JPL Publication 01-18

Proceedings of the Twelfth International Symposium on Space Terahertz Technology

Imran Mehdi, Editor
Jet Propulsion Laboratory, California Institute of Technology
Pasadena, California

February 14–16, 2001
Humphrey's Half Moon Inn, Shelter Island
San Diego, California

D-21490

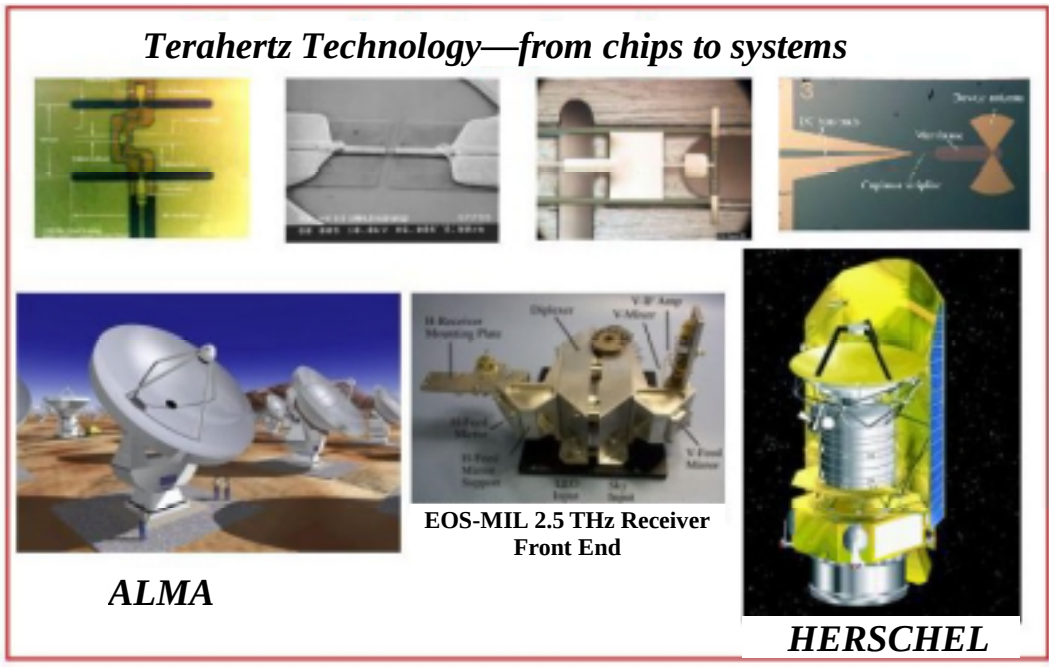

National Aeronautics and Space Administration

Jet Propulsion Laboratory
California Institute of Technology
Pasadena, California

December 2001

PREFACE

On behalf of the Steering committee I wish to thank all of the authors and presenters who have done a wonderful job of making this Symposium productive and enjoyable.

Fifty-three abstracts were accepted for oral presentations and a further sixteen submissions were accepted for poster presentations. The breakdown of the accepted abstracts in terms of broad technology areas is as following:

Hot Electron Bolometers	17
SIS technology	12
LO technology	16
Antennas, measurements etc	18
Direct detectors	6

All of the papers that were submitted on time have been included in the proceedings. Only a handful of papers were not submitted and they have been replaced with the accepted abstracts.

I would like to take this opportunity to thank people who have helped in the organization of this symposium. Pat McLane and her crew from JPL's Conference Administration Office have been instrumental in doing all of the hard work. Wei Lien Dang and Eric Lee for their invaluable assistance with the web and compilation of the proceedings. Dr. Peter Siegel, Dr. Rob McGrath, Dr. Boris Karasik , Dr. Tom Crowe and members of the steering committee helped with the review of the submitted abstracts. Financial support from Dr. Tim Krabach (JPL) was also instrumental and is much appreciated. This publication was prepared by the Jet Propulsion Laboratory, California Institute of Technology, under a contract with the National Aeronautics and Space Administration.

Imran Mehdi
(JPL)

12th International Symposium on Space Terahertz Technology Steering committee:

Raymond Blundell, Harvard Smithsonian Center for Astrophysics
Thomas W. Crowe, University of Virginia
Jack East, University of Michigan
Rob McGrath, Jet Propulsion Laboratory
Gabriel Rebeiz, University of Michigan
Robert M. Weikle II, University of Virginia
Jonas Zmuidzinas, Caltech

Please note the dates and location for the 13th Intl. Symposium on Space Terahertz Technology to be held in 2002:

March 26-28th, 2002
At the Harvard Smithsonian Center for Astrophysics

Program Chair: Dr. Raymond Blundell
rblundell@cfa.harvard.edu

12th International Symposium on Space Terahertz Technology

1. SESSION 1: SIS MIXERS

Session Chair: Dr. Karl Jacobs, KOSMA

2. SESSION 2: HOT ELECTRON BOLOMETER MIXERS I

Session Chair: Dr. Boris Karasik, Jet Propulsion Laboratory

4. SESSION 4: MIXERS AND DETECTORS

Session Chair: Dr. Peter Siegel, Jet Propulsion Laboratory

5. SESSION 5: POSTER SESSION

Session Chair: Dr. Tom Crowe, University of Virginia

6. SESSION 6: HOT ELECTRON BOLOMETER MIXERS II

Session Chair: Prof. Dan Prober, Yale

7. SESSION 7: LO SOURCES II

Session Chair: Dr. Antti V. Räisänen, Helsinki University of Technology

8. SESSION 8: SIS MIXERS II

Session Chair: Dr. Anders Skalare, Jet Propulsion Laboratory

10. SESSION 11: DIRECT DETECTORS

Session Chair: Dr. Jamie Bock, Jet Propulsion Laboratory

11. SESSION 12: LO SOURCES III
Session Chair: Dr. Jean Bruston, ESTEC

12. SESSION 12: MISCELLANEOUS
Session Chair: Dr. S-K. Pan, NRAO

13. SESSION 13: RECEIVERS

Session Chair: Dr. John Pearson, Jet Propulsion Laboratory

NbTiN BASED TUNING STRUCTURES FOR BROADBAND Nb-Al_2O_3-Nb SIS MIXERS FROM 640 GHz– 800 GHz

S. Glenz, S. Haas, C.E. Honingh, K. Jacobs

KOSMA, I. Physikalisches Institut, Universität zu Köln
Zülpicher Strasse 77, 50937 Köln, Germany

We present measurements with a prototype waveguide SIS mixer for band 2 (640 GHz – 800 GHz) of HIFI (Heterodyne Instrument for FIRST). The Nb/Al_2O_3/Nb junctions have an R_nA product from 12–18 $\Omega\mu m^2$. These junctions are embedded in microstrip circuits tuning out the device capacitance using a NbTiN ground layer and various top conductor materials such as NbTiN, Nb and Al. The NbTiN films are fabricated by DC magnetron sputtering which is optimized for a minimum value of the DC resistivity and for a high critical temperature by varying the sputter pressure, sputter power and Ar:N_2 flow. Typical NbTiN film parameters for device fabrication are ρ = 120 $\mu\Omega$cm and T_c = 14.5 K. The best uncorrected noise temperatures we measured so far are for devices with NbTiN/SiO_2/Nb tuning. At 4.2 K bath temperature, a standard Y-factor measurement yields uncorrected receiver noise temperatures of 350 K at 642 GHz and 500 K at 810 GHz for 1.5 GHz intermediate frequency. We discuss the effect of the various tuning circuit materials on the mixer performance. In addition, measurements at IF's between 4 GHz and 8 GHz will be presented.

1. INTRODUCTION

Our aim is to develop an SIS mixer for Band 2 of the HIFI instrument for the Herschel Space Observatory (formerly known as FIRST) [1]. The specifications for this instrument require a broadband and low noise receiver channel which covers frequencies from 640 GHz to 800 GHz. State-of-the-art mixers implementing Nb/Al_2O_3/Nb tunnel junctions and integrated Nb tuning circuits can have quantum limited noise performance up to the gap frequency Δ/h of niobium at about 700 GHz. Above this frequency, RF loss in the niobium tuning structure increases rapidly, whereas the SIS tunnel junction itself can be used as a mixer up to $2\Delta/h$.
Unfortunately, the niobium gap frequency splits band 2 of HIFI, so we have to find the most suitable material or a combination of different materials to obtain the most sensitive device for the complete frequency range.
Over the last few years efforts to find a superconducting material with a higher gap than niobium, compatible to the Nb/Al_2O_3/Nb junction technology, led to the use of NbTiN films for tuning circuits [2] as well as for the junction electrodes [3].

There are also recent developments of SIS mixers with aluminum [4] or a combination of aluminum and niobium [5] for the tuning circuits that resulted an improvement in the mixer sensitivity compared to a pure Nb device.
In this paper we present DC and RF measurements of devices with NbTiN for the ground plane of the microstrip tuning circuit, SiO_2 for the dielectric, and either NbTiN, Nb, or Al as top conductor material, with integrated Nb-Al_2O_3-Nb tunnel junctions.

2. NbTiN FILM FABRICATION AND CHARACTERIZATION

The NbTiN layers are fabricated by reactive DC-magnetron sputtering of NbTi in an Argon/Nitrogen atmosphere. The target (NbTi 78:22 wt.%, 3" diameter) is mounted in a AJA model 330 sputter source with an integrated gas inlet ring positioned in close vicinity of the target. A modular magnet ring allows an unbalanced magnetic field constellation to increase plasma heating of the substrate. The distance between sputter source and substrate is about 8 cm which is the maximum for the system. Tests with different heights (7 cm, 5.5 cm) did not improve the film properties. The sputter chamber is evacuated by a Cryotorr 8 pump to a base pressure $< 1 \cdot 10^{-8}$ mbar. The Ar/N_2 pressure is regulated by throttling the gate valve to the cryopump. The substrate is thermally coupled to a copper pallet which is placed on the water cooled substrate station to achieve stable and reproducible thermal conditions at moderate temperatures during film deposition. To determine the film quality, we measured the normal state resistivity and the critical temperature of NbTiN films with a thickness of 350 nm. The normal state resistivity of the film above T_c (20 K) is taken as an indication of low RF loss, as this loss is difficult to determine directly.
The DC properties of the NbTiN films are measured in a dipstick system for measurements in liquid helium at 4.2 K, where the sample temperature is controlled by the dipstick height above the helium level. A temperature diode is integrated at the sample mount in close thermal contact to the sample. The samples are wire bonded. Using a four point probe and lock-in amplifier technique, resistances down to 10 mΩ can be measured accurately. Both characteristic DC parameters, the critical temperature and the DC resistivity of the film depend on the sputter conditions to varying degrees. Figures 1a – 1c show data sets we measured when sampling the parameter space.
Fig. 1a shows a maximum of T_c at an Ar/N_2 ratio of 91 sccm : 8 sccm. In this regime of the flow ratio, the sputter conditions are very stable and reproducible. The critical temperature shows a strong increase when the sputter power becomes higher than 250 W and attains a maximum at 325 W (Fig. 1b) at these flows, as the N_2 consumption needed for the correct stoichiometry is related to the power. The resulting discharge voltage is around 280 V.
NbTiN films with a low DC resistivity show high compressive mechanical stress, which causes a variety of fabrication difficulties leading to be a certain tradeoff between film stress and DC resistivity. The most decisive parameter to control the resistivity of the NbTiN films is the sputter pressure (Fig. 1c). The increase of the resistivity is due to a change of the film structure [6].

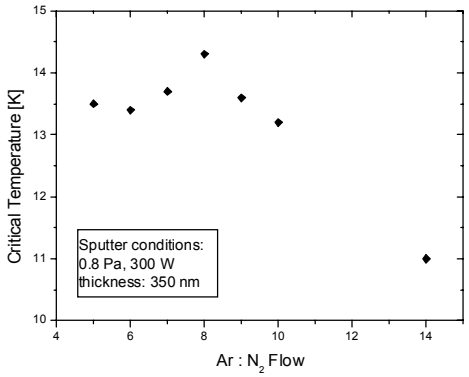

Fig. 1a Tc versus Ar/N_2 flow

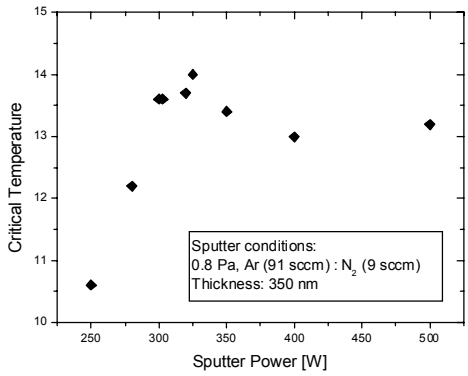

Fig. 1b Tc versus sputter power

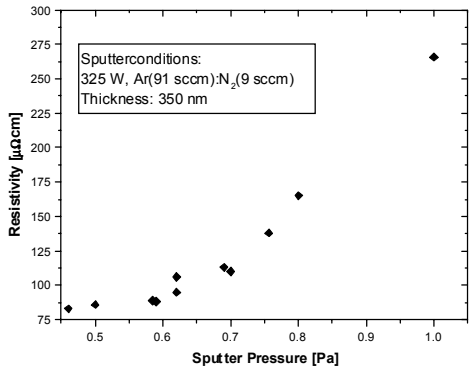

Fig. 1c DC resistivity versus sputter pressure

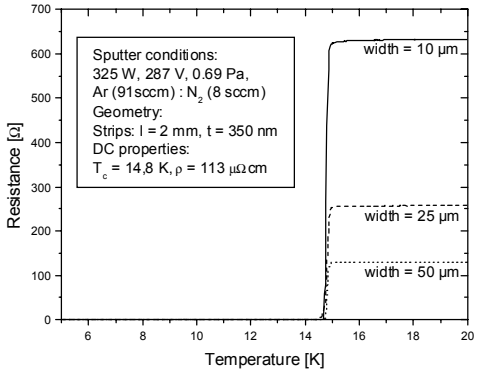

Fig. 2: Typical R-T curves of NbTiN test structures

An example for typical NbTiN films is given in Fig. 2. It shows the R-T curves of three NbTiN strips with different width. The critical temperature is 14.8 K with a sharp transition of $\Delta T_c = 0.3$ K. The DC resistivity $\rho = 113\ \mu\Omega$cm is calculated from the resistance at 20 K and the strip dimensions. These films, sputtered at ~ 0.7 Pa total pressure, exhibit a tolerable stress which still allows a successful integration of tunnel junctions.

3. MIXER DEVICE FABRICATON

In part 5 of this paper we present results. Table 1 gives an overview of three fabrication runs, which are slightly different in fabrication and use several different lithography mask sets. The main differences are the NbTiN quality, the junction barrier oxidation parameters and the deposition method for the SiO_2 dielectric. The results of these fabrication runs will be presented in chapter 5.

An initial stack of four layers is deposited in situ by dc magnetron sputtering on a 250 µm quartz substrate (INFRASIL). It consists a 350 nm NbTiN ground plane followed by the SIS trilayer, composed of a 100 nm Nb bottom layer followed by 8 nm Al for the tunnel

barrier and another 100 nm Nb as top electrode. The oxidation of the barrier is performed in the load-lock of the sputtering machine at a static oxygen pressure of 1.6 Pa for 7 – 8 min, resulting in a current density of j_c = 10–13 kA/cm^2. All four layers are deposited into a bilayer AZ7212 (Clariant) photoresist window with a large undercut profile. This technique [7] permits a clean liftoff process for more than 400 nm layer thickness.
For the junction definition we use standard 300 nm UV lithography with AZ7212. Minimum junction areas of 0.4 – 0.5 µm^2 can be achieved. For smaller junction areas and/or more accurate control of the junction area we will have to change this process to e-beam lithography [8].
A mixture of 6 sccm CCl_2F_2 + 1.2 sccm NF_3 is used for anisotropic reactive ion etching of the 100 nm top Niobium for 1:30 at 0.17 W/cm^2, (-105 V) and 40 µbar [5]. The Al_2O_3-Al barrier is sputter etched with 8 sccm Argon at 10 µbar and 1.1 W/cm^2 (-605 V) for 9 min. To avoid excessive heating of the photoresist and the junction barrier, we etch in 9 intervals of 1 min with 1 min cooling breaks. The Nb bottom electrode is etched again with CCl_2F_2 + NF_3. As a dielectric layer for the RF tuning circuit and for junction insulation we use SiO_2 with a thickness of 230 nm, deposited either by e-beam evaporation or RF sputtering and defined in the usual self-aligned liftoff procedure. The 350 nm thick top wiring layer is DC-magnetron sputtered and defined by a subsequent liftoff. We produced and studied devices with either NbTiN, Al, or Nb top wiring layers, with some wafers having two different wiring material layers which were sputtered sequentially with the other part of the wafer covered by photoresist. The devices with aluminum top wiring are covered with 70 nm Niobium to eliminate the DC series resistance and are passivated with 300 nm SiO_2 to protect the aluminum from chemical attack.

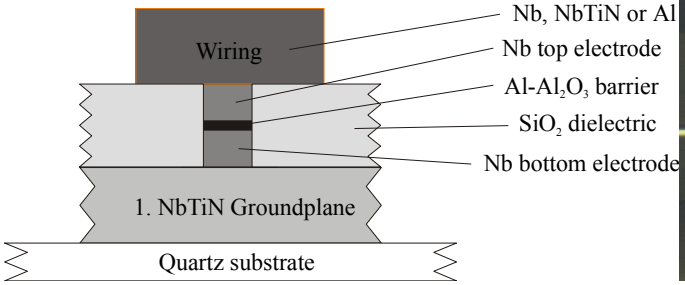

Fig. 3 Sketch of the layer sequence of junction and tuning structure

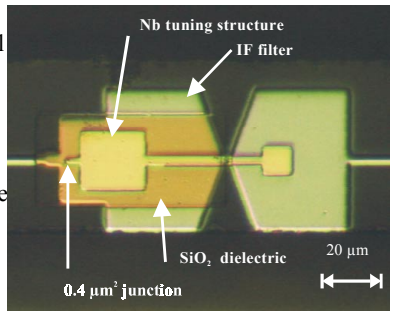

Fig. 4 Microscope photo of a finished device

The fabricated devices have areas of 0.4 µm^2 and 0.6 µm^2. Fig. 4 shows a top view of a finished device after dicing and thinning. The tuning circuit is an end loaded stub followed by two Tchebychev transformer sections. All tested devices are designed for HIFI Band 2 (640-800 GHz). The design is optimized for band flatness with an calculated coupling of 60-70 % over the whole band. For the top wiring we used NbTiN, Nb or Al. Niobium has the advantage to be lossless up to the gap Δ/h = 700 GHz, but above the loss rises rapidly which complicates the flat band design. Aluminum is a normal conductor at 4.2 K with only a small variation in conductivity over the band. This helps achieving a broad bandwidth but has a penalty in noise performance especially at the low end of

band. Having both wiring electrodes made of NbTiN leads to DC and RF heating effects [9].

Table 1: Differences in fabrication between the batches A. B and C

Batch #	Ground layer	Ground plane ρ / T_c	Oxidation time / pressure	Dielectric SiO_2 deposition
A	350 nm NbTiN	134 μΩcm 14.3 K	8:00 1.6 Pa	Evaporated 400 W
B	280 nm NbTiN	125 μΩcm 14.4 K	8:10 1.56 Pa	RF sputtered 1 Pa, 300 W
C	350 nm NbTiN	100 μΩcm 15.1 K	7:00 1.6 Pa	RF sputtered 1 Pa, 300 W

4. DC MEASUREMENTS

After the fabrication the current-voltage characteristics of the devices were DC tested in a dipstick system at 4.2 K which allows the determination of the R_NA product. The voltage of the self induced step resonance of the integrated tuning circuit gives a first indication about the RF performance of the device.

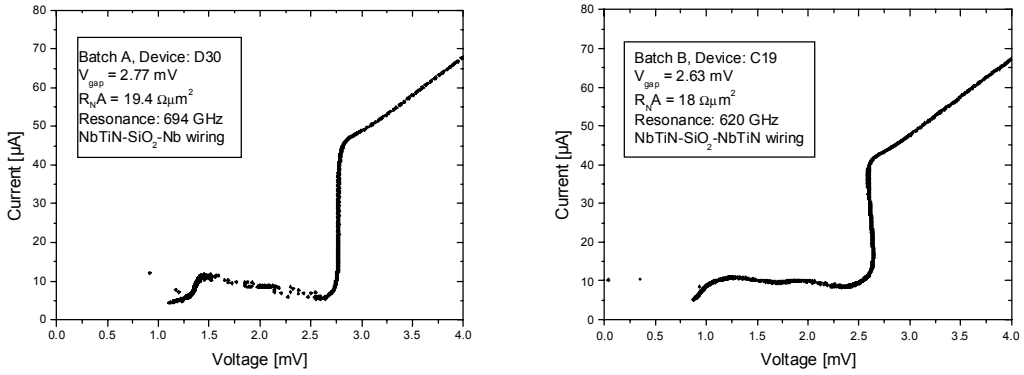

Fig. 5: IV characteristic of a $Nb/Al_2O_3/Nb$ junction with:
5a: $NbTiN/SiO_2/Nb$ tuning 5b: $NbTiN/SiO_2/NbTiN$ tuning

The IV-curves in Fig. 5a and b are measured with a dipstick at 4.2 K. Fig. 5a shows a typical IV-curve for a SIS mixer with a hybrid $NbTiN/SiO_2/Nb$ tuning circuit is shown. The gap voltage is 2.77 mV. The $R_{sg}(2mV)/R_N$ ratio is determined from the I/V-curves with magnetic field in Fig. 6 (R_{sg}/R_N = 7.4 for device A D30). A resonant mode of the integrated tuning circuit shows up as a current peak at 1.43 mV, corresponding to a Josephson oscillation frequency of 694 GHz. The device in Fig. 5b employs a $NbTiN/SiO_2/NbTiN$ tuning circuit and shows backbending at the gap as well as an obvious gap voltage depression (V_{gap} = 2.65 mV). Both effects can be explained by heat trapping in the junction [9].

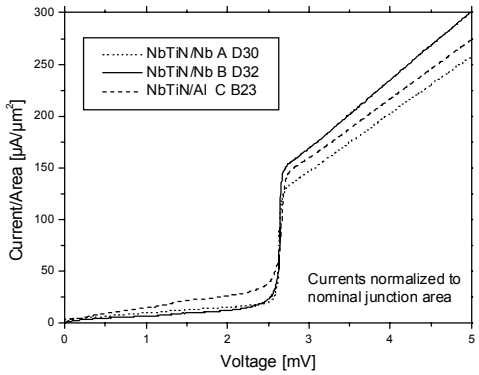

Fig. 6 Comparison between the unpumped IV curves
scaled to the nominal junction areas of different batches

The currents shown in Fig. 6 are normalized to the nominal junction mask size. The self induced resonances are suppressed by a magnetic field. Differences in the current rise at the gap and the subgap current give an indication about the junction quality. The variation in the gap current rise of the devices is mainly due to size variations, which can be as high as 20-30% for device areas of 0.5 μm^2 fabricated by UV lithography. The devices from the batches A and B are of similar quality and their R_{sg}/R_N ratio is 7.4 (Device D30) and 10.9 (Device D32), respectively. The leakage rate of batch C with R_{sg}/R_N = 4.33 (Device B23) is noticeably higher than for the batches A and B and leads to a higher noise temperature of the device. A calculation using the quantum mixer theory [10] shows that the increase in noise temperature can be expected to be between 150-200 K. Table 2 gives an overview of the DC properties of the devices. RF measurements are presented in the next section.

Table 2: DC characteristics of devices from 3 batches

Batch/device	Top wiring Material	Nominal junction area:	R_N	R_{sg}/R_N
A / E17	Nb	0.36 μm^2	49 Ω	8.5
A / D30	Nb	0.36 μm^2	54 Ω	7.4
B / D32	Nb	0.36 μm^2	44 Ω	10.9
B / C19	NbTiN	0.36 μm^2	59 Ω	8.5*
C / B23	Al	0.64 μm^2	29 Ω	4.33
C / B17	Al	0.64 μm^2	22 Ω	4.2
C / D27	Nb	0.64 μm^2	29 Ω	4.3

* The subgap current of device B C19 is noticeably higher than for other devices from this batch with Nb top wiring. This is supposed to be due to the higher temperature of the tunnel junction embedded in the NbTiN wiring which enhances the subgap current and reduces the R_{sg}/R_N ratio.

5. RF MEASUREMENTS

The receiver setup is described in detail in [11]. To verify the response of the junction over the band we use a Fourier Transform Spectrometer to measure the direct detection of the device. The optical path of the FTS beam is evacuated.
The solid state local oscillators have frequency ranges from 630-690 GHz and 780-820 GHz. The LO power and the hot (295 K) / cold (77 K) signal are injected via a 36 µm Mylar beamsplitter, a 500 µm teflon dewar window at 295 K and a 300 µm teflon IR filter at 77 K to the antenna horn of the fixed tuned waveguide (330x90 μm^2) mixer. Using the standard Y-factor method we calculate the uncorrected noise temperature of the receiver.
The IF output signal is connected to a HEMT amplifier on the 4 K stage and further amplified with an IF chain at 295 K by about 70 dB. In our standard setup we use a 1-2 GHz HEMT amplifier [12] and a bandpass filter restricting the IF bandwidth to 100 MHz at 1.4 GHz center frequency. No isolator or matching circuit is used. A second HEMT amplifier [13] is used for IF measurements from 4-8 GHz. The 4-8 IF mixer output signal is coupled to the HEMT amplifier with a 4-8 GHz Pamtech isolator between mixer and amplifier. Both amplifiers have comparable noise temperatures (T_{IF} = 4-8 K).
Fig. 7 shows the trend of the measured receiver noise temperatures as a function of local oscillator frequency for devices from all three batches and with NbTiN, Nb or Al as top wiring layer. All devices are measured at 4.2 K bath temperature with the 1-2 GHz HEMT amplifier. For all measurements (except for the device A E17) a corrugated feedhorn with its center frequency at 675 GHz is used For device A E17 we used a Potter-horn optimized for 800 GHz.

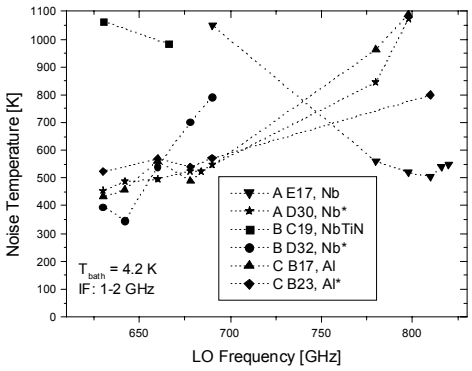

Fig. 7: Overview: Noise Temperatures of devices with different top wiring layers

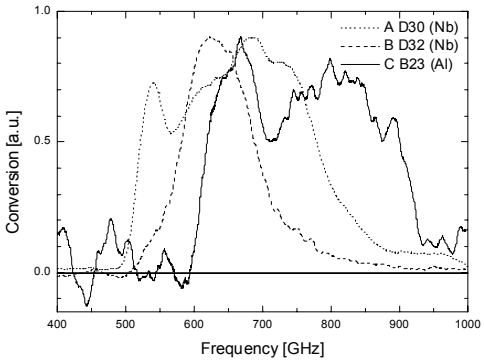

Fig. 8: FTS traces of three devices

The best uncorrected noise temperatures are 350 K at 642 GHz for device B D32 and 500 K at 800 GHz for device A E17. Both devices have a Nb top wiring layer. The noise temperature of the one device with a NbTiN top layer is about a factor of 2 higher than of the devices with Al and Nb. There are devices with Nb (A D30) as well as with Al (C B23) top wiring layer that show broadband response from 640-800 GHz.

This corresponds to the FTS measurements shown in Fig. 8. Both curves are normalized to their peak values. The FTS traces of the devices A D30 with Nb top wiring and C B23 with Al top wiring show a broadband coupling of at least 160 GHz in width but it is obviously difficult to position the band center at exactly 720 GHz. The shift of the band is mainly due to variations in the junction area but also due to resistivity variations of the NbTiN ground layer. The bandwidth of device B D32 is noticeably smaller. We attribute this to the insufficient thickness of the NbTiN ground plane, which is close to or less than one penetration depth.

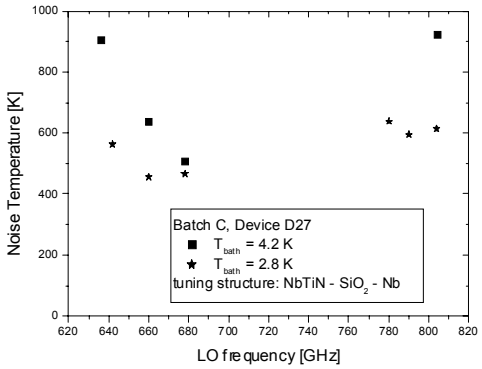

Fig. 9 Results at 2.8 K bath temperature

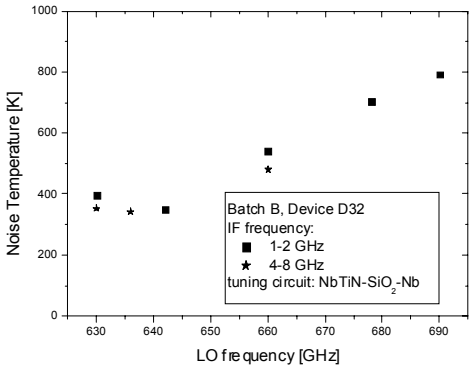

Fig. 10 Results with different IF frequencies

The effect of decreasing the bath temperature from 4.2 K to 2.8. K is shown in Fig. 9 for a device with Nb top wiring layer. The significant improvement in the noise temperature on the upper band side is due to an increase of the Nb gap. The unexpected decrease of the noise temperature at the lower band end can be explained by the strong variation of the phase velocity in the microstrip caused by temperature dependence of the Nb top electrode material. In the present design, this seems results in a shift of the lower band edge to lower frequencies.

The IF band for the HIFI instrument is specified to be 4-8 GHz. Fig. 10 shows a comparison of the noise temperatures of device C D27 measured with both the 1-2 GHz HEMT amplifier and the 4-8 GHz HEMT amplifier. The resulting receiver noise temperatures for both devices are comparable at 4.2 K. The noise temperature with the 4-8 GHz amplifier is measured including the full 4 GHz IF bandwidth while a 100 MHz bandpass filter with 1.4 GHz center frequency was used for the 1-2 GHz IF data.

6. SUMMARY

We developed a deposition process for NbTiN films by using DC reactive magnetron sputtering. The films are optimized for a low DC resistivity and a high critical temperature and high reproducibility. We have shown that films with a resistivity of ρ = 100-140 $\mu\Omega$cm and a critical temperature T_c = 14-15 K can be successfully integrated in a junction fabrication process.

We fabricated and tested Nb-Al_2O_3-Nb tunnel junctions embedded in wiring structures with a NbTiN ground plane, a SiO_2 dielectric and NbTiN, Al, or Nb for the top wiring layer. The quality of the devices varies from is varying from $R_{sg}/R_N = 4.5$ to $R_{sg}/R_N = 9$. The devices are fabricated for the HIFI instrument which requires a fractional bandwidth of 22 %. The FTS results show that we are able to achieve the bandwidth but it is difficult to position the band center, mostly due to the large junction area variation due to the optical lithography of 0.36 μm^2 to 0.64 μm^2 devices. This can be improved by using electron beam lithography.

Based on the heterodyne noise measurements and FTS results there is no clear preference of a tuning circuit top electrode material yet. This decision is complicated by the fact that the DC IV-curves of batch C, which is the first batch with Al devices, have a higher leakage rate which increase the measured noise temperatures.

ACKNOWLEDGMENT

We thank Michael Schultz for dicing, thinning and mounting of the devices, Rafael Teipen and Matthias Justen for most of the RF measurements. This work was supported by DLR (Deutsches Zentrum für Luft- und Raumfahrt), Förderkennzeichen 50 OF 0001 2 and 50 OF 9902 4, by ESA (European Space Agency), CCN5 on ESTEC Contract 11653/95/NL/PB(SC) and also by DFG (Deutsche Forschungsgemeinschaft), Sonderforschungsbereich 494.

REFERENCES

[1] http://saturn.sron.nl/hifi/

[2] J. W. Kooi, J. A. Stern, G. Chattopadhyay, H. G. LeDuc, B. Bumble, J. Zmuidzinas, "Low-loss NbTiN films for THz SIS mixer tuning circuits", Proc. of 8th Int. Symp. on Space Terahertz Techn. 1997, pp. 310-319

[3] B. Bumble, H. G. LeDuc, J. A. Stern, "Fabrication of Nb/Al-N_x/NbTiN junctions for SIS mixer applications above 1 THz", Proc. of 9th Int. Symp. on Space Terahertz Techn. 1998, pp. 295-304

[4] M. Bin, M. C. Gaidis, J. Zmuidzinas, T. G. Phillips, H. G. LeDuc, "Low noise 1 THz niobium superconducting tunnel junction mixer with normal metal tuning circuit", Appl. Phys. Lett., vol. 68, pp. 1714-1716, 1996

[5] S. Haas, S. Wulff, D. Hottgenroth, C.E. Honingh, K. Jacobs, " Broadband Array SIS Mixers for 780-880 GHz with Aluminium tuning circuit", Proc. of 11. Int. Symp. on Space Terahertz Technol. 2000, pp. 95-104

[6] N. N. Iosad, A. V. Mijrishii, V. V. Roddatis, N. M. van der Pers, B. D. Jackson, J. R. Gao, S. N. Polyakov, P. N. Dimitriev, T. M. Klapwijk, "Properties of (Nb, Ti)N thin films deposited on silicon wafers at ambient substrate temperatures", J. of Appl. Phys. vol. 88, issue 10, pp. 5756-5759, 2000

[7] G. J. Dolan, "Offset masks for lift-off photoprocessing", Appl. Phys. Lett. vol. 31 no. 5, pp.337-339, 1977

[8] P. Puetz, K. Jacobs, "E-Beam SIS junction fabrication using CMP and E-Beam defined wiring layer", Proc. of the Tenth Int. Symp. on Space Terahertz Techn. 1999, pp. 118-129

[9] B. Leone, B. D. Jackson, J. R. Gao, T. M. Klapwijk, "Geometric heat trapping in niobium superconductor-insulator-superconductor mixers due to niobium titanium nitride leads", Appl. Phys. Lett. 76, 780-782, 2000

[10] J. R. Tucker, M. J. Feldmann, "Quantum detection at millimeter wavelength", Rev. Mod. Phys., vol. 57, no. 4, 1885

[11] S. Haas, C. E. Honingh, D. Hottgenroth, K. Jacobs, J. Stutzki, "Low noise tunerless waveguide SIS receivers for 440-500 GHz and 630-690 GHz", Int. J. Infrared Millimeter Waves, 17, 1996, pp. 493-506

[12] B. Vowinkel, Ph. Müller, "Cryogenic L-band HEMT-amplifier with a noise figure of less than 0.1 dB", Proc. 5th Microwave and Optronics Conf., Stuttgart, 1990

[13]Yebes: http://www.oan.es/cay/index.shtml.en

Waveguide and Quasi-optical 1 THz SIS Mixers Incorporating NbTiN/SiO_2/Al Tuning Circuits

B.D. Jackson, A.M. Baryshev, G. de Lange, and J.-R. Gao
Space Research Organization of the Netherlands
Postbus 800, 9700 AV Groningen, The Netherlands

N.N. Iosad and T.M. Klapwijk
Department of Applied Physics (DIMES), Delft University of Technology
Lorentzweg 1, 2628 CJ Delft, The Netherlands

S.V. Shitov
Institute of Radio Engineering and Electronics, Russian Academy of Science
Mokhovaya St. 11, Moscow, 103907, Russia

ABSTRACT

The performance of 1 THz waveguide and quasi-optical mixers incorporating NbTiN/SiO_2/Al tuning circuits are evaluated. Both geometries yield low mixer noise temperatures up to 1 THz, with reduced sensitivities at higher frequencies. The drop in sensitivities above 1 THz is attributed to the non-ideal structure of NbTiN films grown at room-temperature, which results in significant losses in the NbTiN ground plane above 1 THz. The design and performance of the quasi-optical lens-antenna is also discussed.

1. INTRODUCTION

The Heterodyne Instrument for the Far-Infrared (HIFI) requires THz mixers with noise temperatures ($T_{N,mix}$) < 3·hν/k (i.e. < 140 K at 960 GHz). Past work has shown that Nb-based superconductor-insulator-superconductor (SIS) mixers yield quantum-limited performance below 680 GHz [1,2]. Above 700 GHz, rf losses in Nb increase [3,4], such that Al wiring is preferred to Nb above 800 GHz [5,6]. Unfortunately, the optimum sensitivity of these mixers is limited to 200-250 K at 1 THz (derived from [6] and [7]). Further improvements in THz mixer sensitivities will require reduced tuning circuit losses (5-9 dB in [6,7]). Although this may be achieved in part by the use of high current-density (high-J_c) SIS junctions [8], truly quantum-limited 1 THz mixers will require low-loss superconducting wiring layers with F_{gap} ~ 1.1 THz, or more.

The recent demonstrations of NbTiN-based SIS receivers with noise temperatures of 205 K at 798 GHz [9] and 315 K at 980 GHz [10] confirm that the use of NbTiN-based tuning circuits can yield low-noise mixers up to 1 THz. However, it remains to be shown that similar performance is attainable above 1 THz – based on $T_{c,\,NbTiN}$ = 14.5-15.5 K, and the measured relationship between F_{gap} and T_c in NbN (F_{gap} = 3.52-4.16·k_BT_c/h [11,12]),

it is predicted that NbTiN is low-loss up to 1.05-1.35 THz.

In this paper, the performance of THz waveguide and quasi-optical mixers incorporating Nb/Al-AlO_x/Nb SIS junctions and NbTiN/SiO_2/Al tuning circuits are compared and analyzed in relation to the measured low-frequency electrical properties of the NbTiN films used as a ground plane. Additionally, the antenna beam-pattern of the quasi-optical lens-antenna system is discussed.

Note that all receiver and mixer sensitivities presented here are calculated using the Callen-Welton formulation [13] for the effective temperatures of the signal loads and optical elements. Also, $T_{N,mix}$, is defined as the DSB input noise of the mixer unit, from the input of the beam-forming element (waveguide horn or quasi-optical lens) to the IF connector. It is calculated from the receiver noise by subtracting the contributions of the IF chain and receiver optics.

2. MIXER DESIGN AND FABRICATION

Waveguide mixers are produced by integrating 7.5 kA/cm^2, 1-μm^2 Nb SIS junctions with a 300-nm NbTiN ground plane, a 250-nm SiO_2 dielectric layer, and a 400-nm Al wiring layer (see Fig. 1). The NbTiN ground plane has $T_c \approx 14.4$ K and $\sigma_{16K} \approx 0.9\times10^6\ \Omega^{-1}m^{-1}$ [14], while the sputtered Al has $\sigma_{4K} \approx 2\times10^8\ \Omega^{-1}m^{-1}$, and is expected to be in the anomalous limit [15]. 100 nm of Nb is added to the Al wiring for chemical passivation, and to reduce the series resistance of the rf-choke filter. For RF measurements, the devices are mounted in a full-height 1 THz mixer block with a diagonal horn. The waveguide mixer and its fabrication process are described in more detail in [16,17].

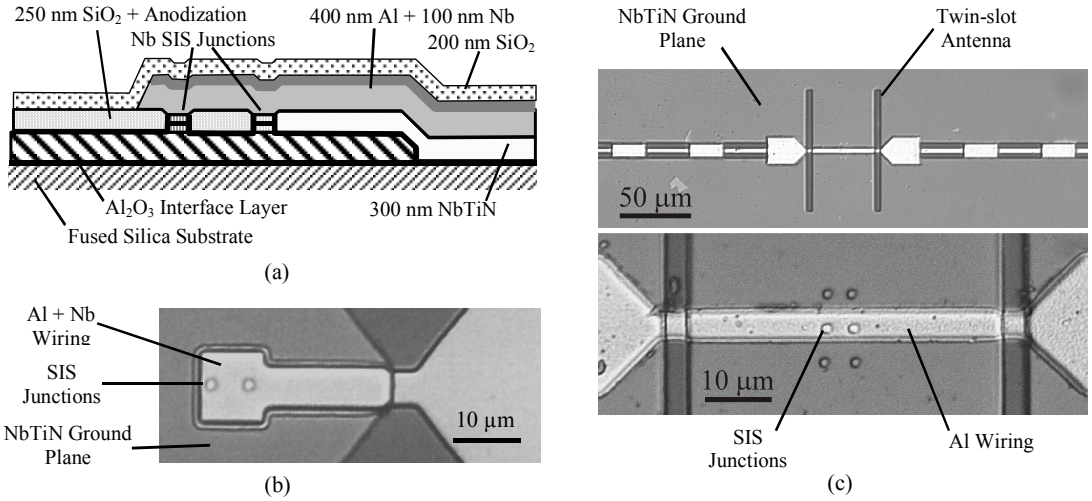

Figure 1. (a) cross-section of the NbTiN/SiO_2/Al tuning circuit (modified from [16]), (b) microscope image of the waveguide device geometry used here (modified from [16]), and (c) microscope images of the quasi-optical device geometry used here (modified from [10]).

Quasi-optical mixers are produced by integrating twin-slot antennas with a double-junction tuning circuit, using the same junction and layer geometry as in the waveguide mixer (note that the 100-nm Nb layer is not present on the wiring of the quasi-optical mixer). For RF measurements, the quasi-optical devices are mounted on a 10-mm elliptical Si lens. The quasi-optical mixer design is described in more detail in [10,18].

3. RF MEASUREMENT SETUP

The quasi-optical and waveguide receivers are described in [10] and [16], respectively. The waveguide receiver includes a 100-μm Mylar window at 295 K, a Zitex G104 heat-filter at 77 K, and a high-density polyethylene lens at 4 K, while the quasi-optical receiver includes a 12-μm Kapton window at 295 K, and Zitex heat-filters at 77- and 4-K. The direct-detection response of each mixer is measured in an evacuated Michelson interferometer, while heterodyne sensitivity is determined from Y-factor measurements with 295- and 77-K loads, BWO local oscillators (LOs) operating between 830 nd 1100 GHz, and Mylar beamsplitters of 6-, 14-, and 49-μm thickness. The IF output from the mixer is cryo-amplied before being further amplified and bandpass filtered at room temperature. Using the unpumped mixers as noise sources, the noise and gain of the IF chain are determined to be 4-5 K and 68 dB in an 85 MHz band at 1.46 GHz.

4. DIRECT-DETECTION MEASUREMENT RESULTS AND THE NBTIN CUT-OFF

The fixed-tuned direct-detection responses of four waveguide mixers and two quasi-optical mixers are shown in Fig. 2 (all at 4.6 K). Both geometries yield high sensitivities below 1 THz. However, all 4 waveguide devices, plus one of the two quasi-optical mixers, have high-frequency cut-offs at ~ 1 THz, despite having significantly different low-frequency roll-offs. This common cut-off is attributed to losses in the NbTiN ground plane at 1 THz and above.

Also shown in Fig. 2b are calculations of the predicted direct detection responses of each quasi-optical device for two possible NbTiN gap frequencies – 1080 and 970 GHz. In these calculations, the NbTiN surface impedance is calculated using the frequency-dependent resistivity of a superconductor in the anomalous limit [3]. Further details of these calculations can be found in [10]. Comparing the measured and predicted device responses, it is seen that the response of device 166 can be relatively well predicted using NbTiN gap frequencies of either 970 or 1080 GHz, but that the high-frequency response of device 162 can only be modeled using a low NbTiN gap frequency (F_{gap}) of 970 GHz.

The apparent NbTiN F_{gap} at 970 GHz is significantly lower than is expected for NbTiN with T_c = 14.4 K (1.05-1.25 THz is expected). However, recent work has shown that there are significant non-homogeneities in the properties of NbTiN films deposited at room temperature [19]. In particular, the T_c and resistivity of these films are strongly thickness-dependent (up to ~ 300-nm), and inductive measurements of T_c yield significantly larger transition widths (ΔT_c) than is observed in resistive measurements (signs of vertical and

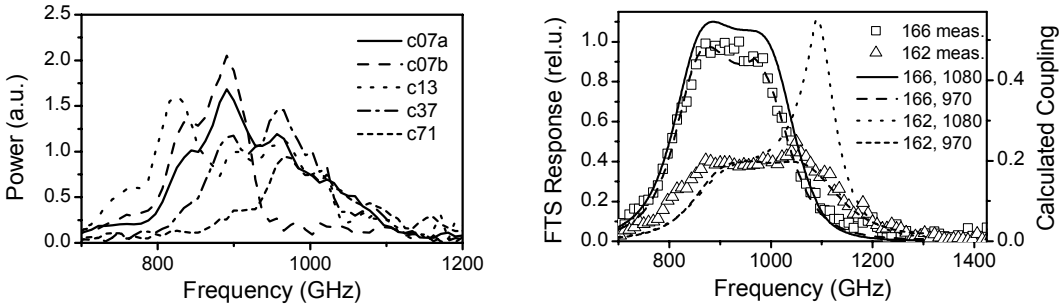

(a) (b)

Figure 2 - (a) Measured direct-detection responses of four waveguide mixers at 4.6 K (modified from [16]). The devices have different junction sizes and separations, and different transformer lengths. (b) Measured direct-detection responses of two quasi-optical mixers at 4.6 K (modified from [10]). The two devices have different junction areas, but are otherwise identical. Also seen are calculated device sensitivities for NbTiN gap frequencies of 970 and 1080 GHz. The predicted response of device 162 matches the measured curve for $F_{gap,\ NbTiN}$ = 970 GHz.

lateral non-homogeneities, respectively). Thus, it is believed that the observed 970 GHz tuning circuit cut-off is due to rf losses in the NbTiN ground plane in a relatively small number of grains with particularly low values of T_c. Fortunately, this argument also implies that it should be possible to increase the cut-off frequency by using higher-quality NbTiN layers (with higher T_c and improved homogeneity), such as those deposited on MgO substrates or at elevated temperatures [19,20].

5. HETERODYNE MEASUREMENT RESULTS

The receiver noise temperatures of four waveguide and two quasi-optical mixers are shown in Fig. 3 for measurements at 4.6 and 2.8 K. In general, the measured heterodyne sensitivities and RF band-widths of these devices agree reasonably well with the direct-detection response curves seen in Fig. 2.

Using the waveguide mixers at 4.6 K, a minimum $T_{N,rec}$ of 425 K is obtained with device c07 at 895 GHz (with a 6 μm beamsplitter), while optimum sensitivity near 1 THz is obtained at 2.8 K with c37 and a 14 μm beamsplitter ($T_{N,rec}$ = 565 K and G_{rec} = -12.9 dB at 970 GHz). The 20 % improvement in the response of waveguide mixer c13 upon cooling from 4.6 to 2.8 K is typical for these mixer geometries (both waveguide and quasi-optical). Also, the sharp dip in the sensitivities of waveguide mixers c13 and c37 at 980-990 GHz is due to water vapour absorption.

Quasi-optical mixer 166 yields significantly higher receiver sensitivities than the waveguide mixers, with an optimum $T_{N,rec}$ of 253 K obtained at 850 GHz and 2.8 K. The noise of this receiver rises slowly approaching 1 THz (315 K at 980 GHz), with a sharp rise in $T_{N,rec}$ at 1 THz (to 405 K at 1015 GHz). Mixer 162 is significantly less sensitive

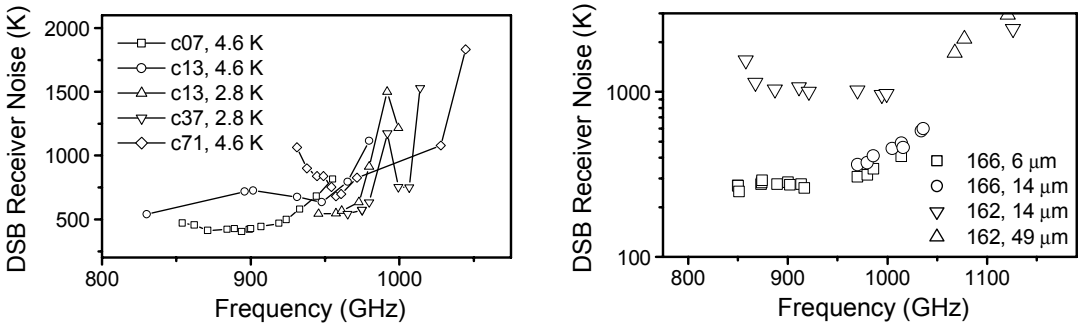

(a) (b)

Figure 3 - (a) Measured $T_{N,rec}$ for 4 waveguide devices measured at 4.6 K (c07, c13, and c71) and 2.8 K (c13 and c37). c13, c37, and c71 are measured with a 14-μm beamsplitter, while c07 is measured with a 6-μm beamsplitter (modified from [16]). (b) $T_{N,rec}$ of 2 quasi-optical mixers measured at 2.8 K with 6-, 14-, and 49-μm beamsplitters (modified from [10]).

than device 166, but it does demonstrate reasonable performance up to much higher frequencies ($T_{N,rec}$ ~ 2200 K at 1120 GHz).

6. RECEIVER SENSITIVITY ANALYSIS

Focusing on the devices with the highest THz sensitivities (waveguide device c37 at 970 GHz and quasi-optical device 166 at 980 GHz, both at 2.8 K), the measured receiver sensitivities are analyzed to estimate the rf loss in the NbTiN ground plane, and to compare the sensitivities of the two mixer geometries. The details of these calculations are contained in [10] and [16], with the results summarized here in Table I.

From this analysis, it is seen that the loss in the NbTiN ground plane is relatively low up to 970 GHz (< 0.6 dB), in both mixer geometries. Additionally, the significantly higher receiver sensitivity obtained with the quasi-optical mixer is found to be

Table I

Receiver noise breakdown and corrected mixer unit sensitivities of waveguide device c37 [16] and quasi-optical mixer 166 [10]

Device	$T_{N,rec}$ G_{rec}	$T_{N,opt}$ G_{opt}	G_{Tucker}	G_{tuning}	G_{Al}	G_{NbTiN}	$T_{N,mix}$ G_{mix}
WG c37 (970 GHz, 2.8 K)	563 - 12.9	146 - 2.5	- 7.2	- 3.2	- 2.5-3	- 0.2-0.7	182 - 10.4
QO 166 (980 GHz, 2.8 K)	315 - 11.1	35 - 1.2	- 7.2	- 2.7	- 2.3	- 0-0.4	171 - 9.9

All gains are in dB, while noise temperatures are Callen-Welton values, and are given in K.
G_{Tucker} is the DSB conversion gain of the SIS junctions, and $-G_{tuning}$ is the estimated tuning circuit loss, which is divided into $-G_{Al}$, the loss in the Al, and $-G_{NbTiN}$, the loss in the NbTiN.
$T_{N,mix}$ and G_{mix} are the effective input noise temperatures and DSB gains of the mixer units.

attributable to the lower optical losses in the quasi-optical receiver – the effective sensitivities of the two mixer geometries are similar ($T_{N,mix}$ = 170-180 K). Furthermore, although additional work is needed to further improve mixer sensitivities (especially above 1 THz), it is noted that these values of $T_{N,mix}$ are already within ~ 30 % of the HIFI goal at these frequencies.

Although the peak sensitivities of the two mixer geometries are similar, it is important to note that the quasi-optical mixers have significantly larger RF band-widths than the waveguide mixers. In particular, quasi-optical mixer 166 yields high sensitivity over most of HIFI mixer band 3 (800-960 GHz), while the waveguide mixers typically have 3-dB band-widths of 100-150 GHz, which is much too narrow for use in HIFI. The narrow band-widths obtained with the waveguide mixers is the result of them having a less-mature RF design relative to that of the quasi-optical mixer (the combined design of the waveguide, waveguide probe, RF choke filters and NbTiN/SiO_2/Al tuning circuit has not been optimized yet). An optimized design, incorporating a reduced-height waveguide [21] should yield much larger RF band-widths than those observed here.

7. QUASI-OPTICAL MIXER BEAM-PATTERN MEASUREMENT SET-UP

The far-field antenna beam-pattern of the quasi-optical mixers is measured in direct-detection using a 2-D rotational setup [18]. In this measurement, a chopped local oscillator is used to pump the mixer while the mixer is rotated around its waist. The junction is biased at ~ 2.4 mV (just below its gap) and the detected signal (current) is measured with a lock-in amplifier. The signal-to-noise ratio at the peak of the co-polar beam pattern is at least 30-dB in this setup (limited by the dynamic range of the lock-in).

Co- and cross-polar beam patterns are obtained using two polarizing grids located near the output of the local oscillator. (Two grids are used to ensure that the incident power is equal in the co- and cross-polar measurements.)

Note that the LO is placed 50-100 cm from the mixer to ensure that the LO beam at the input to the mixer is large relative to offsets in the mixer's beam waist that may occur if the center-of-rotation is slightly misaligned relative to the beam waist location. The spreading of the LO beam also ensures that the power incident on the mixer is low enough to maintain the linearity of the photon-assisted tunneling response of the device.

Differences between the direct-detection and heterodyne beam-patterns of this mixer have not been quantified at this time.

8. MEASURED AND CALCULATED ANTENNA BEAM-PATTERNS

2-dimensional co- and cross-polar beam patterns of the quasi-optical mixer (at 940 GHz) are presented in Fig. 4a and 4b, while 1-dimensional E- and H-plane cuts of the co-polar pattern (at 920 GHz) are presented in Fig. 4c and 4d. Fig. 4c and 4d also include theoretical antenna beam patterns calculated using [22] for two cases: (1) the antenna is

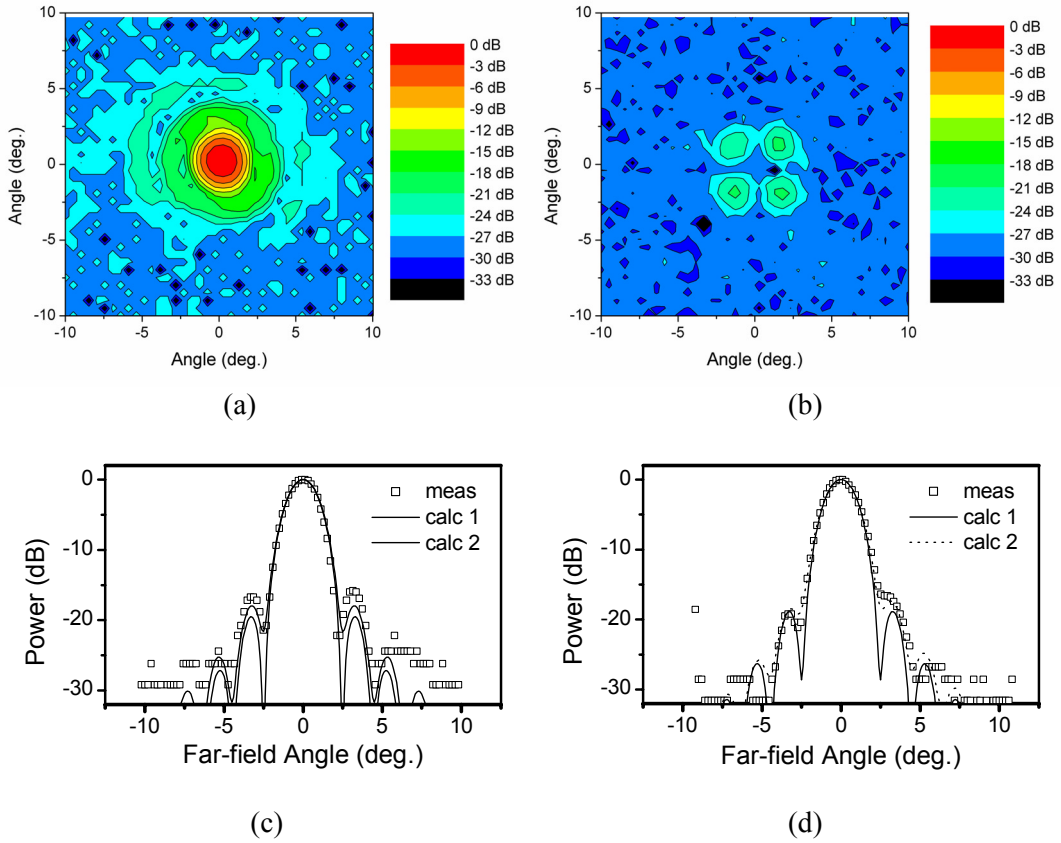

Figure 4 – Antenna beam patterns of a 950 GHz twin-slot antenna mounted on a 10-mm elliptical Si lens. (a) measured 2-D co-polar pattern at 940 GHz, (b) measured cross-polar pattern at 940 GHz, (c) overlay of measured and calculated [22] E-plane cuts of the co-polar pattern in at 920 GHz, and (d) measured and calculated [22] H-plane cuts of the co-polar pattern at 920 GHz..

perfectly aligned to the back focus of the lens; and (2) the antenna is offset 20 μm along the length of the antenna slots and 40 μm behind the back focus of the lens.

Examining the 1-dimensional beam patterns in Fig. 4c and 4d, it is seen that the measured beam-widths are relatively well predicted by theory, with a slight improvement in the agreement if the antenna is assumed to be offset from the focus of the lens. Similar comparisons have been performed at 815, 860, and 1025 GHz, yielding similar agreement between measurement and theory, as summarized in Table II. These calculations are also found to relatively accurately predict the side-lobe levels in the co-polar beam-patterns – the measured side-lobes are ~ 15-18 dB below the main peak, and the predictions typically agree with the measurements to within 2-3 dB. Note that the asymmetry in the measured H-plane beam-pattern (Fig. 4d) may be due to a slight offset of the antenna with respect to the focus of the lens.

The cross-polar beam pattern measured at 940 GHz (Fig. 4b) is similar to those obtained at 812 and 1020 GHz, with four peaks located symmetrically around the co-

TABLE II

Measured and calculated [22] far-field E- and H-plane –10 dB beam-widths of a 950 GHz twin-slot antenna with a 10-mm Si elliptical lens

Frequency (GHz)	$\theta_{E,meas}$	$\theta_{E,calc\ 1}$	$\theta_{E,calc\ 2}$	$\theta_{H,meas}$	$\theta_{H,calc\ 1}$	$\theta_{H,calc\ 2}$
812	3.95	3.8	3.9	4.12	3.9	4.0
860	3.85	3.6	3.6	3.98	3.6	3.8
920	3.4	3.5	3.5	3.7	3.5	3.6
1025	3.25	3.3	3.3	3.65	3.1	3.4

All beam-widths are the far-field angle in degrees.

polar main beam (~ 22-23 dB below the co-polar peak). This general shape is in good agreement with calculations [22], although the peaks are 2-3 dB higher than expected. Note that the quality of the polarizing grids used is demonstrated by the 27-30 dB suppression of the co-polar main lobe in the cross-polar beam pattern.

9. QUASI-OPTICAL LENS DESIGN FOR HIFI

Quasi-optical mixers typically incorporate either the elliptical lens used in this work, or a hyper-hemispherical lens. Unfortunately, these two lens designs produce antenna beam-patterns with relatively extreme far-field divergence angles – the hyper-hemisphere produces a highly divergent beam ($\theta_{-10\ dB} \sim 25^o$), while the ellipse produces a highly collimated beam ($\theta_{-10\ dB} \approx 110 \cdot \lambda/D \sim 3.5^o$ for a 10-mm lens at 920 GHz). The extreme nature of these beam divergences can complicate the integration of a quasi-optical mixer into a complex optical system. For example, the design of the HIFI focal plane system would be simplified by the use of quasi-optical mixers with a relatively moderate beam divergence angle. This would allow the beam-shaping optics in front of a quasi-optical mixer to be similar to those used for a waveguide mixer with a corrugated horn (the horns in HIFI will produce a beam divergence angle of $\theta_{-10\ dB} \sim 18^o$).

It is possible to reduce the far-field divergence angle of the beam produced by a hyper-hemispherical lens by increasing the lens extension length [23], forming an extended-hemispherical lens. However, this method introduces large phase errors to off-axis rays, yielding an aberrated beam-pattern. For this reason, it would be preferable to modify both the surface shape and the extension length to obtain a design that produces the desired beam divergence angle, while also minimizing optical aberrations. The detailed design of this lens is currently in progress.

10. CONCLUSIONS

Waveguide SIS mixers incorporating Nb tunnel junctions and NbTiN/SiO_2/Al tuning circuits $T_{N,rec}$ = 565 K at 970 GHz. Using improved receiver optics, quasi-optical mixers with a similar tuning circuit yield $T_{N,rec}$ = 315 K at 980 GHz. Analyzing the noise and

gain of these receivers, it is shown that the intrinsic sensitivities of these mixers are similar near 1 THz ($T_{N,mix}$ ~ 170-180 K at 970-980 GHz), and that the loss in the NbTiN ground plane is relatively low (< 0.6 dB) up to 980 GHz. Receiver sensitivities are seen to drop above 1 THz, due to increasing loss in the NbTiN ground plane due to rf absorption in a relatively small concentration of NbTiN grains with T_c's that are significantly lower than that measured for a relatively large 300-nm thick film.

Measured antenna beam-patterns for a quasi-optical mixer with a twin-slot antenna mounted on a 10-mm elliptical Si lens are shown to be in relatively good agreement with theoretical predictions. The ongoing optimization of the quasi-optical lens-antenna for integration into the HIFI optical system is also discussed.

ACKNOWLEDGMENT

The authors would like to thank M. Eggens, L. de Jong, W. Laauwen, D. Nguyen, and C. Pieters for their technical assistance and B. Bumble, W. Jellema, P. de Korte, R. LeDuc, H. van de Stadt, J. Stern, N. Whyborn, and J. Zmuidzinas for helpful discussions. This work was supported by the European Space Agency through ESTEC Contract No. 11653/95.

REFERENCES

[1] J. W. Kooi *et al.*, "230 and 492 GHz low noise SIS waveguide receivers employing tuned Nb/AlO_x/Nb tunnel junctions," *Int. J. IR and MM Waves*, vol. 16, pp. 2049-2068, Dec. 1995.

[2] A. Karpov, J. Blondel, M. Voss, and K. H. Gundlach, "A three photon noise SIS heterodyne receiver at submillimeter wavelength," *IEEE Trans. Appl. Supercon.*, vol. 9, pp. 4456-4459, June 1999.

[3] D. C. Mattis and J. Bardeen, "Theory of the anomalous skin effect in normal and superconducting metals," *Phys. Rev.*, vol. 111, pp. 412-417, July 1958.

[4] G. de Lange *et al.*, "Superconducting resonator circuits at frequencies above the gap frequency," *J. Appl. Phys.*, vol. 77, pp. 1795-1804, Feb. 1995.

[5] H. van de Stadt *et al.*, "A 1 THz Nb SIS heterodyne mixer with normal metal tuning structure," in *Proc. of the 6th Int. Symp. on Space THz Technol.*, CIT, Pasadena, CA, pp. 66-77, March 1995.

[6] M. Bin, M. C. Gaidis, J. Zmuidzinas, T. G. Phillips, and H. G. LeDuc, "Low-noise 1 THz niobium superconducting tunnel junction mixer with a normal metal tuning circuit," *Appl. Phys. Lett.*, vol. 68, pp. 1714-1716, Mar. 1996.

[7] P. Dieleman, T. M. Klapwijk, J. R. Gao, and H. van de Stadt, "Analysis of Nb superconductor-insulator-superconductor tunnel junctions with Al striplines for THz radiation detection," *IEEE Trans. Appl. Supercon.*, vol. 7, pp. 2566-2569, June 1997.

[8] J. Kawamura *et al.*, "Very high-current-density Nb/AlN/Nb tunnel junctions for low-noise submillimeter mixers," *Appl. Phys. Lett.*, vol. 76, pp. 2119-2121, Apr. 2000.

[9] J. Kawamura *et al.*, "Low-noise submillimeter-wave NbTiN superconducting tunnel junction mixers," *Appl. Phys. Lett.*, vol. 75, pp. 4013-4015, Dec. 1999.

[10] B. D. Jackson *et al.*, "Low-noise 1 THz superconductor-insulator-superconductor mixer incorporating a NbTiN/SiO_2/Al tuning circuit," *Appl. Phys. Lett.*, submitted for publication.

[11] N. Yoshikawa, H. Su, K. Fukushima, and M. Sugahara, "Study of electron conduction properties of NbN thin films using NbN/MgO/NbN double junctions," in *Proc. of the 5th Int. Superconductive Elec. Conf.*, Nagoya, Japan, pp. 450-452, September 18-21, 1995.

[12] Z. Wang, A. Kawakami, Y. Uzawa, and B. Komiyama, "Superconducting properties and crystal structures of single-crystal niobium nitride thin films deposited at ambient substrate temperature," *J. Appl. Phys.*, vol. 79, pp. 7837-7842, May 1996.

[13] H. B. Callen and T. A. Welton, "Irreversibility and generalized noise," *Phys. Rev.*, vol. 83, pp. 34-40, July 1951.

[14] N. N. Iosad *et al.*, "Source optimization for magnetron sputter-deposition of NbTiN tuning elements for SIS THz detectors," *Supercon. Sci. Technol.*, vol. 12, pp. 736-740, Nov. 1999.

[15] R. L. Kautz, "Miniaturization of normal-state and superconducting striplines," *J. Res. Natl. Bur. Std.*, vol. 84, pp. 247-259, May-June 1979.

[16] B. D. Jackson *et al.*, "**a;sj**," *IEEE Trans. Appl. Supercon.*, submitted for publication.

[17] B. D. Jackson *et al.*, "DC and terahertz response in Nb SIS mixers with NbTiN striplines," in *Proc. of the 10th Int. Symp. on Space THz Technol.*, U. of Virginia, Charlottesville, VA, pp. 144-156, March 16-18, 1999.

[18] A. M. Baryshev et al., "Quasi-optical terahertz SIS mixers," in *Proc. of the 11th Int. Symp. on Space THz Technol.*, U. of Michigan, Ann Arbor, Michigan, pp. 137-146, May 1-3, 2000.

[19] N. N. Iosad *et al.*, "Superconducting transition metal nitride films for THz SIS mixers," *IEEE Trans. Appl. Supercon.,* submitted for publication.

[20] J. A. Stern, B. Bumble, H. G. LeDuc, J. W. Kooi, and J. Zmuidzinas, "Fabrication and dc-characterization of NbTiN based SIS mixers for use between 600 and 1200 GHz," in *Proc. of the 9th Int. Symp. on Space THz Technol.*, CIT, Pasadena, CA, pp. 305-313, March 17-19, 1998.

[21] R. Blundell *et al.*, "A wideband fixed-tuned SIS receiver for 200-GHz operation," *IEEE Trans. Microwave Theory Tech.*, vol. 43, pp. 933-937, Apr. 1995.

[22] All antenna-beam pattern calculations are performed using the "*Program for Integrated Lens and Reflector Antenna Properties – PILRAP*", written by M.J.M. van der Vorst, using a model described in [24].

[23] D. F. Fillipovic, "*Analysis and design of dielectric-lens antennas and planar multiplier circuits for millimeter-wave applications,*" Ph.D. dissertation, University of Michigan, Ann Arbor, USA, 1995.

[24] M. van der Vorst, "*Integrated lens antennas for submillimetre-wave applications,*" Ph.D. dissertation, Technical University of Eindhoven, Eindhoven, The Netherlands, 1999.

Low noise 1.2 THz SIS receiver

A. Karpov, D. Miller, F. Rice, J. Zmuidzinas
California Institute of Technology, Pasadena, CA 91125, USA

J. A. Stern, B. Bumble, H. G. LeDuc
Jet Propulsion Laboratory, California Institute of Technology, Pasadena, CA 91109, USA

Abstract —We present the development of a low noise SIS mixer for the 1.1-1.25 THz heterodyne receiver of FIRST space radiotelescope. The quasi-optical SIS mixer has two NbTiN/AlN/Nb junctions with critical current density 30 kA/cm^2. The individual junction area is close to 0.65 μm^2. The SIS junctions are coupled to the optical input beam through a planar double slot antenna and a Si hyperhemispherical lens. The minimum DSB receiver noise temperature is 650 K, about 12 hν/k.

I. Introduction

In the last decade, SIS receivers using Nb/AlOx/Nb junctions and superconducting Nb circuits have become the best practical solution for the ground-based radio astronomy at mm and submm wavelengths [1]. The minimum submm SIS receiver noise is only three times above the quantum limit [2]. This type of ultra low noise receiver is needed to cover the upper part of the atmosphere transparency band accessible to ground-based radio astronomy facilities. The upper frequency limit of these SIS receivers is determined by the gap frequency of Nb (f_{gap}=0.65-0.7 THz) due to the loss in the Nb circuit. Another frequency limit at about 1.7 f_{gap} =1.0 THz-1.1 THz is due to the cancellation of the quantum assisted tunneling when approaching $2f_{gap}$.

SIS mixers at frequencies over 1 THz are needed for sensitive receivers for airborne and space observatories. This motivates research on alternative materials for low loss THz circuits as well as new types of SIS junctions having a higher gap frequency.

Recent progress in thin film NbTiN technology [3] has given the possibility to create low loss circuits above 0.6-0.7 THz and to improve the performance of the SIS mixers with Nb/AlOx/Nb junctions up to 1 THz [4, 5]. Another approach, using a low loss normal metal circuit to build a low noise 1.05 THz SIS mixer, has been demonstrated in [6, **7**].

The introduction of the NbTiN/AlN/Nb SIS junctions along with NbTiN circuits allows a substantial improvement of the SIS mixer operation up to 900 GHz, with the minimum noise within a factor of ten of the quantum limit [8]. The gap voltage of the existing NbTiN/Nb/AlN/NbTiN junction is about 3.4 mV, potentially allowing the extension of SIS mixer operation above 1.4 THz.

The goal of our work is to extend the low noise performance of the SIS receivers into the THz band using the NbTiN technology. Our approach to build a low noise 1.1-1.25 THz SIS mixer is to use a NbTiN/AlN/Nb tunnel junction with a high critical current density and a low loss circuit made of normal metal and superconducting thin films in a quasi-optical mixer design.

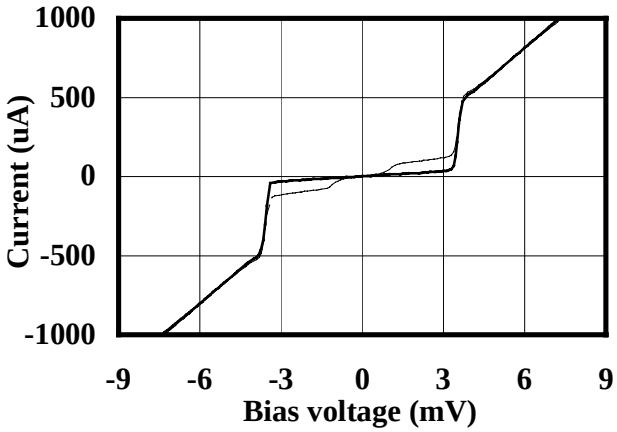

Fig. 1. Current-Voltage characteristic of the NbTiN/AlN/Nb junction with (thinner line) and without radiation at 1130 GHz. Critical Josephson current density is about 30 KA/cm^2.

II. SIS junction

We use NbTiN/AlN/Nb SIS junctions with critical Josephson current densities around 30 KA/cm^2. A current-voltage characteristic (CVC) of a two-junction array with a total area of 1.3 μm^2 is presented in Fig. 1. This junction has a sub-gap to normal state resistance ratio of about Rsg/Rn=12.

A sharp quantum step appears when radiation at 1130 GHz is applied (dotted line). The quantum step width is reduced from hν/e=4.8 mV to hν/e-4Δ/e=2 mV, due to the mutual cancellation of the two quantum steps, at the positive and the negatives branches of CVC. We see only some minor traces of the hot electron effect in this device, appearing like a heating effect in a CVC of a pumped SIS junction.

III. SIS Mixer

We are using a quasi-optical SIS mixer design, similar to one described in [6]. The SIS junction with a double slot planar antenna is mounted at the Silicon hyperhemispherical lens. A polyethylene lens is used to collimate a broad (f/d=2.5) beam coming out of the hyperhemispherical lens into a beam with f/d of about 15 (Fig. 2). The SUPERMIX program [9] was used for the circuit design and optimization. We expect about 1 dB loss in the mixer circuit in the 1.1 THz – 1.25 THz range when using a NbTiN ground plane, Al wiring layer and SiO insulating layer, and around 1.5 dB loss when using a full normal metal circuit.

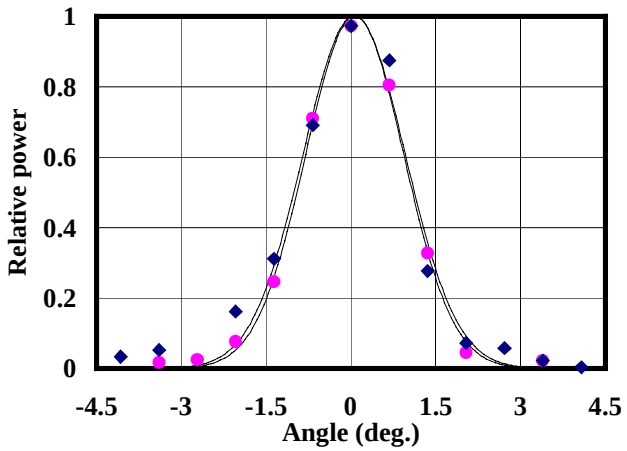

Fig. 2. The measured beam pattern of the SIS receiver at 1.13 THz. The H plane data are shown with dots, and the E plane data with diamonds. The Gaussian fits to the E and H plane data are nearly identical (solid lines) with the f/d ratio about 15 at –10 dB level.

IV. Test SIS receiver

The SIS receiver is mounted in an Infrared Laboratory HL-3 cryostat. The vacuum window is in Mylar 12 μm thick. The infrared filter at the 77 K stage of the cryostat is of Zitex. The local oscillator power is coupled to the mixer beam using a polarizing grid rotated at 45º as a 3 dB coupler.

The intermediate frequency range is 1 GHz – 2 GHz and the IF amplifier noise is about 10 K.

V. Experiment

The receiver beam pattern has been measured using the heterodyne detection of a hot black body (a heater) of a small size. The signal was modulated with a chopper and detected with a lock-in amplifier. The E and H plane measured data are presented in Fig. 2 with diamonds and dots, respectively. The measured beam is symmetrical. The Gaussian fits to the E and H data are identical within the precision of this measurement (solid lines in Fig.2). At the –10 dB level the beam f/d ratio is about 15.

The receiver sensitivity test at 1130 GHz is presented in Fig. 3. Here the solid lines present the receiver output IF power as a function of the SIS junction bias. From upper to lower, the curves are the measured data with the hot load, the cold load, and without local oscillator power. For the hot load experiment, the receiver is looking at a black body at 296 K ambient temperature. For the cold load experiment, we are using a liquid nitrogen cooled black body coupled to the receiver beam with a 3 dB coupler (polarizing grid rotated at 45º). The effective temperature of the cold load is expected to be 186 K. The receiver Y factor is 1.13 and the DSB noise temperature is 650 K. The receiver conversion gain is -13 dB.

The receiver noise may be improved using an IF amplifier with a lower noise temperature, and with a further optimization of the mixer circuit loss.

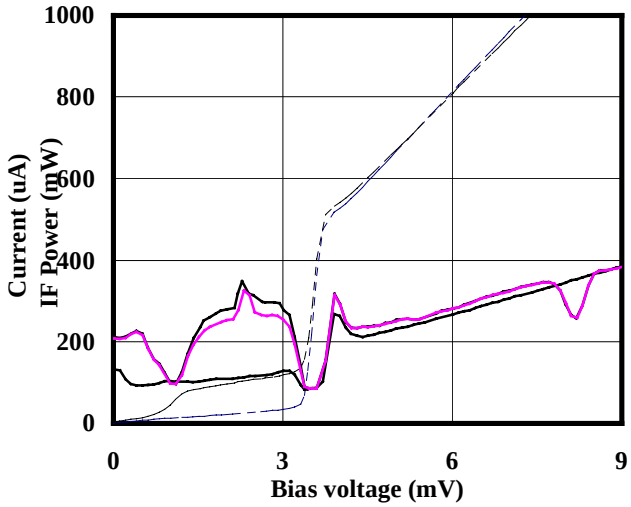

Fig. 3. SIS receiver Y factor measurement at 1.13 THz. The solid lines from upper to lower present the power at the receiver IF output: data with a hot load, with a cold load and data without local oscillator power. The dotted lines are the CVC with and without LO power. The receiver noise temperature is about 650 K. The cold load consists of the liquid nitrogen cooled load coupled via a 3 dB coupler. The hot load effective temperature is 296 K and the cold load is expected to be 186 K.

VI. Conclusion

We developed a SIS receiver for the 1.1-1.25 THz range. At 1.13 THz frequency the receiver double sideband noise temperature is about 650 K. The receiver is using a quasi-optical mixer design with a Si hyperhemispherical lens and twin NbTiN/AlN/Nb SIS junctions with a critical current density of 30 KA/cm^2.

References

[1]. J. E. Carlstrom, J. Zmuidzinaz, "Millimeter and submillimeter techniques", in "*Review of radio science 1993 - 1995*", ed. W. Stone, Oxford, The Oxford University Press, 1996.

[2]. A. Karpov, J. Blondel, M. Voss, K. H. Gundlach, "A three photon noise SIS heterodyne receiver at submillimeter wavelength", *IEEE Trans. on Applied Superconductivity*, Vol. 9, No. 2, pp. 4456-4459, 1999

[3]. B. Bumble, H. G. LeDuc, and J. A. Stern, in *Proc. of the 9th Int. Symp. on Space THz Tech*., edited by W. R. McGrath (Jet Propulsion Laboratory, Pasadena, CA, 1998), pp. 295-304.

[4]. J. W. Kooi, J. A. Stern, G. Chattopady, B. Bumble, and J. Zmuidzinas, "Low-loss NbTiN films for THz mixer tuning circuits", *Int. J. IR and MM Waves*, vol. 19, pp. 373-383, 1998.

[5]. B. D. Jackson, N. N. Iosad, G. de Lange, A. M. Baryshev, W. M. Laauwen, J.-R. Gao, and T. M. Clapwijk, "NbTiN/SiO_2/Al tuning circuits for low noise 1 THz SIS mixers", *IEEE Trans. on Applied Superconductivity*, Vol. 11, N. 1, pp. 653-656, March 2001.

[6]. M. Bin, M. G. Gadis, J. Zmuidzinas, T. G. Phillips, and H. G. Leduc, "Low-noise 1 THz niobium superconducting tunnel junction mixer with a normal metal tuning circuit", *Appl. Physics Letters*, vol. 68, pp.1714-1716, 1996.

[7]. H. van de Stadt et al., "A 1 THz Nb SIS heterodyne mixer with normal metal tuning structure", in *Proc. of the 6th Int. Symp. on Space THz Tech*., CIT, Pasadena, CA, March 21-23, pp. 66-77, 1995.

[8]. J. Kawamura, J. Chen, D. Miller, J. Kooi, and J. Zmuidzinas, "Low noise submillimeter wave NbTiN superconducting tunnel junction mixers", *Appl. Physics Letters*, vol. 75, pp. 4013-4015, 1999.

[9]. J. Ward, F. Rice, G. Chattopadhyay, J. Zmuidzinas, "Supermix", in *Proc. of the 10th Int. Symp. on Space THz Tech*., March 16-18, pp. 268-280, 1999.

Part of the research described in this paper was carried out at the Jet Propulsion Laboratory, California Institute of Technology, under a contract with the National Aeronautics and Space Administration.

DEVELOPMENT OF A 480-640 GHz TUNERLESS SIS MIXER FOR FIRST HIFI/BAND 1

M. Salez[1], Y. Delorme[1], I. Péron[1,2], F. Dauplay[1], B. Lecomte[1], M.-H. Chung[1,4], J. Spatazza[3], M. Guillon[1], K. Schuster[2], J.-M. Krieg[1], A. Deschamps[1]

[1]DEMIRM, Observatoire de Paris, 77 avenue Denfert-Rochereau, 75014 Paris, France
[2]IRAM, Domaine universitaire de Grenoble, 300 rue de la piscine, 38406 Saint-Martin d'Hères, France
[3]CNRS-INSU, Division Technique, 1 place Aristide Briand, 92195 Meudon, France
[4]Taeduk Radio Astronomy Observatory, San 36-1, Whaam-dong, Yusong-gu, Taelon 305-348, South Korea

ABSTRACT

This paper describes the current work at DEMIRM and IRAM to meet the bandwidth-sensitivity specifications of the HIFI Band 1 instrument (480 – 640 GHz). A specific design philosophy was implemented to optimize this Nb-based SIS mixer. We came to design a new tunerless mixer mount, simplified in terms of fabrication and optmized for a 30% bandwidth. It incorporates a high-efficiency electromagnet which can provide several flux quanta to the junction with less than 10 mA. A novel high current density junction fabrication process was set up at IRAM for this project, using negative resist e-beam lithography. Preliminary results based on Fourier Transform Spectroscopy measurements and heterodyne calibrations are presented and discussed. So far, mixer noise values (corrected for the optics) of respectively 65 K and 140 K were measured with a first batch of junctions with a current density of 10 kA/cm^2. More recently, with a new batch of higher current density junctions, receiver noise values (double sideband, uncorrected) of 130 K were measured at some frequencies.

1. INTRODUCTION

Both a very large bandwidth (about 30 %) and a high sensitivity (3 times the quantum limit or less) is required from the Band 1 (480-640 GHz) mixer unit of HIFI, the heterodyne instrument aboard ESA's cornerstone Herschel Space Observatory (formerly FIRST) satellite, scheduled for launch in 2007 [1]. HIFI comprises several SIS and HEB mixers covering a wide range of frequencies through several adjacent bands. Band 1 will consist of two identical tunerless waveguide mixers, with corrugated feedhorns, respectively sensitive to both perpendicular polarizations. The intermediate frequency must cover a 4 to 8 GHz bandwidth with a very low level of ripple (3 dB). The State of the Art (resp. Goal) performance for Band 1 is a linear interpolation between 80 K (resp. 70 K) DSB at 480 GHz and 130 K (resp. 110 K) DSB at 640 GHz. However, achieving a bandwidth of 30% with an SIS mixer is a challenge, and the so-called SOAP truly remains, to this day, a goal yet to be achieved. In addition, the SIS mixers of HIFI must be space qualified, and must satisfy a number of constraints, in terms of mass, volume, power dissipation, EM shielding, which impact on their design.

2. TUNERLESS WAVEGUIDE MOUNT

Since we aim at a large bandwidth mixer, it is essential that input and output impedances of every component of the mixer be well defined. In particular, the embedding impedance of the waveguide mount at the location of the substrate must be well known (and possibly tuned)

over the 480 – 640 GHz, since it must be matched to the SIS device by means of an integrated microstrip circuit. Obviously, the job of conjugate-matching several mixer passive components would be nicer if all the impedances stayed constant within the frequency range of interest, with as little reactive part as possible. From this standpoint, resonant elements such as integrated tuning stubs and waveguide backshorts should be used scarcely, and probably the best 'tunerless' mixer is one with no such tuner at all.

Therefore we have left aside some commonly made assumptions on waveguide mixer embedding impedances and best tunerless waveguide mount geometries — demonstrated by excellent results in several groups [2,3], to carry out extensive EM simulations of a waveguide mixer varying many of its parameters, including the shape of the bow-tie antenna and the first sections of RF choke filter [4]. This was done using a 3D software package [5] allowing to explore, in particular, the influence of the quartz substrate inserted across a reduced-height rectangular waveguide, and the effect of positioning errors and mechanical tolerances. We found the substrate orientation to have a major influence, and we could optimize the geometry in order to provide a nearly frequency-independent and imaginary-part free impedance, close to 70 Ω, to the bow tie center where the SIS circuit is located. Figure 1 shows the calculated evolution of this impedance with backshort location. It is important to note that our simulations have also confirmed some earlier results published by other groups, while this optimum embedding impedance corresponds to a particular substrate orientation and backshort location. The 50 μm-thick quartz substrate has to be mounted with the metallization looking away from the input waveguide, and facing the backshort another 50 μm above it, flush with the top of the substrate channel. This makes the fabrication of tunerless waveguide mixers much easier, since no micromachining of a backshort-terminated waveguide is required.

3. SIS CIRCUIT DESIGN

Following a similar strategy, the SIS junction parameters and the integrated RF microstrip circuit geometry have also been optimized to provide a wide-band match to the mixer mount embedding impedance. The most convenient type of circuit consists of an end-loaded single junction circuit (baseline), in which a two-section Tchebychev impedance transformer is designed so as to stretch the RF coupling bandwith. This solution requires high current density (typically 15 kA/cm^2) SIS junctions. Another approach, more complex because of the advent of Josephson currents, is the use of parallel arrays of junctions (fall-back option).

Regardless of the type of SIS circuits, optimizing them was done in three consecutive stages: first, the electrical lenghts and characteristic impedances of every section of the SIS circuit were optimized using HP Libra. This allowed us to rapidly optimize circuits with a large number of degrees of freedom and to investigate the expected yield. We plugged into the commercial software all the fabrication tolerances and maximum errors associated to all parameters, and did a statistical analysis, leading us to select our circuit designs not on the sole basis of optimum result but also of optimum yield.

In a second stage, the sets of electrical lengths and characteristic impedances were converted into real microstrip circuit dimensions using the theory of superconductive microstrip transmission lines.

To verify the circuit design, the noise performance to expect from any optimized circuit — placed in our tunerless waveguide mount — was calculated at any frequency and for various LO powers and bias voltages, using a numerical code written in C++ using Tucker formalism of quantum mixing in the 3-port aproximation. From these predictions, it became clear (see Fig. 2) that achieving the RF bandwidth specified for Band 1 with a 'flat' receiver noise would be an extremely difficult task using a single junction design and Nb/AlOx/Nb

technology. However, twin-parallel and multi-junction arrays (N>2), as first proposed by NRO [6] should allow to meet the goals. Our own proposed multi-junction array geometries, using non-uniform spacings between SIS junctions, were presented earlier [7].

4. SIS JUNCTION FABRICATION

Considering the maximum RF frequency we need and the degrees of maturity and reliability of various SIS technologies, for current densities up to 15 kA/cm^2 Nb/AlOx/Nb junctions in association with Nb/SiO_2/Nb microstrip circuits appear as the best choice materials for the mixers of HIFI/Band 1.

High-current density (15-kA/cm^2) SIS junctions with areas of 1 μm^2 or smaller are required to avoid shunting by the tunnel barrier capacitance in high frequency applications. Because the standard SIS fabrication process in use at IRAM — UV360 contact lithography — is limited in precision for the definition of junctions smaller than 2 μm^2, a new fabrication process using e-beam lithography for the definition of the HIFI/Band 1 junctions was developed [8]. To make it compatible with the existing process, a mix & match process was chosen, where the same negative resist layer can be both e-beam and UV-exposed to produce self-aligned structures for either the junctions pattern or the larger contact areas. As shown in Fig.3, this process involves less steps than positive e-beam lithography. More details on the fabrication process can be found in [8]. Out of 80 junctions measured, 57% of them displayed good I-V curves with $R_{subgap}/R_n > 20$. The results show that despite earlier claims it is possible to fabricate high quality Nb-Al-AlOx-Nb junctions with current densities well above 10 kA/cm^2 with good yield.

The trilayer consists of a 120 nm niobium (Nb1) bottom electrode, a 10 nm Al layer oxidized in pure oxygen at room temperature, and 60 nm niobium (Nb2). The RF microstrip circuits share the same Nb1 bottom electrode with the trilayer, and use a 200 nm thick dielectric layer (SiO2) and a 430 nm niobium counter-electrode (Nb3). Figure 4 shows a micrograph of a circuit.

5. PRELIMINARY MEASUREMENTS

Fourier Transform Spectroscopy (FTS) measurements and heterodyne hot/cold load calibrations were done with the first SIS circuits produced by IRAM. For the heterodyne tests we made a prototype tunerless waveguide mount, simple—for instance with a plain diagonal horn and a massive conventional superconducting magnet—yet with the substrate positioning and the backshort location found to be optimum from our 3D simulations. We adopted this solution to make rapid validations of the circuits and we expect the next waveguide mount to be of much better quality.

Figure 5 shows on the same plot the FTS response of one such circuit (10 kA/cm2) both mounted in an open structure (prior to dicing of the individual chips) and mounted in the waveguide mount. Several things must be noted. First, the envelopes of both FTS responses are quite similar. This demonstrates that the new tunerless mixer mount is nearly 'transparent' impedance-wise. Indeed, the source impedance seen by the SIS circuit in the open-structure case is close to 100 Ω over most of the band, not too different from the ~70 Ω waveguide mixer environment. With either type of feed, therefore, the computed RF coupling response is dominated by the complex admittance of the SIS circuit itself.

Second, the measured response of the single-junction circuit agrees with the simulations: the 'twin-peaks' like curve is mainly due to the Tchebychev circuit, designed for the widest band possible. This shows the limitations of the microstrip transformer approach

for a 30 % relative bandwidth, since it results, as shown in Fig. 6, in an increase of the receiver noise in the center of the band mirroring the decrease of RF coupling. However, the good agreement between measurements and simulations is encouraging and validates our choice of strategy. In particular, the fact that the 480-640 GHz bandwidth has been obtained from the very first batch of junctions seems to validate our 'best-yield design' approach and the reliability of the new junction fabrication process. The best receiver noise measured for one device always occurs at two frequencies where the RF coupling and the mixer gain peak. An example of these noise values is given in the Table I below, also providing a correction for the optics losses. The influence of the latter was quantified using FTS measurements of refractive indices and absorption coefficients of the optical components at all frequencies (Table II). The calculations assumed a 7 K IF noise and included the contribution of zero-point field fluctuations to the noise, at temperature T_i and frequency ν:

$$T_i \longrightarrow T_{i,ZPF} = \frac{h\nu}{2k_B} \cdot \coth\left| \frac{h\nu}{2k_B T_i} \right|$$

With another device at 15 kA/cm^2, and after removing some optical components (the 3.4-mm thick rexolite lens and one IR filter) in the cryostat we could measure a receiver noise temperature of 130 K around 530 GHz (see fig. 7).

Table I

Frequency (GHz)	T_{rec}, uncor (K)	T_{RF} (K)	G_{RF}	Trec, cor (K)	Trec sim (K)
480	280	95.2	0.35	**65**	60
610	500	73	0.33	**141**	87

Table II

Component	Material	Thickness (mm)	Index *n*	Absorption α(cm^{-1})	Power Transmission
Beam splitter	Mylar	0.009	1.732	0.74	0.97
Vacuum window	Mylar	0.025	1.732	0.74	0.85
Filter 4.2 K	Fluorogold	0.508	1.654-1.657	1.6-2.8	0.74
Lens 4.2 K	Rexolite	3.4	1.6	0.55	0.6

6. LOW-CURRENT ELECTROMAGNET

SIS mixers require the application of a magnetic field in the tunnel barrier plane to null the DC average of Josephson currents. This is commonly achieved with a superconducting electromagnet. In the case of HIFI, the low maximum current allowed—for thermal dissipation reasons—imposes the design of a highly efficient electromagnet, able to provide a few magnetic flux quanta in the SIS junction for a maximum current of 10 mA.

Figure 8 shows the proposed electromagnet for the Band 1 mixers. It consists of a pair of symmetrical electromagnets: the cores are made out of a high magnetic permeability material, coiled with hundreds of turns of NbTi/Cu 100-micron gauge wire, and the polar pieces reach the plane of the SIS substrate. A prototype electromagnet using cryoperm was made and measured at room temperature and 4.2 K. The cryoperm material was provided by Ammuneal Corp [9] then bent into shape and thermally processed [10]. The prototype was

winded in house by hand with 1100 turns of 120-micron formvar-insulated copper wire, then characterized using a Hall probe.

At room temperature, the magnetic field produced by the magnet saturates between 900 and 1100 Gauss, depending on the size of the gap between the polar pieces (~1 mm typ.). As expected, the saturation field, reached for about 150 mA (see Fig. 9), is larger at 4.2 K than at 300 K. These saturation levels are lower than the ~8000 Gauss specified for the bulk cryoperm material, nevertheless sufficient for our application. The magnetic permeability does not vary with temperature, and no hysteresis was noted. These measurements ensure that the electromagnet designed for Band 1 will meet the HIFI specs, providing 300 Gauss — inducing more than 3 flux quanta in a one-micron-square SIS junction — with only 10 mA.

7. DEMONSTRATION MODEL MIXER

Figure 10 shows an Autocad view of the Demonstration Model (DM) mixer for Band 1, as currently designed.

The most important feature for our wideband coupling design is the orientation of the substrate, which lies on the feedhorn section of the mixer. The substrate is surrounded by a set of printed boards supporting various functions: IF output line (with or without an IF impedance transformer) with DC block; grounding of the SIS device with an integrated heater to get rid of occasionnally trapped flux; DC bias circuit with filters. These must be highly efficient in the microwave region, to provide an isolation better than 30 dB and protect the SIS device from EMI/ESD. We propose the use of distributed planar RC filters using lossy suspended striplines. The resistor is a thin TaN film and the dielectric is Ta_2O_5N. These novel filters are attractive because of their smallness and because they will efficiently reject any high frequency noise above a certain cutoff frequency (e.g. 50 MHz), whereas their lumped equivalents provide less rejection and have resonances in the microwave range. We will report on the performance of the filters elsewhere.

Corrugated feedhorns for the DM have been designed (in concertation with the other HIFI mixer designers, for the sake of standardization between bands) and are now fabricated: the mandrels were machined by Société Audoise de Précision [11] out of aluminum 7175; electrodeposition of 24-carat gold—to avoid voids—and copper on the mandrels is done at Protection des Métaux [12]. We will investigate their beam quality (E and H symmetry, sidelobes, crosspolarization, return loss) by amplitude and phase measurements at IRAM. Figure 11 shows the calculated beam pattern and Fig. 12 shows EBM photographs of 70-micron and 20-micron wide corrugations (on a feasibility study prototype).

8. CONCLUSION

We have designed a mixer for HIFI/ Band 1, which we are currently validating by FTS and heterodyne measurements. The Demonstration Model of this mixer will be partially functional (some points at the SOAP specs within the band) and fully compliant with the interface specifications (dimensions, mass and power dissipation budget, ranges of voltages and currents, LO power required). In particular, the DM will include several items which have been specially developed for this project: a high efficiency electromagnet with a cryoperm core, high current density Nb junctions processed by e-beam lithography, and a corrugated feedhorn. We demonstrated with FTS measurements that the waveguide mount needs no fixed length of backshort to provide a wide bandwidth, hence greatly simplifying the manufacture of the mounts. To improve the receiver sensitivity across the band in later deliveries

(upgraded DM or QM, FM), new SIS circuits will be required, including non-uniform parallel arrays of junctions, a developement currently in progress at DEMIRM.

ACKNOWLEDGEMENTS

We thank, for financially supporting the project and Frédéric Dauplay, the Centre National d'Etudes Spatiales and CNRS, the Institut National des Sciences de l'Univers (INSU). We are grateful to Pascal. Fèbvre and Frédéric Garet of Université de Savoie for the measurements of materials at submm wavelengths. We wish to thank Karl Jacobs, Netty Honingh, Gert De Lange, Hans Golstein, and Jaap Evers for open and helpful discussions. We thank for their support Jean-Pierre Ayache, and Raoul Entringer of INSU's Division Technique in Meudon. The feedhorns beam pattern measurements are to be performed at IRAM by Matt Carter.

REFERENCES

1 H. v.d. Stadt, G. Beaudin, T. De Graauw, K. Jacobs, and N. Whyborn, 'Detectors for the heterodyne spectrometer of FIRST', *Proc. of the ESA Symposium 'The Far Infrared and Submm Universe'*, 457, IRAM, Grenoble, France, April 15-17, 1997.

2 J.Kooi et al., 1994, '180-425 GHz low noise SIS waveguide receivers employing tuned Nb/AlOx/Nb tunnel junctions', *International J. of Infrared and Millimeter Waves*, **15**, 5, 783.

3 C.-Y. Tong, R. Blundell et al., 'A fixed tuned low noise SIS receiver for the 600 GHz frequency band', Proc. 6th *International Symposium on Space Terahertz Technology*, 295, Pasadena, 1995.

4 Microwave Studio, Computer Simulation Technology, http://www.cst.de

5 M. Salez, Y. Delorme, F. Dauplay, B. Marchand, B. Lecomte, and M.-H. Chung, 'Design of a fixed-tuned 30% bandwidth SIS receiver for FIRST/HIFI Band 1 (480-640 GHz) and other space applications', *Proc. 4th European Workshop on Low-Temperature Electronics*, WOLTE-4, ESTEC, Noordwijk, NL, June 21-23, 2000.

6 S.-C. Shi, T. Nogushi, and J. Inatani, 'Analysis of the bandwidth performance of SIS mixers with distributed junction arrays', *Proc. 8th International Symposium on Space Terahertz Technology*, p.81, Harvard University, MA, March 25-27, 1997.

7 M. Salez, Y. Delorme, M.-H. Chung, and F. Dauplay, 'Simulated performance of multijunction parallel array SIS mixers for ultra broadband submillimeter-wave applications', *Proc. 11th International Symposium on Space Terahertz Technology*, pp. 343-358, Ann Arbor, MI, May 1-3, 2000.

8 I. Péron, P. Pasturel, and K.-F. Schuster, 'Fabrication of SIS junctions for space borne submillimeter wave mixers using negative resist e-beam lithography', *Proc. of the Applied Superconductivity Conference*, ASC'00, Virginia Beach, Sept. 17-23, 2000.

9 *Amuneal Corp*, 4737 Darrah Str., Philadelphia, PA 1924-2705; larrym@amuneal.com.

10 *Division Technique INSU*, place Aristide Briand, 92195 Meudon, France; *Bodycote Hit*, 25 rue Louis Ampère, Z.I. des Chanoux, 93330 Neuilly-sur-Marne, France.

11 *Société Audoise de Précision*, Z.A. du Pont, F-81500 Ambres, France.

12 *Protection des Métaux*, 57-59 rue de Saint-Mandé, 93511 Montreuil, France.

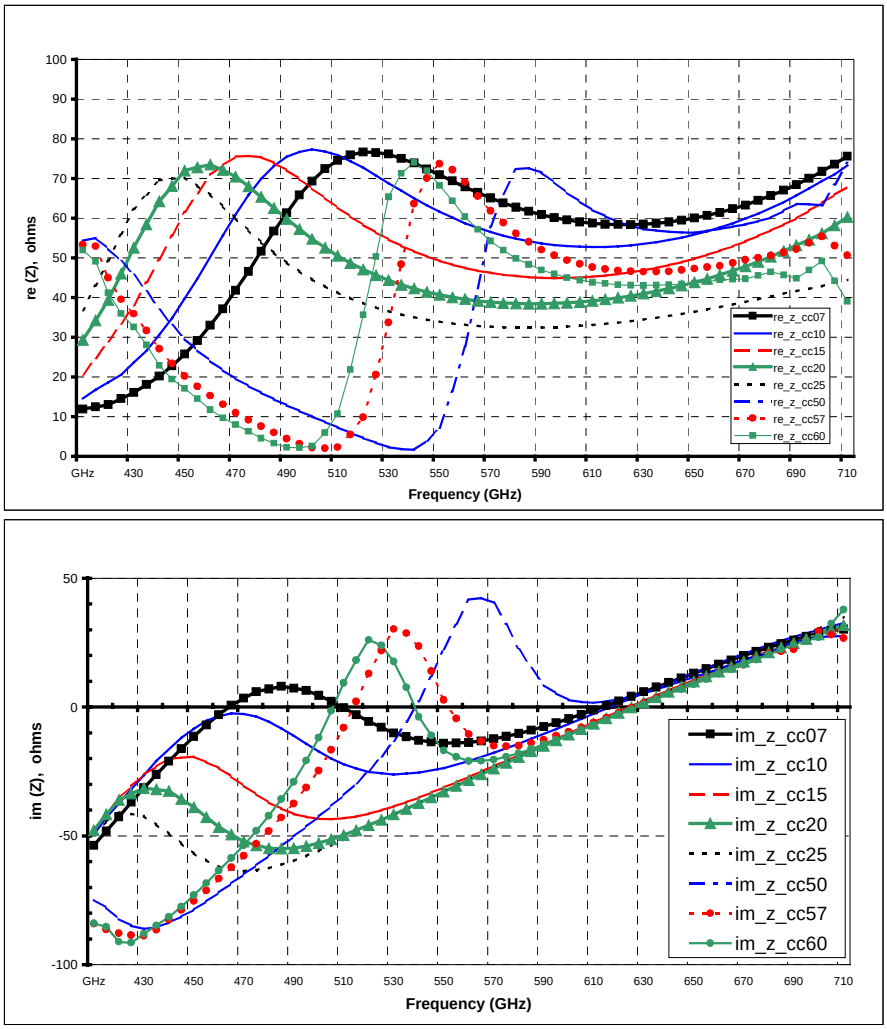

Figure 1. Real and imaginary parts of the waveguide mount embedding impedance seen at the center of the bow-tie probe, simulated for different waveguide backshort locations (distance of backshort from metallization is expressed in the legends in percents of the guided wavelength).

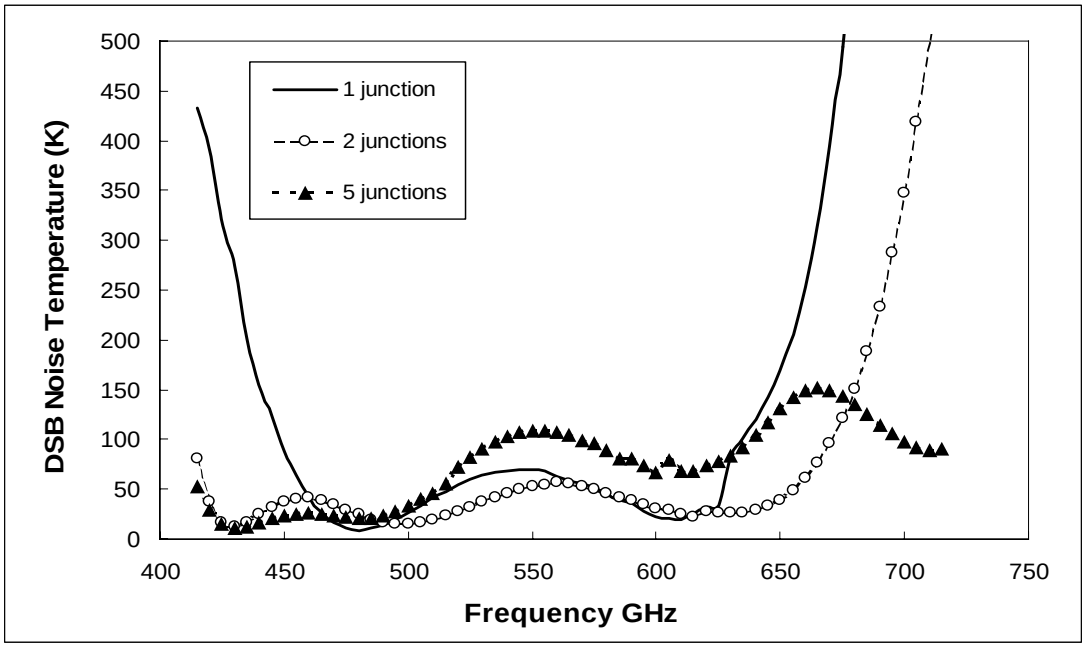

Figure 2. Predicted DSB mixer noise performance for a single-junction, twin-parallel junction, and *N*=5 junction array mixers optimized for Band 1.

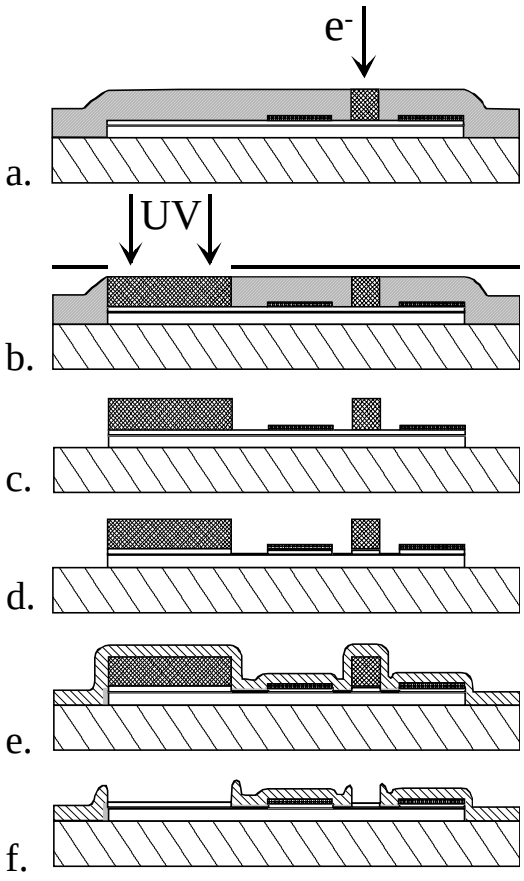

Figure 3. Schematic of the mix & match process: a. e-beam lithography junction definition; b. contact area UV-mask aligner lithography; c. junction and contact pattern after development; d. reactive ion etching of Nb2; e. SiO_2 deposition; f. SiO_2 liftoff.

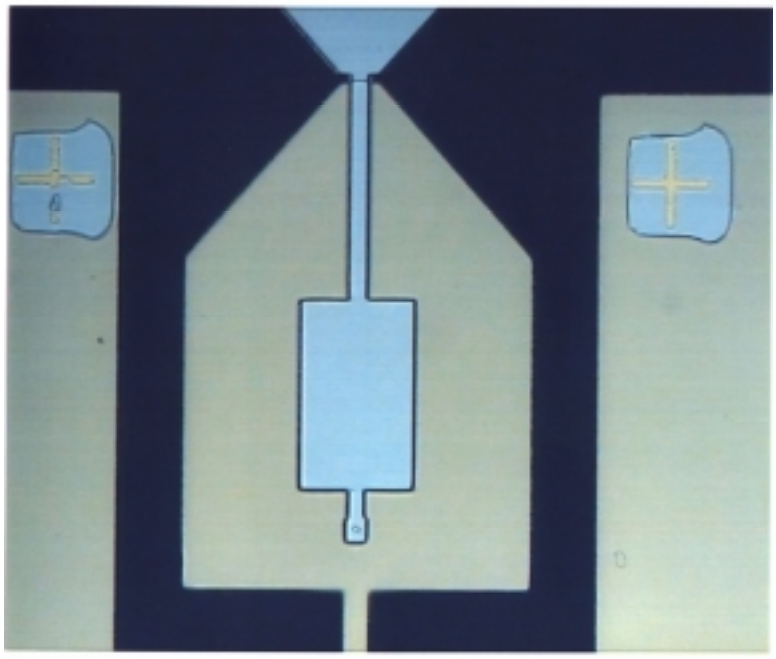

Figure 4. Photograph of a 1-μm^2 junction defined by EBL with the new IRAM process.

(a)

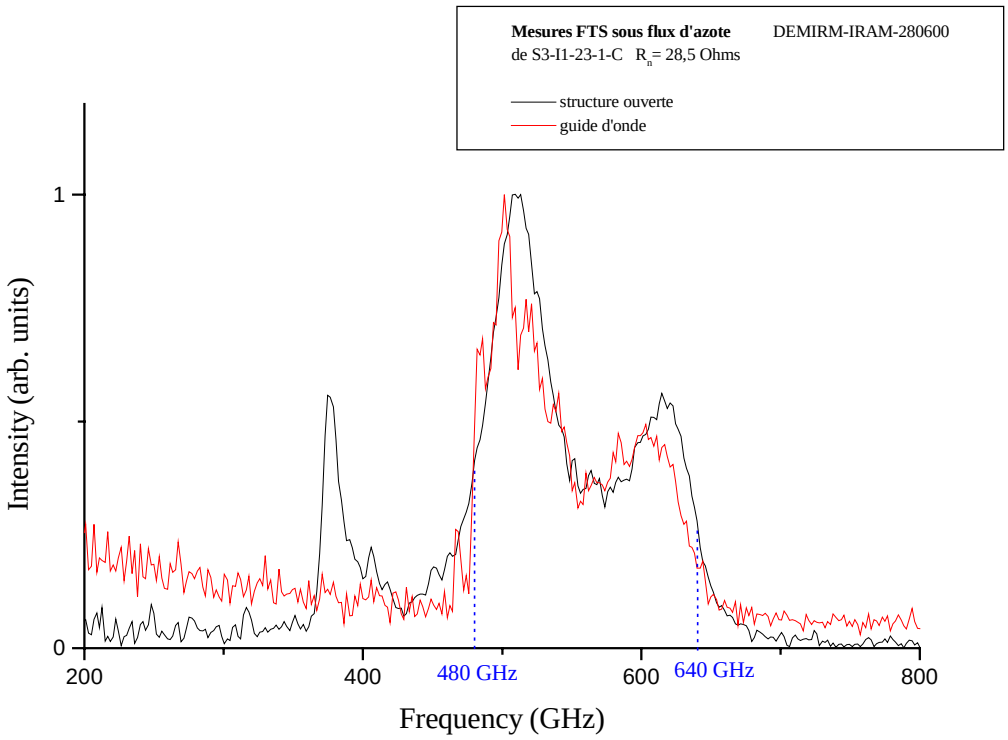

(b)

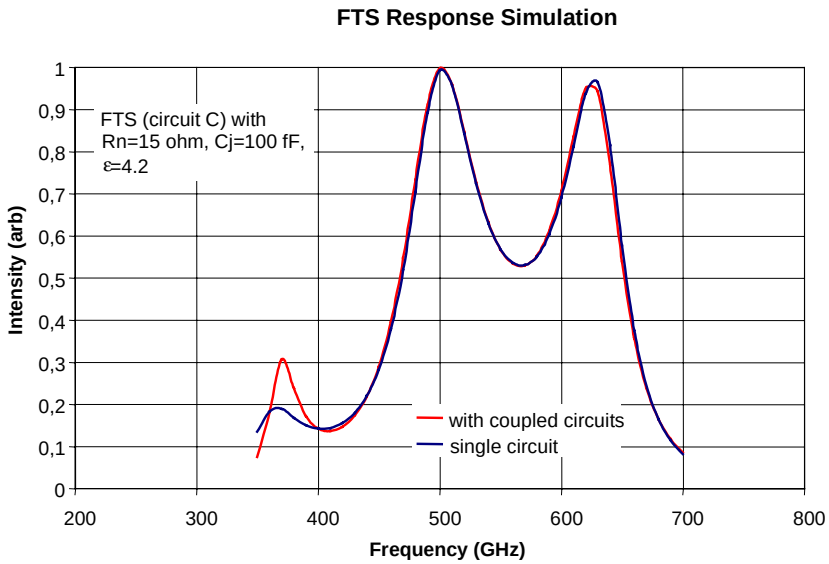

Figure 5. (a) FTS response of a 1 μm^2, 10 kA/cm^2 Nb/AlOx/Nb junction with a Tchebychev transformer (device # S3-I1-23-1-C), coupled to the radiation both quasioptically and in the tunerless waveguide mount. (b) Simulated FTS response: we showed the peak at 380 GHz in the open structure measurement to be a mere consequence of radiation coupling to the nearby devices on the undiced chip.

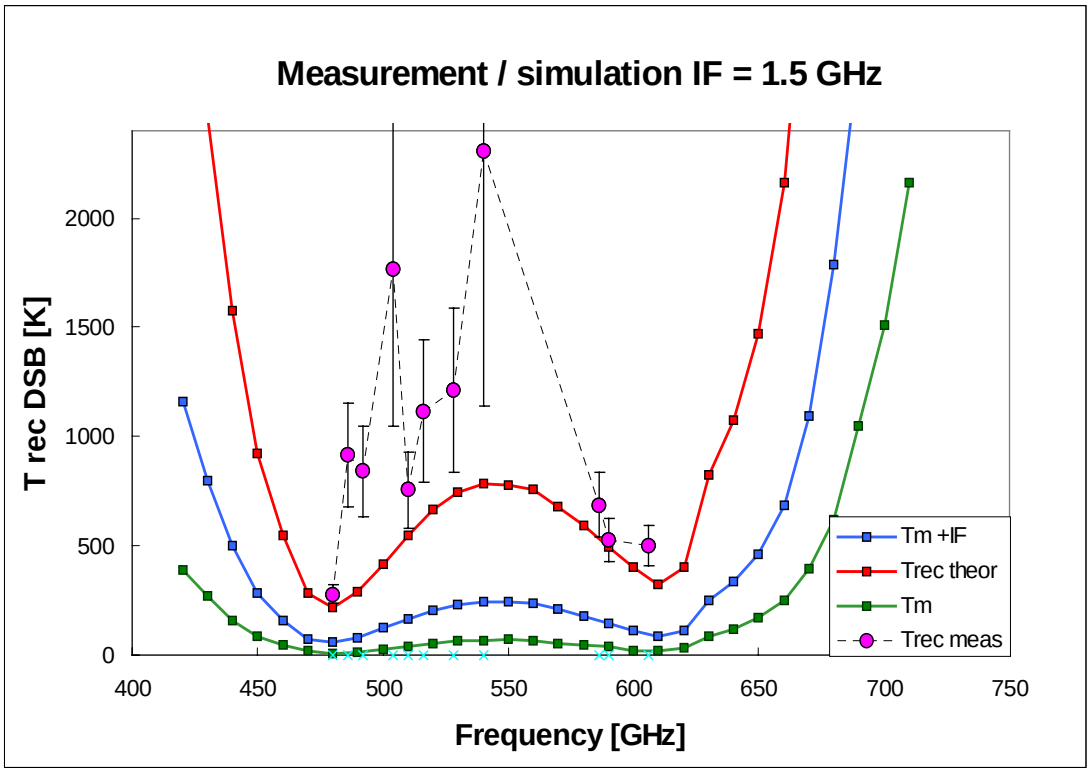

Figure 6. Comparison of heterodyne calibration with simulated DSB noise performance. The calculated noise was optimized (w.r.t. LO power, bias voltage) and includes a 7 K IF system noise at 1.5 GHz. The RF noise contribution was computed after measurements from 100 to 1500 GHz of the refractive index and absorption coefficient of all optical materials used in the experiment. No data is available on this plot below 480 GHz nor above 610 GHz for lack of LO source.

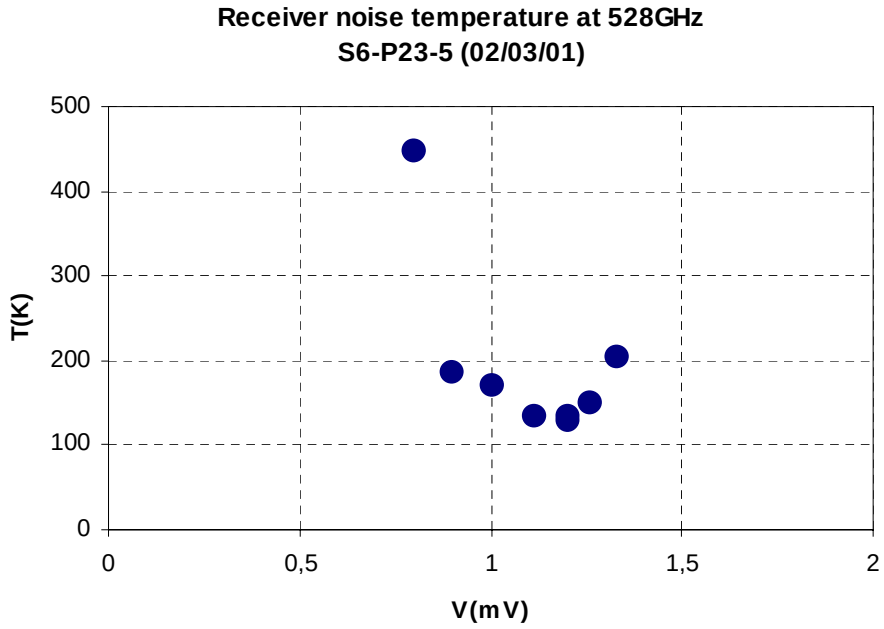

Figure 7. Measured receiver noise temperature versus bias voltage at 528 GHz for device # S6-P23-5 (15 kA/cm^2).

Figure 8. One half of the cryoperm electromagnet designed for Band 1 (1100 turns); artist's view.

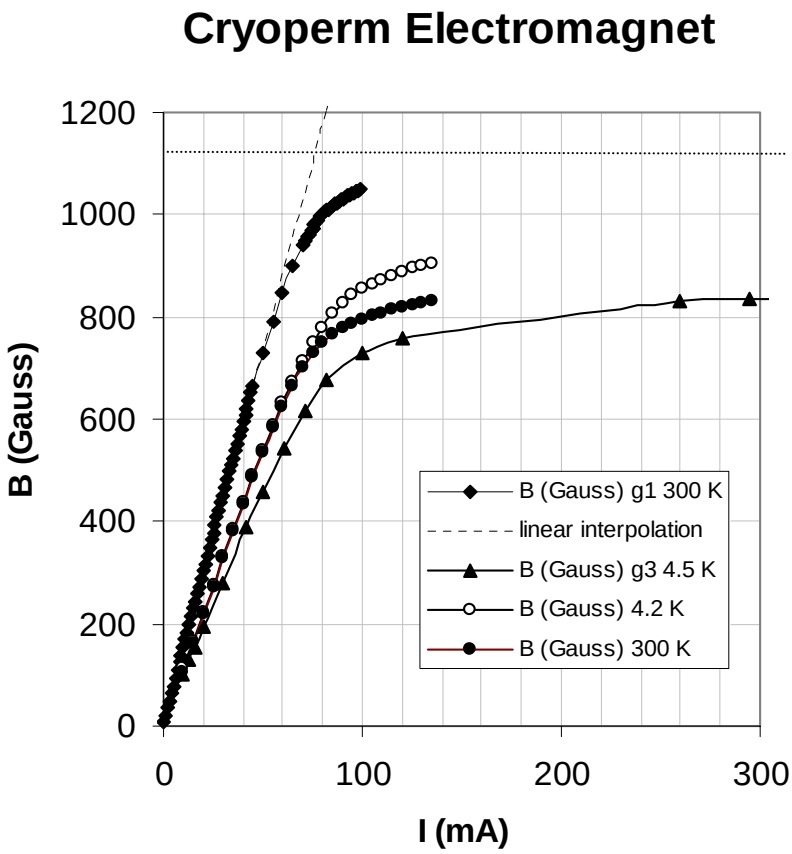

Figure 9. Magnetic field vs. current measured on the Band 1 prototype cryoperm electromagnet, with 1100 turns, at ambiant and LHe temperatures and for three gap values : the permeability decreases as g is increased. The final magnet will have a gap of 1 mm <g1.

(a)

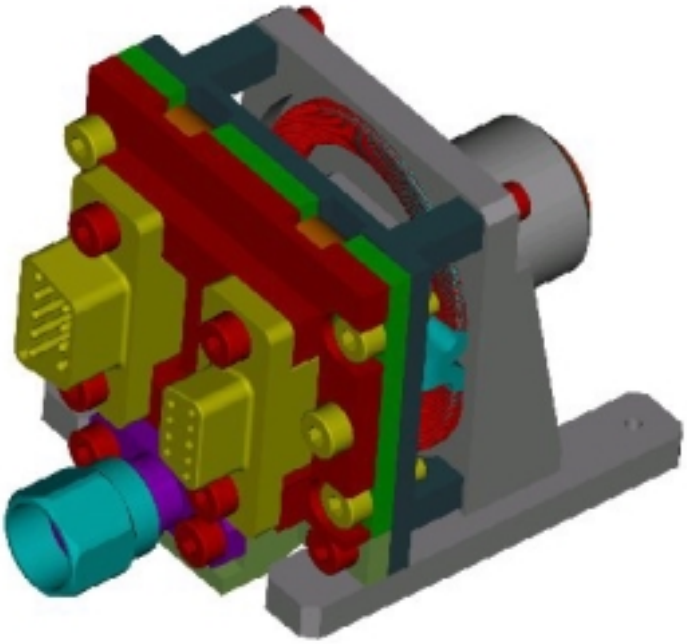

(b)

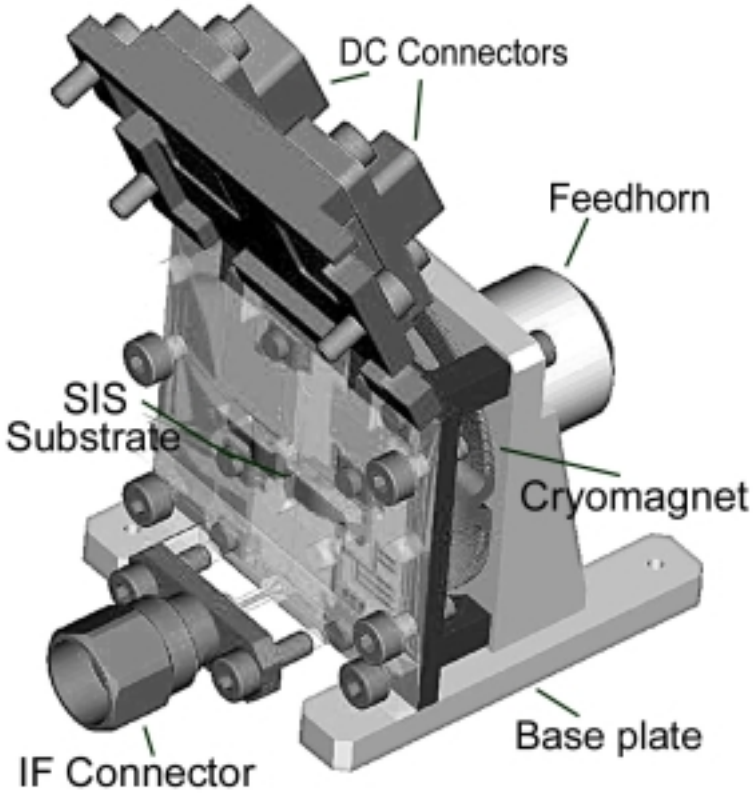

Figure 10. 3D Autocad view of the DM mixer for Band 1: (a) closed; (b) open.

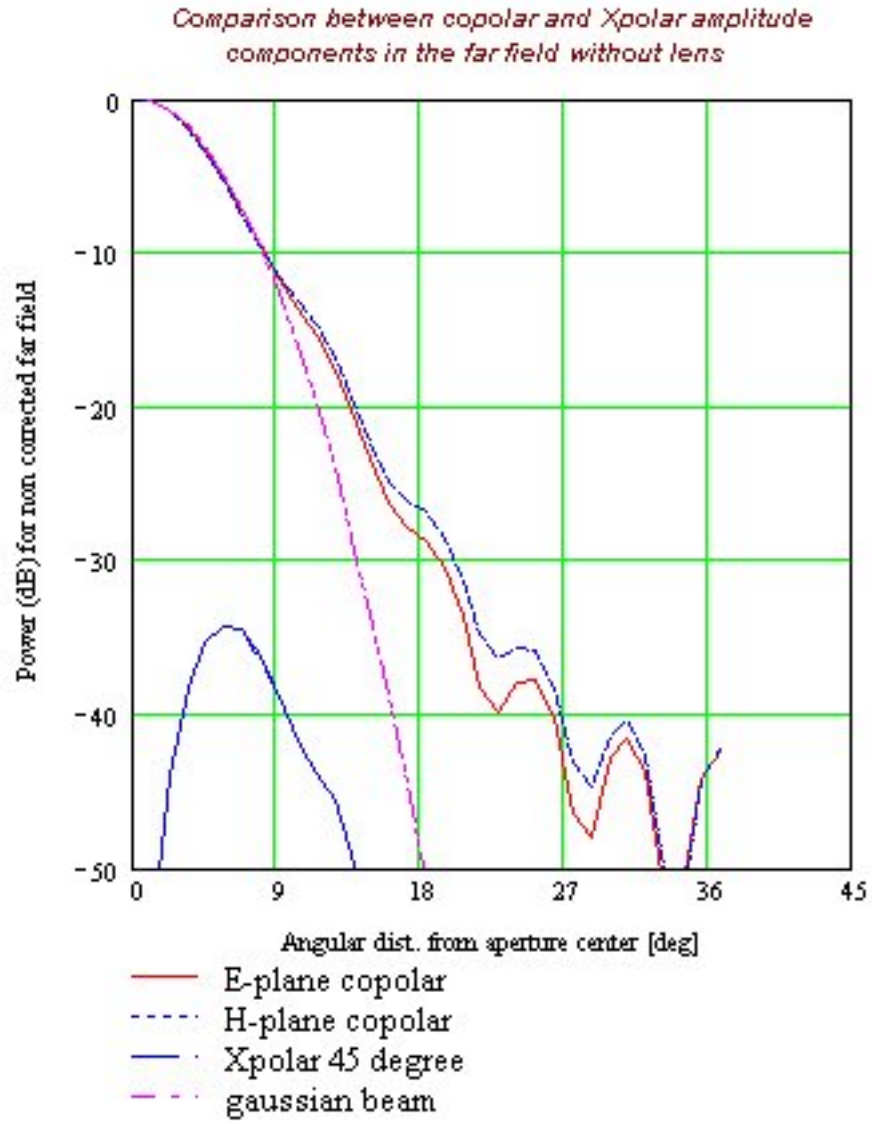

Figure 11. Calculated beam pattern and cross-polarization level for Band 1 (the same horn profile has been adopted for all waveguide mixer bands).

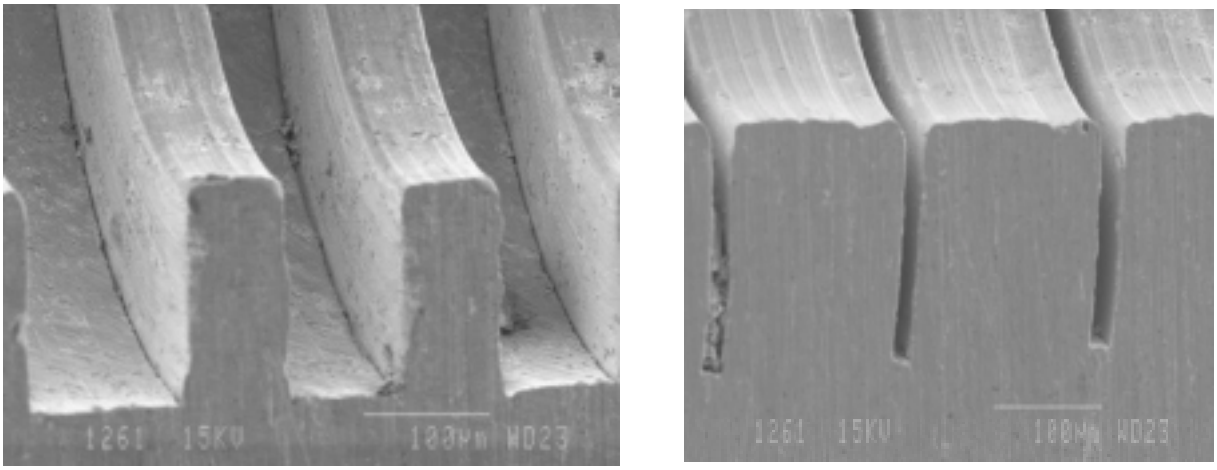

Figure 12. EBM inspection of the corrugated gold parts of two prototype feedhorns with 70 μm (left) and 20 μm (right) wide corrugations.

Reduced T_c Niobium Superconducting HEB Mixers

I. Siddiqi and D.E. Prober
Department of Applied Physics, Yale University, 15 Prospect Street, New Haven CT 06520

B. Bumble and H.G. LeDuc
Jet Propulsion Laboratory, California Institute of Technology, Pasadena CA 91109

A reduction in the mixer noise is expected when using superconductors with a lower transition temperature (T_c) since the thermal noise components of the mixer noise should scale with T_c. Also, the local oscillator (LO) power required for a diffusion-cooled device should decrease as T_c^2 when $T_{bath} << T_c$. We previously studied mixing in aluminum based hot-electron bolometers (HEBs) at microwave frequencies (~30 GHz), and observed a significant improvement in noise performance, and a reduction in LO power as predicted. However, the bias voltage range over which good mixer performance was observed was ~ 5-10 μV. These devices are thus susceptible to saturation effects, in particular output saturation. In the present work, we have investigated Nb HEBs whose T_c is lowered by applying a magnetic field. The goal is to study a case intermediate between Nb and Al, and hopefully to find properties that will allow use in practical receivers. A 15 kOe perpendicular magnetic field was applied to a Nb HEB (L=0.16 μm, W=0.08 μm, R_N=90Ω) to reduce T_c from 5.2 K to 2.4 K. The mixer noise, as inferred from the output noise and the conversion efficiency, decreased from 390 K, DSB to 171 K, DSB. The LO power required for near optimum mixer conversion efficiency (η_{mixer} = - 9 dB in this device) was 8nW in zero field, and ~ 2 nW when T_c was reduced to 2.4K. T_{bath}=0.22K. The conversion bandwidth was previously measured to be 2.4 GHz and the same bandwidth was observed in the presence of a magnetic field. By lowering T_c, the voltage range over which good mixing was observed also decreased. However, even with T_c reduced to 2.4 K, the conversion efficiency dropped by 3dB from its maximum value only when the bias voltage was changed by ~ 90 μV. Saturation effects should thus be much less of a concern in these devices than in Al HEBs. In situations where the application of a large magnetic field is not feasible, we suggest using Ta based HEBs. Ta HEBs should have T_c ~ 3-3.5K and material properties very similar to Nb.

I. Introduction

Nb and NbN hot-electron bolometer (HEB) mixers are promising for spectroscopy applications above 1 THz.[1-3] Diffusion-cooled Nb devices have been shown to have a receiver noise temperature as low as T_R=1800K at 2.5 THz, with an intermediate (IF) bandwidth of ~ 9 GHz in this same device.[1] Mixer noise performance is predicted to improve when the transition temperature (T_c) of the superconducting HEB is lowered. A reduction in the mixer noise temperature and the local oscillator (LO) power is expected.[4]

Recently, we studied diffusion-cooled HEB mixers made of Al. Low frequency studies (f_{LO} ~ 30GHz) indicate that the mixer performance is very good and in agreement with predictions.[5] In the Al devices, optimum mixer performance is observed only within a narrow range of bias voltages, ΔV ~ 5-10 μV. Al HEB tests at 600 GHz indicate that the conversion efficiency is about 10dB lower than that measured at microwave frequencies.[6] It is

possible that the discrepancy between these two measurements is the result of saturation effects. For example, output saturation might be an issue if enough background radiation is down converted to create an IF voltage swing in excess of several microvolts. In Fig. 1, the mixer conversion efficiency is plotted, and it drops when broadband noise is coupled with the mixer input signal. If the frequency of the noise is such that most of it can be down converted to the IF, a significant decrease in conversion efficiency can be observed for even ~10pW ($T_{\text{background noise}} \sim 100$K) of incident power.

Since the voltage range for operation for Al HEBs is small, we consider materials with a T_c that lies between 1K (Al) and 6K (Nb) for practical applications. The approach taken here was to lower the T_c of Nb HEBs by applying a perpendicular magnetic field. These devices should have a lower mixer noise temperature compared to Nb in zero field, but not as low as that obtained with Al. Yet, they should be much less prone to saturation effects. Overall, they should be more like the successful Nb HEBs. The data presented are for a local oscillator frequency of ~ 30 GHz. The motivation for these studies is that the microwave measurements allow for a more thorough exploration of the device physics than can be done with usual sub-millimeter wave measurements. In applications where a magnetic field may be difficult to generate or may interfere with other components, the use of Ta ($T_c \sim$ 3-3.5 K) is suggested. Since Ta and Nb share many material properties,[7] it is hoped that any results obtained with reduced-T_c Nb devices can be reproduced with Ta HEBs.

II. Devices and Experimental Setup

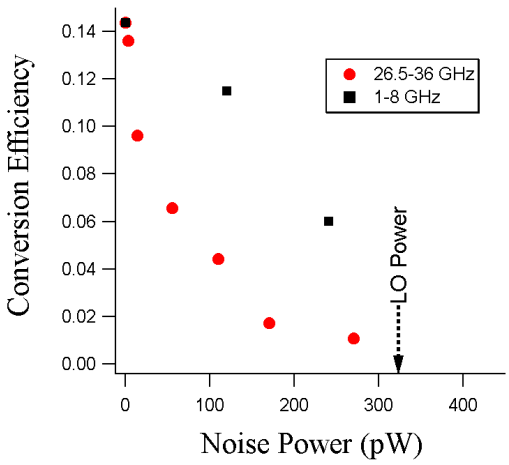

Figure 1: Conversion efficiency for an Al HEB in the presence of background noise. Based on the measured IF bandwidth and the LO frequency chosen, ~85% of the noise in the 26.5-36 GHz can be down converted to the IF.

The devices measured were 10 nm thick Nb HEBs on quartz substrates. The fabrication details of the self-aligned process used are given in Ref. 8. The data presented here are for a device with width 0.08 μm and length 0.16 μm. Thick Au pads (100 nm) are used to contact the Nb microbridge. Measurements were previously made on this device (Device B in Ref. 9) at 20 GHz by Burke, et al.[9] Also, devices from this batch and ones similar to it have been used for HEB mixer tests at ~ 600 GHz, 1.2 THz, and 2.5 THz.[1-2,10]

The device is placed on the cold stage of a variable temperature ^{3}He cryostat. The system described here is similar to the setup in Ref. 5, but differs in instrumentation and functionality. For convenience, all measurements were made at a bath temperature of T=0.22K, and similar mixer performance is expected even at ~ 1.5K. A magnetic field up to 50 kOe could be applied perpendicular to the sample. The LO source is a YIG oscillator

(26.5-40 GHz), and the RF signal source is the internal generator of the HP8722D network analyzer. A path is present for the injection of noise from an external source to simulate background radiation. The first stage IF amplifier is a broadband cooled HEMT. The IF signal was analyzed on a HP8593E spectrum analyzer. Output noise was measured by rectifying the IF signal using a room temperature Schottky diode detector. A block diagram and picture of the measurement setup are given in Fig. 2.

III. Results

A. I-V Curves

The T_c is measured to be 5.2 K in the absence of an applied magnetic field. The critical current is 105 μA with no LO. By applying a 15 kOe perpendicular magnetic field, T_c is reduced to 2.4 K. For this comparison, T_c is taken to be the temperature corresponding to the middle of the resistive transition. The unpumped critical current is reduced to 11 μA. In Figs. 3-4, pumped and unpumped I-V curves for T_c = 5.2 K and 2.4 K are given.

B. LO Power and Conversion Efficiency

The LO power used for mixing was chosen so as to optimize the conversion efficiency. A particular LO power was set and the bias voltage was swept to determine the maximum conversion efficiency for that pump power. The pump power was then incrementally changed to find near optimum operating conditions. Both with and without a magnetic field, the best conversion efficiency obtained was –9 dB.

The LO power required for mixing for a diffusion cooled device is predicted to be

$$P_{LO}=4\,\mathcal{L}\,(T_c^2-T^2)\,/\,R \qquad (1)$$

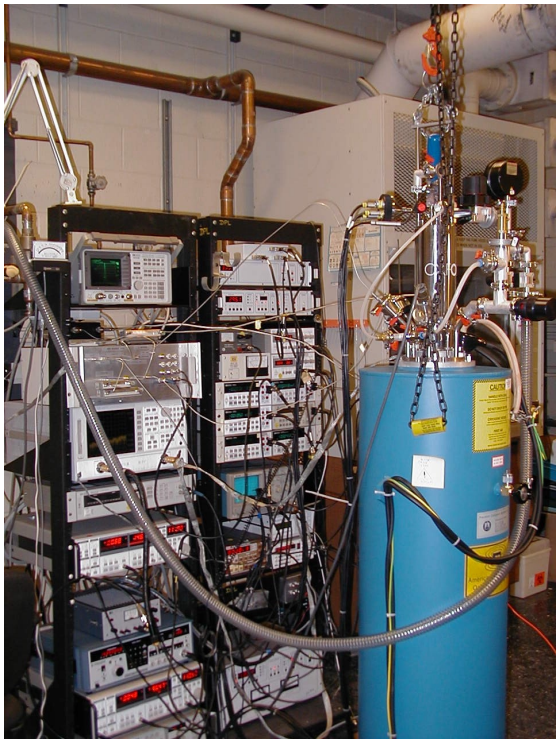

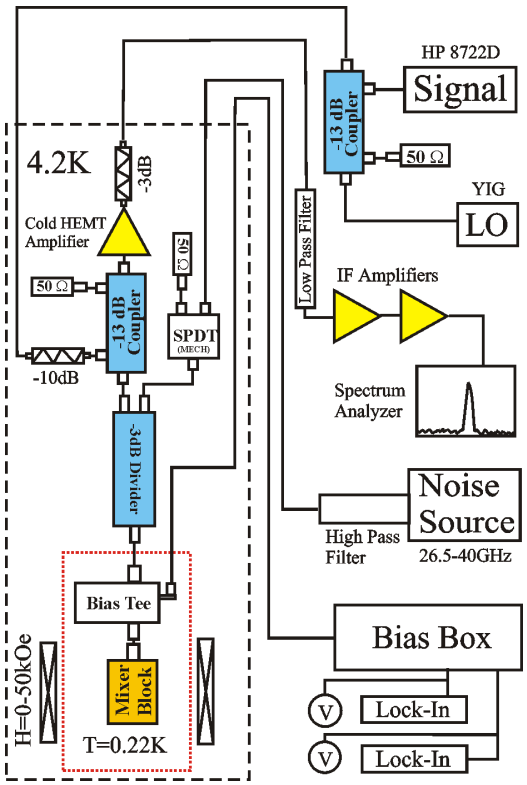

Figure 2: Measurement Setup

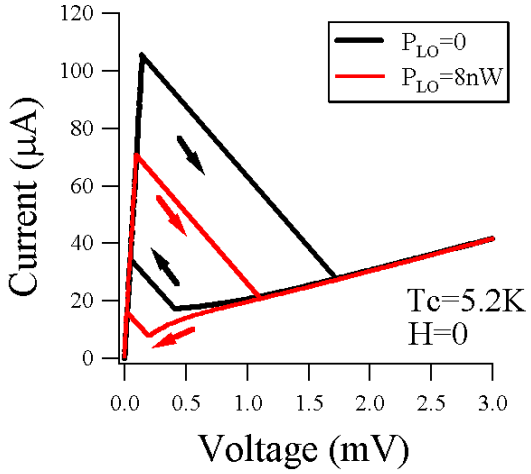

Figure 3: I-V curves in zero applied magnetic field.

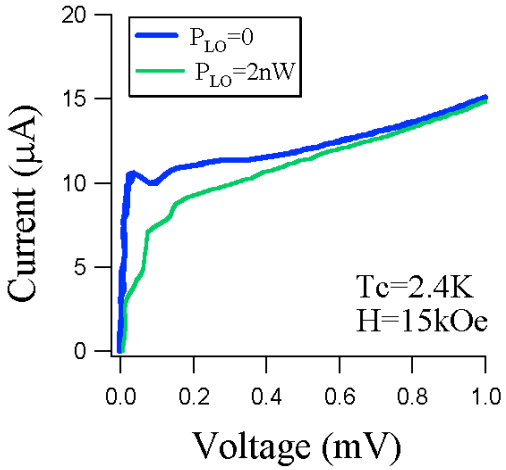

Figure 4: I-V curves in an applied magnetic field.

where L is the Lorenz constant, T_c is the transition temperature, T is the bath temperature, and R is the device resistance.[9,11] Since the bath temperature is 0.22 K, a four fold reduction is LO power is expected in this case. The LO power needed for optimum conversion efficiency with T_c=2.4 K is 6 dB lower than that with T_c=5.2K, as predicted.

C. Conversion Efficiency vs. Bias Voltage

In Fig. 5, the conversion efficiency is presented as a function of bias voltage. The bias voltage is swept from a large positive voltage down to zero. Data points corresponding to lower bias voltages where switching and/or other instabilities were observed are not shown

Both with and without a magnetic field it is possible to obtain a best conversion efficiency of –9 dB. However, the conversion efficiency varies more sharply with bias voltage when T_c is reduced. Without a field, with T_c=5.2 K, the conversion efficiency drops by 3 dB from its maximum value when the bias voltage is shifted by ~ 200 μV. In the presence of the field, the same 3dB drop now occurs when the bias voltage is shifted by ~ 90 μV. This is a considerably larger voltage range that observed with Al devices; see Table I. This Nb device, even with T_c = 2.4 K, should be much less susceptible to saturation effects than an Al HEB.

D. Mixer Noise

The mixer noise temperature is inferred from the output noise temperature and the single sideband conversion efficiency, η ($T_{M,DSB}=T_{output}/2\eta$). The thermal components of the mixer noise – Johnson noise and thermal fluctuation noise – should decrease with T_c. Such a reduction can be significant if the mixer noise is much larger than fundamental quantum noise and is dominated by thermal sources. At 30 GHz, the quantum noise limit ($T_Q=h\nu/k$) is ~ 1.4 K. The output noise when operating with maximum conversion efficiency (-9dB) decreased from 88 K to 46 K when T_c was reduced by a factor of ~ 2 from 5.2 K to 2.4 K. The corresponding mixer noise decreases approximately proportional to T_c, from 390K to 171K when T_c is 5.2K. The mixer noise increases by 3dB from its minimum value when the bias voltage is shifted by ~ 440 μV. This voltage range is smaller when T_c is 2.4K,

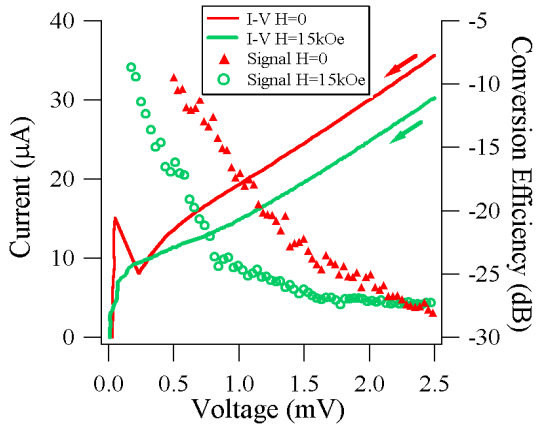

Figure 5:Conversion efficiency versus bias voltage and pumped I-V.

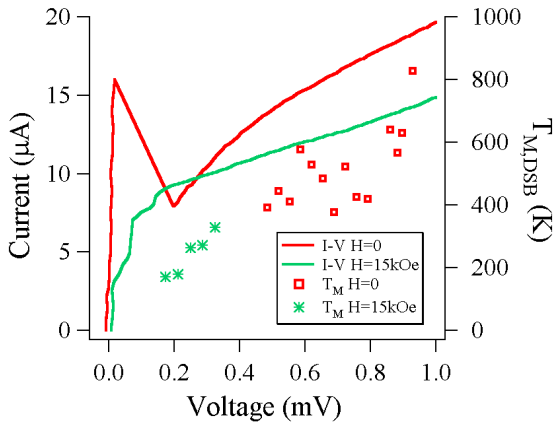

Figure 6: Mixer noise versus bias voltage and pumped I-V.

and the 3dB drop off occurs at a voltage shift of 152μV. The mixer noise as a function of bias voltage is presented in Fig. 6.

IV. Conclusions

The T_c of a Nb HEB was successfully lowered by the application of a magnetic field from 5.2 K to 2.4K. The mixing results for Nb, reduced T_c Nb, and Al HEBs are summarized in table I. The optimum conversion efficiency observed was –9dB for both values of T_c. The mixer noise temperature decreased nearly linearly with T_c. The LO power needed for optimum conversion efficiency decreased from 8nW with T_c=5.2 K to 2 nW with T_c=2.4 K, as predicted in Eq. 1. The bandwidth has previously been measured to be 2.4 GHz and was unchanged when T_c was reduced.

A 3dB drop in conversion efficiency was observed for the device for a bias voltage change of ~ 90μV. This is a considerably larger voltage range than was observed in similar studies of Al HEBs and these reduced-T_c Nb devices are much less prone to saturation effects. For example, for a 300K background and a device IF bandwidth of 10GHz, a noise voltage of ~ 20μV would be generated at the output, and thus not result in significant output saturation. Further tests are in progress to determine when input/output saturation is observable in Nb and reduced-T_c Nb HEBs, and what effects lowering T_c has on these limits. We note that the mixing data for all parameters (output noise, conversion efficiency, LO power, and DC power) obtained in zero magnetic field agree well

DEVICE	L (μm)	R_N (Ω)	P_{LO} (nW)	Conv. Eff. (η) (dB)	$T_{M,DSB}$ (K)	ΔV_{-3dB} Conv. Eff. (μV)	ΔV_{-3dB} Mixer Noise (μV)
Nb (T_c=5.2K)	0.16	90	8	-9	390	200	440
Nb (T_c=2.4K)	0.16	90	2	-9	171	90	152
Al (T_c=1.0K)	0.60	52	0.5	-8	4	~5	~5

Table I: Microwave mixing performance for Nb, reduced T_c Nb, and Al HEBs. The Al data is for device A in Ref. 5. The last two columns give the shift in bias voltage required to produce a 3dB degradation in the conversion efficiency and mixer noise temperature.

with previous microwave measurements ("optimum gain" case, Ref. 9).

Finally, Ta (T_c ~ 3-3.5 K) devices need to be fabricated and tested to see if the results reported here can be reproduced in those devices. Those devices would be used in receivers where a large magnetic field would be impractical.

References

[1] R. A. Wyss, B.S. Karasik, W.R. McGrath, B. Bumble, H. LeDuc, in *Proceedings of the 10th International Symposium on Space Terahertz Technology,* edited by T. Crowe and R.M. Weikle (University of Virginia, Charlottesville, VA, 1999), pp. 215-228.

[2] B.S. Karasik, M.C. Gaidis, W.R. McGrath, B. Bumble, H.G. LeDuc, Appl. Phys. Lett 71, 1567 (1997).

[3] E. Gerecht, C.F. Musante, H. Jian, Y. Zhuang, K.S. Yngvesson, J. Dickson, T. Goyette, J. Waldman, P.A. Yagoubov, G.N. Gol'tsman, B.M. Voronov, and E. M. Gershenzon, in *Proceedings of the 10th International Symposium on Space Terahertz Technology,* edited by T. Crowe and R.M. Weikle (University of Virginia, Charlottesville, VA, 1999), pp. 200-207.

[4] B.S. Karasik and W.R. McGrath, in *P Proceedings of the 9th International Symposium on Space Terahertz Technology,* edited by W.R. McGrath (Pasadena, CA, 1998), pp. 73-80; D.E. Prober (unpublished).

[5] I. Siddiqi et al, in *Proceedings of the 11th International Symposium on Space Terahertz Technology,* edited by J. East (U. Michigan, Ann Arbor, MI, 2000), pp. 82-94.

[6] A. Skalare et al, in *Proceedings of the 11th International Symposium on Space Terahertz Technology,* edited by J. East (U. Michigan, Ann Arbor, MI, 2000), pp. 501-512.

[7] D. W. Face, S.T. Ruggiero, and D.E. Prober, J. Vac. Sci. Technol. A 1, 326 (1983); D. W. Face and D.E. Prober, J. Vac. Sci. Technol. A 5, 3408 (1987).

[8] B. Bumble and H.G. LeDuc, IEEE Trans. Appl. Supercond. 7, 3560 (1997).

[9] P.J. Burke, R.J. Schoelkopf, D.E. Prober, A. Skalare, B.S. Karasik, M.C. Gaidis, W.R. McGrath, B.Bumble, and H.G. LeDuc, J. Appl. Phys. 85, 1644 (1999).

[10] A. Skalare, W.R. McGrath, B. Bumble, H.G. LeDuc, P.J. Burke, A.A. Verheijen, R.J. Schoelkopf, and D.E. Prober, Appl. Phys. Lett 68, 1558 (1996).

[11] P. Burke, Ph.D. thesis, Yale University, 1997, available from the authors.

[12] B.S. Karasik and A.I. Elantiev, Appl. Phys. Lett 68, 853 (1996).

Part of the research described in this paper was carried out at the Jet Propulsion Laboratory, California Institute of Technology, under a contract with the National Aeronautics and Space Administration.

The resistive transition of aluminium hot electron bolometer mixers with normal metal cooling banks

A. H. Verbruggen[a], T. M. Klapwijk[a], W. Belzig[a], and J. R. Gao[a,b]

[a] Department of Applied Physics and DIMES, Delft University of Technology, Lorentzweg 1, 2628 CJ Delft, The Netherlands

[b] Space Research Organization Netherlands (SRON), Utrecht, The Netherlands.

Abstract:

We perform a theoretical analysis based on the superconducting proximity-effect model for the resistive transition of an aluminium superconducting hot electron bolometer mixer when the cooling banks are in the normal state. We compare our calculated result with a recently reported measurement[1]. Our calculation qualitatively reproduces the observed feature in which the resistance drops quickly around T_c with decreasing temperature, but saturates at a value roughly being one half of the normal state resistance. It also opens the question about which type of cooling banks (normal or superconductor) is favourably for low noise performance.

I. Introduction

Superconducting hot-electron bolometer (HEB) mixers are currently the best candidates for heterodyne spectrometers operating at frequencies of a few THz. They combine a high sensitivity with the need for only very low local oscillator (LO) power. The operating principle is absorption of radiation by the electrons leading to an elevated electron temperature, which is thermalized to the bath temperature either by phonons (*phonon-cooled*) or diffusion to large cooling pads (*diffusion-cooled*). The elevated temperature, which is a measure of the absorbed power, leads to a resistance change exploiting the difference in resistance between the superconducting state and the normal state. Originally, it was assumed that the devices would be operating at the transition temperature of the superconductor[2]. Later it was recognized that in practice the devices are brought by a bias current into a state in which part of the bridge is normal (*electronic hot spot*) and part is superconducting[3-6]. The mixing results from a modulation of the length of the hot spot with absorbed power.

The mixers used and studied most thoroughly are based on niobium microbridges using large Au cooling pads at both ends (here we focus on diffusion-cooled HEB's). In response to theoretical estimates, predicting a higher sensitivity, broader IF bandwidth, and lower LO power, aluminium has been proposed as an attractive alternative for diffusion-cooled HEB's[1,7-9]. Unfortunately, the mixing results have so far been disappointing suggesting that a good understanding of the behavior of these nano-scaled microbridges consisting of superconducting and normal parts is lacking. In this paper we present a theoretical analysis of the resistive transition of such a system using the microscopic theory of the proximity-effect.

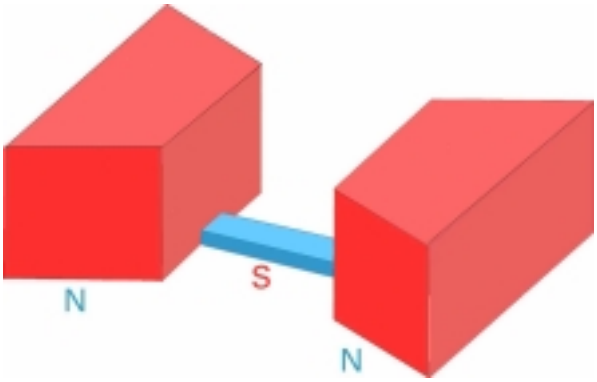

Fig.1. A schematic view of an Al superconducting hot electron bolometer mixer with normal metal cooling banks.

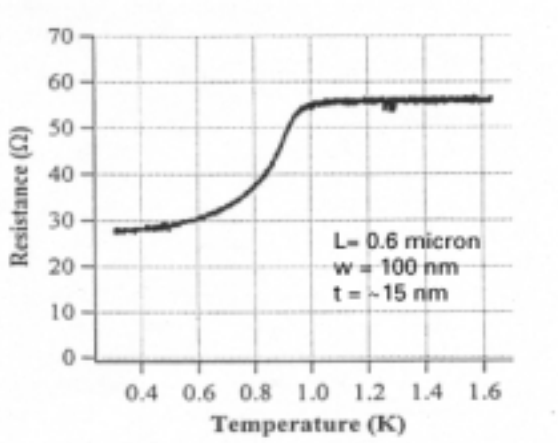

Fig.2. Resistance of 0.6 µm long Al wire as a function of temperature measured by Siddiqi *et al.*[1]

As a starting point we will use a recent observation of Siddiqi *et al.*[1] about the resistive transition of an Al HEB mixer (Fig.2). The resistance drops quickly around a temperature of 1 K, but surprisingly saturates at about 50 % of the normal state resistance even down to very low temperatures. The measured device (Fig.1) consists of a thin, narrow Al microbridge with a length of 600 nm, a width of 100 nm, and a thickness of ~15 nm. The cooling banks are in essence thick and wide Al. The intrinsic superconducting transition temperature of the Al bridge is not exactly known, but expected to be in the range of 1.5-2.4 K. The T_c of the banks is considerably lower than the T_c of the bridge, likely to be ~0.8 K. The diffusion constant of the Al microbridge equals 6 cm^2/s. For the curve shown in Fig.2 the superconductivity of the banks is suppressed by applying a magnetic field, which means that the device consists of normal pads with a superconducting microbridge (NSN).

II. Results of a model-calculation

Since the resistance of the cooling pads is negligible compared to the measured resistance the observations imply that a substantial fraction of the superconducting bridge is resistive. It is well known that the conversion of a normal current to a supercurrent at an N/S interface leads to a resistive contribution due to charge imbalance. This fact has been used by Wilms Floet *et al.*[10] in a previous attempt to model the resistive transition of HEB's. This resistive contribution only appears due to quasiparticles with energies larger than the energy gap and hence, quickly disappears below the critical temperature. Quasiparticles with energies smaller than the energy gap are assumed not to contribute to the resistance and are converted into supercurrent through the process of Andreev-reflection. As pointed out by Siddiqi *et al*[1], their observed anomalous behaviour must be related to the proximity-effect, i.e they find that the measured residual resistance corresponds to a length relating to the coherence length $\xi(T)$. A similar observation has previously been made for Pb-Cu-Pb sandwiches by Harding, Pippard, and Tomlinson[11] and subsequently explained by Krähenbühl and Watts-Tobin[12]. This implies that the assumption of Wilms Floet *et al.*[10] of a negligible contribution to the resistance for quasiparticles with energies smaller than the energy gap must be corrected. To proceed the microscopic theory for the proximity effect, based on the Usadel equations supplemented with the appropriate kinetic equation[13] must be used to calculate the spatial variation of the superconducting gap along the microbridge and the resulting contribution to

the resistance. Since we intend to focus on the issues of interest to the HEB community we neglect the details of the calculation[14] and present only the results.

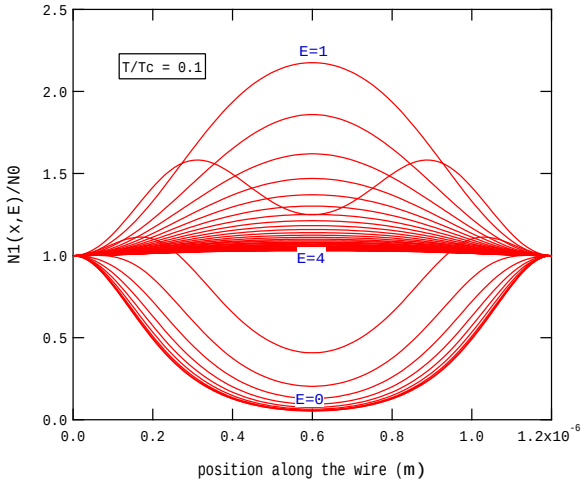

Fig.3. Density of states as a function of position along the bridge for different energies E at T/T_c = 0.1.

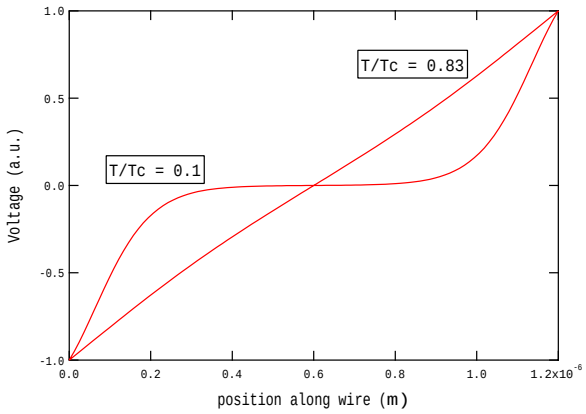

Fig.4. Penetration of the electric field in the bridge at T/T_c = 0.1 and 0.83.

Fig.3 shows the calculated density of state at different positions along the microbridge for different energies E, which is normalized to Δ(0), for T/T_c = 0.1. (The microbridge is assumed to have a length of 1.2 μm, with a bulk energy-gap of Δ(0) = 0.2 meV, and a diffusion constant 100 cm^2/s. T_c is the intrinsic critical temperature of an infinite long bridge consistent with the bulk energy gap). At the boundaries the normal metal density of state is imposed, meaning that Δ is forced to zero in N. Note that even in the middle of the bridge the density of states does not become zero as one would expect for a bulk BCS superconductor. Fig. 4 shows the electrical potential inside the superconducting bridge at T/T_c = 0.1 and 0.83. At low temperatures a substantial drop in voltage is found near the interfaces over a length scale somewhat larger than the coherence length at zero temperature $\xi(0)$, given by $0.88(\hbar D/\Delta(0))^{1/2}$. The final and most relevant result of this analysis is shown in Fig. 5.

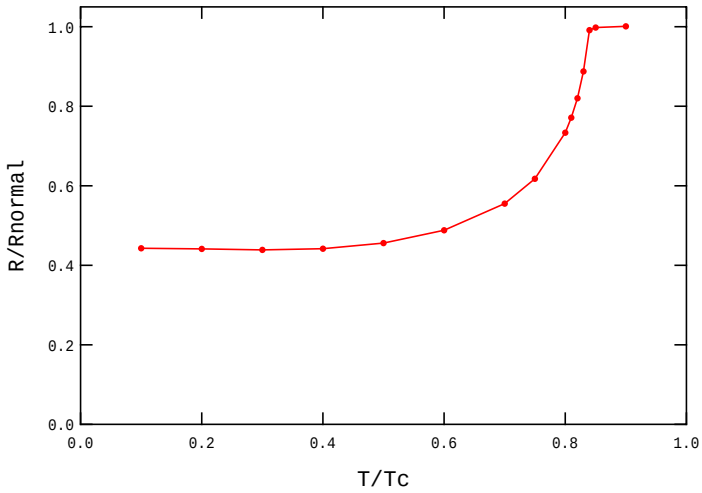

Fig.5. Calculated resistance of an Al bridge (1.2 μm long) when the bath temperature is decreased below T_c.

It shows the resistance of the microbridge as a function of temperature, reproducing very well the measured data given in Fig. 2. Note the apparent lower T_c as well as the large residual resistance of about half the normal state resistance. Unfortunately, a one-to-one correspondence to the experimental data cannot be made because the intrinsic T_c of the measured device is not known. Nevertheless, the calculation is believed to contain the essential physics demonstrating the role of the dominant parameter $\xi(0)/L$.

III. Discussion

The *R-T* curve is an important device characteristic because it provides valuable information about the superconductivity of the bridge and the cooling pads and on the interface between the bridge and the banks. However, this curve is not directly related to the mixer performance. The latter should be determined from the *I-V* curves. Unfortunately, the calculations are performed only for the linear response-regime (zero bias voltage). Nevertheless, the I-V curve is very likely governed by a thermal dissipation process starting at the NS interfaces, which is incompatible with an electronic hot spot concept used successfully for niobium HEB's. Evidently, the proximity effect influences the resistive state stronger for a HEB with a bridge length comparable to $\xi(0)$. Nb devices suffer less from the proximity effect since the length $\xi(0)$ is relatively short.

Over the question about which type of cooling banks (normal or superconductor), although no systematic study has been reported to compare the mixer performance for devices with the cooling banks in the superconducting state or in the normal state, it might be preferable for best sensitivity of also Nb HEB's to work at temperatures where the contacts are superconducting. This analysis suggests that one needs superconducting contacts for good performance of HEB mixers. With superconducting contacts, the electronic hotspot can be formed at the center of the bridge and a high conversion gain is expected from the hot spot mixing model. To avoid heat trapping due to Andreev-reflection, which will reduce the IF bandwidth, the T_c of the banks however should be lower or much lower than that of the bridge.

IV. Acknowledgements

We would like to thank D.E. Prober, I. Siddiqi, and A. Verevkin for providing information about their devices. D. Wilms Floet, W.F.M. Ganzevles, P.A.J. de Korte, and P. Yagoubov have been very helpful in discussing various experimental results on HEB's. This work is financially supported by the Stichting voor Technische Wetenschappen, which is part of the Nederlandse Organisatie voor Wetenschappelijk Onderzoek and, by ESA under contract no. 11738/95/NL/PB and a Feodor Lynen Fellowship of the "Alexander von Humboldt Stiftung" (W.B.).

V. References

1. I. Siddiqi, A. Verevkin, D.E. Prober A. Skalare, B.S. Karasik, W.R. McGrath, P. M. Echternach, and H. LeDuc, in Applied Superconductivity Conference, September, USA, 2000 (preprint)

2. D.E. Prober, Appl. Phys. Lett. **62**, 2119 (1993).

3. D. Wilms Floet, E. Miedema, T.M. Klapwijk, and J.R. Gao, Appl. Phys. Lett. **74**, 433 (1999).

4. H. Merkel, P. Khosropanah, P. Yagoubov, and E. Kollberg, Proceedings Tenth International Symposium Space Terahertz Technology, University of Virginia, Charlottesville, March 16-18, 1999. p. 592

5. A. Skalare, W.R. McGrath, B. Bumble, H.G. LeDuc, Proceedings Tenth International Symposium Space Terahertz Technology, University of Virginia, Charlottesville, March 16-18, 1999, p. 215.

6. A.D. Semenov and H-W. Hübers, in Applied Superconductivity Conference, September, USA, 2000 (preprint).

7. B.S. Karasik, W.R. McGrath, and R.A. Wyss, IEEE Trans.Appl.Superconductivity **9**, 4213 (1999).

8. A. Skalare, W.R. McGrath, P.M. Echternach, B. Bumble, H.G. LeDuc, I Siddiqi, A. Verevkin, D. E. Prober, Proceedings 11th International Symposium on Space Terahertz Technology, (ed), J. East, 1-3 May 2000, Ann Arbor, MI, USA, p. 501.

9. P.M. Echternach, H.G. LeDuc, A. Skalare, W.R. McGrath, Proceedings Tenth International Symposium Space Terahertz Technology, University of Virginia, Charlottesville, March 16-18, 1999, p. 261

10. D. Wilms Floet, J.J.A. Baselmans, T.M. Klapwijk, and J.R. Gao, Appl. Phys. Lett. **73**, 2826 (1998).

11. G.L. Harding, A.B. Pippard, and J.R. Tomlinson, Proc.R.Soc.Lond.**A340**, 1 (1974)

12. Y. Krähenbühl and R.J. Watts-Tobin, J. Low.Temp.Phys.**35**, 569 (1979)

13. A. Schmid and G. Schön, J. Low Temp. Phys. **20**, 207(1975).

14. A.H. Verbruggen, W. Belzig, and T.M. Klapwijk, (in preparation)

FABRICATION AND RECEIVER MEASUREMENTS OF A DIFFUSION-COOLED HOT-ELECTRON BOLOMETER AT 800 GHz

J. Stodolka[1], K. Jacobs
KOSMA, I. Physikalisches Institut, Universität zu Köln,
Zülpicher Str. 77, 50937 Köln, Germany

Abstract

We present a fabrication process for diffusion-cooled niobium hot-electron bolometers using a self-aligned process with gold as an initial protection layer and aluminum as an etch mask that is removed by a wet etch. This process proves to be reproducible and has a yield of ~70 % per batch. Great care has been taken to avoid processing temperatures above 120 °C to minimize degradation of the Nb film.

We have performed heterodyne measurements of an HEB in a fixed tuned waveguide mixer at 804 GHz and at an IF-range from 1-2 GHz. The approximate dimensions of the bridge are 240 x 200 x 14 nm^3. The Niobium bridge has a critical temperature of 6.0 K and a normal state resistance of 16.5 Ω. A standard Y-factor measurement leads to a minimum noise temperature of 1200 K at 1 GHz IF. The coupled LO-power is estimated by the isothermal method to be 21 nW.

Introduction

Superconducting Hot-Electron-Bolometers (HEB) utilizing thin superconducting films have become established as sensitive mixers in the THz region. The thermal response time τ can be very small if the superconductor is thin enough that only the electron gas is heated and the cooling is fast enough. The bolometers described in this paper are cooled by out-diffusion of the hot electrons in normal conducting heat sinks (diffusion-cooled HEB) rather than interactions with phonons of the lattice (phonon-cooled HEB) [1]. To meet the requirements for astronomical applications such as SOFIA, thermal response times down to several picoseconds are needed to get intermediate frequencies up to 10 GHz.

Because of $\tau \sim L^2$ [1] the dimensions of the bolometer bridge have to be very small. We have fabricated diffusion-cooled HEBs with short (L<300 nm) and narrow (<200 nm) bridges consisting of thin (10-14 nm) Niobium (Nb) on z-cut quartz substrates. The normal conducting heat sinks consist of 70 nm Gold (Au). In the following paragraph

[1] e-mail: stodolka@ph1.uni-koeln.de

we discuss problems and merits of several approaches for the fabrication of diffusion-cooled HEBs.

Device Fabrication

Aside from a good reproducibility, the essential requirement for the fabrication of a diffusion-cooled HEB is a good transparency of the interface between the heat sinks and the material of the bolometer bridge. A thermal resistance results in a slower out-diffusion of the hot electrons and thus increases the effective bridge length and thermal response time.

Defining the bolometer bridge by lift-off with subsequent deposition of the heat sinks (Fig. 1) [2] has the major disadvantage of high requirements for the overlap accuracy of the Electron-Beam-Lithography (EBL) system to position the heat sinks on the contact areas of the bridge.

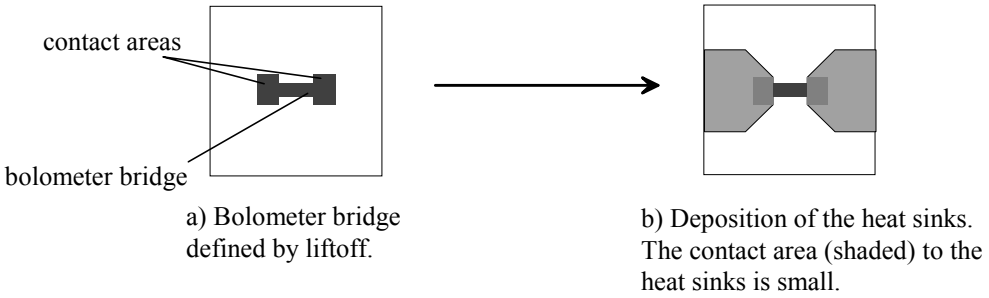

Fig. 1: Outline of HEB fabrication by lift off (top view)

A solution is offered by the self-aligned process (Fig. 2). Here, the substrate is covered with a blanket layer of Nb. The heat sinks and a metal strip of the width of the bolometer bridge are deposited in succession. The bridge is now etched out of the blanket layer by using reactive ion etching (RIE) where the heat sinks and the metal strip serve as etch masks: the spacing between the heat sinks determines the bridge length while the metal strip defines the width. The overlap between Nb and Au heat sinks is large.

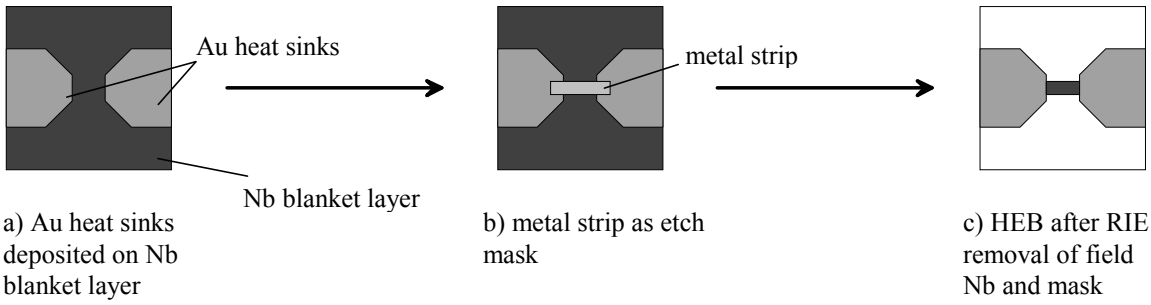

Fig. 2: Outline of self-aligned fabrication process (top view)

A self-aligned process for the fabrication of diffusion-cooled HEBs was developed at JPL [3]. It uses Au as protection layer deposited in-situ subsequent to the Nb blanket layer to prevent the Nb from oxidation and forming a thermal resistance. Au is also used as material of the metal mask for the definition of the bolometer bridge width (Fig.3).
The process requires two gold etch steps which we found difficult to control due to variations in gold thickness after the first gold etch. The second etch step, removing the gold from the bolometer bridge, is then prone to destroy the bridge or leave a Au residue.

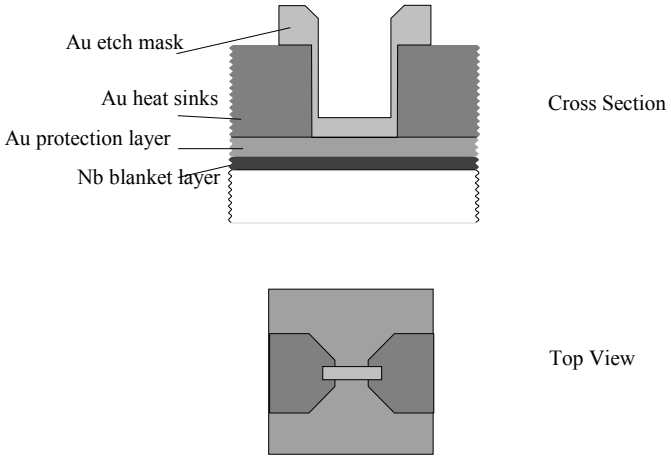

Fig. 3: self aligned fabrication process using a Au protection layer and Au etch mask

In a first effort to solve this problem we tried not to use a protection layer at all. Without a protection this leads to the oxidation of the Nb surface as the wafer is exposed to air. This oxidation layer has to be removed prior to the deposition of the heat sinks, requiring an Ar sputter etch. Unfortunately this clean step turned out to be hard to control due to the small thickness of the Nb film. This lead to irreproducible DC-characteristics of similar-sized HEBs fabricated in the same batch showing contact resistances between 1 to 35 Ohms and irregular resistance versus temperature curves. Hence, the use of an in-situ Au protection layer seems to be crucial for a good transparency of the Nb/Au interface. We chose to change the material of the etch mask from gold to aluminum (Al) to keep the protection layer, distinct from the etch mask, allowing different etch processes for the two layers with good selectivity [4]. In the following we describe the fabrication process that now has been established at KOSMA (Fig. 4).

The small lateral device dimensions down to (100 x 100) nm^2 for the bridge are patterned by Electron-Beam-Lithography (EBL) while larger features above 1 µm are defined using a Karl Süss contact aligner. For EBL we use a 496 K PMMA electron beam resist of 190 nm thickness. All metals are deposited by sputtering. After the deposition of the 12 nm Nb blanket layer and a protection layer of 15 nm Au the heat sinks are defined by EBL, sputtering of 70 nm Au and subsequent lift-off. In a subsequent Ar sputter etch

the thin Au protection layer is removed, reducing the thickness of the heat sinks by 15 nm. For a reproducible etch behaviour it is important to avoid intermetallic diffusion of Au and Nb. To this effect we introduced cooling breaks during the Au etch [Tab. 1] and keep the temperature for baking the PMMA at low 120 °C.

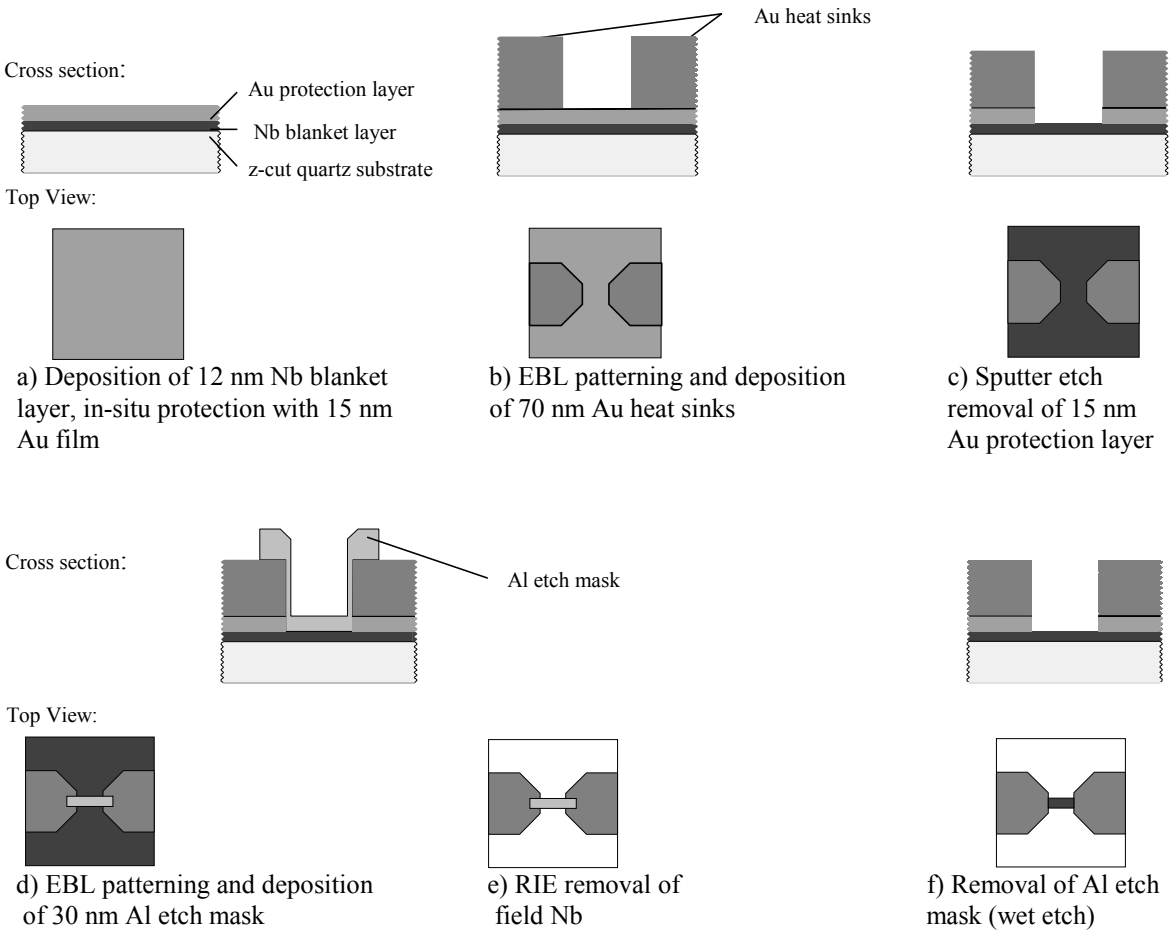

Fig. 4: Self-aligned fabrication process using an Al etch mask

In the next step the Al strip is lift-off defined by EBL and sputter deposition. It is used as etch mask in the subsequent RIE to etch out the bolometer bridge by removing the surrounding Nb. After the definition of the bridge the Al etch mask is removed by a wet etch. We use AZ726 photoresist developer. RF-sputtered SiO_2 is deposited subsequently as a protective coating to avoid degradation of the device by oxidation. The effect of thermal cycling on the coating is unknown.

Material	Process	Process gas	Pressure [Pa]	Flow [sccm]	Power density [W/cm^2]	Duration [min:sec]
15 nm Au	Sputter etch	Ar	4	8	1.1	2 x 0:30 (2:00 cooling break)
12 nm Nb	RIE	CCl_2F_2/NF_3	4	6/1.2	0.13	0:40
30 nm Al	Wet etch	(AZ726)				2:00

Tab. 1: Parameter for Au, Nb, Al etch

The advantage of this process is a very simple removal of the Al etch mask that is rather tolerant against thickness variations of the etch mask. Additionally, the advantage of using a protection layer granting an optimum transparency of the Nb/Au interface is retained. This process offers a high yield of 70-80 % per batch. HEBs of a similar size show similar RT-characteristics (Fig. 5).

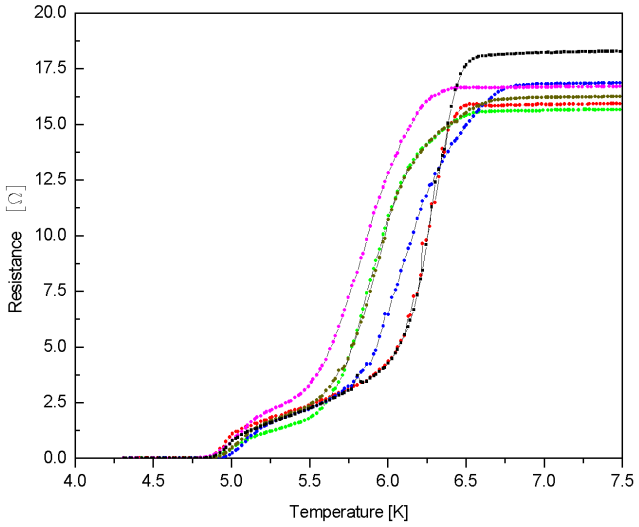

Fig. 5 : RT-characteristics of similar-sized HEBs on one wafer (∅ 22 mm), nominal device dimensions: 240 x 200 x 14 nm^3, R_{sheet}= 14 – 15 Ω. The spread in the R/T curves is probably due to small size variations of the bolometers.

Mixer mount and FTS measurements

The diced quartz substrate carrying the device is lapped down to a thickness of 35 nm and mounted into a fixed-backshort waveguide mixer optimized for performance at 800 GHz [5]. Fig. 6 shows the direct response spectrum measured with a Fourier Transform Spectrometer (FTS). The instantaneous bandwidth from 600 to 980 GHz of the HEB response is determined by the waveguide of the mixer block rather than the device itself.

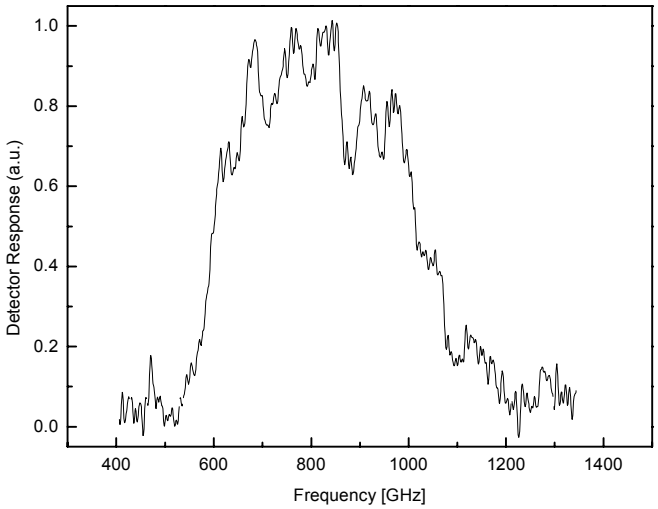

Fig. 6: FTS response of bolometer in fixed-tuned waveguide mount

Heterodyne measurement

For the receiver measurements the LO-signal is superposed with the load-signal with a 36 µm Mylar beamsplitter. A 12 Ohm resistance is connected in parallel with the device. The IF-output is fed through a 50 Ohm coaxial cable to a 1-2 GHz HEMT-amplifier.

The device dimensions and DC characteristics are listed in table 2.

Dev. Dim. [nm^3]	T_C [K]	ΔT_C [K]	I_C [µA]	R_{9K} [Ω]	R_{sheet} [Ω]
240 x 200 x 14	6.0	1.0	230	15	12.5

Tab. 2: Dimensions and DC characteristics of measured device

The device was measured at 800 and 875 GHz at intermediate frequencies from 1-2 GHz. The bath temperature was 4.2 K. The double sideband receiver noise temperature was determined by a standard Y-factor measurement. The LO power requirement was estimated with the isothermal method [6]. Best results are summarized in Table 3.

$T_{Rec, DSB}$ [K]	V_{Bias} [mV]	LO frequency [GHz]	LO power [nW]
1200	0.7	804	21
1500	0.7	875	21

Tab. 3: results of receiver measurement

Fig. 7 shows the LO-pumped and unpumped IV-curve as well as the output power for hot/cold measurements at an LO-frequency of 804 GHz and an IF of 1 GHz.

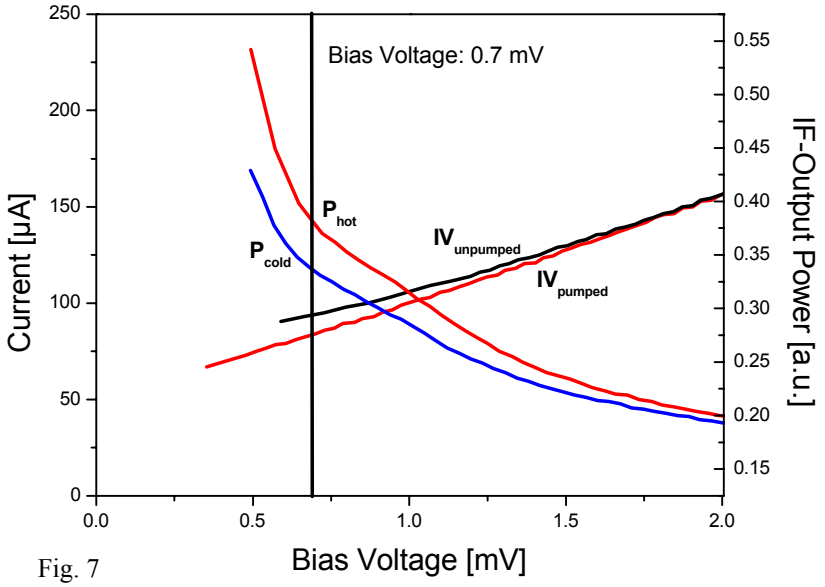

Fig. 7

The bias voltage of 0.7 mV was chosen for stability and did not show any significant shift while changing the loads. Improving the stability of the bias power supply should allow biasing at a lower voltage and thus reducing the noise temperature below 1000 K.

Conclusion

We have established a reproducible self-aligned fabrication process for diffusion-cooled Hot-Electron Bolometers using Al as etch mask. The Al strip can be removed very easily by a wet-etch. A yield of 70-80 % per batch is achieved. First receiver

measurements resulted in a receiver noise temperature (DSB) of 1200 K at an IF of 1 GHz.

Acknowledgment

We thank Michael Schultz for dicing, lapping and mounting the devices, Sybille Haas for FTS measurements and Netty Honingh for discussion. This work was supported by Deutsche Forschungsgemeinschaft (DFG) Sonderforschungsbereich 494.

References

[1] D. E. Prober, Appl. Phys. Lett., **62** (17), pp. 2119-2121, 1993

[2] K. Fiegle, D. Diehl, and K. Jacobs, IEEE Trans. Appl. Superconductivity **7**, pp. 211-214, 1997

[3] B. Bumble, H. G. LeDuc, IEEE Trans. Appl. Superconductivity **7**, 3560, 1997

[4] M. Frommberger, F. Mattiocco, P. Sabon, M. Schicke, O. Laborde, and K.F. Schuster, 11th Int'l. Symp. on Space Terahertz Technology., University of Michigan, pp.489-500, 2000

[5] S. Haas, C. E. Honingh, D. Hottgenroth, K. Jacobs, and J. Stutzki, Int. J. of Infrared and Millimeter Waves, **17** (3), pp. 493-506, 1996

[6] H. Ekström, B. Karasik, E. Kollberg, and K. S. Yngvesson, Proc. 5th Int'l. Symp. on Space Terahertz Technology, University of Michigan, pp. 169-188, 1994

An Active Zone Small Signal Model for Hot Electron Bolometric Mixers

Harald F. Merkel, Pourya Khosropanah, K. Sigfrid Yngvesson, Serguei Cherednichenko,Matthias Kroug, Aurèle Adam, Erik L. Kollberg

***Abstract*— In this paper, the influence of contact resistance between the NbN film and the Au pads on the formation of a hot spot in superconducting hot electron bolometers (HEB) is discussed. Based on a one-dimensional heat transport eq uation for electrons and phonons for the steady state, a distributed small signal model is derived. One finds that the mixing is limited to a small portion of the HEB, where the derivative of the resistivity with temperature is significantly nonzero. It is this small active zone which yields the electrothermal feedback term, not the whole device resistance as in traditional small signal models. Predicted IF bandwidth, receiver noise and conversion gain coincide very well with experimental findings.**

***Index Terms*— hot electron bolometer, hot spot, electrothermal feedback, small signal models**

I. Introduction

One-dimensional hot spot mixer models have been proposed recently for diffusion-cooled [1] and for the phonon-cooled hot-electron bolometers (HEB) [2]. In addition two-dimensional models have been proposed assuming RF skin depth as a major source of frequency dependent losses [3,4]. Here an one–dimensional large signal model incuding contact resistance is presented. From this large signal model, a distributed small signal model is derived which indicates, that only the zones, where the local resistivity of the bolometer has a significant temperature derivative contribute to the conversion gain.

As discussed in [3], hot-spot models provide reasonable predictions of the IV curves - at least for moderate and high bias voltages. There are discrepancies for small bias voltages, where the IV curves in the hot spot model have a tendency to be too resistive. A possible explanation is, that the absorbed radio-frequency (RF)-heating power is not used efficiently for small bias voltages. This can possibly be explained by taking the contact resistance of the NbN layer to the gold antenna pads into account: The superconducting NbN film in devices made at Chalmers extends under the whole antenna structure including ground planes and CPWs. So it is well justified to assume that IF- and DC current flows exclusively in the superconducting NbN layer. This stands in contrast to the RF current with a frequency close to the quasiparticle bandgap (for 600GHz and 4.2K operation temperature) or far above the gap (for 1.6THz). Almost the whole RF current flows in the thick Au top layer except in the vicinity of the NbN bridge where the RF current has to be squeezed into the NbN layer. Given a certain contact resistance and contact capacitance, a transfer region is defined in which the current crosses over from the Au pads to the NbN film. The region to be taken for the integration of the heat balance relations must therefore extend under the Au pads. Adding terms for the thermal capacity of the electrons and assuming a small time-dependent change of the temperature around an operating point results in a time-dependent, one-dimensional integro-differential small signal model. This model depends on the local temperature as well as on the electrothermal feedback where the element as a whole interacts with the load resistance. In previous papers this cumbersome step was avoided and small signal parameters were derived based on the total differential of the resistance with respect to heating powers in the operating point. These traditional small signal models show a conversion gain of the order 10dB too high [7] and various contermeasures have been proposed to explain or avoid this discrepancy ranging from empirical correction factors of the RF heating efficiency or the influence of RF skin effect [4]. For 600 GHz, RF skin depth is far too weak to explain the measured gain data [3]. In this paper, focussing on data at 600GHz, an one-dimensional linearized small signal relation for a small temperature change profile is set up. Transforming this differential equation from a small temperature to a resistance change, allows to restrict the differential equation to parts of the HEB bridge close to the critical temperature, where a small heating power change results in a significant resistance change. Hence only regions, where the derivative of the (local) resistivity with electron temperature is nonzero contribute in conversion gain. These regions are called “active zones”. The remaining part of the bolometer bridge is a passive. It acts merely as a constant parasitic series resistance. The solution of the small signal differential equation can be restricted to the active zones only. The active zones in a HEB are then treated as lumped elements in series with a passive series resistance. It is important to note, that there are two inherently different modes of operation for the HEB – for small heating powers, the center temperature does not exceed the critical temperature significantly giving rise to a single active zone on

Manuscript received February 26 2001.

This work was funded by the European Space Agency under contract number 11738/95/nl/mv.

Harald Merkel, Pourya Khosropanah, Serguei Cherednichenko and Erik Kollberg are with Chalmers University of. Technology, Gothenburg, SWEDEN. Aurèle Adam is with LGEP, Gif-sur Yvette, FRANCE, Karl Sigfrid Yngvesson is with University of Michigan, Amherst, MA. The first author’s email address is harald@ep.chalmers.se.

the center of the HEB. For larger heating powers, a normal conducting hot spot forms acting as a passive series resistance: At the boundary between the normal conducting hot spot and the superconducting rest of the bridge, two independent active zones are formed.
This splitting of the bolometer bridge in a small active part and a parasitic series resistance is also reflected in the form of the expressions for electrothermal feedback: Instead of the "usual" term proportional to $(R_L-R_B)/(R_L+R_B)$ where R_L stands for the load resistance and R_B for the resistance of the HEB in its operating point, the electrothermal feedback term becomes proportional to $(R_L+ R_B -r)/(R_L+R_B+r)$ where r is the resistance in the active zone. This agrees much better with measured results than the traditional relation. Another consequence of the Active Zone model is in the mechanisms of RF- and bias power absorption: For the large signal model it is obvious that the dc bias power (oscillating at the IF frequency at maximum) is only absorbed where the film is normal conducting or whenever the critical current of the film is exceeded. (The latter is usually not the case in the operating points of interest, critical current effects are therefore not treated in this model.) RF power is absorbed uniformly across the bridge – its frequency is above the local quasiparticle bandgap. This led to the definition of different heating efficiencies C_{dc} and C_{RF} in former Hot-Spot models. Now there is no difference in the small signal heating efficiency for RF and DC signals in the active zones – the active zone being close to the critical temperature provides always a very low quasiparticle bandgap which allows uniform RF absorption (in the active zone), for DC absorption, the local critical current is always exceeded. Nevertheless, treating the HEB as a "black" box, different heating efficiencies for RF and DC will be found: In the case of RF power, only the fraction of the power is used for mixing, which is absorbed by the active zone. The same applies to DC power – only the power absorbed in the active zone is relevant for mixing. If there is only a single active zone (surrounded by superconducting material) the whole DC power has to be taken into account. For two active zones, the situation is different, there DC power is also absorbed (and wasted) in the hot spot core, the relevant DC power is only the fraction given by the ratio of the integrated resistance of the active zones divided by the whole resistance in the operating point.

The paper is structured as follows: First, a large signal, steady state hot spot model will be set up. This model serves as a base for the derivation of a time-dependent distributed small signal model. The latter is approximated by the active zone model. Expressions for the heating efficiencies, the electrothermal feedback term, the conversion gain, the IF gain bandwidth based on the new model are derived. Finally, theoretical findings and experiment are compared.

II. Steady State Large Signal Model

The steady state large signal model consists of two parts: the first part solves for the RF and DC current distribution in the NbN film and the Au pads. It results in a concentrated RF heating in the HEB bridge and a decaying "tail" under the Au pads. Therefore even above the quasiparticle bandgap the RF power absorption in the NbN film is not homogenous. Its distribution is then inserted in the heat balance relation which is solved for the electron temperature profile along the HEB bridge. It is important to know, that for "very bad" contacts (with very low electron transparence) the RF current transfer region becomes large up to several micrometers. At the same time, the parameters for the electron conduction term are not influenced by the top layer. The situation is different for "good" contacts: Now the electron transparency is high, shortening the current transfer region to some nanometers and increasing the electron cooling under the antenna pads. This process is associated with a proximity effect reducing the critical temperature under the pads. This effect is easily seen as a "two step transition" in the R(T) curve [1] which has not been observed for NbN HEB. Hence the NbN-Au contacts seem to be of the "bad" type and the model focuses on this case assuming the electron conductivity to be constant and assigning a constant critical temperature to the NbN film all over the modeled structure.

1) Contact resistance

In addition to the resistance of the Au pads and the resistance of the NbN film, there is a detrimental contact resistance between these two metals. In order to enhance contact adhesion, a Ti layer is sputtered on top of the NbN film. This film acts in the worst case as a capacitive layer. Discretising the structure in a lumped element equivalent circuit one arrives at the circuit problem depicted in Figure 1:

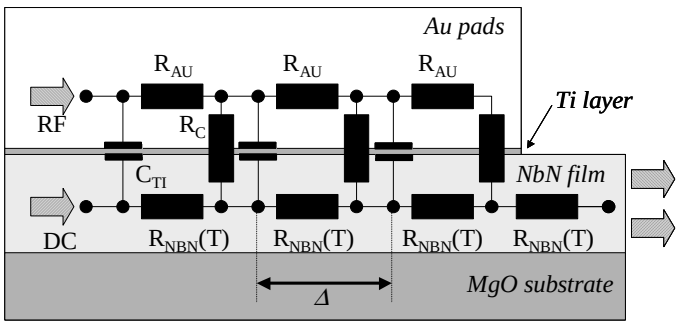

Fig. 1: Equivalent lumped element circuit for the contact resistance problem.

This equivalent circuit must be solved for RF currents and DC current separately due to difference in the capacitive coupling being negligible for DC and IF and very important for RF. IF and DC currents flow only in the gold layer, when the NbN film is heated strongly and turned normal conducting locally. The RF current "sees" a normal conducting NbN film since the RF frequency is far above the quasiparticle bandgap. As a consequence, far away from the HEB bridge, the whole RF current is transported by the thick Au film providing a series resistance two orders of magnitude lower than the thin NbN film. Nevertheless, the RF current must enter the NbN film at a certain place - at least in the bridge, all currents have to flow in the NbN film. This current transfer takes

place in a characteristic length, referred to as "transfer length". Integration of the model differential equation has to extend at least over the bridge and these transfer lengths. It is most convenient to solve the above current problem in terms of the fraction of current flowing in the NbN called n_i where i denotes the index of the current loop i. In total there are N such current loops, *1* located at the beginning of the metal pad, N deep under the pad. With a contact impedance Z_c , a gold pad (R_{AU}) and NbN (R_{NbN}) impedance per length segment Δ, one has to solve the following recurrence relation for all n_i :

$$n_i = n_{i+1} + n_N - 1 - \frac{\sum_{j=i+2}^{N} R_{Au}(1-n_j) - n_j R_{NbN}(T)}{Z_c(\omega)} \quad (1)$$

The values inserted for the resistance of the gold layer for RF calculations take the RF skin depth (30nm at 1THz at 200nm total thickness) into account by assuming the total current to flow in a layer of twice the RF skin depth. A typical result of the current distribution for several contact resistances for 600GHz for 35Å thick NbN films on MgO is depicted in Figure 2. No significant change due to the capacitance caused by the Ti layer could be observed (varying the effective plate distance in the Ti layer from 1Å to 5nm for 600GHz to 2.5THz).

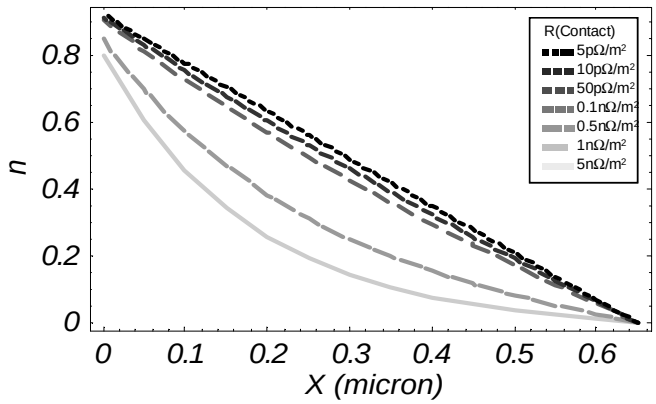

Fig. 2: Fraction of the RF current flowing in the NbN layer for contact resistances ranging from 5pΩ/m^2 to 5nΩ/m^2 for 600GHz. The calculations have been performed for a 35Å thick NbN films covered by a 100nm thick Au layer and a 5nm thick Ti layer

The above current distribution (and resulting RF heating distribution) is used in the subsequent heat balance:

2) Heat balance

For an one dimensional HEB, the heat balance equations for the quasiparticles and for phonons becomes:

$$-\frac{\partial}{\partial x}\lambda(T_e)\frac{\partial}{\partial x}T_e(x,y) + \sigma_{electron}\left[T_e(x,y)^{3.6} - T_{ph}(x,y)^{3.6}\right] = \frac{P_{LO}(y)}{L\cdot W\cdot H} + \rho(T_e)j(x,y)^2 \quad (2)$$

$$\sigma_{electron}\left[T_e^{\,3.6} - T_{ph}^{\,3.6}\right] = \sigma_{phonon}\left[T_{ph}^{\,4} - T_{bath}^{\,4}\right] \quad (3)$$

Here T_e, T_{ph} and T_{bath} are the electron, phonon and bath temperature. The HEB bridge width is denoted by W , the thickness is T and L stands for the length of the analyzed structure and x is the coordinate in length direction. The current density in the bridge is denoted by j and the resistivity is ρ. In (3) phonon diffusion is neglected. The electron-phonon cooling efficiency $\sigma_{electron}$ and phonon escape σ_{phonon} are found in [5]. The electron diffusion data are taken from [3,4,6]. Eliminating the phonon temperature approximately, one is left with a nonlinear ordinary integro-differential equation (in the case of voltage biasing):

$$-\frac{\partial}{\partial x}\lambda(T_e)\frac{\partial}{\partial x}T_e + \sigma\left[T_e^{\,3.6} - T_{bath,eff}^{\,3.6}\right] = \frac{P_{LO}(x)}{L\cdot W\cdot H} + \rho(T_e)\left[\frac{V_0}{\int_{x=0}^{L}\rho(T_e(x))dx}\right]^2 \quad (4)$$

In the above relations, $\lambda(T)$ denotes the electron thermal conductivity, σ is the effective electron-phonon cooling efficiency. L is the length of the whole HEB structure (including the RF current transfer zones under the pads), its width is given by W and the film thickness by H. The bias voltage is V_0 , $\rho(T)$ denotes the film resistivity.

III. Time Dependent Linearised Small Signal Model

Calculating the temperature profile in a one-dimensional HEB bridge during mixing, the RF heating term will consist of a large constant LO heating part and a small time varying "beat term" at the intermediate frequency. This heating power is fed into a time dependent heat balance relation taking thermal capacitance effects into account.

$$+c\frac{\partial}{\partial t}T_e - \frac{\partial}{\partial x}\lambda(T_e)\frac{\partial}{\partial x}T_e + \sigma\left[T_e^{\,3.6} - T_{bath,eff}^{\,3.6}\right] = \frac{P_{LO}(x) + 2\sqrt{P_{LO}(x)P_S}\,e^{i\omega t}}{L\cdot W\cdot H} + \rho(T_e)\left[I_0 + ie^{i\omega t}\right]^2 \quad (5)$$

Knowing a temperature distribution which fulfils the large signal model $T_0(x)$, heated by the a time averaged LO power, a small variation $\tau(t)$ around this "operating point"

temperature profile oscillating at the IF frequency ω is modeled as:

$$T(x,t) = T_0(x) + \tau(t)e^{i\omega t} \tag{6}$$

Inserting this relation in the above differential equation and linearizing

$$T^{3.6} \approx T_0^{3.6}(x) + 3.6T_0^{2.6}\tau(t)e^{i\omega t} \tag{7}$$

a first order small signal model is obtained in Fourier space where p_{DC} denotes the small signal DC power absorbed in the HEB and the thermal conductivity λ and the resistivity ρ depend still on the large signal temperature profile:

$$\begin{aligned} &+i\omega c\tau - \frac{\partial}{\partial x}\lambda\frac{\partial}{\partial x}\tau + 2.6\sigma T_e^{3.6}\tau = \\ &= \frac{2\sqrt{P_{LO}(x)P_S}}{L\cdot W\cdot H} + \frac{p_{DC}}{L\cdot W\cdot H} \end{aligned} \tag{8}$$

IV. The Active Zone Model

Further insight in the above relation is obtained by replacing the small signal temperature profile by the small signal resistivity change profile $\tilde{\rho}$ of the structure :

$$\tilde{\rho}(\tau) \approx \left.\frac{\partial\rho}{\partial T}\right|_{T_0} \tau = R'\tau \tag{9}$$

Formally multiplying (8) with the derivative of the local resistivity (R' in shorthand notation) and after some manipulations one obtains a differential equation for the small signal resistivity change, where the dependence of the thermal conductivity on the large signal electron temperature and therefore on x has been neglected:

$$\begin{aligned} &+i\omega\tilde{\rho} - \lambda\frac{\partial^2}{\partial x^2}\tilde{\rho} + 2\lambda\frac{\partial R'}{\partial x}\cdot\frac{\partial\tau}{\partial x} + \lambda\frac{\partial^2 R'}{\partial x^2}\Big/R'\tilde{\rho} + 2.6\sigma T_e^{3.6}\tilde{\rho} = \\ &= R'\left[\frac{2\sqrt{P_{LO}(x)P_S}}{L\cdot W\cdot H} + \frac{p_{DC}}{L\cdot W\cdot H}\right] \end{aligned} \tag{10}$$

Obviously the RHS of the above relation is only nonzero, where the resistivity change with the large signal temperature is appreciable i.e. around the critical temperature. Small signal power dissipated elsewhere along the HEB does not yield a contribution to the small signal resistivity change and therefore does not produce conversion gain. Hence it is only necessary to evaluate the above relation in the region, where R' is nonzero. This region is referred to as the "active zone" of the bolometer. There are two different regimes of operation for a hot-electron bolometer: For a very small hot spot, there will be a single active zone. If the hot spot grows, the zone will split and two distinct zones around the hot-spot boundary will form.

Inspection of the three diffusion-related terms in the LHS of (10) one finds a differential diffusion term (which has the same form as the large signal diffusion term). This term is reduced by a term depending on the x-derivative of R'. Assuming a single active zone, the x-derivative of the (large signal) temperature will be very small allowing to neglect this term. For two distinct hot spots, there will be indiffusion of electrons into the active zone from the "hot" side which is in principle outbalanced by outdiffusion towards the "cold" side of the active zone. This becomes obvious by assuming a constant (large signal) temperature slope across the active zone and taking into account that R' is at first order symmetric to the hot-spot boundary. The last diffusion-related term accounts for electrons being directly removed to the antenna pads leaving reducing the contribution of diffusion cooling close to the pads. This term is very small in NbN bolometers but may be important in Nb or Al HEBs. Neglecting the small diffusion terms in (9) and assuming the local resistivity derivative R' to be constant ($R'_{\max}/2$) within the active zone with length A and assuming that the small signal resistivity change profile $\tilde{\rho}$ is limited to the active zone one arrives at an algebraic equation for the small signal resistivity:

$$\begin{aligned} &\left[+i\omega c + \frac{\lambda}{2A^2} + 2.6\sigma T_e^{3.6}\right]\tilde{\rho} = \\ &= \frac{R'_{\max}}{2}\left[\frac{\frac{r}{R_N}\cdot 2\sqrt{P_{LO}(x)P_S}}{L\cdot W\cdot H} + \frac{r}{R_B}\frac{p_{DC}}{L\cdot W\cdot H}\right] \end{aligned} \tag{11}$$

In the above relation, r denotes the resistance of the active zone, R_B is the resistance of the HEB structure in its steady state operating point and R_N is the normal resistance, seen by the RF current. It has been taken into account, that the RF beating term is absorbed along the whole structure and only the part actually absorbed in the active zone plays a role for the small signal approach and that the DC power (also at IF frequency) is absorbed only, where the NbN film becomes normal conducting. The rest of the HEB not belonging to the active zone acts as a passive load and the power absorbed there does not affect the small signal conductivity and is therefore wasted. For the resistivity as a function of the IF frequency one obtains:

$$\tilde{\rho}(\omega) = \frac{R'_{\max}}{2}\frac{\left[\frac{\frac{r}{R_N}\cdot 2\sqrt{P_{LO}(x)P_S}}{L\cdot W\cdot H} + \frac{r}{R_B}\frac{p_{DC}}{L\cdot W\cdot H}\right]}{+i\omega c + \frac{\lambda}{A^2} + 2.6\sigma T_e^{3.6}} \tag{12}$$

For the active zone model, the small signal equivalent circuit is depicted in Figure 3:

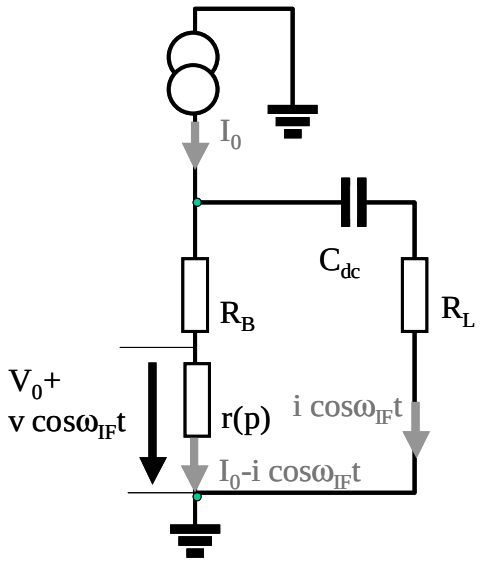

Fig. 3: Small signal circuit for the active zone mode: The heating power sensitive active zone resistor *r(p)* is in series with the resistance of the passive rest of the HEB RB. The HEB is in parallel with a load resistance R_L. The bias current is I_0.

From this equivalent circuit, the dc power dissipated in the active zone as a function of the small signal resistance change is obtained

$$p_{DC} = \left[\frac{R_L + R_B - r}{R_L + R_B + r}\right] \cdot A \cdot \tilde{\rho} \cdot I^2$$

Here r denotes the power dependent resistance of the active zone, A is the length of the active zone and $\tilde{\rho}$ is the small signal change of the resistivity in the active zone as discussed before.

This relation is inserted in (12) and yields the small signal resistance response of the HEB under the influence of electrothermal feedback from which all other small signal parameters are calculated.

In order to be able to compare this model with traditional small signal models, the heating efficiencies (with respect to DC power and RF power on an active zone with length *A*) are obtained as partial derivatives from (12):

$$C_{DC} = A \cdot \frac{\partial \rho}{\partial p_{DC}} = \frac{\frac{r}{R_B} \cdot \frac{A}{L \cdot W \cdot H} \cdot \frac{\dot{R}_{\max}}{2}}{+i\omega c + \frac{\lambda}{A^2} + 2.6\sigma T_e^{3.6}} \qquad (13)$$

$$C_{RF} = A \cdot \frac{\partial \rho}{\partial\left(2\sqrt{P_{LO}(x) P_S}\right)} = \frac{\frac{r}{R_N} \cdot A \frac{\dot{R}_{\max}}{2}}{\frac{L \cdot W \cdot H}{+i\omega c + \frac{\lambda}{A^2} + 2.6\sigma T_e^{3.6}}} \qquad (14)$$

For such a circuit, the well known “electrothermal feedback ” term (ETF) for IF frequencies far above the RC-time constant set up by the load resistance and the DC block capacitance becomes :

$$ETF = \frac{1}{1 - C_{DC} I_0^2 \frac{R_L + R_B - r}{R_L + R_B + r}} \qquad (15)$$

As expected, it is only the active zone resistance *r* which fed back by the sum of the passive zones’ and the load resistance. Taking care about the changed circuit topology, one obtains somewhat changed relations for the conversion gain, the IF gain bandwidth and as a consequence even for the noise properties. Nevertheless, the noise relations being already based on a one-dimensional approach are taken directly from [7]. The mixer time constant is prolonged by electrothermal feedback (15):

$$\tau_{mixer} = \frac{\tau_{electron\ energy\ relaxation}}{1 - C_{DC} I_0^2 \frac{R_L + R_B - r}{R_L + R_B + r}} \qquad (16)$$

This time constant is required for the conversion gain as a function of IF frequency:

$$G = \frac{p_L}{P_S} = 2 \frac{R_L}{\left(R_B + R_L + r\right)^2} \left[\frac{1}{1 + i\omega\tau_{mixer}}\right]^2 \times \times \left[\frac{1}{1 - C_{DC} \cdot \left[\frac{R_L + R_B - r}{R_L + R_B + r}\right] \cdot I^2}\right]^2 \cdot C_{RF}^{\ 2} \cdot P_{LO} \qquad (17)$$

In the following, IV curves obtained by solving a large signal model containing contact resistance and gain, noise and bandwidth curves obtained using the active zone model are summarized and compared with measurements.

V. Comparison with Experiment

Assuming a contact resistance of $25 p\Omega / m^2$ one obtains a (90%) current transfer zone extending 1μm under the antenna pad. Solving the large signal model under these conditions, one obtains IV curves for different RF heating power levels. Figure 4 summarizes measured IV curves and calculated ones for a device with the same geometry.

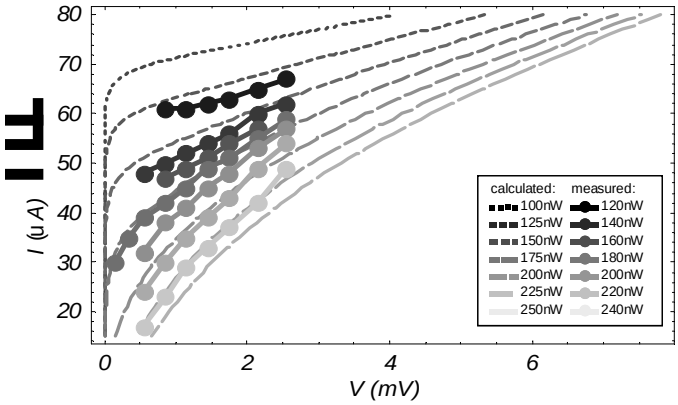

Fig. 4 Calculated and measured IV curves at 0.6THz for device M2-1.The measured curves are dots connected with solid lines; the calculated curves are dashed.

Based on these results, the RF heating efficiency C_{RF} is obtained by solving the small signal relation for the resistivity shown in Figure 5. One observes a sharp peak for the RF heating efficiency where a hot spot is formed .

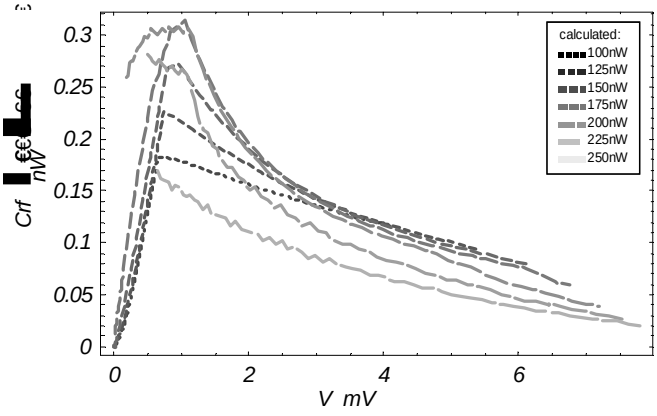

Fig. 5 RF heating efficiency for LO heating powers ranging from 100nW to 250nW in steps of 25nW for device M2-1. The calculated points correspond to the points from Fig.4. (Ed note: vertical scale is Crf(ohms/nW))

Fig. 6 depicts the fraction of RF power absorbed in the active zone related to the total small signal RF power absorbed in the HEB structure. There are clearly two distinct regions – one where the RF fraction increases monotonically (here only a single active zone is present and the hot spot is small) and another, where the RF power fraction decreases (and two separated active zones are found on the HEB).

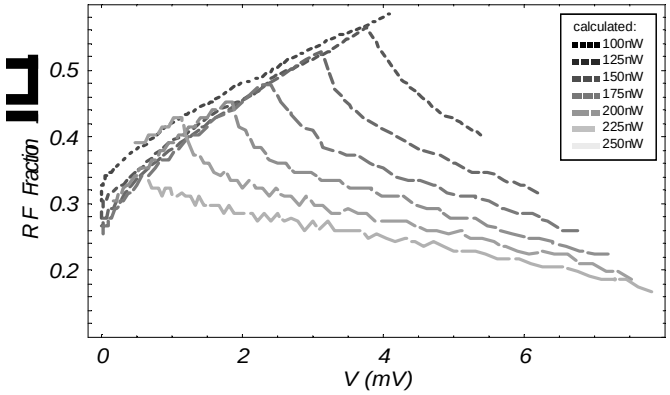

Fig. 6 Fraction of RF power absorbed in the active zone(s) LO heating powers ranging from 100nW to 250nW in steps of 25nW for device M2-1. The calculated points correspond to the points from Fig.4 and 5.

The calculated and experimentally obtained conversion gain at 1.5GHz is shown in Fig. 7. For the experiments, the optical losses have been assumed to be 3.5 dB.

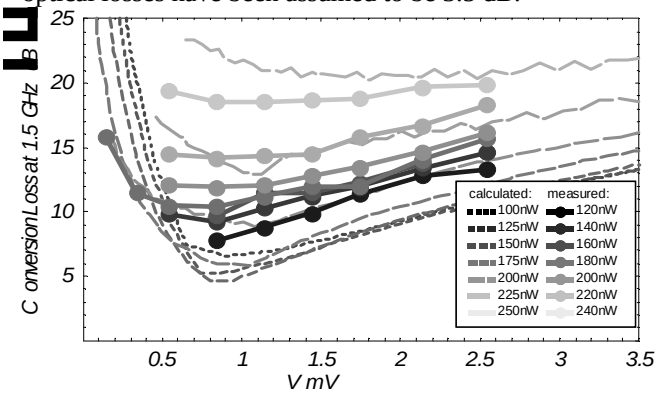

Fig. 7 Conversion loss as a function of bias current and LO power for the device M2-1. The measured and calculated points correspond to the points from Fig. 4 through 6.

For an intrinsic bandwidth of 5.5GHz one obtains an IF bandwidth as a function of bias voltage and LO power as follows. Observe the "peaks" of the bandwidth, where the active zone splits.

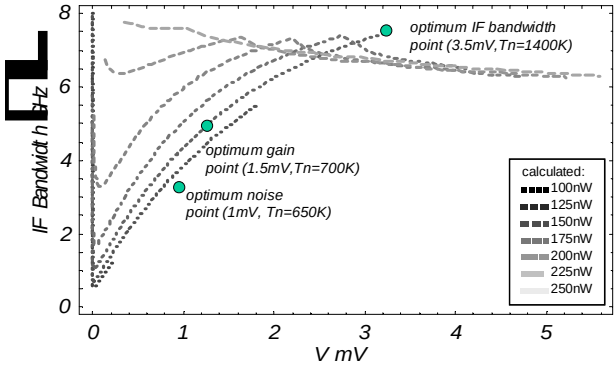

Fig. 8 IF bandwidth for device M2-1. The measured points are obtained for the points with the best noise, the best gain and the best IF gain bandwidth. The measured receiver noises (including optics losses) are indicated.

For the device output noise one assumes the HEB to "see" a room temperature load at its input. This is not really true, since at least a fraction α of the optical losses are cold losses. For the output noise temperature one obtains where T_{noise}^{out} denotes the output noise, T_{TFn}^{out} the Thermal fluctuation noise at the output and T_{Jn}^{out} denotes the Johnson noise at the output:

$$T_{noise}^{out} = T_{TFn}^{out} + T_{Jn}^{out} + 2\times\left[295\alpha + 10(1-\alpha)\right]\times G \quad (18)$$

The (overestimated) output noise assuming 295K at the input and $\alpha=1$ is shown in Figure 9.

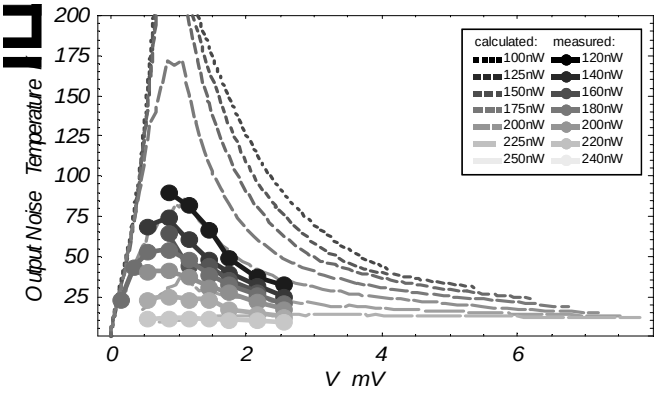

Fig. 9 Total Output Noise for the device M2-1 where the losses are at 295K, optical losses of 3.5 dB have been subtracted.

The DSB receiver noise temperature is then calculated using:

$$T_{RX,DSB} = T_{TFn,DSB}^{in} + T_{Jn,DSB}^{in} + \frac{T_{IF}}{2G} \quad (19)$$

where T_{IF} is the noise contribution from the low noise IF amplifier (≅7 K) and G is the conversion gain. The results are indicated in Fig 10:

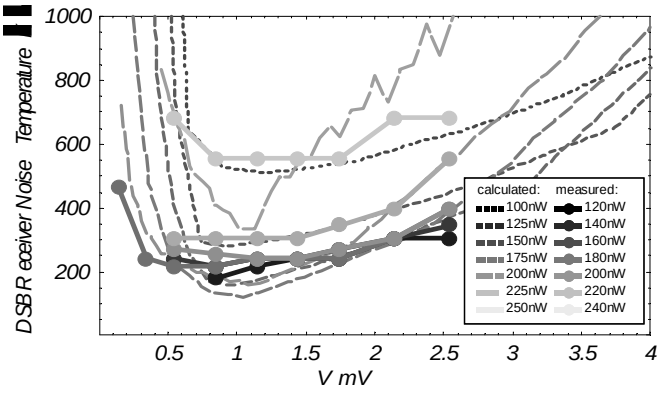

Fig. 10 Total Receiver Noise for the device M2-1. For the optimum point a receiver noise of about 600K is measured. In the measurement data, optical losses of 3.5dB have been subtracted, the IF amplifier's noise temperature is 7K.

VI. Conclusion

Besides the influence of contact resistance between the Au pads and the NbN film, a new small signal model for a hot-electron bolometric mixer is presented. The model uses the fact, that only a small part of the HEB bridge actually takes part in the conversion and mixing process. Therefore the small signal power absorbed in other regions of the HEB is wasted reducing the obtained conversion gain. For measurements at 600GHz, theoretical and experimental results show excellent coincidence improving the prediction capability of hot spot models considerably.

VII. References

[1] D.W. Floet, F. Miedema, J.J.A. Baselmans, T.M. Klapwijk, J.R. Gao, "Resistive Behavior of Nb Diffusion Cooled HEB", IEEE Trans. APS Vol.9 No..2 June 1999, pp.3749-3752

[2] H. Merkel, P. Khosropanah, E. Kollberg, "A hot-spot mixer model for phonon-cooled NbN hot electron bolometric Mixers", IEEE Trans. APS Vol.9 No2 June 1999, pp.4201-4204

[3] H.F. Merkel, P. Khosropanah, S. Cherednichenko, K. S. Yngvesson, A. Adam, E. L. Kollberg, "A Two-Dimensional Hot-Spot Mixer Model For Phonon-Cooled Hot Electron Bolometers " , IEEE Trans. ASC (in press)

[4] Yu. Semenov et al, Proc. THz 2000, Ann Arbor MI .

[5] E.M. Gershenzon, et al. "Wide band High-speed Nb and YBaCuO Detectors", IEEE Trans. Magn. **27**(2). 1991, p.2836-2839

[6] H. Merkel, P. Khosropanah, P. Yagoubov, E. Kollberg "A Self-Consistent Hot-Spot Mixer Model for Phonon-Cooled NbN HEB", Inst. Phys. Conf. Ser. **167**(2) p.699-701

[7] P.Khosropanah, H. Merkel, S. Yngvesson, A.Adam, S. Cherednichenko, E. Kollberg, "A distributed device model for phonon-cooled HEB mixers predicting IV characteristics, gain, noise and IF bandwidth", Proc. 11th ISSTT Ann Arbor, MI May 2000

[8] P.Khosropanah, et al. this issue Proc. 12th ISSTT San Diego, CA February 2001

Ballistic Tunneling Transit Time Devices for THz Power Generation

J. East and G. Haddad
Solid State Electronics Laboratory
The University of Michigan

Abstract

Existing transit time devices such as IMPATT and TUNNETT diodes are based on semiconductor structures. These devices have transit times and operating frequencies that are limited by the saturated velocity in the semiconductor material, the physics of carrier injection, the dielectric constant and the critical field for breakdown.. The combination of a transit time and a capacitive reactance that scales with frequency results in a power and frequency scaling law of the form $P_{rf} \times f^2 \propto C_{material}$, where $C_{material}$ is a constant that depends on the material parameters. An ideal device would have ballistic carriers and a relative dielectric constant equal to 1. This is the basis of the proposed Ballistic Tunneling Transit Time Device (BT^3D), a new transit time device with a vacuum drift region and a tunneling injector. The design and performance of this new device will be described in this paper.

I. Introduction

Local oscillator sources are a key component of submillimeter and THz systems. Fundamental semiconductor sources such as Gunn and IMPATT devices are available at lower frequencies. Harmonic multiplier chains using semiconductor varactor diodes can produce modest amounts of power at THz frequencies. Optical sources based on photoconductive mixing of two locked lasers are under investigation. Gas lasers, although large and complex, can produce milliwatts of power over the desired THZ frequency band. However, these existing sources have limitations for space based applications. The solid state electronic and optical sources do not yet produce enough power to pump Schottky diode mixers and barely produce the required power for HEB mixers. The gas lasers are too large and require too much prime power for space based applications. An alternative source is needed. In this paper

we propose the Ballistic Tunneling Transit Time Device (BT^3D), a vacuum based alternative to conventional transit time devices. The device structure and dimensions will be discussed in the next section. Section III will describe a simple computer simulation to investigate the power and frequency characteristics of these new devices. Several micromachined approaches to the fabrication will be discussed in Section IV. A brief summary and conclusions will be given in Section V.

II. Ballistic Tunneling Transit Time Devices(BT^3D)

Conventional semiconductor transit time devices are limited by saturated velocities and carrier injection physics. The resulting tradeoff between available power and frequency is of the form $P_{available} \times f^2 \propto C_{material}$, where $C_{material}$ is a constant that depends on material parameters such as the saturated velocity, dielectric constant and critical electric field for breakdown. A vacuum is an ideal drift region with a carrier velocity that is ballistic rather than saturated, a relative dielectric constant of 1 and a very high breakdown field. This is the basis of the Ballistic Tunneling Transit Time Device (BT^3D) to be discussed in this paper. An ideal structure is shown in Fig.1 a. The device is a diode with a micromachined field emitter cathode, a drift region and a collecting anode, all sealed in a vacuum. This small structure is mounted across a waveguide as shown in Fig. 1 b. A voltage is applied through a bias circuit that provides RF isolation. The applied voltage combined with the device dimensions will set up an electric field across the drift region. If proper magnitude DC and RF fields are present at the cathode, field emission will occur at the cathode tips. These carriers will be accelerated across the drift region and collected at the anode. The acceleration and resulting transit time will depend on the applied voltage and the dimensions. With a proper design this transit time effect can produce RF power. The combination of the drift region length and the bias voltage will determine the operating frequency of the device. If we assume a transit time equal to the inverse of the frequency, then we can find the required voltage vs. drift region length for different frequencies. This is shown in Fig. 2. The voltages and dimensions for THz structures are within the ranges that can reasonably be fabricated with micromachining techniques.

The next step is to investigate the transit time characteristics of this ballistic

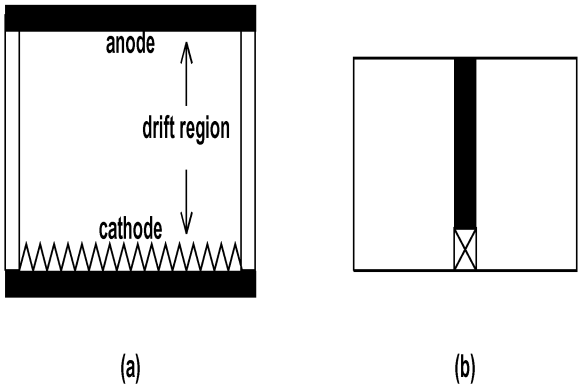

Figure 1: BT^3D (a) Structure (b) Waveguide Mount

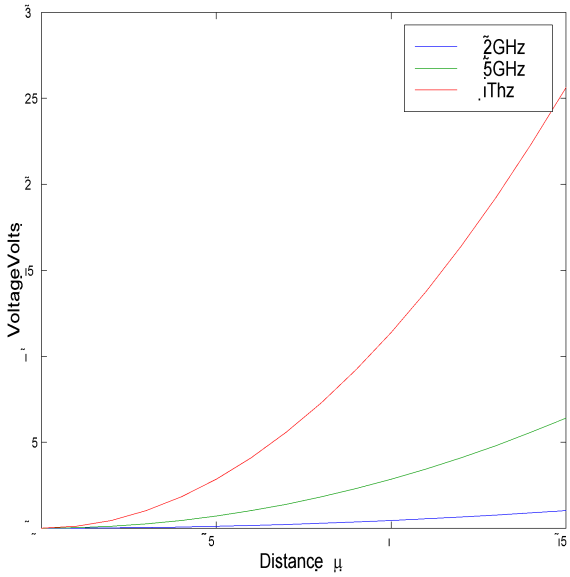

Figure 2: BT^3D Voltages and Transit Region Lengths for Different Frequencies

structure. An ideal semiconductor transit time device has carriers traveling at a constant saturated velocity. The resulting induced current waveform is rectangular, with a starting phase θ_{inj} at the injection angle and a width θ_d equal to the drift angle. The BT^3D carriers will have a constant acceleration so the resulting induced current is triangular, again starting at the injection angle θ_{inj} with a drift angle θ_d. This form of the device injected current can be used to estimate the available power and frequency response for various BT^3D designs. However, a more realistic analysis depends on the properties of the cathode injector.

The cathode is a field emitter with a current vs. voltage characteristic that depends on the electric field at the tip, the geometry of the tip and the preparation of the surface. The properties of the cathode are critical to the device performance. However, the basic form of the cathode current is an exponential dependence on the voltage or the cathode field, with the peak current occurring at the $\pi/2$ phase point. We can write a computer simulation to obtain the injected and induced currents for a range of RF conditions. The analysis is more complex than a corresponding semiconductor transit time device. In a semiconductor all the carriers within the drift region have the same velocity, and the induced current can be obtained by integrating over the charge within the device. For a BT^3D the carrier acceleration is constant and the velocity depends on the amount of time the carriers spend in the drift region. A double integration over time and injection angle is needed to obtain the induced current. A computer simulation has been written to investigate this problem. The simulation predicts the large signal induced current waveform of the device. The ratio of the Fourier components of the fundamental RF current and the RF voltage gives the device admittance. This, along with the RF voltage, the embedding impedance and the parasitic resistance gives the available power into a matched load. This information can then be used to investigate a variety of device structures, bias conditions and operating frequency ranges. Some example calculations will be discussed in the next section.

III. Example Performance Calculations

This section will describe BT^3D performance for a range of bias conditions and operating frequencies. However, before discussing the simulation results,

it is interesting to look at a simple approximation for the device performance. The injected current waveform for constant DC current density and a varying RF voltage is shown in Fig. 3. Although the details of the injected current will depend on the physics of the cathode, the general form is a sinusoidal waveform at small RF voltages that quickly becomes a sharp pulse around $\pi/2$ for larger RF voltages. The resulting induced current waveform under sharp pulse operating conditions will have a fundamental Fourier component that is $\propto J_{dc}$ and is independent of the RF voltage. The device conductance, $G_{electronic}$, will be

$$G_{electronic} \propto \frac{J_{dc}}{V_{rf}}, \tag{1}$$

and the RF power will be

$$P_{rf} \propto G_{electronic} \times V_{rf}^2 \propto J_{dc} V_{rf}. \tag{2}$$

The available RF power depends on the DC current density and the RF voltage. From this approximate large signal model for BT^3D operation we can make some predictions about the power and frequency response that we can expect. First consider the small signal G-B plots for a BT^3D with a design center frequency of 1 THz operating over a frequency range between 700 and 1300 GHz with a DC current density between 100 and 500 A/cm^2. The corresponding small signal G-B plot is shown in Fig. 4. This figure shows many of the basic characteristics of this device. The device has a conductance that depends on the DC current density. Reasonable current densities will be needed to obtain useful powers and to match the device to an external circuit. Second, the device has a very broad bandwidth, 600 GHz in this case for a 1 THz center frequency. Finally, the device has an excellent -Q compared with conventional semiconductor transit time devices. The will allow easier matching and reduce the effect of parasitic resistance. The -Q value for the 500 A/cm^2 case is nearly 1. Next consider this device operating under large signal conditions. Large signal G-B curves for the device of Fig. 4 are shown in Fig. 5 for a device with a DC current density of 200 A/cm^2 and an RF voltage between 0.005 and 0.2 volts. This figure shows the effect of the sharp pulse injection on device operation with the device conductance decreasing with increasing RF voltage. This will effect the device impedance levels, area and output power.

In order to extract power from the device, the circuit impedance must conjugate match the device impedance. This condition sets the device area.

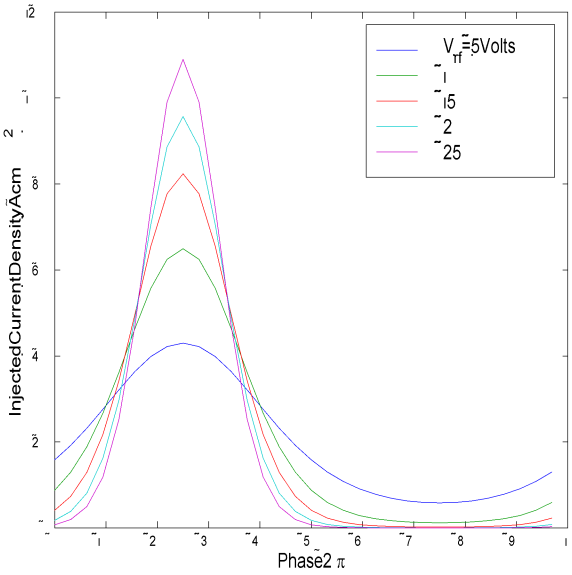

Figure 3: Example Injected Current Waveform

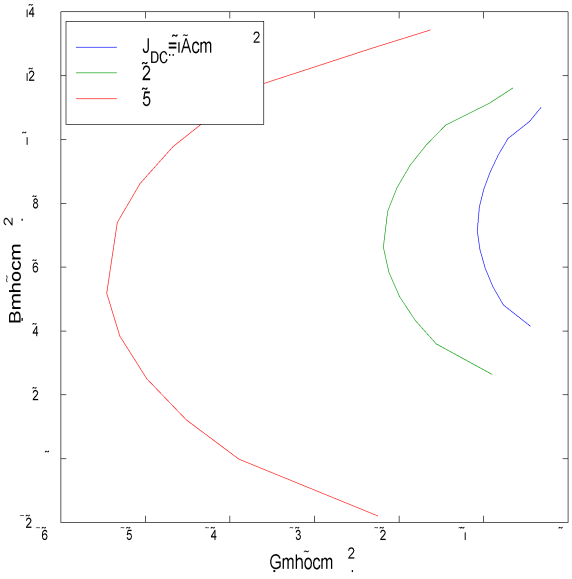

Figure 4: Small Signal G-B Plot, Frequency = 700-1300 GHz, $J_{dc} = 100, 200, 500 A/cm^2$

Typical realistic circuit impedances are several Ω's. We must include the effect of parasitic loss to get a more realistic power prediction. If the load resistance is R_{load} and the parasitic resistance is R_s, then

$$-R_{device} = R_{load} + R_s, \tag{3}$$

where R_{device} is the real part of the device impedance obtained from the inverse of the device admittance including the device capacitance. The power into the load is

$$P_{load} = \frac{R_{load}}{R_{load} + R_s} P_{rf}. \tag{4}$$

We can use this equation along with the calculated device properties to estimate the available RF power. The properties of the device can best be investigated with a sample calculation. Consider a BT^3D with a design center frequency of 1 Thz, a DC current density of 1000 A/cm^2, a drift region length of approximately 0.7 μ and an applied DC voltage of 9.8 volts. We define the small signal admittance at an RF voltage value of 0.025 volts. The area of the device will depend on the external circuit matching resistance. Device areas for matching resistances between 0.5 and 5 Ω are shown in Fig. 6. This figure shows the effect of the higher electron velocity and lower dielectric constant on the device dimensions. This device has a much longer drift region and larger diameter, 20 to 50 μ, than a comparable frequency semiconductor device. This compensates for the lower current density, higher operating voltage and smaller V_{rf}/V_{dc} ratio to produce reasonable powers at THz frequencies. The available power into a matched load depends on the value of the matching resistance and the parasitic resistance. The estimated power for this device is shown in Fig. 7 for RF voltages between 0 and 0.5 volts and small signal load resistances of 1 to 3 Ω. The solid lines are the available power from the device and the dashed lines correspond to a parasitic resistance of 1Ω. This device is producing 2 mW at 1 THz, excellent performance for any electronic device at this frequency.. The low device -Q allows an increase in matching resistance at low RF voltages and reduces the parasitic resistance effect.

The device properties strongly depend on the DC and peak current density of the cathode. The variation in output power with RF voltage for a range of DC current densities is shown in Fig. 8. The device is operating at 1 THz. The load resistance is 3Ω and the parasitic resistance is 1Ω. This figure shows

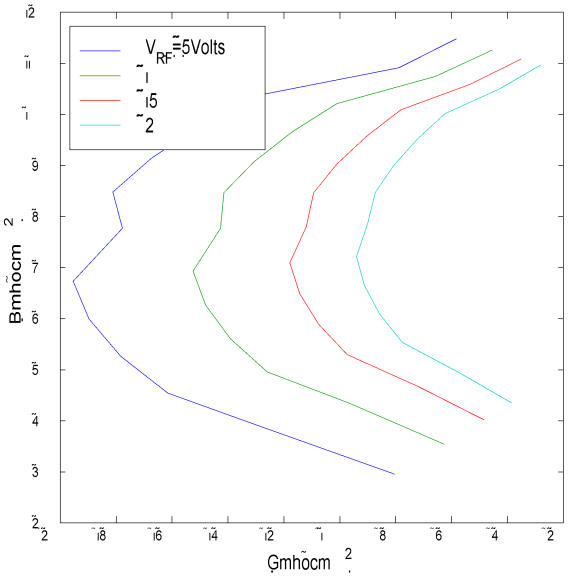

Figure 5: Large Signal G-B Plot, Frequency = 700-1300 GHz, $J_{dc} = 200A/cm^2$, V_{rf} = 0.05,0.1,0.15,0.2 Volts

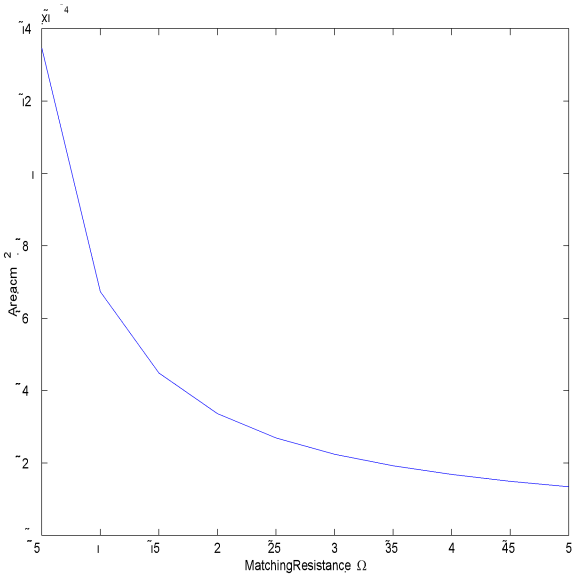

Figure 6: Small Signal Device Area $J_{DC} = 1000A/cm^2$

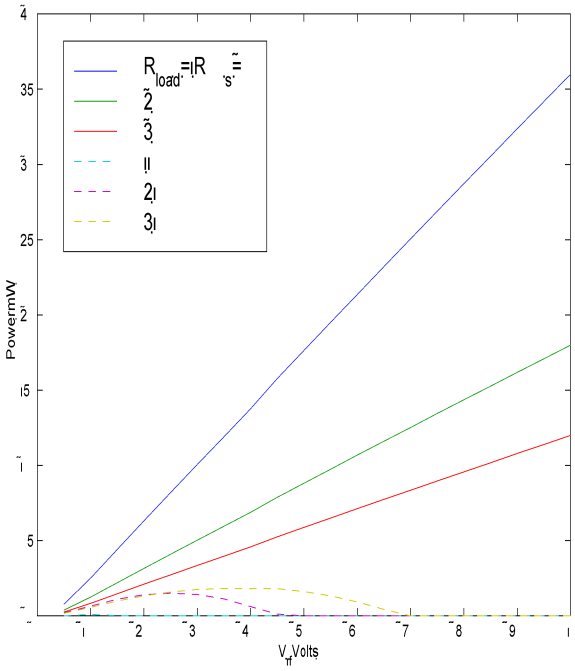

Figure 7: Output Power vs. V_{rf},Frequency = 1THz,$J_{dc} = 2000\ A/cm^2$

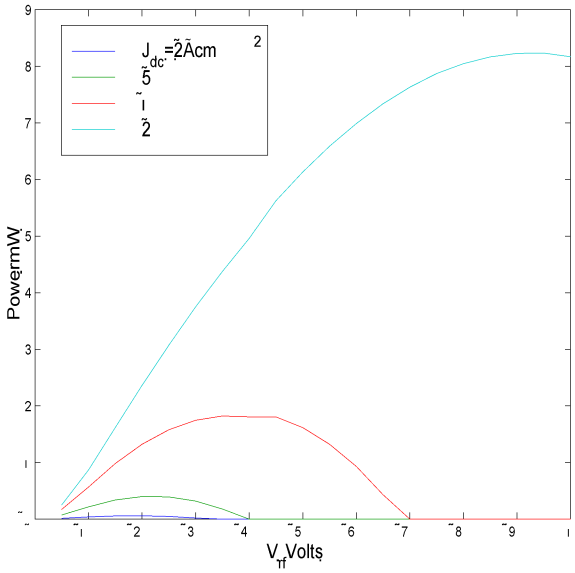

Figure 8: RF Power vs. RF Voltage for a Range of DC Current Densities,Frequency = 1 THz

the critical importance of current density on device performance. Increasing the DC current density increases the device negative conductance and the area required to match the load impedance. The combination produces nearly 10 mW of output power for a current density of $2000 A/cm^2$, excellent performance for any electronic device at THz frequencies.

IV Device Design and Fabrication

The discussion in the first part of this report gave the design dimensions and operating conditions for the proposed BT^3D device. However it is also important to think about the design and fabrication of realistic device structures. A proposed device structure was shown in 1. This would be a vertical emitting structure with the electric field and drift region perpendicular to a planar cylindrical cathode. The critical properties would be the current vs. field characteristics of the cathode, the voltage across the drift region, the length of the drift region and the resonant frequency of the rest of the micromachined cavity. We would also need to couple energy out of the cavity and into a waveguide or quasi-optical coupling network. We would also need to provide DC isolation between the cathode or anode and the rest of the structure. An alternative approach would be to design and fabricate a horizontal emitter with the drift region defined on the same wafer as the cathode. It could be fabricated on the surface of a semi-insulating semiconductor or other support structure. The substrate is assumed to be semi-insulating. A backing conductor material, a thin cathode material and a second support material are deposited onto the substrate. A vertical etch can be used to expose the three layers on the cathode side of the device, and a second etch can be used to etch back the backing material, allowing a very thin pointed cathode tip to be formed. The vertical dimension of the tip depends on the starting material thickness and not on lithography or other nanometer scale process. The width or depth of the cathode can be adjusted to give the proper capacitance and device impedance. A similar set of fabrication steps can be used to form an anode. A natural outcome of the process is a drift region length determined by lithography. A second cavity half would be placed on the top of the wafer to complete the structure. This configuration could be extended to form a portion of a ridge waveguide. In this configuration the resonant frequency could be determined by either a fixed or tunable backshort. Care would be needed to provide a vacuum in the structure. This

alternative structure may have fabrication advantages when compared with the vertical structure.

V Summary and Conclusions

This paper has discussed a new THz device, the BT^3, a vacuum based transit time device. This device appears to be able to generate reasonable and useful amounts of power in the THz frequency range. The transit region dimensions and voltages have reasonable values for devices operating between 500 and 1500 GHz. The unanswered question that most effects the device performance is cathode design. However if cathode current densities in the range of 1000 A/cm^2 can be realized, this should prove to be a very useful new device.

Millimeter Wave Generation Using a Uni-Traveling-Carrier Photodiode

T. Noguchi, A. Ueda, H.Iwashita, S. Takano,
Y. Sekimoto, M. Ishiguro,
T. Ishibashi†, H. Ito†, and T. Nagatsuma††

Nobeyama Radio Observatory
†NTT Photonics Laboratories
††NTT Telecommunications Energy Laboratories

Abstract

We have designed a new photomixer using a uni-traveling carrier photodiode (UTC-PD) for generation of W-band radiation. The UTC-PD is integrated on a InP chip with DC and RF circuits and the chip is mounted upside down on a fused quartz substrate which is placed in a microstrip channel across a quarter-height W-band waveguide. A simple cross-shaped microstrip-waveguide transition printed on the quartz substrate is used to couple power into the waveguide. From the simulation it is found that this microstrip-waveguide transition can give better than -15 dB return loss over 75–120 GHz. The UTC-PD is irradiated by combined two lasers from the back side of the InP chip. We have successfully produced difference-frequency radiation at 100 GHz with a power level of ~1 mW by the photomixer.

Introduction

Millimeter- and submillimeter-wave heterodyne mixers based on the Superconductor-Insulator-Superconductor (SIS) junctions have used a local oscillator (LO) source which is a combination of a Gunn diode and multipliers. Since the LO source with the combination of a Gunn diode and multipliers has a mechanical complexity and poor frequency coverage especially at submillimeter wavelength, a compact and mechanically-simple LO source with broad frequency coverage is highly required for submillimeter-wave SIS receivers in the radio telescopes. Photomixers, which generate a difference frequency of two diode lasers at millimeter and submillimeter wavelength by photoconductive mixing, have been alternatively developed.[1, 2] Photomixers are so compact solid-state sources with broad frequency tunability that they meet the requirement for the LO source of the SIS receivers at millimeter and submillimeter wavelengths.

The low-temperature-grown (LTG) GaAs films have been prevailingly used for a photomixer element. Although the LTG-GaAs photomixers can provide enough output power for a few applications such as molecular spectroscopy, improvement of the output power is

highly required for many applications. It has been recently shown that photomixers using a uni-traveling photodiode (UTC-PD) have a great potential for generation of millimeter-wave radiation with a bandwidth as high as 220 GHz [3]. Based on a simple analysis, it is expected that a 3-dB falloff bandwidth of the UTC-PD determined by carrier traveling time can be in a THz range [4]. The UTC-PD photomixer has emerged as one of the promising candidates to generate the millimeter- and submillimeter-wave radiation.

We have designed a new photomixer using the UTC-PD for generation of W-band radiation. In this paper, a detailed design of the photomixer at W band using the UTC-PD and preliminary results of millimeter-wave generation experiments at 100 GHz will be presented.

Instrument Design

A. UTC-PD device

Since an upper frequency of photo-response in a photodiode is usually limited by a carrier traveling time in a depletion layer in the photodiode, reduction in thickness of the depletion layer is necessary for increasing the upper frequency of photo-response. However, the reduction in thickness of the depletion layer is inevitably accompanied with an increase of capacitance of the photodiode. As a result, the upper frequency of photo-response is sometimes limited by a time constant of the photodiode.

In the UTC-PD, a relatively thick depletion layer made of a wide band-gap material such as InP is adopted to avoid the increase of the diode capacitance. A schematic energy diagram of the UTC-PD is shown in Fig. 1. Photocarriers are generated in an absorption layer of p-type InGaAs and drift into the depletion layer (or collection layer) made of InP. The electron velocity in the InP layer is so high that the traveling time in the depletion layer can be small. Therefore, very fast photo-response in the UTC-PD can be expected.

A 6-μm UTC-PD is integrated on a 150-μm-thick semi-insulating InP chip with DC and RF circuits. A photograph of the UTC-PD chip is shown in Fig. 2. The UTC-PD is assumed to have 25-Ω resistance in parallel with capacitance of 20–30 fF during design of the RF circuit. The UTC-PD is coupled with a tapered stripline transition which transforms an output impedance of the UTC-PD to 50 Ω. The diode capacitance is tuned out by a parallel inductance terminated by radial stubs as RF shorts.

B. Photomixer mount

We have designed a photomixer using the UTC-PD for generation of W-band radiation. Because of efficient transmission of power over a broad bandwidth, our photomixer mount uses waveguide at its output. The UTC-PD chip is placed in a shielded microstrip channel in order to simplify integration of impedance transformers and filters into the photomixer mount.

A simple cross-shaped probe of microstrip-to-waveguide transition printed on a quartz substrate is used to couple power into the waveguide. A surface of the quartz substrate, on which a conducting microstrip is printed, is oriented to an waveguide backshort.[5] Since it

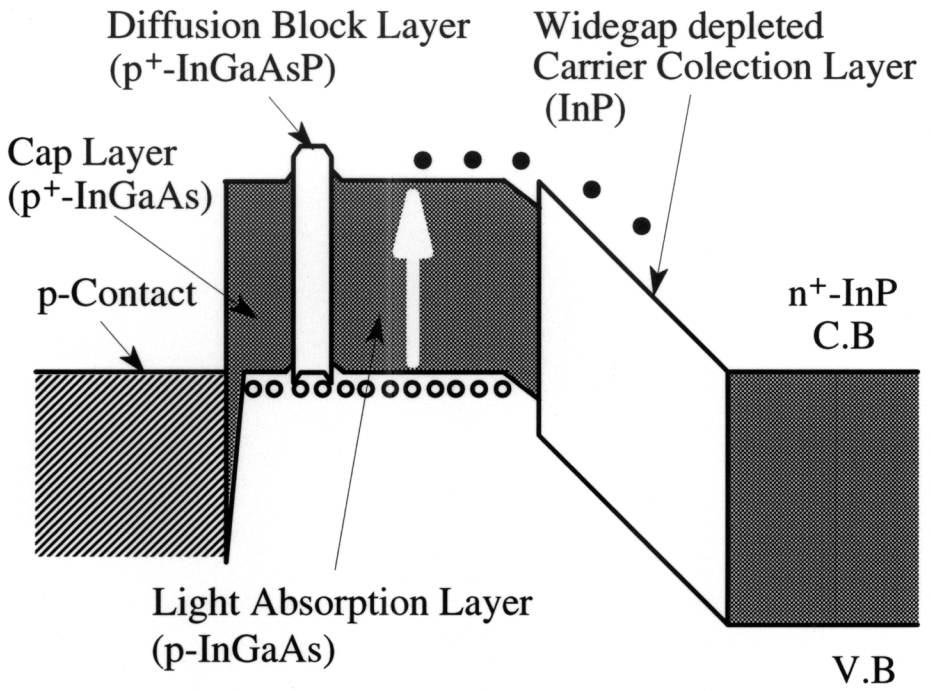

Fig. 1 Schematic energy band diagram of a UTC-PD.

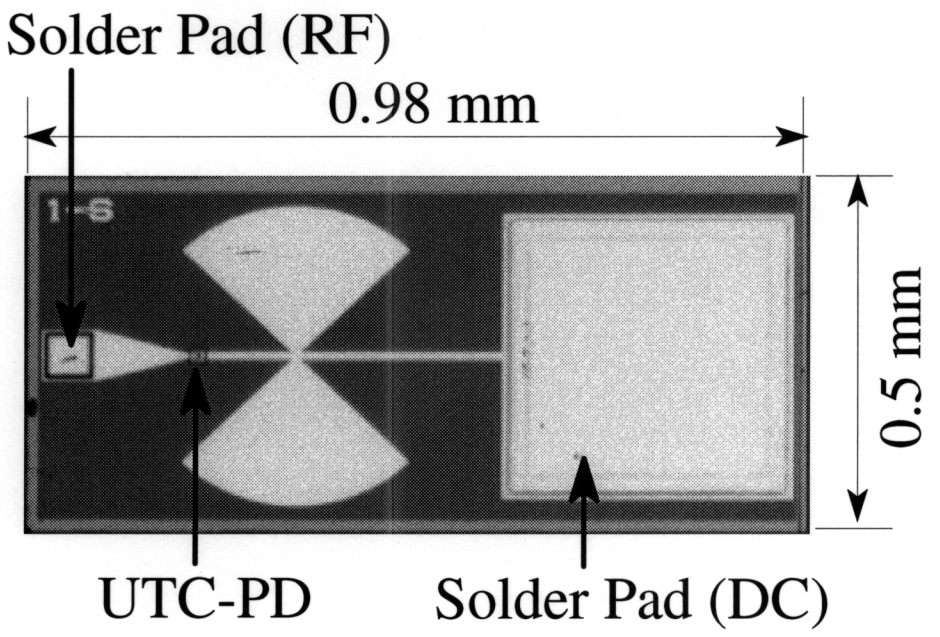

Fig. 2 Photograph of a UTC-PD chip.

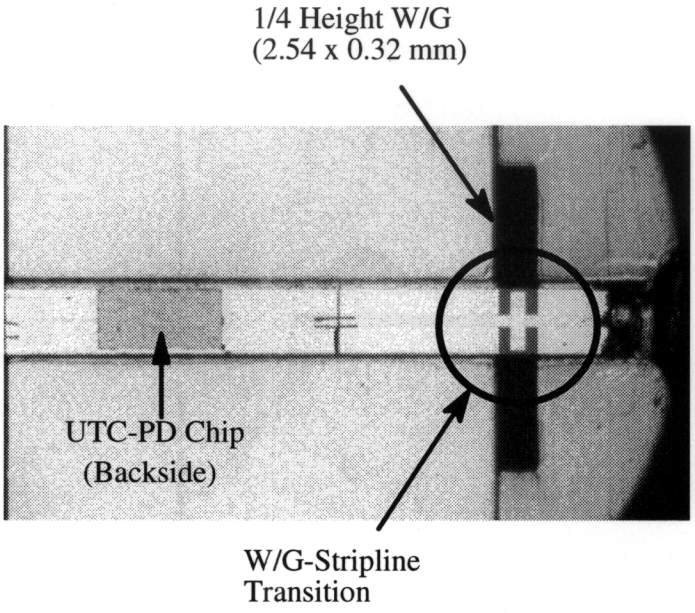

Fig. 3 Waveguide-stripline transition and UTC-PD mounted on a quartz substrate.

is well known that reducing height of an waveguide is effective to extend a operation bandwidth of the transition, a quarter-height waveguide is employed in the mount. A photograph of the waveguide probe is shown in Fig. 3.

The diode chip is soldered upside down on a 0.58-mm wide and 0.15-mm thick fused-quartz substrate as shown in Fig. 3. RF output of the diode is coupled to a stripline with a characteristic impedance of ~80 Ω through 2-stage stripline impedance transformers and then transferred to the quarter-height waveguide by the transition probe. The end of the microstrip channel is short-circuited at some length from the waveguide in order to make a return path of the DC bias applied to the diode. Choke filters made of high- and low-impedance striplines on the quartz substrate are placed in the other end of the microstrip channel. DC bias is applied to the diode through the choke filters. The diode is irradiated by combined two lasers from the back side of the UTC-PD chip. A cross section of the photomixer mount is schematically shown in Fig. 4.

Simulations of the waveguide-stripline transition including the stripline and the impedance transformers were performed using HP's High Frequency Structure Simulator (HFSS) to determine the optimum lengths of the waveguide backshort and the microstrip channel. Figure 5 shows the best bandwidth performance of the transition predicted by the simulation. It is clear that this microstrip-waveguide transition can give better than -15 dB return loss over 75–120 GHz.

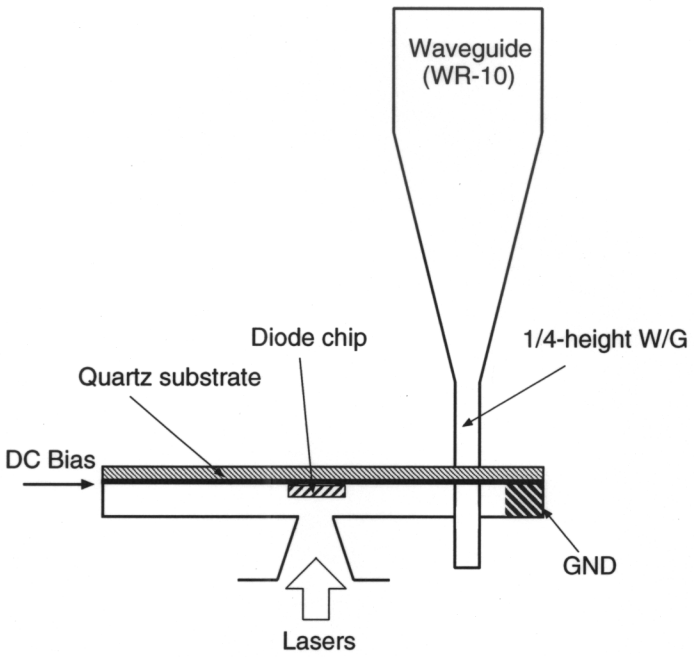

Fig. 4 Schematic of a photomixer mount.

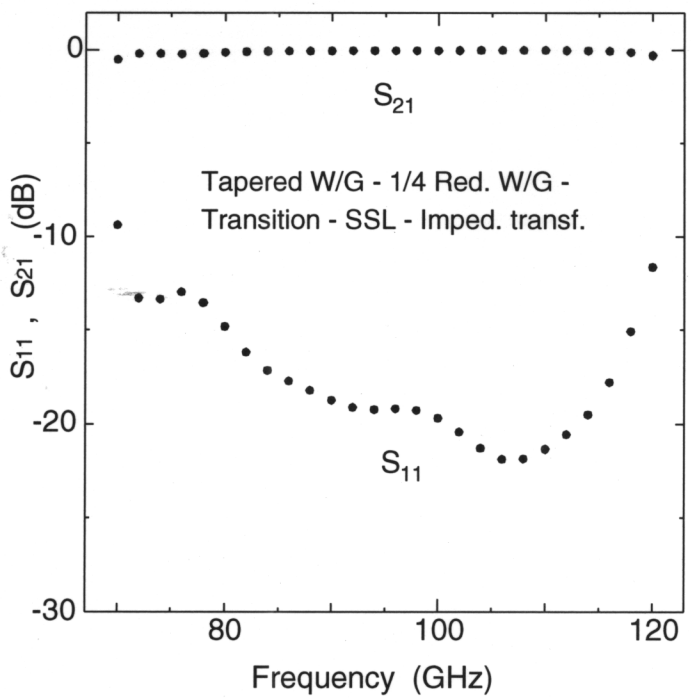

Fig. 5 Predicted performance of the waveguide-stripline transition.

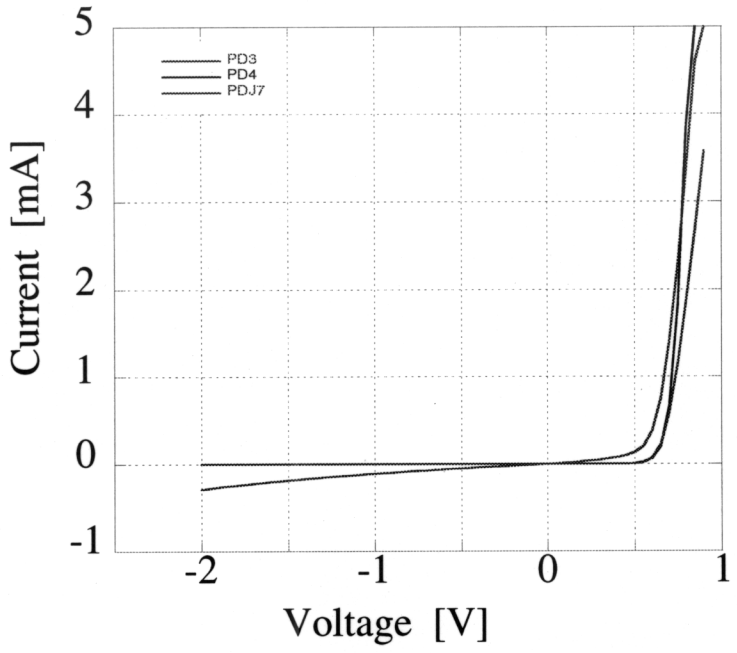

Fig. 6 DC I-V curves of UTC-PD's .

Result and discussion

Lasers ($\lambda = 1.5\mu$m) provided by two semiconductor laser-diodes are separately transferred to optical fibers and then coupled by a coupler into an optical fiber. The output of the lasers from the optical fiber are focused onto the UTC-PD by a lens located in the photomixer mount. The position of the lens is precisely aligned against the photodiode so that maximum power of millimeter-wave radiation is available at the output port of the photomixer mount. The output millimeter-wave radiation from the photomixer is detected by a spectrum analyzer with a harmonic mixer (HP11970) or a Schottky-diode detector.

Typical DC I-V curves of UTC-PD's used in experiments are shown in Fig. 6. The bias voltage applied to the diode is usually in the range from -1 to -2 V. It has been shown that photocurrent of the UTC-PD induced by lasers is approximately proportional to the amount of laser power coupled to the diode in the experiment at lower frequency.[6] In the similar manner, we first measured output radiation power near 100 GHz as a function of photocurrent of the UTC-PD. In Fig. 7 output power measured by a Schottky-diode detector is plotted as a function of the photocurrent of the UTC-PD for bias voltages of -1, -1.5, and -2 V. It is clear that the output power increases in proportion to the photocurrent (or the input laser power) at lower photocurrent. However, a compression or saturation of output power is observed at higher input laser power. The compression or saturation of output power is usually explained by the space charge effect.[7] The output power weakly depends on the bias voltage and increases a little as the bias voltage increases. At the bias voltage of -2 V and photocurrent of 20 mA, highest output power of a half mW is observed.

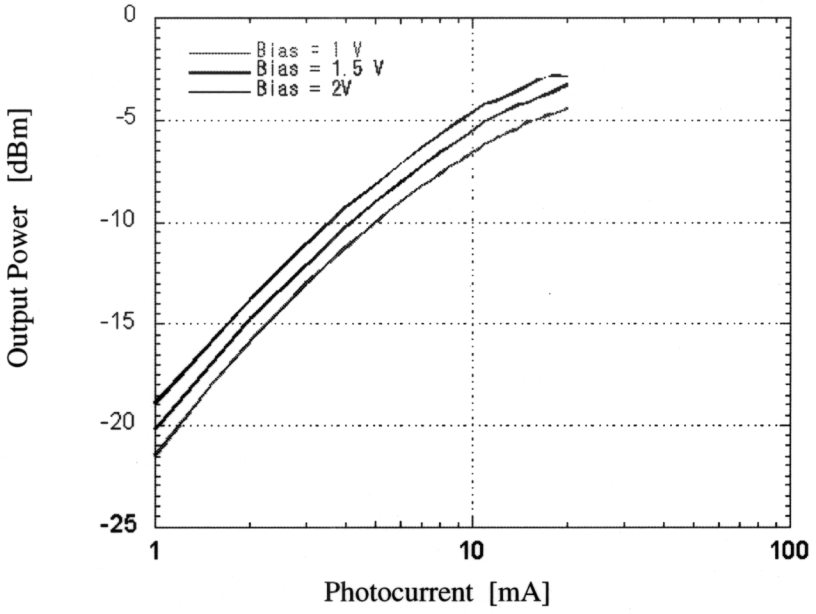

Fig. 7 Millimeter-wave output power as a function of diode photocurrent.

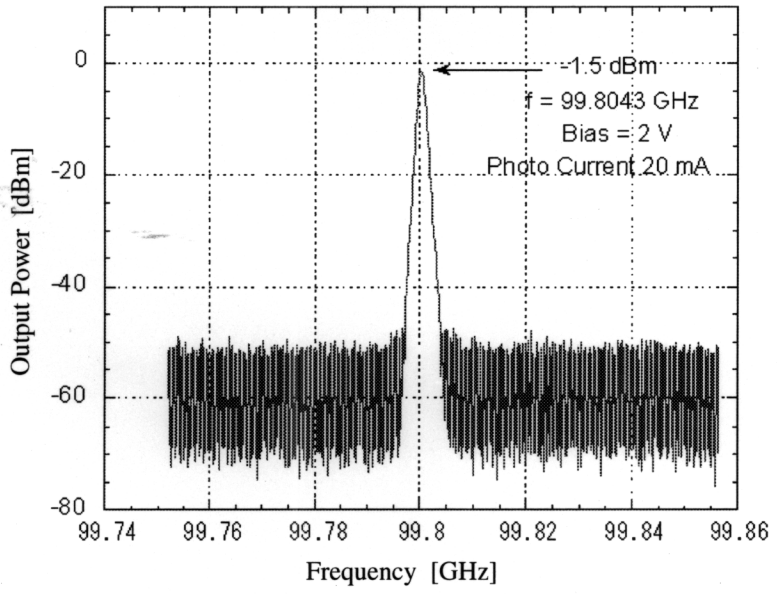

Fig. 8 Spectrum of photomixer output at ~100 GHz.

In Fig. 8 a spectrum near 100 GHz of photomixer output measured by the harmonic mixer is shown. The peak power in Fig. 8 is about 0.7 μW, which is calibrated from the conversion loss of the harmonic mixer given in an attached data sheet. Width of the output spectrum of the photomixer is less than 10 MHz, which is mainly governed by fluctuation of frequencies of the two lasers, since freely-running lasers are used in the experiment.

Summary

We have exploited a photomixer for generation of millimeter wave at W band using a UTC-PD. We have successfully observed output of millimeter-wave radiation at 100 GHz and obtained output power as high as approximately 1 mW. As far as we know, this is the highest output power ever generated by any kind of photomixers at this frequency band. The bandwidth of the output of the UTC-PD photomixer is less than 10 MHz, which is probably limited by the fluctuation of input lasers.

Acknowledgment

The authors would like to thank S. Matsuura of Institute of Space and Astronautical Sciences (ISAS) for stimulative discussion. This work was supported by a Grant-in-Aid for Scientific Research from the Ministry of Education, Culture, Sports, Science and Technology.

References

[1] S. Verghese, K. A. McIntosh, and E. R. Brown, "Highly tunable fiber-coupled photomixers with coherent terahertz output power", *IEEE Trans. Microwave Theory Tech.*, **45**, 1301–1309, 1997.

[2] S. Matsuura, G. A. Blake, R. A. Wyss, J. C. Pearson, C. Kadow, A. W. Jackson, and A. C. Gossard, "A traveling-wave THz photomixer based on angle-tuned phase matching", *Appl. Phys. Lett.*, **74**, 2872–2874, 1999.

[3] H. Ito, T. Furuta, S. Kodama, N. Watanabe, and T. Ishibashi, "InP/InGaAs Uni-Traveling-Carrier Photodiode with 220 GHz Bandwidth", *Electron. Lett.*, **35**, 1556–1557, 1999.

[4] T. Ishibashi, H. Fushimi, T. Furuta, and H. Ito, "Uni-Traveling-Carrier Photodiodes for Electromagnetic Wave Generation", *Proc. IEEE 7th Int. Conference on Terahertz Electron.*, pp. 36–39, Nara, Japan, Nov. 1999.

[5] J. L. Hesler, K. Hui R. M. Weikle, II, and T. W. Crowe, "Design, Analysis and Scale Model Testing of Fixed-Tuned Broadband Waveguide to Microstripline Transitions", *Proc. 8th Int. Symp. Space Terahertz Technology*, Cambridge, Massachusetts, March, pp. 319–325, 1997.

[6] H. Ito, T. Ohno, H. Fushimi, T. Furuta, S. Kodama, and T. Ishibashi, "60 GHz high output power uni-traveling-carrier photodiodes with integrated bias circuit", *Electron. Lett.*, **36**, 747–748, 2000.

[7] T. Ishibashi, N. Shimizu, S. Kodama, H. Ito, T. Nagatsuma, and T. Furuta, "Uni Traveling Carrier Photodiodes", *Tech. Dig. Ultrafast Electronics and Optoelectronics*, Incline Village, Nevada, pp. 166–169, 1997.

Nanoklystron: A Monolithic Tube Approach to THz Power Generation

Peter H. Siegel, Andy Fung, Harish Manohara, *Jet Propulsion Laboratory California Inst.of Tech.*
and
Jimmy Xu, Baohe Chang, *Brown University*

ABSTRACT

The authors propose a new approach to THz power generation: the "*nanoklystron.*" Utilizing silicon micromachining techniques, the design and fabrication concept of a monolithic THz vacuum-tube reflex-klystron source is described. The nanoklystron employs a separately fabricated cathode structure composed of densely packed carbon nanotube field emitters and an add-in repeller. The nanotube cathode is expected to increase the current density, extend the cathode life and decrease the required oscillation voltage to values below 100V. The excitation cavity is based on ridged-waveguide and differs from the conventional cylindrical re-entrant structures found in lower frequency klystrons. A quasi-static field analysis of the cavity and output coupling structure show excellent control of the quality factor and desired field distribution. Output power is expected to occur through an iris coupled matched rectangular waveguide and integrated pyramidal feed horn. The entire circuit is designed so as to be formed monolithically from two thermocompression bonded silicon wafers processed using deep reactive ion etching (DRIE) techniques. To expedite prototyping, a 600 GHz mechanically machined structure has been designed and is in fabrication. A complete numeric analysis of the nanoklystron circuit, including the electron beam dynamics has just gotten underway. Separate evaluation of the nanotube cathodes is also ongoing. The authors will describe the progress to date as well as plans for the immediate implementation and testing of nanoklystron prototypes at 640 and 1250 GHz.

INTRODUCTION

The millimeter and submillimeter-wave frequency bands, from 100 GHz to 3 THz (3 to 0.1 mm wavelength), are some of the least explored and yet information rich regions of the electromagnetic spectrum. The development of technology specifically aimed at remote sensing and identification of chemical species that thermally emit in this wavelength range has been a major thrust area at JPL for more than 10 years. Over this time, enormous progress has been made in both heterodyne and direct detection sensor technology. Significant developments include the realization of near quantum limited superconducting mixers up to 900 GHz, less sensitive but ultra high frequency (2.5 THz) space qualified ambient temperature semiconductor receivers, and most recently helium cooled hot-electron bolometer mixers which will work all the way up to far infrared wavelengths (10 THz). The lower end of the submillimeter band (100-300 GHz) has atmospheric windows that have been long exploited for both civilian and defense applications such as passive remote sensing and imaging, radar, and perhaps very soon ultra

wideband communications systems. Although detector technology has made major inroads towards the realization of these high frequency systems, solid-state source development (a major component in every case) has lagged behind significantly.

Over the years, there have been many attempts to produce CW power above 100 GHz. The most popular method is to use lower frequency oscillators and now power amplifiers (at or slightly above 100 GHz) followed by nonlinear-reactance-based frequency multiplier chains (Schottky diodes) to get to higher frequencies. This process becomes dismally inefficient for multiplication factors of 4 or greater. All attempts at making direct solid-state oscillators at these frequencies have so far failed from lack of efficient output coupling schemes, too low RF power levels, low Q, or internal device parasitics that limit the effective cutoff frequency. Optical downconversion, through laser heterodyning or photomixing, have also proven to be extremely inefficient as well as being difficult to stabilize and fairly bulky. The only methods of THz power production that have proven sufficient for submillimeter-wave heterodyne, communications or radar applications to date are direct laser-to-laser pumping, i.e. using a CO_2 laser to pump a methanol gas laser, or slow-wave tube structures, like backward wave oscillators and carcinotrons. Both of these sources are large and heavy, are extremely expensive (>$100,000), require high power, have limited operational lifetimes and are restricted in their frequency coverage. Backward wave tubes die off above 300 GHz (although a few tubes have been constructed with small amounts of output power up to 1.2 THz), and the number of available submillimeter-wave laser lines with reasonable output power are few and far between. So far as the author knows, no viable THz solid-state source exists with sufficient power to drive even a THz superconductor mixer at this time. Our concept addresses this situation with a new approach to the generation of radiation hard, frequency agile, phase lockable, high frequency power: a micromachined vacuum tube oscillator, the "*nanoklystron*."

TECHNICAL CONCEPT AND RATIONALE:

In the 1930's and 40's a great deal of effort was put into the design and manufacture of thermal emission devices (vacuum tubes) that worked at millimeter wave frequencies (up to 30 GHz). Much of this work involved extensions of the simple vacuum triode which relies on an electron beam pulled from a hot cathode and accelerated through a grid. The grid serves the purpose of bunching the electrons with a resulting high frequency oscillation and amplification of the grid current as the beam is collected at the anode. Variations on the triode (tetrode, pentode etc.) were of course widely employed as oscillators and amplifiers well before the advent of the transistor.

In the push towards higher frequencies the triode was ultimately abandoned because it is limited by parasitics between the emitter and grid as well as the transconductance of reliable cathodes. Two differing techniques emerged in the high frequency vacuum emitter world – slow wave or magnetically confined beams (backward wave tubes, carcinotrons, extended interaction oscillators, gyrotrons) and focused cavity oscillators (kly-

strons). Slow wave structures require high magnetic fields for focusing or steering the electron beam and hence are currently large and enormously heavy. Klystrons rely on passing the electron beam through one or more weakly coupled resonant cavities for the bunching operation and from which the accumulated RF oscillations are removed. Since no magnetic field is required, klystrons are small and lightweight compared to slow wave devices. They can be configured as single or multiple cavity oscillators or, if an RF input is applied to one of the cavities, as amplifiers.

The reflex klystron, [1] and Fig. 1, is a compact form of klystron oscillator that uses only a single cavity and a repeller or reflector to focus the accelerated electron beam back onto itself through a small gap in the walls of the resonator. The gap plays a critical role in establishing and maintaining oscillation at a frequency determined by the surrounding cavity. It takes the form of a precisely spaced set of grids (or gridless gap) at the center of a cylindrical re-entrant cavity that produces an alternating field from random oscillations in the impinging electron beam. This in turn causes bunching of the electron stream and upon proper reflection in phase from the repeller results in significant energy coupling to the surrounding cavity. The reflex klystron is a particularly useful short wavelength oscillator, as far as tubes go, and has been made to work at frequencies as high as 212 GHz [2]. However, the last commercial millimeter-wave reflex klystron was made almost 20 years ago and interest in these devices, at least for high frequency applications, has almost wholly disappeared (although room sized klystrons are still used for mega-watt power generation at microwave frequencies in accelerators and plasma fusion reactors!).

In the meantime, revolutionary advances in microfabrication techniques have enabled researchers to fabricate traditional emitter cathodes on a micron scale, photolithographically, with unprecedented packing densities and uniformity [3,4]. These emitters have even been formed into miniature vacuum tubes and operating triodes with ultra small (<1 micron) grid and emitter-collector gap lengths [5-7]. Again, the triode arrangement makes the high frequency potential of these structures very limited and even the most optimistic projections show the response falling off below 100 GHz [4].

This paper describes an approach which capitalizes on the use of MEMS (micro-electro-mechanical machining) and deep reactive ion etching (DRIE) microfabrication techniques as well as recent advances in monolithically fabricated cold cathodes to realize a miniaturized reflex klystron – the "nanoklystron" [8]. By scaling the gap, cavity and repeller dimensions of a working 100 GHz klystron to dimensions consistent with microlithographic techniques (factors of 5-10) we expect to realize oscillations at frequencies at least as high as 1.2 THz and power levels/device in the milliwatt range. We also plan to overcome a major limitation of existing cold cathodes – breakdown due to non uniformity of the emitter tips – by utilizing newly developed carbon nanotube emitter arrays [9] which have unprecedented packing densities and uniformity, high thermal conductivity and a metallic support substrate. In addition, the required beam voltage (typically 2-3kV in a standard klystron) is expected to go down drastically with shrinkage of the cathode-repeller distance and the use of a packaged carbon nanotip array and emitter

grid. Experimental emitters using carbon nanotubes have threshold voltages as low as a few volts/micron [10]. Finally, taking advantage of the monolithic design implementation, we will incorporate frequency agility, high levels of redundancy, multiple power or multiple beam capability into the nanoklystron [11].

TECHNICAL APPROACH

Our proposed "nanoklystron" (Fig. 2.) consists of a cathodic array of highly uniform carbon nanotubes with a built in emitter grid sealed in a micromachined vacuum cavity with a photolithographically produced microresonator, a deposited microgrid, and a weakly coupled micromachined RF waveguide and beam forming horn for removal of the output signal. We plan to fabricate the entire structure monolithically from two silicon wafers that are thermocompression bonded and vacuum sealed in the final steps. The dimensions obtainable with existing micromachining and photolithography processes are consistent with klystron operation at frequencies from 300 GHz to at least 2 THz. Simple scaling of an existing millimeter wave klystron tube [2] at N band (120 GHz) can potentially yield THz oscillator designs without inventing any new lithographic processes. Decreasing the repeller-to-cathode distance will also reduce the required beam voltage to levels approaching those of traditional solid-state devices (10-100V). The use of high aspect ratio carbon nanotubes for the cathode rather than tapered silicon tip arrays [3,4] will greatly increase packing density, thermal conductivity and lifetime, which translates into higher current density and hence higher frequency operation. Finally, the klystron designers of the 1970's were at a great disadvantage. There were no electromagnetic modelling tools that allowed those early pioneers to verify grid, repeller and cavity designs, let alone optimize the performance of the tubes. All high frequency designs were established by trial and error and limited by mechanical machining techniques to gap dimensions greater than 50 microns [12]. The authors have access to several excellent electromagnetic simulator codes that they plan to apply to the design and optimization of a nanoklystron circuit. A recent calculation from a group at University of Leeds [13] supports the advantages of this approach.

We believe the three most significant hurdles for realizing a THz nanoklystron are: (1) basic cavity and output circuit realization compatible with monolithic processing, (2) implementation of a low voltage, high current density, miniature field emission cathode, (3) demonstration of a micro-scale high-vacuum-sealing technology compatible with low loss THz output. We are addressing each of these areas in turn.

RF Cavity and Output Circuit: In order to realize an appropriate resonant structure and compatible THz output coupling circuit in a wafer level process we have abandoned the traditional cylindrical re-entrant cavity and magnetic coupling probe design often used in millimeter wave reflex klystrons [1] in preference to a simple aperture coupled vertical E field layout. The resonant cavity is designed around single ridged waveguide, which has both an attractive mechanical layout as well as a field distribution and mode behavior that makes vertical E field aperture coupling straight forward. The layout is

shown in Figs. 3-5, where the output Q and load impedance are easily varied by the iris width and the height of the rectangular waveguide step immediately outside the cavity. For optimal coupling to the outside world, the waveguide height is sequentially increased (using quarter wave impedance transformers [14]) from the very reduced height ridge guide (5 microns at 1200 GHz) until the width to height is 2:1. In the first design iteration the vacuum seal occurs at this waveguide output plane and a separately attached and aligned feed horn is added on the outside of the RF transparent window. Eventually we plan to incorporate the horn into the substrate itself and make the vacuum seal at the horn aperture, where its impact on the impinging field will be reduced. The result of a simple EM field analysis (no electron beam present) showing S_{11} from a z-directed gap excitation of the cavity and output waveguide transition is shown on the right in Fig. 3. A commercial finite difference time domain simulator (Quickwave [15]) was used for this analysis. Field cuts at two different planes are given in Fig. 4. Finally, Fig. 5 shows the assembled unit as it would look at 640 GHz.

The wafer processing steps for realizing the nanoklystron cavity structure are given in Fig. 6. The bunching grids are formed during the RIE process. The cathode and repeller are added afterwards by dropping them into via holes that have been appropriately sized and placed in the top and bottom wafers. The critical dimensions are the gap spacing and electron beam hole which are 5 microns and 20 microns respectively at 1200 GHz. This is no problem for the lithographic process but poses a significant hurdle to traditional metal machining techniques.

In order to speed up the development of a prototype, a scaled 640 GHz design (the highest frequency at which we felt we could reasonably machine the cavity and beam guides), was drawn up and, at time of writing, is being machined in the JPL Space Instruments shop. Representative drawings of this design, which includes a 20dB directivity standard gain horn, are given in Fig. 6.

Field Emission Cathode: The cold cathode for the nanoklystron must be capable of generating beams with current densities of at least 100A/cm^2. Traditional Spindt type microcathodes [3,4] have been able to achieve 20X this current density [16]. Carbon nanotube emitters offer potential advantages over more traditional micro-emitter structures, including less susceptibility to tip breakdown and lower emission voltages as well as very high thermal conductivity (same order as diamond). In the case of the highly ordered nanotube arrays recently introduced by the research team now at Brown University [9] and shown in Fig. 7, the tip spacing and height is extremely uniform and the density of emitters can easily be as high as 10^{10}/cm^2. In nonuniform nanotube emitters, threshold voltages of 5V/micron or less are typical and 2.5 V/micron has been realized commercially [17]. For use in the nanoklystron, 30,000 emitter tips of the type shown in Fig. 7 will fit within the electron beam hole at 1200 GHz. With even a modest emitter current of 100nA/tip [18], this means current densities (without focusing) of several kA/cm^2 are feasible. In order to measure the nanotube emitter properties we have developed a simple test jig that allows a small (3x3mm) emitter sample to be tested with a

commercially installed grid (Fig. 8). Although this arrangement has yielded data on the commercial disordered nanotube arrays [17] it does not take advantage of the array uniformity in the same manner as the Spindt integrated grid cathodes [4]. For this reason a procedure for fabricating and inserting a close spaced (<1 micron) grid onto the carbon nanotube arrays has been developed (Fig. 9). This arrangement has not yet been tested, but is scheduled to be completed very soon.

Vacuum Sealing: Vacuum sealing of the cavity, cathode, repeller and output structure requires both high vacuum (10^{-8} Torr or better) and compatibility with low loss RF transmission through the output coupling window. This can be accomplished either with evaporated dielectrics or with a separately attached dielectric window. As a first attempt to accomplish the sealing, a simple microlithographic technique, using an etched-in-place ultrathin (5-10 micron) silicon window, will be tested. For the machined 640 GHz nanoklystron, a separately processed quartz window will be sealed in place with a commercial hermetic process.

Since we have not as yet completed the fabrication of either the machined 640 GHz nanoklystron or the micromachined 1200 GHz nanoklystron we cannot predict all the hurdles that will have to be overcome to produce oscillation and significant output power. Both detailed numeric analysis and sophisticated fabrication process steps are still to be worked out.

SUMMARY

The authors have presented a conceptual design as well as some early progress on the layout and fabrication of a THz nanotube power source. This is clearly a "work in progress" and we apologize for the conceptual nature of the paper. Several important first steps have been made, however, including the design of a new form of re-entrant cavity and coupling structure amenable to lithographic processing, the testing and incorporation into the design of advanced carbon nanotube cold-cathode emitters which should significantly improve the potential current density, the design and incorporation of an integrated microgrid directly on the nanotube cathode, and the wafer processing steps needed to realize the full nanoklystron structure. If all the milestones in the program can be realized, then the concept of a nanoklystron beam switching array, such as that shown in Fig. 10, will be close at hand.

ACKNOWLEDGEMENTS

The authors would like to thank Dick Fink of FEPET for supplying commercial nanotube emitter structures and making measurements on the TO-5 packages, Dr. Colleen Marrese and Dr. Brian Hunt of JPL and Dr. Jeff Hone of Caltech for useful discussions, Maurice Viant and the klystron team at CPI Canada for detailed discussions and an allowed site visit, and Dr. Tracy Lee, now at Copely Networks, for his work at the start of this program. We would also like to acknowledge the financial and programmatic support of

Tim Krabach and Carol Lewis in their roles as managers in the NASA BSICT program. This work was supported by the California Institute of Technology Jet Propulsion Laboratory under contract with the National Aeronautics and Space Administration. The work at Brown University was also sponsored by AFOSR.

REFERENCES:

[1]. See for example: D. Hamilton, J. Knipp and J.B. H. Kuper, Klystrons and Microwave Triodes, chapter12, M.I.T. Radiation Lab Series, vol. 7, McGraw Hill Book Co., c.1948.
[2]. M. Viant, retired klystron designer, Varian Electron Tubes, private comm.
[3]. C.A. Spindt, C.E. Holland, P.R. Schwoebel and I. Brodie, "Field-emitter-array development for microwave applications," J. of Vacuum Science and Technology B, vol. 14, no. 3, May/June 1996, pp. 1986-1989.
[4]. C.A. Spindt, C.E. Holland, P.R. Schwoebel and I. Brodie, "Field-emitter-array development for microwave applications II," J. of Vacuum Science and Technology B, vol. 16, no. 2, March/April 1998, pp. 758-761.
[5]. A.A. G. Driskoll-Smith, D.G. Hasko and H. Ahmed, "The 'nanotriode:' A nanoscale field-emission tube," Applied Physics Letters, vol. 75, no. 18., Nov. 1, 1999, pp. 2845-2847.
[6]. H. W. P. Koops and C. Schossler, "Construction of a three-dimensional microtriode by nanolithography with electron-beam induced deposition," 9th Int. Vacuum Microelectronics Conf., St. Petersburg, pp. 458-462, 1996.
[7]. C.E. Holland, A. Rosengreen and C.A. Spindt, "A study of field emission microtriodes," 1990 IEEE Int. Electron Devices Meeting, IEDM 90, pp. 979-983, 1990.
[8]. P.H. Siegel, T.H. Lee and J. Xu, "The Nanoklystron: A New Concept for THz Power Generation," JPL New Technology Report, NPO 21014, submitted March, 24, 2000.
[9]. J. Li, C. Papadopoulos and J. M. Xu, "Highly-ordered carbon nanotube arrays for electronics applications," Applied Physics Letters, vol. 75, no. 3, July 19,1999, pp. 367-369.
[10]. M. Stammler, J. Ristein, T. Habermann, A. Gohl, K. Janischowsky, D. Nau, G. Muller and L. Ley "Field emission measurements with micrometre resolution on carbon nanostructures," Diamond And Related Materials, vol. 8, March 1999, pp. 792-797.
[11] P.H. Siegel, "A Frequency Agile Nanoklystron," JPL New Tech. Report, March, 2000.
[12]. Chris Nilsen, former klystron designer, CPI Corp., Palo Alto, CA., private comm.
[13] R.E. Miles, J. Garcia, J.R. Fletcher, D. P. Steenson, J.M. Chamberlain, C.M. Mann and E.J. Huq, "Modelling of micromachined klystrons for Terahertz operation," 8th Int. Conf. on THz Electronics, Darmstadt, Germany, Sept. 28-29, 2000, pgs. 55-58.
[14]. G. Matthaei, L. Young and E.M.T. Jones, Microwave Filters, Impedance Matching Networks, and Coupling Structures, Aertech House Books, Dedham, MA c. 1980.
[15]. QWED, ul. Zwyciezcow 34/2, 03-938, Warsaw, Poland, http://www.qwed.com.pl
[16]. J. A. Nation, L. Schachter, F.M. Mako, L.K. Len, W. Peter, C.M. Tang and T. Srinivasan-Rao, "Advances in cold cathode physics and technology," Proc. IEEE, vol. 87, no. 5, May 1999, pp. 865-889.
[17]. R. Fink, FEPET Silicon Diamond, Texas. private communication.
[18]. K.A. Dean and B. Chalamala, "Current saturation mechanisms in carbon nanotube field emitters," Appl. Phys. Letters, vol. 76, no. 3, 17 Jan 2000, pp. 375-377.

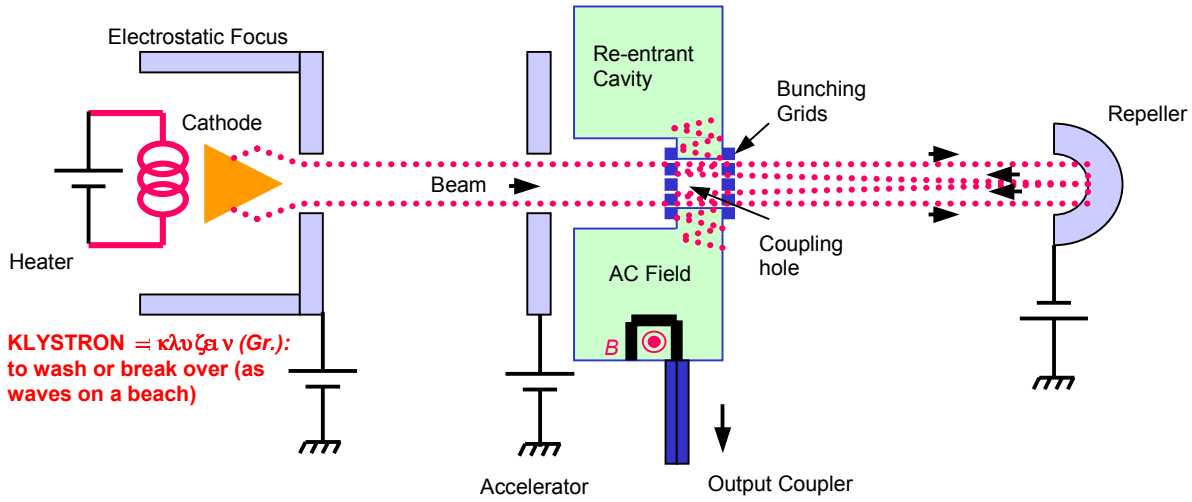

Fig. 1. Schematic cross-section of a simple reflex klystron. All items are cylindrically symmetric. Output coupling is shown via a magnetic field loop. For scale the cavity diameter can be taken as approximately one half wavelength. Actual millimeter wave klystron geometries are significantly more complicated and, at least in the case of Varian designs, still proprietary.

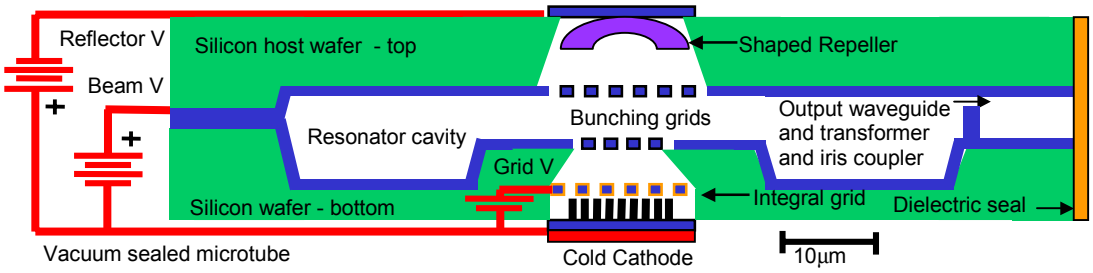

Fig. 2. Schematic cross section of proposed nanoklystron. The cathode is composed of a carbon nanotube field emitter array (Fig. 7) with a built-in grid. The cavity, beam and output waveguide are etched from two silicon wafers which are later joined by thermocompression bonding. The wiring and grid layers are formed lithographically. The repeller and cathode are drop-in parts and vacuum sealing is performed in the last step.

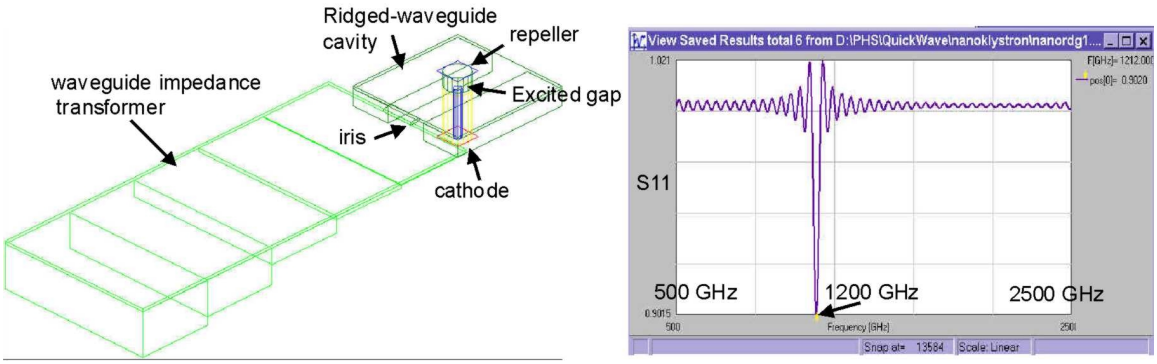

Fig. 3. Left: Transparent construction of nanoklystron re-entrant cavity, coupling iris and output waveguide stepped transformer. Excitation for the S parameter plot (right) is via a coaxial probe that produces a Z oriented field across the cavity grid gap. Right: S_{11} vs. frequency from 500-2500 GHz for gap excited ridged waveguide resonant cavity shown at left. The ripple and greater than unity excursions are an artifact of not waiting for full program convergence. The sharp resonance is due to the fact that the cavity is assumed to be lossless. The resonant frequency is≈ 1200 GHz. The analysis was performed using Quickwave [15].

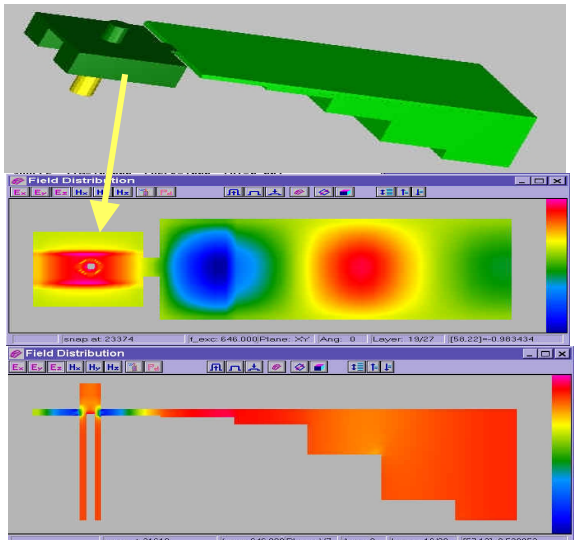

Fig. 4. Top: Solid view of nanoklystron cavity and output waveguide. Middle: Top view field plot showing E_z at the height of the grid gap. Bottom: Side view field plot showing E_z through the center of the cavity ridge and output waveguide. The coax excitation used to set up the fields can be seen at the left in the bottom plot.

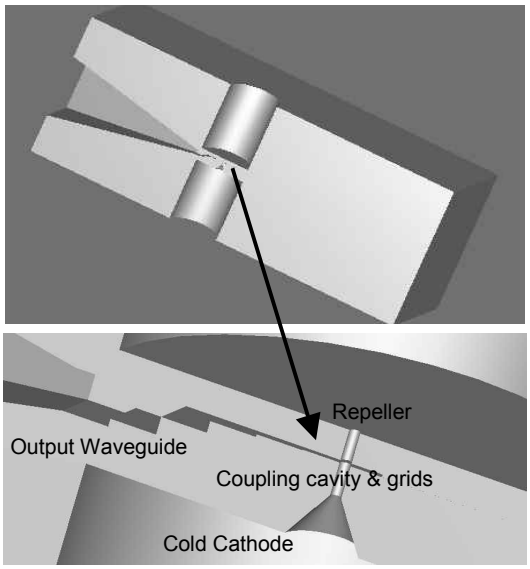

Fig. 5. Cross section and assembled view of 640 GHz machined nanoklystron. The smallest features are the 40μm diameter electron beam hole and the 10μm deep ridged waveguide cavity.

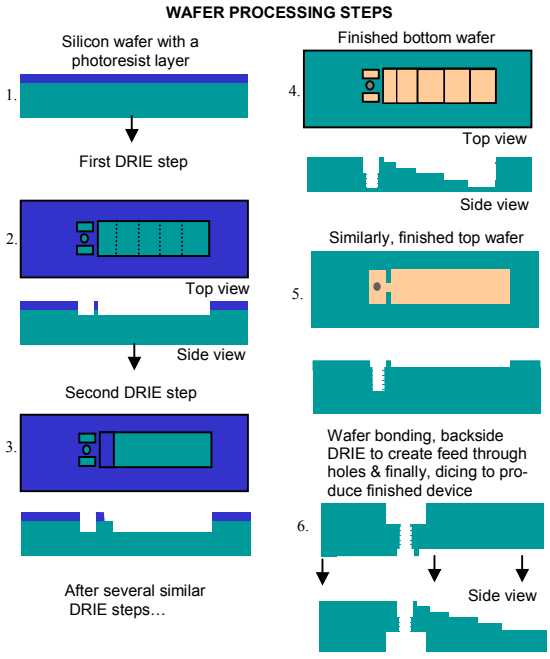

Fig. 6. Wafer processing steps needed to realize nanoklystron cavity, iris and output waveguide transformer from two SI silicon wafers. Each cell is approximately 1x2 mm for circuits between 600 and 1200 GHz allowing many hundreds of variations/wafer.

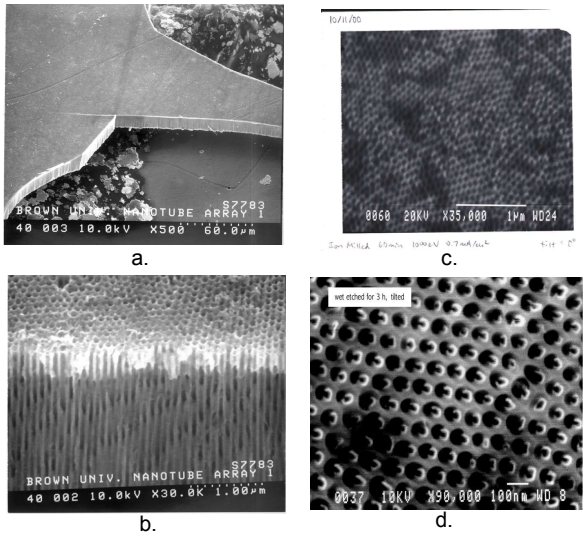

Fig. 7. Brown University highly ordered nanotube array at different magnifications. a. 500 X, b. 30 kX (tilted), c. 35kX (top), d. 90kX (top).

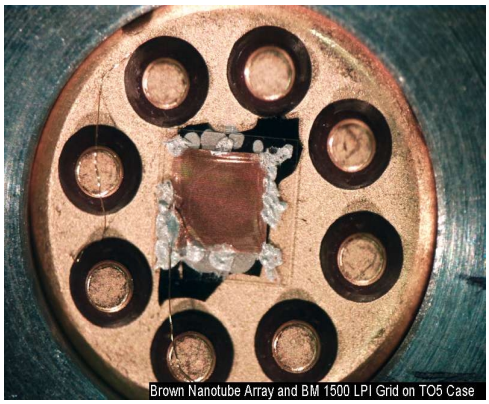

Fig. 8. Nanotube cathode and separate commercial emitter grid (1500 LPI) mounted on a fused quartz spacer for testing in a high vacuum emission test chamber. The grid and cathode are mounted on a T0-5 transistor header. Grid and anode current vs. voltage can be determined. The chamber has been assembled by Colleen Marrese of JPL.

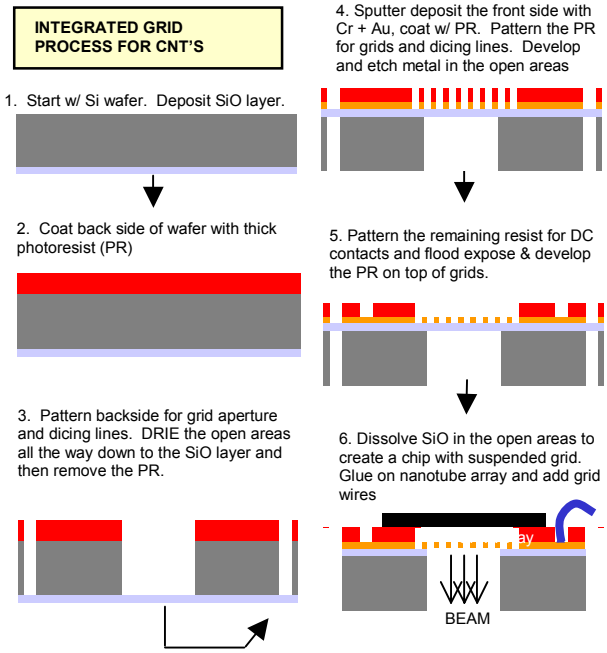

Fig. 9. Steps for fabricating integral grid nanotube cathode.

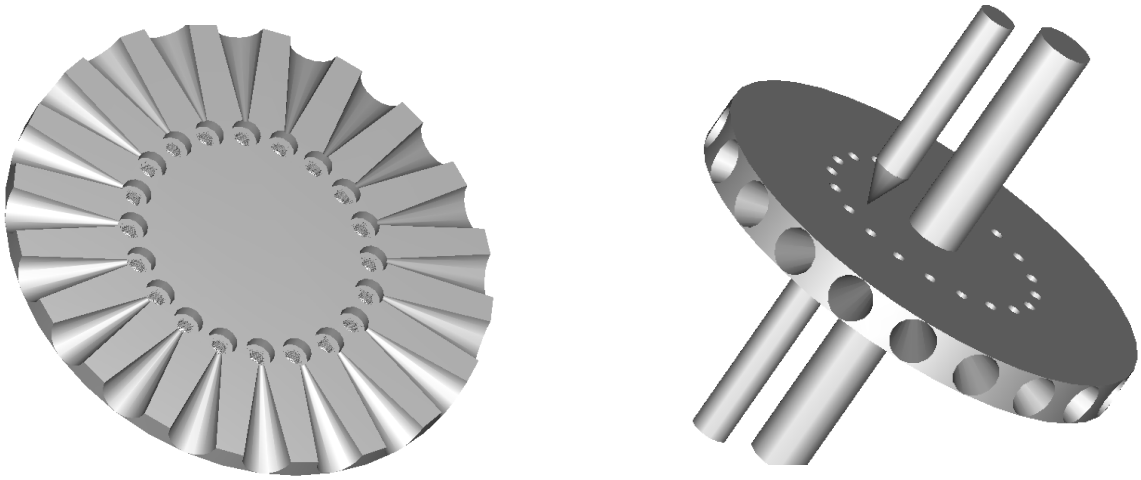

Fig. 10. Left: Possible nanoklystron array for multiple frequency or multiple power output. Right: Frequency switching or redundancy is obtained by mechanical indexing.

The research described in this paper was carried out at the Jet Propulsion Laboratory, California Institute of Technology, under a contract with the National Aeronautics and Space Administration.

EMBEDDED COPLANAR STRIPS TRAVELING-WAVE PHOTOMIXERS

R.A. Wyss, T. Lee, J.C. Pearson,

Jet Propulsion Laboratory, California Institute of Technology, Pasadena, CA 91109

S. Matsuura[†], G.A. Blake,

Division of Geological and Planetary Sciences, California Institute of Technology, Pasadena, CA 91125

C. Kadow[‡] and A.C. Gossard

Materials Department, University of California – Santa Barbara, Santa Barbara, CA 93106

Abstract

The electric field distribution in photomixers with electrodes deposited on the surface has already been calculated[1]. It was shown that the strength of the electric field diminishes rapidly with depth. It was argued that the resulting reduction of the effective interaction volume of the device lowers the optical-to-heterodyne conversion. In this paper, we will present the results of our investigation on the influence of the electrode placement on the performance of photomixers.

We have fabricated and measured traveling-wave photomixer devices which have both embedded and surface electrodes – the nominal spacing between the electrodes was 2 μm. Devices were made using either low-temperature-grown (LTG)-GaAs or ErAs:GaAs as the photoconductive material. The dark current, photocurrent and RF emission were measured at nominally 1 THz. The experimental data show a surprising difference in the behavior of ErAs:GaAs devices when the electrodes are embedded. A factor of two increase in RF radiation is observed for electric fields < 20 kV/cm. No such improvement was observed for the LTG-GaAs devices. We argue that the distinctive behavior of the two photoconductive materials is due to differences in the crystal structure – LTG-GaAs is isotropic, while ErAs:GaAs is uniaxial. We find that the carrier mobility in-plane (parallel) to the ErAs layers in the ErAs:GaAs superlattice is larger than orthogonal to these layers. The data indicate that carrier velocity overshoot is responsible for the excess radiation produced for the embedded electrode ErAs:GaAs devices.

Present address: [†]Institute of Space and Astronautical Sciences, Kanagawa, Japan; [‡]Nortel Networks, Wilmington, MA 01887.

[1]E.R. Brown, "A photoconductive model for superior GaAs THz photomixers," *Appl. Phys. Lett.* **75**, 769 (1999).

HgCdTe Photoconductive Mixers for 2-8 THz

A.L. Betz, R.T. Boreiko
Center for Astrophysics & Space Astronomy
University of Colorado, CB 593
Boulder, CO 80309

and

S. Sivananthan and R. Ashokan
Microphysics Laboratory
University of Illinois, Chicago
Chicago, IL 60607

Introduction

Heterodyne spectroscopy has been taken to wavelengths as short as 63 μm with Schottky-diode mixers [Boreiko and Betz 1996]. Schottkys, however, are relatively insensitive compared to superconducting mixers such as the hot-electron microbolometer (HEB), which has an effective quantum efficiency of 3% at 120 μm (2.5 THz). Although HEB sensitivities are bound to improve, there will always be losses associated with antenna coupling of radiation into sub-micron size devices. Another approach to FIR mixer design is to use a photoconductive device which can be made much larger than a wavelength, and thus act as its own antenna. For example, HgCdTe photodiodes have been used as mixers in the λ=10 μm band for over 25 years [Betz 1981], with sensitivities now only a factor of 2 from the quantum-noise-limit. HgCdTe can also be applied at FIR wavelengths, but surprisingly little work has been done to date. The exception is the pioneering work of Spears (1988) and Kostiuk and Spears (1987), who developed HgCdTe photomixers for the 20-120 μm region.

The spectral versatility of the HgCdTe alloy is well recognized for wavelengths as long as 8-20 μm. What is not so recognized, however, is that theoretically there is no long wavelength limit for appropriately composited HgCdTe. Although Spears (1988) successfully demonstrated a photoconductive response from HgCdTe at 120 μm, this initial effort was apparently never followed up, in part because of the difficulty of controlling the HgCdTe alloy composition with liquid-phase-epitaxy (LPE) techniques. With the availability of precise molecular-beam-epitaxy (MBE) since the early 1990's, it is now appropriate to reconsider HgCdTe for detector applications longward of λ=20 μm.

We recently initiated an effort to fabricate detectors and mixers using II-VI materials for FIR wavelengths. Of particular interest are device structures called *superlattices*, which offer a number of advantages for high sensitivity direct detectors and very long wavelength heterodyne mixers.

Existing Technology

Only Schottky-diode mixers have been used for heterodyne spectroscopy of astronomical objects at FIR wavelengths. This technology is now considered to be obsolete for high sensitivity observations, and has been supplanted (at least in the lab) with the technology of Hot-Electron micro-Bolometer (HEB) mixers. One of the best HEB results in the wavelength region of interest is the 119 μm (2.5 THz) noise-temperature measurement of the JPL group (Wyss *et al.* 1999). With a niobium HEB mixer cooled to 2 K, they achieved an 1850 K (DSB) noise temperature. From a noise viewpoint, this is equivalent to an effective quantum efficiency (QE) of 0.03 at 2.5 THz. Improvements over the next 2 years are likely to raise the effective QE of HEB mixers to 0.06, with a goal of 0.1. These mixers will remain relatively narrow-band, because of the types of coupling antennas that are used, and the necessity of limiting spectral bandwidth to avoid device saturation. At even higher frequencies, HEB mixers will have difficulty achieving quantum-noise-limited performance because of the increased losses in the antenna coupling structures.

Some work has been done to develop *extrinsic* semiconductors for FIR mixer applications. Park *et al.* (1988) investigated Ga-doped Ge as a heterodyne detector for the λ=100 μm region. The low absorption of this material leads to a large detector size of several mm in order to get 10% photon absorption. The large size in turn leads to a long transit time and lifetime for photogenerated carriers. For mixer applications, the carrier lifetime must be short. One technique to speed recombination is to introduce compensation impurities, but this also reduces the photoconductive gain. Regardless, even with high compensation, Park *et al.* (1988) were only able to achieve a 60 MHz IF bandwidth, which is about a factor of 10 less than the minimum needed for remote sensing applications with fixed-frequency local oscillators.

Proposed New Technology HgCdTe

What is needed for FIR wavelengths is an *intrinsic* rather than *extrinsic* detector material. Intrinsic semiconductors have absorption cross-sections 100 times stronger than that of extrinsic (doped) semiconductors. No simple intrinsic materials exist, however, with bandgaps appropriate for λ=50-150 μm detection. Fortunately, one can fabricate intrinsic detectors from mixed materials to obtain a peak photoconductive response at any infrared wavelength. Alloys and superlattices made from HgTe and CdTe can be fabricated with bandgaps engineered between -0.26 eV and +1.60 eV (corresponding to DC to 100 THz response). The absorption coefficient of intrinsic HgCdTe is about 100 cm^{-1} in the λ=50-150 μm range, and so devices as thin as 5-10 μm can provide good quantum efficiency.

Bandgap Engineering

Two approaches are available for the synthesis of "zero-gap" semiconductors. The first is the well-known alloy process in which the bandgap is tailored by varying the mole fraction x of CdTe in an $Hg_{1-x}Cd_xTe$ alloy. The second is a superlattice structure, in which the bandgap is determined by the relative thicknesses of alternating HgTe and CdTe layers in a composite semiconductor.

$Hg_{1-x}Cd_xTe$ Alloys

At 77 K, the band gap of the semimetal HgTe is –0.26eV, and that of the semiconductor CdTe is 1.6 eV. These materials can be combined with various fractional compositions x to tune the bandgap E_g(eV) of the $Hg_{1-x}Cd_xTe$ alloy according to the formula (Hansen and Schmit 1983):

$$E_g = -0.302 + 1.93x + 5.35\times10^{-4}T(1-2x) - 0.810x^2 + 0.832x^3.$$

Figure 1 shows the cut-off wavelength, defined as $\lambda_{co}(\mu m)=1.24/E_g(eV)$, as a function of fractional composition x at various temperatures. It is evident that by choosing x between 0.16 and 0.17, a wide range of cut-off wavelengths in the FIR can be obtained. For the approximate 0.01 eV band gap needed for 100 μm response, x would be close to 0.17. As the band gap approaches zero, small fractional changes in x lead to large fractional changes in the gap energy, and generally we need to control x to within 0.2% to have a 10% uncertainty in peak response. It should be apparent that compositional inhomogeneities in this case lead to variations in the gap throughout the material resulting in non-uniformity in the response of array detectors. Nevertheless, with MBE deposition techniques adequate control can be achieved. Pioneering work on low-gap HgCdTe alloys by Spears (1988) was done with much less precise LPE techniques, and yet usable photoconductive devices were produced for the 20-120 μm region.

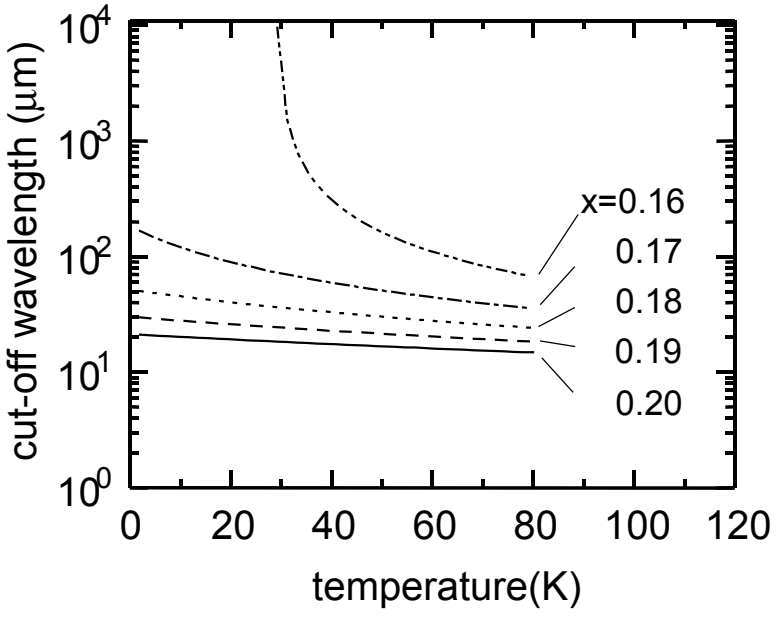

Fig.1: Cut-off wavelength versus temperature for various compositions.

HgTe/CdTe Superlattices

In a superlattice (SL) device, the bandgap is controlled by adjusting the thickness of alternating material layers with very precise molecular-beam-epitaxy (MBE) techniques. Possible material choices are the II-VI compounds HgTe for the *wells* and CdTe (or high-gap HgCdTe) for the *barriers* of the superlattice. Typically, the barrier thickness is 40 Å and the well thickness is many times greater to synthesize a "zero-gap" composite semiconductor. Alternating well and barrier layers are deposited until the total thickness required for the active layer (typically 5-10 μm) is built up. Over a hundred layer pairs are required. Schulman and McGill (1979) first proposed HgTe-CdTe superlattices (SLs) as promising new infrared materials, but few results have been published so far. Since MBE is now a mature manufacturing technology for HgCdTe devices, we believe that it is now possible to fabricate SL structures for FIR applications. We favor the II-VI compounds over III-V materials such as InAs/InGaSb because of their higher electron mobility, which is important for high speed mixers. The UIC Microphysics Lab also has extensive experience with II-VI materials, and a demonstrated proficiency with epitaxial growth on a variety of substrates (Mahavadi *et al.* 1990; Sporken *et al.* 1989; Wang *et al.* 1996).

Superlattices have a number of potential advantages over alloy detectors in the FIR: (i) the band gap of the material is much easier to control; (ii) growth-direction effective masses of electrons and holes in the SL are decoupled from the band gap, so FIR detectors with larger effective masses should display orders of magnitude reductions in the tunneling current; (iii) the carrier degeneracy problem near band edge (longest wavelengths) is less significant; and (iv) a SL can suppress Auger recombination at long wavelengths by intentionally inducing strain.

Although theoretically one can fabricate low band gap SLs from CdTe barriers and HgTe wells, the well thicknesses get large and hard to control for zero bandgap devices. A better approach might be to use HgTe wells and HgCdTe alloy barriers, where the positive gap energy of the alloy is nearly matched to the negative –0.26 eV gap of HgTe. The required +0.26 eV HgCdTe alloy has x = 0.18, and is 4 times less sensitive to compositional variations than an alloy with x=0.168 designed to work at 0.01 eV directly. Furthermore, possible diffusion of Hg from the wells during processing can be allowed for in designing the deposition process for the barriers. A SL designed with pure CdTe barriers would require more stringent controls on Hg diffusion.

FIR Mixers

Photoconductive materials can be used to make two device types that are applicable as FIR heterodyne mixers: a reverse-biased photodiode (PD), and a DC-biased photoconductor (PC). A heterodyne mixer needs an extremely fast response time to achieve a reasonable IF bandwidth of 2 GHz. Consequently, a PD mixer must be reverse biased with a relatively high field to minimize the device capacitance and to maximize the depth of the depletion region where photogenerated carriers can be collected quickly. Whereas this can be done effectively with high bandgap materials (E_g>0.03 eV), for low-gap materials, the high space-charge field leads to excess tunneling currents that degrade

mixer sensitivity. Of course, for FIR applications, low gap materials must be chosen, and we are left with the PC device structure as our only choice if *alloy* devices are used. A PC mixer can operate with electric field strengths 10 times less than those required by a PD device, provided carrier transit times are kept short, and that means a small interelectrode spacing. On the other hand, if tunneling currents can be reduced as predicted with the *superlattice* structure, then PD devices may become practical out to 100 μm and perhaps 150 μm wavelength.

To minimize the LO power required by a photoconductive mixer, it is important to maximize the current responsivity, or equivalently the photoconductive gain g , given by:

$$g = \frac{\tau}{T} = \frac{\tau \mu E}{d}.$$

Here T is the transit time, μ is the electron mobility, E the applied electric field, τ is the carrier lifetime which sets the IF bandwidth $B=(2\pi\tau)^{-1}$, and d is the electrode spacing. For the high-speed devices of interest here, the maximum value of g is 1 when all the electrons and holes are collected. Another possible condition is that the electrons are collected quickly by the electrodes but the slow moving holes are not. This leads to a condition called minority carrier sweepout where $g(max) = 0.5$. The electron and hole mobilities of HgCdTe are high ($\mu_e = 10^5$ cm^2 V^{-1}s^{-1} and $\mu_h=\mu_e/200$), and the carrier velocity μE readily saturates at about 3×10^7 cm s^{-1} in HgCdTe.

Given that we also want a minimum IF bandwidth of 2 GHz and hence carrier lifetime of 10^{-10} s^{-1}, the only variable available to adjust is the electrode spacing d. Maximum gain with 2 GHz IF bandwidths requires that d be no larger than 20 μm. On the other hand, a certain detector cross-section D is needed for efficient coupling to an optical field - generally $D=2\lambda$. The solution is to use interdigitated electrodes (IDE) on the detector surface, with the required electrode number N being just D/d. For λ=120 μm, D=240 μm and we need at least 12 interdigitated electrodes. Surface electrodes are efficient collectors of photogenerated carriers when the absorption depth is not much greater than the electrode spacing. The preferred signal polarization is perpendicular to the long electrode dimension. Another approach would be to couple radiation via a Si immersion lens (n=3.416) so that the required mixer size is only 70 μm. These size trade-offs must be considered when designing 8-element heterodyne arrays.

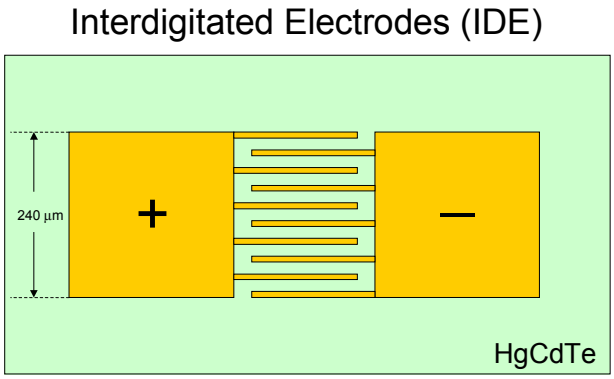

Figure 2: Front Surface View of IDE device

The general expression for the NEP of a photoconductive heterodyne receiver is given by the formula (Kingston 1978):

$$NEP = \left(\frac{h\nu B}{\eta}\right)\left(1 + \frac{P_{Min}}{P_{LO}}\right).$$

Normally, a photoconductive mixer with both generation and recombination noise would have an NEP twice the value given above. However, when recombination is not random, but rather occurs only at the contacts (as with reverse-biased photodiode mixers), then the NEP is as stated. Contact recombination occurs in a photoconductor when the minority carriers are all swept out, and this condition will likely obtain for the IDE devices.

In the NEP equation, η is the quantum efficiency, B is the IF bandwidth, and P_{LO} is the local oscillator power. P_{Min} is the LO power for which the noise power of the LO-induced photocurrent is equal to the input noise power $kT_{IF}B$ of the IF amplifier stage, and is given by:

$$P_{Min} = \frac{2kT_{IF}h\nu}{e^2 g\eta R_{IF}}\left(1 + \omega^2\tau^2\right).$$

Here R_{IF} is the input impedance of the IF amplifier and T_{IF} is its noise temperature. The variable ω is the IF signal frequency. We see that a high value of g (with a maximum of 1) minimizes the required LO power. LO power levels much higher than P_{Min} raise the system gain but do not improve the NEP sensitivity significantly, except at frequencies beyond the –3dB IF signal bandwidth. This can be seen in Figure 3, where the above power equation is plotted for two sets of conditions. Under ideal conditions (η=1, g=1), and with T_{IF}=10 K, R_{IF}=50Ω, and ν=3 THz, P_{Min} is about 2 µW. With more realistic conditions (η=0.4, g=0.5), P_{Min} is 10 µW. Even for an array of 8 such mixers, adequate LO power is available from a 1 mW FIR laser coupled via a 10% beamsplitter.

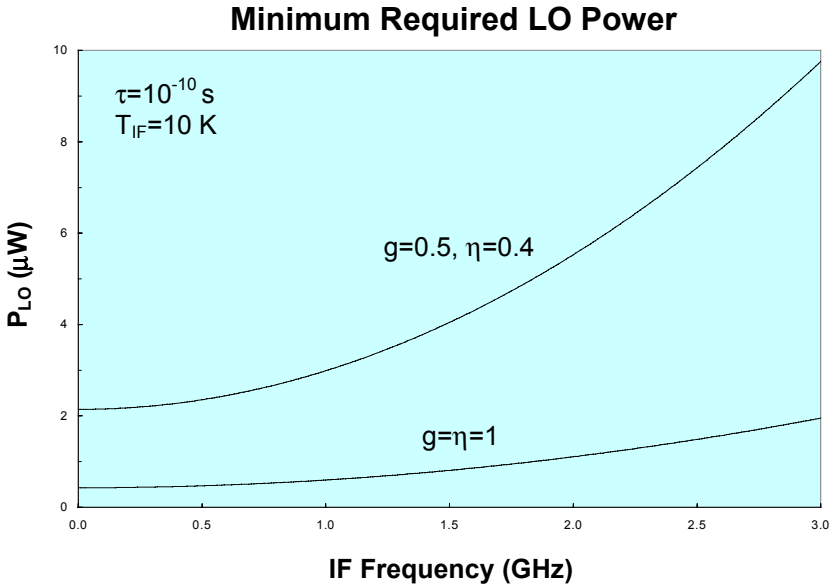

Figure 3: LO Power Requirements

Ideally, p-type HgCdTe should be used to fabricate a PC mixer. The mobility of holes is low enough that a device impedance of >50 Ω is possible with as many as 10 interdigitated electrodes across a 200 μm surface, provided the carrier density at the operating temperature is $< 3\times10^{15}$ cm^{-3}. P-type material also eliminates the conduction band filling problems encountered with n-type material that lead to bleaching of the detector's long wavelength response. Proper control of materials with MBE deposition should allow one to construct a PC mixer with good quantum efficiency (>0.25) over the entire 50-150 μm (2-6 THz) band, except for a "dead-spot" between 70-90 μm where HgCdTe has a lattice band absorption.

We can be fairly certain of good results with HgCdTe alloy material because FIR devices have already been made this way. Spears in the late 1980's developed PC mixers with $Hg_{1-x}Cd_xTe$ (x=0.168) that showed a response as long as λ=118 μm [Spears 1988]. At that time only bulk (ingot grown) materials were available, and the exact alloy composition could only be fixed by selection from material with a composition gradient. In addition, that material was n-type, and device impedances were too low for optimal IF coupling. Nevertheless, Spears was successful in demonstrating the utility of IDE biasing and also the use of resonant reflector-enhanced absorption to increase the quantum efficiency to as high as 0.6 in 5 μm thick PC devices. Although IF bandwidths between 1.7 GHz and 6.0 GHz were measured for devices with different photoconductive gains, no heterodyne sensitivity tests were made.

Resonant Cavity Enhanced (RCE) Photodetectors

If interdigitated surface electrodes are to be used effectively, the thickness of the absorbing region must be kept smaller than the interelectrode spacing so that photogenerated carriers see high electric fields. This imposes the requirement that the active absorber be less than 10 μm thick. We can use thin absorbers and still get high quantum efficiencies if we put the absorber in a resonant cavity. Figure 4 shows a cross-sectional view of the resonant device structure. A Fabry-Perot cavity is defined by the front surface of the mixer and a suitably spaced rear surface. The reflectance R_1 of the front surface is just the specular reflection from the uncoated material. The rear surface is metallized to produce a reflectance R_2 close to 1. The pure silicon substrate underneath the active region provides the required spacing.

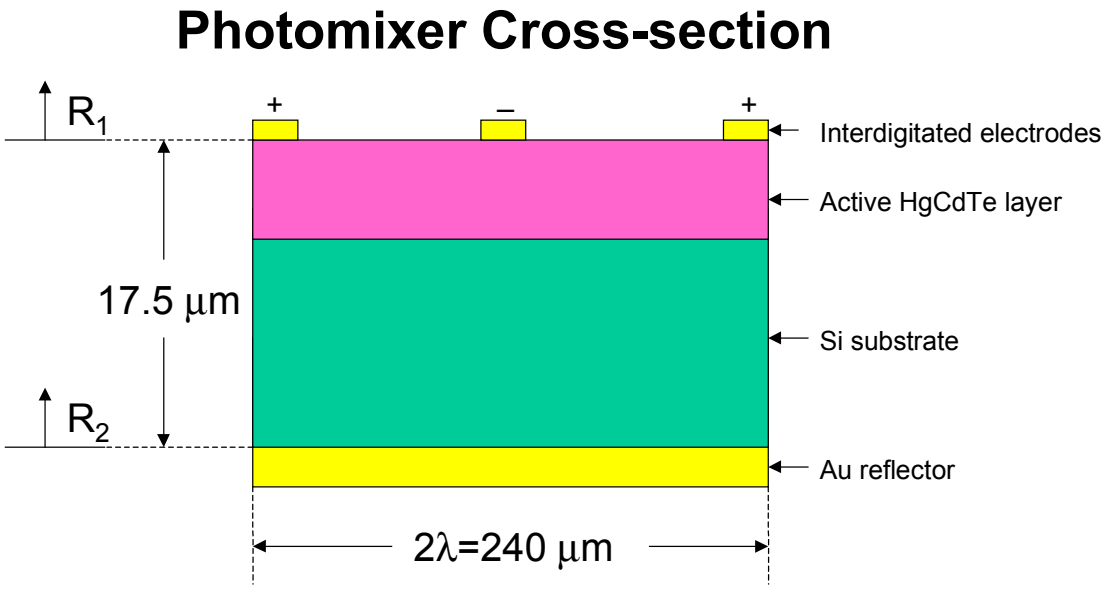

Figure 4: RCE Device Structure

The enhancement in absorption, and hence quantum efficiency, is given by the equation:

$$\eta = \frac{1 + R_2 e^{-\alpha d}}{1 - 2\sqrt{R_1 R_2}\, e^{-\alpha d} \cos[4n\pi L/\lambda + \psi_1 + \psi_2] + R_1 R_2 e^{-2\alpha d}} (1 - R_1)(1 - e^{-\alpha d}).$$

Here ψ_1 and ψ_2 are the small phase shifts at the two surface reflections (here assumed = 0), α the absorption coefficient, and d the thickness of the active layer. R_1 is the front-surface (power) reflection coefficient, and R_2 is that for the rear surface. The overall device thickness is L, and the average index of refraction is given by n. This equation is plotted in Figure 5 for two sets of conditions. When $R_1=R_2=0$, we have single pass absorption for AR coated surfaces. We see that for realistic conditions we can enhance the quantum efficiency by greater than a factor of 4 over a 16% bandwidth (in first order). Quantum efficiencies greater than 0.4 are possible, and hence heterodyne sensitivities only a few times worse than the quantum limit are feasible. Spears fabricated devices of this type in the late 1980's, but was unable to obtain the high efficiencies predicted here because of low absorption efficiencies at long FIR wavelengths. The n-type material available at the time had excessive conduction band filling (Burstein-Moss effect) that "bleached away" the long wavelength response. This problem can be corrected in MBE work by controlling impurities so as to keep the material p-type with hole densities less than $3x10^{15}$ cm^{-3}. The low mobility of majority holes also keeps the dark current low and ensures that the IDE device impedance will be high enough for IF matching.

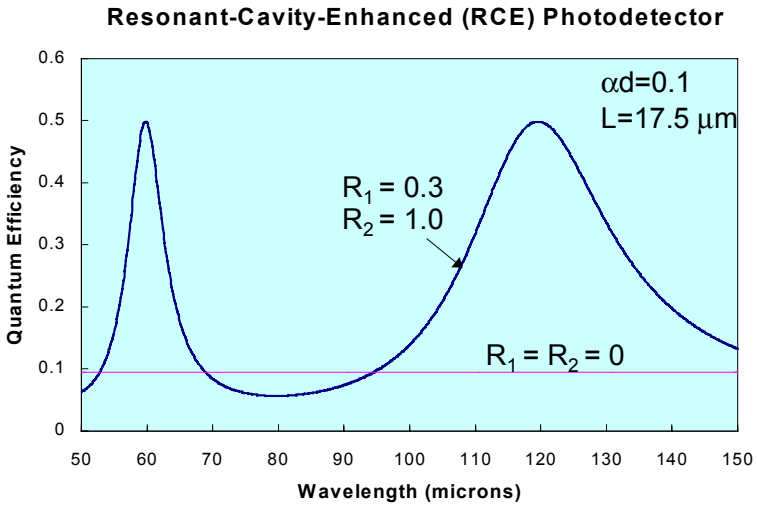

Figure 5: Resonant Enhancement of Quantum Efficiency

We believe that a quantum efficiency of η=0.1 can be obtained in early generation devices at 3 THz. Our 3-year goal is η=0.4. At 6 THz (λ=50 μm), initially η=0.2 should be possible in a resonant-cavity device structure. The 3-year goal at this wavelength is η=0.6. A photoconductor (PC) is inherently a broadband mixer for frequencies higher than the energy gap. In contrast to antenna coupled devices, a HgCdTe PC mixer becomes easier to fabricate as the cutoff wavelength decreases.

This work is supported in part by NASA under grant NAG5-10213.

Bibliography

Betz, A.L., in *Laser Spectroscopy V*, Springer Series in Optical Sciences (Springer-Verlag: Berlin, New York 1981), pp. 81-88

Boreiko, R.T., and Betz, A.L., *Astrophys. J. Lett.,* **464**, L83-L86 (1996)

Hansen, G. L., and Schmit, J. L., *Jour. Appl. Phys.* **54**, 1639 (1983)

Kingston, R.H., *Detection of Optical and Infrared Radiation,* Springer Series in Optical Sciences (Springer-Verlag: Berlin, New York 1978), pp. 41-42

Kostiuk, T., and Spears, D.L., *Int. Journal of Infrared and Millimeter Waves,* **8**, 1269-1279 (1987)

Mahavadi, K.K., Sivananthan, S., Lange, M.D., Chu, X., Bleuse, J., and Faurie, J.P., *J. Vac. Sci. Technol*. **A8**, 1210 (1990)

Park, I.S., Haller, E.E., Grossman, E.N., and Watson, D.M., *Applied Optics,* **27**, 4143-4150 (1988)

Schulman, J. N., and McGill, T. C., *Appl. Phys. Lett*., **34**, 663-665 (1979)

Spears, D.L., *Technical Digest of CLEO 88*, "Wideband Interdigitated-Electrode p-HgCdTe Photomixers at 25 μm" (1988)

Sporken, R., Sivananthan, S., Faurie, J.P., Ehlers, D.H., Fraxedas, J., Ley, L., Pireaux, J.J., and Caudano, R., *J. Vac. Sci. Technol.,* **A7**, 427 (1989)

Wang, L., Sivananthan, S., Sporken. R., and Caudano, R., *Phys.Rev.B*, **54**, 2718 (1996)

Wyss, R.A., Karasik, B.S. McGrath, W.R., Bumble, B., and LeDuc, H., *in Proc. Tenth Int. Symp. Space Terahertz Tech.*, Charlottesville, VA, 16-18 March 1999

Very Wide IF Bandwidths in High Mobility Two-Dimensional Electron Gas Semiconductor Heterostructure Mixers

Mark Lee, Loren N. Pfeiffer, and Ken W. West
Bell Laboratories – Lucent Technologies, 600 Mountain Ave., Murray Hill, New Jersey 07922

There has been great progress in the development of superconducting hot-electron bolometers (HEBs) for use as millimeter and sub-millimeter wave mixers. In particular, the diffusion-cooled niobium HEB has demonstrated low noise, low local oscillator (LO) power requirement, and an intermediate frequency (IF) bandwidth of 2 to 10 GHz in devices with deep sub-micron channel lengths.[1] Yngvesson has suggested[2] that the same principle could be applied to the two-dimensional electron gas (2DEG) in a GaAs-AlGaAs heterostructure. Because of the extremely high electron mobilities obtainable in a 2DEG, IF bandwidths much wider than possible in a superconductor should be achievable in much larger devices, with acceptable compromises in terms of gain, noise, and LO power.

We fabricated antenna-coupled HEB mixers using very high mobility 2DEGs in a GaAs–$Al_{0.28}Ga_{0.72}As$ heterostructure. The 2DEG mobility is 3.1 x 10^5 cm^2/V-s at 77 K and 7.5 x 10^6 cm^2/V-s at 1.5 K, with a sheet carrier density of 2.4 x 10^{11} cm^{-2}. HEB mixers with channel lengths L ranging from 2 to 10 μm were fabricated by etching mesas into the heterostructure, and the ohmic contacts to the 2DEG were coupled to log-periodic antennas and co-planar waveguides. Heterodyne mixing was done using a fixed 115 GHz source and a tunable 115 to 140 GHz source, both coupled in quasi-optically. The IF bandwidth of the measurement system was 20 GHz, limited by an IF low-noise amplifier.

Operating at 77 K, we directly measured 3 dB IF bandwidths ranging from 3 up to 19 GHz corresponding to mixers with L of 10 μm down to 4 μm, respectively. In mixers with shorter L, bandwidths as high as ~ 70 GHz in a 2 μm long device can be extrapolated from Lorentzian fits to the conversion gain roll-off. These bandwidths are all limited by the transit time of a hot electron to move across the channel. For mixers with $L > 4$ μm, the 3 dB frequency scales as L^{-2}, indicating that the hot electrons diffuse across the channel. The diffusion constant obtained from the data is 1.9 x 10^3 cm^2/s. When $L < 4$ μm, the transit time becomes limited by ballistic motion across the channel.

The conversion gain measured is about –16 dB at 0.5 GHz IF using approximately 10 μW of LO power. The conversion gain is only weakly dependent on L, but appears to have some correlation with the DC contact resistance. Preliminary noise power measurements show a system noise temperature of 3500 K operating at 77 K. These results and their relation to calculated expectations[2] will be discussed.

---

[1] B. S. Karasik, M. C. Gaidis, W. R. McGrath, B. Bumble, and H. G. LeDuc, Appl. Phys. Lett. **71**, 1567 (1997)

[2] K. S. Yngvesson, Appl. Phys. Lett. **76**, 777 (2000)

Terahertz Detection by High Electron Mobility Transistor: Effect of Drain Current

J.-Q. Lu and M.S. Shur

Center for Integrated Electronics and Electronics Manufacturing,
Rensselaer Polytechnic Institute, Troy, New York 12180
Tel: (518) 276-2201, luj@rpi.edu, shurm@rpi.edu

Abstract

We report on a new regime of operation of High Electron Mobility Transistor (HEMT) terahertz detectors, in which we apply a constant (*dc*) drain bias. The measured responsivity increases with the drain current by more than an order of magnitude and saturates at the *dc* bias corresponding to the saturation of the *dc* drain current for given gate voltage. We link this increase in the detector responsivity to the drain bias dependence of the gate-to-source and gate-to-drain capacitances, which results in a much greater asymmetry in the boundary conditions for plasma waves. These results confirm our model linking the HEMT detector response to the propagation of overdamped plasma waves in the device channel.

Introduction

Plasma waves in short-channel High Electron Mobility Transistors (HEMTs) have a resonant response at terahertz frequencies [1]. The HEMTs operating in a plasma wave regime should respond at much higher frequencies than conventional, transit-time limited devices, since the plasma waves propagate much faster than electrons. We refer to such devices as *plasma wave electronics* devices. The rectification of the plasma waves (linked to the asymmetry of the boundary conditions at the source and the drain) can be used for the tunable detection of electromagnetic radiation at terahertz frequencies.

This plasma wave electronics short-channel HEMT detector produces an open circuit *dc* voltage, which is proportional to the intensity of the incoming terahertz radiation with a resonance response to electromagnetic radiation at the plasma oscillation frequency. The resonant plasma frequency can be tuned by the gate bias, which makes the plasma wave electronics detector suitable for many applications involving far infrared spectroscopy for the detection of chemical and biological substances. The dynamic range of such a detector is limited by the gate voltage swing, since the responsivity decreases when the terahertz radiation induced *ac* voltage becomes on the order of a few percent of gate voltage swing.

Longer HEMTs exhibit a non-resonant, broadband response to electromagnetic

radiation caused by overdamped plasma waves that degenerate into space charge waves in very long devices. Such devices can still be used as broadband detectors for frequencies up to several tens of terahertz.

Our recent experimental data (see [2,3]) confirm many features of the theoretical predictions but also pose many questions. We have demonstrated non-resonant detectors fabricated using AlGaAs/GaAs [4] and AlGaN/GaN HFETs [5] operating at frequencies below 20 GHz. More recently, we have reported on the implementation of the AlGaAs/GaAs terahertz HEMT detector [3,6], where the devices operated at 2.5 THz, which is about 30 times higher than the transistor cutoff frequency.

In this paper, we report on a new regime of operation of such HEMT terahertz detectors that allowed us to increase the device responsivity by more than an order of magnitude. The motivation for this new regime comes from our theoretical analysis of the effect of the boundary conditions [5,7], which shows that the maximum detector response occurs when the asymmetry between the boundary conditions at the source and drain contacts of the device is the largest. (For a completely symmetrical structure with symmetrical boundary conditions, we, of course, expect and predict a zero detector response.)

Experimental Results

Device Characterizations

The experimental results reported in this paper were obtained using a GaAs/AlGaAs low noise HEMT chip (Fujitsu FHR20X) [8]. Figures 1 through 4 show the measured device characteristics. The estimated threshold voltage for this device V_T = -0.6 V. The device gate width was W = 100 μm (two section of 50 μm each). The estimated gate length was approximately L = 0.15 μm.

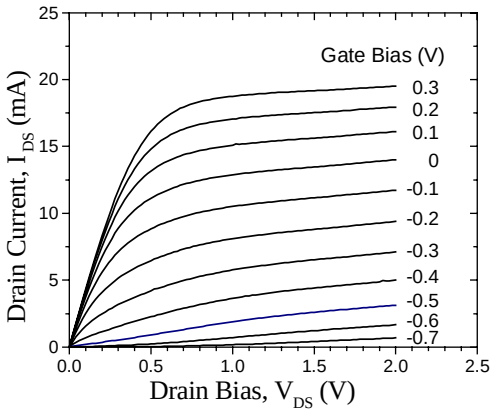

Fig. 1. I-V characteristics of the HEMT. The data was taken when only left source is grounded and the right source is floating.

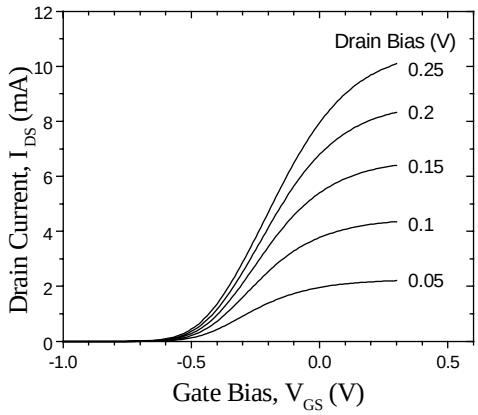

Fig. 2. HEMT transfer characteristics. The data was taken when only left source is grounded and the right source is floating.

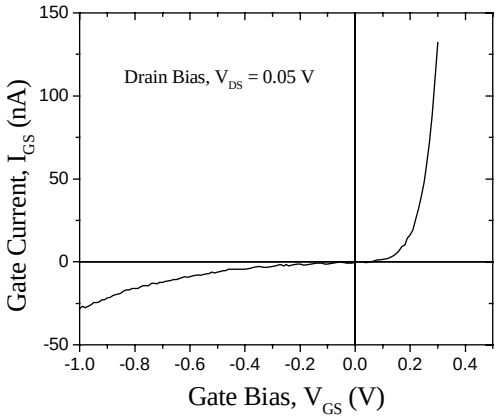

Fig. 3. HEMT FHR20X gate leakage current versus gate bias. The drain source bias is 0.05 V.

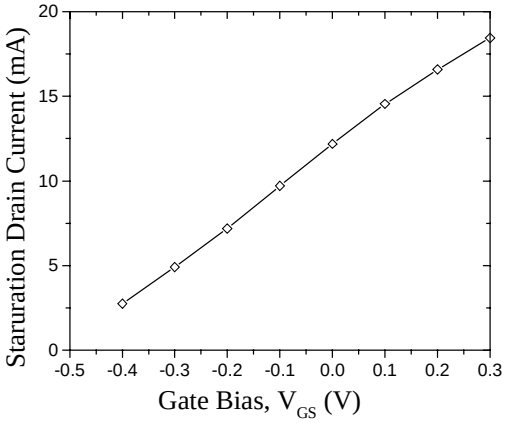

Fig. 4. Saturation drain current vs. gate bias, Isat vs V_{GS}. The data are extracted from the device I-V characteristics shown in Fig. 1.

Figure 5 shows the gain versus frequency of the HEMT, calculated from the scattering parameters taken from the Fujitsu Databook [8], where the bias condition is as follows: V_{DS} = 2 V, I_{DS} = 5 mA.

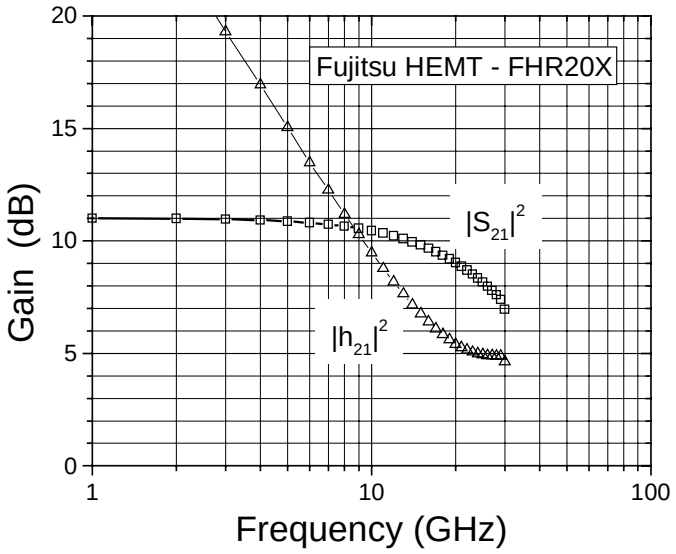

Fig. 5. The gain versus frequency of the HEMT.

Both the device operating frequency (~18 GHz) and the cutoff frequency are orders of magnitude smaller than the terahertz frequency of the radiation used in our experiments. This makes it difficult to use lumped equivalent circuit for the interpretation of our experiments, even though we believe that the asymmetry in the values of the gate-to-source and gate-to-drain capacitances still represent a crude measure of the boundary conditions for the terahertz signal (see our discussion below).

Terahertz Detection

The terahertz detector was fabricated using a Fujitsu FHR20X HEMT mounted on a quartz substrate. The device threshold voltage is close to V_T = -0.6 V, extracted from the measured device *dc* characteristics. A CO_2-pumped far-infrared gas laser served as a source of 2.5 THz radiation. The polarized laser beam was chopped and focused on the sample as shown in Fig. 6. The induced *dc* drain voltage, U_{DS} (that appeared in response to the THz radiation), was superimposed on the drain bias voltage (causing a *dc* drain current, I_{DS}). U_{DS} was measured using lock-in technique. The detector was tuned by a *dc* gate bias, V_{GS}, and the response was a strong function of I_{DS}.

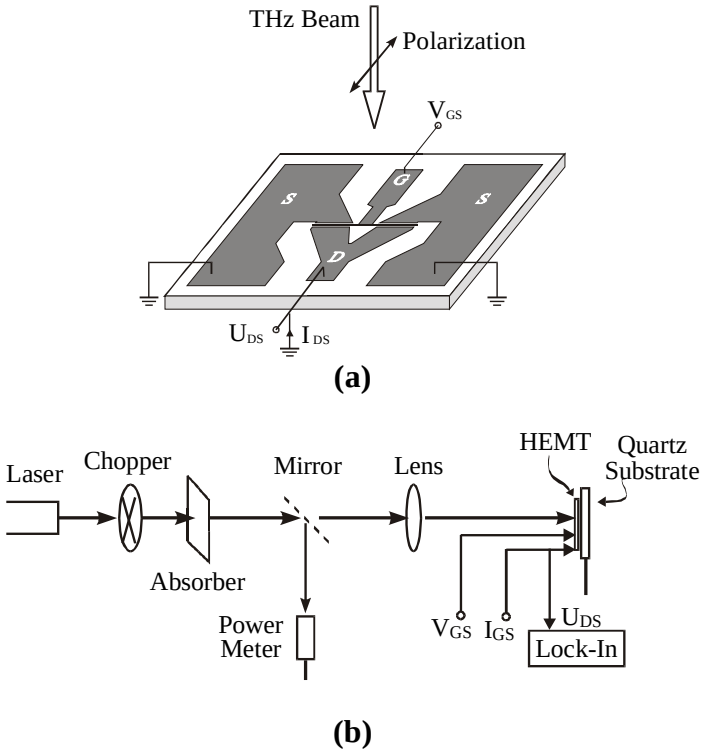

Fig. 6. Detector layout using a Fujitsu FHR20X HEMT with V_T = -0.6 V, and (b) measurement setup with a 2.5 THz laser. The detector response - the *dc* drain voltage, U_{DS}, was measured using lock-in technique.

In the new regime of operation, we apply a *dc* drain bias. The drain bias dependence of the gate-to-source and gate-to-drain capacitances leads to a much greater asymmetry in the boundary conditions for plasma waves and greatly enhances the detector responsivity. As can be seen in Fig. 7, the detector response, *dc* drain voltage, U_{DS}, increases significantly with the applied *dc* drain current, compared with the response without drain current (see the inset of Fig. 7).

We should also notice sharp spikes in the response at the gate bias near the threshold for drain currents from 0.1 to 0.5 μA. These spikes were quite reproducible. However, at the moment we have no explanation for these peaks.

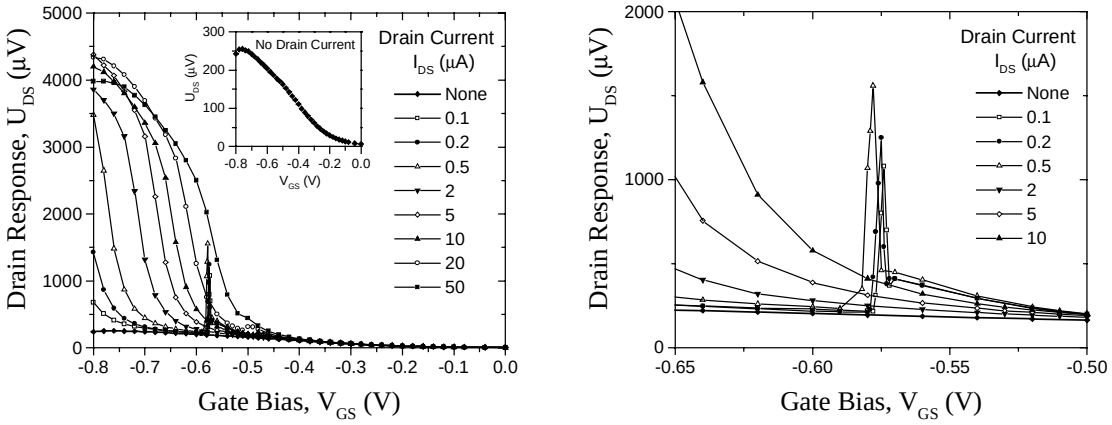

Fig. 7. Measured detector responses (U_{DS}) versus gate bias (V_{GS}) at different *dc* drain currents (I_{DS}). Inset is the drain response without a *dc* drain current. Also shown the measured spikes in response in an expanded scale (left figure).

We also notice that the response peaks at the gate bias somewhat below threshold (see Fig. 8). This is predicted by our theory that links the reduction in the response at the gate bias well below threshold due to the gate leakage current [9].

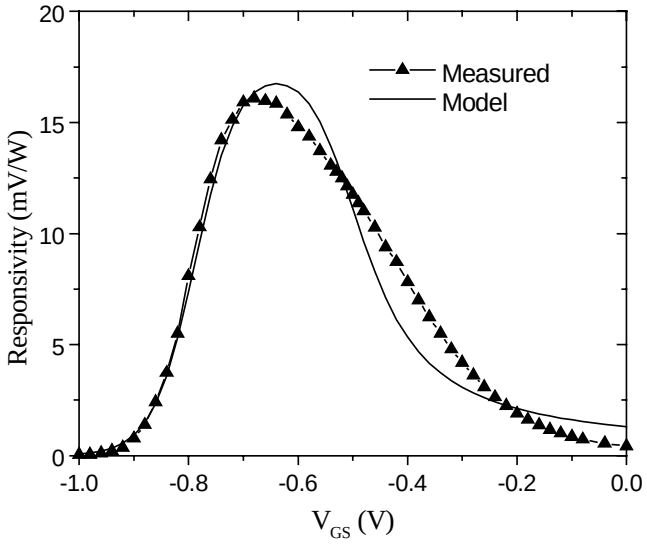

Fig. 8. Typical detector responsivity as a function of gate bias. The solid line is a first order simulation using a HEMT detector model, which is good also for the subthreshold regime [9]. The parameters used for the simulation are threshold voltage, V_T = -0.52 V, ideality factor extracted from Fig. 2, η = 1.5, and the leakage factor, $\Gamma = 10^{-3}$.

Fig. 9 shows detector response versus the drain current at different gate bias. The response increases with the applied *dc* drain current and saturates at a saturation drain current for given gate bias.

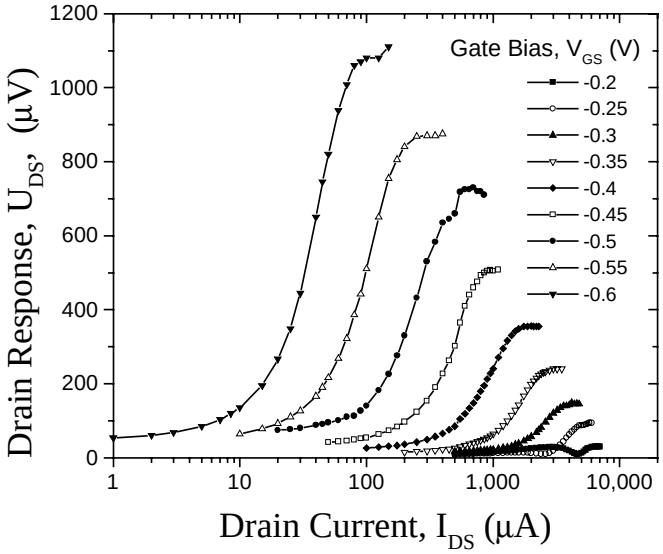

Fig. 9. Measured detector responses (U_{DS}) versus *dc* drain current (I_{DS}) at different gate biases (V_{GS}) at 2.5 THz.

Fig. 10 shows the gate bias dependence of the saturation currents extracted from I-V characterization and from Fig. 9, U_{DS} versus I_{DS} curve. These results confirm our model linking the responsivity increase to the drain bias dependence of the HEMT capacitances.

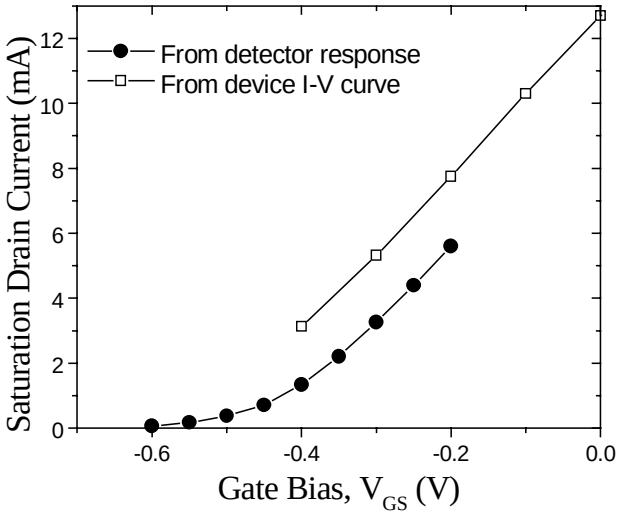

Fig. 10. The saturation drain currents versus gate bias. The circle data are extracted from Fig. 9, U_{DS} versus I_{DS} curve. The square data are extracted from the device I-V characteristics in Fig. 1, where the drain current saturates at certain drain bias for a given gate bias.

Discussion

Fig. 11 shows the calculated dependencies of the gate-to-source and gate-to-drain capacitances for zero and -0.3 V gate bias for an AlGaAs/GaAs HEMT with parameters corresponding to our devices. The gate-to-source and gate-to-drain capacitance values, C_{GS} and C_{GD}, are given as [10]:

$$C_{GS} = \frac{2}{3} C_{ch} \left[1 - \left(\frac{V_{GT} - V_{DSe}}{2V_{GT} - V_{DSe}} \right)^2 \right],$$

$$C_{GS} = \frac{2}{3} C_{ch} \left[1 - \left(\frac{V_{GT}}{2V_{GT} - V_{DSe}} \right)^2 \right],$$

where C_{ch} is gate channel capacitance of the HEMT at zero drain-source bias, the gate bias swing $V_{GT} = V_{GS}-V_T$, and V_{DSe} is the effective intrinsic drain-source voltage given by:

$$V_{DSe} = \frac{1}{2} \left[V_{DS} + V_{GTe} - \sqrt{V_d^2 + (V_{DS} - V_{GTe})^2} \right].$$

Here, V_d is a constant voltage that determines the width of the transition region and V_{GTe} is an effective gate voltage overdrive (equal to V_{GT} above threshold and of the order of thermal voltage in the subthreshold regime). The details of the capacitance model are described in Reference [10].

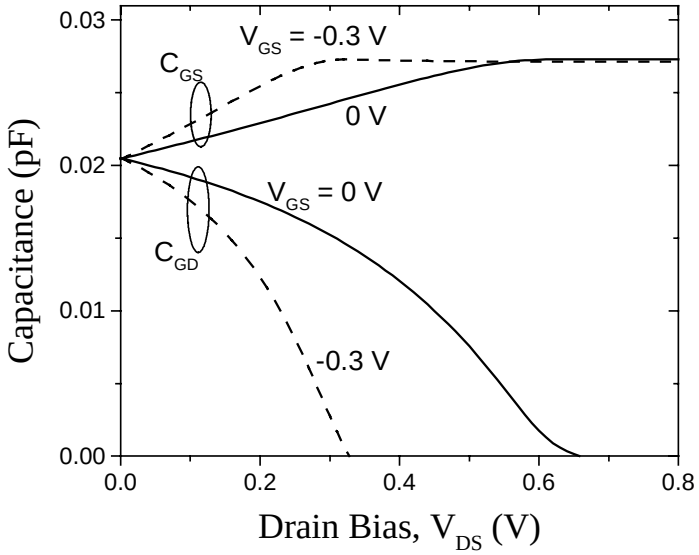

Fig. 11. Gate-to-source and gate-to-drain capacitances for zero and -0.3 gate biases: C_{GS} and C_{GD} versus drain bias. Parameters used in the calculation: threshold voltage, V_T = -0.6 V, gate width and length W = 50

μm and L = 0.15 μm, respectively, AlGaAs thickness, d_i = 25 nm, maximum density of the two-dimensional (2D) electron gas, n_{smax} = $2.5x10^{16}m^{-2}$.

As can be seen from the Fig. 11, at the saturation voltage, which is approximately 0.6 V in the frame of this model for V_{GS} = 0 (0.3 V for V_{GS} = -0.3 V), C_{GD} is nearly zero, whereas C_{GS} reaches its maximum value. Hence, the drain bias dependence of the gate-to-source and gate-to-drain capacitances leads to a much greater asymmetry in the boundary conditions for plasma waves and greatly enhances the detector responsivity. This asymmetry reaches its maximum at smaller drain biases for smaller (larger negative) gate biases (compare the curves for V_{GS} = -0.3 V and V_{GS} = 0 V).

Figure 12 shows that the response saturates as a function of the drain bias at approximately the *dc* drain saturation voltage of I-V characteristics. This is in agreement with our data shown in Fig. 10 and with our interpretation linking this behavior to the enhanced asymmetry in the boundary conditions (see Fig. 11).

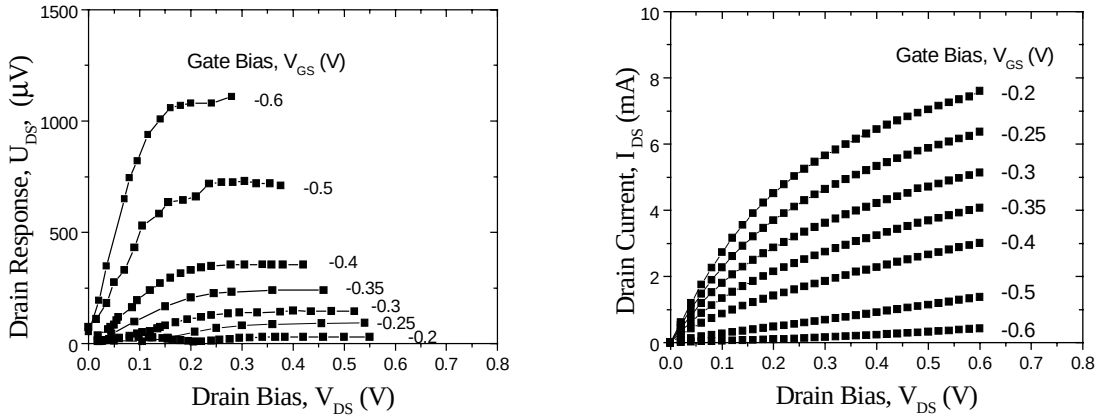

(a) **(b)**

Fig. 12. Comparison of the drain response versus drain bias to *dc* drain current versus drain bias. (a) The drain response versus drain bias curve was converted from Fig. 9. (b) The I-V characteristics are part of Fig. 1.

Conclusions

Our experimental data support the plasma wave mechanism of the terahertz detection by High Electron Mobility Transistors. These results confirm that the gate leakage current does not play a role in the terahertz detection in the above threshold regime, since this current decreases with the drain bias. A strong enhancement of the detector responsivity by a constant drain current and the saturation of this response when the *dc* drain current reaches saturation point confirm the dominant role of the asymmetry in the boundary conditions in determining the detector responsivity.

Acknowledgments

This work has been supported by DARPA (Program Manager, Dr. Edgar Martinez) and by ARO (Program Manager, Dr. Dwight Woolard). We are also grateful to Dr. J. Hesler and Mr. L. Suddarth of University of Virginia for their help with the measurements and to Professor M. Dyakonov for useful discussions.

References:

[1] M. Dyakonov and M. S. Shur, "Detection, mixing, and frequency multiplication of terahertz radiation by two dimensional electronic fluid", *IEEE Trans. Electron Dev.*, vol. 43, no. 3, pp. 380-387, 1996.

[2] M.S. Shur, J.-Q. Lü, and M. Dyakonov, "Plasma Wave Electronics: Terahertz Sources and Detectors Using Two Dimensional Electronic Fluid in High Electron Mobility Transistors", *Proceedings of 1998 IEEE 6th International Conference on Terahertz Electronics*, Leads, UK, pp. 127-130, 1998

[3] J.-Q. Lü, M. S. Shur, J. L. Hesler, L. Sun, and R. Weikle II, "A Resonant Terahertz Detector Utilizing a High Electron Mobility Transistor", *IEDM Technical Digest*, pp. 453-456, San Francisco, CA, 1998

[4] R. Weikle, J.-Q. Lü, M. S. Shur, M. I. Dyakonov, *Electronics Letters*, vol. 32, no. 23, pp. 2148-2149, 1996

[5] J.-Q. Lü, M. S. Shur, R. Weikle, M. I. Dyakonov, and M. A. Khan, *Proceedings of 16th Conference on Advanced Concepts in High Speed Semiconductor Devices and Circuits*, Ithaca, NY, pp. 211-217, 1997

[6] J.-Q. Lü, M. S. Shur, J. L. Hesler, L. Sun, and R. Weikle, *IEEE Electron Dev. Lett*., vol. 19, No. 10, pp. 373-375, 1998

[7] J.-Q. Lu and M.S. Shur, "Effect of Loading on Plasma Wave Detector Utilizing Two-Dimensional Electron Fluid", http://www.rpi.edu/~luj/loadeffect.htm, Dec. 2000.

[8] Fujitsu Microwave Semiconductor Databook (1999), Fujitsu Compound Semiconductor, Inc., 2355 Zanker Rd., San Jose, CA 95131-1138, USA.

[9] V.Katchorovski, J-Q. Lu, and M.S. Shur, "Broad Band Plasma Wave Detector Below Threshold Voltage in High Electron Mobility Transistors: Theory and Experiment", unpublished.

[10] T. A. Fjeldly, T. Ytterdal, and M. S. Shur, Introduction to Device Modeling and Circuit Simulation, John Wiley & Sons, New York, 1998.

Kinetic Inductance Photodetectors Based on Nonequilibrium Response in Superconducting Thin-Film Structures

A.V. Sergeev [a,d], B.S. Karasik[b], I.G. Gogidze[c], and V.V. Mitin[a]

[a]Dept. of Electrical and Computer Engineering, Wayne State University, Detroit, MI 48202
[b]Jet Propulsion Laboratory, California Institute of Technology, Pasadena, CA 91109
[c] Winncom Technologies Corp., Solon, OH 44139
[d] Contact author: tel.: (313) 577-5507, fax: (313) 577-1101,
e-mail: sergeev@ciao.eng.wayne.edu

Abstract **-- While experimental studies of kinetic-inductance sensors have been limited so far by the temperature range near the superconducting transition, these detectors can be very sensitivity at temperatures well below the transition, where the number of equilibrium quasiparticles is exponentially small. In this regime, a shift of the quasiparticle chemical potential under radiation results in the change of the kinetic inductance, which can be measured by a sensitive SQUID readout. We modeled the kinetic inductance response of detectors made from disordered superconducting Nb, NbC, and MoRe films. Low phonon transparency of the interface between the superconductor and the substrate causes substantial re-trapping of phonons providing high quantum efficiency and the operating time of ~1 ms at ≈ 1 K. Due to the small number of quasiparticles, the noise equivalent power of the detector determined by the quasiparticle generation-recombination noise can be as small as ~10^{-19} W/√Hz at He4 temperatures.**

Bolometric sensors are currently the detector of choice for space astrophysics missions in a broad range from millimeter waves to X-rays. In the submillimeter wave range bolometers are the only option having currently demonstrated the noise equivalent power (*NEP*) of the order of 10^{-17} - 10^{-18} W/√Hz at ~0.1 K [1]. Future space radio telescopes will require two orders of magnitude greater sensitivity [2], which may be difficult to achieve with a conventional mechanical design of the bolometers based on Si_3N_4 membranes. An alternative approach to the problem of increasing sensitivity relies on the electron heating in superconducting structures. The corresponding detectors do not require thermal mechanical insulation and can be fabricated on bulk substrates. For example, recently proposed hot-electron resistive microbolometer with disorder-controlled electron-phonon coupling [3] promises the *NEP* ~ 10^{-19} W/√Hz and the time constant, $\tau \sim 10^{-5}$ s at 0.3 K, and *NEP* ~ 10^{-20} W/√Hz and $\tau \sim 10^{-4}$ s [4] at 0.1 K. Another

way to make a hot-electron sensor is to use a kinetic inductance of a superconducting film. In this case, the detector will be able to operate at temperatures above 1 K with very high sensitivity.

There has been significant interest to the kinetic-inductance detectors (KID) operating near the superconducting transition [5,6,7,8,9,10]. Near T_c, the kinetic inductance has strong temperature dependence and can be used as superconducting thermometer. Both bolometric [5-7] and hot-electron [8-10] components have been observed in the response of superconducting microbridges to electromagnetic radiation. Infrared bolometers using kinetic inductance thermometers have been developed in Refs. 5 and 6. In the superconducting state near T_c, the electron and phonon heat capacities and characteristic relaxation rates are close to those in the resistive state. Therefore, the kinetic-inductance detectors offer approximately the same *NEP* and the response time as corresponding resistive bolometers and hot-electron detectors. The main advantage of the inductive detectors operating near T_c in comparison to the resistive counterpart is the absence of Johnson noise. To our knowledge, the non-equilibrium (hot-electron) mode of operation of the KID at $T << T_c$ has not been considered yet. Meanwhile, this regime is advantageous for the detector operation since the number of quasiparticles is exponentially small and the corresponding generation-recombination noise is small as well.

In the current paper, we consider a hot-electron KID operating in the superconducting state far below the superconducting transition but still at temperatures accessible with sorption He3 or He4 cryostats. Such a detector made from a superconductor with T_c ~ 6-10 K allows for the *NEP* ~10^{-19} W/√Hz determined by the quasiparticle generation-recombination noise. The background radiation is effectively cut off below the superconducting gap frequency, $f_c = 2\Delta/h$ (Δ is the superconducting gap). As well as the resistive hot-electron detector [3], the kinetic-inductance one has a number of attractive features for submillimeter and far-infrared operation: the devices can be fabricated on Si or sapphire substrates, the rf impedance can be easily matched to that of a planar antenna, and the detectors has a large array scalability.

The schematic circuit of the KID with a SQUID readout is shown in Fig. 1. The constant bias current, I_b, splits between two branches of a superconducting loop. The change of the kinetic inductance, δL_k, of the detector results in a signal electric current, δI, circulating in the superconducting loop and producing a magnetic flux, which is detected by a sensitive dc SQUID. If the inductance in the second branch, L_2, is significantly larger than that in the first branch, the magnetic flux generated by radiation is given by

$$\delta\Phi = \delta I\, L_2 = \delta L_k I_1 . \qquad (1)$$

Under the radiation, the kinetic inductance is determined by the nonequilibrium distribution function of quasiparticles, $f(\varepsilon)$, and by the value of Δ, which is function of $f(\varepsilon)$ [11],

$$\frac{1}{L(\Omega,T)} = \frac{\sigma_n}{\hbar} \int_{\Delta-\hbar\Omega}^{\Delta} d\varepsilon\,[1-2f(\varepsilon-\hbar\Omega)] \frac{\varepsilon(\varepsilon+\hbar\Omega)+\Delta^2}{(\Delta^2-\varepsilon^2)^{1/2}[(\varepsilon+\hbar\Omega)^2-\Delta^2]^{1/2}}. \quad (2)$$

Far below the superconducting transition, the nonequilibrium distribution function under the radiation is described by the Boltzmann function, $f(\varepsilon)=\exp[(\mu-\varepsilon)/k_BT]$, with a non-vanishing chemical potential [12]:

$$\mu = \frac{k_BT}{2}\ln\left(1+\frac{2rP_0\tau_{qp}}{\hbar\Omega n_0}\right). \quad (3)$$

Here P_0 is the power of electromagnetic radiation absorbed in a unit volume of the superconducting microbridge, Ω is the radiation frequency, r is the coefficient of quasiparticle multiplication due to electron-electron and electron-phonon interactions, τ_{qp} is the quasiparticle lifetime, and n_0 is the concentration of equilibrium quasiparticles:

$$n_0 = \nu(0)\left(\pi k_BT\Delta/2\right)^{1/2}\exp(-\Delta/k_BT), \quad (4)$$

$\nu(0)$ is the electron density of states at the Fermi surface.

The quasiparticle lifetime is determined by the recombination time, τ_R, enhanced by phonon re-trapping. Every time two quasiparticles with energy Δ recombine, a phonon with energy 2Δ is emitted. Even in thin films (thickness $d \sim 10$ nm) with $T_c \geq 5$K, the mean free path of such phonons, $\lambda_{ph}=\eta v_F/\pi\Delta$ (v_F is the Fermi velocity), is smaller than the effective film thickness d/K (K~0.01-0.1 is the acoustic transparency of the film/substrate interface [13]). As a result of the phonon re-trapping, the quasiparticle lifetime, τ_{qp}, is substantially longer than the recombination time:

$$\tau_{qp} = \tau_R\frac{4d}{K\ell_{ph}} = 0.8\,\tau_{e-ph}(T_c)\frac{d}{K\ell_{ph}}\left(\frac{T_c}{T}\right)^{1/2}\exp\left(\frac{\Delta}{k_BT}\right), \quad (5)$$

where $\tau_{e-ph}(T_c)$ is the electron-phonon relaxation time in the normal state. The quasiparticle lifetime is the characteristic response time of the hot-electron KID. Due to exponential temperature dependence and strong dependence on the phonon transparency, the characteristic time can be varied in a broad range 10^{-5}-10^{-3} sec at 1 K.

To model the detector performance, we fist find the inductive response to radiation. Under condition of strong phonon re-trapping, the quasiparticle multiplication factor $r=\hbar\Omega/\Delta$ [14]. According to Eqs. 1 and 2, the shift of the kinetic inductance at $T << T_c$ is given by the change of the non-equilibrium distribution function,

$$\frac{\delta L_k}{L_k} = \frac{2\delta f(\Delta)}{1-2f_0(\Delta)} = \frac{2P_0\tau_{qp}}{\hbar\Delta n_0}\exp(-\Delta/k_BT) \propto \exp(\Delta/k_BT). \qquad (6)$$

The basic noise mechanism of the inductive detector is intrinsic fluctuations of the number of quasiparticles (generation-recombination noise). Exponentially small number of equilibrium quasiparticles (N_{eq}) well below the superconducting transition in micron size film structures may provide unparallel performance of the KID at $T \approx 1$ K. The NEP_{GR} conditioned by the generation-recombination noise is given by [14]:

$$NEP_{GR} = 2\Delta\sqrt{N_{eq}/\tau_{qp}} \propto \exp(-\Delta/k_BT) \qquad (7)$$

Here τ_{qp} is the quasiparticle lifetime, Δ is the superconducting gap.

Assuming that τ_{qp} is adjusted to 1 ms and the total number of equilibrium quasiparticles in the inductive sensor of volume V is statistically sufficiently large, $N_{eq}=n_0V \approx 100$, the noise equivalent power is $NEP_{GR} \approx 600\Delta\sqrt{\text{Hz}} \approx 10^3 k_B T_c\sqrt{\text{Hz}} \approx 10^{-19}$ W/$\sqrt{\text{Hz}}$.

The total *NEP* includes the contribution of the SQUID readout. Typical flux sensitivity of modern SQUIDs, $\delta\Phi \approx 1$ $\mu\Phi_0/\sqrt{\text{Hz}}$ (Φ_0 is the quantum of magnetic flux), and the corresponding NEP_{SQUID} can be calculated as

$$NEP_{SQUID} = \frac{\delta\Phi}{2L_kI_1}\frac{N_{eq}V\Delta}{\tau_{qp}}\exp(\Delta/k_BT). \qquad (8)$$

As an example, we calculated performance of a Nb sensor operating at 1 K. We considered a 4.0×1.0 μm^2 Nb microbridge made from a 10 nm thick film. The transition temperature of such a film is 6.5 K, the sheet resistance $R_{sq} \approx 20\ \Omega$ [15,16], and the electron-phonon relaxation time is 0.6 ns at 6.5 K [16]. According to Eq. 5, the recombination time at 1 K is 1.4×10^{-5} sec. The film-substrate acoustic transparency for 2Δ-phonons, K, is not well known. In our modeling we used experimental data for NbN thin films on sapphire substrate [13] which suggest the parameter τ_{qp}/τ_R to be equal 4.4 d/nm. Thus, we expect the quasiparticle lifetime in a 10 nm Nb film to be 0.62 ms. Such a response time is short enough for most of applications. Note, that substrates with rigid lattice and large acoustic impedance (e.g, diamond) would provide strong acoustic mismatch to the superconducting films, and, therefore, increase the quasiparticle lifetime.

The results of modeling of the noise characteristics are shown in Fig. 2 (the kinetic inductance of the Nb microbridge was 18 pH and the electric current was chosen be 1 mA). The NEP_{SQUID} is significantly smaller than the NEP_{GR}, and $NEP_{GR} \approx 0.6\times10^{-19}$ W/$\sqrt{\text{Hz}}$ is achievable at $T = 1$ K. The reduction of volume might produce additional decrease of the *NEP* but at the same time the number of quasiparticle would become too small to obtain reasonable dynamic range. A thin-film inductive sensor is naturally well

matched to a planar antenna impedance (Z =40-100 Ω) at wavelengths $\lambda < \lambda_c = hc/2\Delta \approx$ 0.4 mm, whereas the background radiation with $\lambda > \lambda_c$ is not absorbed by the sensor. Note, that since the device length is much smaller than $(D\tau_{qp})^{1/2}$ = 200-400 μm (D is the electron diffusion constant) the Andreev contacts with the superconducting gap larger than Δ should be used to prevent the diffusion loss of quasiparticles from the sensor volume. In our example, thicker Nb films, or NbN and NbC films can be used for contact material.

In Table 1 we summarize characteristics of the Nb detector and also present film parameters and characteristics of NbC and MoRe KIDs with the *NEP* ≈ 10^{-19} W/√Hz at 1-1.6 K. We used parameters of available films (NbC [17] and MoRe [18]) and optimized the characteristics in the following way. The operating temperature was chosen to provide the response time of ~1 ms (Eq. 5 with the trapping factor τ_{qp}/τ_R = 4.4 d/nm). The volume of the sensor was taken sufficiently large to accommodate ~100 equilibrium quasiparticles. The number of squares was adjusted to match the sensor rf impedance to that of a planar antenna impedance.

Note, that despite NbN thin films have been also well characterized and can have large T_c, they are not useful for sensitive KIDs since its electron-phonon relaxation time in this material is too short [13]. Our analysis is not applicable to high-temperature cuprates, which are d-wave superconductors with large number of quasiparticles in nodal regions. New s-wave superconductor MgB_2 with T_c = 40 K may be an interesting material for mid- and near-infrared KIDs offering a broad temperature range for adjusting of the lifetime and the sensitivity.

In conclusion, we have analyzed the kinetic inductance detector in the hot-electron mode well below the superconducting transition. The detector noise equivalent power of the order of 10^{-19} W/√Hz has been found to be possible at temperatures above 1 K. The detector output can be read out by a conventional dc SQUID amplifier. A high rf impedance and possibility to fabricated sensors on bulk dielectric substrates are attractive for making a submillimeter monolithic array of antenna-coupled detectors.

We acknowledge useful discussions with W.R. McGrath.

The work of A.S. and V.M. was supported by a NASA and NSF grants. This research was carried out, in part, at the Jet Propulsion Laboratory, California Institute of Technology, under a contract with the National Aeronautic and Space Administration.

References

1. J.J. Bock, J. Glenn, S.M. Grannan, K.D. Irwin, A.E. Lange, H.G. LeDuc, and A.D. Turner, *Proc. SPIE* **3357**, 297 (1998).
2. D. Leisawitz, W. Danchi, M. DiPirro, L.D. Feinberg, D. Gezari, M. Hagopian, W.D. Langer, J.C. Mather, S.H. Mosley, Jr., M. Shao, R.F. Silverberg, J. Staguhn, M.R. Swain, H.W. Yorke, and X. Zhang, *in UV, Optical and IR Space Telescopes and Instruments*, *Proc. SPIE* **4013**, 36 (2000).
3. B.S. Karasik, W.R. McGrath, M.E. Gershenson, and A.V. Sergeev, *J. Appl. Phys*., **87**, 7586 (2000).
4. M.E. Gershenson, D. Gong, T. Sato, B.S. Karasik, W.R. McGrath, and A.V. Sergeev, *Proc. 11th Int. Symp. on Space Terahertz Technology*, May 1-3, 2000, University of Michigan, Ann Arbor, MI, pp.514-523; M.E. Gershenson, D. Gong, T. Sato, B.S. Karasik, and A.V. Sergeev, *submitted to Applied Physics Letters*.
5. E.N. Grossman, D.G. McDonald, and J.E. Sauvageau, *IEEE Trans. Magn.* **27**, 2677 (1991).
6. M.D. Audley, R.L. Kelley, and G.L. Rawley, *J. Low Temp. Phys.* **93**, 245 (1993).
7. N. Bluzer, *J. Appl. Phys.* **71**, 1336 (1992).
8. F.A. Hegmann and J.S. Preston, *Phys. Rev. B* **48**, 16023 (1993).
9. M.W. Johnson, A.M. Herr, and A.M. Kadin, *J. Appl. Phys.* **79**, 7069 (1996).
10. I.G. Gogidze, P.B. Kuminov, A.V. Sergeev, A.V. Elantev, A.I. Menshcikov, and E.M. Gershenzon, *Sov. Phys. - Tech.Phys.* **43**, 1193 (1998); I.G. Gogidze, P.B. Kuminov, A.V. Sergeev, and E.M. Gershenzon, *Sov. Phys. - Tech.Phys.Lett.* **25**, 47 (1999).
11. M. Tinkham, *Introduction to Superconductivity*, 2nd ed., McGraw-Hill, New York (1996).
12. T.S. Owen and D.J. Scalapino, *Phys. Rev. Lett.* **28**, 1559 (1972).
13. A.D. Semenov, M.A. Heusinger, K.F. Renk, E. Menschikov, A.V. Sergeev, A.I. Elantev, I.G. Goghidze, and G.N. Goltsman, *IEEE Trans. on Appl. Supercond.* **7**, 3083 (1997).
14. A. Sergeev and M. Reizer, *Int. J. Mod. Phys.* **10**, 635 (1996).
15. B. Bumble and H.G.LeDuc, *IEEE Trans. Appl. Supercond.* **7**, 3560 (1997)
16. E.M. Gersenzon, M.E. Gershenzon, G.N.Gol'tsman, A.M. Lyul'kin, A.D. Semenov, and A.V. Sergeev, *Zh. Eks. Teor. Fiz.* **97**, 901 (1990) [*JETP* **70**, 505 (1990)].
17. K.S. Il'in, N.G. Ptitsina, A.V. Sergeev, G.N. Gol'tsman, E.M. Gershenzon, B.S. Karasik, E.V. Pechen, and S.I. Krasnosvobodtsev, *Phys. Rev. B* **57**, 15623 (1998).

Table 1. Parameters of kinetic inductance detectors made from different superconductors.

Material	d nm	R_{sq} Ω	T_c K	$\tau_{e\text{-}ph}(T_c)$ ns	$\nu(0)$ 10^{22} eV^{-1}cm^{-3}	$W\times L$ μm×μm	T K	τ_{qp} ms	NEP_{GR} 10^{-19} W/√Hz
NbC	20	27	10	0.5	2.6	1.5×3.0	1.6	1.0	1.0
Nb	10	20	6.5	0.6	16	1.0×4.0	1.0	0.62	0.91
MoRe	30	150	6.1	0.7	8.7	1.3×0.8	1.0	1.0	0.60

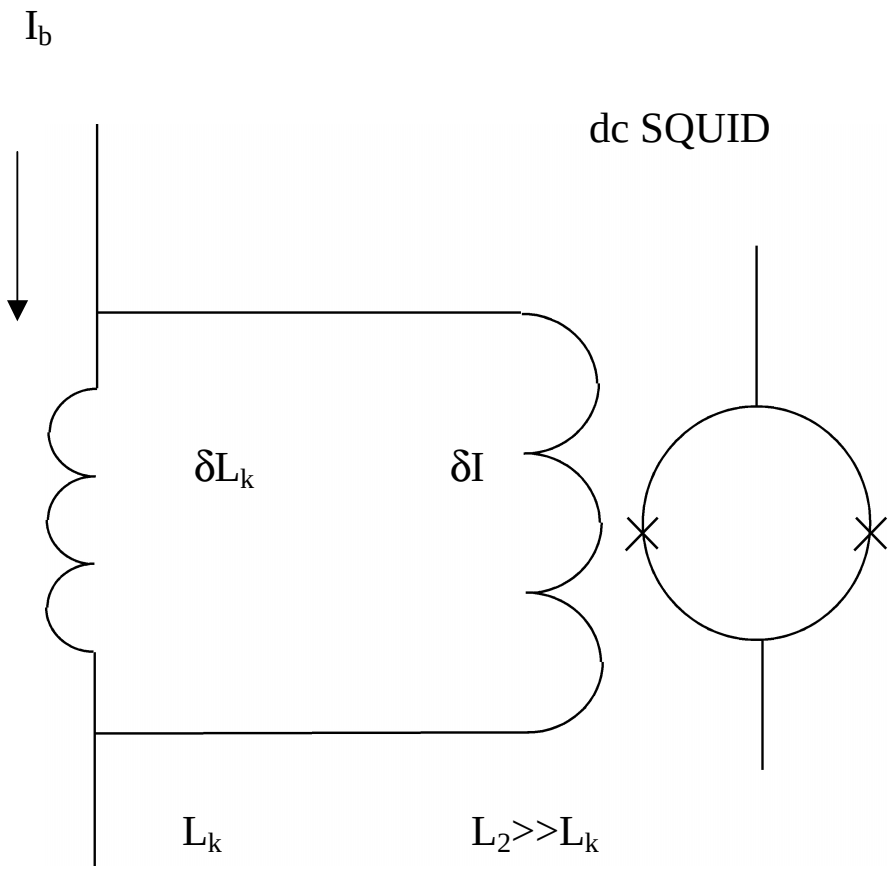

Fig. 1. The schematic circuit demonstrating redistribution of the signal current in a KID/SQUID loop. An increase of the kinetic inductance caused by radiation decreases the current flowing through a SQUID coil producing detectable magnetic field.

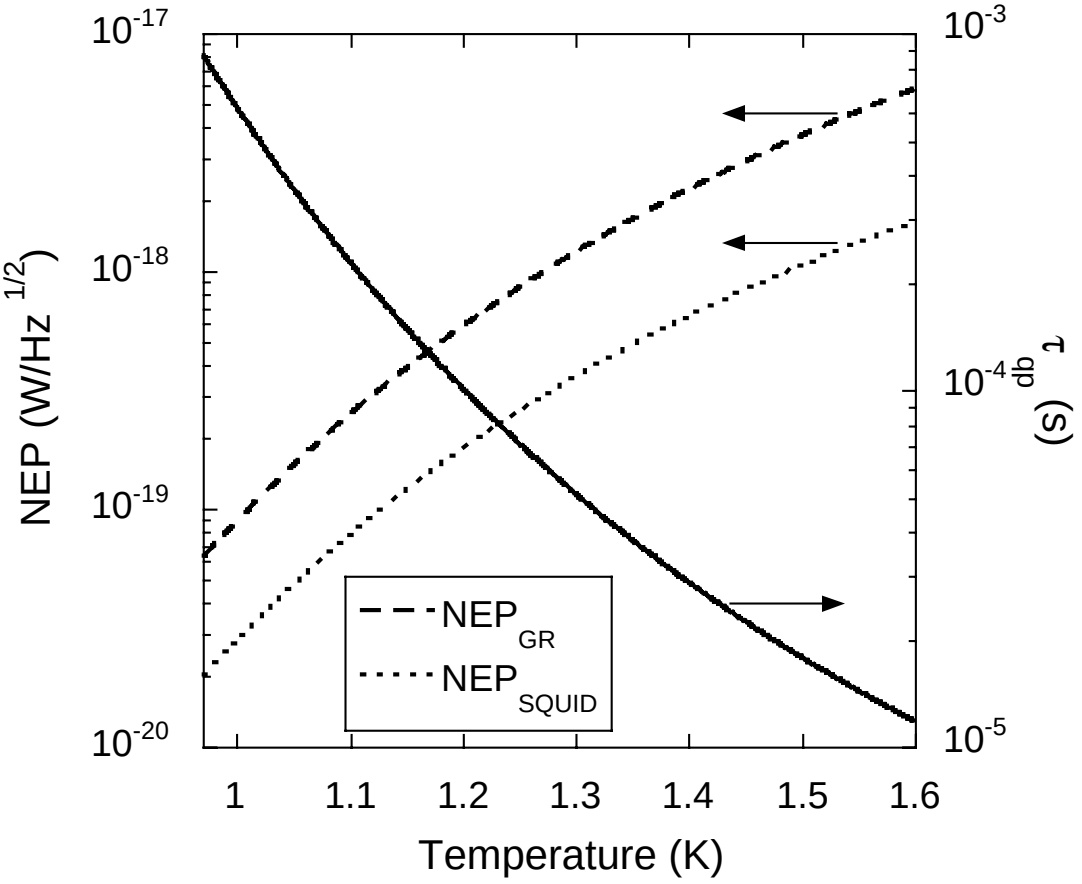

Fig. 2. Temperature dependencies of the NEP and the quasiparticle lifetime in the Nb KID.

ADVANCES IN COMPOSITES FOR TERAHERTZ RADIO ASTRONOMY

S.J. Connell, D.A. Giles
Composite Optics, Inc. (COI)
9617 Distribution Ave.
San Diego, CA 92121
(858) 621-5700
sconnell@coi-world.com

In recent years, Composite Optics, Inc. (COI) has made significant advances in the use of carbon fiber reinforced polymer (CFRP) composite materials for astronomical instrument applications. The inherent low density, high stiffness, and excellent thermal stability of CFRP makes this class of material a natural candidate for many astronomy applications, particularly for space-borne instruments. In recent years, research and development at COI has focused on how to reap these inherent benefits in astronomical applications where other demanding requirements also exist. Basic research has focused on material and process improvement, resulting in an 4 – 5X improvement in the accuracy, homogeneity, isotropy, and thermal stability of the basic material. This has been accompanied by the design, fabrication, and test of large prototype reflectors that cover a broad wavelength spectrum of astronomical interests. Three examples are: a passively adjusted 3-meter aperture prototype reflecting surface for the Large Millimeter Telescope (LMT), the 2-meter aperture prototype mirror for the Far InfraRed and Submillimeter Space Telescope (FIRST), and a 1.6-m prototype for the Next Generation Space Telescope (NGST).

These recent accomplishments have two important implications for the design and fabrication of primary reflectors that can meet the requirements of terahertz astronomy. First, COI has demonstrated a variety of techniques for fabricating large reflecting surfaces from composites to a few microns of accuracy. In addition to high as-manufactured accuracy, an all-composite reflecting surface will have a coefficient of thermal expansion (CTE) of less than 0.1 ppm/°C. This may be the only material that can meet the thermal stability requirements for a ground-based terahertz instrument approach. Secondly, material advances can be applied to primary and secondary support structure, where unparalleled thermal stability may also be enabling for terahertz instruments. New design and manufacturing approaches also have the potential to dramatically minimize the need for high-expansion metallic fittings in these areas.

Multiplexed Readout of Thermal Bolometers with Superconducting Transition Edge Thermometers

Dominic J. Benford, Christine A. Allen, James A. Chervenak, Mino M. Freund, Alexander S. Kutyrev†, S. Harvey Moseley, Richard A. Shafer & Johannes G. Staguhn†

NASA - Goddard Space Flight Center, Code 685, Greenbelt, MD 20771
† Raytheon/ITSS

Erich N. Grossman, Gene C. Hilton, Kent D. Irwin, John M. Martinis, Sae-Woo Nam & Carl D. Reintsema

NIST - Boulder, MS 814.03, Boulder, CO 80305

Abstract

History shows that in astronomy, more is better. In the near future, direct detector arrays for the far-infrared and submillimeter will contain hundreds to thousands of elements. A multiplexed readout is necessary for practical implementation of such arrays, and has been developed using SQUIDs. The technology permits a 32 × 32 array of bolometers to be read out using ~100 wires rather than the >2000 needed with direct wiring. These bolometer arrays are made by micromachining techniques, using superconducting transition edge sensors as the thermistors. We describe the development of this multiplexed superconducting bolometer array architecture as a step toward bringing about the first astronomically useful arrays of this design. This technology will be used in the SAFIRE instrument on SOFIA, and is a candidate for a wide variety of other spectroscopic and photometric instruments.

Keywords: bolometer, far-infrared, submillimeter, superconducting, SQUID, detector array, multiplexer, transition edge sensor

Introduction

Advances in bolometer fabrication have made possible the construction of submillimeter-wavelength cameras with up to 100 direct-detection bolometer elements (e.g., CSO - SHARC (Wang *et al.* 1996), JCMT - SCUBA (Holland *et al.* 1996), IRAM 30m (Kreysa *et al.* 1998)). Currently, the sensitivity of these instruments is background-limited, so deep- and wide-field surveys are limited by the number of detectors and the amount of observing time available. During the past decade, the number of bolometers in large arrays has doubled approximately every 2 years. Within the next few years, kilopixel arrays will be needed for the next generation of astronomical instruments for ground-based, airborne (SOFIA) and spaceborne platforms. In order to achieve a leap to a thousand detectors, a scalable detector architecture must be demonstrated. Such an architecture should deal with both the fabrication of an array and the electronics used to read it out. Specifically, multiplexed readouts are necessary for kilopixel-class arrays. In this paper, we present first results for an architecture which can be readily scaled

to kilopixel arrays using superconducting sensors and a multiplexed amplifier technique (Chervenak *et al.* 1999) to reduce the wiring overhead.

Detector arrays using this technology are currently being developed for use in the SAFIRE instrument for SOFIA (Shafer *et al.* 2001) and for a ground-based spectrometer (Benford *et al.* 2001). A common figure of merit for bolometers is the Noise Equivalent Power (NEP). This is the power that yields a signal-to-noise ratio of unity in a 1Hz bandwidth, and is expressed in units of W/√Hz. For SAFIRE, observations of the CII line at 1900GHz (158μm) with a spectral resolving power of 1000, the maximum NEP for the detectors must be 10^{-17} W/√Hz. NEP can be converted into an equivalent noise temperature $T_N = \mathrm{NEP}/(2k\sqrt{\Delta\nu})$ (Phillips 1988). In the above case, this yields a noise temperature of around 8K. While not achievable with heterodyne spectrometers due to the quantum limit, direct detection has no such restriction.

Superconducting Thermal Bolometers

The transition between a superconducting and a normal state can be used as an extremely sensitive thermometer. A thin film, held at its transition temperature, requires only a tiny amount of power to warm it above its transition, increasing the resistance by a large fraction. In fact, the superconducting transition can be very sharp, yielding a dimensionless sensitivity defined as $d\,logR / d\,logT \approx 1000$ at best. Recently, we have fabricated thin film superconducting bilayers of molybdenum and gold (Benford *et al.* 2000) and molybdenum and copper (Irwin *et al.* 2000). One such transition is shown in Figure 1; it features a bilayer with 400Å of molybdenum and 750 Å of gold, yielding a normal resistance of 220mΩ. Near its transition temperature of 450mK, the sensitivity approaches 1100. By varying the thicknesses of the bilayer materials, the transition temperature may be selected to suit the astronomical application.

Because the transition region is narrow (~1mK) compared to the temperature above the heat sink (150mK above a ^{3}He refrigerator at 300mK), the TES is nearly isothermal across the transition. In use as a detector, the power applied to raise the TES into its transition region is nearly constant. This has the effect that the response becomes linear to better than 1%, substantially better than the typical linearity achieved with semiconducting thermistors.

In order to make a detector of the appropriate sensitivity, we have fabricated monolithic linear silicon bolometers using micromachining techniques (Figure 2). These bolometers have slim silicon legs that provide thermal isolation and a 1mm^2 absorber to couple to the far-infrared light. The thermal conductance at the operating temperature determines the optical power that the device is optimized for; current arrays are being fabricated for operation with ≈1pW of optical loading. These linear bolometer arrays can be folded such that the legs (and, therefore, electrical connections) are hidden completely behind the absorber, allowing close-packing perpendicular to the array. The folding is possible because the silicon membranes become flexible at the 1μm thickness used. In this way, a two-dimensional array of large size can be made with near unity filling factor.

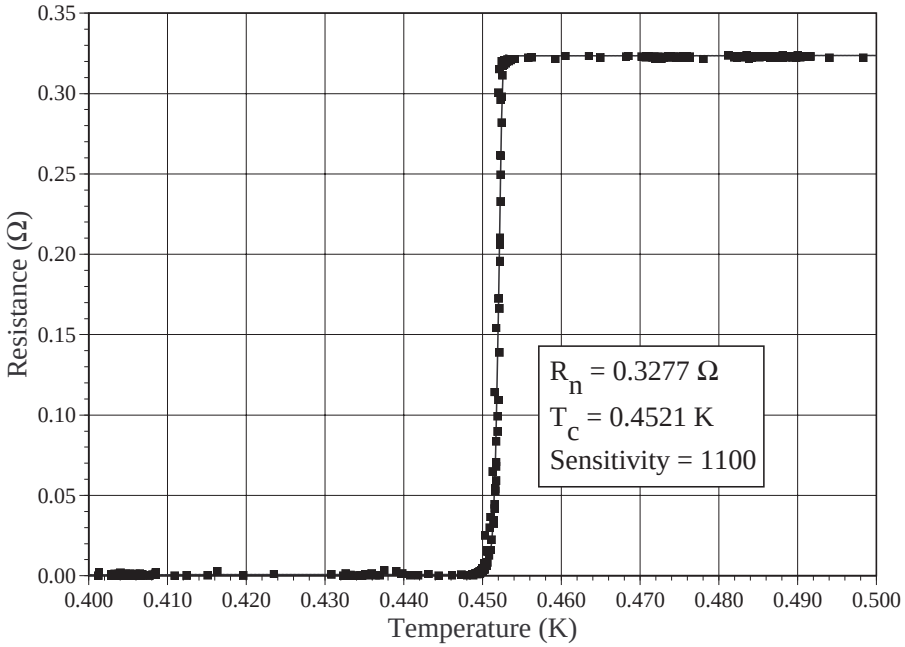

Figure 1. Superconducting transition at 444mK for a Mo/Au bilayer.

Figure 2. A single element from the middle of a linear array of TES bolometers. The absorber is 1mm on a side.

SQUID Multiplexer / Amplifier

A low-impedance detector such as a superconducting TES is well-matched by a superconducting SQUID amplifier. From a fundamental standpoint, a SQUID amplifier functions as a magnetic flux to voltage converter, with extremely low output voltage noise. A voltage-biased TES in series with a pickup inductor placed near a SQUID will induce a changing flux through the SQUID when the TES resistance changes. This changing flux results in an output voltage which is a periodic function of the input, as shown in Figure 3. The SQUID amplifier uses the technique of Welty & Martinis (1993), in which the first stage SQUID is used to drive a series array of SQUIDs which yield a voltage gain of 100. This Series Array Amplifier can produce an output voltage of the order of a millivolt, readily amplified by room-temperature electronics.

In order to remove the inconvenience of a periodic and strongly nonlinear output, a digital linearization circuit has been built. A second inductor, for feedback, is also placed near the SQUID. Any change in the output voltage of the SQUID is reapplied to the feedback coil with opposite sign, bringing the SQUID back to its original total input flux. This has the effect of nulling the SQUID (i.e., its net flux can be kept near zero at all times) and linearizes the SQUID response so that the problem of handling a periodic output need not be tackled.

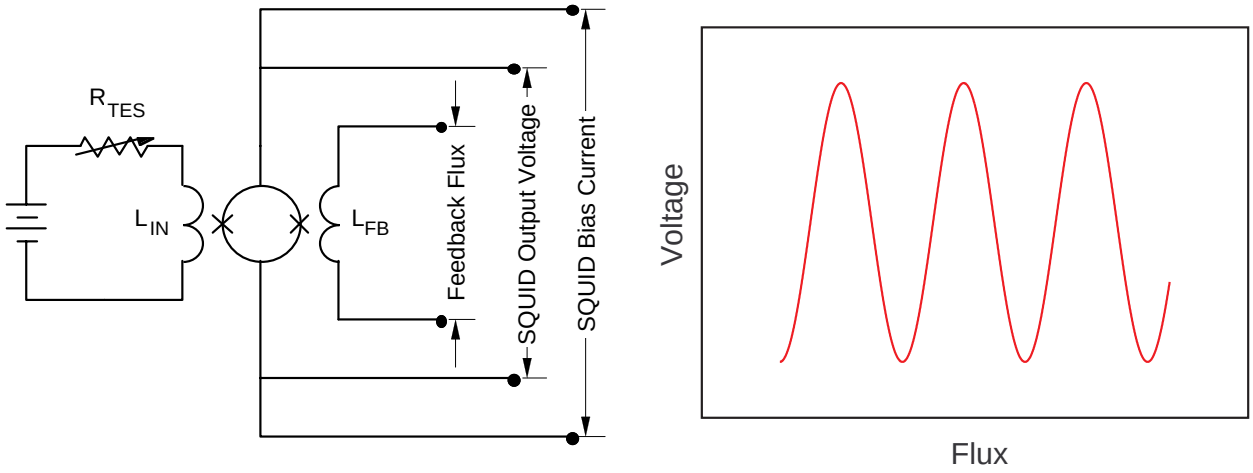

Figure 3. (L) A single SQUID amplifier circuit and (R) its transfer function.

A SQUID amplifier can be switched rapidly between an operational state and an inoperational, superconducting state by biasing the SQUID with roughly 100μA of current. If we stack *n* SQUIDs in series with *n+1* electrical address leads as shown Figure 4, driving current between an adjacent pair of leads will result in only one SQUID being operational. With the other SQUIDs in the superconducting state, the output voltage across the entire array is exactly the voltage across the one active SQUID. In this manner, only one amplifier is necessary for *n* detectors, although at a data rate *n* times faster. This is *time-division multiplexing*. Adding in connections for a common TES bias and feedback signal, and a total of *n+7* wires are needed.

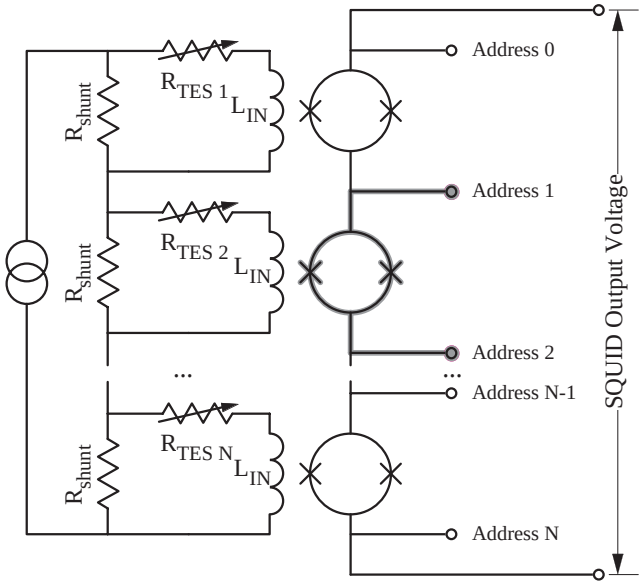

Figure 4. A multiplexed SQUID amplifier reading out *n* detectors. A total of *n+7* wires are needed (assuming ganged biases).

A 1×8 SQUID multiplexer has been built (Figure 5) and tested using the circuit described in Chervenak *et al.* (1999). One triangle and one sine wave inputs were fed into a cold electronics setup so as to mimic the modulation of a signal from infrared light. The multiplexed amplifier was switched between these inputs, amplified, and digitized. A sample time series of data at this point is shown in Figure 5 of Chervenak *et al.* (1999). This data can be demultiplexed to recover the original input waves, which demonstrates the excellent fidelity of the amplifier (Figure 6). Furthermore, crosstalk between channels is a maximum of 2% (although this depends on the readout speed). Adjacent channels in a Nyquist-sampled detector array would have many times this level of optical crosstalk, so the multiplexer has sufficient adjacent channel rejection for most purposes.

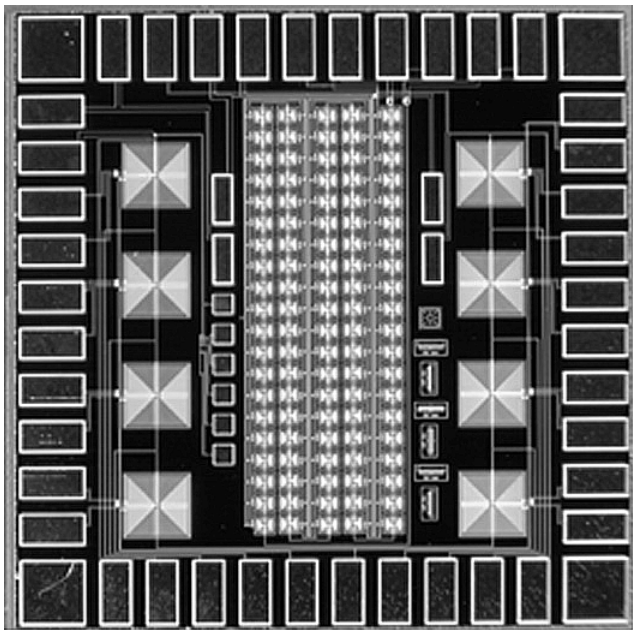

Figure 5. SQUID Multiplexer/Amplifier for 8 detectors; the 4 input coils flank the 100-element series array on the left and right sides.

It should be pointed out that the TES is biased at all times, and is low-pass filtered using an inductor with time constant L/R≈2μs to a response time slower than the multiplex switching time. Effectively, the TES self-integrates so that the multiplexer *samples* an integrated signal; no loss of signal-to-noise is introduced even though the signal from each TES is read out for a shorter time. This is true provided that the noise of the SQUID is substantially less (by a factor of more than $\sqrt{n}$) than that of the TES. Furthermore, in order to remain stable, the devices must be sampled faster than $f_{L/R}=(3+2\sqrt{2})f_{TES} \approx 100$ kHz.

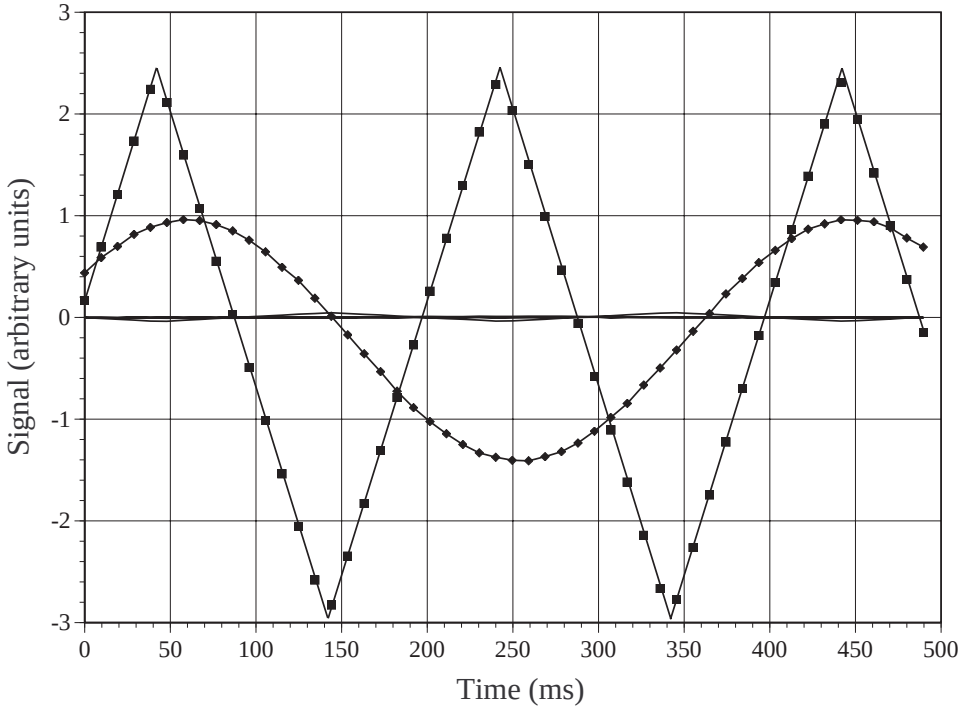

Figure 6. Crosstalk measured for 8 detectors read out simultaneously; one triangle wave and one sine wave excitation were applied.

Performance of Multiplexed SQUID Readout

Optical performance was measured in a test setup designed to calibrate low-background detectors for SPIRE (Hargrave *et al.* 1999). This setup used a helium-cooled blackbody consisting of a textured, black, carbon-loaded epoxy (Epotek 920) wall in a gold-coated cavity. Selectable apertures allow the throughput to the blackbody to be chosen. The blackbody can be heated to cover temperatures between 2K and 40K. A metal-mesh bandpass filter at 350μm wavelength (850GHz) with a fractional bandpass of ~1/10 reduced the total transmitted power to be within the range of our bolometers, which were designed to saturate (i.e., be driven normal) at 5pW. The result of the blackbody calibration is shown in Figure 7, where the measured power has been corrected for a bolometer absorptivity of 90%. The measured response follows the theoretical power very well up to a saturation power of 2.1pW, about half the designed value. The excellent linearity of TES bolometers is one of their best features.

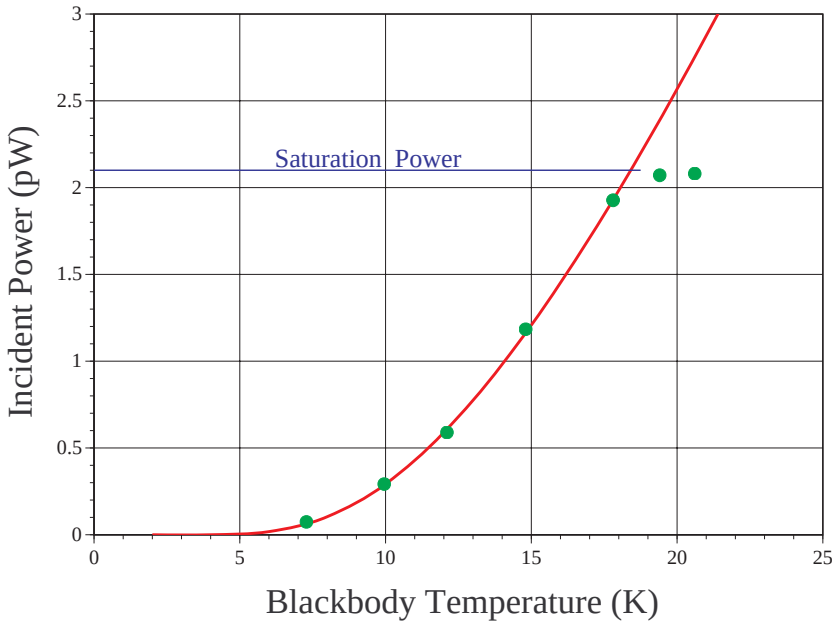

Figure 7. Measured and theoretical power versus blackbody temperature for a helium-cooled calibration source, assuming a detector absorptivity of 90%.

In addition to calibration with the blackbody, the test setup permits an external source to be used. In order to reduce the optical load to an acceptable level, a 1% transmissive neutral density filter is placed in the beam. The time constant was measured by using a rapidly chopping blade with a hot/warm load. An upper limit of $\tau \leq 2$ms was found, limited by the speed of the chopper. A Fourier transform spectrometer was used to measure the frequency response, which was limited by the bandpass filter. No bandwidth degradation due to inefficiencies in the absorbing coating were seen. Also, a beam map was made, and excellent rejection of out-of-beam power was found.

In Figure 8, we show the Noise Equivalent Power (NEP) of a TES bolometer using an Aluminum/Silver bilayer operating at a transition temperature of 568mK. The NEP over the desired 10-100Hz bandwidth is 2.8×10^{-17}W/$\sqrt{\text{Hz}}$. The phonon noise calculation is shown as a solid line, demonstrating that phonon-limited performance has been obtained. Over a 100GHz bandwidth at 850GHz, this noise level corresponds to a detector noise temperature of 3.2K. The measured noise levels of lower-transition (440mK) devices have been about 20% above the phonon noise level, indicating excess noise which is believed to arise from edge effects where the bilayer thicknesses are not well defined. Recent results using Molybdenum/Copper bilayers appear not to have this excess noise.

Finally, we have used the multiplexer to read out 8 detectors simultaneously while observing a chopped hot/cold load. The data, read out in real time like a strip chart, are shown in Figure 9. This demonstration showed that time domain multiplexing/demultiplexing of the signals from 8 bolometers was feasible in real time with high fidelity. Furthermore, we have measured the photon noise in this situation, showing that it is ~10 times the electrical noise including the detector and multiplexer noise contributions.

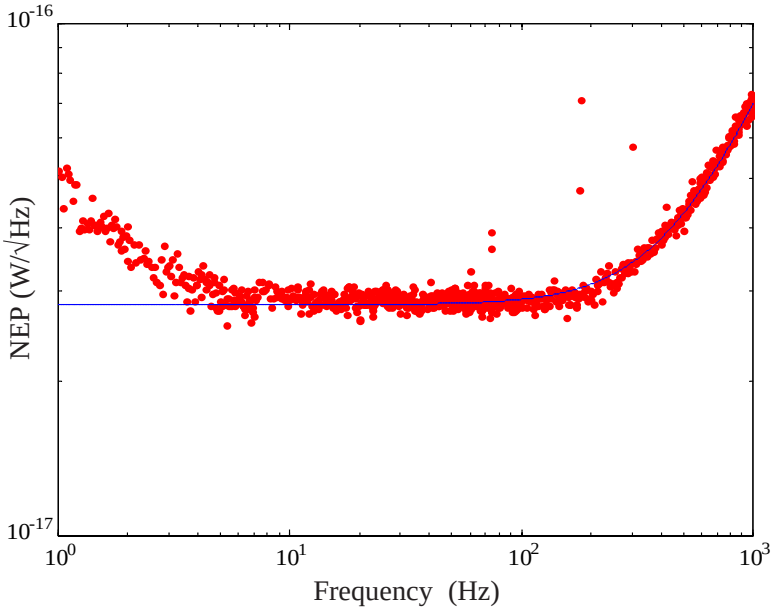

Figure 8. NEP of a detector operating at 568mK. The phonon noise calculation is shown as a solid line, demonstrating that phonon-limited performance has been obtained over the 10-100Hz signal band.

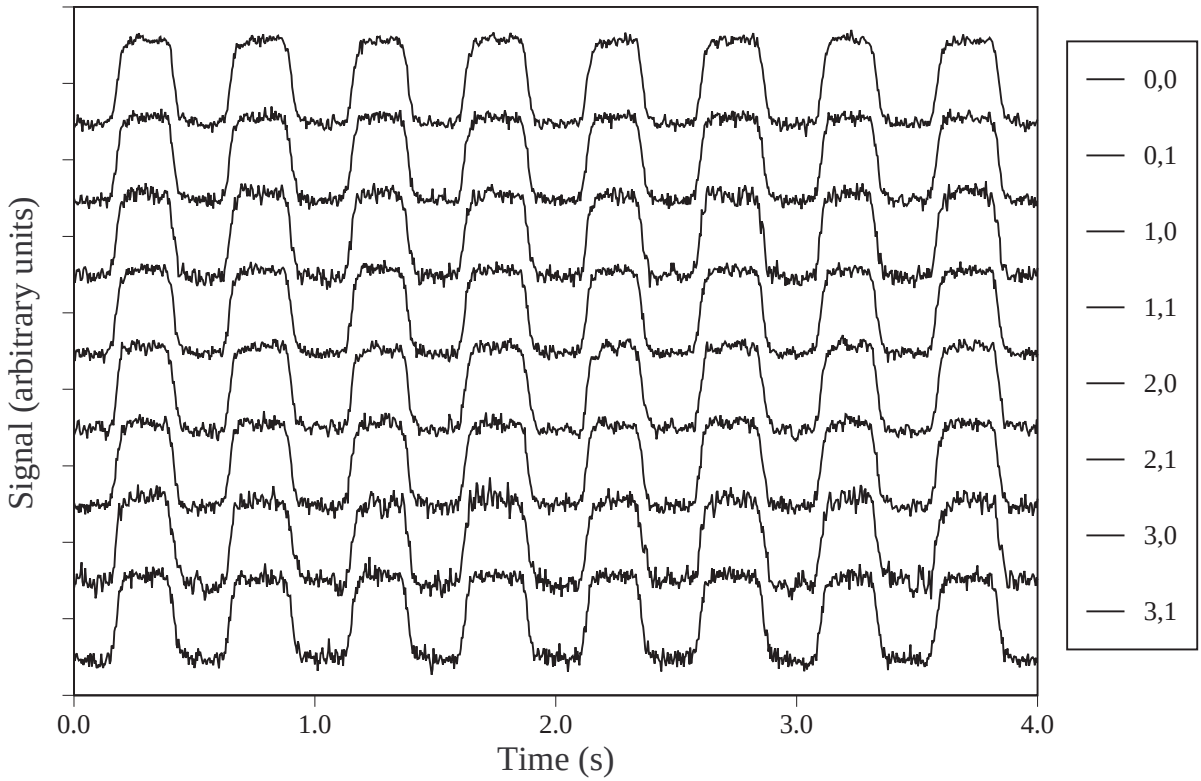

Figure 9. Multiplexed detection of 8 detectors viewing a chopped hot/cold load, read out simultaneously and demultiplexed on-the-fly.

Conclusion

We have demonstrated superconducting transitions in Mo / Au and Mo / Cu bilayers which look promising for use as TES films on sensitive bolometers. Noise Equivalent Powers consistent with phonon noise have been measured, and optical efficiency of 90% has been achieved. A multiplexed SQUID amplifier has been fabricated and is shown to provide low-noise, high-fidelity readout of several TES detectors with a single signal output. We have validated the use of time-division multiplexing for reading background-limited TES bolometers while observing optical sources. This architecture can be extended to large-format (thousands of detectors) bolometer arrays, having application in future far-infrared instruments such as SPIFI on the AST/RO telescope and SAFIRE on the SOFIA observatory.

References

Benford, D.J. *et al.*, 2000 , Int J. IR MM Waves, **21** (12), 1909.

Benford, D.J., Maffei, B., Moseley, S.H., Pajot, F., Phillips, T.G., Rioux, C. & Shafer, R.A. 2000, BAAS, **197**, 53.03

Chervenak, J.A., Irwin, K.D., Grossman, E.N., Martinis, J.M., Reintsema, C.D. \& Huber, M.E. 1999, Appl. Phys. Lett., 74, p.4043

Hargrave, P.C. *et al.* 2000, NIMA, **444**, 427-431

Holland, W.S. *et al.* 1996, Int J IR MM Waves, 17, p.669

Irwin, K.D., Hilton, G.C., Martinis, J.M., Deiker, S., Bergren, N., Nam, S.W., Rudman, D.A. & Wollman, D.A. 2000, NIMA, **444**, 184-187

Kreysa, E. *et al*. 1998, Proc. SPIE #3357, Advanced Technology MMW, Radio, and Terehertz Telescopes , T.G. Phillips, ed., p.319

Phillips, T.G. 1988, in Millimetre and Submillimeter Astronomy , Wolstencroft & Burton, eds., p.1

Shafer, R.A., Moseley, S.H., Ade, P.A.R., Benford, D.J., Dwek, E., Pajot, F., & Stacey, G.J. 2000, BAAS, **197**, 53.02

Wang, N.W. *et al.* 1996, Applied Optics, **35**, p.6639

Welty, R.P. & Martinis, J.M. 1993, IEEE Trans. App. Superconductivity, 3, p.2605

Negative Resistance Effects in NbN HEB Devices

Yan Zhuang and K. Sigfrid Yngvesson
Department of Electrical and Computer Engineering, University of Massachusetts, Amherst, MA, 01003

ABSTRACT -It is well known that HEB devices, whether phonon-cooled or diffusion-cooled, exhibit unstable regions of their IV-characteristics. These phenomena occur when the device is not pumped by the LO, or when the LO power is decreased sufficiently compared with the power level required for optimum operation. The bias voltage is between the critical value at which the device stops being superconducting, and the point where a stable hotspot is formed. We have studied the instabilities occurring in un-pumped NbN devices that are also being used in our THz mixer receivers. The aim is to understand the physical processes, which produce the instabilities in the device under these conditions. Eventually, this should also be useful for understanding the device models in the LO-pumped regime. Whereas other researchers have reported sidebands of the IF in diffusion – cooled devices, we find that a variety of different frequencies and waveforms may be produced in the NbN devices, with frequencies varying from about 300 Hz to several hundreds of MHz. A typical range is a few hundred kHz, however. During our measurements the device is mounted on a circuit board and enclosed in a small box in order to present well – defined circuit conditions. We then add chip components to the circuit and study the effect these have on the instabilities. We have identified some conditions for which the device is stabilized, which may be useful in practical mixer applications, and also present in this paper preliminary results for a model which can be used to interpret the physical processes which occur in the devices. In this model the device is in a metastable hotspot state in which heating and cooling recur periodically.

I. INTRODUCTION

The theory of NbN Hot Electron Bolometric (HEB) Mixers has primarily been based on the "standard model" in which the device is regarded as a point bolometer[1]. Newer models extend the treatment to one or two-dimensional bolometers [2,3], and have contributed toward a more complete understanding of these new devices. Our new approach to this question is to observe the NbN HEB mixers' behavior when the device is biased in the instability region, in which the device shows negative dynamic resistance, and to present a possible model to interpret the experimental data obtained in this region. Studying the negative resistance effects in HEBs is important in understanding how to optimize the bias circuit for the device's best performance, how to protect the device and achieve a long lifetime, and how to model the device, especially vortex phenomena.

In the superconducting state the current through the device increases with applied bias voltage until it exceeds the critical current I_C, whereupon the device makes a transition from the superconducting state to the resistive state at a voltage of a few mV and a lower current. Since the voltage increase is associated with a decrease in current, this transition thus represents a negative differential resistance. By adjusting the bias voltage to values between these two states, we find a region of the I – V curve in which the device is potentially unstable due to the negative resistance. We can observe periodical or quasi – periodical waveforms on an oscilloscope with frequency components typically ranging from about 100 kHz to 6 MHz, and in some cases considerably lower (300 Hz) or higher (hundreds of MHz).

II. EXPERIMENT AND RESULTS

The device was fabricated from a sputtered 3.5nm NbN thin film on a silicon substrate, and was integrated with a log – periodic antenna [4]. The critical temperature of the film is 10.5K. Fig. 1 shows the experimental set up. The device was mounted on a circuit board in a small metal box to reduce the outside radiation interference, and then connected to a semi – rigid coaxial cable, which was built into a dipstick used to insert the device into a liquid helium dewar. The bias voltage was applied to the device through a low pass filter and the coax. The oscillation frequency was observed by a Tektronix 11403A digitizing oscilloscope.

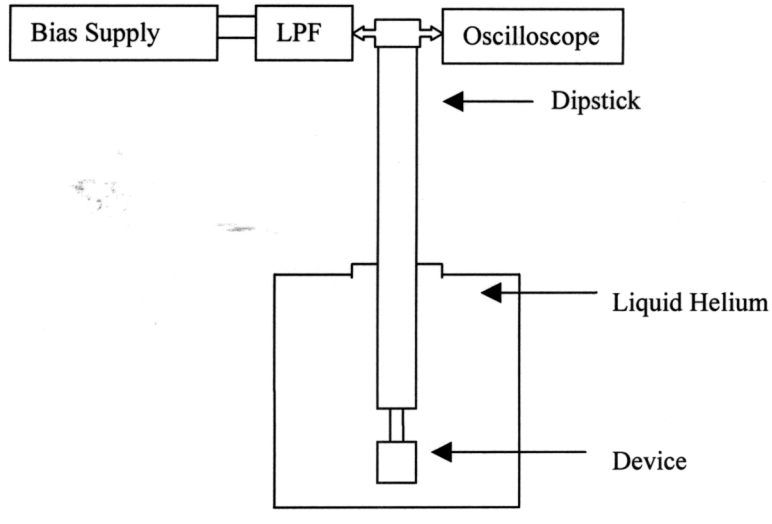

Fig. 1: Experimental set up for the HEB negative resistance study

There are five different regions in the typical I – V characteristics as shown in Fig. 2. The entire device is superconducting in region (1), reaching a critical current, I_{CS}, at which the

current drops and instabilities of different kinds can be observed. First, slow jumps occur in region (2), which are picked up directly by our Labview I – V recording system. We have found that the jumping frequency depends mainly on the opamp circuit in the bias supply, and can be as slow as 300 Hz. Quite large amplitude oscillations occur in this region. A stable hotspot occurs in region (4), which will expand gradually with the bias voltage until the whole film goes normal. LO power is applied in region (5). The current through the device is then suppressed to a lower level. In between regions (2) and (4) is region (3), in which the recorded DC current and voltage are relatively stable, and oscillations can be detected on an oscilloscope. We believe the oscillation frequencies in region (3) are related to both the physical characteristics of the device, and to other

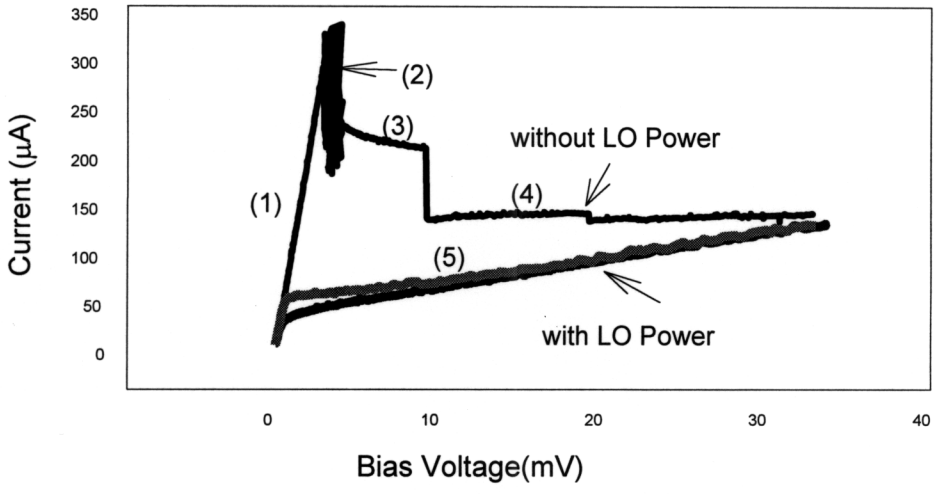

Fig. 2: Typical I – V Characteristics of NbN HEB Device

components connected to it, and our HEB negative resistance study is focussed on this region. From stability theory a network is stable if the real part of the impedance is greater than zero; thus it is possible to stabilize the HEB device in its negative resistance region by inserting a series resistor in the circuit, as shown in Fig. 3. R_S is the internal resistance of the bias supply, which is very low due to a feedback circuit. R_{STAB} is the series – stabilizing resistor. Increasing R_{STAB} will eventually make the circuit stable. There will be no oscillations detected after the circuit is stable. We tested several devices, and the measured R_{STAB} value ranges from 6Ω to 20Ω. Fig.4 shows the I – V characteristics after inserting the stabilizing resistor. The I – V curve without the stabilizing resistor is also included in order to provide a comparison. Based on this simple

model we can conclude that the negative resistance of the HEB devices we tested is around – 6Ω to – 20Ω.

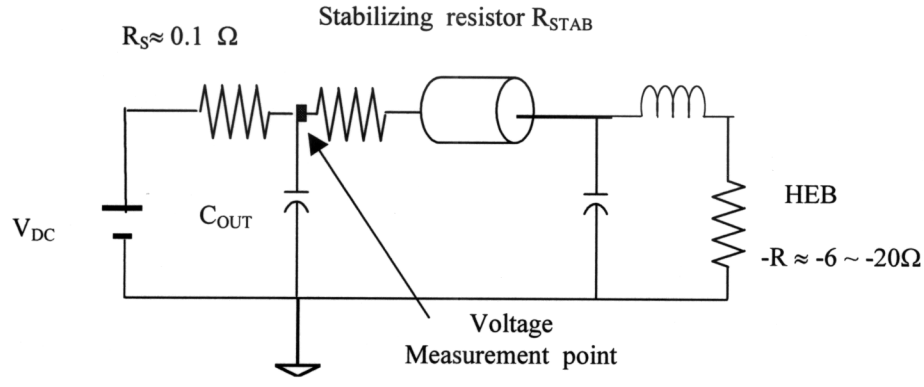

Fig. 3: HEB measurement circuit diagram after inserting stabilizing resistor

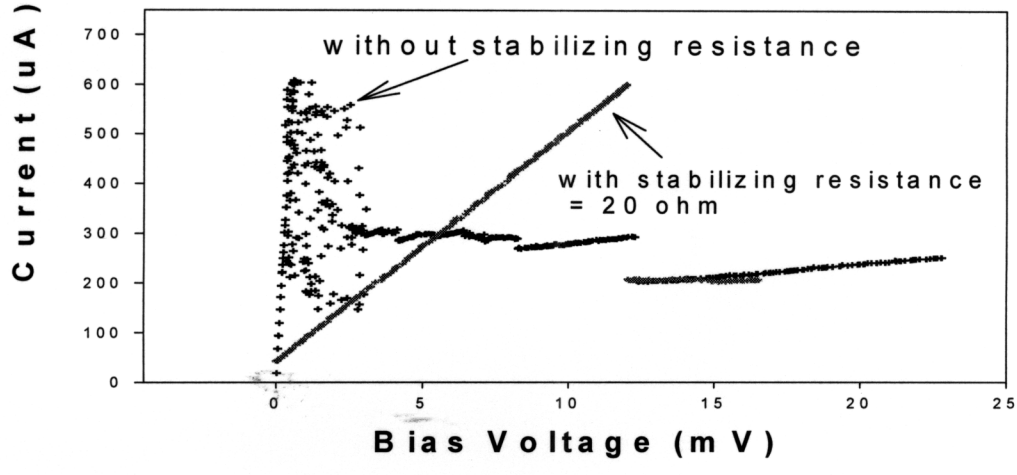

Fig. 4: I – V Characteristics of HEB Device with stabilizing resistor

Typical oscillation waveforms measured in region (3) are shown in Fig. 5. The bias point at which the measurements were made is shown in Fig. 7. The current measurement was done by measuring the voltage across a series resistor inside the bias supply, which doesn't affect the internal resistance of the supply. Fig. 5(a) shows that the voltage periodically has sharp spikes with relaxation oscillations that almost die out before the next spike comes. The repetition rate of the spikes is about several hundred kHz. It increases with the bias voltage, and can also be decreased by adding some series inductance. Fig. 5(b) is the corresponding current waveform. The current drops a little bit

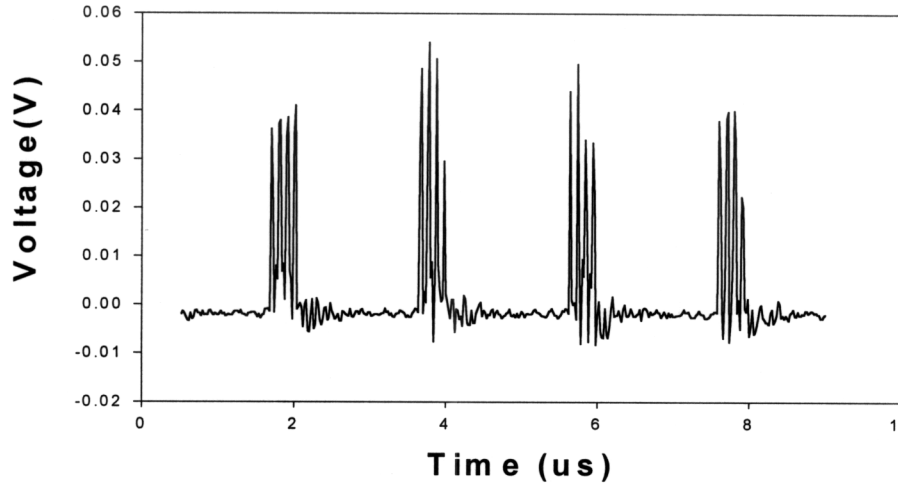

Fig. 5(a)

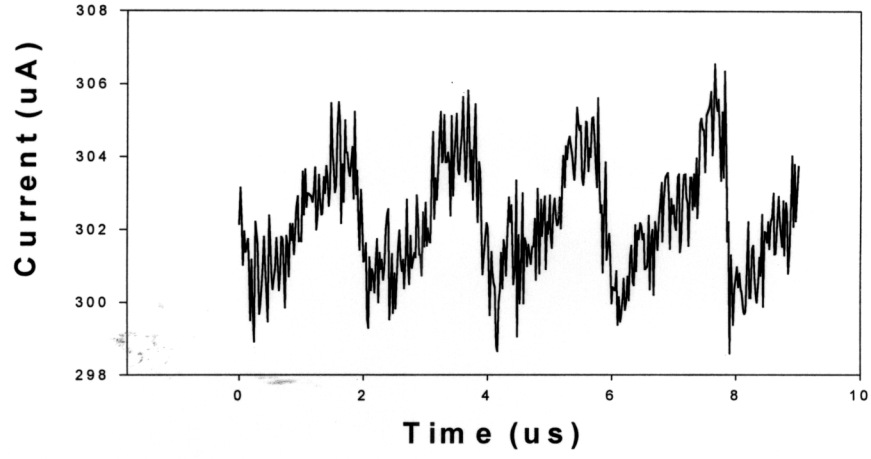

Fig. 5(b)

Fig. 5: (a): Voltage waveform in region (2); (b): Current waveform in region (2)

as the voltage spikes occur, and then recovers with a relatively longer time constant as the voltage spikes die out. The percent change in current is only about 1%. The device was also measured with a microwave vector network analyzer from 300 kHz to 400 MHz, and showed a *positive resistance*, essentially independent of frequency over this range (Fig. 6). The measured microwave resistance is equal to the average DC resistance, as shown

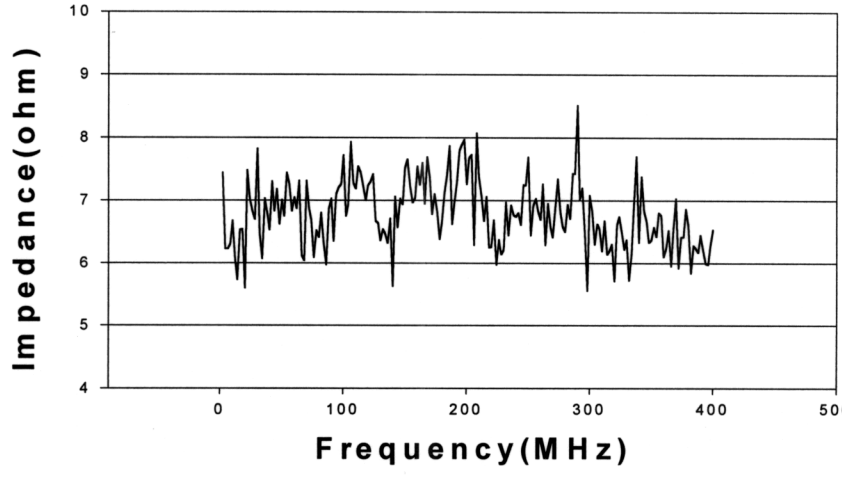

Fig. 6: Impedance of HEB device measured from network analyzer

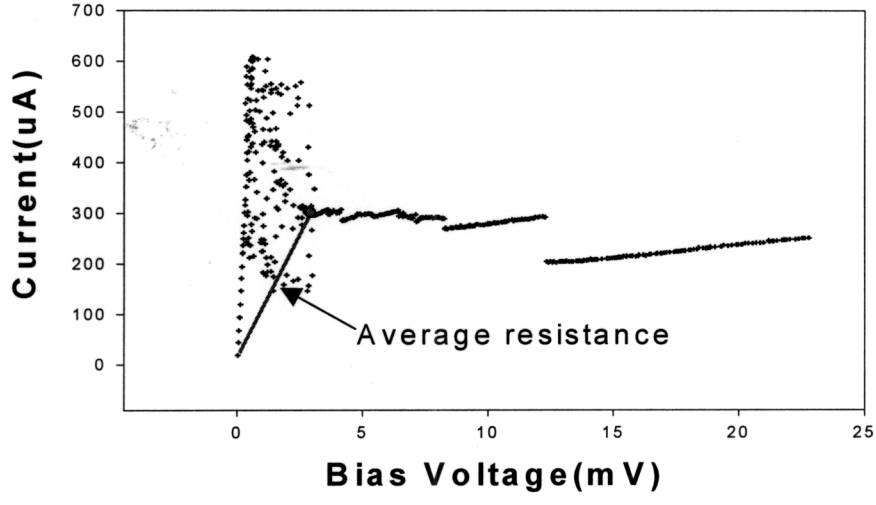

Fig. 7: Average resistance of HEB at the operating point during ANA measurement

in Fig. 7. It follows the DC resistance of the bias point as the bias voltage is increased. The simple negative resistance model we used above cannot explain this behavior – it would predict that the network analyzer should measure a *negative resistance* value. Instead, we will introduce a version of the hotspot model which is related to the one – dimensional models studied by Merkel et al [2,3]. Fig. 5 clearly indicates that most of the time both the voltage and the current are stationary, and thus the device resistance is essentially constant: the current only changes by 1%, and the voltage is constant except for a brief interval when the voltage spikes are detected. We believe that the device is heated or cooled periodically due to the negative resistance effect, and correspondingly the hotpot expands or shrinks at the same rate. Thus, the hotspot formed in region (3) is different from that in region (4), where the hotspot is stable with a length determined by the bias voltage. We will introduce the term "*metastable hotspot*" to describe the device in region (3), and will expand further on this idea in section III. The clearest evidence for this model is furnished by the network analyzer measurements, which indicate that the average resistance is positive. The instability represented by the negative resistance effect is then limited to the brief interval when the voltage spikes occur. The voltage spikes are not seen by the network analyzer, partly because they are at a too low frequency to pass the bias tee of the ANA, and partly because the phase detector of that instrument will not detect them.

III. DISCUSSION

We now discuss our interpretation of the measured results in terms of a one – dimensional hotspot model.

The superconducting state

First, in **region (1)** the device is superconducting and the magnetic field associated with the current begins to penetrate the NbN film, forming a number of vortices. This is typical of all type II superconductors. The fact that we do not detect a voltage indicates that the vortices are not moving; they are pinned by defects in the film. At the critical current (I_{CS}, the critical current in the superconducting state) the Lorentz force between the current and the magnetic field exceeds the pinning force, and the vortices move transverse to the film, inducing a voltage. The voltage dissipates power which heats the film, increasing its resistance and decreasing the current. This represents the basic negative resistance effect.

The metastable hotspot state

Skipping region (2) for a moment, **we will now discuss region (3).** The suggested first order model for the metastable state in this region is shown in Fig. 8. Refer to Fig. 5 for the voltage and current versus time. In the middle of the device there is a metastable hotspot with electron temperature $T_e > T_c$, and with vortices located outside of it. After

the initial decrease in current the vortices will again be pinned since the Lorentz force has decreased. The device has a resistance due to the hot spot shown in the figure. Less power is also being dissipated, and the current rises again. When the current reaches a new and lower critical current I_{CM} (critical current in the metastable state) the vortices begin to move again, which gives rise to the voltage spikes. The device is then again heated. The hotspot expands slightly, but there is not enough heating power to complete the process and form a stable hotspot as in region (4), so the voltage spikes die out. The device then begins to cool down, and the hotspot decreases in length. The resistance reduction causes the current to increase until it reaches I_{CM} again. This model then shows that the voltage and current are close to the metastable bias point, except for the brief voltage spikes. It appears reasonable to assume that the heat transfer equations of the hotspot model [2,3] have metastable solutions of the above type. Further theoretical explorations of this model will have to be pursued to prove this point, however.

Critical current

The average current **in region (3)** (about 300 μA, see Fig. 4) is roughly equal to the critical current under the conditions which correspond to a hotspot in the middle of the device, since the measured current only oscillates by 1 %. It is well known that the critical current decreases with the temperature. As shown in [2,3] the electron temperature T_e close to the hotspot is a little less than the critical temperature T_c, and therefore the critical current (I_{CM}) is less than that when the device goes from the superconducting state to the unstable state (I_{CS}). The latter critical current has a higher value (600 μA, Figure 4) since the entire device is at a lower temperature (4.2K) in this case.

Voltage dependence of the repetition frequency

The voltage spikes appear to produce about the same amount of heating each time, independent of the bias voltage. This is consistent with the fact that the current (and not the voltage) determines the density of the vortices, as well as the Lorentz force they are exposed to; note that the current is observed to be roughly constant in region (3). The cooling effect produced by the hotspot, however, is proportional to the area of the hotspot (the cooling is due to phonons emitted from the film through the film/substrate interface). As the bias voltage increases, the hotspot expands, and it is then able to remove the heat produced by the voltage spikes faster. Therefore, the current reaches I_{CM} faster, and the repetition rate of the periodic heating and cooling cycle increases, as observed.

Effect of the stabilizing resistor

We can now also explain the effect of the stabilizing resistor in terms of the metastable hotspot model. Without a stabilizing resistor we have a fairly wide range in voltage over which the unstable state occurs. We finally reach **region (4)**, and a stable hotspot, when the hotspot is large enough to produce sufficient cooling to take care of the extra heating periodically produced by the vortices (see Fig. 4). If we insert a sufficiently large stabilizing resistor in series with the bias source, then when the current reaches I_{CS},

the voltage is large enough to produce a hotspot which is again large enough to cool the device, and prevent the heating due to the vortices from recurring periodically.

Effect of the external circuit

The repetition frequency of the waveforms shown in Fig. 5 can be decreased if an inductance is added in series with the bias supply. With other circuit configurations, we have recorded oscillations which were more sinusoidal, down to about 300 Hz, and as high as several hundred MHz. The oscillations in **region (2)** also tend to be more sinusoidal.

Instabilities in an LO-pumped device

At the previous Space THz Technology Symposium, sidebands on either side of the IF frequency were reported, when recording the output of diffusion-cooled HEB mixers on a spectrum analyzer [5]. The sidebands occur when the IV-curve shows a negative slope (or a close to zero slope). We believe that these sidebands are related to the type of oscillations we have recorded through the bias line.

In terms of the hotspot model, there should be a continuous transition from a stable hotspot state when sufficient LO power is applied, to the unstable region, as the LO power is decreased. We will extend our studies to this transition in future work. We will design an improved bias circuit for the NbN mixer based on the new data presented here. Vortices should occur in the stable hotspot state as well, and a comparison of the hotspot models in regions (3), (4) and (5) should be illuminating in regard to the performance of THz NbN HEB mixers in general.

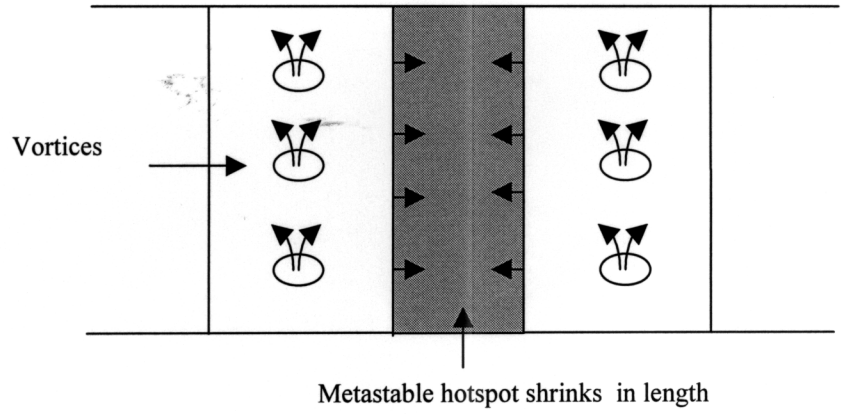

Fig. 8: Suggested first order model for the metastable state

IV. CONCLUSION

In this paper we have studied un – pumped NbN HEB devices in the instability region. Inserting a series resistor can stabilize the devices. The negative resistance of the tested devices is around – 6Ω to – 20 Ω. Measured voltage and current waveforms in the instability region imply that the devices exist in a metastable state in which the unstable hotspot expands or shrinks periodically at the device is heated or cooled. This preliminary first order model was used to interpret the experimental data.

ACKNOWLEDGEMENTS

We gratefully acknowledge support for this project from the NSF program for Advanced Technologies and Instrumentation, Division of Astronomical Sciences, NSF award # AST 9987319. We would like to thank C.F. Musante for fabricating the HEB devices, Dr. Gregory Gol'tsman and Dr. Boris Voronov for growing the NbN films, and F. Rodriguez-Morales for assistance during the measurements. We would also like to acknowledge stimulating discussions with Drs. Erich Grossman and Harald Merkel.

REFERENCES

[1] K. S. Yngvesson and E. L. Kollberg, "Optimum Receiver Noise Temperature for NbN HEB Mixers According to the Standard Model", Tenth Intern. Symp. Space THz Technology, Charlottesville, VA, March 1999, p. 563.

[2] E. Gerecht, C. F. Musante, Y. Zhuang, M. Ji, K. S. Yngvesson, T. Goyette and J. Waldman, " Development of Focal Plane Arrays Utilizing NbN Hot Electron Bolometric Mixers for the THz Regime", Eleventh Intern. Symp. Space THz Technology, Ann Arbor, MI, p. 291.

[3] H. Merkel *et al*, "A Hot Spot Mixer Model for Superconducting Phonon – Cooled HEB Far Above the Quasi – Particle Bandgap," Tenth Intern. Symp. Space THz Technology, Charlottesville, VA, March 1999, p. 580.

[4] H. Merkel et al., "An Active Zone Small Signal Model for Hot Electron Bolometric Mixers," this conference.

[5] I.Siddiqi, A. Verevkin, D.E. Prober, A. Skalare, B.S. Karasik, W.R. McGrath, P. Echternach, and H.G. LeDuc, "Aluminum Sub-Micron Superconducting Hot-Electron Bolometer Mixers", Eleventh Intern. Symp. Space THz Technology, Ann Arbor, MI, p. 91.

Development of Nb/Au bilayer HEB mixer for space applications

**P. Yagoubov, X. Lefoul*, W.F.M. Ganzevles*, J. R. Gao,
P. A. J. de Korte, and T. M. Klapwijk***

Space Research Organization of the Netherlands
Landleven 12, 9747 AD Groningen
The Netherlands

*Department of Applied Physics and DIMES
Delft University of Technology
Lorentzweg 1, 2628 CJ Delft
The Netherlands

Abstract

In this paper we propose to use a metal-superconductor bilayer as an RF detecting element for a diffusion-cooled hot electron bolometer mixer. The motivation is to engineer a superconducting material with a low transition temperature, T_c, (below T_c of commonly used Nb) and higher diffusion constant. With this it is expected to improve the overall HEB mixer performance, i.e. obtain lower noise and wider intermediate frequency bandwidth as well as reduce a local oscillator power requirement.

We report our initial experimental results. A couple of Nb/Au bilayer films with different thickness combinations have been fabricated on either glass or Si substrates. The measured sheet resistance and transition temperature of the bilayers are close to those desired for the fabrication of HEB mixers.

1. Introduction

Development of HEB mixers for space applications is now focused on both optimization of the current NbN (phonon cooled HEB) [1-6] and Nb (diffusion-cooled HEB) [7-10] technology, as well as on investigation of alternative superconducting materials, which may lead to an overall improvement of the HEB mixer performance [11-13]. The three basic parameters of HEB mixers are being addressed: sensitivity, IF bandwidth and local oscillator power requirement.

As it was shown in [11], for diffusion-cooled HEB (DHEB) improvement of the mixer performance is expected by implementation of a superconductor with lower critical temperature. First, the sensitivity is improved since the intrinsic mixer noise is

proportional to the effective electron temperature, which is about the T_c. Secondly, for DHEB the LO power requirement has quadratic dependence on the superconducting temperature T_c. Finally, a larger diffusivity D can be expected in some of superconductors with lower T_c. This would lead to a shorter thermal time constant since it is inversely proportional to D and thus increase the intermediate frequency bandwidth of the mixer.

Originally considered Al has been shown to allow for very small LO power requirement of the HEB [14]. However, the mixers tested in a quasioptical setup exhibited very low gain of about –30 dB. This was explained by the saturation in the IF port due to the very small optimum bias range. The IF bandwidth was not improved with Al based HEBs compared to Nb HEB due to the limitation imposed on the bolometer length because of the proximity effect of the normal cooling pads. The influence of the normal cooling pads on the resistive transition of Al HEB has been modeled in the limit of a very short superconducting bridge (order of coherence length ξ or less) [15].

In this paper we propose using a superconductor-normal metal bilayer as a sensitive element of the HEB mixer. We show that it is possible to obtain desired parameters such as sheet resistance and transition temperature if we choose a bilayer of Nb and Au. The diffusivity is expected to be higher than that of the single layer of Nb due to the presence of Au. Ability to tune the individual layer thicknesses to meet the requirements for particular applications is considered to be a significant advantage of the bilayer based HEB mixer.

2. Material considerations for the bilayer

To make a decision on which materials to use for the bilayer, the following requirements have been considered:

a) T_c of the bilayer should in principle be easily tunable in a temperature range between 1-5 K;

b) the desired T_c of the bilayer for the first tests is around 3-4 K since this temperature is compatible with ^{4}He cryostats facilitating the lab tests. The LO power requirement of the DHEB mixer based on a superconductor with T_c of 3 K is expected to be ~ 20 nW. Further reduction of the T_c would lower this number and may cause saturation of the mixer by the 300 K background in the conventional lab tests;

c) the sheet resistance of the bilayer film should not be too small, order of 10 Ohm/□ or larger, to match the mixer with a planar antenna;

d) It is preferable to have a fabrication process being compatible with the existing clean-room technology and experience;

e) the larger diffusivity and shorter electron-electron interaction time constant of both superconductor and normal metal are desired. The large diffusivity will

provide a wider IF bandwidth of the mixer for a given bolometer length and the fast electron-electron interaction favors the thermalization.

Different materials have been considered and finally the combination Nb/Au was chosen. We expected that the bilayer with film thicknesses: d_n~5 nm, d_s~5 nm may meet the requirements mentioned above. The main parameters of the Nb and Au we used are listed in the Table 1.

Table 1. Material parameters: v_f is the Fermi velocity, ρ is the resistivity, ξ is the coherence length, and l is the electron mean free path.

Material	v_f, $*10^8$cm/s	ρ, μOhm cm	ξ, nm	l, nm
Au	1.4	8-10	50	5
Nb	0.27	20-25	10	3

Here we estimate T_c and the sheet resistance of such a Nb(5 nm)/Au(5 nm) bilayer. The T_c of a bilayer can be predicted using a Golubov model [16] if the T_c of the superconducting layer is known. It is however known from experience that a layer of 5 nm thick Nb can have a varying T_c, depending strongly on the sputtering condition. At the same time it is also not possible to determine T_c experimentally due to fast film oxidation (which proximitizes the superconductor as well). For our estimates we use T_c of 5 nm Nb being about 5-7 K. The model [16] is valid for arbitrary film thicknesses and interface transparencies. Initially the interface resistance was estimated as being simply a mismatch between the Fermi velocities v_f of the normal (N) and superconducting (S) layers. A calculation shows that the T_c of such a Au/Nb bilayer will be about 60 % of the T_c of the Nb, in the range 3-4 K.

To estimate the sheet resistance we have considered the N and S layers as two resistors connected in parallel:

$$R_{sq} = \left(\frac{d_n}{\rho_n} + \frac{d_s}{\rho_s} \right)^{-1}.$$

One should note, however, that the resistivity of very thin films is not equal to the bulk resistivity, but includes a "size" contribution due to the scattering of the electrons at the film surfaces. This causes the electron mean free path to be limited by the film thickness.

For a rough estimate of the Nb resistivity we took the measured value of 15 μOhm cm for the 10nm Nb film, and estimated it to increase to about 20-25 μOhm for the 5 nm film. To our knowledge there is no experimental data on so thin Au films resistivity. The estimate in the Drude model gives a value of 2 μOhm cm with the mean

free path 40 nm. The thickness of our Au is smaller than that value so the "size" contribution to the resistivity may be large. Moreover, Au may not grow very uniformly likely having "island" structure in such thin films, so that the resistivity may increase due to this effect even further. For a crude estimate we took the resistivity of Au to be of the order of 8-10 μOhm cm for thickness 5 nm. With these numbers on resistivity of Nb and Au we expect a sheet resistance of the bilayer to be about 10-15 Ohm/□.

3. Films fabrication and dc characterization

Based on these considerations, the test samples on glass substrate with different film thickness combinations have been produced: "6/6", "5/5", "5/4". The first number corresponds to the thickness of Nb, the second one to the thickness of Au in nm; for instance "6/6" means a bilayer made from 6 nm Nb and 6 nm Au. The layers were sputtered *in situ* to avoid oxidation of Nb. The samples were cut into 4 mm long and 2 mm wide pieces. Critical temperature of the bilayers was measured by a four-probe method. The temperature is controlled by an electrical heater and measured by a calibrated germanium resistor with an accuracy of 10 mK.

The results of the critical temperature measurements are presented in Figure 1. The critical temperatures of the samples made in different runs are consistent, correlating with the thickness combinations and lie within 3.5-4.2 K, close to the designed values and have a very sharp transition of about 50 mK. The sheet resistance of the films of about 15 Ohm/□ is also in a good agreement with the predictions and large enough to match the bolometer to the receiver antenna.

Table 2. dc parameters of the non-patterned Nb/Au bilayer films on glass substrate.

Nb / Au thicknesses, nm	T_c	Sheet resistance at 300 K, Ohm	Sheet resistance at 10 K, Ohm
6/6	4.25	18	13
5/5	3.5	20	16
5/4	3.7	21	16

As it was mentioned in the introduction, one of the very important material parameter to be considered for the DHEB mixer fabrication is the diffusion constant D, since it plays a crucial role in determining an intermediate frequency bandwidth of the device. In case of bilayer we expect the diffusivity to be largely influenced (however not necessarily determined) by the diffusivity of the cleaner material, which is Au. If we use the Drude model to predict diffusion constant of Au, we get a number of 40 cm^2/s. However, it is necessary to verify the diffusivity of a bilayer experimentally.

In case of a single superconductor the diffusion constant can be estimated from the residual resistivity and the density of states at the Fermi level. There is also a straightforward experimental way to determine this parameter, namely by measuring a temperature dependence of the perpendicular critical magnetic field H_{c2}. However, in the

case of thin films bilayer the situation is more complicated and the above mentioned method are not applicable *a priory*. We used the formalism of Fominov and Feigel'man [18] to model the system but came to the conclusion that in our particular case magnetic field measurements can not be used directly for the predictions of the diffusion constant of the bilayer system [19]. Instead, the microwave measurements of the impedance or direct measurements of the HEB IF bandwidth have to be performed.

4. HEB mixer fabrication and dc test results

Figure 2 shows an SEM micrograph of a Nb/Au bilayer HEB mixer using a spiral antenna. In this device the Nb/Au bridge with a length of 250 nm and a width of 190 nm is in the middle, between the antenna arms. Pads directly contacting to the bridge are thick Au, functioning as cooling pads for hot electrons. The structures above the cooling pads are the thick Nb layer as a part of spiral antenna. Due to misalignment in the lithographical process, the thick Nb structure locates not symmetrically with respect to the cooling pads.

The fabrication process of the bilayer mixers is as following. The substrate is a highly resistive Si (111) wafer. The Nb/Au bilayer is sputtered on the whole wafer. Au cooling pads (80 nm) are formed by evaporation in combination with e-beam lithography and lift-off. Then, the antenna structure is realized by sputtering thick Nb (80 nm) followed by a layer of Au and by lift-off. The last step is to etch the Nb/Au bilayer to form a superconducting bridge. The etch mask used is a thin, narrow strip of Al.

The resistance of this device is measured as a function of temperature, shown in Figure 3. The observed R-T characteristic resembles very much those obtained in Nb HEB mixers [20], characterized by two T_c's, one corresponding to the T_c of the bridge (~3.5 K) and the other to the bilayer under the cooling pads (~2 K). The normal state resistance is 13 Ω. The current-voltage characteristic is measured at 1.4 K, which is also included in Figure 3. We observe a critical current of 100 μA and also hysteresis in the IV curve. However, the hysteretic effect is so small that it is hard to be seen in the plotted IV curve. Although no detailed analysis for the R-T and I-V data is done, they can be further evaluated at high frequency, judging from the understanding of Nb HEB mixers.

5. Summary

We present a new approach for diffusion-cooled HEB mixers by using Nb/Au bilayer as a superconducting bridge instead of Nb or Al. We have fabricated Nb/Au bilayer films with different thickness combinations on glass substrate. The dc parameters of the films are close to the designed values. HEB mixers based on 5 nm Nb + 5 nm Au bilayer films on Si substrate have been fabricated and the first dc results are obtained. The next step is rf characterization of the mixer.

Acknowledgement

A. Golubov is greatly acknowledged for the discussions on the bilayer physics and providing us with the numerical computing code to calculate T_c of the bilayers using his model. We are thankful to N. Iosad for his help with the Nb/Au bilayer fabrication.

References

1. E. M. Gershenzon, G. N. Gol'tsman, I. G. Gogidze, Y.P. Gusev, A. I. Elant'ev, B. S. Karasik and A. D. Semenov, "Millimeter and submillimeter range mixer based on electronic heating of superconducting films in the resistive state", *Sov. Phys. Superconductivity*, 3, 1582, 1990
2. J. Kawamura, C.-Y. E. Tong, R. Blundell, D. C. Papa, T. R. Hunter, G. Gol'tsman, S. Cherednichenko, B. Voronov, and E. Gershenzon, "An 800 GHz NbN Phonon-cooled Hot-electron Bolometer Mixer Receiver", IEEE Trans. on Appl. Superconductivity, vol. 9, No 2, 3753, 1999
3. P. Yagoubov, M. Kroug, H. Merkel, E. Kollberg, J. Schubert, H.-W. Huebers, S. Svechnikov, B. Voronov, G. Gol'tsman, and Z. Wang, "Hot Electron Bolometric Mixers Based on NbN Films Deposited on MgO substrates", *Proc. Europ. Conf. on Appl. Superconductivity (EUCAS'99),* Barcelona, 14-17 September, 1999
4. H.-W. Huebers, A. Semenov, H. Richter, G. Gol'tsman, B. Voronov, and E. Gershenzon, "Antenna pattern and noise temperature of the phonon-cooled hot-electron bolometric mixer at the frequencies", presented at the *12th Int. Symp. on Space Terahertz Technology*, San Diego, CA, 2001, this issue
5. E. Gerecht, C. Musante, Y. Zhuang, M. Ji, K. Yngvesson, T. Goyette, and W. Waldman, "Development of focal plane arrays utilizing NbN hot electron bolometric mixers for the terahertz regime", *Proc. 11th Int. Symp. on Space Terahertz Technology*, Ann Arbor, MI, 209, 2000
6. S. Cherednichenko, M. Kroug, A. Adam, N. Wadefalk, M. Choumas, P. Khosropanah, H. Merkel, E. Kollberg, B. Voronov, G. Gol'tsman, H.-W. Huebers, and H. Richter, "HEB quasioptical heterodyne receiver for terahertz frequencies", presented at the *12th Int. Symp. on Space Terahertz Technology*, San Diego, CA, 2001, this issue
7. D.Prober. "Superconducting Terahertz Mixer using a Transition Edge microbolometer", *Appl. Phys. Lett*. 62(17), 2119, 26 April 1993
8. R. Wyss, B. Karasik, W. McGrath, B. Bumble, and H. LeDuc, "Noise and Bandwidth Measurements Of Diffusion-Cooled Nb Hot-Electron Bolometer Mixers at Frequencies Above the Superconductive Energy Gap", *Proc. 10th Int. Symp. on Space Terahertz Technology*, Charlottesville, VA, 214, 1999
9. D. Wilms Floet, J.R. Gao, T.M. Klapwijk, W.F.M. Ganzevles, G. de Lange and P.A.J. de Korte, "Receiver Measurements at 700 GHz with a Niobium Diffusion-Cooled Hot-Electron Bolometer Mixer", *Proc. 10th Int. Symp. on Space Terahertz Technology*, Charlottesville, VA, 229, 1999C. E.
10. W.F.M. Ganzevles, L.R. Swart, J.R. Gao, T.M. Klapwijk, and P.A.J. de Korte, "Direct and Heterodyne Response of Quasi optical NB Hot-Electron Bolometer Mixers designed for 2.5 THz Radiation Detection", *Proc. 11th Int. Symp. on Space Terahertz Technology*, Ann Arbor, MI, 69, 2000
11. B. Karasik, W. McGrath, "Optimal Choice of Material for HEB Superconducting Mixers", *Proc. 9th Int. Symp. on Space Terahertz Technology*, Pasadena, CA, 214, 1999
12. Tong, J. Stern, K. Megerian, H. LeDuc, T. Sridharan, H. Gibson, R. Blundell, "A low-noise NbTiN hot electron bolometer mixer", presented at the *12th Int. Symp. on Space Terahertz Technology*, San Diego, CA, 2001, this issue
13. I. Siddiqi, D. Prober, B. Bumble, H. G. LeDuc, "Reduced Tc Nb Superconducting HEB Mixers", presented at the *10th Int. Symp. on Space Terahertz Technology*, Charlottesville, VA, 214, 1999, in this proceedings

14. A. Skalare, W. McGrath, P. Echternach, H. LeDuc, I. Siddiqi, A. Verevkin, and D. Prober, "Diffusion cooled Aluminum hot-electron bolometer mixers at submillimeter wavelength", *Proc. 11th Int. Symp. on Space Terahertz Technology*, Ann Arbor, MI, 501, 2000
15. A.H. Verbruggen, T.M. Klapwijk, and W. Belzig, and J.R. Gao, "The resistive transition of Aluminium hot electron bolometer mixers with normal metal cooling pads", in this proceedings
16. A. Golubov, E. Houwman, J. Gijsbersten, V. Krasnov, J. Flokstra, H. Rogalla, and M. Kupriyanov, "Proximity effect in superconducting-insulator-superconductor Josephson tunnel junctions; theory and experiment", Phys. Rev. B 51, 1073, 1995; A. Golubov has also provided us with a numerical code
17. M. Frommberger, F. Mattiocco, P. Sabon, M. Schicke, K. Schuster, and O. Laborde, "Properties of Nb thin films and their applications for diffusion-cooled hot-electron bolometer", *Proc. 11th Int. Symp. on Space Terahertz Technology*, Ann Arbor, MI, 489, 2000
18. Ya. Fominov, and M. Feigel'man "Superconductive properties of thin dirty SN bilayers", Phys. Rev. B, 63, 094518, 2001
19. Results of this modeling will be published elsewhere
20. D. Wilms Floet, J. Baselmans, T.M. Klapwijk and J.R. Gao, "Resistive Transition of Niobium Diffusion-Cooled Hot Electron Bolometers", Appl. Phys. Lett.,73, 2826-2828, 1998

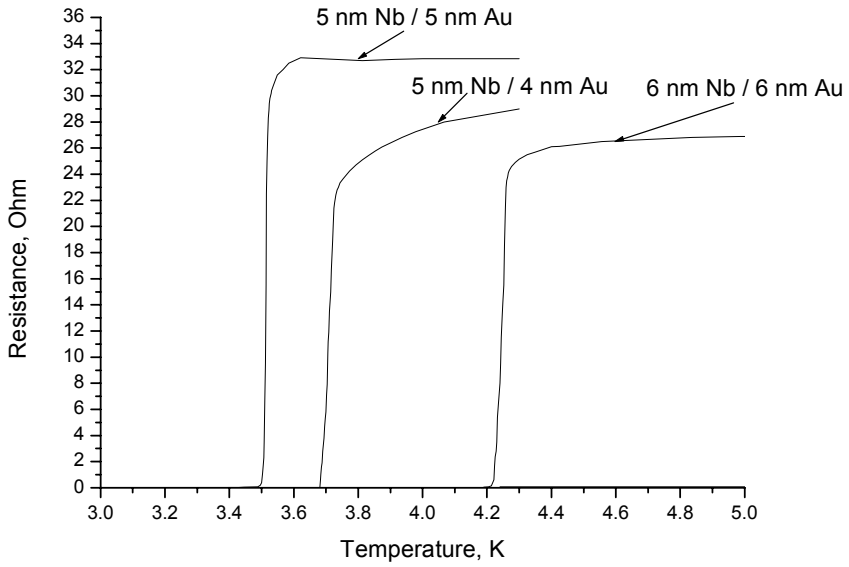

Figure 1. Critical temperatures of Nb/Au bilayer films with different thicknesses combinations. The films are fabricated on a glass substrate and are non-patterned.

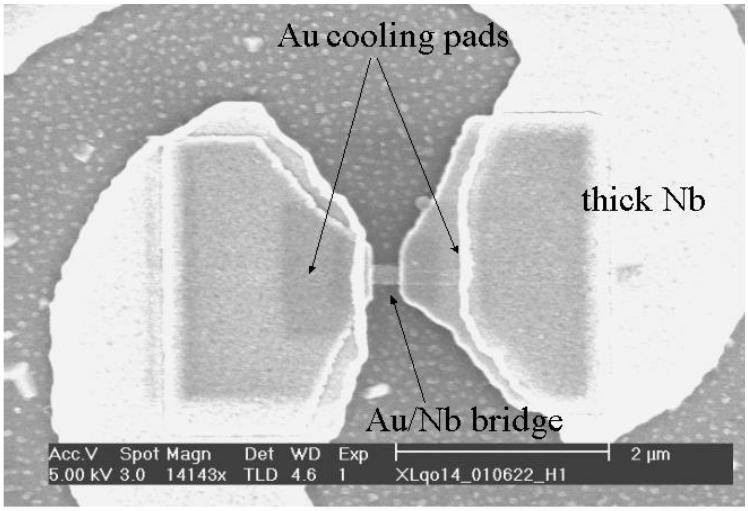

Figure 2. SEM micrograph of a part of Nb/Au bilayer HEB mixer using spiral antenna, fabricated on Si substrate. In the center is the Nb/Au bridge. Two sides of the bridge are contacted to thick Au cooling pads. Above the cooling pads is the antenna structure with thick Nb(80 nm)/Au layer. The bar in the photo is 2 µm.

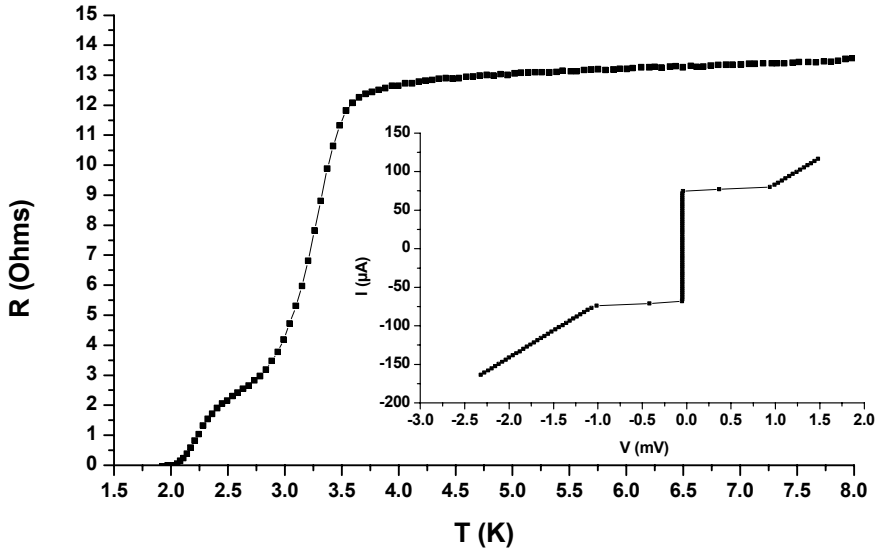

Figure 3. The resistance of the Nb/Au HEB mixer (shown in Fig. 2) as a function of temperature. The current-voltage characteristic at ambient temperature 1.4 K is shown in the inset.

RF current distribution in HEB and a 2-dimensional device model

P. Khosropanah[*], A. Adam[§], H. Merkel[*], S. Cherednichenko[*],

S. Yngvesson[#], E. Kollberg[*]

[*]Chalmers University of Technology, Department of Microelectronics, Microwave electronics Laboratory, 412 96 Gothenburg, Sweden

[#]University of Massachusetts, Department of Electrical and Computer Engineering, Amherst, MA 01003

[§] Laboratoire de Génie Électrique de Paris, Groupe SFMD, 91192 Gif sur Yvette, France

Abstract

The RF current distribution in the bolometer bridge is investigated by solving the Maxwell's field equations analytically and by using commercial packages *QuickWave-3D*® (Finite-Difference Time-Domain, FDTD Method) and *Sonnet*® (Method of Moments). The outcomes of analytical calculations and *QuickWave-3D*® indicate non-uniform RF current distribution where *Sonnet*® results show completely uniform current at 2 THz. This controversial result is subject to discussion. By accepting the non-uniform scenario one can explain the dependence of the conversion loss on LO frequency. A 2-dimensional device model is presented which is based on non-uniform LO power absorption.

I. Introduction

In earlier one-dimensional models [1] RF heating is assumed to be uniform all over the bolometer bridge. The predicted conversion loss by such a model was far too high compared to measured data. Therefore a tuning factor was needed to fit the predicted conversion loss, receiver noise and output noise to the measured data. Recent work by Semenov *et al.* [2] has suggested a non-uniform heating across the bolometer bridge due to RF skin effect.

Since this effect is supposed to have a large impact on the bolometer performance the RF current distribution in the bolometer bridge is investigated in more detail.

In section II the RF current distribution in an infinite long NbN strip is calculated analytically. Section III presents the simulation results of various structures done by a FDTD package (*QuickWave-3D*® [3]). In section IV the effect of non-uniform RF current distribution on bolometer performance is discussed. Section V presents the outcome of a moment method approach (*Sonnet*® [4]). Finally the discussion and conclusion come in section VI.

II. RF current distribution in an infinite long resistive strip

In this section we derive an analytical expression for current distribution in an infinite long conductor strip. Figure 1 shows a schematic top view of a long strip.

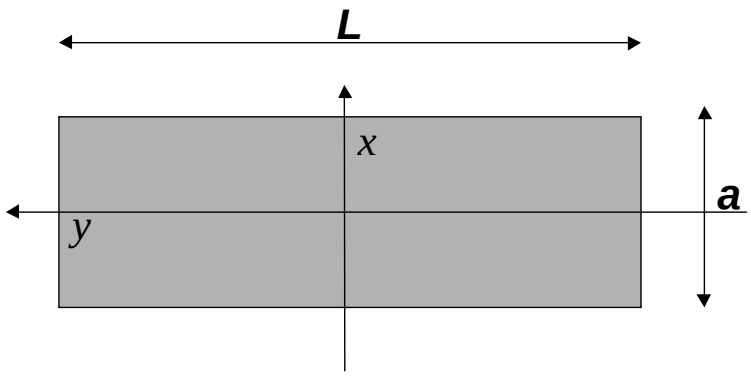

Figure 1. Top view of a long strip with length *L* and width *a* where L>>a

Here it is assumed that the strip is resistive and electrically very thin. This is the case in NbN bolometer bridge which is 5 nm thick with conductivity about 3.5×10^{-6} Ωm

The wave equation in a medium with finite conductivity is:

$$-\nabla^2 \vec{E} = -j\omega\mu(\sigma + j\omega\varepsilon)\vec{E}.$$

In our case $\sigma >> \varepsilon\omega$. For NbN σ is about 3×10^5 S/m where εω is about 100 S/m at 2 THz. So the second term on the right hand side of the above equation is negligible and the equation is reduced to:

$$\nabla^2 \vec{E} = j\omega\mu\sigma\vec{E} \Rightarrow \nabla^2 \vec{E} = k^2 \vec{E}$$

where: $k^2 = j\omega\mu\sigma$.

The electric field in the strip can be written as: $\vec{E} = E_x(x).\vec{x} + E_y(x).\vec{y}$. Since we assume that the strip is infinitely long, the field does not depend on *y* along the strip. Under this assumption we get:

$$\nabla^2 \vec{E} = \frac{\partial^2 E_x}{\partial x^2}\vec{x} + \frac{\partial^2 E_y}{\partial x^2}\vec{y} = k^2 E_x \vec{x} + k^2 E_y \vec{y}$$

which implies:

$$\frac{\partial^2 E_x}{\partial x^2} = k^2 E_x \text{ and } \frac{\partial^2 E_y}{\partial x^2} = k^2 E_y.$$

Assuming that the potential is constant across the strip, requires $E_x = 0$. So one is left with:

$$\frac{\partial^2 E_y}{\partial x^2} = k^2 E_y.$$

Solving for E_y gives: $E_y(x) = C_1 e^{kx} + C_2 e^{-kx}$.

Because of the symmetry we have: $E_y(-x) = E_y(+x)$, so $E_y(x) = C\left(e^{kx} + e^{-kx}\right)$.

If I_0 is the total current and *t* is the thickness of the strip:

$$I_0 = t\int_{-a/2}^{a/2} j(x)dx = t\int_{-a/2}^{a/2} \sigma E_y(x)dx = t\sigma\int_{-a/2}^{a/2} E_y(x)dx = t\sigma\int_{-a/2}^{a/2} C\left(e^{kx} + e^{-kx}\right)dx =$$

$$t\sigma\frac{C}{k}\left[e^{kx} - e^{-kx}\right]_{-a/2}^{a/2} = t\sigma\frac{2C}{k}\left(e^{\frac{ka}{2}} - e^{-\frac{ka}{2}}\right) \Rightarrow C = \frac{kI_0}{2t\sigma\left(e^{\frac{ka}{2}} - e^{-\frac{ka}{2}}\right)}$$

And the final result becomes:

$$j(x) = \frac{kI_0}{2t\sigma}\frac{\left(e^{kx} + e^{-kx}\right)}{\left(e^{\frac{ka}{2}} - e^{-\frac{ka}{2}}\right)}.$$

Figure 2 shows the normalized amplitude of *j(x)* inside the NbN strip at 0.6, 1.6 and 2 THz for 2 micron wide strip.

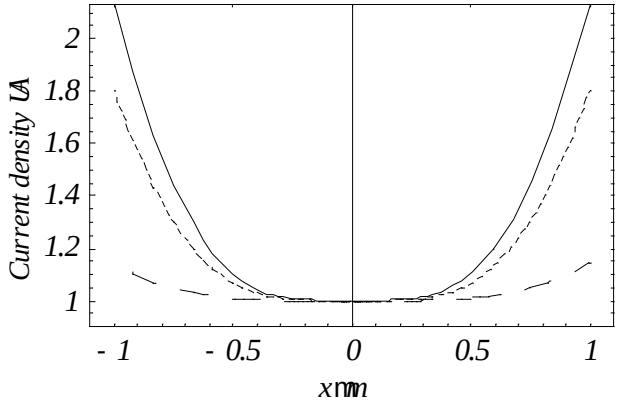

Figure 2. The current distribution along 2 micron wide NbN strip at 0.6 THz (dashed line), 1.6 THz (dotted line) and 2 THz (solid line).

Although the expression derived here for the current distribution is different from [2] the plotted curves coincide very well.

The above derivation is based on the assumption of an infinitely long strip to simplify the problem and make it possible to solve analytically. In reality the bolometer bridge is very short (0.2 micron), limited by two thick (80 nm) golden antenna pads. Since the current distribution in the thick golden antenna arms are presumably very different from what calculated above for NbN strip, one can speculate that the current distribution in the short bolometer bridge is affected by the antenna pads. Also the influence of the substrate is completely ignored in above calculation.

In order to reveal the current distribution in the whole bolometer structure an electromagnetic simulator (*QuickWave-3D*®) was used.

III. *QuickWave-3D*® simulated results

The first simulated structure was a simple 10 μm long, 2 μm wide and 5 nm thick NbN strip on a substrate with ε_r = 2.2. Figure 3 shows the structure and the current density across the strip.

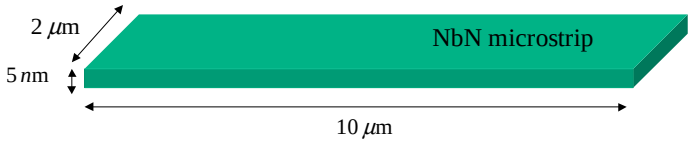

(a)

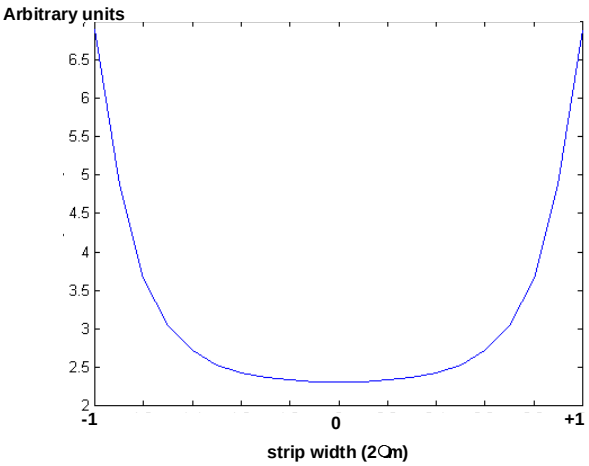

(b)

Figure 3. (a) NbN thin microstrip structure and (b) the current distribution inside NbN at 2 THz.

QuickWave-3D® gives the electromagnetic fields solution using Finite-Differences in Time-Domain (FDTD). Since the current density along the strip is proportional to the *E* field in that direction one can estimate the current density using *QuickWave-3D*®.

Secondly the bolometer structure is simulated. The bolometer bridge is 0.2 μm long, 2 μm wide and 5 nm thick NbN strip. The gold pads are 80 nm thick. Figure 4 shows the schematic picture of the structure and the current density distribution inside the NbN strip under the gold pads and the gap.

(a)

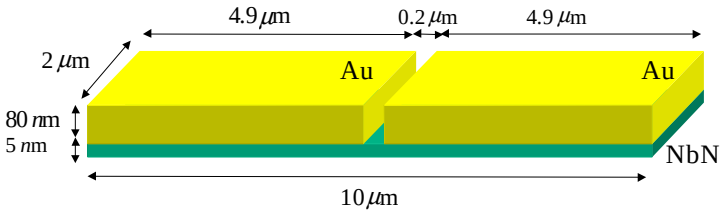

(b)

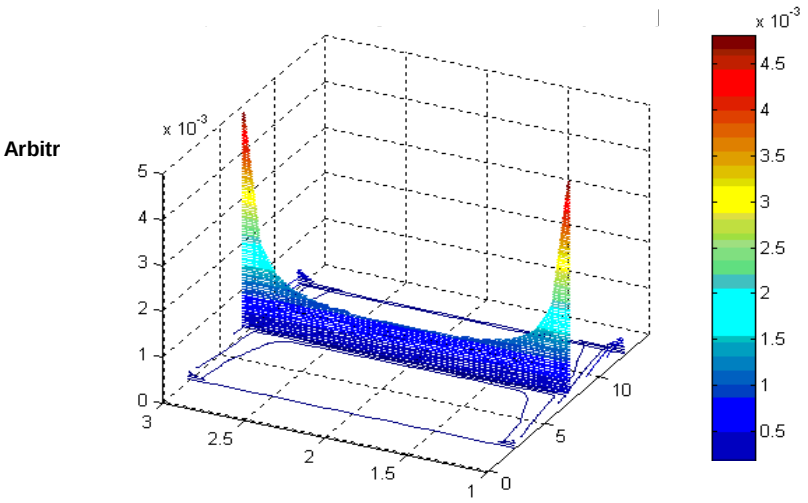

Figure 4. (a) Simulated bolometer structure and (b) the current distribution in NbN layer

The current density in NbN strip under the gold pads is almost zero. This means that almost all the RF current flows in the gold as expected. Figure 5 summarizes the simulated and analytical results. In QuickWave there is an option that applies edge singularity correction. When long strip was simulated with edge singularity option on, the current distribution was slightly different as plotted in figure 5.

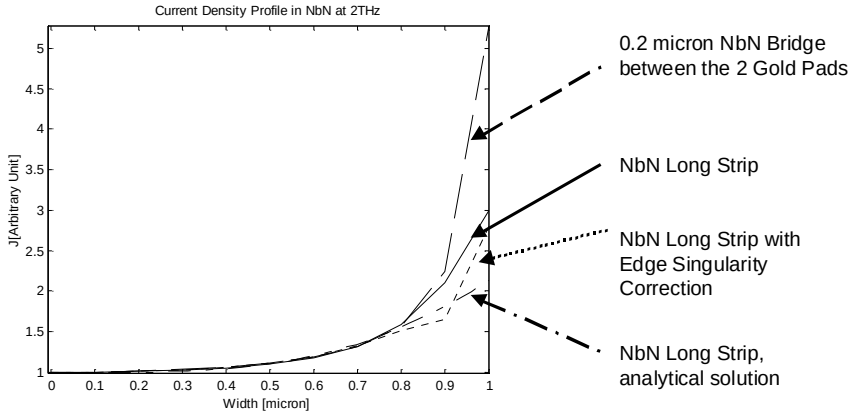

Figure 5. Simulated and analytically calculated results of RF current distribution in half of the 2 micron wide NbN strip. 0 is in the middle of strip and 1 is at the edge.

The RF current distribution in the NbN bolometer structure shows a strong non-uniformity, even more than for the long NbN strip. This is an indication that the current

distribution in the NbN bridge is clearly affected by the current distribution in the gold contacts.

IV. 2D bolometer model

In order to estimate the effect of non-uniform absorbed LO power across the bolometer bridge on the conversion loss of the device, the bolometer is divided into several parallel strips. If the number of these parallel strips is large enough the RF current distribution on each of these strips is approximately uniform. So they can be modeled by a one-dimensional hot spot model [1]. All these parallel strips share the same voltage but they have different resistance and different DC current because the absorbed LO power in each strip is different. It is also assumed that the there is no lateral current in the bridge.

In order to estimate the conversion loss of such system one should first calculate the current and resistance of the device at certain bias voltage and absorbed LO power using the large signal model [1]. The absorbed LO power in each of the parallel strips depends on the LO frequency and the width of the bolometer. Knowing the absorbed LO power one can solve for the DC currents in each strip. The requirement is that the absorbed DC power together with the absorbed LO power in each strip should cause a resistance, which holds the relations:

$R_i I_i = V$ for all i.

Figure 6 shows the schematic picture of a bolometer divided in to several parallel strips.

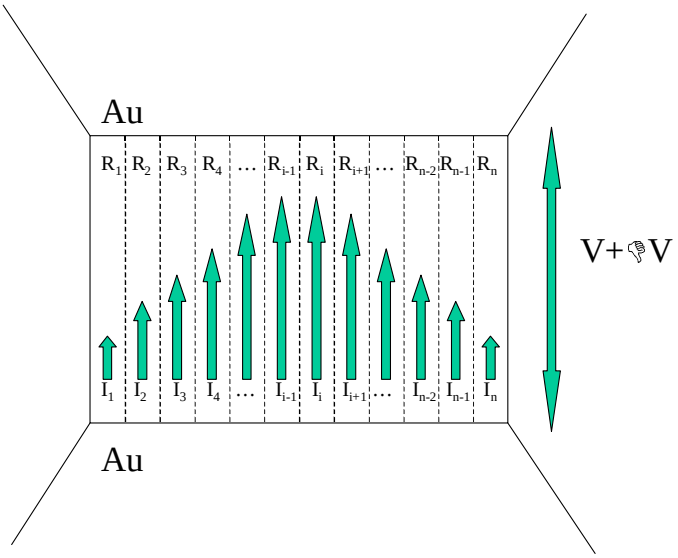

Figure 6. Schematic top view of a bolometer divided into several parallel strips.

The resistances of the middle strips are lower than of the edge strips. Therefore the DC current flows more in the middle. Consequently the size of the hotspot on the edges is larger than in the middle.

Figure 7 shows an estimated two-dimensional electron temperature profile of a bolometer around optimum operating point.

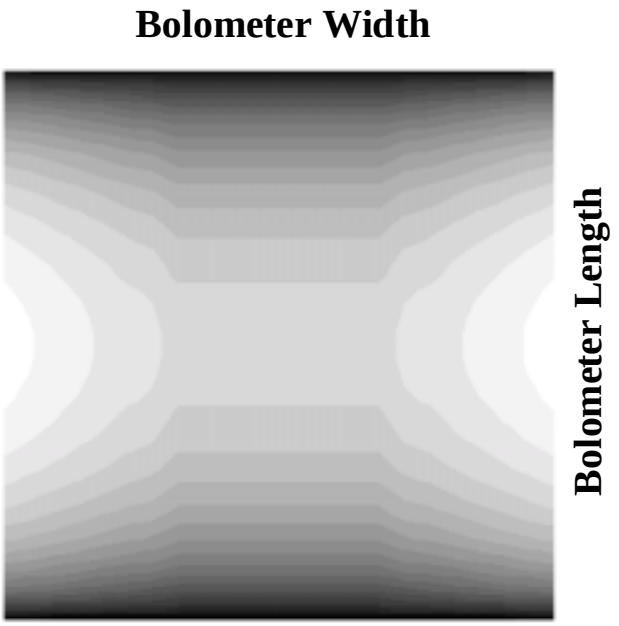

Figure 7. 2D-electron temperature profile of a bolometer. The light color stands for high temperature

Literally we can say that this is as if we have similar bolometers that are biased with the same bias voltage but different absorbed LO power.

By solving the small signal current in each of the strips using the hotspot model [1] one can estimate the conversion loss of the bolometer. Our calculation shows that due to the non-uniform RF current distribution at 2 THz the conversion loss can be up to 6 dB higher that what we calculate at 0.6 THz.

V. *Sonnet*® simulated results

The RF current distribution was also simulated by *Sonnet*®, which is based on moment method. On the contrary to *QuickWave3-D*®, it shows uniform current distribution in the bolometer bridge. Figure 8 shows the simulated result at 2 THz for a 0.2 μm long, 2 μm wide and 5 nm thick NbN bolometer.

The same uniformity was observed when simulating a long thin NbN strip. Non-uniform current was only in thick NbN strips (100 nm). *Sonnet*® does not show any edge singularity at frequencies lower the frequency where the resistance per unit length equals the inductive reactance per unit length [5]. In thin NbN strip where resistance is high this frequency is much higher than 2 THz and the edge singularity does not appear.

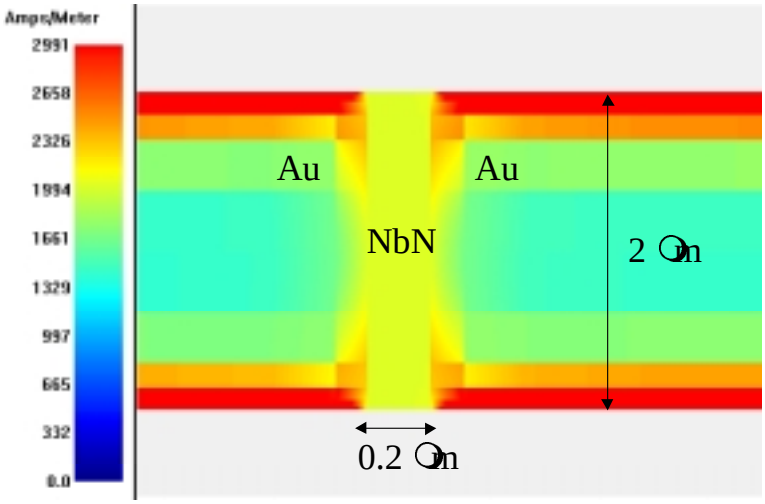

Figure 8. RF current distribution simulated by *Sonnet*®.

VI. Discussion and conclusion

Non-uniformity in RF current distribution has a large impact on the performance of the bolometer. Our QuickWave simulated results are in agreement with analytical calculations indicating a strong non-uniform LO power absorption across the bolometer bridge at 2 THz. However Sonnet simulated results do not agree with that. Since QuickWave is based on FDTD 3-dimensional electromagnetic simulation and confirms the analytically calculated results the authors tend to believe in non-uniformity of RF current in the bolometer. Accordingly less degradation is expected for a device with smaller width when operating at higher frequencies, which is a subject of further investigation.

Novel designs such as thin parallel bolometer strips with different antenna pads configuration have to be investigated to achieve more uniform RF current distribution and eventually decrease the intrinsic conversion loss.

Rejecting the non-uniform current distribution, other reasons for observed increase of conversion loss by increasing the RF frequency must be found.

VII. Acknowledgements

This project is supported by Swedish National Space Board (SNSB) and Swedish Foundation for Strategic Research (SSF).

References

[1] P.Khosropanah *et al.* 11th ISST THz 2000. Ann Arbor, MI. Page: 474

[2] A.Semenov *et al*. 11th ISST THz 2000. Ann Arbor, MI. Page: 39

[3] *QuickWave 3-D*®. http://www.qwed.com.pl/

[4] *Sonnet*®. http://www.sonnetusa.com/

[5] An Investigation of Microstrip Conductor Loss. IEEE Microwave Magazine December 2000. Page 60.

Characterization of NbN Thin Films produced on Quartz Substrates using MgO Seed Layers for phonon cooled Hot-Electron Bolometer Devices

M. Frommberger, P. Sabon, M. Schicke and K.F. Schuster

Institut de Radioastronomie Millimétrique
300, rue de la piscine, Domaine Universitaire
38406 St. Martin d'Hères, France
frommber@iram.fr

INTRODUCTION

NbN phonon-cooled hot-electron bolometer (HEB) mixer devices have turned out to be very useful for space terahertz applications. High intermediate frequencies in the range of several GHz are demanded for those applications. The intermediate frequency bandwidth of phonon-cooled HEBs can be increased by reduced film thickness [1].

Thin NbN films of about 3 nm produced on fused quartz substrates are not superconducting at liquid helium temperature [2]. To improve the film properties, one can use crystalline substrates as MgO, silicon or sapphire but those high-ε materials pose particular problems in terms of electromagnetic impedance matching and are fairly expensive.

We present an investigation on NbN thin films deposited on MgO seed layers on 2" fused and crystal quartz substrates. This MgO layer improved significantly the superconducting properties of our NbN films, sputtered at ambient temperature. Atomic force microscopy and x-ray diffraction were used to examine the surface properties and crystallinity of our thin films.

We present preliminary results using small angle x-ray reflectometry to determine the thickness of our sputtered NbN/MgO bilayers. The results are compared to ellipsometry and anodization measurements.

Phonon-cooled NbN/MgO HEBs have been produced with a new process, using a negative resist for the definition of the width of the microbridge by electron beam lithography.

First results, obtained at a frequency of 800 GHz showed an IF-gain bandwidth of 1.8 GHz and a receiver noise temperature of 670 K (corrected for beam splitter loss).

I. Crystalline Properties of the Bilayer

The influence of an MgO seed layer on fused quartz and crystal quartz on the crystalline properties of the NbN thin films has been investigated by x-ray diffraction measurements.

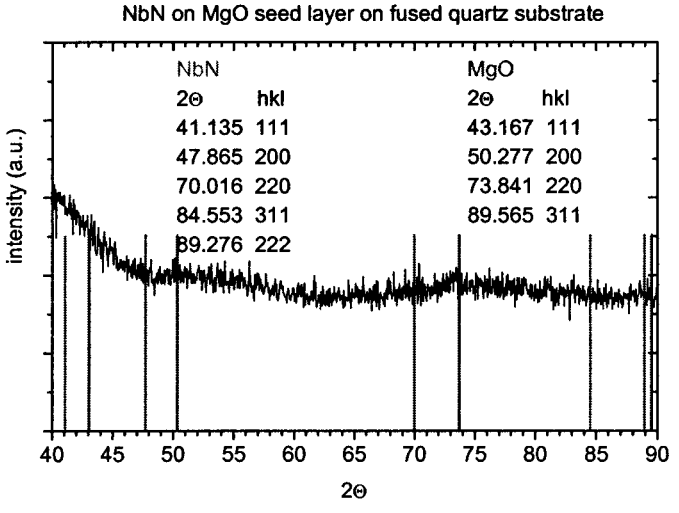

Fig.1.1.: θ/2θ scan of an NbN/MgO bilayer on a fused quartz substrate

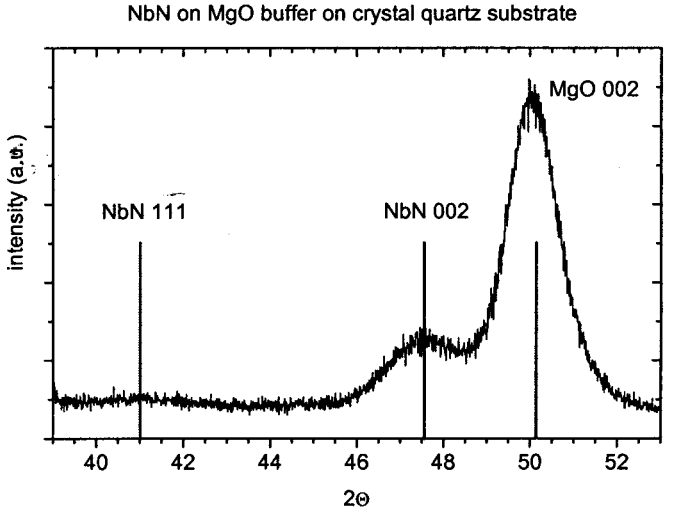

Fig.1.2.: θ/2θ scan of an NbN/MgO bilayer on a crystal quartz substrate.

The pictures show x-ray diffraction data (Co K_α 1.789 Å) of an approximately 5 nm thick NbN film on a 45 nm MgO seed layer on a fused (fig.1.1) and crystal quartz substrate (fig.1.2). On the fused quartz substrate the films are growing amorphously. The crystalline substrate allows the MgO and the NbN layer to grow mainly in (002) orientation. From the full width half maximum value of the (002) peak of NbN (fig.1.2) we can estimate a NbN grain size of 5 nm.

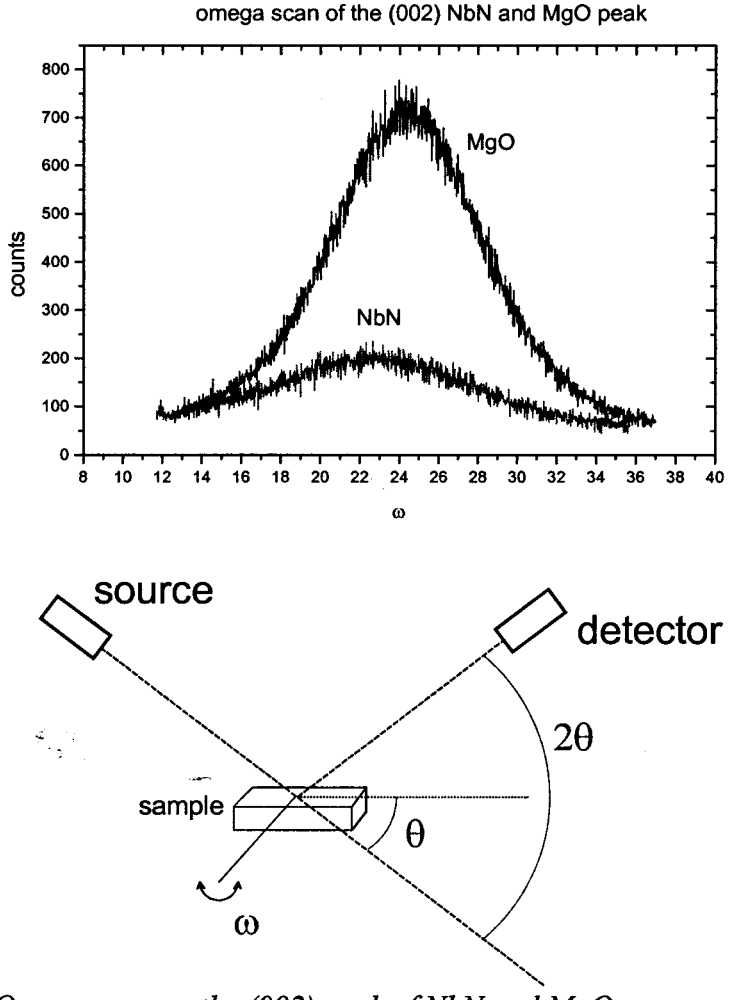

Fig.1.3.: Omega scan on the (002) peak of NbN and MgO

If one fixes the θ/2θ geometry for a given peak and turns the sample around the angle ω (= θ), one obtains a so called omega scan. The omega scan is a measure of the desorientation of the crystallites in the deposited layers. Figure 1.3 shows a scan, carried out on the NbN and MgO (002) peaks which confirms that the NbN growth is following the MgO seed layer.

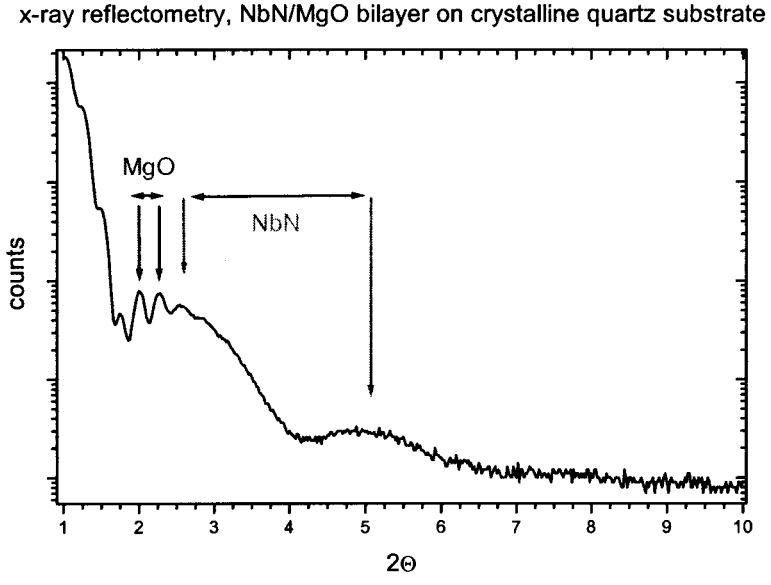

Fig.1.4.: Kiessig fringes of the NbN/MgO bilayer on a crystal quartz substrate.

As the equipment at DRFMC (Department of fundamental research on condensed matter) allowed also small angle measurements, we observed the Kiessig fringes of an NbN/MgO bilayer on crystal quartz (fig.1.4). The small oscillations correspond to the thicker MgO film and give a thickness of about 46 nm. The large oscillation is due to the ultrathin NbN layer and results in a thickness of 4 nm ±1. Surface, interface and substrate roughnesses determined from the x-ray small angle measurements could be estimated as 0.5 nm. This is about twice the RMS values obtained by AFM measurements carried out individually on a crystal quartz substrate, an MgO layer on crystal quartz and an NbN/MgO bilayer on crystal quartz.

II. Thickness Control by Ellipsometry and Anodization

The MgO layer thickness obtained by the reflectivity measurement was verified by ellipsometry of a film sputtered on a 2" Si wafer with the same deposition parameters. We obtained an average seed layer thickness of 42 nm in good agreement with the x-ray results (fig.2.1).

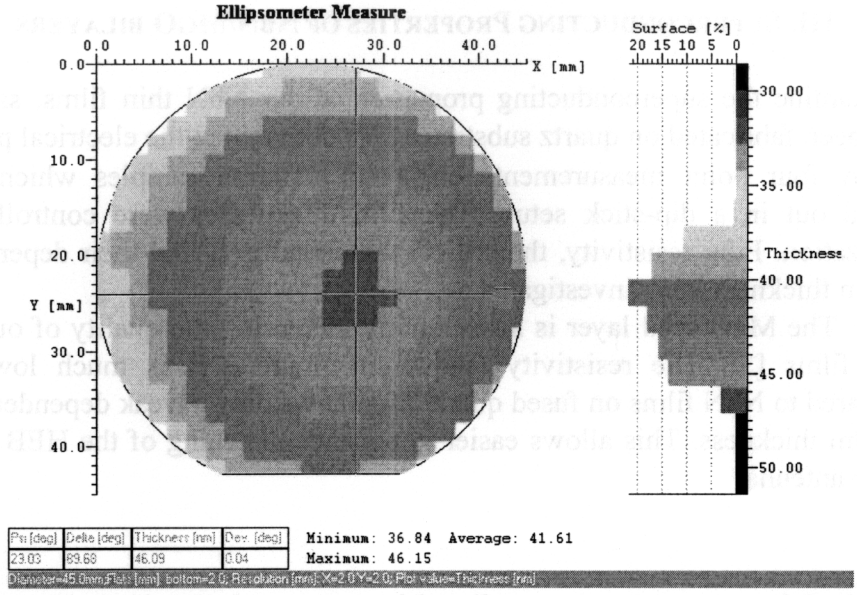

Fig.2.1.: MgO film thickness control by ellipsometry. Mapping of the hole 2" Si wafer.

The thickness of our NbN layers is always measured directly after deposition by anodization [4]. The graph in figure 2.2 shows an anodization curve of a 5 nm ±1 NbN film. The thickness of the superconducting layer determines the resistivity of the film in the normal conducting state and so the length and the width of the final NbN microbridge of a HEB.

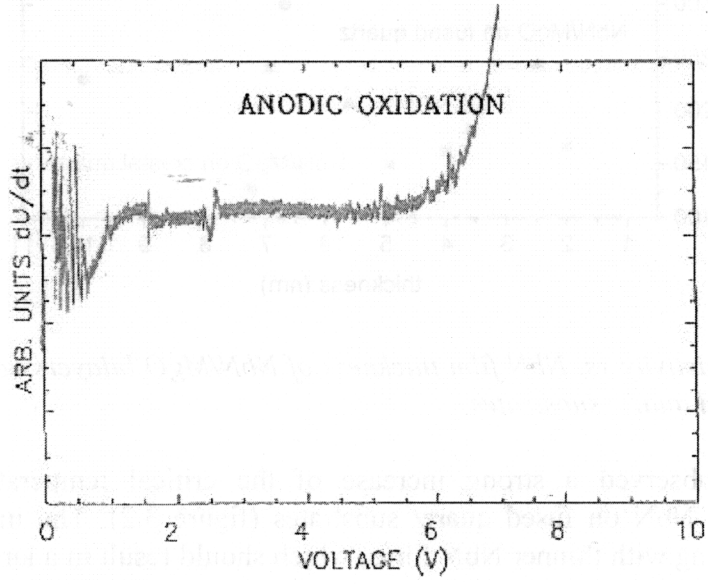

Fig.2.2.: NbN film thickness control by anodization. The plot shows the curve of a ~5 nm NbN thin film.

III. Superconducting Properties of NbN/MgO bilayers

To examine the superconducting properties of our NbN thin films, samples have been fabricated on quartz substrates. We determined the electrical properties by four point measurements on 1 mm × 10 mm samples which were carried out in a dip-stick setup. The film thicknesses were controlled by anodization. Film resistivity, the critical temperature T_c and their dependence on film thickness were investigated.

The MgO seed layer is substantially increasing the quality of our thin NbN films [3]. The resistivity (shown in figure 3.1) is much lower as compared to NbN films on fused quartz and shows only a weak dependence on the film thickness. This allows easier impedance matching of the HEB to the planar antenna.

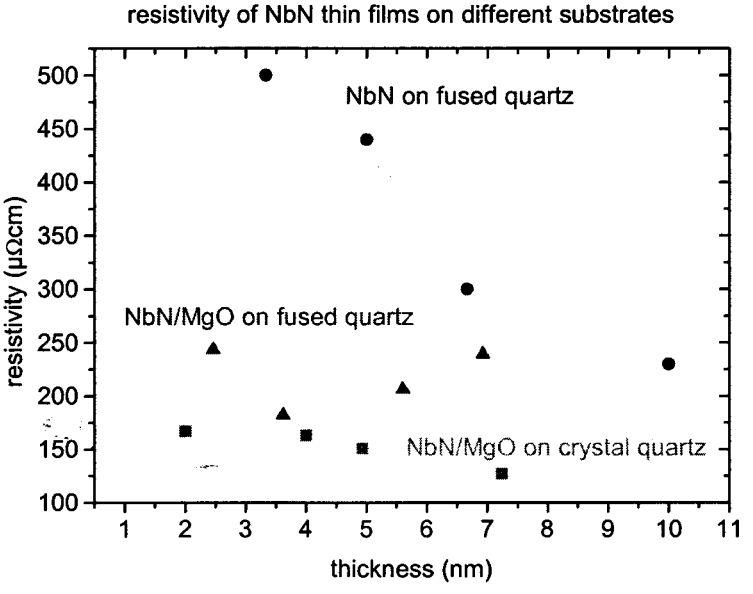

Fig.3.1.: Resistivity vs. NbN film thickness of NbN/MgO bilayers compared to NbN on fused quartz substrates.

We observed a strong increase of the critical temperature T_c as compared to NbN on fused quartz substrates (figure 3.2). The increased T_c allows working with thinner NbN films, which should result in a larger IF-gain bandwidth.

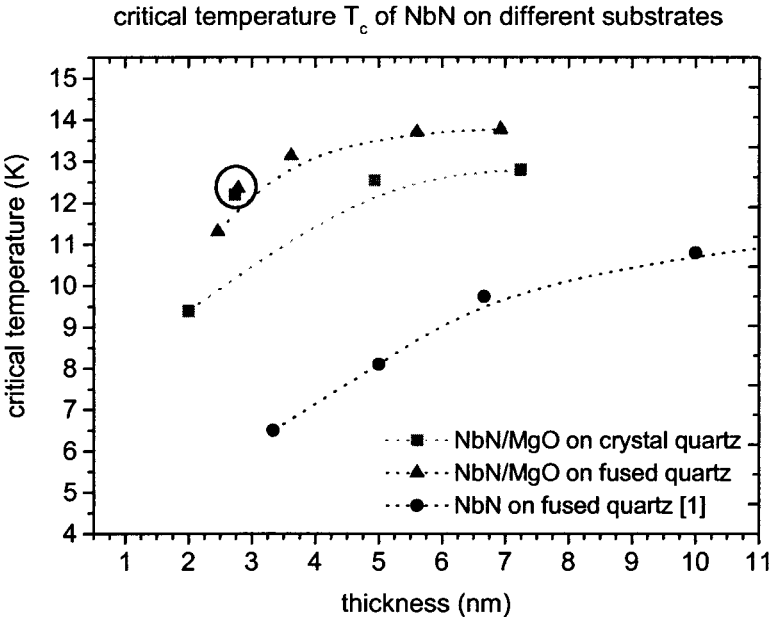

Fig.3.2.: Critical temperature vs. film thickness of NbN/MgO bilayers compared to NbN on fused quartz substrates.

The thickness of the MgO seed layer was 42 nm for the tested films, except for the two encircled points shown in fig.3.2. The latter were measurements on NbN films using a 15 nm thick MgO seed layer, showing that this thickness already provides a better film quality of NbN [5]. The spread in the data is mostly due to the uncertainty of the NbN layer thickness [4].

IV. Device Fabrication

In order to investigate the influence of an MgO seed layer on the properties of a phonon-cooled NbN HEB we first produced devices on fused quartz substrates. The HEBs have been produced with a new process, using a negative resist for the definition of the width of the microbridge by electron beam lithography.

After an overall deposition of a 42 nm MgO seed layer, the NbN film is deposited *in situ*. Antenna and filter structures are defined by photolithography. To define the lateral dimensions of the microbridge we use

Ebeam lithography. In a first step we fix the microbridge length by defining the Au contact pads by a single PMMA layer lift-off process.

In a second Ebeam step we generate a thin resist line using a negative Ebeam resist (Microsresist ma-N 2405) [6,7]. This resist line is used as an etch mask. We remove the surrounding NbN by reactive ion etching (CF_4, O_2). The resist etch mask is removed in aceton. Finally the substrate is diced and the individual devices are characterized by dc-measurements.

V. Characterization of an NbN/MgO HEB on a fused Quartz Substrate

We determined the noise temperature of our NbN/MgO HEB by a Y-factor measurement. The improved film quality (as compared to NbN on fused quartz [2]) increased the critical current of our standard 5 nm NbN thin film and made higher pumping power necessary. With a beam splitter of 60% transmission at 300 K the best receiver noise temperatures were of the order of 670 K (corrected for beamsplitter loss) at 798 GHz and 1 GHz IF.

The IF-gain bandwidth was measured in a heterodyne mixing experiment with two local oscillators (LO), using LO1 to pump the device and LO2 as a signal. The variation of the IF was obtained by changing the frequency of LO2 and observing the output signal with a frequency analyzer. The NbN/MgO HEB showed a -3 dB IF-gain bandwidth of 1.8 GHz, as shown in figure 5.1.

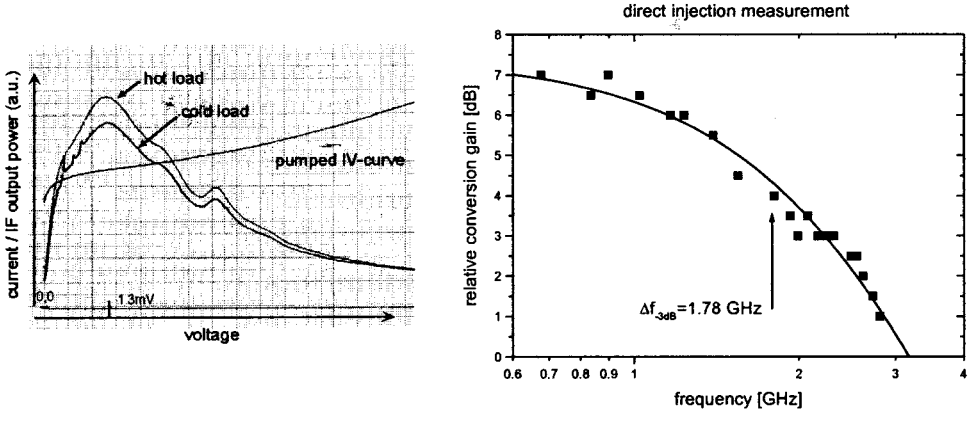

Fig.5.1.: Pumped I(V)-curve and conversion curves of an NbN/MgO HEB; IF bandwidth determined by double local oscillator injection.

VI. Conclusion and Outlook

An MgO seed layer on fused quartz, or crystal quartz substrates, provides a better crystal growth of our NbN thin films, resulting in lower normal state resistivity and higher critical temperature.

High frequency measurements on phonon cooled NbN HEBs fabricated on fused quartz substrates using an MgO seed layer showed a better noise temperature and a higher IF-gain bandwidth than comparable devices on fused quartz [2].

We are currently investigating the influence of the MgO seed layer on the acoustic matching between the bolometer and the substrate.

NbN/MgO HEBs were produced on crystal quartz substrates showing critical currents of about 150 μA and a T_c of 10 K. The high frequency properties of such devices are currently investigated.

Acknowledgement

The authors like to thank V. Fasquelle (LEPMI, INPG Grenoble) for the AFM observations and I. Schuster (DRFMC, CEA Grenoble) for helpful discussions concerning the x-ray measurements.

References

[1] A. V. Sergeev, M. Yu. Reizer, *Photoresponse mechanisms of thin superconducting films and superconducting detectors*, Int. J. of Mod. Phys. B 10 (6), 1996

[2] C. Rösch, *Herstellung und Charakterisierung supraleitender Hot-Electron-Bolometer als Frequenzmischer für Submillimeterwellen*, Ph.D. thesis, IRAM, University of Cologne, January 2000

[3] M. Frommberger, P. Sabon, M. Schicke, F. Mattiocco and K. F. Schuster, *Fabrication and Characterization of Hot-Electron Bolometers for THz Applications*, IEEE Trans. Appl. Supercond., Proceedings of the ASC'2000, Virginia Beach, September 2000

[4] M. Schicke, *Superconducting Mixer Elements for terahertz Frequencies*, Ph.D. thesis, Forschungs-Report, VDE Verlag, 1999

[5] V. Larrey, *Etude et réalisation de jonctions SIS à base de nitrure de niobium et d'une barrière tunnel adaptée permettant la montée aux fréquences THz des instruments hétérodynes*, Ph.D. thesis, CEA, Grenoble, 1998

[6] I. Péron, P. Pasturel and K. F. Schuster, *Fabrication of SIS junctions for space borne submillimeter wave mixers using negative resist e-beam lithography*, IEEE Trans. Appl. Supercond., Proceedings of the ASC'2000, Virginia Beach, September 2000

[7] Microresist technology, Berlin, Germany

Superconducting Nb DHEB Mixer Arrays for Far-Infrared Spectroscopy

E. Gerecht, C. D. Reintsema, and E. N. Grossman

National Institute of Standards and Technology
Boulder, CO 80305

A. L. Betz and R. T. Boreiko

Center for Astrophysics & Space Astronomy, University of Colorado
Boulder, CO 80309

ABSTRACT **-** We are developing a heterodyne focal plane array with up to eight elements to study lines of the interstellar medium and planetary atmospheres with frequencies of 2 THz and above. Our fabrication process utilizes selective ion milling techniques to produce Nb Diffusion-Cooled Hot Electron Bolometeric (DHEB) mixers from a bi-layer thin film of Au/Nb deposited on a silicon substrate. A micro-bridge of 10 nm thick Nb forms the HEB device. The first generation of devices with lateral dimensions of 100 nm by 80 nm were fabricated at the feed of a broadband spiral antenna with a frequency response designed for up to 16 THz. Harmonic multiplier sources becoming available within the next few years should have sufficient power to provide a local-oscillator source for small-format, quasi-optically coupled arrays of these mixers. First generation devices measured at our laboratory have demonstrated a critical temperature (T_c) of 4.8 K with a 0.5 K transition width. These DHEB mixers are expected to have an optimum operational temperature of 1.8-2.0 K. The current four element array mixer block will ultimately be replaced by a dual polarization slot-ring array configuration with up to eight elements.

I. INTRODUCTION

Spectral line observations have played a major role in expanding our understanding of the interstellar medium and planetary atmospheres. Improvements in receiver design have enabled observations at ever shorter submillimeter and far-infrared wavelengths. Improved instrumentation justifies the construction of specialized ground-based observatories for

submillimeter spectroscopy. The complexity and expense of the latest telescopes for both air and space borne platforms designed for astronomical observatories (FIRST, SOFIA, etc.), as well as space-based remote sensing of the Earth's atmosphere (EOS-MLS), demand that spectrometers perform close to the theoretical limits which imply that heterodyne receivers need to have sensitivities close to the quantum noise limit. Heterodyne spectroscopy is capable of providing the required sensitivity and spectral resolution over the entire far-infrared spectral region. The development of low-noise receivers in the THz frequency region is primarily motivated by the need for low noise and low power consumption receivers. Up until recently GaAs Schottky Barrier Diodes (SBD) were used almost exclusively for heterodyne receivers in the THz region. THz SBD mixer technology has recently made a transition from cumbersome whiskered diodes in corner-cube mounts to planar versions in waveguide. Fabrication technology and material parameters limit the size of the monolithic junction and therefore limit the noise temperature performance. Below 1 THz, SIS (Superconductor/Insulator/Superconductor) mixer receivers have excellent noise temperature (only a few times the quantum noise limit). The noise performance is limited to frequencies below or about equal to the superconducting bandgap frequency.

Hot Electron Bolometric (HEB) mixers, which use nonlinear heating effects in superconductors near their transition temperature [1], have become an excellent alternative for applications requiring low noise temperatures at frequencies from 1 THz up to the near IR. There are two types of superconducting HEB devices, the Diffusion-Cooled (DHEB) version [2][3] and the Phonon-Cooled (PHEB) version [4]. The two versions differ mainly by the cooling mechanism of the hot electrons. The devices under development here are DHEBs with a projected Local Oscillator (LO) power requirement of less than 100 nW and bath temperature of less than 2 K. The only practical LO source presently available is an FIR gas laser, although solid state LO sources with sufficient amount of power are under development and will be available in the future. The present state-of-the-art of different THz receivers is compared in FIG. 1.

The Intermediate Frequency (IF) bandwidth for the conversion gain is determined by the thermal time-constant (τ_m) of the DHEB device. The DHEB dissipates the power it absorbs by diffusion of hot electrons through the contacts. This requirements dictates that the dimension of the device be very small in order to maximize the IF gain bandwidth. The receiver noise temperature bandwidth (BW_{NT}) is wider than the conversion gain bandwidth (BW_G). The fact that the receiver noise temperature bandwidth is two to three times wider

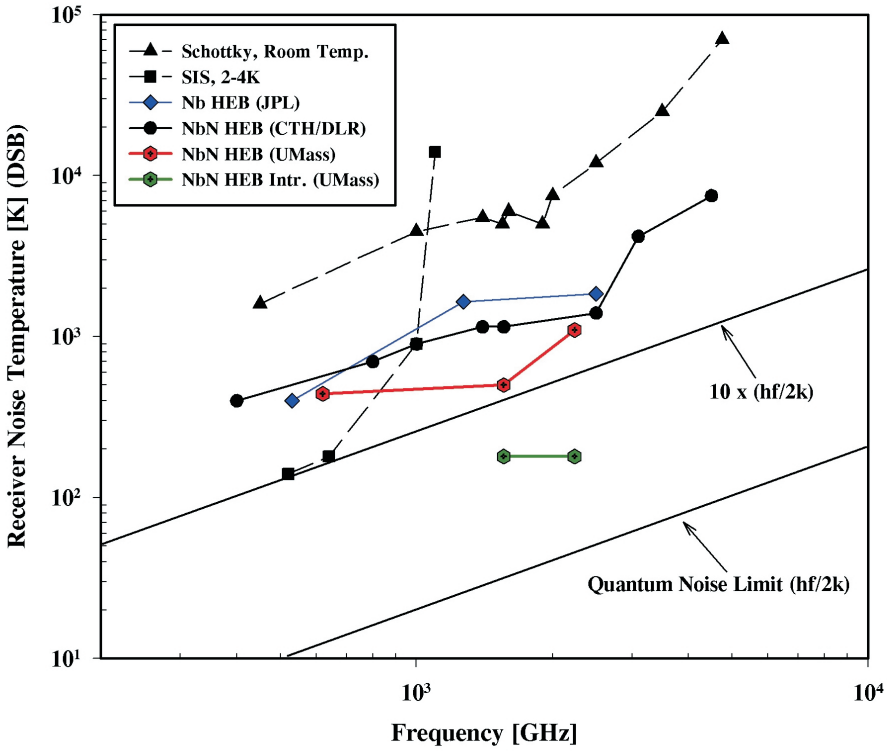

FIG. 1. Noise temperatures vs. frequency for receivers in the terahertz regime.

than the conversion gain bandwidth is a well-known feature of HEB mixers. For these devices, the main noise process in the device (temperature fluctuation noise) yields a noise output which falls at the same rate as the conversion gain, flattening the net receiver noise dependence on the IF frequency.

II. DEVICE DESIGN AND FABRICATION

A quasi-optical coupling design was chosen. The focal plane array is of the "fly-eye" configuration, with individual substrate lenses for each pixel. (Obviously, this configuration is suitable only for relatively small format arrays.) The incoming energy couples to the device through an elliptical lens 4mm in diameter, made from high-purity silicon, and a spiral antenna with a maximum frequency response of 16 THz [5]. The spiral wrap angle is 20 degrees, with a nominal separation of the feedpoints of 1.2 μm. The spiral design is self-complementary, implying an antenna impedance of 75 Ω. The array includes two an-

tennas with 2 1/4 turns and two with 2 3/4 turns, which imply lower frequency limits of 520 GHz and 160 GHz, respectively. (These approximate frequency limits are derived from the criterion that the antenna radius be equal to 1/4 of an effective wavelength. The radius of the inner edge of the antenna is used for the lower frequency limit and the outer edge for the upper frequency limit, with an additional quarter-turn left for engineering margin.) The IF signal is coupled out of the bolometer thru a 50 Ω coplanar waveguide (CPW), the center conductor of which contacts the center conductor of a microminiature K-type connector. The CPW groundplane is common to all four array elements, and directly contacts the body of the mixer block through an indium foil "gasket". The four-element array configured with lenses and spiral antennas is shown in FIG. 2. We are planning to implement a dual polarization design with eight devices in the future.

A typical device fabrication begins with the deposition of a uniform bilayer metallic film across a 75 mm silicon wafer which has been wet oxidized to a thickness of 300 nm. The bilayer is composed of a 12 nm niobium base layer capped by 20 nm of gold. The films are deposited in-situ using DC magnetron sputtering. The HEBs are ultimately formed in the base Nb layer as the last step of the process. The gold cap layer is intended to protect the Nb during initial fabrication steps as well as to mitigate contact resistance problems between the device and overlying metallic layers. Following the bilayer deposition, a 100 nm thick gold layer is deposited through a photoresist liftoff mask patterned using conventional

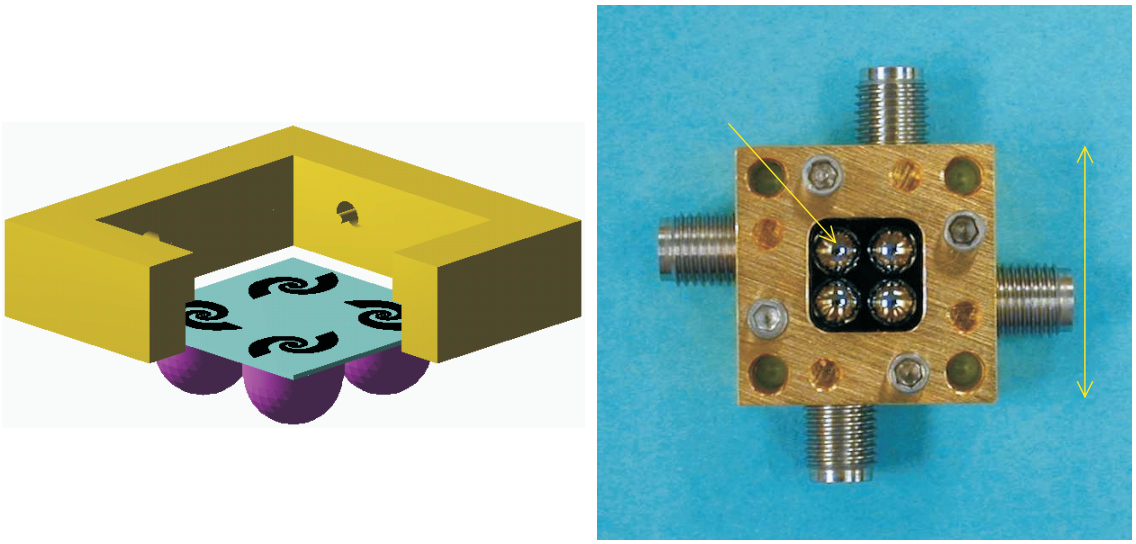

FIG. 2. Array configuration; on the left, a conceptual rendering showing the chip with four elements and substrate lenses nested in the mixer mount, on the right, a photograph of the assembly.

UV lithography. This mask defines the log spiral antennas, ground plane, and the coplanar waveguide (CPW) feed structure to the four array elements. The gold is deposited using thermal evaporation following a 1 minute Ar *rf* plasma cleaning step to treat the contact regions. These steps take us through step (b) in the accompanying FIG.3.

Since optical lithography was used for the antenna deposition, the lead separation at the feed of the antenna remains much too large (~ 2 μm) for useful HEB device dimensions. Therefore, a second contact metallization step, using E-Beam Lithography (EBL), to define the length scale of the devices was performed. Again gold lift-off is used only through

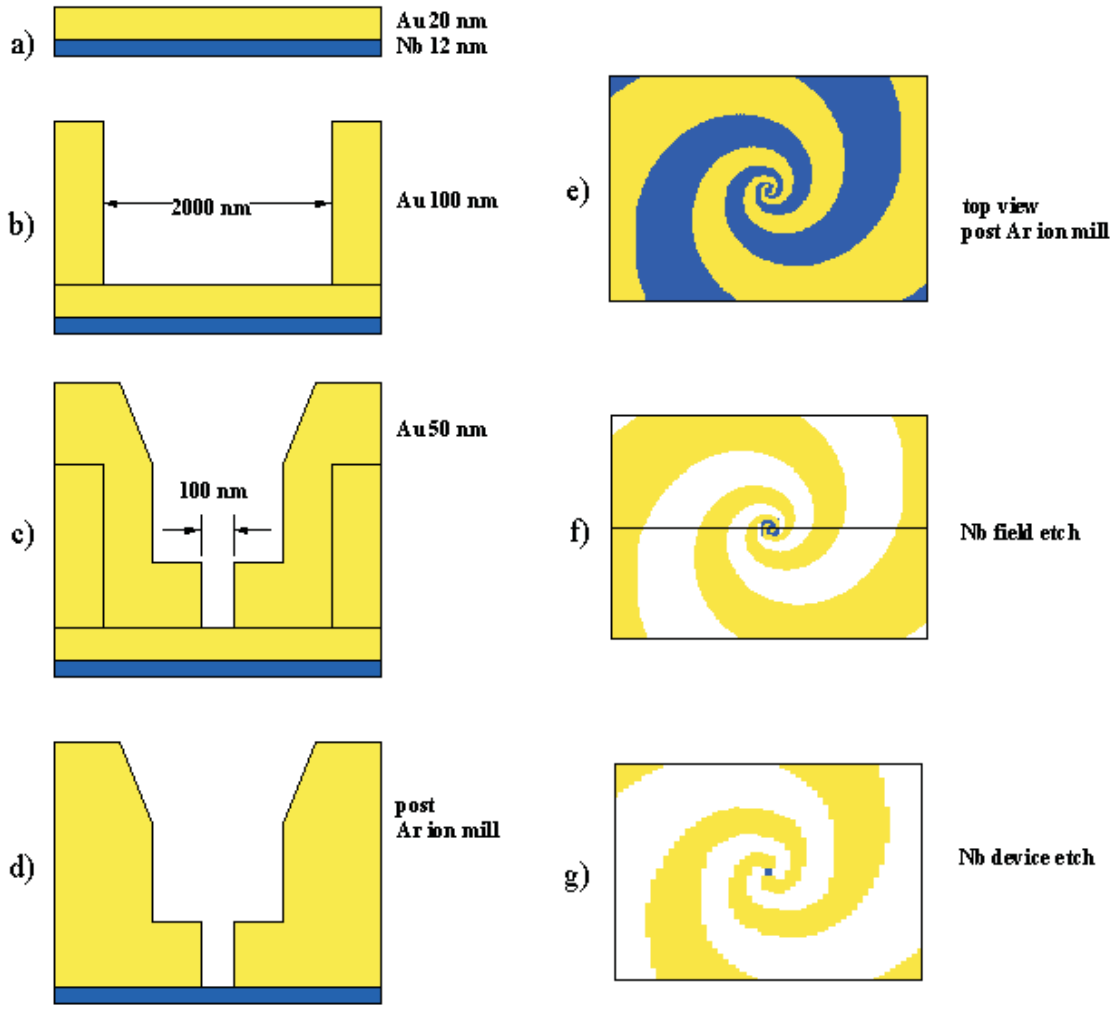

FIG.3. Device fabrication schematic.

an EBL patterned PMMA mask in this case. 50 nm of Au are deposited with an electrode separation of between 80-100 nm at the antenna feed. The deposition process is the same as for the antenna layer.

The last few steps of the process have produced a structure, depicted in FIG.3(c), which includes a complete antenna structure over a blanket Nb/Au bilayer. The 20 nm Au bilayer cap is then removed in an Ar ion mill step using the thick gold as a sacrificial mask. There is no additional patterning associated with this step. 30 nm of the antenna and contact Au are sacrificed to clear the bilayer surface gold from the underlying Nb in the open field areas. The ion mill process has reasonable selectivity to Au as compared to Nb (>5:1).

At this point the device has a Nb layer underlying the entire structure as evident in FIG. 3(e). This Nb must be cleared everywhere except for the final device region. This is accomplished in a two step Reactive Ion Etch (RIE) process. The first step uses optical lithography to pattern a mask which protects a 6 μm × 6 μm square region centered over each device. The chip is then subjected to a SF_6 RIE process to clear the Nb in the exposed field regions (FIG.3(f)). The chip is then patterned one last time using EBL to leave a narrow strip of PMMA bridging the gap between the Au contacts and protecting the final device area. The width of this strip, nominally 80–200 nm, defines the final width of the HEB. There is a 10 μm × 10 μm window around this strip which fully encompasses the 6 μm × 6 μm Nb patch which was protected during the first RIE step. The chip then undergoes an identical SF_6 RIE step to remove the last of the Nb. The resulting final dimensions of a typical HEB are 100 nm length × 100 nm width × 12 nm thickness (FIG.3(g)).

Following device fabrication an elliptical Si lens is affixed to the backside of the substrate. The lens is positioned within a well etched into the backside of the substrate. The well position is registered to within ±5 μm of the device using an infrared backside contact aligner. This well is etched early in the process before device fabrication. The lens is affixed using a low melting point wax.

III. OPTICAL LAYOUT

An apparatus for characterizing the devices and measuring noise temperature has been constructed and is illustrated in FIG. 4. The mixer block is attached to an OFHC Cu pedestal on the cooled plate of a dewar. The base temperature is below 2 K, which is needed for Nb DHEB operation. The THz radiation enters the dewar through a quartz window and a

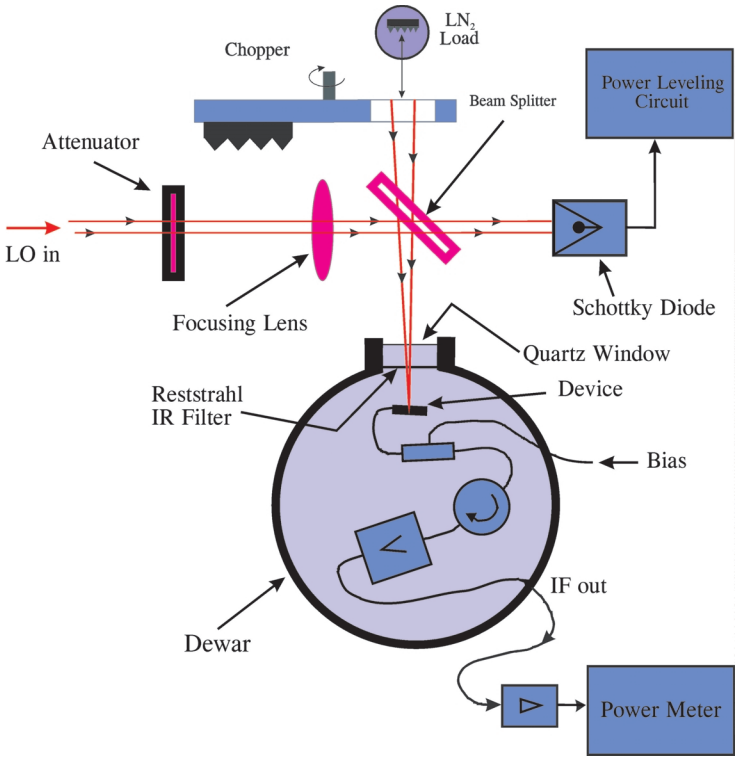

FIG. 4. Measurement setup for noise temperature.

reststrahl filter designed to block radiation above about 6 THz. The mixer is connected through a bias tee and a semi-rigid coaxial cable to a commercial cooled HEMT IF amplifier (L band) with a noise temperature about 5 K.

The local oscillator signal is produced by an optically-pumped far-infrared laser. The laser is 1 m long and operates on most FIR laser lines between 30-300 μm. The polarization of the linearly polarized EH_{11} output mode can be rotated or converted to circular (if desired) by a polarization diplexer. The FIR laser and its CO_2 pump source run sealed off, but can be refilled with gas of any isotopic composition. Initially, tests of HEB mixers are being done with the $^{15}NH_3$ line at 153 μm. The output power of the free-running FIR laser is stable to better than 1% over a period of several minutes, but is normally actively stabilized to better than 0.01 % long term by a closed-loop leveling circuit. FIG. 4 shows the GaAs Schottky diode sensor used for power control. An error signal generated from the difference between the diode output and a reference voltage is used to control the CO_2 pump laser frequency, and hence the FIR laser output power.

IV. RESULTS

We have successfully fabricated several devices using the method described in this paper. The extreme restriction on the dimensions of the device required for maximizing the IF gain bandwidth (and minimizing LO power requirements) were achieved in all cases,

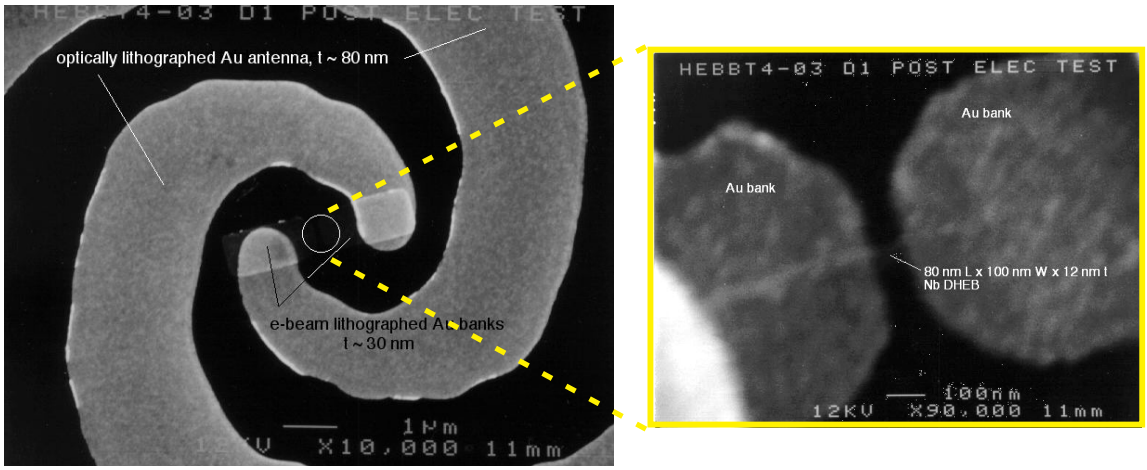

(a)

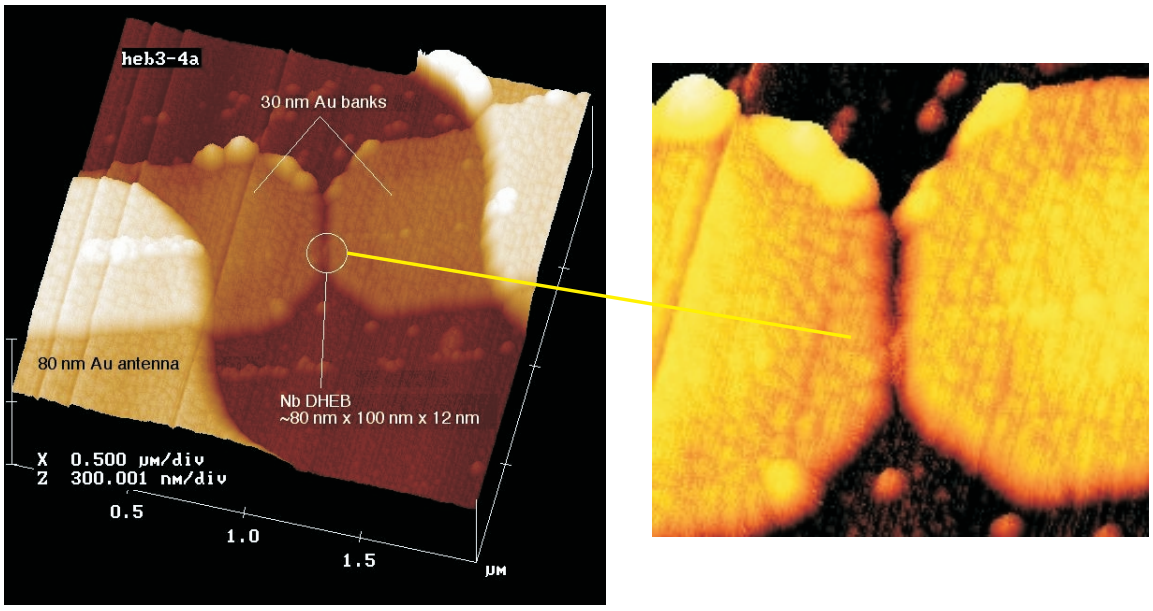

(b)

FIG.5. (a) SEM pictures of the DHEB, (b) AFM pictures of the DHEB.

i.e. device lengths less than 100 nm. The thickness of the Nb in all cases was 12 nm. The critical temperatures exhibited by the devices was 4.8 K with a transition width in the range of 0.5 K. FIG.5(a) shows SEM images of the devices including the spiral antenna, whereas FIG. 5(b) shows AFM images of the microbolometer at the antenna feeds.

ACKNOWLEDGMENTS

This work is supported by the NASA Explorer/SOFIA Technology Development Program under Grant NAG5-8538.

REFERENCES

1. E. M. Gershenzon, G. N. Gol'tsman, I. G. Gogidze, Y. P. Gousev, A. I. Elant'ev, B. S. Karasik, and A.D. Semenov, "Millimeter and Submillimeter Range Mixer Based on Electronic Heating of Superconducting Films in the Resistive State", *Soviet Physics: Superconductivity*, **3**, 1582, 1990.

2. D.E. Prober, "Superconducting Terahertz Mixer Using a Transition-Edge Microbolometer," *Appl.Phys.Lett.*, 62, 2119, 1993.

3. R.Wyss, B.Karasik, W.R. McGrath, B. Bumble, and H. LeDuc, "Noise and Bandwidth Measurements of Diffusion-Cooled Nb HEB Mixers at Frequencies Above the Superconductive Energy Gap," *Proc. Tenth Intern. Space THz Technol.* Symp., U.Virginia, March 1999, p. 214.

4. E. Gerecht, C.F. Musante, Y. Zhuang, M. Ji, K.S. Yngvesson, T. Goyette, J. Waldman, "Development of Focal Plane Arrays Utilizing NbN Hot Electron Bolometric Mixers for the THz Regime," *Proc. Eleventh Intern. Space THz Technol.* Symp., U.Michigan, May 2000.

5. E. N. Grossman, J. E. Sauvageau, D. G. McDonald, "Lithographic Spiral Antennas at Short Wavelengths," *Appl. Phys. Lett.*, v. 59, p.3225, 1991.

VECTOR MEASUREMENTS UP TO THE THz and BEYOND, AT SEVERAL FREQUENCIES AT THE SAME TIME

P. Goy, S. Caroopen, M. Gross,
AB MILLIMETRE,
52 rue Lhomond, 75005 Paris, France,
tel: 33 1 47 07 71 00, fax: 33 1 47 07 70 71,
Email: abmillimetre@wanadoo.fr
Web: www.abmillimetre.com

Abstract.

The Vector Network Analyzer developed by AB MILLIMETRE since 1989 permits vector measurements in the frequency range from 8 to 1000 GHz (with a single pair of extensions) and beyond (with mutiplication chains). It is used in electrical engineering field, like in antenna measurements, and also in the domain of research in Physics, like in the magnetic resonances at high magnetic field. In this last case, working at several frequencies simultaneously saves a lot of time. In the case of antenna measurements, such possibility could also demonstrate the phase center frequency dependence without needing extremely accurate mechanical positioning.

I. Single Schottky Multipliers.

At the beginning of this new century, a large variety of research work is exploring the possibility of new sources at the THz range. See the sessions "Sources" (1). However, the most common, and traditional, way for obtaining coherent millimeter-submillimeter waves from solid-state electronics devices above 200 GHz is the use of Gunn oscillators feeding Schottky multipliers. See the sessions "Multiplication" (2). Such multipliers can be made from a single Schottky. In this case the non-linear effects generate a comb of harmonics Ma at frequencies Fmm from a Gunn A at frequency Fa:

$$Fmm = Ma \times Fa$$

where the integer Ma can take values large enough so that Fmm is above the cutoff of the multiplier's output. With appropriate mechanical tunings, one can optimize the desired harmonic. When making use of high-pass filters, undesired lower harmonics can be suppressed. When associating a widely mechanically tunable Gunn (typically Fa = 95 +/- 15 GHz), there is an overlapping of successive harmonics, so that one has the availability of a continuous frequency coverage source (we call it ESA-1-FC). Naturally, the emitted power decreases with frequency, being of the order of 1 mW ca 200-300 GHz, 0.1 mW ca 400-500 GHz, and decreasing then typically by 10.7 dB per 100 GHz (being typically 1 uW at 700 GHz, 0.6 nW at 1 THz).

II. Simultaneous scalar detection of several harmonics from the same source (multi-harmonic multiplier, or multiplication chain).

In August 2000, in order to make easier the developments and adjustments of the multi-harmonic multipliers that we needed for our "Full Coverage" submillimeter source described above (Gunn at Fa feeding a single-Schottky multiplier), we have created a new instrument called SIMUHADE (SImultaneous MUlti-Harmonic DEtector). In the SIMUHADE, a centimeter source at frequency F1 (between 8 and 18 GHz) is PLL-controlled so that its harmonic k is maintained at 10 MHz from the millimeter frequency Fa. This centimeter source is, through a flexible coax cable, the Local Oscillator LO of a sensitive tunable Harmonic Mixer HM which detects the microwaves at the multiplier output.

Visualization of the harmonics generated by the Multiplier is made easy using a 0-100 MHz scale spectrum analyzer. Each harmonic Ma appears at the frequency Ma x 10 MHz. See for instance Fig.1 the harmonics M=3-4-5 at 309-412-515 GHz, created from a Gunn at 103 GHz, and Fig.2, the harmonics M=5-6-7 at 480-576-672 GHz, from a Gunn at 96 GHz. The effects of possible adjustments on the mutiplier (bias on the Schottky, mechanical tunings) are immediately visible on the spectrum analyzer. With the smallest bandwidth compatible with a fast scan (ca 10 kHz), and with the conversion loss in the harmonic mixer HM (from 46 dB at 250 GHz, to 80 dB at 1 THz) the smallest detectable powers vary from -70 dBm at 250 GHz, to -40 dBm at 1 THz (3). Notice that the SIMUHADE can also be used when testing cascaded multiplication chains. In this case, one can observe the desired harmonic with a sensitivity better than that of a calorimeter, and also sometimes unexpected spurious signals, like M=5 after a sextupler made of a tripler cascaded by a doubler.

III. Simultaneous vector detection of two harmonics from the same source (multi-harmonic multiplier).

For the vector measurements in the range 250-1000 GHz, we associate to the Full Coverage source ESA-1-FC (a multi-harmonic multiplier) described in I., a similar single Schottky device, called ESA-2-FC (a multi-harmonic harmonic mixer), having as LO a Gunn B at the frequency Fb (Fb ≈ Fa). Both Gunns, A & B, are referenced, with PLL controls of different offsets, to the same centimeter LO inside the Vector Network Analyzer MVNA-8-350. The Gunn frequencies are maintained at a small fixed frequency difference:

Fa - Fb = f

the phase noise between them is eliminated, and the oscillator giving f can also give the phase reference to the Vector Receiver VR of the Vector Network Analyzer (4). After harmonic mixing detection, the comb of successive harmonics Ma x Fa (submillimeter waves) gives a comb Ma x f (radiofrequencies below 100 MHz) at the ESA-2-FC output. We operate the vector detection simultaneously at two frequencies when using the two channels of the Vector Receiver tuned respectively at Ma x f (on Channel 1, called "major" harmonic), and at (Ma'=Ma-1) x f (on Channel 2, called "minor" harmonic). At Gunn B, the corresponding harmonic mixing ranks are the same: Mb=Ma, and Mb'=Ma'=Ma-1. This dual-frequency capability has been intensively used in the domain of spectroscopy at high magnetic fields (5). It has also been used, for instance, in the search of resonances in whispering gallery resonators, see Fig.3.

IV. Comparison of Full-Coverage (single-Schottky), or dedicated (several Schottkys), multiplier sources.

Notice that the noise floor Pn of the MVNA-8-350 is very low, of the order of Pn=-155 dBm, due to a small equivalent detection bandwidth. If the ESA-1-FC emitted power is Pmm, and if the ESA-2-FC detector conversion loss is L, the dynamic range S/N will be given by:

S/N (dB) = Pmm (dBm) - L (dB) - Pn (dBm)

With the pair of extensions ESA-1-FC/ESA-2-FC associated to the MVNA, the observed S/N varies from ca 130 dB at 300 GHz, to ca 30 dB at 1000 GHz (see Fig.4, branch a, slope -14.3 dB/100 GHz). The corresponding conversion loss L of the harmonic mixer ESA-2-FC is typically 48 dB at 700 GHz, and its frequency dependence gives a slope of 3.6 dB/100 GHz. Let us remark that this loss L evolution with frequency, on the ESA-2-FC detection side, is three times slower than the power decrease on the ESA-1-FC source side (-10.7 dB/100 GHz as seen in section I.). For experiments beyond 1 THz, the single-Schottky ESA-2-FC extension could still be used for detection, if the single Schottky multiplier source ESA-1-FC is replaced by dedicated multiplication chains (optimized to generate a single harmonic). With such state-of-the-art chains, the available microwaves can be 20 uW ca 1THz, 1 uW ca 1.7 THz (6). By extrapolating the linear evolution of the loss L of ESA-2-FC observed from 300 to 1000 GHz, one predicts a dynamic range which permits experiments up to 1.8 THz, see Fig.4, branch b.

V. Simultaneous vector detection of two freq uencies from different sources (two multiplication chains).

The dynamic range shown in Fig.4 is a clear indication that dedicated multiplication chains give more comfortable signals above 600 GHz, and are quite necessary above 1 THz. However, contrary to the single-Schottky multipliers, multiplication chains are built for delivering a single frequency. The dual-frequency experiments remain possible with two separate multiplication chains, detected by the previous ESA-2-FC harmonic mixer, which is a single Schottky device, and can detect simultaneously two harmonic mixing ranks Mb and Mb'. These ranks will be, most of the time, successive integers:

$$Mb' = Mb - 1$$

Mb and Mb' can be prime numbers. On the contrary, the multiplication ranks Ma and Ma' cannot be prime numbers, since the multiplication chains combine cascaded doublers and triplers. Possible Ma and Ma' values are: 4, 6, 8, 9, 12, 16, 18, 24... Fig.5 gives the schematic diagram of the two multiplication chains (Gunn A, and Gunn A') detected by the single-Schottky Harmonic Mixer ESA-2-FC (Gunn B). Each Gunn is PLL-controlled so that its frequency is related to the frequency F1 of the 7.4-18.6 GHz centimeter source inside the MVNA, with a harmonic rank K and an offset Fo. For Gunns A, A', B:

$$Fa = Ka\ F1 - Foa$$
$$Fa' = Ka'\ F1 - Foa'$$
$$Fb = Kb\ F1 - Fob$$

The harmonic mixing ranks at detection are Mb for the frequency Fmm coming from the Gunn A after multiplication by Ma, and Mb' for Fmm' coming from Gunn A' multiplied by Ma'. The intermediate frequencies Fvr and Fvr', appearing together at the ESA-2-FC output, obey similar equations. For instance:

$$Fvr = (Ma\ Ka - Mb\ Kb)\ F1 + Mb\ Fob - Ma\ Foa$$

where F1 can be eliminated if:

$$Ma\ Ka = Mb\ Kb$$

and, similarly:

$$Ma'\ Ka' = Mb'\ Kb$$

Practically, one chooses a fixed frequency for Fob (37.5 MHz), the Channel 1 receiver frequency is at Fvr=59.0105 MHz, and the Channel 2 receiver frequency at Fvr'=34.0105 MHz, the offsets Foa and Foa' being generated by synthesizers at frequencies:

$$Foa = (Mb / Ma)\ Fob - Fvr / Ma$$
$$Foa' = (Mb' / Ma')\ Fob - Fvr' / Ma'$$

Preliminary experiments have demonstrated a good behaviour, for several cases (see Table 1), with a crosstalk (detection of Fmm in Channel 2, detection of Fmm' in Channel 1) below -80 dB.

References.

1-2. 8th International Conference on Terahertz Electronics, 28th-29th September 2000, Darmstadt, Germany, sessions: Sources I-II-III, Multiplication I.
3. SIMUHADE, User's Manual, AB MILLIMETRE, 16 Aug 2000.
4. French Patent CNRS-ENS September 1st 1989, extended by AB Millimetre to Europe and to the USA: European Pat. EP 0 420 767 April 3rd 1991, US Patent P. Goy, M. Gross, N° 5 119 035, June 2nd 1992.
5. K. Katsumata, H. Yamaguchi, M. Hagiwara, M. Tokunaga, H-J. Mieska, P. Goy, M. Gross, "Single-ion magnon bound states in antiferromagnet with strong uniaxial anisotropy", *Phys. Rev. B **61**, pp.11632-11636 (2000).* P. Goy, S. Caroopen, M. Gross, K. Katsumata, H. Yamaguchi, M. Hagiwara, H. Yamazaki, "Dual-frequency vector detection in the 8-800 GHz interval. Application to spectroscopy at high magnetic field", 23rd Internat. Conference on Infrared and Millimeter Waves, Colchester, University of Essex, UK, 7-11 September 1998.
6. T. Klein, C. Kaseman, MPI für Radioastronomie Bonn, Germany, private communication.

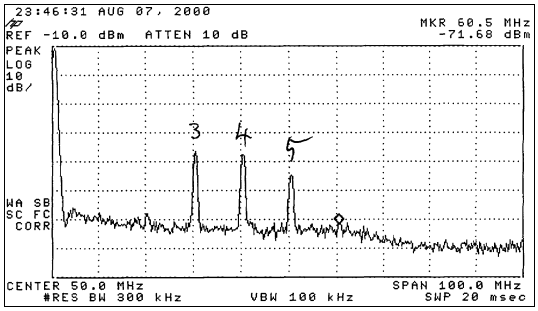

Fig.1.
Vertically : 10dB/div. Horizontally : 10 MHz/div, Span 0-100 MHz. Signal detected by the SIMUHADE with a Gunn at 103 GHz feeding a single-Schottky multi-harmonic multiplier with a F>285 GHz high-pass filter at its output. The successive harmonics M=3-4-5, observed at 30-40-50 MHz, correspond to the microwaves at 309-412-515 GHz.

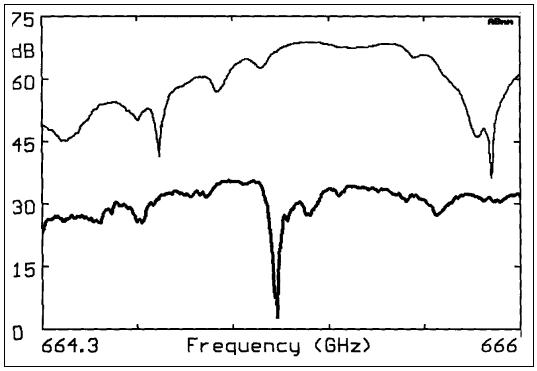

Fig.3.
Search for whispering gallery mode resonances in a quartz disc, 18mm diameter, thickness 1mm. The frequency sweep is operated from 664.3 GHz to 666 GHz on the harmonic M=7 of the multiplier (lower trace, resonance found at 665.1 GHz), and, simultaneously, on the harmonic M=6 of the multiplier, from 569.4 GHz to 570.9 GHz (upper trace, resonances found at 569.8 and 570.8 GHz).

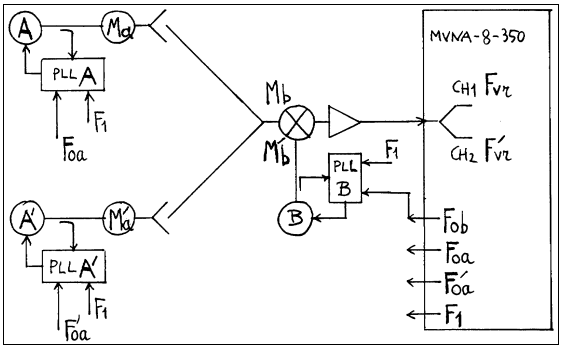

Fig.5.
Experimental setup for dual-frequency detection of two independent multiplication chains.

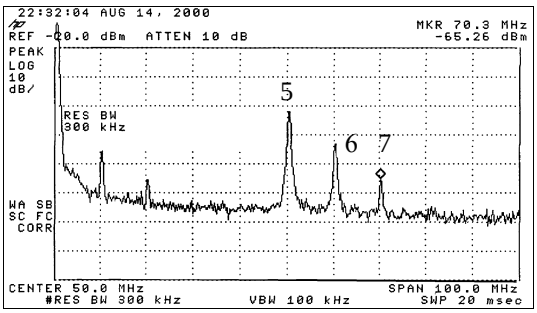

Fig.2.
Same as Fig.1, with a F>475 GHz high-pass filter at the multiplier's output, and a Gunn tuned at 96 GHz. The harmonics M=5-6-7 observed at 50-60-70 MHz, correspond to microwaves at 480-576-676 GHz.

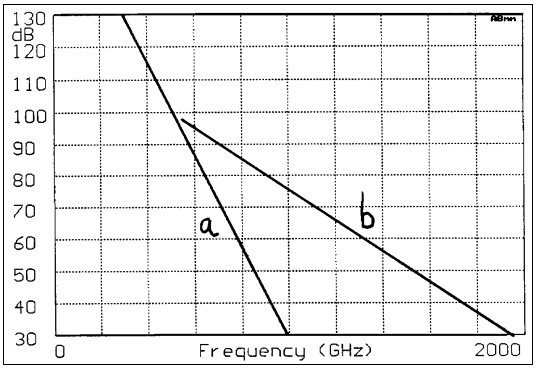

Fig.4.
Dynamic range, MVNA-8-350 with extensions. In a) : observed with a single pair of extensions (source ESA-1-FC, detection ESA-2-FC) covering continuously the interval 250-1000 GHz. In b) : extrapolated from available powers from different multiplication chains, all detected with the single extension ESA-2-FC.

Fmm Fmm' (GHz)	Ma Ma'	Mb Mb'	Fa Fa'	Ka Ka'	Fb	Kb	F1 (GHz)
597 497.5	6 6	6 5	99.5 82.92	6 5	99.5	6	16.58
768 672	8 8	8 7	96 84	8 7	96	8	12
832 936	8 12	8 9	104 78	8 6	104	8	13
1080 990	12 12	12 11	90 82.5	12 11	90	12	7.5

Table 1.
Parameters of the observed pairs of frequencies.

Time-Domain Pulsed THz Near-Field Scanning Microscope with ~ λ/50 Resolution

Oleg Mitrafanov,[*+] Mark Lee,[*] and John Federici[+]
[*]*Bell Laboratories – Lucent Technologies, 600 Mountain Ave., Murray Hill, New Jersey 07922*
[+]*Dept. of Physics, New Jersey Institute of Technology, Newark, New Jersey 07102*

The technique of time gating single-cycle picosecond pulses is known to have several advantages over continuous wave (CW) methods in far-infrared spectroscopy. Because the short pulses have a very broad frequency content typically peaked around 1 THz, a large spectral range can be covered simultaneously with a single source. Also, because measurements are in the time domain, full phase information is maintained when performing a Fourier transform, something generally not done with CW methods. The absorption resonances many chemicals, dielectrics, and organic materials have in the THz frequency range make THz spectroscopy very useful.[1] Unfortunately, with a free-space wavelength of order ~300 μm, diffraction-limited THz spectroscopy lacks the spatial resolution necessary to study the internal structure of electronic devices and biological cells. To do this requires resolution < 10 μm.

We have adapted near-field optical methods to construct a time-domain pulsed THz scanning microscope with spatial resolution well below the diffraction limit. Using an antenna-coupled low-temperature grown GaAs photoconductive switch, we generate single-cycle pulses having a spectrum that peaks near 600 GHz (500 μm) with a ~ 300 GHz half-width. These pulses are broadcast through free-space and detected by a second synchronously time-gated photoconductive switch. The high spatial resolution is achieved by fabricating a sub-wavelength aperture integrated on the chip face opposite the detector switch. The sub-wavelength aperture is a 10 to 50 μm lateral dimension, ~ 1 μm high GaAs protrusion in a surrounding thick Au screen. The aperture is place between 5 to 50 μm from the detector switch by polishing down the GaAs wafer.

Our most recent measurements show that a minimum aperture dimension of 10 μm can produce an acceptable signal-to-noise ratio > 10 dB when placed < 10 μm in front of the detector. Under these conditions, the spatial resolution is set by the aperture size, not by the diffraction limit or by the exact aperture-to-detector distance. Resolution tests performed by scanning across the edge of a patterned Au film on a sapphire substrate showed a resolution of 11 μm based on a 10% to 90% intensity rise criterion. This corresponds to approximately λ/50, using the peak 600 GHz for λ. Scanning across a metal edge, the resolution is polarization dependent, with higher resolution when the polarization is parallel to the edge. The aperture is also observed to act as a high-pass filter for the transmitted pulse, attenuating strongly the frequency content below ~ 300 GHz. Details of the techniques and results will be presented.

---

[1] S. Hunsche, D. M. Mittleman, M. Koch, and M. C. Nuss, IEICE Trans. on Electronics **E81C**, 269 (1998)

DESIGN OF SUBMILLIMETER-WAVE CAMERA WITH SUPERCONDUCTING DIRECT DETECTORS

Seiichirou Ariyoshi[a], Hiroshi Matsuo[b], Masanori Takeda[c] and Takashi Noguchi[c]

[a] *Astronomical Institute, Tohoku University, Sendai, Miyagi 980-8578, Japan*
[b] *National Astronomical Observatory, Mitaka, Tokyo 181-8588, Japan*
[c] *Nobeyama Radio Observatory, Minamimaki, Minamisaku, Nagano 384-1305, Japan*

Abstract

We have designed and are fabricating submillimeter-wave focal plane array based on superconducting direct detectors for Atacama Submillimeter Telescope Experiment (ASTE). Antenna-coupled SIS junctions with low leakage current can be used as sensitive submillimeter-wave detectors. Distributed junction array coupled to log-periodic antenna is designed to realize high quantum efficiency and wide frequency coverage. The observing center frequency using Nb/Al-AlOx/Nb junctions is about 650 GHz (450 μm). The electrical characteristics of the single SIS junction are measured. The achieved leakage current and current noise at 0.5mV-bias is 6.3 pA and 1.8 fA/$\sqrt{\text{Hz}}$, respectively. This measured current noise is consistent with the calculated shot-noise limited one. The expected noise equivalent power (NEP) is an order of 10^{-18} W/$\sqrt{\text{Hz}}$. Bandwidth of the antenna-coupled SIS junctions is calculated to be more than 60 GHz (FWHM)@650 GHz with $J_c = 1$ kA/cm^2.

1 Introduction

The submillimeter-wave region plays an important role in the next generation of radio astronomy as the most suitable probe to realize the search of primordial galaxies and the observational clarification of galaxy formation epoch. It is necessary for astronomical continuum observations to develop a submillimeter-wave camera with wide frequency coverage and wide field of view. Bolometer arrays have been widely used for submillimeter-wave continuum observations. But these systems have many difficulties because of low operating temperature and fabrication of two-dimension arrays. On the other hand, antenna-coupled SIS junctions with low leakage current can be used as sensitive submillimeter-wave detectors and are expected to have capabilities beyond these bolometer systems. Direct photon detection at microwave band was first predicted theoretically by Tucker and Millea (1978) [1], and then proved experimentally by Richards et al. (1979) [2]. They tested a Pb(In,Au) SIS junction which cooled down to 1.4 K, and succeeded in the 36 GHz photon detection. NEP was 2.6 $\pm$ 0.8 x 10^{-16} W/$\sqrt{\text{Hz}}$. They pointed out the need of fabricating SIS junctions with low leakage current for further improvement. Until recently, we have discussed the possibility for realization of superconducting direct detectors (SIS photon detectors) [3] [4].

In this paper, we propose to use SIS photon detectors for future instrument as submillimeter-wave wide field imaging array. We also discuss the design of the antenna-coupled SIS photon detectors and present situations.

2 Atacama Submillimeter Telescope Experiment

The Atacama Submillimeter Telescope Experiment(ASTE) is a Japanese experimental project previous to the Atacama Large Millimeter/Submillimeter Array(ALMA), as the first large submillimeter telescope in the southern hemisphere. The ASTE 10m-diameter telescope will be

Figure 1: ASTE 10m-diameter telescope

equipped with submillimeter-wave focal plane array based on superconducting direct detectors for astronomical continuum observations and SIS mixers (100, 230, 345, 490, 670, 850 GHz) for spectral line observations at Pampa La Bola(4800m altitude), Atacama, Northern Chile. Nobeyama Radio Observatory of Japan manages the ASTE project. Figure 1 shows a picture of the ASTE 10m telescope in Nobeyama Radio Observatory to be installed in Atacama in late 2001. Figure 2 shows the atmospheric transmission at ASTE site [5]. We plan to observe using

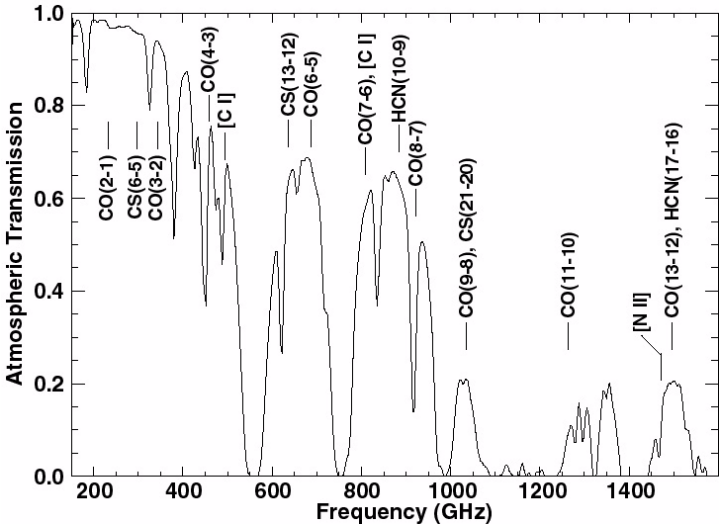

Figure 2: Measured atmospheric transmission spectrum at ASTE site

the atmospheric windows at 650 GHz and 350 GHz using niobium and tantalum based SIS junctions, respectively.

3 The submillimeter-wave camera

The submillimeter-wave camera for the ASTE project requires low noise superconducting direct detectors for continuum observations. The superconducting direct detectors have two kinds of operating principles. One is called 'photon detection', when an incident photon energy($h\nu$) is larger than the gap energy(2Δ) of Cooper-pair. In this case, Cooper-pair can be broken directly by a photon. This principle is often used as the photon-counting UV and optical detectors. The other is called 'video detection', when $h\nu$ is less than 2Δ, then SIS junction need to be connected to an antenna, and an incident photon can be detected by the principle of 'photon-assisted-tunneling(PAT)'. Niobium SIS junctions have 2Δ of about 3 meV which correspond to the radiation frequency of about 700 GHz. As shown in Figure 2, because the observable center frequency is about 650 GHz, we adopt the latter case. It is necessary to apply the bias voltage of 0.5 mV at both sides of a SIS junction.
Distributed junctions coupled to a log-periodic antenna are designed to realize high quantum efficiency and wide frequency coverage. First, the electrical characteristics of niobium SIS junctions are measured. Second, we estimate the input coupling efficiency of SIS distributed junction array with a log-periodic antenna.

3.1 Electrical characteristics of the SIS junction

Before we show our measurement of the leakage current and current noise of the single SIS junction, we estimate the parameters of detector performance. Johnson noise (N_j) and the shot noise (N_s) associated with the leakage current is expressed as follows.

$$N_j = \sqrt{\frac{4k_BT}{R}} \quad \mathrm{A}/\sqrt{\mathrm{Hz}} \tag{1}$$

$$N_s = \sqrt{2eI_0} \quad \mathrm{A}/\sqrt{\mathrm{Hz}} \tag{2}$$

T, R, I_0, e and k_B indicate temperature, resistance, leakage current of the SIS device, electron charge and Boltzmann's constant, respectively.
According to Tucker's theory[6], the current responsivity(S_ν) using as 'video detection' is expressed by

$$S_\nu = \eta \cdot \frac{e}{h\nu} \quad A/W. \tag{3}$$

η and h indicate the quantum efficiency and Planck's constant.
When $N_j \ll N_s$, Noise Equivalent Power(NEP) is expressed by

$$\begin{aligned} \mathrm{NEP} &= \frac{N_s}{S_\nu} \\ &= \frac{h\nu}{\eta} \cdot \sqrt{\frac{2I_0}{e}} \quad \mathrm{W}/\sqrt{\mathrm{Hz}} \end{aligned} \tag{4}$$

For example, when I_0 and η are 10 pA and 0.1 respectively, the expected shot-noise limited NEP is an order of 10^{-17} $\mathrm{W}/\sqrt{\mathrm{Hz}}$ @650 GHz. We need to fabricate SIS junctions with low leakage current and high coupling efficiency to input radiation. It is advantageous to use low current density junctions to achieve low leakage current, but this degrade the coupling efficiency. In the following sections, we show that the current density of 0.5-1 $\mathrm{kA/cm^2}$ is a good compromise to achieve low current density and high quantum efficiency at the same time.

3.1.1 I-V characteristic

The critical temperature of niobium is 9.2 K. A single SIS junction is cooled down to 0.3 K in order to reduce the leakage current caused by thermal excitation of Cooper-pair. The read-out circuit in this experiment is composed of a silicon J-FET used as a source follower and trans-impedance amplifier, as shown in Figure 3.

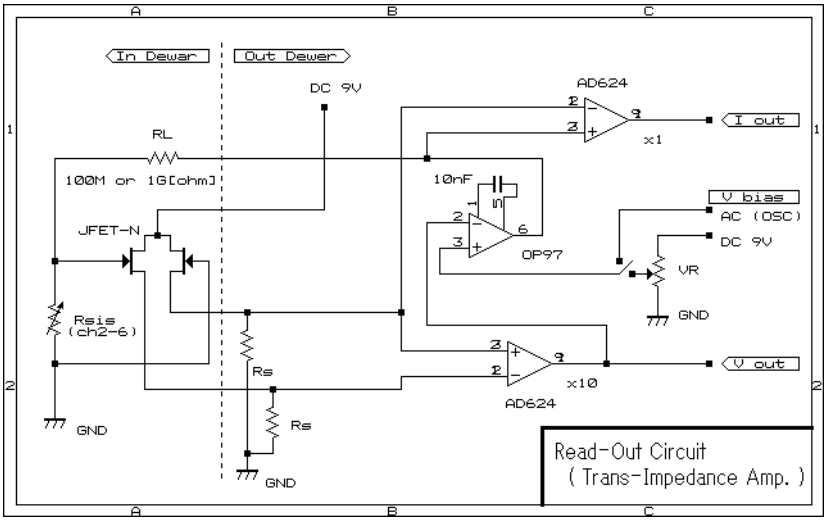

Figure 3: Read-out circuit

We measured the I-V characteristic of a single element niobium junction as shown in Figure 4. The critical current density(J_c) is 0.5 kA/cm^2 and the size is 4×4 μm^2 square. The achieved

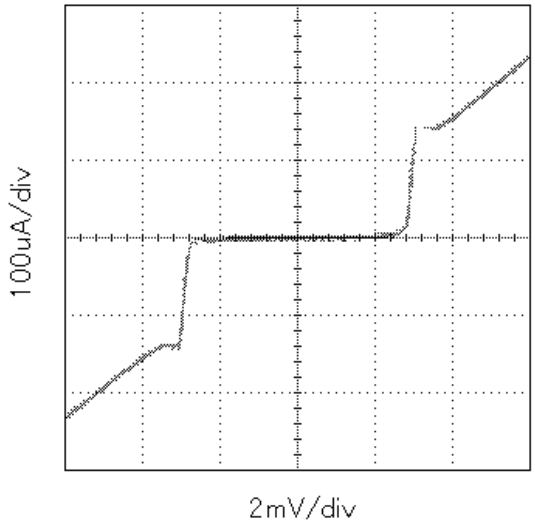

Figure 4: Bias-voltage vs. Leakage-current characteristic

leakage current is 6.3 pA at bias voltage of 0.5 mV, as shown in Figure 5.

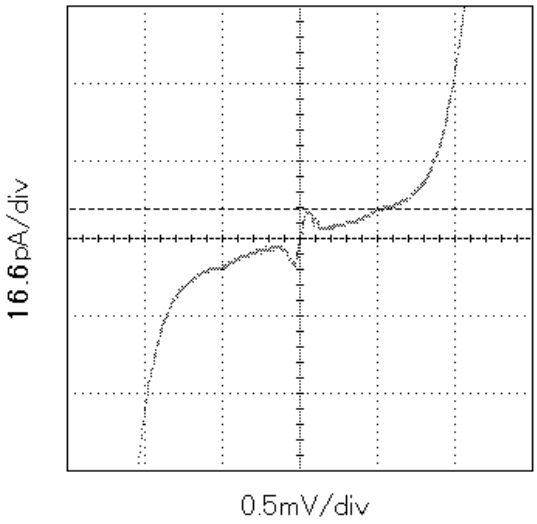

Figure 5: Bias-voltage vs. Leakage-current characteristic (magnified)

3.1.2 I-T characteristic

Figure 6 shows the leakage current as a function of temperature of the single SIS junction. In this figure, the fitted curve indicates temperature dependence of the leakage current associated with thermal excitation of Cooper-pair. We can see that the leakage current at 0.3 K decreases

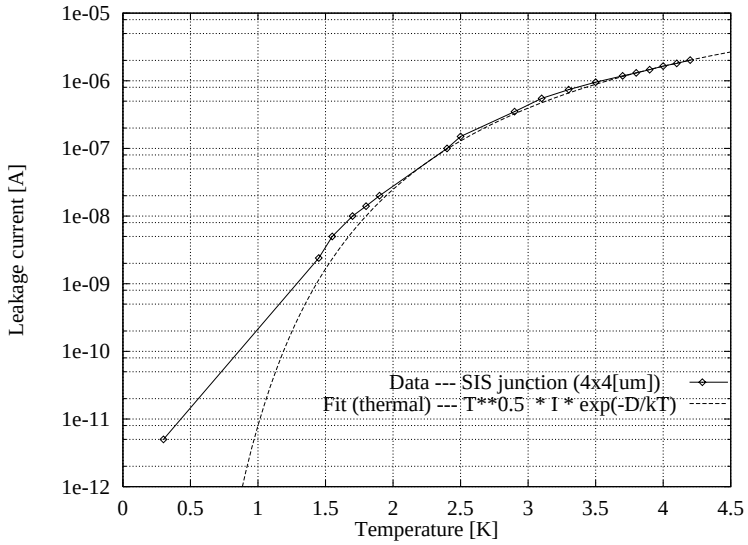

Figure 6: Temperature vs. Leakage-current characteristic

about 6 orders of magnitude as compared to the leakage current at 4.2 K. According to equation (4), when I_0 and η are 6.3 pA and 1, respectively, the expected shot-noise limited NEP is an order of 10^{-18} W/$\sqrt{\text{Hz}}$ @650 GHz. This measurement suggests that the operating temperature of less than 0.9 K is required to achieve NEP of an order of 10^{-18} W/$\sqrt{\text{Hz}}$, although we do not have measured value around 0.9 K.

3.1.3 Noise characteristic

Figure 7 shows the current noise as a function of frequency. The measured current noise is about 1.8 fA/$\sqrt{\text{Hz}}$ at white-noise level. This current noise is consistent with the shot-noise limited value calculated using I_0 at 0.3 K . Using the equation (4), the noise equivalent power (NEP) can be 4×10^{-18} W/$\sqrt{\text{Hz}}$.
Because the 300K atmospheric background limited NEP is an order of 10^{-16} W/$\sqrt{\text{Hz}}$, this detector NEP is sufficient for ground-based observations.

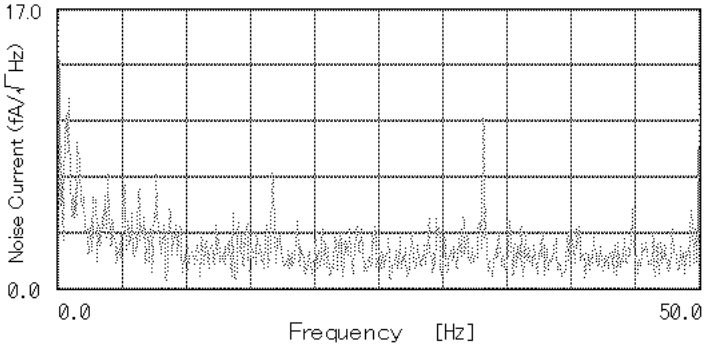

Figure 7: Noise Characteristic

3.2 Design of submillimeter-wave camera

3.2.1 SIS Distributed Junction Array

Using a low critical current density junction, the bandwidth of the detector becomes much narrower compared to the atmospheric window. For instance, when our single SIS junction

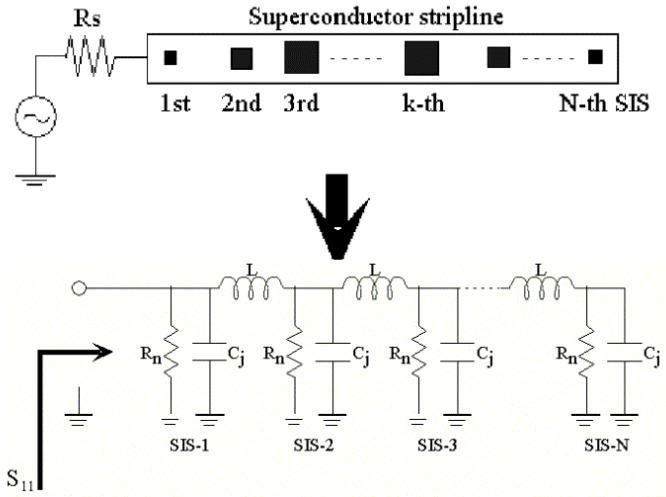

Figure 8: Equivalent circuit of SIS Distributed Junction Array

with $J_c = 1$ kA/cm^2 have the normal state resistance $R_n \simeq 220\ \Omega \cdot \mu$m^2 and the capacitance $C_j \simeq 85$ fF/μm^2, the $\omega R_n C_j$ product is about 75 at 650 GHz, when bandwidth is narrower about one order of magnitude as compared to atmospheric window around 650 GHz. Therefore, We need to fabricate the SIS junction with higher J_c ($\geq$1 kA/cm^2) and smaller size ($\simeq$ a few μm^2). To realize the much wider frequency coverage, we adopt distributed junction array proposed by Shi et al.(1997) [7] and inhomogeneous distributed junction array by Takeda et al.(2000) [8], that each SIS junction connected in parallel through superconducting micro-strip as shown in Figure 8. To optimize its frequency response, we modeled the distributed junctions with the equivalent circuits, and calculate its coupling efficiency. We adopt that the number of junctions is 6, each junction size is 4 μm^2 and J_c is 1 kA/cm^2. Each junction has same size, because we want to suppress DC Josephson current at same magnetic field. The frequency response is tuned by different inductance of each micro-strip line. According to our numerical calculations, the optimized input coupling efficiency is more than 0.5 with a bandwidth of more than 60 GHz where the observing center frequency is 650 GHz as shown in Figure 9. This frequency coverage is comparable to the bandwidth of good atmospheric transmission at 650 GHz.

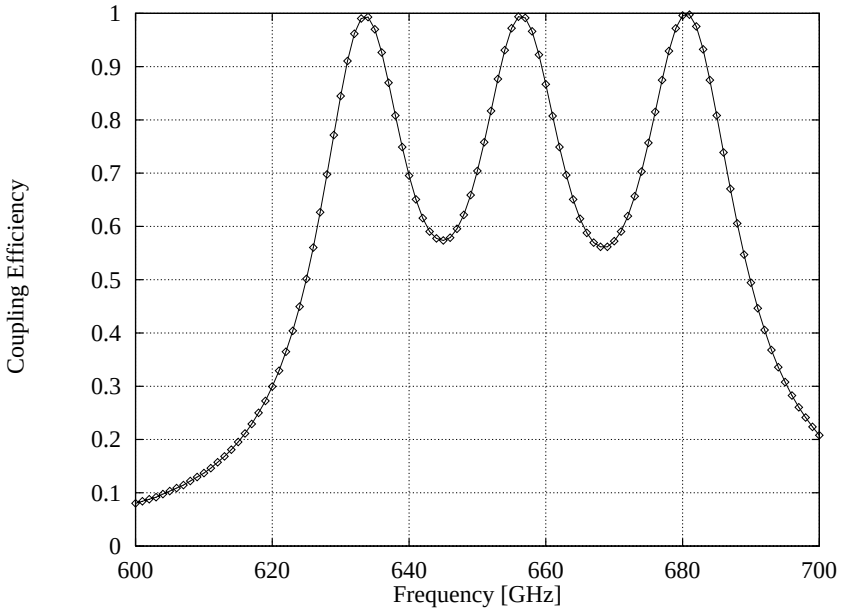

Figure 9: Coupling efficiency of SIS Distributed Junction Array

3.2.2 Superconducting direct detectors

Figure 10 shows the design of superconducting direct detectors based on the simulation in the previous section. Table 1 summarizes the design parameters. It is necessary for wide field and deep imaging observation to realize large two-dimensional imaging array. We adopt the log-periodic planner antenna, which have wide frequency bandwidth and can be fabricated easily in large number of pixels. It is designed to cover the frequency range of 200-1600 GHz and F-ratio of 1 for the compact optics.

The 6 junctions are fed symmetrically at both wings of a log-periodic antenna, which has the diameter of about 420 μm on sapphire substrate. A piece of hyper-hemispherical lense made of Sapphire focuses the input to the log-periodic antenna. The impedances of the log-periodic antenna and SIS distributed junction array are 41.3 and 9.1 Ω respectively, so

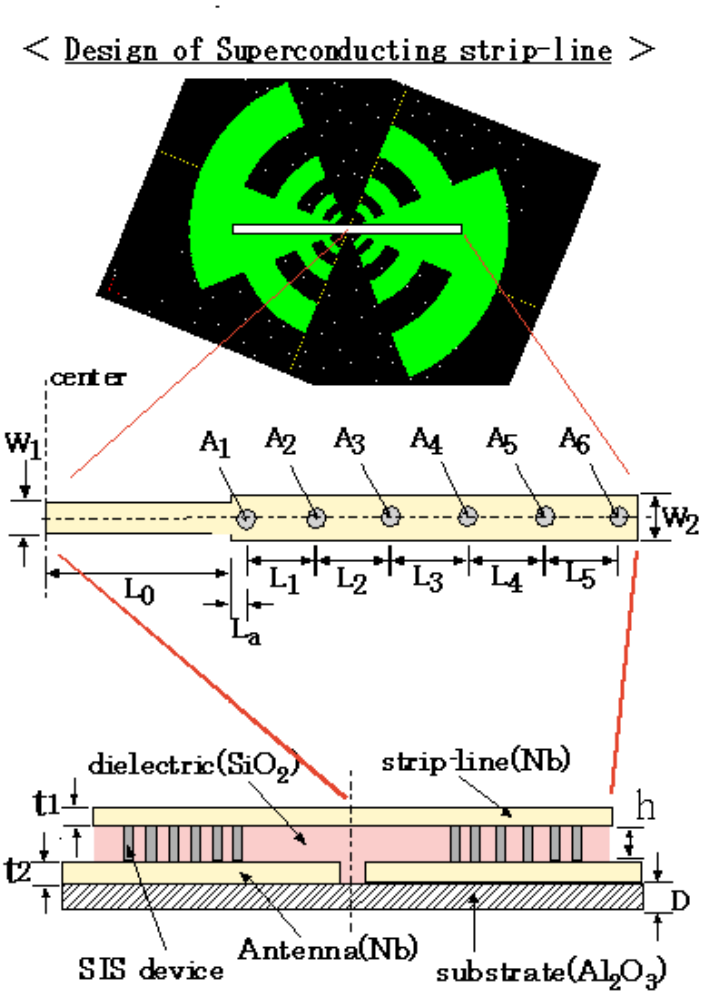

Figure 10: Design of superconducting direct detectors

that these two components are connected by an impedance transformer with a characteristic impedance of $\sqrt{41.3 \times 9.1} = 19.4\ \Omega$ with a quarter wavelength long($= 60.5\ \mu$m). At present, we have prepared the photo-masks in collaboration with RIKEN(The Institute of Physical and Chemical Research, Japan). Figure 11 shows the design of the photo-mask, on five millimeter square silicon wafer.

4 Summary and Future

We have designed and are fabricating submillimeter-wave focal plane array based on superconducting direct detectors for Atacama Submillimeter Telescope Experiment (ASTE). We have designed the antenna-coupled SIS junctions with a relatively low current density ($\simeq 1$ kA/cm^2), low leakage current($\leq$10 pA at 0.5mV-bias voltage) and small size ($\simeq 4\ \mu$m^2). It is estimated that NEP is an order of 10^{-18} W/$\sqrt{\text{Hz}}$ using SIS junctions at less than 0.9 K. We have designed the antenna-coupled Nb junction with 3x3 pixels, and its fabrication and evaluation are underway. We are going to fabricate 10x10 pixels imaging array with superconducting direct detectors for the ASTE telescope in Atacama.

parameter name	parameter		unit
Width of Impedance Transformer	W1	3.0	μm
Width of DJ Array	W2	5.0	μm
Size of SIS junction	A1-A6	4.0	μm^2
Length of Inductance	L0	60.5	μm
	La	3.0	μm
	L1	4.6	μm
	L2	20.0	μm
	L3	4.8	μm
	L4	30.0	μm
	L5	4.6	μm
Thickness of upper strip-line(Nb)	t1	0.2	μm
Thickness of lower antenna(Nb)	t2	0.2	μm
Thickness of dielectric(SiO_2)	h	0.2	μm
Thickness of substrate(Al_2O_3)	D	$\simeq$ 500	μm

Table 1: Design parameters of a superconducting direct detector

Acknowledgments

The ASTE project is managed by Nobeyama Radio Observatory, National Astronomical Observatory of Japan. The low leakage SIS junction presented in this paper is provided by Oxford Instruments. The photo-mask with antenna-coupled SIS junction is made in RIKEN(The Institute of Physical and Chemical Research, Japan). We are gratful to these institutes.

References

[1] Photon detection in nonlinear tunneling devices, J.R. Tucker and M.F. Millea, *Appl. Phys. Lett.*, **33**, pp.611-613(1978).

[2] Superconductor-insulator-superconductor quasiparticle junctions as microwave photon detectors, P.L.Richards, T.M.Shen, R.E. Harris and R.L. Lloyd, *Appl. Phys. Lett.*, **36**, pp.480-482(1979).

[3] Development of Submillimer-wave Camera for Atacama Submillimeter Telescope Experiment, H.Matsuo, M.Takeda, T.Noguchi, S.Ariyoshi, H.Akahori, *Advanced Technology MMW,Radio, and Terahertz Telescopes, Proc.SPIE*, **4015**, pp.228-236(2000).

[4] Development of Submillimer-wave Camera for Atacama Submillimeter Telescope Experiment, H.Matsuo, S.Ariyoshi, H.Akahori, M.Takeda and T.Noguchi, *IEEE Trans. Appl. Supercond.*, in press (2000).

[5] FTS Measurements of Submilimeter-Wave Atmospheric Opacity at Pampa la Bola II : Supra-Terahertz Windows and Model Fitting, S.Matsushita, H.Matsuo, J.R.Pardo and S.J.E.Ranford, *Publ. Astron. Soc. Japan*, **51**, pp.603-610(1999).

[6] Quantum detection at millimeter wavelengths, J.R.Tucker, M.J.Feldman, *Review of modern physics*, **57**, No.4(1985).

[7] Analysis of the bandwidth performance of SIS mixers with Distributed Junction Arrays, S.-C.Shi, T.Noguchi and J.Inatani, *Proc. of Eighth Int. Symp. on Space Terahertz Tech.*, pp.81-90(1997).

[8] Predicted Performance of Superconductor-Insulator- Superconductor Mixers with Inhomogeneous Distributed Junction Arrays, M.Takeda, T.Noguchi and S.-C Shi, *Jpn. J. Appl. Phys.*, **39**, pp.5095-5098(2000).

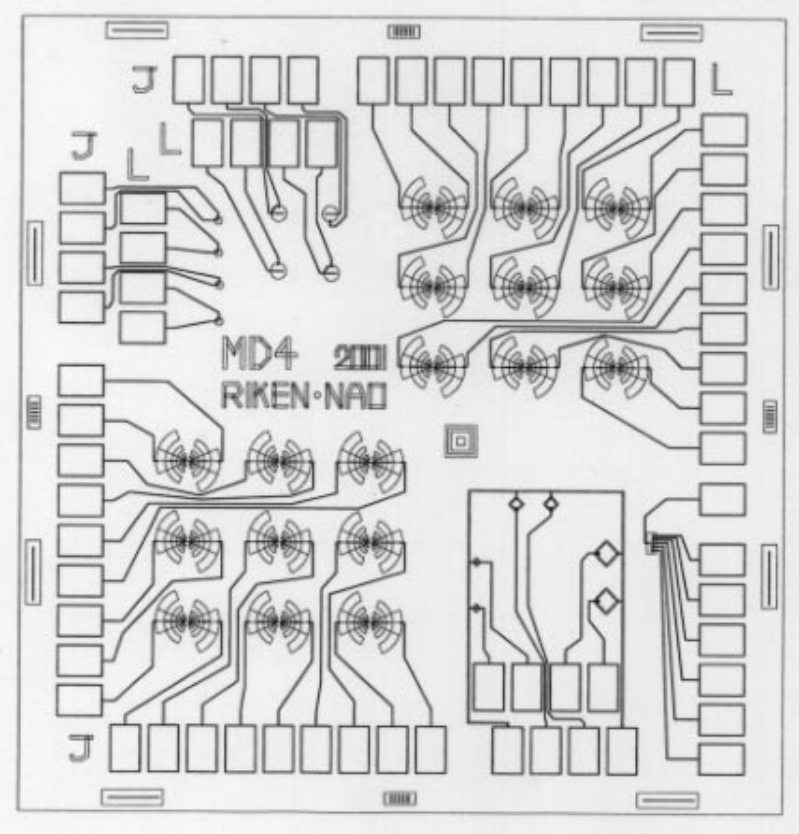

Figure 11: Mask design for 3x3 array

Characterization of an integrated lens antenna at terahertz frequencies

P. Yagoubov, W.-J. Vreeling, P. de Korte

Sensor Research and Technology Division
Space Research Organization Netherlands
Postbus 800, 9700 Groningen, The Netherlands

Abstract

Results of beam pattern and polarization measurements on quasioptical integrated lens antennae at terahertz frequencies are presented. The integrated antenna consists of a planar spiral antenna mounted on the flat surface of an extended hemispherical lens. The planar antenna used is an equiangular logarithmic spiral, which comprises 1.5 turns with a spiral expansion rate of 3.2 per turn. The RF bandwidth of the antenna is designed to 0.3-2.5 THz. We have investigated the optical performance of such an integrated antenna and observed that the polarization is changing from almost circular at frequencies below 1.4 THz to elliptical with an axial ratio equal to 3 at 2.5 THz. The beam patterns have been measured up to 2.5 THz for two orthogonal polarization directions aligned with the elliptical polarization axes. The main lobes are primarily diffraction limited by the aperture of the lens. The first order sidelobe level equals -16 dB at 0.6 THz and increases to –8-12 dB at 1.4 THz and -7-10 dB at 2.5 THz.

Introduction

Properties of the receiver antenna play a very important role in the overall coupling efficiency of the detector to the incoming signal and have to be carefully optimized. In the millimeter wave region the best antenna performance is obtained with the waveguide technology. However for terahertz frequencies the waveguide fabrication becomes difficult and costly, while its losses also increase with frequency. An alternative approach is a quasioptical planar antenna lens combination [1]. It was theoretically shown that the best coupling to the incoming Gaussian beam is obtained when the planar antenna is placed on the backside of the hyperhemispherical lens [2]. However, many research groups developing prototype quasioptical receivers for the submillimeter wavelength prefer to use elliptical lens (EL) instead. This is because the hyperhemispherical lens antenna requires a small f-number lens in front of the

receiver causing additional loss in the signal path. If the planar antenna is placed at the distant focus of the EL, the Gaussian beam coupling efficiency is about 10% worse than in case of the hyperhemispherical lens, but the resulting beam pattern is very narrow since it is diffraction limited by the aperture of the lens. The system is then compatible with large f-number optics. The synthesized elliptical lens (SEL), which is in fact an extended hemispherical lens with an extension equal to 0.39 the lens radius (in case of Si), has been shown to be a good approximation of the EL case [2]. The calculated Gaussicity and reflection loss at the lens-air interface for the SEL and EL are basically the same. The difference is only in the directivity, which is larger with the EL, but the sidelobe level is slightly higher in this case as well.

Different types of planar antennas have been successfully used in combination with extended hemispherical and EL. Because of the diffraction limit, the far-field of the integrated antenna based on EL or SEL is primarily determined by the size of the lens. So the main difference between the beam patterns of various antennae are the side-lobe level and the polarization. It has been demonstrated that double-slot antennas have superior performance in case both low side-lobe level and cross-polarization are required. The first sidelobe level of the twin slot antenna EL combination is measured between –15 to –18 dB at frequencies up to 1 THz [3] and -10 dB at 2.5 THz [4]. Recently the measurements of the beam pattern have been done at 2.5 THz also with the spiral antenna SEL combination [6]. The 1-D pattern is obtained with the symmetric sidelobe level of about –8 dB. However, the pattern was measured only in the E-plane of the source and no results on the polarization were reported.

It is beyond discussion that receivers designed for operation at a telescope must have the best possible coupling efficiency to the single mode Gaussian beam and have low cross-polarization level. Thus the antenna polarization, beampattern profile, sidelobe level, loss etc. play a crucial role in the final receiver performance. However, during the development stage of a specific type of mixer, most of the heterodyne measurements in the laboratory do not require perfect coupling to a Gaussian beam and beam pattern, side lobe and polarization characteristics are only of secondary importance. For instance, to determine the receiver noise temperature, the Y-factor technique with the blackbody loads as signal sources is typically used. Since blackbodies are multi-modal sources all components of the receiver beam pattern, which are not blocked by the aperture of the input window or a beamsplitter, will be fully coupled to the signal. So for mixer development purposes broad frequency antennae, like logarithmic spirals, are frequently used given the advantage of multi-frequency measurements at one and the same mixer.

In this paper we investigate the performance of an integrated antenna system based on the logarithmic spiral antenna and a SEL for frequencies up to 2.5 THz. The device is a NbN Hot Electron Bolometer (HEB), originally designed as a mixer for submillimeter wavelength [5]. Historically a spiral antenna has been chosen as a receiving antenna for the HEB mixer development due to its wide bandwidth. The

spiral antenna belongs to a class of so-called frequency independent antennas, thus allowing one to perform all tests with one selected device in a wide spectral range. This was an important issue because the HEB mixers are aimed to be used at terahertz frequencies and thus have to be finally tested there. At frequencies below 1 THz, however, the mixer evaluation and optimization in the laboratory is appreciably easier, given the availability of stable LO sources, like Backward Wave Oscillators (BWOs) or Gunn-multiplier chains. In addition, some of the measurements, like the intermediate frequency (IF) roll-off determination, can only be done at frequencies below 1 THz, where frequency tunable sources are available. Above 1.5 THz frequency only a CO_2 pumped far-infrared (FIR) laser system is currently an option to deliver sufficient amount of power. This only allows for a limited number of discrete lines and stability is more difficult obtained. Obviously, the results on mixer noise and gain variations at various frequencies give additional information for the further analysis and better understanding of the device physics.

Antenna design

The planar antenna is an equiangular spiral with a 90° arm width yielding a self-complementary design. This implies that the antenna impedance should be purely real and equal to 75 Ohm for the antenna on a Si substrate [7]. The spiral structure of the antennas extends 1.5 turns and the spiral expansion rate is 3.2 per turn. A photo of the final device is shown in the Fig. 1.

The total antenna arm length, calculated from its radii and the expansion rate, is about 300 μm. Setting this equal to a maximum effective wavelength yields a lower cutoff frequency for the antenna of 300 GHz in free space. The higher cutoff frequency of the antenna is defined [8] as the frequency at which the antenna polarization changes from circular to elliptical with an axial ratio of 2. This frequency depends on the construction precision of the antenna feed. Since the spiral arms naturally converge to a point, one has to terminate the center in a tapered section, see Fig. 1. According to [8] the cut-off frequency is set by the length of the tapered section, since it equals about half the cut-off effective wavelength. This length is roughly 20 μm for the spiral used in this paper, setting the upper frequency limit to 2.2 THz. The axial ratio of elliptical polarization increases towards higher frequencies until the polarization becomes linear. This happens when the tapered section is equal to the effective wavelength and the antenna starts to act as a dipole. The impedance and the beam pattern of the antenna are expected to have wider than the polarization bandwidth so that the antenna can still work efficiently although the polarization is not circular.

The bolometer is located between the antenna arms, as shown in the Fig. 1. The chip is placed on the backside of the lens, as shown in Fig. 2. The lens is a SEL with a diameter of 10 mm, made from a high resistivity Si. The extension length (the distance from the geometrical center of the sphere to the antenna) is 1.95 mm. No

antireflection coating is applied yet to the lens curved surface to reduce the reflection loss.

Polarization

The polarization of the antenna has been measured at two frequencies: 1.4 THz and 2.5 THz. The schematic of the setup is shown in the Fig. 3. The 1.4 THz source is a Schottky diode based tripler fed by a 465 GHz carcinotron. For the 2.5 THz we use a CO_2 pumped far infrared (FIR) ring laser. The first grid is used to define the polarization of the source and is fixed. The two other grids are rotated independently during the measurements, each by 180 degrees in steps of 15 degrees. The RF power is modulated with a 35 Hz mechanical chopper. The HEB is biased with a constant voltage source and the current change, due to the incident power modulation, is monitored by a lock-in amplifier. The bolometer is operated in a linear regime, which was checked beforehand by means of polarizing grids as attenuators.

The experimental data were compared to the calculated transmission through the system of three grids and a modeled coupling to the antenna. We assumed a general case of elliptical polarization of the antenna with the axial ratio α. α has been defined as the ratio of amplitudes of the electrical field along the long and short axis of the ellipse. Thus $\alpha=1$ corresponds to the circular polarization of the antenna, whereas $\alpha=\infty$ to the linear one. The second parameter in the calculations is angle φ, which we define as the angle between the line along the tapered section of the antenna and the long axis of the ellipse.

The polarization was found to be elliptical at both frequencies, although closer to the circular at 1.4 THz ($\alpha=1.3$), and strongly elliptical at 2.5 THz, with $\alpha=3$. φ equals about -25 degrees. This means that the long axis of the ellipse is *25* degrees counterclockwise from the direction of the tapered section in the antenna center, as shown in Fig. 1.

The results on the antenna polarization at 2.5 THz disagrees slightly with that reported in [8], where the case of elliptical polarization of the spiral antenna with $\alpha=2$ happens at a frequency where the length of the tapered section is equal to the effective half-wavelength. In our case the length of the tapered portion is about the half-wavelength but the axial ratio is 3 instead of 2. This is an indication that in this case the center part of the antenna has a larger influence on the polarization.

It is useful to compare the results of the polarization measurements with those reported in [9]. The antenna design in [9] is very similar to the one we use here, but all the dimensions of the antenna, including the size of the tapered section, are scaled down by a factor of 3. If we assume that just the size of the tapered section is important, and basing on our result $\alpha=1.5$ at 1.4 THz, we would expect to have $\alpha=1.5$ at 4.2 THz with the 3 times smaller antenna. However, the authors of [8] reported the

larger axial ratio of 1.7 already at 2.5 THz [10]. This is also an indication of the fact that α tends to increase much faster with frequency than one could expect from the antenna geometry alone. We do not have a solid explanation for this yet. One of the thinkable reasons is an increase with frequency of the surface resistance of Au forming the antenna arms. This resistive loss may cause the field to decay faster along the antenna arms and therefore make the influence of the antenna center larger. The size and geometry of the bolometer in the antenna center as well as a possible mismatch between them are obviously also very important and could modify the radiation properties of the antenna.

Beam pattern measurements

Far-field beam pattern measurements have been done at three frequencies: 0.6 THz, 1.4 THz and 2.5 THz in an experimental setup similar to that shown in the Fig. 3. The submillimeter source at 0.6 THz is a BWO. The dewar is placed on a rotation/tilt table to allow for the angular measurements. The tilt movement will be referred to as the vertical scan and the rotation as the horizontal scan. The angle resolution of the system is 0.1°. The integrated antenna is located in the center of rotation. The measured beam pattern of the antenna is therefore expected to be independent of the beam pattern of the signal source. There are no focusing elements between the signal source and the detector and the distance between them is 70-100 cm. By using two grids, the polarization of the incoming signal is set either vertical or horizontal. The antenna is positioned in the dewar in such a way that the direction of the long axis of the polarization ellipse (see Fig. 1) is close to vertical.

Let us start discussion with the 0.6 THz measurements. The beam pattern profiles at this frequency are very similar for both polarizations and scans. A typical result is shown in the Fig. 4. The pattern is symmetric with the first sidelobe level of -16 dB. It is worth noticing that this is close to the theoretically predicted diffraction pattern and similar to the patterns measured with the double slot or double dipole antennas at these frequencies. The full width half maximum (FWHM) is 3.47°.

The results of the measurements at 1.4 THz are shown in the Fig. 5. The patterns are still pretty symmetric relative to the boresight but noticeably different for the horizontal and vertical scans. The FWHM is 1.7° for the horizontal scan and 1.4° for the vertical one. There is no big influence of the polarization on the beamwidth and side-lobe positions within one scan direction but the sidelobe levels are polarization dependent.

Similar patterns are observed at 2.5 THz, see Fig. 6. The FWHM here is about 1° for the horizontal scan and 0.7°-0.9° for the vertical. We have also made a 2-D scan of the antenna pattern at 2.5 THz and the result is shown in the Fig. 7.

To summarize the data, we established that the width of the main lobe scales with the frequency, and is close to the expected diffraction limit of the lens aperture. The

asymmetric beam patterns at high frequencies for the different scans may be attributed to the variation of the planar antenna pattern. A significant change of the shape and the phase of the antenna pattern may also explain the increase of the sidelobe level with frequency. However, there might be other reasons for this as well. For instance, a displacement of the planar antenna has a frequency dependent effect on the beampattern of the integrated antenna.

Conclusions

We have tested the integrated lens antenna, a logarithmic spiral in combination with a SEL, in a wide frequency range from 0.6 THz to 2.5 THz and have found that the polarization is changing from almost circular at relatively low frequencies to elliptical with an axial ratio of 3 at 2.5 THz. The far-field pattern of the antenna has been measured. The sidelobe level increases towards higher frequencies. However, due to the diffraction limit the beam pattern becomes narrower at higher frequencies. The total width of the main lobe and the first sidelobes is about 4 degrees at 2.5 THz. Since most of the power is contained within this angle, we can expect that this antenna couples efficiently with a multimode source and is a good choice for prototype mixers to evaluate in the laboratory.

Acknowledgments

The authors are thankful to A. Baryshev, H. van de Stadt, W. Ganzevles and D. Nguyen for the useful discussions and assistance in the measurements. M Kroug is acknowledged for the fabrication of the device.

References

[1] D.B.Rutledge and M.Muha, "Imaging antenna arrays," IEEE Trans. Antennas Propagat, vol. 30, pp. 535-540, 1982

[2] D.F.Filipovic, S.S.Gearhart, and G.M.Rebeiz, "Double-slot antennas on extended hemispherical and elliptical silicon dielectric lenses," IEEE Trans. Microwave Theory Tech., vol. 41, pp. 1738-1749, 1993

[3] A.M.Baryshev, B.D.Jackson, G.deLange, S.V.Shitov, N.Iosad, J.R.Gao, T.M.Klapwijk, ”Quasi-Optical Terahertz Mixer”, Proceedings of the 11th Int. Symp. on Space Terahertz Technology, The University of Michigan, Ann Arbor MI, 149, 2000

[4] R. Wyss, B. Karasik, W. McGrath, B. Bumble, H. LeDuc, “Noise and Bandwidth Measurements Of Diffusion-Cooled Nb Hot-Electron Bolometer Mixers at Frequencies Above the Superconductive Energy Gap”, Proceedings of the 10th Int. Symp. on Space Terahertz Technology, Charlottesville, VA, 214, 1999

[5] P. Yagoubov, M. Kroug, H. Merkel, E. Kollberg, G. Gol’tsman, S. Svechnikov and E. Gershenzon, “Noise temperature and local oscillator power requirement of NbN phonon-cooled hot electron bolometric mixers at Terahertz frequencies”, *Appl. Phys. Lett.*, 73, 2814, 1998

[6] H.-W.Hübers, A.Semenov, J.Schubert, G. Gol'tsman, B.Voronov, E.Gershenzon, "Performance of the Phonon-Cooled Hot-Electron Bolometric Mixer between 0.7 THz and 5.2 THz", Proceedings of the THz Electronics Conference, Darmstadt, September 2000

[7] S.S. Gearhart, J.Hesler, W.L.Bishop, T.W.Crowe, and G.M.Rebeiz, "A Wide-band 760-GHz Planar Integrated Schottky Receiver," IEEE Microwave and Guided Wave Lett., vol. 3, pp. 205-297, 1993

[8] J.D.Dyson, "The Equiangular Spiral Antenna," IRE Trans. Antennas Propagat., pp. 181-187, April 1959

[9] P. Yagoubov, M. Kroug, H. Merkel, E. Kollberg, J. Schubert, H.-W. Huebers, G. Schwaab, G. Gol'tsman, and E. Gershenzon, "NbN Hot Electron Bolometric Mixers at Frequencies Between 0.7 and 3.1 THz", *Proc. 10th Int. Symp. on Space Terahertz Technology*, Charlottesville, VA, 214, 1999

[10] The axial ratio in [9] is defined as the ratio of powers. To compare the result with ours we took a square root of the number reported there.

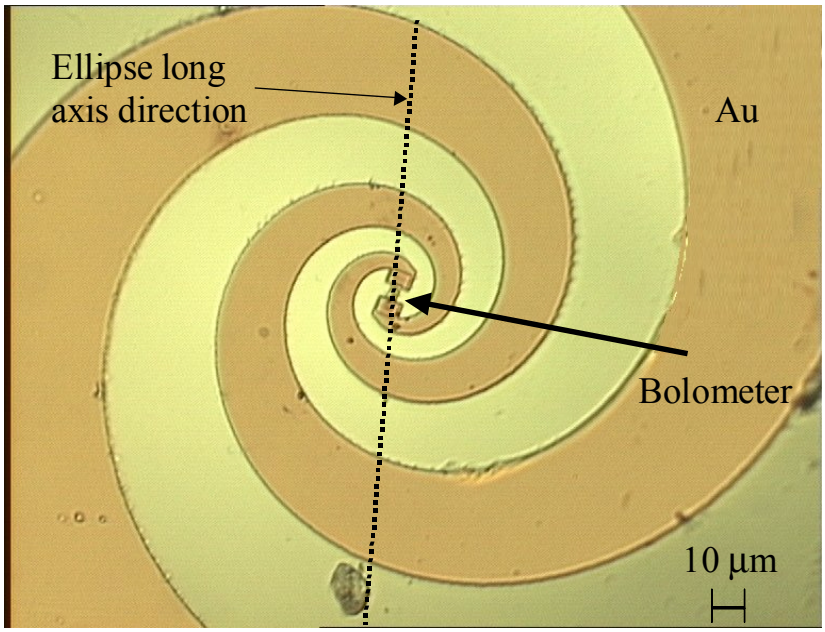

Figure 1. Micrograph of the device. The antenna is a planar spiral made from Au. The darker area is Au. The HEB bolometer is at the center of the spiral arms. The dotted line shows the measured direction of the long axis of the polarization ellipse.

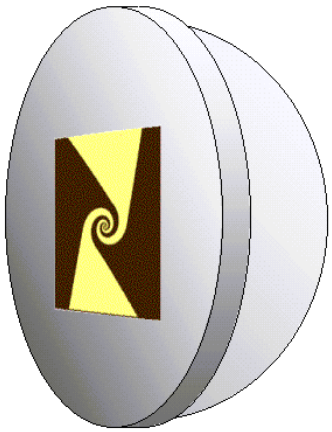

Figure 2. Schematic of the antenna – lens combination.

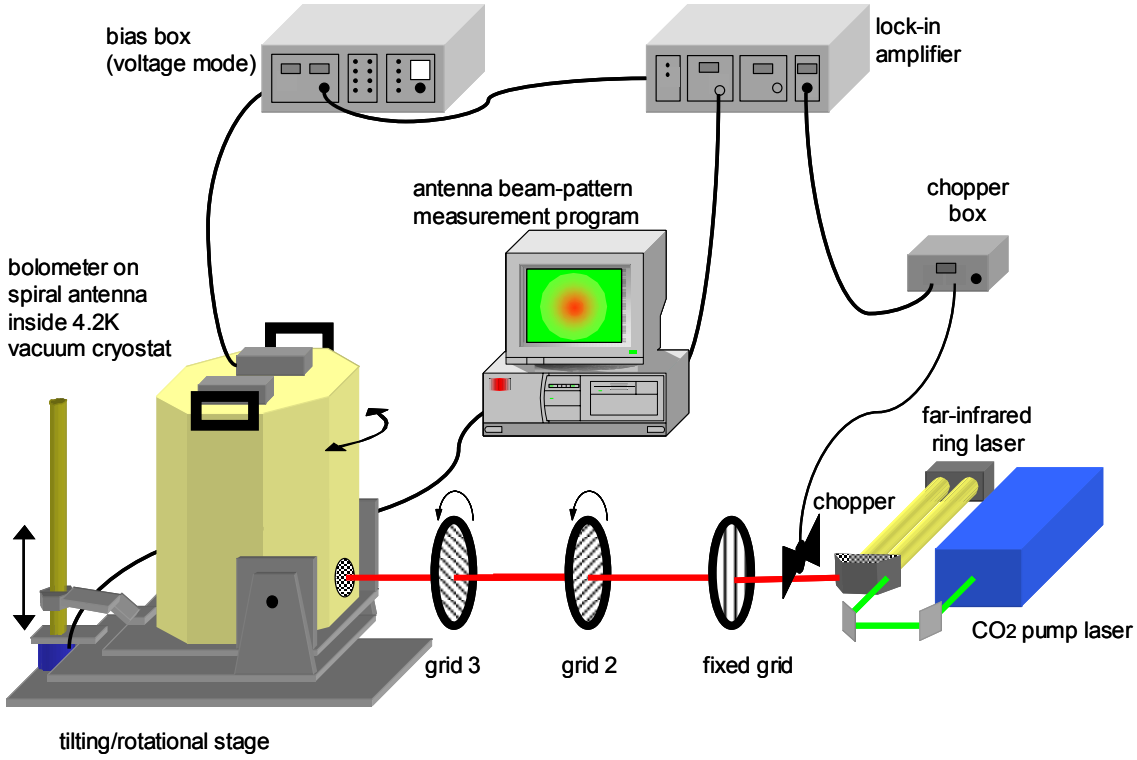

Figure 3. Schematic drawing of the measurement setup. Three submillimeter sources are used for the measurement of polarization and far-field beam pattern, i.e. a BWO at 0.6 THz, a carcinotron + tripler at 1.4 THz, and a CO2 pumped FIR laser at 2.5 THz. Only the laser is shown here.

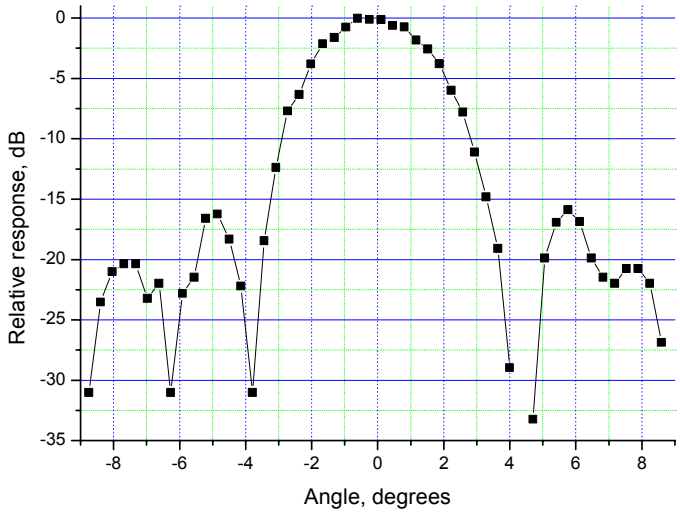

Figure 4. The measured beam pattern of the integrated antenna at 0.6 THz. Symbols are the measurement points, the solid line is a guide for eye.

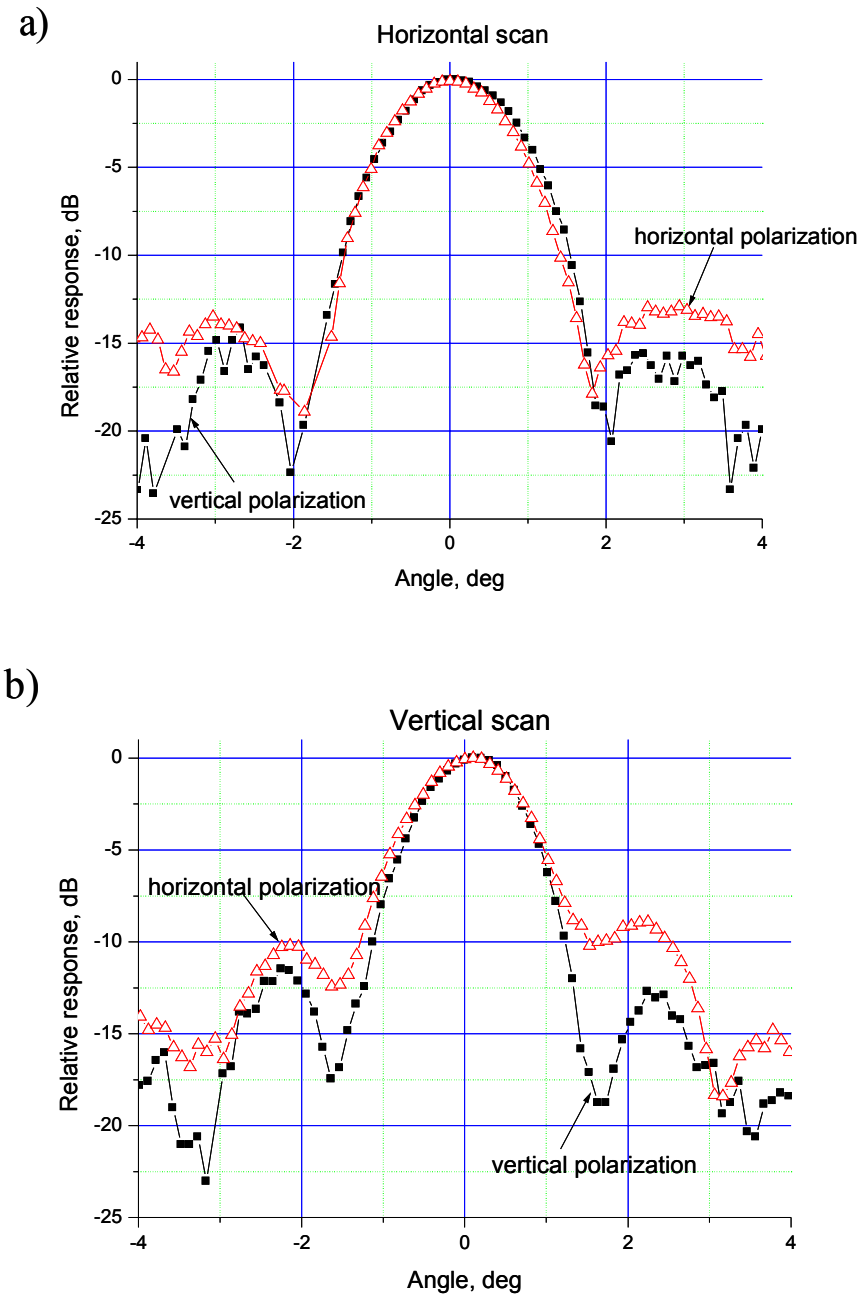

Figure 5. The measured beam pattern of the integrated antenna at 1.4 THz. The horizontal scan (a) is done by rotating the dewar around the vertical axis, and the vertical one (b) by tilting the dewar. The measurements are done for two orthogonal polarizations of the signal. When the polarization is vertical, the electrical field coincides with the direction of the long axis of the ellipse.

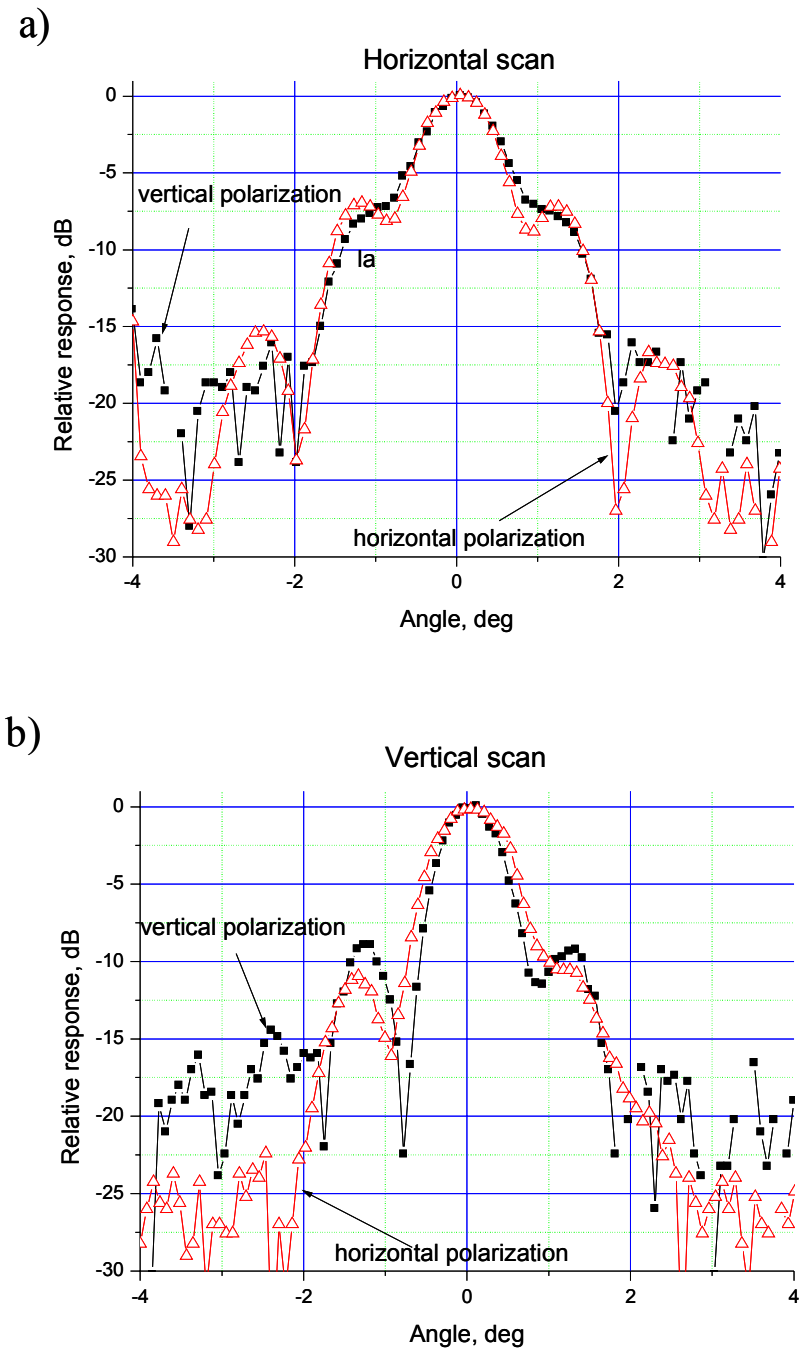

Figure 6. The measured beam pattern of the integrated antenna at 2.5 THz. The horizontal scan (a) is done by rotating the dewar around the vertical axis, and the vertical one (b) by tilting the dewar. The measurements are done for two orthogonal polarizations of the signal. When the polarization is vertical, the electrical field coincides with the direction of the long axis of the ellipse.

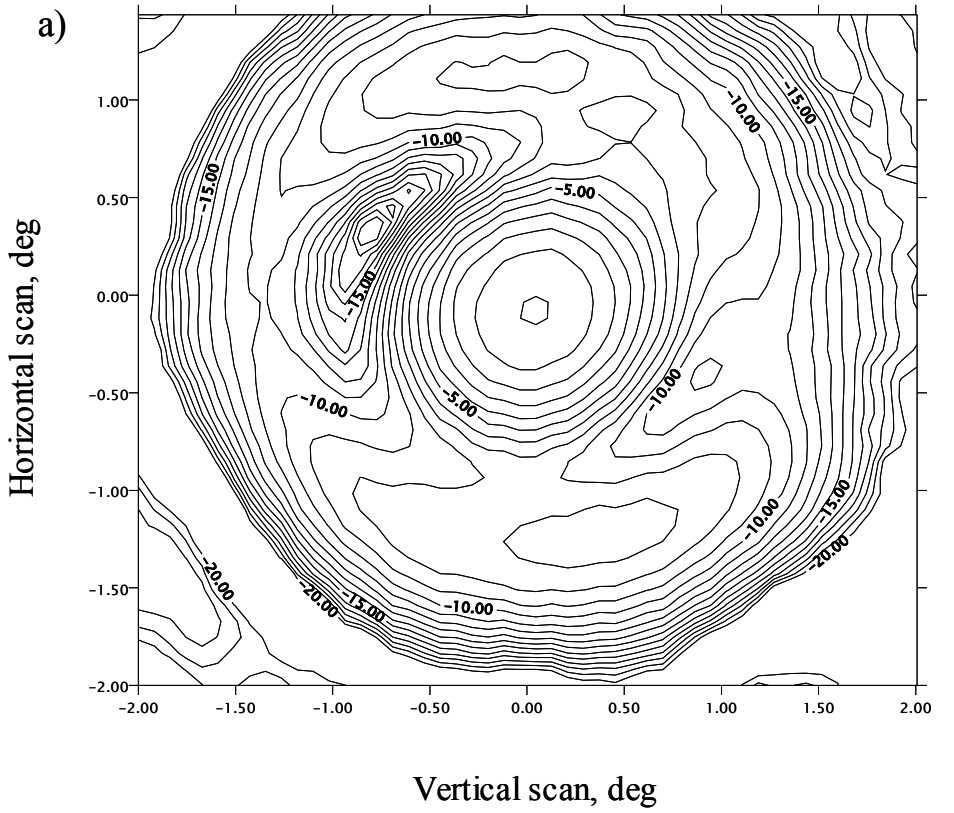

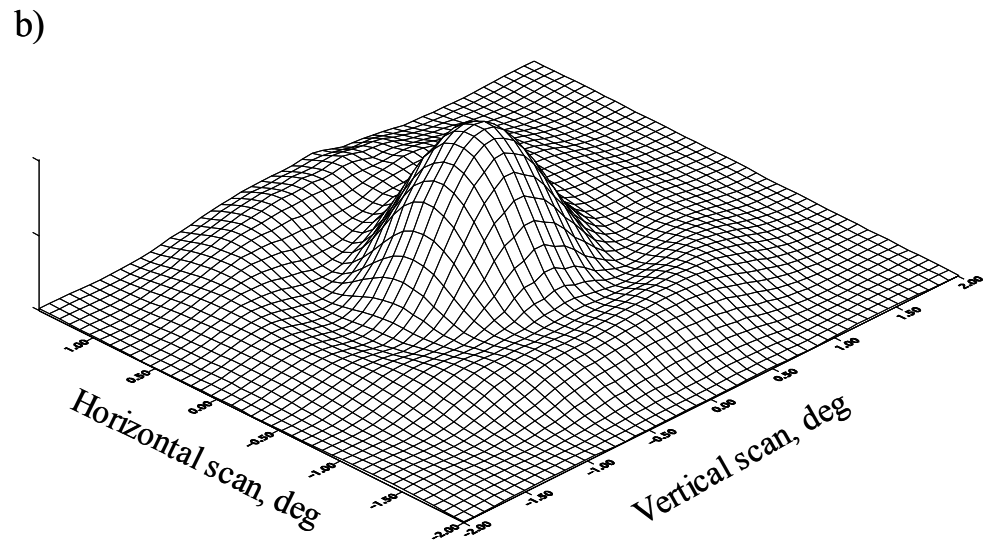

Figure 7. a) 2-D scan of the spiral antenna SEL combination at 2.5 THz. The relative response is in dB; b) 3-D view of the scan.

Design of a 275-370 GHz SIS mixer with image sideband rejection and stable operation

A. Navarrini, D. Billon-Pierron, K.F. Schuster, B. Lazareff

IRAM (Institut de Radio Astronomie Millimétrique)

300, rue de la Piscine – 38406 St. Martin d'Hères -France

Abstract

We discuss the design and optimisation of a SIS Single Side Band (SSB) mixer covering the 275-370 GHz frequency band for astronomical applications. The junction is probe-coupled to the full height waveguide. An adjustable circular noncontacting backshort allows SSB tuning in either USB or LSB in the whole RF band. A ≈30 % operating bandwidth can be achieved by using parallel inductive tuning of the junction capacitance. The calculated SSB receiver noise temperature referred to the mixer input is in the range 25-38 K.

A stability criterion for an SSB mixer with distinct signal and image termination impedances under typical operating conditions is derived. We show that when an inductive series matching structure with a two-stage impedance transformer is used to compensate the junction capacitance, the mixer cannot be operated over a wide frequency range in a stable way. An inductive parallel matching structure with a single-stage transformer allows us to fulfill the necessary conditions of stability.

1 Introduction

Radio astronomical spectroscopy is the main driver for the development of low-noise heterodyne receivers in the mm and submm range. In a practical implementation on a telescope, the losses associated with infrared filtering, local oscillator injection, telescope spillover and atmospheric attenuation all contribute to degrade the actual figure of merit for astronomical spectroscopy: SSB system noise temperature. Referring the system noise to the mixer input, it can be expressed in a simplified form as:

$$T_{SSB} = G_S^{-1} \cdot (T_{out} + T_{IF}) + (1 + G_I / G_S) \cdot T_{in} \qquad (1)$$

where G_S and G_I are the coupled mixer gain in the signal and image band, T_{out} is the mixer noise temperature referred to its output, T_{IF} is the noise temperature of the IF amplifier and T_{in} is the input noise temperature including noise contributions from optics, spillover and sky. For a typical ground-based receiver, the second term is often

dominating the sum. Its impact can be minimized by realizing an SSB mixer. Another requirement is to cover the atmospheric transmission windows with a minimum number of distinct receivers; this is a driver for a wide tuning range of the mixer (and of the LO system). A third requirement is for stable operation to be achieved without critical tuning. Accordingly, our three main goals in the present work are: single sideband operation, wide RF tuning range, low noise and stable operation.

2 Full height waveguide to microstrip transition

The 275-370 GHz mixer waveguide (0.76×0.38 mm^2) supports single TE_{10} mode operation from 197 GHz to 394 GHz. To achieve a good match over the desired frequency band it is imperative that a probe impedance $Z_{ant}(\nu)$ is selected which can easily be tuned over the entire frequency range. A waveguide whose height is reduced relative to the normal b/a ratio is often used in SIS mixers to help achieve the impedance match between the waveguide and the junction. We found desirable to use a full-height waveguide (b/a=1/2) for two reasons : i) lower losses ; ii) easier transition to the circular section used for the backshort described in a later section.

Yassin and Withington [1] give analytical results for a transition from a full height waveguide to a TEM port, that achieves a very good match to a real, low impedance (20-50 Ω) over a full waveguide band, making it well suited for an SIS mixer. We used their results as a starting point for an optimization of the actual configuration, where the probe feeds a microstrip line, itself running atop a base metallization patterned as a choke to provide a virtual short at the waveguide entrance. The electromagnetic simulations, using the FDTD package Microwave Studio from CST [2], take into account the presence of the quartz substrate, the microstrip channel, and the first two sections of the suspended microstrip choke.

We adopted a substrate 250 μm wide, 80 μm thick, with 100 μm air below, and 50 μm air above. The placement of the probe perpendicular to the waveguide's E-plane (see Figs. 1, 3) allows to decouple the first non-TEM propagation mode of the suspended stripline, which otherwise would have required to decrease the substrate width to reject its cutoff above the operating frequency range, and resulted in a more delicate fabrication. The driving-point impedance at the base of the antenna, versus frequency (or versus backshort position) periodically returns through a fixed impedance Z_C, whose real and imaginary parts can be controlled by the probe angle and length, respectively (see Fig.1). Adopting L = 200 μm and $a = 90^0$ results in Z_C = 75 Ω. We find that a better broadband match can be obtained when the quartz substrate does not extend across the full width of the waveguide.

3 Circular non-contacting backshort

A mechanically rugged, noncontacting circular backshort has been adopted. Its role is to provide simultaneously a good match and a high mismatch at, respectively, the

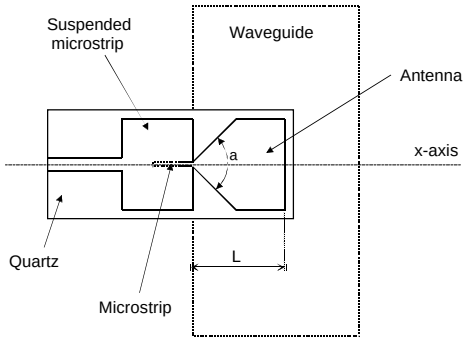

Fig. 1: Geometry of the probe transition from full-height waveguide to microstrip.

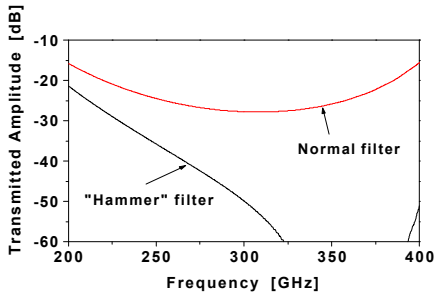

Fig. 2 : Amplitude of the transmission coefficient of six sections ²Hammer² type and normal type filter as a function of frequency.

signal and image frequencies; see sections 5 and 6 for a more complete discussion. It is located inside a circular waveguide of 880 µm diameter, and comprises 4 sections (Fig. 3). It has been optimized to provide a reflection coefficient better than -0.1dB across the operating band, taking into account imperfect contact of the rear part and a possible radial misalignment of 10 µm. For a given frequency range, the fabrication of a non-contacting backshort is easier in a circular (lathe) than in a rectangular (milling machine) waveguide, especially if the latter has reduced height. A conical transition between the rectangular and circular waveguide sections ensures that the reflected amplitude is dominated by the backshort itself, and ensures a regular tuning curve (see Fig. 7).

4 RF Filter

The base metallization on the quartz substrate is patterned into a six-section low-pass filter whose role is to provide a virtual short to the mixer block at the waveguide wall, and to reject the propagation of RF energy in the substrate channel. We found that a "hammer" type structure (visible on Figs 3 and 8) provides a superior rejection compared to the more common rectangular quarter-wave sections (see Fig. 2). A rectangular shape is kept for the first section to provide the space required for the microstrip tuning structures (section 7).

5 SSB Tuning

We start this section with an approximate, analytical discussion of SSB tuning. The principle of SSB operation is to locate the backshort so that its impedance in the plane of the waveguide to microstrip transition is an open at the signal frequency, and a short at the image frequency, which results in the junction being isolated from the mixer input and seeing a reactive termination at that frequency. Disregarding the fact that the

waveguide is non-uniform between the probe and the backshort, the shortest backshort distance that achieves that condition is such that:

$$l_{bs} = \frac{1}{2} n \lambda_g(\nu_l) \quad \text{and} \quad l_{bs} = \frac{1}{2}(n+\frac{1}{2}) \lambda_g(\nu_u) \tag{2}$$

where we have assumed that the lower sideband is the image, and the upper sideband the signal. These two equations can be combined:

$$l_{bs} = \frac{1}{4(\lambda_g^{-1}(\nu_u) - \lambda_g^{-1}(\nu_l))} \approx \frac{c}{8\nu_{IF}} \sqrt{1 - \left(\frac{\nu_c}{\nu_{LO}}\right)^2} \tag{3}$$

This simple equation gives, for ν_{LO} = 300 GHz and ν_{IF} = 6 GHz, $l_{bs} \approx$ 4.6 mm. We now discuss more detailed results from FDTD electromagnetic modeling. Figure 4 shows the driving point impedance $Z_P(\nu)$ of the probe, in the range 275–370 GHz, for a backshort distance from the probe $l_{bs} \approx$ 8 mm. Z_P describes a circle, that slowly sweeps around the Smith chart. At periodic intervals, Z_P passes through a fixed point of real impedance Z_C = 75 Ω, for which the probe was optimized, and, halfway through each rotation, Z_P touches the circle $\Gamma = 1$. For a different value of l_{bs}, the rate of rotation, and the total number of loops between 275–370 GHz, would be different, but the general region swept in the Smith chart would remain the same.

At this point, one might believe that all is needed is a suitable circuit to match the junction to Z_C, a problem for which several solutions are well known. We must, however, pay attention to the stability of the mixer operating in the SSB mode, which will be addressed in the two next sections.

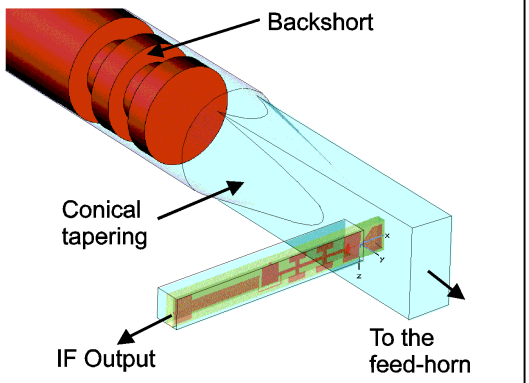

Fig. 3 : Full height waveguide SSB mixer. The circular section backshort is used for image rejection.

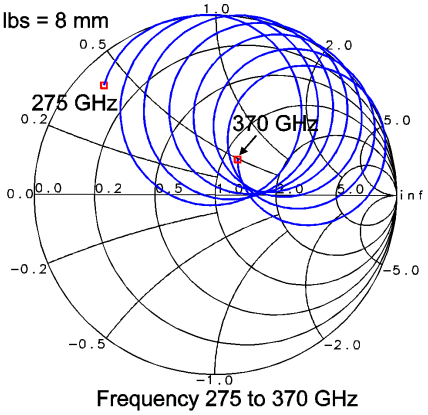

Fig. 4 : Driving point impedance of the probe for the mixer geometry shown in Figs.3 and 8 : The circular backshort is located at a distance l_{bs}=8mm away from the antenna plane. The Smith chart is normalised to 50 W.

6 Stability of SSB Mixer

In this section, we use Tucker's theory of quantum mixing [3] to derive a stability criterion for a SSB mixer operating in the 275-370 GHz range. We use the three-port approximation, treating only signals at $\nu_m = \nu_{LO} + m\,\nu_{IF}, m = 0,\pm 1$ and assuming higher harmonics to be shorted out by the junction capacitance. The geometry of the waveguide mount and the tuning circuit (including the junction's geometric capacitance) define the admittances seen by the junction at the three frequencies ν_m. Note that in the present case, $Y_{-1} \neq Y_1^*$. The dimensionless LO amplitude α defines the conversion matrix $Y_{mn}, m,n = 0,\pm 1$; we use the results and notations of Tucker and Feldman [4]. From these one can compute the augmented *Y* matrix and its inverse *Z*. The output IF admittance of the mixer is given by:

$$Y_{IF} = Z_{00}^{-1} - Y_0 \qquad (4)$$

It is physically clear (although slightly less obvious from the algebra) that Y_{IF} is independent of Y_0, and represents the IF output impedance of the mixer, when the RF ports are terminated at definite impedances, and for a given LO pumping level.

For a purely DSB mixer ($Y_{-1} = Y_1^*$), including the case of zero IF, Y_{IF} is real and equal to the slope of the pumped I-V curve. These two conditions do not hold any more in the general case [5]. The stability condition when the mixer's IF output is connected to a load Y_0 can be written: $\mathrm{Re}(Y_{IF}) + \mathrm{Re}(Y_0) > 0$. For the mixer to be stable for an arbitrary passive load, we require: $\mathrm{Re}(Y_{IF}) > 0$. The optimum operating conditions for a SSB mixer have been discussed by L.R. D'Addario [6]. In the present work, we have restricted the parameter space by assuming that the bias voltage is at the middle of the first photon step, $V_{DC} = V_g - hn_{LO}/2e$, and that the normalized pump voltage is unity: $\alpha = eV_{LO}/h\nu_{LO} = 1$; such parameters usually result in near-optimum noise performance. Moreover, we have assumed Z_S to match the normal-state resistance of the junction R_n, $Z_S = R_n$, and Z_I to be purely reactive ($Z_I = j\cdot X$ with X arbitrary reactance) which implies that the image band is completely rejected. Using an analytic fit to the I-V curve at 4.2 K of a good quality junction, we have used a three-frequency approximation to the quantum theory of mixing to constrain the Z_I values necessary to ensure $\mathrm{Re}[Y_{IF}] > 0$. We find that the lowest frequency in the range, 275 GHz, constrains the limits of the "stability region" :

$$-3.27 \leq \frac{Z_I}{jR_n} \leq +0.12 \qquad (5)$$

The stability region derived in eq. (5) is plotted in Figs. 5 and 6 in a Smith chart normalised to R_n.

7 RF Matching Circuit

The 1 μm^2 Nb/Al-AlO_x/Nb junction has a critical current density of the order of 10 kA/cm^2 and a normal-state resistance R_n = 25 Ω [7]. It has been realised by e-beam lithography. The small-signal impedance of the tunnel barrier $R_{RF} = G_{11}^{-1}$ is, at the center frequency of 320GHz, $R_{RF} \approx 0.72 R_N \approx 18\Omega$. The parallel combination of R_{RF} and the junction capacitance, estimated to be 75 fF ($\omega RC \approx 2.7$), must be matched, at the signal frequency, to the impedance of the waveguide probe. Two of the most common means to achieve this are series inductive tuning (end-loaded stub) and parallel inductive tuning.

In the rest of this section, we first show that a matching circuit comprising an end-loaded stub and a two-section quarter wave transformer does not allow to meet the criterion for stable SSB operation; then we discuss the results obtained with parallel inductive tuning.

7.1 End-loaded stub with two-section transformer

Impedance matching by an end-loaded stub has been discussed by several authors [8]. The end-loaded stub puts a small section transmission line in series with the junction. This results in the transformation of the complex junction impedance to a purely real impedance

$$R_S \approx \frac{R_j}{2 \cdot (w R_j C)^2} \approx 1.2\ \Omega \qquad (6)$$

Matching such a relatively low R_S value to the 75 Ω antenna probe requires a two-section quarter-wave Chebyshev transformer. All transmission lines are implemented in superconducting microstrips with their lines and ground planes made of Nb (120 nm and 430 nm respectively) separated by a 200 nm thick insulating layer of SiO_2 ($\varepsilon_R \cong 4.3$). The widths and lengths of the transmission lines have been optimised for maximum coupling of the RF junction resistance to the antenna probe in the 275-370 GHz frequency range using a commercial software (HP-EEsof Series IV EEsof, Libra-Touchstone), with appropriate corrections for field penetration.

The Smith chart (Fig. 5) shows the embedding impedance $Z_{emb}(\nu)$ in the 275-370 GHz frequency band for a backshort position l_{bs} = 8 mm (increased for clarity) away from the antenna plane. At alternate frequencies, the junction sees a match and a reactive mismatch, respectively, as required for SSB operation. However, the reactive termination at the image frequency lies, in some cases, in the region of instability; this is due to the phase dispersion caused by the two quarter-wave sections of the transformer. This matching circuit must be rejected.

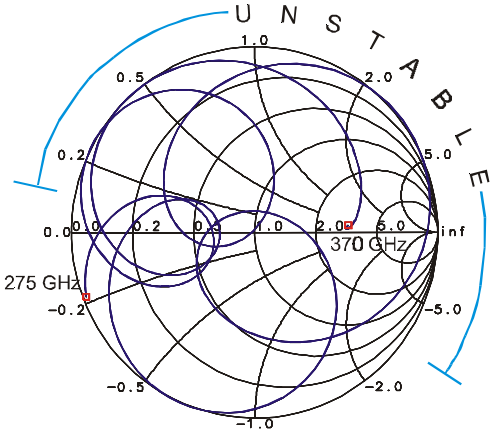

Fig. 5 : Series inductive tuning with two-section l/4 transformer. Impedance seen by the junction. Note that the reactive termination used for image rejection lies, in some cases, in the "unstable" region. The Smith chart is normalised to $Z_S=R_n$.

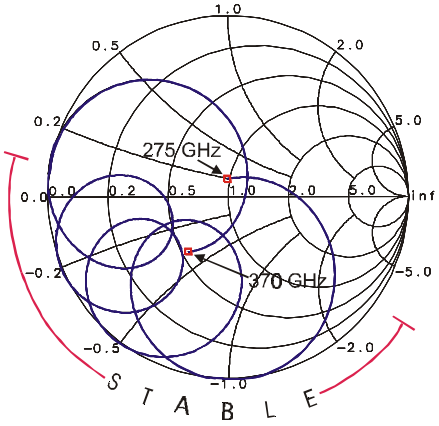

Fig. 6: Parallel inductive tuning with single-section l/4 transformer. Impedance seen by the junction. The reactive termination used for image rejection is always within the "stable" region. Here the backshort distance is 4.2 mm, appropriate for USB operation at 320 GHz.

7.2 Parallel inductive tuning with single-section transformer

A better control of this impedance is obtained by using a lower value for the electrical length between the antenna probe and the junction. This is achieved by adopting a parallel inductive tuning. The required transformation ratio is smaller and can be achieved with a single section λ/4 transformer. The layout of the mixer chip is illustrated in Fig. 8. The parallel inductive tuning is achieved with a short (≈λ/8) length of microstrip, terminated to a virtual ground provided by a radial stub (opening angle 130^0). We found, using simulations [9], that, with respect to the conflicting requirements of lowest impedance at the apex on one hand, and minimum capacitive loading of the IF on the other hand, a radial stub offers no clear advantage over a λ/4 low-impedance rectangular stub. The parallel tuned junction presents, at the centre of the RF band, a real impedance $R_j \approx 18\ \Omega$ as discussed above. This is matched to the ≈ 75 Ω driving point impedance of the probe by a λ/4 line with an impedance $Z_L \approx 35\ \Omega$. This falls between the impedances that can be realised in, respectively, microstrip and coplanar superconductive lines. We have realised this λ/4 section in Capacitively Loaded CoPlanar Waveguide (CLCPW), consisting of 3 sections of microstrip and 2 sections of coplanar lines.

The lengths of the individual sections were optimised, taking into account the actual impedances across the RF band of the inductively tuned junction and of the probe, while ensuring at the same time that the stability criterion for SSB operation was met. Sonnet ***em*** was used to compute de-embedded S-parameters for the microstrip-

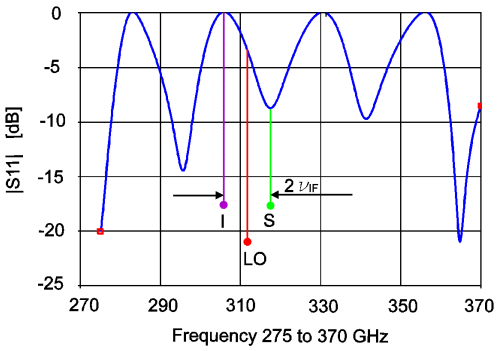

Fig. 7 Amplitude of the reflection coefficient |S11(n)| seen by the junction.

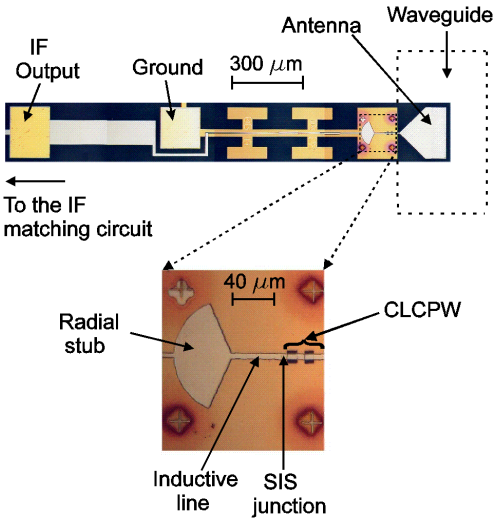

Fig. 8: Quartz substrate used for the mounting of the SIS junction and the integrated tuning structure

coplanar discontinuities, which were used in the Libra simulation of the global circuit. The final result of the optimisation is shown in Figs. 6 and 7.

8 Junction bias and IF Matching Circuit

To bias the junction and provide a path for the IF signal, a narrow microstrip line (3 μm) is connected to the external part of the radial stub as shown in Fig. 8 using alternate $\lambda/4$ sections to reject RF leakage.

9 Modelling results: Gain and mixer noise temperature

Using the standard quantum theory of mixing in the three-port approximation, we have computed the coupled mixer gain, the image band rejection, the SSB mixer noise temperature and the SSB receiver noise temperature of our designed system. We assumed a noise temperature of the IF amplifier $T_{IF}=6\,K$. We also assumed a bias voltage at the half of the first photon step and a LO pumping power such that $\alpha=1$. The receiver has been optimised for SSB operations by tuning the backshort distance from the antenna plane l_{bs} to allow operations with low G_I/G_S in either USB or LSB at each frequency in the RF band. Fig. 9 shows the estimated SSB *mixer* noise temperature T_M and the coupled signal mixer gain G_S. This result shows that the mixer can operate with low mixer noise temperature and reasonable signal conversion gain. Fig. 10 shows the calculated SSB *receiver* noise temperature and the backshort to antenna plane distance l_{bs} expressed in mm required for the SSB tuning. We can see that a worst-case $T_{rec} \approx 38$ K ($\approx 2.4\ h\cdot\nu/k$) occurs at 330 GHz. The result shown in

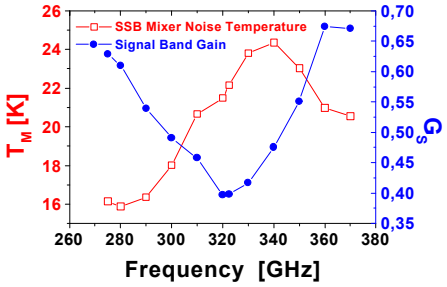

Fig. 9: Calculated SSB mixer noise temperature and coupled mixer gain in the signal band G_S (linear scale) in the 275-370 GHz frequency band.

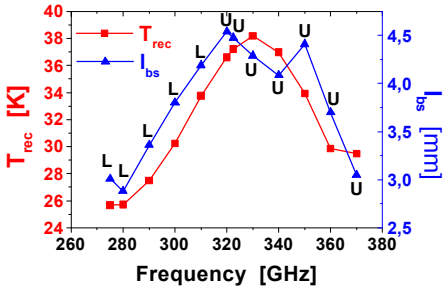

Fig. 10: Calculated SSB receiver noise temperature T_{rec} and backshort in the 275-370 GHz frequency band, in LSB (L) or USB (U).

Fig. 10 indicates that a SSB receiver noise temperature as low as ≈ 2÷3 times the quantum limit hν/k might be achieved over the whole 275-370 GHz frequency band.

10 Mixer block construction

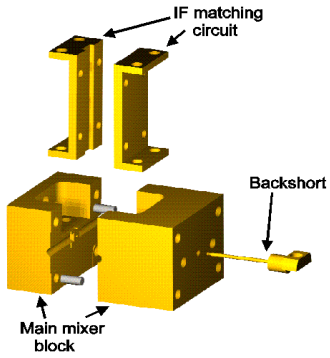

Fig. 11: Mixer block configuration: the two main parts of the mixer used for the SIS junction mounting are shown together with the circular section backshort and the shielded microstrip used as IF matching transformer.

The main mixer block is split in two parts, which are machined in brass. The mixer block includes magnetic field concentrators for the suppression of the Josephson current. The whole device is illustrated in Fig. 11. Here the two main parts of the mixer are shown together with the circular section backshort and the shielded microstrip used as IF matching transformer. The main mixer block has external dimensions $25 \times 20 \times 25$ mm^3. One part of the mixer includes the circular waveguide, housing the backshort, the conical transition circular to rectangular waveguide and a short section of rectangular waveguide. This part of the mixer is used for SIS junction mounting. The other part of the main block includes a 10 mm long rectangular waveguide which has been realised by spark erosion technique. The other parts of the block have been micromachined in a standard way.

11 Conclusions

A new type of SIS heterodyne quasi-particle mixer has been designed for the 275-370 GHz band. The mixer employs a tuned junction mounted in a full height waveguide block and a circular section backshort used for SSB operations. The RF matching network consists of an open-ended stub including a radial stub and an inductive microstrip line. The mixer and its external circuit have been optimised to give wide RF

bandwidth, low mixer noise temperature and high gain. SSB mixer noise temperatures in the range 16-25 K are expected in the RF band with a mixer conversion gain better than -4.0 dB. SSB receiver noise temperatures are in the range 25-38 K in the same frequency band.

Acknowledgements

The authors are grateful to M. Carter and F. Mattiocco for helpful discussions. I. Peron played in crucial role in developing the E-beam lithography in IRAM's SIS laboratory. This work was supported in part by the Institut de Radio Astronomie Millimétrique IRAM (Grenoble, France), and by the CNAA, Astrophysical Observatory of Arcetri (Florence, Italy).

References

[1] G. Yassin and S. Withington, "Analytical Expression for the Input Impedance of a Microstrip Probe in Waveguide", *Int. J. Infrared and Millimetre Waves*, **17**, 1685-1705, 1996

[2] CST Microwave Studio, Büdinger Str. 2 a, D-64289 Darmstadt, Germany

[3] J.R. Tucker, "Quantum limited detection in tunnel junction mixers", *IEEE J. Quantum Electron.*, **6**, 1234-1258, 1979

[4] J.R. Tucker and M.J. Feldman, "Quantum detection at millimetre wavelengths", *Rev. Mod. Phys.,* **57,** 1055-1113, 1985

[5] S.-K. Pan and A.R. Kerr, "SIS mixer analysis with non-zero intermediate frequencies", *Seventh International Symposium on Space Terahertz Technology*, Charlottesville, March, 1996

[6] L. D'Addario, "Noise Parameters of SIS Mixers", *IEEE Trans. Microwave Theory and Techniques*, **36**, (7), 1196-1206, 1988

[7] K.F. Schuster, IRAM Technical Memo, 1998

[8] T.H. Büttgenbach, H.G. LeDuc, P.D. Maker, T.G. Phillips, "A Fixed Tuned Broadband Matching Structure for Submillimetre Astronomy ", *IEEE Trans. Applied Supercond.*, **2**, (3), 165-175, 1992

[9] Sonnet Software, Inc., 1020 Seventh North Street, Suite 210, Liverpool, NY 13088, USA

Development of a 600-720 GHz SIS Mixer for the SMART

S.C. Shi[1], C.C. Chin[2], M.J. Wang[2], W.L. Shan[1], W. Zhang[1], and T. Noguchi[3]
1. Purple Mountain Observatory, Chinese Academy of Sciences, China
2. Institute of Astronomy and Astrophysics, Academia Sinica, Taiwan
3. Nobeyama Radio Observatory, NAOJ, Japan
Email: scshi@pmo.ac.cn, chin@asiaa.sinica.edu.tw
mjwang@mx.nthu.edu.tw, noguchi@nro.nao.ac.jp

Abstract: The SMART (Sub-Mm-ARray-Taiwan) is an expansion project of SAO's SMA project. A 600-720 GHz SIS mixer for this project is under development. The SIS mixer is incorporated with a fixed-tuned waveguide mixer mount, which was originally designed by the receiver team at SAO, and a twin-junction (in parallel) tuning circuit. Individual Nb junctions have an area of 1.2x1.2μm^2 and a critical current density of 10kA/cm^2. Detailed simulation and experimental results are presented in this paper.

1. Introduction

The submillimeter-wave array (SMA) is a unique eight-element interferometer array, sited on Mauna Kea in Hawaii, being jointly developed by the Smithsonian Astrophysical Observatory (SAO) and the Academia Sinica Institute of Astronomy & Astrophysics (ASIAA) [1]. The array will cover a frequency range of 176-900 GHz, in which the 600-720 GHz band will be the first submillimeter band to operate. As it is well known, this frequency band is located just around the gap frequency of Nb SIS junctions. The performance of Nb SIS mixers is well close to $3h\nu/k$ below the junction's gap frequency, but can be further improved beyond that frequency. Developing good performance SIS mixers at submillimeter wavelengths is of particular interest for ground-based observational facilities because of large atmospheric attenuation.

2. SIS Mixer Design

Submillimeter-wave SIS mixers usually adopt SIS junctions in association with an integrated tuning circuit (an inductive thin-film superconducting microstrip line in general), which tunes out the junction's geometric capacitance. The surface resistance of superconducting films becomes considerable beyond the junction's gap frequency (~670 GHz for Nb junctions), due to Cooper-pair breaking by energetic photons. Hence it might be better to develop the 600-720 GHz SIS mixer using either junctions of a higher gap

frequency [2] or Nb junctions incorporated with tuning films of smaller surface impedance (e.g., NbTiN/Al combination [3]), as far as the loss effect of superconducting films is concerned. All Nb junctions were indeed chosen for the first phase development, as the Nb-junction fabrication process is much mature in our labs. The mixer mount adopted for this development is the same as that by the receiver group at SAO [4].

Using all Nb junctions to develop a good performance SIS mixer for 600-720 GHz, we need to understand two points. One is how large the effect of the Nb thin-film loss on the mixer performance is, and the other is if the thin-film loss has similar impact for different junction tuning circuits.

2a. Loss effect for Nb thin-film microstrips

Let us consider a superconducting microstrip line of conductor width *w* and insulation-layer thickness *h*. The distributed parameters of the microstrip line, surface resistance *R*, inductance *L*, and capacitance *C* per unit length are given by

$$R = \frac{2}{Kw}\mathrm{Re}(Z_s) \qquad (\Omega / length) \tag{1}$$

$$L = \frac{\mu_0 h}{Kw} + \frac{2}{Kw}\mathrm{Im}(Z_s)/\ j\omega \qquad (H / length) \tag{2}$$

$$C = \frac{\varepsilon_r \varepsilon_o Kw}{h} \qquad (F / length) \tag{3}$$

where *K* is a fringe field factor [5] and Z_s is the film's surface impedance, which can be calculated by Mattis-Bardeen theory [6].

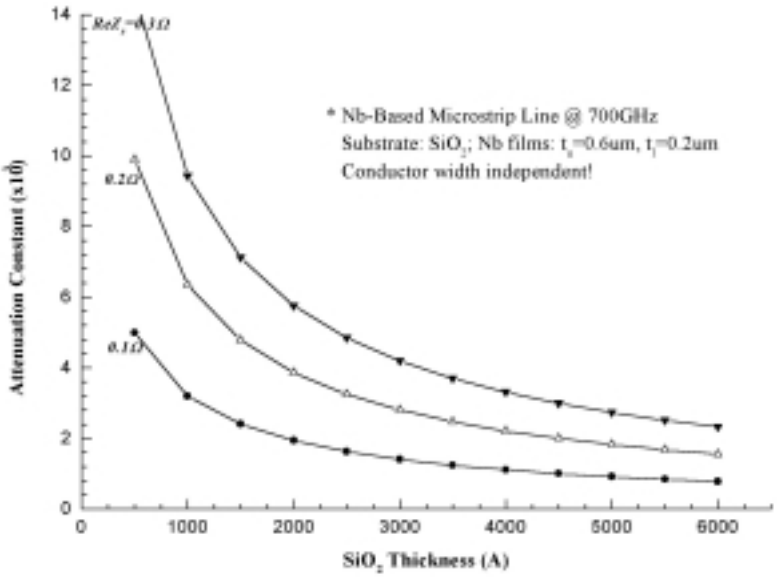

Fig. 1 Attenuation constant vs. substrate thickness.

The attenuation constant of Nb-based superconducting microstrip lines was studied for

different insulation-layer thicknesses and conductor widths. The insulation layer in this case was assumed simply as one single SiO_2 layer. The calculation was done at 700 GHz for three examples of the real surface impedance $Re(Z_s)$ equal to 0.1, 0.2, and 0.3 Ω. It has been demonstrated that as plotted in Fig. 1, the attenuation constant is almost independent of the microstrip width, but decreases with the increase of the insulation-layer thickness (nearly saturated at a certain thickness).

2b. Twin junctions vs. end-loaded SIS

Two junction tuning circuits (refer to the insets in Fig. 2) were investigated to evaluate the effect of lossy thin-film microstrip lines on the performance of SIS mixers. One tuning circuit is commonly referred as the end-loaded type [7], while the other is parallelly connected twin junctions [8]. A quarter-wavelength impedance transformer was assumed in front of both tuning circuits to match a 35-Ω source impedance (i.e., the feed-point impedance of the mixer mount). The thin-film microstrip lines for the tuning inductance and impedance transformer were made up of two Nb films (0.6-μm thick for the wiring layer and 0.2-μm thick for the ground layer, assuming each an 0.1-Ω surface resistance) and a combined insulation layer as $Al_2O_3/SiO_2/Nb_2O_5$ (0.09/0.27/0.1 μm thick, ε_r=9/4/29).

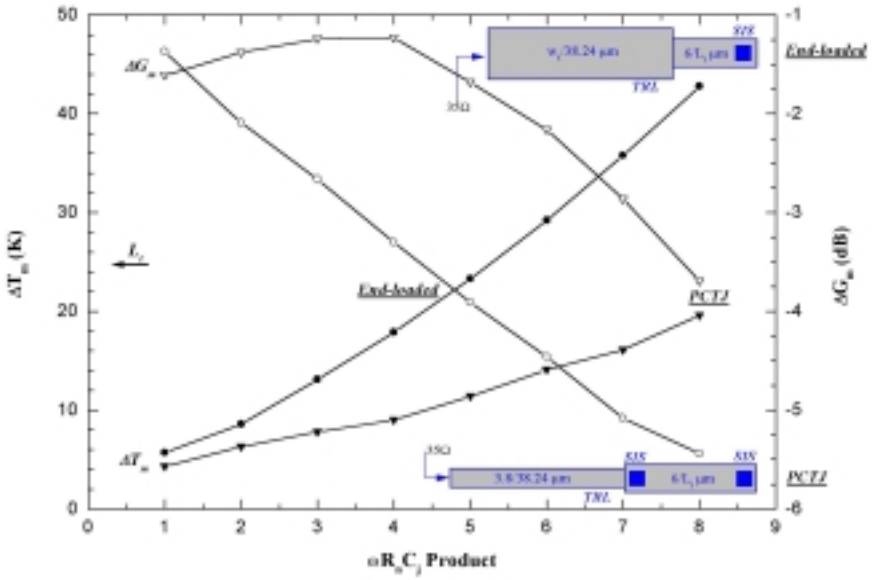

Fig. 2 Differences of the noise temperature and conversion gain as a function of junction's ωR_nC_j product.

The mixing performance (i.e., noise temperature and conversion gain) was simulated at 700 GHz for both tuning circuits. The junction's ωR_nC_j (with R_n fixed at 13.6 Ω) product was varied from one to eight for this simulation. Notice that after changing the junction's ωR_nC_j product we re-optimized the impedance-transformer width and the

tuning-inductance length (indeed only the latter for the twin-junction case). Another simulation was done for the case of the thin-film microstrip lines without any losses for comparison. Fig. 2 demonstrates the noise temperature and conversion gain differences between the two simulated instances. Obviously, both the noise temperature and the conversion gain degrade while taking account of the film loss. Such performance deterioration is more evident for larger junction's $\omega R_n C_j$ product. It is interesting that for the end-loaded tuning circuit, the performance deterioration is rather sharp in comparison to the twin-junction circuit. We had found it was indeed caused by the transformer in the end-loaded tuning circuit, which has a larger impedance transforming ratio. It is also apparent that for both tuning circuits the conversion-gain difference is much larger than the total transmission loss of the thin-film microstrip lines (~1.6 dB per 153 μm). Lossy terminations at other frequency sidebands might contribute partly, as this difference depends strongly on the junction's $\omega R_n C_j$ product.

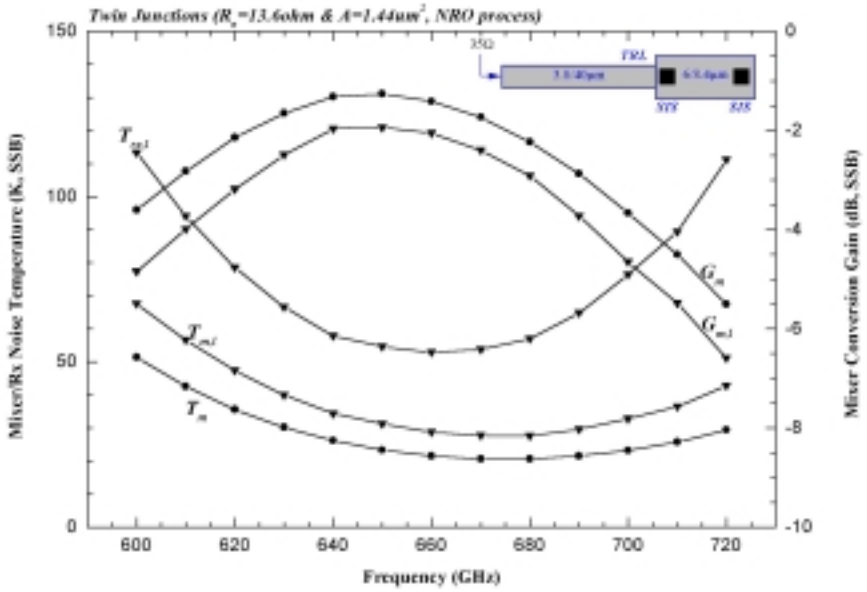

Fig. 3 Simulated Mixer performance for the 670-GHz SIS Mixer. Subcript m and m,l denote the mixer performance without and with the film loss taken into account, while subscript rx,l the receiver performance with the film loss.

2c. Simulated mixer performance

The twin-junction tuning circuit was adopted for the development of the 600-720 GHz SIS mixer, as it is less sensitive to the superconducting film loss than the end-loaded tuning circuit according to our simulation results. The junction's critical current density and area were taken as 10 kA/cm^2 and 1.2x1.2 μm, respectively. Correspondingly, the normal state resistance for individual junctions is 13.6 Ω and the junction's $\omega R_n C_j$ product is equal to

6.9 at 660 GHz by assuming a specific capacitance of 85 fF/μm^2. A quarter-wavelength impedance transformer, which has a width of 3.8 μm and a length of 40 μm, was utilized to match the twin junctions (of an input impedance equal to 6.8 Ω approximately) with the feed-point impedance of the mixer mount (~35 Ω). The tuning inductance between the twin junctions was optimized for the mixer performance by taking account of the loss effect of the superconducting films. Its width and length were found to be 6 μm and 8.4 μm, respectively. Fig. 3 exhibits the simulated mixer performance. Obviously, the receiver noise temperature (SSB) is less than 120 K in the frequency range of 600-720 GHz, with an assumption of 15-K IF noise temperature. It should be pointed out that the junction-chip structure was based on the fabrication process at Nobeyama Radio Observatory (NRO, as given in Section 2b).

3. Mixer Mount Simulation

The feed-point (refer to Fig. 4) impedance of the 660-GHz mixer mount was initially assumed to be 35 Ω (according to a scale model measurement [4]) for the mixer design. With the help of the Ansoft's HFSS simulator [9], we have calculated the feed-point impedance of the actual mixer structure including both choke filters on the IF and ground sides. The feed point was taken as a lumped gap source port (10.56μm x 2.0μm, «λ/10), while the waveguide and IF ports were the other two ports for simulation. All the structural parameters used here followed the original SAO design [4]. As plotted in Fig. 5a, the calculated resistance is well close to 35 Ω, while the reactance is around -30 Ω.

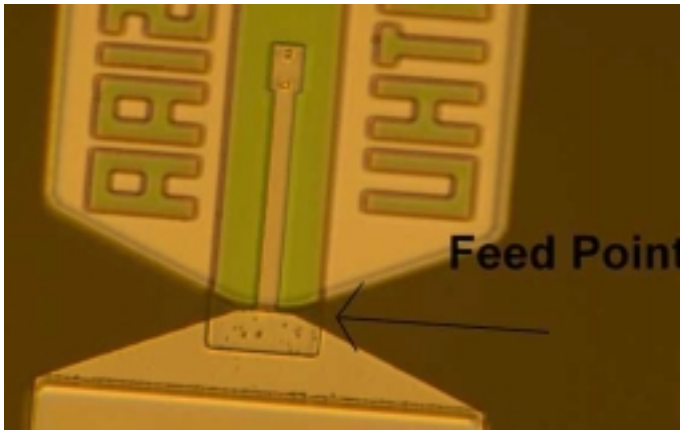

Fig. 4 Photograph of fabricated SIS junction at NRO.

We also studied the dependence of the feed-point impedance upon the size of the lumped gap source port, as the port size (mainly its width) is pre-assumed for HFSS simulation. As shown in Fig. 5b, the feed-point impedance varies with the width of the lumped gap source

port. Given the fact that the lumped gap source port has a uniformly distributed field, we suggest its width should be taken exactly as that of the impedance transformer connected between the feed point and the junction tuning circuit. As it is well known, displacement often occurs when we align the SIS junction chip in the mixer mount. Hence we also examined the effect of the displacement of the feed point in waveguide. Calculation results have demonstrated that the impedance variation is not considerable for the feed-point position shift in both vertical and horizontal directions, but rather evident when the quartz-substrate thickness is reduced down to 30 μm from 40 μm.

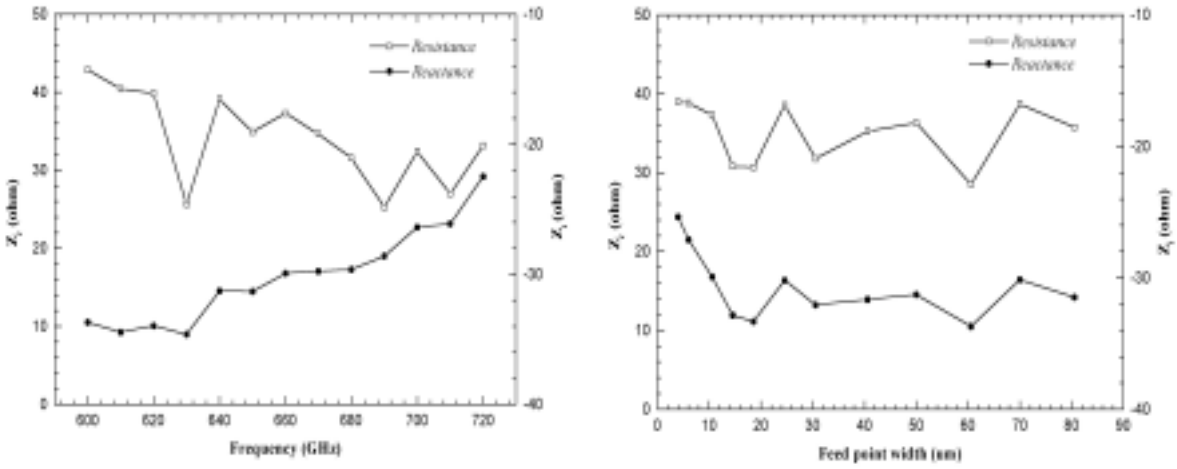

Fig. 5a Feed point impedance vs. frequency; Fig. 5b Feed point impedance vs. feed width

4. Experimental Results

The 660-GHz SIS junctions fabricated at NRO, which have a critical current density of about 10 kA/cm^2, were tested in a 640-GHz mixer mount [10]. It should be pointed out that due to over estimation of the junction shrinkage in the photomask the actual junction area was found approximately 30% larger than the design value, and that the feed-point impedance of the mixer mount used here is fairly close to that shown in Fig. 5a. The measured IF frequency was 6 GHz, at which the IF noise temperature is around 22 K. Fig. 6 shows the measured receiver noise temperature (DSB) from 618-660 GHz. Notice that there are no any corrections on the receiver noise temperature. Clearly the frequency response of the receiver noise temperature is shifted to a lower frequency than the designed center frequency of 660 GHz. The bandwidth appears not clear because of a limited frequency coverage for this measurement. In spite of that, we did observe a noise temperature of 145 K around 620 GHz.

Given the fact the twin SIS junctions had a larger area, we indeed tested the twin junctions of a tuning inductance which is 30% shorter than the designed length. The frequency response of the measured receiver noise temperature, however, was not well compensated, just as shown in Fig. 6. There are two possible causes for this frequency shift. One is a narrower wiring layer for the tuning inductance (i.e., of a higher characteristic impedance) due to over etching, and the other is a parasitic inductance being around individual SIS junctions (of non-uniform current distribution for a relatively large area). In terms of the resonance steps observed on the junction's I-V curve (refer to Fig. 7), we can estimate the resonance frequency of the twin-junction tuning circuit. Therefore, it may be possible to extract the junction's parasitic inductance by comparing the measured resonance frequency with the one derived form an equivalent circuit model for the twin-junction tuning circuit including the parasitic inductances.

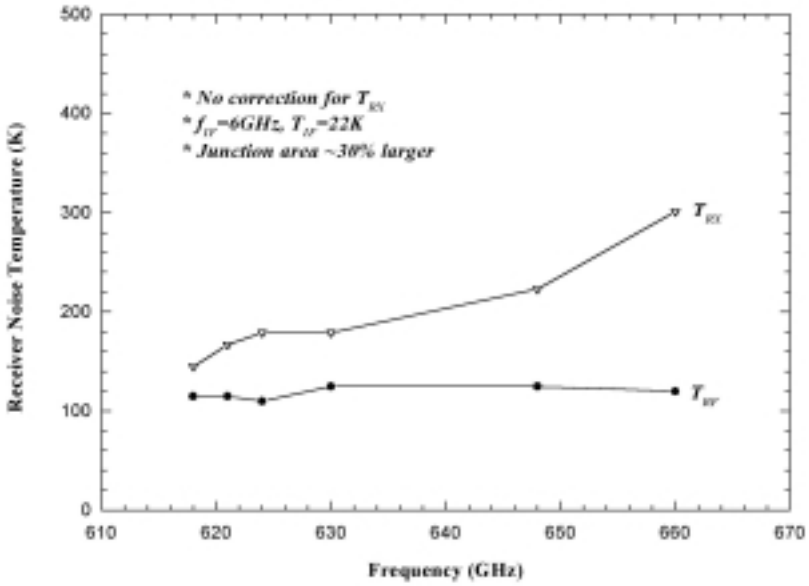

Fig. 6 Measured receiver noise temperature (DSB) for the 660-GHz SIS mixer.

5. Summary

We have designed a 600-720 GHz SIS mixer using Nb twin junctions, with the surface impedance rise of Nb films beyond its gap frequency taken into account. The simulation results are quite promising, giving a receiver noise temperature (SSB) of below 120 K. The feed-point impedance of the 660-GHz mixer mount is well understood through HFSS simulations. A preliminary experiment has demonstrated a receiver noise temperature as low as 145 K at 618 GHz, although its frequency response is still far from satisfied.

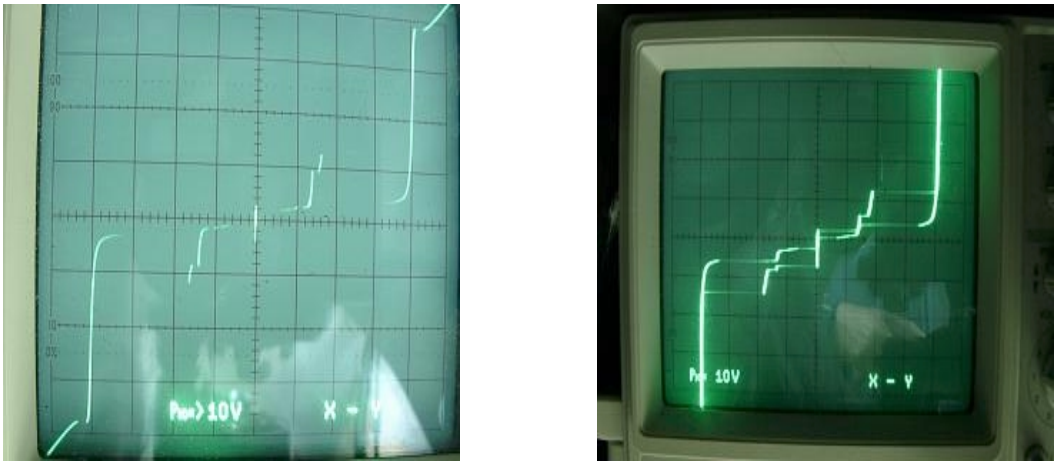

Fig. 7 I-V curves of the twin junctions (a: with a design tuning inductance; b: with a 30% shorter one; 0.677mV/div)

References

1. J. Moran, "The submillimeter array," *SMA memo*.
2. J. Kawamura et al, to appear in *Appl. Phys. Lett.* (2000).
3. S.V. Shitov et al, this proceddings.
4. C.-Y. E. Tong, et al, *Proc. 6th Int. Symp. Space Terahertz Tech.* (1995).
5. W.H. Chang, *J. Appl. Phys.* **50**(12), 8129 (1979).
6. D.C. Mattis and J. Bardeen, *Phys. Rev.*, 111, 412 (1958).
7. B⎮ttgenbach et al, *Int. J. IR & MM Waves*, 11, 1 (1988).
8. T. Noguchi, S.C. Shi, and J. Inatani, *IEICE Trans. Electronics*, E78-c, 481 (1995).
9. HFSS, Ansoft, Pittsburgh, PA 15219-1119, USA.
10. Y. Irimajiri, et al, *Int. J. IR & MM Waves*, 21 (4), 519 (2000)

Development of a High Efficiency 600-700 GHz Backward Wave Oscillators for Submillimeter Applications

Jeff Neilson, R. Lawrence Ives, and Malcom Caplan

Calabazas Creek Research, Inc.
20937 Comer Drive
Saratoga, CA 95070, USA
(408) 741-8680
jeff@CalCreek.com

Calabazas Creek Research, Inc. is funded by the National Aeronautics and Space Administration to develop efficient, light-weight, backward wave oscillators (BWOs) for applications from 300 GHz to 1 THz. These devices are needed as local oscillator (LO) sources in heterodyne receivers. Very low noise heterodyne receivers are needed at submillimeter wavelengths for low-background radio astronomy observations and remote sensing of comets, Earth and other planetary atmospheres. Above 100 GHz, only BWOs have broad tunability (over 100 GHz) and high output power (~1 mW); however, they are heavy (over 20 kg), consume a lot of power (270 W), required water cooling, and have poor output mode purity.

Development is continuing on advanced backward wave oscillators that will incorporate energy recovery, air cooling and significant weight reductions by use of lighter advanced magnetic materials. An improved coupler has been developed to transform the generated RF power to a high purity Gaussian output mode. The design of a 600-700 GHz BWO incorporating these improvements is currently underway. Construction of this tube is expected to begin in late 2001.

ELECTROMAGNETIC MODELING OF DISTRIBUTED-SOURCE-EXCITATION OF COPLANAR WAVEGUIDES: APPLICATIONS TO TRAVELING-WAVE PHOTOMIXERS

Davide Pasqualini[1], Andrea Neto, Rolf A. Wyss

Jet Propulsion Laboratory, California Institute of Technology, Pasadena, California, 91109

I. ABSTRACT

In this work an electromagnetic model and subsequent design is presented for a traveling-wave, coplanar waveguide (CPW) based source that will operate in the THz frequency regime. The RF driving current is a result of photoexcitation of a thin GaAs membrane using two frequency-offset lasers. The GaAs film is grown by molecular-beam-exitaxy (MBE) and displays sub-ps carrier lifetimes which enable the material conductivity to be modulated at a very high rate. The RF current flows between electrodes deposited on the GaAs membrane which are biased with a DC voltage source. The electrodes form a CPW and are terminated with a double slot antenna that couples the power to a quasi-optical system. The membrane is suspended above a metallic reflector to launch all radiation in one direction. The theoretical investigation and consequent design is performed in two steps. The first step consists of a direct evaluation of the magnetic current distribution on an infinitely extended coplanar waveguide excited by an impressed electric current distributed over a finite area. The result of the analysis is the difference between the incident angle of the laser beams and the length of the excited area that maximizes the RF power coupled to the CPW. The optimal values for both parameters are found as functions of the CPW and membrane dimensions as well as the dielectric constants of the layers. In the second step, a design is presented of a double slot antenna that matches the CPW characteristic impedance and gives good overall performance. The design is presently being implemented and measurements will soon be available.

II. INFINITELY EXTENDED CPW FED OVER A FINITE LENGTH ACTIVE REGION

An infinitely extended x-oriented CPW is considered (Fig. 1), which is etched on an infinite conducting plane between two multi-layered half spaces.
In the photomixer structure the active dielectric layer is a GaAs film, which is modeled as a dielectric homogeneous slab with relative permittivity $\varepsilon_{r2} = 12.9$. On top of the CPW ground plane there is a thin protective Si_3N_4 film ($\varepsilon_{r2} = 7.0$). The multi-layer structure has been subdivided in two regions. Region 1, $z > 0$, represents the protective layer (h_1, ε_{r1}), while region 2, $z < 0$, represents the active grounded slab (h_2, ε_{r2}), backed by an

[1] Currently with the Department of Information Engineering, University of Siena, Via Roma 56, 53100 Siena, Italy

infinitely extended metallic reflector separated by a vacuum layer ($\varepsilon_{r0}=1$) with a thickness of h_0. The cross section of both the arms of the CPW (slot "1" and "2") is uniform (w_s) and small in terms of the wavelength.

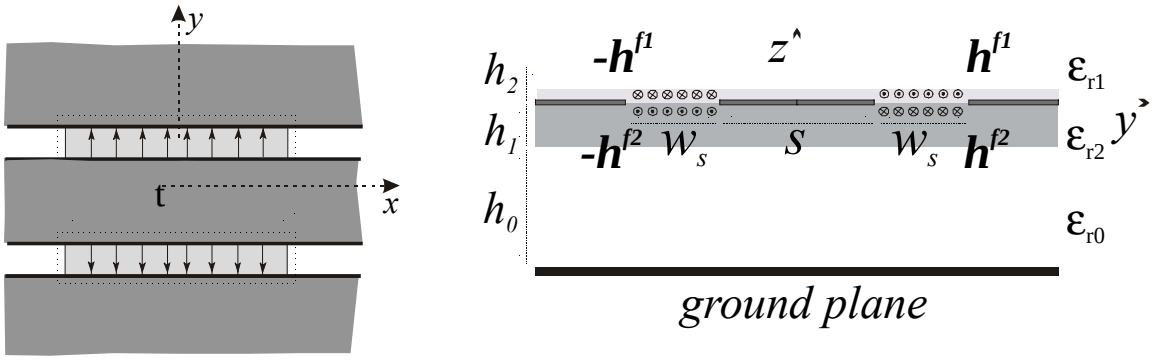

Fig. 1 Investigated geometry, top view and cross section

The separation between the internal edges of the slots is indicated as *s*. The induced RF currents $j_f \, \boldsymbol{i}_y$ may be interpreted by means of the equivalence principle as an x-oriented magnetic field discontinuity $(h^{f+}-h^{f-})\cdot\hat{i}_x = h^f\cdot\hat{i}_x$, impressed at $z=0^{\pm}$. The forcing magnetic fields are required to be equal and opposite in phase in slot "1" and slot "2" in order to be compatible with a propagating mode on the structure: $h^f(x,y)=-h^f(x,-y)$. Resorting to the equivalence principle the slotted regions are replaced by infinite, perfectly conducting surfaces with two unknown magnetic current distributions $\pm\boldsymbol{m}$ (immediatety above and below the CPW plane). These currents have equal amplitude and opposite signs, to ensure the continuity of the electric tangent fields through the CPW. Moreover, they are assumed x oriented due to the small cross sections of the two slots, i.e. $\pm\boldsymbol{m}=\pm m\cdot\hat{i}_x$. Thus, a scalar integral equation can be formulated which enforces the continuity of the total (impressed plus radiated) magnetic field on the CPW:

$$\int_{\Sigma_y}\int_{-\infty}^{+\infty}[g_{xx}(x-x';y-y')]\cdot m(x,x')dx'dy' = -h^f(x,y), \qquad (1)$$

where $\Sigma_y=[(-s/2-w_s,-s/2)\cup(s/2,s/2+w_s)]$ is the region of the slots; and $g_{xx}(x,y)$ is the sum of $g^1_{xx}(x,y)$ and $g^2_{xx}(x,y)$, the Green's functions pertinent to the lower and upper multi-layered half spaces, respectively. This integral equation is enforced on the two axis of the slots that compose the CPW by employing a point matching procedure – this is formally equivalent to weighting Eq. (1) over the transverse domain Σ_y with a two Dirac delta functions having opposite signs centered on $\pm a$. As anticipated, the magnetic current distribution dependence is separable in *x* and *y*, i.e. $m(x,y)=m_x(x)\cdot m_y(y)$. An edge singular behavior is assumed for the *y* dependence of the magnetic currents:

$$m_y(y)=\frac{2}{\pi w_s}\left[\frac{\mathrm{rect}(y+a,w_s/2)}{\sqrt{1-\left[\frac{2(y+a)}{w_s}\right]^2}}-\frac{\mathrm{rect}(y-a,w_s/2)}{\sqrt{1-\left[\frac{2(y-a)}{w_s}\right]^2}}\right], \tag{2}$$

where the $\mathrm{rect}(y,T)$ is the existence function equal to unity for $|y|\le T$ and zero elsewhere. The normalization of m_y is chosen to give unitary value when integrated on the transverse dimension of each of the slots. Moreover, the currents have opposite signs since a propagating mode is being excited on the CPW.

The integral equation can then be solved in the spectral domain and it is only dependent on the x variable. After a few algebraic manipulations it can be shown that the magnetic current distribution can be expressed as an inverse Fourier-transform:

$$m_x(k_x)=\frac{1}{2\pi}\int_{-\infty}^{+\infty}M_x(k_x)\,e^{-jk_x x}\,dk_x \tag{3}$$

with

$$M_x(k_x)=\frac{-2H_x^f(k_x)}{\frac{1}{2\pi}\int_{-\infty}^{+\infty}G_{xx}(k_x,k_y)\cdot J_0\left(k_y\frac{W_s}{2}\right)\cdot\left[-j2\sin(k_y a)\right]^2\,dk_y}. \tag{4}$$

Equations (3)-(4) constitute the basic tools for the investigation of the distributed source characterization of the CPW that will follow in the next section. The integration path selection criteria for Eq. (3) and the properties of the singularities that arise from denominators in Eq. (4) are treated in detail in [1], [2] for a slot line printed between two different homogeneous dielectric half spaces. The integral in Eq. (3) can be performed by adopting a deformation in the complex plane below the real axis for $\mathrm{Re}(k_x)<0$ and above the real axis for $\mathrm{Re}(k_x)>0$.

III. DISTRIBUTED CURRENT SOURCE IN THE CPW: DESIGN CRITERIA

Equation 3 provides the framework to quantitatively determine the design parameters that optimize the coupling of power from the photo-induced current to the quasi-optical system. The reason for investigating distributed sources is the necessity to avoid the high laser densities required for operation of the small area photo-mixer devices. An active area with a length on the order of a few effective wavelengths would allow reducing the laser power density significantly below the damage threshold. Choosing an arbitrary length for the gain region may or may not guarantee preferential coupling to a forward traveling wave rather than to a backward traveling one. The backward traveling wave would render the design sensitive not only to the location of the CPW-antenna transition but also the opposite end where the DC bias leads attach. The following three guidelines were followed to obtain an optimal design:

a) The phase velocity of the impressed current distribution should match the group velocity of the quasi-TEM guided mode of the CPW.
b) The length of the active area in the extended CPW should guarantee that RF power is coupled only to the forward traveling wave.
c) The characteristic impedance of the CPW line should be matched to the antenna impedance.

III.1 Phase matching.

The CPW quasi-TEM guided mode propagation constant can be found by numerically investigating the dispersion equation $D(k_x) = 0$. The search for a solution can be restricted to the real axis and the two poles of the structures, $\pm k_{xp}$ are found in the top Riemann sheet for $k_{zi} = \sqrt{k_i^2 - k_x^2 - k_y^2}$, $i = 0,1$ and 2.

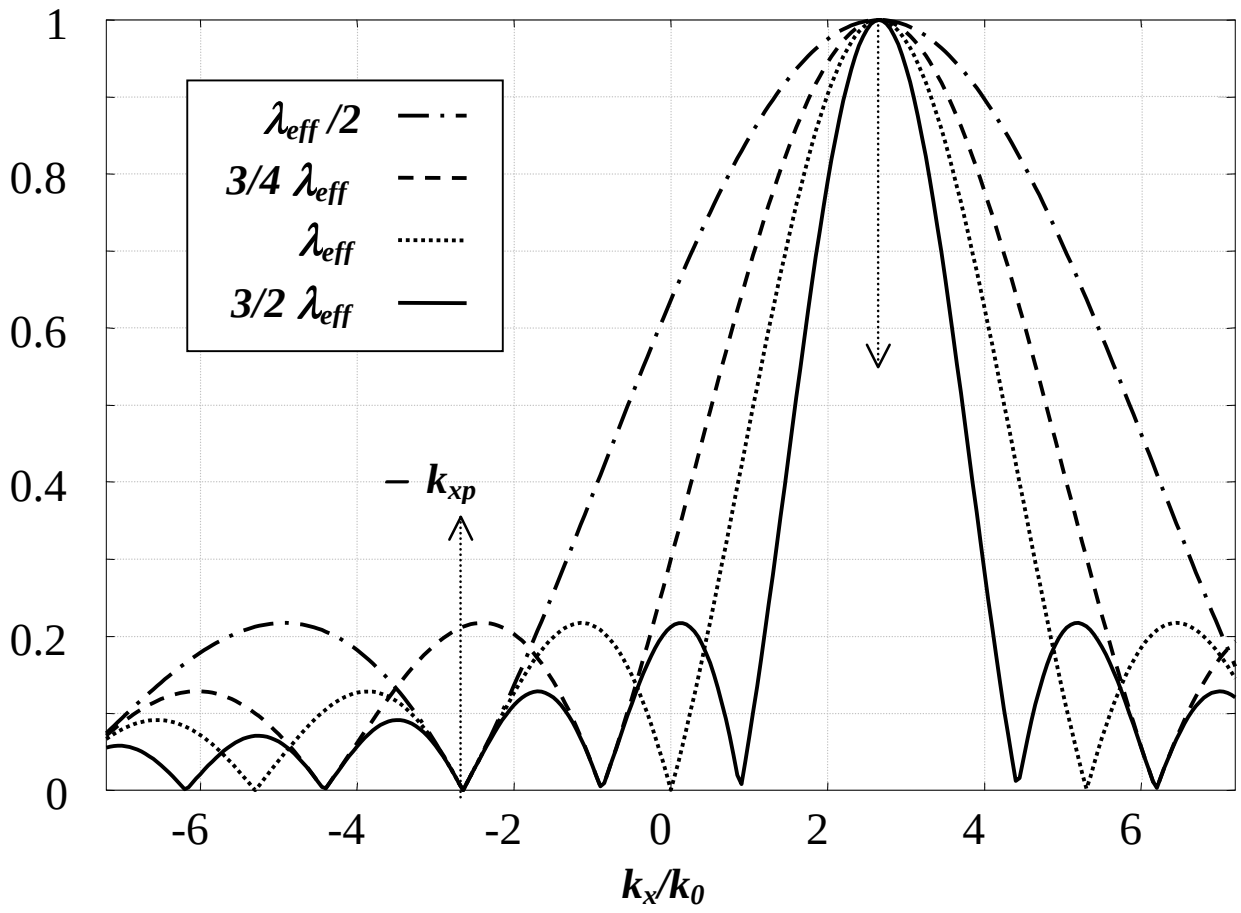

Fig. 2 Fourier transform of the impressed magnetic field for distributed excitations over different active area lengths

Thus, possible branch point singularities and branch cuts in the k_x-plane, arising from the fact that $D(k_x)$ is a multi-valued function [2], are avoided when the attention is restricted to the main quasi-TEM mode. Once k_{xp} is known we verified numerically the well

known principle that an impressed RF current tends to couple to the CPW when the phase velocity of the current (k_{x0}) matches the intrinsic quasi-TEM propagation constant of the structure, i.e. $k_{x0} = k_{xp}$.

III.2 Optimal length of the active area.

The second key design parameter can be extracted from the analysis is the optimal extension of the active area. Figure 2 shows the Fourier transforms of the impressed magnetic fields when distributed on different active area lengths of the CPW. In all cases the Fourier transforms are sinc functions where the maximum corresponds to $k_x = k_{xp}$. It should be noted that when the dimension of the active area is an integer multiple of half the effective wavelength the spectrum of the distribution is equal to zero in

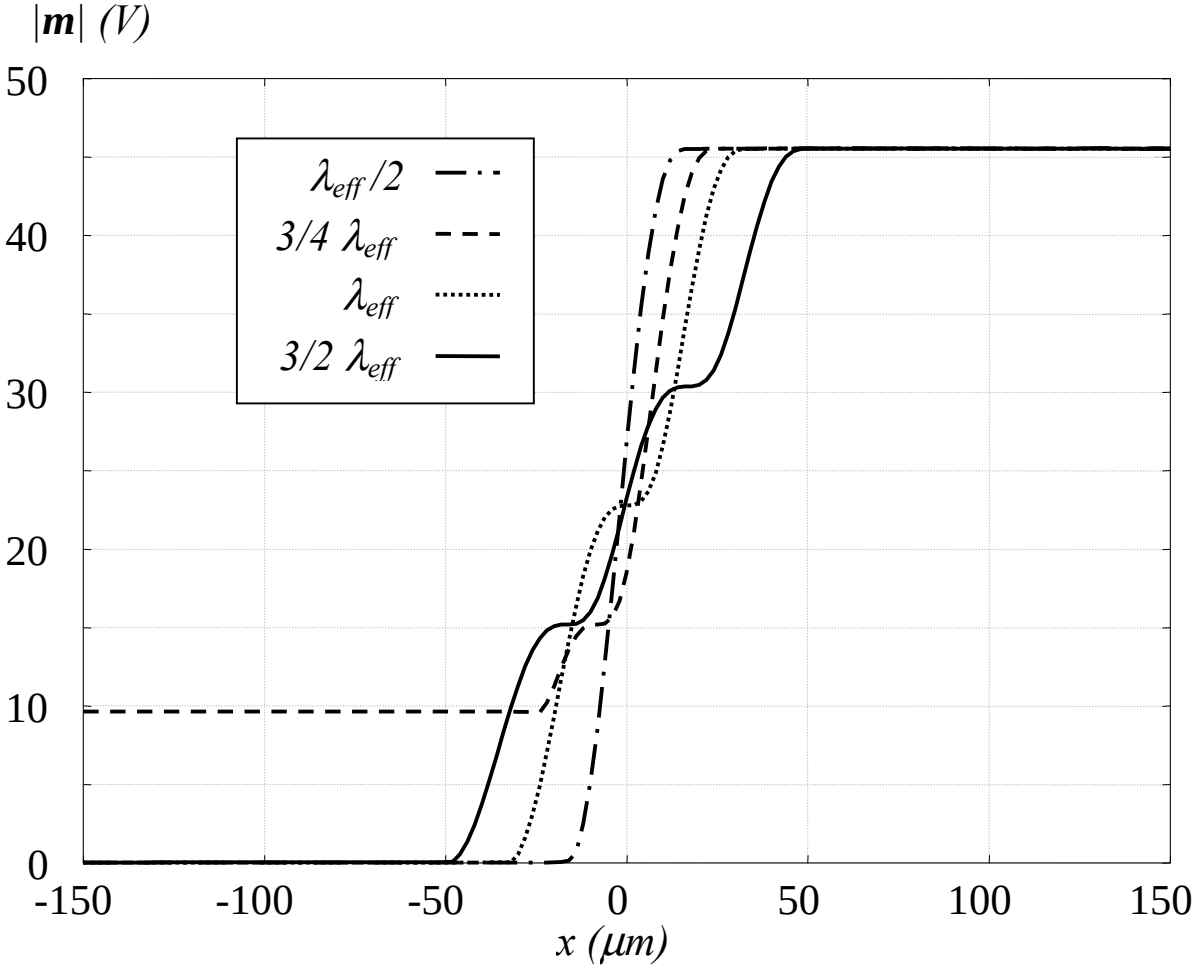

Fig. 3 Magnetic current amplitude on CPW line at the end point of an excitation region indicated in the inset

$k_x = -k_{xp}$. Since the integration in Eq. (6) is widely dominated by pole contributions on the real axis, a zero in $k_x = -k_{xp}$ provides a zero-pole cancellation such that no power is

coupled to the backward traveling wave. For gap excitations over small areas, the power would be equally distributed in the forward and the backward propagating traveling wave.

This is shown in **Fig 3** where the magnetic current distributions are shown as a function of x for the same total forcing field (impinging laser power). The selected CPW is characterized by h_2 = 2.25 μm, ε_{r2} = 12.9, h_1 = 0.1 μm, ε_{r1} = 7.0, h_0 = 35.0 μm , w_s = 0.7 μm, s = 1.5 μm. It is worth noting that for an active area of $3/4\,\lambda_{\text{eff}}$ a significant fraction of the power is also launched backward.

III.3 Impedance matching antenna-CPW.

The asymptotic value of the magnetic current amplitude at large distance from the active area, when the phase velocity of the impressed field matches the phase velocity of the quasi TEM mode in the CPW is the characteristic impedance of the line. Two considerations determined the transverse geometrical dimensions of the CPW:

a) The characteristic impedance needs to be as low as possible since it is difficult to achieve a high impedance with slots operating on the second resonance in the given dielectric configuration.
b) The width of the CPW inner conductor should be small in order to minimize the laser power reflected from the metal.

A value of 45 Ω has been set as target for the characteristic impedance. Taking into account that the fabrication tolerance is on the order of 0.1 μm a width of >0.5 μm seemed feasible. In order to achieve such an impedance level a double slot antenna configuration has been chosen. The slots are series fed by the optically pumped CPW, and they are separated by one effective wavelength (λ_{eff}) in order to obtain the mandatory broadside radiation requirement that is guaranteed by equal magnetic currents in the two slots. The slots are designed to present purely real active impedance (the impedance of each slot when also the other are excited) at the design frequency. So the λ_{eff} separation guarantees, by simple transmission line considerations, that the eventual input impedance of the entire antenna system is the sum of these active impedance's.

IV. DOUBLE SLOT DESIGN *(1.7 THz)*

Two slots of length 90μm and width 12 μm are sufficient to provide about 45 ohms of input impedance. The slots are separated by a distance equal to 64 μm. The stratification is the same used for fig. 5. The reflection coefficient in the band 1.6 THz to 1.9 THz is shown in Fig. 4. It shows a match better than 20 dB at a central frequency of 1.77 THz and 6% relative bandwidth at –10 dB. The normalized magnetic currents in the two different slots are shown to be equal in Fig. 5, where the real and imaginary part of the currents at the frequency of 1750 GHz are superimposed. The separation between the two slots ($\lambda_{eff} \cong 0.38\ \lambda_0$) represents a slightly over-sampled array and this causes a non

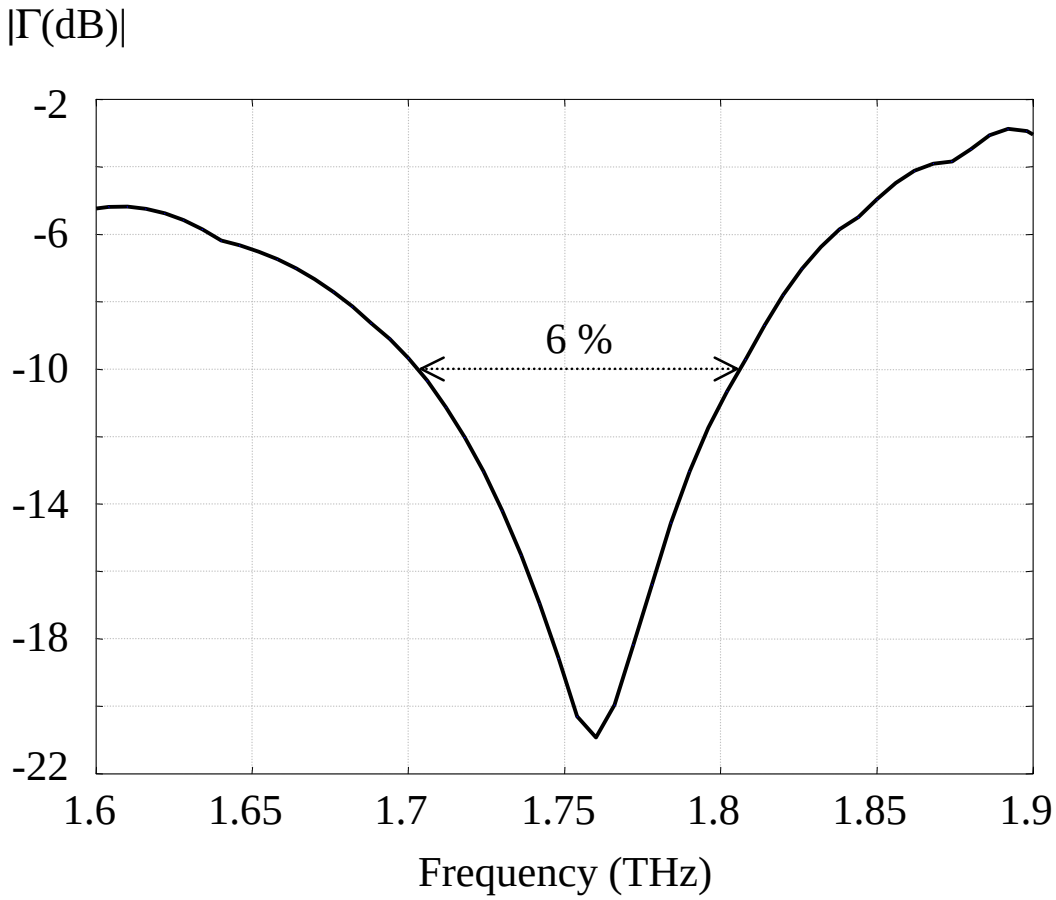

Fig. 4 Reflection Coefficient for a double slot antenna

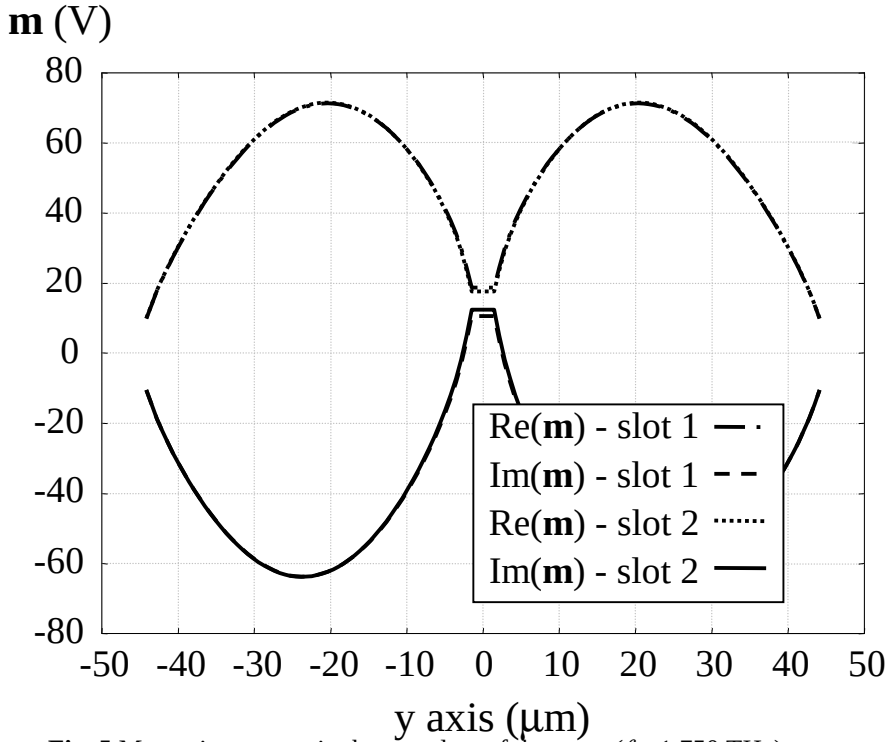

Fig. 5 Magnetic currents in the two slots of the array (*f* = 1.750 THz)

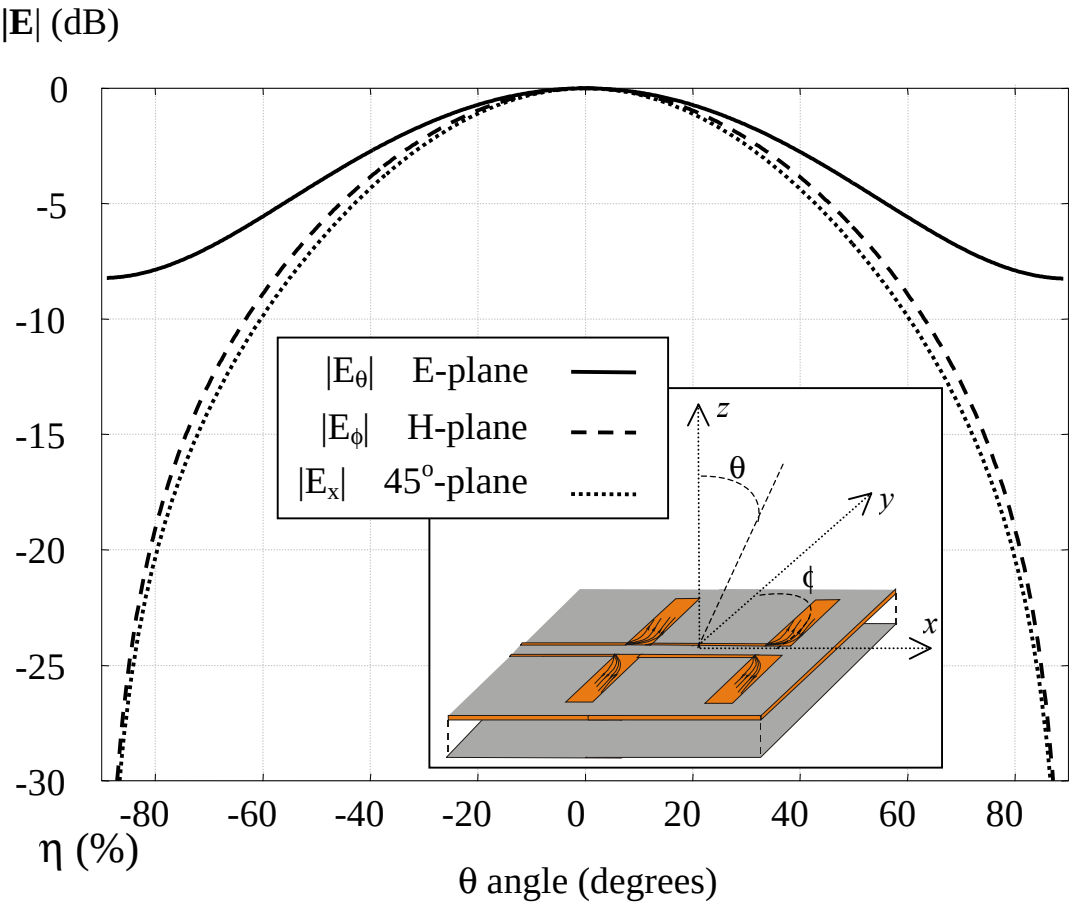

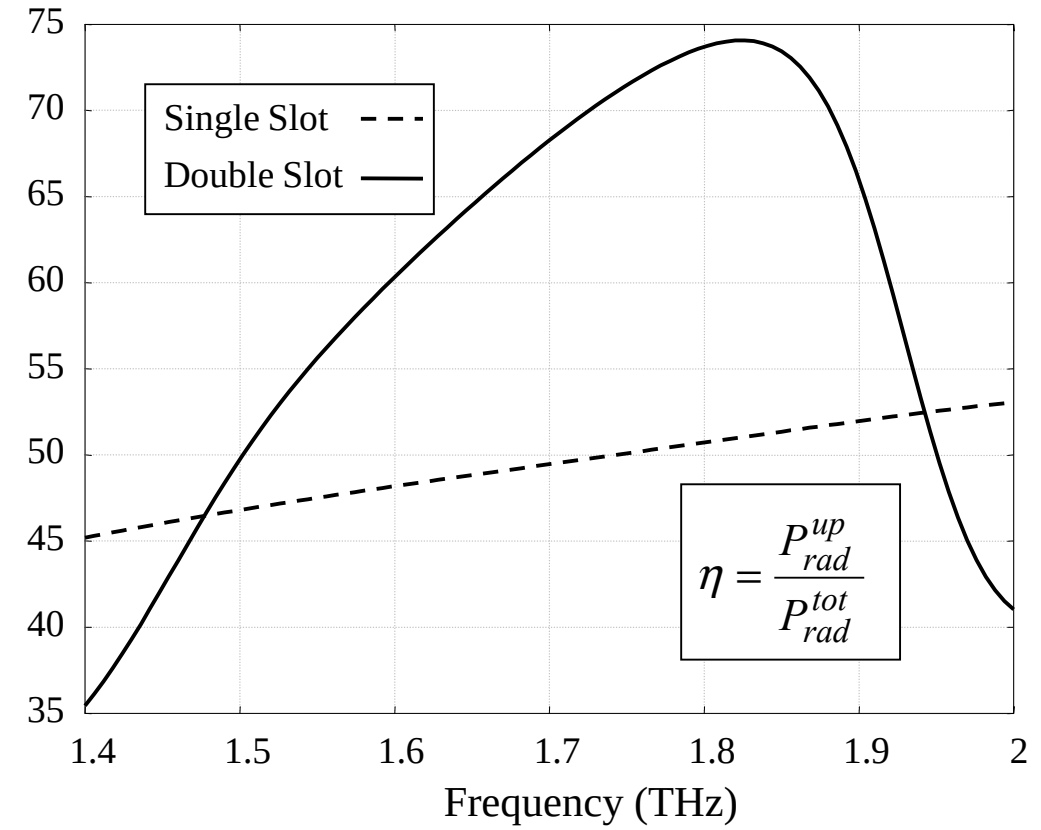

Fig. 6 (a) Copolar radiation pattern of double slot array antenna. (b) Radiation efficiency: comparison between the double slot array and a single slot

perfectly rotationally symmetric pattern, as in Fig. 6a where the copolar radiation pattern of double slot array antennais shown. E_θ field in E-plane (continuous line); E_ϕ field in H-plane (dashed line); E_x field in diagonal plane (dotted line). On the other hand, with this separation a good efficiency (η), intended as the ratio of the power radiated in free space and the power lost in the parallel plate wave-guide mode is obtained (Fig 4b). The efficiency is significantly better than the one of the single slot antenna, also reported in Fig. 6b, thanks to the cancellation of the waves launched in the inhomogeneous PPW by the two slots.

VI. CONCLUSIVE CONSIDERATIONS

A travelling wave, CPW based designs of optically pumped LO's for 1.7 THz frequencies has been presented. The designs are based on separate steps to optimize first the coupling from the R.F. currents photo-induced to a forward traveling wave on the CPW, and then the coupling from the CPW to free space by means of double slot antenna. The theoretical aspects of the distributed source excitations of CPW on thin membranes. The validity of the design considerations presented has been verified by means of full wave MoM simulations of the entire structure. The designs are at the present time being manufactured and the results achieved will be the object of a future publication.

Reference

[1]A. Neto, S. Maci "Analytical Solution for Gap-Excitated, infinite Printed Slot Lines", to be presented to IEEE Antennas and Propagation Symposium (Boston July, 2001) and in preparation as full paper.

[2] Mesa, F.; di Nallo, C.; Jackson, D.R. "The theory of surface-wave and space-wave leaky-mode excitation on microstrip lines" on IEEE Transactions on Microwave Theory and Techniques, Volume: 47 Issue: 2 , Page(s): 207 -215, Feb. 1999

TRAVELING-WAVE MEMBRANE PHOTOMIXERS

R.A. Wyss, S.C. Martin, B.J. Nakamura, A. Neto, D. Pasqualini[†], and P.H. Siegel

Jet Propulsion Laboratory, California Institute of Technology, Pasadena, CA 91109

C. Kadow[‡] and A.C. Gossard

Materials Department, University of California – Santa Barbara, Santa Barbara, CA 93106

Abstract

Traveling-wave photomixers[1] have superior performance when compared with lumped area photomixers[2] in the 1 to 3 THz frequency range. Their large active area and distributed gain mechanism assure high thermal damage threshold and elimination of the capacitive frequency roll-off. However, the losses experienced by the RF wave traveling along the coplanar strips waveguide (due to underlying semi-infinite GaAs substrate) were a serious drawback. In this paper we present device designs and an experimental setup that make possible the realization of photomixers on membranes which eliminate the losses.

Present address: [†]Department of Information Engineering, University of Siena, Italy; [‡]Nortel Networks, Wilmington, MA 01887.

[1]S. Matsuura, G.A. Blake, R.A. Wyss, J.C. Pearson, C. Kadow, A.W. Jackson, and A.C. Gossard, "A traveling-wave THz photomixer based on angle-tuned phase matching", *Appl. Phys. Lett.* **74**, 2872 (1999).

[2]S. Verghese, K.A. McIntosh, and E.R. Brown, "Optical and terahertz power limits in the low-temperature-grown GaAs photomixers", *Appl. Phys. Lett.* **71**, 2743 (1997).

Photomixer as a self-oscillating mixer

Shuji Matsuura

The Institute of Space and Astronautical Sciences, 3-1-1 Yoshinodai, Sagamihara, Kanagawa 229-8510, Japan. e-mail:matsuura@ir.isas.ac.jp

Abstract

Photomixing with low-temperature-grown (LTG) GaAs photomixers is known as a promising technique to generate the coherent radiation in the terahertz (THz) range. In principle, the photomixer could also be used for detecting the THz radiation as a tunable heterodyne mixer with an internal local oscillator, and such a self-oscillating mixer would allow us to construct a simple and tunable receiver system without external local oscillator source. According to a simple photoconductor theory, the conversion efficiency and the noise of the LTG-GaAs photomixer receiver are estimated. It is shown that the performance of the photomixer receiver is reasonably high, if the device design is optimized to get a high photoconductivity, and if the device is cooled down to minimize the thermal noise contribution.

1. Introduction

Optical heterodyne mixing (photomixing) in photoconductors (photomixers) with miniature planar antenna has recently become an attractive method to generate the coherent radiation in the THz range. It has been demonstrated that the photomixer offers relatively high efficiency and extremely wide tuning range [1, 2]. The low-temperature-grown (LTG) GaAs is the most widely used material for the photomixing because of its short response time (carrier lifetime) in the sub-picosecond range (τ <1 ps) and relatively high mobility (μ >100 cm^2/V/s). The LTG-GaAs photomixer have already been used for laboratory spectroscopy, and it has been shown that its spectral purity and THz output power are sufficient for such spectroscopic applications [3].

A schematic view of the LTG-GaAs photomixer as a THz source is shown in Fig. 1.

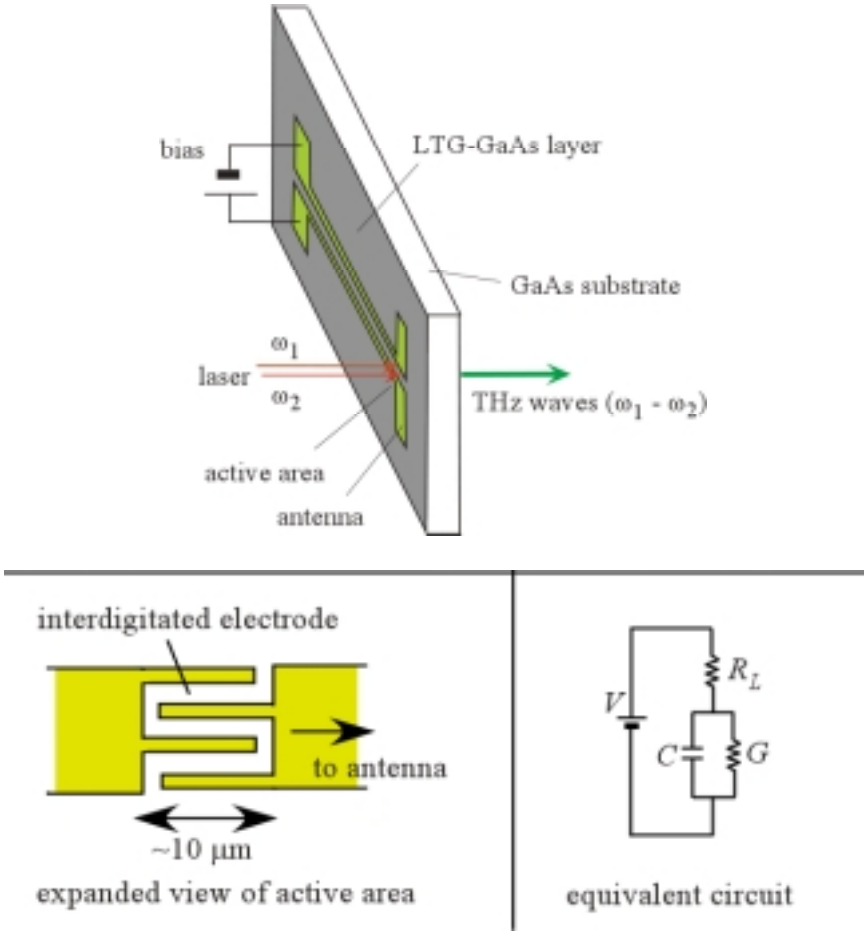

Fig. 1: Schematic view of the photomixer as a THz source.

The active area, consisting of the DC-voltage biased interdigitated electrodes fabricated on the LTG-GaAs layer, is simultaneously illuminated by two single-mode cw lasers at λ850 nm. Beating between the two overlapping laser beams creates a varying optical power at the difference frequency, which modulates the photoconductance. The resultant AC photocurrent is then coupled to a miniature planar antenna patterned on the LTG-GaAs surface. Most of the radiation power goes into the substrate, which has a high dielectric constant (ε=12.8 for GaAs).

According to the reciprocity between transmitting and receiving antenna, the photomixer should be usable not only for the wave generation but also for the detection. The detection principle is the inverse process of the wave generation as illustrated in Fig. 2; small perturbation in the photocurrent induced by the incoming THz field can be measured as the DC current or the IF signal. The LTG-GaAs photomixer receiver has in

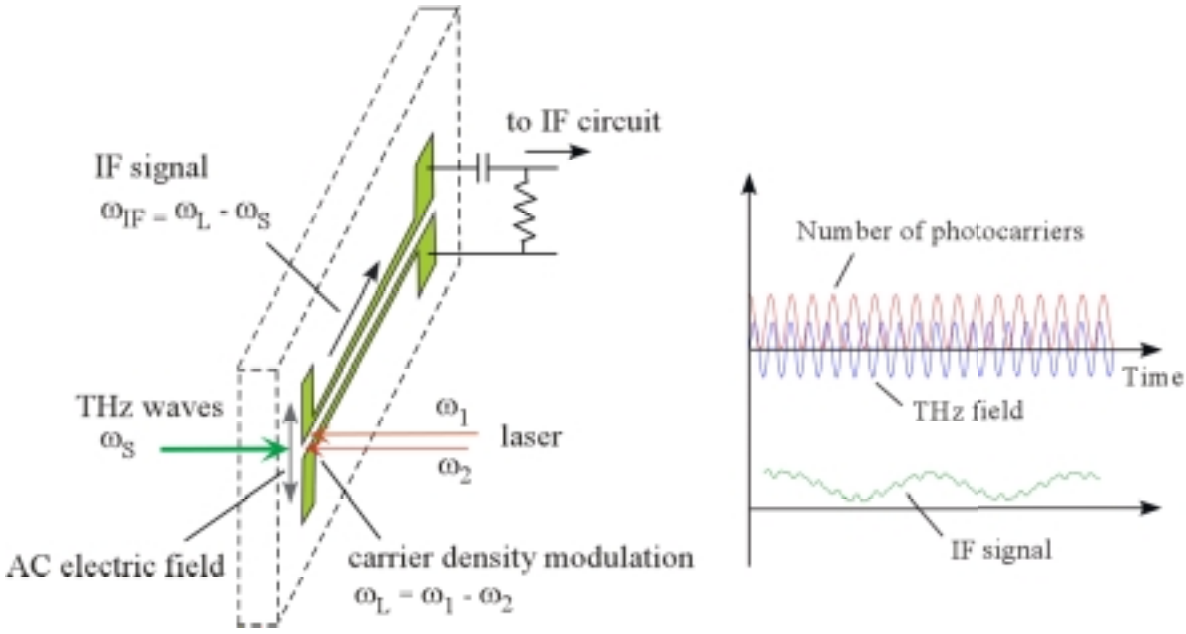

Fig. 2: The principle of the photomixer receiver.

fact been used in the THz homodyne system and has provided high signal-to-noise frequency-domain spectroscopy data even at the room temperature [4, 5].

In principle, the photomixer can be used to detect not only the coherent radiation but also the incoherent radiation as a tunable heterodyne receiver with an internal local oscillator. Such a self-oscillating mixer would allow us to construct a very simple receiver system without external local oscillator. In this paper, the operation of the photomixer as a self-oscillating mixer is proposed, and its performance, the conversion efficiency and the noise temperature, is estimated for the LTG-GaAs photomixer.

2. Photomixer operation in heterodyne mixer mode

The principle of wave detection by the photomixer is regarded as the inverse process of the wave generation by photomixing as illustrated in Fig. 2. When the THz radiation is externally injected to the photomixer whose active area is illuminated by two lasers, the THz field induces the AC bias voltage to the electrode via the antenna. If the temporal change of the photoconductivity at the difference frequency of the two lasers coincides with the external THz field in phase, the rectification of the THz waves takes place, and then the DC current is generated. In the case that the difference frequency is different from

that of the incident THz waves, the intermediate frequency (IF) current signal instead of the DC current should be generated. The IF signal is transmitted to the post-mixer amplifier the same as conventional heterodyne mixers. The photomixer should be operated at zero-bias or minimum DC current in order to minimize the current noise as discussed later, in contrast that for the emitter higher bias voltage is required to obtain higher photocurrent.

The photocurrent induced by the electric field, *E*, is given by

$$I = \frac{ne\mu E}{l} = GV\,, \tag{1}$$

where μ is the mobility, l is the gap size of the interdigitated electrodes, G is the photoconductivity, and V is the voltage corresponding to $E=V/l$. The photoconductivity modulated at the difference frequency of the two lasers, $\omega_L = \omega_1 - \omega_2$, is expressed as

$$G = G_0\left(1 + \frac{\sin\omega_L t}{\sqrt{1+(\omega_L\tau)^2}}\right), \tag{2}$$

where

$$G_0 = \frac{\eta P_L \tau}{h\nu}\cdot\frac{e\mu}{l^2}\,, \tag{3}$$

τ is the carrier lifetime of the photomixer material, η is the external quantum efficiency of the photomixer, and P_L is the total input laser power. The initial phase of the oscillation is set to be zero. The AC bias voltage induced by the THz field, $V = V_0\sin(\omega_S t + \phi)$, and the temporal change of the photoconductivity induced by the laser beating create the photocurrent at the intermediate frequency (IF), $\omega_{IF} = \omega_L - \omega_S$,

$$I_{Ph} = \frac{G_0 V_0 \cos(\omega_{IF} t - \phi)}{\sqrt{1+(\omega_L\tau)^2}\sqrt{1+(\omega_L R_A C)^2}}\,, \tag{4}$$

where the second term of the denominator represents the roll-off due to the device time constant; R_A is the antenna impedance, and C is the electrode capacitance. If the bandwidth of the IF circuit is sufficiently wide compared with the reciprocal of the coherence time of the input THz radiation, the amplitude of the IF signal power should be comparable to that for the coherent radiation.

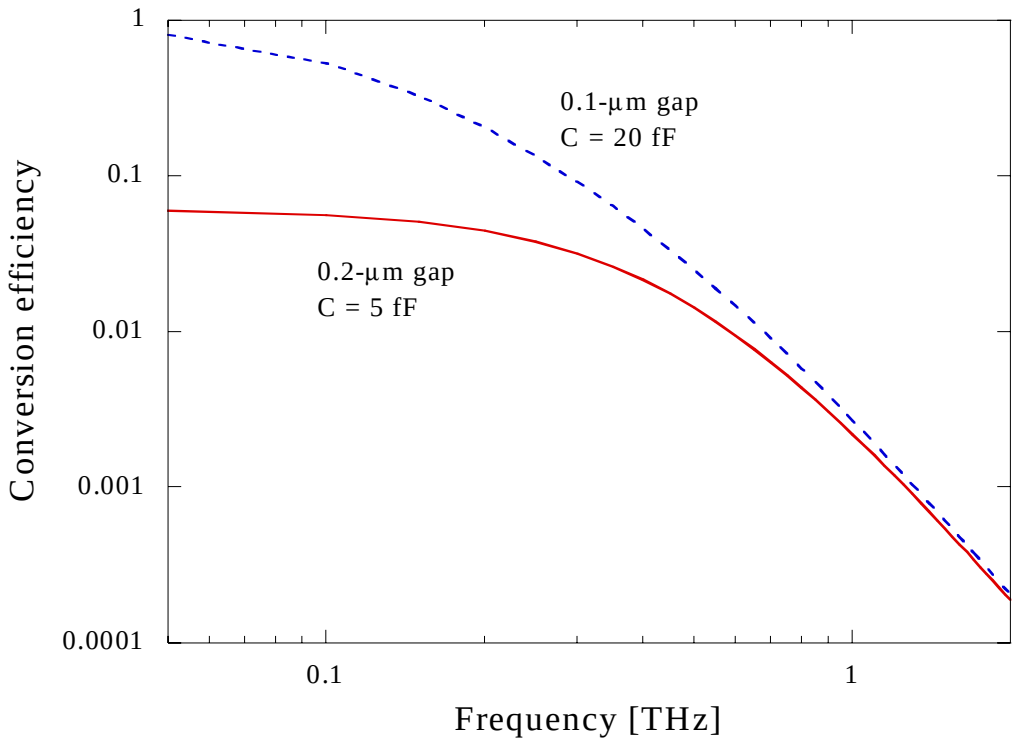

Fig. 3: The conversion efficiency of the photomixer receiver. The solid and dashed curves represent the estimation for the self-complimentary broadband antenna (R_A=72 Ω) device with 0.2-μm and 0.1-μm gap electrodes, respectively.

3. Conversion efficiency

When the THz radiation is injected to the photomixer, the induced voltage across the electrode gaps is

$$V_0 = \sqrt{2P_S R_A}\,, \tag{5}$$

where P_S is the injected THz power, and R_A is the antenna impedance. The average power delivered to the IF load is given by

$$P_{IF} = \overline{I_{Ph}{}^2} Z_L\,. \tag{6}$$

From Equations 4, 5 and 6, the conversion efficiency is obtained as

$$\Gamma \equiv \frac{P_{IF}}{P_S} = \frac{{G_0}^2 R_A Z_L}{[1+(\omega_L \tau)^2][1+(\omega_L R_A C)^2]}. \qquad (7)$$

From Equations 3 and 7, it is clear that the conversion efficiency can be greatly improved by narrowing the electrode gaps ($\Gamma \propto l^{-4}$).

By substituting the parameters for the LTG-GaAs photomixer into above equations; η = 1, P_L = 40 mW, τ = 0.3 ps, μ = 200 cm^2/V/s, R_A = 72 Ω for the self-complimentary antenna on GaAs, Z_L = 50 Ω, and 20 interdigitated electrodes with the width of 0.2 μm and 19 gaps with l = 0.2 μm (C = 5 fF) [6], the conversion efficiency is calculated to be about 6% at DC. The frequency dependence of the conversion efficiency is shown in Fig. 3. Although these efficiency values are much lower than that for superconducting mixers, they are still in a useful range.

4. Mixer noise

There are several possible noise sources in the photomixer receiver, photocurrent fluctuation and Johnson noise. The current fluctuation due to the random process of generation and recombination of the photocarriers in the photoconductor is known as the G-R noise. The current fluctuation due to the G-R noise in the IF bandwidth of Δf is given by

$$\overline{I_{GR}^2} = 4\overline{I_{Ph}^2} \cdot \frac{h\nu}{\eta P_L} \cdot \Delta f . \qquad (8)$$

It is assumed that the photomixer is operated at zero-bias field and that only the AC bias induced by the THz radiation is applied. The signal-to-noise power ratio is

$$\frac{S}{N} = \frac{P_{IF}}{P_{GR}} = \frac{\eta P_L}{4h\nu\Delta f}. \qquad (9)$$

The G-R noise limited S/N depends only on the input laser power but the incident THz power. Once the input laser power is set, the S/N cannot exceed this value, even if the THz signal is very strong compared with the other noise. The situation is similar to that the quantization noise of the A/D converter limits the maximum S/N. For the laser power of 40 mW and the bandwidth of 1 GHz, the S/N is higher than 10^7. Therefore, in most cases, this noise should not limit the minimum detectable THz power.

For real setup, it would not be very easy to obtain the perfect zero bias condition, because the electrode contact may not be ohmic and the photovoltaic effect may occur in

the device [5]. If the DC electric field ($V_{DC} = l\,E_{DC}$) exists, the minimum detectable power (MDP) is calculated as

$$MDP_{GR} = \frac{2h\nu V_{DC}^{\ 2}}{\eta P_L R_A} \cdot \Delta f \ . \qquad (10)$$

If P_L=40 mW and V_{DC}=0.1 V are assumed, the mixer noise temperature limited by the photocurrent noise is T_M~70 K. Since the assumed DC field is close to the maximum available value for LTG-GaAs, in most cases this noise level would be close to the upper limit and small compared with thermal noise described as follows.

Thermal fluctuation of the photoconductivity, the laser power fluctuation, and the background photon noise are also possible noise sources, and their noise levels should be similar to the photocurrent noise estimated here.

At relatively high temperature, Johnson noise contributes to the photomixer noise. For the parameter used before, the resistance of the photomixer, R=1/G_0, is approximately 240 Ω. The noise current is given by

$$\overline{I_J^{\ 2}} = \frac{4kT}{R} \cdot \Delta f = 4kTG_0 \Delta f \ , \qquad (11)$$

and the MDP is

$$MDP_J = \frac{2kT}{G_0 R_A} \cdot \Delta f \ . \qquad (12)$$

When the photomixer is operated at the room temperature (T=290 K), the active area is locally heated up by the laser to T~190 K [2], and the mixer noise temperature is T_M~1300 K at low frequency limit.

5. Possible improvement

The conversion efficiency could be improved by using the photomixer material with longer carrier lifetime, in particular at lower frequencies. Even at higher frequencies the efficiency may become better by increasing the carrier lifetime, because the mobility may also increase with increasing the carrier lifetime. Same argument should be concluded for the photomixer THz source, but we have actually used the LTG-GaAs with the shortest carrier lifetime by the following reason. When the material with much longer carrier lifetime is used, the AC current oscillating at the THz frequency is a small fraction in the total photocurrent, and it may be easily destructed by the random fluctuation of the

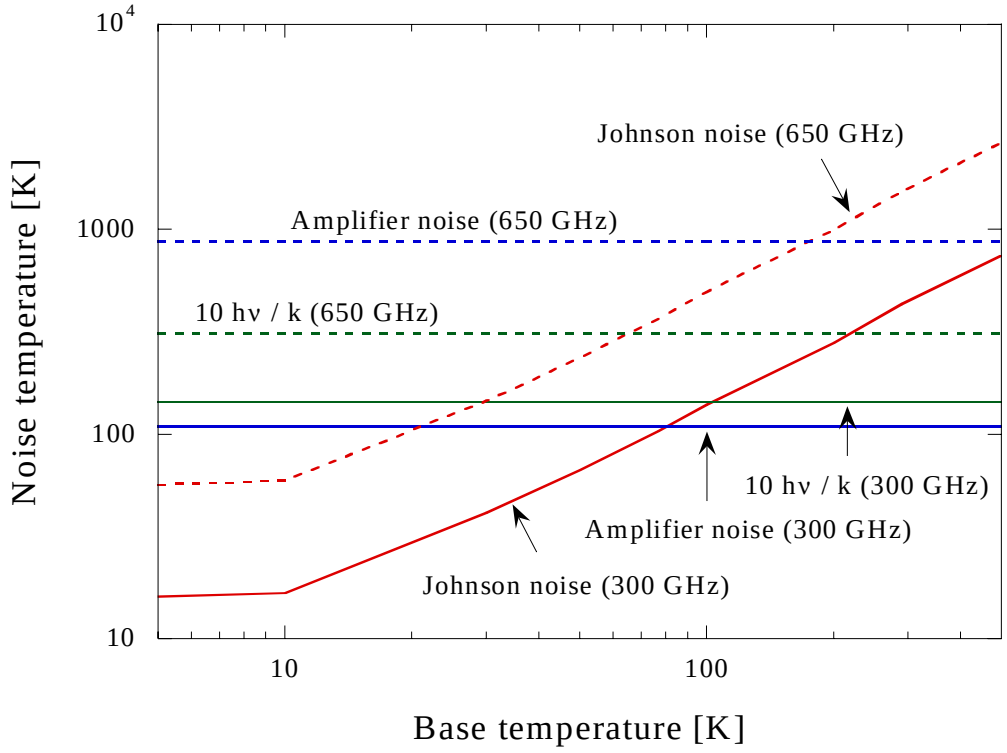

Fig. 4: The noise temperature for the 0.1-μm gap device at 300 GHz and 650 GHz as functions of the ambient temperature. The noise contribution from the post-mixer amplifier, $\Gamma^{-1}T_A$, for T_A=10 K and the quantum noise limit $10h\nu/k$ are also indicated.

DC photocurrent. The optimum carrier lifetime for the receiver may be much longer than that for the source, because it is operated at the zero bias, which the photocurrent fluctuation is small.

As shown before, the conversion efficiency is highly dependant on the electrode gap. The conversion efficiency of the device with 0.1-μm wide and 0.1-μm gap electrodes and with the same active area as the 0.2-μm gap device is shown in Fig. 3. This device shows great improvement in the efficiency at lower frequencies but not much at higher frequencies because of its large capacitance, C=20 fF. If the resonant antenna device is used, the capacitive part of the antenna impedance can be canceled out, and then high efficiency can be achieved at a certain frequency. The traveling-wave photomixer has also potential to overcome the RC-limited bandwidth problem, and it would offer better

efficiency at higher frequencies [7].

If the photomixer is cooled down to the liquid nitrogen temperature, the temperature of the active area becomes T=90 K [2], and the Johnson-noise-limited noise temperature for the 0.1-μm wide gap device becomes T_M~100 K at the low frequency limit. Shown in Fig. 4 is the noise temperature of the 0.1-μm wide gap device operated at 300 GHz and 650 GHz as functions of the base (ambient) temperature. According to the conversion efficiency shown in Fig. 3, the contribution of the post-mixer amplifier noise of T_A=10 K to the mixer noise, $\Gamma^{-1}T_A$, is also shown in Fig. 4. The mixer noise temperature of the photomixer receiver can approach to the quantum limit, if the device is cooled down to the liquid nitrogen temperature. Cooling the device should be also helpful to improve the conversion efficiency, because the carrier mobility increases with decreasing the temperature.

6. Conclusion

The idea on the use of the photomixer as a self-oscillating mixer (receiver) was presented. By assuming the use of the LTG-GaAs photomixer with sub-μm electrode structure, the conversion efficiency and the noise were estimated. The conversion efficiency of the photomixer receiver is low, and the post-mixer amplifier would limit the receiver noise temperature especially at higher frequencies, but the sensitivity would be still in a useful range for some applications. The improvement of the photoconductivity by narrowing the electrode gap is crucial for the improvement of the conversion efficiency and the reduction of the mixer noise. At the room temperature, the thermal (Johnson) noise dominates in the mixer noise. Therefore, the mixer noise can be greatly reduced by cooling the device. The experimental study to prove the principle is in progress.

If the device works as is expected, it allows us to construct a very compact, highly tunable, heterodyne receiver system without external LO source. Although its sensitivity is not very high compared with present-day fixed-tuned superconducting mixers, its overwhelmingly wide frequency tunability should be useful especially for space-based remote sensing applications. It is also worthy to note that the THz-wave detection technique presented here is quite general and applicable to not only the LTG-GaAs photomixer but the other types of photomixers, e.g. ultra-fast PIN photodiodes.

References

[1] E. R. Brown, F. W. Smith, and K. A. McIntosh, *J. Appl. Phys.*, **73**, 1480 (1993).

[2] S. Verghese, K. A. McIntosh, and E. R. Brown, *IEEE Trans. Microwave Theory and Tech.*, **45**, 1301 (1997).

[3] S. Matsuura, P. Chen, G. A. Blake, J. C. Pearson, and H. M. Pickett, *IEEE Trans. Microwave Theory and Tech.*, **48**, 380 (2000).

[4] S. Verghese, K. A. McIntosh, S. Calawa, W. F. Dinatale, E. K. Duerr, K. A. Molvar, *Appl. Phys. Lett.*, **73**, 3824 (1998).

[5] N. Zamdmer, Ph.D thesis, MIT (1999).

[6] Y. Chen, S. Williamson, T. Brock, F. W. Smith, and A. R. Calawa, *Appl. Phys. Lett.*, **59**, 1984 (1991).

[7] S. Matsuura, G. A. Blake, R. A. Wyss, J. C. Pearson, C. Kadow, A. W. Jackson, and A. C. Gossard, *Appl. Phys. Lett.*, **74**, 2872 (1999).

HEB Quasi–optical Heterodyne Receiver for THz Frequencies

M. Kroug, S. Cherednichenko, M. Choumas, H. Merkel, E. Kollberg
Chalmers University of Technology, Gothenburg (Sweden)
H.W. Huebers, H. Richter
DLR Institute of Space Sensor Technology, Berlin (Germany)
D. Loudkov, B. Voronov, G. Gol'tsman
Moscow State Pedagogical University, Moscow (Russia)

Abstract

The performance of NbN based HEB mixers has been investigated at THz frequencies in a receiver with quasi–optical coupling. The best performance is achieved with devices made from NbN films deposited on crystalline MgO substrates, with film thickness $d = 3.5\,\mathrm{nm}$ and a critical temperature $T_\mathrm{c} = 9 - 10\,\mathrm{K}$. Double–side band receiver noise temperatures are 530 K at 0.6 THz, 650 K at 1.6 THz and 1100 K at 2.5 THz. The intermediate frequency (IF) bandwidth is 4.5 GHz under operating conditions yielding the lowest noise temperature. Operating the bolometer at high bias voltages can increase the IF bandwidth up to 9 GHz at the expense of a drop in sensitivity by a factor of two.

1 Introduction

Superconducting hot–electron bolometers (HEB) are suitable mixers for heterodyne receivers at frequencies at and above 1 THz. Their high sensitivity and comparitively low local oscillator (LO) power requirement make them superior to other mixers like SIS junctions or Schottky diodes.

Two concepts of HEB, employing different cooling mechanisms, are under development. The diffusion cooled type, suggested by Prober [1], is a *short* bridge of niobium and cooling takes place by diffusion of hot electrons out of the ends of the bridge. In the phonon cooled type, a microbridge made from *ultrathin* niobium nitride films, electrons are predominantly cooled by inelastic scattering with phonons in the film and subsequent heat transfer into the substrate [2]. Both HEB types have been integrated into receivers with quasi–optical or wave guide coupling and have shown low noise figures at THz frequencies along with an intermediate frequency (IF) bandwidth of up to 9 GHz [3–5].

The technology for NbN based HEB mixers has been continously improved during the last years. At a level of comparitively low noise temperatures, $T_\mathrm{rec,DSB} = 650\,\mathrm{K}$ at 1.6 THz and 1100 K at 2.5 THz, less than 20 times the quantum noise $hf/2k_\mathrm{B}$, the question arises what are the limiting factors in receiver performance. In particular, what are the contributions from coupling loss and mixer conversion loss. There are methods to measure the sum of both [6], but more detailed investigations face the difficulty that different loss contributions in the submillimeter circuit (antenna, bolometer) can not easily be studied separately. For

the performance of the HEB mixer itself, predictions based on existing models can not explain experimental results in all cases, which makes it at this stage difficult to give exact design rules in order to further optimize the receiver.
This paper gives an overview of recent results obtained with quasi–optically coupled NbN based HEB mixers, possible improvements in receiver technology are discussed.

2 Measurement Set–up

Figure 1 shows the set–up used for receiver noise temperature measurements. Local oscillator sources are a BWO for 0.6 THz or a far infrared laser for 1.6 and 2.5 THz. The signal from hot/cold black body loads is combined with the LO by means of a beam splitter, a 12 μm thin Mylar foil, and injected into the cryostate through a polyethylene window. A 0.25 mm thick Zitex filter on the 4 K shield blocks IR radiation from entering the mixer. The mixer chip is clamped onto the flat side of an elliptical lens and mounted into a copper block. Lenses with a $\lambda/4$ antireflex coating made from Parylene are used for measurements at 1.6 THz and 2.5 THz. The read out line for the IF signal consists of a bias–T, a low noise amplifier (LNA) with center frequency 1.5 GHz, a room temperature amplifier, a bandpass filter and a power meter.

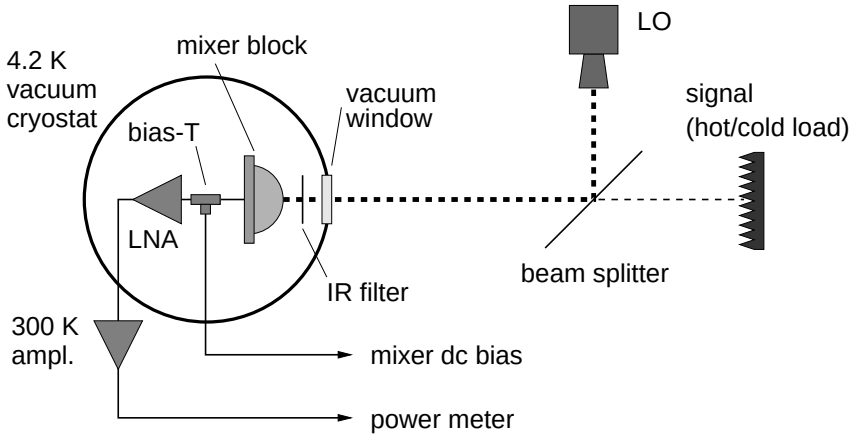

Figure 1: Schematics of the measurement set–up. The radiation coupling optics consists of "hot" (beam splitter, vacuum window) and "cold" (IR filter, lens + antenna) parts.

The absorption/reflection losses in the optics are $\sim$ 2.5 dB at 0.6 THz and increase to $\sim$ 3.5 dB at 2.5 THz (using a lens without anti reflection coating). Data for material absorption losses are taken from [7,8]. The contribution from hot parts in the optics (beam splitter, cryostat window) to the receiver noise temperature $T_{\rm rec,DSB}$ has been measured to be $\sim$ 60 K at 0.6 THz. The IF chain contributes with $25 - 75$ K, calculated from the equivalent noise temperature of the LNA, $T_{\rm IF}(1.5\,{\rm GHz}) \simeq 5$ K, and a total conversion loss of $L_{\rm tot} = 10 - 15$ dB.

3 HEB Device

The mixing element is a thin film strip of superconducting NbN on a dielectric substrate. The strip is integrated into an on–chip logspiral antenna with the antenna terminals serving as rf input and IF output port at the same time. The in–plane geometry width/length is chosen such that it yields a normal resistance R_n of the film strip close to the antenna impedance Z_A. Fig. 3 shows an SEM micrograph of one of the mixer chips.

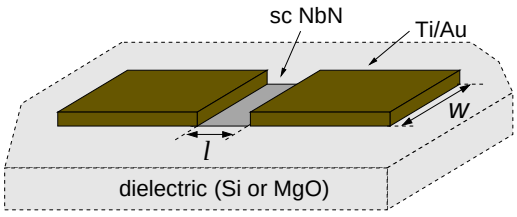

Figure 2: Schematics of the bolometer. The NbN strip with, is contacted by normal metal pads made of 5 nm Ti + 70 nm Au. The width w and length ℓ are of the order μm.

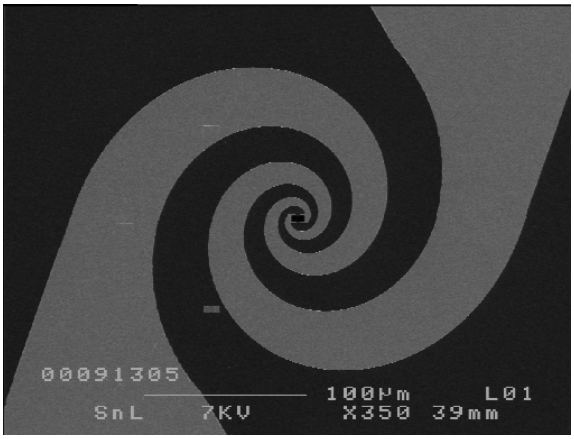

Figure 3: SEM micrograph of the antenna integrated HEB mixer.

3.1 Fabrication

The fabrication makes use of standard thin film and lithographic techniques and has been described earlier [9, 10]. Here, one aspect is looked at in more detail since it is likely to be critical for the device performance. It concerns the quality of the contact between the NbN film strip and the antenna terminals. This contact is established through pads of Ti/Au defined by e–beam lithography in a lift–off technique. The metallization process, using thermal evaporation without in–situ cleaning, requires a thin layer of Ti to achieve good adhesion. There are several reasons why the interface between the Ti/Au pads and NbN film is not ideal:[1]

- Formation of an oxide layer on the NbN film: (a) While being exposed to atmosphere (for some samples as long as months or years), (b) during resist ashing in oxygen plasma (prior to metallisation).
- The highly reactive Titanium will form compounds with contaminants on the sample surface and in the vacuum: (1) a layer of hydro carbones naturally exists on surfaces exposed to atmosphere, (2) remaining gases in the evaporation chamber, mainly oxygen, are gettered by Ti [11].

[1] The "ideal" interface could be obtained with *clean* materials deposited *in–situ*.

In a seperate study, a standard method [12] has been used to measure the specific contact resistance ρ_c between NbN film and Ti/Au pads. The results show that values vary greatly between fabrication batches, with ρ_c falling in the range $10^{-7} - 10^{-6}\,\Omega\,\mathrm{cm}^2$. We attribute this large variation to poorly controlled process parameters as described above. The absolute values for ρ_c are comparable to what is achieved with other ex–situ metallization processes and might not be critical, but in case of small contact areas $\sim \mu\mathrm{m}^2$ a resistance of up to $100\,\Omega$ can occur. The presence of such a contact resistance and consequences for device performance will be discussed in the next section.

3.2 Coupling between antenna and bolometer

Let us discuss the distribution of rf currents close to the NbN bridge: At a frequency higher than $2\Delta/h$ (with Δ the gap energy of the superconductor) the surface impedance of the NbN film equals the normal sheet resistance [13], $R_\Box \simeq 500\,\Omega$ and thus much higher than the one of gold. RF currents are therefore concentrated in the gold and will go into the NbN film only within a certain distance from the bridge edge. A first estimate is to assume this length to be of the order of the skin depth in the gold film, $\delta_{\mathrm{Au}} \approx 0.1\,\mu\mathrm{m}$ at 1 THz.

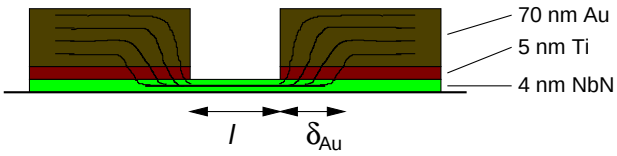

Figure 4: RF current distribution along the length of the NbN bridge.

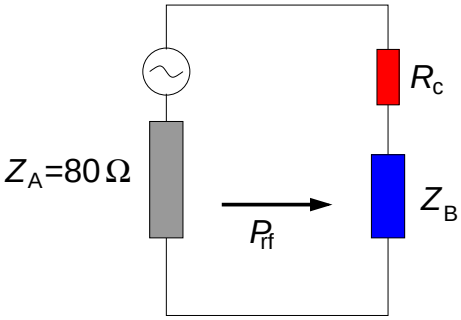

Figure 5: RF ircuit model of the antenna integrated bolometer with contact resistance.

The conclusion from this consideration is that the effective contact area $w \times \delta_{\mathrm{Au}}$ for rf currents is of the order $\sim \mu\mathrm{m}^2$, giving rise to a contact resistance R_c *in series* with the bolometer, see Fig. 5. Hence, coupling of rf–power P_{rf} into the bolometer with impedance Z_B is less efficient, additional losses will scale with the ratio R_c/Z_B.
Even though no exact values for degradation in coupling efficiency can be taken from this study, the badly controlled interface quality might explain why devices with similar film parameters differ in sensitivity performance. In order to improve reliability and reproducibility of the technology, we suggest to have initially an in–situ deposited gold layer on top of the NbN film. The gold layer is removed after patterning the micro bridge, similar to a process successfully used for fabrication of Nb diffusion cooled mixers [14, 15].

4 Receiver Noise Temperature

Noise temperature measurements have been performed at three different LO frequencies: 0.6 THz, 1.6 THz and 2.5 THz. The IF signal is measured at 1.5 GHz and the standard Y–factor method, with hot (295 K) and cold (77 K) loads in the signal path is used to determine the equivalent input noise temperature of the receiver.[2]
We will first present the data for $T_{\rm rec}$ at $f_{\rm LO} = 0.6\,{\rm THz}$ and discuss absolute values of $T_{\rm rec}$ obtained with different mixers. The frequency dependence of the receiver noise temperature is discussed in section 4.2.

4.1 Absolute value

Data of noise temperature measurments have been obtained with mixers where device parameters have been varied within a certain range, see Tab. 1.

Table 1: HEB device parameters. The critical temperature $T_{\rm c}$ is measured on the film *prior* to further processing, values of $j_{\rm c}$ are calculated from the critical current of the bolometer at 4 K.

parameter	value
d	$3-5\,{\rm nm}$
$T_{\rm c}$	$9-11.5\,{\rm K}$
w	$0.15-1\,\mu{\rm m}$
ℓ	$1-4\,\mu{\rm m}$
$R_{\rm n}$	$50-300\,\Omega$
$j_{\rm c}$	$2-8\cdot10^6\,{\rm A/cm^2}$

Lowest noise temperature, $T_{\rm rec,DSB} = 500-550\,{\rm K}$, is achieved with devices having a *low* critical current density, $j_{\rm c} = 2-3\,{\rm A/cm^2}$ corresponding to a critical temperature $T_{\rm c} = 9-10\,{\rm K}$. Their normal state resistance falls into the range $R_{\rm n} = 80-110\,\Omega$, close to what is expected to give good matching to the antenna impedance $Z_{\rm A} = 80\,\Omega$. A dependence of performance on the bolometer in–plane geometry is not observed.

4.2 Frequency Dependence

Fig. 6 shows results from receiver noise temperature measurements with 3 mixers. The devices have different in–plane geometry and are taken from 3 separated fabrication runs. The first conclusion is that the frequency dependence is similar for all mixers, irrespective of the absolute value. Quantitatively, the increase of the noise temperature is $4-5\,{\rm dB}$ when going from 0.6 THz to 2.5 THz.
The degradation in performance is partly explained by about 1 dB higher absorption losses in the optics. It is not clear yet, to which extent other loss mechanisms contribute. While

[2]The *noise temperatures* of hot and cold loads are calculated according to the formulae of Callen & Welton [16].

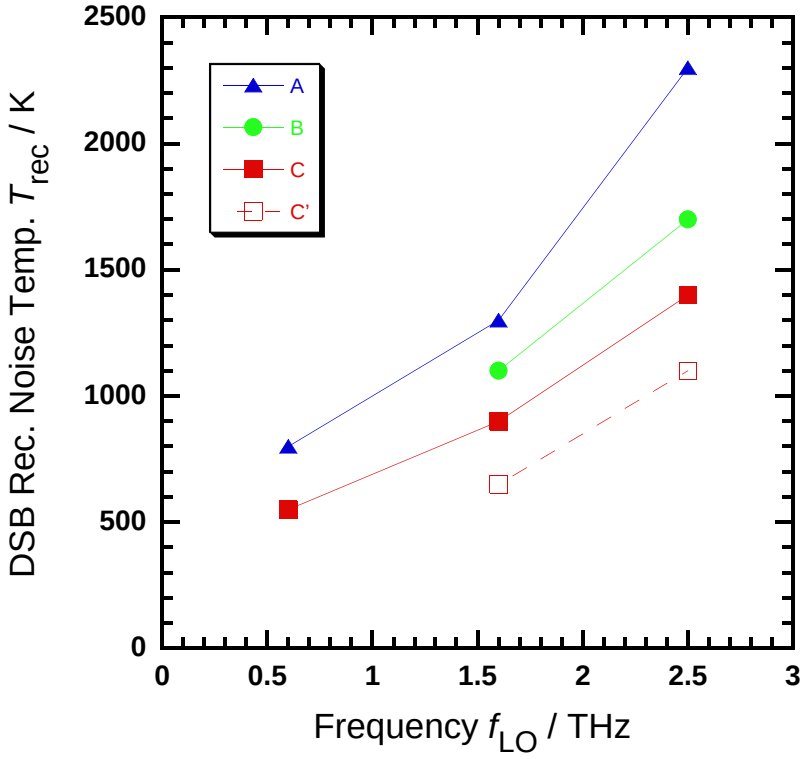

Figure 6: Frequency dependence of the receiver noise temperature for three different HEB mixers. The device in plane dimensions $w \times \ell$ are: $2 \times 0.15\,\mu$m (A), $1 \times 0.15\,\mu$m (B) and $4 \times 0.4\,\mu$m (C). Data (C′) are obtained using Si lenses with a $\lambda/4$ antireflex coating. reducing the coupling loss by about 20 % [4].

the intrinsic conversion loss of the mixer may increase, also other parts of the receiver have frequency dependent characteristics and should be investigated, it concerns:

- Coupling efficiency between free space and the lens antenna.
- Ohmic losses in the antenna.
- Losses between antenna and bolometer due to mismatch.

It has been suggested by Semenov et al. [17], that a non–uniformity in the current distribution across the width of the NbN strip due to the skin effect should be more pronounced at higher frequencies and, as a consequence, lead to increased conversion loss. This problem can be overcome by choosing a device geometry with a small width, comparable to the skin depth in the NbN film, $\delta_{\mathrm{NbN}} \approx 1\,\mu$m at 1 THz. Results from computer simulations using this approach are presented in [18].

5 IF Bandwidth

The maximum speed of a hot electron mixer is set by the electron temperature relaxation time τ_θ which is a function of the film parameters [9]. However, due to electro thermal

feedback from the IF circuit with load impedance $R_{\rm L}$, the effective bolometer time constant $\tau_\theta^\star$ differs from τ_θ depending on bias conditions. In the frame of a uniform heating model, the IF band width reads [19]

$$f_{3\,\rm dB} = \frac{1}{2\pi\,\tau_\theta^\star} = \frac{1}{2\pi\,\tau_\theta}(1-C)\,, \quad \text{with } C = C_0 I_0^2\,\frac{R_{\rm L}-R_0}{R_L+R_0}\,, \tag{1}$$

$R_0 = U_0/I_0$ is the dc resistance in the operating point and $C_0 = dR/dP_{\rm dc}|_{R=R_0}$ the dc responsivity. Hence, by choosing operating conditions with $R_0 > R_{\rm L}$, the value of the self–heating parameter C becomes negative and one can in principle obtain a large band width $f_{3\,\rm dB}$.

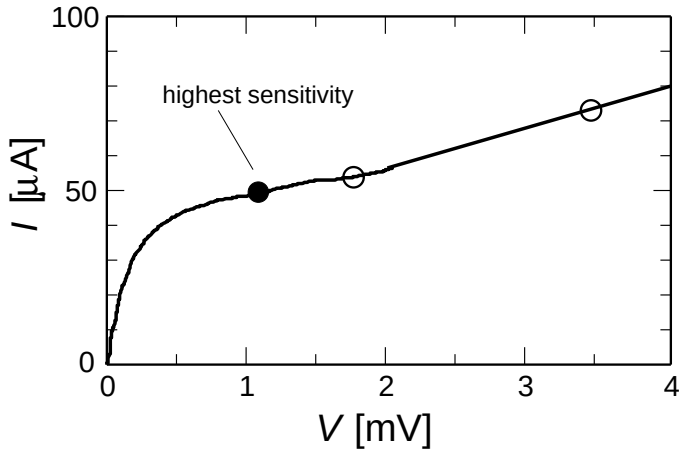

Figure 7: IV curve with the bias points for bandwidth and noise temperature measurements indicated.

The bias dependence of mixer performance has been investigated with an HEB device made from a 5 nm thin film. IF bandwidth as well as receiver noise temperature has been measured in three different bias points as indicated in Fig. 7.

Table 2: Data of IF band width and receiver noise temperature. The self heating parameter C is calculated according to Equ. 1, with $R_{\rm L} = 50\,\Omega$ (input impedance of the IF amplifier) and C_0 obtained from the IV curve in the actual bias point.

R_0 / Ω	C	$f_{3\,\rm dB}$ / GHz	$T_{\rm rec}$ at 0.6 THz	$T_{\rm rec}$ at 1.6 THz
24	0.23	2.7	600 K	650 K
34	0.1	3.5	600 K	700 K
51	0	9	1200 K	1400 K

The change in bandwidth from $f_{3\,\rm dB} = 2.7$ GHz to 3.5 GHz is due to the reduced heating parameter C in the second bias point. The increase to $f_{3\,\rm dB} = 9$ GHz at the highest voltage, can not be explained by the effect of electro thermal feed back alone, since $C = 0$ in this bias point. Within the same bias range, the noise temperature increases by a factor of two, showing that a wide IF bandwidth and still good sensitivity can be achieved with this type of mixer.

6 Conclusions

Sensitivity and IF bandwidth of phonon–cooled HEB mixers based on NbN, integrated into a quasi–optical receiver, have been measured at THz frequencies. The lowest DSB receiver noise temperatures are 530 K at 0.6 THz, 650 K at 1.6 THz and 1100 K at 2.5 THz. For optimization of the receiver it will be necessary to have a more accurate characterisation of the optics and the rf–embedding circuit of the mixer. This will allow a break down of receiver input losses and may allow conclusions about degradation in sensitivty performance at higher frequencies. In addition the fabrication process needs to be developed for better control of the contact resistance at the mixer rf input.

References

[1] D.E. Prober. Superconducting terahertz mixer using a transition–edge microbolometer. *Appl. Phys. Lett.*, 62(17):2119–2121, April 1993.

[2] E.M. Gershenzon, M.E. Gershenzon, G.N. Gol'tsman, A.M. Lyul'kin, and A.D. Semenov. Electron–phonon interaction in ultrathin Nb films. *Sov. Phys. JETP*, 70(3):505–511, March 1990.

[3] R. Wyss, B. Karasik, W. McGrath, B. Bumble, and H. LeDuc. Resistive Behaviour of Nb Diffusion–cooled Nb Hot–Electron Bolometers. In *10th Intl. Sym. on Space Terahertz Technology*, pages 215–228, Charlottesville (USA), March 1999.

[4] M. Kroug, S. Cherednichenko, H. Merkel, E. Kollberg, H.W. Huebers, H. Richter, G. Gol'tsman, and B. Voronov. NbN Hot Electron Bolometric Mixers For Terahertz Receivers. To be published in March 2001 issue of IEEE Transactions on Applied Superconductivity.

[5] C.E. Tong, J. Kawamura, R. Blundell, G. Gol'tsman, and E. Gershenzon. Low–Noise Terahertz Waveguide Hot–Electron Bolometer Heterodyne Receiver. In *1999 IEEE 7th Int. Conf. on THz Electronics*, pages 44–47, Nara (Japan), November 1999.

[6] H. Ekström, E. Kollberg, P. Yagoubov, G. Gol'tsman, E. Gershenzon, and S. Yngvesson. Gain and noise bandwidth of NbN hot–electron bolometric mixers. *Appl. Phys. Lett.*, 70(24):3296–3298, June 1997.

[7] D.J. Benford, J.W. Kooi, and E. Serabyn. Spectroscopic Measurements of Optical Components around 1 Terahertz. In *9th Int. Sym. on Space Terahertz Technology*, Pasadena (USA), March 1998.

[8] D.J. Benford, M.C. Gaidis, and J.W. Kooi. Transmission Properties of Zitex in the Infrared to Submillimeter. In *10th Int. Sym. on Space Terahertz Technology*, pages 405–413, Charlottesville (USA), 16–18 March 1999.

[9] S. Cherednichenko, P. Yagoubov, K. Il'in, G. Gol'tsman, and E. Gershenzon. Large bandwidth of NbN phonon–cooled hot–electron bolometer mixers on sapphire substrates. In *8th International Symposium on Space Terahertz Technology*, pages 245–257, Cambridge (USA), March 1997.

[10] M. Kroug, P. Yagoubov, G. Golt'sman, and E. Kollberg. NbN Quasi optical Phonon Cooled Hot Electron Bolometric Mixers at THz Frequencies. In *3rd European Conference on Applied Superconductivity*, pages 405–408, Veldhoven (The Netherlands), June 1997.

[11] P. Hanarp. Nanofabrication with Colloidal Particles. Technical report, Chalmers University of Technology, 2000.

[12] G.K. Reeves and H.B. Harrison. *IEEE Electron Device Lett. EDL–3*, 111, 1982.

[13] S. Sridhar. Microwave response of thin–film superconductors. *J. of Appl. Phys.*, 63(1):159, January 1988.

[14] Bruce Bumble and Henry G. LeDuc. Fabrication of a Diffusion Cooled Superconducting Hot Electron Bolometer for THz Mixing Applictions. *IEEE Trans. on Appl. Superc.*, 7(2):3560–3563, 1997.

[15] J. Stodolka and K. Jacobs. Receiver Measurements of a Diffusion–Cooled Hot–Electron–Bolometer at 800 GHz. In *12th Int. Sym. on Space Terahertz Technology*, San Diego (USA), February 2001.

[16] A.R. Kerr, M.J. Feldman, and S.K. Pan. Receiver Noise Temperature, the Quantum Noise Limit, and the Role of the Zero–Point Fluctuations. In *8th Int. Sym. on Space Terahertz Technology*, Cambridge (USA), March 1997.

[17] A.D. Semenov, H.-W. Hübers, J. Schubert, G.N. Golts'man A.I. Elantiev, B.M. Voronov, and E.M. Gershenzon. Design and Performance of the Lattice Cooled Hot–Electron Terahertz Mixer. *J. Appl. Phys.*, 88(12), December 2000.

[18] P.K̃hosropanah et. al. RF Current Distribution in HEB and a 2–Dimensional Device Model. This Proceedings.

[19] H. Ekström and B.S. Karasik. Electron temperature fluctuation noise in hot–electron superconducting mixers. *Appl. Phys. Lett.*, 8(6):3212–3214, June 1995.

A Low-noise NbTiN Hot Electron Bolometer Mixer

C. Edward Tong[1], Jeffrey Stern[2], Krikor Megerian[2], Henry LeDuc[2],
T. K. Sridharan[1], Hugh Gibson[1], Raymond Blundell[1]

[1] Harvard-Smithsonian Center for Astrophysics, 60 Garden St., Cambridge, MA 02138.

[2] Jet Propulsion Lab, California Institute of Technology, 4800 Oak Grove Drive, Pasadena, CA 91109.

Abstract

Hot electron bolometer (HEB) mixer elements, based on Niobium Titanium Nitride (NbTiN) thin film technology, have been fabricated on crystalline quartz substrates over a 20 nm thick AlN buffer layer. The film was patterned by optical lithography, yielding bolometer elements that measure about 1 μm long and between 2 and 12 μm wide. These mixer chips were mounted in a fixed-tuned waveguide mixer block, and tested in the 600 and 800 GHz frequency range. The 3-dB output bandwidth of these mixers was determined to be about 2.5 GHz and we measured a receiver noise temperature of 270 K at 630 GHz using an intermediate frequency of 1.5 GHz. The receiver has excellent amplitude stability and the noise temperature measurements are highly repeatable. An 800 GHz receiver incorporating one of these mixer chips has recently been installed at the Sub-Millimeter Telescope in Arizona for field test and for astronomical observations.

I. Introduction

In recent years, heterodyne receivers based on the superconductive Hot Electron Bolometer (HEB) mixer have begun to emerge as the instrument of choice for ultra-sensitive spectroscopic applications at THz frequencies. Two types of HEB mixers have been developed: the phonon-cooled mixer [1] and the diffusion cooled mixer [2]. In a phonon-cooled HEB mixer, hot electrons produced by THz photons are cooled through interaction with the lattice. Phonons are responsible for transferring the excess energy to the substrate on which the film is deposited. Until now, NbN has been the material of choice for this type of mixer [3]. Diffusion cooled HEB mixers, on the other hand, depend on the out diffusion of the hot electrons in extremely short niobium or aluminium thin film bridges to large metal electrodes [4].

Niobium Titanium Nitride (NbTiN) has largely been developed [5] for Superconductor-Insulator-Superconductor (SIS) mixers which now operate beyond 1 THz. NbTiN is a solid solution of NbN and TiN (both B1 phase superconductiors), and it has properties that resemble NbN, and it is reasonable to assume that NbTiN thin films can also be used in phonon-cooled HEB mixers. In this paper, we report on the first successful demonstration of NbTiN thin film technology to low-noise HEB receivers. We present both laboratory and field data in the frequency range 600 – 800 GHz.

II. Fabrication Process

We chose Z-cut crystalline quartz as the substrate material because our NbTiN HEB mixers are designed to work in a waveguide mount. In order to improve the quality of the NbTiN film, we have added an Aluminium Nitride (AlN) buffer layer. Details of the fabrication process can be summarized as follows:

a) A 20 nm thick AlN layer is first deposited onto the crystalline quartz substrate using RF sputtering of Al in an atmosphere of Ar and N_2. The deposition rate is 10 nm/min.
b) The quartz substrate is then heated to a temperature of 375^o C.
c) The NbTiN thin film is deposited by DC sputtering of NbTi alloy target in an atmosphere of Ar and N_2. The substrate is also RF biased during this operation. Following a short period of pre-sputtering, the substrate is moved into the normal sputtering position for 6 seconds, after which the power is shut off. The deposition rate for thick NbTiN layers made under the same conditions is 40 nm/min.

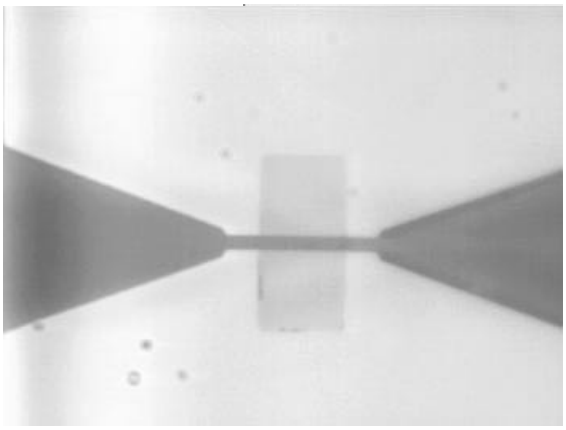

Fig. 1 Photograph of an NbTiN HEB device. The width of the element is 8 μm. The distance between the normal electrodes is about 1 μm. This photo is taken on an optical microscope looking from the back side of the quartz substrate.

d) The NbTiN thin film is next patterned by using Reactive Ion Etching.
e) The normal metal electrodes, which also form the IF filters, are deposited after a brief ion beam cleaning of the NbTiN surface. The electrodes consist of 5 nm of titanium and 30 nm of gold, and are patterned using a lift-off technique with optical lithography.

The length of our HEB devices is about 1 μm. In order to provide a range of impedances, we have fabricated HEB devices of variable width, from 2 to 12 μm. Fig. 1 shows a typical device which is 8 μm wide.

III. Device Characteristics

As a result of the short deposition time of the NbTiN thin film and the deposition process, the thickness of the film is not uniform over the whole wafer. We estimate that the thickness of the film is about 5 nm on average. The resistance ratio R_{20}/R_{300} is typically 1.14. The critical current density is about 1 MA/cm^{-2} and the sheet resistance of the finished device varies between 850 and 1150 Ω／•.

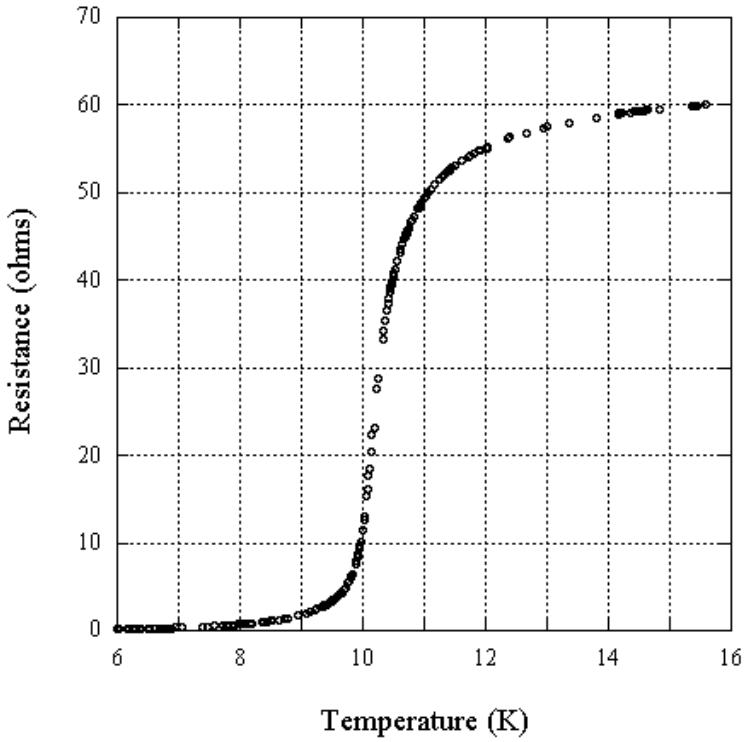

Fig. 2 Resistance – Temperature curve of a typical NbTiN HEB device around the critical temperature.

The Resistance – Temperature curve of a typical device is plotted in Fig. 2. It can be seen that the critical temperature of the device is about 10 K and that the R-T curve has a long tail on the high temperature side. The reason for this non-ideal behavior is not yet understood.

To determine the IF bandwidth of the NbTiN mixers, we have performed heterodyne mixing experiments with two phase-locked 600 GHz sources, one used as a signal source and one as an LO source. The signal power and frequency were kept constant as the IF was varied between 0.5 and 7 GHz by tuning the LO source and regulating the LO power to maintain a fixed operating point. The results are summarized in Fig. 3, where it can be seen that the 3-dB IF bandwidth varies with the applied bias voltage. For a bias of 1 mV, the measured bandwidth is 1.7 GHz. It rises to 1.9 GHz at 2 mV bias, and 2.5 GHz at a bias of 4 mV. These values are marginally better than the data from NbN HEB deposited directly on crystalline quartz [6].

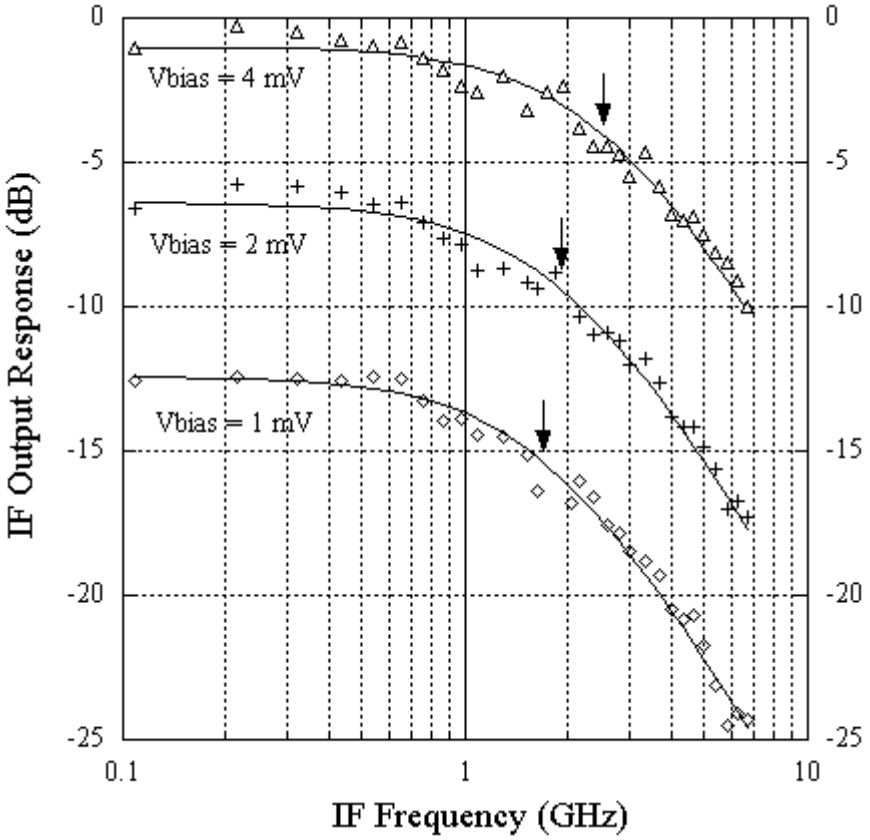

Fig. 3 IF Gain Bandwidth measurement of NbTiN HEB mixers operating at around 600 GHz. The solid curves are the best fit single pole roll-off response for each bias voltage setting. Note that the curves are shifted vertically relative to each other for display purposes only. The 3-dB rollover frequencies are marked by arrows. The error of the fit is about 0.2 GHz.

IV. Noise Measurement

NbTiN mixer chips were installed in our fixed-tuned waveguide mixer block for noise measurement using the standard Y-factor technique. This setup has been described previously [7]. The IF center frequency is 1.5 GHz and the bandwidth is 100 MHz. At 630 GHz, a 12 μm wide device gives a Y-factor of 1.65 at a bias voltage of 3 mV. Both the pumped and unpumped Current-Voltage characteristics, as well as the receiver output in response to the hot and cold loads, are recorded in Fig. 4. Note that the maximum receiver output power occurs at a bias voltage of 2.3 mV.

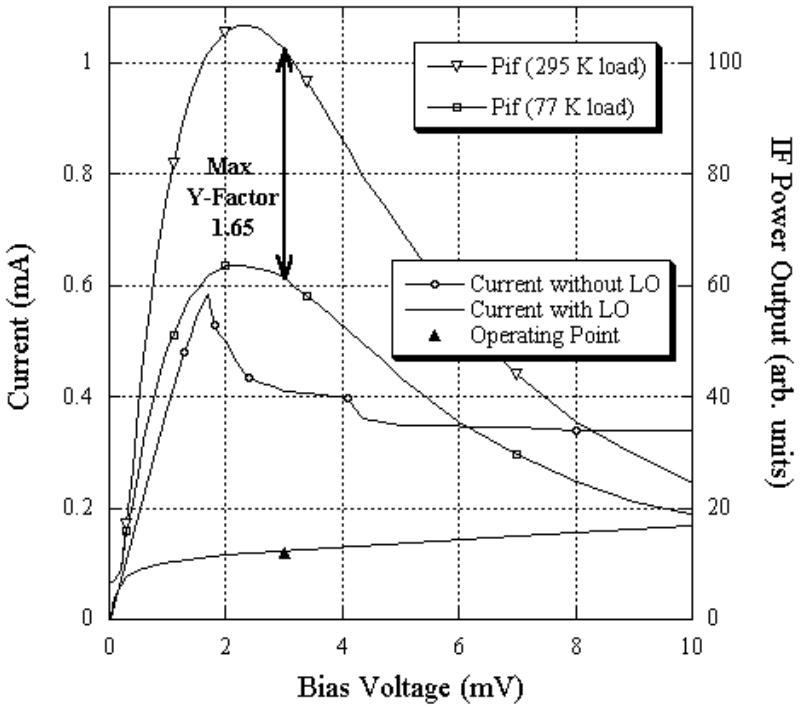

Fig. 4 Current-voltage characteristics of a 12 μm wide NbTiN HEB mixer, with and without LO drive at 630 GHz. Also shown is the receiver IF power as a function of bias voltage in response to hot (295K) and cold (77K) loads. A maximum Y-factor is recorded at a bias voltage of 3 mV and a bias current of 115 μA.

A number of 600 GHz chips have been tested. The results at 636 GHz are summarized in Table I. The measured data show that the performance improves as the resistance of the mixer is reduced. This is in line with our waveguide embedding impedance of about 40 ohms. Also, since the optimal bias point is about 3.5 mV, the achievable IF bandwidth should be close to 2.5 GHz.

Device Width (μm)	Normal State Resistance (Ω)	Critical Current (mA)	DSB Noise Temp. (K)	Estimated DSB Conversion Loss (dB)	Optimum Bias Point
5	170	255	525	-9	3.5 mV, 65 μA
8	110	330	445	-8	3.5 mV, 95 μA
12	95	500	375	-7	3.8 mV, 130 μA
12	80	600	270	-6	3 mV, 115 μA

Table I DC Characteristics and RF performance measured at 636 GHz of different NbTiN HEB mixer chips. Length of device is 1 μm.

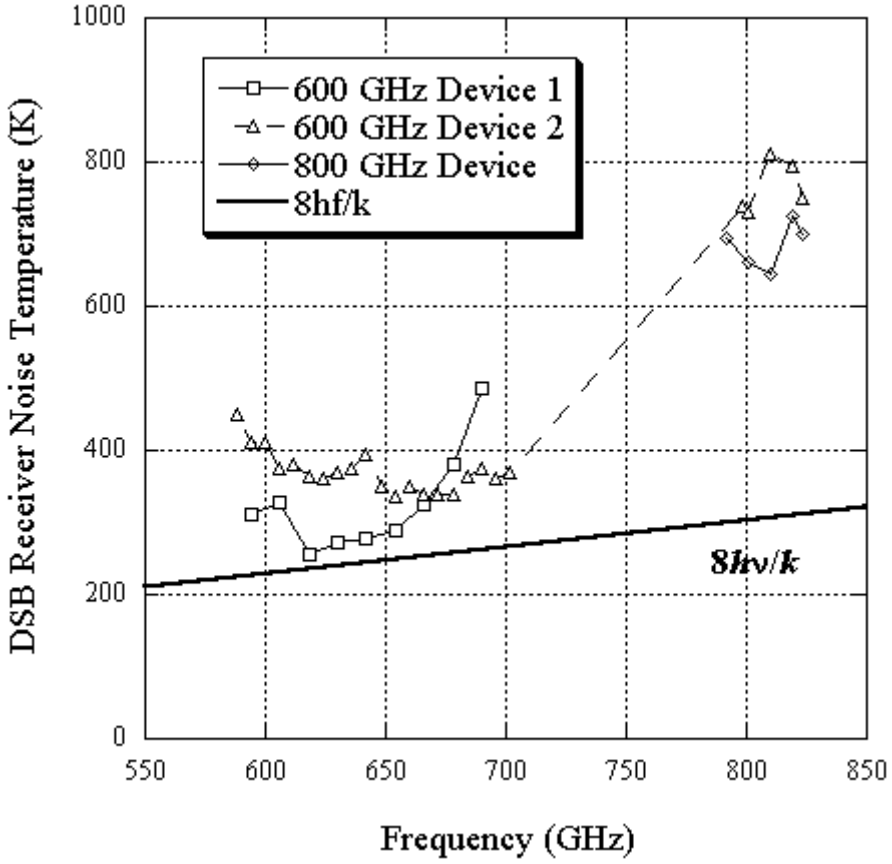

Fig. 5 Double-side-band receiver noise temperature measured for two 600 GHz and one 800 GHz NbTiN mixer chips.

The frequency response of the NbTiN mixers has also been measured for both 600 and 800 GHz chips. Fig. 5 shows the measured noise temperature as a function of frequency for two 600 GHz chips and one 800 GHz chip. The results show that a sensitivity of about 10 *hn/k* is achieved in the 600 GHz band.

The receiver is also extremely stable and its performance is highly repeatable. Once the system is well aligned, amplitude fluctuations of the IF power output are very small over time scales of minutes. In a typical hot/cold load measurement, the measured Y-factor is repeatable to better than 1%. From the direct power measurements, we believe that the receiver amplitude stability is < 0.004. This is comparable to SIS receivers, and far better than most other HEB receivers.

V. Field Testing

Last year, we deployed an NbN based HEB receiver at the Submillimeter Telescope on Mount Graham, Arizona for use primarily in the 800 – 900 GHz atmospheric window. That receiver was used in the first ground-based heterodyne detection of a celestial source above 1 THz [8]. This year, we have substituted the NbN mixer with an 800 GHz NbTiN HEB mixer. According to measurements taken at the telescope, the NbTiN receiver has a noise temperature of about 850 K at 810 GHz, similar to the performance of the NbN based HEB receivers installed on the telescope during the two previous years [6,9]. To demonstrate the true heterodyne performance of this NbTiN receiver, we have measured the emission spectra of CO (7—6) in an astronomical source, IRC+10216. The observed spectrum is recorded in Fig. 6.

VI. Conclusion

NbTiN thin films deposited on crystalline quartz substrate with an AlN buffer layer have successfully been used in a phonon-cooled HEB mixer. The 3-dB IF bandwidth of this mixer is about 2.5 GHz. The mixer chips have been incorporated in a fixed-tuned waveguide receiver which exhibits very good noise performance in the 600 and 800 GHz frequency bands, close to 8 *hn/k* at 630 GHz. This receiver has good gain stability and is currently being used for astronomical observations at the Sub-Millimeter Telescope in Arizona.

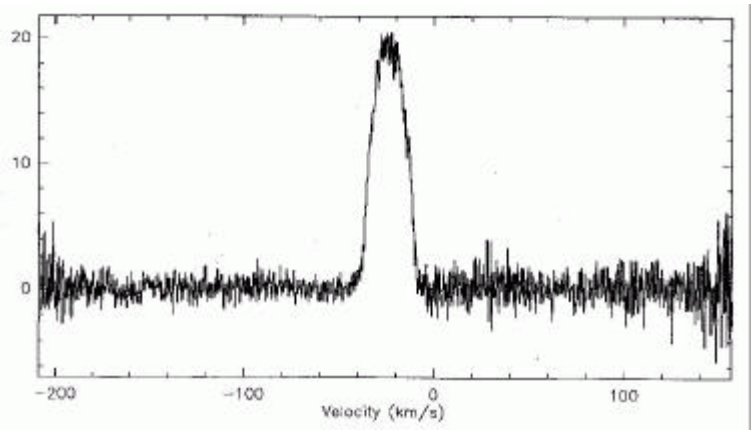

Fig. 6 CO (7—6) emission spectrum recorded by the NbTiN HEB receiver at a signal frequency of 806.65 GHz. The astronomical source, IRC+10216, was at an elevation angle of 69 degrees during the observation. The total system noise temperature was estimated to be 7700 K and the atmospheric opacity at zenith was 1.2. The integration time was 4.2 minutes.

Acknowledgements

We would like to thank Tom Wilson of Sub-Millimeter Telescope Observatory (SMTO) for his valuable support of the field testing of our HEB receiver. We would also like to thank Michael Smith for his meticulous work on the mixer block.

References

[1] E.M. Gershenzon, G.N. Gol'tsman, I.G. Gogidze, Y.P. Gusev, A.I. Elant'ev, B.S. Karasik, and A.D. Semenov, "Millimeter and submillimeter range mixer based on electronic heating of superconducting films in the resistive state," *Soviet Phys. Superconductivity*, vol. 3, pp. 1582-1597, 1990.

[2] D.E. Prober, "Superconducting Terahertz mixer using a transition-edge microbolometer," *Appl. Phys. Lett*., vol. 62, pp. 2119-2121, 1993.

[3] G.N. Gol'tsman, A.D. Semenov, Y.P. Gousev, M.A. Zorin, I.G. Gogidze, E.M. Gershenzon, P.T. Lang, W.J. Knott, and K.F. Renk, "Sensitive picosecond NbN detector for radiation from millimeter wavelengths to visible light," *Supercond. Sci. Technol*., vol. 4, pp. 453-456, 1991.

[4] B.S. Karasik, W.R. McGrath, and R.A. Wyss, "Optimal choice of material for HEB

superconducting mixers," *IEEE Trans. Appl. Supercond*., vol. 9, pp. 4213-4216, 1999.

[5] J.A. Stern, B. Bumble, H.G. LeDuc, J.W. Kooi, and J. Zmuidzinas, "Fabrication and DC characterization of NbTiN based SIS mixers for use between 600 and 1200 GHz," *Proc. 9th Intl. Symp. Space THz Tech.*, pp. 305-313, Pasadena, CA, 1998.

[6] J. Kawamura, R. Blundell, C.E. Tong, D.C. Papa, T.R. Hunter, G. Gol'tsman, S. Cherednichenko, B. Voronov, and E. Gershenzon, "First light with an 800 GHz phonon-cooled HEB mixer receiver," *Proc. 9th Intl. Symp. Space THz Tech.*, pp. 35-43, Pasadena, CA, 1998.

[7] C.E. Tong, R. Blundell, D.C. Papa, M. Smith, J. Kawamura, G. Gol'tsman, E. Gershenzon, and B. Voronov, "An all solid-state superconducting heterodyne receiver at Terahertz frequencies," *IEEE Microwave & Guided Wave Lett.,* vol. 9, pp. 366-368, 1999.

[8] C.E. Tong, J. Kawamura, T.R. Hunter, D.C. Papa, R. Blundell, M. Smith, F. Patt, G. Gol'tsman, and E. Gershenzon, "Successful operation of a 1 THz NbN hot electron bolometer receiver," *Proc. 11th Intl. Symp. Space THz Tech.*, pp. 49-59, Ann Arbor, MI, 2000.

[9] J. Kawamura, R. Blundell, C.E. Tong, D.C. Papa, T.R. Hunter, S.N. Paine, F. Patt, G. Gol'tsman, S. Cherednichenko, B. Voronov, and E. Gershenzon, "Superconductive hot-electron bolometer mixer receiver for 800 GHz operation," *IEEE Trans. Microwave Theory & Tech*., vol. 48, pp. 683-689, 2000.

Part of the research described in this paper was carried out at the Jet Propulsion Laboratory, California Institute of Technology, under a contract with the National Aeronautics and Space Administration.

TERAHERTZ RECEIVER WITH NbN HEB DEVICE (*TREND*) - A LOW-NOISE RECEIVER USER INSTRUMENT FOR AST/RO AT THE SOUTH POLE

K.S. Yngvesson, C.F. Musante, M. Ji, F. Rodriguez, and Y. Zhuang
Department of Electrical and Computer Engineering, University of Massachusetts at Amherst, Amherst, MA 01003; yngvesson@ecs.umass.edu

E. Gerecht
Department of Astronomy, University of Massachusetts at Amherst, Amherst, MA 01003; gerecht@astro.umass.edu

M. Coulombe, J. Dickinson, T. Goyette, and J. Waldman
Submillimeter-Wave Technology Laboratory, University of Massachusetts at Lowell, Research Foundation, Lowell, MA 01854;

C. K. Walker
Department of Astronomy and Steward Observatory
University of Arizona, Tuscon, AZ

A. Stark and A. Lane
Smithsonian Astrophysical Observatory
Cambridge, MA 02138

ABSTRACT

Based on the excellent performance of NbN HEB mixer receivers at THz frequencies which we have established in the laboratory, we are building a *Terahertz REceiver with NbN HEB Device* (*TREND*) to be installed on the 1.7 meter diameter AST/RO submillimeter wave telescope at the Amundsen/Scott South Pole Station. *TREND* is scheduled for deployment during the austral summer season of 2002/2003. The frequency range of 1.25 THz to 1.5 THz was chosen in order to match the good windows for atmospheric transmission and interstellar spectral lines of special interest. The South Pole Station is the best available site for THz observations due to the very cold and dry atmosphere over this site. In this paper, we report on the design of this receiver. In particular, we report measured beam patterns and polarization sensitivity at THz frequencies for a log-periodic antenna/lens combination, accurate measurements of the frequencies of two laser lines which are suitable for two of the spectral lines of greatest interest (NII and CO), as well as the mixer block design and other aspects of the design of the receiver system.

I. INTRODUCTION

We will describe the work done so far on the TREND project, which will build and install a low-noise THz receiver on the 1.7 meter diameter AST/RO submillimeter wave telescope at the South Pole. Most of the work has dealt with issues such as the development of a laser local oscillator, and characterizing the quasi-optical lens/antenna system in order to match it to the telescope. We plan to begin installing the receiver in the fall of 2002, and commence observations during the austral winter of 2003.

II. SITE CONSIDERATIONS

Terahertz astronomy will eventually be pursued with the help of HEB low-noise receivers from platforms in space (FIRST), or in the upper atmosphere (SOFIA, balloons). Until that time, it is important to gain experience of this new technology by installing and employing HEB receivers on ground-based telescopes at the best available sites. It has only recently been realized that observations above 1 THz are feasible at such sites. One can also support an argument in favor of continuing the use of such receivers on ground based telescopes in the future, given the fact that they can be dedicated to specific tasks for longer periods of time compared with facilities such as SOFIA or FIRST, and that larger diameter telescopes are feasible, such as the proposed 10 meter telescope at the South Pole Station [1]. Presently, the 1.7 meter diameter AST/RO submillimeter wave telescope is operated at the South Pole by the Smithsonian Astrophysical Observatory [2], and has been successfully used up to the 800 GHz (350 μm) window for several years (see for example the paper by C. Walker et al. at this symposium [3]).

The Antarctic Plateau, with an altitude of 2847 meters, is unique among observatory sites for unusually low wind speeds, absence of rain, and an extremely cold and dry atmosphere. The median Precipitable Water Vapor (PWV) value is less than 0.3 mm during the austral winter season. Available atmospheric models can be used with the measured amount of PWV to predict the atmospheric transmission in two windows near wavelengths of about 200 μm, occurring from about 1.25 THz to 1.4 THz, and from 1.45 THz to 1.6 THz [4]. Expected *median* transparency at frequencies corresponding to important spectral lines is from 5 % to 11 %, and on unusually good days may reach values 2 or 3 times higher than this. Fourier transform spectrometer measurements were performed in this frequency range at another site, Chajnantor in the Atacama desert, Northern Chile, planned for the ALMA millimeter array. These measurements show similar atmospheric transparency and confirm the above model predictions. However, the good conditions for THz observations at the South Pole are available more often than in the Atacama desert and for more extended periods of time. The Chajanantor measurements are shown in Figure 1 [5]. It is clear that installing a low noise THz receiver at the South Pole site is thus well justified.

We have identified three spectral lines in the above atmospheric windows, which are of special interest: (i) NII (singly ionized nitrogen) at 1461.3 GHz (205 μm), the second strongest spectral line overall in a typical galaxy (only CII at 156 μm is stronger); NII should be ubiquitous in the interstellar medium (ISM) of our galaxy, especially its warm ionized component; (ii) H_2D^+ at 1370.0853 GHz, an important probe for gas phase chemistry; and (iii) the J=13→12 and J=11→10 lines of CO; the latter line is at 1267.014

GHz. It is important to observe higher order CO lines, and compare these with the well-studied millimeter lines of CO in warmer, denser sources. The locations of the spectral lines for the above three species relative to the atmospheric transmission spectrum are marked in Figure 1.

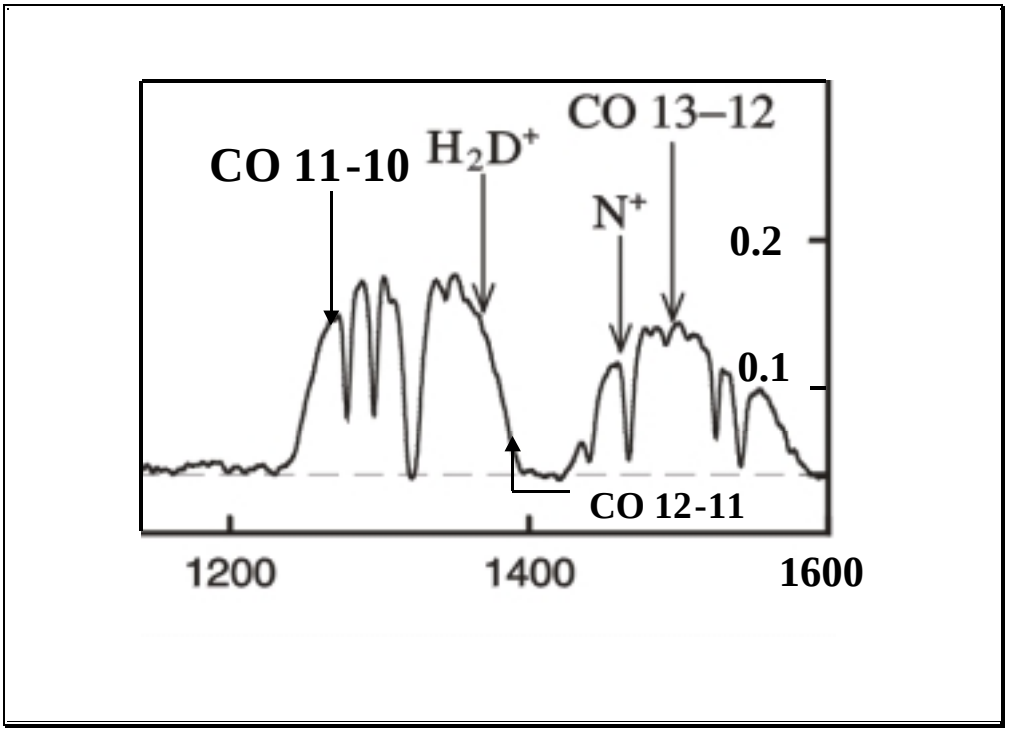

Figure 1. Atmospheric transmission from 1,200 GHz to 1,600 GHz at Chajnantor on a day with very low humidity, FTS measurement by SAO Submillimeter Receiver Lab. [5]

III. RECEIVER DESIGN

A. General considerations

Waveguide-coupled NbN HEB mixers have been used on astronomical telescopes up to 1.04 THz [6] and have proven to be easy to operate in this environment. For the 200 μm window, we will make use of quasi-optical coupling as in most laboratory experiments with HEB mixers. The lowest receiver noise temperatures measured so far at about 1.5 THz are 500 K [7] and 650 K [8]. NbN HEB mixers are also very insensitive to changes in bias conditions and LO power and should be easy to adapt to the observing logistics at AST/RO, where all observations in the Austral winter season are performed by a single Post-doctoral scholar operator. Whereas multiplier LO sources are expected to be available in the future, a laser was chosen for TREND, since it is a mature technology in the THz regime and will lend itself well to a future upgrade of the system incorporating a multi-pixel focal plane array. Laser sources can also be made tunable over +/- 100 GHz by using Sideband Generator Technology [9].

B. Active Device

Phonon-cooled HEB mixers are typically fabricated from NbN films on either silicon or MgO substrates. The MgO substrate has the advantage that the phonon transmission probability is higher than for NbN on silicon. Since the phonon escape time contributes substantially to the thermal time-constant of NbN bolometers, NbN mixers on MgO have wider IF bandwidth for a given NbN film thickness, t. There is also some evidence that NbN/MgO devices may yield lower receiver noise temperature [8]. We are testing films on both substrates and expect to choose the one which yields the lowest receiver noise temperature for the TREND receiver. The IF (conversion gain) bandwidth is typically 3 GHz for NbN/silicon, and up to 4.8 GHz for NbN/MgO [10]. It is important to note that the receiver *noise* bandwidth is about twice these numbers. As explained in section D below, we expect to be able to accommodate the three target spectral lines within an IF band of about 1.3 GHz to 2.3 GHz; the IF bandwidth thus poses no problem for either material combination. Future needs for other spectral lines which yield IF frequencies up to 5 to 6 GHz can easily be satisfied as well, with a change of IF amplifier. Present devices are 1 μm x 5 μm and are fabricated with UV lithography. Smaller devices can be made with e-beam lithography. Both processes are much simpler than the one required for diffusion-cooled HEBs.

C. Quasi-Optical Coupling

In our NbN HEB development work [7], we have made use of a quasi-optical coupling scheme consisting of a 4 millimeter diameter elliptical silicon lens, coupled to a self-complementary toothed log-periodic antenna on a silicon substrate, see Figure 2. The log-periodic antenna has a (design) bandwidth from about 300 GHz to 3.5 THz. The dielectric constant of MgO is very similar to that of silicon and it has been shown that devices on MgO substrates perform well with silicon lenses without modification [8]. Since the required RF bandwidth for TREND is only 1.25 THz to 1.5 THz, we have designed an alternative double-slot antenna and plan to use this antenna if it yields the same or a lower receiver noise temperature. Our NbN HEB mixers do not saturate on the total thermal noise picked up by the antenna. Moreover, choosing a double-slot antenna with a narrower bandwidth than the log-periodic antenna makes the receiver even less sensitive to saturation and direct detection effects. We will make use of a parylene AR coating in order to reduce the receiver noise temperature by about 30 %, as described in [11].

The beamwidth of the quasi-optical system is determined primarily by the diameter of the elliptical lens and has been measured by using a new method. The beam of a THz laser was expanded until it had a diameter of 5 cm (at the -3 dB level). The laser beam was injected through the window of the dewar onto the elliptical lens using a plane mirror

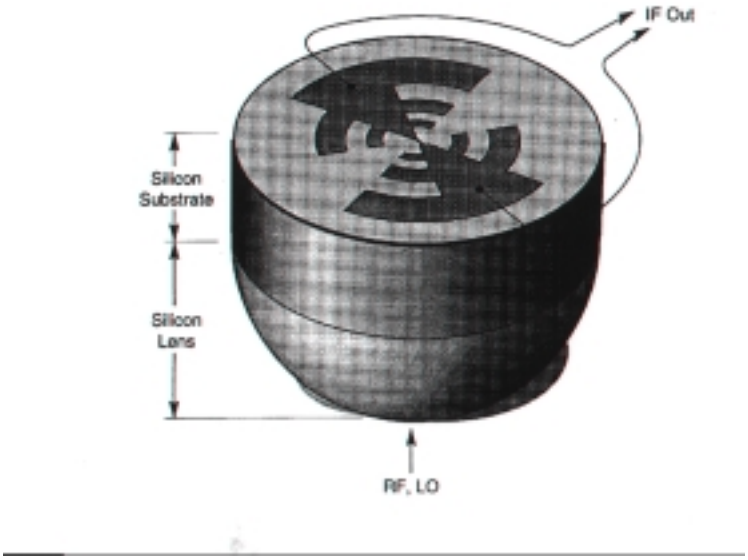

Figure 2. The logperiodic antenna coupled to the silicon lens

close to the dewar. The mirror could be turned in both the horizontal and the vertical plane, thereby changing the angle of incidence of the entire laser beam. The change in the

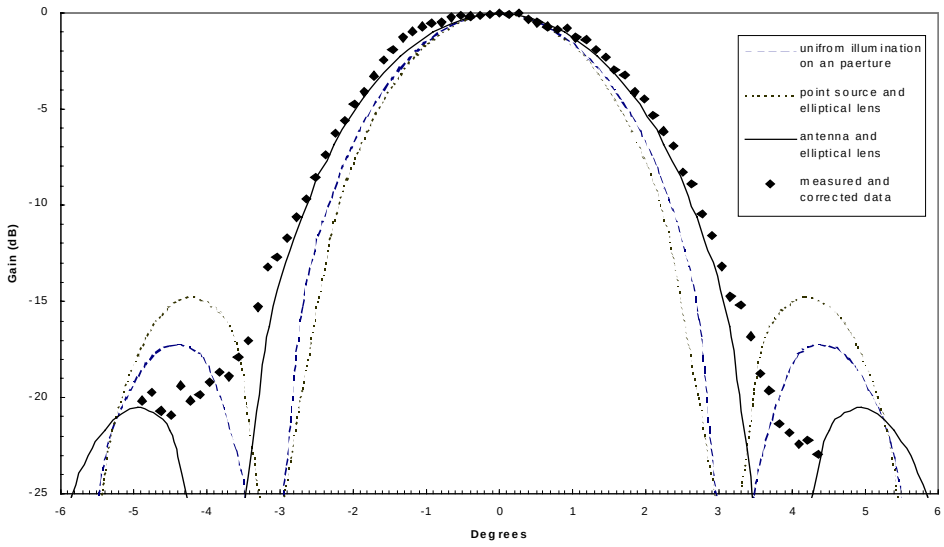

Figure 3. The radiation pattern in the H-plane for the log-periodic antenna/lens combination, measured at 1.56 THz.

actual angle of incidence at the position of the silicon lens can be calculated from the angle by which the mirror is turned if one knows the location of the center of curvature of the incident laser beam. This was determined by making accurate scans of the laser beam in planes at different distances from the dewar. These scans were performed by translating a small hole coupler with a sensitive bolometer detector behind it across the beam. The beam scans also determined the amplitude variation over the cross-section of the beam. The laser operated in a good single mode, and thus emitted a gaussian beam, as verified by the beam scans. The HEB device was used in the direct detector mode for these experiments. Apart from this, the device and the lens/antenna were identical to what is used for the HEB mixer receiver. The operating temperature was 8.43 K and the device was brought to an electron temperature about equal to the critical temperature (9.5 K) by applying a DC bias current of 70 μA. The laser power was attenuated until tests showed that the detector operated in its linear region. The responsivity (up to 2,400 V/W) and NEP (1×10^{-11} $W/Hz^{1/2}$) were sufficient for measuring the radiation pattern down to about 20 dB below the peak. Further details of this method will be published separately [12], [13].

The 3 dB beamwidth was determined to be 3.4 degrees at 1.56 THz and 2.15 degrees at 2.24 THz. Figure 3 shows the radiation pattern of the system at 1.56 THz in the H-plane. Note that there are no sidelobes down to the -20 dB level. The E-plane pattern is very similar. The beamwidth will be matched to the beam of the AST/RO telescope in the plane used for installing receivers. The TREND mixer block and IF amplifier will be housed in an existing dewar together with a 492 GHz SIS receiver system. Both will be able to observe simultaneously by using a polarization splitter.

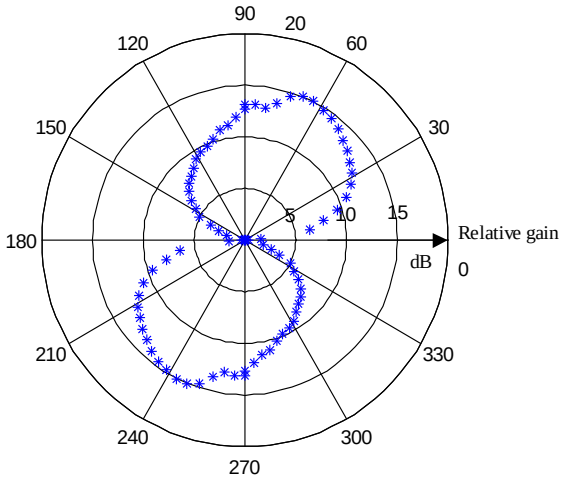

Figure 4. Polarization sensitivity of the log-periodic antenna measured at 1.56 THz.

We also measured the polarization sensitivity of the log-periodic antenna, which has not been documented in the THz region before. As is known from measurements at millimeter waves [14], the angle of polarization which yields the maximum response varies

periodically with the frequency. We confirmed this by measurements at two different wavelengths. The polarization response in Figure 4 was measured at 1.56 THz. The 2.24 THz polarization response "lobe" peaked at an angle which was about 45 degrees from the one at 1.56 THz, but was also wider. The log-periodic antenna measured at millimeter wavelengths in [14] also had five teeth on each side, and can be scaled in size to ours, while scaling the frequency by the same factor. One then finds that our measurements were performed at a (normalized) frequency higher than the highest frequency used at millimeter waves. We can therefore not do a direct comparison, but qualitatively the same features of polarization for maximum response which depends on frequency remain.

D. Local Oscillator

A common source of LO power for THz HEB mixers operated in the laboratory is a CO_2 laser pumped gas laser. By choosing various combinations of CO_2 pump laser frequencies and submillimeter laser gas, an enormous choice of discrete submillimeter laser frequencies is available. Each of these laser lines is typically tunable over a small frequency range of from 2-20 MHz. The spacing between the laser lines tends to be on the order of a few GHz, and it should thus in principle be possible to match a specific interstellar spectral line close enough to be within the band of a typical IF amplifier. One complication is that the reference literature lists the absolute frequency of most of these lines to an accuracy of only a few GHz. This is due to the optical technique usually used to measure the wavelength. A case in point is the NII line planned for the TREND receiver at 1461.3 GHz. The closest laser line appeared to be one due to CD_3OH, pumped by the 10P36 CO_2 line, with a listed wavelength of 205.8 μm. This wavelength converts to a frequency of 1456.7 GHz, and would result in an IF of 4.6 GHz. An accurate frequency measurement, described below, determined that this laser line occurs instead at 1459.3913 GHz, yielding a quite different IF of 1.7 GHz.

The much more accurate technique we used for measurement of the laser frequency was to heterodyne the laser frequency with a calibrated local oscillator (LO[1]). The easiest way to obtain a calibrated THz LO source is to drive a submillimeter mixer with a low frequency source which generates harmonics internally which will mix with the laser producing a number of IF products. The frequency products found at the IF are described by

$$f_{IF} = m\, f_{RF} \pm n\, f_{LO} \qquad (1)$$

where f_{RF} is the laser frequency, $n\, f_{LO}$ is the nth harmonic of the frequency synthesizer, and f_{IF} is the intermediate beat frequency.

The frequency of the CD_3OH line was measured at the UMass/Lowell Submillimeter-Wave Technology Laboratory (STL) using an existing receiver designed to operate over the range of 145 - 175 GHz. Despite being designed for a much lower

[1] The use of the term "LO" in this section refers to the multiplied signal used for frequency reference, whereas in the rest of the text, "LO" is used for the laser source itself.

frequency, this receiver proved able to conveniently measure laser frequencies in the THz range. The receiver uses an LO multiplied up from 10 GHz consisting of a quadrupler followed by an amplifier and a doubler producing a few mW at 80 GHz to drive the receiver's balanced mixer at the 2nd harmonic (160 GHz). Higher order harmonics of the LO (i.e 240 GHz ± 22.5, 320 GHz ± 30, 400 GHz ± 37.5…) generated within the mixer should mix with higher frequency RF sources to produce beat frequencies which if within the IF detection bandwidth may be strong enough to measure. For example, the 18th harmonic of 81 GHz is 1458 GHz could be mixed with the 1456.7 GHz line to produce an IF within the operating range of this mixer.

A diagram of the measurement setup is shown in figure 5. The laser radiation was coupled into the mixer using a fast off-axis parabolic mirror to focus the energy down to a waist-size comparable to the input waveguide dimensions. The laser power at the mixer was measured at 1-2 mW. The mixer input was a simple smooth conical horn. The spectrum analyzer sweep width was set to 100 MHz during the search phase. The resolution BW of the spectrum analyzer was set to 10 KHz to offer the lowest practical noise floor and sweep speed.

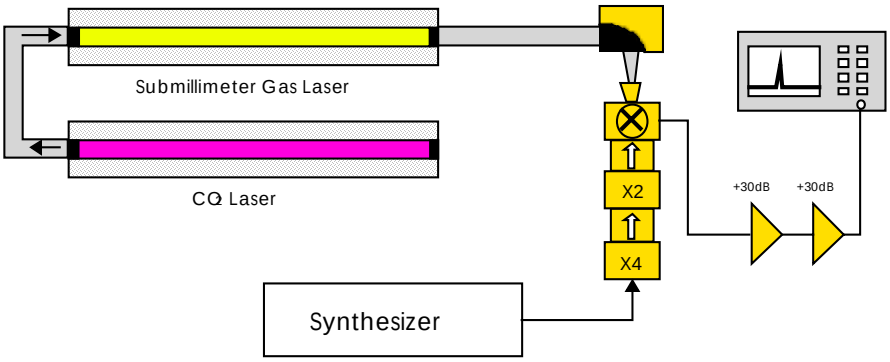

Figure 5. Diagram of the setup used for measurement of THz laser frequencies

To perform the measurement, the synthesizer was set to generate a harmonic output within 3 GHz of the estimated laser frequency. The synthesizer was adjusted until a beat with the laser was detected on the spectrum analyzer. The laser was then tuned over its gain bandwidth to determine the band edges and then tuned to the estimated center of the line. The synthesizer was adjusted to tune the beat to exactly 3 GHz. As a final check, the LO was shifted by 6 GHz to check for a 3 GHz beat with the other sideband. Although the measurement system was determined to be accurate to much better than one MHz, the uncertainty in the laser line center determines the ultimate measurement accuracy. Accurate frequencies of many other laser lines have been determined previously, but the techniques employed have been much more laborious than the one we used here. In order to explore the accuracy and limits of our technique, we measured previously measured lines in CH_3OH up to 3.1 THz and found excellent agreement with the published frequencies. The signal-to-noise ratio (S/N) in the measurement of the 1459.361 GHz line

(after optimization) was as high as 30 dB, as is evident from the spectrum analyzer recording in Figure 6. Even at 3.1 THz, a S/N ≈ 10 dB was obtained.

As a practical note, it appears that the accurate frequency of any laser line to be used for THz heterodyne astronomy needs to be determined by an actual measurement, unless such data is available in the literature. On the other hand, once the frequency is known, the laser can be tuned to its maximum power, which establishes the absolute frequency to

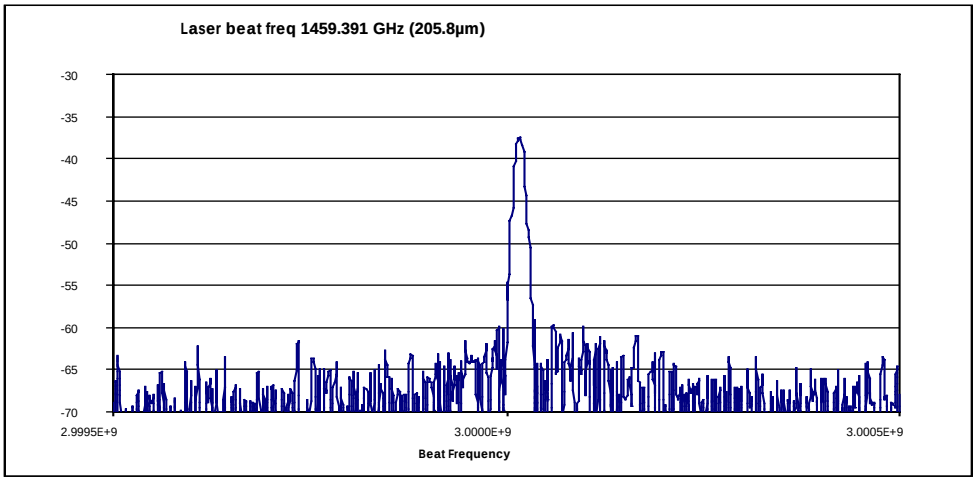

Figure 6. Beat frequency between the CD_3OH laser and the frequency measurement receiver, recorded on a spectrum analyzer.

within about 1 MHz, without the need for using a multiplier chain to control the frequency.

The CD_3OH laser line also demonstrates some of the other constraints on obtaining a laser local oscillator at any specific THz frequency. It was operated at STL with a maximum output power of about 2 mW. This required a quite large amount of CO_2 laser pump power (70 W), however, and lasing was only obtained when a very small (1 mm diameter) hole coupler was used, indicating low laser gain for this particular line. Because the center of the CO_2 pump laser line (10P36) is offset from the center of the CD_3OH line to be pumped by apparently more than 50 MHz, the laser cannot be operated at the optimum pump frequency, since this was outside the free spectral range of the pump laser. This appears to explain the lower than normal gain. We are working with DEOS, Inc. to design a laser which can yield sufficient THz power output while being pumped by a smaller CO_2 laser, appropriate for being installed at the South Pole site.

CD_3OH has a second line which we also operated at STL and measured to be at 1265.513 GHz. This line matches that of the J = 11→10 transition of CO, with a conveniently low IF of 1.5 GHz. There is no equally good match for the J = 13 → 12 CO transition. We have not yet settled on the optimum laser line for H_2D^+.

E. Mixer block and biasing

We have designed a new mixer block which can directly replace another mixer block presently mounted in the designated dewar at the AST/RO facility. The mixer block will contain the lens, the substrate on which the NbN device and the antenna have been fabricated, and a circuit board which supplies the DC bias and connects the mixer to the IF amplifier. Figure 7 shows the present configuration of the circuit board, which is compatible with the wiring for the SIS mixer to be replaced. We are studying different versions of connecting a stabilizing resistor, as described in greater detail in another paper at this symposium [15]. We have shown, for example, that a series resistor in the bias lead of about 6 to 20 ohms (depending on the individual device) will stabilize the device even in its negative resistance region (without LO power).

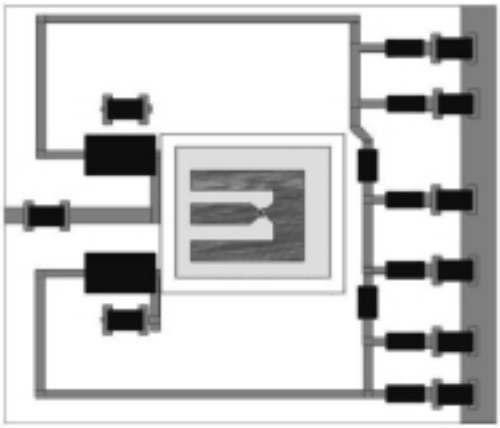

Figure 7. Bias/IF circuit for the TREND NbN receiver

IV. FUTURE EXTENSIONS

Given the availability of the laser LO at the AST/RO site, sufficient LO power is available such that future extensions to THz focal plane arrays are possible. Such arrays will also include MMIC IF amplifiers integrated with the HEB mixers/antennas, which will be developed under a new grant from the NASA Cross-Enterprise Technology Development program. We also plan to develop a capability for NbN film fabrication in collaboration with NIST/Boulder. This capability will benefit future implementation of NbN HEB mixer receivers for THz astronomy.

V. ACKNOWLEDGEMENTS

We gratefully acknowledge support for this project from the NSF program for Advanced Technologies and Instrumentation, Division of Astronomical Sciences, NSF award # AST 9987319. We also want to thank Dr. Eric Mueller of DEOS, Inc. for

generously giving us of his time for discussions and tests related to the TREND laser system.

VI. REFERENCES

[1] A.A. Stark et al, "Plans for a 10-m Submillimeter Wave Telescope at the South Pole," SPIE Proceedings, Advanced Technology: Millimeter Wave, Radio and Terahertz Telescopes, Vol. 3357, pp. 495-506, 1998.
[2] Stark, A. A., et al., "The Antarctic Submillimeter Telescope and Remote Observatory (AST/RO)", Publications of the Astronomical Society of the Pacific, May 2001, in press.
[3] C. Walker et al., "Pole Star: An 810 GHz Array Receiver for AST/RO," this symp.
[4] A.P. Lane, "Submillimeter Transmission at South Pole", in *Astrophysics From Antarctica*, A. S. P. Conf. Ser., eds. G. Novak and R. H. Landsberg, (San Francisco, CA: Astr. Soc. of the Pacific), 141, 289-295.
[5] S. Paine et al., "A Fourier Transform Spectrometer for Measurement of Atmospheric Transmission at Submillimeter Wavelengths," Publications Of the Astronomical Society of the Pacific, **112:** 108-118, 2000.
[6] J. Kawamura et al., "Successful Operation of a 1 THz NbN Hot-Electron Bolometer Receiver," Eleventh Intern. Symp. Space THz Technology, The University of Michigan, Ann Arbor, MI, May 2000, p. 57.
[7] E. Gerecht et al, "Development of Focal Plane Arrays Utilizing NbN Hot Electron Bolometric Mixers for the THz Regime," Eleventh Intern. Symp. Space THz Technology, The University of Michigan, Ann Arbor, MI, May 2000, p. 57.
[8] M. Kroug et al., "NbN Hot Electron Bolometric Mixers for Terahertz Receivers," Applied Superconductivity Conference, Newport Beach, VA, Sept. 2000.
[9] E.R. Mueller, "Widely Tunable Laser-Sideband THz Source for Spectroscopy and LO Applications," this symposium.
[10] S. Cherednichenko et al., "IF Bandwidth of Phonon Cooled HEB Mixers Made from NbN Films on MgO Substrates," Eleventh Intern. Symp. Space THz Technology, The University of Michigan, Ann Arbor, MI, May 2000, p. 228.
[11] M. Ji et al., "Study of Parylene as Anti-Reflection Coating for Silicon Optics at THz Frequencies," Eleventh Intern. Symp. Space THz Technology, The University of Michigan, Ann Arbor, MI, May 2000, p. 407.
[12] M. Ji, "Lens Coupled Printed Antenna Characterization," M.Sc. thesis, University of Massachusetts at Amherst, Department of Electrical and Computer Engineering, May 2001.
[13] M.Ji et al., to be submitted for publication.
[14] B.K. Kormanyos et al., "A Planar Wideband 80-200 GHz Subharmonic Receiver," IEEE Trans. Microwave Theory Techniques, MTT-41, p. 1730, 1993.
[15] Y. Zhuang and K.S. Yngvesson, "Negative Resistance Effects in NbN HEB Devices," this symposium.

Local oscillator power requirement and saturation effects in NbN HEB mixers.

S. Cherednichenko[1], M. Kroug, H. Merkel, E. Kollberg

Department of Microwave Technology, Chalmers University of Technology, Gothenburg, S-412 96, Sweden

D. Loudkov, K. Smirnov, B. Voronov, G. Gol'tsman, E.Gershenzon.

Department of Physics, Moscow State Pedagogical University, Moscow 119435, Russia

[1] e-mail: serguei@ep.chalmers.se

Abstract The local oscillator power required for NbN hot-electron bolometric mixers (P_{LO}) was investigated with respect to mixer size, critical temperature and ambient temperature. P_{LO} can be decreased by a factor of 10 as the mixer size decreases from $4\times0.4\ \mu m^2$ to $0.6\times0.13\ \mu m^2$. For the smallest volume mixer the optimal local oscillator power was found to be 15 nW. We found that for such mixer no signal compression was observed up to an input signal of 2 nW which corresponds to an equivalent input load of 20,000 K. For a constant mixer volume, reduction of T_c can decrease optimal local oscillator power at least by a factor of 2 without a deterioration of the receiver noise temperature. Bath temperature was found to have minor effect on the receiver characteristics

Introduction.

Hot-electron bolometric (HEB) mixers are the most sensitive heterodyne receivers at frequencies above 1 THz. Their all-planar technology allows fulfillment of HEB mixers in both waveguide and quasioptical variants. HEB mixers do not need any RF or IF matching circuits. That is very important, since at terahertz frequencies only normal metal can be used for such circuits and it would cause big input losses.

HEB mixers work at a condition when superconducting gap is suppressed by the radiation of the local oscillator (LO) and effective electron temperature is equal or close to T_c. Under such circumstances the mixer resistance is very sensitive to the oscillation of the electron temperature caused by the beating of LO and RF waves. It has been shown that

that phenomenon is frequency independent in a wide frequency range, from MM up to near IR [1]. Relaxation of the electron temperature can occur via either electron-phonon interaction (phonon cooling, dominates in thin dirty superconducting films) or heat out-diffusion (diffusion cooling, dominates in short bridges of clean superconducting films).

In this paper we consider phonon-cooled HEB mixers based on NbN film. DSB receiver noise temperature for such mixers is from 650 K to 1100 K in the band from 1.6 THz to 2.5 THz[2]. Receiver noise temperature from 3000 to 8000 K was measured up to 5 THz [3]. Stable and reliable operation of NbN HEB mixers has been proved by a set of radio telescope sessions [4]. A gain bandwidth of 4 GHz is achieved at the most sensitive bias point (while noise bandwidth is up to 8 GHz), but can be extended up to 9 GHz with larger bias voltages [2, 5].

Unfortunately, technology of tunable solid state local oscillators (LO) for the terahertz range does not develop so fast. Output power from such sources decreases rapidly with frequency (Fig.1). That is an obstacle for applications in satellite-based receivers and in large arrays. It brings up the task to develop mixers, which require as low local oscillator power as possible.

It has been reported that P_{LO} required for NbN mixers scales with the mixer volume and mixers with P_{LO} of 100 nW can be made [6, 7, 8, 9]. For this mixers 1 dB compression point was found to be from 15 dB to 25 dB below LO power level.

In this paper we investigate the question: which mixers or operation parameters have the strongest effect on the optimal value of the LO power. We fabricated a mixer which requires LO power not more that 15 nW and showed that no saturation occurs up to a load temperature of 20000 K. The investigation was performed at frequency 650 GHz.

Device fabrication and experimental Set-up.

HEB mixers were fabricated from 3.5 nm superconducting NbN film. NbN films were deposited on 350 μm thick single crystal MgO and silicon substrates by reactive dc magnetron spattering. Details about NbN film deposition and device fabrication can be found in [10, 11]. The NbN microbridge was placed in the center of planar spiral antenna made of 200 nm gold film. NbN bridge size was from 4x0.4 μm^2 to 0.6x0.13 μm^2. Device geometry was controlled by a scanning electron microscope.

Experimental set-up is presented in Fig.2. Two backward wave oscillators (650 GHz) were used as LO and RF sources. Variable quasioptical attenuators allowed smooth tuning of both LO and RF power. 12 μm Mylar film served as a beam splitter. Cryostat vacuum window was made of 1.2 mm polyethylene. 250 μm thick Zitex G108 was mounted on the 4.2 K shield as a IR filter. In the frequency band of 3 THz (estimated for the spiral antenna used in the experiment) background radiation at 300 K is of the order of nanowatts. So, it can not be neglected in comparison with LO power for the smallest

mixers. In order to cut-off the background radiation a thin layer of Ecosorb was attached to 4.2 K shield just behind IR filter. Its attenuation was at least 17 dB. Mixer chip was mounted on a 12mm elliptical silicon lens without antireflection coating. The intermediate frequency (IF) chain consisted of bias-T, isolator, HEMT low noise amplifier, room temperature amplifier and band-pass filter. IF band was 30 MHz centered at 1.5 GHz. IF signal was measured by a microwave power meter.

Local oscillator power

The absorbed local oscillator power was measured with an isothermal technique [12]. In brief, that technique is based on the assumption of the equal effect of both P_{LO} and P_{dc} on the mixer dc resistance R_0. So, for a constant resistance line ($I=U/R_0$) $P_{LO} + P_{dc}$ is constant. Therefore, for points 1 and 2 (Fig.7 a) one can write $P_{dc,A}= P_{dc,B}+ P_{LO}$. This technique has been widely used for the estimation of the absorbed LO power for HEB mixers. But we have to note that the error of about 20% shall be assumed for this technique. That value comes from the scattering of P_{LO} data obtained for the same mixer but for different R_0 value. Such accuracy was also confirmed by comparing the relative change of the absorbed P_{LO} (obtained from the isothermal technique) for the mixers with different volume and the change of the attenuation level of the attenuator 1 (Fig.2). Output power of BWO 1 corresponded well to its bias conditions and was the same through all experiments.

In the first part of the investigation DSB receiver noise temperature was measured as a function of the local oscillator power at the bath temperature 4.2 K. Fig.3 (a and b) presents the data for mixers with the same size 4x0.4 μm^2 but different critical current density. As can be seen the optimal value of P_{LO} can be reduced by a factor of 2 just using NbN film with smaller T_c, and therefore smaller j_c. For both mixers minimum of the function $T_r(P_{LO})$ was quite broad and deviations of P_{LO} from the optimum up to 10÷15% did not cause noticeable change of the mixer performance. Fig.3 demonstrate that "underpumping" of the mixer with LO even with an expense of an increase of T_r did not give any significant benefit for P_{LO}. For the sample M12-2 at the optimum bias voltage (around 1 mV) the minimum P_{LO} at which the mixer is still stable for superconducting oscillations is only 30% of the optimum P_{LO}. Sample M10-2 at the optimum bias voltage became unstable if P_{LO} decreased below to 200 nW. For higher bias voltage the stable mixer operation was possible even for smaller P_{LO}. But as it can be seen from Fig.3 it will lead to a degradation of the mixer performance.

The possibility of decreasing of P_{LO} for smaller Tc of NbN film seems to be more interesting perspective. As it can be seen from Fig.3 a decrease of Tc did not lead to the degradation of the receiver sensitivity. At the absolute minimum of T_r both conversion efficiency and output noise temperature was about the same for both mixers (-12 dB and

50 K). We compared obtained data with a uniform heating model [13]. In this model the local oscillator power required to elevate electron temperature to T_c depends on T_c and the mixer volume:

$$P_{LO} = \frac{\gamma}{3.6 \cdot \tau_\Theta \cdot T_c^{1.6}} \cdot V \cdot (T_c^n - T^n - n \cdot T_c^{n-1} \cdot \Delta T_c) \qquad (1)$$

where γ=2.1·10^2 J/(cm^{3}K^2) is Sommerfeld constant, τ_Θ=35 ps is electron cooling time (measured for 3.5 nm NbN films on MgO substrate [5]), V is the mixer volume, T is the bath temperature, ΔT_c is superconducting transition width, n=3.6 is a constant determined for NbN film.

For the mixer size 4×0.4×0.0035 μm^3, and T_c values of 9.5 K and 8 K P_{LO} from (1) are 540 nW and 260 nW respectively. So, the uniform heating model can describe P_{LO} behavior and we will confirm it once more by the next data.

Receiver noise temperature and absorbed local oscillator power was also measured for the mixer M12-2 at different bath temperatures (see Fig.5). We should note that the temperature of the IF chain was kept unchanged, i.e. 4.2 K. During the experiment the mixer critical current was measured at each temperature and then the mixer temperature was estimated from [14] (see also Fig. 4)

$$I_c(T) = I_c(0) \cdot \left[1 - \left[\frac{T}{T_c}\right]^2\right] \cdot \left[1 - \left[\frac{T}{T_c}\right]^4\right]^{0.5} \qquad (2)$$

The validity of (2) we have checked for one of the sample.

Solid line represents Eq.1 that is in a reasonable agreement with experimental points. So, equation (1) was found to describe well the general tendencies of the optimal local oscillator power with respect to the superconducting critical temperature and the bath temperature.

From Fig.3 and 5 an important conclusion can be made. Reduction of T_c from 9.5 K to 8 K leads to a decrease of j_c by 50%. It is followed by a reduction of P_{LO} by a factor of 2 but the mixer sensitivity is not affected. On contrary, a suppression of j_c down to the same value by means of higher bath temperature does not lead to a noticeable benefit with P_{LO}. Although, in this case T_r is not changed much too. Further suppression of j_c finally lead to the drop of P_{LO} but that is followed by a significant increase of the noise temperature.

As a next step we present the data of the optimal LO power for mixer with different volumes (Fig 6). NbN film thickness is 3.5 nm for all mixers and the mixer volume is represented by the product of the mixer length L by the mixer width W taken in micrometers. Therefore, two mixers considered just before, are positioned at L·W=1.6. The smallest mixer had the size 0.6×0.13 μm^2 and the local oscillator power 15 nW. The general tendency is a decrease of the LO power as the mixer volume decreases. The scattering of

the data is connected with the same effect which we have discussed in Fig.3 (a,b), i.e. different critical temperatures and therefore critical current density values. For the same mixer volume the heating of the electrons from the bath temperature up to T_c, where HEB mixers have the best sensitivity, consumes more local oscillator power. As a measure of the required local oscillator power we propose to introduce a "volume coefficient" which equals to the $L \cdot W \cdot j_c$, where L and W are taken in micrometers and j_c is taken in 10^6 A/cm^2. This coefficient can be calculated from a mixer dc parameters and then an expected local oscillator power in the optimum point can be estimated. As it can be seen from Fig. 6 b P_{LO} is a monotonous function of the volume coefficient.

Saturation effects in NbN HEB mixers.

As it can be seen from the previous chapter the requirement for LO power for NbN HEB mixers can be substantially decreased with small volume devices. But then, as it has been shown [7], the dynamic range of the mixers reduces too. In this chapter we present investigation of the saturation effects for different volume mixers.

Table 1. Parameters of the mixers used for saturation measurements. L and W are the mixers length and width, P_{LO} is the optimal local oscillator power absorbed in the mixer (obtained from the isothermal technique), T_{load} is a equivalent load temperature corresponded to 3 dB compression point.

Sample	***L×W, μm²***	***P_{LO}, nW***	***3 dB compression, nW***	***T_{load}, K***
M10-4, 1	2×0.3	70	2	20,000
2			4	40,000
L10-2-2	0.6×0.13	15	2	20,000
			4	40,000
		14.5	5	55,000

For this purpose we choused two mixers M10-4 and L10_2_2 (see also Tab.1). IV-curves of these mixers under LO radiation are presented in Fig.7a and 8a. Dependence of the IF signal vs. RF signal was measured in several points for each mixer. Obtained data are presented in Fig.7b and 8b. Solid line shows the linear regime of the mixer. For mixer M10_4 deviation from the linearity occurs at the input signals –57 dBm (2 nW) and –54 dBm (4 nW) for bias point 1 and 2 correspondingly, i.e. 15÷12 dB below absorbed LO power (70 nW). Taking into account the mixer gain bandwidth B=4 GHz one can calculate the effective load temperature of the receiver at the 3 dB compression point:

$T_{load} = \frac{P_{in}}{2 \cdot k \cdot B}$, where k is the Boltzmann constant. Calculated load temperatures are presented in the top x-axis. Saturation signal corresponds to a load temperature around 20,000 K and 40,000 K for point 1 and 2 correspondingly. The difference in the compression points for bias points 1 and 2 can be easy understood if we plot IF signal swing on the IV plane. The arrows mark amplitudes of the voltage oscillations on the mixer along 50 Ohm load line. If the mixer conversion efficiency changes within IF swing, mixer deviates from the linearity. So, saturation occurs at smaller signals for those mixers, which have stronger bias dependence of the conversion efficiency and operate at smaller bias voltages.

More pronounced bias dependence of the saturation point one can observe for a very small mixer. Data for the mixer L10_2_2 are presented in Fig.8 a and b. Absorbed LO power was only 14.5÷17.5 nW. The saturating power was measured at three bias points. As one can see, the saturation for both mixers occurs at the same input signal. It confirms our suggestion that the saturation is caused by IF signal but not by overheating with RF signal. Equivalent load temperatures corresponding to 3 dB compression points were also calculated (Fig.8b). So, even with smallest volume NbN mixers no deviations from the linear regime was observed up to 20,000 K of the load temperature. That allows a practical operation of even smaller mixers. In this case LO power can be of a few nW.

Conclusion.

From the presented data we can conclude, that by decreasing the mixer volume the required LO power can be decreased substantially. For the mixer with size $0.6 \times 0.13\ \mu m^2$ the LO power is only 15 nW. Regardless of the mixer volume, the input signal at which 3 dB compression occurs is of the order of 2-5 nW. That corresponds to an input load temperature of 20,000 K. We conclude that fabrication of even smaller mixers requiring LO power of the order of a few nW can be reasonable.

Critical temperature has a big impact on the required LO power. As T_c changes from 9.5 K to 8 K, P_{LO} decreases from 480 nW to 230 nW for $4x0.4\ \mu m^2$ mixer. Bath temperature plays a minor role for both P_{LO} and T_r. Only at $T=0.75\ T_c$ P_{LO} starts to decrease but it is followed by a growth of T_r.

In order to estimate P_{LO} at the optimum operating point one has to take into account both mixer volume and critical temperature. A product of the mixer volume and critical current density, measured at 4.2 K, is a good measure of P_{LO}.

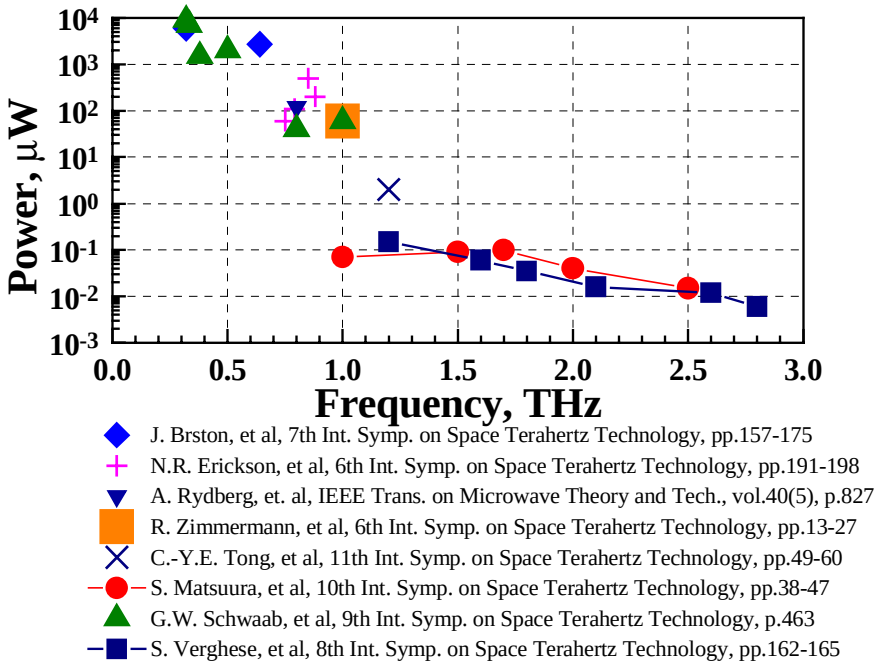

Fig. 1 Output power available from local oscillator sources reported in press.

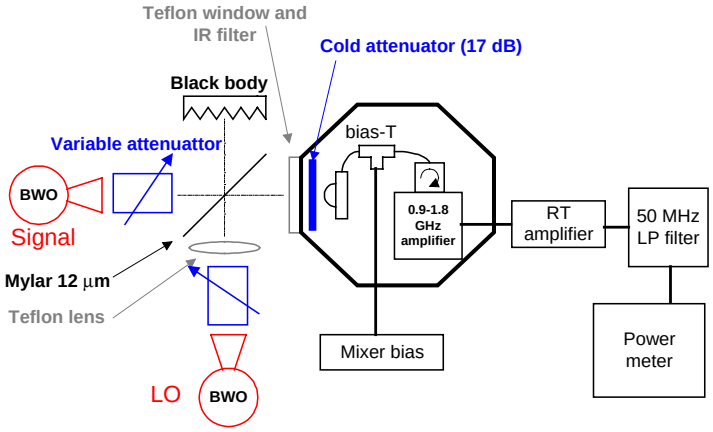

Fig. 2 Experimental set-up used for saturation measurements of HEB mixers. For the receiver noise temperature measurements, the cold attenuator in the cryostat was removed, signal BWO was replaced by 300K/77K black body.

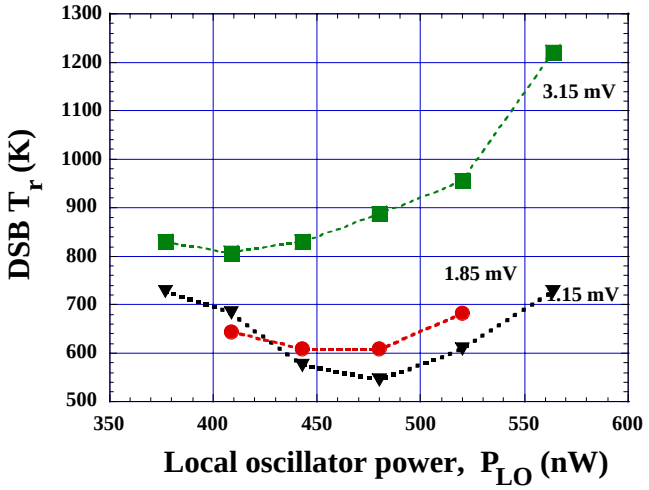

Fig. 3 a DSB receiver noise temperature vs LO power for different bias voltages. Mixer M12-2, width W=4μm, length L=0.4μm. j_c(4.2 K)=2.7·10^6 A/cm^2, T_c=9.5 K.

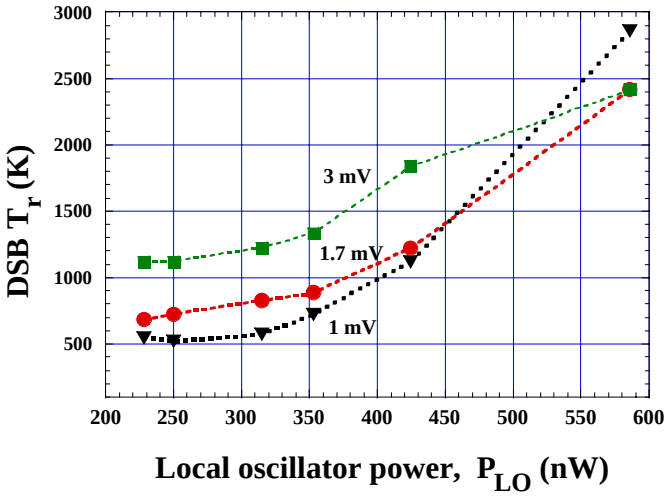

Fig. 3 b DSB receiver noise temperature vs LO power for different bias voltages. Mixer M10-2, width W=4μm, length L=0.4μm. j_c(4.2 K)=1.75·10^6 A/cm^2, T_c=8 K.

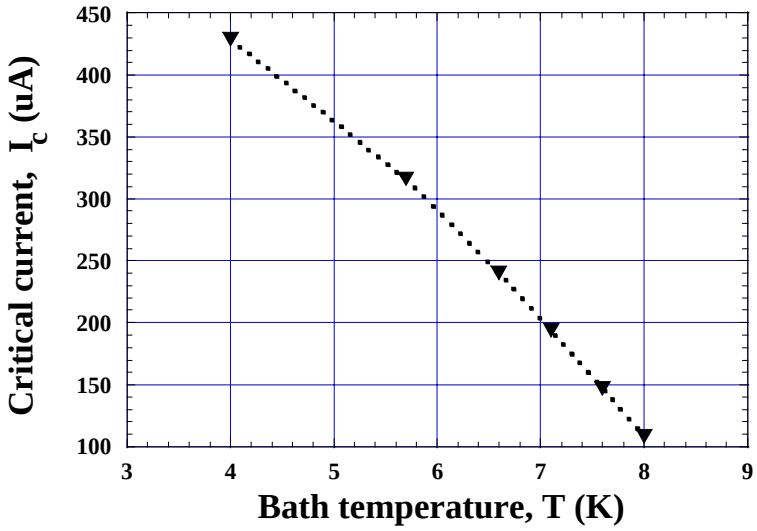

Fig. 4 Critical current vs bath temperature. Sample M12-2, T_c=9.5 K.

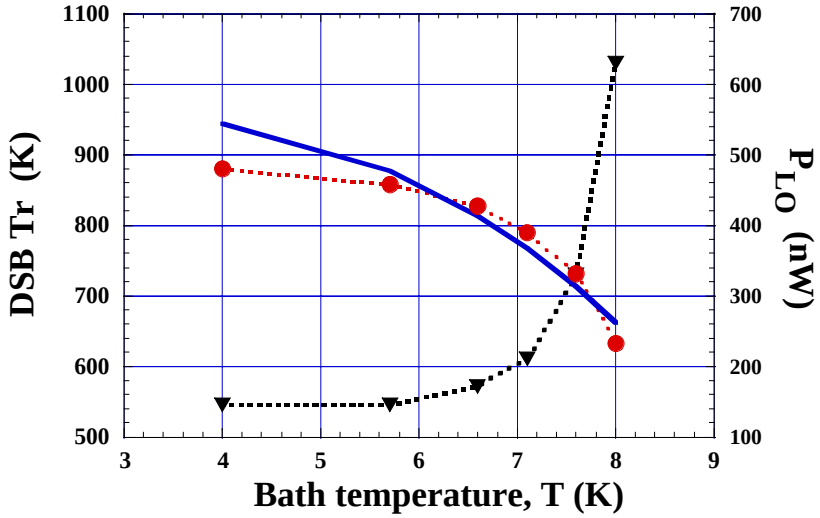

Fig. 5 DSB receiver noise temperature and optimum LO power vs bath temperature. Mixer M12-2, width W=4μm, length L=0.4μm, T_c =9.5 K. Solid line is obtained from Eq.1

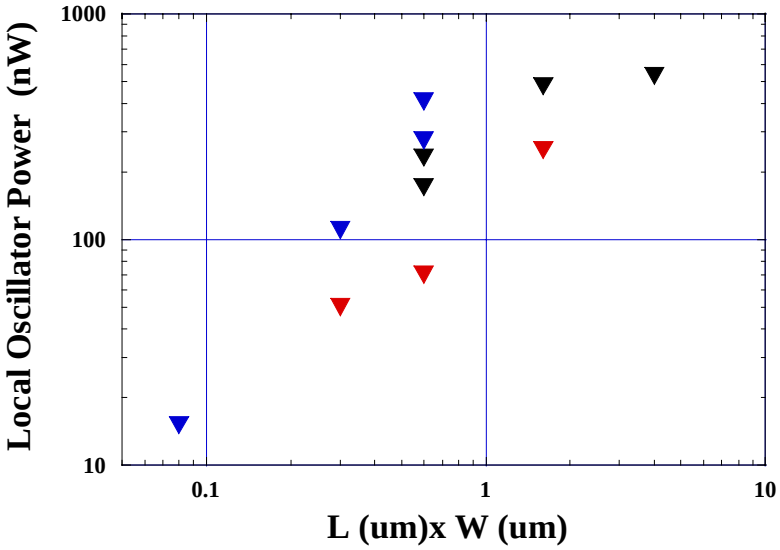

Fig. 6 a) Optimum local oscillator power for different mixer volume. Mixer volume is represented by a product of mixer length L and mixer width W taken in micrometers.

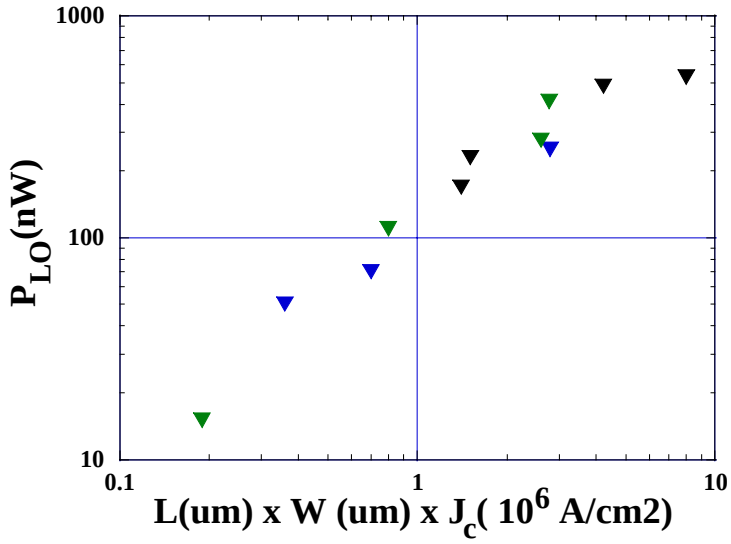

Fig. 6 b) Optimum local oscillator power P_{LO} vs "volume coefficient", i.e. a product of mixers length L, width W and critical current density J_c. J_c is measured at 4.2 K.

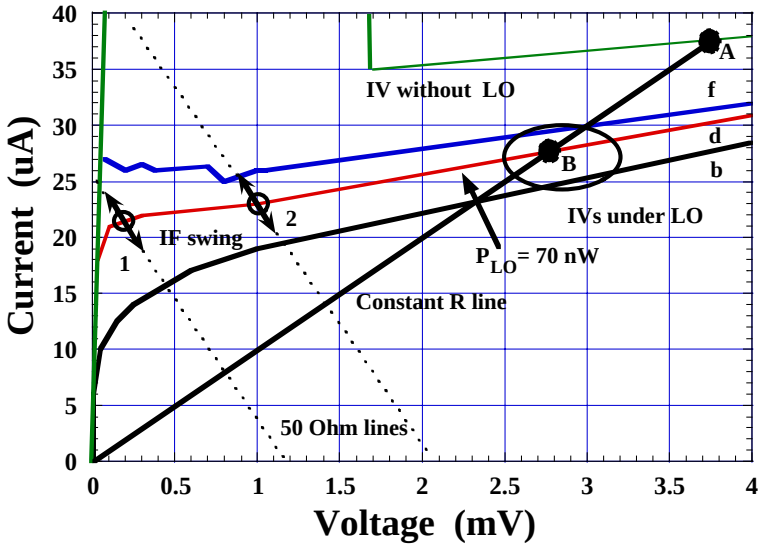

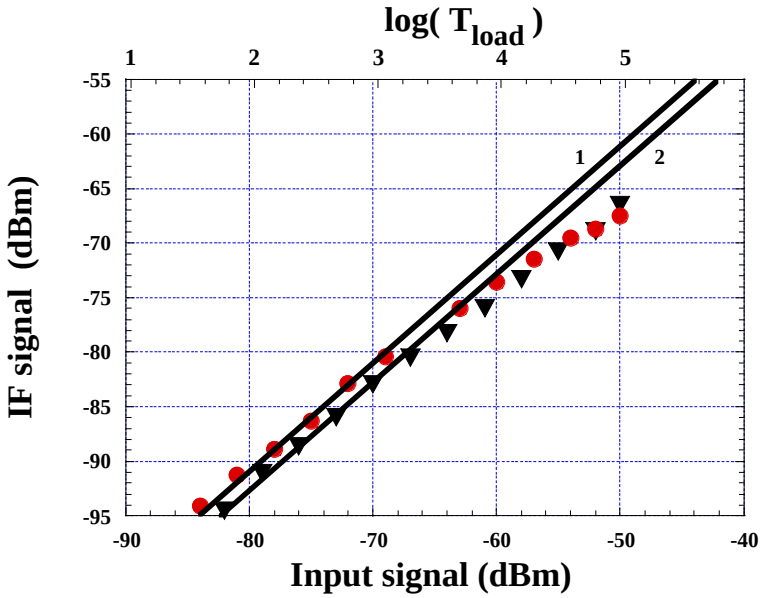

Fig. 7 a) Current-voltage curves of the mixer M10_4. Arrows show the amplitude of the voltage swing corresponding to 3 dB compression point. b) intermediate frequency signal vs. RF input signal for two bias points; bias point 1 (circles), bias point 2 (triangles). 3 dB compression occurs at a load temperature around 20,000 K.

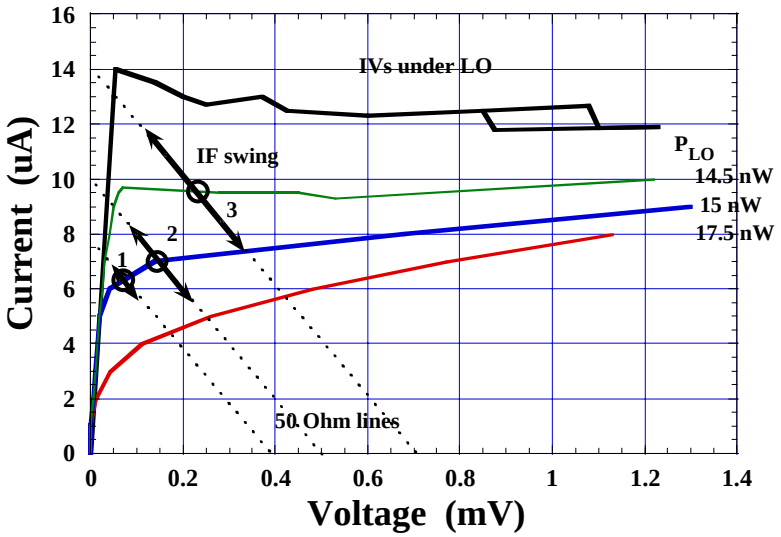

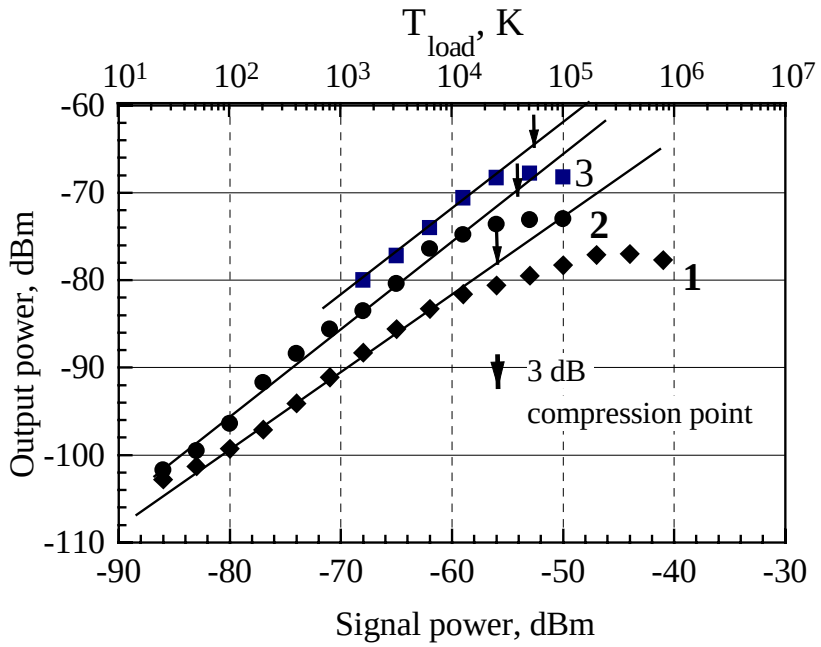

Fig. 8 . a) Current-voltage curves of the mixer L10_2_2. Arrows show the amplitude of the voltage swing corresponding to 3 dB compression point. b) intermediate frequency signal vs. RF input signal for three bias points; 3 dB compression occurs at a load temperature around 20,000 K.

References.

1 E. M. Gershenzon, G. N. Gol'tsman, I. G. Gogidze, A. I. Elant'ev, B. S. Karasik and A. D. Semenov, "Millimeter and submillimeter range mixer based on electronic heating of superconducting films in the resistive state", Sov. Phys. Superconductivity, 3, 1582, 1990.

2 M.Kroug, S.Cherednichenko, H.Merkel, E.Kollberg, B.Voronov, G.Gol'tsman H.-W.Huebers, H.Richter" "NbN HEB mixer for terahertz heterodyne receivers", ASC2000, Virgivia Beach, VA, USA,2000, to be published in IEEE Trans. on Appl. Superconductivity.

3 A.D. Semenov, H.W. Huebers, J. Schubert, G. Gol'tsman, A.I. Elantiev, B. Voronov, and G. Gershenzon, "Design and performance of the lattice cooled hot-electron terahertz mixer", J.Appl.Phys. **88** (11), p.6758, 2000.

4 J. Kawamura, C.-Y. E. Tong, R. Blundell, D. C. Papa, T. R. Hunter, G. Gol'tsman, S. Cherednichenko, B. Voronov, and E. Gershenzon, "An 800 GHz NbN Phonon-cooled Hot-electron Bolometer Mixer Receiver", IEEE Trans. on Appl. Superconductivity, vol. 9, No 2, 3753, 1999.

5 S. Cherednichenko, M. Kroug, H. Merkel, E. Kollberg, et al., "Phonon cooled HEB mixers made from NbN films on MgO substrates", 11th Int. Symp. on Space Terahertz Technology, Ann Arbor (MI), 2000

6 J. Kawamura et al, Appl.Phys.Lett. 70 (12), 24 March, 1997

7 J. Kawamura et al, *Proc. 9th Int. Symp. on Space Terahertz Technology*, Pasadena, CA, p.35, 1998.

8 P.Yagoubov et al, ", IEEE Trans. on Appl. Superconductivity, vol. 9, No 2, 3757, 1999.

9 P. Yagoubov, M. Kroug, H. Merkel, E. Kollberg, G. Gol'tsman, S. Svechnikov, E.Gershenzon, "Noise temperature and local oscillator power requirement of NbN phonon-cooled hot electron bolometric mixers at terahertz frequencies", Appl.Phys.Lett. 73 (19), p.2814, 1998

10 S. Cherednichenko, P. Yagoubov, K. Il'in, G. Gol'tsman and E. Gershenzon, "Large bandwidth of NbN phonon cooled hot-electron bolometer mixers on sapphire substrates", *Proc. 8th Int. Symp. on Space Terahertz Technology*, Cambrige, MA, 245, 1997.

11 M. Kroug, P. Yagoubov, G. Gol'tsman and E. Kollberg, "NbN quasi-optical phonon cooled hot electron bolometric mixers at THz frequencies", Proc. of the 3rd. European Conference on Applied Superconductivity, Veldhoven (Netherlands), Inst. Phys. Conf. Ser. No 158, p. 405, 1997.

12 H. Ekstrom, E. Kollberg, P. Yagoubov, G. Gol'tsman, E.gershenzon, Appl.Phys.Lett. **70** 3296, (1997)

13 B.S. Karasik and A.I. Elantiev, "Noise temperature limit of a superconducting hot-electron bolometer mixer", Appl.Phys.Lett, **68** (6), p.853, 1996

14 V.V.Smidt, "Introduction to Superconductivity", Moscow, "Nauka", 1982.

Antenna Pattern of the Quasi-Optical Hot-Electron Bolometric Mixer at THz Frequencies

H.-W. Hübers[a)1], A. D. Semenov[a)], H. Richter[a)], J. Schubert [a)2], S. Hadjiloucas [b)], J. W. Bowen [b)], G.N. Gol'tsman[c)], B.M. Voronov[c)], and E.M. Gershenzon[c)]

a) DLR Institute of Space Sensor Technology and Planetary Exploration, 12489 Berlin, Germany
b) Department of Cybernetics, The University of Reading, Whiteknights, Reading RG6 6AY, United Kingdom
c) Physical Department, State Pedagogical University of Moscow, 119891 Moscow, Russia

Abstract

An investigation of the antenna pattern of a quasi-optical hot-electron bolometric mixer at terahertz (THz) frequencies is presented. The antenna consists of a logarithmic-spiral planar feed antenna which was mounted on the back side of a hemispherical lens with an extension length optimized for 2.5 THz. The power patterns were measured at several frequencies between 0.7 THz and 4.3 THz for two orthogonal polarizations. The level of the first sidelobe is smallest at 2.5 THz. The sidelobes are different for both polarizations and the main lobes are wider than predicted by diffraction at the diameter of the lens. This indicates that the pattern is not only determined by the lens but also by the feed antenna. The antenna pattern measured by heterodyne detection has almost the same width as the power pattern but significantly higher sidelobes. At 1.6 THz the phase pattern of the hybrid antenna was measured with a quasi-optical interferometric technique.

1. Introduction

The hot-electron bolometer (HEB) is the mixer of choice for heterodyne receivers at terahertz (THz) frequencies, where SIS mixers and Schottky mixers are not sensitive enough for ultimate, quantum limited performance. It has been shown that quasi-optically coupled HEB mixers have noise temperatures close to the quantum limit [1,2,3,4], an intermediate frequency bandwidth up to 9 GHz [3,4,5,6], and require local oscillator power less than 1 μW [1,2,3,4].

At this quite advanced stage of HEB mixer development it becomes increasingly important to characterize precisely the antenna pattern of the quasi-optical HEB mixer at

[1] heinz-wilhelm.huebers@dlr.de
[2] Present address: Max-Planck Institut für Extraterrestrische Physik, 85740 Garching, Germany

THz frequencies. The knowledge of the antenna pattern is of prime importance for any practical application since it allows to achieve optimal coupling of the receiver to a telescope as well as accurate retrieval of atmospheric data. At frequencies below about 1 THz waveguide coupled mixers are commonly used. The performance of waveguide antennas is excellent at these frequencies. However, beyond 1 THz losses of the waveguide increase. Additionally, fabrication becomes more difficult and costly. An alternative approach is the combination of a planar antenna with a lens. In this quasi-optical design the mixer and a planar antenna are fabricated on a substrate which is mounted on the back side of a lens. The lens is made from the same material or a material with similar refractive index as the substrate. Different types of lenses and planar antennas have been investigated [7,8]. Depending on the actual requirements such as Gaussian coupling efficiency and directivity either extended hemispherical lenses or elliptical lenses are used. If the feed antenna is placed in the aplanatic focus of a hemispherical lens it is called hyperhemispherical lens. At a certain extension length the antenna pattern is determined by the diffraction limit of the lens. If the planar feed antenna is placed at this position it is called hybrid antenna [7]. In fact the hybrid antenna is a good approximation to the elliptical lens-antenna. The hyperhemispherical antenna yields a better Gaussian coupling efficiency than the hybrid antenna or the elliptical lens-antenna but the directivity is worse [8]. In this paper we investigate the antenna performance of a HEB mixer integrated in a hybrid antenna with a logarithmic-spiral feed.

2. Antenna Design

The investigated HEB mixers were made from a 3.5 nm thick superconducting NbN film. The film was deposited by dc reactive magnetron sputtering onto a 350 μm thick high resistivity Si substrate (5 kΩcm). The bolometer itself is a 1.4 μm wide and 0.2 μm long bridge. It has a transition temperature of about 9 K. The HEB is located in the center of a planar two-arm logarithmic-spiral antenna, which couples both the signal and the local oscillator (LO) radiation with the bolometer (Fig. 1). The central part of the antenna was patterned using electron beam lithography while the outer part was defined by conventional UV photolithography. The diameter of the circle that circumscribes the spiral structure is 130 μm. This effectively determines the longest wavelength above which the properties of the feed antenna are no longer independent of the wavelength. The wavelength inside the silicon should be less than twice the diameter of this circle. In our case this yields a long wavelength limit outside the silicon of 884 μm (0.34 THz). The shortest wavelength should be at least 10 times larger than the radius of the inner circle, inside which the antenna arms form inner terminals and deviate from the ideal spiral shape. The inner circle has a diameter of about 2.2 μm yielding a short wavelength cut-off of 37 μm (8 THz). However it should be pointed out that the wavelength limits are an estimate and have to be verified experimentally. Between the circles, the antenna arms make two full turns. A radial line from the origin of the antenna intersects a spiral arm at an angle of 70°.

The substrate supporting the HEB with the planar antenna was glued onto the flat side of an extended hemispherical lens. The lenses are spheres with either 6 mm or 12 mm diameter, which were cut off from optically polished, high resistivity (>10 kΩ cm) silicon. Lenses with and without an antireflection coating from Parylene C were investigated [9]. The extension of the lens together with the substrate yields a total extension length of 1.2 mm and 2.4 mm for the 6 mm lens and for the 12 mm lens, respectively. This is the optimal extension length, for which the beam pattern of the hybrid antenna is predicted to be diffraction limited, i.e. the pattern is rather determined by the diameter of the lens than by the beam properties of the planar feed antenna. It is worth mentioning that in the range of the diameter to wavelength ratios, which we covered in the experiments, the optimal extension length weakly depends on the wavelength [7].

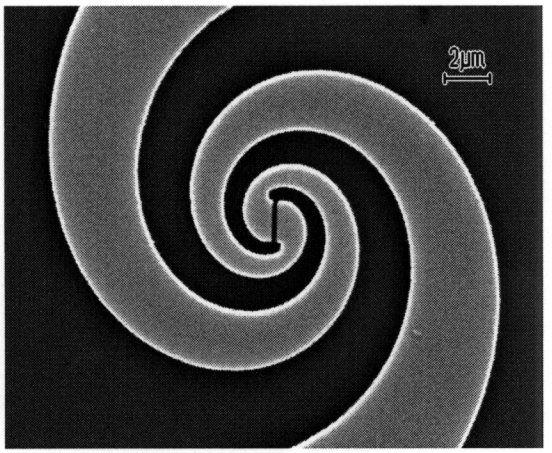

Fig. 1: Layout of the logarithmic-spiral antenna. The HEB is located in the gap in the center of the spiral arms. It is 0.2 µm long and 1.4 µm wide. The inner circle where the spiral deviates from the ideal shape has a diameter of 2.2 µm.

3. Antenna Power Pattern

The power patterns of different hybrid antennas have been measured 0.7 THz, 1.4 THz, 1.6 THz, 2.5 THz, 3.1 THz and 4.3 THz. The temperature of the HEB was set slightly below the transition temperature of the superconducting bridge and the HEB was biased with constant current. The dewar with the HEB was placed on a rotation table in the far field (3-10 × Rayleigh distance) of an optically pumped far-infrared gas laser. The HEB was located in the center of rotation. The laser radiation was chopped and the signal delivered by the HEB was measured as a function of the angle of rotation. Patterns were measured by rotating the HEB around the axis parallel to its length. The polarization of the incoming radiation was determined by a wire grid. For E-plane measurements the vector of the electric field of the laser radiation is parallel to the width of the superconducting bridge while for H-plane measurements it is parallel to the length. Some examples of the power patterns are shown in Fig. 2.

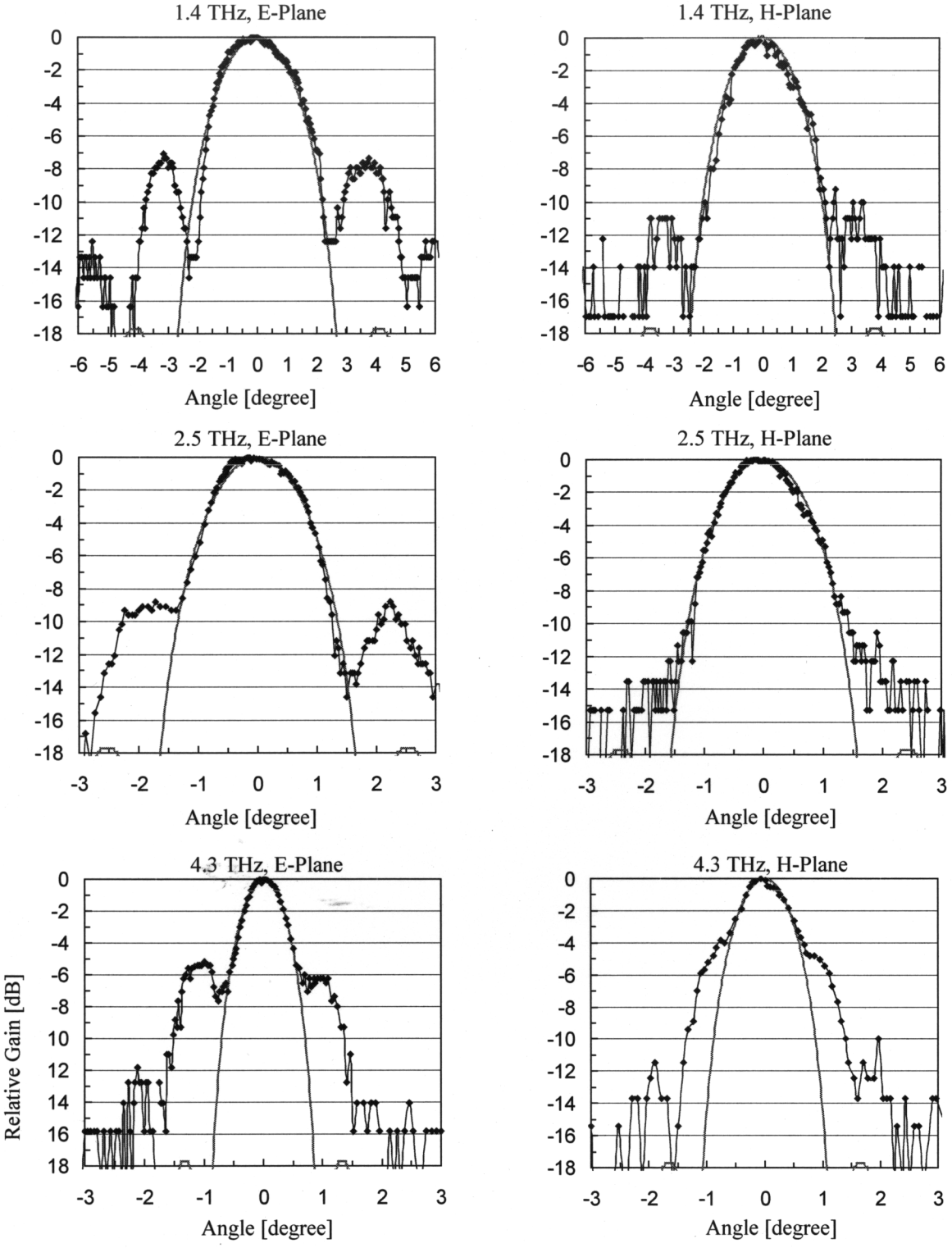

Fig. 2: Antenna power patterns at different frequencies and in two orthogonal polarizations (E- and H- plane refer to polarization of the laser radiation, see text).

The solid lines represent the diffraction limited antenna patterns that were simulated according to the expression $(2J_1(v)/v)^2$, where $v = (\pi \tan(\theta)\, d)/\lambda$, J_1 is the Bessel function of the first kind, θ is the angle of rotation and d is an effective diffracting aperture, which was varied to yield the best fit to the main lobe of the measured pattern. In Fig. 3 the results are summarized. The first sidelobe is lowest at 118.8 µm (2.5 THz) which is the wavelength for which the extension length of the hybrid antenna is optimal. Towards longer wavelengths the level of the first sidelobe increases slightly because the extension length is longer than the optimum one. At the two shortest wavelengths the first sidelobes are highest. This might be attributed to contributions from the inner part of the feed antenna where the spiral deviates from the ideal shape. In general the sidelobes are higher than predicted by simple diffraction theory of a uniform wave at a circular aperture. This is partly due to internal reflections. Additionally, the sidelobes in the E-plane are always higher than in the H-plane except for the two shortest wavelengths. These findings indicate that the pattern of the log-spiral feed antenna is not rotational symmetric and does not illuminate the diameter of the lens uniformly.

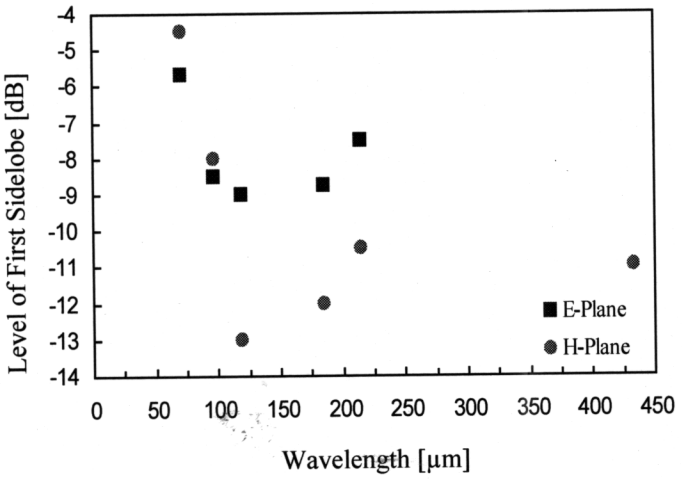

Fig. 3: Level of the first sidelobe as a function of wavelength for E- and H-plane.

Fig. 4 displays the FWHM as a function of the wavelength for E- and H-plane patterns. The dashed line is a linear fit to the data while the solid line represents the FWHM as expected for an antenna pattern which is diffraction limited by the diameter of the lens. The optimum extension length of a hybrid antenna made from silicon is almost constant in the wavelength range considered here. Therefore the linear dependence of the FWHM on the wavelength indicates that diffraction dominates the width of the antenna pattern. The difference between measurement and prediction might be explained by a non-uniform illumination of the lens by the feed antenna. Because of the high refractive index of silicon compared to quartz, this effect is more pronounced in a hybrid antenna made from silicon than in one made from quartz. The optimum extension length at given wavelength and diameter of the lens is smaller in silicon than in quartz. This results in a lower edge taper for a silicon hybrid antenna than for a quartz hybrid antenna. This in turn yields a smaller FWHM for the silicon hybrid antenna. For a quartz hybrid antenna the FWHM is larger and agrees better with the width determined by diffraction the lens diameter.

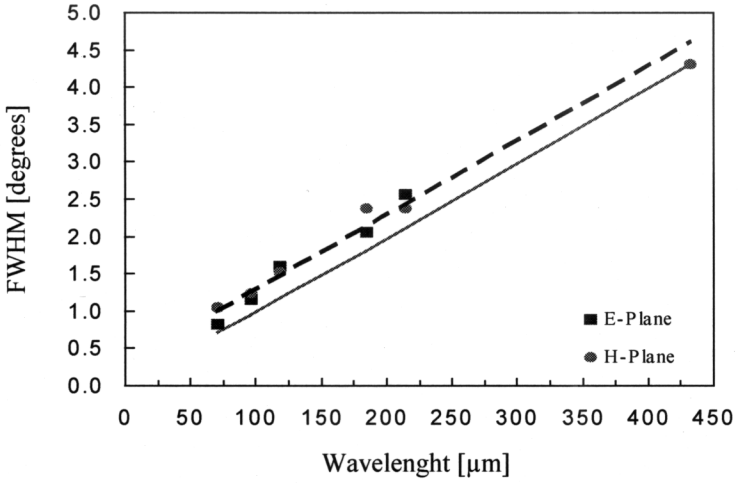

Fig. 4: FWHM as a function of the wavelength. The solid line represents the diffraction limit as given by the diameter of the lens while the dashed line is a linear fit to the measured FWHM.

4. Heterodyne Antenna Pattern

For designing a practical heterodyne receiver the antenna pattern measured in the heterodyne mode is the relevant one. This pattern may differ from the antenna power pattern since heterodyne detection preserves the phase information. We have performed measurements of the antenna pattern in the heterodyne mode. The hybrid antenna consisted of a 12 mm diameter silicon lens with a Parylene anti-reflection coating and a log-spiral feed antenna as described above. Again, the extension length was optimized for 2.5 THz. In principle, a standard Y-factor measurement setup as described previously [1] is used. However, instead of a liquid nitrogen cold load a small (0.14° angular width) metal halide hot source is used. It can be moved in a plane orthogonal to the axis defined by the center of the main lobe of the antenna. The double sideband (DSB) signal is measured as a function of the position of the hot source. The heterodyne antenna pattern is given by the DSB signal as a function of the angle under which the hot source is seen by the HEB mixer. Fig. 5 displays the antenna patterns measured at 0.7 THz, 1.6 THz and 2.5 THz. The polarization of the FIR laser local oscillator is arbitrary since a rotatable wire grid is used to adjust the power from the FIR gas laser to the level which yields the best signal to noise ratio. At all frequencies the first sidelobe is significantly higher in the heterodyne pattern than in the power pattern and it increases with frequency. The FWHM is almost the same in the heterodyne and power patterns except at 2.5 THz where it is bigger in the heterodyne pattern. This is possibly due to a contribution from the high sidelobe to the main lobe. The reason for the high sidelobes is not clear yet. One possible explanation could be a strong change of the phase across the main lobe of the power pattern as it will be discussed in the next section. However, the power patterns were measured with an uncoated 6 mm lens while the heterodyne patterns were measured with a 12 mm anti-reflection coated lens. We would like to emphasize here that the spectral properties of our antenna are effected not only by the smaller radius of the spiral but also by the actual size of the HEB. This seems to be a general feature of planar antennas, since it was also noticed for twin-slot antennas [10]. For our log-spiral

antenna we found that, according to simulations [1], decrease of the HEB width flattens the frequency dependence of the noise temperature. The difference in the DSB noise temperature between 0.6 THz and 2.5 THz was reduced from 2.8 dB for a 1.7 μm wide HEB to 1.5 dB for a 1.4 μm wide HEB. Here again, the 1.7 μm HEB was mounted on the uncoated 6 mm lens while the 1.4 μm HEB was mounted on the 12 mm coated lens. All this makes comparison and interpretation of antenna patterns at different frequencies more difficult.

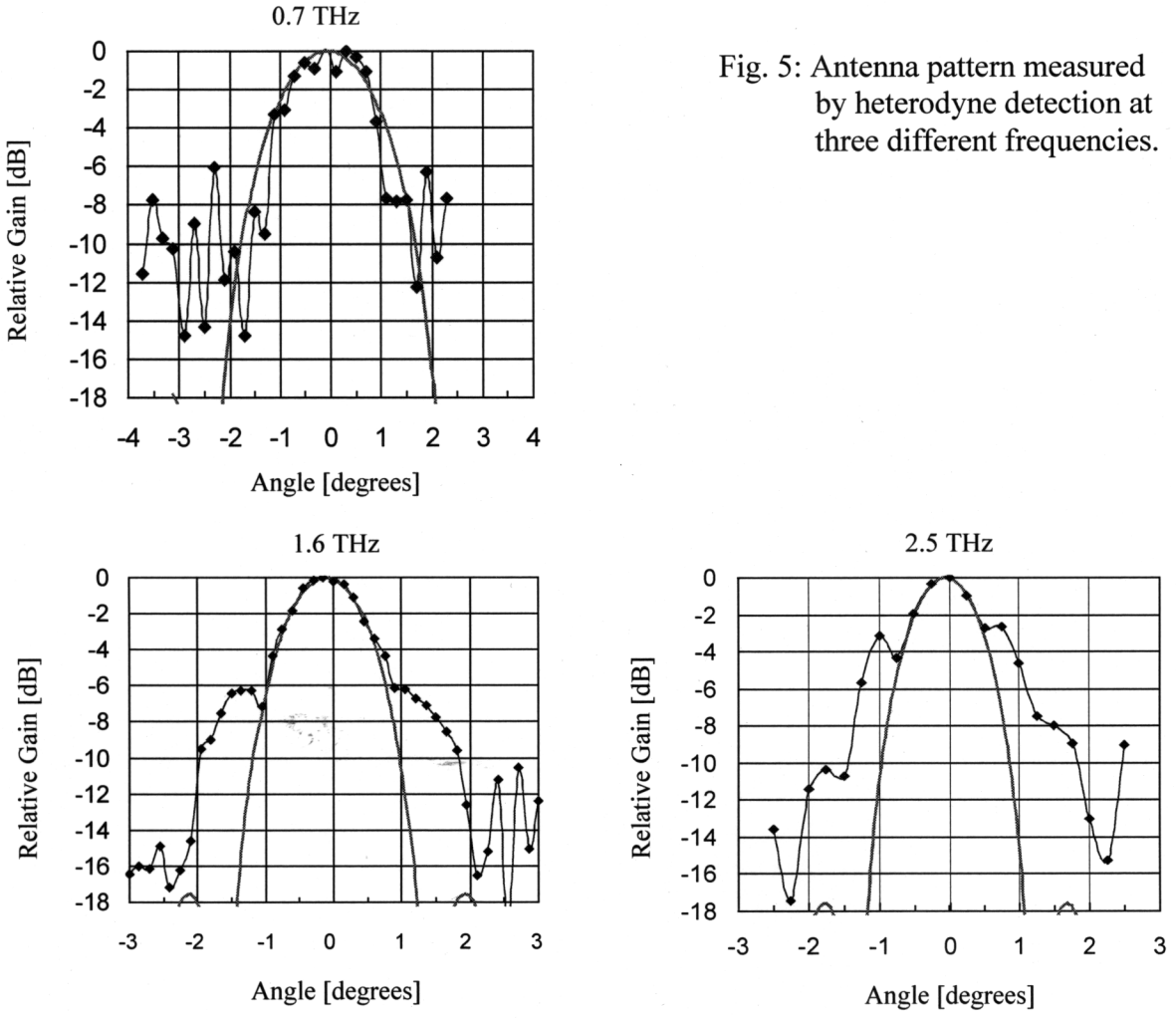

Fig. 5: Antenna pattern measured by heterodyne detection at three different frequencies.

5. Phase Measurements

Phase pattern measurements at frequencies towards or above 1 THz become increasingly problematic because it is difficult to provide a coherent phase reference. In our measurements we use a novel, quasi-optical interferometric technique to record both amplitude and phase pattern of antenna [11]. This method has been verified with a

Schottky mixer in a corner cube mount at 1.4 THz [12]. The principle is depicted in Fig. 6. The output radiation from a FIR gas laser is split by a 45° wire grid. A vertical wire grid is used in transmission and a horizontal wire grid is used in reflection. This set-up results in two mutually coherent co-polar sources S_1 and S_2, each launching a beam towards a test antenna at slightly different angles θ and $\theta+\theta_S$, where θ_S is the angle subtended by the two sources. The two beams have a phase delay ϕ_d. By blocking first one source and then the other, the power patterns V_1 and V_2 are measured as a function of the angle θ. Finally, the power pattern V_{12} is measured when both sources launch a beam towards the HEB. The phase relation is extracted from the three power patterns according to

$$\Phi(\theta + \theta_s) - \Phi(\theta) + \Phi_d = \cos^{-1}\left\{\frac{V_{12}(\theta) - V_1(\theta) - V_2(\theta)}{2\sqrt{V_1(\theta) \cdot V_2(\theta)}}\right\} \qquad (1)$$

Since Φ_d is independent of θ and the phase reference it can be set to zero. If $V_{12}(\theta)$, $V_1(\theta)$, and $V_2(\theta)$ are measured the relative phase between successive directions which are separated by θ_s can be determined.

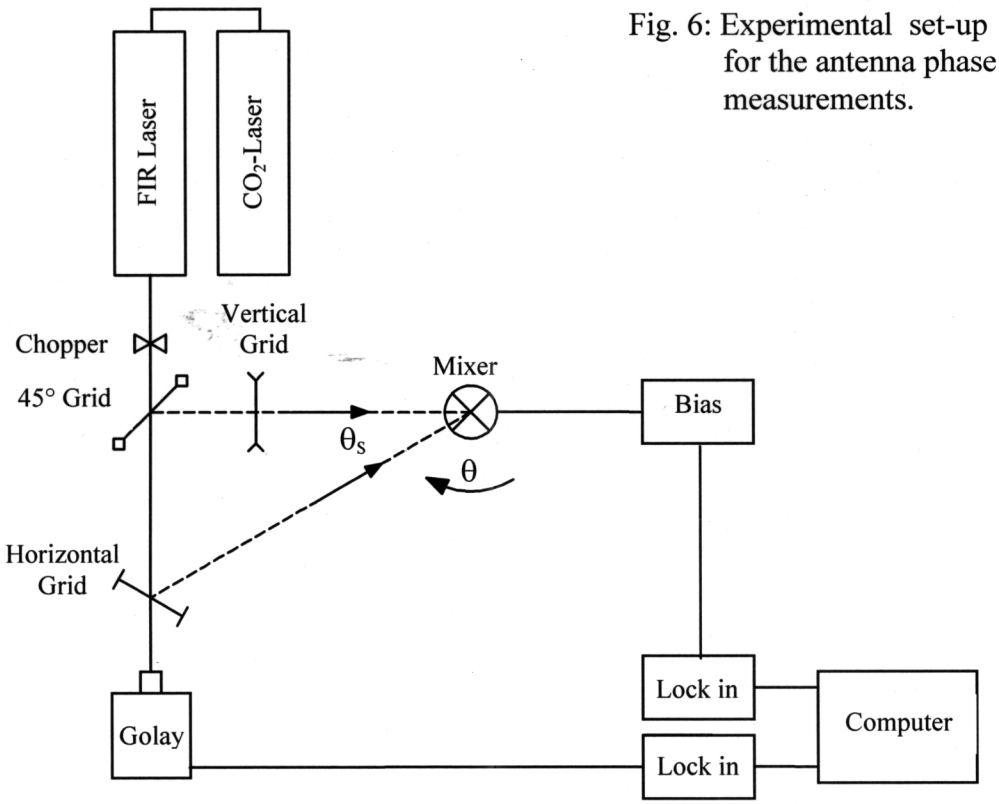

Fig. 6: Experimental set-up for the antenna phase measurements.

In Fig. 7 power and phase patterns measured at a frequency of 1.6 THz in the E-plane of the FIR laser are shown. The hybrid antenna consisted of a 6 mm lens without anti-reflection coating and the above described log-spiral feed antenna. FWHM and the level of the first sidelobe agree with the power patterns presented in section 3. The minimum phase difference occurs at a different position than the maximum of the main lobe. Also, there is no flat part of the phase inside the main lobe of the power pattern. This indicates that the HEB was not exactly positioned at the phase center. This position has to be determined by finding the pivot position that gives maximum phase flatness over the main lobe. However, the phase pattern of the hybrid antenna has changes quite drastically by about 0.3 –1.2 rad/degree. In contrast, the 4λ quasi-optical Schottky mixer at 1.4 THz has a flat phase within the -6 dB points of the main lobe and the change of the phase outside the main lobe of the power pattern is < 0.2 rad/degree. This indicates that the strong change of the phase of the hybrid antenna may contribute to the high level of sidelobes seen in the heterodyne antenna pattern. However, further investigations are necessary.

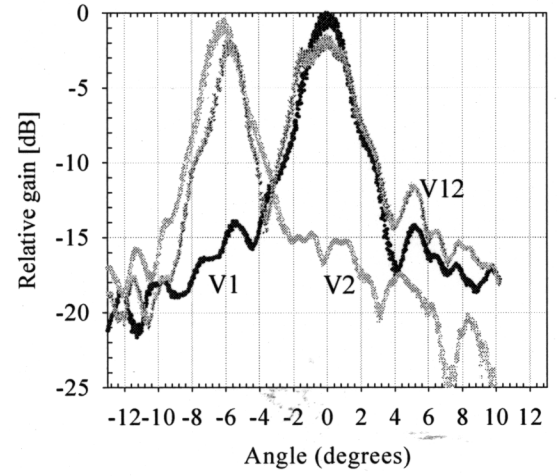

Fig. 7: Power patterns V_1, V_2 of two co-polar sources and the interference pattern V_{12} (left). Power pattern (bottom left) and extracted phase pattern (bottom right). All patterns are measured at 1.6 THz in E-plane.

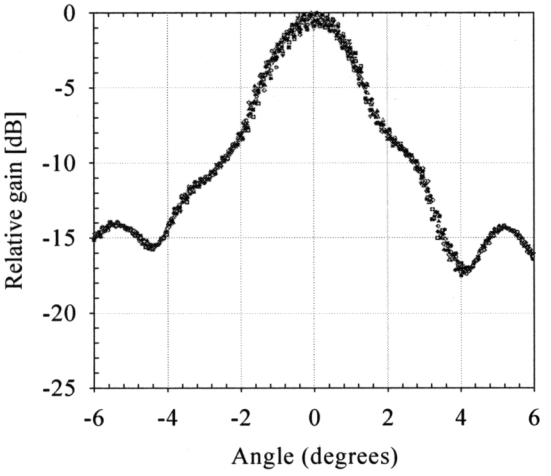

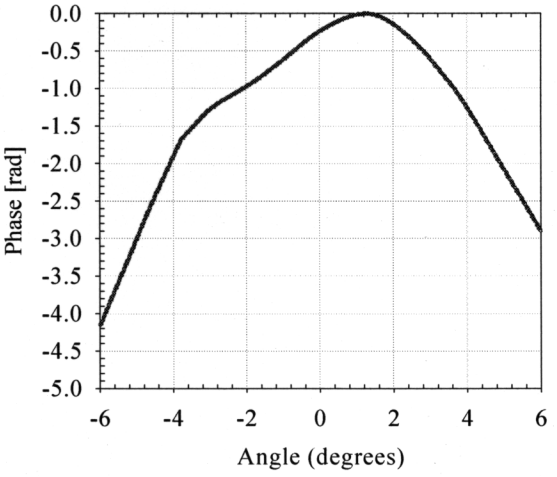

6. Summary and Conclusions

We have investigated the beam pattern of a HEB mixer with a hybrid antenna. The antenna consists of a log-spiral feed antenna and a silicon lens. The power pattern was measured in the frequency range from 0.7 THz to 4.3 THz. It was found that the FWHM of the main lobe is wider and the sidelobes are higher than predicted by diffraction of a uniform wave at the aperture given by the diameter of the silicon lens. This can be attributed to a non-uniform illumination of the lens by the feed antenna. Measurements of the antenna pattern by heterodyne detection at 0.7 THz, 1.6 THz and 2.5 THz reveal that the sidelobes are higher than in the power patterns while the FWHM is almost the same. The phase of the hybrid antenna has been determined by a quasi-optical interferometric method. It is not constant across the main lobe of the power pattern. The results emphasize the importance of heterodyne antenna measurements and phase measurements. However, further investigations are necessary in order to get a complete understanding of the antenna pattern of a hybrid antenna at THz frequencies.

Acknowledgement

This work was financially supported by the German Ministry of Science and Education (WTZ RUS-149-97), the European TMR project "INTERACT", NATO Division of Scientific Affairs, and the INTAS grant 99-0569.

References

[1] A. D. Semenov, H.-W. Hübers, J. Schubert, G. N. Golt'tsman, A. I. Elantiev, B. M. Voronov, and E. M. Gershenzon, "Design and performance of the lattice-cooled hot-electron terahertz mixer", J. Appl. Phys. **88**, 6758 (2000).
[2] E. Gerecht, C. F. Musante, Y. Zhuang, M. Ji, K. S. Yngvesson, T. Goyette, and J. Waldman, "Development of focal plane arrays utilizing NbN hot electron bolometric mixers for the THz region", Proc. of the 11th Int. Symp. on Space Terahertz Technol., 209 (2000).
[3] M. Kroug, S. Cherednichenko, H. Merkel, E. Kollberg, B. Voronov, G. Gol'tsman, H.-W. Hübers, and H. Richter, "NbN HEB mixer for terahertz heterodyne receivers" Proc. of the Int. Conf. on Appl. Superconductivity, Virginia Beach (2000).
[4] R. Wyss, B. Karasik, W. McGrath, B. Bumble, and H. LeDuc, "Noise and bandwidth mesurements of diffusion cooled Nb hot-electron bolometer mixers at frequencies above the superconductive energy gap", Proc. of the 10th Int. Symp. on Space Terahertz Technol., 214 (1999).
[5] S. Cherednichenko, M. Kroug, P. Yagoubov, H. Merkel, E. Kollberg, K. S. Yngvesson, B. Voronov, and G. Gol'tsman, "IF bandwidth of phonon cooled HEB mixers made from NbN films on MgO substrates", Proc. of the 11th Int. Symp. on Space Terahertz Technol., 219 (2000).

[6] A. D. Semenov, H.-W. Hübers, "Frequency Bandwidth of a Hot-Electron Mixer According to the Hot-Spot Model", Proc. of the Int. Conf. on Appl. Superconductivity, Virginia Beach (2000).
[7] T. H. Büttgenbach, "An improved solution for integrated array optics in quasi-optical mm and submm receivers: the hybrid antenna", IEEE Trans. Microwave Theory Tech. **41**, 1750 (1993).
[8] D. F. Filipovic, S. S. Gearhart, and G. M. Rebeiz, "Double-slot antennas on extended hemispherical and elliptical silicon dielectric lenses", IEEE Trans. Microwave Theory Tech. **41**, 1738 (1993).
[9] H.-W. Hübers, J. Schubert, A. Krabbe, M. Birk, G. Wagner, A. Semenov, G. Gol'tsman, B. Voronov, and E. Gershenzon, "Parylene anti-reflection coating of a quasi-optical hot-electron bolometric mixer at terahertz frequencies", Infrared Phys. and Technol. **42**, 41 (2000).
[10] R. A. Wyss, A. Neto, W. R. McGrath, B. Bumble, H. LeDuc, "Submillimeter-wave spectral response of twin-slot antennas coupled to hot-electron bolometers", Proc. of the 11th Int. Symp. on Space Terahertz Technol., 388 (2000).
[11] J. W. Bowen, S. Hadjiloucas, and B. M. Towlson, "An interferometric technique for measuring terahertz antenna phase patterns", Proc. of the 24th Int. Conf. on Infrared and Millimeter Waves, Monterrey (1999).
[12] S. Hadjiloucas, H.-W. Hübers, J. W. Bowen, and J. Schubert, "Quasi-optical measurements of corner cube antenna amplitude and phase patterns at 1397.1 GHz", IOP Proc. of the Appl. Optics and Opto-Electronics Conf., 77 (2000).

Monolithic THz Frequency Multipliers

N.R. Erickson, G. Narayanan and R.M. Grosslein
Dept. of Astronomy, University of Massachusetts, Amherst, MA 01003

S. Martin, I. Mehdi, and P. Smith
Jet Propulsion Laboratory, California Institute of Technology, Pasadena, CA 91109

M. Coulomb and G. DeMartinez, Submillimeter-Wave Tech. Lab.,
University of Massachusetts, Lowell, MA, 01854

Introduction

Frequency multipliers are required as LO sources for frequencies up to 2.7 THz for FIRST and airborne applications. Multipliers at these frequencies have not previously been demonstrated, and the object of this work was to show whether such circuits are really practical. A practical circuit is one which not only performs as well as is required, but also can be replicated in a time that is feasible. As the frequency of circuits is increased, the difficulties in fabrication and assembly increase rapidly. Building all of the circuit on GaAs as a monolithic circuit is highly desirable to minimize the complexity of assembly, but at the highest frequencies, even a complete monolithic circuit is extremely small, and presents serious handling difficulty. This is compounded by the requirement for a very thin substrate. Assembly can become very difficult because of handling problems and critical placement. It is very desirable to make the chip big enough to that it can be seen without magnification, and strong enough that it may be picked up with tweezers. Machined blocks to house the chips present an additional challenge. Blocks with complex features are very expensive, and these also imply very critical assembly of the parts. It would be much better if the features in the block were as simple as possible and non-critical to the function of the chip. In particular, grounding and other electrical interfaces should be done in a manner that is highly reproducible.

A complete realization of all of these desires is not presently possible, but we can come fairly close. The primary contribution to the solution is to fabricate all circuitry on 3 μm thick GaAs, and add to this a 50 μm thick frame to support it and provide a handle [1]. The thin GaAs is separated from the thick substrate by an etch stop layer, and so the fabrication of this structure is quite practical. The 3 μm membrane is surprisingly robust, and while it can not be touched by hand, it can contact the block and have beam leads for grounding. An external connection for DC bias may connect to the frame, which is much stronger. Figure 1 shows a framed circuit for a THz doubler, which incorporates a side arm to the circuit membrane in addition to the beam leads.

The metal mounting block provides a frame holder, and waveguides to external interfaces. With the correct circuit design the exact placement of the circuit in the block is not excessively critical, although with THz circuits, even this reduced sensitivity still

demands micron level accuracy. The blocks are in general much simpler to machine than those involving frameless circuits, because the block does not need to touch the membrane, and most clearances can be made fairly generous. Beam lead grounding can be designed to bridge an expected gap.

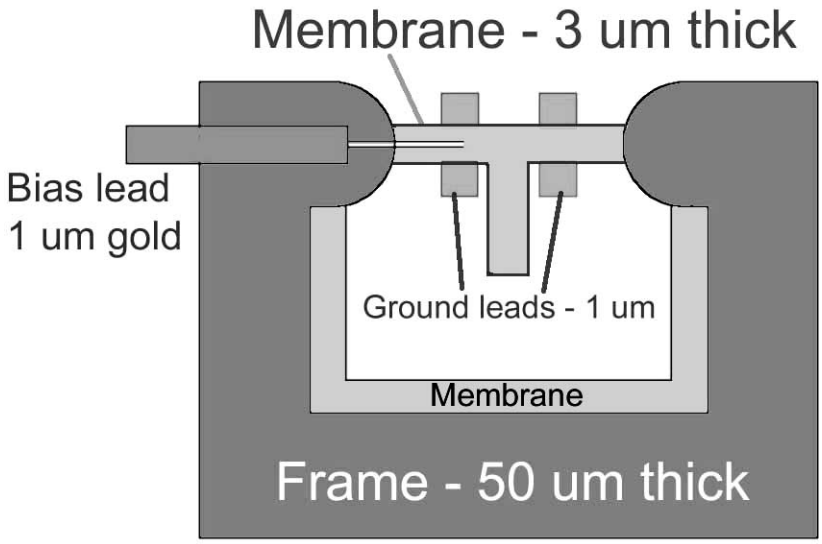

Figure 1. A membrane and frame circuit showing typical features. This circuit is used for a doubler, but the tripler uses similar features.

THz Circuits

Bands from 0.5 - 2.7 THz are required for the FIRST mission, and performance of planar circuits above 1 THz is largely unknown. For this reason test circuits were designed for a range of frequencies corresponding to actual required bands from 1 to 2.7 THz. Triplers were designed for 1.0 and 1.2 THz using a varactor balanced design, while doublers were designed for 1.5 and 2.5 THz using a resistive balanced design. Diode properties are essentially unknown at these frequencies but it was believed that the highest practical frequency for varactor operation was around 1 THz.

The design of the circuits is challenging within the constraints, which include a fixed substrate thickness regardless of frequency, an absence of backside metal, and minimum diode mesa dimensions which sometimes exceeded the available circuit space. The completely unknown mechanical behavior of the circuit led to a somewhat conservative design. Despite these constraints, high performance circuits are practical, and suffer no significant limitations beyond those inherent to THz circuits. Design of these circuits requires lots of HFSS simulations to verify operation. Dimensions in nearly all cases are at the maximum limit for higher mode propagation, leading to significant effects from evanescent modes.

Doubler Design

At frequencies near 2 THz, carrier velocity saturation effects seriously limit varactor operation. An approximate value for the peak junction current, estimated from the carrier concentration in the junction, times the maximum saturated carrier velocity, is 3 mA/fF. At 1 THz, a sinusoidal wave has only a 1 V peak-peak amplitude at this current. This means little voltage modulation is possible, and varactor efficiency will be very low. Resistive multiplication requires lower voltage amplitude, and still should work with reasonable efficiency, although it is inherently less efficient. These circuits are required to produce only a few microwatts of output power to drive HEB mixers, and the input power is likely to be very limited as well. Little data is available on multipliers above 700 GHz, and those that have been built have not been intended to produce high power. Projections of optimized drive levels are in the 0.25 to 1 mW level at most. At low power, simulations show that DC forward bias is essential for best efficiency, and zero bias is favored only for power levels far higher than would be available. A balanced design was chosen because it requires no filters, and is very simple, despite the fact that it uses two diodes which double the required input power. Losses in filters can easily exceed the penalty for using two diodes. For the 2.5 THz design, diodes with Cj(0) = 0.5 fF were chosen to minimize the required input power. Even smaller diodes seemed desirable but were too far outside the known range for planar diode fabrication. For 1.5 THz, diodes may be significantly larger, at 0.9 fF, and circuit design is easier, because these diodes more closely match the typical circuit impedance levels. Figure 2 shows the predicted efficiency vs. power for a 1.5 THz doubler.

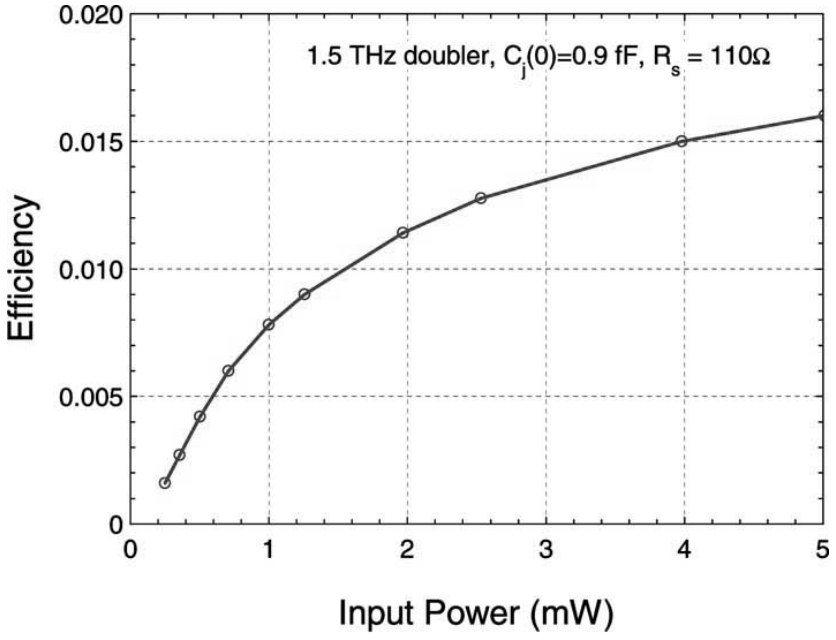

Figure 2. Predicted efficiency vs. input power for a doubler to 1.5 THz using a pair of diodes with $C_j(0)$ = 0.9 fF and R_s = 110Ω, biased in the forward direction.

Doubler Construction

A fairly conventional design was chosen in which the diodes are in the output waveguide, for lowest loss at the output frequency. The diodes are easy to bias in series, without affecting RF performance, using an integrated Si_3N_4 capacitor which bypasses the bias circuit. Probe coupling was used in the input waveguide, which requires no contact, and converts the waveguide impedance to a value near 50 Ω. A two section transformer was used to match to the diode impedance in a very short section of quasi-TEM line joining the two waveguides. At the output frequency, the diodes are a fairly good match to full height waveguide without any tuning except the choice of finger length and backshort location, which is close to the diodes. The mounting block provides full height input and output waveguides, a frame holder and a bias connection, with no really critical dimensions. Outside the immediate circuit area, both waveguides step up to square or circular cross sections, which facilitate the further transition to feed horns on both ports. The input has a conical horn while the output uses a diagonal horn. This device was intended to be optically coupled on both ports in initial tests. The closed frame forces the input waveguide to be at a right angle to the frame, and this was the most difficult aspect of this circuit to accommodate in the machining, which did not use electroforming. The inner details of the doubler block and device mounting are shown in Figures 3 and 4. The predicted frequency response for the doubler is shown in Figure 5. The bandwidth is very wide, despite the circuit simplicity, because a doubler operating in a resistive mode has a very low input Q. A flatter response may be obtained in a more optimized block.

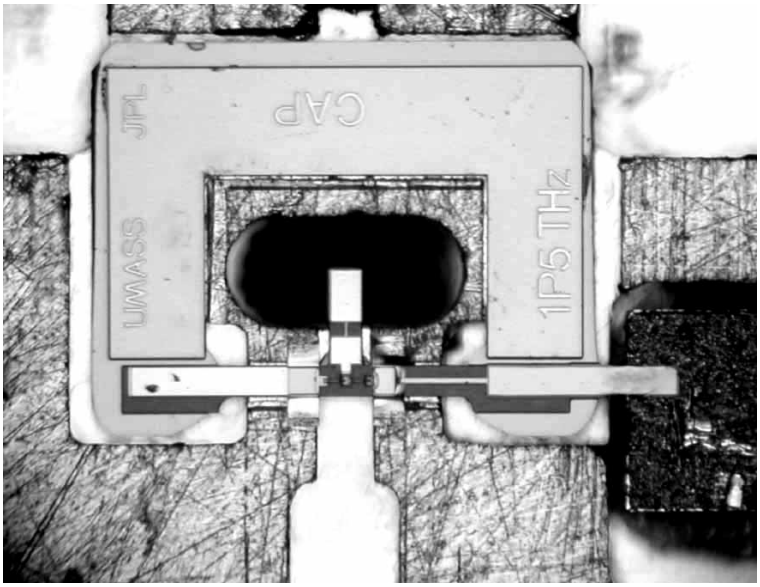

Figure 3. 1.5 THz doubler construction with the device mounted in the doubler block. The device frame surrounds the input waveguide (with rounded corners). The input coupling probe extends into this waveguide, and converts the power to a quasi-TEM mode. The bias beam lead is seen to the extreme right.

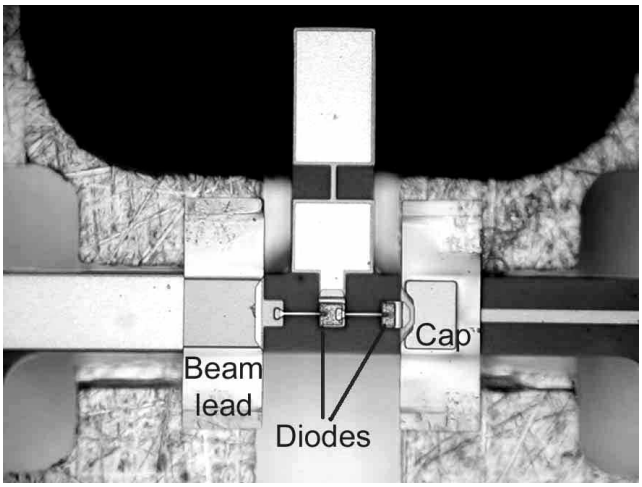

Figure 4. 1.5 THz doubler detail showing the connection of the input probe to the center point between the diodes, which are mounted in the output waveguide. There are four grounding beam leads. The right hand ground includes an integrated SiN capacitor to bypass the bias line.

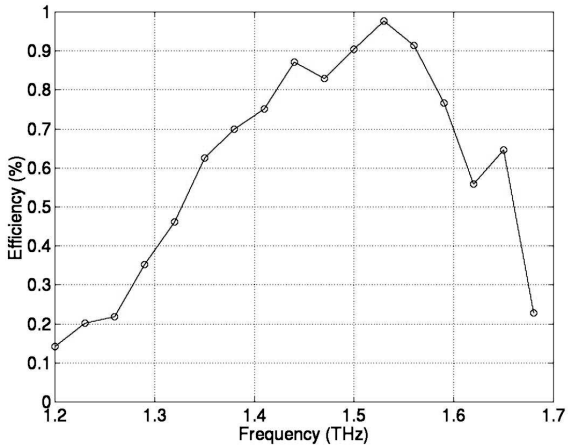

Figure 5. 1.5 THz doubler predicted efficiency vs. frequency at 2 mW input.

Devices

All of the devices were fabricated at JPL on a pair of nominally identical wafers, which included many other designs. The wafer is undoped GaAs having a final thickness of about 50 μm, with an epi structure (grown by MOCVD by Epitronics) as shown in Table 1.

	Mat'l	Thickness	Doping
Epi layer	GaAs	0.15 μm	5.0×10^{17} Si
N++ layer	GaAs	1.0 μm	5.0×10^{18} Si
Etch stop	$Ga_{0.5}Al_{0.5}As$	0.05 μm	undoped
Membrane	GaAs	3.0 μm	$<3 \times 10^{14}$
Etch stop	$Ga_{0.5}Al_{0.5}As$	0.4 μm	undoped

Table 1

An SEM photo of a 1.5 THz doubler device is shown in Figure 6. The curvature to the beam leads and the diode fingers occurs as a result of their non-planar fabrication, rather than strain. Only the membrane portion of the diode circuit is shown in the figure.

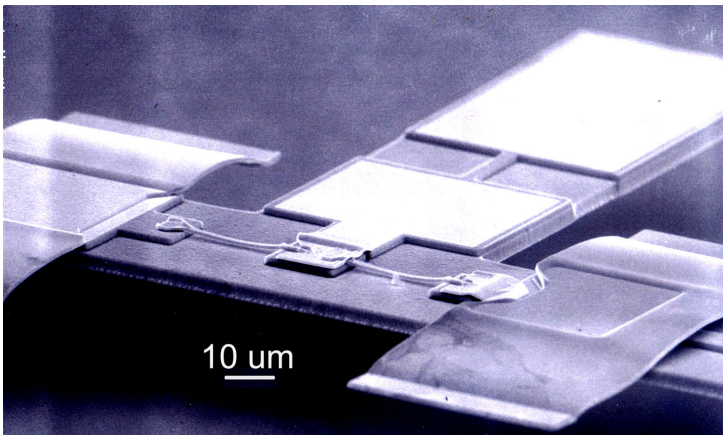

Figure 6. 1.5 THz doubler SEM photo showing the same region as in Figure 4.

1.5 THz Doubler Tests

No solid state driver source is presently available near 750 GHz with enough power to drive this doubler. A preliminary test was needed to determine the feasibility of such a doubler and the required drive level. The results of this test would be used to develop the driver. Tests were performed in the Submillimeter Technology Lab of the Univ. of Mass Lowell, using formic acid laser lines at 692, 716 and 761 GHz. Typical output power is 5 -10 mW in all three lines. The laser was focused using a teflon lens into the input horn. The coupling to the horn was relatively poor, because the laser focal spot was somewhat larger than the horn. In order to determine the effective input power, the power was measured using a similar horn on the input to a broadband waveguide calorimeter [2]. The same calorimeter was used with a smaller conical horn to couple to the output waveguide.

In order to monitor the input power, which would very slowly drift during the tests, and to determine the power with the beam attenuated, the laser beam was sampled with a mylar beamsplitter. The sample was measured with one calorimeter having a horn matching that on the doubler input, while the output power was measured with a second calorimeter of the same type.

Three doubler chips from two wafers were tested in the same block. One had a peculiar IV curve, and gave very low efficiency ~0.1%. Two other devices from the other wafer gave similar good results. The maximum output power is 55 μW at 1522 GHz, at an efficiency of 1.0 %. The output power and efficiency vs. input power are shown in Figure 7. The best operation is with a current bias of 0.5-1 mA, while the bias

voltage is always in forward direction. An output power of 40μW was obtained at 1384 GHz, and 25 μW at 1432 GHz. At frequencies other than 761 GHz, the input power was not so well calibrated, but the efficiency at 692, 716 and 761 GHz input is the same within ±1.5 dB.

An important concern is the minimum input power required to drive an HEB mixer. The input power was reduced with attenuators until an indicated output power of 1 μW was seen. The room environment and the power sensor were sufficiently stable to clearly read this low power. The required input power was 0.4 mW for this output, and this power seems quite attainable with a solid state driver consisting of 3 cascaded planar doublers. Thus far a power of 6 mW has been produced at 378 GHz from 2 cascaded doublers operated at room temperature [3] (which should nearly double at 150 K), and a subsequent doubler with an efficiency of 4% seems consistent with available data at higher and lower frequencies.

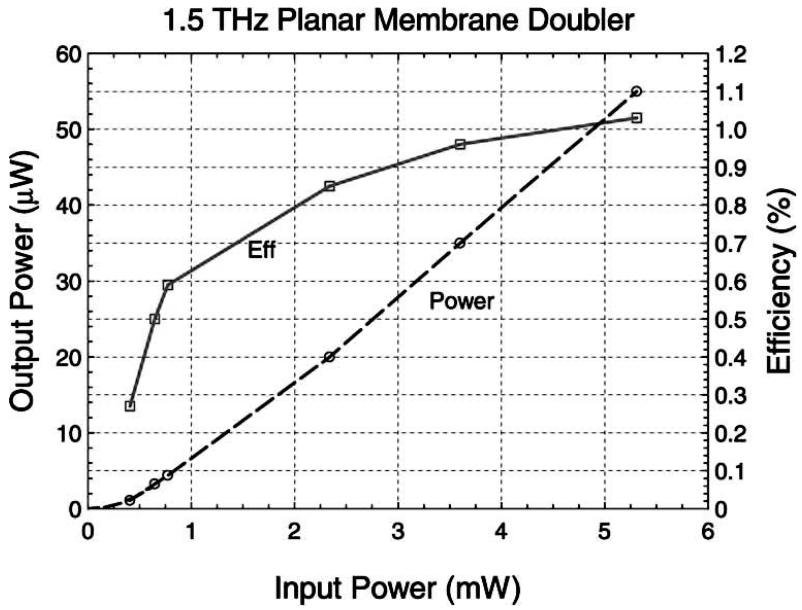

Figure 7. Output power and efficiency vs input power for the doubler at 1522 GHz.

Cryogenic tests

Diode properties improve at lower temperature due to increased carrier mobility. This is observed in all lower frequency multipliers. However, for highly doped THz diodes, we expect much reduced variation in mobility with temperature. A test was needed to determine if any large efficiency benefit would be seen at this high frequency. The doubler survives cooling to 100K, although one device appeared to short out in the bypass capacitor below 200K. The diode IV curve shows a 1.7x increase in slope at 100K, but no change in R_s. A steeper IV should reduce the input power required, even if the efficiency is otherwise unchanged.

A fairly crude test was done with the doubler tested over a LN_2 bath with the laser input at 2.5 mW. At a temperature of 230K the output increased ~10%, but at lower temperature frost began to build up on the input horn, and the output power showed no further increase, with an actual decrease below 180K. A proper test would require a real dewar, but this test suggests that no major efficiency improvement will occur, since the frost build up did not appear to be sufficiently large to produce a very large loss.

Machining

The machining of the block was very easy, considering the small sizes involved. The small features were machined with a 50 μm diameter end mill on a micro-milling machine [4], while the larger features used a 150 μm diameter mill in a second spindle. All critical features used the smaller mill so registration of the tools was not a problem. The one difficult feature was the right angle waveguide, which required plunging a conical horn through a thick block and then meeting this feature with a milled cut from the opposite side. It would be much simpler to machine if this waveguide could be rotated into the same plane as other features, so that both waveguides are split in the E-plane.

The input waveguide can not cross the frame because the presence of the GaAs in the waveguide produces a very large mismatch. However, the frame can be removed. In a test, the frame was glued down at the corners and the frame was then broken in the required area without damage to the membrane. Rotating the input waveguide 90° has no effect on the input match, and the required backshort location fits within the remaining frame. The doubler for 2.5 THz will be machined this way, greatly simplifying this smaller and more difficult part, and also will be tested with a laser.

1 THz Tripler

The 1.0 and 1.2 THz triplers are based on a successful monolithic tripler tested in the 230-330 GHz range [5]. The change is mostly just a scaling in size, but the membrane is significantly thinner than the scaled substrate thickness for the 300 GHz version. The circuit includes two antiparallel diodes in a loop with nearly optimized second harmonic inductance, having an integrated Si_3N_4 capacitor for DC bias bypass. Beam leads are used for dc and rf grounding, and two radial stubs are used to prevent loss of output power to the input circuit. In this smaller size there is some considerable doubt about the effective dielectric constant for radial stubs on the GaAs membrane which depend on the metal of the block for a ground plane. The design assumed that there would be a 1 μm gap under the GaAs, and the stubs were sized accordingly. Variation in this gap is not too critical, and it is unlikely to exceed 2 μm in the worst case. Surface roughness insures that it will never drop below 0.5 μm. An input waveguide probe was added to the THz models to fully integrate the circuit. Because the input probe dominates

the length of the membrane strip, in order to minimize its length, the input waveguide was reduced to 0.6× normal height. The probe was then tuned for this waveguide height, and the transition worked much the same as for full height. The best transition to full height (for bandwidth of the tripler as a whole) was found to be an abrupt step, a short distance from the probe.

The output waveguide for 1 THz is reduced in height to 25 μm at the circuit, but steps to full height very close by. It is broached (scraped out) with a thin tool on the same NC machine used to make the other features. The backshort position and quality is critical, so the waveguide is cut with an integral backshort. It is not possible with this type of machining to cut a vertical wall, but the tool may be brought out of the metal at a 60° angle. This V shaped backshort works as well as a conventional flat wall but the location must be shifted to produce the same effect. The output waveguide includes an additional section of reduced height to increase the bandwidth. The entire waveguide coupling circuit is in one plane, since in this case the circuit topology permits both waveguides to leave the same side of the frame. The output waveguide continues straight to a diagonal horn, while the input wraps around 180° to the input waveguide flange. These details are shown in Figures 8 and 9.

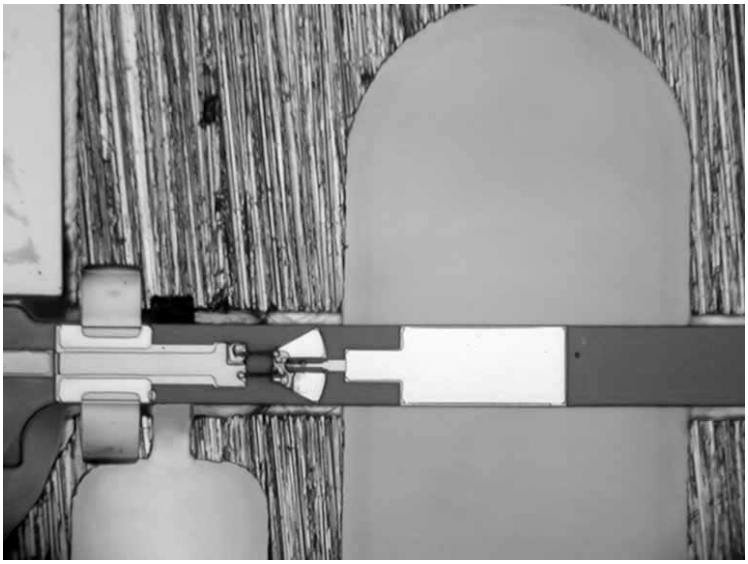

Figure 8. Photograph of the details of the 1 THz tripler, showing the beam leads at far left, output waveguide (next to the beam leads), diodes and radial stubs, and the waveguide probe in the reduced height input waveguide (right).

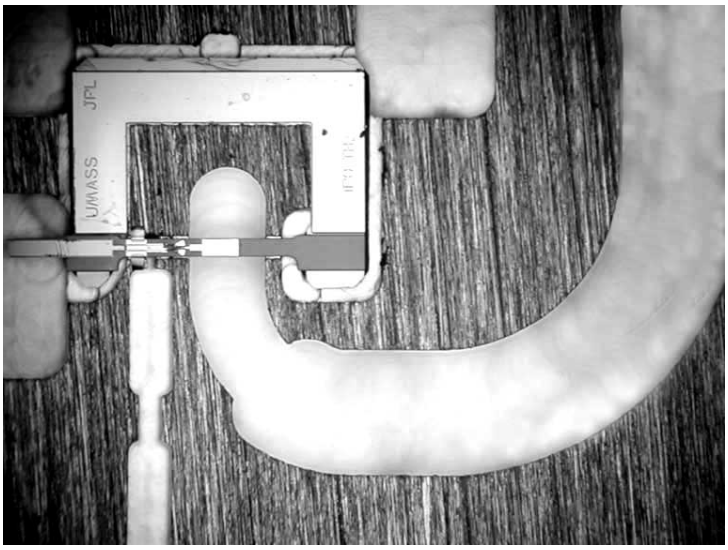

Figure 9. Overall view of the 1 THz tripler showing the complete frame, bias beam lead on the left, and the wrap-around input waveguide on the right.

Tripler Results

The drive source used in the tests is a Gunn oscillator followed by a MMIC power amplifier producing up to 100 mW output in the 100-110 GHz band, driving a monolithic tripler. The tripler tunes 300-330 GHz with 4-6 mW output power, dropping rapidly at 330 GHz. No source at higher frequency was available, so much of the final tripler's design band corresponding to 320-350 GHz input, could not be tested. Only one device was tested, which gave sufficiently good results that it was not exchanged. The diodes had an odd IV curve, with a very high value for η, but this could be due to the very limited space for ohmic pads, rather than a problem with the diode junctions themselves.

The efficiency is very good, particularly for low available input power, and the low end of the band is nearly at the expected frequency. The highest output power is 80 μW, at 978 GHz, which is comparable to the best seen with a whisker contacted tripler at 800 GHz [6]. Results are shown in Figure 10, with all powers measured with the same waveguide calorimeter as referenced earlier. The typical bias voltage is low, in the range of 0.2 V forward to 0.45 V reverse, with about 0.5 mA bias current. This is not consistent with the optimal varactor mode of operation but the reason for this could be either a diode capacitance below the design value, too little input power, or a limited useful voltage amplitude due to carrier velocity saturation. More tests are needed to determine the cause.

Measurement of the efficiency is not so simple as measuring output power and the input power delivered into a matched load. It is essential to actually measure the power delivered into the load in use, and this requires a directional coupler. A special low-loss

high-directivity WR3 coupler was built for this work [7]. In these tests the true efficiency was measured to be 0.8-1.1% in the 965-980 GHz range, with input powers ~4 mW. No rapid change with input power was noted, although this power should be too low for best efficiency. The input reflected power was 10-20%.

Operation of the full chain, shown in Figure 11, is extremely simple. There are no tuners on the multipliers, and their only adjustment is the bias level. The input frequency is set with Gunn tuner and power with the voltage bias on the power amp. This makes the chain fully compatible with space or remote operation. The interaction between driver multiplier and THz tripler is acceptable, in that any input frequency may be chosen without seeing large output power variations. However, the band tested so far is quite limited relative to that required for FIRST, and full tests are planned when the actual driver chain (consisting of two cascaded doublers) is completed. At low temperature, much higher output power is expected, because the driver tripler is known to show a 57% increase in power [5], and the final tripler should show at least some improvement.

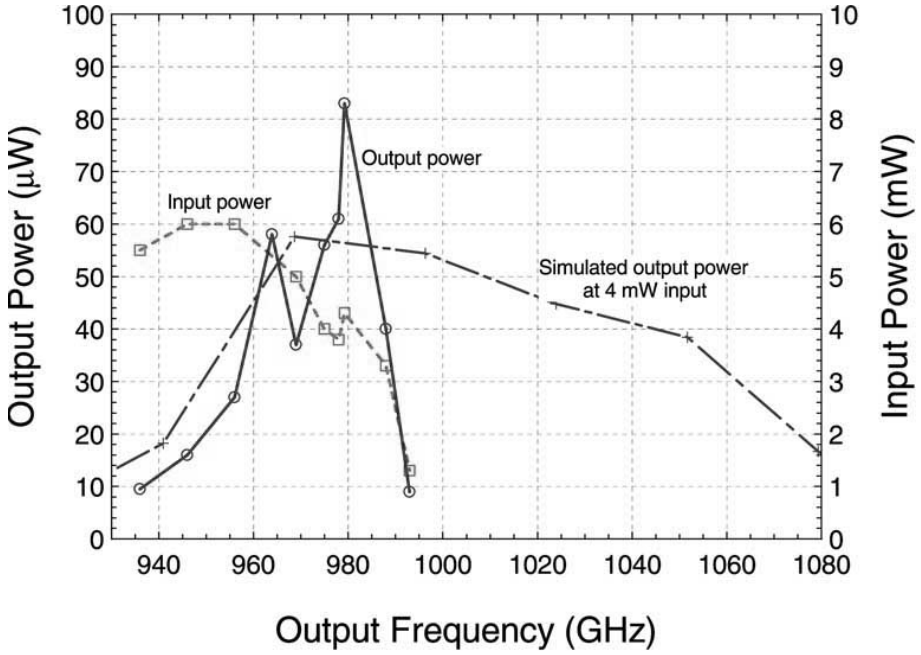

Figure 10. Input power (delivered to a matched load), and output power for the 1 THz tripler, as well as the predicted output power with 4 mW input. Actual input differs due to interactions. No source was available above 330 GHz.

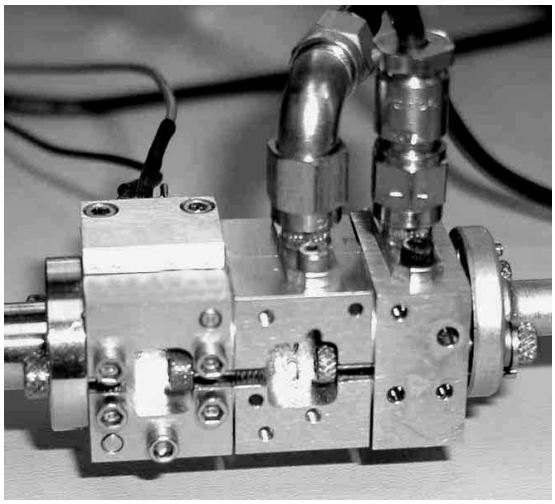

Figure 11. Photo of the complete 1 THz multiplier chain, consisting of (left to right) 100-110 GHz power amp, 320 GHz tripler and 1 THz tripler. The output waveguide on the tripler is a transition from circular to WR10, to match to the power sensor.

Conclusions

The results of this work show that THz monolithic frequency multipliers are quite practical, with excellent performance. A very limited data set indicates that they are also reproducible. These results now make whiskered devices obsolete at all frequencies. At all lower frequencies, planar devices have already shown their superiority, particularly when integrated with most of the multiplier circuitry. The requirement to achieve such good performance is that the circuit must be simple, and there must be an absolute minimum of microstrip or other planar transmission line circuitry. Any such circuitry must be used with careful attention to the losses that will be produced.

The efficiency is high enough to make practical THz solid state sources, which only need to produce a few μW in order to drive SIS or HEB mixers. Cascaded sources are possible with little power ripple vs. frequency, although this may apply only over limited bandwidths. Membrane circuits are quite fragile, yet are quite robust in actual use since they never need to be subjected to significant strain. Machining of the blocks is quick and easy relative to any previous designs, requiring nearly a factor of ten less time than is needed for a whiskered device at the same frequency. Assembly is remarkably easy for such high frequency, and a block may be taken from machined parts to fully functional in a time of ~4 hours.

The large (3 inch) wafer size means that many devices are available, even with a low yield, and a single wafer may contain 10's of different designs, with 100's of each design. This meets the requirements for a major space mission such as FIRST, and also enables a very wide range of other uses. While a wafer run is quite expensive, this

enormous productivity makes circuits in the THz region quite affordable, relative to their whiskered equivalents, and the long term reliability is certain to be much better as well.

References

[1] P.H. Seigel, R.P. Smith, S. Martin, and M. Gaidis, "2.5 THz GaAs Monolithic Membrane-Diode Mixer," *IEEE Trans. Microwave Theory Tech.*, v. 47, pp. 596-604, May 1999.

[2] N. Erickson, "A Fast and Sensitive Submillimeter Waveguide Power Meter," *Tenth International Symposium on Space Terahertz Technology*, pp. 501-507, Mar. 99.

[3] E. Schlecht, J. Bruston, A. Maestrini, S. Martin, D. Pukala, R. Tsang, R.P. Smith, and I. Mehdi, "200 and 400 GHz Schottky Diode Multipliers Fabricated with Integrated Air-dielectric "Substrateless" Circuitry," *Eleventh International Symposium on Space Terahertz Technology*, pp. 287-295, May 2000.

[4] G. Narayanan, N. Erickson, and R. Grosslein, "Low Cost Direct Machining of Terahertz waveguide Structures," *Tenth International Symposium on Space Terahertz Technology*, pp. 518-528, Mar. 99.

[5] N. Erickson, R. Smith, and S. Martin, "High Efficiency MMIC Frequency Triplers for Millimeter and Submillimeter Wavelengths," *IEEE MTT-S Int'l Microwave Symposium*, June 2000, Boston.

[6] N.R. Erickson, and J. Tuovinen, ``A Waveguide Tripler for 720-880 GHz," *Sixth Int'l Symposium on Space Terahertz Tech.*, pp. 191-198, 1995.

[7] N.R. Erickson, "High Performance Dual Directional Couplers for Near-mm Wavelengths," to be published in *IEEE Microwave and Guided Wave Lett*, 2001

Part of the research described in this paper was carried out at the Jet Propulsion Laboratory, California Institute of Technology, under a contract with the National Aeronautics and Space Administration.

A 1.2 THz Planar Tripler Using GaAs Membrane Based Chips

J. Bruston*, A. Maestrini, D. Pukala, S. Martin, B. Nakamura and I. Mehdi

Jet Propulsion Laboratory, California Institute of Technology, Pasadena, CA 91109
**now at ESA – ESTEC, Noordwijk, NL*

1 ABSTRACT

Fabrication technology for Submillimeter-wave monolithic circuits has made tremendous progress in recent years and it is now possible to fabricate sub-micron GaAs Schottky devices on a number of substrate types, such as membranes [1], frame-less membranes [2] or substrateless circuits [3]. These new technologies allow designers to implement very high frequency circuits, either Schottky mixers or multipliers, in a radically new manner.

This paper will address the design, fabrication, and preliminary results of a 1.2 THz planar tripler fabricated on a GaAs frame-less membrane, the concept of which was described previously [2]. The tripler uses a diode pair in an antiparallel configuration similar to designs used at lower frequency [4]. To date, this tripler has produced a peak output power of 80 μW with 0.9% efficiency at room temperature (at 1126 GHz). The measured fix-tuned 3 dB bandwidth is about 3.5%. When cooled, the output power reached a peak of 195 μW at 120 K and 250 μW at 50K. The ease with which this circuit was implemented along with the superb achieved performance indicates that properly designed planar devices such as this tripler can now usher in a new era of practical very high frequency multipliers.

2 INTRODUCTION

For a number of years astrophysicists and radio astronomers have been demanding a full submillimeter survey-type mission to investigate phenomena such as star formation and galaxy evolution. The Far Infrared and Submillimeter Telescope, FIRST [5], now renamed the Herschel Space Observatory, HSO, is the most comprehensive mission for these frequencies. In the initial planning of HSO it became obvious that while the detector elements have improved considerably over time the available technology for broad band local oscillator sources left much to be desired. Cascaded multipliers following a fundamental driving source have been the working horse of local oscillators for years For mass and volume reasons, solid state technology is favored over heavy and bulky molecular lasers, although these are being used when the mission permits [6. Unfortunately limitations on maximum output power didn't allow their use for flight above about 300 GHz (although lab demonstrations had been done up to 1.4 THz [7].) First made with whisker contacted diodes, frequency multipliers have recently been developed with the preferred, more reliable, more reproducible, and easier to assemble, planar technology. Improvements in GaAs processing technology have allowed for the design of GaAs Schottky varactor multipliers up to the higher end of the submillimeter-wave range.

In our attempt to push the fully integrated Schottky diode technology to supra THz frequencies, we have benefited from the recently available power amplifiers that operate around 100 GHz [8],

along with improvements in multipliers at sub-terahertz frequency [3]. Previously, we introduced the frameless membrane and presented a number of design concepts to reach supra THz frequency [2]. This paper will detail the concept and final design methodology, fabrication and preliminary test of a GaAs membrane based 1.2 THz tripler. We believe that the work presented in this paper is a major step in meeting this challenge of implementing supra-THz Local Oscillator for space-borne receivers.

3 DESIGN AND FABRICATION

GaAs membrane based planar Schottky devices have been demonstrated as mixers at 2.5 THz, with very impressive results [1, 6]. They use a 3 μm thick GaAs membrane suspended across the RF waveguide by means of a sturdier, 50 μm thick GaAs frame. This requires that the waveguide be perpendicular to the membrane, as a traditional split waveguide block would see the thick, high dielectric constant, lossy frame in the waveguide. This results in several design constraints. To gain in design flexibility, we decided to design and fabricate devices without any frames [2]. Handling and assembly turned out not to be an issue, as we will discuss later. To allow for "drop-in" assembly, and provide simple bias connections, we decided to make extensive use of beam leads. The availability of the membrane allows one to move the diodes away from the waveguides, to which they are coupled by means of stripline matching circuits and waveguide probes. The main advantage of using diodes remote from the waveguides is that it simplifies the diode analysis and optimization. Also, and in the case of a balanced tripler, the quasi TEM coplanar structure with grounds on chip permits the two diodes to be biased in series, simplifying the biasing circuit. Finally, it ensures that only the TEM mode propagates at every harmonic, simplifying the matching circuit design. The ground planes are shorted to the block by means of wide beam leads, which also provide support for the membrane assembly [2]. A sketch of the final design is shown in Figure 1.

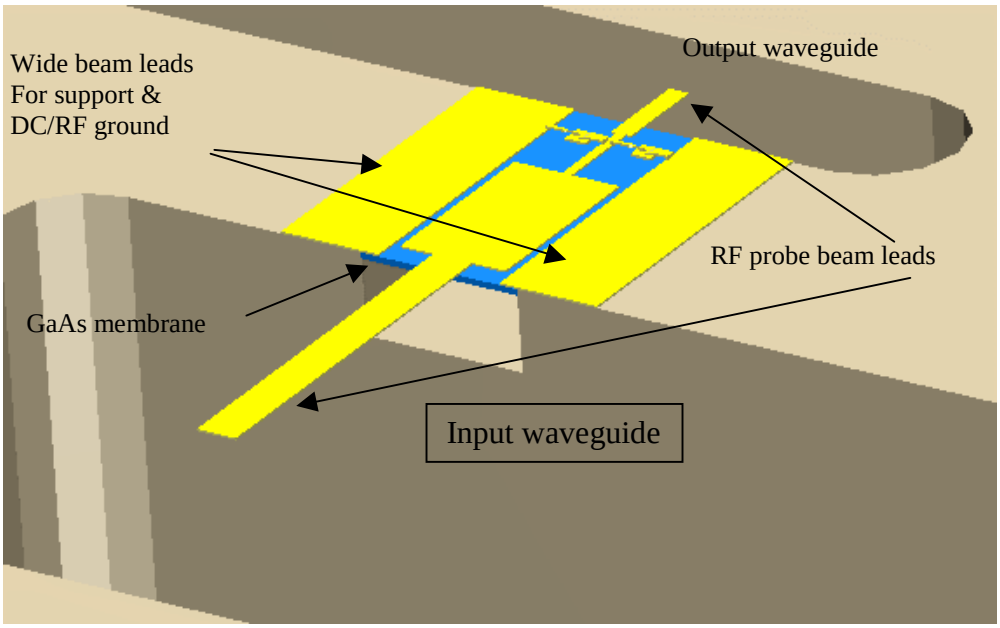

Figure 1: *Final design of the frameless tripler is shown placed inside the split waveguide block.*

3.1 Device optimization and Diode loop

The tripler utilizes a diode pair in an antiparallel configuration similar to designs used at lower frequency [4]. This configuration has the distinct advantage that only odd harmonics are generated. However, it requires a carefully designed second harmonic idler tuning circuit. The second harmonic current flows in the diode loop (fig. 2a), which needs the adequate series reactance for resonating the third harmonic [9]. The value of this reactance can be calculated, like the other embedding impedance of the diode, by means of harmonic balance simulation and optimization. We used our in house diode model of the JPL made planar Schottky diode [10], that we updated for THz frequency, introducing harmonic dependent series resistance. The optimum diode doping and size is found using only one diode and half the input power. We used a doping of $5x10^{17}$ cm^{-3} and an anode of $0.4x1.3$ μm^2. However, this approach can not provide the embedding impedance of the final configuration. The reactive series impedance required for the idler in the diode loop directly impact the embedding impedance at the first and third harmonic. It is therefore important to first optimize this loop and then calculate the embedding impedance.

Our approach was semi empirical and iterative. The diodes, the diode mesas, and the air bridges constitute the diode loop (fig. 2 b and c). A first step consisted of developing an electrical equivalent circuit for this structure, where the air bridges are replaced by inductances modeled as suspended ribbon (fig. 2 a). This allows a first optimization leading to a starting value of the inductance for best idler tuning. In turn, this inductance permits the definition of the corresponding air bridges (the mesas dimensions were fixed in the design, by fabrication considerations). However, this approach is approximate, and the inductance value in the diode loop is not well described by the equivalent model. This is due to the fact that the idler reactance is also impacted by the dimensions of the channel in which the circuit resides. We therefore use the now well developed technique of 3D electromagnetic simulation [10] (with Ansoft HFSS) to evaluate the inductance in the loop (fig. 2 b). The computed S-parameters of the structure are inserted into the harmonic balance for performance calculation. This time, we use terminations only at the first and third harmonics, as the second harmonic idler is contained in the S-parameters. Fine tuning of the air bridges length and width permits some further performance improvement. However, we never matched the diode maximum performance computed with ideal embedding impedance and idler. The air bridge length and width provide some flexibility in tuning the inductance, but one must also tune the cavity in which the circuit resides to obtain optimum values. However, for our first iteration, we decided not to use this parameter as a tuning variable, to simplify the design. This shall be optimized in future iterations. In spite of this, the compromised performance is a good trade off. As a matter of fact, the idler inductance makes the diode structure very high Q at the third harmonic, compromising the final design bandwidth. The non-optimum idler reduces this effect, allowing for a relatively wide band design.

3.2 Waveguide probes

Removing the diodes from the waveguide, either input or output, provides a safe quasi TEM mode environment for the diodes and circuits, together with a simple bias scheme. Furthermore, it allows us to separate carefully the different issues inherent to this kind of design: the diode optimization and implementation, the waveguide to planar circuit transitions, the waveguide to open propagation (horn, see below), and finally the matching between the different pieces.

One doesn't need to design the CPW to waveguide probe to have any particular impedance termination, as the matching circuit between the probes and the diodes does not need to transform to 50 Ohms, the value usually used to design probes. The impedance of the diodes nominally has a fairly low real part and some reactive part. It will greatly help the matching circuit design to obtain a probe termination impedance close to the diode's conjugate impedance.

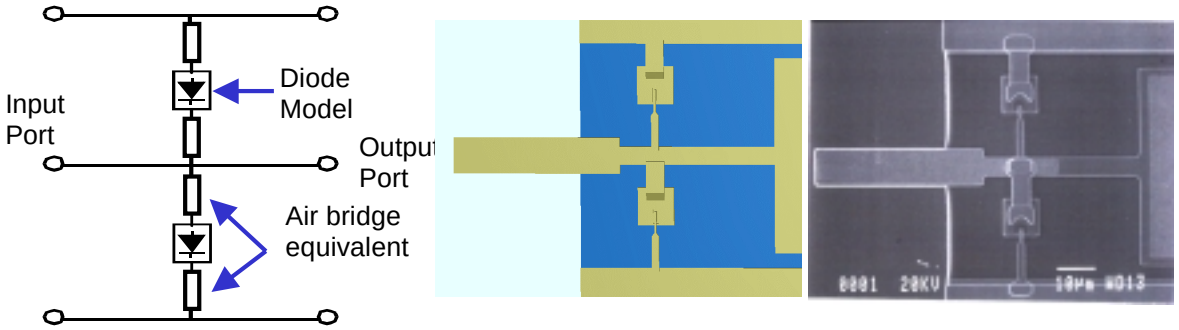

***Figure 2**: (a) The diodes have an antiparallel configuration restraining the second harmonic current in the diode loop. This loop must have the right impedance at the second harmonic to maximize third harmonic production. (b) The diode structure as simulated with HFSS showing the mesas and air bridges part of the diode loop seen by the second harmonic current. (c) Photograph of the same diodes after fabrication.*

We used this philosophy in our design, picking any probe dimension (length and width) that we knew would work somewhat without introducing too much resonance. We only provided for length optimization, by simulating a few with HFSS and, having inserted the aggregate results as a 2 dimensional matrix in the harmonic balance, letting the simulator extrapolate the best length. This worked so well that we actually found an output probe with a termination impedance almost perfectly matching the diodes at the third harmonic. This is a great result, as this means the diodes could be almost in the plane of the transition, which, due to the waveguide cut-off, provides for the required first harmonic short without the need for additional lossy circuit features. However, this also introduced an iteration in the calculation of the embedding impedance, as the close proximity of the diodes to the output waveguide, meant that some effect due to evanescent modes had to be taken into account.

The probes are designed as metal beam leads, with all the GaAs removed from the waveguide. This implementation yields a wider bandwidth transition and reduced loss. The aspect ratio of the probe (20 µm wide, 175 µm long, 1 µm thick) provides enough mechanical robustness and sturdiness.

3.3 Matching circuit

The output match was non existent as the probe provided the right impedance. The remaining match, to the horn, was made using waveguide sections (see below).

The input matching circuit had to match from the diode impedance at the first harmonic to the input waveguide probe impedance, together with providing a short at the third harmonic. This

was done using a two sections high-low impedance Chebyschev transformer. It is desirable to work with a small number of sections, in order to reduce loss, and maintain a small robust circuit. The price is reduced bandwidth. As we did not need to go through 50 Ohms, two sections provided sufficient bandwidth and a simpler design for our first iteration. If the bandwidth appears too narrow, additional sections can be added in subsequent design iterations.

3.4 Bias circuit

The diode optimization and performance computation showed an optimum bias close to 0V. This allowed for an unbiased nominal circuit design, which would provide testable devices in the event that implementation of the bias circuit failed. However, we provided for bias on some circuits, to help debugging, and to test the concept for future designs that may require bias.

Since the two diodes are in series between the two ground planes of the CPW circuit, to provide for bias, we needed to keep one ground plane, via its beam lead, DC grounded, by shorting to the block. The connection of the diodes to the opposite ground plane, therefore, has to provide for DC decoupling. The solution is to run an air bridged interconnect line from one of the diodes to a MIM capacitor on the CPW ground plane. This capacitor provides for RF short and DC decoupling. A narrow, high inductance MIM line connects the capacitor to a DC bond pad located in a side channel in the block. The quasi TEM mode nature of the circuit prevents any leakage of the RF through the bias channel. We ensured that was the case using HFSS simulation of the whole structure and looking at RF leakage at the end of the channel.

However, the narrow ground plane on membrane didn't provide much space for the MIM decoupling capacitor. The calculated capacitor impedance at the first harmonic is 4 Ohms. In spite of this fairly high value, the measured results show that the bias circuit has little, if any, impact on performance. Figure 3 shows the bias circuit after fabrication.

3.5 Housing block and output horn

The housing block uses a traditional split waveguide configuration, with the tripler chip positioned in a channel joining the two parallel waveguides. This configuration allows for in line input - output waveguides, low loss waveguide split as the cut is placed in the E plane of the TE_{10} dominant mode, and simple machining using high precision NC milling tools.

The 400 GHz input waveguide is terminated by an in house designed flange used as a standard for all our high frequency designs. The transition from the output waveguide to free space propagation is made by means of a built-in transition from rectangular to circular waveguide and Picket Potter horn [11].

3.6 Circuit fabrication

The membrane chip fabrication was described in detail in [2]. Extensive use of a projection aligner, dry etch techniques and etch stop layers all contributed to high circuit yields. The biasable circuits had somewhat reduced yields, due to the presence of circuit designs with thick GaAs support frames that interfered with some of the backside lithography. This problem could be eliminated in the future by processing the 1.2 THz circuits separately. The fabricated chip is shown in fig.3.

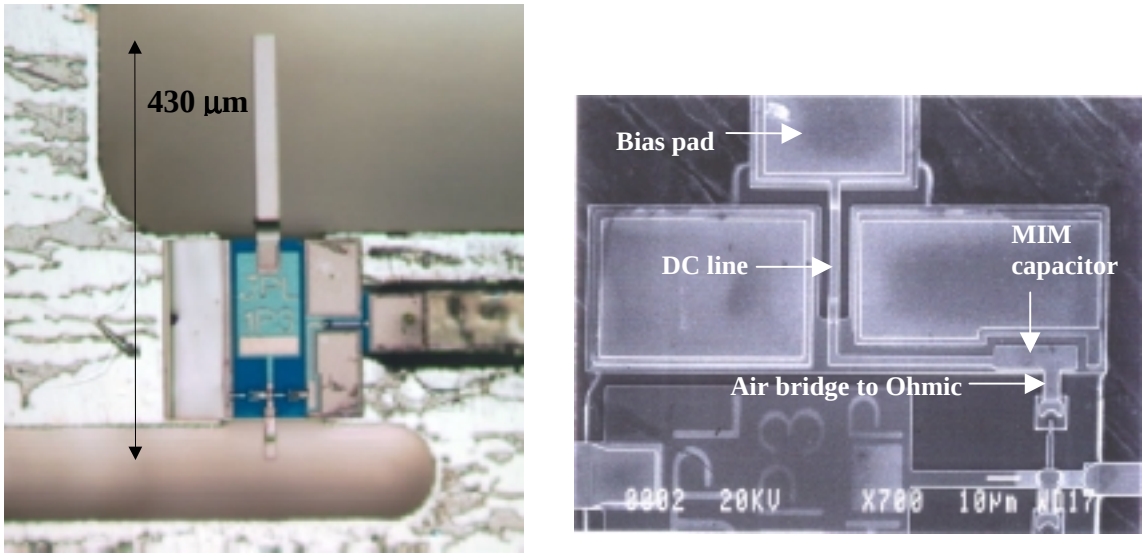

(a) **(b)**

***Figure 3**: **a)** A fabricated 1.2 THz tripler after assembly into the waveguide block, showing bias circuit, RF probes and "drop in" support beam leads. **b)** SEM of the bias circuit showing MIM capacitor with Air-bridge to ohmic, and DC line to bias pad.*

4 PERFORMANCE

4.1 Simulation

It is difficult to accurately predict multiplier performance at supra THz frequencies. Performance calculation is based on harmonic balance simulation of the active elements (the Schottky diodes), and 3D electromagnetic simulation of the circuit topology (mesas and air bridges, CPW matching circuit, waveguide to CPW transitions, etc.).

The harmonic balance accuracy relies on the analytical model developed for the JPL made Schottky diode [10]. This model has been verified at least to 100 GHz by means of comparison to vector network measurements of JPL diodes. However, several effects render this model approximate at supra THz frequencies [12]. When the classical model is used (as described in [10]), we find a tripling efficiency of about 8%. This is obviously an overestimation. An improved model, including a frequency dependent series resistance (Rs) that more than triples its value at the third harmonic (1.2 THz) yields an efficiency of about 2 %. To further evaluate the impact of Rs on performance, we can apply a correction factor, as illustrated in figure 4b. As will be seen later, measurements yielding efficiencies of nearly 1% indicate that a correction factor of no more than 1.5 is necessary at these frequencies. In any case, current models provide a 3 dB estimation of the performance, which while not perfect can allow for further optimization of the device structure.

Similarly, the accuracy of the 3D electromagnetic simulation relies on the ability to simulate the fabricated structure. At supra THz frequencies, small details such as mesa height, ignored at sub THz frequencies, become important parameters. However, simulating these fine structures becomes computationally intensive, and often it is not possible to obtain convergence. Furthermore, the sheer size of these features is within the accuracy of device fabrication, and it becomes difficult to guaranty exact feature sizes.

These restrictions make the prediction of performance somewhat academic at supra THz frequencies. However, as part of the design process, this calculation is used to establish a nominal design. Doing so, we found a calculated performance of better than 1% over a 15% bandwidth centered around 1200 GHz, with 10 mW input power. The design performance is summarized in Fig 4a.

Finally, it is important to evaluate the tolerance of our design to one of the most critical fabrication issue, the anode size. Using the tools described above, we were able to calculate the efficiency of the tripler as a function of the anode length. This simulation shows a clear optimum, close to the designed length value. One important result is that, although the performance degradation can reach 50% for a 50% change in anode size, it is negligible for variations within 20% of nominal. As illustrated by figure 4, the efficiency is more strongly influenced by small variations on the series resistance model than by anode size for a fixed model.

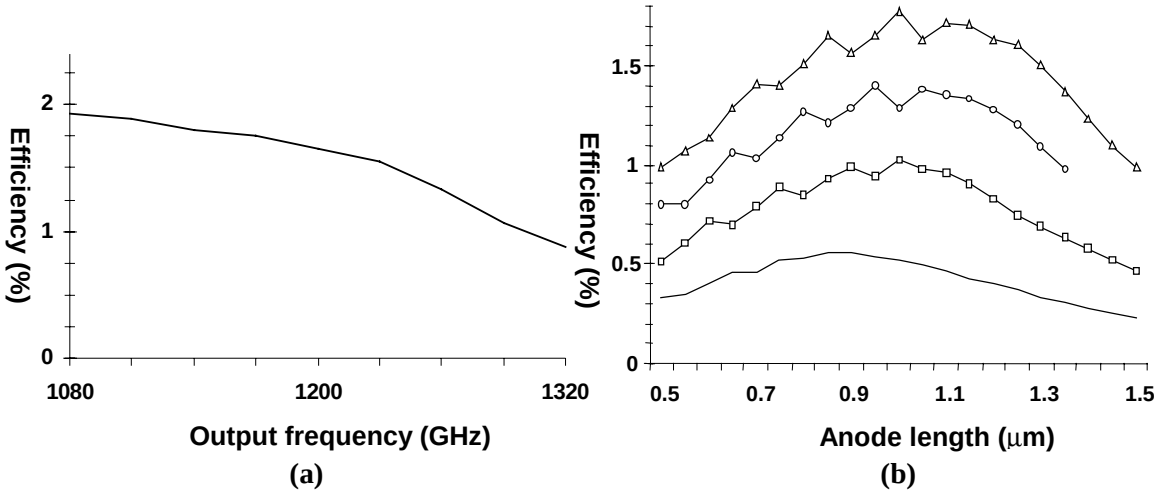

***Figure 4**: **a)** Efficiency as a function of frequency, for the final tripler design computed with harmonic balance, using JPL diode model, and S-parameters from Ansoft HFSS: input power is 10 mW over 360 to 440 GHz, 0V bias. **b)** Efficiency as a function of anode length and series resistance, with 10 mW input power at a fixed frequency of 400 GHz, and 0V bias. It is important to note that these results are for the specific design, and not the intrinsic diode performance with ideal embedding.*

4.2 Assembly

Assembly of the tripler chip in the housing block is made straight forward by the "drop-in" approach. As the nominal device needs no bias, it is sufficient to drop the chip in place, tuning its

position for proper probe alignment in the waveguides. The mating of the two halves of the split housing waveguide block holds the chip in place by "clamping" the ground beam leads thus ensuring a good RF ground. No soldering or bonding is necessary. The assembly of the biasable version requires a more complex procedure, as it is necessary to either bond or solder the DC feed to the bias pad that extends from the membrane. The original design did not permit bonding, and soldering is difficult due to the small size of the pad. A new design shall provide for clamping the bias pad beam lead in a similar manner to the ground beam leads.

4.3 Measurements

Preliminary measurements have been performed using the set up described in [13]. The tripler is driven using a 400 GHz solid state source composed of a 100 GHz HEMT power amplifier module [8] followed by two doublers. The fundamental source is a 100 GHz BWO used for convenience and lab availability. This chain delivers a peak output power of approximately 8mW at 375 GHz. The 1.2 THz tripler output power is measured by means of a Thomas Keating calorimeter [13].

Room temperature RF measurements of the tripler have provided a maximum output power of about 70 μW at 1126 GHz, or a 0.9% conversion efficiency, with a 3 dB fix-tuned bandwidth of 3.5 %. Measured output power of the tripler along with the input power are shown in Figure 5. Note that there are no movable tuners on the entire chain. The output power follows the input power level and the efficiency is fairly independent of frequency over the measured band. This performance is achieved with the smaller than nominal anode of 0.9x0.4 μm2, as the nominal design (1.3 x 0.4 μm2) was optimized for 10 mW of input power. With only 8 mW of input power, the nominal diodes are under-pumped, hence the need for a smaller anode to provide a diode impedance compatible with the circuit. This is encouraging, as we think that the design will show an increased efficiency and bandwidth with an increased and flat input power profile.

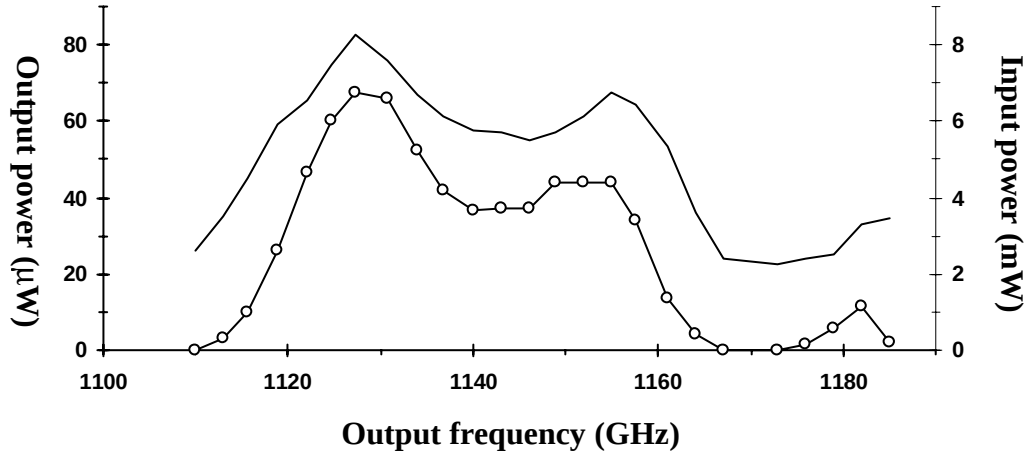

Figure 5*: Measured frequency response of the fix-tuned tripler along with the available input power. The bandwidth and maximum output are restricted by the limited input power.*

Room temperature measurements made with a different first stage doubler yielding higher power at 400 GHz provided 80 μW, or 0.9 % efficiency, at 1126 GHz. When cooled, the two doublers and tripler chain yielded 195 μW at 120K, and 250 μW at 50K.

Measurements of the biased chip were made with the nominal size anode devices only, as the other anode sizes lacked bias circuitry. The biased chips did not show any improved performance when compared to non biased ones of similar size. Furthermore, the optimum bias voltage was found to be close to 0 V, confirming our design analysis.

5 CONCLUSION

We have designed, fabricated and done preliminary measurements on a 1.2 THz planar tripler that incorporates a free standing GaAs membrane and multiple beam leads. This design has proven robust, easy to assemble, with, at the time of this writing, record performance for a supra THz multiplier. This result validates the use of integrated planar technology for THz multiplier, and demonstrates the viability of the technology for projects such as HSO.

6 ACKNOWLEDGEMENTS

We are highly appreciative of the numerous technical discussions that we have had with Neal Erickson (UMass), Peter Zimmermann (RPG), Chris Mann (RAL) and Tom Crowe (UVa). We also wish to acknowledge the technical help provided by Pete Bruneau and Ray Tsang (of JPL) for block fabrication and device assembly respectively. The research described in this publication was carried out at the Jet Propulsion Laboratory, California Institute of Technology, under a contract with the National Aeronautics and Space Administration

7 REFERENCES

[1] P.H. Siegel, R.P. Smith, S. Martin and M. Gaidis, “2.5 THz GaAs Monolithic Membrane-Diode Mixer”, *IEEE Transactions Microwave Theory and Techniques*, vol. 47, no. 5, pp. 596-604, May 1999.

[2] J. Bruston, S. Martin, A. Maestrini, E. Schlecht, R.P. Smith, I. Mehdi, “The Frame-less Membrane: A Novel Technology for THz Circuits,” *Proc. Eleventh International Symposium on Space THz Technology*, Ann Arbor, May 2000.

[3] E Schlecht, J. Bruston, A. Maestrini, S. Martin, D. Pukala, R. Tsang, A. Fung, R. P. Smith , I. Mehdi, “200 And 400 GHz Schottky Diode Multipliers Fabricated with Integrated Air-Dielectric "Substrateless" circuitry,” *Proc. Eleventh International Symposium on Space THz Technology*, Ann Arbor, May 2000.

[4] C.P. Hu, “Millimeter wave frequency multipliers employing semiconductor diodes in a balanced configuration,” *Proc. 16th European Microwave Conf.*, Dublin 1986, 247-251.

[5] G. Pilbratt, “The FIRST mission,” *Proc. ESA Symp., The Far Infrared and Submillimetre Universe 1997*, ESA SP-401

[6] Michael C. Gaidis, Herbert M. Pickett, C. D. Smith, Suzanne C. Martin, R. Peter Smith, and Peter H. Siegel, “A 2.5 THz Receiver Front End for Spaceborne Applications,” *IEEE Trans. Microwave Theory and Tech.*, v. 48, no. 4, April 2000, pp. 733-739.

[7] P. Zimmermann, *private communication*.

[8] L. Samoska, T. Gaier, A. Peralta, S. Weinreb, J. Bruston, I. Mehdi, Y.C. Chen, H.H. Liao, M. Nishimoto, R. Lai, H. Wang, Y.C. Leong, "MMIC Power Amplifiers as Local Oscillators for FIRST," *Proc. SPIE UV, Optical, and IR Space Telescopes and Instruments*, SPIE 4013, Munich, Germany, March 2000, not yet published

[9] P. Penfield, R.P. Rafuse, "Varactor Applications," M.I.T Press, 1962.

[10] J. Bruston, R.P. Smith, S.C. Martin, A. Pease and P.H. Siegel, "Progress Toward the Realization of MMIC Technology at Submillimeter Wavelengths: A Frequency Multiplier to 320 GHz," *Proc. IEEE Intl. Microwave Symp. Dig.*, Baltimore, MD, June 1998, pp. 399-402.

[11] H.M. Pickett, J.C. hardy and J. Farhoomand, "Characterization of a Dual Mode Horn for Submillimeter Wavelengths," *IEEE Trans. Microwave Theory and Techniques*, vol. MTT-32, no. 8, pp. 936-8, Aug. 1984.

[12] J. Grajal, V. Krozer, E. Gonzalez, F. Maldonado, and J. Gismero, "Modeling and Design Aspects of Millimeter-Wave and Submillimeter-wave Schottky Diode Varactor Frequency Multipliers," *IEEE Transactions Microwave Theory and Techniques*, vol. 48, no. 4, pp. 700-712, April 2000.

[13] A. Maestrini, D. Pukala, F. Maiwald, E. Schlecht, G. Chattopadhyay, and I. Mehdi, "Cryogenic operation of GaAs based multiplier chains to 400 GHz", *proceeding of the 8th International Conference on Terahertz Electronics, Darmstadt*

Design and Performance of a 2.7 THz Waveguide Tripler

Frank Maiwald, S. Martin, J. Bruston[1], A. Maestrini, T. Crawford and P. H. Siegel
Jet Propulsion Laboratory, California Institute of Technology, Pasadena, CA 91109
[1] European Space Research and Technology Centre (ESTEC), Noordwijk, Holland

ABSTRACT

The design and performance of a 0.9 THz to 2.7 THz waveguide tripler are presented. An unusual split block configuration with parallel input and output waveguides accommodates a monolithic membrane diode (MoMeD) circuit [1, 2]. Submicron planar GaAs Schottky diodes in single and antiparallel pairs are implemented with matching filters on a 3 μm thick suspended substrate as part of the MoMeD structure. The filters are a combination of short hammerheads [3] and high-low impedance elements. Only a few circuit variations have been measured to date. The best current performance shows an output power of 0.1 μW and an efficiency of 0.002% at the band center frequency of 2.55 THz.

INTRODUCTION

The submillimeter-wave spectral bands from 300 THz to 3 THz are some of the least explored, yet information rich, regions of the electromagnetic spectrum with applications in radio astronomy, planetary science, and Earth remote sensing. To reach the frequency regime above one THz with high resolution, high sensitivity spectral line detectors, local oscillators (LO) sources are desperately needed. For space applications it is essential that such sources be realized with robust, low power consuming, solid-state technology. Likewise the source must be strong enough (1 to 50 μW) to pump superconductor-insulator-superconductor (SIS) mixers or hot-electron-bolometer (HEB) mixers. Recently a 1.2 THz solid-state source with 70 μW output power was demonstrated at JPL using planar Schottky diode multipliers and a power amplifier at W-band [4]. The highest reported LO-frequency generated by a multiplier using planar Schottky diodes is 1.5 THz (a doubler pumped by a far infrared laser). The observed output power was 40 μW [5]. With a traditional whisker contacted frequency tripler, 15 μW at 1.4 THz was obtained [6] using a backward wave oscillator (BWO) at 450 GHz. The advantages of using planar diode multiplier designs instead of whisker-contacted diodes are mechanical robustness, reproducibility, and simplified handling and mounting. These features are of great advantage for space applications.

In this paper we present the design and performance of a 2.7 THz waveguide tripler which was originally intended to be one of the upper stages of a multiplier chain on the Far Infrared and Submillimeter Space Telescope (FIRST/Herschel). Since a solid-state pump source at 850 GHz was not available, we used a far infrared laser as an input source for the measurements reported.

MONOLITHIC MEMBRANE DIODE (MOMED) CIRCUIT

The 0.9 THz to 2.7 THz frequency tripler uses the monolithic membrane diode (MoMeD) fabrication techniques [7] developed for a 2.5 THz Schottky diode mixer [1]. The performance of high frequency circuits suffers dramatically due to substrate losses. In order to keep the circuit losses as low as possible the active and passive high frequency structures are defined on a very thin GaAs membrane, as shown in Figure 1. The dimensions of the membrane are: 3 μm thick, 30 μm wide, and approx. 700 μm long. The membrane is attached to a sturdy 50 μm thick GaAs frame (outer dimensions: 1.5 mm x 1.0 mm) to provide mechanical rigidity and facilitate the handling of the device during fabrication and mounting. The complexity of the multiplier circuit is higher than the mixer circuit [1] because we implemented beam leads on top of the thin membrane (Figure 1b). They provide the connection to ground for the DC bias loop and for the RF. The dimensions of the beam leads (Fig. 1b) are: 1 μm thick, 15 μm long, and 10 μm wide. The complete MoMeD circuit is defined on a MBE grown semi-insulating GaAs wafer with a heavily doped ($5x10^{17}/cm^3$) epitaxial layer of 100 nm thickness.

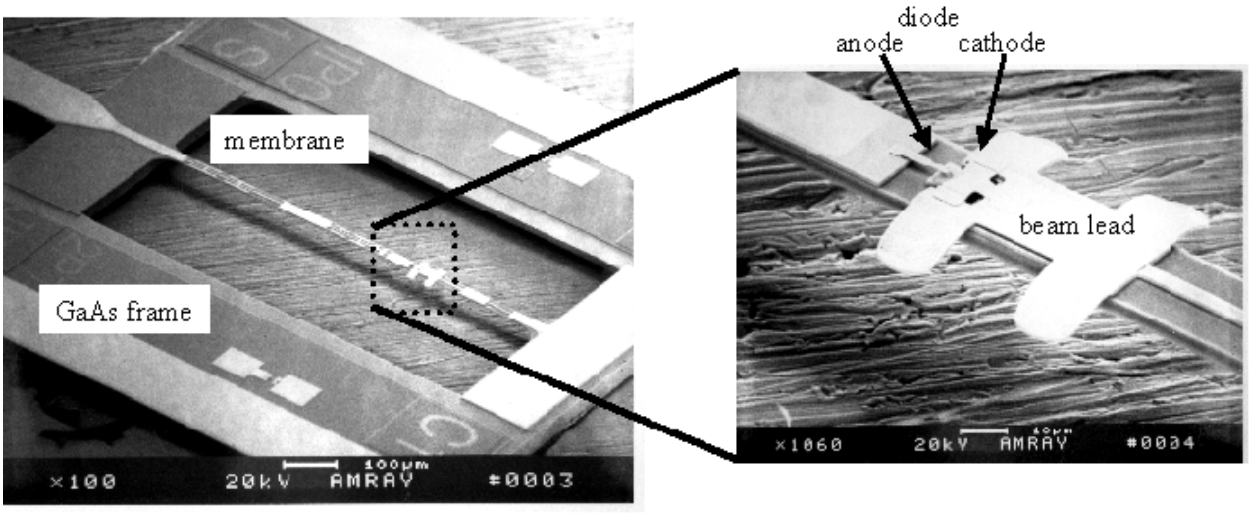

Fig. 1. Left (1a): SEM photo of the MoMeD circuit. Right (Fig 1b): Close up of the diode and the beam lead on the membrane.

The planar Schottky diode and the RF filters are defined on top of the membrane (Figure 2), which is suspended at the center of a 50x50 μm^2 rectangular channel. The cutoff frequency for this channel is 3 THz. Therefore only the propagation of a coaxial mode through the membrane is possible. This mode is transformed into a TE fundamental waveguide mode at the output, where the diode is defined, and at the input where an E plane probe is located. The waveguides are separated by a distance of 250 μm and orientated perpendicular to the membrane [Fig. 2]. Between the waveguides an input band-pass filter is implemented which passes the fundamental frequency and rejects the second and third harmonics. To provide the diode with DC bias an input band-stop and RF/DC short (including λ/4 band-stop) were necessary. The GaAs frame supports the bias return and the DC bias beam lead for connection off the frame.

The ability to bias the diode is important for monitoring the coupling of input power and optimization of the output power while the diode is operating mainly in the resistive mode.

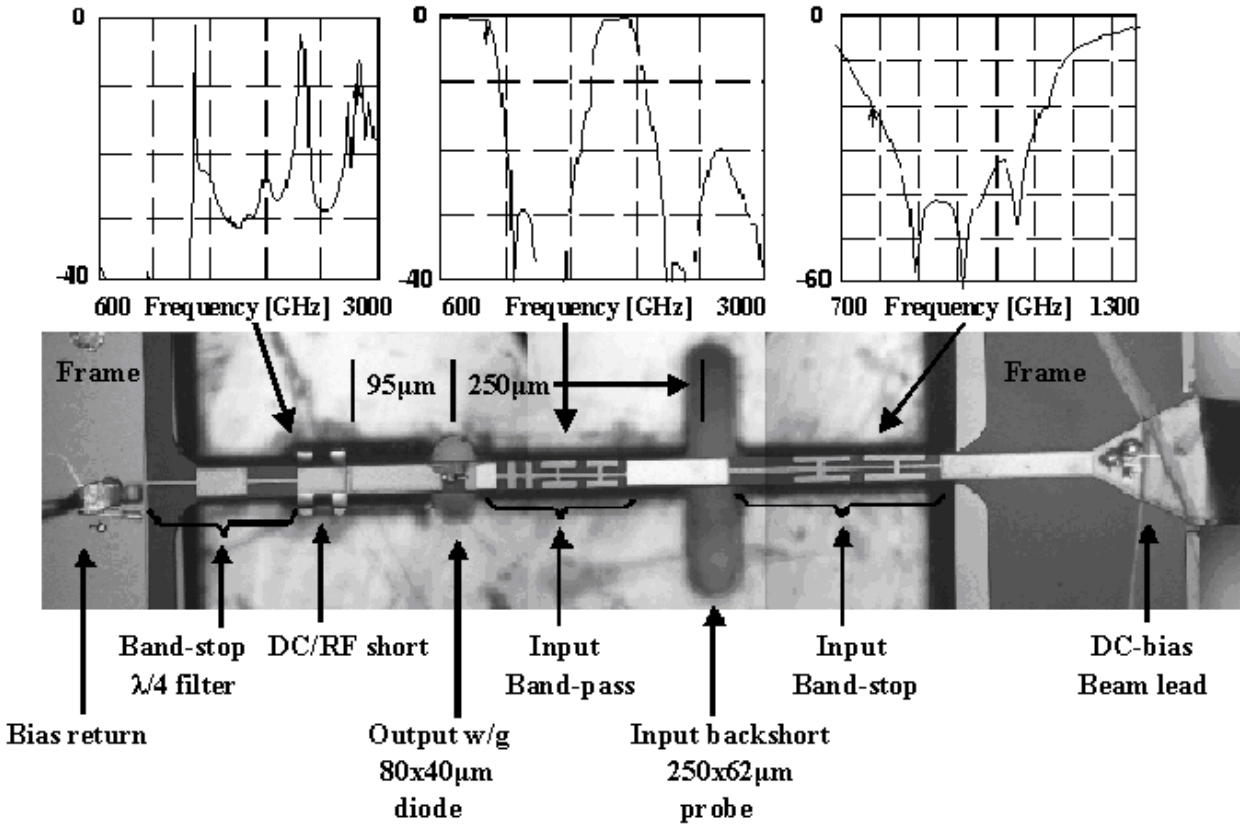

Fig. 2: MoMeD circuit and filter performance (modelled). Top: Filter responses of: the RF/DC short including λ/4 band-stop (left), the band-pass (middle), and the band-stop (right); Bottom: Mounted single diode circuit close up.

Two circuits using different diode configurations were designed and implemented on the membrane. One configuration has a single submicron diode (Fig. 1b) and the other consists of an antiparallel diode pair arrangement. The antiparallel pair circuit generates only odd harmonics and is similar to designs used at lower frequencies [8]. In both configurations the diodes are defined in the output waveguide, which is cutoff at the second harmonic. The antiparallel diode pairs are centered in the output waveguide while the single diode circuits include variations with the diodes centered, as well as next to, the output waveguide wall. During the circuit simulations both locations were found to have reasonable performance. The complete MoMeD circuit integrated in the filter channel (Figure 2) was simulated using a high frequency structure simulator (HFSS) as well as modeled on an X/Ka band mockup (1:135 scale) with commercial beam lead devices. For simulating the individual filter response we also used an electromagnetic simulator based on conformal finite-difference time-domain (FDTD) [9]. Final locations for the filter elements followed more detailed non-linear numeric analysis in Microwave Design System (MDS) [10] with the diode model developed in [11]. In order to compensate for inaccuracies in the diode model at frequencies above 500 GHz we varied the anode size on the GaAs wafer. The single diode designs have anodes of 0.4 to 0.8 μm^2 (Cjo varies from 1.1 fF to 2.5 fF) and the antiparallel diodes have a nominal anode area of 0.5 and 1 μm^2 (C_{j0} = 1.25 fF, 2.5 fF) per anode.

During the simulations it was found that the position of the RF short on the membrane had a large effect on the predicted conversion efficiency. Therefore we implemented two variations of the RF/DC short position to define a virtual ground at the wall of the output waveguide. One variation has the beam lead ground exactly at the output waveguide wall and the other has it λ/2 (95 μm) away, as shown in figure 2. Likewise the input band-stop filter was found to impact the band-pass filter response between the input and output waveguides significantly. A further constraint was to design the filters to be as compact as possible to reduce high frequency losses. Therefore we used a combination of hammerhead [3] sections and high-low impedances. All filters were first optimized separately and then integrated in the MoMeD circuit design. One challenge was to reduce the interaction of the filter elements. By iteratively changing the relative position and slightly varying the filter element dimensions we were able to move the undesirable resonances out of the desired frequency bands (fundamental, 2nd, and 3rd harmonic).

WAVEGUIDE BLOCK

The housing for the MoMeD circuit (Fig. 3) was designed to minimize mechanical complexity. It employs an unusual split-block configuration in which the waveguides lie parallel to one another (Fig. 4). Dual mode horns are integrated in both parts of the split block. The MoMeD circuit is mounted in the half which contains the output horn. When the blocks are joined together they can be optically aligned using a microscope viewed through the horn aperture. The precision for this procedure was better than 5 μm.

Fig. 3: Assembled MOMED tripler. The outer block dimensions are: HxWxL = 16 x 20 x 10 mm (without the SMA connector).

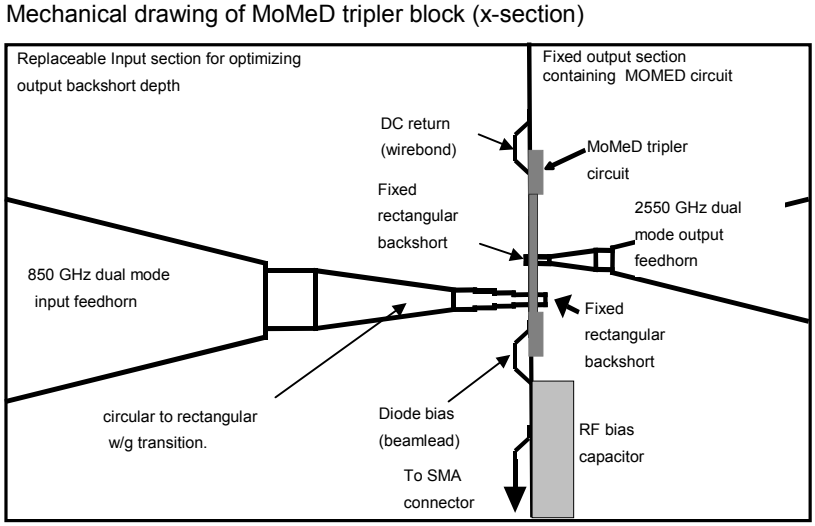

Dual frequency metal machined waveguide block with electroformed RF inserts, inline input/output feedhorns, micromachined backshort cavities, single suspended substrate cavity, GaAs MOMED diodes and support frame, and DC bias port.

Fig. 4: MoMeD multiplier block shown in cross section.

Power coupling at the input and the output of the MoMeD circuit is accomplished with dual mode Pickett-Potter feed horns [12]. We machined the horns, together with a short waveguide section, in an aluminum mandrel (Fig. 5). After the machining, the mandrels were electroformed with copper and the aluminum was etched out. The finished copper inserts were then pressed into a bore hole in the two halves of the split block.

The horns and waveguide transitions were analyzed with the aid of an electromagnetic simulator (HFSS). The calculated return loss of the rectangular-to-circular transition (left in Fig. 3) is better than 20 dB. Note that the input waveguide is ½ height to reduce the impedance for better diode matching. The return loss for the output transition was better 30dB.

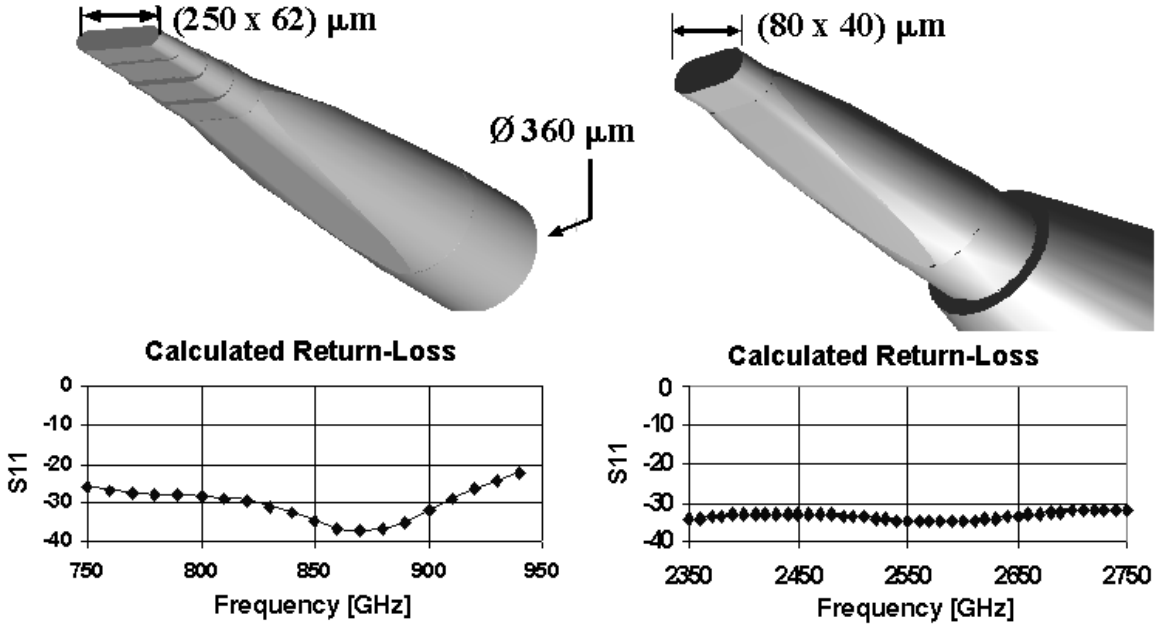

Fig. 5: Calculated return-loss of input and output circular to semi-circular-sided waveguide transition.
Left: The input transition with integrated full height to reduced height waveguide transformer is displayed. S11 is better than 20dB.
Right: The output transition with a part of the output feedhorn is also displayed. S11 is better than 30dB.

In order to house the MoMeD circuit, a relief hole was machined into the output block as shown in Fig. 6. The output backshort cavity depth was varied in several blocks and machined directly into the opposite block half. A similar cavity was milled in the half containing the device to serve as an input tuning short. The suspended substrate channel with a cross section of 50x50 μm^2 was milled only in the output block. The channel crosses the output waveguide and the input backshort cavity at their centers and accommodates the membrane of the MoMeD circuit. The membrane is mounted at the vertical center of the suspended substrate channel with an accuracy of better than 2 µm. Cyanoacrylate glue was used to hold the MoMeD circuit in the output block. The DC bias input beam lead formed on the GaAs frame was bonded to a capacitor. A bond wire connects the capacitor with the center pin of an SMA connector. The beam leads on the membrane itself were intended to provide both DC and RF shorts near the output waveguide, but they did not always provide adequate contact, hence extra bond wires were connected from the MoMeD frame to ground.

Variable depth waveguide backshort cavities (Fig. 2) were directly micro-machined into both halves of the split block. The depth of the output backshort was varied in steps of 0, 10, 20, 30 and 45 µm with a cross-section of 80x40 µm. The input backshort cavity in the output block (Fig. 6) has two different depths, 175 µm and 95 µm. Its cross-section is 250x62 µm. The direct

machining simplified the block fabrication and allowed the backshort cavity to be positioned within 2 μm total accuracy relative to the waveguide of the feedhorn (Fig. 6). However this design means many separate blocks are required to perform RF tuning. Because the tuning shorts were cut with a single pass of an endmill whose diameter was equal to the waveguide height, the resulting guide has semi-circular-sided broad walls. In order to reduce mismatch, the same shape was machined into the waveguide sections of both horn mandrels (Fig 5.). A similar waveguide is used on the much lower frequency Pacific Millimeter power detectors. Simulations indicate that the width must be increased slightly over that of a straight sidewall rectangular waveguide to match the desired cutoff frequency [13], but the performance is otherwise unaffected.

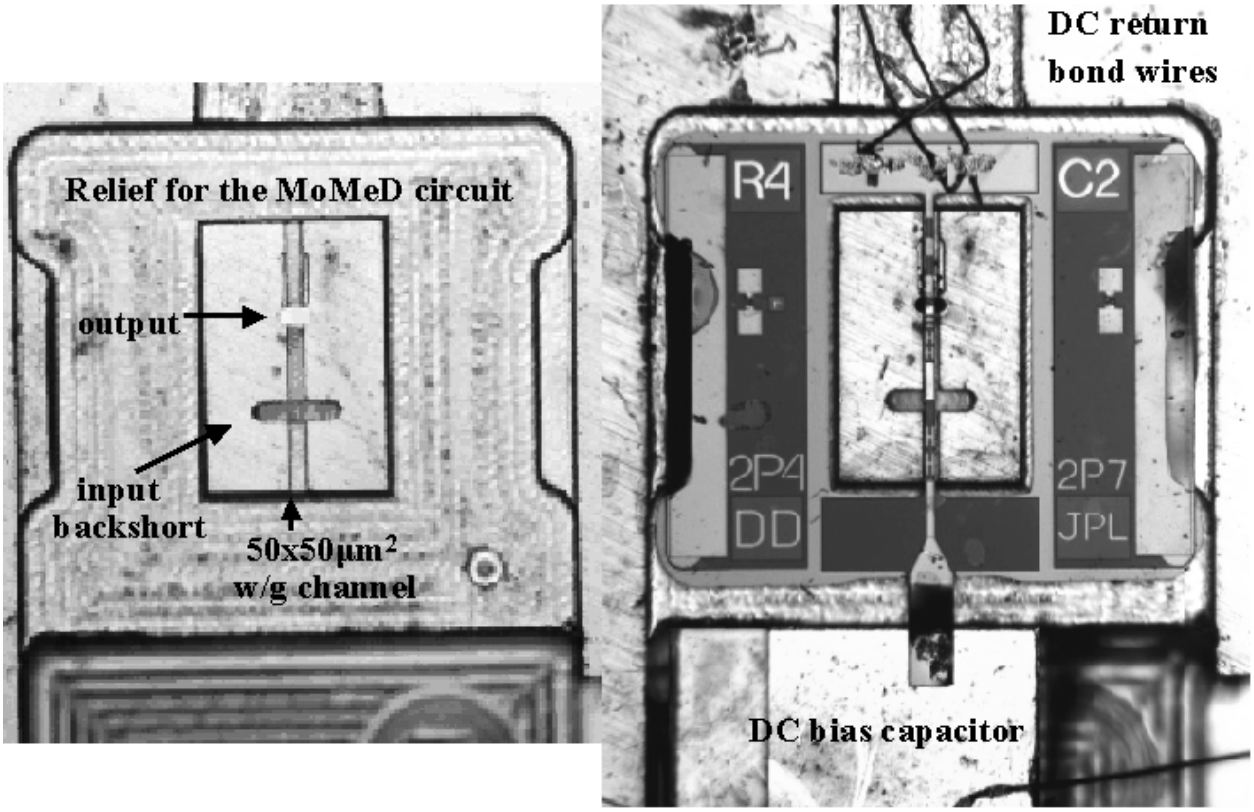

Fig. 6: Output block of the 2.7 THz tripler, with mounted MoMeD circuit.
Left side: A relief with approx. 100 μm depth for the MoMeD circuit is shown, the output waveguide (80x40 μm) is lightened, the 50x50 μm rectangular waveguide is crossing the input backshort cavity (250x62 μm) and the output waveguide in the center.
Right side: Assembled MoMeD device. On the top the bias loop is grounded, on the bottom there is the bias capacitor and the bond wire to the SMA visible.

To optimize the output power, the depth of the input waveguide cavity was varied by swapping block halves. To optimize the input power similar MoMeD devices were used in a series of blocks each with a different cavity depth for the input waveguide. The diodes bias current was monitored in video detection mode for these measurements. The advantage of this split-block arrangement is short input/output waveguide lengths. Although the calculated waveguide loss at 2.5 THz is very low (<.05 db/100 microns [14,15]), the actual measured loss will be much higher.

MEASUREMENT SYSTEM

The tripler measurement setup is shown in Figure 7. As no solid-state source was available at the time, a strong (>100W) carbon dioxide (CO_2) laser [16] was used to pump a far-infrared (FIR) laser. Sufficient output power of the FIR laser at two frequencies in the range from 780 to 900 GHz was produced to pump the tripler. A Fabry Perot filter was used to stabilize the CO_2 laser at the selected pump frequency. The output power of the FIR laser was measured with a commercial power head with 30% accuracy, since it could not be calibrated for this frequency range. The FIR output was mechanically chopped and focused into the input horn of the tripler. The output power of the multiplier was detected with a 4K-cooled Silicon-bolometer in direct detection video mode. A pre-amplifier with 200x and 1000x magnification is integrated on the cold stage of the bolometer. With a magnification of 200x the bolometer was calibrated at 2.5 THz. The measured sensitivity was $Rv=(5.5\pm1.0)x10^5$ Vp-p/W. To shorten the output path the detector was mounted as close as possible to the output feedhorn of the tripler. This was necessary since a strong water absorption line at 2523 GHz is present. Further we suppressed standing waves by placing absorber strategically around the input window of the detector. Output power was optimized by adjusting the DC bias on the diode.

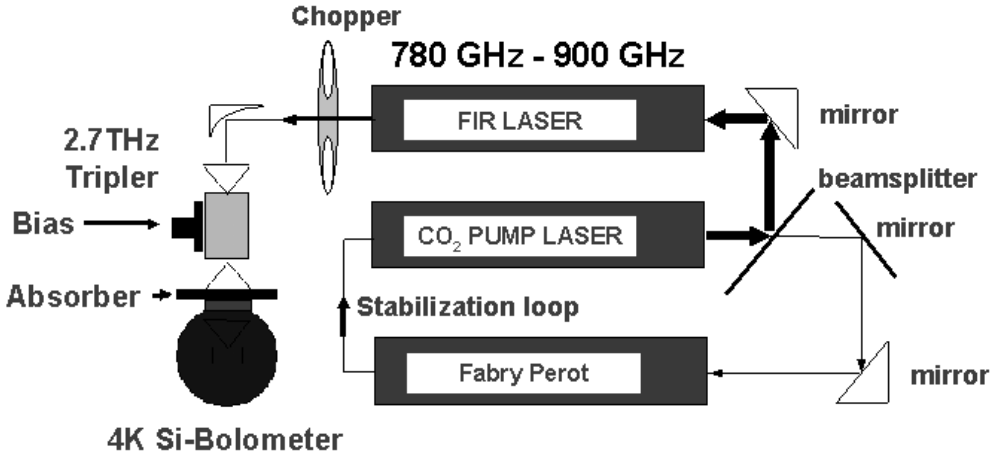

Fig. 7: FIR laser tripler test setup.

RESULTS

Preliminary results were obtained with two single diode circuits mounted in the waveguide block. In both cases the anode size was 0.4 x 1.9 μm^2 (C_{j0} = 2 fF). The RF/DC short was placed at a distance of 94 μm from the waveguide wall as displayed in Fig. 6. Typical measured device I/V characteristics are: series resistance $R_s = 6\ \Omega$, saturation current $I_{sat} = 1x10^{-12}$ A, and ideality factor $\eta = 1.5$.

We used the 10R16 line of carbon dioxide (CO_2) to pump deuterated methanol (CD_3CD). The measured output power at 850 GHz was (6±2) mW. With this power the diode bias point at constant bias voltage was driven from 10 μA (with no input power) to more than 1 mA. The output signal from the tripler was detected with the Silicon bolometer. With the pre-amplifier set to 200x, the output voltage was 50 to 60 mV. This corresponded to an output power of about. 0.1 μW at 2550 GHz. The tripler was also measured using a deuterated formic acid (DCOOD)

line pumped by the 10R12 line of CO_2 (110 W). The FIR laser generated (7±2.5) mW at 787 GHz. Our best estimate of the tripler efficiency and output power (available input to detected output) is 0.0003 % and 0.025 μW at 2360 GHz and 0.002 % and 0.1 μW at 2550 GHz. Currently only two single diode and one antiparallel-pair diode circuits have been measured. At this point only the single diode circuit can be pumped sufficiently to generate measurable output power above 2 THz.

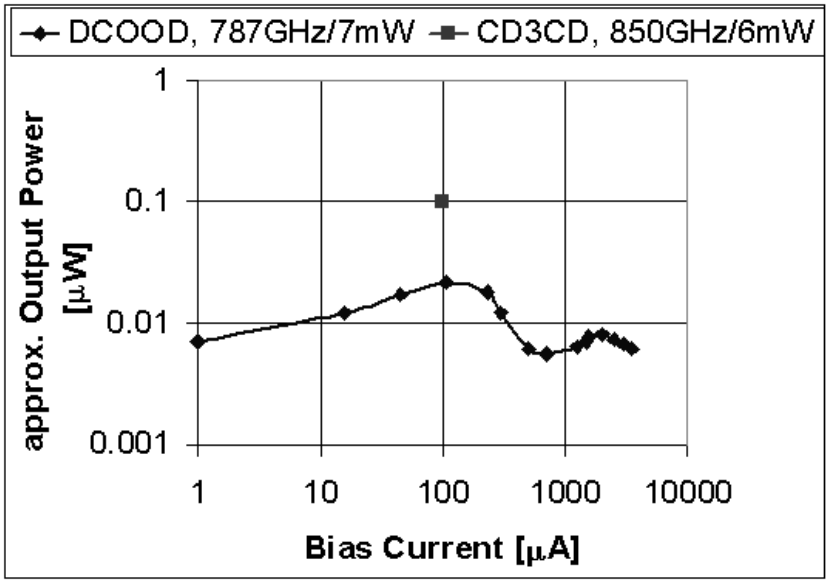

Fig. 8: Measured performance (approximate output power vs. bias current) of the MOMED tripler at 2361 GHz and 2550 GHz at fixed input power. Maximum output power was obtained at 100 μA and 0.7 V bias.

We also investigated the video responsivity as well as the isolation between the input and output horns. The output waveguide tuning cavity depth was optimized in this way. A cavity depth of 20 μm (λ/4) was optimal. Fourth and second harmonic content were checked by measuring the output standing waves when the detector was moved with a micrometer mount along the propagation axis. Harmonic content was below detectable limits.

SUMMARY

The first measurements of a 2.7 THz planar diode frequency tripler have been reported. By pumping with a laser source at 850 GHz, we estimate that 0.1 μW was detected at 2550 GHz. Although the conversion efficiency is very poor and the output power is low, the circuit and device topology are robust and there is much room for improvement. Further research is needed to find a more accurate way to measure the power at THz frequencies. The device structure is identical to that used for THz mixing and it has been qualified for flight [1, 17]. It is expected that similar circuit realizations could be used for multipliers at other frequencies in the submillimeter regime in order to produce flight qualified all-solid-state sources. Additional measurements are in progress, over a greater frequency range, and with other design variations available on the mask set.

ACKNOWLEDGEMENTS

The authors would like to acknowledge the support of Peter Bruneau for fabrication of the waveguide blocks, Erich Schlecht for technical discussions, John Lichtenberger (Metaplate) for electroforming the horns, Herb Pickett for providing the laser used for output measurements, and Dave Orozco for support with measurements of the video response. This work was performed at the Jet Propulsion Laboratory, California Institute of Technology, under a contract with the National Aeronautics and Space Administration (NASA). The European Space Agency (ESA) supports Frank Maiwald under Fellowship program ADM-H/vp/607.

REFERENCES

[1]. P.H. Siegel, R.P. Smith, S. Martin, and M. Gaidis, "2.5 THz GaAs Monolithic Membrane-Diode Mixer", IEEE Trans. Microwave Theory and Tech., v. 47, no. 5, May 1999, pp. 596-604.

[2]. R.P. Smith, S. Martin and P.H. Siegel, "GaAs Membranes for Millimeter and Submillimeter Wave Circuits and Devices," JPL New Technology Report, NPO-20314, Nov. 10, 1997.

[3]. J.E. Oswald and P.H. Siegel, "The application of the FDTD method to millimeter-wave filter circuits including the design and analysis of a compact coplanar strip filter for THz frequencies", TU3F-28, pp. 309-312, MTT-S Digest 1994.

[4]. A. Maestrini, J. Bruston, D. Pukala, S. Martin and I. Mehdi, "Performance of a 1.2 THz frequency tripler using GaAs frameless membrane monolithic circuits," to appear in 2001 IEEE MTT-S Int. Mic. Sym., Feb. 2001.

[5]. N.R. Erickson, G. Narayanan, S. Martin, R. P. Smith and I. Mehdi, M. Coulomb, G. DeMartinez, "Monolithic frequency doublers and triplers for THz frequencies", 12th Int. Sym. on Space THz Tech., San Diego, CA, Feb. 14-16, 2001.

[6]. R. P. Zimmermann, RPG, Germany, private communication.

[7]. Suzanne Martin, Barbara Nakamura, Andy Fung, Peter Smith†, Jean Bruston, Alain Maestrini, Frank Maiwald, Peter Siegel, Erich Schlecht, and Imran Mehdi, "Fabrication of 200 to 2700 GHz Multiplier Devices using GaAs and Metal Membranes", to appear in 2001 IEEE MTT-S Int. Mic. Sym., Feb. 2001.

[8]. C.P. Hu, "Millimeter Wave Frequency Multipliers Employing Semiconductor Diodes in a Balanced Configuration," Proc. of the 16th European Micr. Conf., Dublin, Ireland, 1986, pp. 247-251.

[9]. QuickWave, 3D electromagnetic simulator based on conformal finite-difference time-domain method (FDTD), Version 1.7, QWED s.c., Zwyciezcow 34/2, 03-938 Warsaw, PL, info@qwed.com.pl.

[10]. Microwave Design System (MDS) from HP, Agilent

[11]. J. Bruston, R.P. Smith, S.C. Martin, D. Humphrey A. Pease and P.H. Siegel, "Progress Towards the Realization of MMIC Technology at Submillimeter Wavelengths: A Frequency Multiplier to 320 GHz," IEEE MTT-S International Microwave Symposium, Baltimore, MD, pp. 399-402, June 1998.

[12]. H.M. Pickett, J.C. Hardy and J. Farhoomand, "Characterization of a Dual Mode Horn for Submillimeter Wavelengths," IEEE Trans. Microwave Theory and Tech., vol. MTT-32, no. 8, Aug. 1984, pp. 936-938.

[13]. P.H. Siegel and H. Javadi, "Semi-Circular-Sided Waveguide Millimeter-Wave Dichroic Plate for High Incidence Angles", JPL New Technology Report, NPO 20826, 8/18/1999, 5 pages.

[14]. N.J. Cronin, Microwave and optical waveguides, 1995, IOP Publishing Ltd, ISBN 0 7503 0216 X pbk.

[15]. R.E. Collin, Foundations for Microwave Engineering, 1966, McGraw-Hill, Inc

[16]. H.M. Pickett, J.C. Hardy and J. Farhoomand, "Characterization of a Dual Mode Horn for Submillimeter Wavelengths," IEEE Trans. Microwave Theory and Techniques, vol. MTT-32, no. 8, Aug. 1984, pp. 936-8.

[17]. Michael C. Gaidis, H.M. Pickett, C.D. Smith, R.P. Smith, S.C. Martin and P.H. Siegel "A 2.5 THz Receiver Front-End for Spaceborne Applications," IEEE Transactions on Microwave Theory and Techniques, MTT-48, no. 4, April 2000, 733-739.

The research described in this paper was carried out at the Jet Propulsion Laboratory, California Institute of Technology, under a contract with the National Aeronautics and Space Administration.

A New Pillar Geometry for Heterostructure Barrier Varactor Diodes

[1]B.E.J.Alderman, [2]J.Stake, [2]L.Dillner, [1]D.P.Steenson, [2]M.Ingvarson, [2]E.L.Kollberg, [3]C.M.Mann and [1]J.M.Chamberlain

[1]Institute of Microwaves and Photonics, School of Electronic and Electrical Engineering, University of Leeds, Leeds, LS2 9JT, UK
[2]Microwave Electronics Laboratory, Chalmers University of Technology, SE-412 96 Göteborg, Sweden
[3]Rutherford Appleton Laboratory, Chilton, Oxon, OX11 0QX, UK
Email: eenbeja@electeng.leeds.ac.uk

Abstract

We report on a novel diode geometry, with reduced thermal resistance, for Heterostructure Barrier Varactor, HBV, diodes. The pillar geometry presented here involves the complete removal of the substrate, electrical contact is made by the forward and reverse side processing of metallic pillars.
We propose that there is a limit to the maximum number of barriers that can be used to increase the power capability of a HBV. An analytical model has been developed to study these effects. In considering the case of a perfect thermal heat sink the limit is found to be fourteen, in applying this model to the new pillar structure this is reduced to six.

1) Introduction

The Heterostructure Barrier Varactor, HBV, has received considerable attention since its proposal in 1989 by Kollberg and Rydberg [1]. The HBV is a symmetric varactor which gives rise only to odd harmonic generation, simplifying the circuit geometry for higher harmonic multiplication, due to the absence of idler circuits. For this reason, together with the ability to epitaxially stack any number of these devices and increasing the power handling capacity, recent results are comparable with the best reported Schottky based multipliers [2-5].

Present interest in HBV frequency multipliers is focused towards changes in the device geometry and increased integration. A variety of material systems are used, and theoretical work continues with the goal of increasing the capacitance modulation whilst reducing the conduction current. However, theoretical and experimental results continue to show the domination of thermal effects.

As the intrinsic HBV temperature is raised, the conduction current, which results primarily from thermionic emission over the barriers, increases. This increase in conduction current reduces the capacitance modulation. Hence, together with the increase in series resistance, the overall device efficiency is reduced. Moreover, the breakdown voltage decreases with temperature, reducing the power handling capacity [6]. These effects are well known and reflected by the many device designs in which the thermal impedance is of considerable importance.

In this paper we demonstrate a new pillar diode geometry which is optimised for a reduction in the thermal resistance. Our results suggest a limit to the number of barriers; this limit is based on the dominance of thermal effects.

2) Pillar Geometry

2.1) Device Concept

With the move from whisker to planar devices, the twin air-bridge structure has become a popular fabrication process for HBV diodes. Typically, the thermal impedance from the edge of the mesas, contacted via air-bridge technology on a flip-chip, to the multiplier block is estimated to be of the order 0.7 K/mW [7]. The thermal conductivity of the substrate and the length of the bond fingers give the main limitations to the thermal resistance. The latter of these must also be optimised with respect to the parasitic capacitance, such that a decrease in their length reduces the thermal resistance at the cost of increased parasitic capacitance.

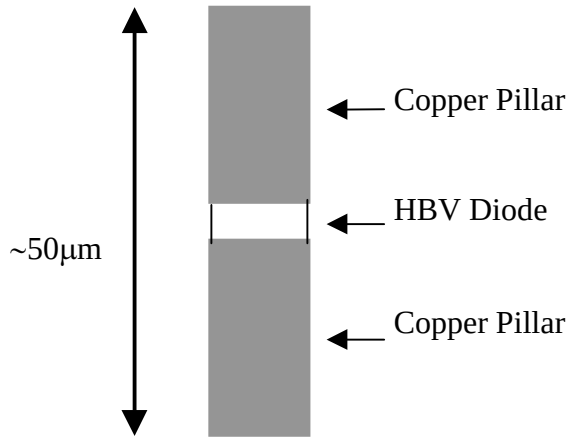

Figure 1) Schematic diagram of pillar HBV structure.

The new pillar geometry presented here is conceptually very simple. The semiconductor mesa is contacted symmetrically by two metallic pillars, and all other substrate material is removed. Figure 1 shows a schematic of the pillar structure.

This structure can be soldered directly into a circuit or, as is planned, soldered into a flip-chip and mounted in the traditional planar manner. A schematic of this structure is shown in figure 2. The estimated thermal contact resistance of the pillar structure, when soldered into an adjoining flip-chip, is 0.2 K/mW.

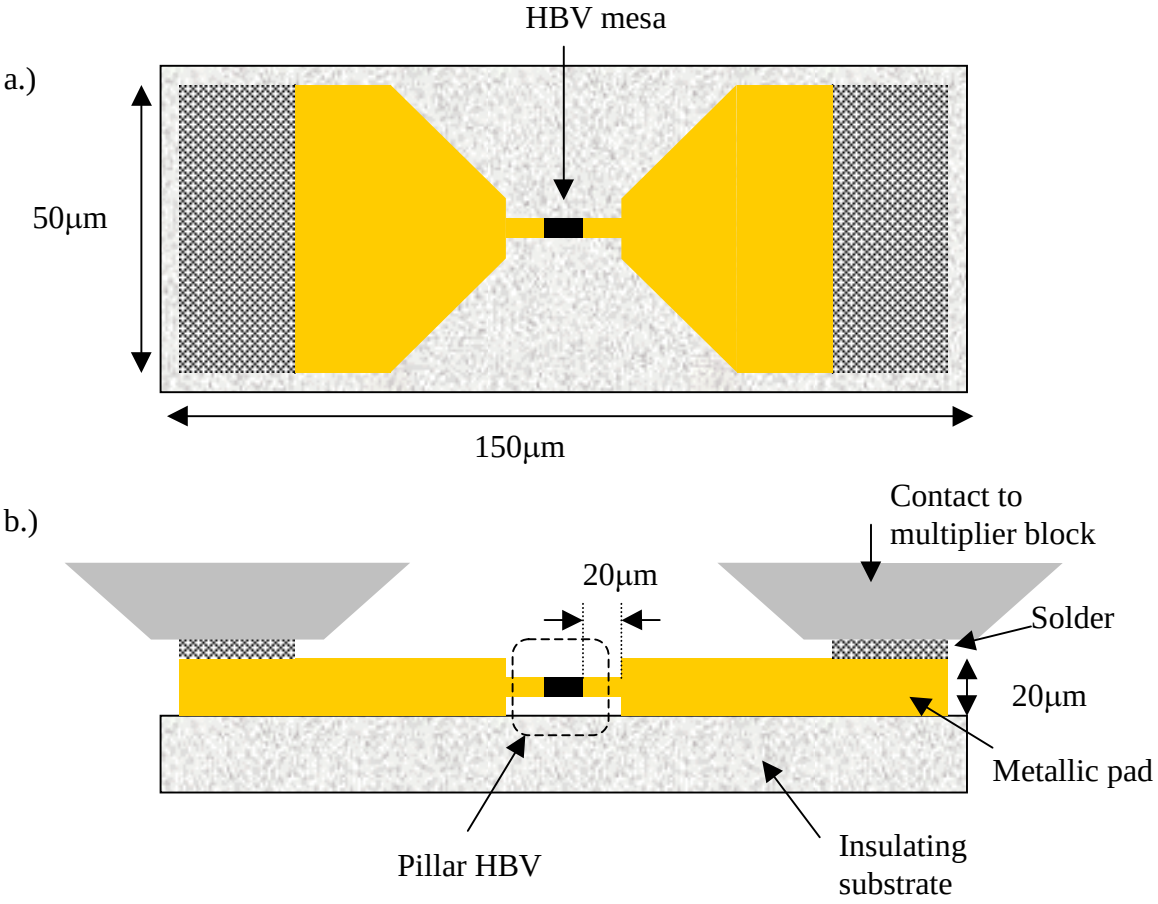

Figure 2) Top (a.) and cross-sectional (b.) representation of flip-chip mount for pillar HBV.

One of the significant advantages the twin air-bridge structure has over alternative approaches is the fact that two mesas are electrically contacted back-to-back. Asymmetries within the epi-layers are effectively cancelled; however, this is at the cost of increased series and spreading resistance formed in the connecting n^+ region. These

terms together represent a significant fraction of the total electrical resistance. This new geometry is, therefore, reliant on good quality material with symmetrical material characteristics. However, the resulting electrical and thermal resistances are significantly reduced, together with the parasitic capacitance. The on-wafer device density also approaches the maximum possible value; the most significant wastage derives from edge-bead effects during fabrication.

2.2) Device Fabrication

The HBV material structure, ITME 1817, shown in Table 1,was grown by MOVPE. The device fabrication was performed using standard photolithography techniques and alloyed ohmic contacts. The mesa was initially etched by chlorine based Reactive Ion Beam Etching, RIBE, followed by a short wet etch. Thick film resist was used to define the top side pillar structure which was copper electroplated to the top level of the resist. An additional sputtering process was employed before electroplating a sacrificial copper substrate to ~50μm. The InP wafer substrate was subsequently removed by wet chemical etching. Evaporating the contact metalisation and repeating the pillar electroplating process was the final stage of the device fabrication. The devices were separated by carefully etching the sacrificial substrate. A single device soldered on a gold-on-quartz filter can be seen in figure 3.

Table 1
The HBV Material Structure (ITME 1817)

Layer	Material	Doping [cm^{-3}]	Thickness [Å]
Contact	InAs	$>5x10^{18}$	100
Contact	$In_{.53\rightarrow1}Ga_{.43\rightarrow0}As$	$>5x10^{18}$	6000
Modulation x 6	$In_{.53}Ga_{.47}As$	$3x10^{16}$	4000
Spacer x 6	$In_{.53}Ga_{.47}As$	undoped	200
Barrier x 6	$Al_{.48}In_{.52}As$	undoped	50
Barrier x 6	AlAs	undoped	30
Barrier x 6	$Al_{.48}In_{.52}As$	undoped	50
Spacer x 6	$In_{.53}Ga_{.47}As$	undoped	200
Modulation	$In_{.53}Ga_{.47}As$	$3x10^{16}$	4000
Contact	$In_{.53}Ga_{.47}As$	$>5x10^{18}$	3000
Substrate	InP	N^{++}	

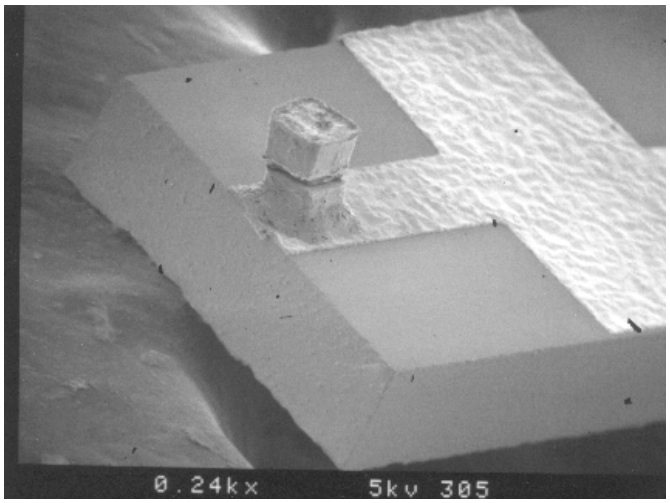

Figure 3) Pillar HBV structure soldered on a gold-on-quartz filter.

3) Thermal Estimations

3.1) Thermal Models

In this section, we propose that a limit exists for the maximum number of effective barriers for the HBV. Based on first order approximations and steady-state thermal analysis, it is argued that additional barriers beyond this limit act predominately as electrical series losses. The value of this limit is also shown to be dependent on the external thermal contact resistance.

We have solved the one-dimensional temperature profile analytically in a section of GaAs given a point source and a distributed source of power dissipation, this has been combined with linear and nonlinear models for the thermal conductivity of GaAs. The nonlinear thermal conductivity is as follows;

$$K_{GaAs} = \frac{A}{T^{1.2}} \qquad (1)$$

where the constant, A, varies with doping. For GaAs doped at $N_D=1x10^{17}cm^{-3}$, A=48800 [8], which we have used here. In the linear model we assume a fixed temperature of 300K.

The temperature differential developed over a section of material is calculated as the product of the thermal power flow through and the thermal resistance of the element. The

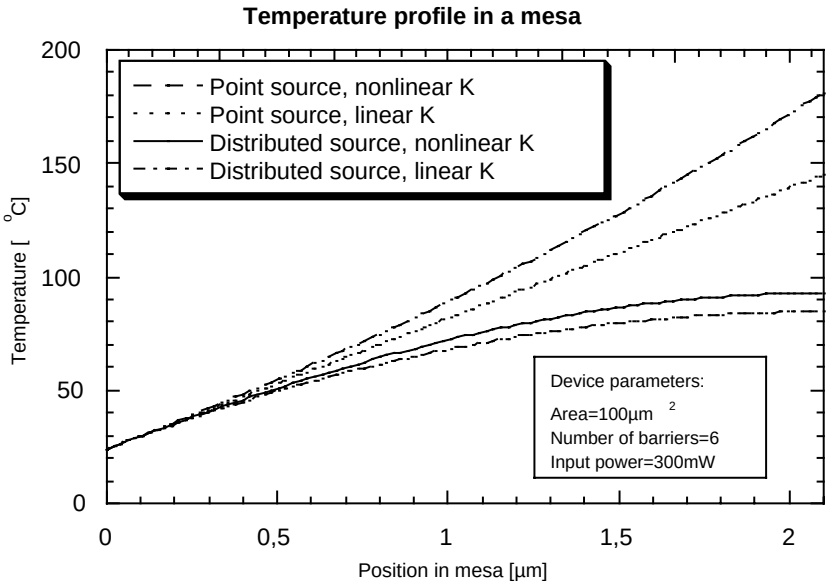

Figure 4) Comparison of thermal models.

thermal resistance of a bulk section of material surrounded by air can be solved directly as

$$R_{Thermal} = \frac{t}{K\pi r^2} \qquad (2)$$

where t is the thickness of the section, K is the material's thermal conductivity and r is the equivalent radius based on the cross-sectional area of the section.

Evaluation of the above formulae reveal four distinct trends, which are plotted in figure 4 for typical values of area, number of barriers and input power for a moderately high powered HBV. It is also assumed that one edge of the mesa is at room temperature and that the total heat flow, resulting from the power dissipation in the active region, is in one direction only, towards the heat sink. Although the values taken are appropriate from an electrical prospective, by ignoring the contacting geometry, the temperature scale is in effect arbitrary. In estimating the mesa thickness, L, we have assumed a typical modulation layer thickness, l, of 300nm together with the relationship

$$L \approx l(N+1) \qquad (3)$$

where N is the number of barriers. Hence, assuming the contact and barrier layers to be of negligible thickness. The power dissipated thermally in the device is approximated to the input power.

The model involving a distributed power source with nonlinear thermal conductivity was considered as the most appropriate for the analysis which follows. Under these assumptions, the temperature, $T(x)$, at point x, for a mesa of length, L, and equivalent cross-sectional radius, r, is given by

$$T(x) = \left(\frac{1}{T_0^{0.2}} - \frac{0.1\left(2Lx - x^2\right)P_{Total}}{LA\pi r^2} \right)^{-5} \quad \text{for} \quad 0 \le x \le L \qquad (4)$$

where T_0 is the temperature of the mesa at the heat sink. P_{Total} is the total power dissipated in the active region.

3.2) Operating temperature of Pillar HBV diode

Thermal analysis of the pillar HBV structure is simplified by the symmetry of the device. For a given dissipated power and mesa length we are able to solve for half the power dissipated by half the length of the mesa. The asymmetry of the air-bridge structure and the essentially one directional heat flow of the whisker structure, do not allow this simplification.

The temperature in centigrade at the centre of an N barrier HBV mesa is shown in figure 5; this follows from the solution of equation 4 for a symmetrically contacted device. In this figure the contact is assumed to be a perfect heat sink, such that the edges of the mesa are kept at 300K. Lines of constant peak temperature are given as a function of power density per barrier and the number of barriers. The contour lines are only shown within the approximate validity of the nonlinear model. Taking 100^0C as a reasonable maximum acceptable temperature rise in a mesa and a power density per barrier of 0.5mW/μm^2, the limiting number of barriers can be estimated at fourteen. In assuming a perfect thermal contact, this analysis implies an effective maximum in the number of barriers. Incorporating the additional effect (thermal resistance) of a 20μm copper pillar, of the same equivalent radius as the mesa, reduces the maximum number of barriers to approximately six. This is shown in figure 6.

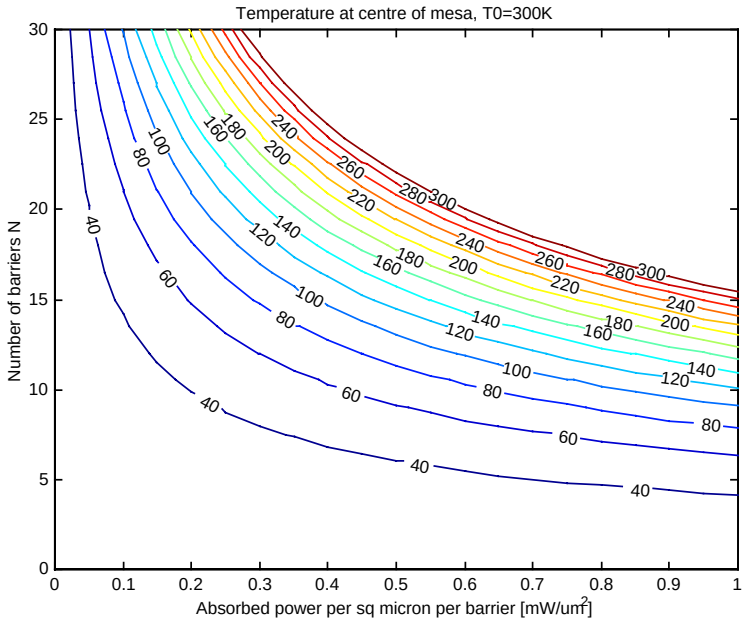

Figure 5) Temperature at the centre of a symmetrically contacted HBV mesa. The contacts are assumed to be perfectly conducting and at 300K.

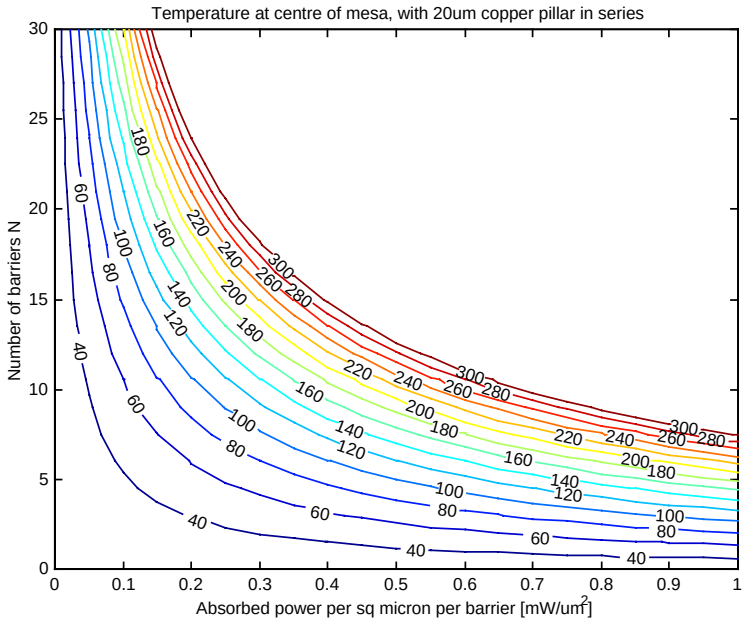

Figure 6) Temperature at the centre of a HBV mesa. The mesa is assumed to be contacted symmetrically by 20μm copper pillars to a perfect thermal conductor at 300K.

3.3) Power Handling

The analysis above is generalised in the form of power density, such that the maximum power dissipated by a symmetrically contacted HBV is linked to the area. For high powered applications, increasing the device area, for a given number of barriers, would allow higher dissipated power. However, this results in a decreased operating impedance which can present matching difficulties. The total ohmic contact resistance is also reduced with larger area such that increasing the number of barriers is usually preferable but is a trade-off with the power density per barrier.

4) Conclusions

We have demonstrated a novel device geometry for the HBV diode. These diodes have been fabricated using standard fabrication techniques, they are also robust and easy to integrate into existing circuits.

A steady-state thermal model of the HBV has demonstrated that a maximum number of barriers exists for a HBV. This is shown to be fourteen for a device contacted symmetrically by two perfect thermal heat sinks, however, this reduces to six for the new pillar structure.

The thermal approach we have taken here is by no means conclusive. No account has been taken for the output circuit delivering power at the various harmonics, nor the thermal generation in the ohmic contacts. Together, these effects represent a significant fraction of the input power. The heat generation within the diode is also a nonlinear effect where the electrical losses are strongly dependent upon temperature. A self-consistent approach involving thermal conductivity with harmonic balance estimates of individual barrier performance is required to investigate these effects further. However, we present here clear evidence, based upon thermal considerations, which indicates a limit to the maximum number of barriers for a HBV diode. Moreover, this limit is within the range typically considered for device fabrication, and therefore is an important aspect in overall device optimisation.

Acknowledgements

The authors would like to thank W. Strupinski of the Institute of Electronic Materials Technology, Epitaxy Department, Warsaw, Poland, for the HBV material used in these studies.

References

[1] E. Kollberg and A. Rydberg, "Quantum-barrier-varactor diodes for high-efficiency millimetre-wave multipliers," *Electronics Lett*., vol. 25, pp. 1696-1698, 1989.

[2] A. Simon, C. Lin, M. Rodriguez-Gironés, H. Hartnagel, P. Zimmermann, R. Zimmermann and R. Henneberger, "High efficiency frequency multipliers using substrateless Schottky diodes," IEEE Sixth Int. Conf. On Terahertz Electronics, pp. 72-73, 1998.

[3] J. Bruston, R. P. Smith, S. C. Martin, D. Humphrey, A. Pease and P. H. Siegel, "Progress towards realization of MMIC technology at submillimeter wavelengths: A frequency multiplier to 320 GHz." 1998 IEEE MTT-S International, pp. 399-402, vol. 2, 1998.

[4] J. Thornton, C. M. Mann and P. de Maagt, "Optimization of a 250 GHz Schottky triplier using novel fabrication and design techniques," IEEE Trans. Microwave Theory Tech., vol. 46, pp. 1055-1061, 1998.

[5] X. Mélique, A. Maestrini, R. Farré, P. Mounaix, M. Favreau, O. Vanbésien, J. Goutoule, F. Mollot, G. Beaudin, T. Närhi and D. Lippens, "Fabrication and performance of InP-based heterostructure barrier varactors in a 250 GHz waveguide triplier," IEEE Trans. Microwave Theory Tech., vol. 48, no. 6, 2000.

[6] J. Stake, L. Dillner, S. H. Jones, C. Mann, J. Thornton, J. R. Jones, W. L. Bishop and E. Kollberg, "Effects of self-heating on planar heterostructure barrier varactor diodes," Trans. Electron Devices, vol. 45, pp. 2298-2303, 1998.

[7] J. Stake, C. Mann, L. Dillner, M. Ingvarson, S. H. Jones, S. Hollung, M. Henini, B. Alderman, J. M. Chamberlain and E. L. Kollberg, "Improved diode geometry for Heterostructure Barrier Varactors," Tenth International Symposium on Space Terahertz Technology, Charlottesville, 1999.

[8] Properties of Gallium Arsenide, 2nd Edition, (INSPEC: The Institution of Electrical Engineers, London, United Kingdom, 1993), pp. 46-49.

Temperature Effects in Varactors and Multipliers

J. East and I. Mehdi
Solid State Electronics Laboratory
The University of Michigan
JPL

Abstract

Varactor diode multipliers are a critical part of many THz measurement systems. The power and efficiencies of these devices limit the available power for THz sources. Varactor operation is determined by the physics of the varactor device and a careful doping profile design is needed to optimize the performance. Higher doped devices are limited by junction breakdown and lower doped structures are limited by current saturation. Higher doped structures typically have higher efficiencies and lower doped structures typically have higher powers at the same operating frequency and impedance level. However, the device material properties are also a function of the operating temperature. Recent experimental evidence has shown that the power output of a multiplier can be improved by cooling the device.We have used a particle Monte Carlo simulation to investigate the temperature dependent velocity vs. electric field in GaAs. This information was then included in a nonlinear device circuit simulator to predict multiplier performance for various temperatures and device designs. This paper will describe the results of this analysis of temperature dependent multiplier operation.

I Introduction

The goal of this paper is to investigate the temperature dependent performance of GaAs based Schottky diode frequency multipliers. The performance of these multipliers is an important limitation on the overall performance of submillimeter and THz imaging systems. Recent experimental evident indicates that these multipliers can have improved performance with cooling. This paper will discuss a simplified device model to investigate this temperature dependence. The next section of the paper will present a temperature and doping dependent transport model for GaAs obtained from a Monte Carlo based transport model. The results of this model were parameterized

to provide information for a device model. Section III describes the nonlinear device circuit model used to include velocity saturation effects and the conditions used in the multiplier simulation. Section IV presents results for doping, temperature and frequency dependent multiplier performance. The paper is summarized in Section V.

II Monte Carlo Modeling of GaAs Transport

The transport properties of GaAs play an important part in the operation of high frequency GaAs Schottky barrier frequency multipliers. The velocity characteristics in the undepleted region of the diode determine the saturation characteristics and thus the power and the efficiency. To date, most varactor designs have been based on room temperature heat sink operation. However, recent measurements have shown that cooling improves the operation, so we need a better understanding of temperature dependent transport. We have used a Monte Carlo simulation of GaAs electron velocities vs. electric field, doping and temperature to quantify the transport. The simulation is a simple 2 valley parabolic band approximation [1], [2]. The code includes most of the characteristics of a more complex approach, yet is fast enough for the type of parameter extraction needed for this study. The simulation was run for temperatures between 150 and 450 K, corresponding to a range between a cooled heat sink and typical higher temperature operation. The data was fit to a velocity vs. electric field curve of the form [3].

$$v(E) = \frac{\mu E + v_{sat}(\frac{E}{E_p})^4}{1 + (\frac{E}{E_p})^4}, \tag{1}$$

where μ,v_{sat} and E_p are fitting parameters that depend on the temperature and doping. In the low field limit $v(E) = \mu E$ and at high fields $v(E) = V_{sat}$. Typical results are shown in Fig. 1 for a doping of $10^{17}/cm^3$. The peak velocities based on Eqn. 1 can then be collected and plotted. A plot of the peak velocity vs. temperature and doping is shown in Fig. 2. The peak velocities and the mobilities can be fit to equations of the form

$$V_{peak}(T) = V_{peak}(300)(T/300)^x. \tag{2}$$

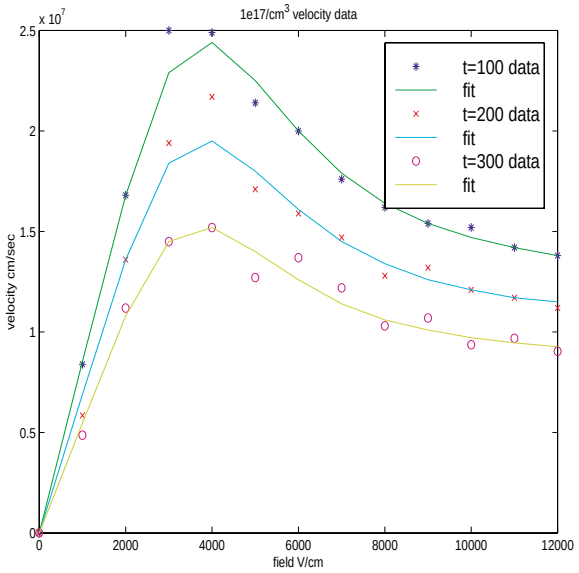

Figure 1: GaAs temperature and field dependent velocities $N_d = 10^{17}/cm^3$

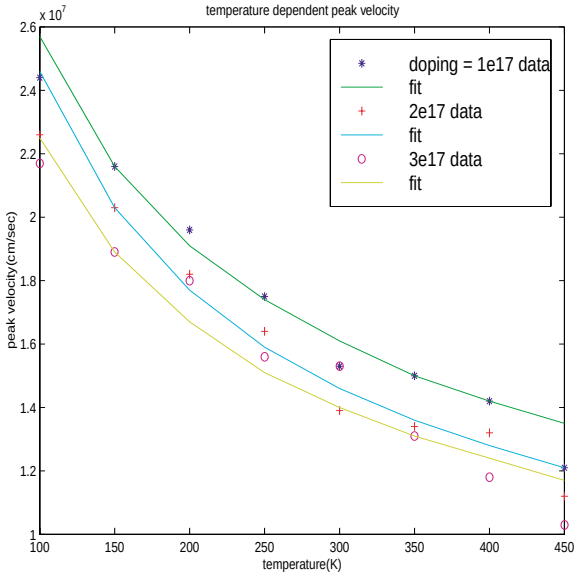

Figure 2: GaAs temperature and doping dependent peak velocities

and

$$\mu(T) = \mu_{300}(T/300)^{x}. \tag{3}$$

These expressions can then be used in a nonlinear multiplier simulation to investigate temperature dependent operation. We also need to model the breakdown voltage. The breakdown voltage will depend on the doping profile and the temperature. If we assume an abrupt junction and neglect the temperature dependence, the breakdown voltage can be approximated by

$$V_{breakdown}(N_d) = 60(N_d/10^{16}cm^{-3})^{y}. \tag{4}$$

This expression is shown in Fig. 3. We can use this material information to investigate device operation.

III Multiplier Modeling

The next step is to simulate multiplier performance for a variety of operating temperatures, frequencies and powers levels. We need a device model that takes velocity saturation effects into account. These effects were first described by Kollberg et.al. [4] A simple physical model for this effect based on separating the structure into an abrupt depletion layer and an undoped epitaxial layer with transport in the bulk determined by a velocity vs. electric field curve was described by East et.al. [5] This model has been used in a nonlinear circuit simulator to investigate devices under different operating conditions.

We need a way to compare devices for a range of operating conditions. However, the multiplier performance will strongly depend on the bias point, the frequency and the embedding impedances. We need a consistent comparison. In this paper we fix the input Q of the circuit. This in effect sets the type of operation, with lower Q devices acting more like nonlinear resistors and higher Q devices acting more like nonlinear capacitors. With a fixed source impedance, the device can be tuned to match the circuit, rather than the more conventional approach of designing a circuit around a given diode. Adjusting the device area scales the impedance level and adjusting the bias changes the ratio of the input real and reactive impedance. The combination inside an optimization loop can adjust the nonlinear input impedance

to match the source impedance. The harmonic load will also effect the input impedance and efficiency of the multiplier. The device harmonic output impedance will conjugate match the harmonic load. We need to search the output impedance plane to find the embedding impedance that produces the highest efficiency for a given input power. This search becomes the inner loop in the simulation. The outer loop is the available local oscillator power. The input parameters of the simulation are the epitaxial layer doping and length, the frequency, the device breakdown voltage, the peak velocity, the mobility and a local oscillator power step. The simulation loops through the code increasing the available power until the maximum voltage across the semiconductor depletion layer becomes larger than the breakdown voltage. The outputs of the simulation are the pump frequency input impedance as a check on the convergence of the simulation, the output power and efficiency, the optimal output embedding impedance, the device area and bias and useful internal parameters such as the peak electric field in the bulk and the peak depletion layer voltage. The simulation can use the temperature dependent velocity characteristics described in the last section to investigate the temperature characteristics of multipliers.

IV Temperature, Doping and Frequency Dependent Performance

Before we investigate temperature dependent multiplier operation, we first consider constant temperature characteristics. The first example is a multiplier operating with an input frequency of 50 GHz with a peak velocity of $1.6 \times 10^7 \mathrm{cm/sec}$ corresponding to an operating temperature of 300 K and an input impedance of 50 + j100. Fig. 4 shows the efficiency vs. available input power and Fig. 5 shows the output power for a range of epitaxial layer dopings. These two figures show many of the design tradeoffs in multipliers. For this 50 GHz room temperature operation, the $3 \times 10^{16}/\mathrm{cm}^2$ device is operating in velocity saturation . The multiplier efficiency decreases over the entire operating range. Increasing the doping to $4 \times 10^{16}/\mathrm{cm}^2$ reduces the saturation effects. The $6 \times 10^{16}/\mathrm{cm}^2$ device is showing little saturation and is operating with a nearly constant efficiency over it's entire operating range. The corresponding power plot shows the effect of the breakdown voltage on the power output. The lower doped structure have a larger breakdown voltage and can support a larger input power before breakdown, nearly 300 mW. However, the larger input power doesn't produce a larger output power due

to to effiency reduction caused by velocity saturation. The $4 \times 10^{16}/\mathrm{cm}^2$ device is operating near the onset of saturation. It's efficiency is decreasing at higher drive levels, causing the output power to nearly saturate at higher drive levels. The higher doping level reduces the breakdown voltage and the corresponding input power, but this structure produces the most power of the 3 cases in this figure. Finally, the $6 \times 10^{16}/\mathrm{cm}^2$ device, with the best efficiency of the group, is limited by it's smaller breakdown voltage to an input power of 100 mW. It's peak output power is similar to the lowest doped case. Further increasing the doping will reduce the breakdown voltage and allow the device to operate without saturation effects. This will have only a small effect on the efficiency but will further reduce the output power due to the reduced breakdown voltage and input power.

Next lets consider the effect of varying the temperature. Consider a multiplier doped at $3 \times 10^{16}/\mathrm{cm}^3$operating with an input frequency of 50 GHz and a source impedance of 50+j100. The operating temperature varies between 100 and 400 K with a variation in the saturated velocity, given by Eqn. 2, ranging between 1.4 and 2.5×10^7 cm/sec. This design showed strong saturation effects in Figs. 4 and 5. The resulting temperture dependent efficiency is shown in Fig. 6. This device shows a strong temperature dependent performance. At 300 and 400K the multiplier is strongly saturated, with efficiencies that are monotonically dropping with pump power. Decreasing the temperature from 300 to 200K, with a corresponding increase in the saturated velcoity from 1.6 to $1.9 \times 10^7 \mathrm{cm/sec}$ improves the efficiency at the peak pump power point from 10 to 20%. An additional decrease in the temperature to 100K increases the velocity enough to eliminate most of the saturation effects. The efficiency is nearly constant with pump power. These efficiency variations will have a strong effect on the available power from the multiplier. The temperature dependent output power is shown in Fig. 7. The 100K device can produce more than 4 times the power of the room temperature structure.

This improvement in power and efficiency at lower temperatures occurs because the higher saturated velocities at lower temperatures can support more current. An example of a structure that does not have much improvement at reduced temperatures is shown in Fig. 8. This is the optimal room temperature device from Fig. 4. This device has a large enough doping to support the cuurent at room temperature. Lowering the temperature will increase the

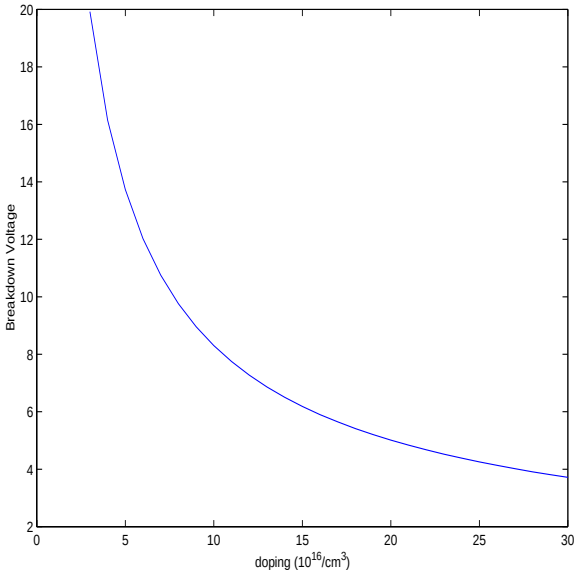

Figure 3: GaAs Junction Breakdown Voltage vs. Doping

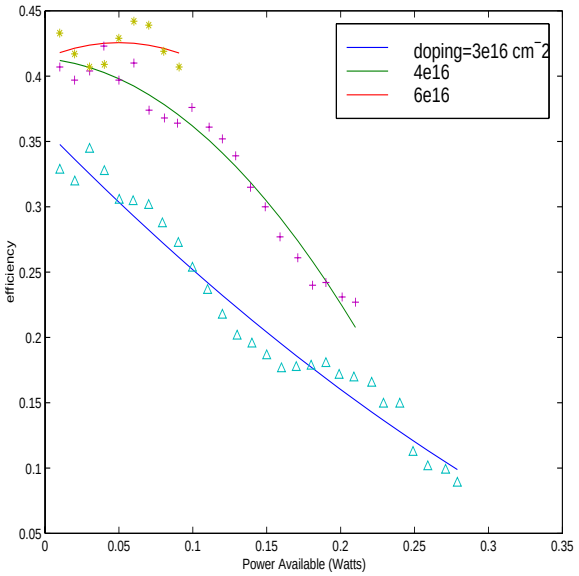

Figure 4: Doping Dependent Efficiency for F=50 GHz, T=300, Z_{in}=50+j100

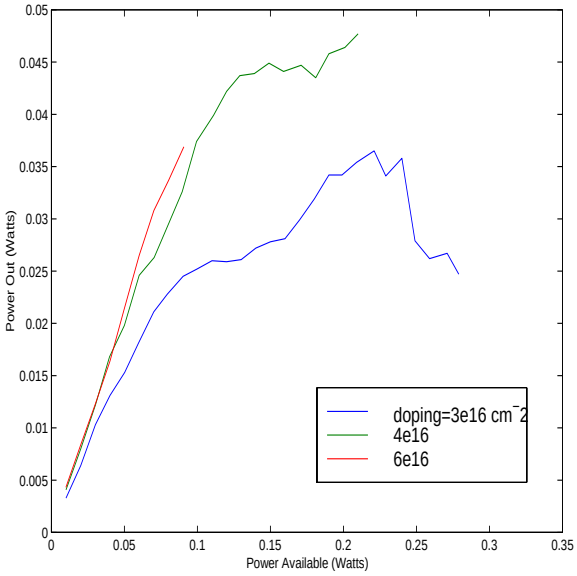

Figure 5: Doping Dependent Power for F=50 GHz, T=300, Z_{in}=50+j100

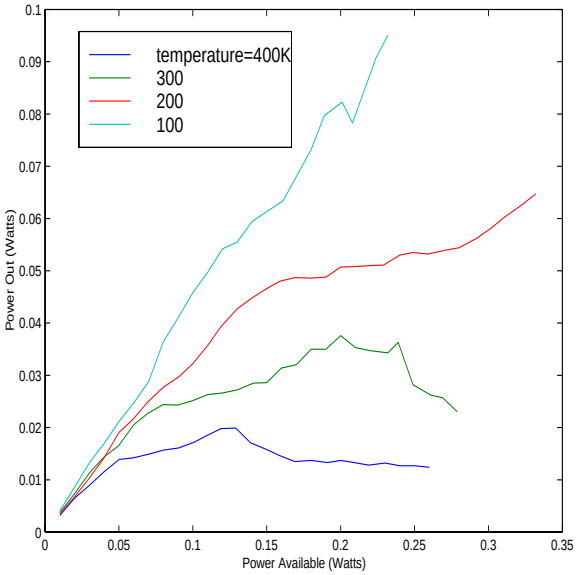

Figure 6: Temperature Dependent Efficiency for F=50 GHz,$N_d = 3 \times 10^{16}/cm^3$, Z_{in}=50+j100

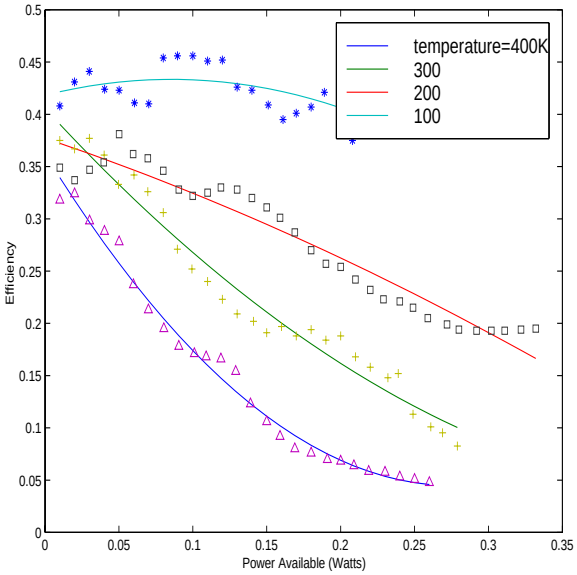

Figure 7: Temperature Dependent Power for F=50 GHz,$N_d = 3 \times 10^{16}/cm^3$, Z_{in}=50+j100

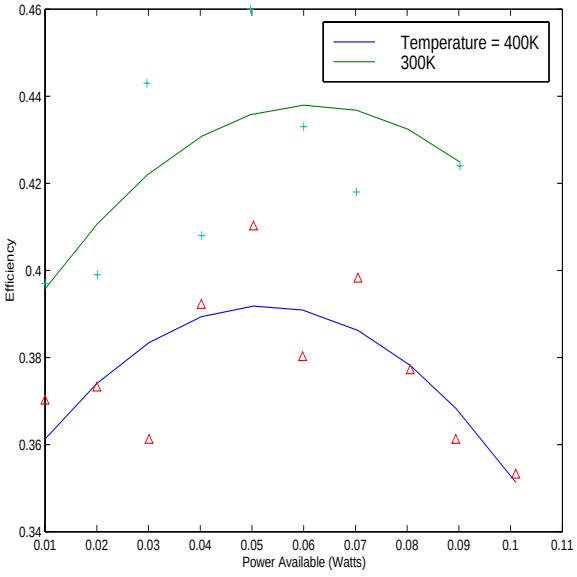

Figure 8: Temperature Dependent Power for F=50 GHz,$N_d = 6 \times 10^{16}/cm^3$, Z_{in}=50+j100

saturated velocity, but the additional velocity is not utilized by the device, so there is only a modest improvement in the efficiency at the lower temperature. This device is limited by it's breakdown voltage, and the higher current available at lower temperatures gives only a small performance improvement.

Similar temperature and doping dependent calculations were carried out for input frequencies of 100 and 200 GHz. The resulting power vs. frequency at room temperature and 100 K is plotted in Fig. **??**. The figure shows that a properly designed low temperature device can produce approximately twice the power of a room temperature one.

V Summary

This paper has discussed the results of a frequency dependent investigation of multiplier performance. The results show that the temperature dependent peak velocity plays an important role in performance. The optimal design depends on the tradeoff between current saturation and breakdown and the design for peak power can be different than the peak efficiency design. The power and efficiency also depend on the temperature. Reducing the temperature increases the peak velocity and can change the mode of operation. Devices designed for room temperature operation can have modest improvement with reduced temperature. A device that is current saturated for room temperature operation can greatly improve it's performance with cooling. The difference in output power for a well designed room temperature device and a corresponding low temperature design can be as much as a factor of 2.

References

[1] Fawcett,W.,Boardman,A.D. and Swain,S.,"Monte Carlo Determination of Electron Transport Properties in Gallium Arsenide," J.Phys.Chem. Solids vol. 31, no. 9,pp. 1963-1990,September, 1970.

[2] Ruch,J.G. and Fawcett,W., "Temperature Dependent of the Transport Properties of Gallium Arsenide Determined by a Monte Carlo Method," Journal of applied Physics, vol. 41, no. 9, pp. 3843-3849, August, 1970.

[3] Bauhahn,P.E.,"Properties of Semiconductor Materials and Microwave Transit Time Devices," Ph.D. Thesis, The University of Michigan, 1977.

[4] Kollberg,E., Tolmunen,M., Frerking,M. and East,J., "Current Saturation in Submillimeter Wave Varactors," IEEE Trans. on Microwave Theory and Techniques, vol. 40, no. 5, May,1992, pp. 831-838.

[5] East,J., Kollberg,E. and Frerking,M., "Performance Limitations of Varactor Multipliers," Fourth International Conference on Space Terahertz Technology,March, 1993, pp. 98-114.

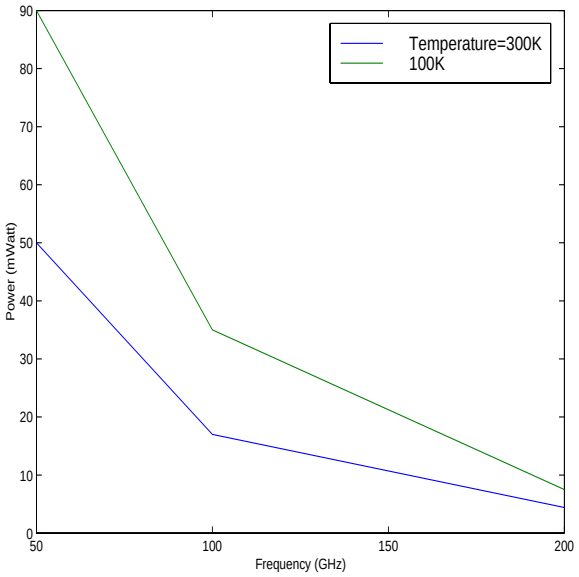

Figure 9: Summary of Frequency Dependent Power vs. Frequency and Temperature

Part of the research described in this paper was carried out at the Jet Propulsion Laboratory, California Institute of Technology, under a contract with the National Aeronautics and Space Administration.

PERFORMANCE OF AN ALL-NBN QUASI-OPTICAL SIS MIXER FOR THE TERAHERTZ BAND

Yoshinori UZAWA, Zhen WANG, Akira KAWAKAMI,
Kansai Advanced Research Center, Communications Research Laboratory,
588-2 Iwaoka, Iwaoka-cho, Nishi-Ku,
Kobe, 651-2492 JAPAN
e-mail: uzawa@crl.go.jp

and Shigehito MIKI
Graduate School of Science and Technology, Kobe University

Abstract

We designed an all-NbN SIS mixer with low-noise and wideband operation at terahertz frequencies. The mixer consists of a self-compensated NbN/AlN/NbN tunnel junction and an epitaxially grown NbN/MgO/NbN microstripline. The junction as a distributed element is 0.8 μm wide and 2.4 μm long, and its current density is 50 kA/cm^2. The microstripline consists of a 200-nm-thick NbN ground plane, a 180-nm-thick MgO insulator, and a 350-nm-thick NbN wiring layer. The frequency dependence of the receiver noise temperature was investigated by using an optically pumped far-infrared laser and backward-wave oscillators as local oscillators at frequencies from 760 to 980 GHz. The mixer showed flat noise characteristics at frequencies from 780 to 960 GHz, as predicted in our design process. The lowest receiver noise temperature was about 550 K at 909 GHz, including a 9-μm-thick Mylar beam splitter loss and other optical losses. Some large optical losses may be possible in the quasi-optical receiver configuration based on the standard method of input-loss estimation.

1. Introduction

Terahertz mixers with quantum limited noise sensitivity and wideband characteristics are needed in radio-astronomy projects, such as the Atacama Large Millimeter Array (ALMA), the Far-Infrared Space Telescope (FIRST), and so on. For the frequency bands above the gap frequency of Nb (about 700 GHz), for example, the ALMA specifies SSB noise temperatures of about 450 K for the band 10 (787-950 GHz, the relative bandwidth is 18.8%), and the FIRST needs low-noise SIS mixers for much higher frequency bands of up to 1.25 THz. Recently, SIS mixers consisting of conventional Nb/AlOx/Nb and Nb/AlN/NbTiN tunnel junctions and NbTiN-based tuning circuits have been developed and tested to enable low-noise operation at terahertz frequencies [1, 2]. However, these mixers had low-noise operation with DSB noise temperatures of 205 K at 798 GHz and 565 K at 970 GHz, their RF bandwidths were narrow due to the use of low-current density junctions (≅10 kA/cm^2). It was also found that heat trapping at the Nb/NbTiN interface degraded the junction properties, increasing the subgap leakage current and suppressing the gap voltage, which would degrade the noise performance [3].

We are currently developing SIS mixers based on NbN that have a high gap frequency of up to 1.4 THz. In principle, all-NbN SIS mixers should perform well below the gap frequency, just like all-Nb SIS mixers do. To develop wideband and low-noise mixers by designing all-NbN SIS mixers that can operate at terahertz frequencies, very high-current-density SIS junctions and

high-quality NbN films are needed to reduce the $\omega C_J R_N$ products and enable extremely low-loss transmission lines. For example, to cover the ALMA band 10 for below –10-dB matching, the maximum allowable value for $\omega C_J R_N$ products should be about 7 [4]. Assuming that the junction specific capacitance is 120 fF/μm^2, the required current density of the NbN tunnel junction should be about 40 kA/cm^2. Usually, the polycrystalline structure of NbN films is a problem because this structure has a large surface resistance on conventional insulators, such as SiO. This results in a large RF loss, which greatly degrades the mixer noise performance [5].

Another problem is that the relatively long penetration depth of NbN (even if NbN is a single crystal of, let's say 200 nm) makes the circuit design difficult because the large slow-wave factor shortens the circuits at terahertz frequencies. It was found that a conventional integrated tuning circuit did not work as effectively as it was designed to work because the spreading inductances introduced by the embedding of small junctions in the wide microstrip lengthened the tuning section [6]. As a result, there have been few reports of all-NbN SIS mixers with wideband and low-noise operation at teraherz frequencies.

Earlier, we developed NbN/AlN/NbN tunnel junctions epitaxially grown on MgO substrates that have current densities as high as 127 kA/cm^2 [7]. These tunnel junctions showed excellent noise performance at submillimeter-wave frequencies [8, 9]. Recently, we also developed NbN/MgO/NbN microstriplines epitaxially grown on a single-crystal MgO substrate that can be used in extremely low-loss tuning circuits [10]. In this report, we describe the design, fabrication, and testing of a quasi-optical SIS mixer with this NbN/MgO/NbN microstripline and a self-compensated NbN/AlN/NbN tunnel junction. This mixer dose not have a conventional tuning structure consisting of a microstrip inductor and a SIS junction as a lumped element [11].

2. Mixer Design

Our mixer uses an MgO hyperhemispherical lens, 3 mm in radius, with an antireflection (AR) cap. The AR cap is thermoformed Kapton JP polyimide film with a thickness of 50 μm, which corresponds to the thickness of a quarter-wavelength at around 800 GHz [5]. An optical micrograph of our mixer chip is shown in Fig. 1. A rectangular NbN/AlN/NbN junction and an NbN wiring on an MgO insulator were integrated with an NbN log-periodic antenna on a 0.3-mm-thick single-crystal MgO substrate. Because the NbN/MgO/NbN microstripline and the high-current-density NbN/AlN/NbN tunnel junction were grown epitaxially [12], we assumed in the mixer design process that the upper and lower NbN films had the same gap frequency of 1.27 THz and a normal state conductivity of 1.5 x 10^6 Ω^{-1}m^{-1}. These values were obtained from our measurements.

We designed the tuning circuit so that it had a center frequency of 1 THz. In this frequency region, NbN-based μm-sized SIS junctions must be considered as distributed elements, not lumped elements, because the slow-wave factor in these junctions is much larger than that in Nb junctions [11, 13]. This means that an NbN junction must be treated as a microstrip transmission line with a quasi-particle tunneling loss. It is well known that an imaginary part of the impedance in transmission lines becomes zero at a length of $n \times \lambda/4$, where n is an integer. For distributed SIS junctions, this means that the junction capacitance is tuned out, and the input impedance becomes the only real component. The impedance must be the largest at the $\lambda/2$ length for an open-ended junction. We calculated the size of the junction, including the NbN/MgO/NbN microstrip overhanging layer, as shown in Fig. 2. For the calculations, the distributed series impedance per unit length, *Z*, and the distributed shunt admittance per unit

length, *Y*, must be known. For a given distributed-SIS-junction geometry, *Z* and *Y* are defined as

$$Z = j\omega\mu_0 \frac{s}{W_J} + \frac{1}{W_J}\left(Z_{SU} + Z_{SL}\right) + j\omega\mu_0 \frac{d}{W_S - W_J} + \frac{1}{W_S - W_J}\left(Z_{SU} + Z_{SL}\right), \quad (1)$$

$$Y = \frac{W_J}{R_{rf}} + j\omega C_S W_J + j\omega\varepsilon_r\varepsilon_0 \frac{W_S - W_J}{d}, \quad (2)$$

where Z_{SU} and Z_{SL} are, respectively, the surface impedance of the upper and lower electrodes calculated from the Mattis-Bardeen theory of the anomalous skin effect [11], W_J and W_S are the widths of the NbN/AlN/NbN junction and the NbN/MgO/NbN microstripline, respectively, and R_{rf} represents the specific resistance of the quasi-particle loss due to the tunneling current through the insulator. The specific junction capacitance in pF/μm^2, C_S, was calculated based on the following equation obtained from the measurements of our high-current-density NbN/AlN/NbN tunnel junction:

$$\log C_S = 0.16 \log J_C - 1.15, \quad (3)$$

where J_C is the current density in kA/cm^2. The tunneling barrier thickness, *s*, was assumed to be 1 nm based on the observation of the high-current-density junction by using a transmission electron microscope (TEM) [12]. We used the relative dielectric constant, ε_r, of 9.6 for MgO, and the thickness was expressed as *d*.

The input impedance of this lossy transmission line was calculated using the parameters described in Table I. We decided that the width of the junction should be small to prevent transverse mode propagation. Figure 2 shows the real and imaginary parts of the input impedance. It can be seen that the junction capacitance is self-compensated at around 1 THz, i.e., the imaginary part becomes zero, while the real part becomes the maximum value of about 11 Ω. This relatively large resistance can be easily matched to the source impedance of the log-periodic antenna on the MgO lens (about 80 Ω) by using a λ/4 impedance transformer. The 13.5-μm length of the NbN/MgO/NbN microstripline enables good matching of below –10 dB at frequencies ranging from 900 to 1080 GHz, as shown in Fig. 3. Theoretically, a relative bandwidth of 18% can be achieved at terahertz frequencies.

3. Results and Discussion

A. Fabrication and I-V Measurements

The mixer chips were prepared by the fabrication process described in [14]. First, NbN/AlN/NbN trilayers were deposited in situ on an ambient-temperature MgO substrate by rf-magnetron sputtering in a load-locked sputtering system. One side of the antennas was formed by conventional photolithography and reactive ion etching (RIE). Then, rectangular junctions were defined using photolithography and RIE. After the MgO films were deposited by rf- and dc-magnetron sputtering to electrically insulate the base electrodes and the contact-wiring layer [10], an NbN film was deposited and patterned on the other side of the antennas and the contact-wiring layer to form a tuning circuit and to make contact with the junction. The actual thicknesses of the lower NbN, the lower MgO, and upper NbN were 200, 180, and 350 nm, respectively. The measured width was about 1.4 μm. The Josephson critical current of the junction was 950 μA at 4.2 K, and the junction was 0.8 μm wide and 2.4 μm long. This resulted in a current density of about 50 kA/cm^2. In the liquid helium measurement, we observed a slightly lower gap voltage of about 5 mV with backbending characteristics because of the large current through the junction. The normal state resistance was about 4 Ω.

To roughly define the tuning frequency, we also observed resonance-induced Josephson steps, as shown in Fig. 4. A dc current step could be seen at a voltage of about 1.9 mV, which corresponds to 920 GHz according to the Josephson frequency relationship, $f_J = 2eV_0/h$. This result indicates that the tuning frequency was slightly lower than the design frequency of 1 THz, because the fabricated junction was a little bit longer and the overhanging layer was a little bit narrower than the design junction and layer.

We analyzed the properties of the tuning circuit at terahertz frequencies by monitoring the dynamic resistance of the photon-assisted tunneling (PAT) steps induced on the *I-V* curves by a backward-wave oscillator (BWO). Figure 5 shows the pumped *I-V* curves at the RF irradiation of 900, 990, and 1030 GHz. As can be seen, there were changes in the dynamic resistance of the *I-V* curves at the PAT steps indicating that the capacitance of the junction was tuned out toward the lower frequency of 900 GHz.

B. Noise Measurements

The heterodyne receiver noise measurements were cunducted using the standard *Y*-factor method for room-temperature (295 K) and liquid-nitrogen-cooled (77 K) loads used as signals. The receiver set-up was basically the same as the one described in [5], except that an isolator was used instead of the 180-degree hybrid coupler. Local-oscillator (LO) power was introduced into the signal path through 9-μm and 16-μm-thick Mylar beam splitters. The signal and LO entered the dewar through a 0.5-mm-thick Teflon vacuum window, and the Zitex infrared filters cooled to 77 and 4.2 K. No corrections were made for the losses in front of the receiver.

Figure 6 shows the *I-V* characteristics of the receiver at 909 GHz with and without the LO power. The LO source was the BWO, and the 9-μm-thick Mylar beam splitter was used. As can be seen there was a suppression of the gap voltage in the pumped *I-V* curve. In addition, the width of the voltage measured at the PAT step, which was 3.25 mV, was narrower than the estimated width of 3.76 mV. These results show that the SIS junction suffered from the heating effects of the applied DC and RF power, because NbN has a low thermal conductivity. This local overheating increased the sub-gap leakage current of the junction and the loss in the NbN electrodes, which would degrade the noise performance. To reduce this heating effect, a normal metal, such as Al, should be deposited on the top electrode [15]. Figure 6 also shows the receiver IF output in response to the hot and cold loads as a function of the bias voltage. At voltages above the half-gap voltage of about 2.7 mV, the maximum *Y*-factor was about 1.25, which corresponded to the double-sideband (DSB) receiver noise temperature of 800 K. Below the half-gap voltage, the *Y*-factor was 1.35 (550 K) at 2.2 mV. However, the IF outputs around the first-Shapiro-step voltage of 1.88 mV were not stable because of the high dynamic resistance of the pumped *I-V* curve, as mentioned above. To obtain a better performance, a stronger magnetic field should be applied to the junction to suppress unwanted noise resulting from the Josephson effect.

The frequency dependence of the receiver noise temperature was investigated at frequencies ranging from 760 to 980 GHz. We used two BWOs for the 800-980 GHz measurements and an optically pumped CH_2F_2 far-infrared laser for the 760- and 783-GHz measurements. Figure 7 shows the receiver noise temperature as a function of the LO frequency. The 16-μm-thick Mylar beam splitter was used at all the measured frequencies, and a bias voltage was applied to the junction above the half gap to obtain stable operation. Wideband and flat-noise characteristics were observed at frequencies ranging from 780 to 960 GHz. Although the measured center

frequency of about 870 GHz was lower than the design frequency, the characteristics of the tuning bandwidth were almost consistent with the design ones, which means that the NbN films fabricated for the tuning circuits had no significant losses at terahertz frequencies. The fact that the center frequency was slightly lower than the observed resonance frequency of 920 GHz may be attributed to the increase in the effective penetration depth of the NbN due to the increase in the effective temperature in the NbN films by the DC and LO power.

At the higher and lower ends of the tuning frequencies, we could apply a bias voltage below the half-gap easier because the dynamic resistance of the pumped *I-V* curve became slightly smaller than that around the center frequency. Figure 8 shows the heterodyne response at 809 GHz when the 16-μm thick Mylar beam splitter was used. The maximum *Y*-factors below and above the half-gap voltage were, respectively, 1.33 (584 K) and 1.22 (914 K), including the Mylar-beam-splitter loss and other optical losses. Using the intersecting lines technique [16, 17], we estimated the input loss around this frequency from the IF responses biased below the half-gap voltage. A large input-noise contribution of about 350 K was derived that included the loss from the 16-μm-thick Mylar beam splitter. The most likely reasons for the high input noise are the following.

1) In the fabricated log-periodic antenna structure, at terahertz frequencies, the size of the teeth in the active region on the base (ground) side of the antenna was approximately 15% smaller than that on the other (wiring) side, due to shrinking by overetching. This unsymmetrical antenna structure results in an impedance mismatch and a poor beam pattern.
2) The loss of the thick MgO lens reduces the coupling efficiency at terahertz frequencies.

Using a high-efficiency input-coupling configuration, such as a waveguide structure, can improve the performance. We believe that all of the improvements described here can reduce the noise temperatures. We also believe that self-compensated NbN/AlN/NbN junctions and NbN/MgO/NbN microstriplines are more capable of low-noise and wideband operation at terahertz frequencies of up to 1.4 THz than conventional mixers that use lumped elements.

4. Conclusion

We designed, fabricated and tested at terahertz frequencies an all-NbN SIS mixer that has no conventional tuning structure. We demonstrated that tuning circuit, which consisted of a self-compensated NbN/AlN/NbN tunnel junction and an NbN/MgO/NbN microstripline, had effective low-noise and wideband operation in the terahertz band. The mixer had a simple structure and was fabricated by using conventional photolithography. Our fabricated NbN device remained stable throughout more than ten repetitions of the thermal cycle. We believe that the all-NbN SIS mixers with these excellent characteristics can be effectively used in projects, such as the ALMA, FIRST, and so on.

Acknowledegments

We thank Prof. V. Yu. Belitsky of Chalmers Univ. of Tech. for helpful suggestions about the tuning circuit and valuable discussions of the results. We thank Prof. T. Noguchi of the Nobeyama Radio Observatory and Dr. J. Inatani of NASDA for their constructive comments on the results. This work was supported in part by the ALMA Joint Research Fund of the National Astronomical Observatory of Japan.

References

[1] J. Kawamura, J. Chen, D. Miller, J. Kooi, J. Zmuidzinas, B. Bumble, H. G. LeDuc, and J. A. Stern, *Appl. Phys. Lett.*, vol. 75, pp. 4013-4015, 1999.

[2] B. D. Jackson, N. N. Iosad, G. Le Lange, A. M. Baryshev, W. M. Laauwen, J.-R. Gao, and T. M. Klapwijk, Submitted to *IEEE Trans. Appl. Supercond.*, March 2001.

[3] B. Leone, B. D. Jackson, J.-R. Gao, and T. M. Klapwijk, *Appl. Phys. Lett.*, vol. 76, pp. 780-782, 2000.

[4] A. R. Kerr, *IEEE Trans. Microwave Theory Tech.*, vol. 43, pp. 2-13, 1995.

[5] Y. Uzawa, Z. Wang, and A. Kawakami, *Appl. Supercond.*, vol. 6, pp. 465-475, 1998.

[6] B. D. Jackson, G. de Lange, W. Laauwen, J. R. Gao, N. N. Iosad, and T. M. Klapwijk, in *Proceeding of the 11th International-Symposium on Space Terahertz Technology*, University of Michigan, Ann Arbor, MI, 1-3 May 2000 (unpublished).

[7] Z. Wang, H. Terai, A. Kawakami, and Y. Uzawa, *IEEE Trans. Appl. Supercond.*, vol. 9, pp. 3259-3262, 1999.

[8] Y. Uzawa, Z. Wang, and A. Kawakami, *Appl. Phys. Lett.*, vol. 69, pp. 2435-2437, 1996.

[9] Y. Uzawa, Z. Wang, and A. Kawakami, *Appl. Phys. Lett.*, vol. 73, pp. 680-682, 1998.

[10] A. Kawakami, Z. Wang, and S. Miki, Submitted to *IEEE Trans. Appl. Supercond*., March 2001.

[11] V. Yu. Belitsky and E. L. Kollberg, *J. Appl. Phys.*, vol. 80, pp. 4741-4748, 1996.

[12] Z. Wang, H. Terai, A. Kawakami, and Y. Uzawa, *Appl. Phys. Lett.*, vol. 75, pp. 701-703, 1999.

[13] V. Yu. Belitsky and E. L. Kollberg, in *Proceeding of the 7th International-Symposium on Space Terahertz Technology*, University of Virginia, Charlottesville, VA, 12-14 March 1996 (unpublished).

[14] Z. Wang, A. Kawakami, Y. Uzawa, and B. Komiyama, *Appl. Phys. Lett.*, vol. 64, pp. 2034-2036, 1994.

[15] P. Dieleman, T. M. Klapwijk, S. Kovtonyk, and H. van de Stadt, *Appl. Phys. Lett.*, Vol. 69, pp. 418-420, 1996.

[16] R. Blundell, R. E. Miller, and K. H. Gundlach, *Int. J. IR & MM Waves*, vol. 13, pp. 3-16, 1992.

[17] Q. Ke and M. J. Feldman, *IEEE Trans. Microwave Theory Tech.*, vol. 42, pp. 752-755, 1994.

Table. 1 Parameters used in the design.

NbN upper electrode thickness:		200 nm
NbN lower electrode thickness:		200 nm
MgO insulator thickness, *d*:		200 nm
NbN/AlN/NbN junction width, W_J:		0.7 μm
	length:	2.25 μm
	current density, J_C:	40 kA/cm^2
	$J_C R_N A$ products	350 kVμm^2/cm^2
NbN/MgO/NbN microstripline width, W_S:		1.7 μm

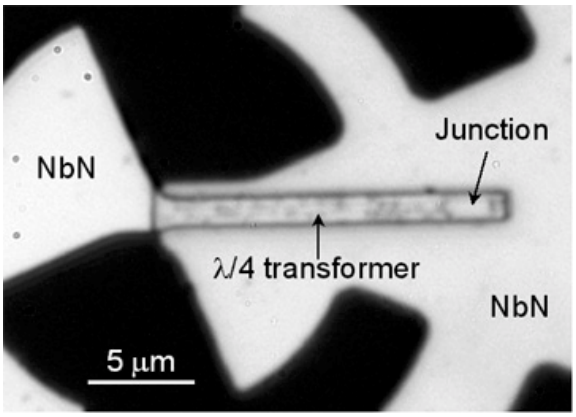

Fig. 1. Optical micrograph of the mixer. A rectangular NbN/AlN/NbN tunnel junction, as a distributed element, and a λ/4 NbN/MgO/NbN microstrip-impedance transformer were integrated with a self-complementary NbN log-periodic antenna.

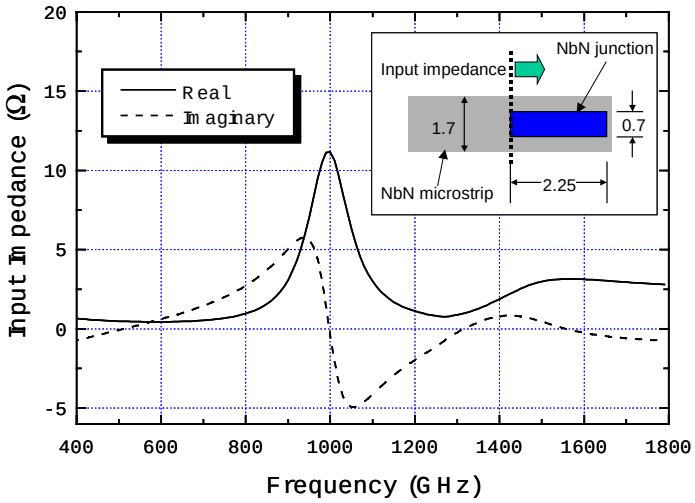

Fig. 2. Input impedance of the self-compensated junction tuning circuit. The junction capacitance was tuned out at the λ/2-wavelength frequency of 1 THz

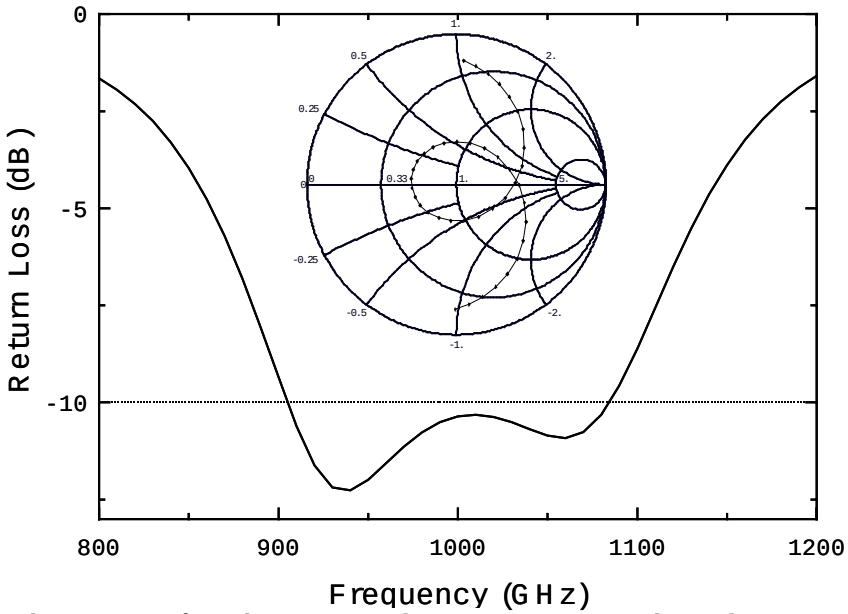

Fig. 3. Return-loss characteristics from the antenna to the tuning circuit. Impedance chart was normalized to the antenna source impedance of 80 Ω.

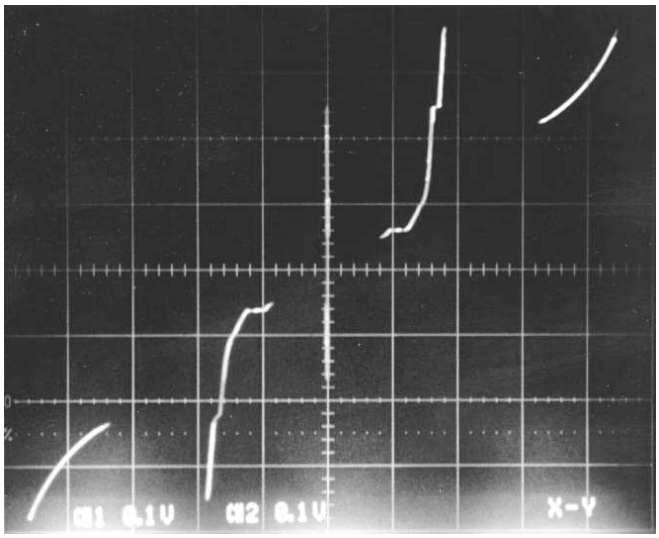

Fig. 4 Observed resonance-induced Josephson steps in the *I-V* curve. The horizontal scale is 1 mV per division, and the vertical scale is 0.1 mA per division.

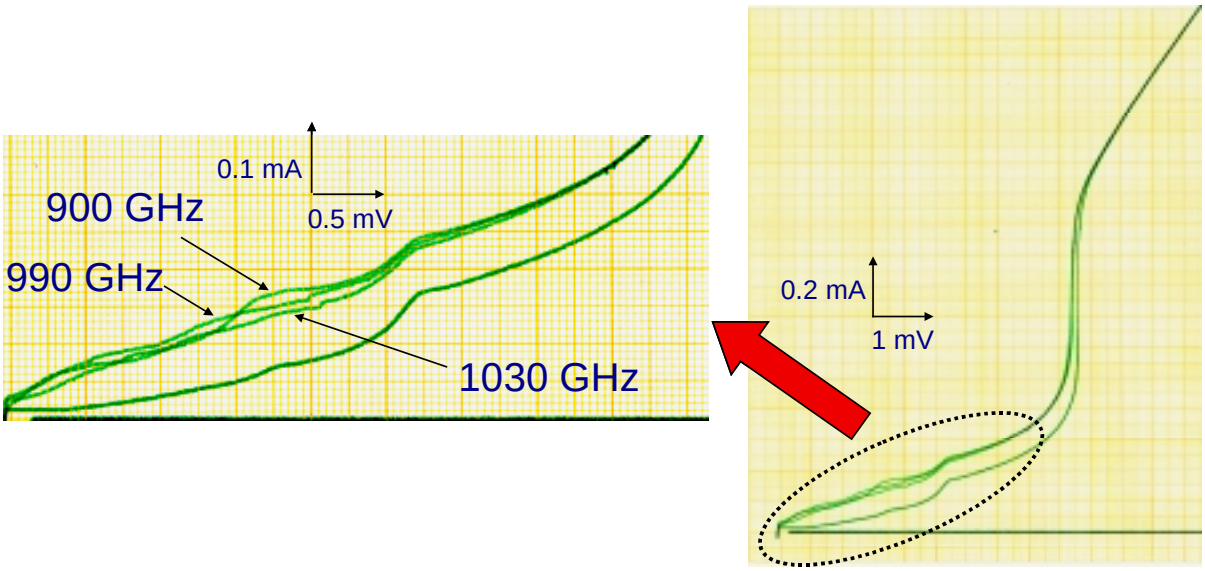

Fig. 5 Pumped I-V curves at the RF irradiation of 900, 990, 1030 GHz. Note that the changes in the dynamic resistance of the I-V curve at the PAT steps are visible.

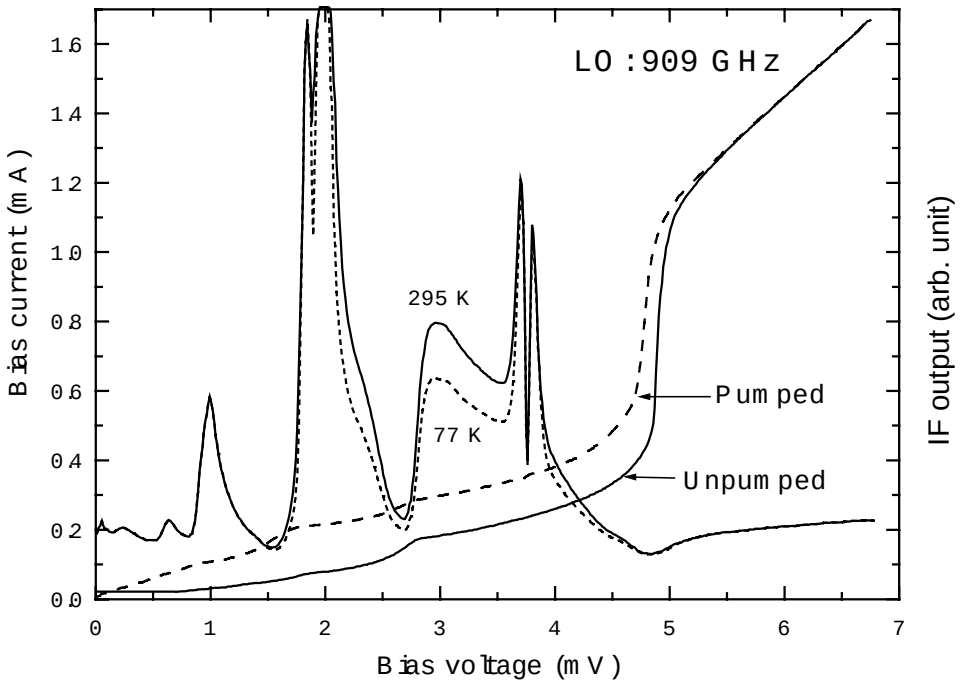

Fig. 6. Heterodyne response of the receiver at 909 GHz. Shown are the I-V characteristics for the self-compensated NbN/AlN/NbN tunnel junctions with and without the LO power. Also shown is the IF power as a function of the bias voltage for hot (295 K) and cold (77 K) loads.

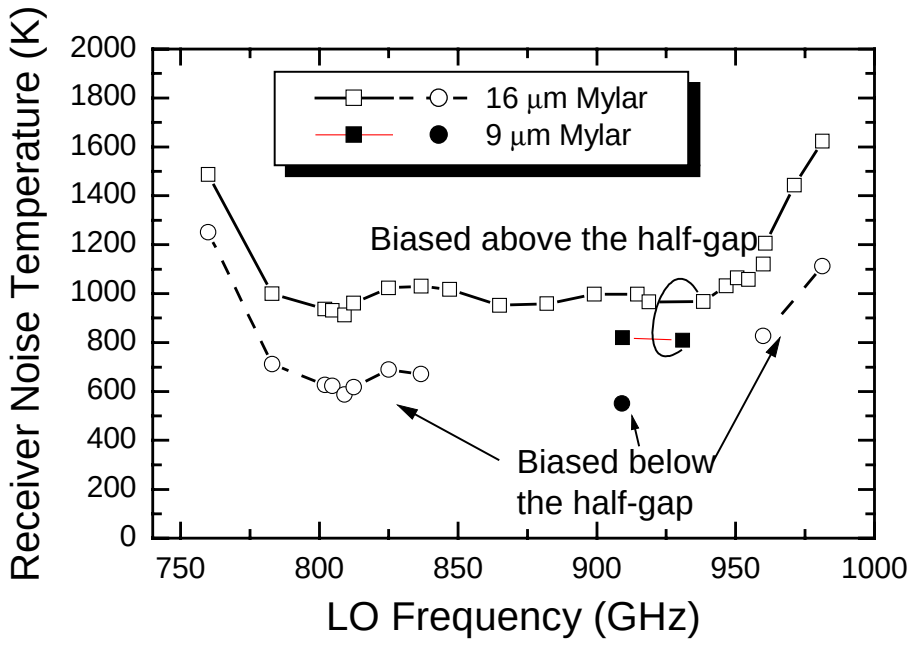

Fig. 7. DSB-receiver noise temperatures as a function of the LO frequency.

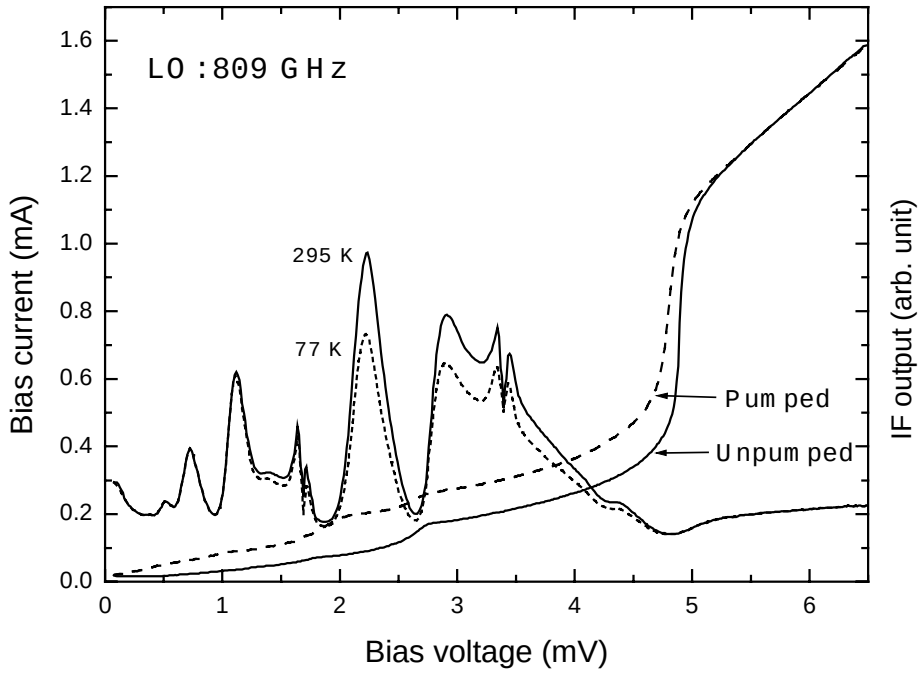

Fig. 8. Heterodyne response of the receiver at 809 GHz. Shown are the I-V characteristics for the self-compensated NbN/AlN/NbN tunnel junctions with and without the LO power. Also shown is the IF power as a function of the bias voltage for hot (295 K) and cold (77 K) loads.

A Low-Noise Double-Dipole Antenna SIS Mixer at 1 THz

S. V. Shitov
Institute of Radio Engineering and Electronics (IREE), Russian Academy of Sciences
101999 Moscow, Russia

B. D. Jackson, A. M. Baryshev
Space Research Organization of the Netherlands (SRON)
P.O.Box 800, 9700 AV Groningen, the Netherlands

N. N. Iosad, J.-R. Gao and T. M. Klapwijk
Department of Applied Physics, Delft University of Technology (DIMES)
2628 CJ, Delft, the Netherlands

Abstract

A quasi-optical mixer employing a Nb/Al/AlO_x/Nb twin-SIS junction with a NbTiN/SiO_2/Al microstrip coupling circuit is tested at 800-1000 GHz. The mixer design is developed as an option for *HIFI* frequency bands 3 and 4. The double-dipole antenna is made from NbTiN/Al; a Nb film is used for the back reflector. The mixer design is optimized for the IF band of 4-8 GHz. The receiver noise temperature $T_{RX} = 250$ K (DSB) is measured at 935 GHz for the bath temperature 2 K at IF=1.5 GHz; T_{RX} remains below 350 K within the frequency range 850-1000 GHz. The double-dipole antenna beam pattern demonstrated good symmetry with sidelobes below –16 dB.

Introduction

Low-noise THz-band heterodyne receivers are needed to realize the full potential of airborne and space-based telescopes currently being developed for sub-millimeter spectral astronomy, e. g. for *HIFI* [1]. To consider the possibility of designing an effective SIS mixer at 1 THz, it is worth to have a brief look at the most critical parameters of SIS mixers.

The Nb/Al/AlO_x/Nb SIS mixers are known as the quantum (photon) noise limited heterodyne down-converters [2], which are tested within frequency range 30-1500 GHz and shown to yield receiver noise temperatures as low as (2-3)*hf/k_B below 680 GHz, the gap frequency of Nb [3], [4]. Theoretically, the frequency range of all-Nb SIS mixers as quantum limited detectors can be extended up to twice the gap frequency, i. e. up to about 1300 GHz [5]. However, a single junction SIS mixer can not cover the entire band because of its high specific capacitance, C, yielding the Q-factor of the circuit of order of 10 at 1 THz. The high Q-factor leads to at least two distinctive problems: a relatively narrow instantaneous bandwidth and increased influence of loss. The real part of the high frequency impedance of a superconducting film [6] is responsible for losses, which are growing as the square of the rf current density in the tuning circuit, i. e. proportional to

Q^2. The Q-factor can, theoretically, be reduced with increasing the junction current density, J_c. However, it is hard to do practically due to degradation of the IV-curve at $J_c > 10$-15 kA [7]. There is, however, a possibility to reduce the *rf* losses employing smaller (sub-micron area) junctions. Nevertheless, it is clear that quantum-limited SIS mixers are hard to realize for a frequency range where losses in the tuning circuit are essential. Unfortunately, the *rf* circuits from Nb become lossy above 680 GHz that is twice lower than the possible operational range of a Nb-based SIS junction. That is why, along with the efforts on high current density and sub-micron patterning of SIS junctions, the development of low-loss tuning circuits, in both electrodynamics and materials [8]-[12], is of great importance for realization of a THz-band quantum-limited SIS mixer.

The capacitance of the *rf* tuning circuit can contribute to the problem of matching the IF port of the mixer to a standard 50 Ω output transmission line due to high dynamic resistance of the SIS junction (up to about 1 kΩ). To reduce this effect, which is more pronounced at higher IF and can also lead to a high Q-value, the capacitance of all tuning and coupling circuits has to be minimized along with use of a special IF matching circuit.

Two main solutions are available for a *rf* feed of a SIS mixer: the waveguide and the open structure. All problems mentioned above are common for both types of mixers. However, a few specific problems exist in production of precision mechanical components for waveguides: corrugated horn antenna, waveguide channel, backshort structure, chip channel, etc. Another critical steps in production of a waveguide mixer are precise dicing and polishing of the SIS chips along with their alignment in the mixer block. In contrast, the quasioptical mixers can be fabricated on relatively large and easy-to-handle substrates, which are a part of the optical system and dependent mostly on accuracy of the photolithography. However, the antenna beam pattern of a lens-antenna is dependent on quality of the microwave lens and the alignment accuracy of the chip [13], [14]. The theoretical level of the first order sidelobes is about –18 dB for most known integrated lens-antennas that is higher than for the corrugated horn antennas used for waveguide SIS mixers.

The double-slot and the double-dipole are two types of antennas widely used in SIS mixers [10], [15]-[18]. Both antennas have, theoretically, similar parameters of the beam if used as an integrated lens-antenna; they have also similar values of the feed-point impedance. In spite a bare slot-antenna operated near its second resonance has a bit higher sidelobes in the H-plane (5% or –13 dB) [17], the beam of the *lens-antenna* can be somewhat corrected by the microwave lens [13], [14]. The double-dipole antenna is used successfully for the integrated receiver [16]. The advantage of a slot-antenna is the shielding ground plane, which allows placing relatively complex circuits very close to the antenna. Unlike the dipole antenna, it is not possible however to return the backlobe using a reflector for the slot antenna. The double-dipole antenna usually has no capacitive coupling elements, so the total capacitance of the structure can be minimized that is important at high IF.

The challenge of the project was to demonstrate a quasioptical double-dipole antenna SIS mixer complying with *HIFI* requirements for the bands 3 and 4 [1].

General Approach

We have chosen the twin-junction SIS mixer with the anti-phase feed circuit [10] integrated with the double-dipole antenna, as shown in Figure 1; the numerical and experimental studies [10], [18] have demonstrated wider instantaneous bandwidth along with lower loss in comparison with the end-loaded tuning structure. The lower loss can be attributed to the lower *rf* current density at the input of the impedance transformer, that is a specific feature of the twin-SIS junction. In spite the all-NbTiN microstrip can, at least potentially, be a low-loss at 1 THz, the NbTiN/SiO_2/Al tuning circuit has been chosen for two reasons: (1) it minimizes effects of heat-trapping observed previously in Nb-based SIS junctions integrated with an all-NbTiN tuning circuit [19]; (2) the poor nucleation of NbTiN on top of the SiO_2 layer may reduce the effective gap frequency of a wiring layer [20]. Two identical mixers are placed at the distance of 500 μm in the center of a high-resistivity silicon chip of size 2 mm x 2 mm x 300 μm. These dimensions allow to accept a non-truncated 120-degree beam of a printed antenna. The second device can be used as a replacement. The diameter of a silicon elliptical lens was chosen to be 10 mm, that defines the alignment accuracy of the chip of about 10 μm. The IF coupling circuit has to operate at the dynamic resistance of the mixer R_d = 100 Ω (200 Ω per junction). The reflection loss has to be kept below –10 dB within the IF band of 4-8 GHz for R_d = 50-150 Ω.

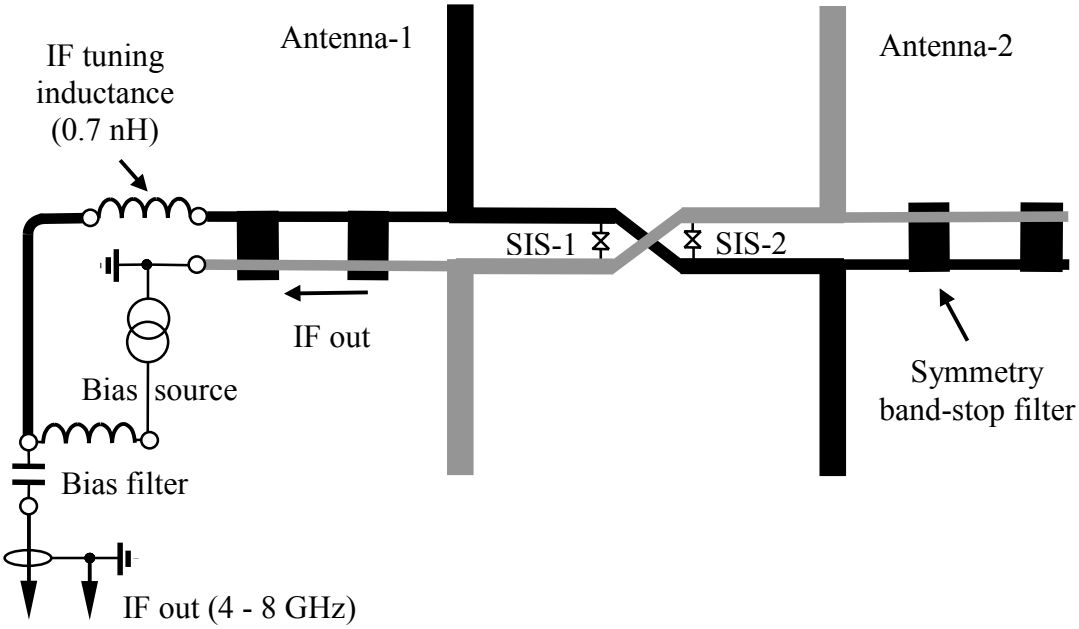

Fig. 1 Simplified electric scheme of quasi-optical planar SIS mixer with double-dipole antenna. The anti-phase mode of the twin-SIS junction (SIS-1 and SIS-2) is used in the mixer. Note that the junctions are connected in parallel for *dc* current, but in series at *rf*.

Details of Design

The devices are designed for two *HIFI* bands: 800-960 GHz and 960-1120 GHz. The optimization of the layout is made for each of two bands separately. The double-dipole antenna from Figure 2 is scaled from 500 GHz integrated receiver [16]. The size of the antenna is 34 μm x 40 μm and the width of its arms is 4 μm. It was initially considered that almost any metal (e. g. Nb) can be used for the back reflector at about 1 THz assuming low current density at the surface of the film. The quarter-wavelength-thick silicon chip (0.5 mm x 0.5 mm x 22 μm) one-side covered with 200 nm of Nb is placed onto the antenna as the back reflector. The calculated feed point impedance of the double-dipole antenna with the back reflector is shown in Figure 3. The anti-reflection coating of the microwave lens is optimized for 960 GHz using the 46-μm layer of Stycast™ 1264 epoxy ($\varepsilon \approx 2.9$).

Two 1-micron area SIS junctions Nb/Al/AlO_x/Nb are integrated with the antenna as shown in Figure 1 and Figure 2. The transmission line connecting the two junctions (placed 3.6 μm or 3 μm apart) and antennas is a microstrip line with narrow ground plane – just 1 μm wider than the strip which is 3 μm or 4 μm wide for the two bands respectively. Due to the nearly symmetric structure of the transmission line its strip and ground plane can be exchanged, so they are equally connected to the antennas picking up the anti-phase signals. The symmetry of the coupling structure provides also a virtual ground (a zero potential plane) at halfway between the junctions, that is equal to a tuning inductor connected in parallel to each junction at high frequency [10].

The calculated coupling at *rf* is presented in Figure 4 along with the best fit of the experimental FTS data. In these calculations the base electrode from NbTiN is assumed to be a perfect superconductor with London penetration depth 300 nm. The surface (sheet) resistance of 0.15 Ω was used for Al. Two band-stop filters are connected to the double-dipole antenna, as shown in Figure 1, but only one filter is connected to the IF channel providing the best symmetry of the structure at *rf*. This is assumed to be essential for symmetry of the beam of the array antenna. To achieve a combination of compactness and efficiency, the filters are designed with alteration of coplanar strips and microstrips. It is found that losses in the antenna band-stop filters are not negligible. The 3% absorption of the *rf* signal is estimated for the three-stage band-stop filter. This value can be actually made lower by adding extra

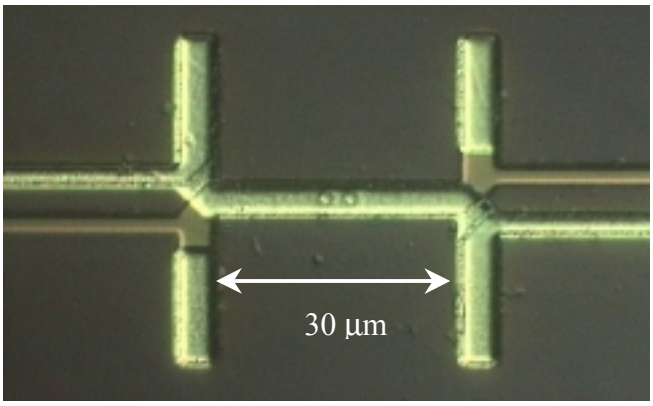

Fig. 2 Photograph of the double-dipole antenna SIS mixer fabricated on silicon substrate. The light metal strips are Al wiring; the darker ones are NbTiN strips at the bottom.

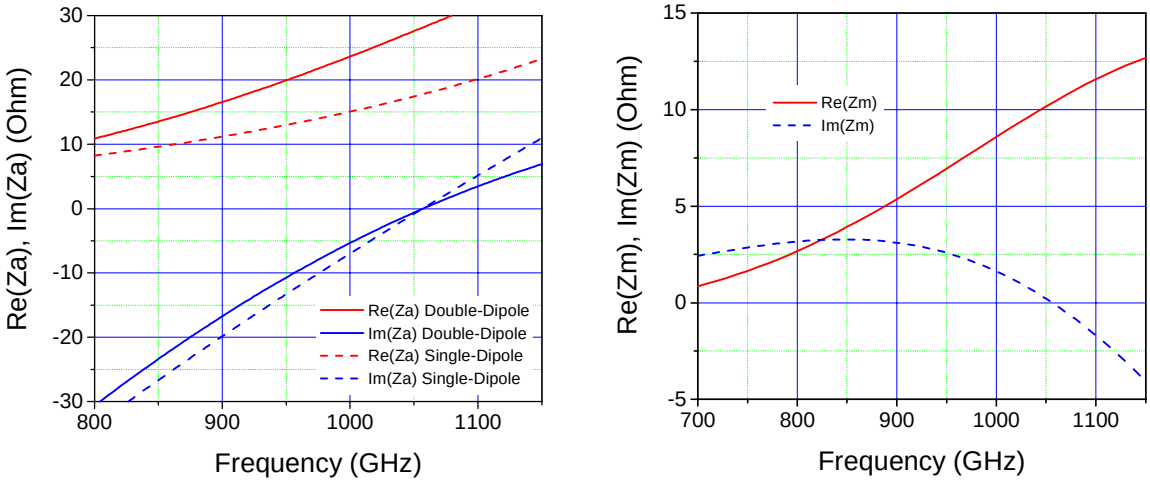

Fig. 3 Feed-point impedance calculated for the planar double-dipole antenna on semi-infinite silicon medium with a quarter-wave reflector (left graph); mutual impedance of the antenna array is plotted on the right graph.

sections, but the IF coupling would suffer from the growing capacitance of the filters. To obtain curves shown in Figure 4, both stray inductance of the SIS "tablet" and stray inductance of the microstrip, that is caused by the greater density of the *rf* current near the junction window, are included in the calculation. The stray inductance can be estimated roughly as 0.1-0.2 pH [21].

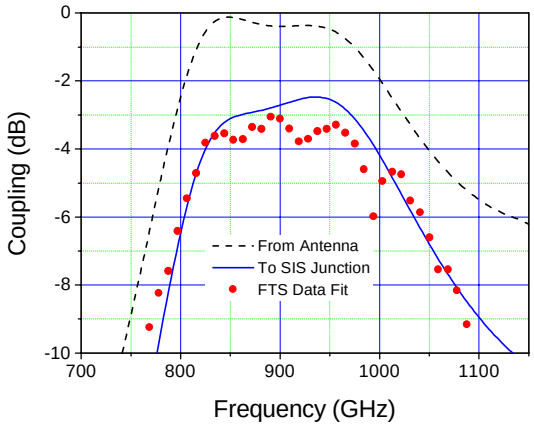

Fig. 4 Best fit of FTS data to the calculated coupling between the antenna and the mixing SIS junction. The drop of the antenna coupling (dashed) to the junction (solid) is caused by surface loss in the aluminum layer of the NbTiN/SiO_2/Al tuning stripline.

Experimental Results

The mixers are fabricated using a process similar to that described previously for waveguide devices with NbTiN and Al tuning circuits [20]. The standard optical lithography is used. The NbTiN ground plane 300 nm thick is deposited at ambient temperature. The SiO_2 dielectric layer is 250 nm thick. The Al wiring layer (400 nm) has conductivity at 4 K, $\sigma_{4K} \approx 2\times10^8\ \Omega^{-1}m^{-1}$, and is expected to be in the anomalous limit [22]. The Al wiring layer is protected against chemical attack by 200 nm of SiO_2. The typical IV-curve of the experimental twin-junction is presented in Figure 5. A few devices of band 4 (960-1120 GHz) were tested in the standard vacuum cryostat with optimized IR filters,

which optical losses are estimated as 1.2 dB at 1 THz [23]. The FTS data demonstrated a feature that looks very much like a high-frequency cut-off just above 1 THz. This feature was found to be almost independent on variation in the junction size and other important tuning parameters. The noise temperature of about

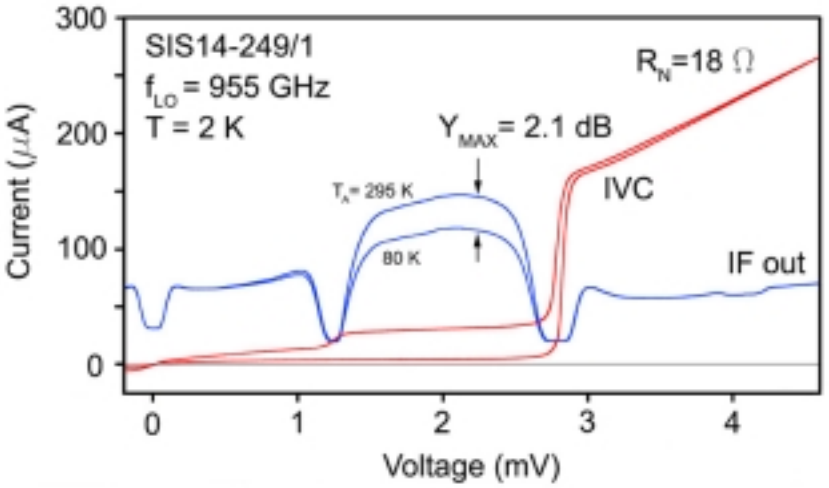

Fig. 5 Unpumped and pumped IV-curves of experimental SIS mixer along with hot/cold response at 955 GHz measured at IF=1.5 GHz. Bath temperature is about 2 K.

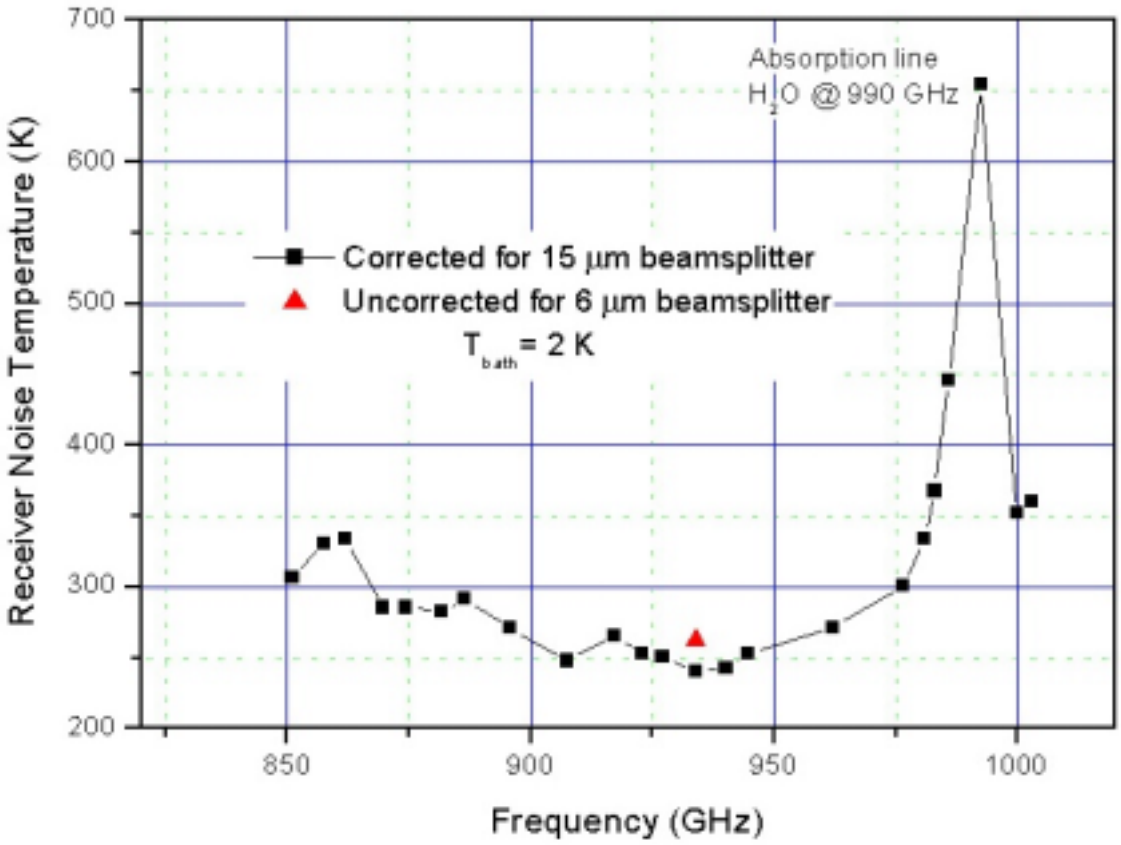

Fig. 6 Receiver noise temperature (DSB) measured for double-dipole antenna SIS mixer at bath temperature about 2 K.

500 K was measured for a couple of devices above 950 GHz. A device with the tuning frequency a bit lower than 1 THz was eventually selected. This device demonstrated a 3 dB FTS range of 800-1050 GHz as shown in Figure 4. The heterodyne response of 1.6 dB at 4.2 K and 1.8 dB at about 2 K was measured with a 15-μm beam splitter at the frequency of 935 GHz (see Figure 5). The response increased to 2.1 dB with a thinner (6 μm) beam splitter at about 2 K that yield T_{RX} = 260 K (DSB). The correction made for both beam splitters gave very close figures of about 245 K at 935 GHz. The water vapor absorption line at about 990 GHz is clearly seen at the T_{RX} data measured at IF = 1.5 GHz (see Figure 6).

The calculated reflection at the IF port vs. dynamic resistance of the mixer is presented in Figure 7. The complete capacitance of the structure, which includes the twin-SIS

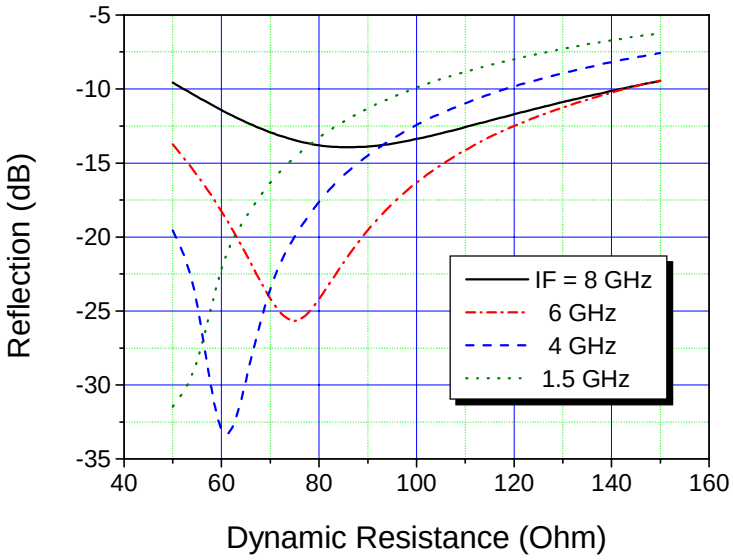

Fig. 7 Reflection loss at the IF port of the double-dipole antenna SIS mixer vs. dynamic resistance of the mixing element. Calculation made for four frequencies 1.5 GHz, 4 GHz, 6 GHz and 8 GHz in presence of inductive IF tuner (see Fig. 1).

junction, all microstrips and antenna filters, has been taken into account. The reflection below –10 dB is predicted for most of the band 4-8 GHz. According to the calculations, such reasonable coupling to a 50 Ω transmission line can be obtained with a series inductor, L=0.7 nH, which can be formed by two 1 mm long bond wires of 20-50 μm in diameter separated at the distance of 0.2 mm (see Fig. 1).

The antenna beam is measured in the direct detection mode using a relatively narrow beam source that provide the dynamic range up to 40 dB (see Figure 8). The receiver was being rotated about the phase center of the antenna. It is found that the antenna mainlobe at 915 GHz is almost round and its half-width is about 1.8° at –11 dB, the first-order sidelobe appeared below –16 dB, and the beam quality is not degrading at 850 GHz. The width of the beam is somewhat decreasing at higher frequency that fit expectations for the diffraction limited optics. To obtain the exact beam width required by *HIFI* (F/3-F/5), an ellipsoid correction mirror is suggested in front of the mixer. The cross-polarized component of the beam is also measured at 850 GHz and found to be below –22 dB.

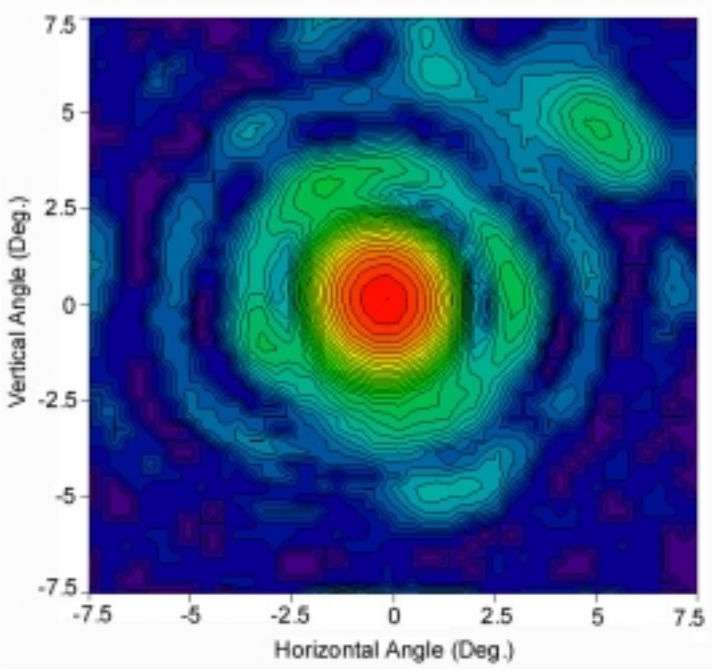

Fig. 8 Antenna beam pattern of experimental double-dipole SIS mixer with NbTiN/SiO_2/Al tuning microstrip at 915 GHz. The chip is mounted at elliptical lens of diameter 10 mm. Contours are at 1 dB step. All sidelobes are below –16 dB. The distant spot at the top-right corner is caused most probably by unknown reflection.

Conclusions

A double-dipole antenna THz-band *SIS receiver* with noise of only 10 photons is demonstrated experimentally. The receiver can cover *HIFI* band 3 and the part of band 4 demonstrating however cut-off just above 1 THz. We conclude that NbTiN/SiO_2/Al tuning microstrip sputtered at ambient temperature can be low loss at least up to 1 THz yielding the SIS receiver noise temperature of 250 K at 935 GHz and 360 K at 1 THz. These experimental results support the design value of effective sheet resistance of the NbTiN/SiO_2/Al microstrip in the range 0.1-0.15 Ω. It is demonstrated numerically that IF coupling is achievable in the range of 4-8 GHz for this type of SIS mixer. We may conclude that a diffraction limited double-dipole lens-antenna can provide effective *rf* coupling for a THz-band SIS mixer with sidelobes less than -16 dB. The cross-polarized component is found below –22 dB. It looks worth to try the back reflector from Al or NbTiN that can further improve both the noise temperature of the receiver and the sidelobes of the array antenna.

Acknowledgments

The authors thank Th. de Graauw and V. P. Koshelets for continuous encouraging and D. Nguyen for technical assistance. The work was supported in parts by the European Space Agency under ESTEC Contract No.11653/95, Russian SSP "Superconductivity", RFBR project 00-02-16270, INTAS project 97-1712 and ISTC project 1199.

References:

[1] *HIFI* for *Herschel Space Observatory* (known formerly as *FIRST*), http://www.sron.nl

[2] J. R. Tucker, M. J. Feldman, "Quantum detection at millimeter wavelengths," *Reviews of Modern Physics*, vol. 57, No. 4, pp. 1055-1112 (1985).

[3] J. W. Kooi, M. Chan, B. Bumble, H. G. LeDuc, P. Schaffer, T. G. Phillips, "230 and 492 GHz low noise SIS waveguide receivers employing tuned Nb/A10$_x$/Nb tunnel junctions," *Int. J. IR and MM Waves,* vol. 16, pp. 2049-2068 (1995).

[4] A. Karpov, J. Blondel, M. Voss, K. H. Gundlach, "A three photon noise SIS heterodyne receiver at submillimeter wavelength," *IEEE Trans. Appl. Supercond.,* vol. 9, pp. 4456-4459 (1999).

[5] J. A. Stern, B. Bumble, H. G. LeDuc, J. W. Kooi, J. Zmuidzinas, "Fabrication and characterization of NbTiN based SIS mixers for use between 600 and 1200 GHz," *Proc. 9 Int. Symp. Space Terahertz Technol*., pp. 305-313 (1998).

[6] D. C. Mattis and J. Bardeen, "Theory of the anomalous skin effect in normal and superconducting metals," *Phys. Rev.,* vol. 111, pp. 412-417 (1958).

[7] P. Dieleman, T. M. Klapwijk, J. R. Gao, H. van de Stadt, "Analysis of Nb superconductor-insulator-superconductor tunnel junctions with Al striplines for THz radiation detection," *IEEE Trans. Appl. Supercond.,* vol. 7, pp. 2566-2569 (1997).

[8] H. van de Stadt, A. Baryshev, P. Dieleman, Th. de Graauw, T. M. Klapwijk, S. Kovtonyuk, G. de Lange, I. Lapitskaya, J. Mees, R. A. Panhuyzen, G. Prokopenko, H. Schaeffer, "A 1 THz Nb SIS heterodyne mixer with normal metal tuning structure," *Proc. 6 Int. Symp. Space Terahertz Technol.*, pp. 66-77 (1995).

[9] V. Yu. Belitsky, S. W. Jacobsson, L. V. Filippenko, S. A. Kovtonyuk, V. P. Koshelets, E. L. Kollberg, *Proc. 4 Int. Symp. Space Terahertz. Technol.*, U. of California, Los Angeles, CA, p. 538 (1993).

[10] J. Zmuidzinas, H. G. LeDuc, J. A. Stern, and S. R. Cypher, "Two-junction tuning circuits for submillimeter SIS mixers," *IEEE Trans. Microwave Theory Tech.,* vol. 42, No. 4, pp. 698-706 (1994). M. Bin, M. C. Gaidis, J. Zmuidzinas, T. G. Phillips, H. G. Leduc, "Low-noise 1 THz niobium superconducting tunnel junction mixer with a normal metal tuning circuit," *Appl. Phys. Lett.,* vol. 68, pp.1714-1716 (1996).

[11] V. Yu. Belitsky and E. L. Kollberg, "Superconductor-insulator-superconductor tunnel strip line: features and applications," *J. Appl. Phys.,* vol. 80, pp. 4741-4748 (1996). Y. Uzawa, Z. Wang, A. Kawakami, and S. Miki, "Performance of all-NbN quasi-optical SIS mixers for the terahertz band", this conference.

[12] N. N. Iosad, V. V. Roddatis, S. N. Polyakov, A. V. Varlashkin, B. D. Jackson, P. N. Dmitriev, J.-R. Gao, T. M. Klapwijk, "Superconducting transition metal nitride films for THz SIS mixers", Appl. Supercond. Conf. ASC'2000, Sept. 2000, Rep. 5MD04, to be published in *IEEE Trans. on Appl. Supercond.* (2001).

[13] D. F. Filipovic, S. S. Gearhart, and G. M. Rebeiz, "Double-slot antennas on extended hemispherical and elliptical silicon dielectric lenses," *IEEE Trans. on Microwave Theory Tech.,* vol. 41, vol. 10, pp. 1738-1749 (1993).

[14] M. J. M. van der Vorst, P. J. I. de Maagt and M. H. A. J. Herben, "Matching layers for integrated lens antennas," *Proc. Int. Symp. Antennas,* (JINA '96), pp. 511-515 (1996). M. J. M. van der Vorst, *PILRAP,* the software for design of integrated lens-antennas.

[15] A. Skalare, Th. de Graauw, H. van de Stadt, "A planar dipole array antenna with an elliptical lens," *Microw. and Opt. Technol. Lett.,* vol. 4., pp. 9-12 (1991).

[16] S. V. Shitov, V. P. Koshelets, A. B. Ermakov, L. V. Filippenko, A. M. Baryshev, W. Luinge, J.-R. Gao, "Superconducting chip receivers for imaging application," *IEEE Trans. on Appl. Supercond.,* vol. 9, pp. 3773-3776 (1999).

[17] J. Zmuidzinas and H. G. LeDuc, "Quasi-optical slot antenna SIS mixers," *IEEE Trans. Microw. Theory Tech.,* vol. 40, pp. 1797-1804 (1992).

[18] S. V. Shitov, A. M. Baryshev, V. P. Koshelets, J.-R. Gao, J. Jegers, W. Luinge, H. van de Stadt, Th. de Graauw, "Wide-band quasi-optical SIS mixers for integrated receivers up to 1200 GHz," *Proc. 7 Int. Symp. Space Terahertz Technol.*, pp. 525-534 (1996).

[19] B. D. Jackson, N. N. Iosad, B. Leone, J. R. Gao, T. M. Klapwijk, W. M. Laauwen, G. De Lange, and H. Van de Stadt, "DC and RF Properties of Nb SIS Mixers with NbTiN Striplines," *Proc. 10 Int. Symp. Space Terahertz Tech.*, p. 144 (1999). B. Leone, B. D. Jackson, J. R. Gao, and T. M. Klapwijk, "Geometric heat trapping in niobium superconductor-insulator-superconductor mixers due to niobium titanium nitride leads," *Appl. Phys. Lett.,* vol. 76, pp. 780-782 (2000).

[20] B. Jackson, G. de Lange, W. M. Laauwen, J. R. Gao, N. N. Iosad, T. M. Klapwijk, "NbTiN/SiO2/NbTiN and NbTiN/SiO2/Al tuning circuits for 1 THz waveguide SIS mixers," *Proc. 11 Int. Symp. Space Terahertz Technol.*, pp. 238-250, U. of Michigan, Ann Arbor, Michigan (1-3 May 2000).

[21] M. M. Khapaev, "Extraction of inductances of a multi-superconductor transmission line", *Supercond. Sci. Technol.*, vol. 9, pp. 729-733 (1996). M. Yu. Kupriyanov, Private communication on the inductance calculation.

[22] R. L. Kautz, "Miniaturization of normal-state and superconducting striplines," *J. Res. Natl. Bur. Std.,* vol. 84, pp. 247-259 (1979).

[23] A. M. Baryshev, B. D. Jackson, G. de Lange, S. V. Shitov, N. Iosad, J. R. Gao, T. M. Klapwijk, "Quasi-optical terahertz SIS mixer," *Proc. 11 Int. Symp. Space Terahertz Technol.*, pp. 129-138, U. of Michigan, Ann Arbor, Michigan (1-3 May, 2000). B. D. Jackson, A. M. Baryshev, G. de Lange, W. M. Laauwen, L. de Jong, J. R. Gao, N. N. Iosad, T. M. Klapwijk, S. V. Shitov, "The Development of THz SIS mixers for HIFI," this conference.

Design of Sideband Separation SIS Mixer for 3 mm Band

V. Vassilev and V. Belitsky
Onsala Space Observatory, Chalmers University of Technology

ABSTRACT

As a part of Onsala development of a single sideband mixer for ALMA band 7 (275-370 GHz), we present the design of a prototype sideband separation mixer for 85-115 GHz. The mixer is designed using a quadrature scheme with two identical DSB SIS mixers pumped by a local oscillator (LO) with 90° phase difference. The mixer employs a new device, a double-probe coupler, which splits the input RF signal and provides transition from a waveguide to a microstrip line, allowing the integration of all mixer components on the same compact substrate and thus ensure a high degree of similarity in the SIS junction performance and the geometry of all the mixer elements including integrated tuning circuitry. The RF and the LO power are coupled on the substrate by using microstrip directional coupler; the remaining LO power at the idle port of the coupler is terminated by unbiased (or weakly biased) SIS junction acting as a lumped load. To obtain feasible dimensions of the LO directional coupler and the SIS tuning circuitry the mixer is designed using two types of dielectric: 150 μm thick crystal quartz substrate and two layers (400 nm and 200 nm) of sputtered SiO_2. The presence of the two dielectrics (quartz and SiO_2) requires step in the ground plane, which is achieved by using a choke structure as a virtual ground [1].
We present the design of all the mixer components, detailed simulation results using High Frequency Structure Simulator and measurements of the double probe coupler.

INTRODUCTION

In [2] Jewell and Mangum examine in details single versus double sideband operation in terms of the signal-to-noise ratio and optimum receiver performance. They found that SSB observations are more efficient not only for spectroscopic observations in one sideband, but even if spectral lines of interest are present in both sidebands. With SIS mixer noise temperature approaching level of 2-5 times the quantum noise, the noise performance of a double-side band (DSB) super-heterodyne receiver can be limited by the atmospheric noise fed into the system via the image band. A separation of the atmospheric noise introduced by the image band can improve the sensitivity of a SSB receiver up to a factor of two over the DSB receiver with balanced sideband gains [4].
A quadrature scheme with two identical DSB SIS mixers pumped by a local oscillator (LO) with 90° phase difference as shown in Figure 1 does not use any RF filter components and has been demonstrated for mm-wave band [3, 4].

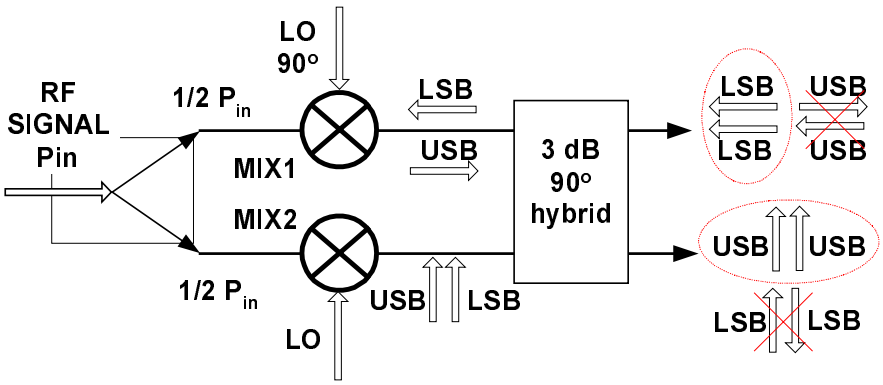

Figure 1 Block diagram of the sideband separation mixer. The crossed out items at the hybrid outputs are the rejected sidebands (180° phase difference).

The RF and the LO amplitude and phase *balance* at the two mixers is the limiting factor [5] in the separation of the image band (more than 10 dB is a typical specification).

MIXER DESCRIPTION

The whole mixer circuitry is design on a single crystal quartz substrate 9mm/ 0.7mm/ 150µm as shown in Figure 2.

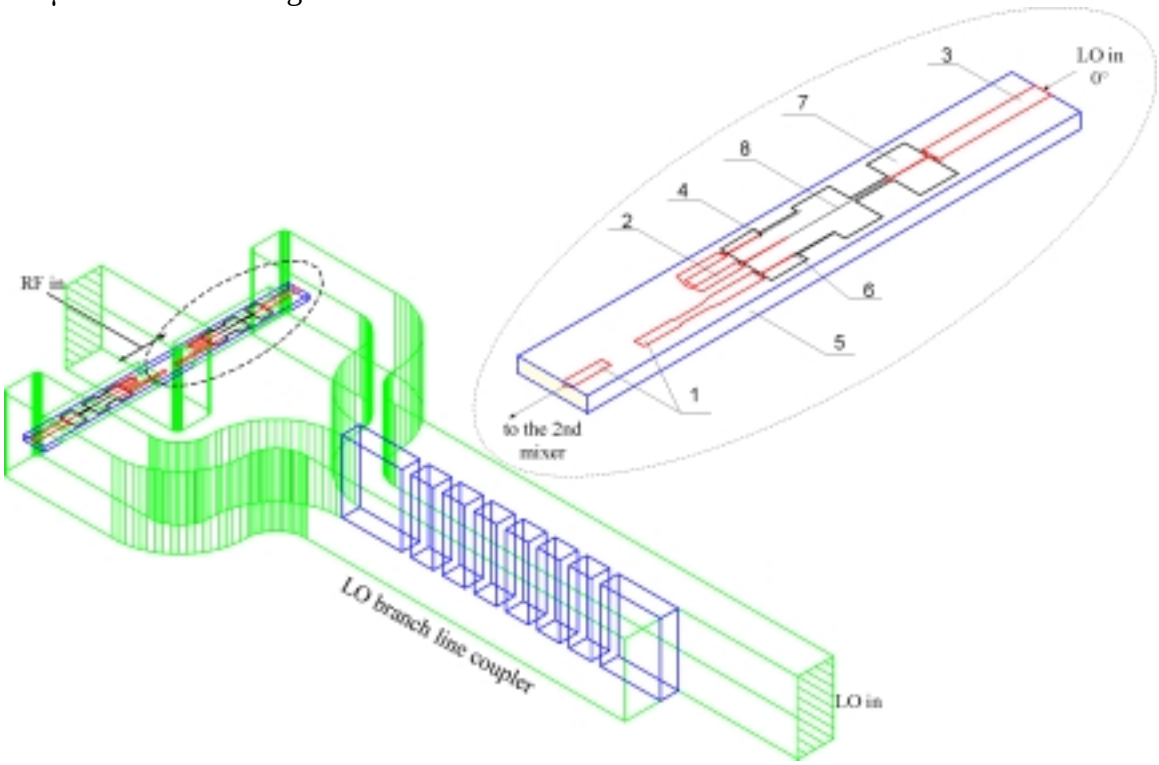

Figure 2 Layout of the sideband separation mixer. 1- double probe 3 dB coupler, 2- 15dB LO directional coupler, 3- LO waveguide to microstrip transition, 4- SIS junction as an absorbing load, 5- crystal quartz substrate, 6- SIS mixer junction, 7- choke structure, 8- 3 sections transformer matching the LO probe to the LO injection coupler.

The substrate is coupled to the RF waveguide via a double-probe 3dB coupler (1). A waveguide branch line coupler provides 90° phase shift and splits the LO power which is then coupled at the ends of the substrate. Three section transformer (8) matches the impedance of the LO probe (3) to the LO injection coupler (2). To keep the signal path loss small the LO power is coupled to the RF via –15dB directional coupler (2). SIS junction (4) is used as a load for the idle ports of the substrate LO coupler to terminate the remaining LO power.

Two types of transmission line media are used: microstrip lines (the lines linked to 1, 2 and 3 from Figure 2) which use the 150μm crystal quartz substrate as dielectric and 'narrow' microstrip lines (the lines located above the choke 7) which are placed on the top of a thin sputtered SiO_2 layer. To increase the upper limit of the attainable impedances of SiO_2 based line, two layers of SiO_2 are used- 200nm layer, which is placed over the last sections of the choke and accommodates the SIS junctions and a second 200nm layer (on top of the first one) over the middle choke sections allowing increase in the line impedance by a factor of 2 up to ≈ 25 Ω.

THE DOUBLE-PROBE COUPLER

In attempt to simplify the design by combining the low-loss, wide band power division with the waveguide to microstrip transition, we suggest a device where a double-probe structure is coupled to the E-field in a waveguide as shown in Figure 3. The probes split the input RF signal over a frequency band limited by the dominant mode of the waveguide and simultaneously provide transition from waveguide to microstrip line for easy integration with the associated mixer circuitry [6].

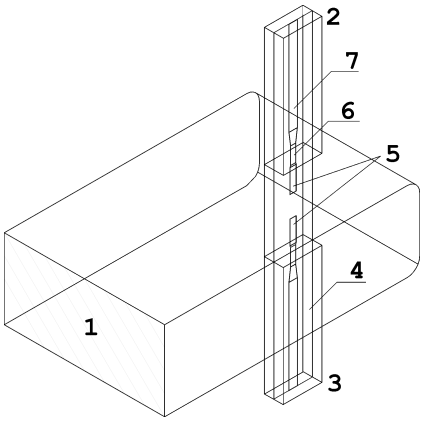

Figure 3 Waveguide to microstrip power divider. 1 – the input port, 2,3 – the output ports, 4 – channel with the substrate, 5 – probes, 6 – high impedance line, 7 – output microstrip line.

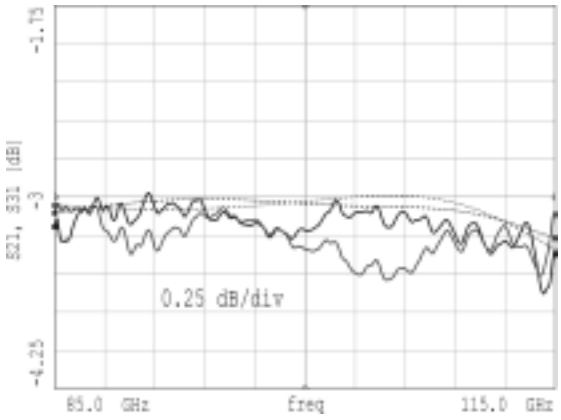

Figure 4 Measured transmission magnitude of the power divider (solid lines) and the simulated transmission (dashed lines).

The transmission S_{21} and S_{31} were measured between 85-115 GHz and are plotted in Figure 4, the typical total loss is ≈0.3dB over 30% of bandwidth. In this measurement

only response calibration was performed, the observed amplitude asymmetry is ≤ 0.3 dB and is likely caused by the interaction between the system's source and loads mismatch. The double probe coupler is a perfect phase-splitter, since the E-field vector oscillates in the direction parallel to the probes; phase difference of 180° is introduced between the output ports for all frequencies of the waveguide dominant mode. Thus the suggested power divider provides perfect phase symmetry. Good amplitude symmetry is observed as long as the output ports are terminated with identical loads. The power divider transducer power gain was examined for different values of possible loads mismatch and the resulting asymmetry is compared to that of the ideal Wilkinson in [6], it was shown that for small load impedance deviations Z_L/Z_0 the asymmetry of the suggested power divider converges to the one of the ideal Wilkinson divider.

LO DIRECTIONAL COUPLER

A number of attempts were made to design a LO injection directional coupler by using the SiO_2 as transmission medium. However due to the small dielectric thickness, the gap required between the coupled lines appears to be critically small even if periodic capacitive coupling is introduced on top of the lines. To ease the processing requirements the LO injection coupler was designed using the crystal quartz substrate as a dielectric which also facilitates its connection to the double probe coupler. The LO coupler together with the power divider is shown in Figure 5.

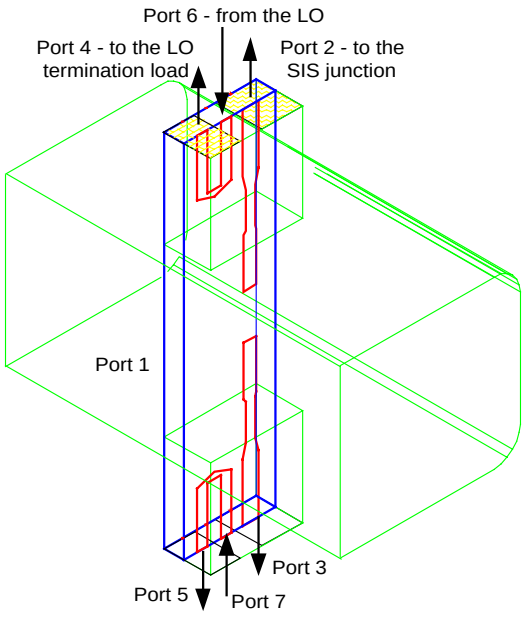

Figure 5 LO injection directional coupler together with the power divider. Port 1 is the RF waveguide input, ports 2, 3 are connected to the SIS junctions via a λ/4 transformer section, the LO power is applied at ports 6 and 7, ports 4 and 5 are connected to the LO termination load (unbiased SIS junctions).

The transmission lines were designed as wide as possible in order to decrease the impedance at the ports to ease the matching to the SIS junctions. The resultant 7 ports

structure was analyzed using HFSS simulator [8], and the simulated performance is shown in Figure 6. The shape of the line that provides 180° bend in the LO path was optimized to minimize the reflection caused by the 'sharp' bend.

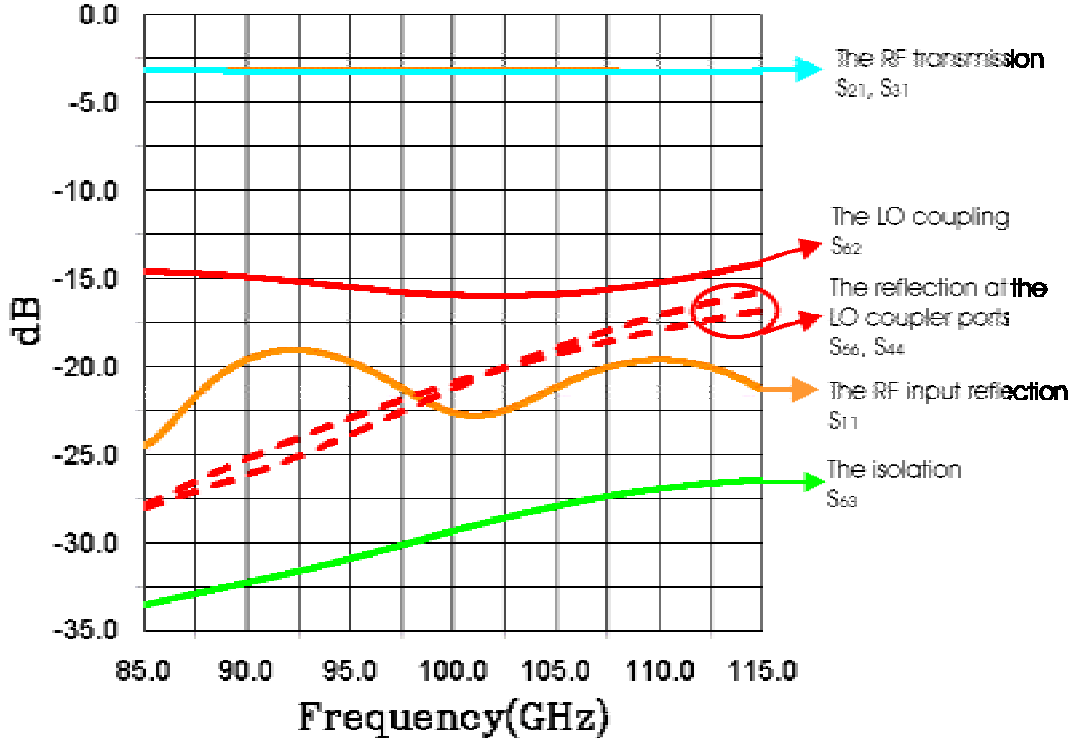

Figure 6 Simulated performance of the RF power divider and LO injection coupler.

The LO to RF coupling is nearly constant –15dB, the return loss at all the ports is > 17 dB and the directivity is > 14dB.

CHOKE

Incorporating the two types of dielectric– 150 μm crystal quartz substrate and the two layers of SiO_2 (200nm and 400 nm) for the lines surrounding the SIS junctions requires transition between the two ground planes. More effective step in the ground can be achieved by shaping the upper ground plane as a 'choke' or band-stop filter as suggested by [1]. This idea is illustrated in Figure 7 where a line is placed on top of the choke structure separated by a thin SiO_2 layer. The direct way to evaluate the efficiency of such a step in the ground plane is to observe what amount of the power is directed between the choke and the line and what fraction of the power remains trapped between the choke and the first ground plane. This would require to represent the structure as a 2 ports / 2 modes device. However to perform an electromagnetic simulation on such a structure is difficult and impractical since the thickness of the SiO_2 layer is much smaller (factor of 10^{-4}) compared to the choke dimensions. As a result the number of cells required to properly mesh the structure exceeds the workable amount of cells typical for a reasonable simulation. Therefore the SiO_2 layer and the transmission line are omitted in the

simulation and the choke is considered only as a band-stop filter with open ports. The performance of the above-defined structure is shown in Figure 8.

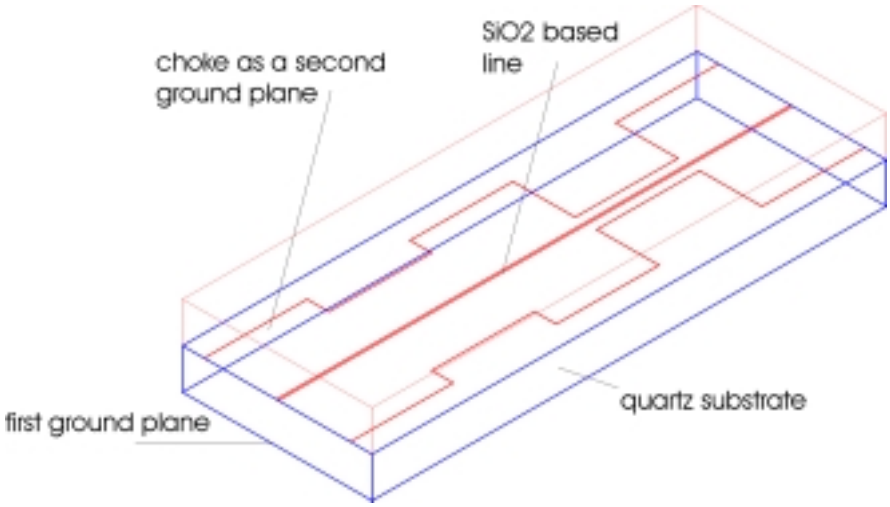

Figure 7 Choke structure on top of the quartz substrate and a line separated by a thin SiO_2 layer (not visible in the picture).

Since the ports of the choke are virtually short-circuited to the first ground plane (S_{11}, S_{22} in Figure 8) we can make the assumption that the power, which is not locked in between the choke and the first ground plane is directed between the choke and the transmission line. Therefore the loss, which is due to the step in the ground plane, should not exceed -3.10^{-3} dB (-22dB leak in the quartz substrate).

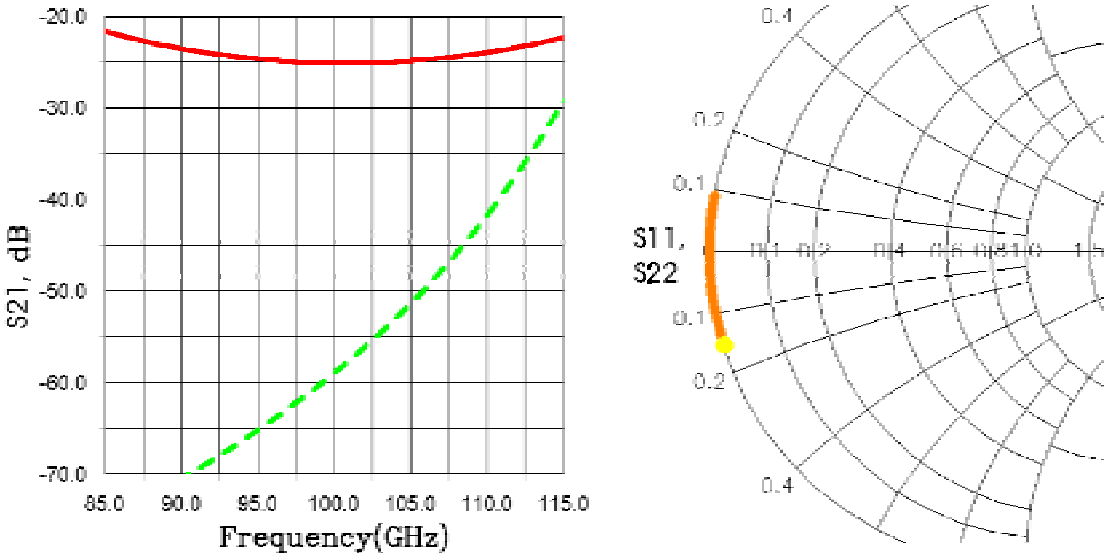

Figure 8 Transmission of the choke with open ports (terminated with the channel impedance) and the reflection at the ports. The solid line in the first plot represents the power in the main TEM mode, which remains trapped between the choke and the first ground plane, the dashed line illustrates the growth of the transverse resonant mode caused by the low impedance choke sections.

The dashed line in Figure 8 shows the appearance of the transverse resonant mode at ≈ 125 GHz, which restricts further increase of the width of the low impedance choke sections, the width of the high impedance sections is chosen to accommodate the SIS tuning circuitry.

LINE TRANSITION BETWEEN THE TWO DIELECTRICS

The line transition from 150 μm quartz to 400 nm SiO_2, as shown in Figure 9, creates significant geometrical and electrical discontinuity causing reflection even if the lines have identical impedances. Bringing the 'wide' quartz-based line close to the SiO_2 layer shunts the signal due to its excessive capacitance with respect to the 2nd ground plane. Different configurations of tapered shapes, to connect the two lines, were simulated to minimize the effect of the discontinuity. The distance *L* was optimized and for this particular example is about 30 μm.

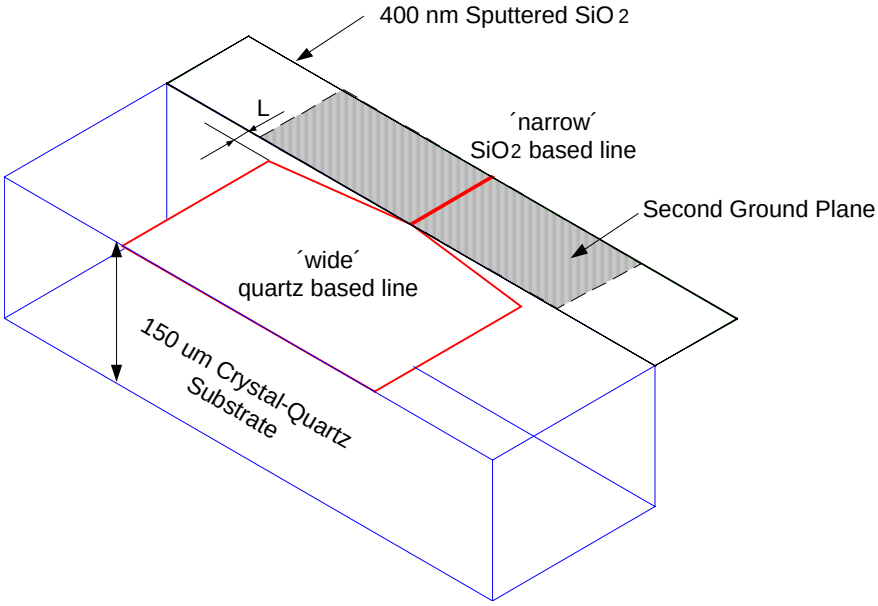

Figure 9 Quartz-based line to SiO_2-based line transition. Two lines having the same impedance but using dielectrics with different thickness are connected via a "tapered line" with optimized length.

In our simulations all the lines were modeled as perfect conductors, therefore the London penetration depth in a superconductor is not taken into account in the calculation of the line impedances. Therefore the actual line impedance exceeds the impedance computed by HFSS with factor of 1.15 for 400 nm SiO_2 substrate and line impedance of ≈ 30Ω. In other words a superconducting line having the same impedance as the line in HFSS would have been wider with a factor of 1.15. Nevertheless in terms of discontinuity this would not make any difference that may possibly affect the result of the simulation. The reflection produced by such a transition is presented in Figure 10.

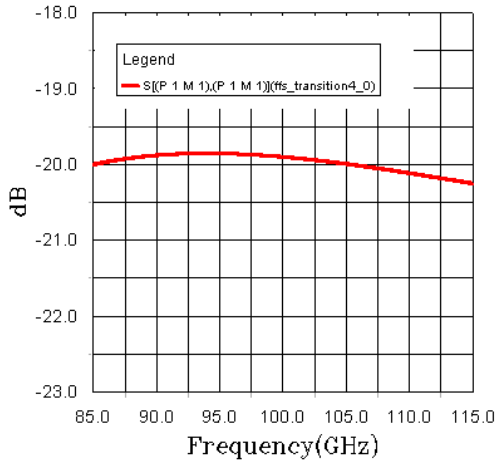

Figure 10 The reflection caused by the discontinuity in the line transition between quartz and SiO_2 dielectrics.

LO BRANCH LINE COUPLER

Finally to divide the LO power between the two mixers and to introduce the 90° phase difference a waveguide branch line coupler was designed. Since the required LO band is narrower compared to the RF band with 2 times the IF highest frequency, introducing the 90° phase difference in the LO path will benefit better phase and amplitude symmetry of the coupler due to the reduced bandwidth. To facilitate the machining the LO coupler (Figure 2) employs symmetrical branch sections [7].

The important parameters in the branch line coupler performance relevant for the image band isolation are the magnitude and the phase symmetry. Figure 11 shows the magnitude difference and the phase shift between the two channels.

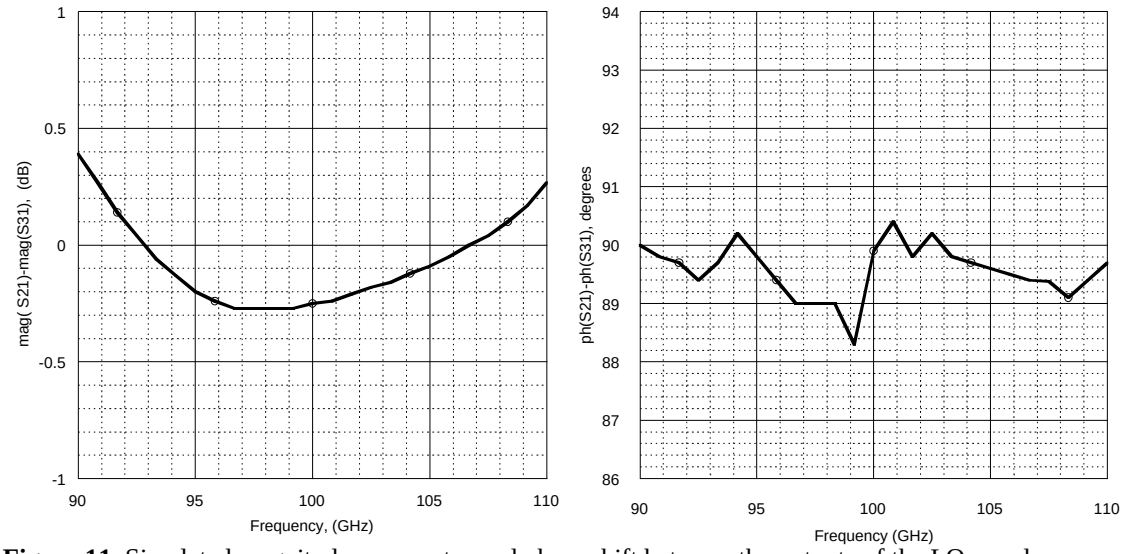

Figure 11 Simulated magnitude asymmetry and phase shift between the outputs of the LO coupler.

SIS INTEGRATED TUNING CIRCUIT

SIS junction tuning circuitry is designed using microstrip lines based on sputtered SiO_2 as a dielectric and consists of inductive section followed by an open stub (short circuit) as shown in Figure 12. This configuration is used for both SIS mixer junction and LO termination load and both circuits were optimized for source power match. Similar tuning circuitry was employed by [Carpenter] except we use the open stub input to connect DC bias and IF output.

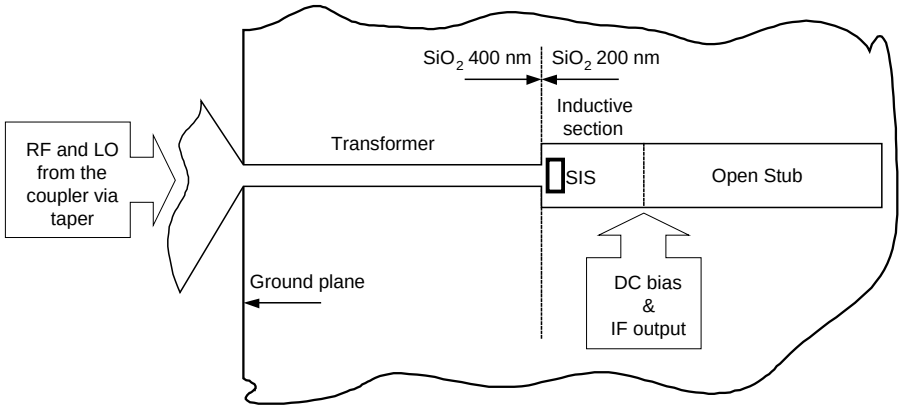

Figure 12 SIS tuning circuitry. This configuration is identical for both SIS mixer junctions and SIS LO termination junctions.

The mixer tuning was designed for source impedance of $\cong 69\Omega$ and frequency range 85 – 116 GHz. To provide matching between the SIS junction and the relatively high source impedance, the required transformer section impedance is of about $25\,\Omega$. In order to obtain the line with such impedance while keeping reasonable line dimensions we introduced a second 200 nm SiO_2 layer giving total dielectric thickness in the transformer section of ≈ 400 nm.

Using SIS junction with its tuning circuitry for LO termination gives the opportunity to produce it within the same processing steps as the mixer junction while the thin film resistors need additional and somewhat critical processing steps to achieve the required high resistivity of the normal metal film. The LO termination was optimized for the frequency band ΔF-$2F_{IF}$, where ΔF is the SIS mixer RF band (85 – 116 GHz) and F_{IF}=4.6 GHz is the upper intermediate frequency. The level of RF power at SIS junction is defined by parameter $\alpha = eV_{rf}/hf$, here **e** is the electron charge, **h** is Planck's constant and **f** is the operating frequency. The RF voltage across the LO termination junction, $\mathbf{V_{rf}}$, is 15 dB higher than the V_{rf} across the mixer junction (the coupling of the LO coupler is –15 dB). Assuming that the SIS mixer junction operates at α_m=1 at the SIS LO termination junction this will give $\alpha_t \approx 5$. The result of the circuit optimization is presented in Figure 13.

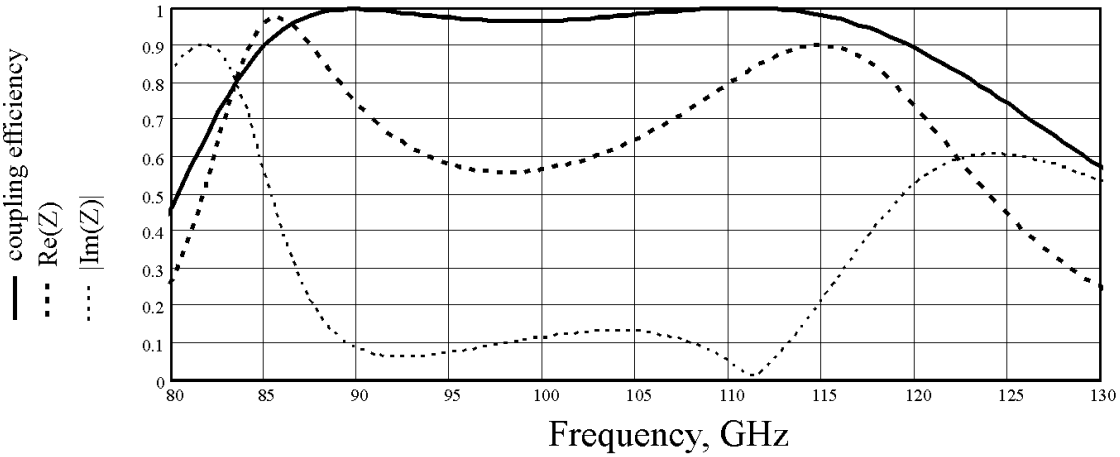

Figure 13 Coupling efficiency and impedance of the LO termination SIS junction together with its tuning circuitry. The values for the impedance are normalized to 69Ω which is the required impedance for matched LO coupler termination.

CONCLUSION

We present the design of a sideband separation mixer for 85-115 GHz. The mixer is based on a new device - a double-probe coupler, which makes possible the integration of all mixer components on the same compact substrate and thus ensures a high degree of similarity in the SIS junction performance and the geometry of all the mixer elements. Together with the good symmetry provided by the double-probe coupler and the LO branch line coupler, this gives the prospect of very good image band suppression.

REFERENCES

[1] Approach proposed by J. Kooi (private communication).
[2] P. R. Jewell, J. G. Mangum, "System Temperatures, Single Versus Double Sideband Operation, and Optimum Receiver Performance", MMA Memo. 170, National Radio Astronomy Observatory, Charlottesville VA, May, 1997.
[3] A. R. Kerr, S.-K. Pan and H. G. LeDuc, "*An integrated sideband separating SIS mixer for 200-280 GHz*", Proc. of the Ninth Space Terahertz Technology Symposium, Pasadena, USA, March, 1998.
[4] R. L. Akeson, J. E Carlstrom, D. P. Woody, J. Kawamura, A. R. Kerr, S. -K. Pan and K. Wan, "*Development of a Sideband Separation Receiver at 100GHz*", Proc of Fourth International Symposium on Space Terahertz Technology, pp.12-17, March, 1993.
[5] A. R. Kerr and S.-K. Pan, "*Design of Planar Image Separating and Balanced SIS Mixers*," Proc. of Seventh International Symposium on Space Terahertz Technology, March 12-14, 1996.
[6] V. Vassilev, V. Belitsky, Denis Urbain, S. Kovtonyuk, "*A New 3 dB Power Divider for MM-Wavelengths*" Accepted for publication in IEEE Microwave and Wireless Components Letters.
[7] S.M.X. Claude, C.T. Cunningham, A.R. Kerr, S.-K. Pan, "Design of a Sideband-Separating Balanced SIS Mixer Based on Waveguide Hybrids", ALMA Memo 316, http://www.alma.nrao.edu/memos.
[8] Agilent High Frequency Structure Simulator, HFSS, Agilent Technologies, 395 Page Mill Road, Paolo Alto, CA 94304, U.S.A.

Reflectivity Measurements of Commercial Absorbers in the 200–600 GHz Range

Jussi Säily, Juha Mallat, Antti V. Räisänen

MilliLab, Radio Laboratory, Helsinki University of Technology
P.O. Box 3000, FIN-02015 HUT, Finland
Email: jussi.saily@hut.fi

Abstract

Reflection properties of several commercial absorbers measured at frequencies of 200, 300, 400, 500, and 600 GHz with different incident angles are presented in this paper. The measurements were done using a specially built test setup with a vector network analyzer and a linear scanner. The presented results show the measured peak reflectance values, i.e., the maximum reflection from the object. The reflectance requirement for absorbers used in compact antenna test ranges (CATRs) is usually –40 dB for all incident angles. According to our measurements, this is not possible with the tested absorbers over the whole frequency range.

1. Introduction

High quality radiation absorbing materials (RAM) with reflectivities below –40 dB are needed for antenna test ranges operating at submillimeter wavelengths [1]. This limit is chosen to allow low enough added fields in the quiet-zone region. If the antenna needs to be measured pointing directly to the back-wall, even lower absorber reflectivity is required. Conventional carbon-loaded convoluted and pyramidal foam absorbers do not provide the necessary absorption performance. A large-sized antenna test range, like the compact antenna test range (CATR), needs very large quantities of absorbers.

MilliLab (HUT Radio Laboratory) is developing a submillimeter wavelength CATR facility using a planar hologram in a contract for the European Space Agency (ESA) [2,3]. This CATR is planned for testing reflector antennas in the 1.5 meter class at frequencies of 300–650 GHz. It is desirable that one type of absorber can cover the whole operational frequency range. In this paper, the measured reflectances for several commercial absorber types at different incident angles and polarisations over the frequency band of 200–600 GHz are presented.

2. Tested absorbers

The tested absorbers (FIRAM-500, TERASORB-500, TK THz RAM, Eccosorb LS-22) are based on different materials. FIRAM-500 is made of iron oxide loaded silicon [4],

TERASORB-500 of carbon loaded EVA (ethylene vinyl acetate) plastic [4], TK THz RAM of carbon loaded polypropylene plastic [5], and Eccosorb LS-22 of carbon loaded polyurethane foam [6]. FIRAM and TERASORB panels have a wedged-type surface design, TK THz RAM a sharp pyramidal surface, and the Eccosorb surface is flat. Eccosorb LS-22 is designed for operation below 30 GHz, but it was tested just like the others. Reflectivity results for other absorber types in the 100–200 GHz range can be found in [7].

3. Instrumentation and test procedures

The test instrumentation was built around a millimeter wave vector network analyzer AB Millimétre MVNA-8-350 equipped with submillimeter wave extensions ESA-1 and ESA-2 [2]. The source ESA-1 consists of a phase-locked Gunn oscillator and a frequency multiplier. The receiver ESA-2 has a similar phase-locked Gunn oscillator which acts as the local oscillator for a sensitive waveguide-type Schottky mixer. Fixed positions of the transmitter and receiver modules were used for precise alignment of the angle and to ensure good repeatibility.

The test setup is shown in Figure 1 for vertical E-field polarisation. A photograph of the test setup is presented in Figure 2. The used incident angles of $\theta_i = 26.5^o, 45^o, 63.4^o$ were chosen for easing precise alignment on the optical table. Alignment guides were mounted to the optical table and then the transmitter and receiver modules were fixed to the guides. In the $\theta_i = 63.4^o$ measurements, a thick absorber sheet between the transmit and receive antennas was used to reduce direct coupling due to antenna sidelobes (see Figure 2). Direct coupling between the antennas without the target was tested to be always below –70dB or the measurement noise floor (whichever higher).

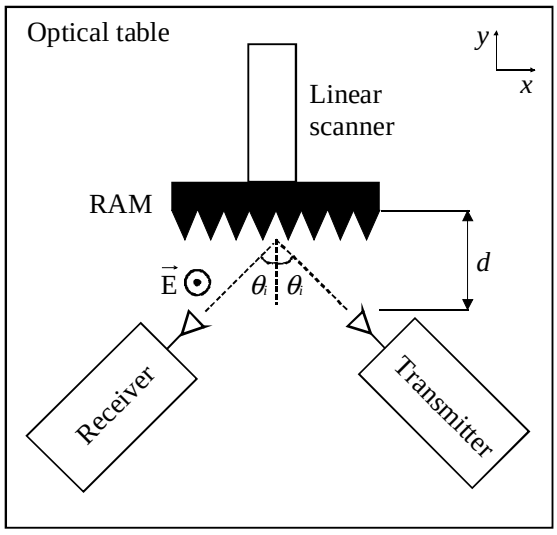

Figure 1. Schematic drawing of the test instrumentation.

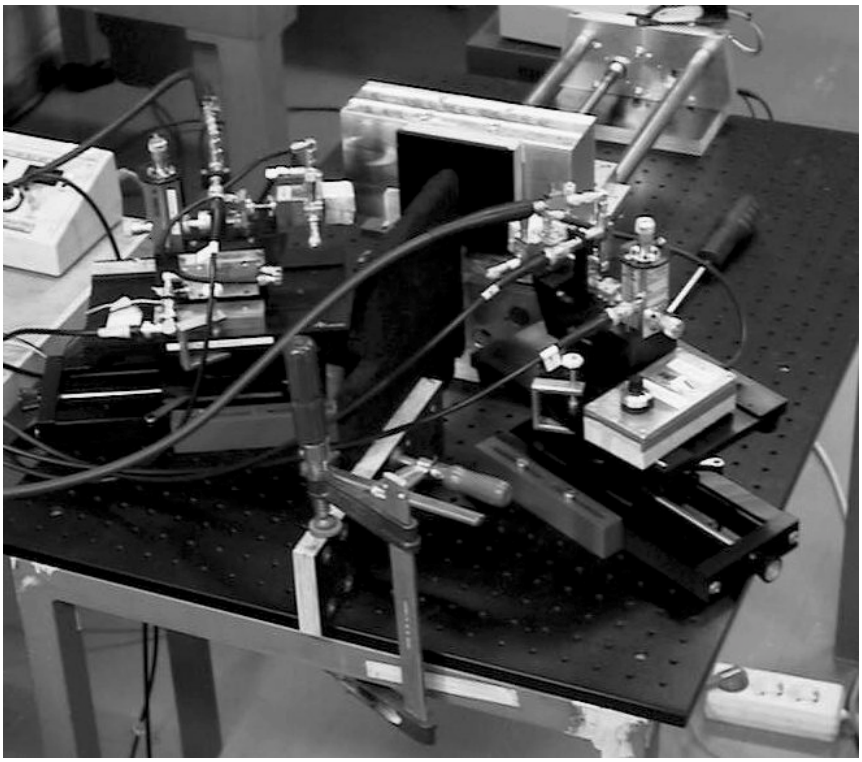

Figure 2. Photograph of the test setup.

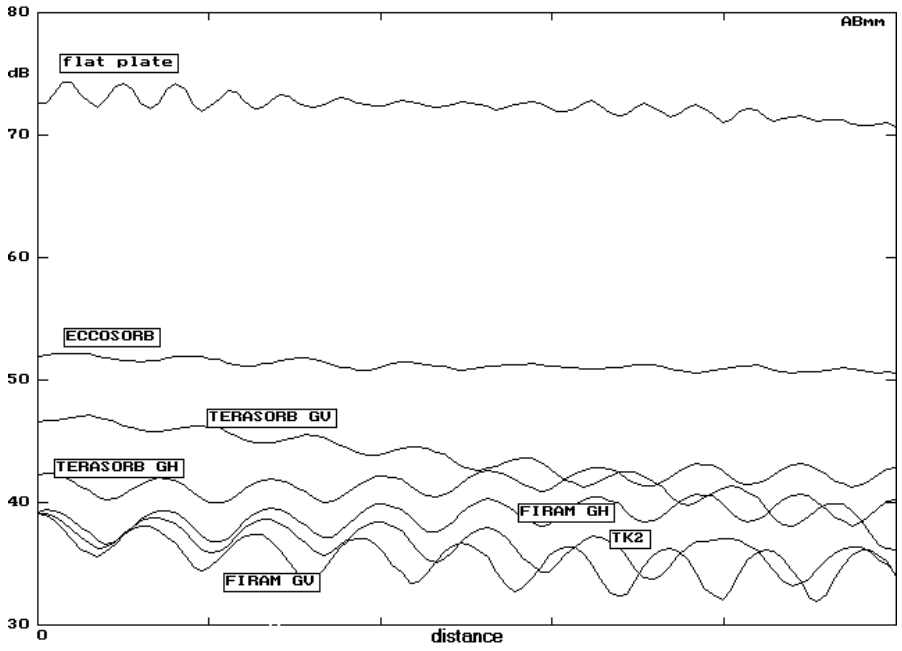

Figure 3. Amplitude data from the network analyzer (300 GHz, 45 degrees and H-H pol).

The flat metal plate used for calibration and the tested absorbers were mounted to a linear scanner. The distance of the test object (*d* in Figure 1) was varied a few wavelengths around its center value determined by geometry. The measured reflected powers have clearly periodical patterns, as can be seen from Figure 3, due to field scattering from the target. At least ten averaged amplitude and phase values were taken for each wavelength in the reflectance measurements.

The surface area illuminated by the incident beam is relatively small and the reflectance results depend on the position of the absorber. To find out the effect of this, the absorbers were tested in three different mounting positions along the x-axis.

Accuracy of the reflection measurement depends on the analyzer dynamic range, which degrades with increasing frequency (from about 100–60 dB at 200–600 GHz). The amplitude measurement accuracy for both vertical and horizontal polarizations at 200–400 GHz is estimated to be ± 0.1 dB, and about ± 0.5 dB at 500–600 GHz.

4. Measurement results

The reflected power from a flat aluminium plate was measured first for each incident angle. After that, the reflected powers from different absorbers were measured. The presented absorber reflectivity dB-values in this paper are all relative to the reflectivity of the flat plate. They show the highest measured reflectivity, i.e., the worst performance over three subsequent linear scans with the absorber mounted in different position. For the wedged-type absorbers FIRAM-500 and TERASORB-500 the results are given for both vertical (gv) and horizontal (gh) groove directions.

The measured and calibrated absorber reflectivities for $\theta_i = 26.5^o, 45^o, 63.4^o$ using vertical and horizontal polarizations are shown in Tables 1 and 2, and also presented in Figures 4–6. The lowest measured reflectivities for each test are printed in bold in Tables 1 and 2. Reflectivities of even the best absorbers are always higher than –40 dB. The measured reflectivity values increase with larger incidence angles. The frequency dependence, however, is not so clear. FIRAM-500 and TERASORB-500 materials are specifically optimized for 500 GHz, and they clearly have better performance in the 400–600 GHz range than in the 200–300 GHz range. In the lower frequencies TERASORB has somewhat lower reflectivities than FIRAM, but in the 400–600 GHz range the results are quite similar with both groove directions. TK THz RAM has the lowest reflectivity in almost all angles and frequencies. Eccosorb LS-22 has the worst performance, as can be expected for a standard microwave absorber intended for frequencies well below 30 GHz.

5. Conclusions

The reflectivities of several commercially available absorbers have been measured at 200–600 GHz. The measurements were carried out with incident angles of

$\theta_i = 26.5^o, 45^o, 63.4^o$. The results presented in this paper show the measured peak reflectivity values taken over three different positions of the absorbers. The reflectivity requirement for high performance compact ranges is usually –40 dB in all angles of incidence. This is clearly not yet possible at submm-waves with commercially available materials. TK THz RAM manufactured by Thomas Keating Engineering Physics, Inc., was found to have the best overall performance in the tests.

Acknowledgements

The hologram CATR project is partly funded by ESA/ESTEC (Contract No. 13096/NL/SB), Tekes (Finland), and the Academy of Finland. The first author has also received personal grants for the research work from Nokia Foundation, TES (Finland), and EIS (Finland) which are greatly appreciated. The authors would also like to thank Mr. Eino Kahra and Mr. Lauri Laakso from the Radio Laboratory workshop for help with the mechanical constructions.

References

[1] Foster, P.R., Martin, D., Parini, C., Räisänen, A., Ala-Laurinaho, J., Hirvonen, T., Lehto, A., Sehm, T., Tuovinen, J., Jensen, F., Pontoppidan, K., "Mmwave antenna testing techniques - Phase 2", 1996, *MAAS Report 304*

[2] Säily, J., Ala-Laurinaho, J., Häkli, J., Tuovinen, J., Lehto, A., Räisänen, A.V., "Instrumentation and testing of submillimeter wave compact antenna test ranges", *11th International Symposium on Space Terahertz Technology*, Ann Arbor, MI., USA, May 1-3, 2000, pp. 590–597

[3] Säily, J., Ala-Laurinaho, J., Häkli, J., Tuovinen, J., Lehto, A., Räisänen, A.V., "Test results of a 310 GHz hologram compact antenna test range", *Electronics Letters*, Vol. 36, No. 2, 2000, pp. 111–112

[4] University of Massachusetts Lowell Submillimeter Technology Laboratory, "Design and manufacture of submillimeter-wave anechoic structure", Product sheet, http://stl.uml.edu/stlweb/stl_firam.html

[5] Thomas Keating Engineering Physics, Inc., "Space qualified tessalating THz RAM for the 100 to 1000 GHz region and beyond", Product sheet, http://qmciworks.ph.qmw.ac.uk/TKI/RAM/ram.html

[6] Emerson&Cuming Microwave Products, Inc., "Eccosorb LS lossy flexible microwave absorber", http://www.emersoncumingmp.com/catalog/ECCOSORB/LS.htm

[7] Lehto, A., Tuovinen, J., Räisänen, A.V., "Reflectivity of absorbers in 100–200 GHz range", *Electronics Letters*, Vol. 27, No. 19, 1991, pp. 1699-1700

Table 1. Reflectivity measurement results for vertical-vertical polarization (values in dB relative to the flat-plate reference).

26.5 deg vertical-vertical

f (GHz)	firam gv	firam gh	terasorb gv	terasorb gh	tk thz ram	eccosorb
200	-21.7	-26.2	-21.3	-29.5	**-34.6**	-13.2
300	-25.2	-27.7	-23.5	-32.6	**-33.4**	-14.6
400	-23.5	**-32.4**	-27.9	-27.9	**-32.4**	-18.8
500	-21.4	-27.6	-25.3	-24.8	**-28.5**	-10.7
600	-25.2	-25.7	-25.3	-25.7	**-29.5**	-22.7

45 deg vertical-vertical

f (GHz)	firam gv	firam gh	terasorb gv	terasorb gh	tk thz ram	eccosorb
200	-17.8	-24.7	-17	-27.3	**-35.5**	-12.4
300	-19.5	-27	-16.3	-30	**-31.1**	-14.4
400	-19.7	-29.7	-21.8	-26.3	**-31.9**	-18.8
500	-20.7	-24.7	**-28.3**	-23.8	-27.8	-9.9
600	-22.8	-24.6	-24.2	-21.9	**-28.1**	-16.5

63.4 deg vertical-vertical

f (GHz)	firam gv	firam gh	terasorb gv	terasorb gh	tk thz ram	eccosorb
200	-14.2	-18.2	-12.7	**-22.3**	-20.1	-9
300	-12	-16.7	-9.55	-19.9	**-20.1**	-7.3
400	-10.6	**-20.5**	-12.7	-22.3	**-20.5**	-11.7
500	-9.7	**-19**	-12.7	-17.7	-18	-12.6
600	-14.4	-18.5	-15.4	-16.9	**-24.9**	-13.7

Table 2. Reflectivity measurement results for horizontal-horizontal polarization (values in dB relative to the flat-plate reference).

26.5 deg horizontal-horizontal

f (GHz)	firam gv	firam gh	terasorb gv	terasorb gh	tk thz ram	eccosorb
200	-31.5	-27.1	-30.4	-25.3	**-33.1**	-17
300	-31.5	-28.6	-37.4	-28.5	**-39.1**	-19.3
400	-33.1	-30	-30.7	-28.5	**-35**	-25.9
500	-28.3	-25.4	**-30.6**	-24.6	-25.3	-17.3
600	-24.9	-23.5	-25.7	-24.5	**-26.9**	-17.2

45 deg horizontal-horizontal

f (GHz)	firam gv	firam gh	terasorb gv	terasorb gh	tk thz ram	eccosorb
200	-23.5	-23.9	**-24.5**	-23.7	-18.5	-19.6
300	**-33.6**	-30.4	-25.4	-27.9	-33.4	-20
400	-34.7	-28.2	-30.6	-30.9	**-35.6**	-24.5
500	-29.5	-25.3	-30.1	-28.5	**-30.4**	-20
600	-25.8	-28.1	-28.8	**-33.2**	-30.4	-21.8

63.4 deg horizontal-horizontal

f (GHz)	firam gv	firam gh	terasorb gv	terasorb gh	tk thz ram	eccosorb
200	-16.8	-18.7	-15.4	-18.7	-12.4	**-20.4**
300	-15.4	-16.3	-12.8	-15.9	**-22**	-16.3
400	-12	**-21.3**	-15.6	-18.1	-16.2	-15
500	-14.6	-20.8	-17.6	**-21.6**	-19.4	-14.4
600	-19.8	-23.4	-19.4	-24	**-25.7**	-18.7

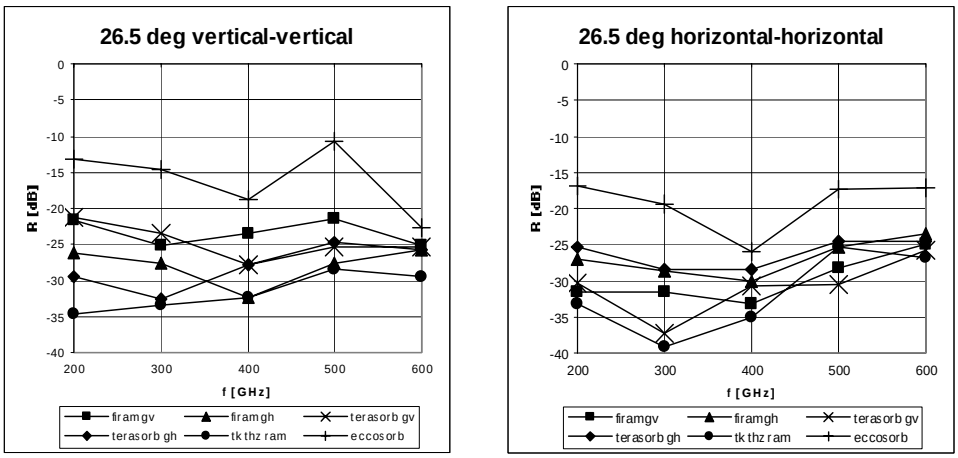

Figure 4. Measured reflectivities for θ_I = 26.5 degrees.

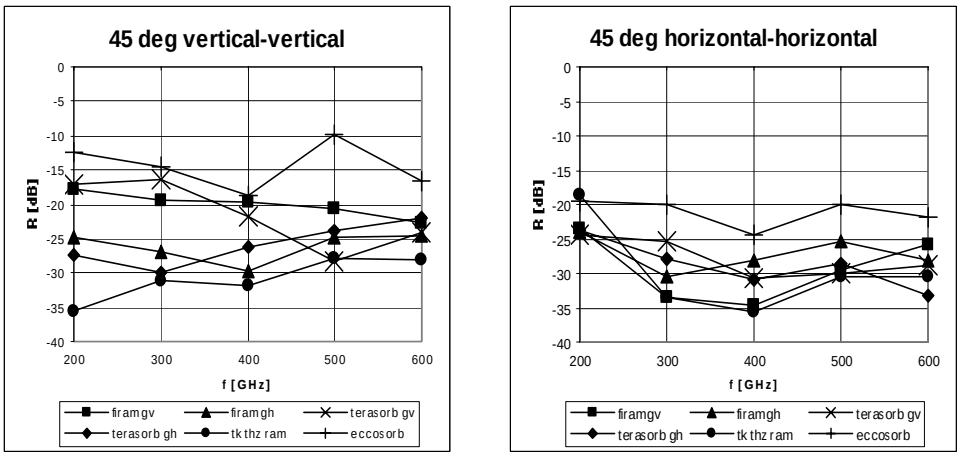

Figure 5. Measured reflectivities for θ_I = 45 degrees.

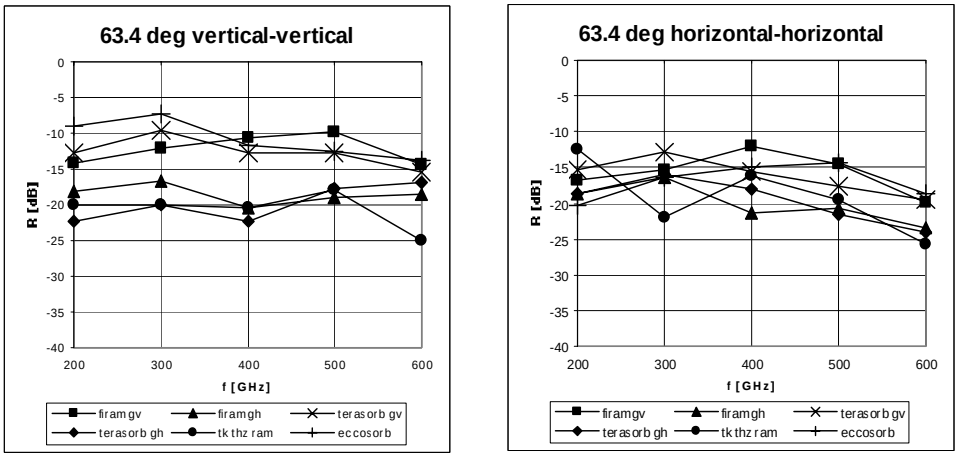

Figure 6. Measured reflectivities for θ_I = 63.4 degrees.

Development of a Hologram CATR for Submm-wavelengths

Janne Häkli, Jussi Säily, Juha Ala-Laurinaho, Tomi Koskinen, Anne Lönnqvist, Arto Lehto, Jussi Tuovinen*, Antti V. Räisänen

MilliLab, Radio Laboratory, Helsinki University of Technology
P.O. Box 3000, FIN-02015 HUT, Finland
Email: janne.hakli@hut.fi

*MilliLab, VTT Information Technology
P.O. Box 1202, FIN-02044 VTT, Finland

Abstract - The hologram based compact antenna test range (CATR) is a potential method for measuring large antennas at submillimeter wave frequencies. The test results of a demonstration CATR for 310 GHz are shown. Also, further development of the hologram CATR is discussed; the hologram manufacturing and possible improvements to the hologram CATR with a dual reflector feed system is described.

INTRODUCTION

In the near future, several scientific and remote sensing satellites with submillimeter wave instruments and antennas (for example Planck and MASTER by ESA) are scheduled for launch. The testing of electrically large submillimeter wave antennas presents some technical challenges to be met, because the testing cannot be done or is problematic with existing antenna measurement facilities.

Conventional far-field measurements cannot be used for large submillimeter wave antennas. The required far-field distance may be tens or hundreds of kilometers, which makes these measurements impossible because of the high atmospheric attenuation. The radiation pattern and other properties of the antennas can also be determined by measuring the electromagnetic near-field of the antenna and performing a computational near-field-to-far-field transformation. The near-field of an antenna has to be sampled with sample spacing less than $\lambda/2$. For electrically large antennas the required number of samples is very large – several millions of measurement points are needed. The measurement is time consuming and requires great stability and positioning accuracy from the measurement equipment. Compact antenna test ranges (CATRs) are seen as the potentially most suitable measurement technique for submillimeter wave antennas [1].

The compact antenna test ranges allow the measurements to be done indoors in a controllable environment. In a CATR, a focusing element forms a planar wave into a so-called quiet-zone (QZ) from the spherical wave emitted by a feed antenna. The focusing element can be a reflector or several reflectors, a lens, or a hologram. The most commonly

used CATRs are based on the use of reflectors. The highest usable frequency of a reflector CATR is limited by the surface accuracy of the reflectors. The required high surface accuracy makes manufacturing of the reflectors expensive. Lenses are not used for large CATRs, because of the lack of suitable homogenous low-permittivity lens materials.

The hologram is a transmission type focusing element with lower surface accuracy requirements than reflectors. This makes hologram manufacturing potentially much more economical than manufacturing of large reflectors. The hologram is a binarized interference pattern of the incoming spherical wave and the desired planar wave. When the hologram is illuminated with the spherical wave, the planar wave is generated into the quiet-zone. The interference pattern is realized by etching radiotransparent slots to a metallization layer on a dielectric substrate. To avoid edge diffraction the slots are tapered, i.e. narrowed, at the edges of the hologram pattern. The basic structure of the hologram CATR is presented in Figure 1.

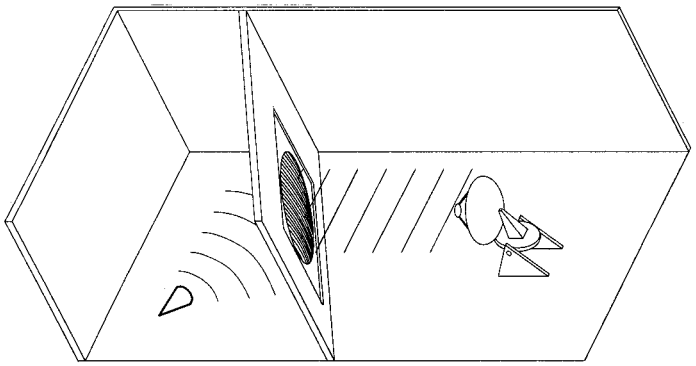

Figure 1. CATR based on a hologram.

The holograms used for CATRs are numerically generated [2]. The holograms are simulated using finite difference time domain method (FDTD) to compute the aperture field and physical optics (PO) is used for computing the quiet-zone field. The holograms are designed iteratively; a hologram is generated and after the simulation a modified hologram is generated to improve the quiet-zone. The plane wave in the quiet-zone is typically required to have an amplitude ripple less than 1 dB peak-to-peak and maximum phase ripple of 10° peak-to-peak. An example of a hologram pattern is presented in Figure 2.

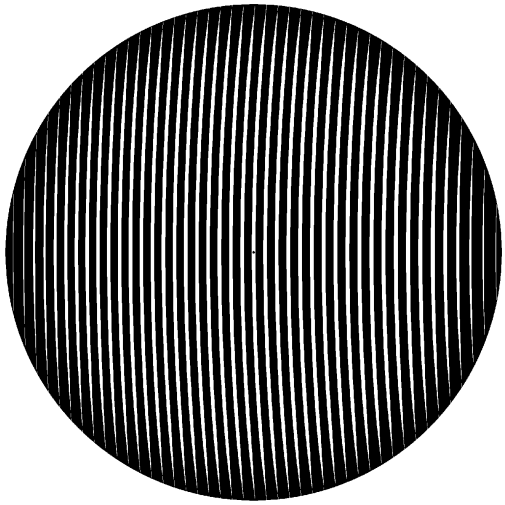

Figure 2. A binarized hologram pattern.

DEMONSTRATION COMPACT ANTENNA TEST RANGE FOR 310 GHZ

A 60 cm diameter hologram was designed for demonstration purposes. The hologram was manufactured by a commercial printed circuit board (PCB) manufacturer. The measurement instrumentation was based on a millimeter wave vector network analyzer MVNA-8-350 (by AB Millimètre). The MVNA-8-350 can be used with various source and receiver configurations. The source was a phase-locked Gunn oscillator with a frequency multiplier. The receiver was a harmonic Schottky mixer pumped with a phase-locked Gunn oscillator.

The source was mounted on a small *xyz*-scanner, which allowed precise adjustments of the source location relative to the hologram. The transmitting antenna was a 310 GHz corrugated horn antenna. The receiver was mounted on a large planar *xy*-scanner. The probe antenna was an open-ended WR-3 waveguide. The quiet-zone field of the CATR was scanned at a distance of 1.5 meters from the 60 cm hologram. The measured contour map of the quiet-zone amplitude is presented in Figure 3. The horizontal phase scan at the center of the quiet-zone is shown in Figure 4.

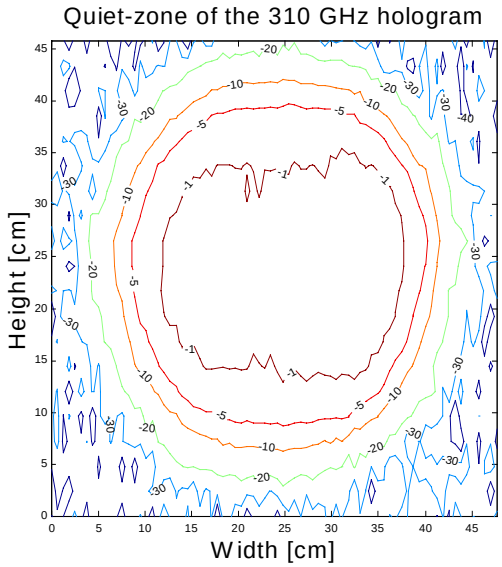

Figure 3. Measured quiet-zone amplitude of the 310 GHz demonstrator CATR.

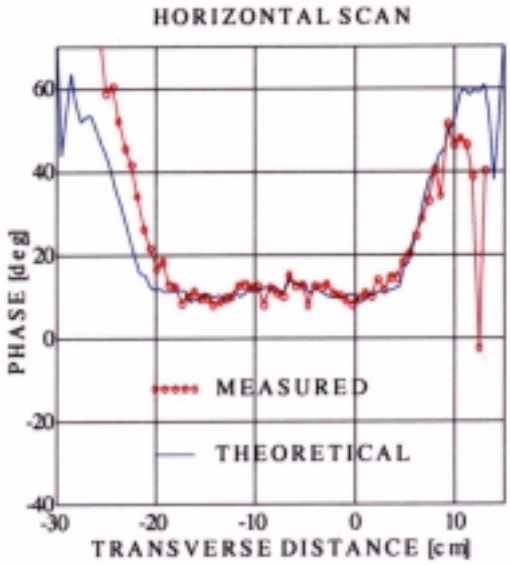

Figure 4. Measured and theoretical phases in horizontal direction.

The peak-to-peak amplitude ripple was found to be about 1 dB and the phase ripple within 10°. The quiet-zone size was found to be approximately 25 cm x 20 cm. With visual inspection of the hologram, it was found out that the narrowest slots at the edges of the hologram had not been properly etched and the hologram had actually a diameter of 52 cm instead of the designed 60 cm. The truncated slots cause the elliptic shape of the quiet-zone seen in Figure 3.

DEVELOPMENT OF HOLOGRAM MANUFACTURING

The quiet-zone of the CATR is required to be larger than the antenna-under-test. To realize a quiet-zone with a diameter of over two meters for testing of two-meter antennas, the hologram has to be 3–4 meters in diameter. The required surface flatness can be achieved by tensioning the hologram into a frame. The required hologram pattern accuracy, i.e., slot width and slot spacing accuracy in the pattern, is estimated to be about 20 and 5 μm for frequencies of 300 and 1000 GHz, respectively. Tapering of the slots, i.e., narrowing of the slots, is needed at the edges of the hologram pattern to reduce edge diffraction. The tapering causes the narrowest slots to be about 20 μm at 600 GHz. These narrow slots are difficult to manufacture. The hologram operation is, however, quite tolerable to localized manufacturing errors.

Several test holograms were manufactured by different manufacturers and these holograms were tested in the MilliLab, Radio Laboratory. The manufacturing methods tested were mainly conventional printed circuit board processes (photolithography) and modifications of these by different exposure methods. Selective metallization of mylar substrate was also tested with laser-induced chemical liquid-phase deposition (LCLD) [3]. The quiet-zone of one of these 20 cm diameter test holograms was measured in three dimensions by taking crosscuts of the quiet-zone field at several locations along the direction of the wave propagation. The resulted 3D scan of the quiet-zone is presented in Figure 5.

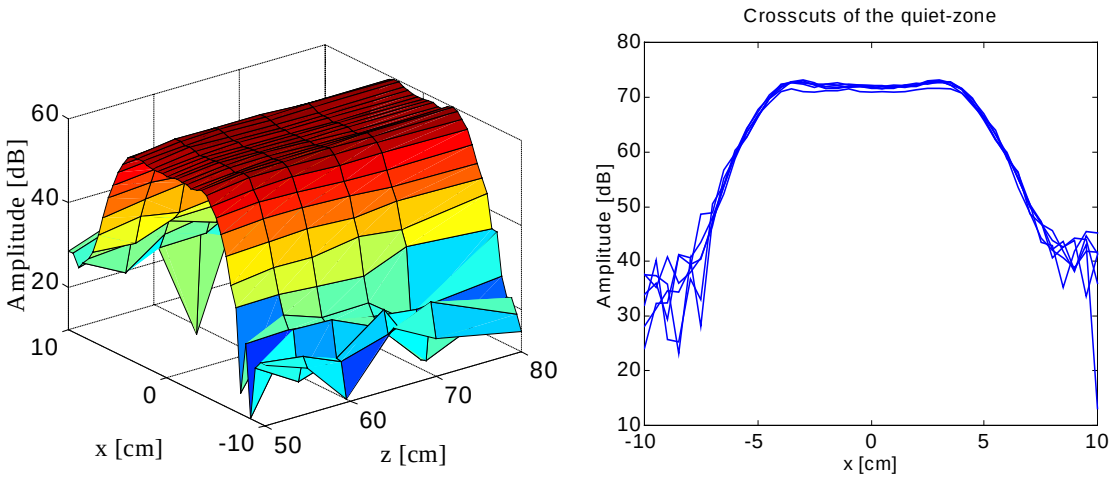

Figure 5. Quiet-zone of a small hologram along the direction of propagation.

Commonly available commercial printed circuit board (PCB) processes are usually limited to the circuit board size of 600 mm x 600 mm and etching of narrow slots at the edges of the area is problematic. In a conventional PCB process phosensitive resist is applied over the metallization on the dielectric substrate. For 310 GHz holograms, the substrate was 75 μm thick Mylar with 17 μm thick copper layer. Photomasks were used for selective

exposure of the photosensitive resist. The copper was removed from the slots by chemical wet etching.

The maximum manufacturable pattern size can be increased with so-called stepwize exposure, where a rectangular area is exposed with a photomask and another photomask is then joined to the previous photomask. The pattern length can be increased by joining several masks to form several meters long pattern strips with fixed width (600–900 mm). These strips could be then joined to form a large hologram. The joining of the photomasks reduces achievable overall pattern accuracy because of the potential misaligning of the photomasks. Photomask distortions may also occur when large masks are used.

The hologram pattern can also be written directly to the photosensitive resist with a laser. The metallization is chemically etched after the laser exposure. The direct laser writing of the pattern is currently seen as the most interesting manufacturing technique for large submillimeter wave holograms. Patterns up to 1.5 m x 6 m can be manufactured in a single piece with line widths down to 40 μm.

To realize large holograms up to 3–4 meters in diameter, the holograms have to be joined from several separately manufactured pieces or custom made large-sized special equipment has to be used. Taping and glueing have been investigated as potential joining methods of hologram pieces. A seam causes a discontinuity to the hologram pattern and acts as a diffraction source. The effect of horizontal and vertical tape strips and seams were tested with 30 cm diameter test holograms. The quiet-zone was scanned in vertical direction in case of the horizontal tape, and vice versa. The tape was 23 μm thick and 5 cm wide mylar tape by Scotch. According to the tests, horizontal seams perpendicular to the hologram slots and to the used polarization affect the hologram quiet-zone the least. Therefore, the hologram should be formed by joining long horizontal strips. Measured effect of vertical and horizontal strips of tape at the center of the hologram are presented in Figure 6 (the curves have been shifted in vertical direction to avoid overlapping). The investigation on the joining techniques of hologram pieces continues and different glueing experiments will be done to find the most suitable joining method.

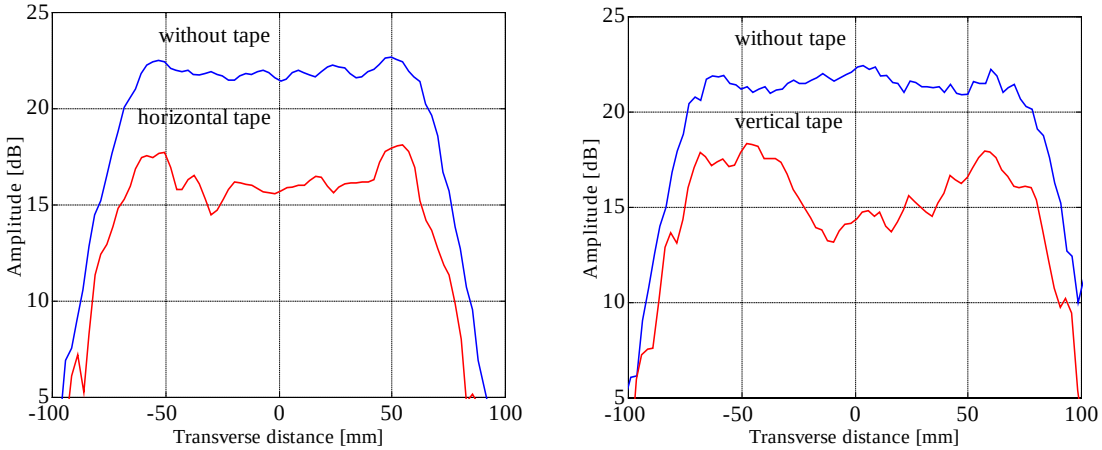

Figure 6. Effect of horizontal and vertical tape to the hologram quiet-zone.

There are some challenges to be met in the manufacturing of large submillimeter wave holograms. The required hologram size cannot be realised without joining several hologram pieces together, which reduces the achievable pattern accuracy and the operational frequency range of the hologram CATR. The tapering of slots to avoid edge diffraction leads to very narrow slots at the edges of the hologram. These narrow slots are difficult to etch.

DUAL REFLECTOR FEED SYSTEM FOR HOLOGRAM CATR

The needed tapering of the slots can be reduced by modifying the electromagnetic field that illuminates the hologram. Narrow slots are difficult to manufacture and the narrow slots increase the polarization sensitivity of the hologram. Furthermore, by modifying the hologram illumination the hologram size efficiency, i.e., the relative size of the quiet-zone compared to the hologram, can also be increased. The hologram illumination can be modified by using a dual reflector feed system (DRFS).

The DRFS modifies the radiated field of a feed horn both in amplitude and phase. The reflectors are shaped non-classical surfaces, that have to be determined numerically. The basic configuration of the DRFS is shown in Figure 7. The reflectors have elliptical rims and the surface shape is hyperbolical type with a focal point behind the reflectors. The sizes of the reflectors needed for the modified hologram illumination are approximately 20–25 % of the hologram diameter. The reflector surfaces can be determined with geometrical optics (GO) based reflector antenna synthesis from the feed horn radiation pattern and from the desired hologram illumination [4]. Ray-tracing based GO synthesis software is currently being developed.

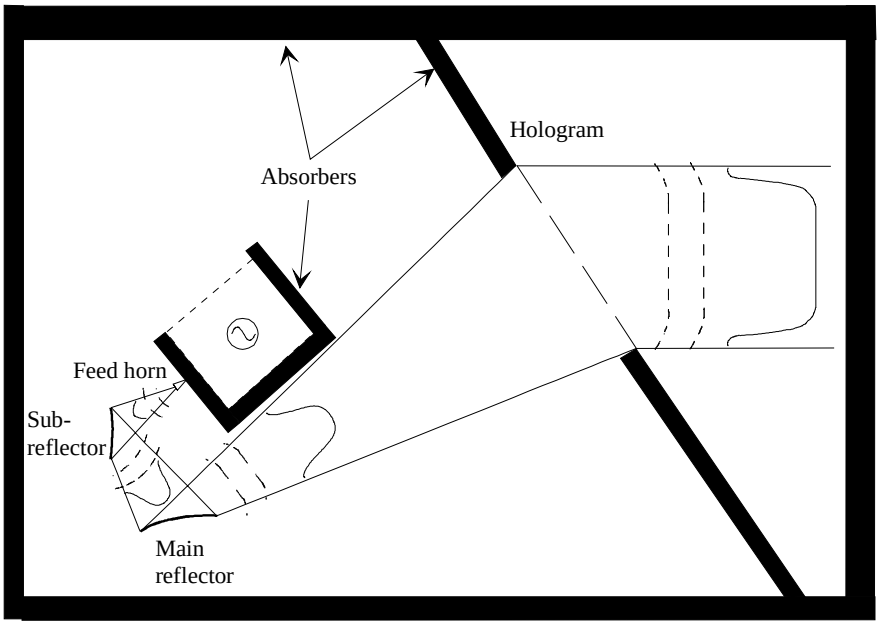

Figure 7. Hologram CATR with a dual reflector feed system.

The main advantages gained by introducing a DRFS to the hologram CATR are the increased relative quiet-zone size and the reduced need for narrow slots at the edges of the hologram pattern. The spill-over of the feed system is also slightly decreased, which increases the dynamic range of the CATR. Also, the cross-polarization level of the hologram CATR will be slightly decreased, because the hologram effective focal length can be increased. The increased focal length results to less curved slots, which reduces cross-polarization caused by the hologram. In Figure 8, the simulation results for a 60 cm hologram are presented. For example, with a third order Butterworth-type flat illumination with amplitude taper of -7 dB at the hologram edges, the quiet-zone diameter of a 60 cm hologram increases by a third compared to a hologram illuminated directly with a feed horn.

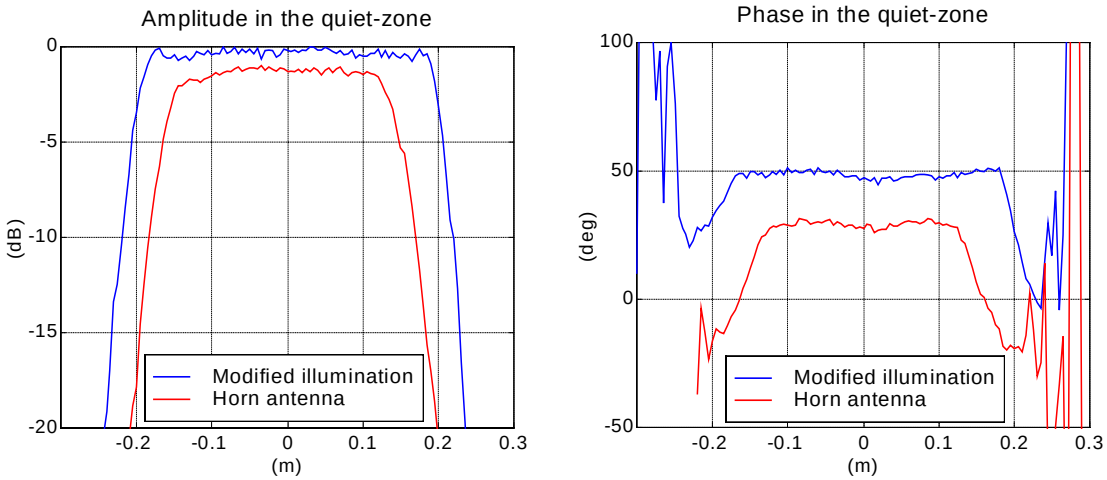

Figure 8. The increase in the quiet-zone size with modified hologram illumination.

The improved hologram illumination by the DRFS also simplifies the hologram manufacturing by widening the slots near the hologram edges. The hologram pattern slot spacings and widths with a simple Gaussian illumination, and with a more optimized illumination are presented in Figure 9. The main disadvantages of introducing a DRFS to the hologram CATR are the increased cost of the CATR and the cross-polarization caused by the reflectors itself in the DRFS.

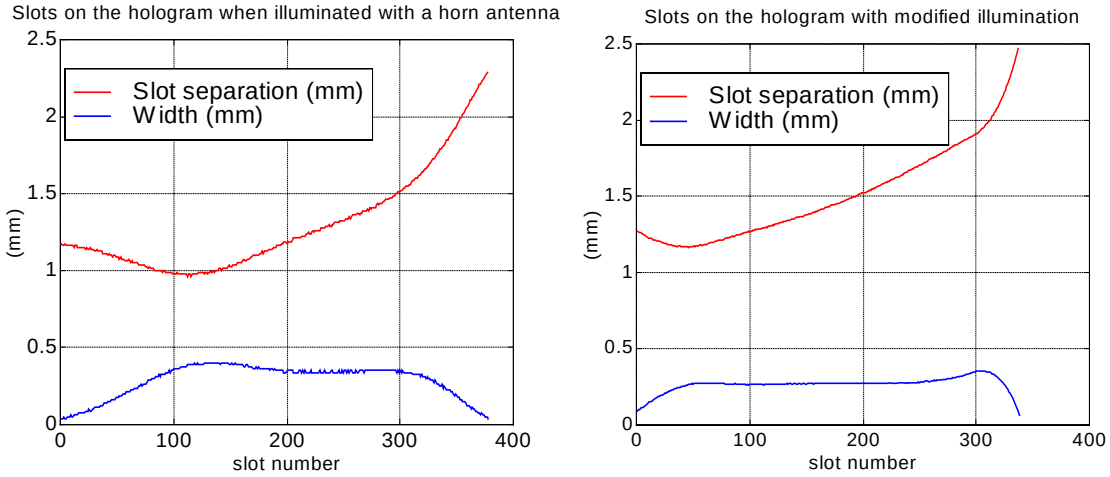

Figure 9. Hologram slot separations and widths with Gaussian and modified illumination.

CONCLUSIONS

The hologram CATR is a potential method for testing large submillimeter wave satellite antennas. The feasibility of the CATR has been demonstrated with quiet-zone testing of a 60 cm diameter hologram for 310 GHz. Progress in the hologram manufacturing is presented here, but some manufacturing challenges still have to be met before practical large-sized compact antenna ranges based on the hologram can be realized. The continuing research on the hologram manufacturing has been presented. The hologram performance and the manufacturability of the hologram can be improved with a dual reflector feed system (DRFS). The DRFS modifies the hologram illumination, which increases the achievable quiet-zone size of the hologram. The reflectors of the DRFS are shaped non-classical surfaces. The surfaces can be determined with geometrical optics based reflector synthesis.

ACKNOWLEDGEMENTS

The authors are grateful to Mr. Lauri Laakso and Mr. Eino Kahra for their valuable help with mechanical aspects of the hologram testing. This work was supported by ESA/ESTEC (Contract No. 13096/98/NL/SB), Tekes (Finland) and the Academy of Finland.

REFERENCES

[1] Foster, P. R., Martin, D., Parini, C., Räisänen, A., Ala-Laurinaho, J., Hirvonen, T., Lehto, A., Sehm, T., Tuovinen, J., Jensen, F. , Pontoppidan, K., *Mmwave antenna testing techiniques - Phase 2,* MAAS Report 304, Issue No. 2, ESTEC Contract No. 11641/95/NL/PB(SC), December 1996.

[2] Ala-Laurinaho, J., Hirvonen, T., Räisänen, A., Optimization of a submillimeter wave hologram CATR, *Proceedings of the 1997 IEEE AP-S International Symposium*,1997, pp. 136–139.

[3] Kordás, K., Bali, K., Leppävuori, S., Uusimäki, A., Nánai, L., Laser direct writing of copper on polyimide surfaces from solution, *Applied Surface Science*, Vol. 154–155, 2000, pp. 399–404.

[4] Kildal, P-S., Synthesis of multireflector antennas by kinematic and dynamic ray tracing, *IEEE Transactions on Antennas and Propagation*, Vol. 38, No. 10, 1990, pp. 1587–1599.

Optical Characterization of Absorbing Coatings for Sub-millimeter Radiation

T.O. Klaassen[1], M.C. Diez[1†], J.H. Blok[1], C. Smorenburg[2], K.J. Wildeman[3], G. Jakob[4],

[1]Department of Applied Physics, Delft University of Technology, The Netherlands, [2]TNO Institute of Applied Physics, Delft, The Netherlands, [3]SRON, Groningen, The Netherlands, [4]Max-Planck-Institut für Extraterrestrische Physik, Garching, Germany.
[†]Now at Centro Astronómico de Yebes, Observatorio Astronómico Nacional, Guadalajara, Spain
Information: T.O. Klaassen, P.O. Box 5046, 2600 Delft, The Netherlands, T.O.Klaassen@tnw.tudelft.nl

Abstract. Experimental results are presented on the specular and diffuse reflectance (BRDF) of a variety of surfaces that can be used to absorb sub-millimeter radiation. Although the emphasis of this study is on the development and optical characterization of black absorbing coatings, intended for use in the spectrometers aboard the FIRST satellite, also some convenient materials for laboratory use are discussed. The here presented data have been collected room temperature

Introduction. The optical properties of the coatings have been studied in the 0.1 - 0.9 mm wavelength region in order to comply with the wavelength bands covered by the HIFI and PACS spectrometers. Optical characterization has been performed using monochromatic light at selected wavelengths across the 100-900 micron wavelength region. (96.5µm, 118.8µm, 184.3µm, 496µm and 889µm) created by an optically pumped far-infrared laser.

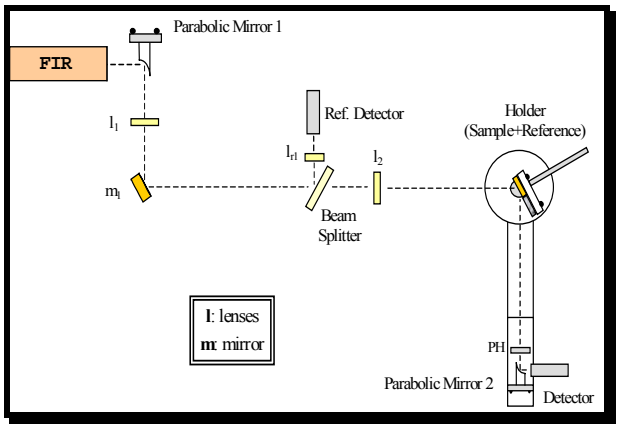

Fig.1 *Experimental set-up*

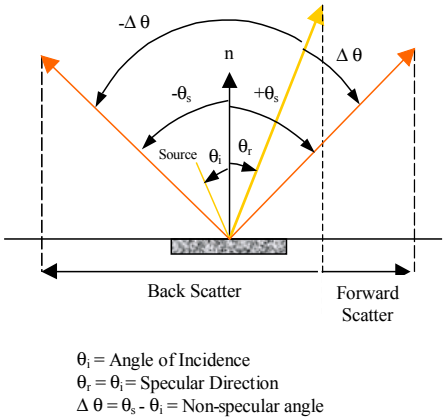

Fig.2 *Angular relations in the optical plane*

Measurements on samples for a range of directions of incident and reflected light and for different polarization directions have been done. The influence of variations in shape and intensity of the laser beam has been eliminated by comparing all samples with reference samples that have been characterized accurately. Experiments have been performed at room temperature, employing the experimental setup shown in Fig. 1. In Fig. 2 the definition of various angles in the optical plane is given. The Bi-directional Reflectance Distribution Function (BRDF), used to describe the scattering properties of surfaces, is defined as the reflectance per unit projected detector solid angle as a function of the azimuthal coordinates θ and ϕ. It is given in units of inverse steradians (sr^{-1}) and is usually measured in the plane of incidence (ϕ=180°) versus the non-specular angle $\Delta\theta$,

$$BRDF(\Delta\theta,\lambda,\theta_i)=\frac{P_s(\Delta\theta,\lambda,\theta_i)}{P_o(\lambda,\theta_i)\Omega\cos\theta_s}$$

Here P_s is the power, diffusely scattered by the surface, in the direction θ_s, and P_o the total incoming optical power at the sample. The factor $\Omega\cos\theta_s$ (in general $\Omega \approx 8\times10^{-3}$ sr in our experimental set-up) is the projected detector solid angle. For a non-absorbing perfect diffuse scatterer, a so-called Lambertian surface, the BRDF is independent of direction and equals π^{-1}. A reference sample basically consists of a gold-coated rough surface, acting as a near Lambertian reflector, accurately calibrated against the total reflection of a gold-coated mirror.
The near Gaussian like sub-millimeter beam is shaped such that the waist (with a $1/e^2$ diameter of 10-15 mm) is situated at the sample surface in to assure a well-defined angle of incidence of the light. To average out the effects of the non-perfect "random roughness" of the coating surfaces, especially important for very rough surfaces, the samples are rotated around their surface normal at a speed of about 300 rpm. The scattered light is detected with a (room temperature) 2 mm diameter pyroelectric detector (Eltec) with homemade sensitive read-out electronics [1].

Experimental results.
Commercial absorbers. To allow for a comparison with the coatings developed for FIRST, we have also studied the scattering characteristics of two commercially available materials used as (sub-) millimeter absorbers. Marconi LAO 5, a carbon loaded soft open foam microwave absorber, and (Tessalating Terahertz) RAM from Thomas Keating Ltd., injection molded 25mm squares with sharp pyramidal surface formed in conducting plastic. In Fig. 3 the specular reflection of both samples is shown at 4 different wavelengths; the reflection increases with increasing wavelength and angle of incidence. In Fig. 4 the BRDF of LAO 5 is shown for 3 wavelengths. Its value is seen to increase again with wavelength and angle of incidence. Evidence of specular reflection is observed, that is, a peak develops for $\Delta\theta = 0$. The BRDF value of 0.02-0.04 means a Total Hemispherical Reflection (THR) of 6-12% (-12- -9 dB).

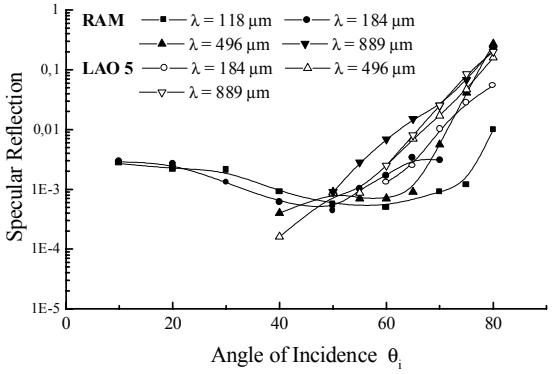

Fig. 3. *Specular reflection of RAM and LAO 5*

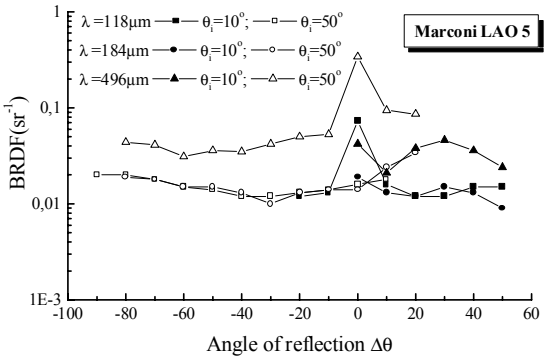

Figure 4. *BRDF of LAO 5*

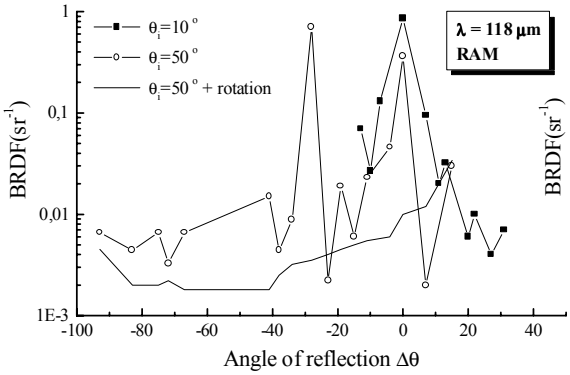

Fig. 5 *BRDF of RAM at 118μm*

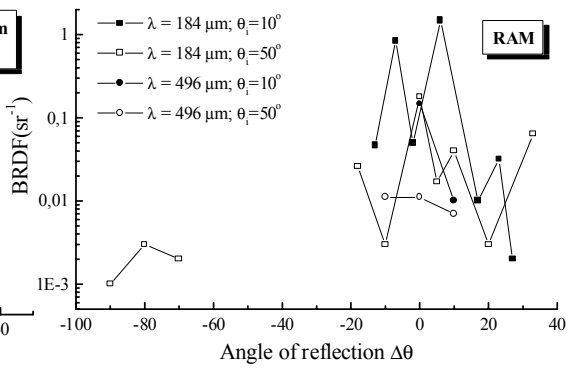

Fig. 6 *BRDF of RAM*

The BRDF data of RAM in Fig.5 and 6 show, in contrast to those of LAO 5, sharp peaks in the angular dependence. These reflections result from the regular 1x1 mm^2 structure of the sharp needles at the surface that acts as a reflection grating. These grating reflections are observed only when the optical plane is parallel to the needle rows. For other directions, or if the sample is rotated around it's surface normal, these peaks disappear, and quite a low BRDF value is observed, resulting in a THR of about –20dB. This grating effect is similar to that observed for the pyramidal structured absorber reported earlier [2].

2. MPI coatings for PACS

In the table, the different coatings developed by MPI are given. They are fabricated on an Aluminium substrate, first coated with a thin layer of Nextel Primer (5523:5524; 10:1) diluted with Nextel Thinner 8061, and then coated with either DeSoto Gunship Black (828X310:910X376; 1:1) or Nextel Suede Coating (3101:6018; 8:1). Part of the samples also contains 100μm size SiC grains that have been applied immediately after the DeSoto or Suede coating. The samples have been dried at 60°C for 1 hour. (In view of the thickness of MPI 10, possibly the last two layers are absent.)

Sample	Thickness	Layer sequence
MPI 3	0.15 mm	Primer-Suede-Suede
MPI 4	0.20 mm	Primer-Suede-Suede-Suede
MPI 9	0.50 mm	Primer-Suede-Sic grains-Suede
MPI 10*	0.55 mm	Primer-Suede-Sic grains-Suede- Suede-Suede
MPI 7	0.15 mm	Primer-DeSoto-DeSoto
MPI 8	0.20 mm	Primer-DeSoto-DeSoto-DeSoto
MPI 5	0.50 mm	Primer-DeSoto-SiCgrains-DeSoto
MPI 6	0.90 mm	Primer-DeSoto-SiCgrains-DeSoto-SiCgrains-DeSoto

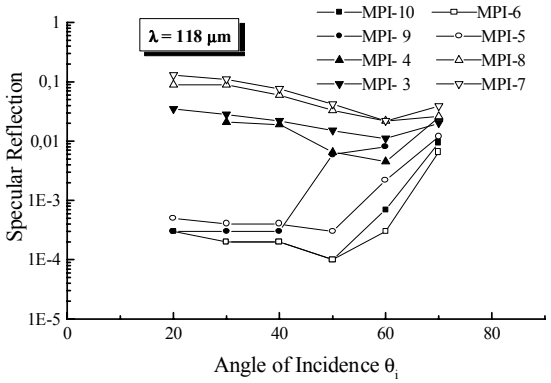

Fig. 7 *Specular reflection of MPI coatings*

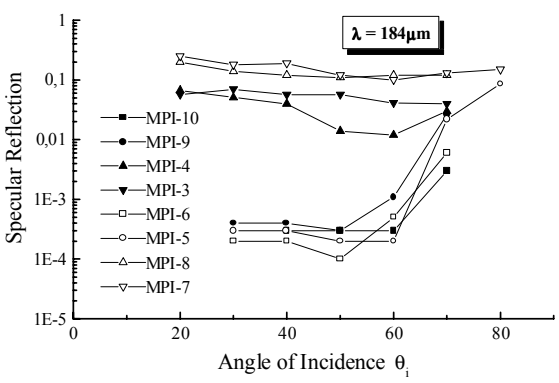

Fig. 8 *Specular reflection MPI*

The data on specular reflection in Fig.'s 7 and 8 clearly demonstrate the influence of the SiC grains on the scattering properties; their presence is crucial to suppress the specular reflection. Although the SiC itself does not contribute to the absorption, it causes multiple reflections at the rough surface and inside the layer, and thereby increases the effective absorption.

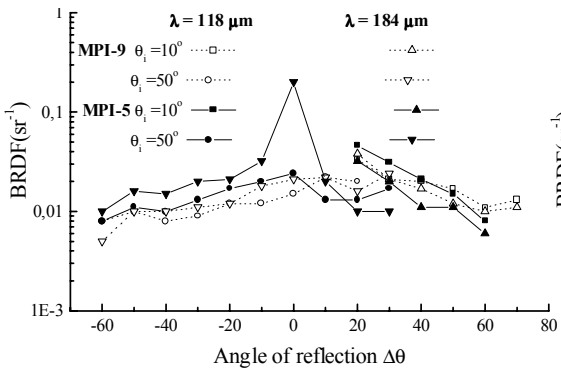

Fig. 9 *BRDF of single SiC layer MPI*

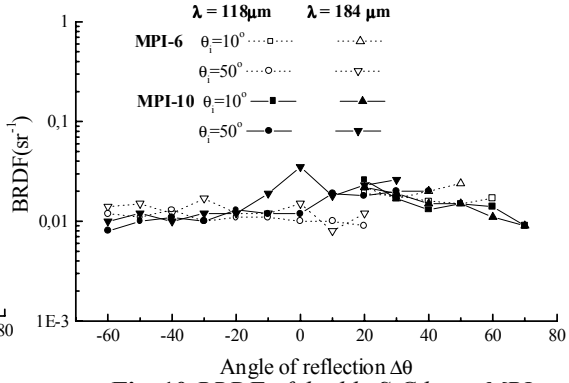

Fig. 10 *BRDF of double SiC layer MPI*

The experimental data in Fig.'s 7-10 indicate that both specular reflection and BRDF increase with wavelength, angle of incidence and diminishing surface roughness and thickness. The Suede samples show slightly better absorbing characteristics, possibly due to a larger absorption coefficient (see later). The approximate value of the BRDF of the SiC loaded coatings is 0.02 sr^{-1}, corresponding to a THR of about 6% (–12dB) Further developments of these coatings are in progress.

3. Delft/SRON coatings for HIFI

Also these coatings have been fabricated on Aluminium substrates. First a thin layer of Stycast 2850 FT + 24 LV Catalyst is applied and subsequently a mixture of Stycast 2850 FT + 24 LV Catalyst and SiC grains of various sizes. The samples are then dried for 2 hours at 60° C. Coatings have been made with SiC grain sizes of 125µm, 250 µm, 500 µm, 750 µm and 1000 µm respectively. Because of the much longer upper wavelength of HIFI, these coatings have been studied for wavelengths up to 889 µm.

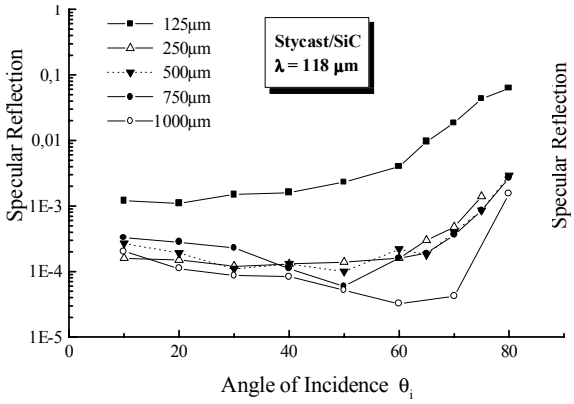

Fig. 11 *Specular reflection at 118 µm*

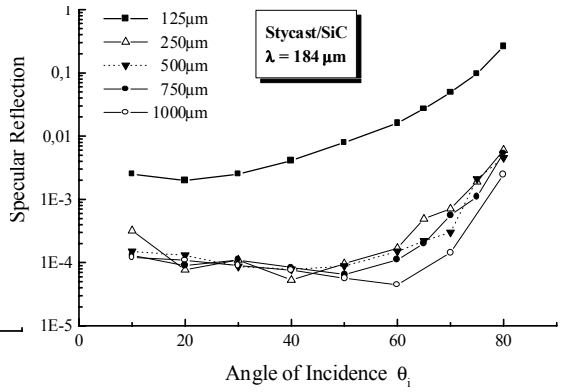

Fig. 12 *Specular reflection at 184 µm*

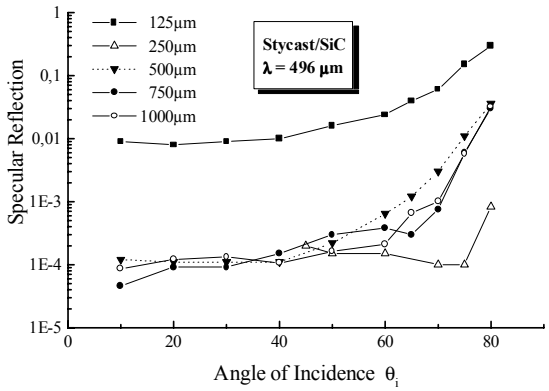

Fig. 13 *Specular reflection at 496µm*

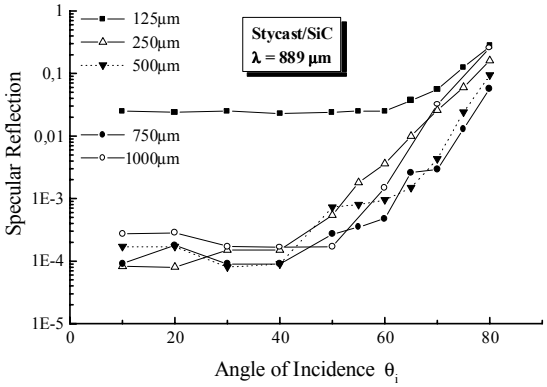

Fig. 14.*Specular reflection at 889 µm*

Similar to the findings for the MPI coatings, also for this series of coatings the specular reflection increases with increasing wavelength, angle of incidence and

diminishing surface roughness, as is clearly visible in Fig.'s 11-14. Therefore, to ensure a minimum (specular) reflection at the longest wavelength, the coating containing 1000 μm SiC grains is preferable. Properties of that coating are:

Optimum weight ratio Stycast/SiC	1:4
Coating thickness	2.3 (3) mm
Mass of coating (ex substrate)	0.34 (3) gram/cm^2

This intimate relation between scattering intensity, wavelength and surface roughness is also observed in the BRDF data. A concise summary of those data is shown in Fig.'s 15-18, with emphasis on the properties of the 1000 μm SiC coating.

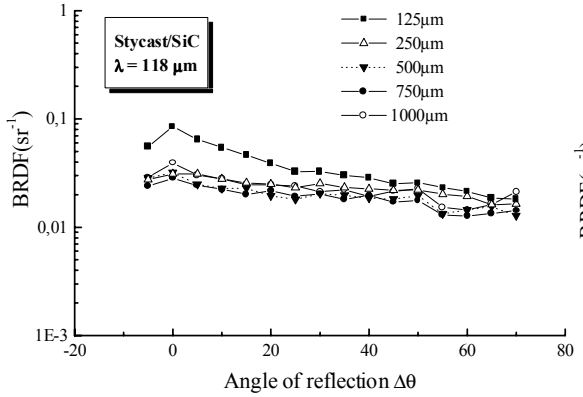

Fig. 15 *BRDF of Stycast/SiC samples at 118μm*

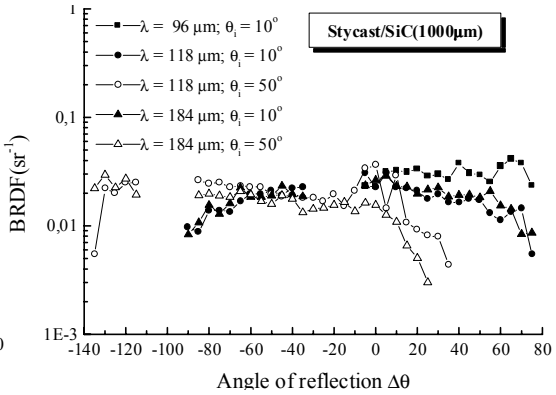

Fig. 16. *BRDF of 1000 μm sample at 3 wavelengths*

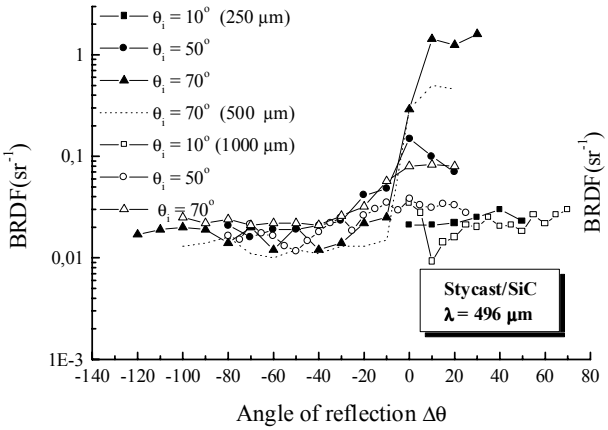

Fig. 17 *BRDF of Stycast/SiC samples at 496 μm*

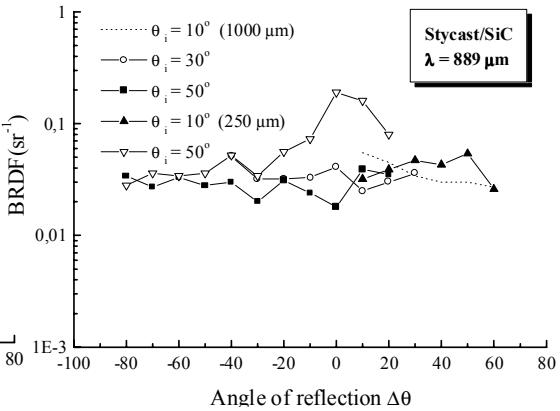

Fig. 18 *BRDF of Stycast/SiC at 889 μm*

The nearly wavelength, polarization [2] and directional independent - value of the BRDF (also for out of plane scattering [2]) of this coating is about 0.02. That means a THR of 6%, i.e. –12dB. This number agrees very well with the measured emissivity e = 0.93(2) at λ = 435 μm and T = 70K [2].

The disadvantage of this very rough surface however is two-fold. First of all, because of the large grain size, the coating layer is rather thick. Secondly, in those cases where the optical beam has a relatively small waist at the coating surface, the scattering is observed to be not random anymore, due to the limited number of SiC grains (size ≈ 1mm!) within the illuminated area. Strongly angular dependent variations, up to a factor 5, in the reflected intensity have been observed. In order to measure a representative and reproducible value for the BRDF, the samples have to be rotated around their surface normal to measure an "averaged" reflection signal. For critical applications, such as beam dumps, these unpredictable variations may be harmful. Therefore, in the near future it will be investigated whether the coating with 500μm SiC grains, which shows this effect much less, can serve, after further optimization, as an alternative.

Absorption coefficients. The wavelength dependent absorption coefficients of some of the materials used for the coatings discussed in this paper have been derived from transmission through thin layers, not loaded with SiC grains. In the table the values are given in cm^{-1}. Those for DeSoto and Suede have been estimated from reflection data on unloaded samples.

Material	**118 μm**	**184 μm**	**496 μm**	**889 μm**
Stycast 2850FT	89	41	11.5	7.8
DeSoto	65	45		
Suede	100	70		
RAM	100	62	22	19

Table: Absorption coefficients(cm^{-1})

The increase of absorption coefficient with decreasing wavelength is in accordance with data reported by Halpern et al [3] on Stycast 2850FT for wavelengths above 300 μm , although their values are somewhat lower than ours. It is interesting to observe that the large decrease of the absorption coefficient from 118 μm towards 889 μm does not lead to a similar increase of the BRDF values of the Stycast/SiC (1000μm) sample. It should be mentioned that the SiC crystalline grains only show an absorption band near a wavelength of 12 μm; in the sub-millimeter range no absorption occurs. The nearly wavelength independent BRDF value shows that the absorption processes in such a rough layer is due to a complicated interplay between absorption of the binder material and scattering of the grains. In the very near future the scattering properties of these coatings at cryogenic temperatures will be studied. In view of the small sensitivity of the BRDF for changes in the absorption coefficient,

it is expected that the decrease of the absorption coefficient towards low temperature, as reported in [3], will not strongly influence the BRDF values.

Qualification test. First qualification tests of the 1000μm SiC coating have been performed at SRON; these included:

- Thermal shock: cool-down from 294 K to 88 K in 15 min + subsequent heating to 300 K
- Thermal cycling: 5x cool-down from 290 K to 88 K in 60 min + increase of temperature gradient by attaching conducting straps to the sample
- Extended bake out: T = 80 C at p < 1mbar for 48 hours.
- Vibration test: T = 70 K perpendicular to surface; random and sinus up to g=30

In all cases, no flakes or loose grains, no blistering coating, no bending of sample and no colour changes were observed. The adhesion test gives an averaged tensile strength of 14.6N/mm^2, not influenced by the above mentioned treatments.

Still to be performed: out gassing and influence of treatments on optical properties.

Possible surfaces for a black body calibration source. Requirements for a black body calibration source for HIFI are: 2 cm^2 emission area at T = 100K with a maximum electric power of 2 mW. The emitting surface must have an optimum emissivity and a minimum temperature gradient.

Following the results of study of the optical properties of various types of absorbing surfaces, so far three types of surfaces could qualify.

1. A standard SiC/Stycast coating on an Aluminium substrate.

The heater and temperature sensor(s) can be placed on the back side of the Al substrate.

For the 1000μm SiC coating surface at T = 77K and λ = 435 μm, the emissivity e=0.93; emissivities of the 250 μm and 500 μm coating are expected to be about the same.

Further specifications for the 1000 μm coating at T = 100K are:

Mass (excluding the Al substrate) :		0.34 gram/cm^2.
Heat capacity:		43 mJ/cm^{2}K
Thermal conductivity:	(low purity) SiC :	1 W/cmK
	Aluminium:	3 W/cmK
	Stycast 2850 FT:	0.014W/cmK @300K

2. Aluminium foam (ERG Materials and Aerospace Corp., Oakland, CA, USA).
40 pores per inch (ppi) coated with Stycast 2850 FT + 24 LV Catalyst.

In Figure 19 the BRDF data of this surface at λ = 496 μm are given. From the average BRDF of about 0.06 an emissivity of approximately 0.80 is calculated. The advantage of this material is that only 1 cm^2 is needed because both sides will emit equally well. Heater and temperature monitors could be attached to an aluminium ring around the (approximately 4 mm thick) outer contour of the surface; the excellent heat conduction of the aluminium grid will establish a good temperature homogeneity across the sample.

Moreover a finite sub-millimetre transmission through the sample is present. Transmission data at different wavelengths show that the overall transmission of a 4 mm thick sample is in the range of 1%.
This finite transmission might be profitable in establishing a homogeneous optical field distribution, if the emitter is placed inside an integrating sphere.

General properties of such a surface:
Density of foam: 8-10 %
Al filament diameter: 0.11 mm
Mass: 0.29 gram/cm^2
Mass of foam + Stycast: 0.87gram/cm^2
e ≈ 0.80 @300K

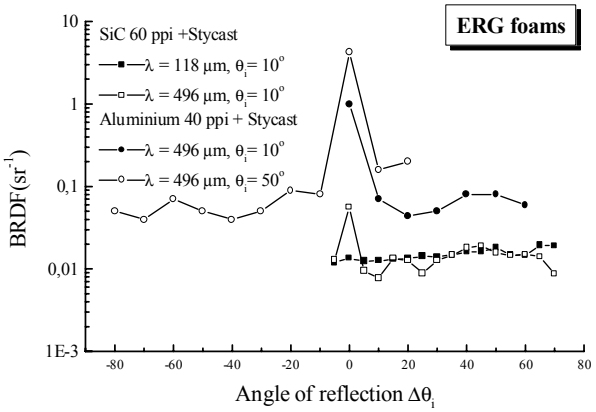

Fig. 19 *BRDF of Stycast coated foams*

3. SiC foam (ERG), 60 ppi, with relative density of 12-14%, coated with Stycast 2850 FT.
As can be seen from the BRDF data in Figure 19, the emissivity of this material will be quite the same as found for the SiC/Stycast home made coatings, i.e. e ≈ 0.93. These samples with 3.2 mm thickness, show an sub-millimeter transmission of the order of ≤ 10^{-3}. The incorporation of heater and temperature sensors in such a material however, might cause some problems.
The properties at 100 K are:

Mass of foam	0.18	gram/cm^2
Mass of foam + Stycast	0.25	gram/cm^2
Thermal conductivity foam:	4	W/cm^{2}K
Specific heat of foam	18	mJ/cm^{2}K
Specific heat foam + Stycast:	78	mJ/cm^{2}K

Conclusions
A number of home made absorbing surfaces have been developed that are suitable as sub-millimeter absorbers for the spectrometers aboard the FIRST satellite. In order to achieve a sufficient suppression of the specular reflection, the absorbing binder materials such as DeSoto, Suede or Stycast 2850FT, have to be mixed with (SiC) grains to produce a rough surface.
The size of the SiC grains should be about equal to the wavelength region of interest. Typical BRDF values are 0.02 sr$^{-1.}$ The corresponding Total Hemispherical Reflection equals 6%, or –12dB. Because of the low specular reflection under non-grazing incidence, the occurrence of standing wave patterns will be effectively cancelled.

These coatings might also be employed as emitting surfaces for black body radiation sources. Alternatively, some rigid foam materials, coated with for instance Stycast 2850FT, could also be useful for that purpose.

References

[1]. R.N. Schouten, A new amplifier design for fast low-noise far-infrared detectors using a pyroelectric element, Meas. Sci. Technol. 9(1998)686-91.
[2]. M.C. Diez, T.O. Klaassen, C. Smorenburg, V. Kirschner, K.J. Wildeman, Reflectance measurements on sub-millimeter absorbing coatings for HIFI, SPIE Vol 4013(1999)122
[3]. M. Halpern, H.P. Gush, E. Wishword, V. De Cosmo, Far infrared transmission of dielectrics at cryogenic and room temperatures, Appl. Optics. 25(1986)565.

Acknowledgements. This work is supported by The Netherlands Agency for Aerospace Programs (NIVR) under contract NRT nr. 2901 TU.

Design and Fabrication of Quartz Vacuum Windows with Matching Layers for Millimeter-Wave Receivers

Daniel Koller, A. R. Kerr, G. A. Ediss, and D. Boyd
National Radio Astronomy Observatory*
Charlottesville, VA 22903

Abstract

Sensitive radio receivers operating at frequencies above approximately 100 GHz require the use of cryogenic detectors, often SIS mixers, cooled to liquid helium temperatures. A vacuum window is required to couple the radiant energy through the chamber walls to the detector element with as little loss as possible. While seemingly simple to make, the optimization of windows for high transparency and low leak rate is a non-trivial problem requiring the construction of multi-layer dielectric structures.

The Atacama Large Millimeter Array (ALMA) telescope, to be built in Chile, will require over 600 vacuum windows covering ten frequency bands. In support of ALMA and its own in-house development needs, NRAO has developed a number of crystal quartz vacuum windows utilizing Zitex, Goretex, Teflon and other plastic anti-reflection coatings to improve the window's overall transmission within specific bands. The design, fabrication details and testing of some of these windows are discussed.

Introduction

For many years, NRAO has used plastic film vacuum windows on its millimeter-wave receivers [1]. The most recent version of this window has the plastic film vacuum barrier supported by a 0.125″-thick sheet of open-cell expanded PTFE. Such windows offer very low absorption over a very wide frequency range, but are easily damaged and have a significant leak rate for air, water vapor, and helium. Cryogenic receivers using similar windows on the 12 Meter Telescope became noticeably less sensitive after one or two months of continuous operation, and required periodic warming up and evacuation to remove condensed air and water. The high permeability to helium precludes the use of a helium leak detector on receivers with such windows. For these reasons, plastic film vacuum windows are considered inappropriate for use on ALMA receivers.

To develop a more robust window with negligible air or helium leakage, we decided in 1996 to explore the use of crystal quartz with various anti-reflection layers to reduce the insertion loss within a desired frequency band. This report describes the design and construction of several crystal quartz multi-layer windows. Some of these windows are now in use in VLBA receivers, and others are intended for use in receivers for testing the ALMA antennas and for production testing of SIS mixers for ALMA.

The Choice of Crystal Quartz

Crystaline quartz has very low loss at millimeter wavelengths and high physical strength [2-6]. The z-orientation was selected to minimize the effects of birefringence and so have minimal effect on the

* The National Radio Astronomy Observatory is a facility of the National Science Foundation operated under cooperative agreement by Associated Universities, Inc.

polarization of the incoming beam. With optically polished surfaces, a quartz window can be sealed to the cryostat using a standard o-ring. The minimum thickness of the quartz plate is determined by the desired clear aperture of the window and the safety factor, as described in Appendix 1. However, the relatively high dielectric constant, $\varepsilon_r = 4.45$ [2-6], causes large interference fringes to be generated so a quartz window requires matching layers to reduce the insertion loss. For narrow-band operation, a quarter-wave layer is needed with $\varepsilon_r = (\varepsilon_{r,\,quartz})^{0.5}$. To achieve wider bandwidth, multiple matching layers can be used if it is possible to find materials with the desired dielectric constant and low loss. The three- and five-layer windows described below use PTFE, high density polyethylene (HDPE), and expanded PTFE as matching layers.

Three-Layer PTFE/Z-Quartz/PTFE Window

The three-layer Teflon/z-Quartz/Teflon windows described here are currently in use on the VLBA receivers for the 80-96 GHz band. These windows consist of a z-cut crystal quartz plate, 0.2260″ thick, as determined by the desired 3.5″ clear aperture as shown in Figure 7 of Appendix 1. Each face is covered with a Teflon layer 0.0220″ thick. Teflon, with a dielectric constant of 2.1 [7], is a nearly Ideal anti-reflection layer. The construction is described in Appendix 2.

The goal was to keep the return loss of the window >20 dB and the absorption loss < 0.05 dB, for a total insertion loss < 0.1 dB, over the widest possible range within the WR-10 waveguide band (75-110 GHz), including the 80-96 GHz VLBA band. Note that a window at room temperature with an insertion loss of 0.1 dB adds approximately 7 K to the noise temperature of a low noise receiver, assuming all power entering the receiver by reflection or scattering from the window originates at room temperature. The microwave circuit analysis program MMICAD [8] was used to simulate the window and optimize the thickness of Teflon and quartz for maximum transmission within the desired band. The resulting design allows machining errors of ±0.0002″ in the Teflon thickness without compromising the window specifications. A model calculation is shown in Figure 1.

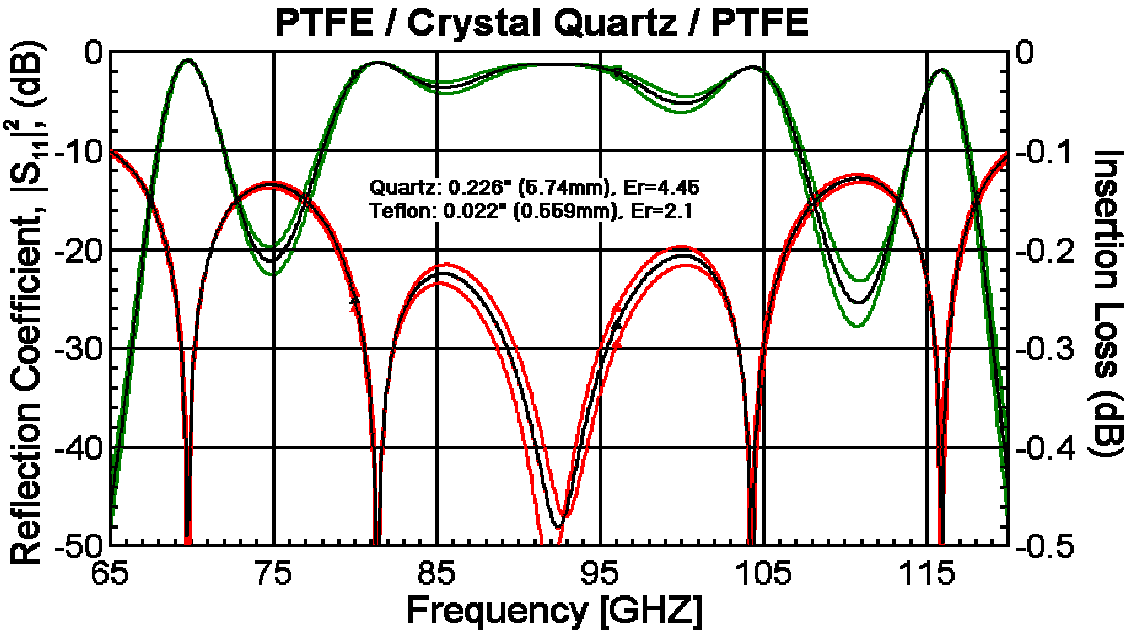

Figure 1. MMICAD model of a Teflon / quartz / Teflon window for the VLBA. Upper trace is insertion loss (right scale), and lower curve is reflection coefficient. Markers denote the edges of the 80-96 GHz VLBA band. Adjacent lines show the effect of changing the Teflon thickness by ±0.0002″, indicating the design tolerance to machining errors. Absorption of the glue is included.

The calculations in all of the figures shown here include the attenuation due to approximately 0.0002″ of EpoTek 301-2 epoxy used to bond the plastic to the quartz (see Appendix 4). Optical properties of the glue were measured on a Fourier Transform Infrared Spectrometer (FTS) from 300 GHz to approximately 1 THz and extrapolated to lower frequencies [9]. The dielectric constant of the epoxy is 2.8, and the attenuation is best fit by the expression

$$\alpha\ (\mathrm{dB}/\mathrm{m}) = 2.10\, f + 0.00571\, f^2, \ldots \text{where } f \text{ is the frequency in GHz.}$$

Measurements of the loss of a window with useful frequency resolution and amplitude accuracy are very difficult to obtain at millimeter wavelengths. Short of measuring the window one frequency at a time in front of a low-noise receiver, the best results have been obtained with a time-domain-gated vector network analyzer, as described in [10]. Results are shown in Figure 2 with the model calculation for comparison. Attenuation of the quartz and Teflon were taken from [2] and [7]. Within the ±0.1 dB accuracy of the measurements, the window performs as predicted. The quartz for this window was 0.22590″ thick, and the Teflon faces were 0.0220″ thick.

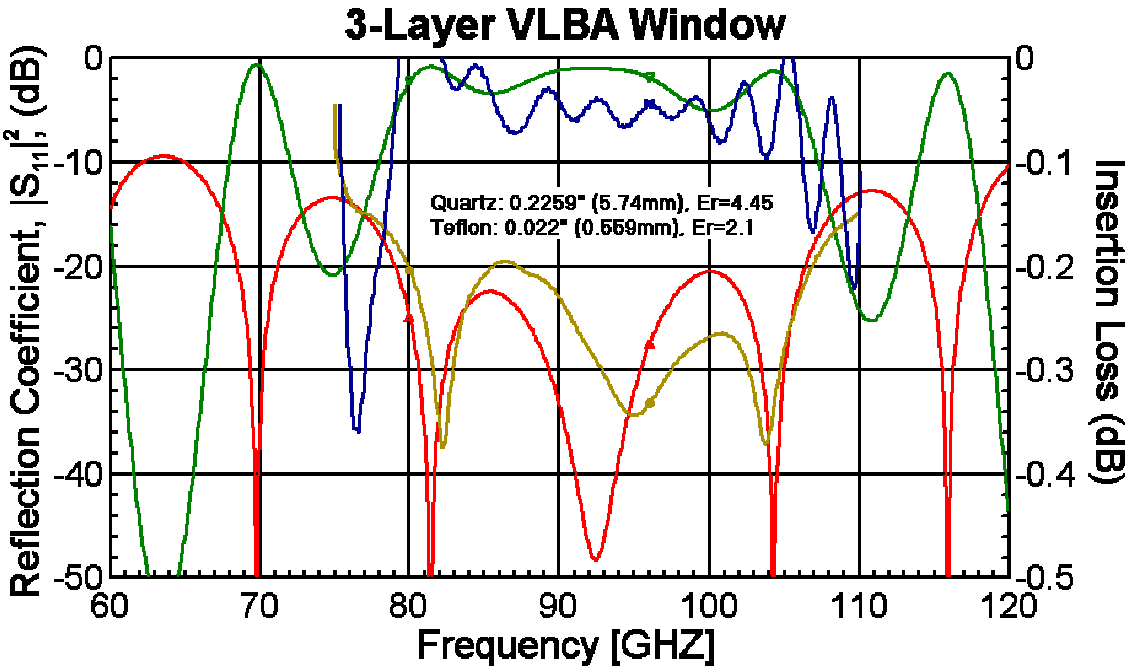

Figure 2. Predicted reflection coefficient and insertion loss of VLBA window "SN6," along with actual performance recorded on the HP 8510 network analyzer, as described in [10].

The first three-layer windows had the Teflon AR layers completely covering both faces of the quartz. The vacuum seal was made by an o-ring in contact with the machined Teflon. Reports from the VLBA in February 2000 indicated that the windows had good vacuum integrity when delivered, but after six months to a year began to leak, sometimes significantly. Turned over in their frames, the windows again worked initially, but eventually began to leak again. It was determined that the leaks were due to the roughness of the machined Teflon surfaces; apparently vacuum grease would allow a good seal at first, but would gradually flow under pressure, opening small leaks. To remedy the problem, 0.55″ was removed from the diameter of the Teflon, leaving the quartz exposed in a 0.275″ ring at the edge of the window. The quartz produces a superior seal against the o-ring, as verified with a helium leak detector.

ALMA Evaluation Receiver

A three-layer window has recently been completed for 86-100 GHz to be used in the ALMA antenna test receiver. The window consists of a 0.226″ thick quartz plate, 3.75″ in diameter, faced with Teflon sheets, 0.023″ thick. The performance of this window, as measured on the HP 8510 network analyzer, is shown in Figure 3 and compared with the model calculations. Note that the bandwidth exceeds the requirements of the evaluation receiver, but not that of ALMA band 3 (89-116 GHz[1]). In order to cover the ALMA bands, additional matching layers are required.

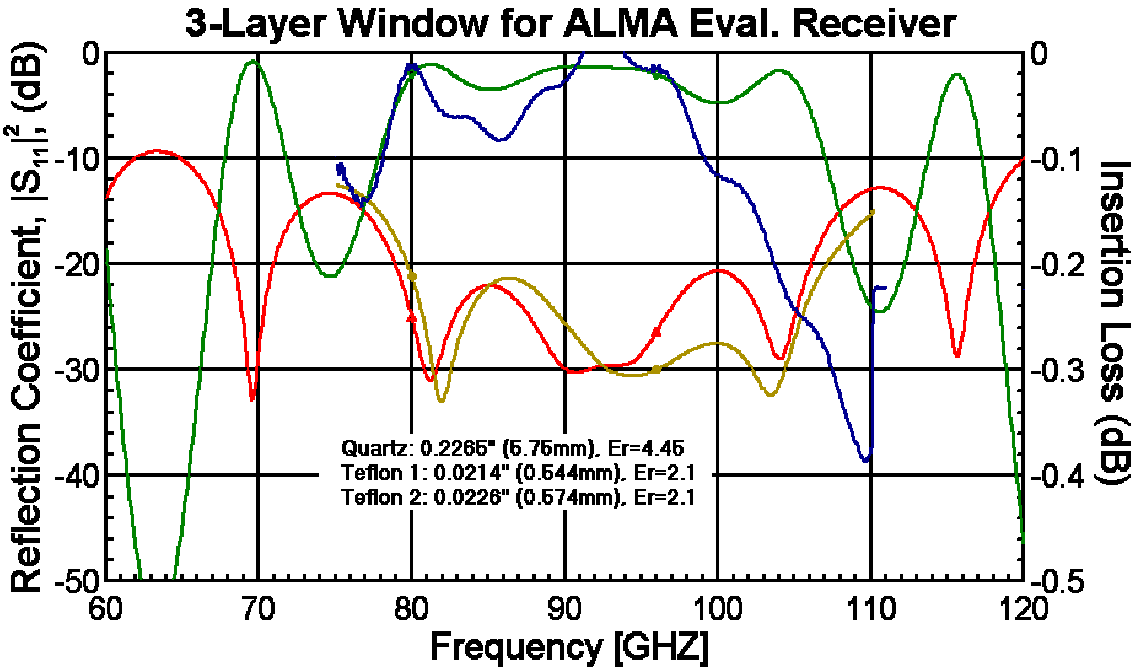

Figure 3. Simulated and measured results for a three-layer Teflon / quartz / Teflon window for the ALMA evaluation receiver band 3 (86-100 GHz). The quartz is 0.2265″ thick. Teflon AR layers are 0.0214″ and 0.0226″ thick, the latter having been made thicker to compensate for a thinner than desired layer 1. The premature increase in measured absorption above approximately 100 GHz may be instrumental.

Five-Layer Expanded PTFE/HDPE/Z-Quartz/HDPE/Expanded PTFE Window

For the relatively wide bandwidths of ALMA receivers, three-layer windows are insufficient to cover the full band and a five-layer design is required. The original five-layer designs at NRAO were for the proposed 4-beam 3-millimeter receiver for the 12 Meter Telescope, before it was decommissioned. These windows were to cover 86-116 GHz with <0.05 dB insertion loss and >20 dB return loss at the band edges. Few materials have suitable dielectric constant and low loss for anti-reflection layers; the best were high density polyethylene (HDPE) and Gore RA7957 Radome material[2], referred to here as "Goretex" [11,12]. Goretex is a pure expanded PTFE (X-PTFE) open-cell material made by a proprietary process. The slightly more complicated procedures for constructing a five-layer window are discussed in Appendix 3 and network analyzer data are compared with the model for an ALMA band 3 window in Figure 4.

[1] At the time of writing, there is a proposal pending to increase band 3 to 84-116 GHz.

[2] There was considerable difficulty in obtaining Goretex in the appropriate thickness and there is some question as to whether it will be available from the manufacturer in the future. See [12] for more details on this material.

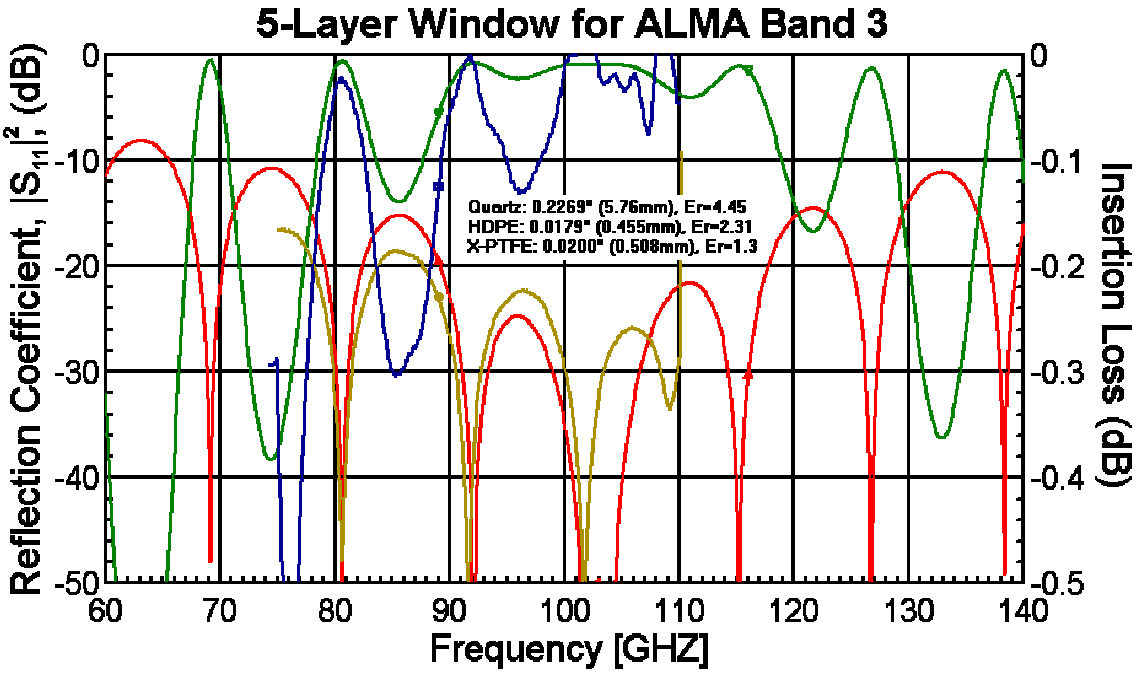

Figure 4. A five-layer window design for the ALMA 89-116 GHz band, utilizing Expanded PTFE / Polyethylene / Quartz / Polyethylene / Expanded PTFE. The expanded PTFE is Goretex RA7957, as described in the text. Thickness of layers are indicated in the figure.

Discussion

As designs for new quartz vacuum windows progress towards higher frequencies, Goretex RA7957 becomes unsuitable as the outer layer for the five-layer windows as it is not available in thickness of less than 0.020″, precluding its use above approximately 200 GHz [12]. Fortunately, a similar expanded PTFE material, known as Zitex-G, has been identified as a good candidate replacement [13]. Using methods similar to those described in [12], the dielectric constant of Zitex G has been found to be 1.45, slightly higher than that of Goretex. However, the material is much more mechanically robust than Goretex and is available in sheets as thin as 0.004″ and up, in increments of 0.002″. Using Zitex G-104 (0.004″ thick), a window has been designed for the ALMA evaluation receiver's 210-275 GHz band, and the model performance is shown in Figure 5.

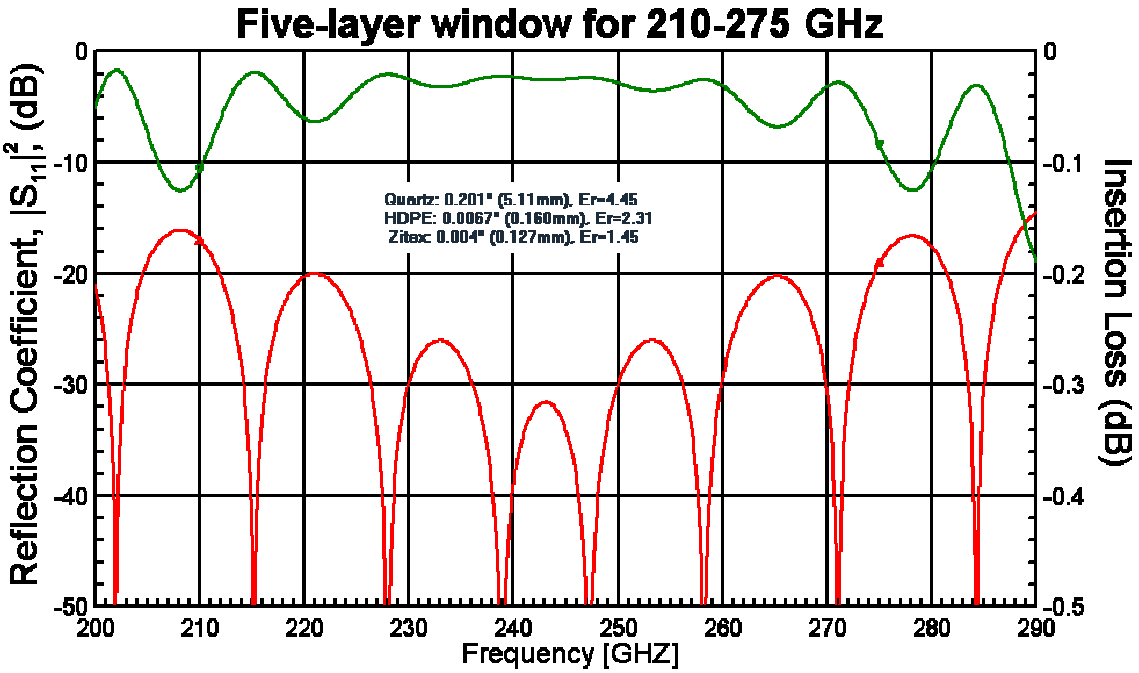

Figure 5. A five-layer window for the ALMA evaluation receiver's 210-275 GHz band, utilizing Zitex G-104 as the outer AR layers. Zitex G is an expanded PTFE material similar to RA7957, but available in thinner sheets.

At higher frequencies, wide bandwidth measurements of the window performance become increasingly difficult and extending the network analyzer capabilities to each of the bands of interest becomes prohibitively expensive. A workable solution may be the use of a Fourier Transform Spectrometer (FTS) optimized for use at very long wavelengths. Figure 6 shows the MMICAD model calculations and

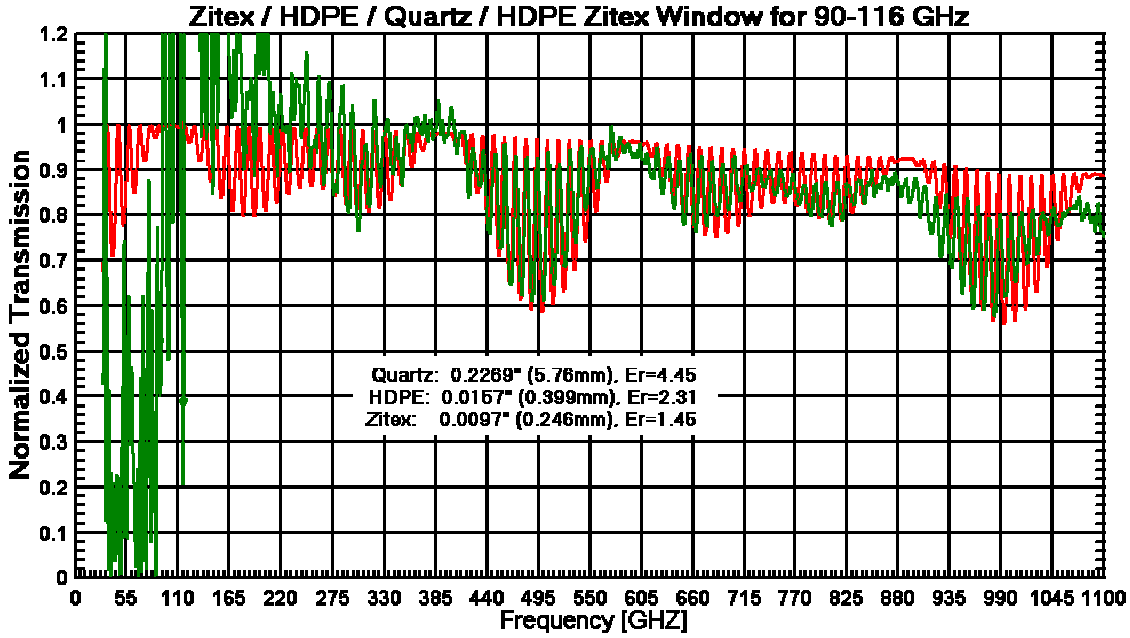

Figure 6. Calculated and measured performance of a Zitex/HDPE/quartz/HDPE/Zitex window for the 90-116 GHz band. Though the long wavelength, high-resolution Fourier Transform Spectrometer was not capable of measuring in-band performance, it does confirm the very good agreement with the model.

measured performance of a five-layer window originally designed for the 90-116 GHz band. The instrument used was Science Tech STS-200 FTS, installed at the National Synchrotron Light Source at Brookhaven National Labs [14]. The instrument is in theory capable of $0.03cm^{-1}$ (approximately 1 GHz) resolution with useable signal at frequencies above approximately 60 GHz. Numerous technical difficulties compromised the measurements of the window at low frequencies, but the second pass band, centered around 385 GHz, is clearly resolved. The data also show very good agreement between the modeled and actual window performance. An improved instrument is expected to function down to approximately 60 GHz, allowing verification of window designs at higher frequencies.

If the total insertion loss specification is allowed to slip to 0.1 dB, using Zitex G in the five-layer configuration, it is expected that quartz vacuum windows can be designed up to at least 600-720 GHz.

After we had completed most of this work, QMC instruments [15] agreed to make multi-layer quartz windows to specification. Tests of these windows were reported in [16]. The performance of the QMC windows was consistent with our own measurements.

Appendix 1: Notes on Z-Quartz — Data, Calculations, Assumptions

The minimum thickness of the crystal quartz windows was chosen to withstand a pressure difference of 4 atmospheres, *i.e.*, with a safety factor of 4. Formulas for the stress in loaded circular plates with clamped and free rims are given in [17]. The tensile strength of z-cut crystal quartz was taken as 5400 PSI [18]. Figure 7 gives the minimum quartz thickness required to achieve a 4 atmospheres bursting pressure, as a function of the clear aperture, with clamped and free rims. Because the window clamping arrangement is always somewhat flexible, it is safest to use the thicker quartz as required for a free rim.

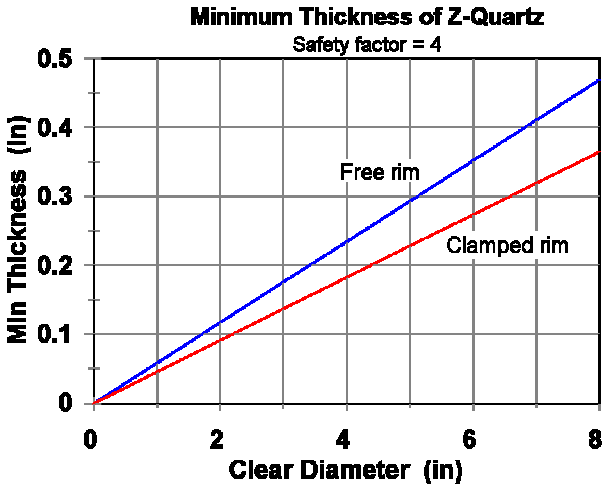

Figure 7. Minimum thickness of crystal quartz required to achieve a 4 atmospheres bursting pressure.

The quartz windows must have a diameter substantially larger than the clear aperture of the window to allow contact with a standard size o-ring. According to one supplier, quartz crystals larger than approximately 4.5″ diameter are very difficult to obtain. For the VLBA windows, having a diameter at the o-ring of approximately 4″, 0.225″ was chosen as the minimum thickness for the quartz, based on the figure above. The thickness was then *increased* using the MMICAD model as a guide to minimize the effect of the fringing due to the unmatched quartz, and so maximize the effect of the matching layers.

Appendix 2: Construction of the Three-Layer PTFE / Z-Quartz / PTFE Window

Construction of the quartz vacuum windows might appear relatively straightforward, but there are many subtleties to the procedures that have been worked out over several years. For this reason, the complete procedure is described here in detail.

Preparing the Quartz:

Quartz blanks were obtained from Boston Piezo Optics (see Appendix 4). The blanks, as specified, vary in thickness by ± 0.0005″ and so must be measured accurately to make adjustments to the Teflon layer thickness as required by the model. Blanks are measured on a flat granite slab using an Ono-Sokki digital micrometer accurate to 50 microinches with a 0.125″ diameter flat foot. Calibration was checked using high precision gauge blocks.

After measuring, the quartz blanks are scrubbed on one side with a Kimwipe cloth soaked with hexanes to remove fingerprints. If the quartz has not been handled with bare hands, this step can be omitted. The quartz is next scrubbed with acetone, using a Kimwipe, to remove more organics, then distilled water to remove the acetone, and isopropyl alcohol to dry the surface. After blowing the surface with clean nitrogen, blanks are baked for 1 hour at approximately 100 C, in a vacuum oven.

Preparing the Teflon:

Teflon sheets are obtained in pre-etched form (see Appendix 4). Discs are cut to approximately 1" larger diameter than the quartz blank. The bonding surface, which should be brown and smooth, is cleaned and baked with the same procedure used for the quartz.

Preparing the Epoxy:

Epo-Tek 301-2 low-viscosity epoxy (Appendix 4) has been found to give the most consistent glue layer with the procedure described here. The layer is of uniform thickness, approximately 0.2 mils thick for the construction parameters given here, and free of bubbles and voids. As described in the epoxy instructions, mix 3.00 g of part A and 1.05 g of part B in a small container. Components are weighed to the nearest 10 mg on a digital balance, and part B is added by syringe to facilitate the operation. Approximately 2 g is needed for one surface, but the epoxy should not be mixed in quantities of less than approximately 4 g. The epoxy is stirred by hand for 5 minutes, and then vacuum degassed for approximately 1 hour. Pot life is well over 6 hours at room temperature so the epoxy can be left pumping longer if desired. Release the vacuum slowly to avoid trapping air in the degassed mixture.

Glueing PTFE to Quartz:

Glueing under pressure was found to be the best means of achieving a durable, bubble-free glue line. In order to reduce the curing time to approximately 12 hours, the press is heated to 65 C. Figure 8 shows a cross section of the various components of the press and window. An aluminum pressure distribution plate sits on the foot of the press. On top of that lies a piece of pressboard ceiling tile to serve as a thermal insulator. A thin film heater (McMaster Carr #35765K143) lies between the insulator and the bottom of the window jig.

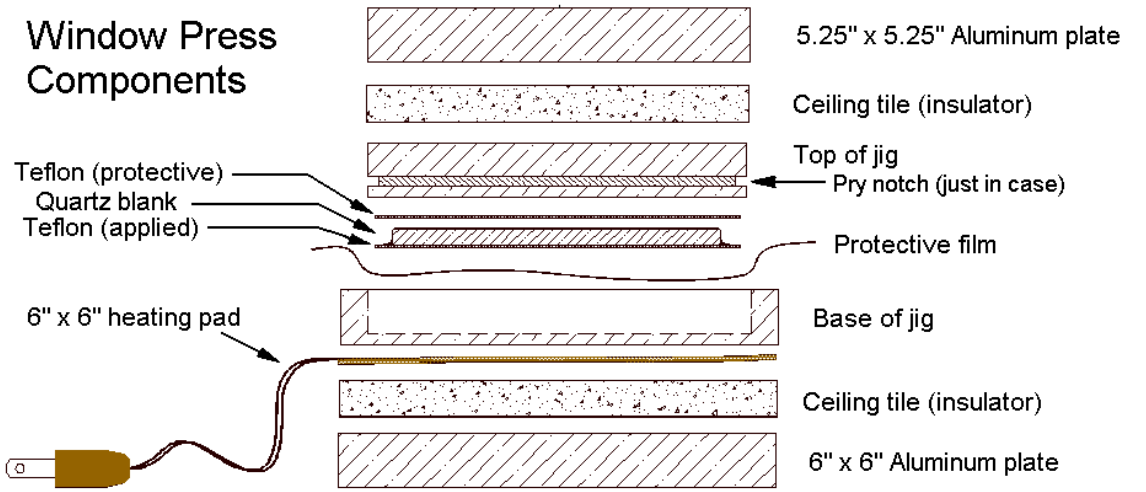

Figure 8. Components of the window press, in cross-section.

A wide piece of plastic film (Mylar or HR500 film) protects the jig bottom from epoxy over-spill and the inside of the jig is sprayed with a PTFE-based mold release agent. The Teflon sheet is placed glue-side up on top of the film and approximately 2 g of epoxy is poured out and allowed to spread to about half the window diameter. The quartz blank is laid gently on top of the epoxy and held centered while it settles. It can be pressed down to drive bubbles to the edge of the epoxy if desired but this step is generally unnecessary, as the bubbles will be completely squeezed out under pressure. A spare piece of Teflon is

placed on top of the quartz blank to protect the surface, and the press is closed with the top of the window jig, a piece of ceiling tile for thermal insulation, and the thicker aluminum pressure plate, in that order. A photograph of the assembled stack is shown in Figure 9.

Figure 9. Photograph of the assembled window press. The Variac and heating pad are used to increase the temperature of the jig and so decrease the curing time of the epoxy. Note the thin film thermometer on the lower half of the jig.

Pressure is applied to the air press from a regulator attached to a nitrogen cylinder and must be increased VERY SLOWLY to avoid smashing the piston into the jig and breaking the window. Pressure is raised slowly over the next 5-10 minutes to allow the glue to be squeezed out uniformly before reaching the final value of 16 PSI at the window surface. With a 4.5″-diameter quartz blank and the McMaster Carr #2373A14 press, the operating pressure corresponds to 35 PSI air at the piston.

The heater is turned on as soon as the pressure has stabilized, and remains on for 12 hours (typically overnight). A Variac was found to be an effective means of adjusting the temperature. For the 90 W heaters described in Appendix 4, a Variac setting of 32% typically stabilizes the jig temperature at 65 C within several hours. To aid in monitoring the temperature, a liquid-crystal self-adhesive thermometer strip is applied to the lower half of the jig. After at least 12 hours, the Variac is turned off and the jig allowed to cool for at least 2 hours before releasing the pressure.

Trimming and Machining the Teflon:

After removal from the press, excess Teflon is cut off with heavy duty hand scissors as close to the window as the hardened epoxy will allow. The remaining epoxy must be ground off. It was found that sanding the epoxy off on a belt sander can compromise the bond layer, and can also cause chips at the edge of the quartz disk. Instead, a dedicated table router is used to grind the Teflon and epoxy away with a high-speed motion parallel to the window surfaces. A standard alumina grinding bit, with a ¼" diameter shank, is mounted in place of the router bit. The router is additionally jigged to prevent grinding the quartz once all the excess epoxy is removed. The alumina grinding bits have little effect on the crystal quartz, but can cause small chips if the disk is forced.

Teflon can be machined on a lathe using a sharp high-speed steel tool. A vacuum chuck, custom made for a particular window diameter, is used to hold the window securely in place. A facing cut is first taken from the face of the chuck, and the digital gauges zeroed on that face. The quartz is wiped clean with acetone to remove grease and debris, and placed on the vacuum chuck for cutting. After the final cut, the window is removed from the chuck, and the edges of the Teflon are beveled with a razor blade. The window thickness as cut on the lathe is typically within ± 0.2 mils of the desired thickness. In the event that the plastic is too thin, some compensation can be made by increasing the thickness of the Teflon on the opposing face, as determined by the model calculations (see, for example, Figure 3 above).

Finishing the Windows:

The second side of the window is completed just as the first side. The quartz must be cleaned to remove machine oil and fingerprints, and a new sheet of Teflon is glued on. As before, the Teflon to be applied is placed in the bottom of the jig to prevent epoxy from running onto the window, and a spare sheet of Teflon is placed on top to protect it. Additional care must be taken not to scratch the finished surface of the first side during pressing, grinding and machining.

After turning down the second surface, an annulus of Teflon is cut away around the perimeter to expose the quartz surface, which will contact the o-ring. This must be done slowly and carefully to avoid scoring the crystal. It is best to stop when most of the Teflon has been removed, exposing the brownish etched Teflon just above the epoxy. At this point the epoxy can be scraped off manually with a razor blade. After a final degreasing and cleaning, the window is measured to confirm the total thickness and it is ready for testing (Figure 10).

Figure 10. A nearly completed 4.5″ diameter, three-layer window for the VLBA. The outer surfaces are PTFE, which has not yet been trimmed for the o-ring seal.

Appendix 3: Construction of a Five-Layer X-PTFE / HDPE / Z-Quartz / HDPE / X-PTFE Window

Construction of the five-layer windows proceeds in much the same fashion as the three-layer windows but differs significantly in the way the polyethylene and X-PTFE are handled. Like PTFE, polyethylene is extremely inert and its surface must be chemically activated to make bonds available for glueing. However, HDPE is not readily available in sheets with a pre-treated surface so it must be etched prior to use. The solution of choice is a chromic/sulfuric acid solution:

		Parts By Weight
H_2SO_4	(Sulfuric acid)	100
$Na_2Cr_2O_7 \bullet 2H_2O$	(Sodium Dichromate)	5
H_2O	(Water)	8

The solution should be mixed with care as it is an extremely strong oxidizer. When fresh, it is dark brown, and gradually becomes dark green upon exposure to air and in use – a practical indicator that it should be replaced. The solution will naturally etch through a polyethylene container and should be stored in safety-glass bottles. Note that in past decades Emerson and Cuming manufactured "Ecoprime PP" as a recommended treatment for polyethylene prior to bonding. Though the solution is no longer available, it appears to be very similar to the mixture above as deduced from the Material Safety Data Sheets.

The polyethylene sheets are cut from HDPE rod stock and turned on a vacuum chuck to approximately 20-mils thickness. They are then rubbed with an acetone soaked Kimwipe to remove gross dirt and organics, then placed in the etching solution. The disks are etched for approximately 1 hour with intermittent stirring, then rinsed for 5 minutes under warm running water, and given a final rinse with distilled water. Baking is *not* recommended for the surface treated polyethylene, nor is wiping the surface. Instead, the windows should be blown dry with clean nitrogen gas. If a bake is necessary to dry them, the temperature should be kept at approximately 50 C.

The polyethylene is applied to the quartz with Epo-Tek 301-2 epoxy, as for the three-layer windows. Machining the polyethylene layers to the desired thickness is more complex, however. The trimmed window is first chucked in the lathe and the polyethylene turned down to be approximately 1-2 mils thicker than desired. Machining HDPE on the lathe leaves undesirable tool marks, a surface which is convex near the center, and other features greater than 1 mil in height. As a result, the plastic must be ground to the correct thickness on a surface grinder. The proper grinding wheel to use is designated #32A46-GVBEP (see Appendix 4), operated at 2850 RPM (1492 in/sec at the wheel surface). Feed rates are on the order of in/sec longitudinal, and in/minute transverse. Only 0.2-mils may be removed per pass or scoring will result.

To apply either Goretex or Zitex outer layers, a minimal glue transfer method is used to minimize the amount of glue available to soak into the porous materials, thereby affecting their dielectric properties. The polyethylene covered window is given a 5 minute etch in the chromic/sulfuric acid mixture, rinsed, and baked 30 minutes under a partial vacuum of approximately 5 PSI in a vacuum oven. Epo-Tek 301-2 epoxy is prepared in the usual manner, and about 2 drops of it are squeezed between a pair of 6″-diameter, 3/8″ thick aluminum disks for 1 minute at 40 PSI air pressure in the air press. The excess is wiped from around the disk edges, and the disks are separated. An X-PTFE disk, pre-cut to match the diameter of the window, is pressed against each glue surface for 1 minute at 10 PSI air to transfer the epoxy. The plastic disks are then placed on their respective quartz window faces. The window is sandwiched in the air press with Goretex sheets protecting the window's Goretex or Zitex faces and the press is operated at 10 PSI air overnight, with the heater set to approximately 65 C.

To complete the window, the plastics are trimmed from the window to expose the quartz sealing surface, as for the three-layer window. The expanded PFTE will not cut off neatly with the turning tool on the lathe, so it must first be sliced with a razor blade and peeled off. The HDPE can then be turned down to the quartz with a standard tool to expose the o-ring contact surface.

Appendix 4: Sources of Materials

Quartz: Obtained from Norman Benoit and Steve Wickstrom of Boston Piezo Optics, Medway Massachussetts. In March of 2001 the facilities are expected to move to Bellingham, MA, (508) 966-4988.

Teflon: McMaster-Carr #8711K12. 12″ x 12″ x 1/32″-thick sheet, etched on one side. Also available in 0.015″ and 0.020″ thicknesses.

EpoTek 301-2 is available from Epoxy Technology Inc., 14 Fortune Dr., Billerica, MA 01821-3972. 301-2 is a two-part, slow curing optical epoxy.

Heating Pad: McMaster-Carr Model #35765K143. 6″ x 6″ semi-flexible rubberized heating pad, 2.5 Watt/square inch.

Press: Air Mite, Model # AP 19, Air Mite, Chicago, IL 60641. 2″ stroke, 5″ diameter cylinder, 120 PSI maximum pressure. Available as McMaster-Carr #2373A14.

Grinding wheel: Sears Craftsman. ½″ diameter x 1-½″ long with ¼″ shank. Aluminum oxide.

Router: Sears Craftsman router, Model #917506. 2 HP variable speed with work light and dust collection. 15,000 – 25,000 RPM, run at its fastest speed for removing epoxy. Cheaper models don't have the dust collection system which is essential.

Router table: Sears Craftsman router table, Model #925560. 13″ x 18″ with adjustable fence.

Grinding wheel: Norton Bonded Abrasives, Worcester Massachussetts, (508) 795-5000. The applications engineer checked the records and recommended a 32A (Aluminum Oxide), 46 grit, G hardness, Vitrified (V) bonded wheel with a porous structure. The complete designation of the wheel is: 32A46-GVBEP. In a 10″ x 1″ x 3″ wheel, the 10 digit ID number is 6253160932. The wheel is available from Manhattan Supply Company (MSC) as part number 05986013.

Polyethylene: High density polyethylene (HDPE) rod stock. Avoid sheet stock due to the possibility of polarization effects caused by the extrusion process. McMaster-Carr #8624K56, 5″ diameter.

Goretex: See [11].

Zitex: See [13]. Zitex G is available in thicknesses of 4, 6, 8, 10, 15 mils, and larger thicknesses up to 150 mils. A 5″ wide, 26 foot long roll of Zitex G110 (10 mils) is the minimum order available.

References

[1] A.R. Kerr, ALMA Memo, in preparation. Will be available on-line at http://www.alma.nrao.edu/memos/

[2] M. E. Thomas, R. I. Joseph, G. J. Simonis, and M. Stead, "Characterization of the Infrared and Far-Infrared Properties of Sapphire and Quartz," *Proceedings of 13th Int'l. Conf. on Infrared and Millimeter Waves*, pp. 339-341, Dec. 1988.

[3] S. Roberts and D. D. Coon, "Far-Infrared Properties of Quartz and Sapphire," *J. Opt. Soc. Am.*, v. **52**, pp. 1023-1029 (1962).

[4] E. E. Russell and E. E. Bell, "Measurement of the Optical Constants of Crystal Quartz in the Far Infrared with the Asymmetric Fourier-Transform Method," *J. Opt. Soc. Am.,* v. **57**, pp. 341-348 (1967).

[5] E. V. Loewenstein, D. R. Smith, and R. L. Morgan, "Optical Constants of Far Infrared Materials. 2: Crystalline Solids," *Appl. Opt.*, v.**12**, pp. 398-406 (1973).

[6] Roger W. Ward, "The Constants of Alpha Quartz," 14th Piezoelectric Devices Conference and Exhibition, Sept. 1992.

[7] M. N. Afsar, "Dielectric Measurements of Common Polymers at Millimeter Wavelength Range," *1985 IEEE MTT International Microwave Symposium Digest*, pp. 439-442, 1985.

[8] MMICAD is a microwave circuit analysis and optimization program available from Optotek Ltd., 62 Steacie Drive, Kanata, Ontario, Canada K2K 2A9. http://www.optotek.com/

[9] Thanks to Charles Cunningham, National Research Council of Canada, Herzberg Institute of Astrophysics, Victoria, BC, Canada, for use of the Spectrometer on which these data were obtained. See also Daniel Koller, Geoff Ediss, Jeff Hesler, and Charles Cunningham, "FTS Measurements of Some Window Materials", NRAO Electronics Division Technical Note No. 184, August 1999. Available on-line at http://www.gb.nrao.edu/sshears/electronics/

[10] G. A. Ediss, A. R. Kerr, D. Koller, "Measurements of Quasi-Optical Windows with the HP 8510," ALMA Memo #295, March 2000. Available on-line at http://www.alma.nrao.edu/memos/

[11] W. L. Gore and Associates, Inc., 1901 Barksdale Rd., P. O. Box 9236, Newark, DE 19714-9236.

[12] Daniel Koller, G. A. Ediss and A. R. Kerr, "Dielectric Constant of Goretex RA7956/7957 Radome Material," ALMA Memo #309, May 2000. Available on-line at http://www.alma.nrao.edu/memos/

[13] Norton Performance Plastics, 150 Dey Road, Wayne, NJ.

[14] Thanks to Prof. Laszlo Mihaly, and Dr. Larry Carr of the State University of New York, Stony Brook, and Brookhaven National Laboratories, respectively, for use of their STS-200 FTS.

[15] QMC Instruments LTD, Mile End Road, London, UK. http://qmciworks.ph.qmw.ac.uk/homepage.htm

[16] G.A. Ediss, S-K. Pan, J. Effland, and T.Globus, "Measurements of Commercial Vacuum Windows for ALMA Bands 3 and 6," ALMA Memo #340, December 2000. Available on-line at http://www.alma.nrao.edu/memos/

[17] *Mark's Standard Handbook for Mechanical Engineers*, 8th Ed., 1978. See sect. 5, p.53.

[18] S. Wickstrom, Boston Piezo-Optics, Inc., Medway, MA. Private communication.

Characterization of Various Quasi-Optical Components for the Submillimeter Limb-Sounder SMILES

A. Murk[1], N. Kämpfer[1], R. Wylde[2], J. Inatani[3], T. Manabe[4] and M. Seta[4]

E-mail: axel.murk@mw.iap.unibe.ch

[1] *University of Bern*, Sidlerstr. 5, Bern, Switzerland

[2] *Thomas Keating Ltd.*, Billingshurst, West Sussex, RH14 9SH, UK

[3] *National Space Development Agency*, Tsukuba, Ibaraki 305-8505, Japan

[4] *Communications Research Laboratory*,Koganei, Tokyo 184-8795, Japan

Abstract

The submillimeter-wave limb-emission sounder called SMILES is currently being developed for the Japanese Experiment Module of the International Space Station. It will observe the spectral emission lines of several stratospheric trace gases related to ozone chemistry. We present transmission and reflection measurements with a submillimeter-wave vector-network analyzer of various optical sub-components of SMILES, which include corrugated feed horns and corrugated back-to-back horns, a novel single sideband filter and a conical calibration load.

1 Introduction

SMILES is a submillimeter-wave limb-emission sounder which is currently developed for the Japanese Experiment Module of the International Space Station [2]. It will obtain global maps of ClO, BrO, HCl, O_3 and other stratospheric trace gases related to ozone chemistry by observing their spectral emission lines in two frequency bands at 624.32–626.32 and 649.12–650.32 GHz. Two superconducting SIS mixers cooled by a mechanical cooler will guarantee the very highest sensitivity.

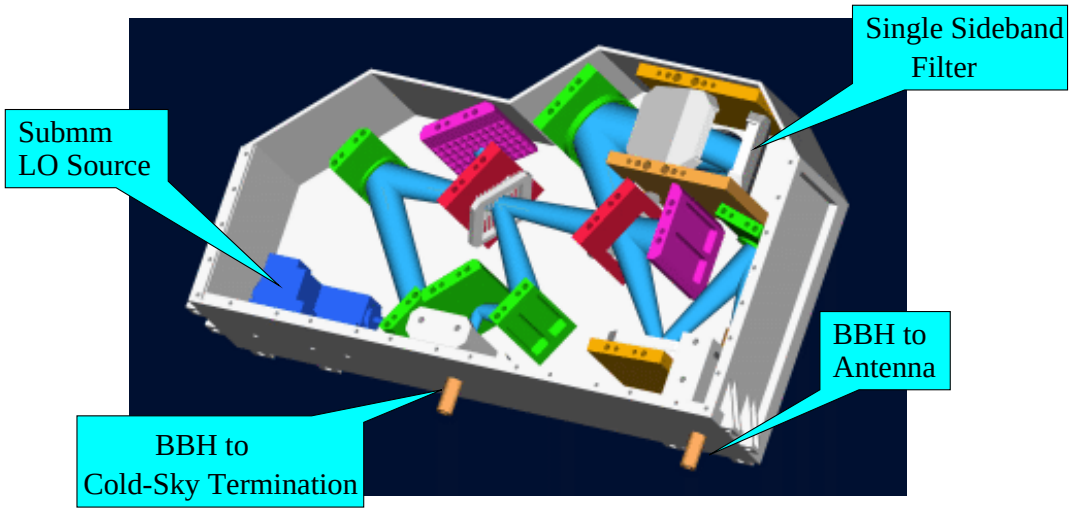

Figure 1: Ambient Temperature Optics (AOPT) module of SMILES. Submillimeter radiation from the cold sky and the atmosphere enters the AOPT through two corrugated Back-to-Back Horns (BBH). The output to the cryogenic mixers is hidden underneath the single sideband filter.

The Ambient Temperature Optics subsystem as shown in Figure 1 provides LO injection, single sideband filtering and EMC isolation for the radiometer. This is achieved by freestanding wire grids, a novel configuration of the Martin-Puplett Interferometer based on Frequency Selective Polarizers (FSP) and corrugated Back-to-Back (BBH) horns, respectively. Other optical elements outside of the AOPT are the corrugated feed horns of the SIS mixers and a black-body calibration load.

This paper reports on measurements of these critical quasi-optical components in the submillimeter range. Their transmission- and reflection characteristic were determined with a vector-network analyzer from the company *AB-Millimetre*[1]. In our configuration of this instrument coherent submillimeter radiation is generated from a phase locked Gunn oscillator using harmonic multiplication. A harmonic mixer with a second Gunn oscillator phase-locked to the same reference frequency as the first one is used for the detection and allows amplitude and phase measurements with high dynamic range [3].

2 Corrugated Feed Horns

The two SIS mixer blocks of SMILES will be equipped with corrugated feed horns that are known to produce symmetric Gaussian beam patterns with low side-lobes [9]. However they are not easy to manufacture for frequencies in the submillimeter region and detailed antenna pattern measurements are mandatory.

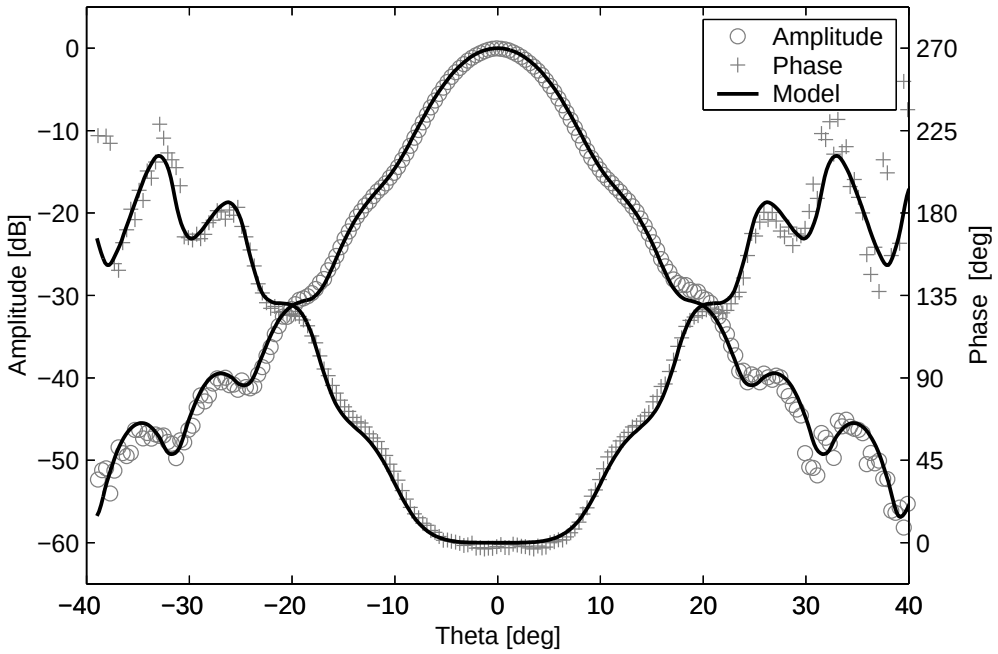

Figure 2: Measured amplitude and phase of the SMILES corrugated horn antenna together with model predictions. This measurement is a cut through the E-plane at a frequency of 602.5 GHz.

[1] *AB-Millimetre*, 52 rue Lhomond, 75 005 Paris, France, http://www.abmillimetre.com

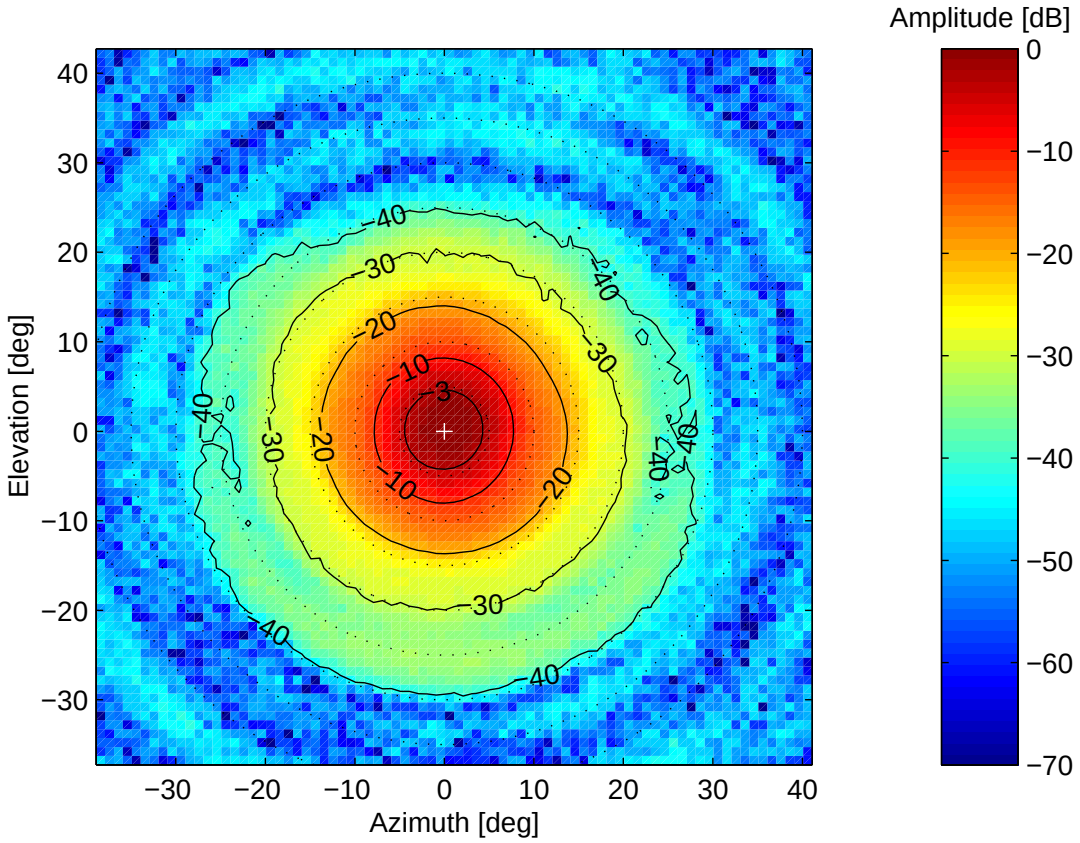

Figure 3: 2-D antenna pattern of the corrugated horn antenna. Solid lines represent the 3 dB and the first 10 dB contours of the measurement, dotted lines are circles with 5° difference between their radii.

A first prototype of the SMILES horn antenna was mounted on the harmonic detector of the *ABmm* system and rotated in azimuth and elevation using a motorized 2-axis rotational stage. The submillimeter source with another corrugated horn antenna was operated at a frequency of 602.5 GHz and remained fixed in a distance of 250 mm. Since the aperture diameter of the horn under test is 4.2 mm this distance is more than three times larger than the far field requirement $2D^2/\lambda$. Three micro-positioners are used to adjust the position of the phase center of the horn under test with respect to the rotational axes to achieve a flat phase response in the main beam.

Amplitude and phase of the 1-D antenna patterns in Figure 2 are in good agreement with the predictions of the mode-matching model CORRUG [1] down to the -50dB level. Other corrugated horns with a different design showed a similar good match between measurements and model.

The symmetry of the horn is revealed by the 2-D antenna pattern in Figure 3. Small deviations on the -40 dB level at elevations beyond 20° are caused by artifacts of the antenna test range. This is indicated by the fact that the asymmetry does not change when the horn is rotated by 180°.

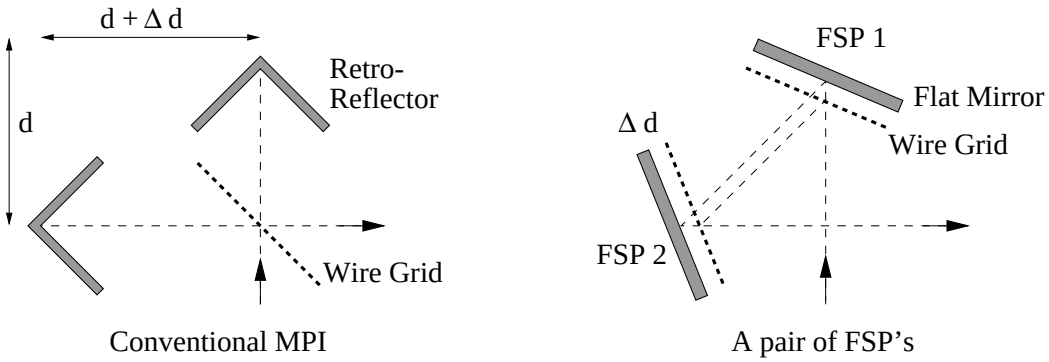

Figure 4: Schematic setup of a conventional MPI and a pair of FSP's. The wires of each grid have an orientation of 45° with respect to the polarization of the incoming radiation.

3 Sideband Filter

Many millimeter- and submillimeter-wave receivers make use of the Martin-Puplett interferometer (MPI) to achieve single sideband operation [7]. The frequency characteristic of a MPI can be easily tuned by changing the optical path difference in one of the two interferometer arms. For fix-tuned applications in space this has the disadvantage that the dimensions of the whole interferometer have to be machined to an accuracy in the order of 1μm and that these tight tolerances have to be maintained over the whole temperature range of operation. Another drawback is that residual reflections due to the imperfect performance of the grid cause standing waves in the optics which could limit the accuracy of the instrument.

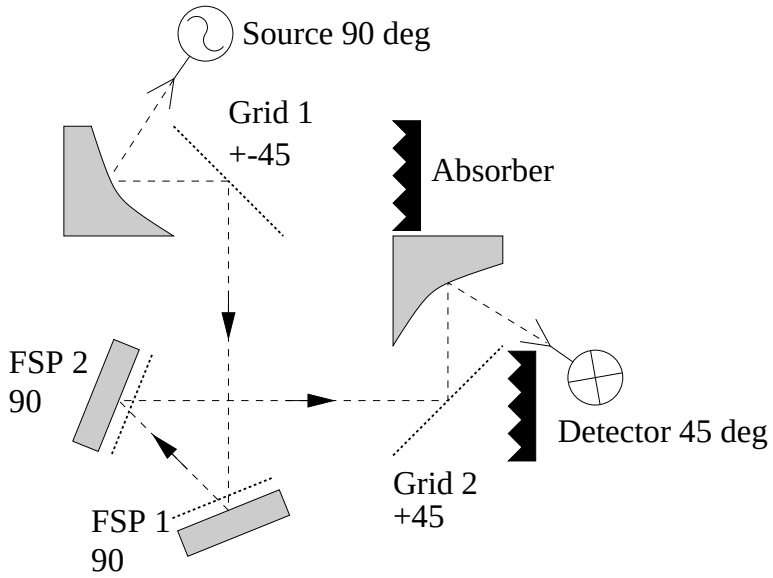

Figure 5: Quasi-optical network for transmission measurements through a pair of FSP's

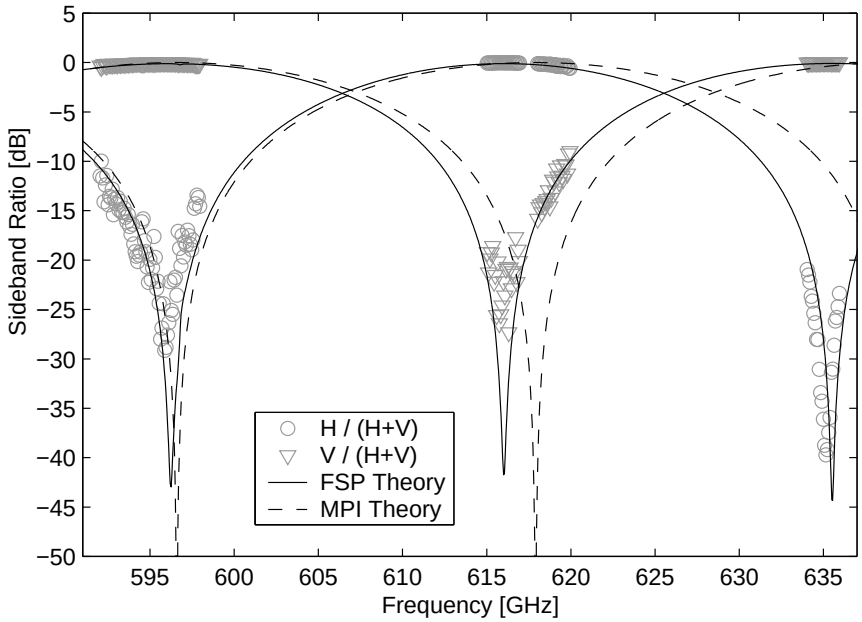

Figure 6: Transmission measurements through a pair of FSP's with $\Delta d = 1.9$ mm together with the theoretical curves for the corresponding MPI and FSP interferometers.

To avoid these problems a new configuration of the MPI as show in Figure 4 will be used for SMILES [4]. It is based on two Frequency Selective Polarizers (FSP) which consist of a wire grid placed in a specific distance Δd parallel in front of a flat mirror. This device is free of residual reflections and more suitable for fixed-tuned applications since the critical tolerances have to be met only within the FSP.

When the theoretical transmission through such a device is calculated the non-ideal behavior of the wire grids has to be modelled in detail because it has a significant influence on the frequency characteristic of the FSP's. As discussed in [6] the cross-polar components of the signal transmitted and reflected by the grids shift the frequency of the bandpass minima and maxima of the FSP filter compared to a conventional MPI with similar path difference.

The transmission through a first prototype of two FSP's with $\Delta d = 1.9$ mm was measured on a quasi-optical test bench using the network analyzer (Fig. 5). Two elliptical mirrors produce a Gaussian beam with a beam-waist radius of $\omega_0 = 10$ mm between the FSP's. The wires of both FSP's have a vertical orientation, while the wires of the reflecting grids are set for 45° polarization. The first grid after the vertically polarized source can be rotated by 90° to obtain two measurements H and V.

The normalized ratios $H/(H+V)$ and $V/(H+V)$ as displayed for different frequency bands in Figure 6 are a measure for the sideband suppression. The transmission minima are already below the noise floor of this measurement and can be smaller than the observed values. This figure also shows the expected characteristics of a conventional MPI and of the FSP filter with the same nominal path difference. The frequency shift between the theoretical FSP curve and the measurement is about 300 MHz, which corresponds to 1 μm machining accuracy of Δd.

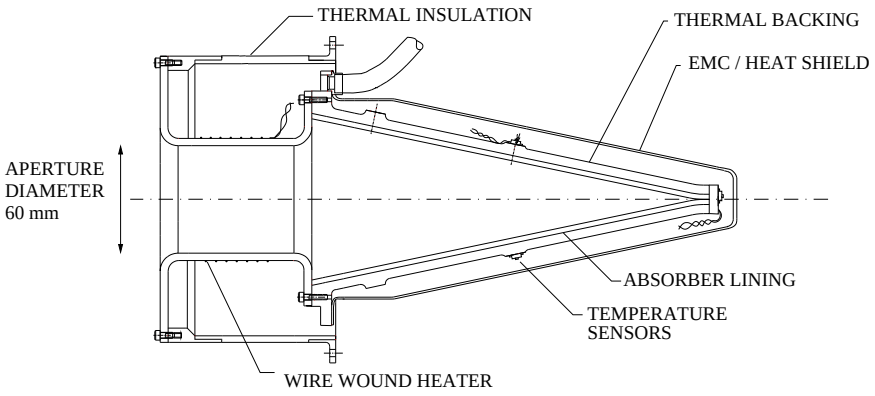

Figure 7: Design of the Calibrated Hot Load CHL. The aperture has a diameter of 60 mm, total length is 317 mm.

4 Calibration Load

The radiometric on-board calibration of SMILES will be realized by alternate observations of the cold sky and of a black-body calibration target at ambient temperature. The design of this load will be based on the Calibrated Hot Load (CHL) which was developed by *Thomas Keating Ltd.* and *AEA Technologies* within an previous submillimeter limb-sounder study of the European Space Agency ESA [5]. Figure 7 displays the design of the CHL based on a tapered aluminum cone lined with microwave absorbing material.

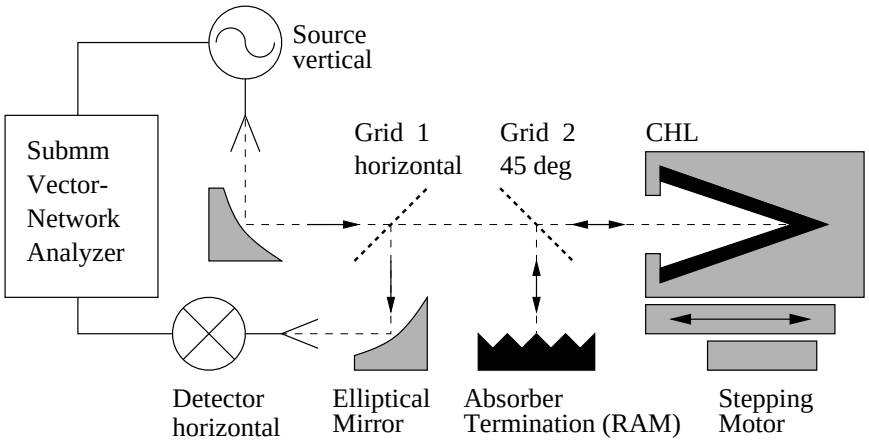

Figure 8: Setup of the quasi-optical reflectometer. Device Under Test is the CHL mounted on a motorized translation stage which allows to alter the phase of the reflected signal.

A quasi-optical reflectometer was used to measure the monostatic reflectivity of the CHL. This property is of special interest because it determines the amount of standing waves between the load and the receiver and thus the baseline ripple of the calibrated spectra. The schematic diagram of the reflectometer setup is given in Figure 8. The vertically polarized beam from the *ABmm* source passes

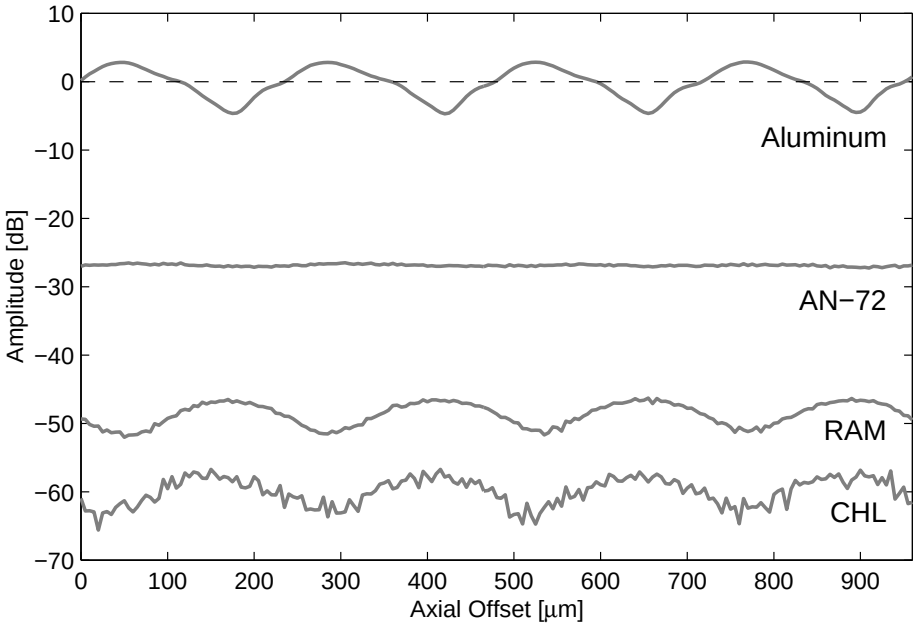

Figure 9: Reflection measurements at 625 GHz of the CHL and other absorbing materials at different axial offsets.

through a first horizontal grid. The second grid, set for a polarization of 45°, acts as a 3 dB beam splitter. Half of the power is transmitted to the device under test (DUT), in this case the CHL, while the other half is reflected to a beam termination made of the submillimeter-wave absorber RAM[2]. The returning signals, which were reflected at the termination or at the DUT, are then recombined with the 45° grid and partly routed to the detector by the horizontal grid. Two elliptical mirrors are included in the reflectometer to form a beam-waist with $\omega_0 = 10$ mm close to the aperture of the CHL.

Amplitude and phase of the detected signal are determined by the reflectivity of the DUT and the absorber termination and by the path difference in the two arms of reflectometer. To separate the two components the DUT is mounted on a motorized translation stage which allows to move it parallel to the beam axis over a distance of one or more wavelengths.

Figure 9 shows such a measurement of the CHL and of two other commercial absorbers RAM and AN-72[3]. The measurement of a flat aluminum plate, also shown in this figure, was used to establish the 0 dB reference. Multiple reflections between the Aluminum and the reflectometer are causing the distinct periodic modulation when this plate is moved. In the case of the CHL and the RAM the modulations are due to the interfering signals of the DUT and the absorber termination. AN-72 produces a flat response because its reflectivity is much higher than that of the RAM termination, but still low enough to avoid a significant contribution from the multiple reflections.

In polar coordinates and on a linear scale the data points of each target lie on a circle due to the phase change from the moving DUT (Fig. 10). The radius of these circles is a measure for

[2]RAM: submillimeter-wave absorber with a pyramidal surface from *Thomas Keating Ltd.*

[3]AN-72: flat foam absorber from *Emmerson&Cuming*

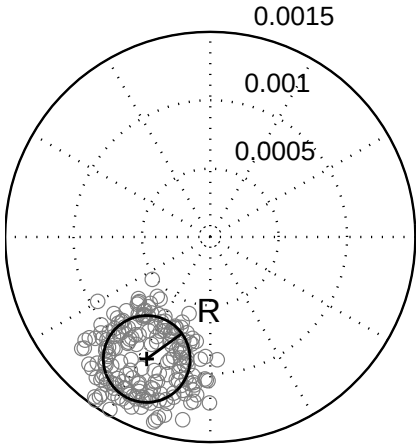

DUT: CHL
Frequency: 625 GHz
Radius R: $3.17 \cdot 10^{-4}$
Reflectivity: -70 dB

Figure 10: The same CHL measurements as shown in Figure 9, but on a linear scale and in polar coordinates.

the monostatic reflectivity of the DUT. The signal reflected at the fixed absorber termination has a constant phase and is responsible for the offset of the circles. From this measurement of the CHL an outstandingly low reflectivity of -70 dB at 625 GHz can be deduced. Similar results at other frequencies between 200 and 700 GHz are reported in [8] together with passive reflection measurements of the CHL at 278 GHz.

5 Back-to-Back Horn

To avoid EMC problems the sensitive receiver of SMILES has to be isolated from the low frequency RF contamination of the space station. This will be achieved by two corrugated Back-to-Back horns (BBH) which couple the atmospheric signal and the cold space view of the sideband termination into the shielded enclosure of the AOPT module. The BBH's have a total length of 130 mm and act as overmoded waveguides for the submillimeter waves while RF radiation with a longer wavelength is prevented from entering the receiver. A major concern are reflections at the BBH's which would cause standing waves in the optics. For that reason different BBH prototypes were tested in a reflectometer setup similar to the one shown in Figure 8. A third elliptical mirror after the second grid has to be added to image the source and detector horns onto the input of the BBH. The lateral position of the BBH can be adjusted manually using two micro-positioners to optimize the alignment for minimal reflections. Another motorized positioner moves the BBH parallel to the beam axis.

Figure 11 displays the amplitude of the detected signal for different axial positions. The modulations again are caused by the superposition of the reflected signals from the BBH and the absorber termination and can be removed by applying the technique described in the previous section on neighboring data points. The resulting monostatic reflectivity of the BBH given by the black line in Figure 11 has a minimum value below -65 dB in the optimum focal position. The lateral position of the BBH is more critical than the axial position since a 1 mm horizontal or vertical offset of the BBH already leads to reflections at the -30 dB level.

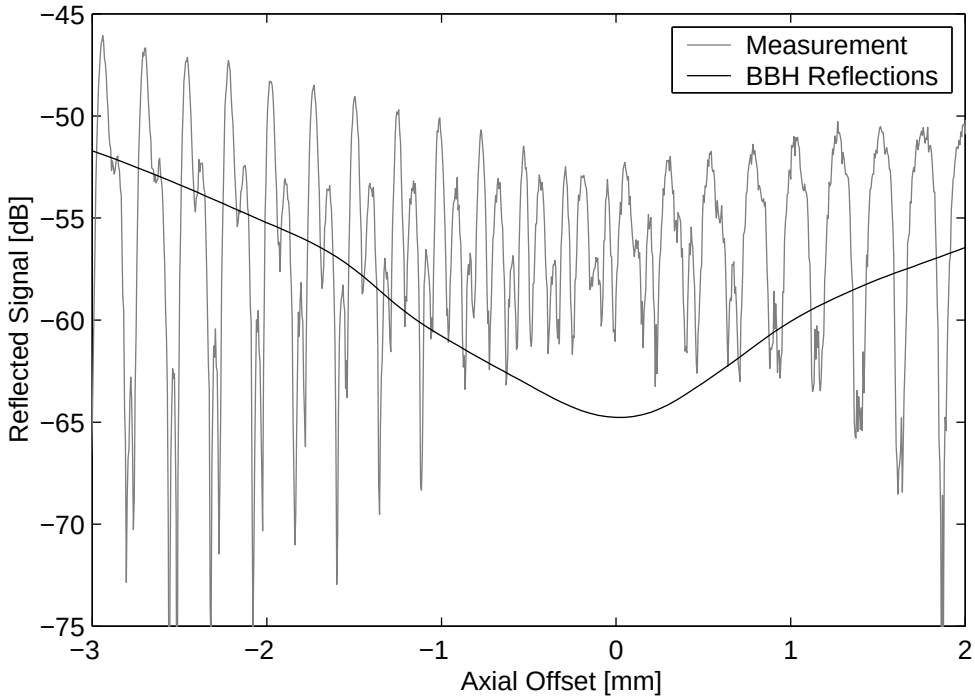

Figure 11: Reflectometer measurement of the BBH for different axial offsets from the optimal focal position and the retrieved BBH reflectivity (black line).

6 Conclusions and Outlook

We have described transmission and reflection measurements of critical quasi-optical components for SMILES in the submillimeter region which were obtained with a vector-network analyzer. Summarizing we conclude:

Antenna patterns of the corrugated feed horns are very close to the predicted values. This is a good proof for theory, manufacture process and measurement technique. Measurements of a novel FSP sideband filter showed that a sideband suppression of more than -40 dB can be achieved with such a device. Only a small frequency shift between the measured and the predicted transmission minima was observed. This shows that the non-ideal characteristic of the grids can be modelled correctly and that the FSP's can be machined with the required μm tolerances. The Calibrated Hot Load CHL has a very low monostatic reflectivity of -70 dB in the frequency bands of SMILES. This will lead to less standing wave problems than with other load designs. Reflections from the Back-to-Back Horns can be as low as -65 dB. However this requires a high accuracy in the alignment of the optics.

Currently an engineering model of the complete AOPT module is manufactured. The electrical characteristics of the whole module will be measured before and after vibration and thermal cycling as soon as it is available.

Acknowledgements
This work was funded by the Swiss National Science Foundation under the grant 2000-055687.98.

References

[1] ASL Antenna Software Ltd., UK. CORRUG mode matching software. http://www.demon.co.uk/asl/corrug.html.

[2] Inatani et al. Submillimeter limb-emission sounder JEM/SMILES aboard the Space Station. In *Microwave Remote Sensing of the Atmosphere and Environment*, volume 4152. Proceedings of SPIE, October 2000. Available at http://smiles.tksc.nasda.go.jp/document/indexe.html.

[3] P. Goy, M. Gross, and S. Caroopen. Millimeter and submillimeter vector measurements with a network analyzer up to 1000 GHz. Basic principles and applications. Technical report, AB Millimetre, Paris, France, May 1998.

[4] J. Inatani, S. Ochiai, T. Manabe, M. Seta, R. Wylde, and D. H. Martin. A new configuration of the Martin-Puplett Interferometer with low reflection. In *7th International Conference on Terahertz Electronics, Nara, Japan*, pages 260–263. IEEE, November 1999. Available at http://smiles.tksc.nasda.go.jp/document/indexe.html.

[5] Nigel Keen, Rob Spurrett, and Richard Wylde. An absolute blackbody source for radiometer calibration at submillimeter wavelength. In *ESA Workshop on Millimetre Wave Technology and Applications*, pages 4.2.1–4.2.10, Noordwijk, December 1995. European Space Agency.

[6] Takeshi Manabe. Transmission characteristics of the Inatani-type SSB filter consisting of wire-grids and mirrors with finite conductivity. Technical Report Ver. 2.1, CRL, Japan, July 2000. Available at http://www.crl.go.jp/ck/ck321/smiles/aopt/ssb-ver8.pdf.

[7] D.H. Martin. *Polarizing (Martin-Puplett) Interferometers for the Near- and Submillimeter Spectra*, volume 6 of *Infrared and Millimeter Waves*, chapter 2, pages 66–149. Academic Press, 1982.

[8] Axel Murk and Niklaus Kämpfer. Reflectivity measurements of a conical calibration load at submillimeter wavelengths. Presented at the *First International Microwave Radiometer Calibration Workshop*, University of Maryland, MA, October 2000. Available at http://mitb.gsfc.nasa.gov/ucal/Murk.PDF.

[9] R. J. Wylde. Millimetre-wave Gaussian beam-mode optics and corrugated feed horns. *IEE Proceedings*, 131-H(4):258–262, August 1984.

Novel Multiplexing Technique for Detector and Mixer Arrays

Boris S. Karasik and William R. McGrath

Center for Space Microelectronics Technology, Jet Propulsion Laboratory, California Institute of Technology, Pasadena, CA 91109-8099.

Future submillimeter and far-infrared space telescopes will require large-format (many 1000's of elements) imaging detector arrays to perform state-of-the-art astronomical observations. A crucial issue related to a focal plane array is a readout scheme which is compatible with large numbers of cryogenically-cooled (typically < 1 K) detectors elements. When the number of elements becomes of the order of thousands, the physical layout for individual readout amplifiers becomes nearly impossible to realize for practical systems. Another important concern is the large number of wires leading to a 0.1-0.3 K platform. In the case of superconducting transition edge sensors (TES), a scheme for time-division multiplexing of SQUID read-out amplifiers has been recently demonstrated [1]. In this scheme the number of SQUIDs is equal to the number (N) of the detectors, but only one SQUID is turned on at a time. The SQUIDs are connected in series in each column of the array, so the number of wires leading to the amplifiers can be reduced, but it is still of the order of N. Another approach [2] uses a frequency domain multiplexing scheme of the bolometer array. The bolometers are biased with ac currents whose frequencies are individual for each element and are much higher than the bolometer bandwidth. The output signals are connected in series in a summing loop which is coupled to a single SQUID amplifier. The total number of channels depends on the ratio between the SQUID bandwidth and the bolometer bandwidth and can be at least 100 according to the authors. An important concern about this technique is a contribution of the out-of-band Johnson noise which multiplies by factor $\sqrt{N}$ for each frequency channel.

We propose a novel solution for large format arrays based on the Hadamard transform coding technique which requires only one amplifier to read out the entire array of potentially many 1000’s of elements and uses ~ 10 wires between the cold stage and

room temperature electronics. This can significantly reduce the complexity of the readout circuits.

As an example of the technique, we consider an implementation using four detectors (TES detectors, for example) and a SQUID amplifier. The electrical diagram is shown in Fig. 1. All detectors are individually voltage biased. The output signal currents, I1 to I4, (from each detector resulting from the far-IR input signal) are summed in the input coil of a SQUID amplifier. In order to de-convolve the individual output signals from the total summed output, four sequential readings are performed. Each time a different polarity pattern is applied to the bias voltages of the detectors (shown in Fig.1). The mathematical basis for the de-convolution procedure uses the Hadamard Transform (HT) and the corresponding voltage polarity patterns are given by the Walsh-Hadamard functions [3,4]. (A very good description of the HT algorithm and its applications for imaging and spectroscopy can be found in [5]). The Walsh-Hadamard functions are binary functions (plus and minus ones) and for our purpose they correspond to positive and negative bias voltages across detectors. This assumes the detector current-voltage (IV) characteristic is symmetrical, which is the case for bolometers.

Let **R** be the vector whose elements correspond to the summed outputs for each of the 4 polarity patterns. Then **R** is the Hadamard transform of **O**:

$$\mathbf{R} = \frac{1}{4}\mathbf{H}_4 \bullet \mathbf{O}, \tag{1}$$

where **O** is the vector whose elements are the detector output currents I1 to I4. Inverting this equation gives **O**, the actual signal output of the array. $\mathbf{H}_4$ is the corresponding Hadamard matrix. One of its possible construction is given by

$$\mathbf{H}_4 = \begin{bmatrix} 1 & 1 & 1 & 1 \\ 1 & -1 & 1 & -1 \\ 1 & 1 & -1 & -1 \\ 1 & -1 & -1 & 1 \end{bmatrix} \tag{2}$$

The Hadamard matrix is especially simple if its order (same as the number of detector elements) is 1, 2, 4, 8, 16, 32, … 2^n where n = integer . The higher order matrices are all based on the basic 2×2 matrix:

$$\mathbf{H}_2 = \begin{bmatrix} 1 & 1 \\ 1 & -1 \end{bmatrix}, \mathbf{H}_4 = \begin{bmatrix} \mathbf{H}_2 & \mathbf{H}_2 \\ \mathbf{H}_2 & -\mathbf{H}_2 \end{bmatrix}, \mathbf{H}_{2N} = \begin{bmatrix} \mathbf{H}_N & \mathbf{H}_N \\ \mathbf{H}_N & -\mathbf{H}_N \end{bmatrix}. \quad (3)$$

Examples of different order matrices can be found in [3,5]

Beside the major advantage of using just one amplifier, this technique provides an improvement in the signal-to-noise ratio (SNR) of the measurements. Indeed, during a single reading event, 4 signals are algebraically added whereas the electrical noise from individual detectors, i_noise_n, (which are independent) is totaled as $I\_noise = \sqrt{\sum_n i\_noise_n^2}$. The average SNR improvement for the aforementioned technique is $N^{1/2}$ [5].

The HT multiplexing technique can also be applied to the detectors with asymmetrical IV characteristics. In this case, instead of reversing the polarity one simply has to turn the bias on and off. The Hadamard matrix then consists of 0's and 1's and can be easily generated as: $\mathbf{S} = (\mathbf{H}+\mathbf{U})/2$, where $\mathbf{U}$ is the unity matrix (we have adopted the "S-matrix" notation of reference 4, in this case). The SNR improvement is somewhat worse in this case: $(N+1)/2\sqrt{N} \approx \sqrt{N}/2$ (for large N) [5]. The multiplexing technique based on the "S-matrix" can be applied to arrays of mixers. However, the problem of feeding many high-frequency IF signals into one amplifier is definitely more severe than that for slow detectors.

The HT multiplexing technique has been used in optical imaging applications and spectroscopy for many years. However, the implementation of the optical masks was strictly mechanical. For example, a coded mask technique has been used in some X-ray telescopes to record an image using a single detector and a set of masks with transparent and opaque segments. The sequence of segments fulfills the aforementioned mathematical ordering sequence (e.g., that of Eq. 3). Since the encoding in this case occurs on the optical side of the detector system, the modification of the SNR is different from what we expect in our electrical scheme [5]. In optical multiplexers, the optical noises are not necessarily independent and after the de-convolution can be redistributed in such a way that the SNR in a pixel with a weak useful signal can become smaller. As a result, despite the potential average increase of the SNR, the contrast of the image can degrade. This *cannot* happen for the scheme which we propose. Our multiplexing of signals occurs on the "electrical" side of the detector system after all optical signals

(useful one and noise) are already detected. The SNR improvement takes place due to suppression of the electrical noise at the detectors output. The optical noise appears after the de-convolution as a part of the optical signal and its rejection is a matter of interpretation of the final data.

As can be expected for most signal processing techniques, the significant advantage of the HT multiplexing technique does not come for free. There are at least two issues which may hamper the use of this technique. Generation of the N electrical bias patterns would certainly take time especially when N is of the order of thousands. Figure 2 illustrates the time diagram which should be expected in bolometers. The required time to hold a certain voltage across a detector must be at least τ (the bolometer time constant). This allows for accumulation of the energy of the signal in the bolometer. So the total time required to obtain one image would be $N\tau$ which may be unacceptably long if τ is large. This becomes less of an issue however if the bolometers are fast. For example, if we consider a hot-electron direct detector (HEDD) which is a recently proposed micron-size version of a TES bolometer [6], the intrinsic time constant given by the electron-phonon relaxation time can be ≈ 1ms [7]. However, modification of the time constant due to the electro-thermal feedback mechanism would reduce it to 30-100 μs. In this case even a 10^4-element array can be read out in ~ 1 sec.

The second issue is the generation of the electrical polarity patterns. If the patterns are generated outside of the dewar then this technique does not have any advantage in reducing the heat load on the cryogenic system. One would need to run $2N$ wires to bias the bolometers. However, due to the binary nature of the Walsh-Hadamard functions and the cyclic properties of S-matrices from which the Hadamard matrices can be originated [5], a better solution is available. We envision a custom-designed digitially-controlled pattern generator circuit located on one of cold stages near the array (see Fig. 3). Such a circuit would generate a new polarity pattern at N serial outputs every time a new control bit arrives at the input. It would need just a few wires for bias and control input. The read-out SQUID would typically need 6 wires. The design of the pattern-generator would depend on the cooling requirements. If the detectors need to be moderately cooled (≥ 1 K), the circuit can be placed on a 4K-stage. In this case, it could use semiconductor transistor technology. For deeper cooling (<< 1 K), very low-power Josephson logic circuits could be used.

The HT multiplexing technique should work well with arrays of HEDD bolometers. In addition to the record sensitivity predicted at submillimeter wavelengths [6], the

HEDD bolometers can be fabricated on bulk dielectric substrates (Si, sapphire) (see Fig.4). It is certainly attractive to combine such an array with an on-chip Walsh-Hadamard function generator. Another advantage, as was mentioned above, is the small time constant which makes the time needed to take one image short enough for most applications.

In conclusion, a new approach based on Hadamard Transform coding is proposed for multiplexing of large array of detectors. The method uses only one amplifier to read out many detectors and does not put any hard limit on the number of detectors (10^4 detectors may be possible). The signal-to-noise ratio for a single reading can be improved by factor of square root of the number of detectors. For subkelvin cryogenic applications this approach can be an important solution drastically reducing the number of wires between the cold stage and the room temperature electronics.

We thank L.A. Luizova, A.D. Khakhaev for sharing their experience with Hadamard Transform based algorithms for image recognition. Fruitful discussions with P.H. Siegel, A. Neto, M. Seiffert, and V. Kapluneko are greatly appreciated.

This research was performed by the Jet Propulsion Laboratory (California Institute of Technology) under a contract with the National Aeronautic and Space Administration and was partly supported by the Caltech President's Fund.

References

1. J.A. Chervenak, K.D. Irwin, E.N. Grossman, J.M. Martines, C.D. Reintsema, and M.E. Huber, *Appl. Phys. Lett*. **74**, 4043 (1999); *Nucl.Instrum.and Methods in Physics Research* **A44**, 107 (2000).
2. J. Yoon, J. Clarke, J.M. Gildemeister, A.T. Lee, M.J. Myers, P.L. Richards, and J.T. Skidmore, *Appl. Phys. Lett.* **78.** 371 (2001).
3. N. Ahmed and K.R. Rao, *Ortogonal Transforms for Digital Signal Processing*, Springer-Verlag, Berlin-Heidelberg-New York, 1975, pp.89-94.
4. L.A. Luizova and A.D. Khakhaev, *private communication.*
5. M.Harwitt and N.J.A.Sloane, *Hadamard Transform Optics*, Academic Press, New York, San Francisco, London 1979.

6. B.S. Karasik, W.R. McGrath, H.G. LeDuc, and M.E. Gershenson, *Superconductor: Science & Technology* **12**, 745 (1999); B.S. Karasik, W.R. McGrath, M.E. Gershenson, and A.V. Sergeev, *J. Appl. Phys.* **87**, 7586 (2000).
7. M.E. Gershenson, D. Gong, T. Sato, B.S. Karasik, W.R. McGrath, and A.V. Sergeev, *Proc. 11th Int. Symp. on Space Terahertz Technology*, May 1-3, 2000, University of Michigan, Ann Arbor, MI, pp.514-523.
8. B.S. Karasik, M.C. Gaidis, W.R. McGrath, B. Bumble, and H.G. LeDuc, *Appl. Phys. Lett.*, **71**, 1567 (1997).

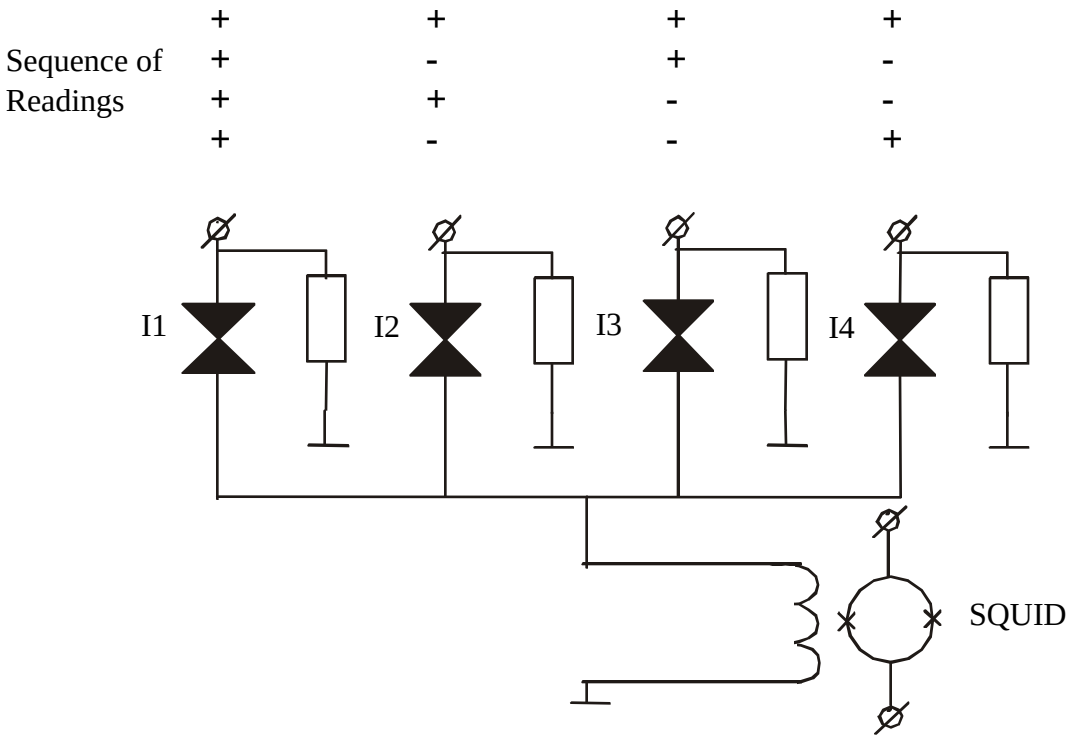

Fig. 1. An electrical circuit for multiplexing of 4 transition-edge sensors. All four detectors are individually voltage biased. Signal currents (I1-I4) from all detectors are summed into a SQUID input coil. The multiplexing is done by applying a sequence of four polarity patterns of bias voltage. The de-convolution of the signal distribution among the detectors is done using the Hadamard Transform algorithm.

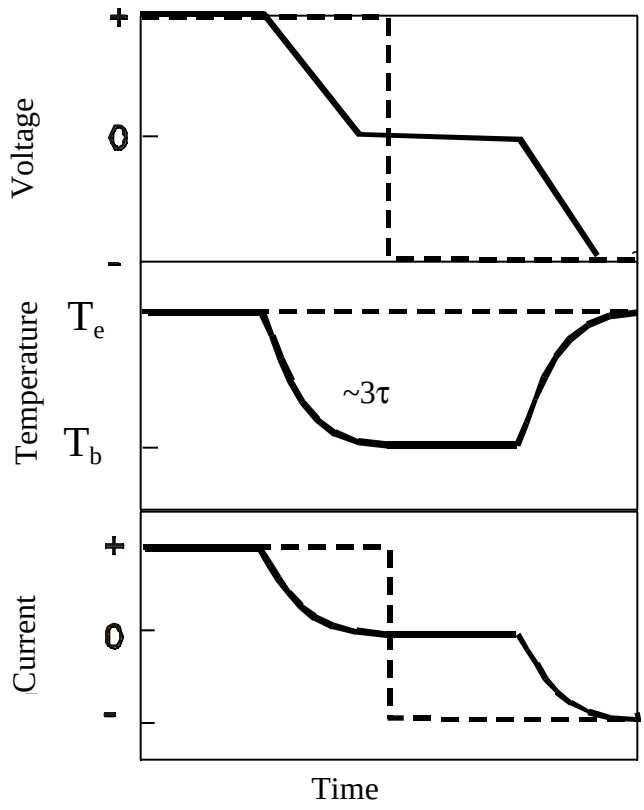

Fig. 2. The time diagram for switching polarity across a bolometer. If the switching is done fast (dashed line) comparing to the bolometer response time τ, the electron temperature does not "sense" that and remains constant. So, the current just changes its polarity and the device is ready again. The polarity pattern should be held during a period of at least τ to let the bolometer collect all the signal energy. If the switching is slow (soild line) then a time of at least 2-times-3τ would add to the signal hold time, which corresponds to the time required for the bolometer to warm-up and cool-down.

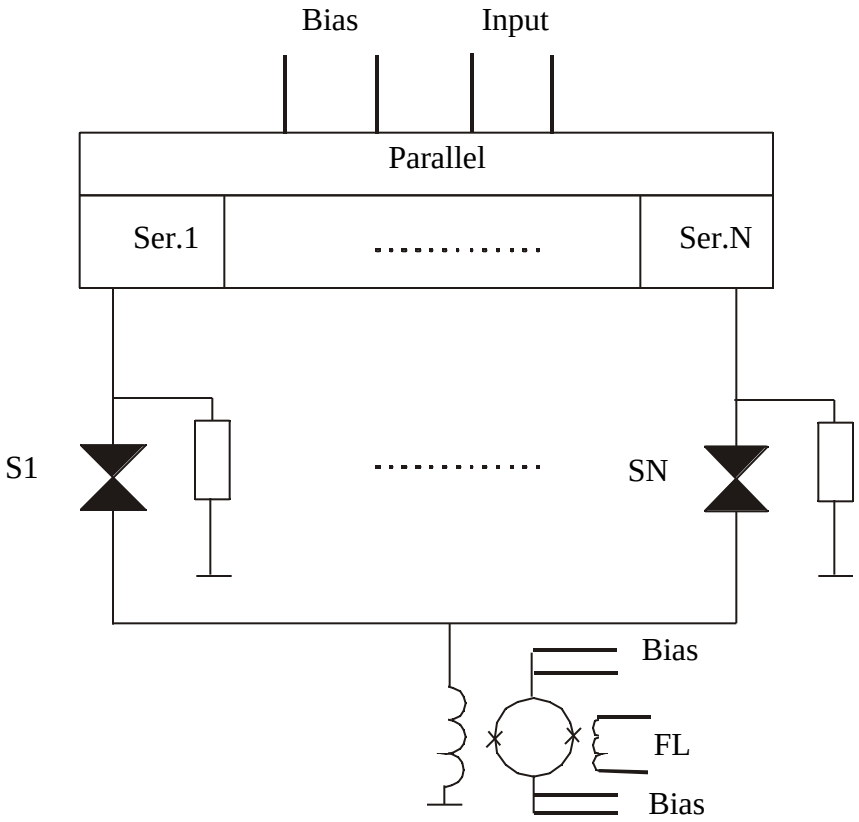

Fig. 3. Schematic block-diagram for generating Walsh-Hadamard electrical bias patterns A new bias pattern is generated each time a bit is received at the input. This circuit may need just a few wires for bias and signal input. A SQUID amplifier would need 6 wires: 4 for bias and 2 for the feedback loop (FL).

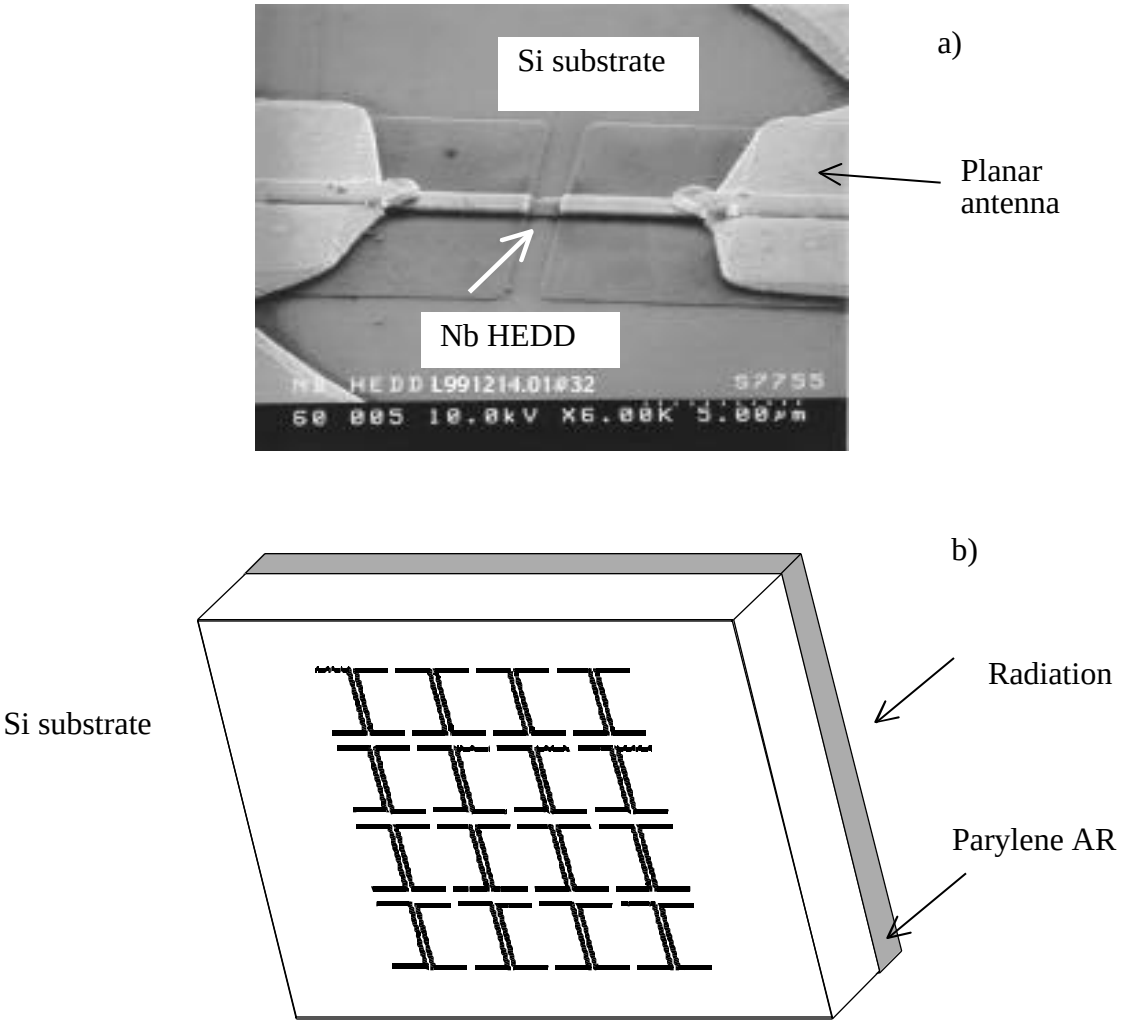

Fig. 4. A monolithic array of antenna-coupled HEDD bolometers for submillimeter wavelengths.

a). an SEM image of a 1×1 μm^2 Nb prototype HEDD bolometer on a Si substrate. The device is combined with a spiral antenna (not shown). The detector was fabricated by H.G. Leduc at JPL.

b). A 4×4 array of bolometers for submillimeter wavelengths. Narrow band antennas will be useful for lower T_c bolometers to limit background loading effects. A twin-slot antenna (shown in the figure) is a possible choice since it has a relatively narrow one octave bandwidth. Such antennas have been used up to 2.5 THz [8] for hot-electron superconducting mixers. A parylene anti-reflecting (AR) coatings works well for Si at THz frequencies.

Optical Qualification of the Normal Metal Hot-Electron Microbolometer (NHEB)

Denis Chouvaev, Daniel Sandgren, Michael Tarasov*, and Leonid Kuzmin

Chalmers University of Technology, Department of Microelectronics and Nanoscience
SE-412 96 Göteborg, Sweden
* On leave from IREE RAS, 103907 Moscow, Russia
e-mail: chouvaev@fy.chalmers.se

Abstract

We are presenting here the first results of optical responsivity measurements for the Normal Metal Hot-electron Microbolometer (NHEB), a hot-electron direct detector for sub-mm wavelengths. The detector is a metallic microresistor coupled to a planar antenna; superconductor-insulator-normal metal (SIN/NIS) tunnel junctions are employed to monitor the temperature of the electron gas. We aim to achieve with this detector sensitivity around 10^{-17} W/√Hz at 0.3 K while the time constant is going to be less than 1 μs. Planar design of the NHEB is favorable for its future expansion into a detector array. Earlier we have measured electrical NEP (noise equivalent power) of 3×10^{-16} W/√Hz for an NHEB at 0.3 K. This time we have performed an optical responsivity measurement for another NHEB at 0.5 K using a hot/cold load. We have obtained an optical responsivity value consistent with the electrical responsivity data, and with the estimated efficiency of the quasioptical coupling.

Introduction

Direct detectors can be used in those astrophysical applications where sensitivity is more important than the spectral resolution. Some examples of studies are observation of the extragalactical objects, observation of remote galaxies radiation from which is highly red-shifted, and study of the early phases of the star formation. For these applications the interesting frequency range is between 400 GHz and 1.2 THz [1]. Another kind of study, where bolometers are employed, is the Cosmic Microwave Background (CMB) study. In the CMB experiments astrophysicists try to resolve fine fluctuations of intensity in the relict radiation with equivalent black-body temperature around 2.7K, that is why the interesting frequency range there is 50..300 GHz.

Today's most common type of bolometers is the NTD-Germanium thermistor suspended on a SiN-mesh. The newer type is a superconducting transition-edge sensor (TES), also suspended on thin SiN or Si supports [2][3]. All these bolometers have noise equivalent power (NEP) around 10^{-17} W/Hz$^{1/2}$, which usually means that their sensitivity is already

limited by noise from fluctuations in the stream of received photons (photon noise). However the time constant is at the level of 1 ms, which means that an experiment requires very long observation time. This problem can be resolved by integrating many bolometers into an array, thus building an imaging camera. Several research groups have proposed different ways how large bolometer arrays could be built, however at present there is still no fully developed solution for a fast, sensitive, and robust bolometer, that could be easily integrated into an array with thousands of pixels.

It would be a great advantage for integrating the detectors if the whole array could be fabricated on a single wafer and processed at the same time instead of assembling it from individual elements as it is usually done nowadays. We are developing a detector which is fully compatible with the planar microtechnology and can be fabricated on a standard silicon wafer without membranes or any suspended structures. This detector, normal-metal hot-electron bolometer (NHEB) is an antenna-coupled device, similar to the widely known hot-electron heterodyne mixers. Its operating temperature is 0.3 K or below, and the sensitivity after optimization can be as good as 10^{-17} W/Hz$^{1/2}$ at 0.3 Kelvin and 10^{-19} W/Hz$^{1/2}$ at 0.1 Kelvin. Furthermore, this bolometer has the time constant as short as 20 μs at 0.1 K (less than 1 μs at 0.3 K), thus allowing for high-speed scans. In the following text we review the prospects of this detector and describe its optical qualification that has been done now for the first time.

The Normal-Metal Hot-Electron Bolometer

The normal metal hot-electron bolometer (fig. 1) has been proposed by M. Nahum *et al* [4][5]. It consists of a normal-metal absorber strip with small volume connected as a matched load to a planar antenna, and a pair of Normal metal-Insulator-Superconductor (NIS) tunnel junctions. The electron gas in the absorber strip receives thermal energy from the high-frequency currents induced in the antenna and gives it away to the lattice phonons in the film. At low temperatures the electron-phonon interaction time is much longer than the electron-electron interaction time, so that the electrons arrive at thermal equilibrium at a temperature which is higher than the lattice temperature (hot-electron effect). In order to avoid energy loss through diffusion of the electrons into the antenna the strip is contacted via superconducting electrodes, since the Andreev effect prohibits energy transport from the normal metal to the superconductor at an NS-interface. Variations of the electron temperature in the absorber strip of the NHEB are detected from smearing of IV-curves of the NIS junctions, which have the strip as their N-electrode. In the latest design of our devices the absorber strip is made of copper and has dimensions 5.6μm×0.25μm×0.03μm. The superconducting electrodes are made of aluminum. The NIS junctions have normal resistance between 1 and 10 kOhms.

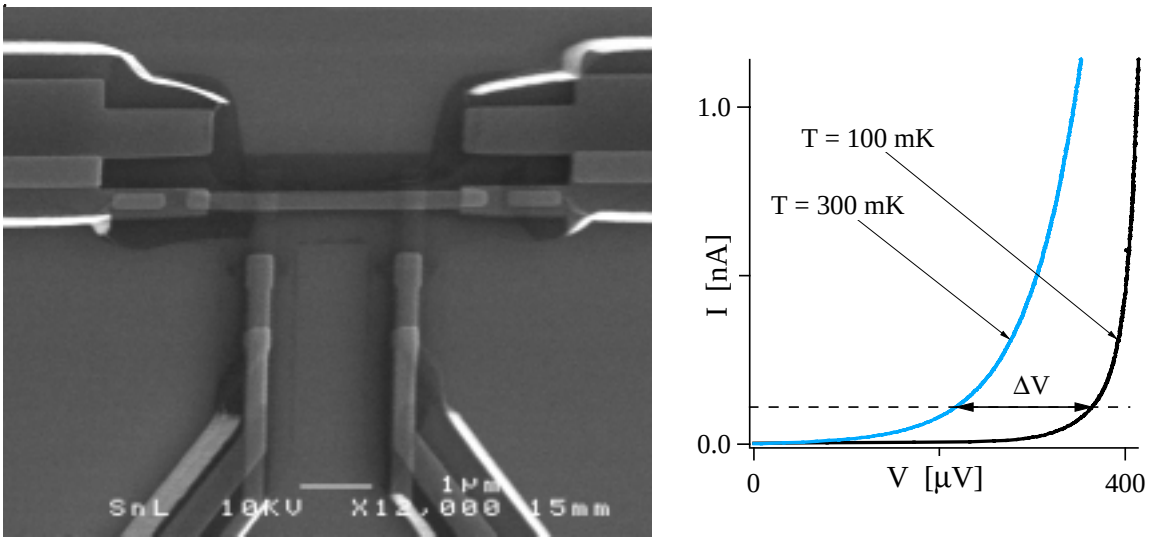

Fig. 1

Left panel – *SEM image of the power sensor (tilted view). The structure is fabricated by e-beam lithography and shadow metal evaporation from different angles.*

Right panel – *principle of operation of the NIS thermometer. Two junctions in series are biased with a constant current. Voltage over the junctions is then almost linearly dependent on the electron temperature in the normal electrode.*

The following expressions can be used for a simple estimation of speed and sensitivity of the detector at various temperatures:

$$NEP = e_n / S$$

is the Noise Equivalent Power (NEP), which is the common measure of sensitivity for bolometers; e_n is the total voltage noise at the output of the bolometer and S is the bolometer's responsivity (output voltage change per unit of input power change). The output noise is a sum of many contributions: thermal fluctuation noise, shot noise in the tunnel junctions, noise from thermal flow fluctuations in the junctions, amplifier noise, and the photon noise. A detailed analysis of the different noise contributions can be found in [6]. Here we can mention that in all experiments reported by now the output noise has been dominated by the noise of a semiconductor amplifier. In our latest experiment we had e_n = 15 nV/Hz$^{1/2}$ at 35 Hz with a room-temperature amplifier, and we estimate that by using a cold amplifier we must be able to reach e_n = 3 nV/Hz$^{1/2}$.

The responsivity is given by

$$S = \frac{dV}{dT} \cdot \frac{dT}{dP} = \frac{dV}{dT} \cdot \frac{1}{G}$$

where T is the electron temperature in the absorber strip, dV/dT is the temperature responsivity of the tunnel junctions, and G is the thermal conductance from electrons to

phonons in the absorber strip. dV/dT for aluminum junctions is nearly constant from 0.15 K to 0.45 K with nominal value of 8×10^{-4} V/K per pair. Low thermal conductance is of the key importance for obtaining high responsivity and low NEP, and it is strongly dependent on the operating temperature. For copper films which we use for the absorber strip in the NHEB, the electron-phonon cooling rate is given by

$$P_{ep} = \Sigma\Omega\left(T^5 - T_0^5\right)$$

where Ω is the volume of the strip (0.045 μm^3), Σ is the material parameter (2.5×10^{-9} W $\mu m^{-3}K^{-5}$ for copper), and T_o is the phonon temperature. Then the thermal conductance will be

$$G = 5\Sigma\Omega T^4 .$$

The time constant of the bolometer is equal to the electron-phonon interaction time in the absorber strip. According to the data that can be found in literature [5] this constant for our type of films is

$$\tau_{ep} = 20 / T^3 \text{ ns.}$$

By substituting the typical values into the formulas above we get the following summary of performance parameters expected for the NHEB:

	T = 0.3 K	T = 0.1 K
thermal conductance G	5×10^{-12} W/K	6×10^{-14} W/K
responsivity S	1.8×10^{8} V/W	9×10^{9} V/W
NEP with e_n = 15 nV/Hz$^{1/2}$	8×10^{-17} W/Hz$^{1/2}$	1.7×10^{-18} W/Hz$^{1/2}$
NEP with e_n = 3 nV/Hz$^{1/2}$	1.7×10^{-17} W/Hz$^{1/2}$	3×10^{-19} W/Hz$^{1/2}$
time constant	0.7 μs	20 μs

In our earlier experiments we measured the so-called electrical responsivity of a NHEB, that is response at the output per unit power dissipated in the absorber strip by a constant current applied through it. We obtained $S_E = 1\times10^8$ V/W at 0.3 K and $S_E = 4\times10^9$ V/W at 0.1 K for a bolometer with absorber strip of double the volume used in the calculations above [7]. Thus the experimental values were in a good correspondence with theory.

In order to measure the optical responsivity, which is the response per unit power of an external sub-mm wave signal coupled to the bolometer, we had to incorporate the NHEB power sensor with a suitable planar antenna. We have chosen the twin-slot antenna because of its reasonably narrow pattern and frequency characteristics. The slot dimensions were designed using the calculation procedure developed at Caltech [8]. To simplify the fabrication process coupling between the slots and the power sensor has been

done by two co-planar waveguides (CPW) with characteristic impedance of 30 Ohms, which is equal to the antenna impedance at the resonance frequency (300 GHz) – see figure 2.

Fig. 2

The twin-slot antenna. The bolometer (in the center) is connected to the slots by a CPW transmission lines with characteristic impedance of 30 Ohms, which matches the calculated impedance of the slots at 300 GHz. The ground plane is divided by another narrow slot in other to allow measurements of resistance of the absorber strip and to make space for the bias wiring of the tunnel junctions.

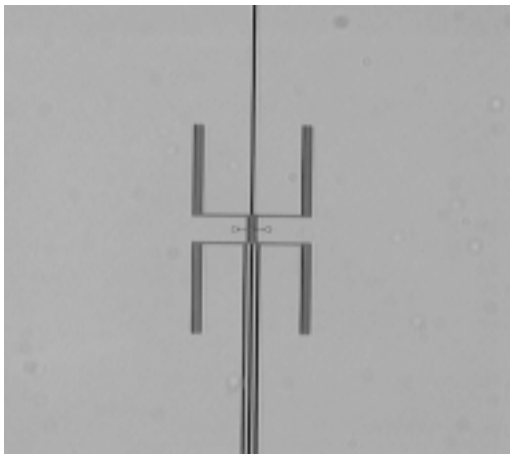

The optical setup

The concept of our optical setup was described in detail in [7]. These are its main elements:

- Helium dewar with an optical window, type HDL-8 from IR-labs; minimum temperature of the cold plate is about 1.5 K achievable by pumping on the helium bath.
- Closed-cycle ^{3}He cryocooler mounted at the cold plate of the dewar and providing cooling of a detector holder to 0.3 K.
- Detector holder containing the detector, a hyperhemispherical silicon lens, and a focusing dielectric lens.
- Filter unit mounted in the dewar window and cooled to the cold plate temperature.

This setup provides coupling of the external radiation to the detector cooled to 0.3 K by a nearly gaussian beam, so that the whole throughput of the antenna is covered by an external load. It also prevents overheating of the bolometer by thermal radiation at high frequencies. For the latter purpose we are using three sequential filters (in order from room to detector):

- metal mesh resonant low-pass filter with sharp edge at 450 GHz
- alkali-halide low-pass filter with edge at 1650 GHz; this filter blocks the resonant leaks of the metal-mesh filter at higher frequencies
- neutral density filter with 1.3% (-18.9 dB) transmission reducing the overall power load on the bolometer from the room-temperature environment.

All the filters are fabricated by QMCI [9]. The schematic diagram of the quasioptical path and a view of the cold work area of the dewar are shown in the figures 3 and 4.

Fig. 3

Ray traces in the quasioptical path (at the -8.7dB relative power level) for frequencies from 180 GHz to 420 GHz. The components on the drawing from left to right are the filter unit aperture, the dielectric lens and the hyperhemispherical lens (shown by a small circle). The traces are calculated in the assumption of the gaussian beam shape.

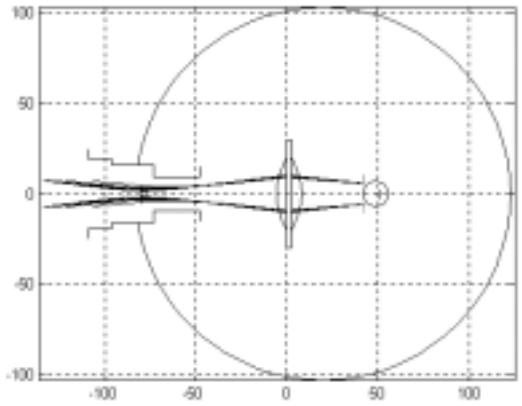

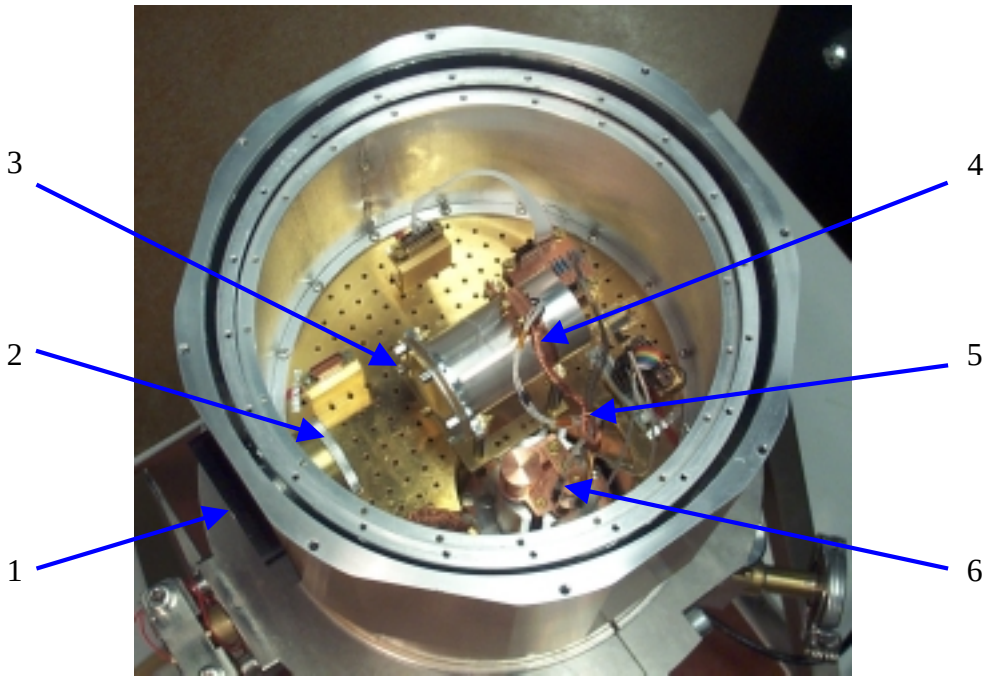

Fig. 4 *View of the cold working area in the cryostat: 1 – the optical window; 2 – the filter unit; 3 – the focusing dielectric lens; 4 – the detector holder (position of the Si lens); 5 – the 0.3 K thermal strap; 6 – the ^{3}He cryocooler.*

The measurement results

In our optical qualification experiment we have measured how voltage across the tunnel junctions of the NHEB changes in response to switching between the hot (room temperature) and cold (liquid nitrogen) loads placed outside the dewar window. View of the experimental setup is presented in the Fig. 5. The measurements were done with a lock-in amplifier and the chopping frequency was 35 Hz. We have also measured the voltage noise at the output of the amplifier in order to determine the NEP of the bolometer. By modulating an external microwave source irradiating the bolometer we could estimate the post-detection bandwidth of the system, which was limited by the RC-constant of the readout.

Fig. 5

Setup used in the optical responsivity measurement: the chopper disk is tilted 45° from the optical axis; the bolometer sees either the lab environment reflected by a chopper blade (hot load) or an Eccosorb pad floating in liquid nitrogen in the foam box behind the chopper (cold load).

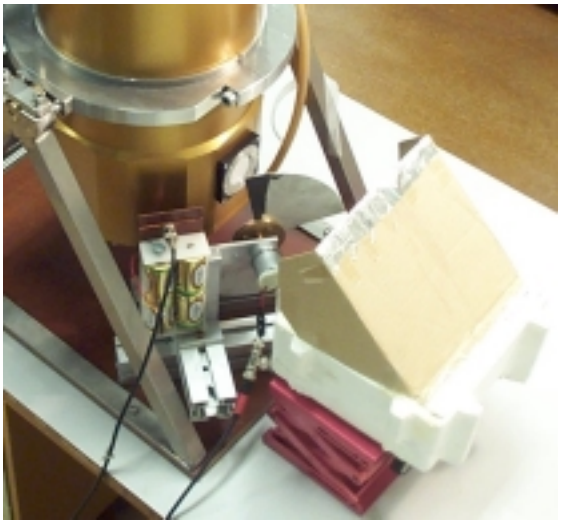

The NHEB used in this experiment had an absorber strip with resistance of 30 Ohms. The detector sample had been tested first electrically in a dilution refrigerator at T = 0.3 K.. 0.5 K. We have recorded IV-curves of the junctions at different temperatures, which has allowed us later to measure the electron temperature of the absorber strip in the optical experiment.

The results of the optical responsivity measurements are shown in the Fig. 6. The maximum response was 4 μV at the optimal bias current of 1.2 nA. By comparison of the junctions' IV-curve with the IV-curves recorded in the dilution refrigerator we could conclude that the electron temperature in the absorber strip was 0.50 K, which also was the minimum electron temperature we could achieve in this experiment, even though the cryocooler's physical temperature was as low as 0.30 K. Presently we suspect that this overheating was due to the rf-interference from outside the cryostat penetrating through the test wiring attached to the antenna plane.

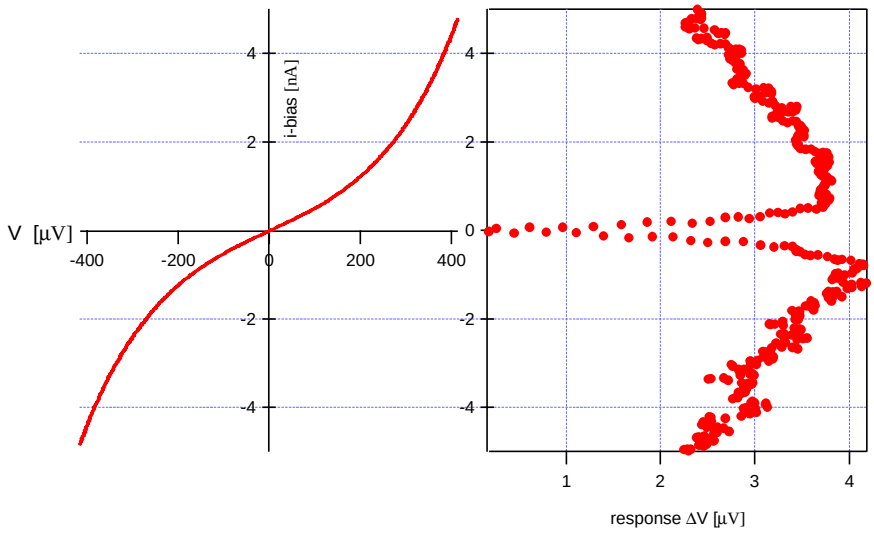

Fig. 6 Left panel: *IV-characteristics of the SINIS tunnel junctions in the optical responsivity measurement; the curve corresponds to the electron temperature of 0.5 K in the N-electrode (absorber strip).* Right panel: *Voltage response corresponding to chopping between cold and hot loads outside the dewar window. The measurement has been done with a lock-in at 35 Hz. The vertical axis is the junctions' bias current (same as in the left panel).*

A simple estimation of how the radiation power coupled to the bolometer changes with switching between the cold and the hot loads can be obtained with the following expression, derived from the Plank's formula for blackbody radiation in the limit of high temperatures and low frequencies:

$$\Delta P = \eta \cdot k_B (297K - 77K) \cdot \Delta f \ .$$

η represents all the optical and coupling losses, and Δf is the detection bandwidth which in our case is determined by the width of the main resonance in the frequency characteristics of the antenna. We have accounted for the following losses:

- Dewar windows (teflon), reflection, -0.4 dB
- Neutral density filter, calibrated by the manufacturer, -18.9 dB
- Focusing dielectric lens (TPX), reflection, -0.2 dB
- Silicon lens, reflection, -1.5 dB

This gives in total -21 dB, or $\eta = 7.9\times10^{-3}$. The unaccounted losses can be absorption losses, interference losses, antenna losses, and antenna-to-bolometer matching losses. The bandwidth Δf has been estimated from a measurement done on a 100:1 scale model of the antenna as $0.3f_o$, or 100 GHz (accurate within about ±50%). Substituting the

estimations for the losses and for the bandwidth into the expression above we get ΔP = 2.4×10^{-12} W and maximum responsivity $S = \Delta V / \Delta P = 1.7\times10^{6}$ V/W.

The theoretical responsivity of the NHEB with this volume of the absorber strip would be $S_{theor} = 1.5\times10^{7}$ V/W at 0.5 K. If we associate the discrepancy solely with the unaccounted losses it would mean that those losses in this experiment were as large as -9.5 dB.

Fig. 7

Voltage noise from the NHEB at the operating conditions and the amplifier's own noise. The optical responsivity has been measured at 35 Hz.

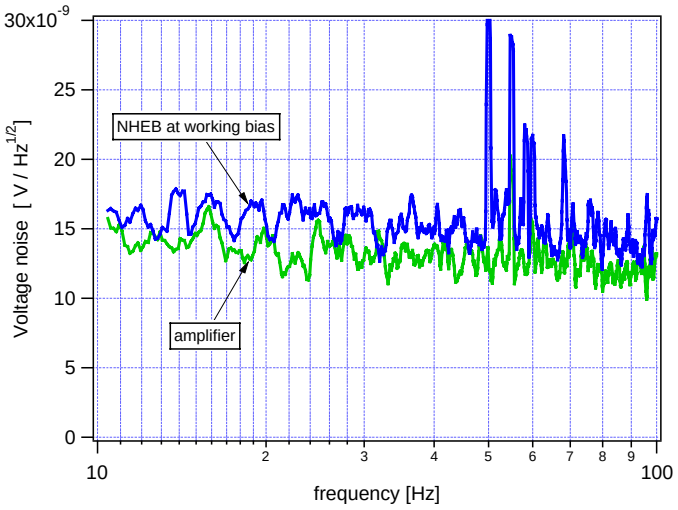

The results of the noise measurements are shown in the Fig. 7. The noise from the amplifier (INA110, differential OpAmp with an FET input) is the dominating contribution (13 nV/Hz$^{1/2}$ at 35 Hz). The total bolometer noise at 35 Hz (the frequency used in the optical responsivity measurement) is about 15 nV/Hz$^{1/2}$ which corresponds to $NEP = e_n/S = 9\times10^{-15}$ W/Hz$^{1/2}$. For the same bolometer operating at 0.3 K and in the absence of coupling losses this output noise would have corresponded to $NEP = 9\times10^{-17}$ W/Hz$^{1/2}$.

Finally, we attempted to measure the time constant of the detector or that of the measurement system, whichever would be shorter. We had placed an IMPATT oscillator radiating at 62 GHz in front of the dewar window and modulated it at frequencies up to 200 kHz. To reduce the incident power the window was blocked by a metal bar, leaving a small gap just enough to get a measurable response from the NHEB. We have observed a –6 dB/octave roll-off with characteristic frequency 20 kHz (Fig. 8). Considering the dynamic resistance of the tunnel junctions at the working point (100 kOhms) and capacitance of the wiring connecting the junctions to the amplifier (about 100 pF), this frequency behavior perfectly corresponds to the low-pass filtering action of the readout circuit. The conclusion has been made that the time constant of the bolometer itself is at least below 10 μs. The theoretical value of the NHEB's time constant at 0.5 K is 0.16 μs (f_{mod} > 6 MHz).

Fig. 8

Dots: *Amplitude of the bolometer's response to radiation from a strong 62 GHz-source modulated at different frequencies.*

Curve: *theoretical frequency characteristics of an RC lowpass filter with f_c=20kHz. This value corresponds quite well to the R and C of the readout circuit. No rolloff contribution from the bolometer itself could be identified.*

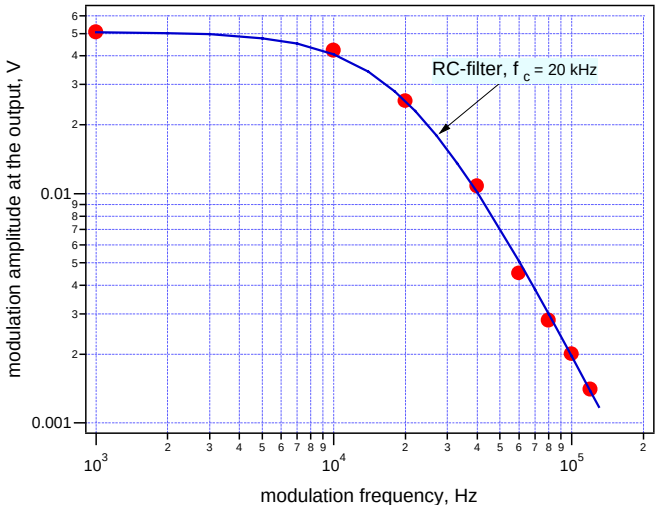

Further development

In the near future we are aiming to improve our experiment and achieve better values of sensitivity. The primary issue is to avoid the rf interference by installing additional filters in the cryostat. In this way we hope to reduce the working temperature of the bolometer to the physical temperature of the cryocooler, that is 0.3 K. The next step will be to minimize the output noise by using a cooled amplifier with noise level below 5 nV/Hz$^{1/2}$ in the vicinity of the detector. These two measures should improve the sensitivity by the factor of 20. At the same time we will need to identify and measure the unknown losses in the optical coupling and measure the true frequency spectrum of the receiver. We plan to do this by using a Fourier Transform Spectrometer.

Later on we would like to improve the performance of the NHEB even more by decreasing the absorber strip volume and by trying out materials other than copper and aluminum. It has been reported that in Hafnium and possibly in some other thin films one could obtain dependence of the τ_{ep} on temperature as T^4 instead of T^3 [10]. This would mean that the electron-phonon thermal conductance might be reduced even more, thus enhancing the bolometer responsivity. And besides the development of the individual detector element we plan to provide eventually also an array solution with a few NHEBs operating simultaneously on the same chip.

Conclusions

We are developing the NHEB - an antenna-coupled hot-electron direct detector particularly suitable for creating rapid bolometer cameras. According to the electrical responsivity measurements this detector can have sensitivity of NEP = 10^{-17} W/Hz$^{1/2}$ and

time constant in the microsecond range at 0.3 K; a greatly better performance is possible at 0.1 K. Functionality of the NHEB has now been demonstrated in an optical qualification experiment with hot/cold load; the detector has been operated at 0.5 K and it has shown the optical NEP = 9×10^{-15} W/Hz$^{1/2}$. In the near future we aim to improve performance of the NHEB at 0.3 K and obtain the predicted level of sensitivity; later on we will also start to develop an array solution.

Acknowledgements

We are grateful for the scientific and technical support from the bolometer group at the University of California at Berkeley (Prof P.L. Richards *et al*).

This project is supported by The Swedish Research Council for Engineering Sciences (TFR) and by Swedish Foundation for Strategic Research (SSF).

References

[1] M. Griffin, B. Swinyard, L. Vigroux, *Proc. SPIE 4013, Munich, 27-31 March 2000*

[2] J.M. Gildemeister, Adrian T. Lee, P.L. Richards, *Appl. Phys. Lett.*, Vol. 74, No. 6, 868 (1999)

[3] D.J. Benford, C.A. Allen, A.S. Kutyrev, S.H. Moseley, R.A. Shafer, J.A. Chervenak, E.N. Grossman, K.D. Irvin, J.M. Martinis, C.D. Reintsema, *Proc. of the 11th Int. Symp. on Space Terahertz Technology, Ann Arbor, MI, May 1-3 2000*, pages 196-205

[4] M. Nahum, P.L. Richards, C.A. Mears, *IEEE Trans. Appl. Supercond.*, Vol. 3, No. 1, 2124 (1993)

[5] M. Nahum, J. Martinis, *Appl. Phys. Lett*., Vol. 63, No. 22, 3075 (1993)

[6] D. Golubev and L. Kuzmin, submitted to the *Journal of Applied Physics*

[7] D. Chouvaev and L. Kuzmin, *Proc. of the 11th Int. Symp. on Space Terahertz Technology, Ann Arbor, MI, May 1-3 2000*, pages 465-473

[8] J. Zmuidzinas, H.G. LeDuc, *IEEE Trans. on Microwave Theory and Techniques*, 40(9):1797-1804, Sept. 1992

[9] Ken Wood /QMC Instruments Ltd., http://qmciworks.ph.qmw.ac.uk/Products_frame.htm; accessed 2000-04-27.

[10] M.E. Greshenson, D. Gong, T. Sato, B.S. Karasik, W.R. McGrath, A.V. Sergeev, *Proc. of the 11th Int. Symp. on Space Terahertz Technology, Ann Arbor, MI, May 1-3 2000*, pages 514-523

Focal Plane Arrays of Voltage-Biased Superconducting Bolometers

Michael J. Myers[1,5], John Clarke[1,4], J. M. Gildemeister[1,4], Adrian T. Lee[1,2,3], P. L. Richards[1,3,4,5], Dan Schwan[1,5], J. T. Skidmore[1,5], Helmuth Spieler[2], Jongsoo Yoon[1,4]

[1] *Department of Physics, University of California, Berkeley, CA 94720*
[2] *Physics Division, Lawrence Berkeley National Laboratory Berkeley, CA 94720*
[3] *Center for Particle Astrophysics, 301 LeConte Hall University of California, Berkeley, CA 94720*
[4] *Material Science Division, Lawrence Berkeley National Laboratory, Berkeley, CA, 94720*
[5] *Space Sciences Laboratory University of California, Berkeley, CA 94720*

Introduction

The 200μm to 3mm wavelength range has great astronomical and cosmological significance. Science goals include characterization of the cosmic microwave background, measurement of the Sunyaev-Zel'dovich effect in galaxy clusters, and observations of forming galaxies. Cryogenic bolometers are the most sensitive broadband detectors in this frequency range. Because single bolometer pixels are reaching the photon noise limit for many observations, the development of large arrays will be critical for future science progress.

Voltage-biased superconducting bolometers (VSBs) have several advantages compared to other cryogenic bolometers. Their strong negative electrothermal feedback enhances their linearity, speed, and stability. The large noise margin of the SQUID readout enables multiplexed readout schemes, which are necessary for developing large arrays. In this paper, we discuss the development of a large absorber-coupled array, a frequency-domain SQUID readout multiplexer, and an antenna-coupled VSB design.

Absorber-Coupled Filled VSB Arrays

A closely packed array of bolometers mounted directly in the focal plane of a telescope can give a higher overall efficiency than other designs. We have developed a monolithic design for large format filled arrays of absorber-coupled voltage-biased superconducting bolometers [1].

The thermal isolation required by a bolometer creates a challenge in developing a close packed array. Our design (Figure 1) makes use of a folded leg suspended structure with a square absorber to allow for an array with a high filling factor while maintaining the requisite thermal isolation. The absorber is an open mesh, allowing for efficient absorption of mm-wave optical power while minimizing the cosmic ray cross section. The open mesh absorber was pioneered with "spiderweb" semiconducting bolometers [2] and VSBs in that geometry have been fabricated by our group [3]. However, the spiderweb geometry is not well suited for a close packed array.

Single pixel prototype devices were constructed using standard microfabrication techniques. The low stress silicon nitride was deposited on a

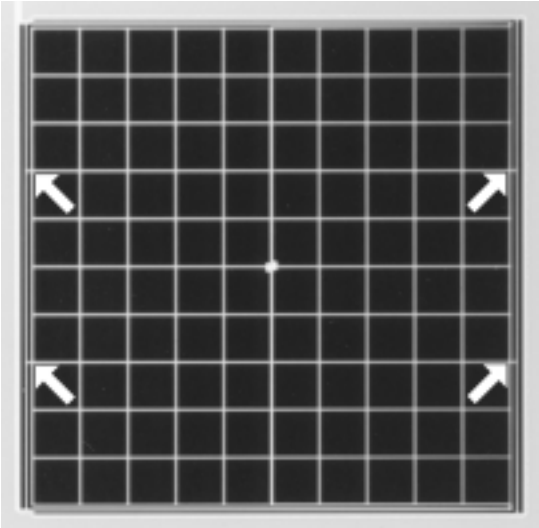

Figure 1 : Prototype single pixel for the filled array design. The absorbing grid is a silicon nitride mesh 1.5 mm on a side. The nitride grid is suspended at four points (arrows) where it is attached to tensioned nitride beams along the left and right sides of the grid. The electrical leads are supported by the nitride beams along the top and bottom of the grid. The leads make contact to the superconducting thermistor on the small patch of nitride at the center of the grid.

standard silicon wafer. The thermistor and leads were then deposited together as four successive layers consisting of Al/Ti/Al/Ti. The thick upper Al layer was etched off the top of the thermistor to create a region with a lower critical temperature (Tc) than the leads around it. Adjusting the thicknesses of the Al and Ti allows the Tc of the thermistor to be controlled. The nitride was then etched into the square mesh pattern using a fluorine plasma etch. A XeF_2 gaseous etch was used to etch the silicon underneath the nitride from the front side of the wafer.

A prototype was tested at a base temperature of 264 mK. The device was voltage biased by current biasing a 20 mΩ shunt resistor and the bolometer current was measured using a SQUID ammeter. The noise spectra were measured with a spectrum analyzer and the noise equivalent power is plotted in Figure 2. The thermal conductance was measured to be G = 2.7 x 10^{-11} W/K.

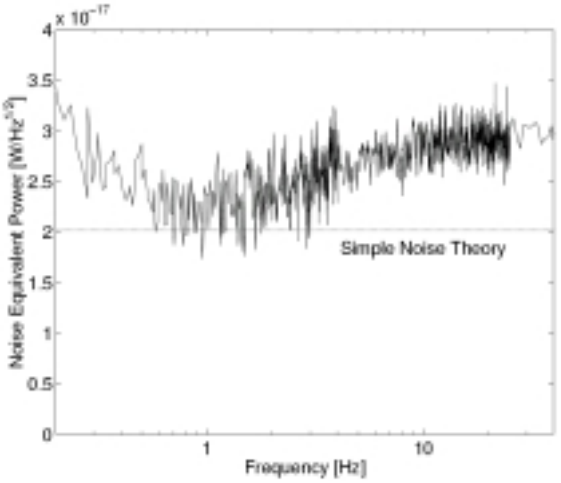

Figure 2 : Measured noise equivalent power for prototype bolometer

To optimize the optical coupling, future devices will have a reflective metal deposited on the back of the wafer as depicted in Figure 3. In free space, the distance between the reflector and the absorber should be ¼ λ to maximize absorption. The presence of silicon over part of the distance modifies the optimal length somewhat. Using SOI wafers and trench etching techniques, the reflector can accurately be placed at the correct distance [4].

In order to test the mechanical stability of this design and its suitability for use in large arrays, several nitride structures were constructed for bolometer arrays ranging from 4 x 4 to 32 x 32 pixels. Pictured in Figure 4 is the nitride mesh structure for a 32 x 32 pixel array. The nitride meshes are spaced to allow 1 μm leads with 1 μm spacing to each pixel. A similarly constructed

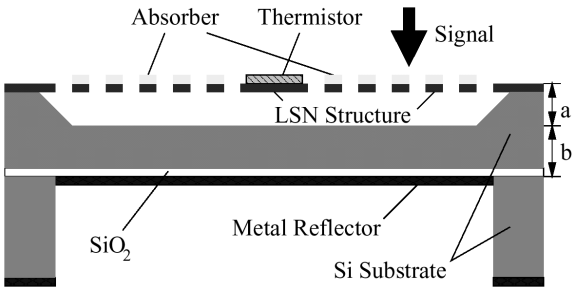

Figure 3 : Cross section of bolometer with the proposed reflector on the back side. The vertical scale has been exaggerated.

bolometer array would give a filling factor of 88%.

All of the elements in the pictured array are intact, but 10 of the 1024 meshes show defects due to dust contamination. The other nitride arrays had a similarly high yield. The devices also proved to be more robust during handling than the previously manufactured spiderweb bolometers [3]. This is likely due to the continuous silicon substrate beneath the nitride suspensions.

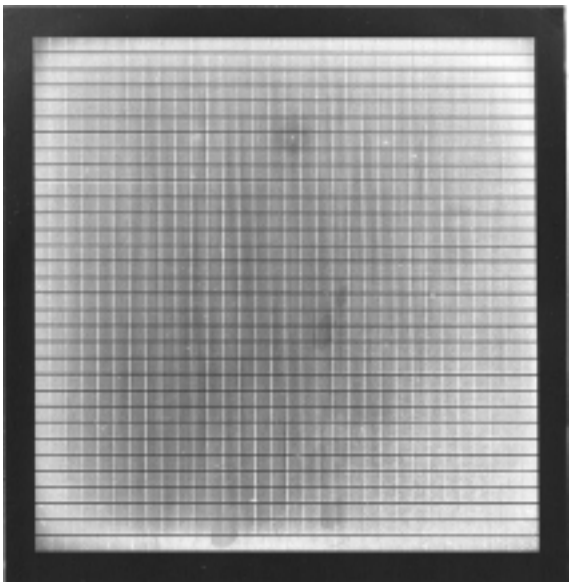

Figure 4 : 32 x 32 array of silicon nitride meshes

Antenna-Coupled VSB Arrays

Using an antenna to couple optical power into a bolometer offers some advantages. The antenna pattern can be used to control the solid angle visible to the bolometer much as a horn does but with much greater scalability. The transmission line typically used to feed the antenna can also incorporate filters, further integrating the required optical components onto the substrate. Planar antennas are also polarization sensitive, which can be quite useful for some experiments. One potential application is the measurement of the polarization of the cosmic microwave background. We are currently developing an antenna coupled bolometer design using planar antennas, transmission line filters, and lithographed VSBs.

Our current design uses a dual slot dipole planar antenna [5]. This antenna is well suited to this application as it has a symmetric beam pattern and provides a good impedance match to microstrip transmission lines. Typically a dielectric lens in direct contact with the antenna is used and the parameters of the lens and antenna can be tuned to provide a good match to the f/# of a telescope. A variant of the dual slot antenna that is sensitive to dual polarizations has been developed by Chattopadhyay and Zmuidzinas [6].

Superconducting niobium microstrip is used to feed the antenna. Superconducting microstrip is very low loss for frequencies well below that corresponding to twice the gap energy of the superconductor. Niobium is in this regime for the frequencies of this design (150-300GHz).

Band defining planar filters will be fabricated in niobium microstrip. There is a considerable amount of knowledge regarding the design of these filters in the literature. After filtering, the transmission line is terminated with a load resistor on a suspended nitride VSB. This places the load in good thermal contact with the superconducting thermistor.

We are currently working to build a prototype antenna-coupled pixel. The highly integrated nature of the design should make it easily scalable to very large arrays. Since the microstrip is low loss, it can be used to route the RF to the perimeter of the antenna array, where there is significant room for the filters, bolometers, and SQUID readout.

Frequency Domain SQUID Multiplexer

Far-infrared to millimeter wave telescopes can accommodate 10^3-10^4 element arrays, but a readout multiplexer will be required to instrument such arrays. The complexity and heat load of the readout limits the number of bolometers in current array receivers to ~10^2. A multiplexer can alleviate these problems by allowing one readout channel to service several pixels, thus reducing the wire count required for a given number of pixels. The SQUID readout of a VSB is well suited to multiplexing schemes due to its low noise and high bandwidth.

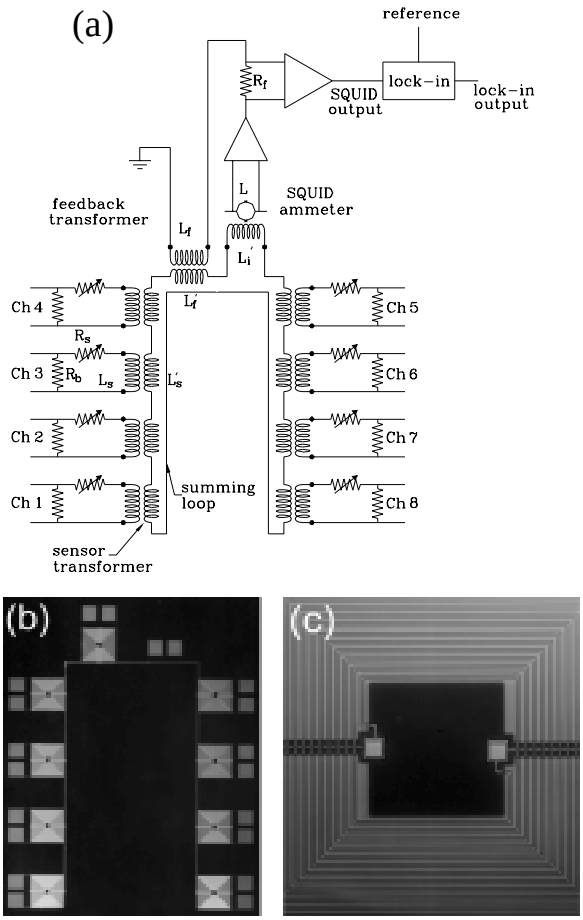

Figure 5 : (a) Schematic of the eight channel multiplexer (b) photograph of the test device (c) close-up of the center of one of the niobium transformers

We have developed a frequency domain single SQUID readout multiplexer suitable for use with superconducting bolometers [7]. A schematic of an 8 channel multiplexer using this design is pictured in Figure 5a. Each bolometer is AC biased at a different frequency and they are then coupled to a superconducting summing loop with a transformer. The current in the loop is measured with a SQUID ammeter. The individual signals are recovered by lock-in detection at the output of the SQUID electronics. The current in the summing loop is nulled by feedback to prevent crosstalk between the detectors.

We fabricated an eight channel multiplexer as depicted by the schematic in Figure 5a. Photographs of an actual chip are shown in figure 5b and 5c. The transformers and summing loop are made of thin film niobium. The transformers consist of two intertwined spiral coils over a split niobium washer to maximize magnetic coupling. A SiO_2 insulating layer separates the niobium layers. The summing loop is connected to the SQUID input coil via niobium wirebonds.

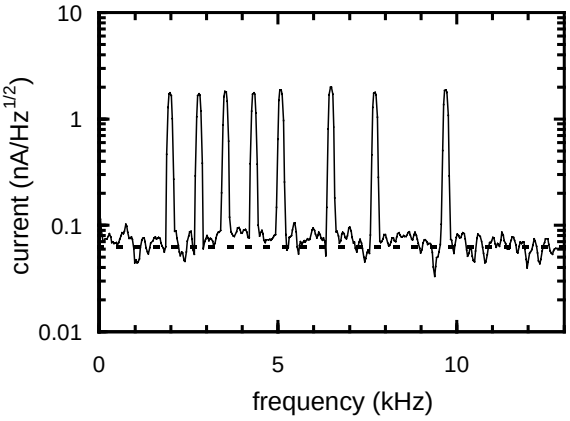

Figure 6 : Spectral density of SQUID output with all 8 channels AC biased

The multiplexer was tested at 4.2K, at which temperature the niobium is superconducting. Resistors were used as simulated bolometers and bias was applied at frequencies ranging from ~2–10kHz. The bias frequencies were spaced so as to avoid the overlap of harmonics. The spectral density of the SQUID output can be seen in Figure 6.

In order to simulate an actual bolometer signal, seven of the eight channels were 2% AC modulated at unique low frequencies from 1.6 to 19Hz. The eighth channel was not modulated in order to simulate a no signal condition. The individual signals were recovered by locking in to the bias frequency for the channel of interest. The spectral density of the lock-in output is shown in Figure 7 for one of the channels with a simulated signal (upper trace) and the eighth channel with no simulated signal (lower trace). A crosstalk of < 1% was measured, which may be due to the drive electronics.

Current work on the multiplexer involves a new design, which will operate at significantly higher bias frequencies making it suitable for faster

bolometers. We are also working to incorporate filters at the input of each channel in order to prevent the broadband Johnson noise of each detector from affecting the other detectors on the same summing loop.

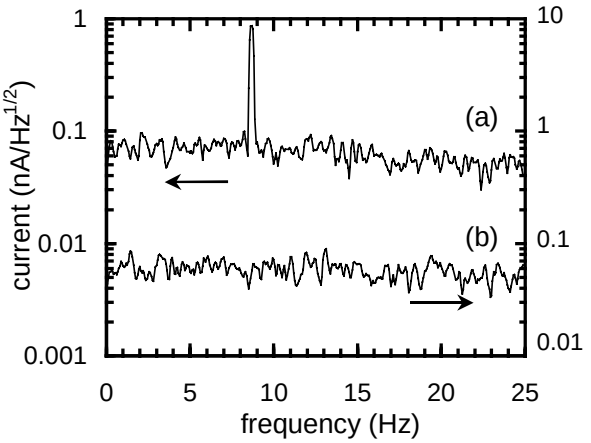

Figure 7 : Spectral density of lock-in detected SQUID output referenced to (a) Channel 5 (simulated signal) and (b) Channel 8 (no signal)

Acknowledgements

This work was supported by National Science Foundation Grant FD97-31200, NASA Grant FDNAG2-1275, and by the Director, Office of Science, Office of Basic Energy Sciences of the U.S. Department of Energy under Contract No. DE-AC0376SF00098. ATL was supported by the National Science Foundation through the Center for Particle Astrophysics (cooperative agreement AST91-20005). All devices were fabricated at the Berkeley Microfabrication Laboratory.

[1] J. M. Gildemeister, Adrian T. Lee, P. L. Richards, *Applied Physics Letters*, Vol. 77, pp 4040-4042, 11 December 2000
[2] J. J. Bock, D. Chen, P. D. Mauskopf, and A. E. Lange, *Space Science Reviews*, 74, Kluwer Academic Publishers, 229, 1995
[3] J. M. Gildemeister, Adrian T. Lee, and P. L. Richards, *Applied Physics Letters*, Vol. 74, pp 868-870, 8 February1999
[4] J. Bhardwaj, H. Ashraf, and A. McQuarrie, *Proceedings of the Third International Symposium on Microstructures and Microfabricated Systems*, Montreal, Canada, Electrochem. Soc., 1997
[5] D. F. Filipovic, G. P. Gauthier, S. Raman, G. M. Rebeiz, *IEEE Transactions on Antennas and Propagation*, Vol 45, No. 5, May 1997
[6] G. Chattopadhyay, J. Zmuidzinas, *IEEE Transactions on Antennas and Propagation*, Vol 46, No. 5, May 1998
[7] Jongsoo Yoon, J. Clarke, J. M. Gildemeister, Adrian T. Lee, M. J. Myers, P. L. Richards, J. T. Skidmore, *Applied Physics Letters*, Vol.78, pp 371-373, 15 Jan. 2001

Superconducting NbN-based ultrafast hot-electron single-photon detector for infrared range

A. Verevkin, Y. Xu, X. Zheng, C. Williams, and Roman Sobolewski

Department of Electrical and Computer Engineering and Laboratory of Laser Energetics

University of Rochester, Rochester, NY 14627-0231, USA

O. Okunev, K. Smirnov, G. Chulkova, A. Korneev, A. Lipatov, and G. N. Gol'tsman

Department of Physics, Moscow State Pedagogical University, Moscow 119435, Russia.

Abstract: *Single-photon detector (SPD) with GHz counting rate for infrared range, based on the supercurrent-assisted hotspot effect in a superconducting NbN thin-film microstructure has been developed. A photon-induced hotspot leads to temporary formation of a resistive barrier across the narrow superconducting sensor stripe and results in an easily measurable voltage pulse. Subsequent hotspot healing in <100 ps time frame, restores the superconductivity (zero-voltage state), and the detector is ready to register another photon. It exhibits an experimentally measured intrinsic quantum efficiency up to ~20% and negligible dark counts. Spectral dependence of the photoresponse is presented.*

I. Introduction

Single-photon detection is the ultimate sensitivity limit on any radiation detector. While single-photon detectors (SPD) for the x-ray to the visible photon counting are currently commonplace using photomultiplier tubes[1] or quantum semiconductor avalanche photodiodes[2], detection of single infrared photons remains a major technological challenge because infrared photons carry significantly less energy than those of visible light, making it difficult to engineer an efficient electron cascade. The most successful silicon avalanche photodiodes have a spectral sensitivity limited to below 1 μm, restricted by the Si bandgap, while photodiodes based on narrow-gap semiconductors currently exhibit unacceptably large dark counts. Vacuum photomultipliers are bulky and have extremely low quantum efficiency for above-1-μm-wavelength photons. Finally,

the most recently proposed far-infrared detectors based on single-electron transistors[3] are slow and require millikelvin temperatures and tesla-level magnetic fields. New superconducting devices are the natural choice for fast and ultrasensitive infrared detection, because of their quantum nature and low-noise cryogenic operation environment. The superconducting energy gap 2Δ is two to three orders of magnitude lower than in a semiconductor; thus, the photon absorption in a superconducting detector creates an avalanche electron charge two to three orders of magnitude higher for the same photon energy. This results in an enhanced resolution in energy-resolving devices, such as superconducting tunnel junctions[4,5], and extends the range of detectable energies well into the infrared range for photodetectors[6]. In addition, as we have recently demonstrated, energy relaxation time constants of excited electrons in superconductors are in the picosecond range for both the low-temperature[7] and high-temperature[8] superconductors, assuring the gigahertz repetition rate for superconducting photon counters.

We have developed simple to manufacture, easy to operate, superconducting SPD's. The approach that we present is to use the hot-electron photoresponse in a superconducting NbN thin-film microstructure with a large active area. This type of device is characterized by a very fast response time (down to ~30 ps), high intrinsic quantum efficiency (up to 20%), and negligible dark counts.

The SPD's detection mechanism is based on supercurrent-assisted hotspot formation of a resistive barrier across a very narrow superconducting stripe, kept at the temperature well below the material's superconducting transition T_c~11 K for NbN. The hotspot formation process includes formation of phase-slip-centers (PSC) and results in a large (above 1 mV), easily measurable voltage signal.

II. Device fabrication and geometry

We use nominally 0.1-0.2-μm-wide meandering strip patterned from ultrathin (5-nm-thick) NbN films deposited on sapphire substrate by reactive dc magnetron sputtering in an Ar + N_2 gas mixture[9]. NbN meander type microstructures that cover either 4 μm by 4 μm, or 10 μm by 10 μm active areas were patterned with using of electron beam lithography technique. SEM image of the 4x4 μm area device is presented in Fig. 1. We used short single stripe devices with sizes either 0.1x0.1μm and 0.2x.02 μm as well.

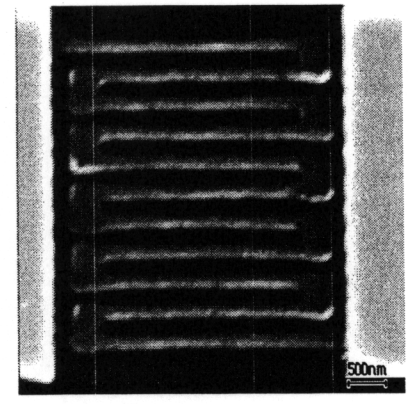

Fig. 1. SEM image of a meander-type SPD structure with 4x4 μm area.

III. Experimental Setup

In our experiments, a NbN SPD was mounted on a cold plate (T = 4.2 K) inside an optical cryostat. We used two cold glass filters to block the room temperature background radiation falling on the sample. The sample was dc biased and mounted on a rigid coplanar transmission line with the ac output connected to a cryogenic low-noise

amplifier with the input cryogenic isolator, characterized by 30-dB gain and 1-2 GHz

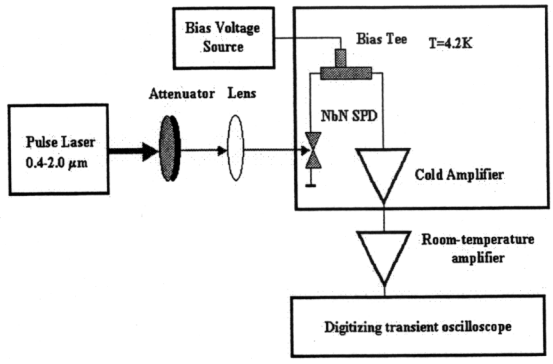

Fig. 2. Experimental Setup.

bandwidth (Fig. 2). Outside the dewar, the signal passed through a second broadband power amplifier (9 GHz; 20-dB gain) before going to a 6-GHz or 12 GHz-bandwidth single-shot oscilloscopes for display and then to a 200-MHz voltage-level threshold counter for real-time event counting and statistical analysis. We worked with 100-fs-wide optical pulses with a 1-kHz repetition rate at 0.4 μm, 0.81 μm, 1.55 μm, and 2.1 μm wavelengths. The intensity of the laser pulses was attenuated using banks of neutral density filters. The diameter of the beam incident on the device was ~ 50 μm. Wavelength dependencies of quantum efficiency were measured using grating spectrometer, or interferometric filters, and CW radiation source.

IV. Experimental Results and Discussion.

The current-voltage (I–V) characteristics of a NbN 0.2x0.2μm^2 microbridge, operated at 4.2 K, is shown in Fig. 3.

The device is normally biased in the superconducting (zero-resistance) state. The dashed-line section of the resistive characteristics corresponds to the metastable region (which cannot be accessed under dc operating conditions) when the device is connected to a 50 Ω load of the output coaxial line, biased below its critical current I_C, and no light is incident upon the microbridge. The device I_C typically is within range of 40-120 μA, while the normal-state resistance is equal to 300-500Ω for 0.2x0.2 and 0.1x0.1μ^2 single strip devices, and 50-70 kΩ for meander type 10x10 μm device. For a device biased near, but below I_C, photon absorption leads to a temporary switch from the stable superconducting state (point A in Fig. 3) to the sub-critical resistive state (point B in Fig. 3). As a result, we observe a voltage pulse whose amplitude corresponds to the voltage level at point B, and time duration that depends on the dynamics of formation and subsequent healing of the resistive state induced by the photon absorption. This process is reversible due to the metastable character of the sub-critical state.

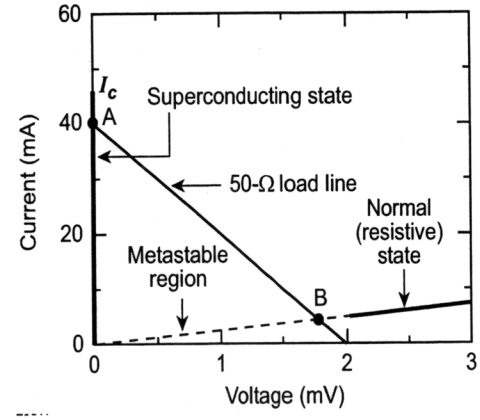

Fig. 3. I-V curve of SPD.

The dynamics of the hotspot formation in a superconductor at

temperature T below its critical temperature T_C, has been described before[10] and studied in details in Ref.11. Absorption of a photon with energy $h\omega >> 2\Delta$ creates, through electron–electron and electron–Debye-phonon interactions, a local nonequilibrium perturbation with a large number of excited hot electrons (above 300 for NbN, excited with 800-nm wavelength light[6]), and an increase of the average electron temperature above T_C. This initial phase is called the thermalization process and for ultrathin NbN films is characterized by the thermalization time $\tau_T = 6.5$ ps[7]. The thermalization process results in the formation of a hotspot—a local nonsuperconducting region (Fig. 4a). After the initial thermalization, the resistive hotspot size grows (Fig. 4b) as hot electrons diffuse out of its hotspot region. At the same time, the supercurrent is expelled from it's the hotspot volume and is concentrated in the "sidewalks" between the hotspot and the edges of the film (Fig. 4c). The microbridge, however, still shows no resistance, unless the bias current I_{bias} is sufficient to exceed the critical current in the sidewalks. In this latter case, superconductivity in the sidewalks is destroyed, and the resistive barrier is formed across the entire width w of the device (Fig. 4d), giving rise to a voltage signal with amplitude proportional to the barrier resistance. Resistance of normal areas is determined by the length of PCS appeared in sidewalk areas, which is close to double charge-imbalance length. From the other hand charge imbalance length is determined by the inelastic scattering length, which is close to characteristic electron-phonon length in NbN[7]. As the result, each the resistive area in NbN SPD has the length of an electron-phonon length. The normal resistance areas formation process competes, with the cooling process, as electrons diffusing out the hotspot loose their energy through electron–phonon scattering. Thus, after the time depending on both the diffusion rate and the quasiparticle relaxation dynamics,[6] the hotspot heals itself, leading to the restoration of the superconducting path along the microbridge.

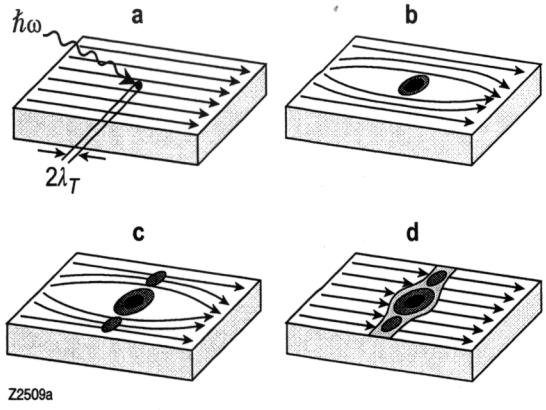

Fig.4. Schematics of a supercurrent-assisted hotspot formation mechanism in an ultrathin and narrow superconducting stripe.

As a result of the hotspot creation and relaxation processes, the device switches temporarily between the superconducting and resistive states (points A and B in Fig. 3) and a voltage pulse is generated at the device terminals. The physical difference between our current-assisted single-photon detection mechanism and an earlier proposed hotspot mechanism[10] is that our response is due to a collaborative effect of the bias current and the radiation quantum, leading to a comparably large, easily measurable output voltage signal. We note that the current-assisted hotspot process creates a nonlinear, multidimensional space of operating parameters, such as w, I_{bias}, $h\omega$, and T.

The time-resolved response of our SPD is shown in Fig. 5. The signal has a pulse width of below 100 ps, with the signal-to-background-noise ratio of above 100:1, and shot-to-shot jitter of less than 30 ps. The measured bandwidth of the output

pulse was limited by the bandwidth of our chain of output amplifiers and the oscilloscope bandwidth. With the proper bandwidth of the output data acquisition system, it is possible to reach the intrinsic

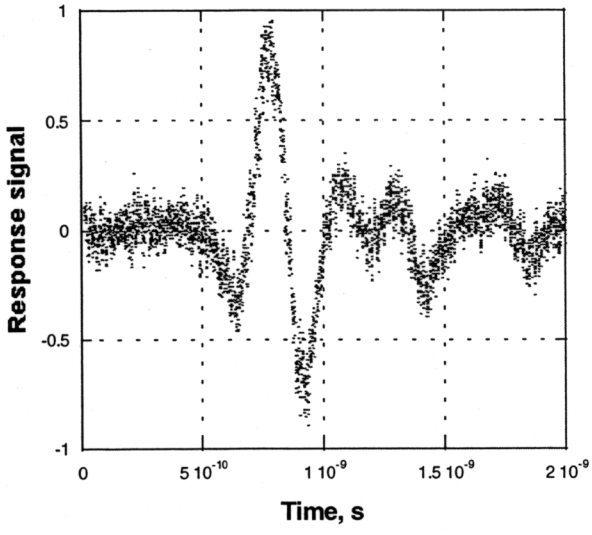

Fig. 5. Time-resolved SPD response.

Truly single-photon counting requires that the photon detection probability is a linear function of the number of photons incident on the device. For a mean number of $m << 1$ photons per pulse (far below detector saturation), the probability $P(n)$ of absorbing n photons from a given pulse is proportional to

$$P(n) \sim \frac{m^n}{n!}. \qquad (1)$$

Consequently, the probability of absorbing one photon is proportional to m, the probability of detecting two photons is proportional to m^2, the probability of detecting three photons is proportional to m^3, and so on.

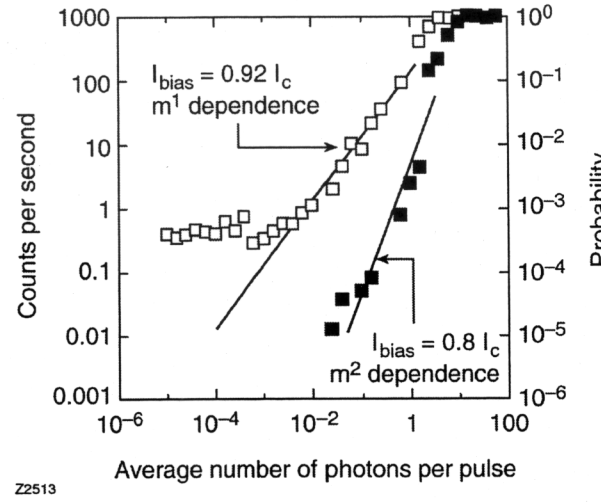

Fig. 6. Counting rate and probability vs. average number of photons per pulse (0.2x0.2μm device).

Figure 6 shows the probability of the detector producing an output voltage pulse as a function of the average number of photons per pulse, incident on the device area for two different values of I_{bias}. The left vertical axis in Fig. 6 indicates the number of detector counts per second (equivalently, per 1000 laser pulses), based on the average number of counts detected by SPD over a 10-s counting period for the highest photon doses, and up to 1000 s for the lowest. The right vertical axis corresponds to the count rate, probability of detecting an optical pulse. Open squares correspond to the SPD performance when it was biased at 0.92 I_C.

There is saturation at high incident photon fluxes, but for smaller fluxes, the experimental data show the linear decrease of detection probability versus the average number of incident photons over four orders of magnitude, which unambiguously demonstrates the single-photon detection. At very low photon doses, our experimental data points leveled off at 0.4 counts/sec, which must be regarded as the laboratory

photon background noise. The intrinsic dark count rate of our SPD was below 0.001 counts/sec, which corresponds to the number of detector responses over the time of 1000 sec when its input was completely blocked. The above limit was set by the long-term stability of our dc biasing box. We strongly believe that the intrinsic dark count of our device is significantly lower and should be limited by electron thermal fluctuations. The system noise temperature of our SPD, including the cryogenic amplifier, is below 15 K, which yields to voltage fluctuations several orders of magnitude below our signal levels. From Fig. 6, we can estimate that the quantum efficiency (QE) of our NbN microbridge device is 20%, as the value corresponding to the probability of detecting a pulse containing an average of one photon incident upon the device. The practical detection efficiency of our SPD is, of course, is determined by S_d/S_{in} ratio of the tested structure. Using proper coupling optics, the incident photon beam could be focused to a diffraction-limited spot size.

The solid squares in Fig. 6 correspond to the same device, operated under the same conditions as those for the open-square data, but with $I_{bias} = 0.8\ I_C$. We note immediately that our experimental data points now follow a quadratic dependence of detection probability showing the two-photon detection [see Eq. (1)]. As expected, for a two-photon process its QE is significantly lower than that for the single-photon detection and is approximately equal to 1%. At the same time we do not see the laboratory photon background noise since the probability of two stray photons arriving at the device at the same time (more accurately, within the hotspot-formation/healing process) is negligibly small.

Spectral dependencies of QE for two meander-type devices with 4x4 μm area size are presented in Fig. 7. As it can be seen, both dependencies have an exponential character with the same slope.

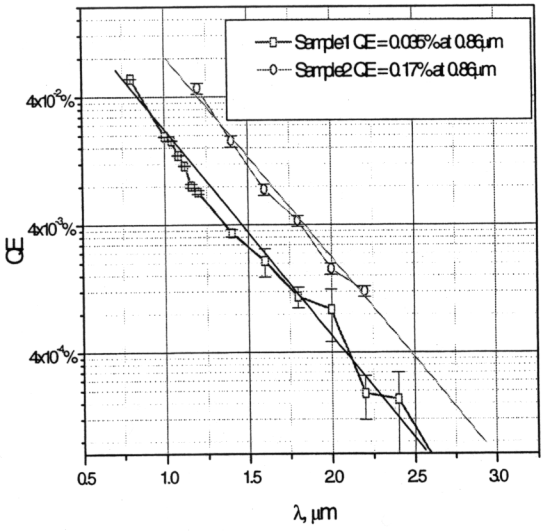

Fig. 7. Spectral dependence of quantum efficiency (meander-type devices).

We have found from our studies of AFM images of devices that the absolute QE values are in good correlation with the nonuniformity level of superconducting stripe edges. An origin of exponential behavior of the QE (λ) needs in future studies.

In conclusion, we have demonstrated that a supercurrent-assisted, hot-spot-formation mechanism can be implemented in ultrathin NbN stripes for ultrafast single-photon detection and counting of visible and infrared photons with experimentally measured quantum efficiency up to 20% and negligible dark counts. The bandwidth-limited measured response time was ~100 ps, corresponding to a 10-GHz photon counting rate. Already identified

applications for our superconducting SPD's range from sensing ultraweak electroluminescence from submicron complementary metal-oxide-semiconductor VLSI circuits[13], to NASA high-data-rate and data-capacity free-space optical communication systems for planetary exploration and earth-orbiting missions[14]. Our devices are also envisioned to be the heart of quantum communication systems, which allow for the implementation of unconditionally secure quantum key distribution for high-speed, real-time Vernam enciphering of large volumes of data[15].

We thank Kenneth Wilsher, Steven Kasapi, Seema Somani, and Gerald Gilbert for helpful discussions and comments. This work was supported by Schlumberger TT, US Office of Naval Research under grant N00014-98-1-0080, and the NATO Linkage Grant No. N98062.

References

[1] Photomultiplier Tubes, Hamamatsu PhotonicsK.K.

[2] F. Zappa, A. L. Lacaita, S. D. Cova, and P. Lovati, Opt. Eng. **35**, 938 (1996).

[3] S. Komiyama, O. Astafiev, V. Antonov, T.Kutsuwa, and H. Hirai, Nature **403**, 405 (2000).

[4] A. Peacock, P. Verhoeve, N. Rando, A. van Dordrecht, B. G. Taylor, C. Erd, M. A. C. Perryman, R. Venn, J. Howlett, D. J. Goldie, J. Lumley and M. Wallis, Nature **381**, 135 (1996).

[5] R. J. Schoelkopf, S. H. Moseley, C. M. Stahle, P. Wahlgren, and P. Delsing, IEEE Trans. on Appl. Supercond. **9**, 2935 (1999).

[6] K. S. Il'in, I. I. Milostnaya, A. A. Verevkin, G. N. Gol'tsman, E. M. Gershenzon, and R. Sobolewski, Appl. Phys. Lett. **73**, 3938 (1998).

[7] K. S. Il'in, M. Lindgren, M. Currie, A. D. Semenov, G. N. Gol'tsman, R. Sobolewski, S. I. Cherednichenko, and E. M. Gershenzon, Appl. Phys. Lett. **76**, 2752 (2000);

[8] M. Lindgren, M. Currie, C. Williams, T. Y. Hsiang, P. M. Fauchet, R. Sobolewski, S. H. Moffat, R. A. Hughes, J. S. Preston, and F. A. Hegmann, Appl. Phys. Lett. **74**, 853 (1999).

[9] S. I. Cherednichenko, P. Yagoubov, K. S. Il'in, G. N. Gol'tsman, and E. M. Gershenzon, Proceedings of the Eighth International Symposium on Space Terahertz Technology (Harvard University, Cambridge, MA, 1997), pp. 245-252.

[10] A. M. Kadin and M. W. Johnson, Appl. Phys. Lett. **69**, 3938 (1996).

[11] A. D. Semenov, G. N. Gol'tsman, and A. Korneev, Physica C, in print.

[12] M. Born, E. Wolf, Principles of Optics: Electromagnetic Theory of Propagation, Interference, and Diffraction of Light (Cambridge University Press, Cambridge, 7th expanded ed., 1999), pp. 752-758.

[13] J. C. Tsang and J. A. Kash, Appl. Phys. Lett. **70**, 889 (1997).

[14] G. G. Ortiz, J. V. Sandusky, and A. Biswas, in Free-Space Laser Communication Technologies XII, edited by G. S. Mercherle, (SPIE, Bellingham, WA, 2000), vol. 3932, pp. 127-138.

[15] G. Gilbert and M. Hamrick, MITRE Technical Report, MTR00W0000052

Background Limited Quantum Superconducting Detector for Submillimeter Wavelengths

Gregory Gol'tsman, Alexei Semenov*, Konstantin Smirnov, and Boris Voronov

State Pedagogical University of Moscow, 119891 Moscow, Russia
** DLR Institute of Space Sensor Technology and Planetary Exploration, 12489 Berlin, Germany*

ABSTRACT

We propose a concept of the background-limited detector for submillimeter radioastronomy that will have the noise equivalent power $\approx 10^{-21}$ W $Hz^{-1/2}$ when operated at 0.3 K and exposed to thermal background radiation with an equivalent temperature of 4 K. The detector is based upon the superconducting photon counter from Titanium film integrated into a planar logarithmic antenna. The planar layout makes feasible integration of the device in a detector array.

Introduction

Future radioastronomy missions will require detectors, which provide ultimate (background limited) sensitivity in the submillimeter wavelength range even when exposed to relatively weak background radiation. In comparison with different detection regimes, the photon counting regime is by definition the one having ultimate sensitivity. There has been recently proposed [1] a single-photon detection mechanism in a current carrying superconducting film that may become a basement for the development of the novel detector meeting observation requirements. The mechanism of the photon detection is the following. Photon absorbed in the superconducting film creates growing normal spot that forces the current to bypass the absorption site. When the current density in the superconducting areas reaches the critical value, the film switches into the resistive state and generates the voltage pulse. Operation of NbN photon counter [2] has been recently demonstrated. Both theoretical estimate [1] and extrapolation of experimental data [3] show, however, that the NbN counter will have a cutoff wavelength for the single photon detection regime of about 10 μm. Implementation of low-transition-temperature superconducting materials and subkelvin operation temperatures will shift the cutoff wavelength towards submillimeter range. Here we present estimates of the performance of the Ti based quantum detector for radiastronomy and first results of device manufacturing and characterization.

E-mail addresses: goltsman00@mail.ru ; Alexei.Semenov@dlr.de

Operation Principle of the Superconducting Quantum Detector

The key element of the quantum detector is a superconducting film patterned into a narrow strip, which is biased along its length with the current slightly less than the critical current at the operation temperature. The film thickness should be comparable or smaller than its width. In order to have significant coupling with radiation, the strip should be integrated into a planar antenna or form the meander-line covering the area larger than squared wavelength. Once a photon is absorbed at some point in the strip, it produces a high-energy electron, which then shares its energy with low-energy electrons by means of electron-electron and electron phonon interaction. The process is commonly called multiplication, since the number of low-energy unpaired electrons grows in time. The maximal number of additional electrons appearing in the film per one absorbed photon is referred as quantum yield or quantum efficiency. This figure increases in proportion to the ratio of the quantum energy and the superconducting energy gap. At any point in the film, the concentration of unpaired electrons increases due to multiplication and decreases due to out-diffusion. Once their concentration has exceeded the value specific for the normal state at $T = T_C$ (T_C is the superconducting transition temperatire), unpaired electrons suppress the energy gap and destroy superconductivity. The normal spot appears at a position where the photon has been absorbed. This forces the supercurrent to flow around the spot through still superconducting portion of the film. With the increase of the spot size the current density in the superconducting sidewalks increases and reaches the critical value. At this very moment the resistive "membrane" is formed across the cross-section area of the film, giving rise to the voltage pulse with the magnitude proportional to the bias current. Thus, the response appears due to collaborative effect of the bias current and the growing normal domain.

From this simple description one can see that the ability of the detector to register a single photon is the trade-off between the film width, the bias current, and the photon energy. The minimal film width is restricted to approximately 100 nm by available structuring technology. The magnitude of the bias current is limited by thermal fluctuations and/or by fluctuations of the superconducting phase. To achieve the background limited performance; fluctuations of the critical current should be less than the difference between the critical current and the bias current. In this case, the detector noise equivalent power is limited by phase fluctuations, which produce voltage pulses (dark counts) indistinguishable from those resulted from absorbed photons.

Since the quantum efficiency drops with the increase of the wavelength, there is a cutoff wavelength for the above described detection mechanism. Low energy photon can not produce the concentration of unpaired electrons, which is sufficiently large in order to suppress superconductivity. For NbN quantum detector, the cutoff occurs in the near infrared spectral range. The quantum efficiency, however, turns to be larger in a superconducting material with smaller transition temperature, because the superconducting energy gap decreases with the transition temperature. The normal-state concentration of the electrons, which should be reached during multiplication in order to destroy superconductivity, also decreases with the transition temperature. Thus, the use of a material with smaller transition temperature will shift the cutoff towards longer

wavelength. Provided a sufficiently high optical coupling, such a detector may compete with traditional background limited thermal detectors in the submillimeter wavelength range.

Quantum Detector from Titanium: Performance simulation

We simulate major figures of merit for the detector from Ti superconducting film making use of the model described in Ref. 1. We do not know some of required film parameters. Although this increases uncertainty of the estimate, we believe that our results are quite realistic. We took the density of states for bulk Titanium [4] and the Bardeen-Cooper-Schrieffer (BCS) energy gap. The electron-electron interaction time at the Fermi level was calculated in the extreme dirty limit [5] using the expression

$$\tau_{ee}^{-1} = \frac{k_B}{4\hbar R_q} R_S T_C \ln\left(2\frac{R_q}{R_S}\right), \quad (1)$$

where $Rq = h/(4e^2) = 6.47$ kΩ is the resistance quanta and R_S is the sheet resistance of our films. Electron diffusivity was concluded from the Lorentz number and the value [4] of the Sommerfeld constant $6.8 \cdot 10^{-4}$ J cm^{-3}K^{-2} for bulk material. The Table below contains the material parameters, which we used for simulation.

Table 1 Material parameters of titanium films.

Transition temperature	Energy gap at T = 0	Electron-electron interaction time	Electron density of states	Electron diffusivity
0.6 K	1.06 K	400 psec	$6.8 \cdot 10^{24}$ m^{-3}K^{-1}	0.4 cm^{2}sec^{-1}

The cutoff wavelength for Ti and NbN films at different bias currents and strip widths is shown in Fig. 1 for the operation temperature 0.5 T_C. Material parameters of NbN films were taken from [1]. The film thickness was assumed 5 nm in both cases. According to our estimate, a detector from Titanium should provide at least an order of magnitude larger cutoff wavelength than NbN photon counters.

Photon counting regime brings peculiarities into the signal processing that do not allow for direct comparison of thermal detectors (bolometers) and quantum detectors in terms of the noise equivalent power. We examine here main performance figures of the Ti quantum detector whereas a detailed analysis of the counting statistics will be published elsewhere. The maximum intensity of the narrow-band background radiation, which the device can sustained while keeping the photon counting capability, is given by

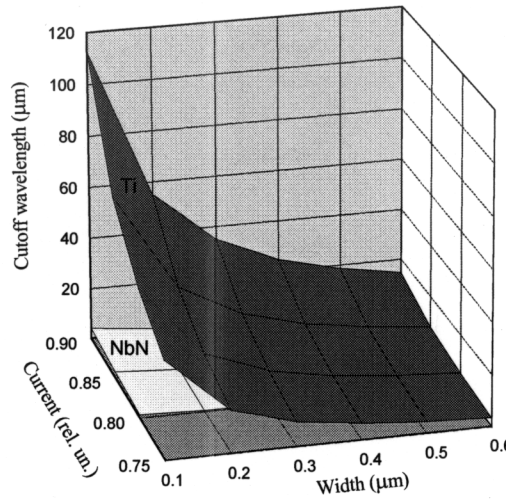

FIG.1 Cutoff wavelength for NbN and Ti quantum detectors. Bias current is plotted in units of the critical current at the operation temperature.

the expression $\eta\, h\nu/\Delta t$ where $\Delta t = 0.2\,\tau_{ee}$ is the duration of the response voltage transient, η is the optical coupling efficiency, and $h\nu$ is the quantum energy. Assuming 100-μm cutoff wavelength and typical optical coupling –10 dB, which has been demonstrated [6] for an integrated antenna in this wavelength range, we obtain an upper limit of $2\cdot10^{-10}$ W for the background radiation power. For a diffraction limited antenna with the 6-mm effective aperture [6], this power corresponds to the 42-K thermal background and results in the background limited noise equivalent power (NEP) $1.2\cdot10^{-15}$ W Hz$^{-1/2}$. The smallest power, at which the detector still has background limited sensitivity, is determined by the dark count rate. Provided that the bias current is sufficiently small in order to prevent switching of the film into the normal state due to thermal fluctuations, the origin of dark counts is the 2π-slippage of the superconducting phase leading to voltage pulses at the device outer contacts. According to [7], the probability of the slippage depends on the reciprocal phase relaxation time (Ginzburg-Landau relaxation time), superconducting condensation energy, and the bias current. Additionally taking into account the dependence of the condensation energy on the bias current, we estimated for the 100-nm wide Ti film biased with the current 0.9 I_C (I_C is the critical current) at $T = 0.5\ T_C$ the mean dark count rate ≈ 10^2 sec^{-1}. For 100-μm cutoff wavelength this corresponds to the input radiation power $1.7\cdot10^{-18}$ W. The same count rate would produce quanta of the thermal background with a temperature of 6.3 K. The background limited NEP decreases in this regime to $5\cdot10^{-20}$ W Hz$^{-1/2}$. Thus, the photon detector is expected to provide background-limited performance within the dynamic range, which approaches eight orders of magnitude. Further decrease of the background radiation intensity does not lead to a better performance, since NEP is limited by dark counts. For a photon counter, the effective signal integration bandwidth equals the reciprocal chopping frequency. Since for a statistical ensemble of 10^2 events the apparent mean square deviation does not

practically differ from the deviation for an infinite number of events, one would need few second observation time at the chopping frequency 1 Hz in order to realize the best noise equivalent power.

In order to compare our detector with alternative hot-electron bolometer detectors [8,9], we specify also the noise equivalent power transformed to the device input. Setting the optical coupling $\eta = 1$, we obtain the NEP of the detector itself $5 \cdot 10^{-21}$ W Hz$^{-1/2}$. The smallest power providing background limited regime will be $1.7 \cdot 10^{-19}$ W, which corresponds to the background temperature of 4 K for the 100-μm cutoff wavelength. It is worth noting that the spectral cutoff of our detector plays the role of a built-in filter that effectively decreases the background radiation intensity and, correspondingly, the noise equivalent power. Without the cutoff, the full power absorbed by our detector from 4 K-background would be $2 \cdot 10^{-15}$ W, which is close to the saturation level predicted [9] for hot-electron-bolometer detectors.

Manufacturing and characterization of the detector

Our detector is a planar device fabricated on a silicon substrate. The detector represents a narrow bridge pattern from Ti film. The bridge connects inner terminals of a logarithmic spiral antenna structured from gold film on the same substrate. Fabrication process included several deposition and lithographic stages. At the first stage the inner part of the spiral antenna was evaporated by electron-beam sputtering through the mask made by lift-off electron-beam lithography. Thickness of the inner spiral was 100 nm. The gap between antenna terminals had the width of 0.2 μm. At the second stage Ti film was deposited through the mask made by electron-beam lithography. The mask opened a rectangular 0.2-μm width and 2-μm long window that overlapped the gap between antenna terminals. The film was deposited by means of dc reactive magnetron sputtering of the pure Ti target in argon atmosphere at a pressure of 10^{-2} mbar. The length of the bridge, i.e. the active area of the detector, was 0.2 μm as determined by the gap between the antenna terminals. The edges of the Ti strip situated on the gold antenna terminals, providing electrical contact to the active area. Finally, outer part of the spiral antenna and contact pads for wiring the detector were made from 200-nm thick gold film by lift-off UV lithography and thermal evaporation. SEM image in Fig. 2 shows the layout of the central part of the detector.

Detector exhibited a superconducting transition temperature of 0.64 K and 0.53 K for 25 nm and 30 nm thick Ti bridge, respectively. In both cases the width of the superconducting transition was less than 0.02 K. The critical current density $1.5 \cdot 10^3$ A cm^{-2} measured at 0.5 T_C was noticeably smaller than the value concluded from the BCS theory. The reason for the discrepancy is not yet clear. We shall mention here that an increase of the critical current density would result in a larger output voltage transient, thus making easier the signal readout. On the other hand, larger bias current would hamper the noise equivalent power because the dark count rate exponentially grows with the bias current.

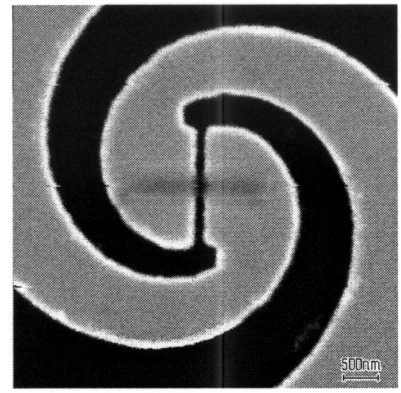

FIG.2 SEM image of the central part of the detector. Ti strip (gray shadow rectangle) bridges the inner terminals of the spiral antenna.

Focal Plane Array and Readout

The planar technology makes integration of our detectors into a detector array relatively simple. An example of possible array architecture is shown in Fig. 3. Detectors are patterned on the rectangular or hexagonal grid on one side of the wafer, which carries an antireflection coating on the irradiation side. The second wafer containing bias lines and SQUID read-out is flip-chipped to the first one carrying detectors. Assuming a single

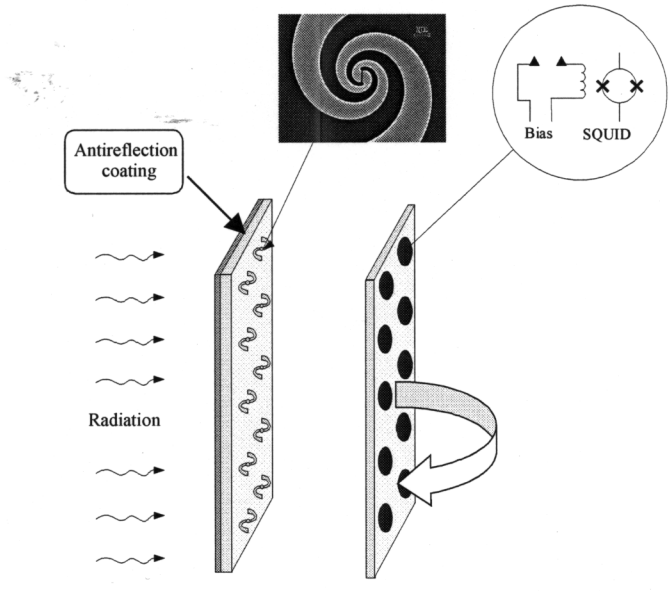

FIG. 3 Focal plane quantum detector array with flip-chip SQUID readout.

pixel with the diffraction limited size, that is ≈ 50 μm for silicon wafer, and the hexagonal grid, we estimate the 5.3 mm radius of the 10^4-pixel array. With the corresponding filling factor of about 0.9, the optical coupling will be mostly determined by the efficiency of individual antennas. However, the array will require an additional lens or mirror to convert its relatively large F-number ≈ 70 into the value of about 10, which is typical for telescopes. Besides the lower dissipated power in comparison to solid state amplifiers, the advantage of the SQUID readout is a larger signal to noise ratio. This is especially important when detectors are biased with the small current resulting in the magnitude of the signal transient below the millivolt level.

Conclusion

We have shown that the novel Ti superconducting quantum detector is a prospective single-pixel element for submillimeter focal plane detector arrays. Our detector offers background limited sensitivity in the range of background intensity much broader than hot-electron bolometers, while its noise equivalent power at a weak background should be comparable or better than NEP projected for hot-electron devices.

References

[1] A.D. Semenov, G.N. Gol'tsman, and A.A. Korneev, "Quantum detection by current carrying superconducting film", *Physica C*, 2001.

[2] G. Gol'tsman, O. Okunev, G. Chulkova, A. Lipatov, A. Dzardanov, K. Smirnov, A. Semenov, B. Voronov, C. Williams, and Roman Sobolewski, "Fabrication and properties of an ultrafast NbN hot-electron single-photon detector", *Applied Superconductivity Conference ASC'2000*, Virginia Beach, VA, September 2000.

[3] A. Verevkin et al., this conference Proceedings.

[4] C.P. Poole, H.A. Farach, R.J. Creswick, *Superconductivity*, Academic Press, New York 1995, ISBN 0-12-561455-1.

[5] B. Altshuler and A. Aronov, *Electron-Electron Interaction in Disordered Systems*, North Holland, Amsterdam 1985.

[6] A.D. Semenov, H.-W. Hübers, J. Schubert, G.N. Gol'tsman, A.I. Elantiev, B.M. Voronov, and E.M. Gershenzon, "Design and performance of the lattice-cooled hot-electron terahertz mixer", *J. Appl. Phys* **88**, 6758 (2000).

[7] D.E. McCumber and B.I. Halperin, "Time scale of intrinsic resistive fluctuations in thin superconducting wires", *Phys. Rev.* **B1**, 1054 (1970).

[8] M.E. Gershenson, D. Gong, T. Sato, B.S. Karasik, W.R. McGrath, and A.V. Sergeev, "Hot-electron direct detectors: towards record sensitivity via disorder-suppressed electron-phonon coupling", *Proc. 11th Int. Symp. on Space Terahertz Technology*, May 1-3, 2000, University of Michigan, Ann Arbor, MI, pp.514-523.

[9] D. Chouvaev, L. Kuzmin, M. Tarasov, Normal-metal hot-eletron microbolometer with on-chip protection by tunnel junctions, Supercond. Sci. Technol. **12**, 985 (1999).

SIS photon detectors for submillimeter-wave observations

Hiroshi Matsuo*[a], Seiichirou Ariyoshi*[b], Masanori Takeda*[c] and Takashi Noguchi*[c]

[a] Advanced Technology Center, National Astronomical Observatory of Japan, Mitaka, Tokyo 181-8588, Japan

[b] Astronomical Institute, Tohoku University, Sendai, Miyagi 980-8578, Japan

[c] Nobeyama Radio Observatory, Minamimaki, Minamisaku, Nagano 384-1305, Japan

We propose to use superconducting direct detectors (SIS photon detectors) for future instruments for submillimeter-wave wide field imaging arrays. Using low leakage (less than 10pA) superconducting tunnel junctions, it is possible to realize submillimeter-wave direct detectors with noise equivalent power of less than 10^(-17)W/Hz^(0.5). We have evaluated leakage current and current noise of 4micron niobium SIS junctions with current density of 0.5-1kA/cm^2 at 0.3K. The measured leakage current is 5pA at 0.5mV and current noise is 1.5fA/Hz^(0.5) with white noise spectrum down to 5Hz. Antenna coupled SIS photon detector is designed as a distributed junction arrays, which is expected to gives good matching in wide frequency range in submillimeter-wave with low current density junctions.

Since the leakage current of the niobium junction saturates at about 0.9K, the operating temperature of the detector can be 0.9K, which greatly ease cooling and readout electronics requirements. Further advantage over bolometric detectors come from their thin film fabrication process and direct photon sensitivity. Because of the thin film fabrication process, the uniformity of the junction is good and large format array can be realized rather easily, and would be less affected by cosmic rays. Because of the direct photon sensitivity, excess noise by temperature fluctuation or electrical interference are not critical like bolometric detectors.

Submillimeter-wave imaging arrays using the SIS photon detectors have been designed and being fabricated. The arrays will be evaluated in Atacama Submillimeter Telescope Experiment.

InP MMIC Chip Set for Power Sources Covering 80-170 GHz

Lorene Samoska, Vesna Radisic†, Miro Micovic†, Ming Hu†, Paul Janke†, and

Catherine Ngo†

Jet Propulsion Laboratory, California Institute of Technology
MS 168-314
4800 Oak Grove Dr.
Pasadena, CA 91109
818-354-0849 - lorene@merlin.jpl.nasa.gov
†HRL Laboratories LLC
3011 Malibu Canyon Road
Malibu, CA 90265

ABSTRACT

We will present a Monolithic Millimeter-wave Integrated Circuit (MMIC) chip set which provides high output-power sources for driving diode frequency multipliers into the terahertz range. The chip set was fabricated at HRL Laboratories using a 0.1-μm gate-length InAlAs/InGaAs/InP high electron mobility transistor (HEMT) process, and features transistors with an f_{max} above 600 GHz. The HRL InP HEMT process has already demonstrated amplifiers in the 60-200 GHz range[1]. In this paper, these high frequency HEMTs form the basis for power sources up to 170 GHz.

A number of state-of-the-art InP HEMT MMICs will be presented. These include voltage-controlled and fixed-tuned oscillators, power amplifiers, and an active doubler. We will first discuss an 80 GHz voltage-controlled oscillator with 5 GHz of tunability and at least 17 mW of output power, as well as a 120 GHz oscillator providing 7 mW of output power. In addition, we will present results of a power amplifier which covers the full WR10 waveguide band (75-110 GHz), and provides 40-50 mW of output power. Furthermore, we will present an active doubler at 164 GHz providing 8% bandwidth, 3 mW of output power, and an unprecedented 2 dB of conversion loss for an InP HEMT MMIC at this frequency. Finally, we will demonstrate a power amplifier to cover 140-170 GHz with 15-25 mW of output power and 8 dB gain.

These components can form a power source in the 155-165 GHz range by cascading the 80 GHz oscillator, W-band power amplifier, 164 GHz active doubler and final 140-170 GHz power amplifier for a stable, compact local oscillator subsystem, which could be used for atmospheric science or astrophysics radiometers.

I. INTRODUCTION

The 140-170 GHz frequency range is interesting for atmospheric science heterodyne radiometers, as several molecular species radiate in that frequency regime, or a multiple of it. A harmonic mixer could make use of a direct local oscillator in the 140-170 GHz range, while a subharmonic mixer operating at 280 - 340 GHz or 560 – 680 GHz could be pumped with a 140-170 GHz LO, or such an LO followed by a doubler. Water has an important spectral line at 557 GHz, and is being studied in the future MIRO (Microwave Instrument for the Rosetta Orbiter) mission, using a heterodyne system with a Gunn oscillator operating at 140 GHz. An aircraft instrument, the Cloud-Ice Radiometer, seeks to study ice in clouds at different altitudes, and makes use of a heterodyne system with local oscillator at 162.5 GHz. Gunn oscillators are increasingly difficult to obtain commercially, and passive multipliers may not offer high enough output power to drive a mixer in a heterodyne receiver. This paper discusses an InP HEMT chip set fabricated at HRL Laboratories, LLC which could provide an alternative to passive components for a local oscillator source in the 140-170 GHz frequency range. All of the measurements discussed here were obtained on-wafer, using waveguide RF wafer probes [2].

II. OSCILLATORS

The first component of the chip set is an 80 GHz voltage controlled oscillator. Other oscillators in this frequency range are included in [3,4]. A photograph of the chip is shown at left in Figure 1. It consists of a 4×37 μm gate periphery HEMT device in a common source configuration. The series feedback element is a CPW transmission line at the source. The varactor element is the gate-source capacitance of a 4×25 μm gate

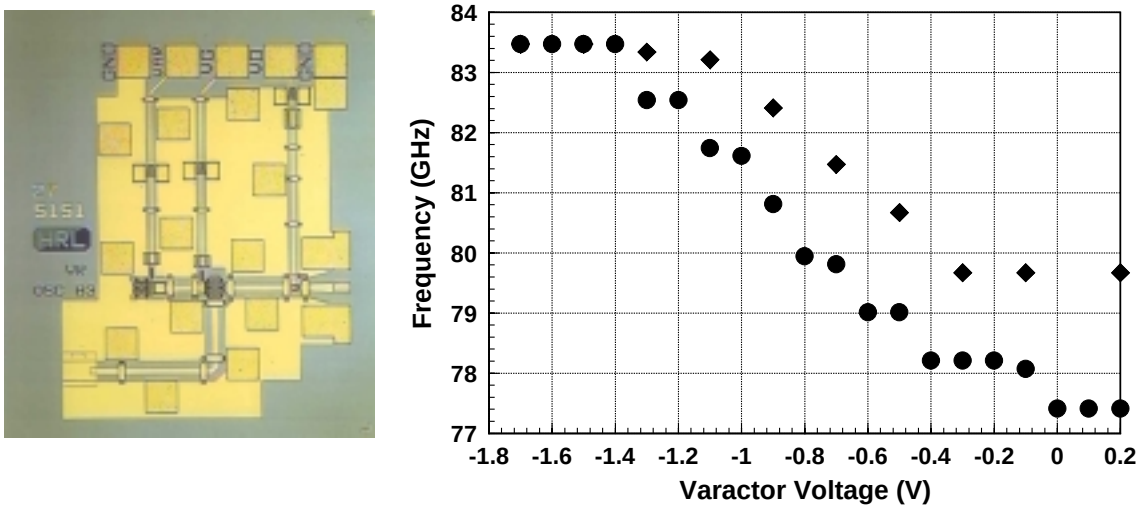

Figure 1. At left, the chip photograph of the 80 GHz VCO is shown. At right, the frequency tuning capability as a function of varactor control voltage is shown. The diamonds and circles represent two stable operating conditions of the VCO, depending on the direction of turning on the varactor voltage.

periphery HEMT, to the left of the larger a 4×37 μm gate periphery HEMT. The larger HEMT is used at the output to maximize output power. The varactor capacitance is varied by changing the gate supply voltage. The graph at right in Figure 1 shows that 6 GHz of tuning is obtained by changing the varactor voltage. The output power achieved between 77.5 and 83.5 GHz is 13 +/- 0.5 dBm. The chip measures 1.2 x 1.3 mm^2, and operates at a drain voltage of V_d=2.5 V and I_d= 30 mA.

A second, fixed-tuned oscillator was designed in addition to the 80 GHz VCO. This oscillator made used of a tuning stub with removable airbridges. Frequency of oscillation was measured by mixing the oscillator output with a Millitech 90 GHz Gunn oscillator. The mixer output was connected to a spectrum analyzer. Figure 2 shows the chip photograph at left. The circuit is biased at the drain voltage of 2.5 V, gate voltage Vg of -.036 V, and the drain current of 25 mA. With the airbridges on the chip intact, the oscillation frequency for this bias condition is 119.8 GHz. The output power at 119.8 GHz is 8.7 dBm, as measured with a WR8 Anritsu power meter. By scribing out the first airbridge, the frequency of oscillation changes to 129 GHz. Removal of the second airbridge results in a frequency of oscillation of 134 GHz. The output power as a function of frequency is shown in the graph at the right in Figure 2.

III. W-BAND AMPLIFIER

Amplification of the 80 GHz VCO may be required in order to drive an active doubler to 160 GHz. A suitable amplifier that could be used is the chip shown in Figure 3. This medium power amplifier makes use of 3 stages of a 4×37 μm gate periphery HEMT

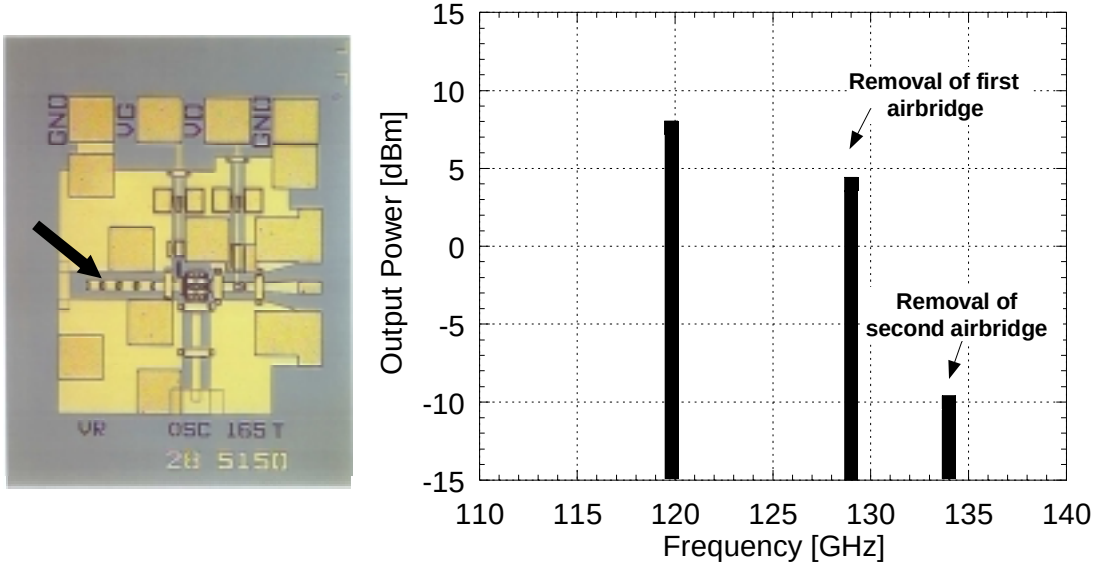

Figure 2. At left is the chip photograph of a 120 GHz fixed-tuned oscillator, showing the tuning stub in the left-center portion of the photograph (arrow). Removal of the first or second airbridge tunes the frequency according to the graph at right.

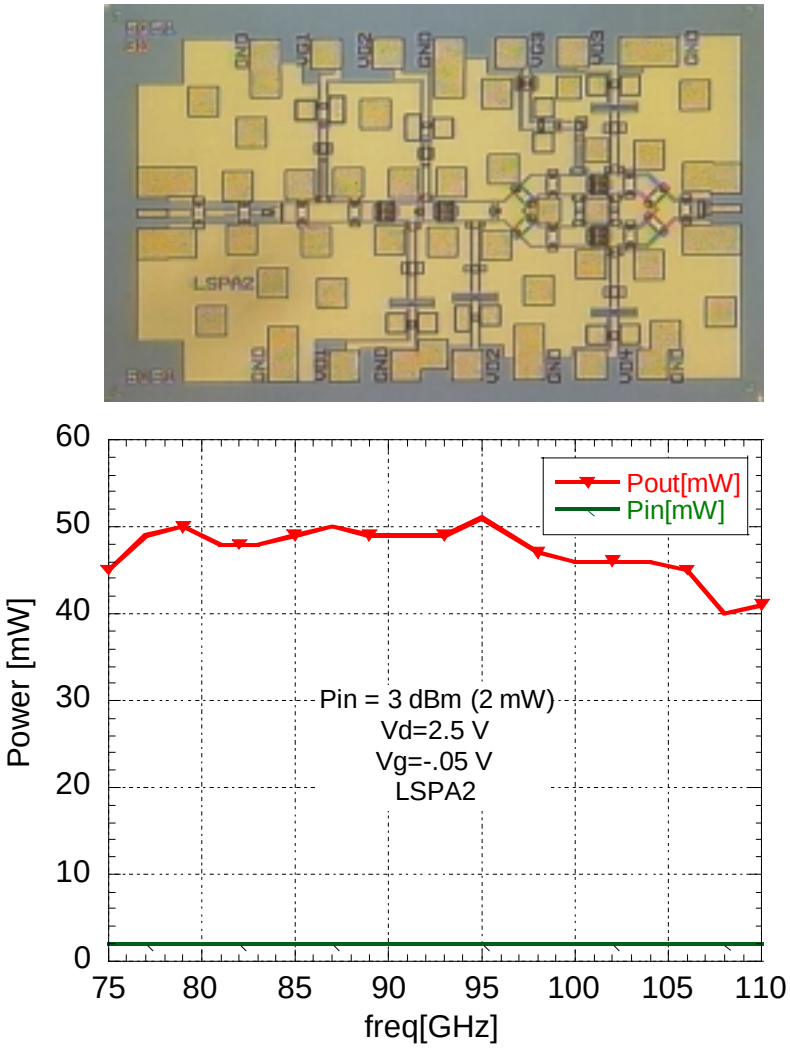

Figure 3. Chip photograph of the W-band power amplifier and output power as a function of frequency for a fixed input power of 2 mW.

devices, with two HEMTs combined in parallel in the last stage to maximize output power. A similar amplifier was described in [5], with 6 dB of large signal gain and at least 25 mW from 75-110 GHz. Our current amplifier was driven by a backward wave oscillator, and the output power was measured using an HP power meter equipped with a WR10 waveguide sensor. The amplifier exhibits 13 dB of large signal gain, and puts out 40-50 mW of output power over the 75-110 GHz WR10 waveguide band. Such an amplifier could find many uses for test equipment, or as a driver for active or passive frequency multipliers in a subsequent stage. The amplifier operates at 2.5 V, 250 mA, for a minimum power-added efficiency of 6%.

IV. ACTIVE DOUBLER

A class B doubler was designed using the harmonic balance simulator from Agilent's Series IV. The matching elements are realized using grounded CPW lines. The fundamental frequency at the output is suppressed using a quarter-wave open stub, which presents a short at the fundamental and an open at the second harmonic. The highest frequency HEMT doubler previously reported is a 180 GHz MMIC with a 6 dB conversion loss at an input power of 0 dBm [6]. For comparison, a 94 GHz Schottky diode doubler demonstrated 6 dB conversion loss at 55 mW of output power[7].

Figure 4 shows a photograph of the fabricated MMIC doubler. The chip size is 1.1×1.2 mm^2. The doubler is biased at the pinchoff condition, with a gate voltage of –0.6 V. The drain voltage was 2.5 V. We measured the doubler on-wafer using a WR10 waveguide wafer probe at the input and a WR5 waveguide wafer probe at the output of the chip. The input was driven by a backward wave oscillator from 75-90 GHz. The output power was measured with a WR5 Anritsu power sensor. The best results were obtained at the input frequency of 82 GHz. The graph at right in Figure 4 shows the output power and conversion loss as a function of output frequency. A conversion loss of 2 dB is measured at an input power at 82 GHz of 7 dBm. This corresponds to an output power of 5 dBm or 3.2 mW at 164 GHz. The RF efficiency of this doubler is 63 %. The 3 dB bandwidth of this active doubler is approximately 158-173 GHz.

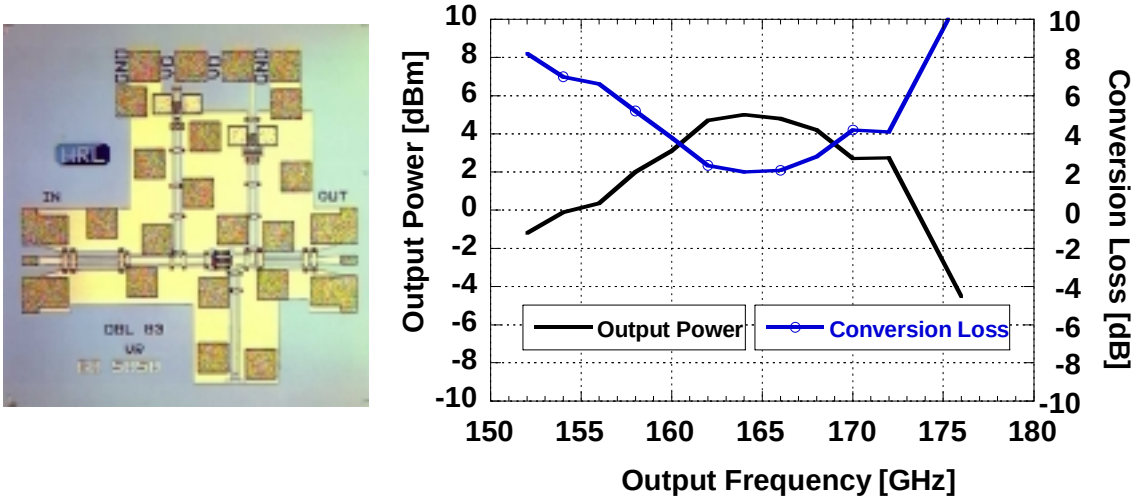

Figure 4. At left, the chip photograph of the 82-164 GHz active doubler is shown. At right, output power and conversion loss as a function of frequency are illustrated.

V. WR5 Power Amplifier

The final stage of our proposed local oscillator source is a power amplifier to amplify the active doubler of section IV. Figure 5 shows a photograph of the power amplifier. The chip features another grounded CPW design, with 3 stages of 4x37 micron gate periphery HEMTs. As in the W-band amplifier, two HEMTs were combined in the output stage to maximize output power. The chip size was 1.1 x 1.9 mm^2.

The power amplifier chip was first measured on-wafer for small signal S-parameters, using a WR5 waveguide frequency extender from Oleson Microwave Labs and an HP 8510A vector network analyzer. The amplifier exhibits 10 dB of small signal gain from approximately 144-170 GHz. The glitch around 143 GHz is a product of the measurement system. The input and output return losses are 10 dB at 165 GHz, and are shown in the middle graph of Figure 5. For these measurements, the chip was biased at Vd = 2.5 V, Id = 240 mA, and Vg = 0 V.

Power measurements on this chip were obtained using a WR10 BWO from 70-85 GHz to drive a Millitech doubler source between 140-170 GHz. The doubler was characterized for its output power using a WR5 Anritsu power meter, and then the BWO and doubler were connected to a WR5 RF wafer probe on the probe station. The power amp chip was biased with DC needle probes, and the output power as a function of frequency was measured again using the WR5 Anritsu power meter and a WR5 RF wafer probe.

The output power as a function of frequency and input power is shown for one of the power amp chips. The input power was varied to give the maximum output power. Peak power was observed at 150 GHz, with a maximum output power of 14.1 dBm or 25 mW, for an input power of 6.3 dBm, yielding a large signal gain of approximately 8 dB. From 140-170 GHz, 15 to 25 mW (11.8 – 14 dBm) of output power is achieved across the band. For the power measurements, a drain voltage of 2.1 V gave the optimized output power, for a drain current of 250 mA and a gate voltage of 0V. This amplifier could be a useful gain stage following the active doubler of the previous section. The power obtainable from the active doubler between 162-166 GHz was 5 dBm (refer to Figure 4). In Figure 5, the power out of the amplifier is at least 15 mW for an input power of 5 dBm (3.2 mW) for these frequencies.

VI. CONCLUSIONS

We have presented results of a chip set fabricated at HRL Laboratories, LLC using InP HEMTs which could form the local oscillator chain of a heterodyne receiver for atmospheric science or astrophysics radiometers. The resultant output power from such a chain could be as large as 15-20 mW from 158-166 GHz.

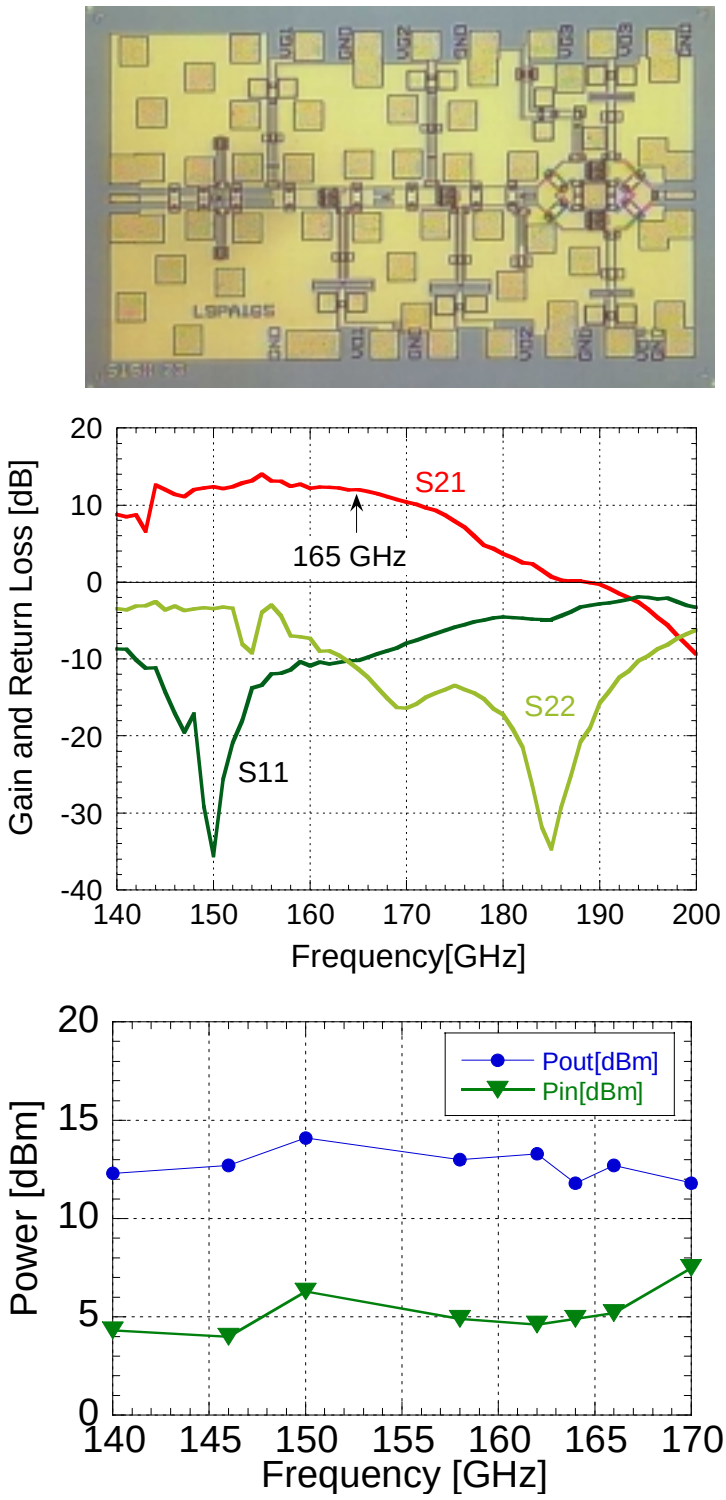

Figure 5. 140-170 GHz power amplifier chip (top photo), showing S-parameters (middle graph) and output power (lower graph) as a function of frequency.

ACKNOWLEDGMENTS

This work was funded by DARPA under contact number F33615-99-C-1512. The authors would like to thank Dr. Edgar Martinez of DARPA for guidance in this project. The research described in this paper was carried out in part at the Jet Propulsion Laboratory, California Institute of Technology under a contract with the National Aeronautics and Space Administration.

Special acknowledgments to Matt Morgan, Dr. Imran Medhi, Dr. Alain Maestrini, David Pukala, Douglas Dawson, Dr. Todd Gaier, Dr. Sander Weinreb, and Dr. Peter Siegel, of the Jet Propulsion Lab-Caltech, for helpful discussions, technical expertise, and the use of lab facilities.

REFERENCES

[1] C. Pobanz, M. Matloubian, V. Radisic, G. Raghavan, M. Case, M. Micovic, M. Hu, C. Nguyen, S. Weinreb, and L. Samoska, "High Performance MMICs with Submillimeter Wave InP-based HEMTs," in *InP & Related Materials, 2000 Conference Proceedings*, pp *67-70.*

[2] T. Gaier, L. Samoska, C. Oleson, G. Boll, "On-Wafer Testing of Circuits Through 220 GHz," presented at the *Ultrafast Optics and Electronics Conference*, Snowmass, CO, April,1999.

[3] H. J. Siweris, H. Tischer, T. Grave, and W. Kellner, "A monolithic W-band HEMT VCO with feedback topology," in *IEEE Intern. Microwave Symp. Dig., MTT-S*, June 1999, pp. 17-20.

[4] Y. Kwon, D. Pavlidis, P. Marsh, T. Brock, and D. C. Steit, " A 100-GHz monolithic cascode InAlAs/InGaAs HEMT oscillator," *IEEE Microwave Guided Wave Lett.*, vol. 4, no. 5, pp. 135-7, May 1994.

[5] Y.C. Leong, S. Weinreb, "Full W-band MMIC medium power amplifier," *IEEE MTT-S Int. Microwave Symp. Dig.*, vol. 2 , pp. 951 -954 , June 2000.

[6] Y. Kwon, D. Pavlidis, P. Marsh, M. Tutt, G.I. Ng, and T. Brock," 180 GHz InAlAs/InGaAs HEMT monolithic integrated frequency doubler", in *IEEE GaAs IC Symp. Dig.*, 1991, pp. 165 –168.

[7] S. W. Chen, T. Ho, F. R. Phelleps, J. L. Singer, K. Pande, P. Rice, J. Adair, and M. Ghahremani, " A high-performance 94-GHz MMIC doubler," *IEEE Microwave Guided Wave Lett.*, vol. 3, no. 6, pp. 167-9, June 1993.

DESIGN CONSIDERATIONS FOR HEAVILY- DOPED CRYOGENIC SCHOTTKY DIODE VARACTOR MULTIPLIERS

E. Schlecht, F. Maiwald, G. Chattopadhyay, S. Martin and I. Mehdi
Jet Propulsion Laboratory, California Institute of Technology
MS 168-314
4800 Oak Grove dr.
Pasadena, CA 91109
310-354-4887 - erichs@merlin.jpl.nasa.gov

Abstract.

Diode modeling for Schottky varactor frequency multipliers above 500 GHz is presented with special emphasis placed on simple models and fitted equations for rapid circuit design. Temperature- and doping-dependent mobility, resistivity and avalanche current multiplication and breakdown are presented. Next is a discussion of static junction current, including the effects of tunneling as well as thermionic emission. These results have been compared to detailed measurements made down to 80 K on diodes fabricated at JPL, followed by a discussion of the effect on multiplier efficiency. Finally, a simple model of current saturation in the undepleted active layer suitable for inclusion in harmonic balance simulators is derived.

The research described in this publication was carried out at the Jet Propulsion Laboratory, California Institute of Technology, under a contract with the National Aeronautics and Space Administration.

I Introduction.

As diode multipliers are applied to higher frequencies (here used to mean above 500 GHz) the frequency dependent effects that can often be neglected at lower frequencies become more important. These include current saturation, carrier inertia, and capacitance of the undepleted epitaxial region [1,2]. More accurate multiplier performance predictions benefit from including these effects in the models used. Furthermore, current and future space missions are being designed to operate the LO multiplier chains at lower temperatures, near 120 K for instance [3]. Again, for accurate modeling temperature effects must be considered. These include the effects on mobility, breakdown voltage, static I/V current and current saturation. To aid in the rapid design of multipliers at many different power levels and frequency ranges, it is desirable to have models which are easy to implement using simple equations, with a minimum of arduous calculation, maximizing the speed of analysis. Thus, the more advanced models should still be fairly simple, suggesting the use of fitted equations.

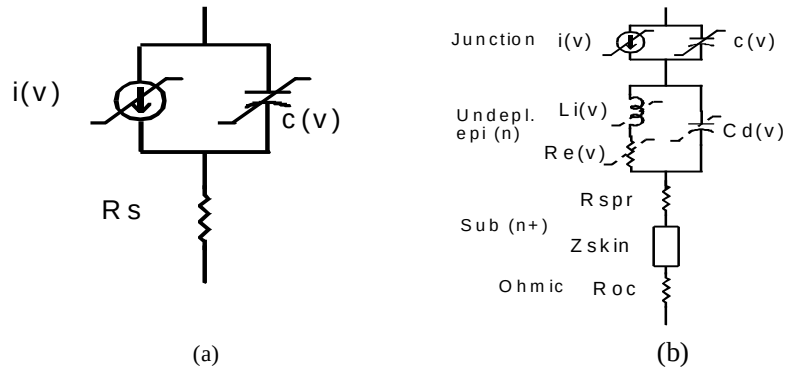

Figure 1. Diode circuit model. (a) Simplified. (b) More complete

As an illustration, Figure 1a shows a widely used diode model, which does a good job at lower frequencies, and can even work higher if well-calibrated. Figure 1b indicates the more sophisticated model discussed in this paper. The elements of the model will be investigated in the following sections. In section II the temperature-dependent material properties are discussed: mobility, resistivity, avalanche current multiplication and breakdown voltage. Section III is an analysis of the static junction current including the effects of tunneling, and its effect on multiplier efficiency. In section IV a simple model for analysis of current saturation in the undepleted epi region is introduced. The conclusions are presented in Section V.

II Diode Properties.

A. Mobility.

One of the primary loss mechanisms in the Schottky diode multiplier is signal absorption in the parasitic series resistance, depicted as R_s in Figure 1a and R_e, R_s, and R_{oc} in Figure 1b. The value of these resistances is proportional to the resistivities in the active epitaxial layer, the highly-doped sub-layer, and ohmic contacts respectively. Resistivity depends on the low field mobility, which can either be calculated by Monte Carlo methods [4-6] or measured [7, 8]. To facilitate calculation of the mobility for rapid design, a fitted algebraic equation is desired, including the effects of temperature and donor concentration. The author is not aware of a good fit, so the following expressions are suggested:

$$\mu = \left(\frac{1}{\mu_0} + \frac{1}{\mu_I} \right)^{-1} \tag{1}$$

$$\mu_0 = \frac{2296 \quad cm^2/Vs}{\left[\exp(490/T) - 0.42\right]^{-1} + (T/3410)^{1.3}} \tag{1a}$$

$$\mu_I = \frac{2.34\times10^5}{\left[\dfrac{1}{(184/T)^{2.3}+1} + \left(\dfrac{20}{T}\right)^{1.4}\right]\left[\dfrac{n_0}{10^{14}}\left(\dfrac{1+\theta}{1-\theta}\right)\right]^{0.86-T/900}} + \frac{10^4\left(e^{-\theta/0.68} - 0.27\right)}{T/163 + 0.8} \quad cm/Vs \tag{1b}$$

where T is the temperature in Kelvins, n_0 is the carrier concentration in cm^{-3}, and θ is the compensation ratio, defined [5] as the ratio of ionized acceptor to ionized donor concentrations. Since the normal donors in GaAs, such as Si, are shallow (~6 meV), as the carrier concentration increases the donor levels merge with the conduction band [9]. This occurs at a donor concentration of around 10^{16} cm^{-3}, and above that all donors are considered ionized except at extremely low temperatures, 10 K or so. Since the range of temperatures considered here is above 50 K and donor concentrations are above 10^{17} cm^{-3}, the carrier concentration is assumed equal to effective donor concentration, $N_D - N_A$, where N_D and N_A are the donor and acceptor concentrations.

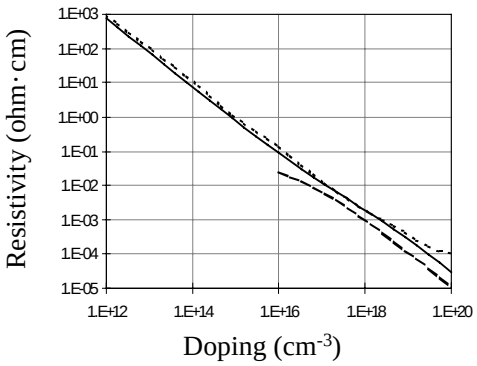

Figure 2. GaAs resistivity doping dependence. Solid line: 300 K calculation. Dotted line: From [10]. Broken line: 100K calculation.

The resistivity ρ is given by the usual formula:

$$1/\rho = q\mu n_0 \tag{2}$$

Figure 2 shows a plot of resistivity versus carrier concentration. Our room temperature and 100K calculations based on the formula above are compared to the room temperature plot in [10].

B. Avalanche current multiplication and breakdown.

Avalanche current multiplication caused by impact ionization is important in the reverse bias regime, especially for the highly doped diodes being used. This is the mechanism for junction breakdown, assuming the epi region is thicker than the depletion width when it occurs. Avalanche multiplication increases the current injected from one side of the depletion region by a factor M. Since impact ionization occurs at high fields, around 5×10^5 to 10^6 V/cm, it occurs first under the anode at high reverse bias, that is, the current being multiplied is comprised of electrons penetrating the barrier from the anode contact. Under these circumstances, M is given by [11]:

$$1 - \frac{1}{M} = \int_0^W \alpha_n \exp\left[-\int_0^{x'} (\alpha_n - \beta_p)\, dx' \right] dx \tag{3}$$

where α_n is the field-dependent electron ionization coefficient, β_p is the corresponding hole ionization coefficient, and W is the depletion width at the given voltage. To determine the breakdown voltage, M is taken to be infinite,

and the right side of (3) is solved iteratively to determine the applied voltage and corresponding field distribution and depletion width that make it unity.

Many researchers over the years have attempted to determine the ionization coefficients of GaAs [12-16]. For this work the measurements reported by Bulman et al. [14, 15] were used. Baraff [17] made calculations parameterizing the ionization coefficients at low temperature in terms of the optical phonon energy E_r, the mean free path between phonon scattering events λ, and the average ionization energy, E_i. These have been extended to all tempertures [18] using the assumption that E_i varies with temperature as the band gap energy and that E_r and λ vary as:

$$\frac{E_r}{E_{r0}} = \frac{\lambda}{\lambda_0} = \tanh\left(\frac{E_{r0}}{2kT}\right) \qquad \textbf{(4)}$$

where the zero subscripts refer to zero Kelvin values. The 0 K phonon energy is known to be 0.036 eV, so only values for E_i and λ_0 must be determined. The calculations in [17] have been fitted by Okuto and Crowell [18] to a simple formula. For our study the expression in [18] has been modified to fit Baraff's data more closely, which seems to model the measurements better. The modified equation is:

$$\alpha\lambda = f\sqrt{\frac{b}{x}}\exp\left[a - \sqrt{a^2 - x^2}\right] \qquad \textbf{(5)}$$

Here α is either α_n or β_p as appropriate, f is a simple factor which accounts both for variations in measurments and for the unknown ratio of impact ionization cross-section to phonon emission cross-section [17]. The expressions for a, b, and x are:

$$a = 0.116\left(\frac{E_i}{E_r}\right)^{1.266} \qquad b = 6.83\left(\frac{E_r}{E_i}\right) + 0.113 \qquad x = \frac{E_i}{qE\lambda} \qquad \textbf{(6,7,8)}$$

with E being the magnitude of the electric field. For this work values for the parameters that fit well to Bulman's data are: E_i = 2 eV and f = 0.44 for both electron and hole ionization coefficients, and λ_0 = 78.6 Å for α_n and 71.1 Å for β_p. As pointed out in [15, 19, 20] the ionization coefficients also depend on location. The effect of this was checked using the model of [15,20] , and it was found that for doping up to about 5×10^{17} the difference in breakdown voltage with and without this correction is only a few tens of millivolts.

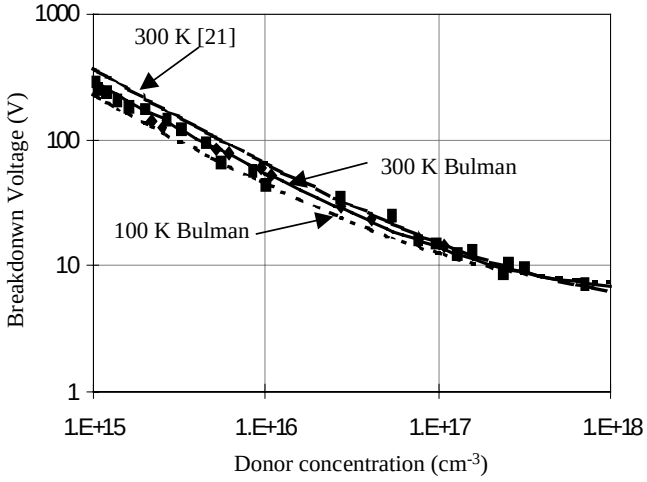

Figure 3. Breakdown voltage doping dependence. Scattered points represent measurements as described in text.

Figure 3 shows the breakdown voltage calculated using the ionization coefficients from equation (5) in equation (6) at 300 K, compared to a plot from [21] based on Pearsall's coefficients [13]. Also shown as scattered points are measurements used to derive the coefficients in [14,15] as well as others as reported in [22, 23]. The fit is better to those using Bulman's data at lower doping, although the difference between the two calculations is very small for the more highly doped diodes. Also shown is a curve indicating the breakdown voltage at 100 K calculated as above. Again, the temperature dependence is small at the higher dopings.

III Junction Current.

Quantum mechanical electron tunneling through the Schottky barrier is the dominant static current mechanism in low temperature and in highly doped diodes. This is because at high doping levels the depletion width is narrow, giving the large number of electrons below the top of the barrier a substantial probablity of tunneling through. At lower donor concentrations the depletion width is great enough that the dominant current mechanism is thermionic emission over the barrier. Several approximate tunneling current calculations were developed by Padovani and Stratton and others [24-27], but due to the approximations in calculating the tunneling coefficient the results are not valid over all current regimes. Recently the transfer matrix technique has been used [28, 29] to calculate the tunneling currents [30, 31]. This is a type of mode matching

algorithm wherein the barrier is divided up into a series of slices, each having a constant or linear potential profile. After the transmission coefficient, $T(E_n)$ is calculated for each value of the normal component of electron energy, E_n, the current density is calculated according to [32, equation (13)]. The transmission coefficient depends on the potential profile, including the barrier height, ϕ_b, which is given for an anode at $x = 0$ by:

$$\psi = \phi_b - qE_{\max} x\left(1-\frac{x}{W}\right)-\frac{q^2}{16\pi\varepsilon_r\varepsilon_0 x} \quad \textbf{(9)}$$

with $\varepsilon_r\varepsilon_0$ the semiconductor dielectric constant. The electric field under the anode is given as:

$$E_{\max} = \sqrt{\frac{2q(N_D - N_A)(\phi_b - V - V_n)}{\varepsilon_r\varepsilon_0}} \quad \textbf{(10)}$$

where V_n is the difference in potential between the Fermi level and the bottom of the conduction band in the semiconductor bulk. The barrier height itself commonly appears to have a dependence on the applied voltage [10, 33, 34]. For this work, the barrier height is characterized by an asymptotic "flat-band" height, Φ_{FB}, which is the barrier height at zero electric field, when the conduction bands would be flat. Additionally, the barrier height is assumed to have a linear dependence on E_{max}:

$$\phi_b = \Phi_{FB} - \alpha E_{\max} \quad \textbf{(11)}$$

Since E_{max} and ϕ_b, are mutually dependent, they must be solved for together as discussed in [33].

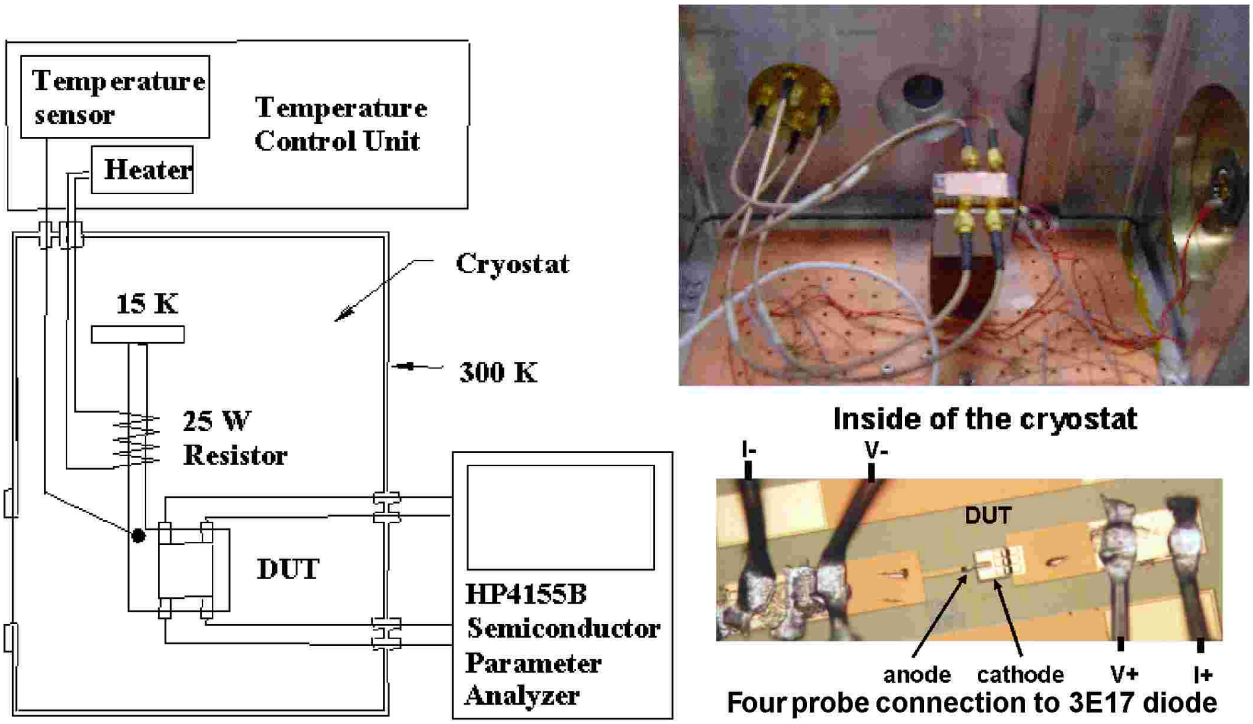

Figure 4. Block Diagram and photo of cryostat set up and wire-bonded diode.

To check the validity and determine the effect of the tunneling current on multiplier performance, several diodes fabricated at JPL have been measured over a wide temperature range in a specially designed cryostat [35]. The cryostat, shown in Figure 4, consists of a vacuum chamber enclosing the device under test (DUT) cooled by a two-stage closed-cycle Helium refrigerator. The temperature of the DUT is adjustable to within ±1 K in the 35-325 K range using a temperature controller with two temperature sensors, a 25 W heater and a bracket that mechanically connects the DUT to the 15 K second stage cold plate of the refrigerator.

The HP 4155B Semiconductor Parameter Analyzer is connected to the DUT with four cables for a four-probe measurement, compensating for the series resistance of the lines (Figure 2). Shielded cables connect the analyzer to SMA adaptors at the vacuum flange of the cryostat where the signals are fed through into the chamber. Inside the cryostat short sections of flexible cable connect the feed-through to the ceramic test socket which is

thermally bonded through a copper block to the temperature-stabilized cold plate. The diode is epoxied to the test socket and connected with four 25 μm bond wires to the carrier as also shown in Figure 4.

A diode fabricated a JPL on material doped to 3×10^{17} with an anode size of 1.5×10.5 μm^2 was measured from 100 to 300 K. The magnitude of the measured and calculated currents are compared in Figure 5. The current calculations included tunneling and avalanche multiplication as described earlier. Values of Φ_{FB} = 0.92 eV and α = 30 Å in equation (11) were used to fit the measurements. The fit is pretty good, but it is desirable to have independent justification for these values. The flat-band barrier height is dependent on the metal/semiconductor system in the contact. Using forward bias measurements of the reverse saturation current and ideality factor, the flat-band barrier height and effective barrier height, $\phi_{b,eff}$ can be determined as discussed in [36-39] based on the fact that as the applied voltage approaches the built-in voltage (flat-band), all current mechanisms except thermionic approach zero. This includes tunneling (because the bulk of electrons are near the barrier top in energy) and any models described by a linear field dependence (since the field approaches zero). This type of analysis was also performed on the above diode, with the results shown in Figure 6a. Since the JPL anodes are fabricated from Ti/Pt/Au, the flat-band barrier height should be compared to those metals. In [38] the reported heights are around 0.83 eV for Ti, 0.92 eV for Au and 0.99 eV for Pt. The measured values fit a line Φ_{FB} = 950–.3T meV, T being the temperature in Kelvin. It is possible that some intermixing may be taking place between the Ti and the Pt, but this cannot be said for certain. As to the α = 30 Å factor, many theories have been proposed explaining non-zero α as due to the imperfect nature of the metal-semiconductor interface [33, 34, 40-44]. Again, there is not enough data to pin this down.

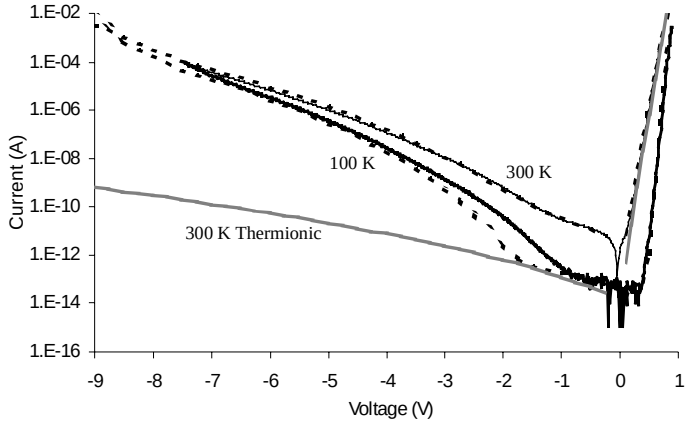

Figure 5. Tunneling/avalanche current calculations compared with measurement. The solid lines are measured currents, broken lines are calculated.

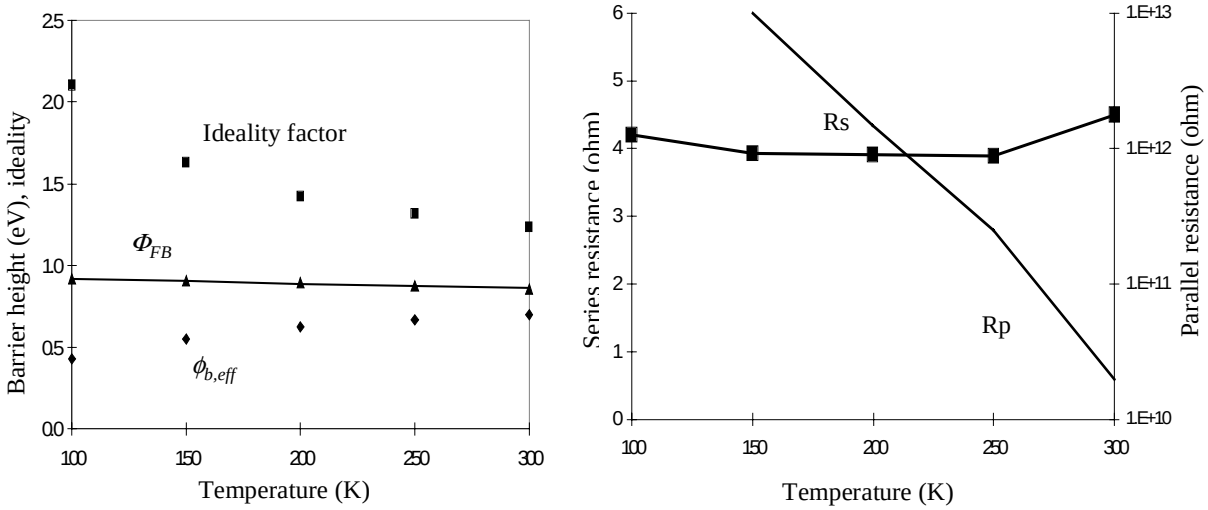

Figure 6. Characteristics of 3e17 diode. (a) Barrier height and ideality. The solid line is a model Φ_{FB} = 0.95-0.0003T eV. (b) Series and shunt resistances.

The series resistance and shunt resistance can also be found from the I/V data. These are plotted in Figure 6b. As expected, the series resistance R_s is independent of temperature (except for deviations ascribable to measurement uncertainty). The shunt resistance, R_p, however rises sharply at low temperatures. This is consistent

with a model wherein the shunt conduction is a surface "hopping" phenomenon, where the carriers do freeze out as the temperature drops. Generation-recombination current was considered, but it is proportional to the product of depletion width W and intrinsic carrier concentration n_i. For GaAs in general n_i is very low and for highly doped diodes W is small, so this current mechanism is insignificant in this case.

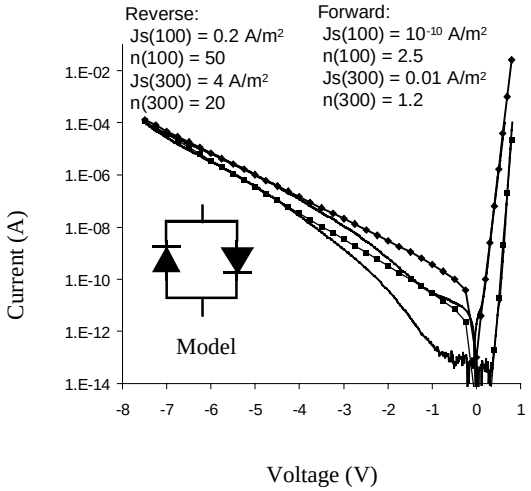

Figure 7. Fitted diode models and measurements, 100 & 300 K. Markers indicate fit models.

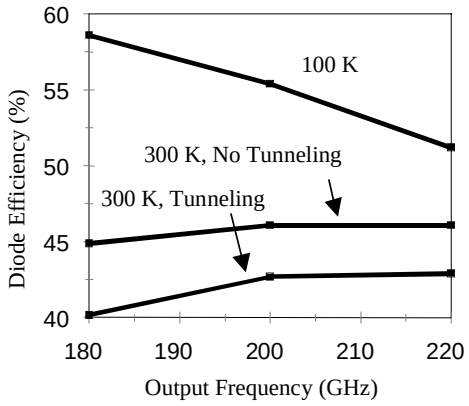

Figure 8. Efficiency of doubler with and without including tunneling current.

To evaluate the effect of these departures from thermionic behavior on multiplier efficiency, a simple model consisting of two diodes back-to-back was incorporated into a commercial harmonic balance simulator. A schematic is shown in Figure 7. One diode models the forward current, the other the reverse. The fit of the modeled current magnitude to the measurements is also shown in Figure 7. The fit is good for the forward bias, and not so good for reverse. However, the fit at the higher reverse currents is good, and the lower currents should have little effect on the performance of the multiplier.

Performance calculations of a 200 GHz multiplier with and without the reverse tunneling component are shown in Figure 8. As can be seen, at room temperature there is a significant reduction in efficiency when tunneling current is considered, but at 100 K there is no substantial difference. There is also no observed difference when the same calculation is performed at 800 GHz. These can be explained by noting that all Schottky multipliers suffer from two loss mechanisms: series resistance loss, which dominates, and conduction current loss. As the temperature is lowered, the conduction current drops (at a given voltage) so the conduction current contribution to the loss is greatly reduced. Hence, little difference in efficiency occurs with or without tunneling at low temperatures. At 800 GHz the efficiency is low and also greatly dominated by the series resistance loss, so the exact conduction current mechanism has little effect on efficiency.

IV Current Saturation.

As the electric field in a GaAs sample is increased, the velocity and hence the current reaches a peak, then begins to decline due to electrons gaining enough energy from the field to scatter into the upper, low-mobility valleys. This acts as a current limit in the undepleted epitaxial region of the diode. Current saturation reduces the efficiency of the diode as a multiplier because it decreases the ability of the charge at the edge of the depletion region to move around at the signal frequency and modulate the capacitance, generating the varactor non-linearity. There are also time constants associated with the transfer, and at the high frequencies being considered here they should be taken into account.

There are several equations used to describe the static current saturation profile. The simplest and oldest is the Kramer and Mircea formula [47]:

$$u(F) = \frac{\mu_0 F + u_s (F / F_N)^4}{1 + (F / F_N)^4} \qquad \textbf{(12)}$$

where u is the velocity, F the magnitude of the electric field, u_s the ultimate saturation velocity at about 20 kV/cm, and F_N is a characteristic field which determines where the peak velocity occurs. Usually current saturation, including transient effects have been modeled using Monte Carlo simulations (see, for example [45, 46]). Since

Monte Carlo calculations take large amounts of computer time, it is desirable to incorporate these effects into a harmonic balance (HB) circuit simulator using a simple model which can be integrated using the Runge-Kutta type integrators normally used in HB simulators. We propose to use a time constant based formulation somewhat similar to that introduced in [48]. The epi current is divided between two resistances representing the dominant two conduction band valleys in which electrons travel, as illustrated in Figure 9. Defining μ_0 as the lower valley mobility, (about 4000 cm^2/Vs or higher at reduced temperatures), and μ_1 is the upper valley mobility (about 400 cm^2/Vs) and n_0 and n_1 as the corresponding valley populations, the velocity in equation (12) can be written:

$$u(F) = \left(\mu_0 \frac{n_0}{n} + \mu_1 \frac{n_1}{n} \right) F \tag{13}$$

with n the total electron concentration in the undepleted epi. Then, several coupled differential equations are used to represent the time-dependent behavior of the velocity. The upper valley population is described by:

$$\frac{dn_1}{dt} = \frac{n_{1s}(V) - n_1(t)}{\tau} \tag{14}$$

where $n_{1s}(V)$ represents the static population of the upper valley, derived by combining equations (12) and (13) and noting that the total electron concentration is the sum of the populations of the two valleys, i.e. $n = n_0 + n_1$. The time constant, τ is dependent on the voltage across the epi, V_{tot}.

The current through the inductor representing carrier inertia has the usual equation:

$$\frac{di}{dt} = \frac{V_{tot}(t) - V(t)}{L_i} \tag{15}$$

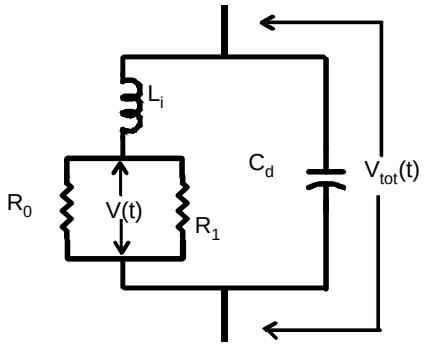

Figure 9. Simplified model of current saturation.

where L_i is the carrier inertia inductance, equal to:

$$L_i = \frac{m^* w}{q^2 n A} \tag{16}$$

with m^* the effective mass, w the thickness of the undepleted epi, and A the area of the diode. The total current through the inductance is simply:

$$i = qnuA \tag{17}$$

To simulate the full diode, of course, other equations must be included to model the epi capacitance, as well as the junction capacitance and conduction current.

As a check on the validity of the model, a test on a sample "undepleted epi" was made. It was assumed that this sample was of constant thickness, so that the equations above could be used, uncoupled from the epi capacitance, since the its current would depend on V_{tot} only, which is given as a boundary condition. In that case, equations (13) through (17) can be integrated using a numerical integrator with any given waveform for V_{tot}. In Figure 10 these calculations are compared with those in [46] for steps from zero electric field to the indicated values.

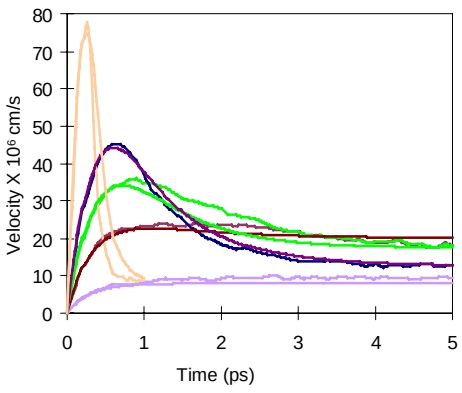

Figure 10. New current saturation model transient response (smooth curves) and results from [6] (rough curves).

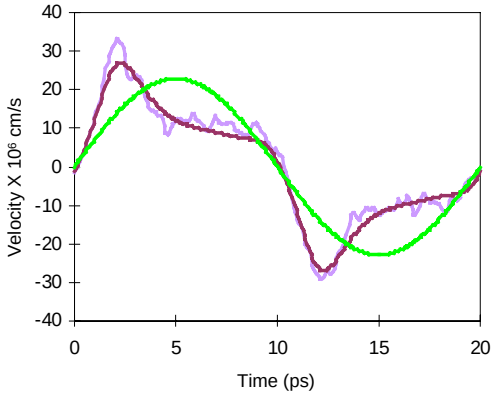

Figure 11. Sinusoidally pumped current saturation model (smooth line) compared to results from [46] (rough) and resistive approximation (sine wave).

It was found that values for τ ranging linearly from 0.2 ps at the 20 kV/cm to 3 ps at 1 kV/cm gave a good fit. As a further test, the same model is compared in Figure 11 with a sinusoidal 60 GHz excitation of 10 kV/cm amplitude. Again, the match is good. Also plotted is the current through a resistance having a mobility one-third that of GaAs (hence three times the resistance), which gives an estimate of the magnitude in performance reduction.

Currently, it appears that the above model, simple as it is, is impossible to incorporate into commercial HB simulators. Work is continuing in this direction, and a version of the Siegel/Kerr reflection algorithm HB simulator [49] is in progress so this model can be used to actually design multipliers.

V Conclusions.

Several suggestions have been made for improving the modeling of Schottky diodes for high doping and frequency, and low temperatures. The effects examined have been low-field mobility, breakdown, conduction current, barrier height and current saturation. Most of the effects serve to merely reduce the achievable efficiency, but not change the designs themselves very much, specifically the matching impedances. This is because the most important design parameter is the reactance tuning, dominated by the diode capacitance, which has been accurately modeled previously. However, the current saturation serves to greatly increase the effective series resistance, which is the dominant loss mechanism. It is possible to estimate the magnitude of the effect by using a series resistance much larger than the measured DC values in the performance estimates [50]. However, by calculating the behavior of current saturation with variations in doping and temperature, it should soon be possible to improve the optimization of the doping and anode sizes of high frequency multiplier diodes.

References

[1] T.W. Crowe, "GaAs Schottky Barrier Mixer Diodes for the Frequency Range 1-10 THz," Int. J. Infrared Millimeter Waves, vol. 10, no. 7, pp 765-777 (1989)

[2] J.T. Louhi and A.V. Räisänen, "On the Modeling and Optimization of Schottky Varactor Frequency Multipliers at Submillimeter Wavelengths," *IEEE Trans. Microwave Theory Tech*., vol. 43, no. 4, pp 922-926, 1995.

[3] N.D. Whyborn, "The HIFI Heterodyne Instrument for FIRST: Capabilities and Performance," in *Proc. ESA Symp. The Far Infrared and Submillimetre Universe 1997*, ESA-401.

[4] D.L Rode, "Low-Field Electron Transport," in *Semiconductors and Semimetals Volume 10*, ed. R.K. Willardson, and A.C. Beer, Academic Press, New York, 1975.

[5] W. Walukiewicz, L. Lagowski, L. Jastrzebski, M. Lichtensteiger, and H.C. Gatos, "Electron Mobility and Free-Carrier Absorption in GaAs: Determination of the Compensation Ratio," *J. Appl. Phys.* vol. 50, no. 2, pp 899-908, 1979.

[6] J.G. Ruch and W. Fawcett, "Temperature Dependence of the Transport Properties of Gallium Arsenide Determined by a Monte Carlo Method," *J. Appl. Phys.* vol. 41, no. 9, pp 3843-3849, 1970.

[7] G.E. Stillman, C.M. Wolfe, and J.O. Dimmock, "Hall Coefficient Factor for Polar Mode Scattering in n-Type GaAs," *J. Phys. Chem. Solids*, vol. 31, pp. 1199-1204, 1970.

[8] C.M. Wolfe, G.E. Stillman, and W.T. Lindley, "Electron Mobility in High-Purity GaAs," *J. Appl. Phys.*, vol. 41, no. 7, pp 3088-3091, 1970.

[9] G.E. Stillman, and C.M. Wolfe, "Electrical Characterization of Epitaxial Layers," *Thin Solid Films*, vol. 31, pp 69-88, 1976.

[10] S.M. Sze, *Physics of Semiconductor Devices*, 2nd Ed., Wiley, New York, 1981.

[11] G.E. Stillman, and C.M. Wolfe, "Avalanche Photodiodes," in *Semiconductors and Semimetals Volume 12*, ed. R.K. Willardson, and A.C. Beer, Academic Press, New York, 1977.

[12] R.A. Logan and S.M. Sze, "," J. Phys. Soc. Jap. Suppl., vol. 21, p 434, 1966.

[13] T.P. Pearsall, "The Band Structure Dependence of Impact Ionization by Hot Carriers in Semiconductors: GaAs," *Solid-State Electronics*, vol 21, pp 297-302, 1978.

[14] G.E. Bulman, V.M. Robbins, K.F. Brennan, K. Hess, and G.E. Stillman, "Experimental Determination of Impact Ionization Coefficients in (100) GaAs," *IEEE Electron Device Lettr.*, vol. EDL-4, no. 6, pp 181-185, 1983.

[15] G.E. Bulman, V.M. Robbins, and G.E. Stillman, "The Determination of Impact Ionization Coefficients in (100) Gallium Arsenide Using Avalanche Noise and Photocurrent Multiplication Measurements," IEEE Trans. Electron Devices, vol. ED-32, no. 11, pp 2454-2466, 1985.

[16] X.G. Zheng, P. Yuan, X. Sun, G.S. Kinsey, A.L, Holmes, B.G. Streetman, and J.C. Campbell, "Temperature Dependence of the Ionization Coefficients of AlxGa1-xAs," *IEEE J. Quantum Electr.*, vol. 36, no. 10, pp

1168-1173, 2000.
[17] G.A. Baraff, "Distribution Functions and Ionization Rates for Hot Electrons in Semiconductors," *Phys. Rev.*, vol. 128, no 6, pp. 2507-2517, 1962.
[18] Y. Okuto and C.R. Crowell, "Energy-Conservation Consideration in the Characterization of Impact Ionization in Semiconductors," *Phys. Rev. B*, vol. 6, no. 8, pp 3076-3081, 1972.
[19] Y. Okuto and C.R. Crowell, "Ionization Coefficients in Semiconductors: A nonlocalized Property," *Phys. Rev. B*, vol. 10, no. 10, pp. 4284-4296, 1974.
[20] Y. Okuto and C.R. Crowell, "Threshold Energy Effect on Avalanche Breakdown Voltage in Semiconductor Junctions," *Solid-State Electronics*, vol 18, pp 161-168, 1975.
[21] M.H. Lee and S.M. Sze, "Orientation Dependence of Breakdown Voltage in GaAs," *Solid-State Electronics*, vol 23, pp 1007-1009, 1980.
[22] B.J. Baliga, R. Ehle, J.R. Shealy and W. Garwacki, "Breakdown Characteristics of Gallium Arsenide," *IEEE Electron Device Lettr.*, vol. EDL-2, no. 11, pp 302-304, 1981.
[23] B.J. Baliga, A.R. Sears, P. Menditto and P.M. Campbell, "Extended Measurements of Gallium Arsenide Breakdown Characteristics Using Punchthrough Structures," *IEEE Electron Device Lettr.*, vol. EDL-5, no. 9, pp 385-387, 1984.
[24] F.A. Padovani and R. Stratton, "Field and Thermionic-Field Emission in Schottky Barriers," *Solid-State Electronics*, vol 9, pp 695-707, 1966.
[25] F.A. Padovani, "The Voltage-Current Characteristics of Metal-Semiconductor Contacts," in *Semiconductors and Semimetals Volume 7A*, ed. R.K. Willardson, and A.C. Beer, Academic Press, New York, 1971.
[26] C.R. Crowell and V.L. Rideout, "Normalized Thermionic-Field (T-F) Emission in Metal-Semiconductor (Schottky) Barriers," *Solid-State Electronics*, vol 12, pp 89-105, 1969.
[27] V.L. Rideout and C.R. Crowell, "Effects of Image Force and Tunneling on Current Transport in Metal-Semiconductor (Schottky Barrier) Contacts," *Solid-State Electronics*, vol 13, pp 993-1009, 1970.
[28] Y. Ando and T. Itoh, "Calculation of Transmission Tunneling Current Across Arbitrary Potential Barriers," *J. Appl. Phys.*, vol. 61, no. 4, pp. 1497-1502, 1987.
[29] W.W. Lui and M. Fukuma, "Exact Solution of the Schrodinger Equation Across and Arbitrary One-Dimensional Piecewise-Linear Potential Barrier," *J. Appl. Phys.*, vol. 60, no. 5, pp. 1555-1559, 1986.
[30] U.V. Bhapkar and R.J. Mattauch, "Numerical Simulation of the Current-Voltage Characteristics of Heteroepitaxial Schottky Barrier Diodes," *IEEE Trans. Electron Devices*, vol. 40, no. 6, 1993.
[31] J. Grajal, V. Krozer, E. González, F. Maldonado and J. Gismero, "Modeling and Design Aspects of Millimeter-Wave and Submillimeter-Wave Schottky Diode Varactor Frequency Multipliers," *IEEE Trans. Microwave Theory Tech.*, vol. 48, no. 4, 2000.
[32] R. Stratton, "Volt-Current Characteristics for Tunneling through Insulating Films," *J. Phys. Chem. Solids*, vol. 23, pp1177-1190, 1962.
[33] E.H. Rhoderick and R.H. Williams, *Metal-Semiconductor Contacts*, Second Edition, Oxford University Press, New York, 1988.
[34] J.M. Andrews and M.P. Lepselter, "Reverse Current-Voltage Characteristics of Metal-Silicide Schottky Diodes," *Solid-State Electronics*, vol 13, pp 1011-1023, 1970.
[35] Maestrini et. al, "Cryogenic operation of GaAs based multiplier chains to 400 GHz, " 8th Intl THz Conf, 2000.
[36] L.F. Wagner, R.W. Young and A. Sugerman, "A Note on the Correlation Between the Schottky-Diode Barrier Height and the Ideality Factor as Determined from I-V Measurements," *IEEE Electron Device Lettr.*, vol. 9 pp320-322, 1983.
[37] H.-W Hübers and H.P. Röser, "Temperature Dependence of the Barrier Height of Pt/n-GaAs Schottky Diodes," *J. Appl Phys.*, vol. 84, no. 9, pp 5326-5330, 1998.
[38] G. Myburg, F.D. Auret, W.E. Meyer, C.W. Louw and J.J. van Staden, "Summary of Schottky Barrier Height Data on Epitaxially Grown n- and p-GaAs," *Thin Solid Films*, vol. 325, pp181-186, 1998.
[39] V.W.L. Chin, M.A. Green and J.W.V. Storey, "Correlation Between Current-Voltage and Capacitance-Voltage Schottky Barrier Height on (100) and (110) GaAs and (110) InP Survaces," *J. Appl Phys.*, vol. 68, no. 7, pp 3470-3474, 1990.
[40] J. Tersoff, "Schottky Barriers and Semiconductor Band Structures," *Phys. Rev. B*, vol. 32, no. 10, pp 6968-6971, 1985.
[41] S.G. Louie, J.R. Chelikowsky and M.L. Cohen, "Ionicity and the Theory of Schottky Barriers," *Phys. Rev. B*, vol. 15, no. 4, pp 2154-2162, 1977.
[42] W. Mönch, "Barrier Heights of Real Schottky Contacts Explained by Metal-Induced Gap States and Lateral Inhomogeneities," *J. Vac. Sci. Technol. B*, vol. 17, no. 4, pp1867-1876, 1999.

[43] R.T. Tung, "Electron Transport at Metal-Semiconductor Interfaces: General Theory," *Phys. Rev. B*, vol. 45, no. 23, pp 13509-13523, 1992.
[44] R.T. Tung, "Chemical Bonding and Fermi Level Pinning at Metal-Semiconductor Interfaces," *Phys. Rev. Lettr*., vol. 84, no. 26., pp 6078-6081, 2000.
[45] T.J. Maloney and J. Frey, "Transient and Steady-State Electron Transport Properties of GaAs and InP," *J. Appl. Phys*., vol. 48, p 781, 1975.
[46] R.O. Grondin, P.A. Blakey, J.R. East, "Effects of Transient Carrier Transport in Millimeter-Wave GaAs Diodes," *IEEE. Trans. Electron Devices*, vol. ED-31, no. 1, pp 21-28, 1984.
[47] B. Kramer and A. Mircea, "Determination of Saturated Electron Velocity in GaAs," *Appl. Phys. Lettr*., vol. 26, no. 11, pp 623-625, 1975.
[48] D.E. McCumber and A.G. Chynoweth, "Theory of Negative-Conductance Amplification and of Gunn Instabilities in "Two-Valley" Semiconductors," *IEEE Trans. Electron Dev*., vol. ED-13, no. 1, pp 4-21, 1966.
[49] Siegel/Kerr NASA report, 1984.
[50] N.R. Erickson, private communicaion.

Experimental investigation of local oscillator chains with GaAs planar diodes at cryogenic temperatures

A. Maestrini, D. Pukala, E. Schlecht, I. Mehdi and N. Erickson[1]

Jet Propulsion Laboratory, California Institute of Technology
[1]University of Massachusetts

Abstract – **This paper will describe a robust test-bed that has been built to measure multiplier performance over a wide range of temperatures and frequencies. In a 182-212 GHz designed balanced doubler the peak efficiency at 201 GHz improves from 22% to 28% upon cooling from 300 K to 120 K. This stage is then used to pump a 362-424 GHz balanced planar doubler. The peak chain efficiency increases from 3.4% to 6% when the two cascaded doublers are cooled from 300 K to 120 K. This enables the production of 10 mW of peak output power at 377 GHz, which ought to be sufficient for driving the next stage multiplier.**

I. INTRODUCTION

GaAs Schottky diode frequency multipliers are being developed at a number of facilities for the Heterodyne Instrument of Herschel Space Observatory (formerly known as FIRST). The planned mission will cover the 80 μm to 670 μm range with a 14-channel instrument that is based on state-of-the-art sensor technologies [1,2,3]. Cooling of multiplier circuits to enhance performance has been demonstrated [4,5] and thus the mission has base lined cooled operation of the local oscillator (LO) unit. In principal, whisker contacted circuits can be used but the inherently mechanically sensitive approach to the building of whisker contacted circuits does not readily lend itself to thermal cycling. Well-designed and appropriately implemented planar technology is better suited for cooled operation and can be designed to handle thermal cycling and heat dissipation.

Cooling of multiplier circuits can have considerable influence on the output power and efficiency of GaAs multipliers as has been demonstrated [4,5]. However, the intricate tradeoff between various diode parameters for optimum cryogenic applications is still under investigation [6]. Electron mobility in GaAs is strongly temperature dependent while circuit losses also improve upon cooling. However, a better understanding of electron transport in doped GaAs as a function of temperature along with an accurate thermal model of the diode chip is required to take full advantage of the cooling. In high input power applications the anode area is substantially hotter than the ambient temperature and accurate thermal models of the chips are required to optimize the anode characteristics for a given frequency, input power and temperature. While work is still under way to obtain a better understanding of temperature related effects in multipliers it is also equally important to experientially characterize multiplier stages and multiplier chains as a function of ambient temperature. The latter objective is being addressed in this paper. A robust test-bed that has been constructed from mostly commercially available items will be

described that simplifies the testing of multipliers as a function of ambient temperature. This setup has been used to measure a planar balanced doubler at 200 GHz and a planar chain of two cascaded doublers to 400 GHz. The results obtained will be discussed.

II. DESCRIPTION OF THE TEST SETUP

The test setup consists of an 87-108 GHz continuously tunable source, a cryostat in which the multipliers under test are installed and a Thomas Keating power meter as shown in Figure 1. The source is composed of a 75-115 GHz BWO followed by an 87-108 GHz power amplifier chain that can deliver up to 280 mW at 92 GHz [7]. Power is adjusted by an attenuator and /or a ferrite modulator that also isolates the BWO from the amplifier chain. Frequency is monitored by a microwave counter via a harmonic mixer. A cross-waveguide coupler and a low-offset, low drift power meter are used to monitor the power delivered by the source.

A low loss wide-band isolator is located inside the cryostat, between the coupler and the multiplier chain, to avoid any load pulling effects that can affect the accuracy of the monitoring of the input power. The temperature of the multipliers is adjustable to within ±1 K in the 35-325 K range using a controller, two temperature sensors, a 25 W resistor and a bracket that mechanically connects the chain to the 15 K cold plate of the cryostat. The vacuum window on the output side is made of a one-mil thick by two-inch diameter Mylar shield. IR radiation going through the window is partly blocked by two 25 μm-thick layers of Zitex 135 material.

We measured the power produced by the multiplier chain with a Thomas Keating power meter. A single 25 μm-thick layer of Zitex 135 material is used to protect the membrane of the Thomas Keating sensor from air-borne acoustic vibration, as well as visible and IR radiation. In addition, the Thomas Keating sensor is installed on an anti-vibration-plate with a 0.16 Hz cut-off frequency to eliminate the low frequency vibration produced by the refrigerator, the BWO, the chopper and the vacuum pumps. The RF output beam is focused on the membrane of the Thomas Keating sensor by an over-sized elliptical mirror that reduces the sensitivity to the optical misalignments. The beam is chopped by a two-blade by ten-inch diameter wheel operating at 20±0.2 Hz. The modulated signal detected by the Thomas Keating sensor is pre-amplified and filtered by a high-rejection, 10-30 Hz band-pass filter. The signal is finally measured by both a high-performance dual-channel digital lock-in amplifier and by the data acquisition card of the Thomas Keating power meter.

We found that the combination of the band-pass filter and the lock-in amplifier greatly improves the sensitivity of the Thomas Keating power meter. 10 μW could be confidently detected with a measurement uncertainty of ±1 μW, whereas the standard configuration results in a 10 μW noise floor.

A commercial power meter is used to monitor the input power. A second power meter, calibrated carefully by the manufacturer, is connected to the last waveguide bend before the multiplier chain, inside the cryostat. Recording at different frequencies the ratio between these two power levels defines a calibration chart. The output power is calibrated

automatically by the Thomas Keating control program. RF losses produced by the IR filters and the Mylar film were measured around 200 GHz and 400 GHz. We found a total absorption of less than 7% at 375 GHz however this was not used to correct the data reported.

Only modulated signals are taken into account by the Thomas Keating power meter. Therefore, in order to modulate the RF signal produced by the frequency multiplier chain, we decided to use a two-blade chopper wheel. This wheel is located outside the cryostat at room temperature. When the RF beam is cut, the Thomas Keating sensor receives only the IR radiation of the blades that can be considered as a black body at 300 K. When the RF beam is not cut, the Thomas Keating sensor receives the RF signal as well as part of the IR radiation emitted by the metallic components located inside the cryostat. This is because the IR radiation is only partially absorbed by the IR filters at the output window of the cryostat. When operating at cryogenic temperature, this IR radiation is the emission of a cold black body. As the Keating sensor is broadband, it detects a modulated IR signal in addition to the modulated RF signal produced by the frequency multipliers. This IR signal is 180° out of phase with the RF signal and, therefore, it is subtractive.

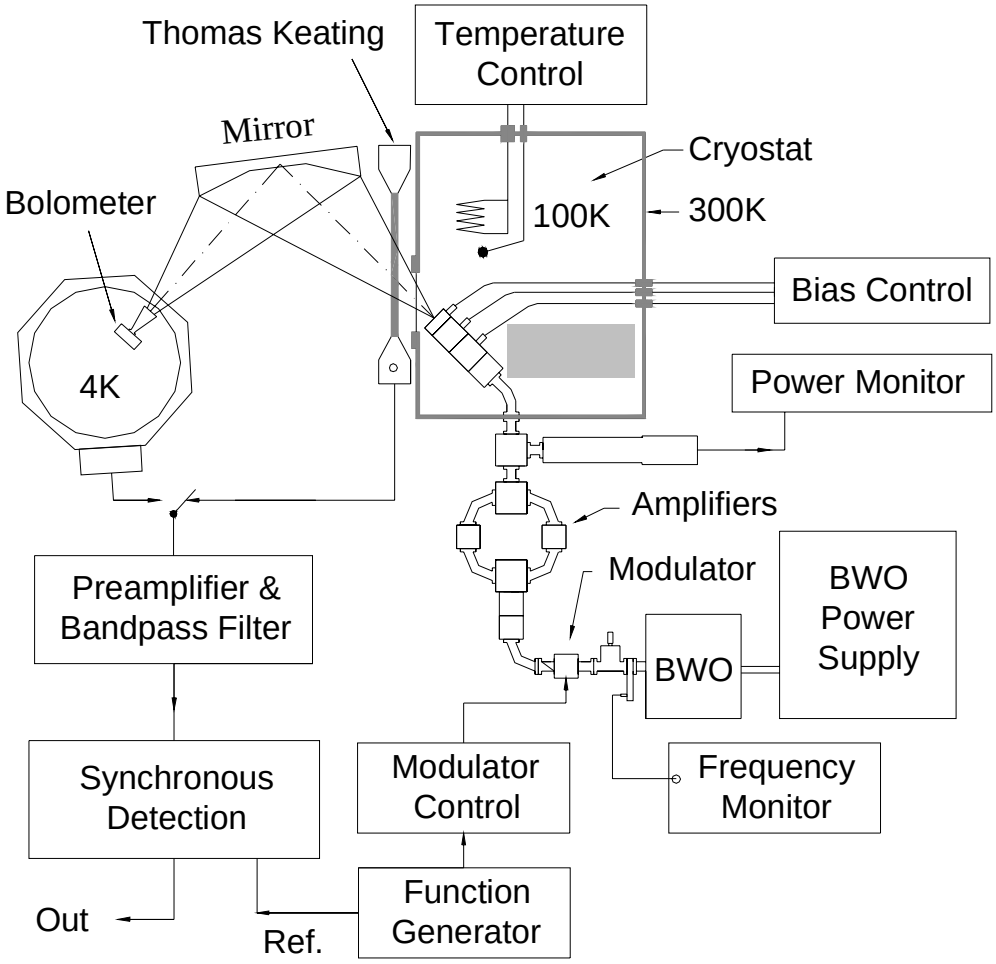

Figure 1: Test-bed for the measurement of output power from multipliers at cryogenic temperatures.

In the configuration shown (Fig. 1) at 100 K this IR radiation is about 150 μW. Consequently, at low output power levels it can have a significant effect on the measurement. One possible solution is to use a better IR filter but this might produce additional RF losses and standing waves. Another solution is to modulate the input power of the multiplier chain. The chopper wheel is removed and the modulation of the IR radiation is eliminated. The validity of this approach was ascertained by making a number of pulsed measurements with the amplifiers and the multipliers. We found that the amplifiers give slightly more power (+4% maximum) when driven with a 50% duty ratio square wave than when driven in CW. This increase of power is taken into account since the input power is monitored with a coupler and a power meter. The measurements show also that the frequency multiplier diodes reach their thermal equilibrium in less than 100 μs. Hence, modulating the input power of the doubler at 20 Hz does not produce any change in the behavior of the multiplier chain.

III. MULTIPLIER MEASUREMENTS

The 184-212 GHz balanced planar doubler with preliminary measurements has been described previously [8]. It is a 6-anode array with each anode being 1.5x14 μm. The doping in this chip was $1x10^{17}$ cm^{-3}. The discrete chip is mounted directly onto the waveguide block and a 1-mil wire is used to connect the chip to the bias capacitor. The close-up of the chip and the chip mounted up-side-down in the waveguide block is shown in Figure 2.

Room temperature performance of the 200 GHz doubler stage is shown in Figure 3. This particular multiplier exhibits a peak efficiency of about 21% at 188 GHz with a peak output power of 36 mW. The 3-dB bandwidth is approximately 20 GHz or 10%. The input and output backshorts are fixed and in obtaining the performance shown in Figure 3 only the device bias is optimized. The optimum bias range is between 11 and 13 volts. Under these pump conditions we have used this device extensively (both at room temperatures and at cryogenic temperatures) and have noticed no degradation in performance.

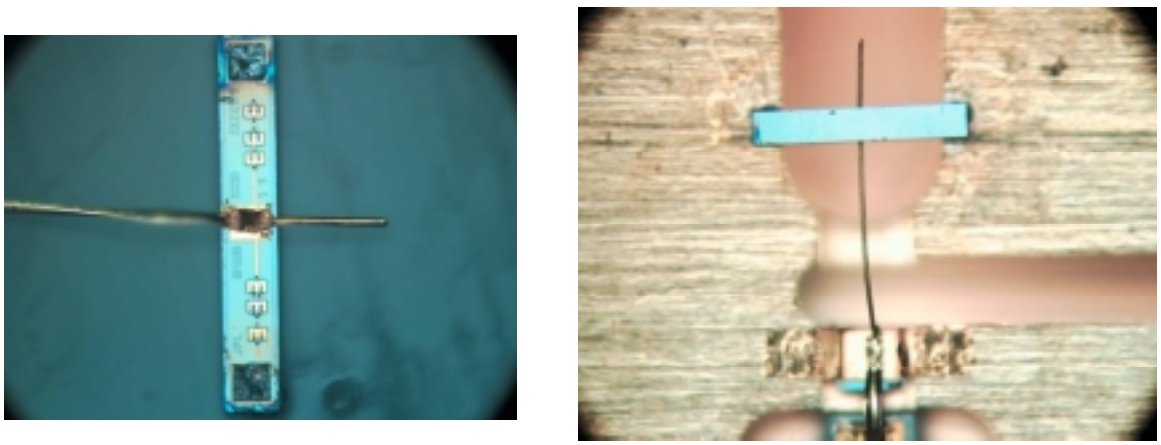

Figure 2: Discrete 6-anode chip (left) mounted up side down in the 200 GHz waveguide multiplier block (right).

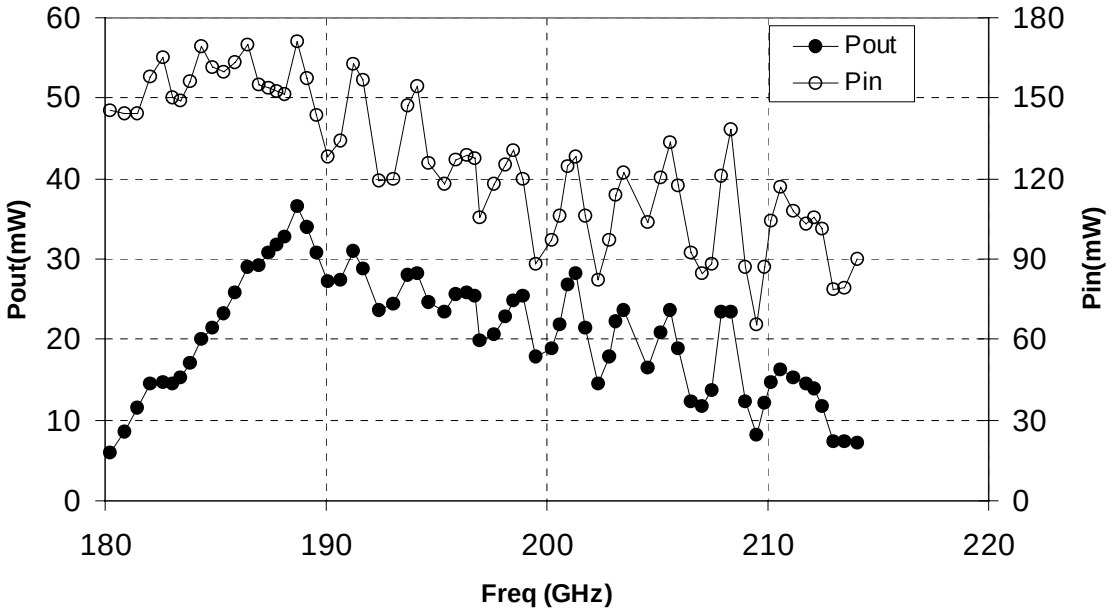

Figure 3: Room temperature performance of the 200 GHz stage doubler. Power-combined power amplifiers are used to increase the input power.

Since the room temperature measurements were made with the Keating meter the only setup change required for low temperature operation was to close the cryostat lid and activate the cryostat. The multiplier was tested at 120 K. This particular temperature is significant only because the multipliers operating on the Herschel Space Observatory are being baselined for this temperature range. The performance of the stage at 120 K is shown in Figure 4 (input power is similar to the curve shown in Figure 3 since the power amplifiers are not cooled). For comparison the output power and efficiency at room temperature have also been plotted on the same graph. For all frequencies a clear enhancement in output power can be observed with cooling. The peak efficiency of the multiplier stage increases from 21% at room temperature to about 28% at 120 K. This represents an increase of 30%. The basis for this increase is the improvement of the mobility of the free carriers in GaAs as the ambient temperature is decreased from room temperature. The enhanced mobility results in reduced series resistance thus improving the multiplier efficiency. The peak output power of the multiplier increases from 36 mW to 42 mW.

The 400 GHz doubler is constructed using the substrateless device technology that has been previously described in detail [9]. Essential features of this technology are that the anodes and the matching circuit are formed together with most of the metallic circuit suspended in air. A 30 micron thick GaAs frame holds the chip together. Extensive use of beamleads is made both for handling and mounting purposes. A picture of the substrateless 400 GHz doubler inside the waveguide block is shown in Figure 5. This is a 4-anode array (anodes are at the far left of the chip) with each anode 1.5x5.4 μm. The doping used for this chip is $2x10^{17}$ cm^{-3}.

The 200 GHz stage described earlier is used to pump the 400 GHz balanced doubler. The two blocks are cascaded with no isolators in between. An external dual mode horn centered at 400 GHz was mounted on the output guide of the second stage doubler and the output power was measured using the Keating meter as described earlier. Output power and the efficiency of the second stage at 120 K are shown in Figure 6. Also, shown is the available input power to the second stage multiplier. A peak in the efficiency of the second stage is observed around 368 GHz approaching 28%. The maximum output power from the cascaded chain is about 10 mW at a frequency of 378 GHz. At this particular point the efficiency of the second stage is 25%. Note that a maximum combined efficiency of 6% is measured and the 3dB bandwidth of output power is about 18 GHz or about 5%. The ripple present in the output power is due to the mismatch between the multiplier stages.

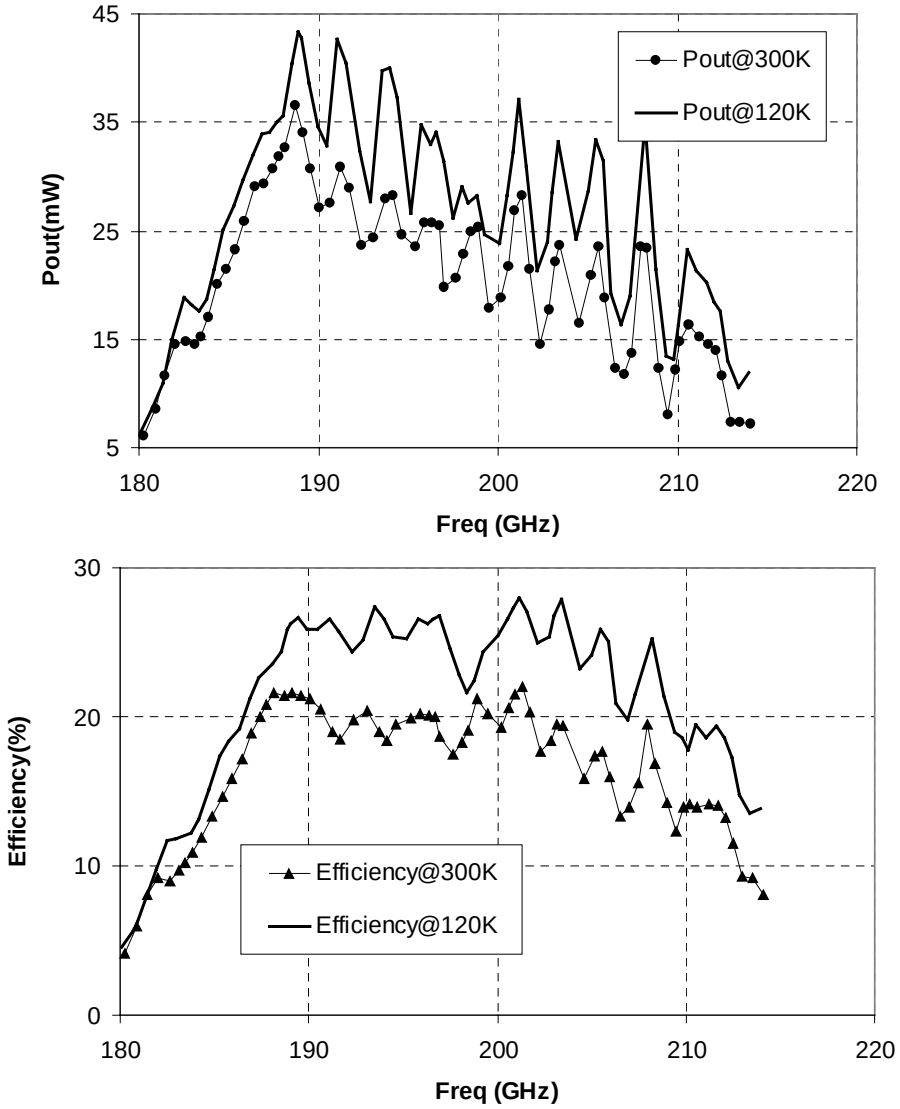

Figure 4: Output power (top) and efficiency (bottom) performance of the 200 GHz stage at 120 K.

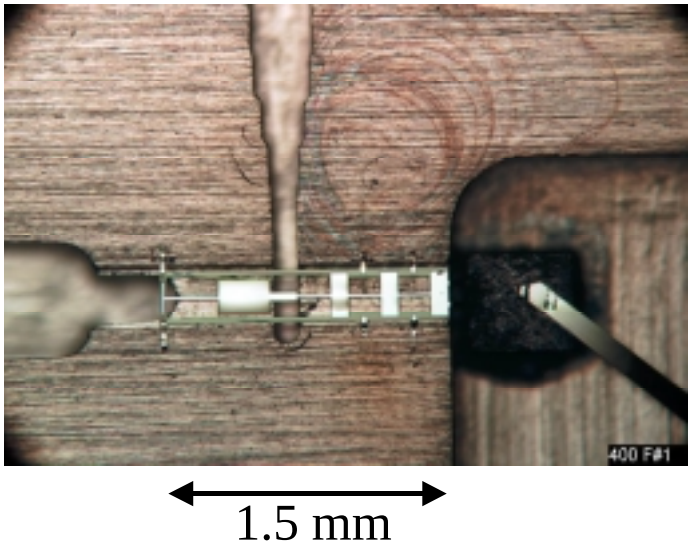

Figure 5: Inside of the 400 GHz balanced doubler with the top half of the split block removed. The output guide is shown in the top half of the photograph. The chips are made with the substrateless technology that requires only a simple assembly process.

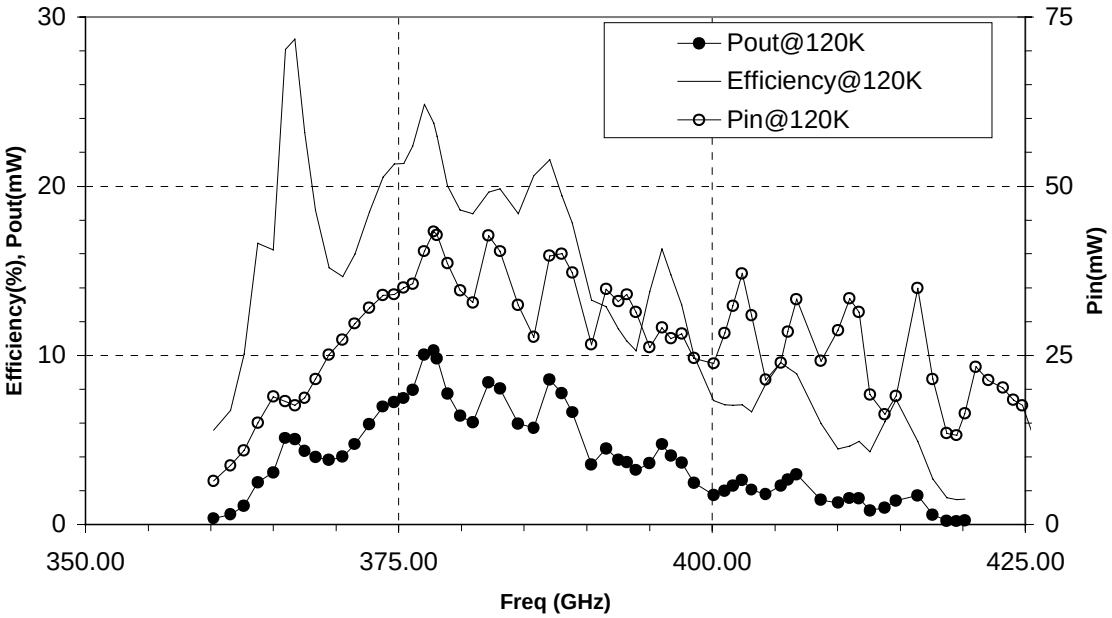

Figure 6: Performance of the cascaded chain at 120 K. The power available to the second stage multiplier is shown as Pin.

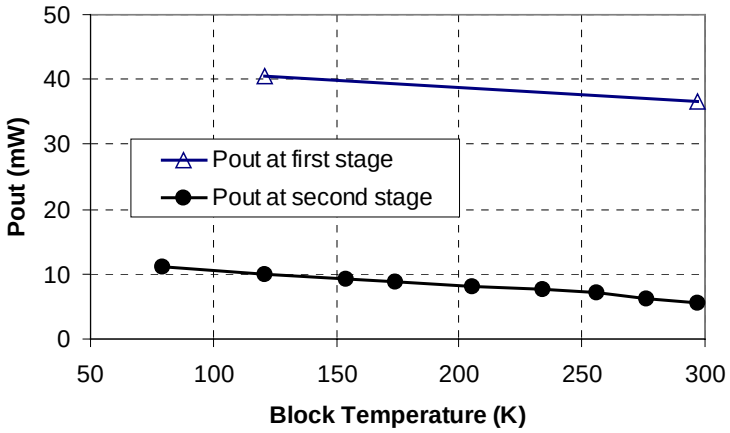

Figure 7: Output power from the two multiplier stages as a function of ambient temperature. The first stage output power is measured at 188.5 GHz while the second stage output power is measured at 377 GHz.

Figure 7 shows the effect of ambient temperature on the power performance of the two stages. We note that in each case the output power is linear with decreasing temperature with the slope for the second stage being sharper than for the first stage. This measurement is made at fixed frequencies of 188.5 and 377 GHz (corresponding to the first and second stages). We note that as the temperature is lowered the efficiency of the second stage approaches the efficiency of the first stage. There can be a number of possible explanations for this effect and further careful analysis is required to draw valid conclusions. It is possible that the anodes on the first stage are considerably hotter than the ambient temperature and thus the mobility improvement in the first stage is not has pronounced as the second stage. Also, one must take into effect current saturation effects, which can dominate the performance of the first stage due to the lower doping and higher input power. The chain efficiency as a function of temperature is also shown in Figure 7. An improvement of about 2.5 dB is observed when cooling from 300 K to 120 K.

IV. CONCLUSION

A test setup built to study performance of cryogenic multiplier stages has been described. Planar balanced doubler stages from 100 to 200 GHz and from 200 to 400 GHz have been measured at cryogenic temperatures. The chain efficiency can be improved by about 2.5 dB when the chain is cooled from 300K to 120 K. This improvement can be attributed to the enhancement of electron mobility and the reduction of current saturation effects in the individual multiplier stages. More work is required to quantitatively understand the interplay between device doping, temperature and input power for each stage.

V. ACKNOWLEDGEMENTS

Technical support from L. Samoska, T. Gaier, S. Martin, B. Nakamura, and A. Fung are greatly appreciated. Technical discussions with J. Bruston, A. Skalare, P. Siegel, and P. Zimmermann are also acknowledged. The research described in this publication was carried out at the Jet Propulsion Laboratory, California Institute of Technology, under a contract with the National Aeronautics and Space Administration.

VI. REFERENCES

1. G. Pilbratt, "The FIRST mission," *Proc. ESA Symp., The Far Infrared and Submillimetre Universe 1997*, ESA SP-401.
2. N. D. Whyborn, "The HIFI Heterodyne Instrument for FIRST: Capabilities and Performance," in Proc. ESA Symp., The Far Infrared and Submillimetre Universe 1997, ESA SP-401.
3. J. C. Pearson, R. Guesten, T. Klein, N. D. Whyborn, "Local oscillator system for the Heterodyne Instrument for FIRST (HIFI)", in Proc. Of SPIE UV, Optical and IR Space Telescopes and Instruments, Vol. 4013, Munich, Germany, March, 2000, SPIE 4013-18.
4. J. Louhi, A. Raisanen, and N. Erickson, "Cooled Schottky Varactor Frequency Multipliers at Submillimeter Wavelengths," IEEE Trans. On Microwave Theory and Techniques, Vol 41, No. 4, April 1991, pp. 565-571.
5. D. Porterfield, "Millimeter-Wave Planar Varactor Frequency Doublers," Ph.D. thesis at the University of Virginia, August 1998.
6. J. East and I. Mehdi, "Temperature Effects in Varactors and Multipliers," presented at the 12th Intl. Symp. on Space Terahertz Technology, San Diego, February 2001.
7. L. Samoska, T. Gaier, A. Peralta, S. Weinreb, J. Bruston, I. Mehdi, Y.C. Chen, H.H. Liao, M. Nishimoto, R. Lai, H. Wang, Y.C. Leong, "MMIC Power Amplifiers as Local Oscillators for FIRST," *Proc. SPIE UV, Optical, and IR Space Telescopes and Instruments*, SPIE 4013, Munich, Germany, March 2000.
8. N. R. Erickson, G. Narayanan, R. P. Smith, S. C. Martin, I. Mehdi, T. W. Crowe and W. L. Bishop, "Planar Frequency Doublers and Triplers for FIRST," Proc. of the 11th Inter. Symp. On Space Terahertz Technology, ann Arbor, Michigan, May 2000, pp. 543-551.
9. E. Schlecht, J. Bruston, A. Maestrini, S. Martin, D. Pukala, R. Tsang, A. Fung, R. P. Smith†, I. Mehdi, "200 and 400 GHz Schottky Diode Multipliers Fabricated with Integrated Air-Dielectric 'Substrateless' Circuitry", 11th International Symposium on Space Terahertz Technology, Ann Arbor, Michigan, May1-3, 2000.

The research described in this paper was carried out at the Jet Propulsion Laboratory, California Institute of Technology, under a contract with the National Aeronautics and Space Administration.

WIDELY-TUNABLE LASER-SIDEBAND THz SOURCE FOR SPECTROSCOPY & LO APPLICATIONS

Eric R. Mueller
DeMaria ElectroOptics Systems, Inc.
1280 Blue Hills Ave.
Bloomfield, CT 06002
(806) 243-9557

Jeffrey L. Hesler, Thomas W. Crowe,
David S. Kurtz & Robert M. Weikle, II
Applied Electrophysics Laboratories
Department of Electrical Engineering
University of Virginia
Charlottesville, VA 22901

Abstract

There has been a recent resurgence of interest in spectroscopy in the THz. The development of "short-pulse" THz sources, and the measurements made with these sources, have pointed to a number of possible applications for THz imaging and spectroscopy in biology, medicine, and semiconductor device packaging characterization. While the "short-pulse" sources offer wide-range, low resolution, THz coverage, they have a number of drawbacks for measurement applications. The work described here represents an alternative that avoids many of these drawbacks.

The work outlined in this paper marries the recent developments in high-reliability, compact THz lasers,[1, 2] with recent advances in Schottky-based sideband generators,[3, 4] to yield a reliable, potentially milliwatt-level, tunable THz source. While this work has been focussed on spectroscopy applications, the results can also be applied to provide tunable THz local oscillators.

Preliminary results & modeling for the tuning range and fixed-wavelength operating range will be presented.

This work is supported by NIST/Gaithersburg under contract number 50-DKNB-0-90072, and the US Army National Ground Intelligence Center, DAHC-90-96-C-0010.

Introduction

The approach taken in the present work, to generate tunable THz, has been in use for a number of years.[5] In this method, a fixed frequency laser and a tunable millimeter-wave (MMW) source are both coupled into a high-frequency Schottky diode and the resulting sidebands are re-radiated out of said Schottky diode. Thus the resulting sideband radiation can be tuned by simply tuning the MMW source.

As there will typically be quite a large amount of non-sideband radiation, at the laser frequency, also present in the re-radiated beam, a method is often employed to "filter" the output – yielding only sideband radiation (often both upper and lower sidebands, though one will typically be noticeably weaker than the other).

Very recently, significant advances over the previous state-of-the-art output power achievable[8] from an SBG have been made.[4] These advances include use of newly available THz waveguides/embedding structures to improve the SBG-mixer-mode (we refer to as FM mode) conversion loss from 31 dB to 25 dB at 1.6 THz, and more significantly a new mode of operation for the SBG[4] where a conversion loss of 14 dB has been demonstrated at 1.6 THz. In this mode of operation, SBG-phase-modulation-mode (PM), the MMW radiation is used to directly modulate the THz impedance of the SBG element/block thus modulating its reflectivity. This avoids the loss associated with coupling THz currents through the Schottky diode whose parasitic parameters

"short-out" a large amount of the available THz energy.

In the present work the above advances in SBG technology are coupled with the recent advances in compact reliable THz laser sources.[1, 2]

The remainder of this paper will: describe each of the key elements/technologies of the system, present measured and calculated performance results for each element, and then present the design for the final system to be constructed for NIST.

Compact Laser Source

The compact laser source will be a DEOS SIFIR-50 FPL FSW. A photograph of this laser system (including its power supply and controller) is presented in Figure 1. The output power vs wavelength for this laser system (using a fixed hole output coupler) is presented in Figure 2, and the

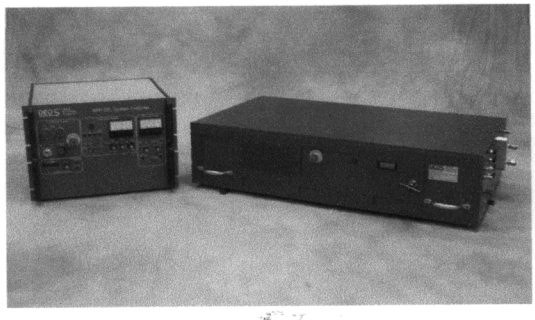

Figure 1: The SIFIR compact laser source.

spatial output mode obtained at 2.5 THz is shown in Figure 3. The short wavelength drop off in output power is due to the quartz output window used, which cuts-off at ~ 65 μm. The slow drop-off at longer wavelengths is due to the FIR waveguide cut-off, and the low power spike at 236 μm is due to the weak pump line for this laser line (9R6). The low frequency performance can be easily improved by using a larger waveguide diameter in the laser.

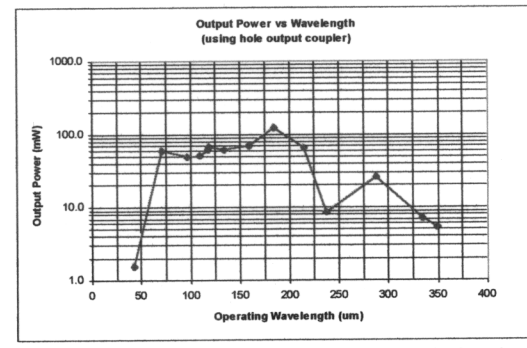

Figure 2: Output power vs wavelength for the laser source. (These data were obtained with a fixed hole output coupler. 2 - 3 times as much output power can in general be obtained at any given line by using a uniform output coupler.)

This laser system utilizes DEOS's permanently sealed-off pump laser technology, DEOS's compact high-vacuum-integrity high-stability THz laser technology, and an integrated design approach. The combination of these provides a reliable, easy to use THz laser.

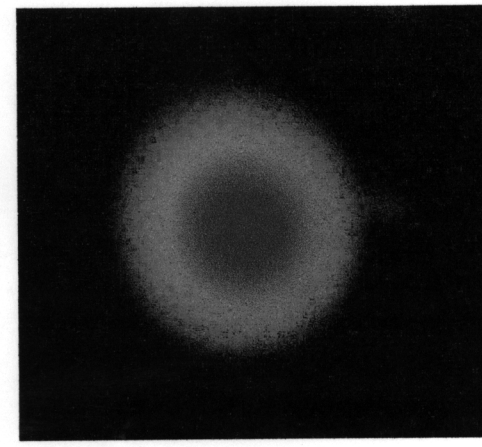

Figure 3: SIFIR spatial output mode at 118.83 μm.

Sideband Generator

The sideband generator used in this work is a University of Virginia 0.8 μm Schottky varactor diode mounted in a machined/electro-formed block. The THz radiation is coupled into and out of the waveguide within the block via a diagonal

feedhorn and the MMW energy is coupled into the block via a standard connector. A photograph of the initial version of this SBG block is presented in Figure 4. The backshort is mechanically-tuned for optimal video response when changing laser lines.

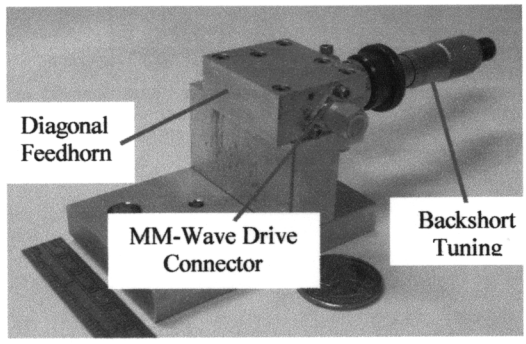

Figure 4: Photograph of the SBG mixer block.

Drawings of the inside of the block and of the planar whisker are presented in

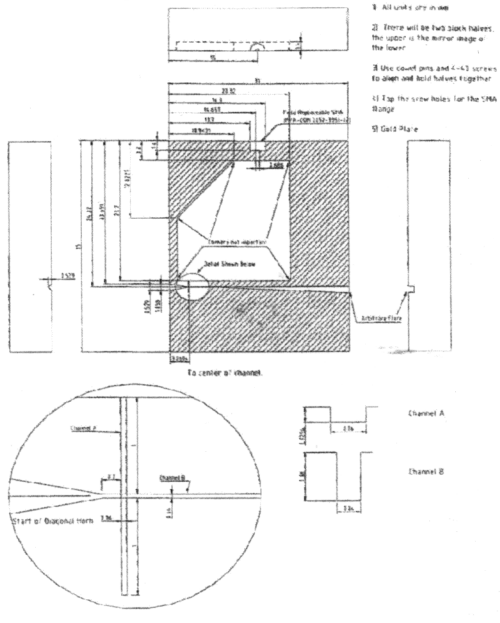

Figure 5: Drawing of the SBG mixer block.

Figure 5, and Figure 6, respectively. The planar whisker type used here is modeled after a technique developed for a 250 GHz tripler.[6]

As will be discussed later, this block was originally designed for operation at low (<18 GHz) offsets. During the present work minor changes were made to extend the block's operating range up to ~50 GHz, and simulations of the next generation design indicate operation up to 110 GHz. This represents a potential tuning range of 220 GHz around each laser line for 1st-order SBG operation.

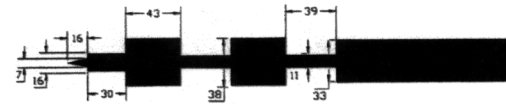

Figure 6: Drawing of the SBG contact/THz-coupling planar whisker. All dimensions are in μm.

MMW Coupling to the SBG

To efficiently generate sideband power, it is necessary that both the THz and the millimeter-wave (MMW) energy be coupled to the SBG diode. To test and optimize this behavior a series of experiments and simulations were conducted. The initial tests were performed on an existing, far-from-optimal, SBG block, and the later measurements were made on the same block after minimal modifications were executed to improve its MMW performance. Following these measurements a series of simulations, and commensurate design changes, were performed so that future SBG blocks could be expected to operate at sideband offsets up to 110 GHz, with the MMW energy coupled into the SBG block via an Agilent 1-mm connector.

- Initial MMW Testing

The SBG block used for this research was a prototype and was not designed for use at high microwave frequencies. A microstrip line on a Duroid substrate 40 mils thick was used to couple the MMW power to the diode, and a standard SMA connector (operating frequency range from DC to 18 GHz) was

used to connect to the block. In spite of this, initial tests were performed on the microwave coupling to the block, as shown in Figure 7. The curves in Figure 7 show the SBG block microwave reflection coefficient as the bias (and thus the diode impedance) is changed.

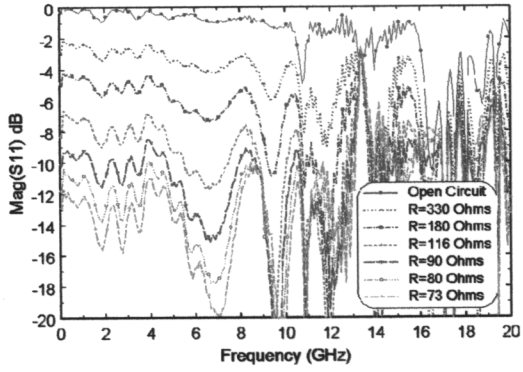

Figure 7: SBG block S_{11} measurements at a variety of diode bias points (bias currents).

When the diode is zero-biased the diode acts as an open circuit, and the amount S_{11} drops below 0 dB represents the microstrip line loss in the block. The line losses are small up to about 10 GHz, at which point resonances in the reflection coefficient begin to appear. Above about 15 GHz the microwave coupling degrades rapidly. The microwave coupling problems for this block are caused by resonances in the electrically-large microwave cavity and by discontinuities and air-gaps in the microstrip line. In order to solve these problems, the MMW circuit needed to be redesigned.

- SBG MMW Circuit Modification

In order to extend the MMW bandwidth for this project it was decided to modify the block again to address some of the MMW coupling issues. To do this, the SMA connector was replaced by a V-connector (operating frequency range from DC to 60 GHz). Also, the 40 mil Duroid substrate (dielectric constant 10.2) was replaced by a much shorter 3 mil thick quartz substrate (dielectric constant 3.8). The modification is pictured in Figure 8. While this modification was expected to solve some of the problems seen previously, the MMW cavity was still much larger

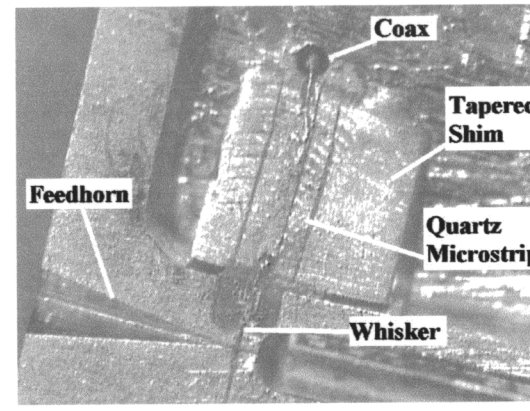

Figure 8: Internal view of the modified SBG block.

than desired for high frequency operation, a point that will be discussed more fully in the MMW simulations section.

- Improved-Block MMW Testing

MMW testing was performed on the modified SBG block, the results of which are shown in Figure 9. The upper curve (for a zero-biased diode) shows that the SBG

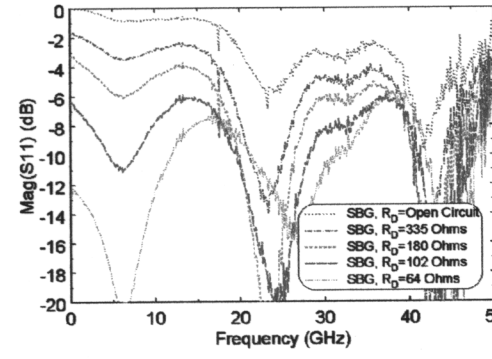

Figure 9: S_{11} measurements of the improved SBG block.

block loss is relatively flat up to 50 GHz (the upper limit of the network analyzer configuration used), although there are soft

resonances at 25 and 40 GHz. A comparison of this performance with the performance before the MMW circuit modification (Figure 7) reveals the dramatic decrease of line loss at high frequencies.

In order efficiently generate sidebands from the laser the MMW signal applied to the SBG must be able to modulate the diode bias, thus allowing phase modulation of the THz to occur. Since the change in capacitance of the diode with changing bias point causes the change in reflected phase, a figure-of-merit that allows us to gauge the ability of the MMW to modulate the diode is the MMW responsivity of the SBG. This is defined as the ratio of diode video response to the applied microwave power. The video response is determined by measuring the change of the diode bias voltage when microwave power is applied with the diode bias current fixed at a forward current of 0.6 mA. This bias point was found suitable for sideband generation during previous experiments.[4] Figure 10 shows the measured responsivity of the SBG block for

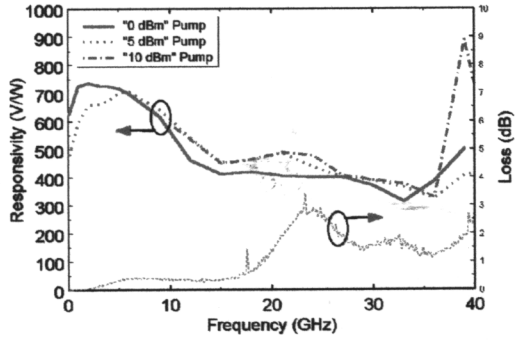

Figure 10: Measured MMW responsivity of the SBG.

several different MMW power levels. The MMW power was found to effectively modulate the diode bias all the way up to 50 GHz. The responsivity is (to within measurement error) constant as the MMW power changes, which is expected since the MMW pump power is still quite low. The scatter in the data at high frequencies is due to a rapid decrease in available MMW power from the network analyzer at high frequencies and also to the video response measurement accuracy of ±½ mV. Above 40 GHz the measured video response was on the order of the measurement accuracy.

- 110 GHz MMW Simulations

In order to determine the proper configuration for future SBGs and also to examine the limitations of the MMW coupling bandwidth, MMW coupling simulations were performed using Ansoft's HFSS, a finite-element analysis package. The key to achieving MMW coupling to the SBG diode is to avoid line discontinuities and cavity resonances. Figure 11 shows transmission plots for several MMW circuit

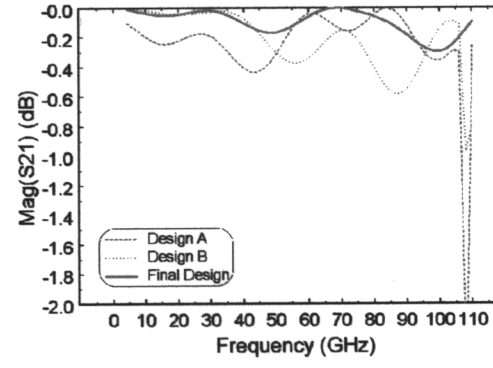

Figure 11: S_{21} simulation results for the future-design SBG block.

configurations that were simulated. The main difference between the various curves is the size of the cavity. By reducing the cavity size sufficiently the higher-order modes at 110 GHz can be cutoff, and the simulations indicate that the coupling of microwave power to the diode is possible up to 110 GHz. The final design uses 5 mil quartz and a cavity configuration that can be easily machined using standard milling techniques. By using this cavity design along with an Agilent 1-mm coaxial connector (operating frequency range from DC to 110 GHz) the

microwave operating range of the SBG can be extended all the way to 110 GHz.

THz Coupling to the SBG

In order to understand the THz coupling to the SBG diode, a series of video

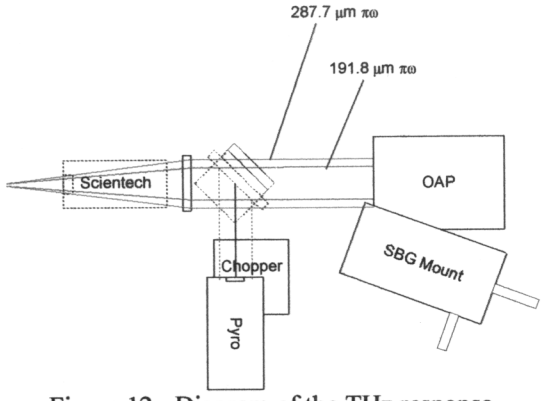

Figure 12: Diagram of the THz response experimental set-up.

responsivity measurements vs THz laser frequency were performed.

A diagram of the optical set-up is presented in Figure 12, and a photograph of the layout is shown in Figure 13. At each

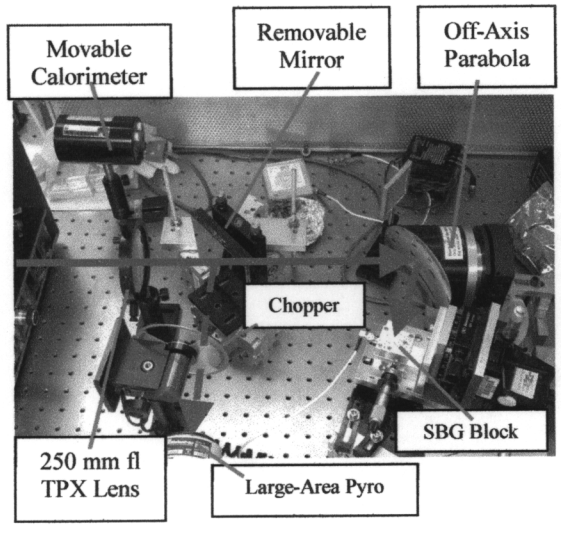

Figure 13: Photograph of the THz response experimental set-up.

test wavelength a measure of the output power from the laser was made and then an attenuator was added to keep the THz power at the diode in the 3-10 mW range. The laser output powers were measured with a Scientech calorimeter and then calibration corrected.[7]

The results of the THz measurements are presented in Figure 14. The "Normalized Response" data were normalized at 1.6 THz, and the "Re-Normalized Response" data are the Normalized data with a $1/\nu^2$ dependence factor applied to remove the natural response characteristic response of the diode (to illustrate the block's THz performance).

The low frequency cut-off is expected due to the waveguide dimensions but the slowness of the high-frequency

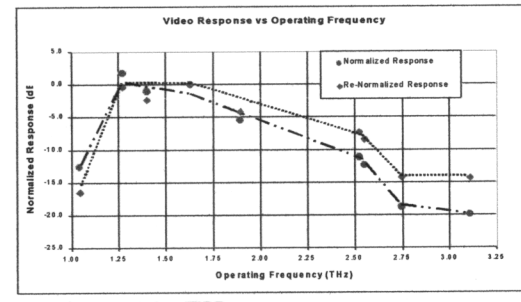

Figure 14: THz response measurement results. The lines are only intended to be an aid to the reader and do not represent a "best-fit" of any kind.

response is surprising. The gradual high-frequency roll-off, combined with improved SBG conversion efficiency, suggests that a large portion of the THz region could be covered, with multi-μW output, with only 1 or 2 SBG blocks. This makes the waveguide block approach much more attractive than previously thought.

In the past SBG's were typically corner-cube mounted. This provided wide THz bandwidth through tuning of the corner-cube and antenna but did not provide the flexibility in embedding impedance offered by the waveguide mounting. The above THz measurements, coupled with simulation results to be presented later, indicate that the

waveguide approach is indeed feasible and in fact may be preferable.

Quasi-Optical Diplexer

To separate the drive laser from the sideband output some type of diplexing device will be required. A number of alternatives for this function were considered including: a series of etalon diplexers,[8] a tunable etalon diplexer, a Mach-Zender diplexer,[9] and a Martin-Puplett[10] diplexer.

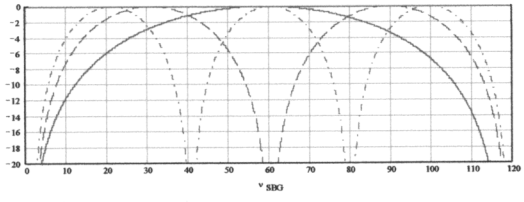

Figure 15: Diplexer SBG frequency coupling efficiency plot. The vertical axis is the SBG-to-output port transmission in dB, and the horizontal axis is the SBG offset frequency in GHz.

The Martin-Puplett topology was selected for a number of reasons including: capability of accommodating either laser polarization through simple adjustment of the first grid and the diplexer spacing, performance of available grids throughout the THz, availablility of components, and cost.

The theoretical performance vs sideband offset frequency is presented in Figure 15. The three plots shown there are for different settings of the diplexer spacing, and illustrate the capability of very wide band performance and end-of-band operation via user tuning of the diplexer spacing.

System Design & Performance Projections

The system design will combine the laser, diplexer, and SBG to form a reliable, easy to use, tunable THz source.

A drawing of the system is shown in Figure 16, and

Figure 17. The SBG and diplexer are integrated directly on the top of the laser housing. The laser housing is ~ 100 cm x 50 cm x 25 cm. The diplexer and 5-axis mount for the SBG are sufficiently small that the remainder of the laser top can be used for additional experimental space.

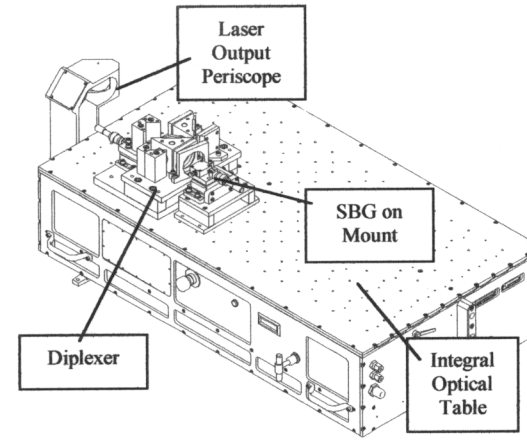

Figure 16: Design drawing of the system.

It is desirable that the optical system for coupling the laser to the SBG be constant vs operating wavelength. We have devised such an optical system. The beam propagation for the optical system is

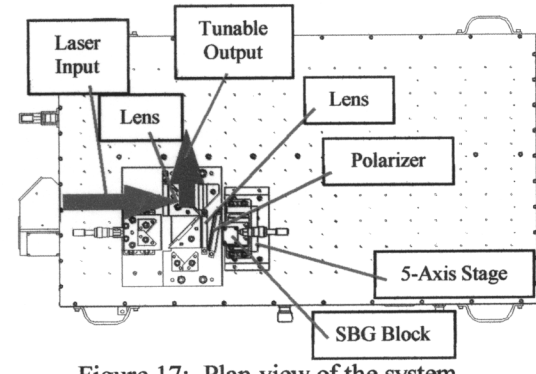

Figure 17: Plan view of the system.

presented in Figure 18. While in that plot it appears that the beam size at the SBG is independent of wavelength, in fact there is some wavelength dependence. The wavelength dependence of the waist at the SBG input is presented in Figure 19. This

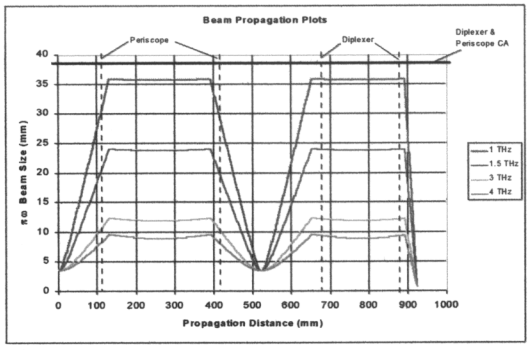

Figure 18: Beam propagation plots.

dependence is due to some slight non-symmetry in the design and corrections due to operating with low f#.[11]

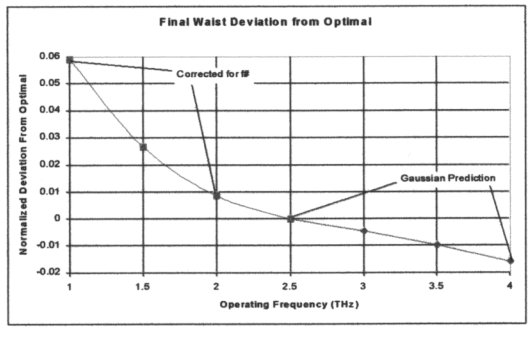

Figure 19: SBG-Coupling beam size predictions vs operating frequency. Note: the low frequency calculations include a correction for small f#[11] and the higher frequency predictions are paraxial Gaussian propagation results.

- Sideband Conversion Efficiency Modeling

It is desirable to make some estimates of output power vs frequency achievable with the envisioned system. To that end, a model of the SBG efficiency vs operating frequency was developed.

This model is broken into two distinct operating regimes: PM-mode operation, and FM-mode operation. It is expected that the achievable PM-mode range will be somewhat limited and that where this mode of operation rolls-off, the more conventional, FM-mode will dominate.

To estimate the PM-mode performance vs frequency the SBG was modeled using the post-in-a-waveguide analysis of Eisenhart.[Error! Bookmark not defined.] The equivalent circuit for the SBG is shown in Figure 20. Note that this equivalent circuit does not model the effect of finite bandwidth of the low-pass filter fabricated on the planar whisker, and assumes the guide is shorted at the edge of the waveguide.

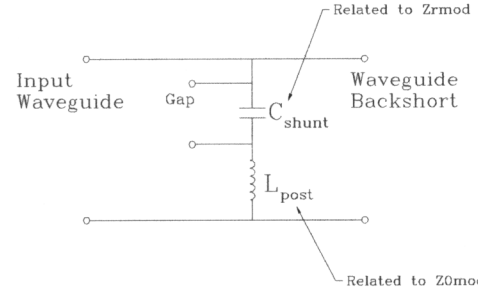

Figure 20: Circuit model of the SBG/block.

Using this simplified model of the SBG and the predicted capacitance variation for the varactor used (i.e. from 0.4 fF to 2.5 fF) the amount of phase modulation achievable at a given THz frequency (where the backshort position is optimized for each THz frequency) is calculated. (For 1st-order SBG operation no more than 180 degrees of PM is desired). These results were then normalized to the 14 dB measured result at 1.6 THz to yield the dashed maroon curve found in Figure 22.

Since the output power of the laser is known, the SBG THz coupling efficiency for the block was measured, and the PM conversion efficiency has been estimated, it is now possible to estimate the output power one would expect when operating the designed system in PM mode. However it is expected that the conversion efficiency will saturate with increasing laser power. At this time there is no existing data on this effect, and so as an approximation, it was assumed that the efficiency would be constant up to

20 mW of input power and roll-of by 6 dB by the time the laser power

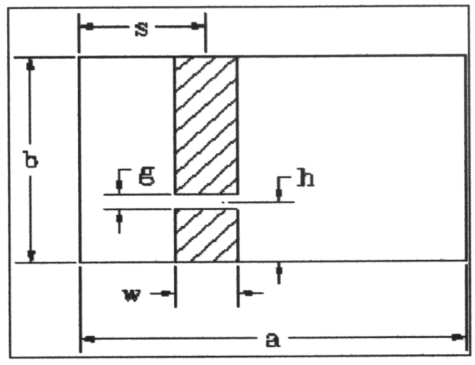

Figure 21: Waveguide/post physical model. a and b are the dimensions of the waveguide (160 x 40 μm); s is the distance from the waveguide wall to the diode post (80 μm); g is the gap between the waveguide post and the end of the wide section of the whisker (10 μm); and h is the height of the diode mounting post – ½ g (0.4 μm), and w is the width of the post and whisker end section just prior to the narrowed contact area (taken to be 40 μm in this model for improved performance at higher frequencies).

is increased to 100 mW. When all of these factors are used the resulting prediction is that shown in the solid blue curve of Figure 22.

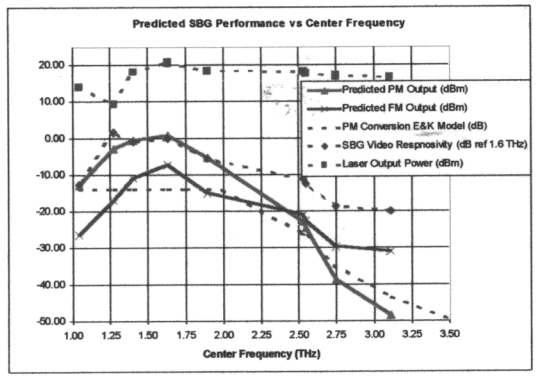

Figure 22: Measured & Predicted Laser/SBG system performance vs center frequency. The laser output power vs operating frequency and normalized SBG responsivity are included for illustration.

It is expected that at the point where the PM-mode of operation falls below the estimated FM-mode of operation, the FM-mode output power will dominate. To estimate this, the THz responsivity and a conservative 28 dB conversion loss at 1.6 THz (measured result in the waveguide SBG was approximately 25 dB but this result was for a mixer diode) were multiplied to yield the solid red curve of Figure 22.

These data are quite encouraging. They suggest that even without using multiple SBG blocks, each optimized for a given band, it should be possible to obtain multi-μW tunable THz output over a very broad range and mW tunable output over a more restricted range.

Conclusions

In this work recent developments in SBG and laser technology have been brought together to yield a design with potentially impressive output power over the entire THz regime.

The experimental data, simulations, and resulting design, should yield an easily used, tunable THz source with >10's of μW of output power over a very broad range, and even possibly mW output power over a more narrow range. The mW levels should also be realizable throughout much of the THz by using optimized SBG blocks at the desired THz center frequencies.

While the present design was evaluated for 1st-order SBG only, 2nd-order operation could also be used to extend its MMW tuning range at any given laser line.

This system should prove to be an excellent source for spectroscopy and LO applications.

Acknowledgements

The authors would like to acknowledge the contributions of D. Porterfield to this project.

References & End Notes

[1] E. R. Mueller, W. E. Robotham, Jr., R. P. Meisner, R. A. Hart, J. Kennedy, and L. A. Newman, "2.5 THz Laser Local Oscillator for the EOS Chem 1 Satellite," Proc. 9th Int. Symp. Space Terahertz Technol., p. 563 (1998)

[2] E. R. Mueller, J. Fontanella, & R. W. Henschke, "Stabilized, Integrated, Far-Infrared Laser System for NASA/Goddard Space Flight Center," Proc. 10th Int. Symp. Space Terahertz Technol., (2000)

[3] D. S. Kurtz, J. L. Hesler, T. W. Crowe, and R. M. Weikle, II, "Millimeter-Wave Sideband Generation Using Varactor Phase Modulators," IEEE Mircowave & Guided Wave Lett., **10**(6), 245 (2000)

[4] David S. Kurtz, Sideband Generation for Submillimeter Wave Applications, Doctoral Dissertation, University of Virginia, Charlottesville, May 2000

[5] H. R. Fetterman, P. E. Tannenwald, B. J. Clifton, W. D. Fitzgerald, and N. R. Erickson, "Far-ir heterodyne radiometris measurements with quasioptical Schottky diode mixers," Appl. Phys. Lett., **33**, 151 (1978); D. D. Bicanic, B. F. J. Zuidberg, and A. Dymanus, "Generation of continuously tunable laser sidebands in the submillimeter region," Appl. Phys. Lett., **32**(6), 367 (1978)

[6] J. Thornton, CM. Mann, and P. de Maagt, "Optimization of a 250-GHz tripler using novel fabrication and design techniques," IEEE MTT, **46**(8) 1055 (1998)

[7] F. B. Foote, D. T. Hodges, and H. B. Dyson, "Calibration of Power and Energy Meters for the Far Infrared/Near Millimeter Wave Spectral Region," Int. J. IR & MMW, **2**(4), 773 (1981)

[8] E. R. Mueller, and J. Waldman, "Power and Spatial Mode Measurements of Sideband Generated, Spatially Filtered, Submillimeter Radiation," IEEE MTT, **42**(10) 1891 (1994)

[9] N. R. Erickson, "A Directional Filter Diplexer Using Optical Techniques for Millimeter to Submillimeter Wavelengths," IEEE MTT, **25**, 865 (1977)

[10] D. H. Martin, and E. Puplett, "Polarised Interferometris Spectrometry for the Millimetre and Submillimetre Spectrum," Infrared Phys., **10**, 105 (1969)

[11] G. P. Agrawal, and D. N. Pattanyak, "Gaussian beam propagation beyond the paraxial approximation," J. Opt. Soc. Am., **69**(4), 575 (1979)

Laser Micromachining Fabrication of THz Components

C. Drouët d'Aubigny, C. Walker, B. Jones, C. Groppi
Steward Observatory, Univ. of Arizona.

J. Papapolymerou, C. Tavernier
Dept. of Electrical and Computer Engineering,
Univ. of Arizona.

ABSTRACT

Laser micromachining techniques can be used to fabricate high-quality waveguide structures and quasi-optical components to micrometer accuracies. Successful GHz designs can be directly scaled to THz frequencies. We expect this promising technology to allow the construction of the first fully integrated THz heterodyne imaging arrays. At the University of Arizona, construction of the first laser micromachining system designed for THz waveguide components fabrication has been completed. Once tested and characterized our system will be used to construct prototype THz 1x4 focal plane mixer arrays, magic tees, AR coated silicon lenses, LO source phase gratings, filters and more. Our system can micro-machine structures down to a few microns accuracy and up to 6 inches across in a short time. This paper discusses the design and performance of our micromachining system, and illustrates the type, range and performance of components this exciting new technology will make accessible to the THz community.

INTRODUCTION

Laser micro chemical etching works by focusing several watts of laser power on a silicon wafer in a low-pressure chlorine ambient (200 Torr). The deposited energy vaporizes a cylindrical region 6 μm wide and 1 μm deep. The vaporized silicon atoms react immediately with chlorine molecules to form silicon tetrachloride, which is gaseous at the pressure used and prevents re-deposition on the substrate (see Figure 1). Melted silicon not captured by chlorine re-deposits epitaxially as soon as the beam is moved to a different position.

Laser micro machining possesses a significant edge over conventional techniques. It does not require the use of masks, and is not confined to any given crystal plane. Since it is a non-contact process, laser micro machining eliminates tool wear and vibration. The etch depth is only limited by the motion range (5mm) of the vertical stages. The laser micromachining process is entirely computer controlled and permits proven complex waveguide designs and quasi-optical components to be scaled to THz frequencies. The system also allows fast prototyping: the magic tee structure presented in this paper took

less than 5 minutes to etch. Larger complex structures such as corrugated feedhorns may take up to 1 hour of actual machining time. Generally, the complexity of the structure has little impact, if any, on the process time. In practice, only the size and volume of the region to be etched have a meaningful impact, making this process ideally suited for THz applications.

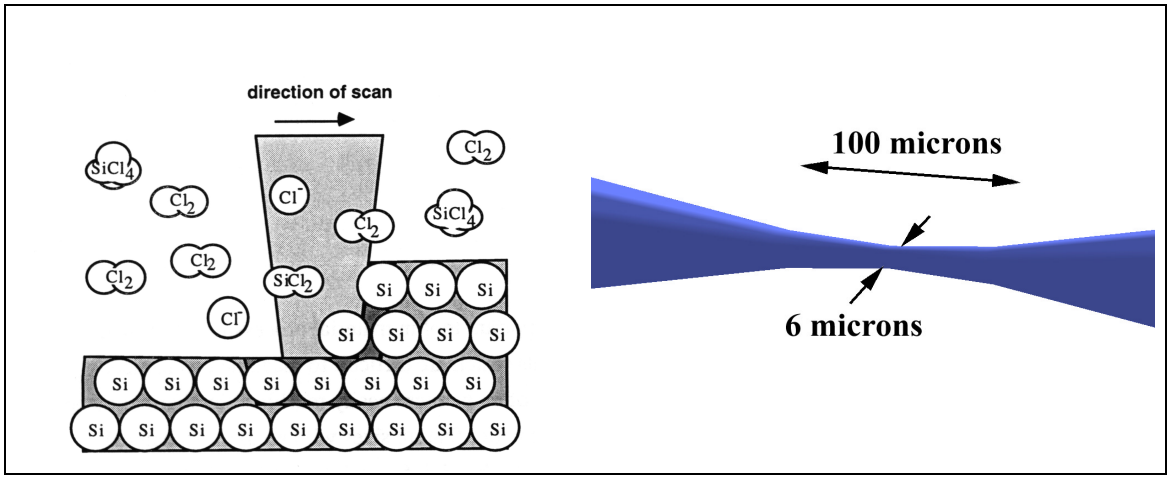

Figure 1-a (left), 1-b (right): a) The focused spot of a laser is scanned across a silicon wafer. Silicon atoms are vaporized, and immediately react with the ambient chlorine molecules preventing re-deposition. Using high numerical aperture optics confines the etch to a region only a few micrometers wide. The trade-off of high NA is a tapering of the beam that can be significant for some applications, eg. vertical walls (Ted Bloomstein, MIT, Ph-D Thesis). b) The Gaussian beam behavior of the laser beam provides a 100 μm deep region where vertical walls can be machined without significant loss in resolution.

The system we have built at Steward Observatory (Fig. 3) is equipped with a 30W, water-cooled, Argon Ion, laser used at 488 and 514nm. While only 4W is actually required on the sample, system losses, and the need to stop the laser to a small aperture to obtain a TEM_{00} Gaussian beam, increase the laser power requirements. The beam waist diameter when focused on the silicon is ~6μm. The F/# of the system is 5, causing a beam taper angle of 6° and an aspect ratio of 10:1. However, in the 100 μm focal region of the laser, vertical walls with an extremely high aspect ratio can be achieved. The currently available scanning range is ~ 5 x 5 mm. Through the use of stitching, structures up to 150 mm in diameter can be machined.

In our design, the laser beam is expanded to 16mm. The beam is then deflected by a commercial X-Y galvo-mirror scanner onto an achromatic scanning lens. The focused beam is then introduced through a fused silica window into a stainless steel reaction chamber containing the silicon substrate (see Fig.2). The wafer surface temperature is biased to roughly 100°C using a parabolic IR illumination source shining through a second window on the backside of the reaction chamber (see Fig 2). The process is monitored through the focusing optics using a CCD with a plate scale of 7 μm per pixel. The scanning system is driven directly from computer-generated patterns, which can be

constructed using Autodesk's AutoCAD. The ensemble is mounted on computer controlled X-Y-Z precision motion stages (see Fig. 3) allowing the stitching of large structures.

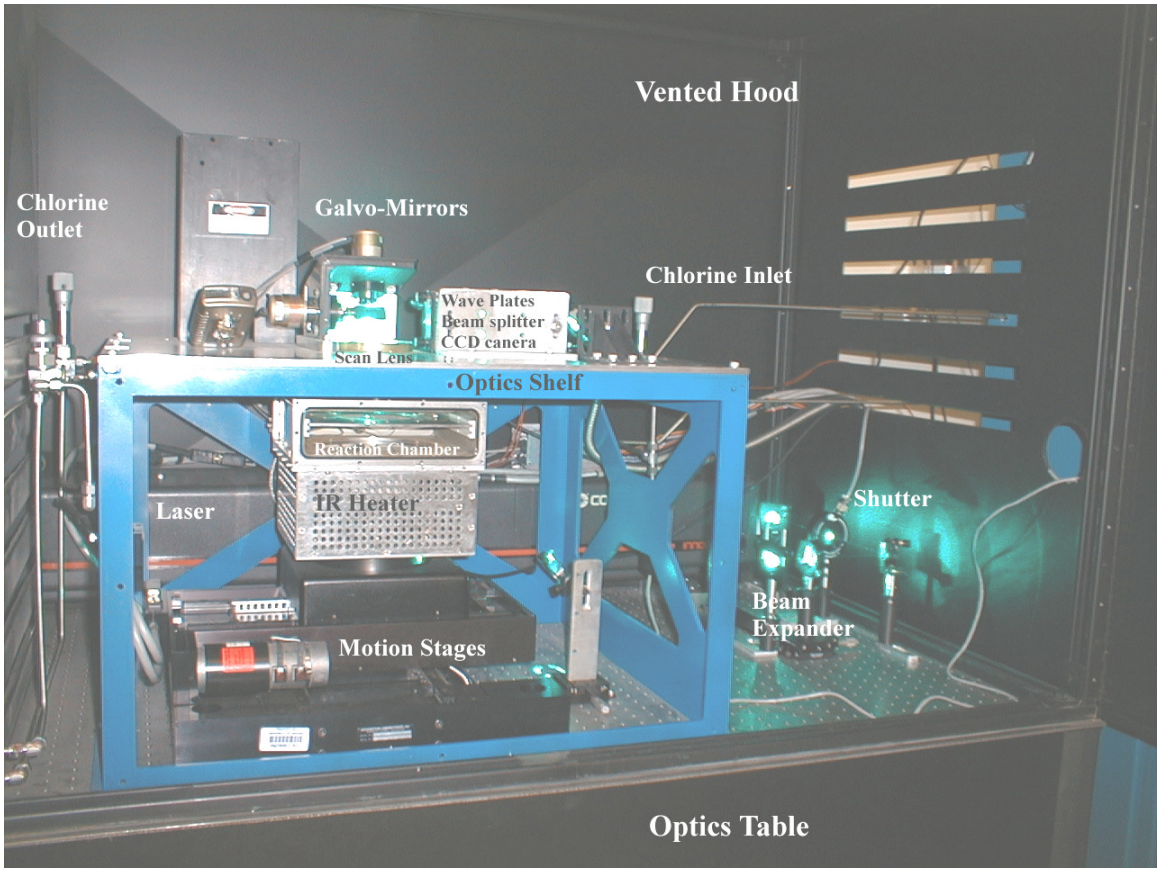

Figure 2: The laser micro machining optical hood. The Argon-Ion laser is visible in the back. On the right side of the image, the beam can be seen reflecting off relay mirrors, passing through the electronic shutter and beam expander. The beam-splitter, wave-plates and CCD camera labeled on the image are not visible from this angle. The open reaction chamber loaded with a silicon wafer can be seen. The entire assembly is mounted on precision motion stages.

Before operation the cell is evacuated, then filled with 99.9 % pure chlorine gas to 100 Torr. After ~2 hours of machining the remaining chlorine gas and silicon chlorides are captured in a scrubbing bubbler. Figure 4 shows the system in our laboratory. The chlorine and nitrogen gas cylinders are stored in the gas cabinet on the right. The central hood houses the laser, reaction chamber, and optics. The vacuum pump and chlorine scrubbers are contained in the small gas cabinet on the left.

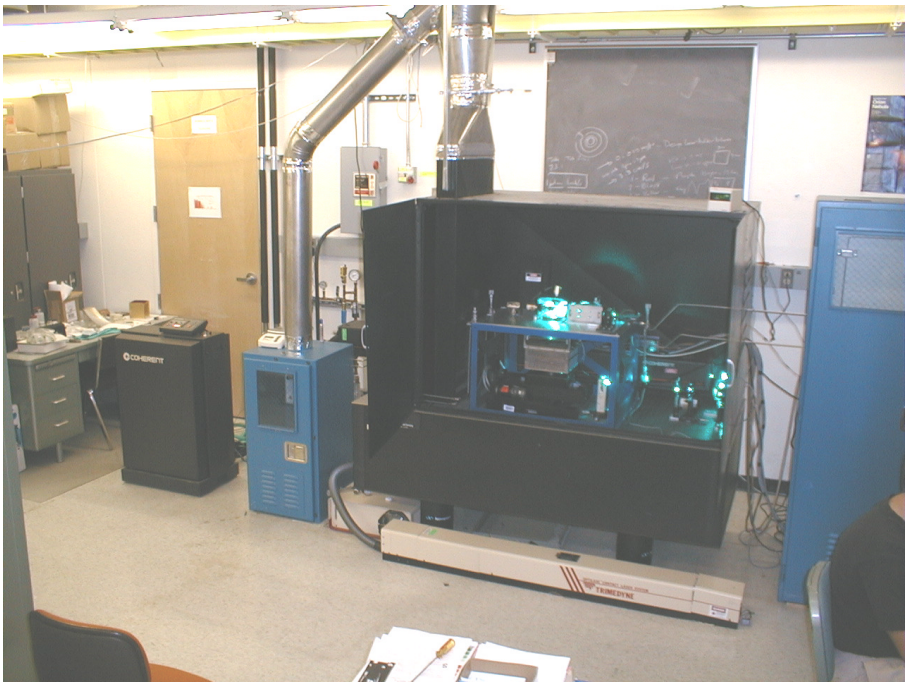

Figure 3: Ensemble view of the Steward Observatory laser micromachining system Chlorine gas cabinets are visible to the right and left of the black laser machining hood in the center.

The operating parameters used to produce the structure presented in this paper were: substrate temperature of ~120°C, chlorine pressure 200 Torr, laser power on the silicon 4W and a scanning speed of 3 cm/s. Using these parameters 1μm deep layers were etched at a rate of 0.27mm^3/hr, consistent with previous MIT Lincoln Laboratories findings (Bloomstein, 1996). From measurements obtained in our previous collaboration with Lincoln Laboratories, the expected surface finish out of the laser micro machining system is ~0.1μm rms. This value can be improved to better than 25nm rms through the use of isotropic etches. With those numbers, the expected losses at 2THz are only 20% more than that of an ideally polished waveguide surface.

IMPROVEMENTS AND FUTURE WORK

In the coming weeks we plan to work on developing a method for precisely mapping, in situ, the distortions (barrel/pincushion) that are caused by our scanning lens. Once a map is established, distortions will be compensated for during the etching process. An essentially distortion free system is essential in order to properly stitch etched fields. A CCD imager looking down into the chamber will be used to supplement the motion stages in properly registering the various components. In the coming months we plan to automate our gas handling system. At present, pumping the reaction chamber down to vacuum, loading it with chlorine, and scrubbing the gas after the process is completed is a time consuming process.

We also plan to improve the opening and closing mechanism of the reaction chamber. and design a better, wider, scanning lens that will permit the production of structures up to 30mm in diameter without stitching. Finally, we are interested in exploring etching parameter space to get higher removal rates and smaller etch depths.

APPLICATIONS OF LASER MICROMACHINED DEVICES

Laser micromachining permits the direct scaling of successful waveguide and quasi-optical components to THz frequencies. The process works best for structures that can be machined directly onto a 2-dimensional surface. For example, `split-block' waveguide components and anti-reflection (AR) grooves are well adapted for fabrication with this process. Here we discuss three specific examples of laser machined components, waveguide magic-Tee's, feedhorns, and AR coatings. These components are needed at THz frequencies to enable the construction of efficient receiver systems for space and airborne astronomy as well as space-based communication systems.

1. Magic-Tee

The magic tee is a four-port network in which an incident signal on any one port divides between two output ports with the remaining port being isolated. The magic tee has been used primarily at microwave frequencies in a number of applications, including coherent power combining and balanced mixers. Figure 4 is a schematic of a basic waveguide magic tee.

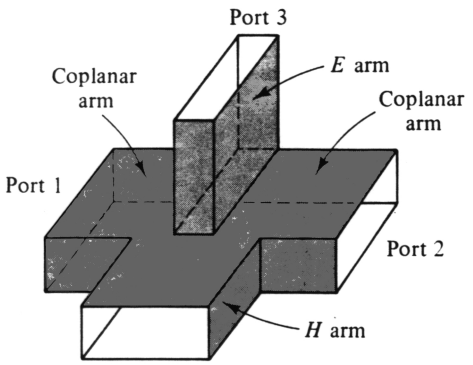

Figure 4: Schematic of magic tee structure (Rizzi, 1988).

If the E-arm (Port 3) is match terminated, then signals incident at Ports 1 and 2 will be isolated from each other and combine in phase at Port 4 (Rizzi 1988). This configuration of a magic tee could be used to coherently combine the local oscillator power from 2 or more independent sources or as the heart of a coherent beam combiner for space interferometry missions.

The match termination for this application can be achieved in silicon using the design shown in Figure 5-a. HFSS simulations show the termination works well across the waveguide pass-band (Fig 5-b).

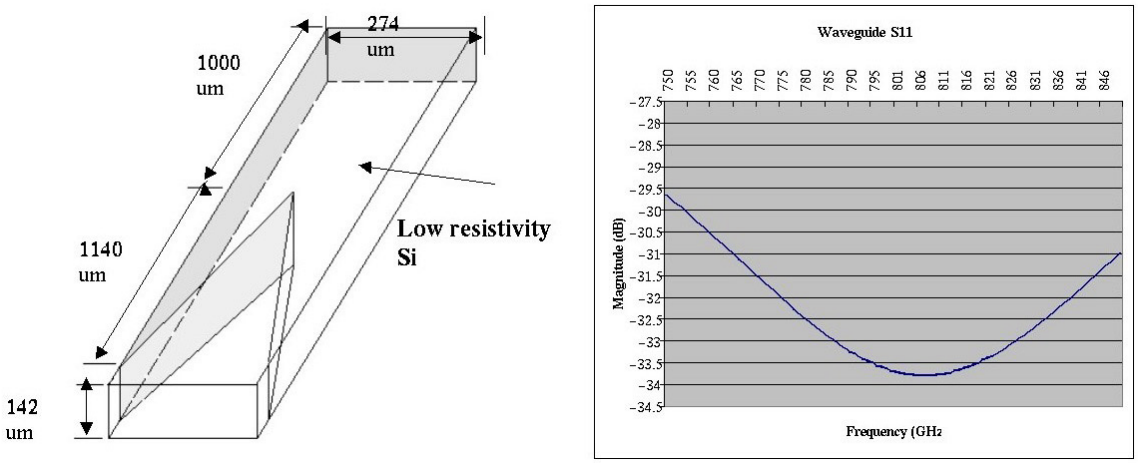

Figure 5-a (left) 5-b (right): Waveguide termination placed on the E arm. The simulated HP HFSS attenuation is better than 30dB over a 100 GHz band centered on 810 GHz.

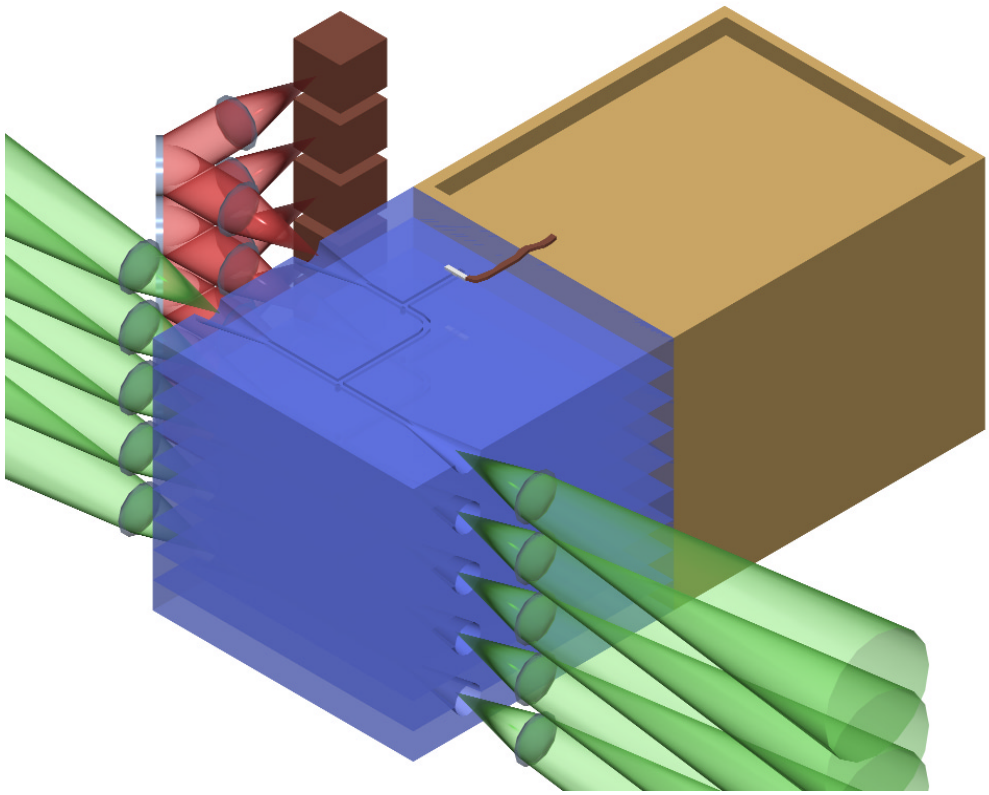

Figure 6: Conceptual 3D rendering of and interferometric array proposed for the Large Binocular Telescope (LBT). The split block uses laser micro machined feedhorns and magic tees to coherently combine the beams from two telescopes. A directional coupler is used to inject LO power.

Figure 6 is a conceptual design for an array receiver at 810 GHz that uses magic tees to coherently combine the power from the two 8.4 m apertures of the Large Binocular Telescope (Drouët d'Aubigny et al 2000). By using waveguide beam combining techniques, the bandwidth limitations imposed by using digital correlators is avoided.

Balanced mixers offer several advantages over single-ended mixers; suppression of local oscillator (LO) amplitude noise, spurious signals, and the potential of ~100 % LO power coupling (Maas 1993; Chattopadhyay et al. 2000). For this application, the input signal enters through the E-arm (Port 3), the LO through the H-arm (Port 4), and there are two mixing devices, one at Port 1 and the other at Port 2 (Collin 1966). The ability to efficiently inject the LO into the mixer is a huge advantage at THz frequencies since the available LO power is often quite limited (Tong and Blundell 1994).

As a proof-of-concept, we have used the laser micromachining system to fabricate a waveguide magic tee at ~1.2 THz. An SEM photograph of the structure is shown in Figure 7. The aspect ratio of the walls is quite high and the surface finish appears almost optical in quality. It should be noted that the structure shown in Figure 7 was our first attempt to make a magic tee and only took ~4 minutes to fabricate.

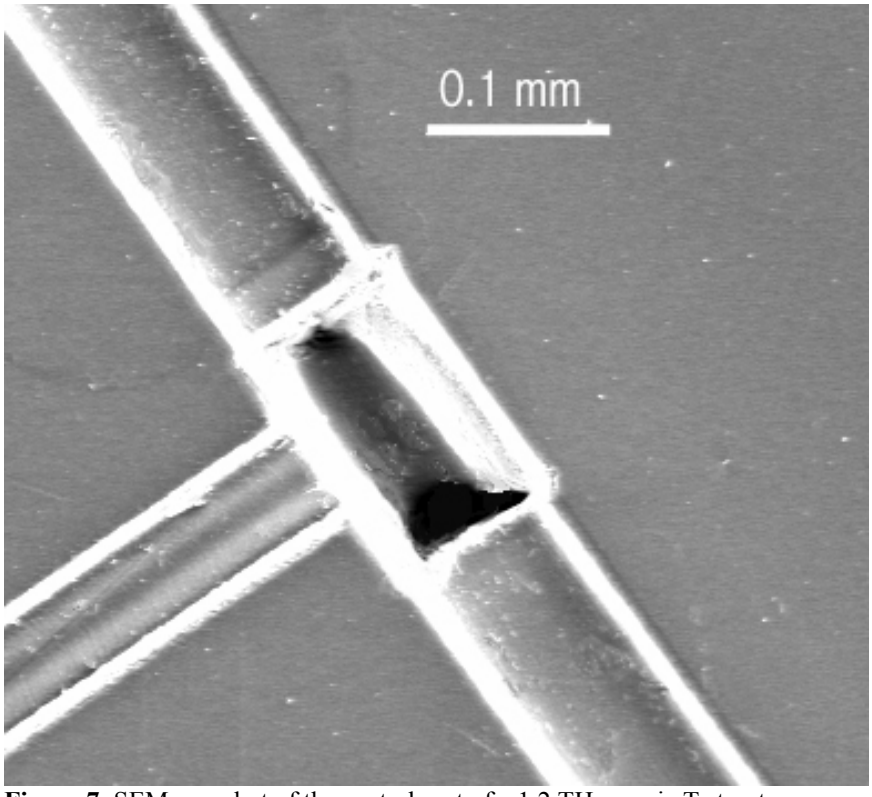

Figure 7: SEM snapshot of the central part of a 1.2 THz magic T structure.

2. Feedhorns

In the diffraction limit, Gaussian beam optics is often used in the design of telescopes and receiver systems. Waveguide feedhorns provide an extremely efficient means of launching Gaussian beams. Indeed, corrugated and dual-mode feedhorns are capable of coupling ~98% of their power into the fundamental Gaussian mode, making them the most efficient means of transferring power into and out of many quasi-optical systems. In comparison, dielectric lens planar antennas have a Gaussian beam coupling efficiency of at best ~89% (Goldsmith 1998).

.

Laser micromachining can be used to fabricate corrugated and dual-mode feedhorns well into the THz range. Test results of a 2 THz laser machined feedhorn are published in an earlier THz conference proceeding (Walker et al. 1997). An SEM photograph of an 850 GHz feedhorn made at Lincoln Labs using a similar system is shown in Figure 8. The throat of the feedhorn terminates in a section of circular waveguide followed by a circular-to-rectangular transition, which is stepped to quarter height waveguide. With laser micro machining this entire structure can be fabricated in one run. There is no need for tool changes or photolithographic masks. With this technology, the fabrication of efficient, large, format feedhorn arrays becomes tractable.

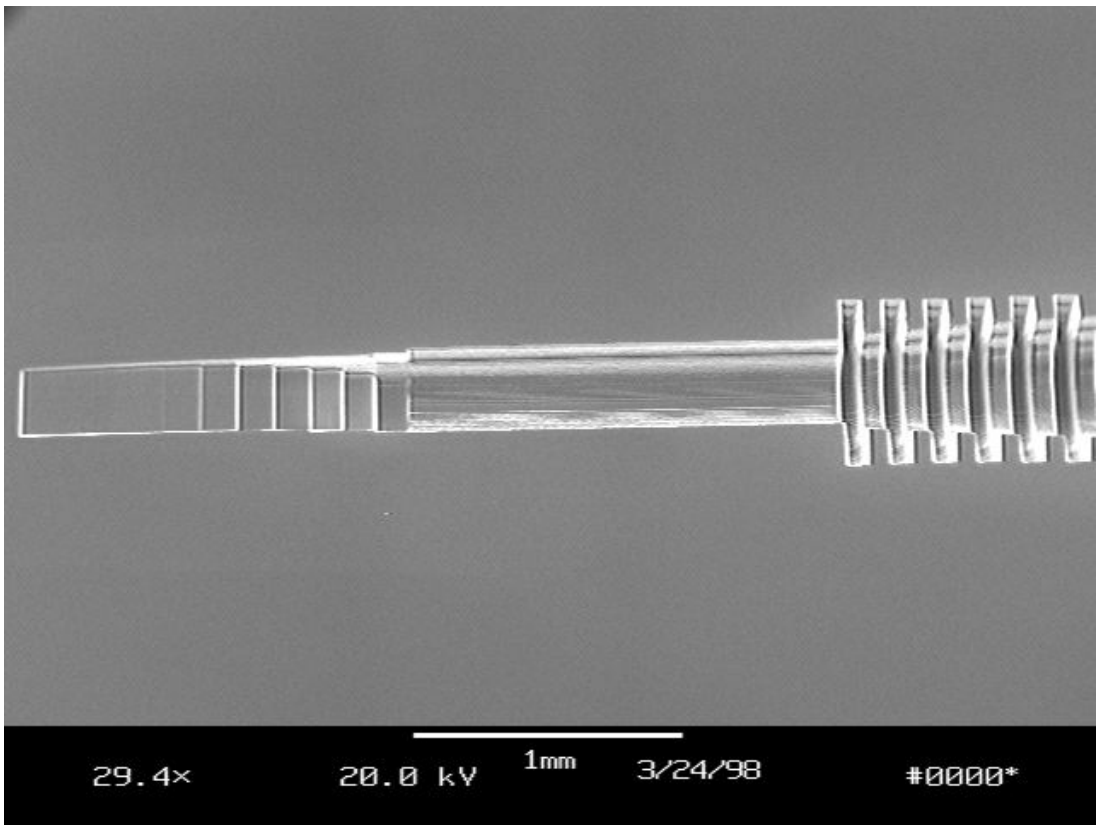

Figure 8: Laser micro machined corrugated circular feedhorn with stepped transition to rectangular waveguide fabricated at MIT Lincoln Laboratories.

Figure 9-a, below, is a conceptual drawing of a 10x10 array of laser machined, dual-mode feedhorns to be used in an 810 GHz prime focus camera for the LBT. The small (1.2 mm diameter) feedhorns are the only quasi-optical components needed. The geometry of a dual-mode feedhorn obviates the need of split-block construction. All 100 feedhorns can be machined in a single small (~1.5x1.5 cm) square of silicon. Metallization of the feedhorns will be performed using an e-beam evaporator. An HFSS simulation of the emergent beam pattern from one of the horns is shown in figure 6-b.

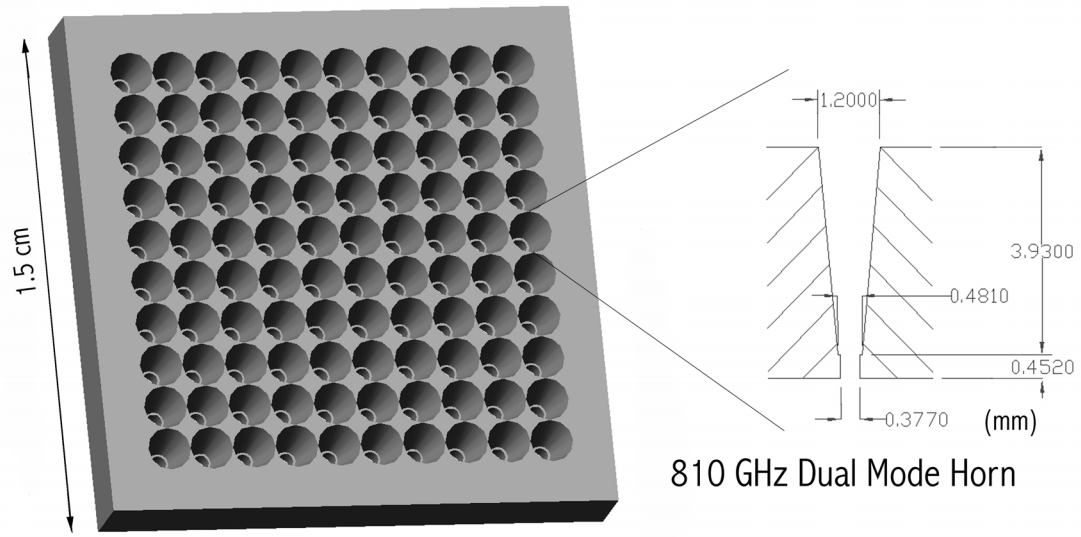

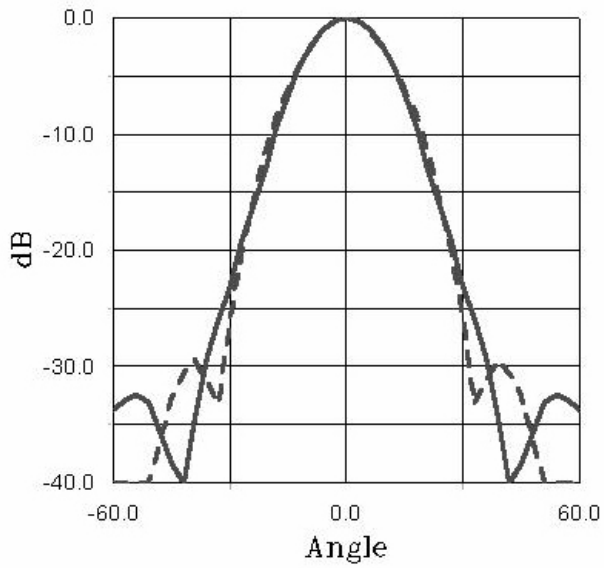

Figure 9-a (top), 9-b (bottom): 3D rendering of a 10x10 array of dual mode feedhorns for a prime focus camera to be used on the Large Binocular Telescope. a) Design of laser machined array. b) Predicted beam pattern from an individual horn made using HP HFSS: E-plane black line, H plane dashed line.

3. Anti-Reflection (AR) Coatings

Dielectric lenses are widely used in sub-millimeter-wave systems. They play a critical role in forming the beam of planar antennas, such as the double slot and dipole. In addition, quasi-optical systems utilizing dielectric lenses are often more compact than comparable systems designed using reflective optics. The main disadvantages of using lenses are reflective losses off their surfaces and absorption of power in the lens material itself. With the proper choice of dielectrics, such as silicon, the absorption losses can often be kept to only a few percent. However, the reflected power off the surfaces of even low index of refraction materials (e.g. Teflon) can be as high as 12%. Lenses made with higher dielectric materials have shorter focal lengths and greater mechanical strength. To overcome the increase in the fractional power reflected from the surfaces of such materials, they must be coated with one or more layers of a dielectric with an index of refraction intermediate between the lens material and free space (Goldsmith 1998). Alternatively, the surface of the lens itself can be machined to simulate the required matching layer (Morita and Cohn 1955). In practice, this is usually achieved by etching concentric, $\lambda/4$ grooves in the dielectric surface.

An example of a 1.5 THz AR grooved silicon window is shown in Figure 8-a. The bandwidth of the matching layer can be increased by etching grooves with a triangular cross-section several wavelengths deep. However, both the rectangular and triangular concentric grooves are polarization sensitive. This sensitivity can be avoided if an array of holes is used instead of concentric grooves to simulate the required dielectric layer. If the holes have a conical cross section and are several wavelengths deep, the surface can also be used over a wide frequency band (Lesurf 1990). A 3-D CAD representation of such a surface made in silicon for operation at 1.5 THz is shown in Figure 10-b.

Due to their small size scales, it has been impossible to use simulated dielectrics as AR coatings at THz frequencies. However, with laser micro machining it is straightforward to machine either concentric grooves or holes like those depicted in Figure 8 directly into silicon quasi-optical components, such as lenses and vacuum windows. We plan to utilize these structures in THz receiver systems we are constructing for AST/RO and SOFIA.

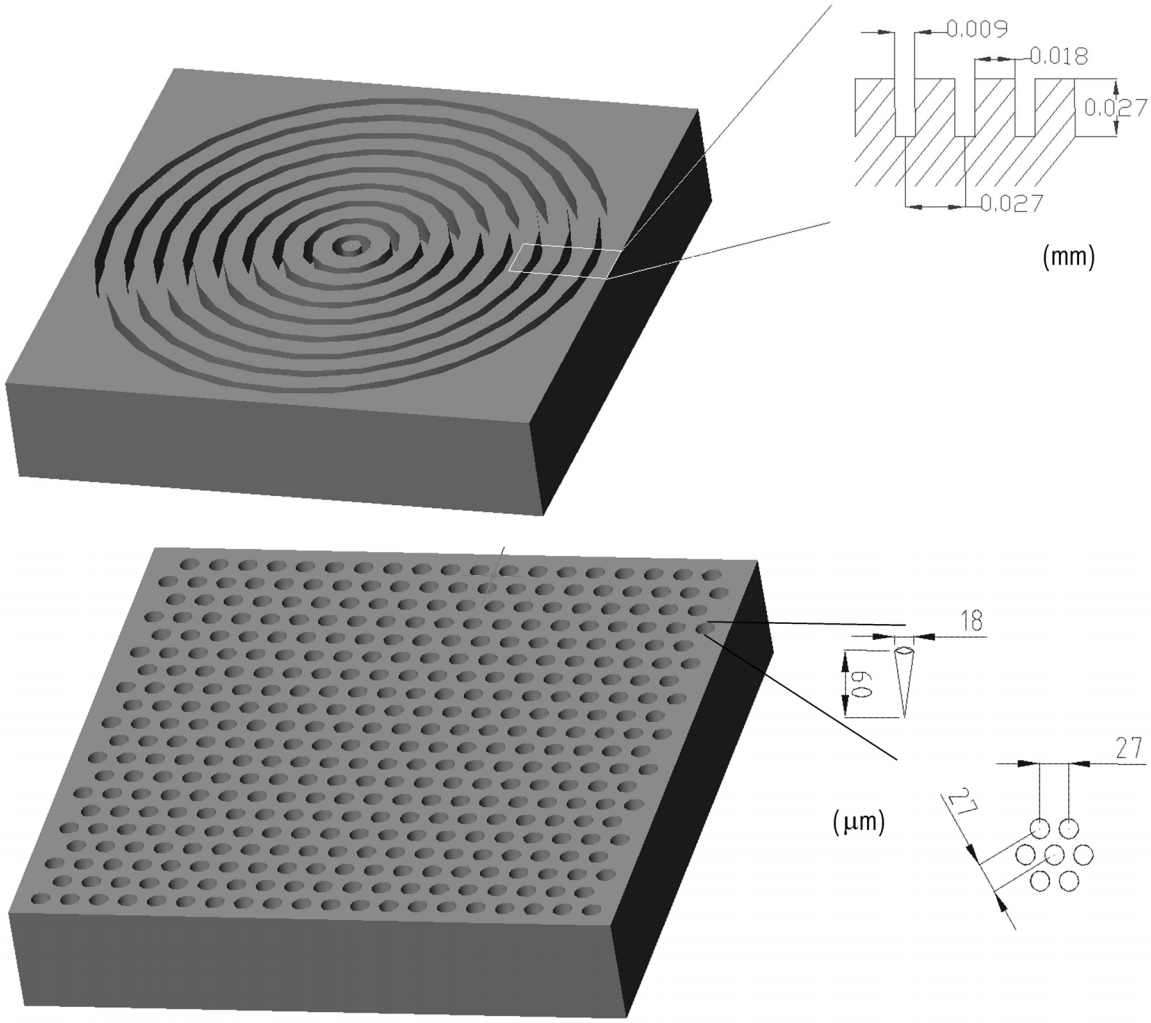

Figure 10: Conceptual 3D rendering of 1.5 THz AR matching layers in silicon. 10-a (top) Using concentric rectangular grooves. 10-b (bottom) Using conical holes.

SUMMARY

Laser micromachining provides a mean of scaling successful waveguide and quasi-optical components to THz frequencies with micron accuracy. A laser micromachining system optimized for THz applications is now in operation at Steward Observatory. We have fabricated a prototype magic tee structure at 1.2 THz and developed conceptual designs for laser machined feedhorn arrays, coherent beam combiner, and AR coatings. We plan to begin fabricating these structures in the near future. With this system, machining accuracy of 6 microns laterally and less than 1 micron vertical are possible.

AKNOWLEDGEMENTS

This work was supported in part by NSF grant ECS 9800260 and NASA grant NAG5 9100. The authors also thank Kevin Righter and Kenneth Domanik of The Lunar and Planetary Laboratory for both optical and SEM pictures of the magic Tee.

REFERENCES

Bloomstein, T., Ph-D Thesis, MIT, 1996,

Chattopadhyay, G., Rice, F., Miller, D., LeDuc, H., and Zimuidzinas, J., 2000, IEEE Microwave and Guides Wave Letters, in press.

Collin, R., 1966, in ``Foundations of Microwave Engineering", pub. McGraw Hill, p. 285.

Drouët d'Aubigny, C., Walker, C., Groppi, C., Hill, J., Bieging, J, and Popmpea, S., 2000, Proc. SPIE, 4015, p. 268.

Goldsmith, P., 1998, in ``Quasioptical Systems", publ. IEEE Press, p. 184.

LeSurf, J., 1990, in ``Millimeter-wave, Optics, Devices & Systems", publ. Adam Hilger, p.22.

Mass, S., 1986, in `` Microwave Mixers", publ. Artech House Inc., p. 213.

Morita, T. and Cohn, S., 1956, IRE Trans. on Antennas and Propagation, vol. AP-3, p.33.

Rizzi, P., 1988, in ``Microwave Engineering (Passive Circuits)", publ. Prentice Hall, p. 358 & 365.

Tong, E. and Blundell, R., 1994, IEEE Trans. Microwave Theory and Techniques, vol. MTT-42, no. 3, p. 383.

Walker, C., Narayanan G., Knoepfle, H., Capara, J., Glenn, J., Hungerford, A., Bloomstein, T., Palmacci, S., Stern, M., and Curtin, J., 1997, Proceedings of the Eighth International Symposium on Space TeraHertz Technology, eds. Blundell and Tong, Harvard University, p. 358.

THE ELECTROMAGNETIC PROPERTIES OF THE SUPERCONDUCTING CO-PLANAR WAVEGUIDE

P. KITTARA, G .YASSIN AND S. WITHINGTON
Department of Physics, University of Cambridge,
Madingley Road, Cambridge CB3 OHE, UK

There is no doubt that advances in predicting the electromagnetic properties of superconducting transmission lines have been a major contributor to the recent impressive improvement in the performance of SIS mixers. This progress has mainly manifested itself in two areas: First, it allowed accurate design of a circuit to tune out the capacitance of the tunnel junction and second it made integration of very useful planar circuits on the mixer chip possible. In most cases, those circuits employed microstrip lines whose modal and superconducting properties have thoroughly been investigated.

The reason for preferring the (CPW) over the more familiar microstrip may arise as a result of one or more of the following reasons:

- It offers a wide range of intermediate characteristic impedance values
- It is insensitive to the oxide thickness.
- It can have low conduction losses
- In some cases the deposition of coplanar structure can be simpler then that of two layer structure.

In this paper we present full analysis of the properties of the superconducting coplanar waveguide with thick metallisation. We first calculate the characteristic impedance and complex propagation constant based on a conformal mapping technique. After computing the geometrical factors of the equivalent TEM transmission line we use the Mattis Bardeen equations to include the effect of superconductivity on the electrical parameters. We then use those results to discuses the possible applications of the (CPW) in mixer circuits and make a thorough comparison with the properties of the conventional microstrip. In particular, we shall discuss the potential of this circuit as a tuning stub and a low loss transmission line in SIS mixers at frequencies near the superconducting gap.

Gap Excitations and Series Loads in Microstrip Lines: Equivalent Network Characterization with Application to THz Circuits

Andrea Neto and Peter H. Siegel
Jet Propulsion Laboratory, California Institute of Technology

Abstract
At submillimeter wavelengths typical gap discontinuities in microstrip, CPW lines or at antenna terminals, which might contain diodes or active elements, cannot be viewed as simple quasi statically evaluated lumped elements. Planar Schotky diodes at 2.5 THz for example have a footprint that is comparable to a wavelength. Thus, apart from modelling the diodes themselves, the connection with their exciting elements (antennas or microstrip) gives rise to parasitics. Full wave or strictly numeric approaches can be used to account for these parasitics but at the expense of generality of the solution and the CPU time of the calculation. In this paper an equivalent network is derived that accurately accounts for large gap discontinuities (with respect to a wavelength) without suffering from the limitations of available numeric techniques.

I. INTRODUCTION

Planar circuits utilizing microstrip or coplanar waveguide are often coupled to active devices or antennas through electrically small gaps. However, at THz frequencies, practical fabrication scales limit devices, such as planar Schottky diodes [1], to dimensions which are comparable to a wavelength. As a consequence, the effect of the gap dimensions on the coupling coefficient or resonant frequency of the associated transmission line or antenna cannot be ignored. Nor can it be modelled as a quasi statically derived [2 and references there cited] single lumped element. In this paper the authors present a new formulation for analyzing the effect of finite gap excitations on microstrip lines. The technique involves separating the excited modes into reactive elements which are confined near to the gap and propagating quasi TEM components, which are coupled to the surrounding transmission line and load (antenna). The formulation is very general and can be applied to a large class of problems involving discontinuities in transmisssion line circuits. Verification of the new method has been obtained using traditional but much more time consuming method of moments (MoM) techniques [3, 4 for example].

Recent investigations [5, 6, 7] present a direct integration method to derive the spectral Green's function for microstrip and strip-line. Most notably they furnish a detailed analysis of the singularities of this Green's function, while enphasizing on the excitation mechanisms of the propagating and leaky modes compatible with strip line and microstrip. This technique can be used to great advantage in the modeling of sub-mm wave circuits. The same formalism was adopted by one of the authors, [8, 9] to derive, analytically in that case, the Green's function of a slot printed at the interface between two different homogeneous dielectrics, and in [10] to derive ad hoc basis functions in the MoM analysis of coplanar waveguide excited slot antennas.

As another application of this methodology, we investigate in this paper the input impedance of gap excited microstrips coupled to planar antennas. A rigorous equivalent network is derived that accurately accounts for the field in-and-near large-or-small (with

respect to a wavelength) gap discontinuities, without suffering from the lack of physical insight of purely numerically derived solutions. On the contrary the network approach will provide the guidelines on the one hand for the efficient coupling to and from the gap, and on the other hand for the separate characterization of the reactive energy associated with the feed. Full wave tools, such as Finite Difference in Time Domain or Finite Element Method may be necessary to characterize the minute details of a complicated diode structure but are typically not needed for the remaining part of the circuit.

In our technique the spectral kernel of the Greens function is first used for the determination of the bound mode wave number. Then the evaluation of the residue contributions associated with this pole allows the derivation of an equivalent transformer that accounts for the gap launching coefficient on the equivalent transmission line of the bound TEM mode in the microstrip. By subtracting the current associated with this main mode on the infinite line from the total current, a source attached current is defined. This current, for the circuit substrates used in many sub millimeter planar devices, is mostly confined in a region very close to the gap. From this current a parallel gap impedance is derived that accurately represents the reactive effects of the gap. The same formalism adopted here for the microstrip configuration, can be used for characterizing a wide variety of other gap excited planar transmission lines and active antennas.

II. FORMULATION: ELECTRIC CURRENTS ON THE MICROSTRIP

The problem under investigation is shown in Fig. 1.

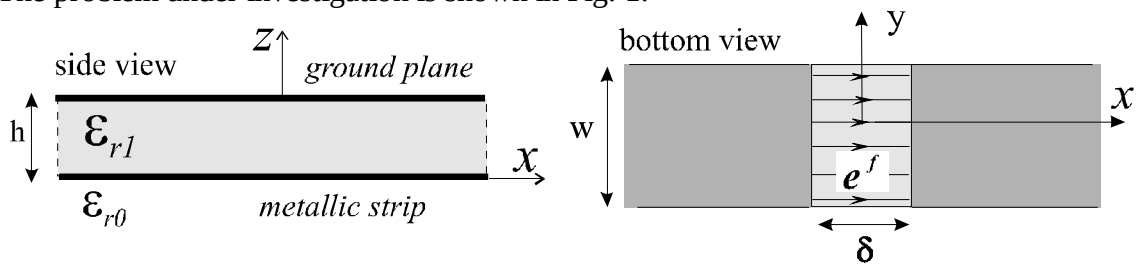

Fig.1 *Infinitely extended microstrip excited with by an impressed electric field distributed over a gap of dimensions (δ,w).*

An infinitely extended (along *x*) microstrip, printed on a grounded dielectric slab (ϵ_{r1}, $\epsilon_{r2}=1$) is considered. The microstrip cross section (*w*, along *y*) is uniform and much smaller than the wavelength. The structure is assumed to be excited by an impressed electric field $\boldsymbol{e_f}(x,y)=e_f(x,y)\boldsymbol{i}_x$. The electric current distribution is assumed to be characterized by a separable space-dependence with respect to *x* and *y*; i.e.,

$$j(x,y)=i(x)\cdot\frac{2}{w\pi}\frac{1}{\sqrt{1-\left(\frac{2y}{w}\right)^2}} \qquad (1)$$

where the transverse *y*-dependence is chosen to verify the quasi-static edge-singularities and the the normalization constant, $\frac{2}{w\pi}$, has been chosen in such a way that $i(x)$ represents a net current flowing in the microstrip at any cross section of the slot line. The method adopted to derive the current of a gap excited microstrip has been presented in [5]-[7]. A

brief review with the minor variations introduced in this paper is presented in the appendix. As a result the electric current in the microstrip is expressed as:

$$i(x)= \frac{1}{2\pi} \int_{-\infty}^{\infty} \frac{-E^f(k_x)e^{-jk_x x}}{D(k_x)} dk_x \qquad (2)$$

where $E^f(k_x)$ is the Fourier Transform (FT) of the impressed electric field, with respect to the variable x, and

$$D(k_x)= \frac{1}{2\pi} \int_{-\infty}^{\infty} G_{xx}(k_x,k_y)J_0(\tfrac{1}{2}w_s k_y)dk_y \qquad (3)$$

with J_0 is the Bessel function of zero order and $G_{xx}(k_x, ky)$ the FT, with respect to the variables x and y of the electric field radiated by a short electric dipole lying at the interface between the slab and the homogeneous half space for $z<0$, in the absence of the metallic strip.

An interesting aspect of (2) is that the impact of the feed is all contained in the numerator and in most practical cases it is a simple anayitic function. When the distribution is uniform over the feed region $e^f(x)=-1/\delta$ for $x \in (-\delta/2,\delta/2)$ the excitation is said to be a δ-gap and $E^f(k_x)= -sinc(k_x\delta/2)$. This case will be considered specifically in the following. The denominator, $\frac{1}{D(k_x)}$, represents the microstrip spectral Green's function and for a detailed discussion on the nature of the branch singularities of $D(k_x)$ the reader is referred to [5, 6].

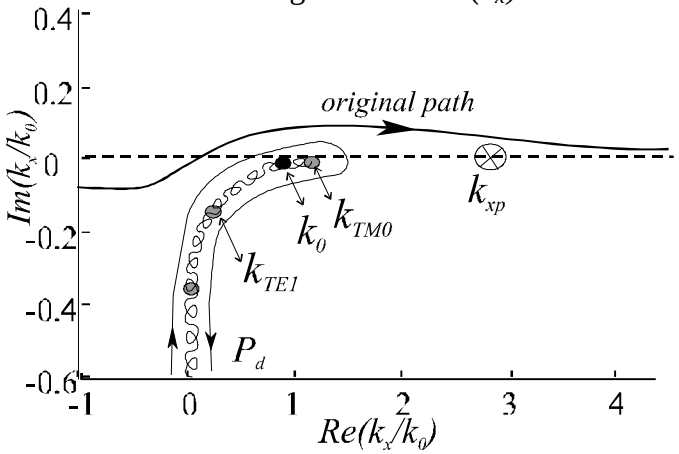

Fig. 2 *Complex k_x plane topology for thin dielectric substrates. Only the TM0 pole of the grounded slab is assumed to be above cut off.*

The outer integral in (2) can be performed by adopting a deformation in the complex plane below the real axis for Re $(k_x)<0$ and above the real axis for Re $(k_x)>0$ (*original path* in Fig. 2), in order to avoid the branch cuts arising from the branch points implicit in $D(k_x)$. Here it is sufficient to know that these branches are square root type or logarithmic when they originate from poles or from the branch (k_0) of the layered Green's function $G_{xx}^{je}(k_x,k_y)$ respectively. For a thin dielectric layer configuration, (that is only the TM0 pole

is above cut off in the grounded slab) the complex plane topology of the microstrip's Green's function, $\frac{1}{D(k_x)}$, is well represented in *Fig. 2* which shows the branch cuts arising from k_{TM0}, k_{TE1} and k_0.

II.1 Case study

It is instructive to perform a parametric study of the currents as a function of the gap dimensions. The information derived will lead to the current representation and equivalent network of the following sections. Fig. 3. shows the real part (3a) and imaginary part (3b) of the current due to a 1 volt uniform excitation for different gap dimensions (δ) from 2 to 18 μm. The width of the microstrip (w) and the height of the slab (h) are 8 μm and 3 μm respectively ($h=\lambda_0/40$ *at 2.5 THz*). The relative dielectric constant considered is ϵ_{r1}=12.85. These parameters and the maximum gap dimension are typical of thin GaAs membrane diode technology [1] for which this analysis is derived.

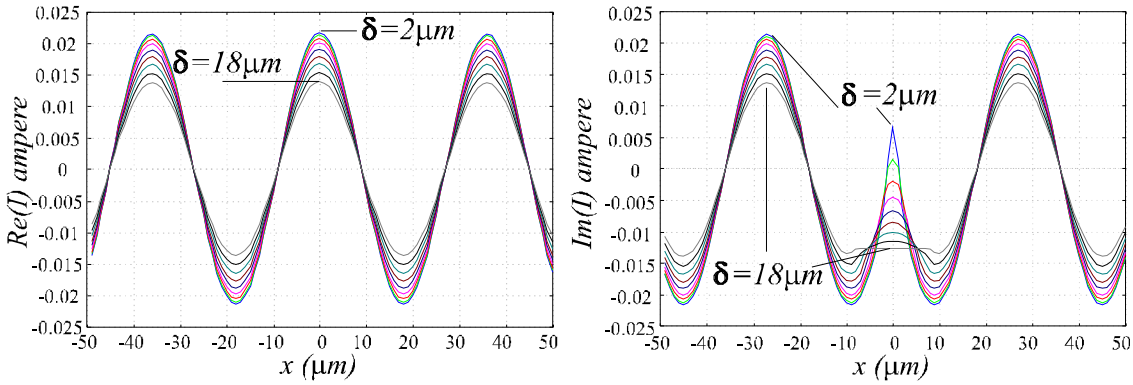

a) b)

Fig. 3 *Current on an example microstrip structure at submillimeter wave frequencies (2.5 THz) obtained using the present direct integration method (equation 2). Real (a) and Imaginary(b) parts are presented for different dimensions of the excitation gap (δ varying from 2 to 18 μm).*

Two aspects of the problem should be noted

i) A launching efficiency issue stands out, since the amplitude of the oscillation of the real and imaginary part of the current at a certain distance from the source is regulated by the gap dimensions. As δ tends to zero, the amplitude of the current is a maximum and tends to one half of the characteristic admittance of the microstrip line. As δ grows the value of the current diminishes.

ii) The reactive energy in the feed zone is strongly affected by the width of the source. When the gap dimensions shrink to zero, the imaginary part of the current tends to grow logarithmically (Fig. 3b) indicating a capacitive reactance. When the dimensions of the gap are large, the imaginary part of the current can be less then zero, indicating an inductive reactance.

II.2 Modal and source attached currents

The dispersion equation, $D(k_x)=0$, defines the position of the pole of the guiding structure. The localization of the zeroes of $D(k_x)$ as a function of the parameters of the structure (w, ϵ_{r1}), can be performed numerically by means of a descent along the gradient algorithm. As

a starting point one can use the analytical formulas [1], knowing that the actual propagation constant is not drastically different. Only one pole, indicated here after as $\pm k_{xp}$, is found for the thin dielectric layers we are interested in ($3\mu m=\frac{\lambda_0}{40}$ *at 2.5 THz*). In the absence of losses, the pole of the structure is found on the real axis of the k_x plane (see *Fig. 2*). Knowingn its location, the integral in *(2)* can be approximated asymptotically for $|x|>\delta/2$, by the residues of the poles in $k_x = \pm k_{xp}$. These residue contributions are expressed as

$$i_{res}(x)= -2\pi j\left(sinc\,(k_{x0}\tfrac{\delta}{2})\right) R\, e^{-jk_{xp}|x|} R=Res\,\left(\frac{1}{D(k_x)}\right)_{k_x=k_{xp}} \qquad (4)$$

It is apparent that this current is the one associated with the quasi TEM mode that propagates in the microstrip. A comparison between the residue evaluation *(4)* of the integral in *(2)* and the original numerical integration is presented in Fig.4a and Fig. 4b, for two unit δ-gap excitation configurations. Outside the source region (gray zone in Fig. 4) the full integration of *(2)* and the sole residue contribution are almost superimposed due to the drawing scale. A source attached current can then be defined and will be indicated by

$$i^s(x)=i(x)-i_{res}(x) \qquad (5)$$

The source attached currents represent an overall current that contains all the separate branch conntributions, without calculating them separately as in [7]. In this respect it is useful to observe that i^s can be calculated for $|x|>\delta/2$, deforming the original integration path on a path P_d (Fig. 2 where only the spectrum for $\mathrm{Re}(k_x)>0$ is shown) that surrounds all the branch cuts on the top Rieman sheet. This is possible because in thin dielectric cases, the only significant singularity encountered in the deformation is the pole in $\pm k_{xp}$.

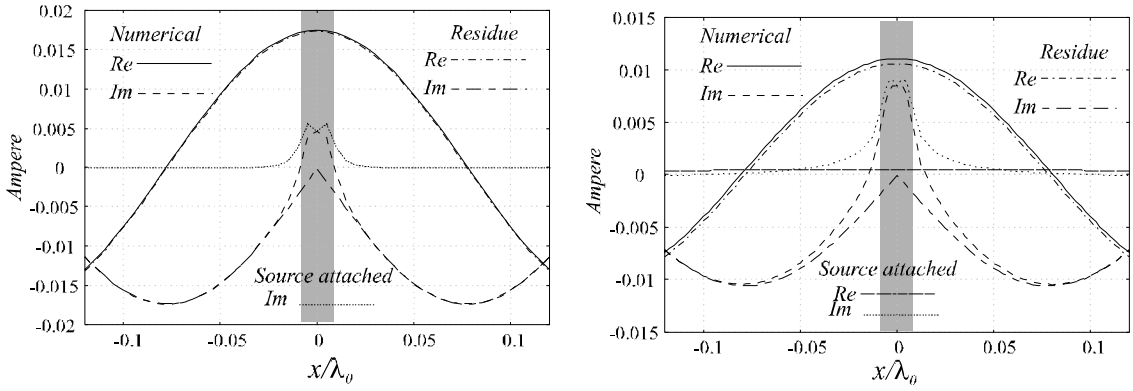

a) b)

Fig. 4 *Comparison between asymptotic evaluation (residue only) and direct numerical integration of the current for a sample microstrip structure at submillimeter wave frequencies (2.5 THz). Also plotted is the source attached field (real and imaginary parts in 4.b and only the imaginary part in 4.a since the real part is almost zero and cannot be distinguished in the drawing scale). The width of the microstrip and the dimensions of the excitation gap (δ) are $\lambda_0/20$ ($6\mu m$), $\lambda_0/60$ ($2\mu m$) respectively. The height of the slab is $\lambda_0/40$ ($3\mu m$) in Fig. 4a and $\lambda_0/20$ ($6\mu m$) in Fig. 4b. The relative dielectric constant considered is ($\epsilon_{r1}=12.85$).*

The integrand decays exponentially in the deformed path P_d. Thus the numerical calculation of i^s is much more efficient than along the original path. The definition of the source attached current is also analytically extended to the source region, $|x| < \delta/2$ (but not this way of calculating it, which must be done in accordance with the definition in *(5)*). The source attached field is also plotted in Fig. 4. In [7] it is demonstrated that each of the branch contributions to the current decays as $x^{-3/2}$, thus also $i^s(x)$ decays this way or faster. It's value in the source zone depends on the thickness of the dielectric considered. In the very thin dielectric slab ($h=\lambda_0/40$) considered in Fig. 4a the real part of $i^s(x)$ is not noticeable on the drawing scale and thus is not reported. Also the imaginary part of $i^s(x)$ is very concentrated in the surrounding of the source. In Fig. 4b the same curves are reported for a thicker dielectric case ($h=\lambda_0/20$). In this case the real part of $i^s(x)$ is noticeable, and significant for larger distances from the source. It is worth repeating at this point that ($h=\lambda_0/40$) corresponds to a 3μm thick dielectric at 2.5 THz, the design target for this work.

III. INPUT ADMITTANCE AND EQUIVALENT NETWORK

The current representation in terms of source attached and mode contributions is particularly significant when only one bound mode is propagating in the microstrip. In this case it is possible to derive a rigorous equivalent network, based on a single transmission line, that characterizes the δ-gap excited infinite microstrip input impedance. We will see in section IV, that finite (loaded) microstrips can also be studied by resorting to the same simple equivalent network. The input admittance of a δ-gap excited microstrip can be expressed in the spectral domain as:

$$y_{inf} = \int_{-\infty}^{\infty} \frac{sinc^2(k_x\delta/2)}{D(k_x)} \, dk_x \qquad (6)$$

Accordingly, the total complex power radiated by the source can be expressed as:

$$P_{tot} = \frac{1}{2} |V_g|^2 y_{inf} \qquad (7)$$

The knowledge of the microstrip characteristic impedance z_0 [3], together with the amplitude of the traveling wave in the microstrip from *(4)*, consents to write the power launched in the microstrip quasi TEM mode as:

$$P_m = |V_g|^2 (R^+)^2 z_0 \qquad (8)$$

where $R^+ = -2\pi j\left(sinc(k_{x0}\frac{\delta}{2})\right)R$. This power actually leaves the excitation zone in form of a couple of outgoing travelling waves ($\pm k_{xp}$). As we will see later on, this power is the only one that might give rise to interactions with components of the circuit which are located at a significant distance, in terms of a wavelength, from the feeding zone. In order to derive an equivalent network that rigorously takes into account the gap effects one may associate all the power that is not launched into the the quasi TEM mode as being assigned to a lumped load indicated as z_{gap}. The power conservation then imposes:

$$P_{gap} = P_{tot} - P_m \qquad (9)$$

This gap impedance is imagined as in parallel to the source and to the modal loading as in fig. 5a. Accordingly both P_m and P_{gap} can also be expressed as:

$$P_m = \tfrac{1}{2} \mid V_g \mid^2 y_m; \qquad P_{gap} = \tfrac{1}{2} \mid V_g \mid^2 y_{gap} \tag{10}$$

thus givin the explicit relation between the various admittance components of the network in fig.5a

$$y_{gap} = y_{inf} - y_m \tag{11}$$

The expression for y_m according to this definition equating the two expression for P_m in *(8)* and *(10)*

$$y_m = 2(R^+)^2 z_0 \tag{12}$$

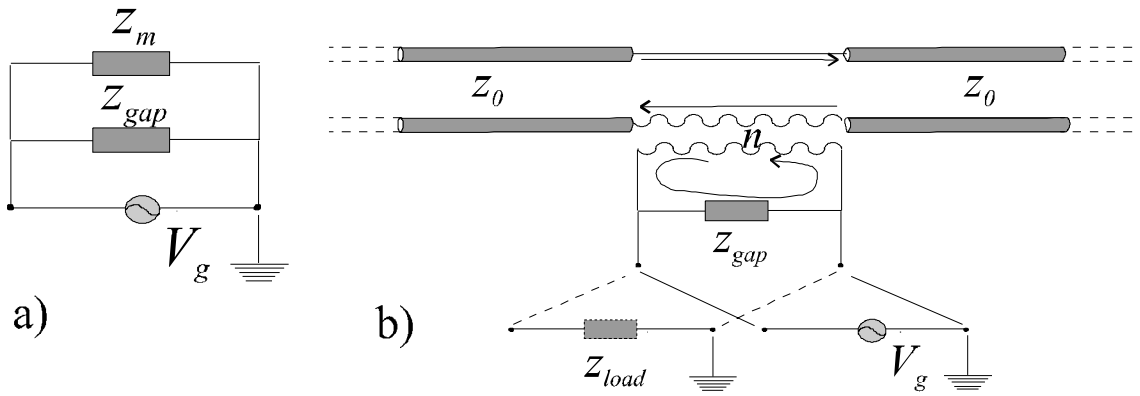

Fig. 5 *Equivalent network for δ gap excited microstrip structure. a) admittance decomposition ($y_{inf} = y_{gap} + y_m$); b)Interpretation of the modal impedance interms of transformer connected equivalent transmission line.*

So that, given *(12)*, *(11)* becomes an operative definition. It is useful to perform a further algebraic manipulation expressing the modal admittance as

$$y_m = \frac{2z_0 R^+ \cdot 2z_0 R^+}{2z_0} = n^2 \frac{y_0}{2} \tag{13}$$

where

$$n = 2z_0 R^+ = 2z_0 (2\pi j R)\ sinc\ (k_{x0} \tfrac{\delta}{2}) \tag{14}$$

The introduction of the coefficient *n* consents to represent the modal part of the impedance associated to the series of two transmission lines representing the quasi TEM mode. These transmission line are series fed, via a transformer of turn ratio *n*, by the parallel combination of the source voltage and the gap impedance. The full circuit is shown in Fig. 5b.

The use of the transformer is a convenient wayof separating the different field behavior associated with the feeding and the propagation of the transmission lines. The electric currents in the source are oriented parallel those in the microstrip, both along x. The electric fields in the source and in the transmission line are orthogonal, (along x and along

z respectively). The value of the transformer *n* for the same microstrip of Fig.3 (operated again at 2.5 THz) is plotted in Fig. 6. as a function of the gap's width, δ.

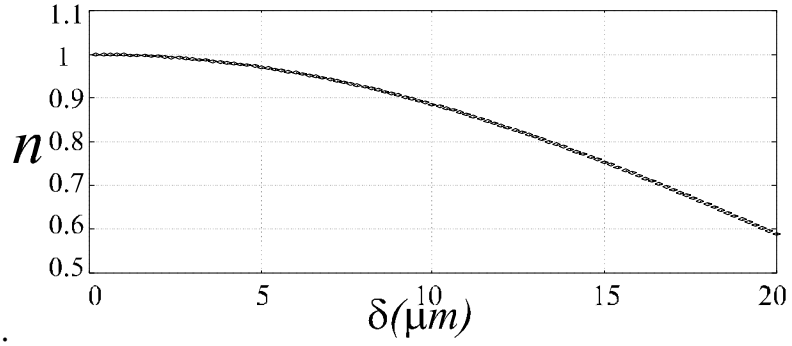

Fig. 6 *Transformer for δ gap excited microstrip structure of Fig. 3*

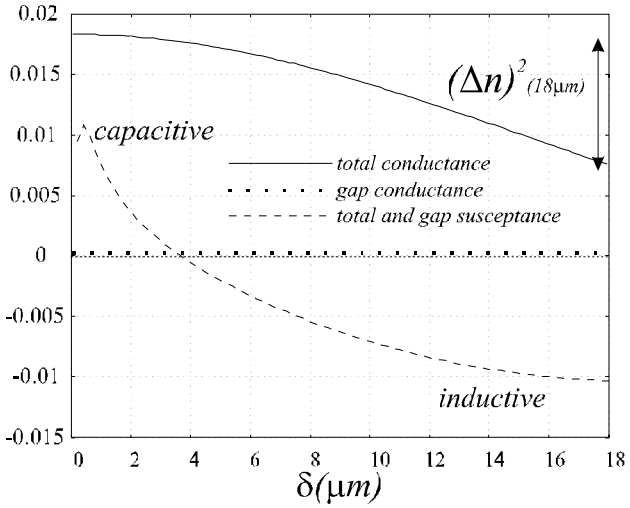

Fig. 7 *Total and gap admittance (gap and total susceptances are equal)*

The gap and total admittance for to the same case are presented in *fig.7*. It should be noted that the gap conductance is virtually zero for the case of the thin dielectric slab, and the gap susceptance, coincident by definition with the total one, goes from being capacitive to inductive for the investigated range of δ.

IV. NUMERICAL EXAMPLES, APPLICABILITY AND CONSIDERATIONS

The purpose of deriving the equivalent network is to characterize the input impedance of finite, as opposed to infinite, microstrips. When the bound mode currents are much more intense than the source attached currents, at a certain distance from the source one may assume that the source attached currents intrinsically satisfy Maxwell's equations for the finite structure. The loading of the end-points of the microstrip will generate a reflection that can be characterized by a load impedance. Thus the interaction between the two outer loads and the source can be accounted for via a complete equivalent network with equivalent lumped elements z_{l1}, z_{l2} (Fig. 8) located at the endpoints of the microstrip.

IV.1 Numerical examples

Two finite length microstrips printed on a GaAs membrane ($\epsilon_{r1}=12.85$) have been investigated using the equivalent network in fig. 8.

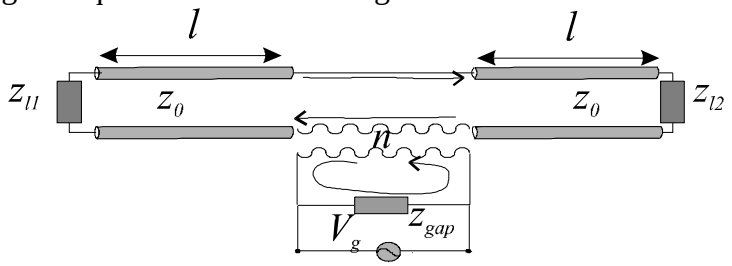

Fig.8 *Equivalent network for a δ-gap excited and loaded microstrip.*

The dielectric thicness and the width of the conductor are 3 μm and 2.5 μm respectively. The pertinent open end impedance has been derived as in [3]. Fig.9a shows the imaginary part of the input impedance for a 60μm long microstrip as a function of the frequency for three different gap dimensions (0.5, 1.15, and 15 μm). It is found that in the three cases the resonant frequency is the same and significant differences are observed at larger values of the impedance. Also the pertinent curves obtained via a full wave Method of Moments are shown for the 1.15 μm and the 15 μm cases. The MoM tool uses piece wise sinusoidal sub-domain basis functions and rectangular weighting functions in the longitidinal dimension and assumes a rectangular distribution in the transverse dimension. The agreement between the network solution and the MoM solution is excellent apart for a minimal (0.5 %) resonant frequency shift, probably due to the different electric current transverse distribution assumed in the two models.

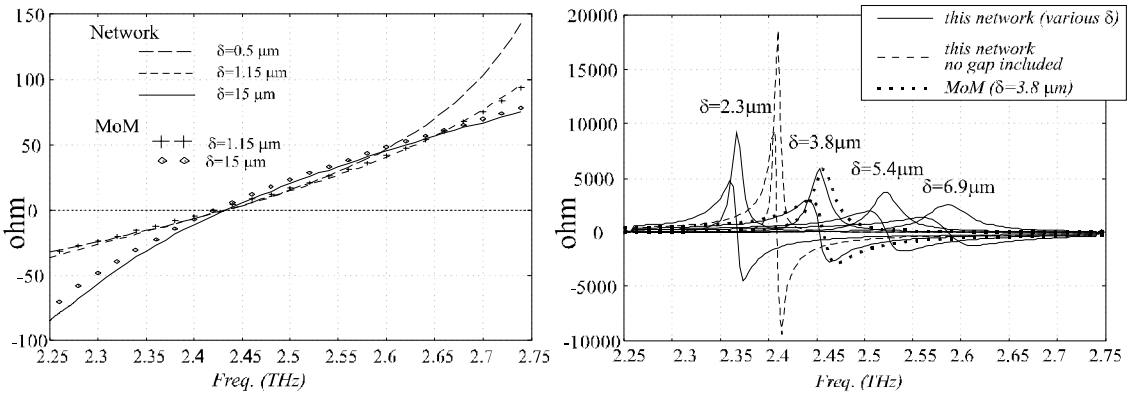

a) b)

Fig. 9 *Impedance of a delta gap excited microstrip as function of the frequency. a) (l=60 μm); b) l=40μm). Also a parametric study as a function of δ and comparison with MoM are shown. The width of the microstrip and the thickness of the dielectric are 2.5 μm and 3 μm respectively. The grounded dielectric is made of Ga-As.*

The case in Fig. 9a ($l=60\ \mu m$) is geometry corresponds to a case in which the load impedance (z_{li}, $i=1,2$), when reflected the excitation zone, is nearly zero. In view of this the gap impedance effect is relatively minimal since it is in parallel to a very low impedance load. The case in Fig. 9b ($l=40\mu m$) corresponds to a very high load impedance

at the excitation zone, and as seen the impact of the gap becomes dramatic. The resonant frequency as a function of the gap width shifts very significantly for δ varying from 2.3 μm to 6.9 μm and the curves can easily be distinguished. For even smaller gaps the resonance frequency shifts out of the figure since the source attached currents tend to be singular as δ tends to zero. In Fig.9a is also plotted a MoM result, for δ=3.84 μm, which again shows excellent agreement with out model. Finally in Fig. 9b the result that would be achieved by using the equivalent network without the transformer and the gap impedance introduced in this paper is plotted. Not only is the resonance frequency poorly modelled but also the absolute values of the impedance vary widely form those of the more accurate equivalent network analysis.

IV.2 Applicability

We will assume than when $|\, i_s(x=l/2)\,| < \frac{|i_{res}(x=l/2)|}{100}$ the accuracy, $A(x=l/2) > \frac{1}{100}$, in the evaluation of input admittance is satisfactory. In fig. 10 $|\, i_{res}\,| / |\, i_s\,|$ is plotted as a function of the frequency at an observation point located at $\lambda_0/10$ from the center of the feed. The microstrip's nominal characteristic impedance is 50 ohms, the dielectric thickness and the width of the conductor strip are 3 μm and 2.5 μm respectively. The dimension of the excited gap is $\lambda_0/40$ and the dielectric is composed of silicon ($\epsilon_{r1}=11.7$). It is found that $|\, i_{res}\,| / |\, i_s\,|$ is always larger than 100 for frequencies up to 3 THz. Thus, since $i_s(x)$ decays algebraically, $x^{-3/2}$, any load at a distance larger than $\lambda_0/10$ can be characterized accurately with the present equivalent network. The same is not true for thicker dielectrics. Also the investigated microstrip is only weakly dispersive, as the normalized propagation constant k_{xp}/k_0 calculated as explained in sect. III varies from *2.8 to 2.9* in the frequency range considered in *Fig. 10.*

IV.3 Considerations

The loads, Fig. (8), typically represent active impedances. For example if they represented slot antennas their impedance should be calculated when both slots are radiating in phase. In this case the load connected at the end points of the microstrip will present a larger real part. Also in this case frequency shifts as significant as in Fig. 9b, can be expected. This has already been experimentally verified in a similar slot circuit [11]. If the actual source under investigation is not well represented by a δ-gap generator, a correction in the equivalent network parameters can be made by simply substituting the *sinc* function in *(6), (14)* with the relevant FT $E^f(k_x)$, provided the more realistic function $e^f(x)$ is still an even function, with respect to x. If $e^f(x)$ also presents some odd components, then a single impedance should not be used, and an even and odd impedance characterization should be adopted. The extra degree of freedom (odd mode) can still benefit from an equivalent network, that can be derived with the same methodology used here for the even mode. At this point $e^f(x)$ could for example the result of the investigation of complicated source in isolation. Indeed the procedures presented in this paper are found to be particularly useful in connecting an isolated load or source to the remaining part of the circuit. Full wave tools such as Finite Difference Time Domain or Finite Element Method may be necessary to caharacterize the tiny details of a complicated source (like a diode) but are often not necessary for analyzing the remaining part of the circuit.

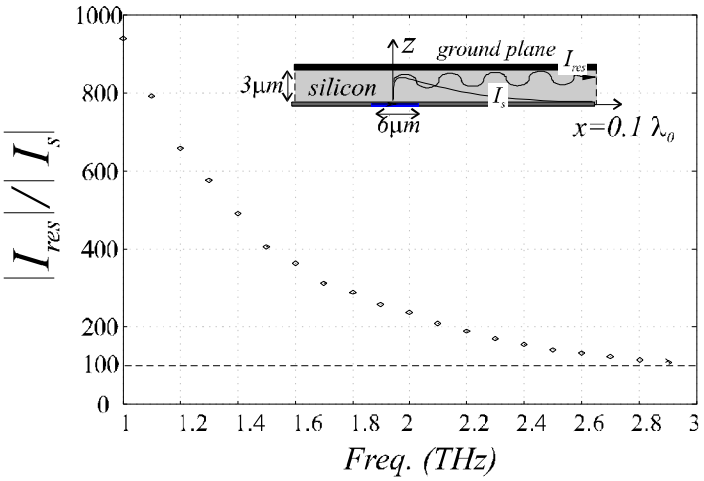

Fig. *10 Ratio between the amplitudes of the residue contribution to the currents and the source attached currents. The graph can be read as 1/(A(l=0.1λ$_0$)). The microstrip impedance is nominally 50 ohm. The width of the microstrip and the thickness of the dielectric are 2.5 μm and 3 μm respectively. The grounded dielectric is made of silicon (ϵ_{r1}=11.7). The width of the gap is λ$_0$/40.*

V. CONCLUSIONS

An equivalent network has been presented for the wide band characterization of the gap in a series fed and loaded microstrip line. The network consists of a transformer and a gap impedance. The transformer accounts for the launching coefficient of the mode on the equivalent transmission line representing the microstrip and is evaluated analytically by simple interpretation of the spectral expression of the microstrip Green's function. The gap impedance accounts for the current distribution in the region surrounding the feed, and is calculated by simple spectral domain numeric integration (less then 3 minutes on a 300 MHz Pentium II). The procedure, validated via MoM, will work for any kind of dielectric stratification, but is meaningful when one bound mode is above cut off in the microstrip. Submillimeter's wave problems in which this equivalent network can be applied include the design of receivers (i.e. diodes as mixers or frequency multipliers) and generators (i.e. photomixer based local oscillators).

APPENDIX: SOLUTION OF THE INTEGRAL EQUATION

According to the equivalence principle an Electric Field Integral Equation (EFIE) is set up and enforced, via a point matching like procedure only on the longitudinal axis of the micro strip *(y=0)*.

$$\iint_{\Sigma} g_{xx}(x-x', 0-y')\, j_x(x', y')\, dx'dy' = -e^f(x, 0) \qquad (A0)$$

where Σ is the entire microstrip domain. The point matching (or razor blade) as testing procedure is selected in order to mantain the same formalism used [8-10] for the characterization of slot antennas printed between two different homogeneous dielectrics. All the quantities are scalar, because of the x-polarisation of all the scattered and impressed electric fields involved in the equation, and neglecting cross polarized electric

currents (in view of the small cross section of the strip). The left hand side of *(A0)* represents the electric field at $z=0$ radiated by the electric current density j_x. The Green's function, g_{xx}, that appears in the kernel of this integral equation, is the electric field radiated by a short electric dipole lying at the interface between the slab and the homogeneous half space for $z<0$, in the absence of the metallic strip.
The electric current distribution is assumed to be characterized by a separable space-dependence with respect to x and y; i.e.,

$$j(x',y')=i(x') \cdot j_t(y') \,. \qquad (A1)$$

The transverse y-dependence is chosen to verify the quasi-static edge-singularities

$$j_t(y)=\frac{2}{w\pi}\frac{1}{\sqrt{1-\left(\frac{2y}{w}\right)^2}}. \qquad (A2)$$

$j_t(y)$ possesses a closed-form Fourier transform,

$$J_t(k_y)=FT\{j_t(y)\}=J_0(\tfrac{1}{2}w\,k_y), \qquad (A3)$$

where J_o is the Bessel function of zero order. The IE (1) is now transformed into the k_x-Fourier domain as

$$I(k_x)\int_{-\infty}^{\infty}\widetilde{G}_{xx}(k_x,\ -y')\ j_t(y')\,dy' = -E^f(k_x), \qquad (A4)$$

where $I(k_x)$ and $\widetilde{G}_{xx}(k_x, -y')$ are the FT, with respect to the variable x, of $i(x)$ and $g_{xx}(x, y)$, respectively. Equating the two spectra in k_x it is apparent that

$$I(k_x)=\frac{-E^f(k_x)}{D(k_x)}; \qquad (A5)$$

where

$$D(k_x)=\int_{-\infty}^{\infty}\widetilde{G}\,(k_x,\ -y')\ j_t(y')\,dy'=\frac{1}{2\pi}\int_{-\infty}^{\infty}G(k_x,k_y)J_0(\tfrac{1}{2}w_s k_y\,)dk_y \qquad (A6)$$

represent the spectral domain Green's function of the microstrip line and $G(k_x,k_y)$ is the FT of $g(x, y)$ with respect to both the variables x and y. The electric current on the microstrip can then be expressed as:

$$i(x)=\frac{1}{2\pi}\int_{-\infty}^{\infty}\frac{-E^f(k_x)e^{-jk_x x}}{D(k_x)}\,dk_x \qquad (A7)$$

References

[1] P.H. Siegel, R. P. Smith, M. C. Gaidis, S. Martin "2.5 THz GaAs Monolithic Membrane-Diode Mixer," *IEEE Trans. Microwave Theory and Techniques, vol. MTT 47*, pp. 596-604, May 1999.

[2] P. Benedek, P. Sylvester, " Equivalent Capacitance for Microstrip Gap and Steps," *IEEE Trans. Microwave Theory and Techniques*, vol. MTT 20, pp. 729-733, Nov. 1972.

[3] P.B. Katehi, N.G. Alexopoulos, "Frequency Dependent Characteristics of Microstrip Discontinuities in mm-Wave Integrated Circuits," *IEEE Trans. Microwave Theory & Techniques.*, vol. MTT 33, no. 10, pp. 1029-35, Oct. 1985.

[4] N.G. Alexopoulos, Shih-Chang Wu "Frequency Independent Equivalent Circuit Model for Microstrip Open-End and Gap Discontinuities," *IEEE Trans. Microwave Theory & Techniques.*, vol. MTT 42, no. 7, pp. 1268-1272, July 1994.

[5] C. Di Nallo, F. Mesa, D.R. Jackson. "Excitation of Leaky Modes on Multilayer Stripline Structure" on *IEEE Transactions on Microwave Theory and Techniques,* Vol. 46, no. 8 , pp 1062 -1071, August 1998.

[6] F. Mesa, C. Di Nallo, D.R. Jackson "The theory of surface-wave and space-wave leaky-mode excitation on microstrip lines" on *IEEE Transactions on Microwave Theory and Techniques,* Vol. 47, no. 2 , pp. 207 -215, Feb. 1999.

[7] D.R. Jackson, F. Mesa, M.J. Freire, D.P. Nyquist, C. Di Nallo, "An Excitation Theory for Bound Modes and Residual-Wave Currents on Stripline Structures" *Radio Science*, Vol. 35, no. 2, pp 495 -510, March-April 2000.

[8] A. Neto, S. Maci, "Analytical Solution for Gap-Excited, Infinite Printed Slot Lines", to be presented at *IEEE Antennas and Propagation Symposium,* Boston July, 2001.

[9] A. Neto, S. Maci, "Green's Function of Gap-Excited, Infinite Printed Slot Lines", *NASA New Technology Report* (April 2001).

[10] A. Neto, P.J.I. De Maagt, S. Maci "Optimized Basis Functions for Slot Anetnnas Excited by Coplanar Waveguides", submitted to *IEEE Trans. Antennas and Propagation* (March 2001)

[11] R.A. Wyss, A. Neto, W.R. McGrath, B. Bumble, and H. LeDuc, "Submillimeter-wave spectral response of twin-slot antennas coupled to hot electron bolometers," Proceedings of the *11-th Int. Symp. on Space THz Tech.*, Ann Arbor, MI, May 1-3, 2000.

The research described in this paper was carried out at the Jet Propulsion Laboratory, California Institute of Technology, under a contract with the National Aeronautics and Space Administration.

PoleStar: An 810 GHz Array Receiver for AST/RO

Chris Walker, C. Groppi, D. Golish, C. Kulesa, A. Hungerford, C. Drouet d'Aubigny
SORAL, University of Arizona, 933 N. Cherry Ave. Tucson, AZ 85721 USA
Tel: +01-520-621-3924, Email: cwalker@as.arizona.edu

K. Jacobs, U. Graf
KOSMA, I. Physikalisches Institut Universität zu Köln Zülpicher Str. 77 50937 Köln Germany

C. Martin
Smithsonian Astrophysical Observatory, MS-78, 60 Garden St. Cambridge, MA 02138 USA

J. Kooi
California Institute of Technology 105-24 Caltech, 1201 East California Blvd, Pasadena CA 91125 USA

Abstract

We have constructed a 4-channel receiver at 810 GHz for use on the Antarctic Submillimeter Telescope and Remote Observatory located at the South Pole (AST/RO). The array was assembled and tested at the Steward Observatory Radio Astronomy Lab (SORAL) and then installed on AST/RO in November-December 2000. In this paper we describe the instrument and its performance both in the lab and on the telescope.

Introduction

The cold, dry conditions at the South Pole, coupled with its relatively high altitude (~10,500 ft) make it an excellent location for observations at submillimeter wavelengths. The Antarctic Submillimeter Telescope and Remote Observatory (AST/RO) with its 1.7 m aperture was designed and built to take advantage of these conditions (Stark et al 2001). Figure 1 shows a CO J=4→3 image of the giant molecular cloud NGC 6334 made with AST/RO. CO J=7→6 and [CI] spectra toward the same object are also shown. These are 'first light' data taken in the middle of the Antarctic *summer* with a dual channel, 460/810 GHz receiver system built by our team a few years ago. Much higher atmospheric transmission is routinely available in the winter. These almost ideal atmospheric conditions and the resulting observing efficiency available from the South Pole motivated us to build an 810 GHz array for use on AST/RO. Figure 2 is a photograph of the receiver 'front-end' as it appeared in the lab before deployment.

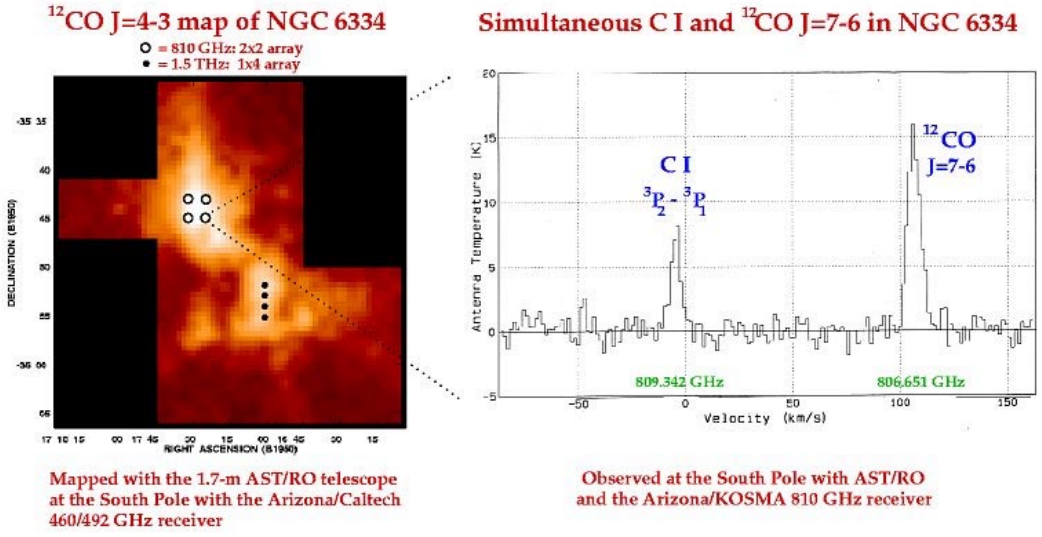

Figure 1

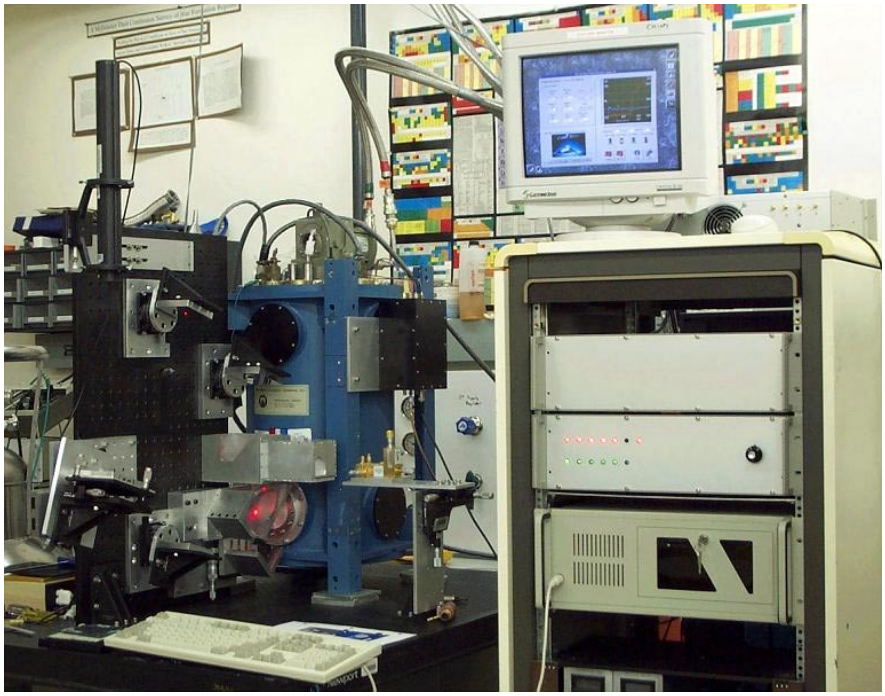

Figure 2: PoleStar frontend and control electronics during testing at SORAL.

Pole Star Optical Design

The purpose of the optical system is to reimage AST/RO's focal plane onto a compact 2x2 array of lenses located in the array cryostat and to efficiently inject local oscillator power into each mixer. Focal plane reimaging is achieved by a pair of parabolic mirrors and two flats (Figure 3). Each AST/RO beam expands from the focal plane located ~900

mm above the receiver pallets on to the first offset parabola (P1). P1 collimates the beams and conveys them via two flats to the second parabola (P2). P2 focuses and re parallelizes the beams so that they arrive at the mixer lenses with the correct size and placement. The beam 'footprint' of the array on NGC 6334 is shown in Figure 1 (open circles). Each diffraction limited, half-power beam diameter is ~54".

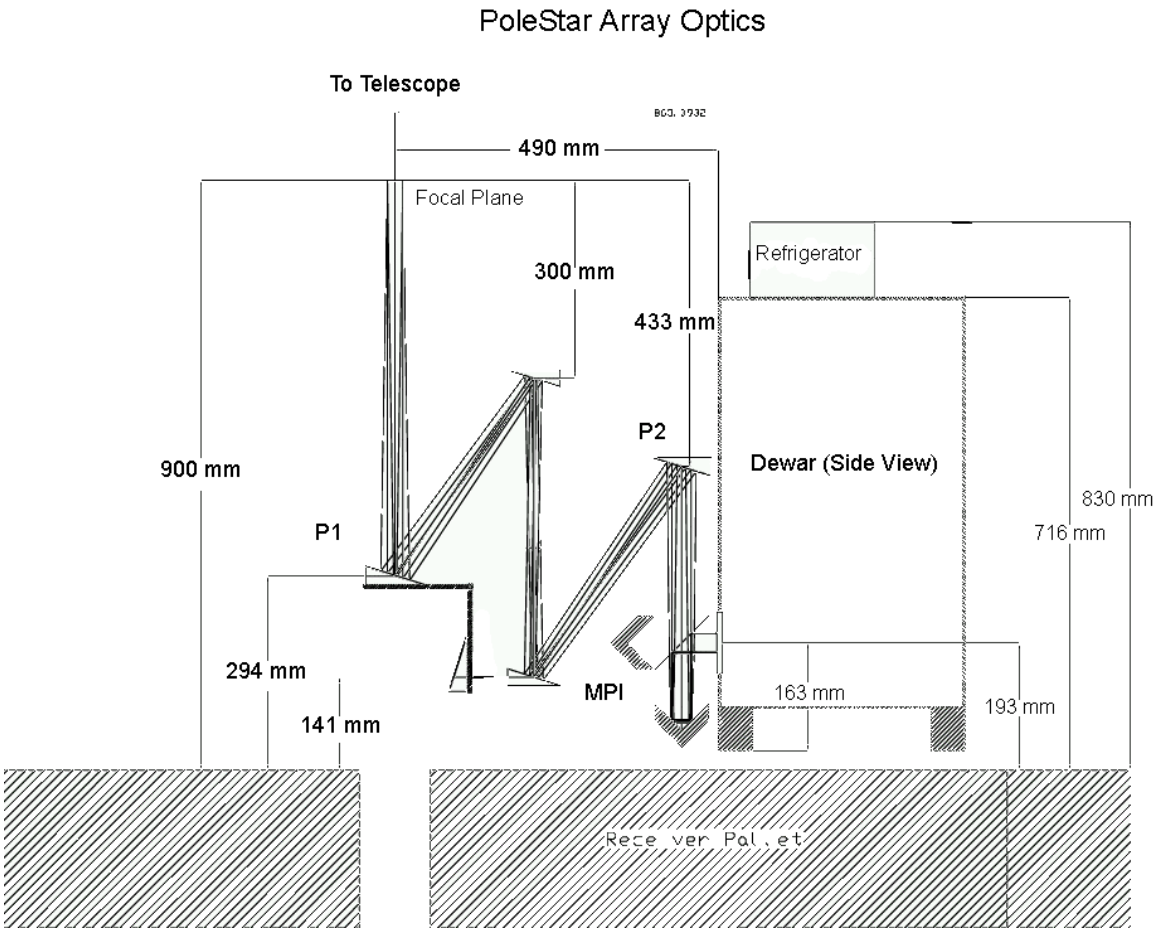

Figure 3

The local oscillator for the array is a single oscillator (J. Carlstrom) and multiplier (Erickson & Narayanan). A quasi-optical LO power divider (Figure 4) is used to split the focused, 42 μW LO beam into 4 equal parts. The power dividing is accomplished by two, low-loss, ~50% crystalline quartz beamsplitters. Each beam splitter is paired with a flat mirror to give the emerging beams the proper horizontal and vertical offsets. After including all loss mechanisms, we estimate that 18% of the incident LO power is in each LO beam at the output of the power divider. The LO polarization is orthogonal to the signal beams. The four beams are then injected into the 'sky' signal path by a high quality wire grid. A Martin-Puplett interferometer then rotates the LO beam polarization

to match that of the sky and directs them into the cryostat. A 2x2 array of HDPE lenses then focuses the beams into the mixer feedhorns.

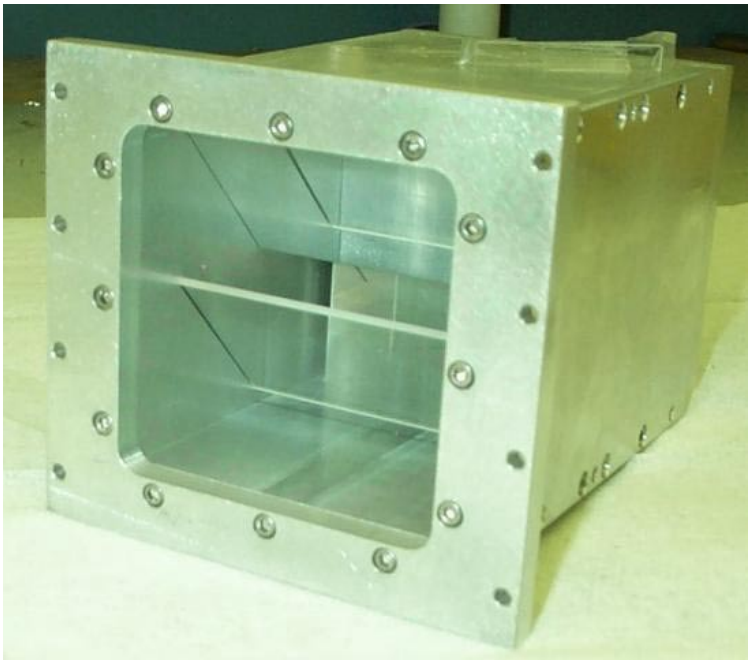

Figure 4: PoleStar's quasioptical LO power splitter.

Pole Star Front-End Design

Cryostat

The Pole STAR cryostat (Figure 5) was constructed by Precision Cryogenics and is based on the successful CSO hybrid design. It uses a CTI model 350 coldhead to cool the outer and inner radiation shields to ~77 and ~12 K, respectively and a 4 liter liquid helium can to maintain the mixers at their operating temperature. This same basic design is used for all AST/RO and CSO receivers. In the single pixel AST/RO receivers, 30.5 mm diameter, Teflon coated, crystalline quartz windows are used at 300 and 77 K. Zytex is used as the IR filter on the 12 K radiation shield. With a good vacuum, hold times of ~6 days can be achieved. With Pole STAR, we have 4 such apertures to contend with in the same cryostat. Furthermore, Teflon coated, crystalline quartz windows are difficult to obtain and the emerging beams from our close-packed lens array makes it impossible to fabricate 4 independent vacuum windows. At 77 K, we have simply substituted an additional layer of Zytex for the 50 mil quartz windows. For the 300K vacuum window, we are using a 7.62 mm thick disk of HDPE in which 4 cylinders with the diameter of the emerging beams have been milled out to a depth of 6.65 mm (see Figure 6). The membrane thickness at the bottom of the cylinders corresponds to 4 lambda at 370 microns. The machining of these windows leaves behind a thick cross member structure

which helps keep the window from collapsing under atmospheric pressure. The absorption loss through the window is estimated to be <5%. With all 4 mixers and amplifiers mounted in the cryostat, the measured hold time is ~3 days. The holdtime is much better than expected based upon the optimum performance of the single pixel receivers. This was achieved by doing away with the 'vent' tube normally used in these cryostats. In the lab we have found that without the vent tube, the fill line is LESS likely to ice up, most likely due to the increased back pressure of helium gas.

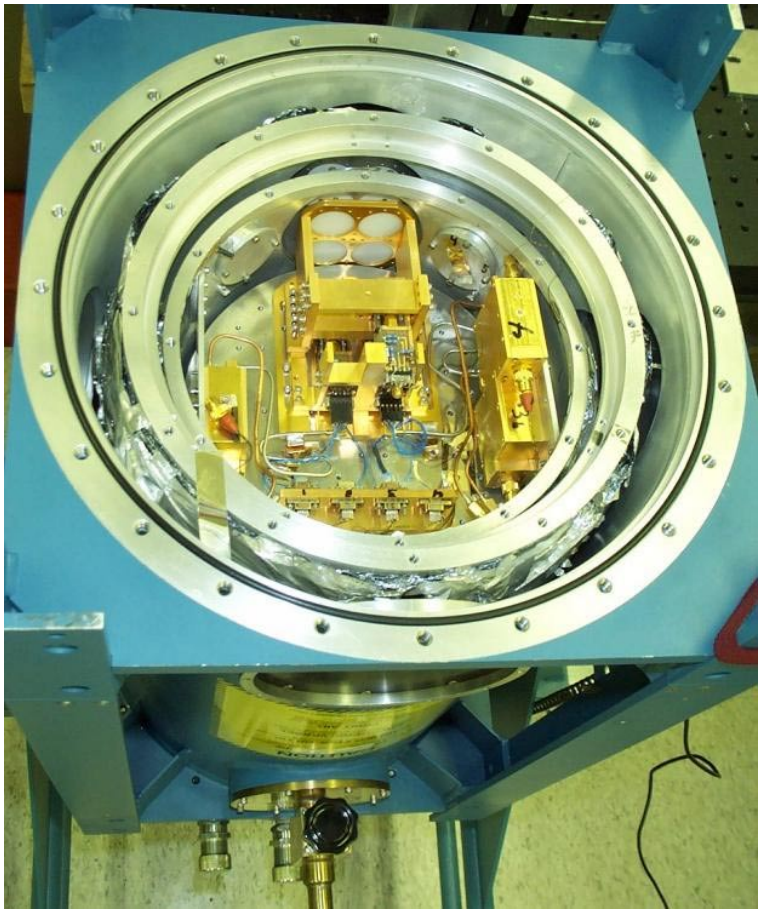

Figure 5: Layout of PoleStar array cryostat.

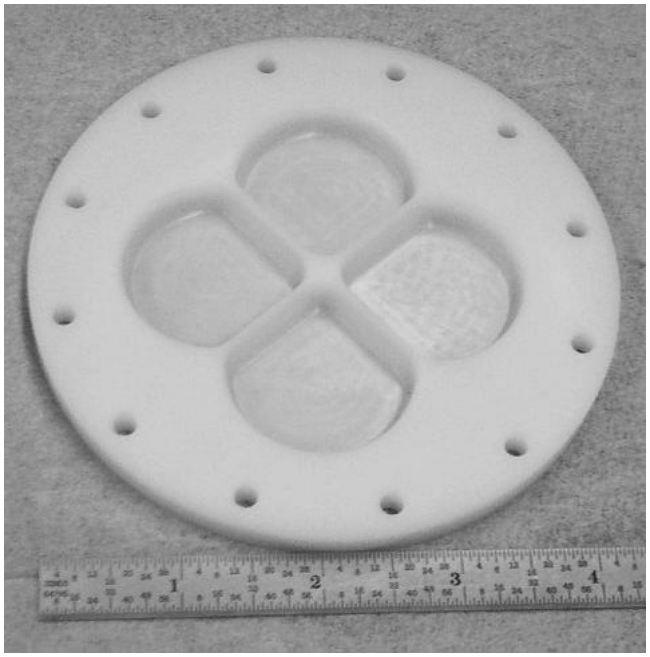

Figure 6: HDPE vacuum window for PoleStar.

Mixers

The SIS mixers used in PoleStar were made by KOSMA. Each mixer uses a Potter horn with a circular to ½ height waveguide transition to couple radiation to a Nb SIS junction. The junctions achieve low noise (~450 - 650K) performance through the use of an on-substrate Al tuning structure and a fixed waveguide backshort. The mixers have embedded magnets to suppress the Josephson effect. A four-wire bias system is used to ensure stable operation of the mixers.

Pole Star IF Processing

Figure 7 provides a global schematic of the IF processing in Pole Star. The 1.5 GHz output of each mixer is amplified ~30 dB by a low-noise, 1-2 GHz amplifier mounted to the cryostat's 12 K radiation shield (Figure 5). The amplifiers are balanced and have a Lange coupler on their input, effectively eliminating the need for an isolator. Each signal is then amplified an additional 35 dB by room temperature Miteq amplifiers mounted on the dewar frame.

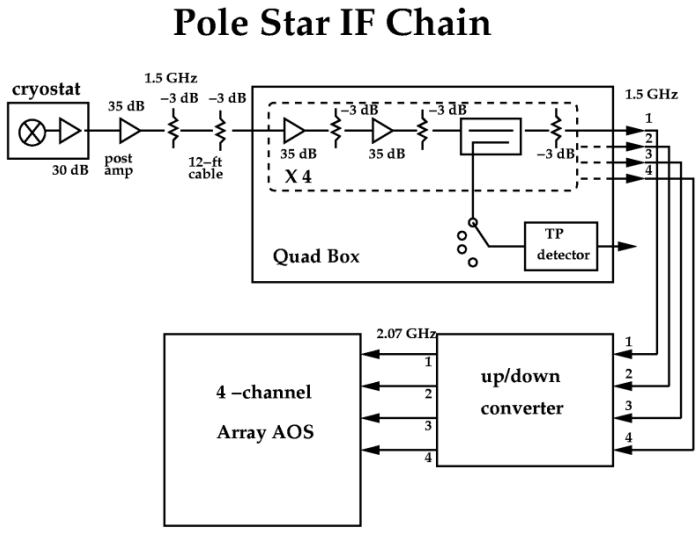

Figure 7

After passing through a 3.6m cable run the array IFs enter a 4-channel total power box. The total power box provides 60 db more amplification and contains a bandpass filter and crystal detector that permits the total power of each receiver channel to be measured either manually or under computer control. Once through the total power box, the 4 IFs enter an up/downconverter box which translates the 1.5 GHz IFs to 14.5 GHz and then down to 2.075 GHz, the center frequency required by the array Acousto-Optical Spectrometer (aAOS) (see the next section).

Pole Star Array AOS

The Array AOS (aAOS) built by KOSMA provides four independent spectrometer channels, each with ~1 MHz of spectral resolution over a 1 GHz bandwidth. At 810 GHz, these numbers translate to 0.37 and 370 km/s respectively. It uses a single laser, a 4-channel, lithium niobate Bragg cell, and a custom CCD to achieve its performance parameters. The aAOS has been successfully tested on the IRAM 30m and CSO.

Pole Star Bias Control

Hardware

The SIS junctions, the electromagnets used to suppress quantum-generated mixer noise, and the Low Noise Amplifiers (LNA's) all require noise-free, accurate electrical biasing for reliable operation. On single-pixel receivers, providing the appropriate biasing voltages and currents is handled adequately by individual boxes with manual potentiometers and LCD panels on the front. With the advent of array receivers, however, the sheer number of boxes required makes this kind of control impractical. The PoleStar

bias system uses proven circuit design used on single pixel receivers at AST/RO and the Henrich Hertz Telescope. We replace the manual potentiometers in these designs with a Xicor digital potentiometer, and package 4 channels of bias on a single Euro 96 card. These modular 4 channel cards can be plugged into a backplane in a 19" equipment rack, allowing easy extensibility to more channels. All digital communications with the bias system are done through a bi-directional optically isolated connection with the control computer. The I^2C bus used for digital communications has a separate clock line. The digital lines, including the clock, are only active when changing a bias setting. The voltages and currents for the SIS junctions, magnets and amplifiers, the total power from the 4 channel total power box and the cryostat temperature information are read through a A/D card in the control computer. Signals from the bias system are multiplexed with Burr-Brown analog mulitplexers, and read through a single BNC output. This design eliminates any clocks or digital signals in the bias rack except when changing to a new bias value.

A block diagram of our bias control system is shown in Figure 8. This design can support up to 16-channels with no modifications, and is extensible to over 100 channels in its current configuration using a single control computer.

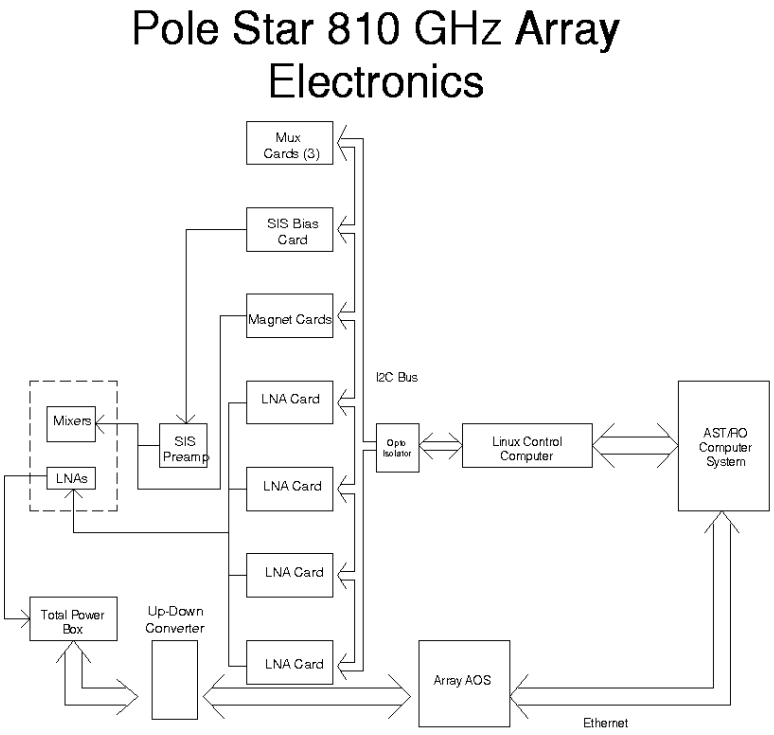

Figure 8

Software

The philosophy of compactness and flexibility, seen in the design of the computer controlled bias electronics, carries into the software design as well. The I^2C signals needed by the electronics is generated at the parallel port of an otherwise normal rack-mounted PC running the Linux operating system. The excellent documentation of system internals, tight use of system resources, remote accessibility via X-Windows, and free compilers and programming tools make Linux an excellent choice for this design. An Intelligent Instrumentation PCI-20428W multi-purpose Data Acquisition (DAQ) card is used for non-I^2C control of the instrument.

The actual array software is highly modular and the source code, written in C and supplemented by Perl CGI is nearly independent of the hardware. The actual graphical user interface takes advantage of the open source, popular and highly capable GTK+ X-Windows toolkit. All bias control functions can be accessed remotely. The mixer bias control window is shown in Figure 9. The current Pole Star PC is powered by a 75 MHz AMD K5 processor, comparable to a 75 MHz Pentium, and with "only" 32 MB of RAM.

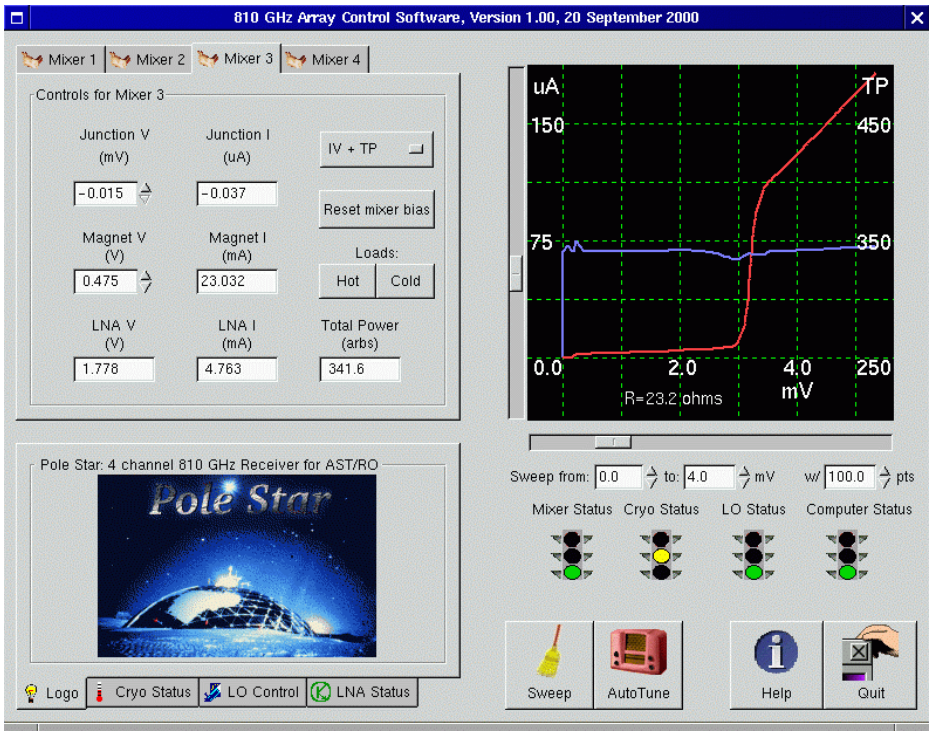

Figure 9: SIS bias control window on PoleStar

Pole Star Performance

Receiver Noise Measurements

Figure 10 shows the LO pumped IV curves of each of the 4 mixers together with IF power sweeps. The red curve shows the IF power output when a HOT (290K) load is placed in front of the receiver. The blue curve shows the response with a COLD (77K) load . When the system performance was optimized for each channel in the lab, a Y-factor of ~1.2 was achieved for receivers channels 1, 2, and 3, Due to a small misalignment of the mixer's feedhorn (later corrected), a Y-factor of 1.12 was achieved on channel 4. A Y-factor of 1.2 corresponds to a receiver noise temperature of ~970K and includes all loss (optics, windows, Martin-Puplett, IF amp, etc.) in the system.

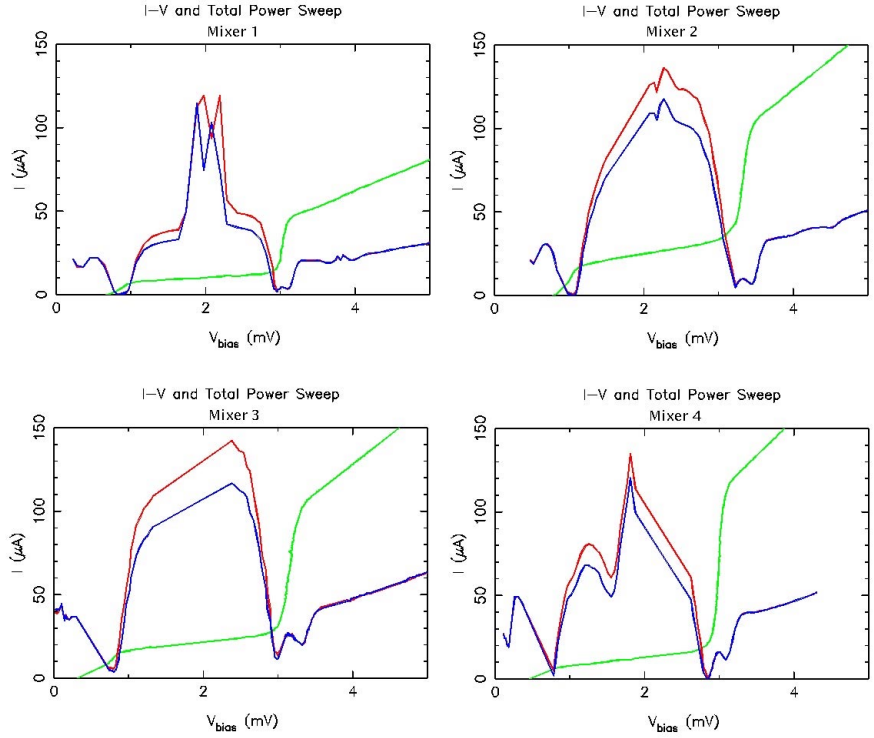

Figure 10: PoleStar receiver performance curves.

These receiver noise temperatures are about a factor of two higher than those obtained with the same mixers in a laboratory receiver system at KOSMA. In the KOSMA measurements reflective optics and a Mylar vacuum window and LO beamsplitter were used. We estimate the HDPE mixer lens and vacuum window used in Pole STAR add ≤100 K to the receiver noise temperature. The balance of the receiver noise temperature appears to come from optical loss in the Martin-Puplett LO diplexer. Due to the long path lengths and relatively large beamwaists required by the array, a loss of 3 dB in the

Martin-Puplett can occur if there is as little as ~0.5° tilt in the entrance beam. With a single pixel system, it is often possible to adjust the relative position of the Martin-Puplett and receiver cryostat to compensate for small alignment errors. When dealing with multiple pixel systems this is much more difficult to do. Indeed, when all 4 receiver channels were optimized for simultaneous operation in Pole STAR, walk-off effects in the Martin-Puplett added an additional ~3 dB of optical loss. These results suggest that the implementation of Martin-Puplett diplexers for large format arrays may in practice be problematic. If a narrower operational bandwidth and some loss (~3 dB) in LO power can be tolerated, a better approach may be to use a thin (~3 mm) silicon etalon (Mueller 2001) as an LO diplexer. The small path lengths through such a silicon beamsplitter would minimize the adverse effects of small optical misalignments.

Receiver stability measurements on Pole STAR were made by monitoring the IF output power of 2 of the receivers over ~1000 sec. The IF power variation was about 1 part in 1000 over this period.

Beam Pattern Measurements

A computer controlled antenna test range was constructed to measure the 4 Pole STAR beams. We used a liquid nitrogen load with a 10 mm aperture as the signal source. The signal was chopped and synchronously detected using a lock-in amplifier connected to the receivers' total power output. Maps of the 4-beams and their relative placement are shown in Figure 11. To within the measurement errors the beams have the right size and shape. One beam (from Mixer 3) had a small squint angle compared to the others. On warm-up, the horn on this mixer was found to be out of alignment and was readjusted.

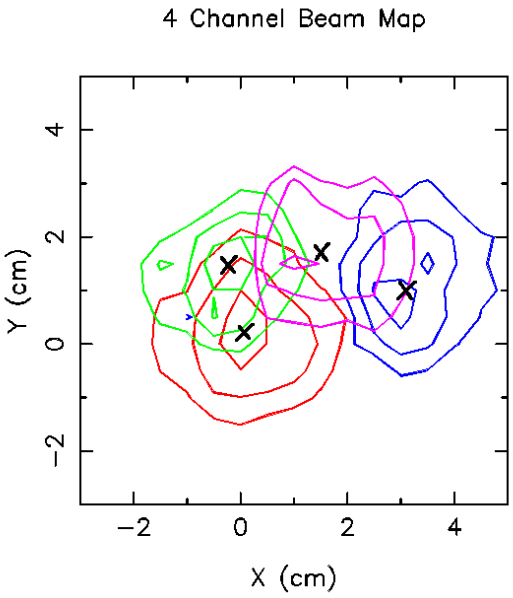

Figure 11: PoleStar beam patterns.

First Light on AST/RO

Pole STAR was installed on AST/RO during a 3 week period from mid November to early December 2000. Figure 12 shows the First Light spectra obtained toward NGC 6334. Two CO J=7→6 and [CI] lines were observed. Pole STAR will remain at the Pole and be used for astronomical observations later this year.

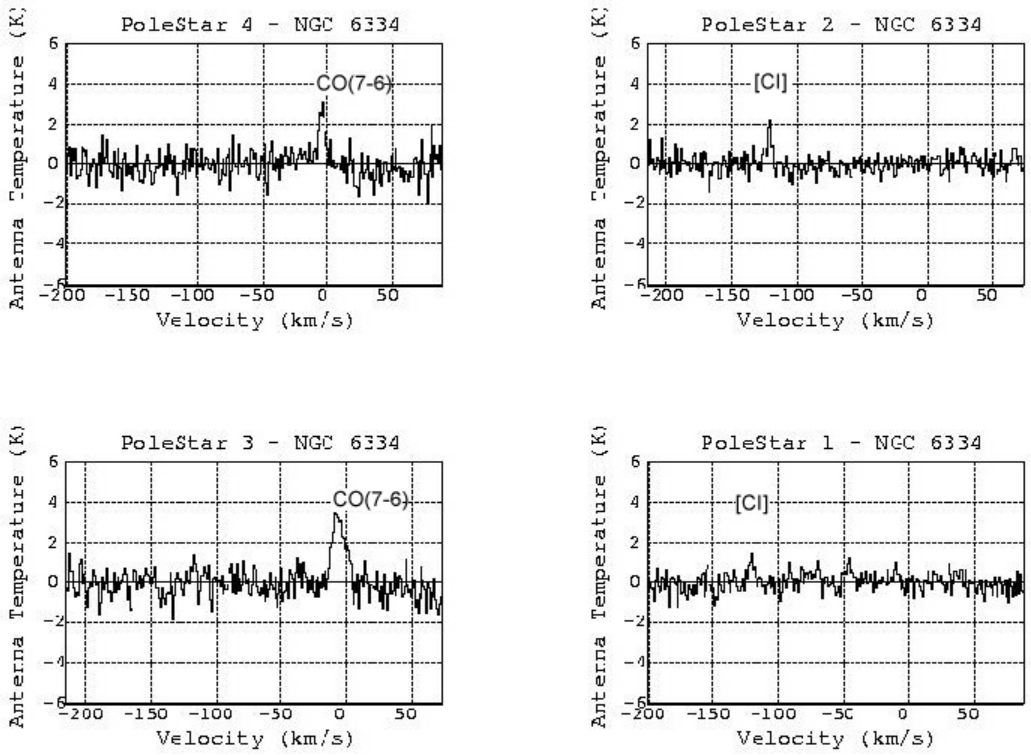

Figure 12: First light spectra taken with PoleStar at AST/RO.

Summary

We have constructed a 2×2, 810~GHz array receiver for the AST/RO telescope. The array utilizes a common set of reimaging optics, an efficient 4-way quasi-optical LO power splitter, a solid-state LO, low noise mixers, a flexible computer controlled bias system, and an array AOS. The system is modular, permitting upgrades to be made as new technologies become available.

References

Mueller, E., 2001, DeMaria ElectroOptics Systems, Inc., 1280 Blue Hills Ave., Bloomfield, CT 06002}.

Stark, A. et al., 2001, *The Antarctic Submillimeter Telescope and Remote Observatory (AST/RO), PASP*, in press}.

KOSMA's 490/810 GHz Array Receiver

U. U. Graf, S. Heyminck, E. A. Michael, S. Stanko

KOSMA, I. Physikalisches Institut, Universität zu Köln, Zülpicher Straße 77, 50937 Köln, Germany. E–mail: *lastname*@ph1.uni-koeln.de

ABSTRACT

We describe the frontend design of KOSMA's new multi frequency SIS array receiver, which is currently being built to be used at our submillimeter telescope. The receiver consists of two 2×4 mixer arrays. One array operates at a frequency of 490 GHz, the other one at 810 GHz. We can thus simultaneously observe eight spatial positions in two frequencies.

After passing through a K–mirror type image rotator, the two frequencies are separated by polarization and individually combined with their local oscillators (LOs), using Martin–Puplett diplexers. Splitting of the LOs is performed with a new type of phase grating, the collimating Fourier grating.

Because of space and weight restrictions at the 3m KOSMA telescope, most of the optics is outside the dewar. The dewar window is located at an image plane of the telescope pupil to reduce the window size. Inside the dewar the two polarizations are split and the individual beams are focused into the feed horns with a faceted mirror. The opto–mechanical design makes extensive use of our CNC machining capabilities. As far as possible we machine complete sub–units from monolithic blocks, in order to reduce the need for optical alignment.

We describe the optical design of the instrument and present the first test results obtained in early 2001.

GENERAL FEATURES

The receiver will be installed at the KOSMA 3m telescope[1] at Gornergrat near Zermatt/Switzerland later this year. It will be capable of observing two frequency bands simultaneously extending from approximately 450 to 500 GHz and from 800 to 880 GHz, respectively. The two frequencies are split by polarization.

Each frequency is equipped with a 2×4 pixel array of waveguide SIS mixers. The two subarrays are superimposed on the sky with a spacing between the array pixels

of 100″, which corresponds to twice the FWHM of a single beam at 490 GHz. We use a K–mirror type image rotator to compensate for the image rotation introduced when tracking an astronomical source with an Alt–Az–mounted telescope.

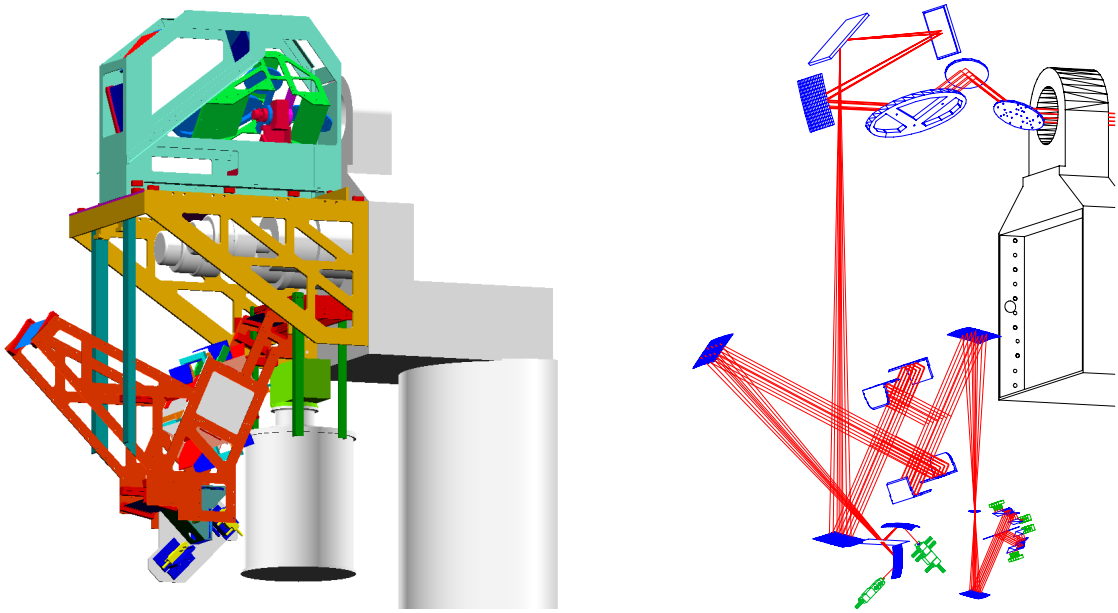

(a) Receiver geometry (b) Beam path

Figure 1. Drawings of the receiver layout and the beam path as it will be mounted at the telescope.

The detectors are fixed tuned SIS waveguide mixers.[2] The IF signals are analyzed with four 4–channel array–acousto–optical spectrometers.[3] In order to speed up the tuning cycle of the instrument, we implemented a computer controlled automatic mixer tuning algorithm, which sets the mixer bias voltages and the magnet currents to suppress the Josephson effect. The software also advises the observer to increase or decrease the local oscillator (LO) power level for optimum mixer performance.

Since the telescope and the observatory are relatively small, we had to make an effort to keep the instrument as compact as possible. We therefore placed most of the optics elements at ambient temperature to reduce the dewar size, although this will increase the receiver noise temperature to some extent.

The two frequencies each use one LO chain which is multiplexed between the 8 mixers using a new variant of the recently developed Fourier grating[4,5], a reflective phase grating.

The optical alignment of the instrument is simplified by the usage of pre-aligned optical building blocks, which are quasi–monolithically machined on a CNC milling machine.

We use a closed cycle Gifford–McMahon refrigerator* to cool the detectors to approximately 4 K.

Fig. 1 shows the receiver mounted to the telescope. In order to keep a compact arrangement, the receiver optics wraps around the telescope structure and the elevation drive motors sticking out of it. The instrument consists of three main parts: the image rotator unit, which is mounted above the triangular receiver mounting brackets, the main optics part, which contains the LO–unit and the diplexer unit, and the dewar.

OPTICAL LAYOUT

The instrument uses one of the Nasmyth ports of the KOSMA telescope (Fig. 1). The first optical element is the image rotator, which consists of three plane mirrors mounted in a K–arrangement on a rotating unit. The subsequent optics contains two Gaussian telescopes. The first Gaussian telescope reimages the focal plane to the center of the diplexer unit. Within the diplexer unit, the signal is split by a polarizer grid to distribute the two input frequencies to two independent Martin–Puplett interferometric diplexers. The same polarizer grid is used to couple the LO signals into the diplexers. The output ports of the diplexers are combined again using a second polarizer grid.

The second Gaussian telescope reimages the diplexer waists to the mixer units inside the dewar. The dewar window is located between the two mirrors forming this Gaussian telescope. To minimize the window size, we put it at an image of the telescope aperture, where the beam cross section is minimal.

The space underneath the diplexer unit is taken up by the LO–unit, creating and distributing the LO signals. This unit is described in detail in the paper by Heyminck and Graf.[5]

The mixer units inside the dewar collimate and combine the beams of the individual mixers before injecting them into the common optics. In contrast to other array receiver designs[6,7,8], we avoided lenses and use only reflective optics in the design of the mixer units.

*Sumitomo, SRDK–415

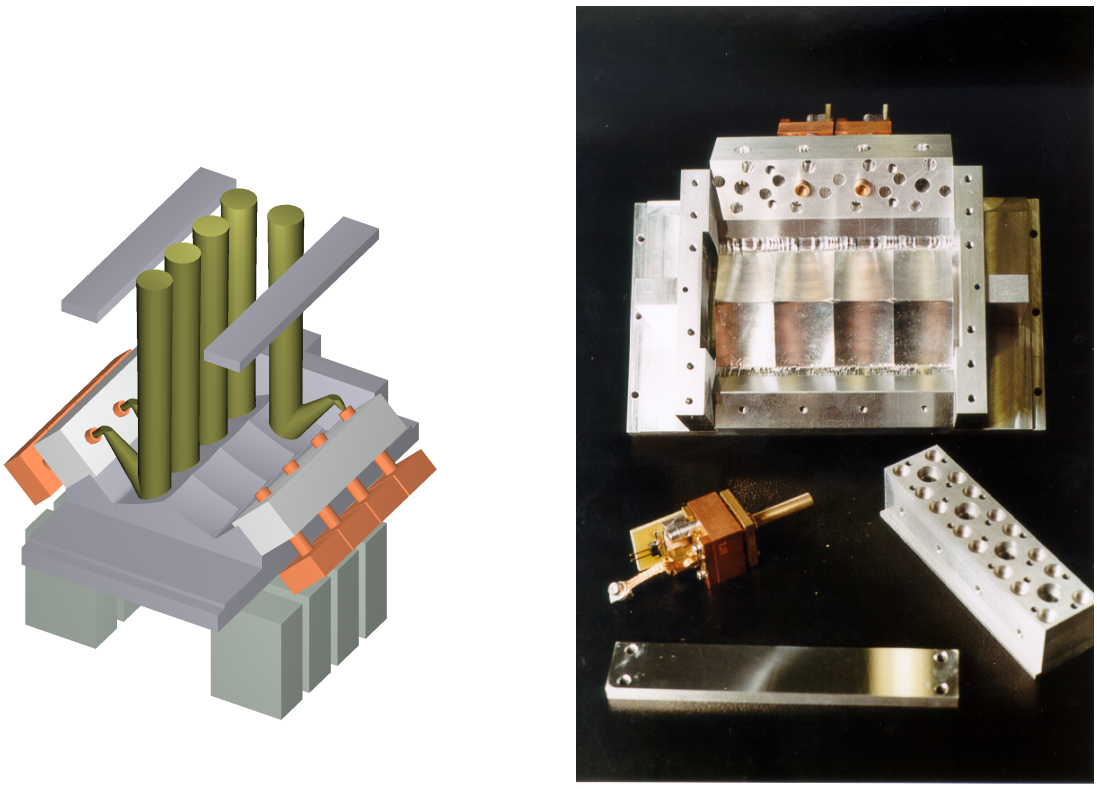

(a) (b)

Figure 2. Drawing (a) and photograph (b) of the 490 GHz mixer unit. The beam from the mixer feed horn is reflected by a plane mirror onto one of eight paraboloidal mirror facets, which collimates the beam for injection into the array optics.

MIXER UNIT

The relative spacing of the array pixels on the sky is determined by the ratio of the beam spacing to the beam waist at the point where the beams enter the common receiver optics. In order to reduce the beam spacing on the sky it is therefore necessary to increase the individual beam waists before injecting them into a common optics. This is most easily done with a collimating optical element directly in front of each mixer. Fig. 2 shows the arrangement we have chosen, to achieve the collimation with purely reflective optics.

The divergent beam from the mixer feed horn is reflected back by a plane mirror (lifted up in Fig. 2(a) to expose the underlying features) onto a paraboloidal collimating mirror. 8 paraboloids for the 8 mixers are combined to create a facetted mirror block. These mirror facets together with the mounting surfaces for the plane mirrors and for the blocks holding four mixers each, are machined in one machining cycle on

a numerically controlled milling machine. This means that from the first to the last cut neither the workpiece nor the tool have been removed from the machine, making sure that all the machining is done in the same machine reference frame. Through this technique the accuracy of the finished workpiece does not depend on the skills of the machinist anymore, but exclusively on the positioning accuracy of the machine. The latter, we estimate is on the order of a few microns for the relative positioning of all the relevant surfaces of the block.

To avoid alignment errors introduced by the mounting of the mixers, we decided not to fix the mixer blocks in place, but rather to hold the feed horns in their exact positions. In this way we exclude alignment errors from the fact that feed horns may not always be perfectly aligned perpendicular to the mixer body. Accurate positioning of the feed horns is achieved by inserting them into tight fit reamed holes in CNC–precision machined blocks, which in turn are mounted to the CNC–machined mounting surfaces on the mixer units.

Fig. 2(b) shows a photograph of the finished parts of the mixer unit for 490 GHz, with two mixer blocks mounted and a third one ready to be mounted. Fig. 3 is a side view of the fully assembled unit, showing four mounted mixer blocks and the HEMT–amplifiers connected to them.

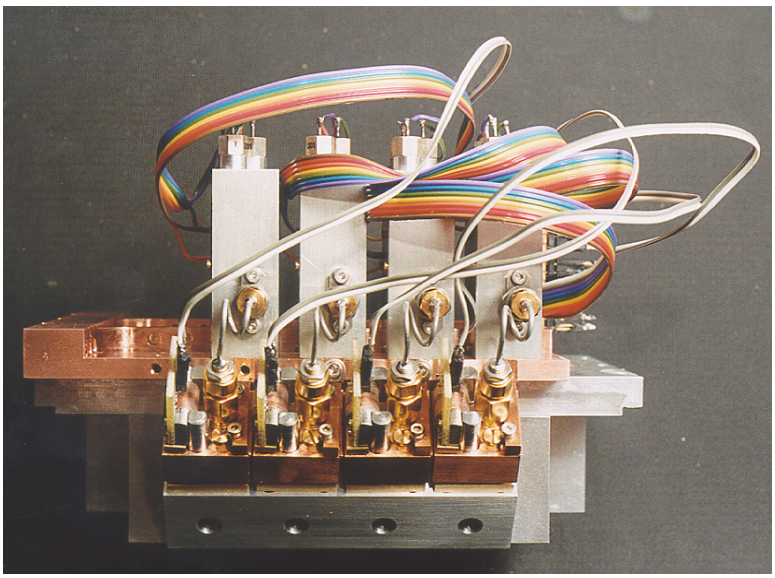

Figure 3. Side view of the assembled 490 GHz mixer unit showing four mixers and their HEMT amplifiers.

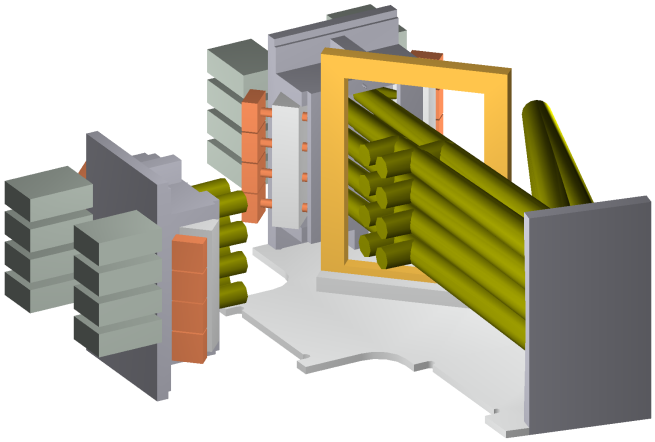

Figure 4. Drawing of the 4K assembly. Two mixer units, the polarizer grid and the first common mirror of the array optics are sandwiched between two identical, CNC–machined plates (top plate not shown here).

THE 4K ASSEMBLY

Two mixer units are mounted together with a polarizer grid and the first common mirror to form the 4K assembly of the receiver (Fig. 4). Again we simplified the alignment by precision machining all the components. The optical elements are sandwiched between two identical plates. The outer contour of these plates has been cut in one machining cycle on the CNC milling machine, thereby creating the mounting surfaces for all the optical elements and a number of stiffening plates with very high accuracy.

There are no adjustable parts in the 4K assembly. When all the pieces are bolted together, it forms a single optical element, which only has to be aligned to the rest of the receiver optics as a whole. In this way the 16 pixel array receiver does not require more optical adjustments than a single pixel receiver.

Mounted inside the dewar, the 4K assembly is hanging down from the dewar top plate by a number of epoxy straps. All the electrical feed throughs as well as the cold head flange are located in the top plate of the vacuum vessel. This design improves the serviceability of the system, since all the components can be accessed easily after removal of the dewar cylinder and the radiation shield.

The refrigerator cold head is connected to the mixer units with flexible copper straps to reduce the mechanical coupling and to provide a thermal low pass to dampen temperature fluctuations.

CLOSED CYCLE REFRIGERATOR

We use a Sumitomo SRDK 415 closed cycle refrigerator to cool the instrument to 4 K. The high cooling capacity of the refrigerator (approximately 1.5 W at 4 K) is very convenient. However, the cold head temperature fluctuates significantly. Fig. 5 shows the temperature fluctuations measured at different places during a 3 second time interval. Directly at the cold head, the peak to peak temperature change is almost 150 mK. This variation is dampened to some extent on the way to the mixer unit, where we measure a peak to peak variation of somewhat less than 20 mK. It is not clear, how much of this variation is seen by the SIS junction, because some of it may also be dampened by the thermal coupling to the mixer block. If further measurements indicate that the temperature change at the junctions is significant, we will either have to compensate it with a regulated heater or dampen it more by adding a passive volume of liquid helium.[9]

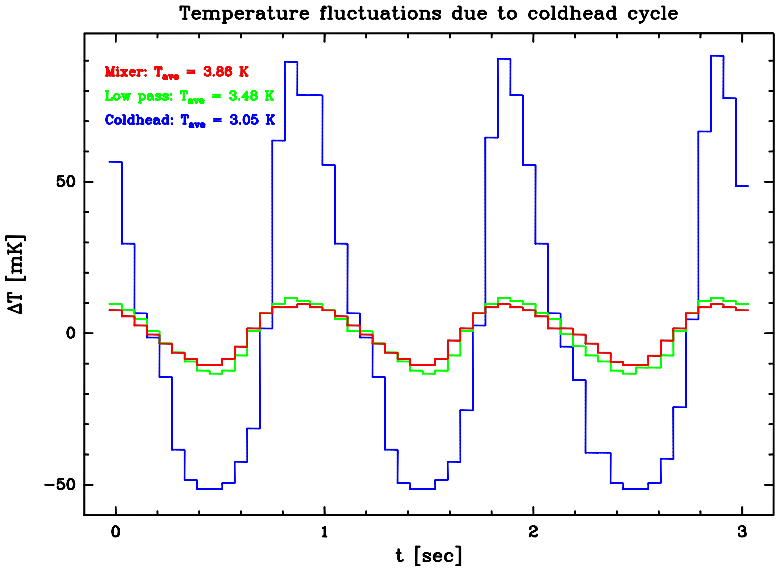

Figure 5. Temperature fluctuation measured at different places.

In addition to the temperature fluctuations, the cold head introduces vibrations to the system. Measurements with an accelerometer indicate that at some places in the receiver these vibrations reach an amplitude of several tens of microns. We are currently developing a vibration damping system to reduce these oscillations.

FIRST RESULTS

Shortly before the Symposium, we obtained our first results with a preliminary setup of only two active mixers inside the dewar. The main purpose of these measurement was to find out whether the optical concept of the receiver is reasonable. We used a chopped cold load mounted on an XY–translation stage to scan the intensity distribution in the receiver beams near the location of the telescope focus. Fig. 6 shows the beam maps measured.

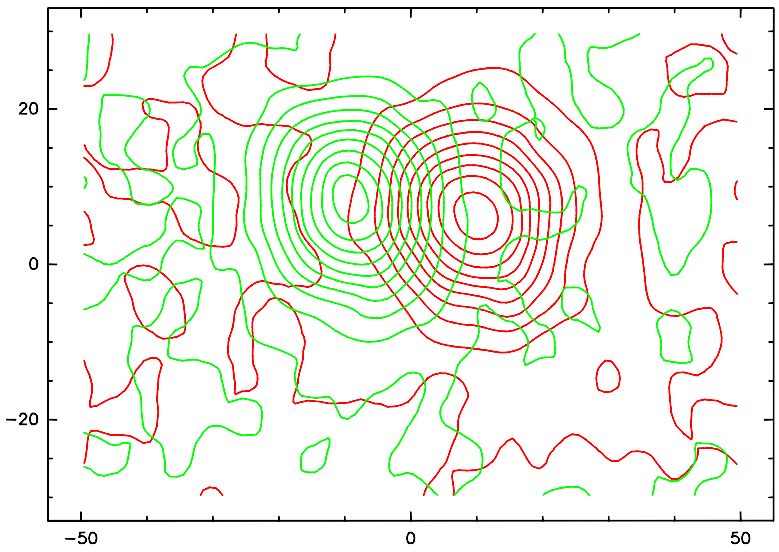

Figure 6. Beam map measured simultaneously with two mixers at 490 GHz.

Both beams are round and have the same size, which coincides with their nominal size to within 5%. Also the spacing between the two beams agrees well with the design value. Although this result is very preliminary, and more beam maps will have to be measured with a complete array, it indicates that the optical setup performs as designed.

Receiver noise temperatures have not been measured yet, because the polarizer grids required in the diplexer unit have not been delivered, due to a severe delay in the manufacturing. Thus, the measurements described above were made with Mylar beam splitters as substitutes for the polarizer grids in the Martin–Puplett diplexer, which results in a high loss in the diplexer and greatly increased receiver temperature.

CONCLUSION

We have built a dual–frequency 490/810 GHz, 16 pixel array receiver system, which is scheduled to be operational at the KOSMA telescope by fall 2001.

The frontend optics design of the receiver makes massive use of our CNC–machining capability. Wherever possible, we precision machine optics building blocks containing several optical elements in one prealigned unit. Through this technique we reduce the alignment effort for the array receiver to a level typical for a single pixel receiver.

We have obtained the first preliminary measurements of the receiver's antenna patterns, indicating that the optical setup works as designed. Further measurements will be made during the testing phase which has just started. Also, we will have to investigate the extent of instabilities introduced by the closed cycle refrigerator and possibly find ways to eliminate them.

ACKNOWLEDGMENTS

This work was supported by the *Verbundforschung Astronomie* through grant 05 AH9PK1, by the *Deutsche Forschungsgemeinschaft* through grant SFB 494, and by the ministry of science of the state Nordrhein–Westfalen.

REFERENCES

1. C.G. Degiacomi, R. Schieder, J. Stutzki, and G. Winnewisser. The KOSMA 3–m Submillimeter-Wave Telescope. *Optical Engineering*, 34(9), 1995.
2. S. Haas, C.E. Honingh, D. Hottgenroth, K. Jacobs, and J. Stutzki. Low noise broadband tunerless waveguide SIS receivers for 440–500 GHz and 630–690 GHz. *Intl. J. IR mm Waves*, 17(3), 1996.
3. R. Schieder, J. Horn, O. Siebertz, C. Möckel, F. Schlöder, C. Macke, and F. Schmülling. Design of Large Bandwidth Acousto–Optical Spectrometers. In Thomas G. Phillips, editor, *Advanced Technology MMW, Radio, and Terahertz Telescopes*. Proceedings of SPIE Vol. 3357, 1998.
4. U.U. Graf and S. Heyminck. A Novel Type of Phase Grating for THz Beam Multiplexing. In *Proceedings of the* 11th *International Symposium on Space Terahertz Technology*, Ann Arbor, 2000. University of Michigan.
5. S. Heyminck and U.U. Graf. Array-Receiver LO Unit using Collimating Fourier Gratings. In *Proceedings of the* 12th *International Symposium on Space Terahertz Technology*, San Diego, 2001.
6. K.-F. Schuster et al. The IRAM 230 GHz multibeam SIS receiver. In R. Blundell and E. Tong, editors, *Proceedings of the* 8th *International Symposium on Space Terahertz Technology*, Cambridge, 1997. Harvard University.

7. R. Güsten et al. CHAMP — the carbon heterodyne array of the MPIfR. In Thomas G. Phillips, editor, *Advanced Technology MMW, Radio, and Terahertz Telescopes*. Proceedings of SPIE Vol. 3357, 1998.
8. C. Walker et al. Pole STAR: An 810 GHz Array Receiver for AST/RO. In *Proceedings of the* 12th *International Symposium on Space Terahertz Technology*, San Diego, 2001.
9. R. Li, A. Onishi, T. Satoh, and Y. Kanazawa. Temperature Stabilization on Cold Stage of 4 K G–M Cryocooler. In Ronald G. Ross, Jr., editor, *Cryocoolers 9*, New York, 1997. Plenum Press.

Array-Receiver LO Unit using collimating Fourier-Gratings

S. Heyminck and U.U.Graf

KOSMA, I. Physikalisches Institut der Universität zu Köln,
Zülpicher Straße 77, 50937 Köln, Germany

Abstract

The local oscillator (LO) unit in our 490/810GHz array receiver needs to transform a divergent beam coming from a horn antenna into an array of well collimated beams. Based on our development of reflective phase gratings (Fourier gratings) we designed a compact LO unit using newly developed collimating gratings.

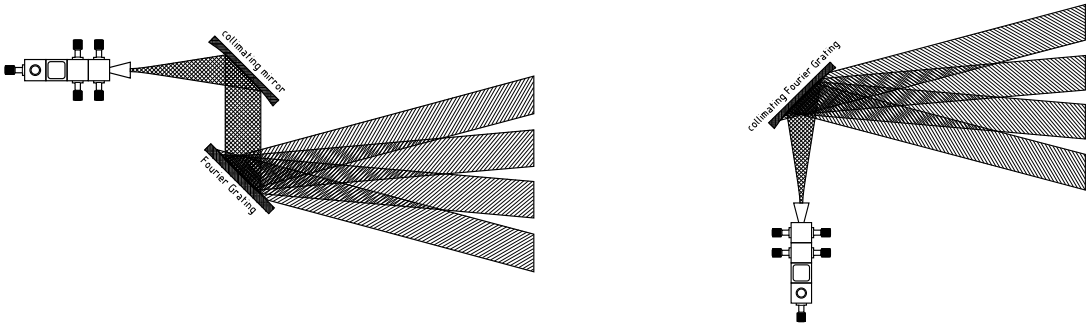

Figure 1. Old arrangement of the LO unit using a collimating mirror and a plane Fourier Grating (left hand side) and the new one with the collimating Fourier grating.

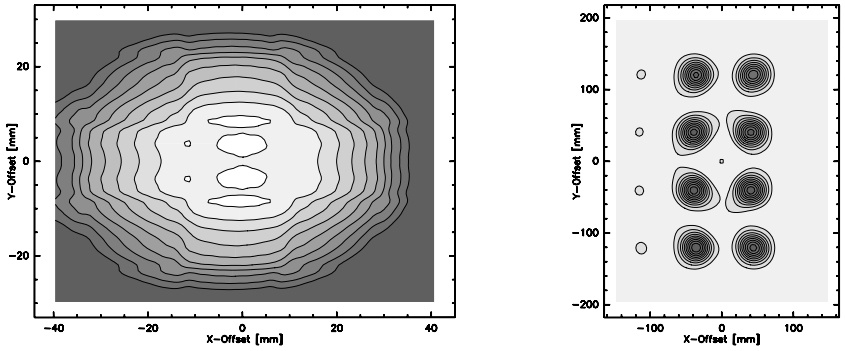

Figure 2. Example of the surface topology of a collimating grating and a computer simulation of its far field diffraction pattern. Contour levels in both plots are from 10% to 90% in steps of 10%.

Further author information: E-mail: lastname@ph1.uni-koeln.de

Using planar gratings, the LO source had to be reimaged to form a plane wave at the location of the grating. The new collimating Fourier grating is matched to the wave front curvature of the divergent beam and does not require an additional collimating element. Because of the smooth grating structure it is possible to produce the collimating Fourier gratings on a commercial numerically controlled milling machine.

We present the design of the grating and the entire LO unit combined with first measurements.

Keywords: phase grating, beam splitter, heterodyne array receiver, submillimeter beam multiplexer, LO unit

Introduction

One problem we had to solve while building the KOSMA Array Receiver was to distribute local oscillator (LO) power to the different mixers. It is impractical in terms of tunability and complexity of the resulting setup to use one LO for each mixer in the array. So it is necessary to use one LO for a larger number of mixers which means multiplexing the LO signal.

Waveguide splitters as they are in use at IRAM[2] work well at longer wavelengths, but are very difficult to manufacture for our frequency range (490GHz and 810GHz).

Using beam-splitters as in the AST/RO - Pole Star array[3] is efficient for a small number of mixers. But with an increasing number of mixers the optics gets more and more complex. For our array of 2 times 2×4 mixers we were looking for a more elegant way of multiplexing the LO.

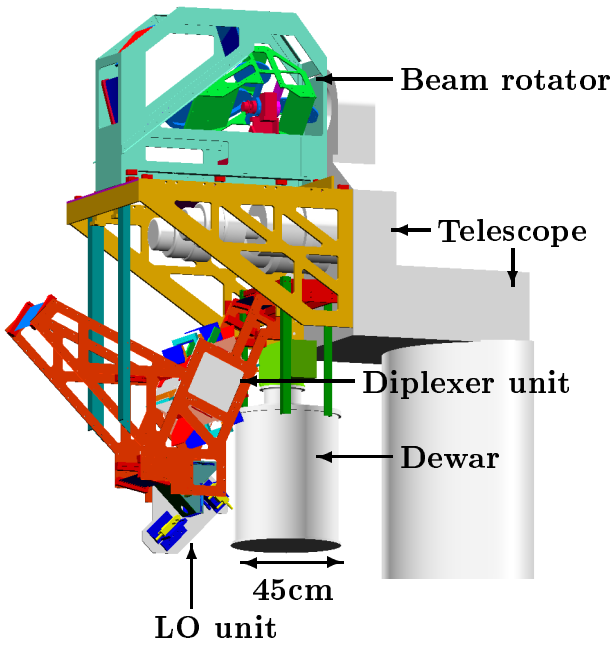

Figure 3. KOSMA Array Receiver[1]

The use of phase gratings to split the local oscillator signal into a given number of equal beams is one other possibility. Binary phase gratings also known as Dammann gratings,[4] or multilevel gratings with higher efficiency, have been used[5,6,7] as LO multiplexers. These stepped gratings are difficult to produce as reflection gratings for a 2 dimensional array of mixers. To overcome this manufacturing problem and to increase the efficiency we introduced the Fourier grating concept.[8,9]

An other important design driver was the need to reduce the number of optical elements to minimize alignment problems. In order to fit the receiver at the relatively small KOSMA telescope[10] on Gornergrat (Switzerland) we also had to shrink some components of the receiver as far as possible.

To reach these goals we combined a parabolic mirror and a Fourier grating to form one optical element. This results in a very compact and simple design of the LO unit (fig. 8).

Fourier gratings[11]

Fourier gratings, as we developed them over the last two years, have a continuous phase modulation. This results directly from the way these gratings are designed. To model the phase structure, we use a finite Fourier series (with typically 13 coefficients per spatial dimension). The coefficients are calculated by a random search followed by an optimization process.

Fourier gratings have a very high efficiency. For most one dimensional diffraction patterns the efficiency is above 90%. In two dimensions it is typically 80% or higher.

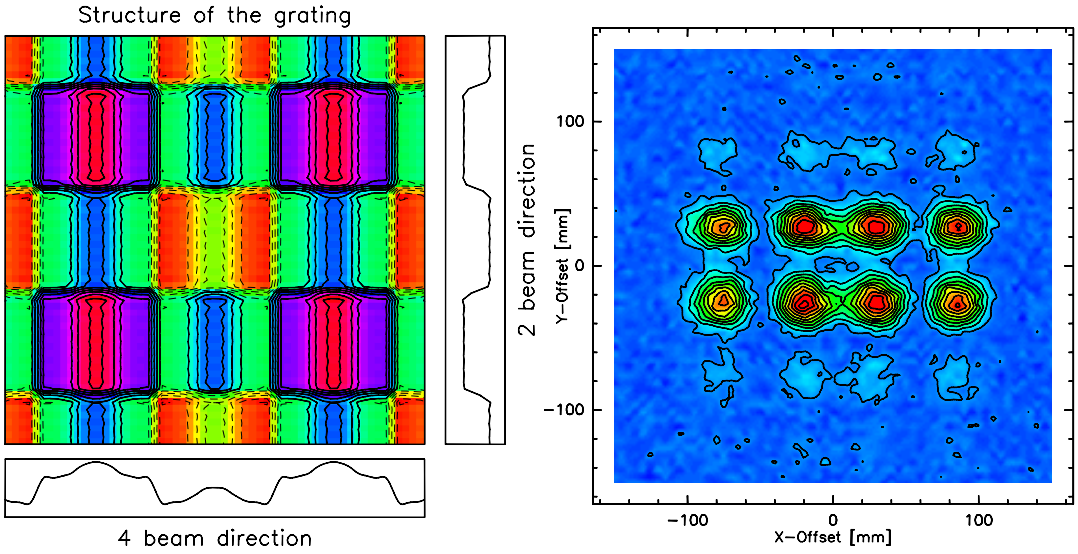

Figure 4. Surface topology of a 2×4 beam grating containing 2×2 unit cells (left hand side). Contour levels are in steps of 0.5 radians. The right hand side shows a measured diffraction pattern produced by this grating structure at 490GHz. Contour levels are from 5% to 95% in steps of 10% of the peak intensity.

Because of the continuous phase modulation, we get a smooth surface structure. This allows a 2 dimensional manufacturing with high accuracy ($\pm 3\mu m$ RMS) on a numerically controlled milling machine. With this manufacturing technique we are not limited to planar gratings, but can also produce grating structures superimposed on a curved surface.

The grating bandwidth is limited to less than ±5% of the design frequency. This range could be stretched somewhat by using a zoom optics setup. However, we considered it simpler to design exchangeable gratings. With a small number (3 to 4) of gratings we can then cover the total bandwidth of a typical astronomical receiver.

An LO unit built with such a planar Fourier grating would look similar to the arrangement shown in figure 1 (left hand side). The divergent beam coming from the horn antenna of the LO has to be reimaged to form a plane wave front at the location of the Fourier grating. This grating is finally multiplexing the signal to the various mixers.

Collimating Fourier gratings

The idea of a collimating Fourier grating is to combine the collimating mirror needed to re-image the LO beam and the grating itself into one optical component. By shrinking the distance between the grating and the collimating mirror (fig. 1 left hand side) to zero, the collimating mirror changes from an ellipsoidal to a parabolic mirror. The grating structure is then superimposed on this mirror.

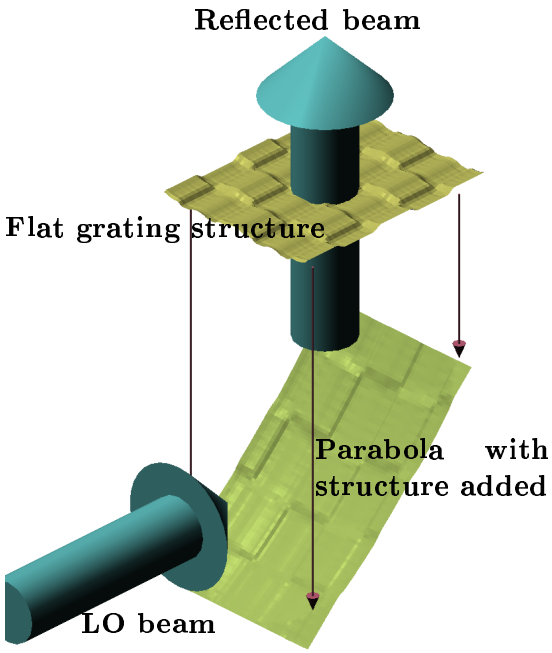

Figure 5. Calculating the grating structure

To do this, the structure of the flat grating is projected onto the parabola along the direction of the reflected LO signal as shown in figure 5. When projecting the grating structure onto the parabola the structure height changes to

$$h = \frac{h_{flat}}{\cos(\alpha)}$$

where α is the local geometrical reflection angle. This height is added along the surface normal of the parabolic mirror. The resulting structure and the theoretical diffraction pattern is shown in figure 2.

A quick and dirty measurement of such a grating is shown in figure 7. The 8 resulting beams and their correct positions are clearly shown. Because of poor alignment the power distribution between the beams is not as expected. Nonetheless, this measurement, together with the numerical simulation and our previous experience with planar Fourier gratings convinced us of the usefulness of these devices.

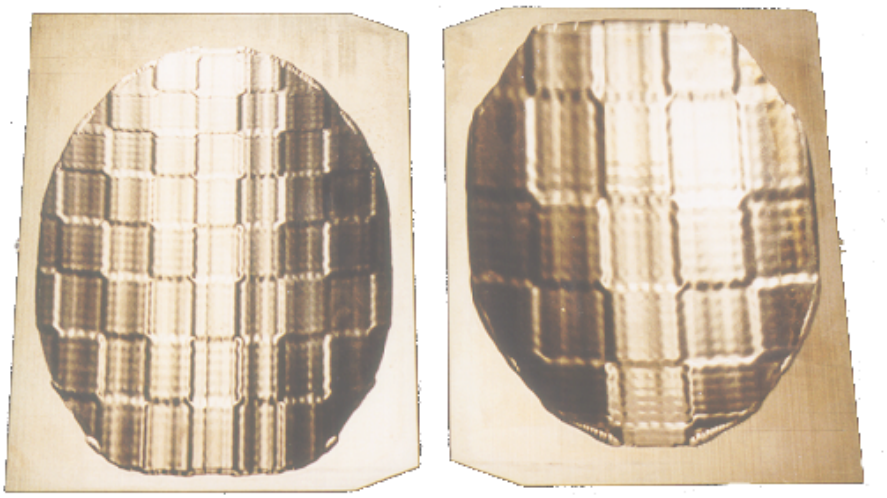

Figure 6. Photograph of the two collimating Fourier gratings for 490GHz (right hand side) and 810GHz. The reference planes around the structure are manufactured along with the grating. One unit cell contains 4 sub cells arranged in a square. The size of the unit cell changes with the design wavelength.

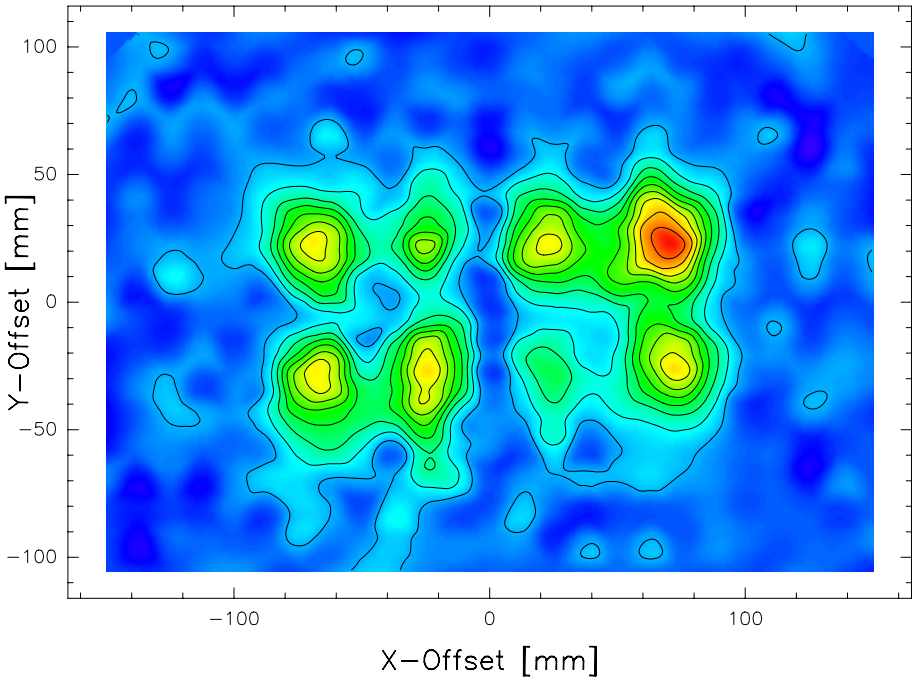

Figure 7. Intensity distribution in the diffraction pattern of a collimating Fourier grating measured at 490GHz. The variations in the intensity of the beams are due to poor alignment in the measurement setup. Contour levels are in steps of 10% of the peak intensity.

KOSMA Array Receiver LO unit

Figure 8 shows the design of the Array Receiver LO unit together with the beam-paths for the two frequencies (490GHz and 810GHz). The two frequencies are superposed onto each other by a polarizer grid.

The gratings and their holders are designed such that the grating can be easily exchanged in order to overcome bandwidth limitations. For different frequencies within the receiver band we can use different gratings to maximize the efficiency of the LO-system. Springs press the grating against three reference surfaces for accurate repositioning. The reference planes on the grating are manufactured along with the grating structure (figure 6). This gives us the position accuracy required and allows a rapid change of the grating without the need for realignment, when the observing frequency is changed.

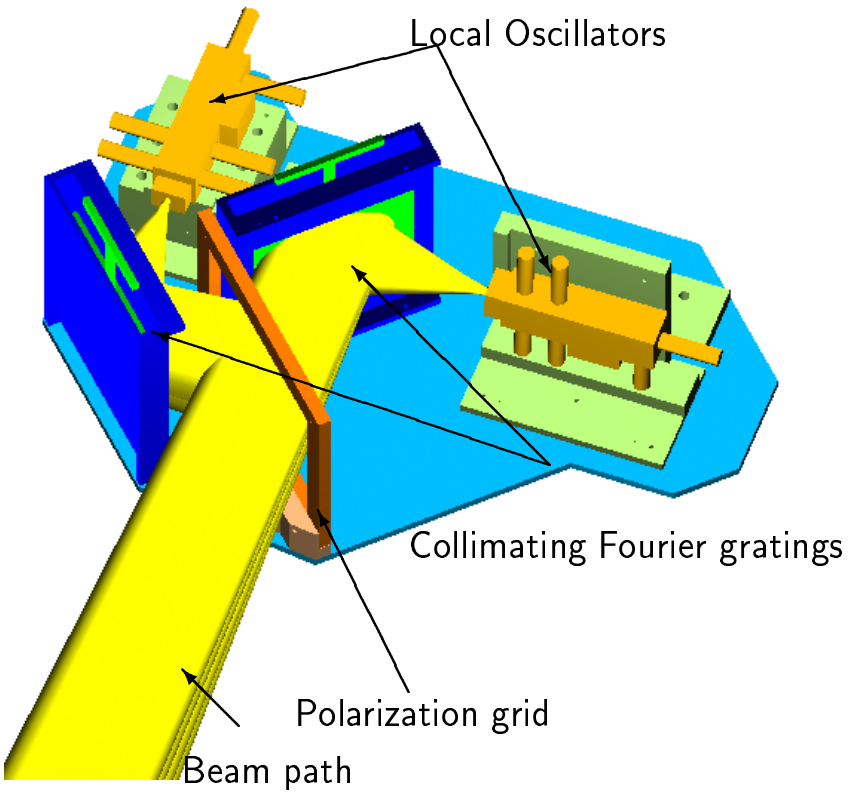

Figure 8. Overview of the LO unit

Equal pump levels were achieved on both mixers during a first test run of the system without doing any alignment work on the LO unit. In figure 9 we show the IV- and the conversion curves of both mixers. Because of the symmetry of the array receiver optics these two mixers represent one half of the array.

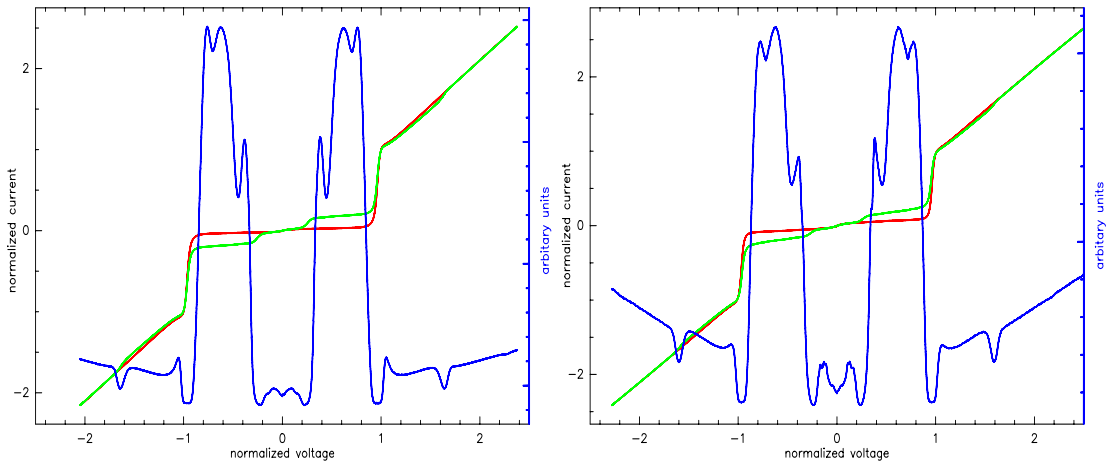

Figure 9. Pumped, un-pumped IV- and conversion curves of the two mixers in the array.

We verified that exchanging of the gratings does not affect the alignment. The pump levels and the conversion curves did not change when removing the grating and putting it back into its holder.

Conclusions

The concept of the collimating Fourier grating works well for the mixer arrangement used in our receiver as is shown by the measured diffraction pattern of the 490GHz grating. Based on earlier tests with flat grating structures for various other mixer arrangements, we are also sure that we can produce collimating Fourier gratings for other diffraction patterns.

In addition to the diffraction measurement, we got equal pump levels in the two mixers we had in the array until now. Removing and putting back the grating has no effect on the pump levels and the conversion curves, indicating that the grating repositions accurately. The additional work in changing the frequency of the array receiver, in comparison to a single pixel receiver, is, therefore, just to swap these gratings.

Simulations and measurements done with the flat Fourier gratings show the high efficiency of the LO splitting by this grating type.

With the LO unit built for the KOSMA 490/810GHz array receiver we reached a compact design which is easy to tune and which is efficient in terms of the LO power distributed to the mixers.

Acknowledgments

This work was supported by the *Verbundforschung Astronomie* through grant 05 AH9PK1, by the *Deutsche Forschungsgemeinschaft* through grant SFB 494 and by the ministry of science of the state Nordrhein-Westfalen.

References

1. U.U.Graf, S.Heyminck, E.A.Michael, and S.Stanko, "KOSMA's 490/810 GHz Array Receiver," in *Proceedings of the 12th International Symposium on Space Teraherz Technology*, (San Diego, California), 2001.
2. K.-F. Schuster, J. Blondel, M. Carter, A. Karpov, J. Lamb, B. Lazareff, F. Mattiocco, S. Navarro, and J.-L. Pollet, "The IRAM 230 GHz multibeam SIS receiver," in *Proceedings of the* 8th *International Symposium on Space Terahertz Technology*, R. Blundell and E. Tong, eds., Harvard University, (Cambridge), 1997.
3. C. Walker, C. Groppi, A. Hungerford, C. Kulesa, D. Golish, C. D. d'Aubergny, K. Jakobs, U. Graf, C. Martin, and J. Kooi, "Pole star: An 810GHz Array Receiver for AST/RO," in *Proceedings of the 12th International Symposium on Space Teraherz Technology*, (San Diego, California), 2001.
4. H. Dammann and E. Klotz, "Coherent optical generation and inspection of two–dimensional periodic structures," *Optica Acta* **24**, 1977.
5. R. Güsten et al., "CHAMP — the carbon heterodyne array of the MPIfR," in *Advanced Technology MMW, Radio, and Terahertz Telescopes*, T. G. Phillips, ed., Proceedings of SPIE Vol. 3357, 1998.
6. J. Murphy, S. Withington, and H. Van de Stadt, "Dammann gratings for local oscillator beam multiplexing," 1995.
7. S. Jacobsson, A. Lundgren, and J. Johansson, "Computer generated phase holograms (kinoforms) for millimeter and submillimeter wavelengths," *Intl. J. IR mm Waves* **11**(11), 1990.
8. S.Heyminck and U.U.Graf, "Reflection gratings as THz local oscillator multiplexer," in *Proceedings of SPIE, Astronomical Telescopes and Instrumentation 2000*, vol. Airborne Telescope Systems, 2000.
9. U.U.Graf and S.Heyminck, "A Novel Type of Phase Grating for THz Beam Multiplexing," in *Proceedings of the 11th International Symposium on Space Teraherz Technology*, 2000.
10. C. Degiacomi, R. Schieder, J. Stutzki, and G. Winnewisser, "The KOSMA 3 m submm telescope," *Optical Engineering* **34**(9), 1995.
11. U.U.Graf and S.Heyminck, "Fourier Gratings as Submillimeter beam splitters," *IEEE TransAP* , in press.

Fabrication and Characterization of a 600 GHz Resonant Distributed SIS Junction for Fixed-tuned Waveguide Receiver

Teruhiko Matsunaga[1], Cheuk-yu Edward Tong[2], Takashi Noguchi[3] and Raymond Blundell[2]

1 Department of Astronomical Science, The Graduate University for Advanced Studies, Nobeyama, Minamimaki, Minamisaku, Nagano, 384-1305 Japan.

2 Harvard-Smithsonian Center for Astrophysics, 60 Garden St., Cambridge, MA 02138 USA.

3 Nobeyama Radio Observatory, Nobeyama, Minamimaki, Minamisaku, Nagano, 384-1305 Japan.

Abstract

The non-linear quasiparticle tunnel current flowing in a distributed superconductor-insulator-superconductor (SIS) transmission line resonator has been exploited in a low-noise heterodyne fixed-tuned waveguide receiver in the 600 GHz band. The mixer employs two half-wave or full-wave distributed SIS long junctions connected in series. These devices have been fabricated with optical lithography. Preliminary results show that a noise temperature of 240 K is routinely obtained at around 600 GHz. The best double-side-band receiver noise temperature measured so far is 161 K at 597 GHz. The achieved RF bandwidth is only about 5 % and the center frequency of the resonance is also shifted towards lower end of the target frequencies.

I. Introduction

Distributed mixer based on the nonlinear quasi-particle tunnel current in a superconductor-insulator-superconductor (SIS) nonlinear transmission line requires a lower current density tunnel barrier, simpler matching circuitry, and lower magnetic field to operate when compared with conventional lumped-element SIS mixers. Waveguide receivers incorporating such long SIS junctions have demonstrated quite wide bandwidth, very low noise temperatures at submillimeter wavelengths [1][2]. However, the widths of these junctions have to be submicron to achieve reasonably high impedance for ease of matching. Consequently, they have to be fabricated using electron beam lithography [3] or with edge junction technique [4].

In standard fabrication process with optical lithography, the junction area is commonly defined through square or round resist stencils. In order to fabricate long distributed

junctions, long, narrow stencils are required. Such geometry is not ideal from the point of view of fabrication process, in particular the reactive ion etching steps. Damaged stencils result in too large variation of the individual junction size over a wafer. In addition, the lift-off process after SiO_2 or Al_2O_3 sputter deposition is difficult or even not possible at very narrow line widths. In this work, we have experimented with wider (> 1 μm) and shorter (=λ_g, $\lambda_g/2$) SIS transmission lines. This type of resonant distributed mixer was proposed by Belitsky [5] and a quasi-optical version of it has been tested by Uzawa [6].

To achieve good matching between the waveguide embedding circuit and such a large distributed junction, we employ 2 resonant junctions connected in series, each with its own quarter-wave transformer section. This design allows for a lower circuit embedding impedance. Also the IF capacitance is reduced by half. The details of fabricated and laboratory test data will be presented below.

II. Non linear transmission line resonator mixer design

The characteristic impedance of our 1.4 μm wide non-linear transmission line is only about 1 Ω. At its half-wave resonant and full-wave resonant frequencies, the input resistance becomes reasonably large and the reactance vanishes. Fig. 1 shows the theoretical [7] input impedance at 660 GHz as a function of the length of the resonator. Note that the resonance structures are clearly observed.

A waveguide horn couples the RF radiation to the waveguide and mixer chip. Fig.2 illustrates the layout of the mixer design, and Fig. 3 is an SEM photograph of a single SIS long junction. Two types of resonant long junctions have been designed: the 5.7 μm long half-wave resonator (labeled HWR) and the 11.4 μm long full-wave resonator (labeled FWR). The nominal junction width is 1.4 μm. Two series connected resonator junctions are each integrated with a quarter-wave transformer. This arrangement has a dual purpose. First, it halves the IF output capacitance. Thus, the output capacitance of a HWR chip is about 0.4 pF and that of an FWR chip is about 0.8 pF. Secondly, the embedding impedance seen by each device is reduced. We need only to match each resonator to an impedance of about 20 Ω. We have incorporated a quarter-wave transformer with a characteristic impedance of 8 Ω on the HWR chip and 6 Ω for the FWR chip.

III. Junction Fabrication

The Nb/AlO_X-Al/Nb tunnel junction was fabricated using standard SNEP (Selective Niobium Etching Process) incorporating the anodization technique [8]. The processing

steps are illustrated in Fig. 4.

Waveguide mixer elements for high frequencies require substrate materials with low dielectric constants and low absorption. Therefore crystalline quartz substrates are used. The fabrication of the SIS mixer circuit starts with the deposition of a Nb/AlO_X-Al/Nb tri-layer in a photoresist mask defining the low-pass filter for the IF output. The base Nb layer is 200 nm thick. The film stress was measured [9] using the film on an extra wafer processed in same batch and it is adjusted to about 0.5 ± 0.1 GPa to achieve high quality (subgap to normal resistance ratio, R_{SG}/R_N~20) SIS junction. The measured stress of films is shown in Fig. 5. Just after the deposition of the base layer, a 6 – 8 nm thick Al film is sputtered in same chamber. The oxidation of the Al film is performed in the load-lock chamber with 53 mTorr Ar + 10%O_2 for 30 min. The target critical current density is 7.5 kA/cm^2. Then 100 nm thick Nb counter electrode is deposited. After the lift-off of the photoresist, 75 nm SiO_2 is deposited on the whole wafer to protect the surface of the Nb counter electrode from being oxidized in the later anodization process. For the definition of the junctions, first lines are patterned on top of the tri-layer using positive resist ip3100HS [10] and the Canon PLA501 contact mask aligner operating Deep-UV. Then the unprotected parts of the SiO_2 and counter Nb film are etched away to obtain the long junctions. In order to avoid short-current at the junction edges, periphery of the junctions are anodized, followed by the deposition a 270 nm SiO_2 and a 90 nm Al_2O_3. After lifting off the resist, the SiO_2 layer is removed, and exposed area of the top Nb electrode is etched with 1.5 Pa Ar plasma for 4.5 min. Finally, the wiring Nb layer was deposited and patterned and, a gold layer was evaporated by e-beam deposition to provide good contact pads for the IF port and ground.

IV. Receiver noise measurement

The mixer chip is installed in a fixed-tuned waveguide mixer block developed for the Sub-Millimeter Array [1]. For laboratory noise temperature measurements, we have employed a liquid helium cryostat. The measurement setup, as shown in Fig. 6, is identical to what was previously described by Tong [8]. The IF is 1.5 GHz. Local oscillator power is provided by a cascade of solid-state multipliers pumped by a Gunn oscillator. The LO beam is collimated by a 90 degree off-axis parabolic mirror. A Martin-Puplett interferometer provides LO and signal diplexing. The beam reflected off the paraboloid passes through several layers of infrared blocking filters, made from porous Teflon sheet, at 77 K and 4.2 K, is then focused on the mixer feed using a parabolic mirror.

The heterodyne receiver noise measurements were made using the standard Y-factor method for room temperature (295 K) and liquid-nitrogen-cooled (77 K) loads. Double-side-band noise temperature is computed from the experimental Y-factor with no correction for Planck's radiation law.

V. Results and Discussion

Using resistance data from large (5.0, 3.0, 2.0, 1.75 and 1.5 μm square) junctions fabricated on same wafer, the current density of the barrier is determined to be about 7.0 kA/cm^2, which is close to the design value. The subgap to normal state resistance ratio (R_{SG}/R_N) is typically > 15. Fig. 7 shows a typical I-V curve of a full-wave long junction (nominally 1.5 μm x 10.8 μm= 16.2 μm^2), together with its measured heterodyne response at 579 GHz to hot and cold loads. From the normal state resistance of this device of 3.98 Ω, we infer that junction size is 13.6 μm^2. This means that there is a difference of around 0.22 μm in both length and width of device compared with the design values. At a bias voltage of 3.8 mV, a Y-factor of 1.72 is obtained. This corresponds to a double-side-band receiver noise temperature of 226 K.

A number of chips have been tested. A noise temperature of 240 K is routinely obtained at around 600 GHz. The measured noise temperature as a function of LO frequency is plotted in Fig. 7 for both an HWR and a FWR chip. When the helium bath temperature is lowered to 2.5 K, the receiver noise temperature is reduced by about 100 K. The lowest noise temperatures measured at 2.5 K is 161 K at 597 GHz. The double sideband conversion loss corresponding to the lowest receiver noise point are estimated to be 8 ± 2 dB and 7 ± 2 dB, for the half and full wave resonators, respectively. The IF-amplifier noise temperature is around 5 K.

The achieved RF bandwidth of all measured devices is only about 5 % that is around 30 GHz. The center frequency of the resonance is also shifted by about 10 % toward the lower end of the target frequencies. We believe that the frequency shift and the narrow RF bandwidth are result of the undersized junctions; we estimate 0.22 μm of shrinkage for a nominally 1.4 μm design. The measurement setup can also be improved to give better sensitivity toward the higher end of the frequency band.

VI. Conclusion

Preliminary tests have been made on a distributed superconductor-insulator-superconductor (SIS) resonant mixer in a fixed-tuned waveguide

mount in the 600 GHz band. The best double-side-band receiver noise temperature measured so far is 161 K at 597 GHz. However, the achieved RF bandwidth of every measured device is only about 5 % (that is about 30 GHz) and the center frequency of the resonance is also shifted 10 % (that is around 60 GHz) towards lower frequencies. These effects are caused by impedance mismatch between waveguide and the junctions, because the design parameters are slightly different, and because the resonator width was shrunk by about 0.22 μm during fabrication process, especially photolithography and RIE. We are currently working on a second batch of devices designed with parameters extracted from the measurement data.

VII. Acknowledgment

We thank Mr. Tadao Yoshizawa at Mitsubishi Electric Logistics Support Co. Ltd., for his assistance about device fabrication.

VIII. References

[1] C. E. Tong, R. Blundell, D. C. Papa, J. W. Barrett, S. Pine, X. Zhang, J. A. Stern, H. G. LeDuc, "A fixed tuned low noise SIS receiver for the 600 GHz frequency band", in *Proc. 6th Int. Sym. Space THz Tech.,* pp.295-304, Pasadena, CA, March, 1995.

[2] R. S. Amos, A. W. Lichtenberger, C. E. Tong, R. Blundell, S. -K. Pan, A. R. Kerr "Nb/Al-AlOx/Nb Edge Junctions for Distributed Mixers," *IEEE Trans. Appl. Super.* Vol. 9, No.2, pp.3878-3881, 1999.

[3] H. G. LeDuc, A. Judas, S. R. Cypher, B. Bumble, B. D. Hunt, J. A. Stern, "Submicron area NbN/MgO/NbN tunnel junctions for SIS mixer applications," *IEEE Trans. Magn.*, Vol. 27, No. 2, pp.3192-3195, 1991.

[4] J. A. Martinis, R. H. Ono, "Fabrication ultrasmall Nb-AlOx-Nb tunnel junctions," *Appl. Phys. Lett.* Vol.57, (6), pp.629-631, 1990.

[5] Y. V. Belitsky, E. L. Kollberg, "Superconductor-insulator-superconductor tunnel strip line: Features and applications," *J. Appl. Phys.*, Vol. 80, 8, pp.4741-4748, 1996.

[6] Y. Uzawa, A. Kawakami, S. Miki, and Z. Wang, "Performance of All-NbN Quasi-Optical SIS Mixers for the Terahertz Band" presented at the *Appl. Superconductivity Conf.*, Virginia beach, VA, Submitted *to IEEE Trans. Appl. Super.*

[7] C. E. Tong, L. Chen, R. Blundell, "Theory of distributed mixing and amplification in a superconducting quasi-particle nonlinear transmission line," *IEEE Trans. Microwave Theory and Tech.*, MTT-45, No. 7, pp.1086-1092, 1997.

[8] T. Noguchi, A. Sakamoto, S. Ochiai, "Fabrication of sub-micron SIS junctions," *Technical Report of IEICE*, SCE93-64, pp.43-48, 1994.

[9] R. S. Amos, P. E. Breyer, H. H. Huang, A. W. Lichtenberger, "Stress and source conditions of DC magnetron sputtered Nb Films," *IEEE Trans. Appl Super.*, vol.5, No.2, p.2326-2329, 1995.

[10] Tokyo Ohka Kogyo, http://www.tok.co.jp

[11] C. E. Tong, J. Kawamura, T. R. Hunter, D. C. Papa, R. Blundell, M. Smith, F. Patt, G. Gol'tsman, E. Gershenzon, "Successful operation of a 1THz NbN-hot electron bolometer receiver," in *Proc. 11th Int. Sym. Space THz Tech.*, pp.49-59, Ann Arbor, , MI, May, 2000.

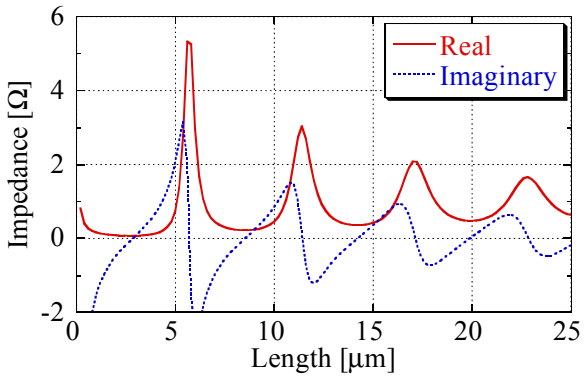

Fig. 1 Calculated real and imaginary parts of the input impedance of a 1.4 μm wide open-ended SIS transmission line. Note that around integer multiples of $\lambda_g/2$ (6 μm in this case), the reactance vanishes and the resistive part becomes larger.

Table 1 Size of sections in a mixer.

		HWR	FWR
Transformer	Width [μm]	9.0	14.0
	Length [μm]	36.5	36.5
Junction	Width [μm]	1.4±0.2	1.4±0.2
	Length [μm]	5.1±0.3	11.4±0.3

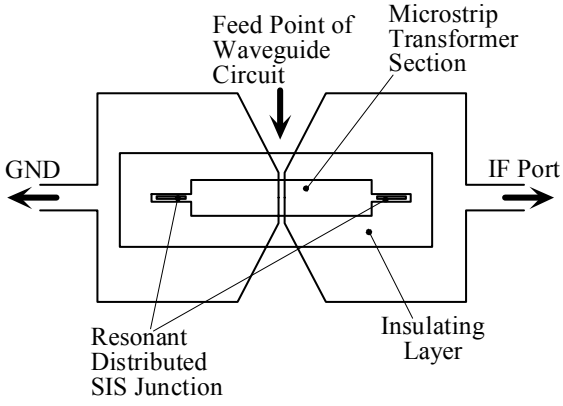

Fig. 2 Layout of the resonant SIS mixer chips.

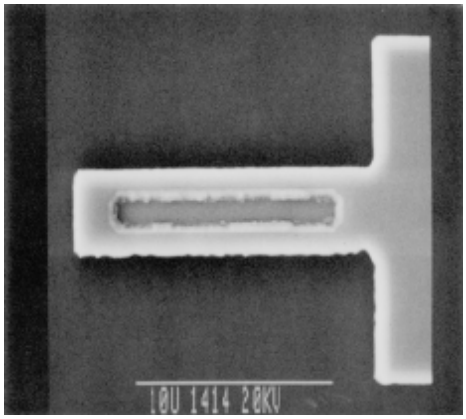

Fig. 3 SEM photograph of a full wave resonant distributed SIS quasiparticle tunnel junction.

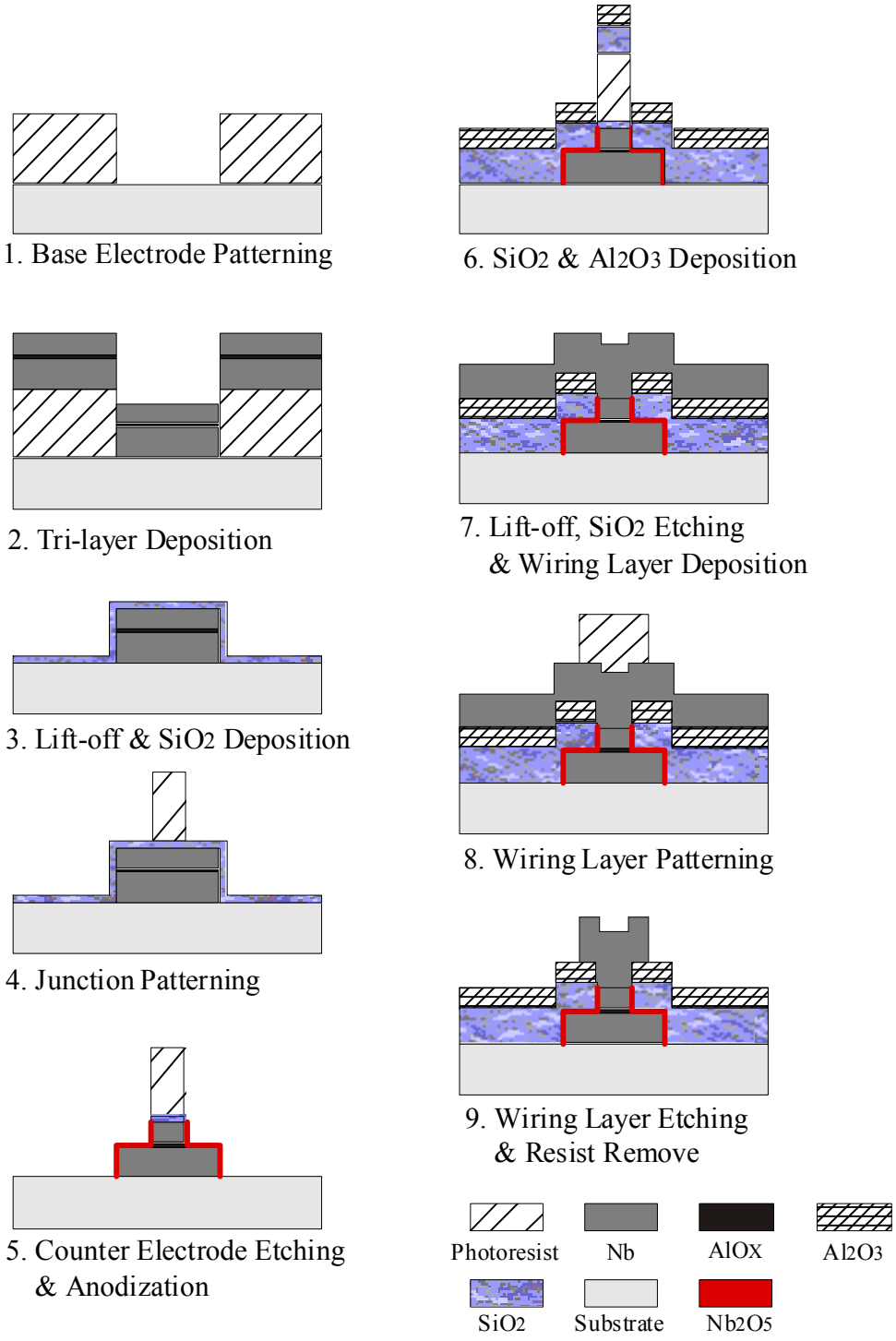

Fig. 4 Fabrication steps for SIS tunnel junction with Selective Niobium Etching Process (Selective Niobium Etching Process) incorporating with the anodization technique.

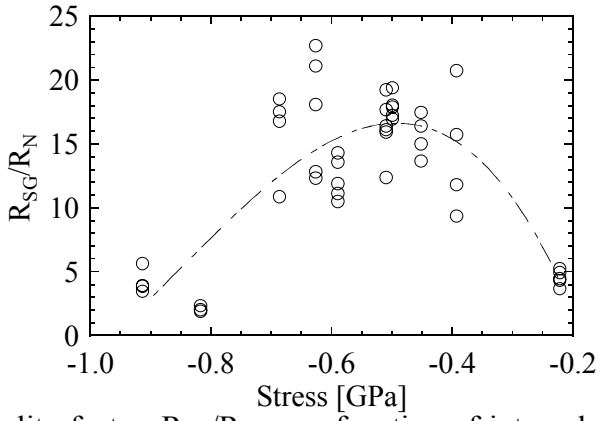

Fig. 5 SIS quality factor, R_{SG}/R_N, as a function of internal stress of base Nb film. Minus sign represents compressive stress. Thin film with about 0.5 GPa compressive stress gives relatively high quality junctions.

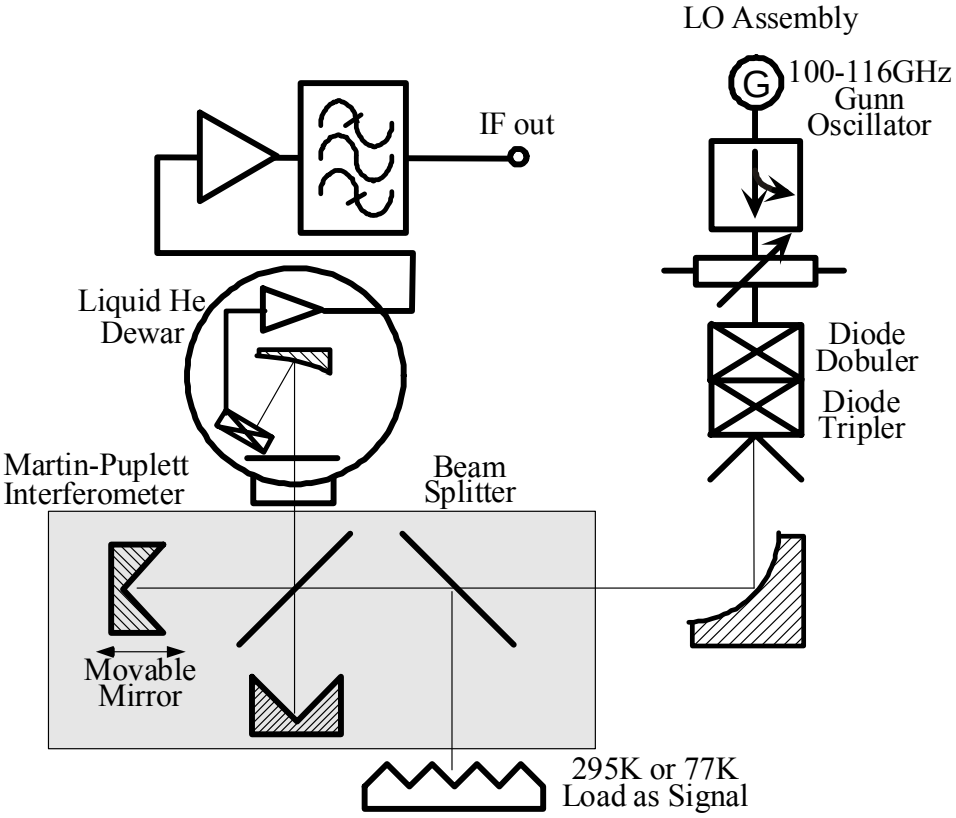

Fig. 6 Layout of receiver experiment. The mixer assembly, parabolic mirror and HEMT amplifier are mounted on the 4.2 K-cold plate.

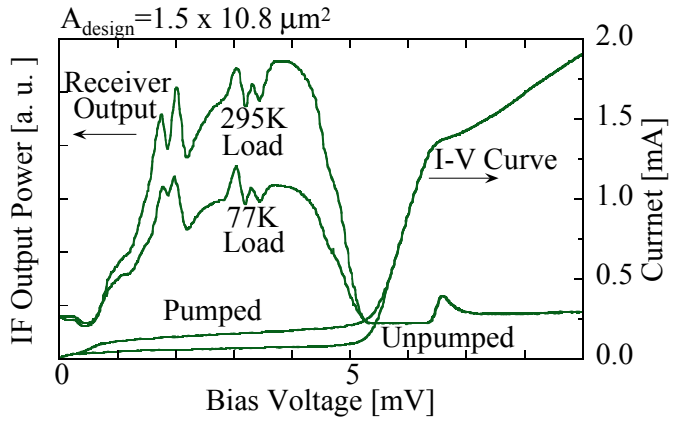

Fig. 7 DC current-voltage characteristics of the resonance distributed SIS junction mixer without and with incident LO power at 579 GHz. Also shown is the receiver IF output power as a function bias voltage for hot and cold loads. A Y-factor of 1.72 is noted at a bias voltage of 3.8 mV.

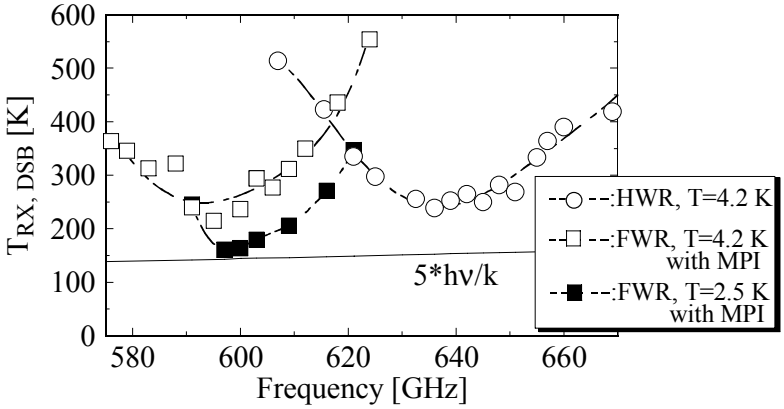

Fig. 8 DSB noise temperature as a function of frequency. Results are shown for FWR (λ_g) and HWR ($\lambda_g/2$) resonator length mixer noise temperature at 2.5 K and 4.2 K, respectively.

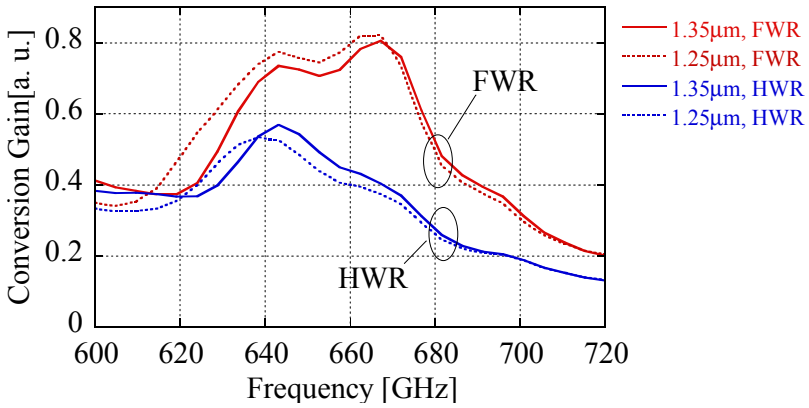

Fig. 9 Simulated conversion gain of resonant SIS mixer. Note that the center frequency changes with the junction width because of changes in the capacitance of the non-linear transmission line.

Development of a 0.6 THz SIS Receiver for ALMA

A.M. Baryshev[2,3], L. de Jong, R. Hesper[2], H. Schaeffer[1], H. van de Stadt[1], W. Wild[2,1], T. Zijlstra[4], M. Zuiddam[4]

[1]SRON-Groningen, Groningen, the Netherlands
[2]NOVA, University of Groningen, the Netherlands
[3]Institute of Radio Engineering and Electronics RAS, Moscow, Russia
[4]Department of Applied Physics (DIMES), Delft University of Technology

ABSTRACT

The Atacama Large Millimeter Array (ALMA) requires low noise SIS receivers for frequencies from about 80 GHz to 950 GHz with very large IF bandwidth (4-12 GHz). Additional requirements for these receivers are high reliability, low cost and the possibility of series production. In this paper we report on mixer designs based on standard Nb/AlO_x/Nb SIS junction technology and an optics design for ALMA band 9 (602 – 720 GHz).

We present the design of a tunerless balanced waveguide SIS mixer and a quasi-optical double slot-antenna mixer as well as an optical design to couple the telescope beam to the mixer. The waveguide balanced mixer is based on a magic T with integrated RF and LO feed horns.

Losses in the Nb film increase at frequencies above the Nb gap frequency of 690 GHz and limit the mixer sensitivity at the high end of ALMA band 9. In this paper we present a layout concept of the optics and the mixers as well as an analysis of its RF properties which shows that efficient mixer operation is still possible across this band without changing the material of tuning elements.

INTRODUCTION

The Atacama Large Millimeter Array (ALMA) requires low noise SIS receivers for frequencies from about 80 GHz to 950 GHz with very large IF bandwidth (4-12 GHz). ALMA will be built in the Atacama Desert (Chili) at the altitude of more than 5 km. The atmospheric conditions for mm wave astronomical observations at this site are among the best in the world. The array will consist of at least 64 antennas, each with a diameter of 12 m.

Table 1, ALMA frequency coverage

Band	Low end frequency (GHz)	High end frequency (GHz)
1	31	45
2	67	90
3	84	116
4	125	163
5	163	211
6	211	275
7	275	370
8	385	500
9	602	720
10	787	950

The Alma frequency band is divided into ten subbands that are shown in table 1. These bands coincide with regions where the atmosphere is relatively transparent and astronomical observations are possible. The receivers for the different subbands will be mounted in a common cryostat supporting three temperature levels: 4.3 K, ~10 K and 80 K. Each subband receiver is contained in an independent "cartridge" that can be mounted in the receiver cryostat without disturbing other subbands. This cartridge contains a complete receiver system including SIS mixers, LO subsystem, IF amplifiers and all necessary optical components.

The remoteness of the site and the large number of receivers impose additional requirements to the receiver design such as: absence of moving parts, an as simple as possible layout, low cost, and the possibility of series production.

In this paper we report mixer designs based on standard $Nb/AlO_x/Nb$ SIS junction technology in waveguide or planar antenna geometries and a concept of an optics design for ALMA band 9 (602 – 720 GHz).

OPTICAL DESIGN

The ALMA telescope baseline design provides a beam with an f-ratio of f/8. Our goal is to design a frequency-independent optical system that matches the telescope beam with a mixer feed which consists of a corrugated horn in the case of the waveguide mixer or an antenna/lens combination in the case of the quasi-optical mixer. Additional requirements are low RF loss, low distortion loss, and low cross polarization loss. The latter is especially important for the polarization observations that are planned for ALMA.

We propose a configuration for the signal path consisting of two elliptical mirror. This creates enough flexibility to accommodate mixer feeds with f-ratios from f/3 to f/10. Two elliptical mirrors can be arranged in such a way that distortions introduced by them are partially compensated [1]. The proposed mirror arrangement is shown in fig 1.

The focal points (*fp1..fp4*) of the ellipses are indicated in the figure. The telescope secondary focus is located in *fp1* and the feed at *fp4*.

The coupling loss L_{dist} between the reflected beam and a symmetric Gaussian beam in each mirror is given by the following formula [1]:

$$L_{dist} = \frac{w_1^{\,2} \tan^2(\alpha 1)}{8 \cdot f_1^{\,2}}, \qquad (1)$$

where w_1 is the beam radius at the mirror, f_1 is focal length of the mirror and $\alpha 1$ is the beam bending angle as indicated in fig. 1. We assume that the second mirror compensates the distortion in the first mirror. Applying equation (1) to each of the mirrors and equating the result in the geometrical optics limit, one can obtain the following relation between the bending angles of the ellipses for full distortion compensation:

$$\alpha 2 = ArcTan\left(\frac{(1 + \mathrm{M1}) \cdot \tan(\alpha 1)}{\left(1 + \frac{1}{\mathrm{M2}}\right)} \right), \qquad (2)$$

where M1 and M2 are the magnifications of the ellipses given by $M1 = \frac{R2}{R1}$ and $M2 = \frac{R4}{R3}$ (parameters are indicated in fig. 1). This equation can also be derived by means of minimizing geometrical aberrations. In the 600-720 GHz band, the beam radii become significantly different from the ones given by the geometrical optics calculation and equation (2) should be modified to incorporate Gaussian beam formalism. The bending angle relation then becomes frequency dependent. However, it is still possible to compensate distortions over a limited frequency range. Using the described approach, equation (2) can be easily extended for three or more mirrors.

The cross polarization loss is twice that given by equation (1) [1] and it can be compensated. Consequently, the approach described above holds for cross-polarization loss as well.

The final signal path layout for ALMA band 9 is shown in fig. 2.

SINGLE-ENDED WAVEGUIDE MIXERS

1. *Mixer design*

The single-ended waveguide mixers have been shown to have a quantum limited sensitivity [2], [3]. In the past, the SRON laboratory in Groningen has made sensitive SIS waveguide mixers for the 540-700 GHz frequency range. In February 2000 two of these were installed at the James Clerk Maxwell Telescope (JCMT) on Mauna Kea, Hawaii. The Double Side Band (DSB) receiver noise temperature of the present tunerless mixers

is below 200 K over the whole band. The SSB system noise temperature, including all optics and diplexers of the W-band receiver at JCMT is below 600 K over the 630-700 GHz band.

Three mixers were made in total, two for the receiver and one spare. They are labeled D5, D6 and D7, where D7 is the spare mixer. We describe the mixer parameters in the following paragraphs:

The mixer consists of two sections: a front part including the corrugated horn and Teflon lens, and a back part with the substrate channel and IF connection.

The corrugated horn was designed by S. Withington of MRAO, Cambridge, England. It has a semi-apex angle of 7.5 degrees and a length of 19 mm, corresponding to a waist of 1.15 mm radius located halfway the horn length for the design frequency of 682 GHz. The waveguide has a cross-section of 100 x 400 μm. The lens is made of Teflon and has a focal length of 32 mm so that it gives good coupling between the horn and a 2.97 mm waist located 86 mm in front of the lens.

In the back part of the mixer the cross-section of the substrate channel is 70 x 100 μm and the backshort cavity is 160 μm deep. The substrate is 2.1 mm long, 50 μm thick and 70 μm wide and it contains a Nb-based SIS tunnel junction. It is glued in the channel and we use silver paint for the ground contact on one end as well as for the IF contact at the other end. For the IF contact we use a standard 50 Ohm glass bead.

The lens, horn and back part are contained in a mounting bracket, which is cooled at the top via a heat strap. The IF pin of the mixer fits into a standard SMA connector which is supported by a separate mounting bracket.

For the magnet we use a coil of about 6000 windings of 63.5 micron diameter Cu-cladded Nb wire. For the core of the magnet and for the field line conductors we use VacoFlux 50, which has a maximum permeability of 9000 and saturation polarization of 2.35 T.

2. *Sensitivity*

The Michelson FTS measurements for the D-band receiver are presented in fig. 4. It shows a relatively flat frequency direct response over the 560-700 GHz band for all three produced D-band mixers. The model calculation fit is shown in the same picture. The model includes Mattis-Bardin theory [2] for losses in the superconductor, standard lossy microstriplines and a waveguide probe approximation. All responses in fig. 4 are normalized. This model produces a remarkably good fit to the experimental data, for large variations of junction area or backshort cavity depths.

The measured noise temperature for the D-band mixers is presented in fig. 5. The measurements were done using standard Y-factor techniques. The center IF frequency was 4 GHz as required for the JCMT. The best noise temperature measured under these conditions is 170 K at 660 GHz (corrected for beamsplitter loss). The main source of

noise in the system appeared to be the IF amplifier chain which at the time of the measurements was around 14 K. This can be demonstrated by a significant improvement in DSB noise temperature that we have obtained with a similar single-ended waveguide mixer at 1.5 GHz IF frequency. The uncorrected noise temperature for this mixer is shown in fig. 6. The best noise temperature, measured at 645 GHz, was 130 K. All noise temperatures are Callen & Welton corrected [5].
The receiver DSB noise temperatures of around 350 K across the band was registered at the JCMT using the fixed-tuned D-band mixers described above. The SSB noise temperature of 600 K was measured at the upper part of the band.

SINGLE-ENDED QUASI-OPTICAL MIXERS

The planar antenna – silicon elliptical lens combination was used successfully before to produce a usable receiver beam [6], [7], [5], [9]. A design similar to the one described in [9] is currently being implemented and tested. The design layout of such a mixer is presented in fig 7.
The RF signal is picked up from the double slotline antenna by means of stubs and then fed through microstripline transformers to a twin junction circuit. The DC and IF signals pass through the choke structure to the edge of the chip. The magnetic field required for Josephson current suppression is applied by means of passing a current through the wiring electrode just above the junction pair.
The FTS measurements of two quasi-optical mixers are presented in fig. 8 (on the same relative scale). One of these mixers was tuned at a somewhat higher frequency because of a smaller junction area. The considerable loss of sensitivity that is observed can be explained by increased loss in the Nb tuning structures above the gap frequency of Nb. The mixer with the optimal junction area produces a good response over the whole ALMA band 9, including the upper edge.
The quasi-optical mixers have certain advantages over waveguide mixers, mainly because of the smaller number of critical technological steps that are required for manufacturing, resulting in reduced production costs. For instance, a lens is cheaper than a good corrugated horn at these frequencies. Also, a few additional features like integrated Josephson current suppression can easily be implemented on-chip, obviating the need for an external superconducting magnet coil.

BALANCED MIXERS

The balanced mixers contain two individual mixer detectors which are pumped by local oscillator signals having a phase difference of 180^{o}. This allows combining the IF signals in a 180^{o} hybrid circuit so that the total signal is directed to one output port, while the LO sideband noise is directed to the other output port where it is dissipated in a load resistor. In this way one separates the local oscillator noise from the signal. This feature is

especially important when using solid state local oscillators with a chain of multipliers, which generate a high level of sideband noise. The exact amount of sideband noise reduction depends on the accuracy of the 180° phase shift and on the amplitude balance between the two mixers [10]. However, it was shown that the amplitude and phase balance requirements are not stringent in this configuration. An additional advantage of balanced mixers is that all of the LO power is used without the additional complexity of having to build an LO diplexer.

The basic property of a balanced set of detectors is the phase-difference of 180° between reflected and transmitted waves. This can simply be achieved by using beamsplitters, as explained by Waite [11] using Stokes' analysis of phase change on reflection at a dielectric surface. Waite shows that this phase difference occurs automatically, independent of wavelength, polarization and angle of incidence, but that it is only exactly 180° for beamsplitters without absorption loss. An early demonstration of balanced mixers for heterodyne detection at a near infrared wavelength of 3.39 micron, or a frequency of 88.5 THz, was given by H. van de Stadt [12].

Instead of one of the conventional LO coupling schemes for balanced mixers (a simple beamsplitter or a more complicated set-up using a Martin-Puplett interferometer), we present here schemes with all-waveguide (Magic Tee) and quasi-optical balanced mixers.

1. *Magic-Tee balanced mixer*

The proposed magic Tee waveguide balanced mixer layout is shown in fig. 9. It is based on D-band mixer layout, described in previous sections. The Magic Tee mixer utilizes two detector backpieces of exactly the same design as in single-ended mixer. The phase difference in LO between the two mixers is achieved due to the symmetry of fields inside magic-T that automatically makes it broadband. In addition, the smallest size of elements in such a design is larger than in branch-line waveguide hybrids designed for the same bandwidth, thereby simplifying the manufacturing process.

CONCLUSIONS

The distortion compensated optical design for coupling the telescope beam into the various mixer feeds is described. The single-ended waveguide mixer operation has been successfully demonstrated at the James Clerk Maxwell Telescope. The best receiver noise temperature of 130 K (uncorrected for optical loss and beamsplitter) was measured at 650 GHz in a similar mixer.

The quasi-optical mixer design which works in 600-720 GHz band is described and preliminary evaluated. Preliminary results show that Nb technology is sufficient to cover the desired frequency range.

The magic Tee balanced mixer is proposed for this band and its layout, based on reusing proven design concepts from the single-ended mixer, is described.

ACKNOWLEDGEMENT

Authors would like to thank Duc Nguen for his help in measurements and assembly of the mixer blocks, Gert de Lange and Brian Jackson for stimulating discussion and help in junction production, as well as Per Friberg and the JCMT receiver team.

REFERENCES

[1] J.A. Murphy, "Distortion of a simple Gaussian beam on reflection from off-axis ellipsoid mirrors", Int. J. Infrared and Millimeter Waves, vol. 17, no 12, pp. 1165-87, 1988.

[2] J. W. Kooi, *et al*., "230 and 492 GHz low noise SIS waveguide receivers employing tuned Nb/A10$_x$/Nb tunnel junctions," *Int. J. IR and MM Waves,* vol. 16, pp. 2049-2068 1995.

[3] R. Blundell *et al.*, "A wideband fixed-tuned SIS receiver for 200-GHz operation," *IEEE Trans. Microwave Theory Tech.*, vol. 43, pp. 933-937, Apr. 1995.

[4] D. C. Mattis and J. Bardeen, "Theory of the anomalous skin effect in normal and superconducting metals," *Phys. Rev.*, vol. 111, pp. 412-417, July 1958.

[5] H. B. Callen and T. A. Welton, "Irreversibility and generalized noise," *Phys. Rev.*, vol. 83, pp. 34-40, July 1951.

[6] D. F. Filipovic, *et al.*, "Double-slot antennas on extended hemispherical and elliptical silicon dielectric lenses," *IEEE Trans. on Microwave Theory Tech.,* vol. 41(10), pp. 1738-1749 , 1993.

[7] V.P. Koshelets, *et al*., "Integrated Superconducting Receivers", *Superconductor Science and Technology,* vol. 13, pp. R53-R69, 2000.

[8] M. Bin, *et al.*, "Low-noise 1 THz niobium superconducting tunnel junction mixer with a normal metal tuning circuit," *Appl. Phys. Lett.*, vol. 68, pp. 1714-1716, Mar. 1996.

[9] A. M. Baryshev et al., "Quasi-optical terahertz SIS mixers," in *Proc. of the 11th Int. Symp. on Space THz Technol.*, U. of Michigan, Ann Arbor, Michigan, pp. 137-146, May 1-3, 2000.

[10] A.R. Kerr and S.K. Pan, *Proc of 7th Int. Symp on Space THz Techn.*, 207, 1996.

[11] T. Waite, Proc. *IEEE.* 54, 334, 1966.

[12] H. van de Stadt, *Astron. & Astrophys*. 36, 341-348, 1974.

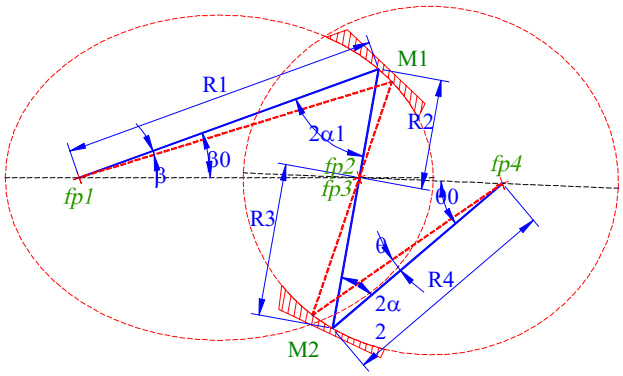

Fig. 1 Two elliptical mirrors distortion compensating arrangement

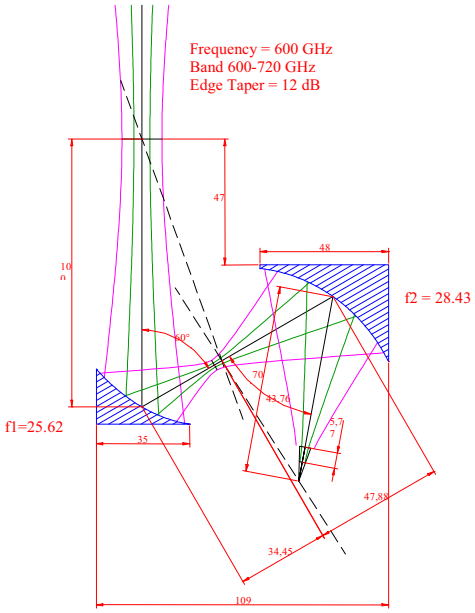

Figure 2: Proposed ALMA band 9 optical layout

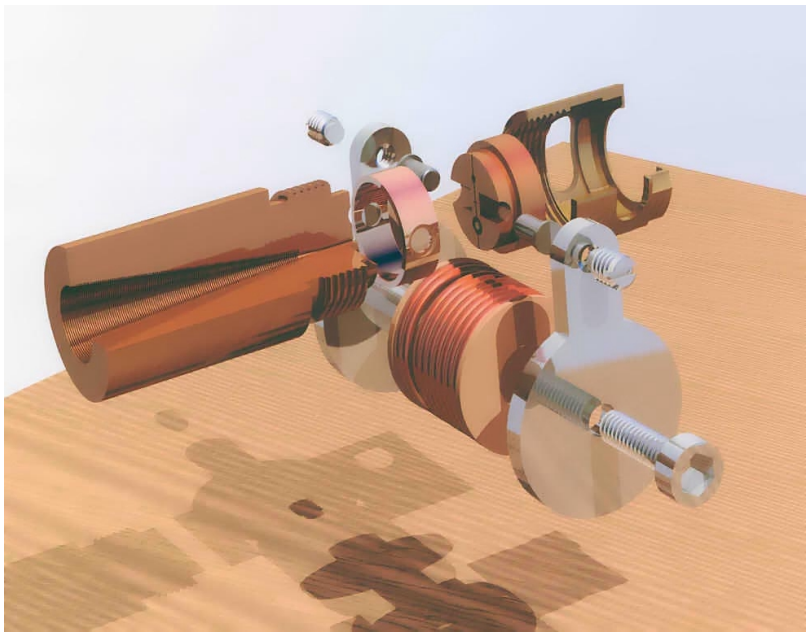

Figure 3: Exploded view of an SRON fixed-tuned waveguide mixer similar to the one installed at JCMT.

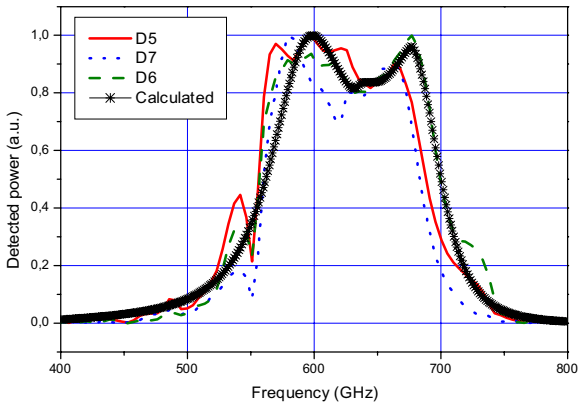

Figure 5: Receiver noise temperatures measured in the lab and at the JCMT.

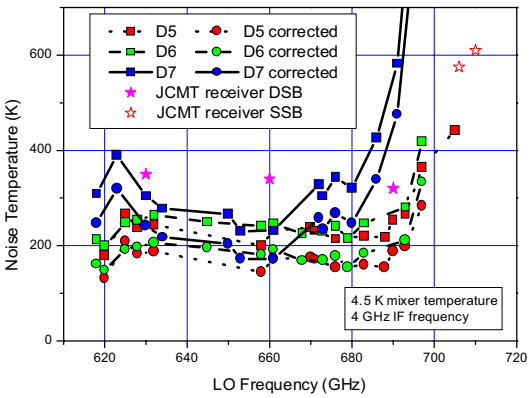

Figure 4: Measured FTS spectra for the three JCMT mixers (D5, D6, D7) and a prediction based on model calculations (crossed line).

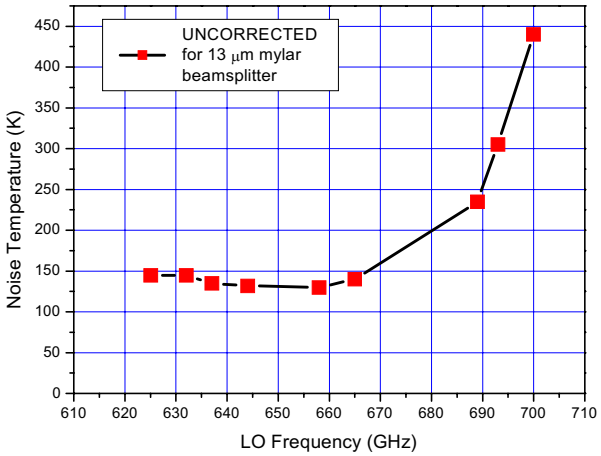

Figure 6: Uncorrected receiver noise temperature of a fixed-tuned waveguide mixer measured at 4.2 K physical temperature at an IF frequency of 1.5 GHz.

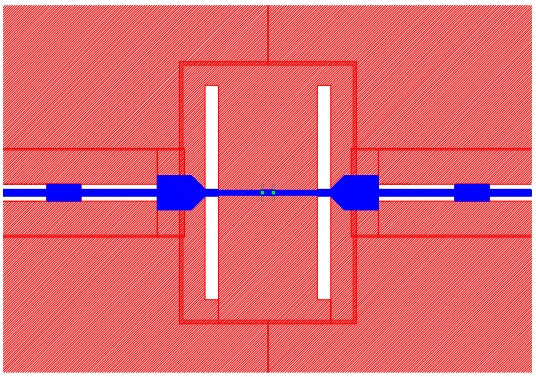

Figure 7: Chip layout of the quasi-optical SIS mixer for the 600-720 GHz ALMA band (not to scale). The SIS junctions are in the middle of the strip, and the double-slotline antenna and tuning structures are shown.

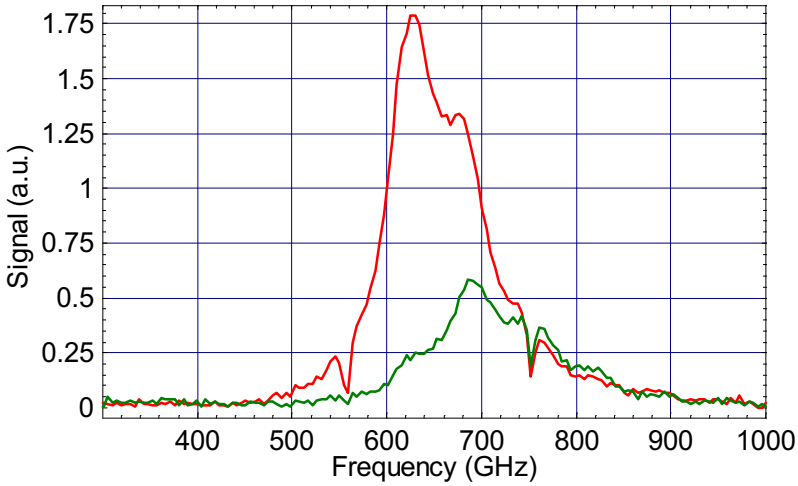

Figure 8: FTS response of two quasi-optical single-ended mixers. The mixer responses are shown in the same scale. The higher frequency peaked response is of the mixer with smaller junctions.

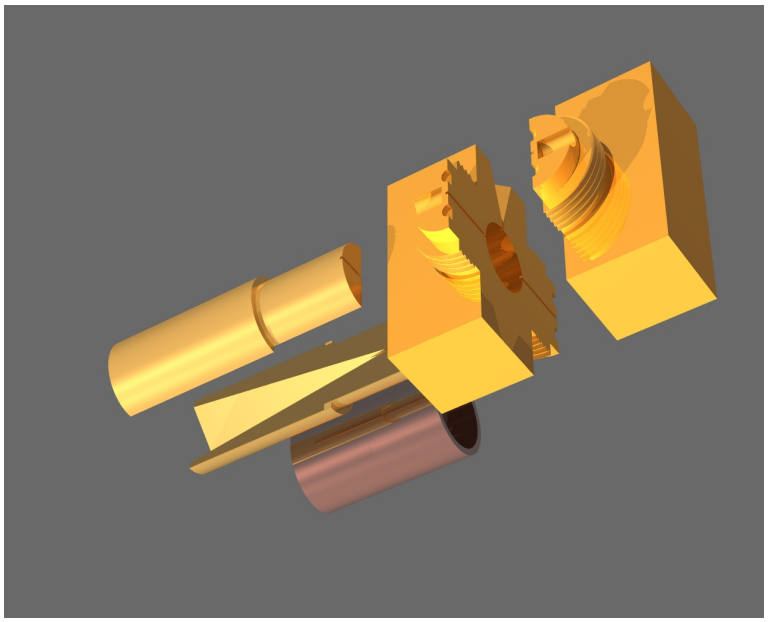

Figure 9: The Magic-T waveguide balanced mixer configuration. The two detector backpieces are not shown.

List of Attendees and Authors for the 12th International Symposium On Space Terahertz Technology

Last Name	First Name	Affiliation	Address	Phone	Fax	E-mail
Adam	Aurele	Chalmers Univ. of Tech	Microelectronics MC2 412 96 Gothenburg Sweden	+46 31 772 1621	+46 31 164513	aurele@ep.chalmers.se
Alderman	Byron	University of Leeds	Leeds LS2 9JT UK	+44(0)113-233-2092	+44(0)113-244-9541	eenbeja@electeng.leeds.ac.uk
Ariyoshi	Seiichirou	Tohoku Univ.	Astronomical Institute Sendai Miyagi 980-8578 Japan	+81 42 2343915	+81 42 2343864	ariyoshi@astr.tohoku.ac.jp
Barrett	Jack	Harvard-Smithsonian Astrophysical Obersvatory	60 Garden St. Cambridge MA 02138	617-496-7667	617-495-7554	jbarrett@cfa.harvard.edu
Baryshev	Andrey	Sron/Nova	Postbus 800 9700 AV Groningen The Netherlands	+31 50 3638287	+31 50 3634033	andrey@sron.rug.nl
Batelaan	Paul	JPL	4800 Oak Grove Drive MS 168-314 Pasadena CA 91109	818-354-6465	818-393-4683	
Belitsky	Victor	Chalmers University of Technology	Gard/MC2 S-412 96 Gothenburg Sweden	+46 31 772 18 93		belitsky@ep.chalmers.se
Benford	Dominic	NASA GSFC	Code 685 Grennbelt MD 20771	301-286-8771	301-286-1617	dominic.benford@gsfc.nasa.gov
Betz	Albert	University of Colorado	1255 38th St. Boulder CO 80303	303-492-4880	303-492-5941	betz@spot.colorado.edu
Blundell	Raymond	Smithsonian Astrophysical Observatory	60 Garden Street Cambridge MA 02138	617-495-7367	617-495-7345	rblundell@efe.harvard.edu
Bradford	Matt	Caltech	Pasadena CA 91125			
Bruston	Jean	ESA/ESTEC				bruston@xe.estec.es.ul
Bumble	Bruce	JPL				
Carter	Matthew	IRAM	300 rue de la piscine 38406 St Martin d'Heres France	+33 47 6824922	+33 47 6515938	carter@iram.fr
Caux	Emmanual	CESR	BP 4346 31028 Toulouse Cedex 04 France	+33 56 1556689	+33 56 1556701	CAUX@CESR.FR
Chattopadahyay	Goutam	Caltech	MC 320-47 Pasadena CA 91125			
Chen	Pin	JPL	4800 Oak Grove Drive MS 183-301 Pasadena CA 91109	818-393-0412	818-354-8460	pine@spec.jpl.nasa.gov
Cerednichenko	S.	Chalmers University of Technology	Microelectronics Dept. Gothenburg SE 412-96 Sweolen	+46 31 772 8499	+46 31 164513	serguei@ep.chalmers.se
Chin	Chi Chung	The Institute of Astronomy & Astrophysics	Academia sinica Nakang Taipe Taiwan	+886 2 26538566	+886 2 27881106	chin@asiaa.sinica.edu.tw

Chouvaev	Denis	Chalmers University of Technology	Dept. of Microelectronics & Nanoscience SE-412 96 Göteborg Sweden	+46 31 7725173	+46 31 7723471	chouvaev@fy.chalmers.se
Claude	Stéphane	IRAM	300 rue de la piscine 38406 St Martin d'Heres France	+33 47 6824987	+33 47 6515938	claude@iram.fr
Crowe	Thomas	University of Virginia	351 McCormick Rd Dept of Elec. Engr. Charlottesville VA 22904-4743	804-924-7693	804-924-8818	twc8u@virginia.edu
Cunningham	Charles	NRC	5071 West Saanich Road Victoria V9E 2E7 Canada	250-363-6937	250-363-0049	karen.rowe@nrc.ca
Dauplay	Frederic	Observatoire de Paris	61 Avenue de l'observatoire 75018 Paris France		+33 14 0512085	frederic.dauplay@obspm.fr
Davidson	Jaqueline					
Delaet	Bertrand	JPL	4800 Oak Grove Drive MS 168-314 Pasadena CA 91109	818-354-0781	818-393-4683	
Delange	Gerhard	SRON	Landleven 12 9700 AV Groningcten Netherlands	+31 50 3634051	+31 50 3634033	gert@sron.rug.nl
Drouet d' aubigny	Christian	Steward Observatory	933 N. Cherry Ave. Tucson AZ 85721	520-621-3924	520-621-1532	cdaudign@as.arizona.edu
East	Jack	University of Michigan	2301 EECS Building Ann Arbor MI 48109	734-763-0212	734-763-9324	jeast@eecs.umich.edu
Edgar	Mick	Caltech	Pasadena CA 91125			
Ediss	Geoff	National Radio Astronomy Observatory	2015 Ivy Road Suite 219 Charlottesville VA 22903	804-296-0245	804-296-0324	gediss@nrao.edu
Effland	John	National Radio Astronomy Observatory	2015 Ivy Road Suite 219 Charlottesville VA 22903	804-296-0216	804-296-0324	jeffland@nrao.edu
Erickson	Neal	Univ. of Massachusetts	Lederle 610 Amherst MA 01003	413-545-1873	413-545-4223	neal@ieee.org
Frommberger	M.	Insitut de RadioAstronomie Millimétrique				
Gao	J.R.	Delft University of Technology	Dept of Appl. Physics Lorentzweg 1 2624CJ Delft Holland			J.r.gao@tnw.tu.delft.nl
Gerecht	Eyal	National Institute of Standards & Technology	325 Broadway MS 814-09 Boulder CO 80305	303-497-4199	303-497-3042	gerecht@boulder.nist.gov
Gibson	Hugu	Harvard-Smithsonian Astrophysical Obersvatory	60 Garden St. Cambridge MA 02138	617-495-7294	617-496-7554	hgibson@cfa.harvard.edu
Glenn	Jason	University of Colorado				

Glenz	Stefan	Univ. of Cologne	Zuelpicherstrasse 77 50937 Cologne Germany	+49(0)221-470-3489	+49(0)221-470-5162	glenz@ph1.uni-koeln.de
Gol'tsman	Gregory	Moscow State Pedagogical University	29 M. Priogojskaya Str. Moscow 119435 Russia	+7 09 54261202	+7 09 52462483	goltsman00@mail.ru
Goldsmith	Paul	Cornel University				
Gossard	Arthur	UCSB				
Goy	P.	AB MILLIMETRE				
Graf	Urs	Univ. of Cologne	Zuelpicherstrasse 77 50937 Cologne Germany	+49(0)221-470-4092	+49(0)221-470-5162	graf@ph1.uni-koeln.de
Groppi	Chris	Steward Observatory	933 N. Cherry Ave Tucson AZ 85721	520-621-6535	520-621-1532	cgroppi@as.arizona.edu
Grossman	Erich	National Institute of Standards & Techonology	325 Broadway MS 814-09 Boulder CO 80305	303-497-5102	303-497-3042	grossman@boulder.nist.gov
Guillon	Matthieu	Observatoire de Paris	61 Avenue de l'observatoire 75018 Paris France	+33 14 4512133	+33 14 0512085	matthieu.guillon@obspm.fr
Häkli	Janne	Helsinki Univ. of Tech.	P.O. Box 3000 FIN-02015 Finland	+358 9 451 2938	+358 9 451 2152	Janne.hakli@hut.fi
Hesper	Ronald	Sron/Nova	Postbus 800 9700 AV Groningen The Netherlands	+31 50 3638287	+31 50 3634033	hesper@sron.rug.nl
Heyminck	Stefan	Univ. of Cologne	Zuelpicherstrasse 77 50937 Cologne Germany	+49(0)221-470-4092	+49(0)221-470-5162	heyminck@ph1.uni-koeln.de
Hübers	Heinz-Wilhelm	German Aerospace Center	Rutherfordstr. 2 12489 Berlin Germany	+49-10130-67055596	+49-10130-67055507	heinz-wilhelm.huebers@dlr.de
Hunter	Todd	Harvard-Smithsonian Astrophysical Obersvatory	60 Garden St. Cambridge MA 02138	617-496-7667	617-496-7554	thunter@cfa.harvard.edu
Ives	Lawrence	Calabazas Creek Research, Inc,	20937 Comer Drive Saratoga CA 95070-3753	408-741-8680	408-741-8831	rlives@calcreek.com
Jackson	Brian	Space Reasearch Organization of the Netherlands	SRON P.O. Box 800 9700 Groningen Netherlands	+31 50 363 4051	+31 50 363 4033	
Jacobs	Karl	KOSMA Univ. of Cologne	Zuelpicher Str. 77 D-50937 Koeln Germany	+49-221-470-3484	+49-221-470-5162	jacobs@ph1.uni-koeln.de
Jones	Bryan	SORAL	933 N. Cherry Ave Tucson AZ 85721	520-621-3924		bdj@u.arizona.edu
Kämpfer	Niklaus	Univ. of Bern	Sidlerstr. 5 Ch-3012 Bern Switzerland	+41 31 6318911	+41 31 6313765	kaempfer@mw.iap.unibe.ch
Karasik	Boris	JPL	4800 Oak Grove Drive MS 168-314 Pasadena CA 91109	818-393-4438	818-393-4683	
Karpov	Alexander	Caltech	Pasadena CA 91125			
Kawamura	Jonathan	JPL	4800 Oak Grove Drive MS 168-314 Pasadena CA 91109	818-393-4779	818-393-4683	jonathan.h.kawamura@jpl.nasa.gov

Khosropanah	Pourya	Chalmers University of Technology	Microtechnology Centre MC2 412 96 Coteborg	+46(0)31 772 1621	+46(0)31 16 45 13	pourya@ep.chalmers.se
Kittara	P.	Univ. of Cambridge				
Klaassen	Tjeerd	Delft University of Technology	P.O. Box 5046 2600 GA Delfs Netherlands	+31 15 2786136	+31 15 2783251	tjeerd@hfwork3.tn.tudelft.nl
Koller	Dan	National Radio Astronomy Observatory	2015 Ivy Road Suite 219 Charlottesville VA 22903	804-296-0293	804-296-0324	dkoller@nrao.edu
Krabach	Timothy	JPL	4800 Oak Grove Drive MS 180-601B Pasadena CA 91109	818-354-9654	818-393-1554	timothy.n.krabach@jpl.nasa.gov
Kroug	Matthias	Chalmers University of Technology	Microelectronics MC2 S-41296 Gothenburg Sweden	+46 31 772 8499		kroug@fy.chalmers.se
Lau	Chun					
Lazareff	Bernard	IRAM	300 rue de la piscine 38406 St Martin d'Heres France	+33 47 6824941	+33 47 6515938	lazareff@iram.fr
Lecomte	Benoit	CNRS	77 Avenue Denfurt Rochereau 75014 Paris France	+33 14 0512381	+33 14 0512232	benoit.lecomte@obspm.fr
LeDuc	Henry	JPL	4800 Oak Grove Drive MS 302-231 Pasadena CA 91109	818-354-2209	818-393-4540	rleduc@vaxeb.jpl.nasa.gov
Lee	Karen	JPL	4800 Oak Grove Drive MS 168-314 Pasadena CA 91109	818-354-6465	818-393-4683	kalee@pop.jpl.nasa.gov
Lee	Mark	Bell Laboratories-Lucent Technologies	600 Mountain Ave Murray Hill Rm 1C-360 NJ 07974	908-582-7697	908-582-3260	markl@lucent.com
Lewis	Carol	JPL	4800 Oak Grove Drive MS 302-205 Pasadena CA 91109	818-354-3767	818-393-5143	carol.r.lewis@jpl.nasa.gov
Lu	James	Rensselaer Polytechnic Institute	110 8th Street Troy, NY 12180	518-276-2909	503-210-1823	luj@rpi.edu
Maestrini	Alain	JPL	4800 Oak Grove Drive MS 168-314 Pasadena CA 91109	818-354-6465	818-393-4683	alain.e.maestrini@jpl.nasa.gov
Maier	Doris	IRAM	300 rue de la piscine 38406 St Martin d'Heres France	+33 47 6824917	+33 47 6515938	maier@iram.fr
Maiwald	Frank	JPL	4800 Oak Grove Drive MS 168-314 Pasadena CA 91109	818-354-0214	818-393-4683	fwm@merlin.jpl.nasa.gov
Mangum	Jeff	NRAO Tucson	949 N. Cherry Ave Tuscon AZ 85721	520-882-8250 x113	520-882-7955	jmangum@nrao.edu

Manohara	Harish	JPL	4800 Oak Grove Drive MS 168-314 Pasadena CA 91109	818-354-6465	818-393-4683	
Martin	Suzanne	JPL	4800 Oak Grove Drive MS 168-314 Pasadena CA 91109	818-354-6465	818-393-4683	suzanne.c.martin@jpl.nasa.gov
Matsunaga	Teruhiko	The Graduate University for Advanced Studies	Nobeyama, Minamimaki, Minamisaku Nagano, 384-1305, Japan	+81-267-98-4364	+81-267-98-2947	teru@nro.nao.ac.jp
Matsuo	Hiroshi	National Astronomical Obersvatory of Japan	2-21-1 Osawa Mitaka Tokyo 181-8588 Japan	+81-422-34-3915	+81-422-34-3864	h.matsuo@nao.ac.jp
Matsuura	Shuji	The Institute of Space & Astronautical Sciences	3-1-1 Yoshinodai Sagamihora Kanagawa 229-8510 Japan	+81 42 459 8211	+81 42 786 7202	matsuura@ir.isai.ac.jp
McGrath	William	JPL	4800 Oak Grove Drive MS 168-314 Pasadena CA 91109	818-354-6465	818-393-4683	william.r.mcgrath@jpl.nasa.gov
Mehdi	Imran	JPL	4800 Oak Grove Drive MS 168-314 Pasadena CA 91109	818-354-6465	818-393-4683	irman.mehdi@jpl.nasa.gov
Meledin	Denis	Harvard-Smithsonian Astrophysical Obersvatory	60 Garden St. Cambridge MA 02138	617-496-7667	617-496-8327	dmeledin@cfa.harvard.edu
Merkel	Harold	Chalmers Univ.	Microelectronics MC2 412 96 Gothenburg Sweden	+46 31 7721848	+46 31 164513	harold@ep.chalmers.sc
Mitrafanov	Oleg	Lucent Technologies				
Mueller	Eric	DeMaria Electro-Optic Systems	1280 Blue Hills Avenue Bloomfield CT	860-243-9557 x325	860-243-9577	e.r.mueller@deoslaser.com
Munier	Jean-Marie	Observatoire de Paris	61 Avenue de l'observatoire 75018 Paris France	+33 14 4512256	+33 14 0512085	jean.marie.munier@obspm.fr
Murk	Axel	Univ. of Bern	Sidlerstrausse 5 Ch-3012 Bern Switerland	+41 31 631 8923	+41 31 631 3765	murk@mw.iap.umibe.ch
Myers	Michael	UC Berkeley	109 LeConte Berkeley CA 94546	510-642-4359	510-643-5204	mmyers@cfpa.berkeley.edu
Narayanan	Gopal	University of Massachusetts at Amherst	Lederle GRC Amherst MA 01003	413-545-0925	413-545-423	gopal@astro.umass.edu
Navarrini	Alessandro	IRAM	300 rue de la piscine 38406 St Martin d'Heres France	+33-476824986		navarrin@irma.fr
Neto	Andrea	JPL	4800 Oak Grove Drive MS 168-314 Pasadena CA 91109	818-354-4424	818-393-4683	neto@merlin.jpl.nasa.gov
Noguchi	Takashi	Nobeyama Radio Observatory	462-2 Nobeyama Minami maki Minami saku Nagano 384-1305 Japan	+81-267-98-4364	+81+267-98-2927	noguchi@nro.nao.ac.jp

Pan	Shing-Kuo	National Radio Astronomy Observatory	2015 Ivy Road Suite 219 Charlottesville VA 22903	814-296-0262	814-296-0324	span2@nrao.edu
Pearson	John	JPL	4800 Oak Grove Drive Pasadena CA 91109	818-354-6822	818-354-8460	jpl@spec.jpl.nasa.gov
Peron	Isabelle	IRAM	300 rue de la piscine 38406 St Martin d'Heres France	+33 67 6824984	+33 67 6515938	peron@iram.fr
Prober	Daniel	Yale University	15 Prospect St. Rm 405 P.O. Box 208284 New Haven CT 06520-8284	203-432-4280	203-432-4283	daniel.prober@yale.edu
Pukala	David	JPL	4800 Oak Grove Drive MS 168-314 Pasadena CA 91109	818-354-4602	818-393-4683	david.m.pakala@jpl.nasa.gov
Raisanen	Anlti	Helsinki University of Technology	P.O. Box 3000 FIN-02015 HUT Finland	+358 9 451 2241	+358 9 451 2152	antti.raisanen@hut.fi
Reintsema	Carl	National Institute of Standards & Technology	325 Broadway MS 814-09 Boulder CO 80305	303-497-5052	303-497-3042	carlr@boulder.nist.gov
Rice	Frank	Caltech	313 Downs Laboratory MC 320-47 Pasadena CA 91125-4700	626-395-4246	626-796-8806	rice@its.caltech.edu
Saily	Jussi	Helsinki Univ. of Tech.	P.O. Box 3000 FIN-02015 HUT finland	+358 9 451 2939	+358 9 451 2152	jsa@radio.hut.fi
Salez	Morvan	Observatoire de Paris				
Samoska	Lorene	JPL	4800 Oak Grove Drive MS 168-314 Pasadena CA 91109	818-354-6465	818-393-4683	lorene@merlin.jpl.nasa.gov
Schlecht	Erich	JPL	4800 Oak Grove Drive MS 168-314 Pasadena CA 91109	818-354-6465	818-393-4683	erichs@jpl.nasa.gov
Schoenthal	Gerhard	Univ. of Virginia	351 McCormick Rd. Rm C-112 Charlottesville, VA 22904-4743	804-982-2262	530-884-5710	gerhard@virginia.edu
Seiffert	Michael	JPL	4800 Oak Grove Drive MS 169-3274 Pasadena CA 91109	818-354-6465	818-393-4683	michael.d.seiffert@jpl.nasa.gov
Sergeev	Andrew	Wayne State University				
Serpa	Gino	Booz-Allen & Hamilton	4001 Fairfax Drive Suite 750 Arlington VA 22203	703-465-5728	703-525-3754	serpa-gimo@bah.com
Shi	Sheng-Cai	Purple Mountain Observatory	2 West Beijing Rd Nanjing JiangSu 210008 China	+86-25-330-3738	+86-25-330-3151	SCSHI@MAIL.PMO.AC.CN

Shitov	Sergey	Institute Radio Engineering & Electronics	Mokhovaya 11 Building 9 Gsp-9 Moscow, Russia 101999	+7(095)2032784	+7(095)2038414	sergey@hitech.cplire.ru
SiddiqI	Irfan	Yale University	15 Prospect St. Rm 405 Becton Center New Haven CT 06520	203-432-4129	203-432-4283	irfan.siddiqi@yale.edu
Siegel	Peter	JPL	4800 Oak Grove Drive MS 168-314 Pasadena CA 91109	818-354-6465	818-393-4683	phs@merlin.jpl.nasa.gov
Skalare	Anders	JPL	4800 Oak Grove Drive MS 168-314 Pasadena CA 91109	818-354-6465	818-393-4683	
Stern	Jeff	JPl	4800 Oak Grove Drive MS 302-231 Pasadena CA 91109	818-354-0029	818-393-4663	jstern@vaxeb.jpl.nasa.gov
Stodolka	Joerg	Univ. of Cologne	Zuelpicherstrasse 77 50937 Cologne Germany	+49(0)221-470-3769	+49(0)221-470-5162	stodolka@ph1.uni-koeln.de
Stringfellow	Guy	NASA HQ	300 ESTSW Code SR Washington DC 20546		202-358-0311	guy.stringfellow@hq.nasa.gov
Sunada	Kazuyoshi	Nobeyama Radio Observatory	Nobeyama 462-2 Minamimaki Minamisaku Nagano 384-1305 Japan	+81 26 7984361	+81 26 7982923	surada@nro.nao.ac.jp
Tong	Edward	Harvard-Smithsonian Astrophysical Obersvatory	60 Garden St. Cambridge MA 02138	617-496-7641	617-495-7345	etong@cfa.harvard.edu
Uzawa	Yoshinori	CRL	588-2 Iwaoka Iwaoka-cho Nishi-ku Kobe 651-2492 Japan	+81 78 9692195	+81 78 9692199	uzawa@crl.go.jp
Vassilev	Vessen	Chalmers University of Technology		+46 31 772 1846		veras@oso.chalmers.se
Verbruggen	Ad	Delft University of Technology				
Verevkin	Aleksandr	University of Rochester	240 East River Rd Rochester NY 14627	716-275-1929	716-273-1014	vererkin@ece.rochester.edu
Walker	Christopher	Steward Observatory	933 N. Cherry Ave Tucson AZ 85721	520-621-8783	520-621-1532	cwalker@as.arizona.edu
Wilner	David					
Wyss	Rolf	JPL	4800 Oak Grove Drive MS 168-314 Pasadena CA 91109	818-354-5958	818-393-4683	randwyss@merlin.jpl.nasa.gov
Xu	Jimmy	Brown Univ.				
Yagoubov	Pavel	SRON	Landleuen 12 P.O. Box 800 9700 Au Groningen Netherlands			
Yassin	Chassan	University of Cambridge	Madingley Road Cambridge CB3 OHE U.K.	+44 0 1223 337309	+44 0 1223 354599	ghassan@mrao.cam.ac.uk

Yngvesson	Sigfrid	University of Massachusetts at Amherst	Dept. of ECE Amherst MA 01003	413-545-0771	413-545-4611	yngvesson@ecs.umass.edu
Zhuang	Yan	University of Massachusetts at Amherst	Department of Electrical & Computer Engineering Amherst 01003	413-545-4607	413-545-4611	yzhuang@ecs.umass.edu
Zmuidzinas	Jonas	Caltech	Pasadena CA 91125			